

Bharat Bhushan *Editor*

# Nanotribology and Nanomechanics II

Nanotribology, Biomimetics,  
and Industrial Applications

*Third Edition*

 Springer

# Nanotribology and Nanomechanics



Bharat Bhushan  
Editor

# Nanotribology and Nanomechanics

Nanotribology, Biomimetics and Industrial  
Applications

Volume 2

 Springer



*Editor*

Bharat Bhushan  
Ohio State University  
Nanoprobe Laboratory for Bio- &  
Nanotechnology &  
Biomimetics (NLB<sup>2</sup>)  
201 West 19th Avenue  
Columbus Ohio 43210-1142  
USA  
bhushan.2@osu.edu

ISBN 978-3-642-15262-7 e-ISBN 978-3-642-15263-4  
DOI 10.1007/978-3-642-15263-4  
Springer Heidelberg Dordrecht London New York

Library of Congress Control Number: 2011928932

© Springer-Verlag Berlin Heidelberg 2011

This work is subject to copyright. All rights are reserved, whether the whole or part of the material is concerned, specifically the rights of translation, reprinting, reuse of illustrations, recitation, broadcasting, reproduction on microfilm or in any other way, and storage in data banks. Duplication of this publication or parts thereof is permitted only under the provisions of the German Copyright Law of September 9, 1965, in its current version, and permission for use must always be obtained from Springer. Violations are liable to prosecution under the German Copyright Law.

The use of general descriptive names, registered names, trademarks, etc. in this publication does not imply, even in the absence of a specific statement, that such names are exempt from the relevant protective laws and regulations and therefore free for general use.

*Cover design:* WMXDesign GmbH, Heidelberg, Germany

Printed on acid-free paper

Springer is part of Springer Science+Business Media ([www.springer.com](http://www.springer.com))

# Foreword

The invention of the scanning tunneling microscope in 1981 has led to an explosion of a family of instruments called scanning probe microscopes (SPMs). One of the most popular instruments in this family is the atomic force microscope (AFM), which was introduced to the scientific community in 1986. The application of SPMs has penetrated numerous science and engineering fields. Proliferation of SPMs in science and technology labs is similar to optical microscopes 50 years ago. SPMs have even made it into some high school science labs. Evolution of nanotechnology has accelerated the use of SPMs and vice versa. The scientific and industrial applications include quality control in the semiconductor industry and related research, molecular biology and chemistry, medical studies, materials science, and the field of information storage systems.



AFMs were developed initially for imaging with atomic or near atomic resolution. After their invention, they were modified for tribological studies. AFMs are now intensively used in this field and have led to the development of the field of nanotribology. Researchers can image single lubricant molecules and their agglomeration and measure surface topography, adhesion, friction, wear, lubricant film thickness, and mechanical properties all on a micrometer to nanometer scale. SPMs are also used for nanofabrication and nanomachining. Beyond as an analytical instrument, SPMs are being developed as industrial tools such as for data storage.

With the advent of more powerful computers, atomic-scale simulations have been conducted of tribological phenomena. Simulations have been able to predict the observed phenomena. Development of the field of nanotribology and nanomechanics has attracted numerous physicists and chemists. I am very excited that SPMs have had such an immense impact on the field of tribology.

I congratulate Professor Bharat Bhushan in helping to develop this field of nanotribology and nanomechanics. Professor Bhushan has harnessed his own knowledge and experience, gained in several industries and universities, and has assembled a large number of internationally recognized authors. The authors come from both academia and industry.

Professor Bharat Bhushan's comprehensive book is intended to serve both as a textbook for university courses as well as a reference for researchers. It is a timely addition to the literature on nanotribology and nanomechanics, which I anticipate will stimulate further interest in this important new field. I expect that it will be well received by the international scientific community.

IBM Research Division  
Rueschlikon, Switzerland  
Nobel Laureate Physics, 1986

Prof. Dr. Gerd Binnig

# Preface

Dr. Bharat Bhushan received an M.S. in mechanical engineering from the Massachusetts Institute of Technology in 1971, an M.S. in mechanics and a Ph.D. in mechanical engineering from the University of Colorado at Boulder in 1973 and 1976, respectively, an MBA from Rensselaer Polytechnic Institute at Troy, NY in 1980, Doctor Technicae from the University of Trondheim at Trondheim, Norway in 1990, a Doctor of Technical Sciences from the Warsaw University of Technology at Warsaw, Poland in 1996, and Doctor Honouris Causa from the National Academy of Sciences at Gomel, Belarus in 2000. He is a registered professional engineer. He is presently an Ohio Eminent Scholar and The Howard D. Winbigler Professor in the College of Engineering, and the Director of the Nanoprobe Laboratory for Bio- & Nanotechnology and Biomimetics (NLB2) at the Ohio State University, Columbus, Ohio. His research interests include fundamental studies with a focus on scanning probe techniques in the interdisciplinary areas of bio/nanotribology, bio/nanomechanics and bio/nanomaterials characterization, and applications to bio/nanotechnology and biomimetics. He is an internationally recognized expert of bio/nanotribology and bio/nanomechanics using scanning probe microscopy, and is one of the most prolific authors. He is considered by some a pioneer of the tribology and mechanics of magnetic storage devices. He has authored 6 scientific books, more than 90 handbook chapters, more than 700 scientific papers (h-index – 45+; ISI Highly Cited in Materials Science, since 2007), and more than 60 technical reports, edited more than 45 books, and holds 17 U.S. and foreign patents. He is co-editor of Springer NanoScience and Technology Series and co-editor of Microsystem Technologies. He has given more than 400 invited presentations on six continents and more than 140 keynote/plenary addresses at major international conferences.

Dr. Bhushan is an accomplished organizer. He organized the first symposium on Tribology and Mechanics of Magnetic Storage Systems in 1984 and the first international symposium on Advances in Information Storage Systems in 1990, both of which are now held annually. He is the founder of an ASME Information Storage and Processing Systems Division founded in 1993 and served as the founding chair during 1993–1998. His biography has been listed in over two dozen Who's Who books including Who's Who in the World and has received more than two dozen awards for his contributions to science and technology from

professional societies, industry, and U.S. government agencies. He is also the recipient of various international fellowships including the Alexander von Humboldt Research Prize for Senior Scientists, Max Planck Foundation Research Award for Outstanding Foreign Scientists, and the Fulbright Senior Scholar Award. He is a foreign member of the International Academy of Engineering (Russia), Byelorussian Academy of Engineering and Technology and the Academy of Triboengineering of Ukraine, an honorary member of the Society of Tribologists of Belarus, a fellow of ASME, IEEE, STLE, and the New York Academy of Sciences, and a member of ASEE, Sigma Xi and Tau Beta Pi.

Dr. Bhushan has previously worked for the R & D Division of Mechanical Technology Inc., Latham, NY; the Technology Services Division of SKF Industries Inc., King of Prussia, PA; the General Products Division Laboratory of IBM Corporation, Tucson, AZ; and the Almaden Research Center of IBM Corporation, San Jose, CA. He has held visiting professor appointments at University of California at Berkeley, University of Cambridge, UK, Technical University Vienna, Austria, University of Paris, Orsay, ETH Zurich and EPFL Lausanne.

# Contents

## **Vol. 1 Measurement Techniques and Nanomechanics**

- 1 Introduction – Measurement Techniques and Applications** ..... 1  
Bharat Bhushan

## **Part I Scanning Probe Microscopy**

- 2 Scanning Probe Microscopy – Principle of Operation, Instrumentation, and Probes** ..... 37  
Bharat Bhushan and Othmar Marti
- 3 General and Special Probes in Scanning Microscopies** ..... 111  
Jason Hafner, Edin (I-Chen) Chen, Ratnesh Lal, and Sungho Jin
- 4 Calibration of Normal and Lateral Forces in Cantilevers Used in Atomic Force Microscopy** ..... 135  
Manuel L.B. Palacio and Bharat Bhushan
- 5 Noncontact Atomic Force Microscopy and Related Topics** ..... 195  
Franz J. Giessibl, Yasuhiro Sugawara, Seizo Morita, Hirotaka Hosoi, Kazuhisa Sueoka, Koichi Mukasa, Akira Sasahara, and Hiroshi Onishi
- 6 Low-Temperature Scanning Probe Microscopy** ..... 239  
Markus Morgenstern, Alexander Schwarz, and Udo D. Schwarz
- 7 Dynamic Modes of Atomic Force Microscopy** ..... 307  
André Schirmeisen, Boris Anczykowski, Hendrik Hölscher, and Harald Fuchs

<b>8 Molecular Recognition Force Microscopy: From Molecular Bonds to Complex Energy Landscapes .....</b>	<b>355</b>
Peter Hinterdorfer, Andreas Ebner, Hermann Gruber, Ruti Kapon, and Ziv Reich	

## **Part II Nanomechanics**

<b>9 Nanomechanical Properties of Solid Surfaces and Thin Films .....</b>	<b>391</b>
Adrian B. Mann	
<b>10 Computer Simulations of Nanometer-Scale Indentation and Friction .....</b>	<b>439</b>
Susan B. Sinnott, Seong-Jun Heo, Donald W. Brenner, Judith A. Harrison, and Douglas L. Irving	
<b>11 Mechanical Properties of Nanostructures .....</b>	<b>527</b>
Bharat Bhushan	
<b>Editor's Vita .....</b>	<b>585</b>
<b>Index .....</b>	<b>587</b>

## **Vol. 2 Nanotribology, Biomimetics and Industrial Applications**

### **Part III Nanotribology: Fundamental Studies**

<b>12 Nanotribology, Nanomechanics, and Materials Characterization ....</b>	<b>3</b>
Bharat Bhushan	
<b>13 Surface Forces and Nanorheology of Molecularly Thin Films .....</b>	<b>107</b>
Marina Ruths and Jacob N. Israelachvili	
<b>14 Interfacial Forces and Spectroscopic Study of Confined Fluids ....</b>	<b>203</b>
Y. Elaine Zhu, Ashis Mukhopadhyay, and Steve Granick	
<b>15 Friction and Wear on the Atomic Scale .....</b>	<b>243</b>
Enrico Gnecco, Roland Bennewitz, Oliver Pfeiffer, Anisoara Socoliuc, and Ernst Meyer	
<b>16 Scale Effect in Mechanical Properties and Tribology .....</b>	<b>293</b>
Bharat Bhushan and Michael Nosonovsky	

**Part IV Molecularly-Thick Films for Lubrication**

<b>17 Nanotribology of Ultrathin and Hard Amorphous Carbon Films ...</b>	<b>347</b>
Bharat Bhushan	
<b>18 Self-Assembled Monolayers for Nanotribology and Surface Protection .....</b>	<b>403</b>
Bharat Bhushan	
<b>19 Nanoscale Boundary Lubrication Studies .....</b>	<b>461</b>
Bharat Bhushan	

**Part V Biomimetics**

<b>20 Biomimetics Inspired Surfaces for Superhydrophobicity, Self-cleaning, Low Adhesion, and Drag Reduction .....</b>	<b>533</b>
Bharat Bhushan and Yong Chae Jung	
<b>21 Gecko Feet: Natural Hairy Attachment Systems for Smart Adhesion .....</b>	<b>701</b>
Bharat Bhushan	

**Part VI Industrial Applications**

<b>22 Micro/Nanotribology and Micro/Nanomechanics of Magnetic Storage Devices .....</b>	<b>771</b>
Bharat Bhushan	
<b>23 MEMS/NEMS and BioMEMS/BioNEMS: Materials, Devices, and Biomimetics .....</b>	<b>833</b>
Bharat Bhushan	
<b>24 Mechanical Properties of Micromachined Structures .....</b>	<b>947</b>
Harold Kahn	
<b>Editor's Vita .....</b>	<b>979</b>
<b>Index .....</b>	<b>981</b>





# Contributors

**Boris Anczykowski** NanoAnalytics GmbH, Gievenbecker Weg 11, 48149 Münster, Germany, [anczykowski@nanoanalytics.com](mailto:anczykowski@nanoanalytics.com)

**Roland Bennewitz** Leibniz Institute for New Materials, Campus D2 2, 66123 Saarbrücken, Germany, [roland.bennewitz@inm-gmbh.de](mailto:roland.bennewitz@inm-gmbh.de)

**Bharat Bhushan** Nanoprobe Laboratory for Bio- & Nanotechnology and Biomimetics, W390 Scott Laboratory, The Ohio State University, 201 W. 19th Avenue, Columbus, OH 43210-1142, USA, [bhushan.2@osu.edu](mailto:bhushan.2@osu.edu)

**Donald W. Brenner** Department of Materials Science and Engineering, North Carolina State University, Raleigh, NC 27695-7909, USA, [brenner@ncsu.edu](mailto:brenner@ncsu.edu)

**Edin I-Chen Chen** Institute of Materials Science and Engineering, National Central University, 300 Jung-Da Rd, Chung-Li, Taoyuan 320, Taiwan, [ichen@ncu.edu.tw](mailto:ichen@ncu.edu.tw)

**Andreas Ebner** Institute for Biophysics, Altenbergerstr. 69, 4040 Linz, Austria, [andreas.ebner@jku.at](mailto:andreas.ebner@jku.at)

**Harald Fuchs** Physikalisches Institut, Wilhelm-Klemm-Str.10, 48149 Münster, Germany, [fuchsh@uni-muenster.de](mailto:fuchsh@uni-muenster.de)

**Franz J. Giessibl** Institute of Experimental and Applied Physics, University of Regensburg, Physics Building, Room PHY 1.1.22, Universitätsstrasse 31, 93053 Regensburg, Germany, [franz.giessibl@physik.uni-regensburg.de](mailto:franz.giessibl@physik.uni-regensburg.de)

**Enrico Gnecco** Institute of Physics, University of Basel, Klingelbergstr. 82, 4056 Basel, Switzerland, [Enrico.Gnecco@unibas.ch](mailto:Enrico.Gnecco@unibas.ch)

**Steve Granick** Department of Materials Science and Engineering, University of Illinois at Urbana-Champaign, 104 S. Goodwin Ave, Urbana, IL 61801, USA, [sgranick@uiuc.edu](mailto:sgranick@uiuc.edu)

**Hermann Gruber** Institute of Biophysics, University of Linz, Altenberger Str. 69, 4040 Linz, Austria, hermann.gruber@jku.at

**Jason H. Hafner** Physics and Astronomy – MS61, Rice University, PO Box 1892, Houston, TX 77251–1892, USA, hafner@rice.edu

**Judith A. Harrison** Chemistry Department, MS 9B, U.S. Naval Academy, 572 Holloway Road, Annapolis, MD 21402, USA, jah@usna.edu

**Seong-Jun Heo** Department of Materials Science and Engineering, University of Florida, 100 Rhines Hall, P.O. Box 116400, Gainesville, FL 32611-6400, USA, heoagyver@ufl.edu

**Peter Hinterdorfer** Institute for Biophysics, University of Linz, Altenbergerstr. 69, 4040 Linz, Austria, peter.hinterdorfer@jku.at

**Hendrick Hoelscher** Institute for Microstructure Technology, Forschungszentrum Karlsruhe, PO Box 36 40, 76021 Karlsruhe, Germany, Hendrik.Hoelscher@imt.fzk.de

**Hiroataka Hosoi** Creative Research Initiative Sousei, Hokkaido University, Kita 21, Nishi 10, Kita-ku, Sapporo, Japan, hosoi@cris.hokudai.ac.jp

**D. L. Irving** Department of Materials Science and Engineering, North Carolina State University, Raleigh, NC 27695-7909, USA, dlirving@ncsu.edu

**Jacob N. Israelachvili** Department of Chemical Engineering and Materials Department, University of California, Santa Barbara, CA 93106, USA, Jacob@engineering.ucsb.edu

**Sungho Jin** Department of Mechanical and Aerospace Engineering, University of California, 9500 Gilman Drive, La Jolla, San Diego, CA 92093, USA, jin@ucsd.edu

**Yong Chae Jung** Samsung Electronics C., Ltd, San #16 Banwol-Dong, Hwasung-City, Gyeonggi-Do 445–701, Korea, yc423.jung@samsung.com

**Harold Kahn** Department of Materials Science and Engineering, Case Western Reserve University, 10900 Euclid Ave, Cleveland, OH 44106–7204, USA, hxx29@po.cwru.edu

**Ruti Kapon** Department of Biological Chemistry, Weizmann Institute of Science, Rehovot 76100, Israel, ruti.kapon@weizmann.ac.il

**Ratnesh Lal** University of California, San Diego PFBH Room 219 9500 Gilman Drive, MC 0412, La Jolla, San Diego, CA 92093–0412, USA, rlal@ucsd.edu

**Carmen LaTorre** Owens Corning, Insulating Systems Business, 2790 Columbus Road, Route 16 (Bldg 20–1), Granville, OH 43023, USA, carmen.latorre@owenscorning.com

**Adrian B. Mann** Department of Ceramic and Materials Engineering and Biomedical Engineering, Rutgers University, 607 Taylor Road, Piscataway, NJ 08854, USA, abmann@rci.rutgers.edu

**Othmar Marti** Abteilung Experimentelle Physik, Universitaet Ulm, Albert-Einstein-Allee 11, 89069 Ulm, Germany, othmar.marti@uni-ulm.de

**Ernst Meyer** Institute of Physics, University of Basel, Klingelbergstr. 82, 4056 Basel, Switzerland, Ernst.Meyer@unibas.ch

**Markus Morgenstern II.** Institute of Physics B, RWTH Aachen University, D-52056 Aachen, Germany, mmorgens@physik.rwth-aachen.de

**Seizo Morita** Department of Electronic Engineering, Graduate School of Engineering, Osaka University, Yamada-Oka 2–1, Suita 565–0871, Japan, smorita@ele.eng.osaka-u.ac.jp

**Koichi Mukasa** Nanoelectronics Laboratory, Graduate School of Engineering, Hokkaido University, Nishi-8, Kita-13, Kita-ku, Sapporo 060–8628, Japan, mukasa@nano.eng.hokudai.ac.jp

**Ashis Mukhopadhyay** Department of Physics, Wayne State University, Detroit, MI, USA, ashis@physics.wayne.edu

**Michael Nosonovsky** Department of Mechanical Engineering, University of Wisconsin, EMS Building, Room E371G, Milwaukee, WI 53201–0413, USA, nosonovs@uwm.edu

**Hiroshi Onishi** Department of Chemistry, Kobe University, Rokko-dai, Nada-ku, Kobe 657–8501, Japan, oni@kobe-u.ac.jp

**Manuel Palacio** Nanoprobe Laboratory for Bio- & Nanotechnology and Biomimetics, The Ohio State University, 201 W. 19th Avenue, Columbus, OH 43210–1142, USA, palacio.1@osu.edu

**Oliver Pfeiffer** Institute of Physics, University of Basel, Klingelbergstr. 82, 4056 Basel, Switzerland, Oliver.Pfeiffer@unibas.ch

**Ziv Reich** Department of Biological Chemistry, Weizmann Institute of Science, Rehovot 76100, Israel, ziv.reich@weizmann.ac.il

**Marina Ruths** Department of Chemistry, University of Massachusetts Lowell, 1 University Avenue, Lowell, MA 01854, USA, [marina\\_ruths@uml.edu](mailto:marina_ruths@uml.edu)

**Akira Sasahara** School of Materials Science, Japan Advanced Institute of Science and Technology, 1-1 Asahidai, Nomi 923-1292, Japan, [sasahara@jaist.ac.jp](mailto:sasahara@jaist.ac.jp)

**Andre Schirmeisen** Physikalisches Institut, University of Muenster, Wilhelm-Klemm-Str.10, 48149 Muenster, Germany, [schira@uni-muenster.de](mailto:schira@uni-muenster.de)

**Alexander Schwarz** Institute of Applied Physics, University of Hamburg, Jungiusstr. 11, 20355 Hamburg, Germany, [aschwarz@physnet.uni-hamburg.de](mailto:aschwarz@physnet.uni-hamburg.de)

**Udo D. Schwarz** Department of Mechanical Engineering, Yale University, P.O. Box 208284, 15 Prospect Street, Rm. 213, New Haven, CT 06520-8284, USA, [udo.schwarz@yale.edu](mailto:udo.schwarz@yale.edu)

**Susan B. Sinnott** Dept. of Materials Science and Engineering, University of Florida, 154 Rhines Hall, P.O. Box 116400, Gainesville, FL 32611-6400, USA, [sinnott@mse.ufl.edu](mailto:sinnott@mse.ufl.edu)

**Anisoara Socoliuc** SPECS Zurich GmbH, Technoparkstrasse 1, 8005 Zurich, Switzerland, [socoliuc@nanonis.com](mailto:socoliuc@nanonis.com)

**Yasuhiro Sugawara** Department of Applied Physics, Graduate School of Engineering, Osaka University, Yamada-Oka 2-1, Suita 565-0871, Japan, [sugawara@ap.eng.osaka-u.ac.jp](mailto:sugawara@ap.eng.osaka-u.ac.jp)

**Y. Elaine Zhu** Department of Chemical and Biomolecular Engineering, University of Notre Dame, 182 Fitzpatrick Hall, Notre Dame, IN 46556, USA, [yzhu3@nd.edu](mailto:yzhu3@nd.edu)

**Part III**  
**Nanotribology: Fundamental Studies**

# Chapter 12

## Nanotribology, Nanomechanics, and Materials Characterization

**Bharat Bhushan**

**Abstract** Nanotribology and nanomechanics studies are needed to develop a fundamental understanding of interfacial phenomena on a small scale and to study interfacial phenomena in micro-/nanoelectromechanical systems (MEMS/NEMS), magnetic storage devices, and other applications. Friction and wear of lightly loaded micro-/nanocomponents are highly dependent on surface interactions (few atomic layers). These structures are generally coated with molecularly thin films. Nanotribology and nanomechanics studies are also valuable in the fundamental understanding of interfacial phenomena in macrostructures and provide a bridge between science and engineering. An atomic force microscope (AFM) tip is used to simulate a single-asperity contact with a solid or lubricated surface. AFMs are used to study the various tribological phenomena, which include surface roughness, adhesion, friction, scratching, wear, detection of material transfer, and boundary lubrication. In situ surface characterization of local deformation of materials and thin coatings can be carried out using a tensile stage inside an AFM. Mechanical properties such as hardness, Young's modulus of elasticity, and creep/relaxation behavior can be determined on micro- to picoscales using a depth-sensing indentation system in an AFM. Localized surface elasticity and viscoelastic mapping of near-surface regions can be obtained with nanoscale lateral resolution. Finally, an AFM can be used for nanofabrication/nanomachining.

The mechanisms and dynamics of the interactions of two contacting solids during relative motion, ranging from the atomic to microscale, need to be understood in order to develop a fundamental understanding of adhesion, friction, wear, indentation, and lubrication processes. For most solid–solid interfaces of technological relevance, contact occurs at multiple asperities. Consequently the importance of investigating single-asperity contacts in studies of the fundamental micro/nanomechanical and micro/nanotribological properties of surfaces and interfaces has long been recognized. The recent emergence and proliferation of proximal probes, in particular scanning probe microscopies (the scanning tunneling microscope and the atomic force microscope), surface force apparatus, and computational techniques for simulating tip–surface interactions and interfacial properties have allowed systematic investigations of interfacial problems with high resolution as well as

ways and means for modifying and manipulating nanoscale structures. These advances have led to the appearance of the new field of nanotribology, which pertains to experimental and theoretical investigations of interfacial processes on scales ranging from the atomic and molecular to the microscale, occurring during adhesion, friction, scratching, wear, indentation, and thin-film lubrication at sliding surfaces [1–14]. Proximal probes have also been used for mechanical and electrical characterization, in situ characterization of local deformation, and other nanomechanics studies.

Nanotribological and nanomechanics studies are needed to develop a fundamental understanding of interfacial phenomena on a small scale and to study interfacial phenomena in nanostructures used in magnetic storage devices, nanotechnology, and other applications [4–20]. Friction and wear of lightly loaded micro/nanocomponents are highly dependent on the surface interactions (few atomic layers). These structures are generally coated with molecularly thin films. Nanotribological and nanomechanics studies are also valuable in the fundamental understanding of interfacial phenomena in macrostructures, and provide a bridge between science and engineering.

The surface force apparatus (SFA), the scanning tunneling microscopes (STM), and atomic force and friction force microscopes (AFM and FFM) are widely used in nanotribological and nanomechanics studies. Typical operating parameters are compared in Table 12.1. The SFA was developed in 1968 and is commonly employed to study both static and dynamic properties of molecularly thin films sandwiched between two molecularly smooth surfaces. The STM, developed in 1981, allows imaging of electrically conducting surfaces with atomic resolution, and has been used for imaging of clean surfaces as well as of lubricant molecules. The introduction of the AFM in 1985 provided a method for measuring ultrasmall forces between a probe tip and an engineering (electrically conducting or insulating) surface, and has been used for morphological and surface roughness measurements of surfaces on the nanoscale, as well as for adhesion measurements. Subsequent modifications of the AFM led to the development of the FFM, designed

**Table 12.1** Comparison of typical operating parameters in SFA, STM, and AFM/FFM used for micro/nanotribological studies

Operating parameter	SFA	STM <sup>a</sup>	AFM/FFM
Radius of mating surface/tip	≈ 10 mm <sup>b</sup>	5–100 nm	5–100 nm
Radius of contact area	10–40 μm	N/A	0.05–0.5 nm
Normal load	10–100 mN	N/A	< 0.1–500 nN
Sliding velocity	0.001–100 μm/s	0.02–200 μm/s (scan size ≈ 1 nm × 1 nm to 125 μm × 125 μm; scan rate < 1–122 Hz)	0.02–200 μm/s (scan size ≈ 1 nm × 1 nm to 125 μm × 125 μm; scan rate < 1–122 Hz)
Sample limitations	Typically atomically smooth, optically transparent mica; opaque ceramic, smooth surfaces can also be used	Electrically conducting samples	None of the above

<sup>a</sup>Can be used for atomic-scale imaging

<sup>b</sup>Since stresses scale inverse of tip radius, SFA can provide low stress measurement capabilities



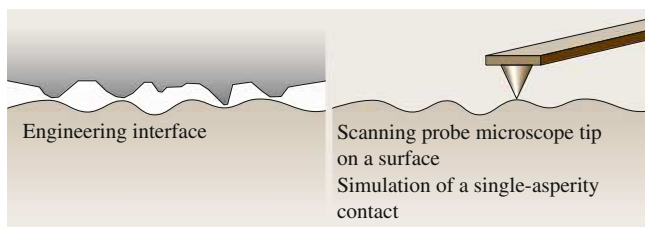


**Fig. 12.1** Schematics of an engineering interface and scanning probe microscope tip in contact with an engineering interface

for atomic- and microscale studies of friction. This instrument measures forces in the scanning direction. The AFM is also being used for various investigations including scratching, wear, indentation, detection of transfer of material, boundary lubrication, and fabrication and machining [14, 21–33]. Meanwhile, significant progress in understanding the fundamental nature of bonding and interactions in materials, combined with advances in computer-based modeling and simulation methods, has allowed theoretical studies of complex interfacial phenomena with high resolution in space and time. Such simulations provide insights into atomic-scale energetics, structure, dynamics, thermodynamics, transport, and rheological aspects of tribological processes.

The nature of interactions between two surfaces brought close together, and those between two surfaces in contact as they are separated, have been studied experimentally with the surface force apparatus. This has led to a basic understanding of the normal forces between surfaces and the way in which these are modified by the presence of a thin liquid or a polymer film. The frictional properties of such systems have been studied by moving the surfaces laterally, and such experiments have provided insights into the molecular-scale operation of lubricants such as thin liquid or polymer films. Complementary to these studies are those in which the AFM tip is used to simulate a single-asperity contact with a solid or lubricated surface (Fig. 12.1). These experiments have demonstrated that the relationship between friction and surface roughness is not always simple or obvious. AFM studies have also revealed much about the nanoscale nature of intimate contact during wear, indentation, and lubrication.

In this chapter, we present a review of significant aspects of nanotribological, nanomechanical, and materials characterization studies conducted using AFM/FFM.

## 12.1 Description of AFM/FFM and Various Measurement Techniques

The AFM was developed by *Binnig* and his colleagues in 1985. It is capable of investigating surfaces of scientific and engineering interest on an atomic scale [34, 35]. The AFM relies on a scanning technique to produce very high-resolution,

three-dimensional images of sample surfaces. It measures ultrasmall forces ( $<1$  nN) present between the AFM tip surface mounted on a flexible cantilever beam and a sample surface. These small forces are obtained by measuring the motion of a very flexible cantilever beam having an ultrasmall mass, by a variety of measurement techniques including optical deflection, optical interference, capacitance, and tunneling current. The deflection can be measured to within 0.02 nm, so for a typical cantilever spring constant of 10 N/m, a force as low as 0.2 nN can be detected. To put these numbers in perspective, individual atoms and human hair are typically a fraction of 1 nm and  $\approx 75$   $\mu\text{m}$  in diameter, respectively, and a drop of water and an eyelash have a mass of about  $\approx 10$  and 100 nN, respectively. In the operation of high-resolution AFM, the sample is generally scanned rather than the tip because any cantilever movement would add vibrations. AFMs are available for measurement of large samples, where the tip is scanned and the sample is stationary. To obtain atomic resolution with the AFM, the spring constant of the cantilever should be weaker than the equivalent spring between atoms. A cantilever beam with a spring constant of  $\approx 1$  N/m or lower is desirable. For high lateral resolution, tips should be as sharp as possible. Tips with a radius ranging from 5 to 50 nm are commonly available. Interfacial forces, adhesion, and surface roughness, including atomic-scale imaging, are routinely measured using the AFM.

A modification to the AFM providing a sensor to measure the lateral force led to the development of the friction force microscope (FFM) or the lateral force microscope (LFM), designed for atomic-scale and microscale studies of friction [4–6, 8, 9, 14, 36–50] and lubrication [20, 51–55]. This instrument measures lateral or friction forces (in the plane of sample surface and in the scanning direction). By using a standard or a sharp diamond tip mounted on a stiff cantilever beam, AFM is used in investigations of scratching and wear [7, 10, 14, 41, 56–59], indentation [10, 14, 17, 41, 60–63], and fabrication/machining [5, 14, 41]. An oscillating cantilever is used for localized surface elasticity and viscoelastic mapping, referred to as dynamic AFM [48, 64–72]. In situ surface characterization of local deformation of materials and thin coatings has been carried out by imaging the sample surfaces using an AFM during tensile deformation using a tensile stage [73–75].

### ***12.1.1 Surface Roughness and Friction Force Measurements***

Surface height imaging down to atomic resolution of electrically conducting surfaces is carried out using an STM. An AFM is also used for surface height imaging and roughness characterization down to the nanoscale. Commercial AFM/FFMs are routinely used for simultaneous measurements of surface roughness and friction force [5, 13]. These instruments are available for measurement of both small and large samples. In a small-sample AFM (Fig. 12.2a), the sample, generally no larger than 10 mm  $\times$  10 mm, is mounted on a piezoelectric crystal in the form of a cylindrical tube (referred to as a PZT tube scanner) which consists of separate

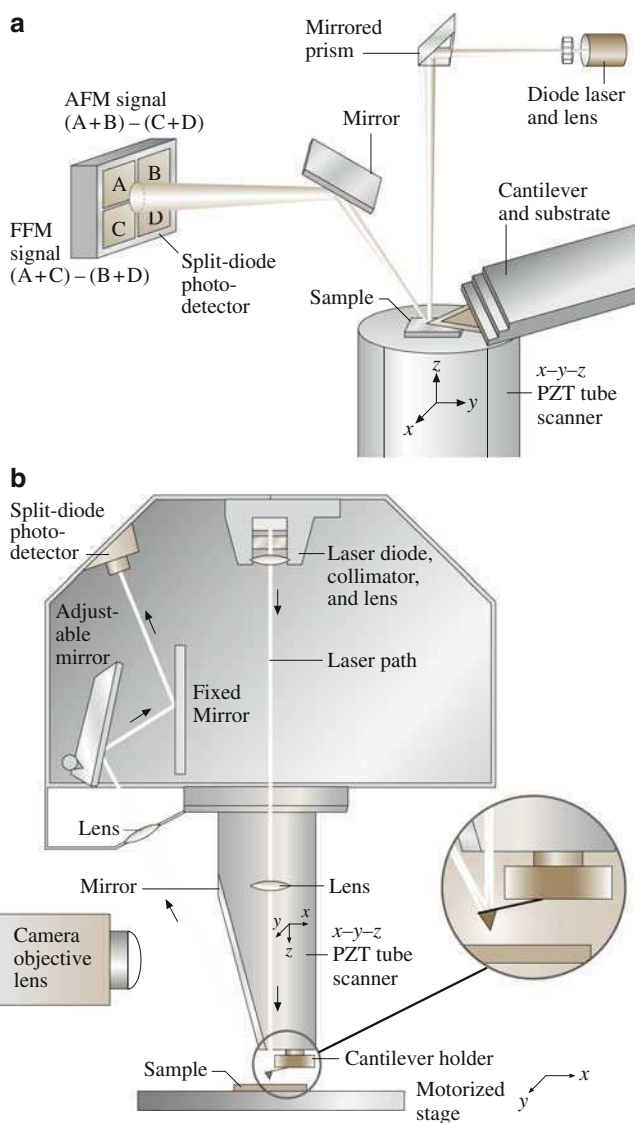


**Fig. 12.2** Schematics (a) of a commercial small-sample atomic force microscope/friction force microscope (AFM/FFM), and (b) of a large-sample AFM/FFM

electrodes to scan the sample precisely in the  $x$ - $y$  plane in a raster pattern and to move the sample in the vertical ( $z$ ) direction. A sharp tip at the free end of a flexible cantilever is brought into contact with the sample. Normal and frictional forces being applied at the tip-sample interface are measured using a laser beam deflection technique. A laser beam from a diode laser is directed by a prism onto the back of a cantilever near its free end, tilted downward at  $\approx 10^\circ$  with respect to the horizontal

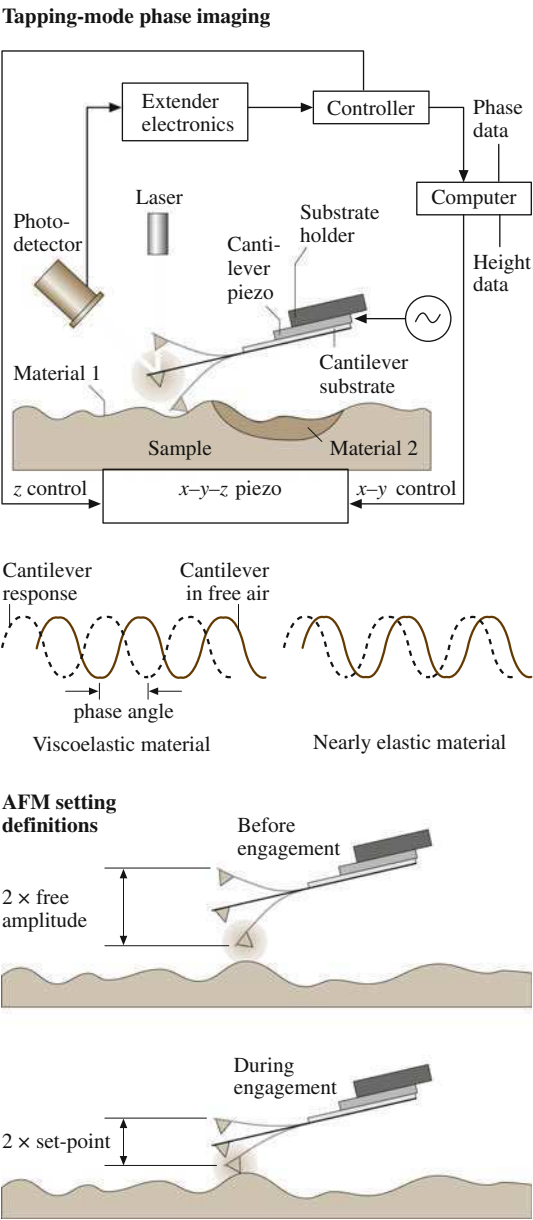
plane. The beam reflected from the vertex of the cantilever is directed through a mirror onto a quad photodetector (a split photodetector with four quadrants). The differential signal from the top and bottom photodiodes provides the AFM signal, which is a sensitive measure of the cantilever vertical deflection. Topographic features of the sample cause the tip to deflect in the vertical direction as the sample is scanned under the tip. This tip deflection will change the direction of the reflected laser beam, changing the intensity difference between the top and bottom sets of photodetectors (AFM signal). In the AFM operating mode called the height mode, for topographic imaging or for any other operation in which the applied normal force is to be kept constant, a feedback circuit is used to modulate the voltage applied to the PZT scanner to adjust the height of the PZT, so that the cantilever vertical deflection (given by the intensity difference between the top and bottom detector) will remain constant during scanning. The PZT height variation is thus a direct measure of the surface roughness of the sample.

In a large-sample AFM, both force sensors using optical deflection method and scanning unit are mounted on the microscope head (Fig. 12.2b). Because of vibrations added by cantilever movement, lateral resolution of this design can be somewhat poorer than the design in Fig. 12.2 in which the sample is scanned instead of cantilever beam. The advantage of the large-sample AFM is that large samples can be measured readily.

Most AFMs can be used for surface roughness measurements in the so-called tapping mode (intermittent contact mode), also referred to as dynamic (atomic) force microscopy. In the tapping mode, during scanning over the surface, the cantilever–tip assembly with a normal stiffness of 20–100 N/m (Digital Instrument (DI) tapping mode etched Si probe or TESP) is sinusoidally vibrated at its resonant frequency (350–400 kHz) by a piezo mounted above it, and the oscillating tip slightly taps the surface. The piezo is adjusted using feedback control in the  $z$ -direction to maintain a constant (20–100 nm) oscillating amplitude (setpoint) and constant average normal force (Fig. 12.3 [5, 13]). The feedback signal to the  $z$ -direction sample piezo (to keep the setpoint constant) is a measure of surface roughness. The cantilever–tip assembly is vibrated at some amplitude, here referred to as the free amplitude, before the tip engages the sample. The tip engages the sample at some setpoint, which may be thought of as the amplitude of the cantilever as influenced by contact with the sample. The setpoint is defined as a ratio of the vibration amplitude after engagement to the vibration amplitude in free air before engagement. A lower setpoint gives a reduced amplitude and closer mean tip–sample distance. The amplitude should be kept large enough that the tip does not get stuck to the sample because of adhesive attractions. Also the oscillating amplitude applies less average (normal) load as compared with the contact mode and reduces sample damage. The tapping mode is used in topography measurements to minimize effects of friction and other lateral forces and to measure the topography of soft surfaces.

For measurement of friction force at the tip surface during sliding, left-hand and right-hand sets of quadrants of the photodetector are used. In the so-called friction mode, the sample is scanned back and forth in a direction orthogonal to the long

**Fig. 12.3** Schematic of tapping mode used to obtain height and phase data and definitions of free amplitude and setpoint. During scanning, the cantilever is vibrated at its resonant frequency and the sample  $x$ - $y$ - $z$  piezo is adjusted by feedback control in the  $z$ -direction to maintain a constant setpoint. The computer records height (which is a measure of surface roughness) and phase angle (which is a function of the viscoelastic properties of the sample) data



axis of the cantilever beam. A friction force between the sample and the tip will produce a twisting of the cantilever. As a result, the laser beam will be reflected out of the plane defined by the incident beam and the beam reflected vertically from an untwisted cantilever. This produces an intensity difference of the laser beam

received in the left-hand and right-hand sets of quadrants of the photodetector. The intensity difference between the two sets of detectors (the FFM signal) is directly related to the degree of twisting and hence to the magnitude of the friction force. One problem associated with this method is that any misalignment between the laser beam and the photodetector axis would introduce error in the measurement. However, by following the procedures developed by Ruan and Bhushan [38], in which the average FFM signal for the sample scanned in two opposite directions is subtracted from the friction profiles of each of the two scans, the misalignment effect is eliminated. This method provides three-dimensional maps of friction force. By following the friction force calibration procedures developed by Ruan and Bhushan [38], voltages corresponding to friction forces can be converted to force units [76]. The coefficient of friction is obtained from the slope of friction force data measured as a function of normal loads typically ranging from 10 to 150 nN. This approach eliminates any contributions due to the adhesive forces [41]. For calculation of the coefficient of friction based on a single point measurement, friction force should be divided by the sum of applied normal load and intrinsic adhesive force. Furthermore it should be pointed out that, for a single-asperity contact, the coefficient of friction is not independent of load (see the discussion later).

Surface roughness measurements in the contact mode are typically made using a sharp, microfabricated square-pyramidal  $\text{Si}_3\text{N}_4$  tip with a radius of 30–50 nm on a triangular cantilever beam (Fig. 12.4a) with normal stiffness on the order of 0.06–0.58 N/m with a normal natural frequency of 13–40 kHz (DI silicon nitride probe or NP) at a normal load of  $\approx 10$  nN, and friction measurements are carried out in the load range of 1–100 nN. Surface roughness measurements in the tapping mode utilize a stiff cantilever with high resonant frequency; typically a square-pyramidal etched single-crystal silicon tip, with a tip radius of 5–10 nm, integrated with a stiff rectangular silicon cantilever beam (Fig. 12.4a) with a normal stiffness on the order of 17–60 N/m and a normal resonant frequency of 250–400 kHz (DI TESP), is used. Multiwalled carbon nanotube tips having a small diameter (a few nm) and a length of  $\approx 1$   $\mu\text{m}$  (high aspect ratio) attached to the single-crystal silicon square-pyramidal tips are used for high-resolution imaging of surfaces and of deep trenches in tapping mode (noncontact mode) (Fig. 12.4b) [77]. The multiwalled nanotube (MWNT) tips are hydrophobic. To study the effect of the radius of a single asperity (tip) on adhesion and friction, microspheres of silica with radii ranging from about 4 to 15  $\mu\text{m}$  are attached at the end of cantilever beams. Optical micrographs of two of the microspheres at the ends of triangular cantilever beams are shown in Fig. 12.4c.

The tip is scanned in such a way that its trajectory on the sample forms a triangular pattern (Fig. 12.5). Scanning speeds in the fast and slow scan directions depend on the scan area and scan frequency. Scan sizes ranging from  $< 1 \text{ nm} \times 1 \text{ nm}$  to  $125 \mu\text{m} \times 125 \mu\text{m}$  and scan rates from  $< 0.5$  to 122 Hz can typically be used. Higher scan rates are used for smaller scan lengths. For example, scan rates in the fast and slow scan directions for an area of  $10 \mu\text{m} \times 10 \mu\text{m}$  scanned at 0.5 Hz are 10 and 20 nm/s, respectively.

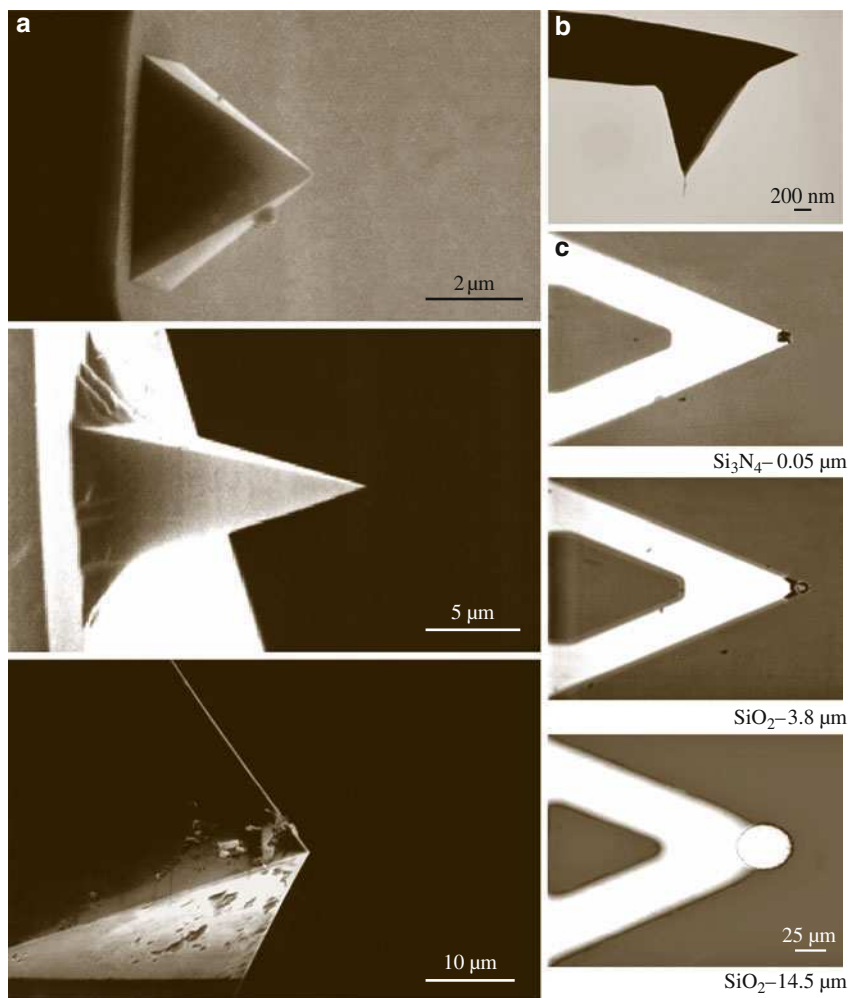


**Fig. 12.4** (a) SEM micrographs of a square-pyramidal plasma-enhanced chemical vapor deposition (PECVD)  $\text{Si}_3\text{N}_4$  tip with a triangular cantilever beam, a square-pyramidal etched single-crystal silicon tip with a rectangular silicon cantilever beam, and a three-sided pyramidal natural diamond tip with a square stainless-steel cantilever beam. (b) SEM micrograph of a multiwalled carbon nanotube (MWNT) physically attached on a single-crystal silicon square-pyramidal tip, and (c) optical micrographs of a commercial  $\text{Si}_3\text{N}_4$  tip and two modified tips showing  $\text{SiO}_2$  spheres mounted over the sharp tip, at the end of the triangular  $\text{Si}_3\text{N}_4$  cantilever beams (radii of the tips are given in the figure)

### 12.1.2 Adhesion Measurements

Adhesive force measurements are performed in the so-called force calibration mode. In this mode, force–distance curves are obtained, for example that shown in

**Fig. 12.5** Schematic of the triangular pattern trajectory of a tip as the sample (or tip) is scanned in two dimensions. During scanning, data are recorded only during scans along the *solid scan lines*

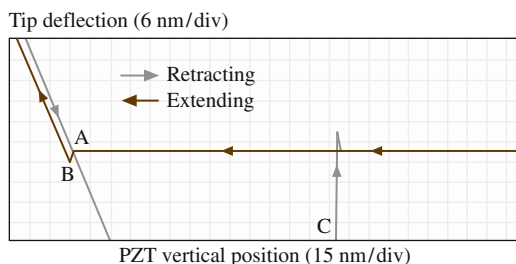
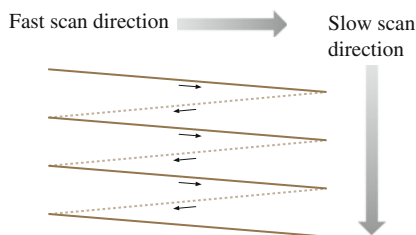


**Fig. 12.6** Typical force–distance curve for the contact between a  $\text{Si}_3\text{N}_4$  tip and a single-crystal silicon surface in measurements made in the ambient environment. Snap-in occurs at point A; contact between the tip and silicon occurs at point B; the tip breaks free of adhesive forces at point C as the sample moves away from the tip

Fig. 12.6. The horizontal axis gives the distance the piezo (and hence the sample) travels, and the vertical axis gives the tip deflection. As the piezo extends, it approaches the tip, which is at this point in free air and hence shows no deflection. This is indicated by the flat portion of the curve. As the tip approaches the sample within a few nanometers (point A), an attractive force exists between the atoms of the tip surface and the atoms of the sample surface. The tip is pulled towards the sample and contact occurs at point B on the graph. From this point on, the tip is in contact with the surface and, as the piezo extends further, the tip gets further deflected. This is represented by the sloped portion of the curve. As the piezo retracts, the tip goes beyond the zero deflection (flat) line because of attractive forces (van der Waals forces and long-range meniscus forces), into the adhesive regime. At point C in the graph, the tip snaps free of the adhesive forces and is again in free air. The horizontal distance between points B and C along the retrace line gives the distance moved by the tip in the adhesive regime. This distance multiplied by the stiffness of the cantilever gives the adhesive force. Incidentally, the horizontal shift between the loading and unloading curves results from the hysteresis in the PZT tube [5, 13].

### 12.1.3 Scratching, Wear, and Fabrication/Machining

For microscale scratching, microscale wear, nanofabrication/nanomachining, and nanoindentation hardness measurements, an extremely hard tip is required.



A three-sided pyramidal single-crystal natural diamond tip with an apex angle of  $80^\circ$  and a radius of about 100 nm mounted on a stainless-steel cantilever beam with normal stiffness of about 25 N/m is used at relatively higher loads (1–150  $\mu\text{N}$ ) (Fig. 12.4a). For scratching and wear studies, the sample is generally scanned in a direction orthogonal to the long axis of the cantilever beam (typically at a rate of 0.5 Hz) so that friction can be measured during scratching and wear. The tip is mounted on the cantilever such that one of its edges is orthogonal to the long axis of the beam; therefore, wear during scanning along the beam axis is higher (about  $2 \times$  to  $3 \times$ ) than that during scanning orthogonal to the beam axis. For wear studies, an area on the order of  $2 \mu\text{m} \times 2 \mu\text{m}$  is scanned at various normal loads (ranging from 1 to 100  $\mu\text{N}$ ) for a selected number of cycles [5, 13, 41].

Scratching can also be performed at ramped loads and the coefficient of friction can be measured during scratching [59]. A linear increase in the normal load approximated by a large number of normal load increments of small magnitude is applied using a software interface (lithography module in Nanoscope III) that allows the user to generate controlled movement of the tip with respect to the sample. The friction signal is tapped out of the AFM and recorded on a computer. A scratch length on the order of 25  $\mu\text{m}$  and a velocity on the order of 0.5  $\mu\text{m/s}$  are used and the number of loading steps is usually taken to be 50.

Nanofabrication/nanomachining is conducted by scratching the sample surface with a diamond tip at specified locations and scratching angles. The normal load used for scratching (writing) is on the order of 1–100  $\mu\text{N}$  with a writing speed on the order of 0.1–200  $\mu\text{m/s}$  [5, 7, 13, 14, 41, 78].

### 12.1.4 Surface Potential Measurements

To detect wear precursors and to study the early stages of localized wear, the multimode AFM can be used to measure the potential difference between the tip and the sample by applying a direct-current (DC) bias potential and an oscillating (alternating current, AC) potential to a conducting tip over a grounded substrate in a Kelvin probe microscopy or so-called *nano-Kelvin probe* technique [79–81].

Mapping of the surface potential is made in the so-called *lift mode* (Fig. 12.7). These measurements are made simultaneously with the topography scan in the tapping mode, using an electrically conducting (nickel-coated single-crystal silicon) tip. After each line of the topography scan is completed, the feedback loop controlling the vertical piezo is turned off, and the tip is lifted from the surface and traced over the same topography at a constant distance of 100 nm. During the lift mode, a DC bias potential and an oscillating potential (3–7 V) are applied to the tip. The frequency of oscillation is chosen to be equal to the resonant frequency of the cantilever ( $\approx 80$  kHz). When a DC bias potential equal to the negative value of the surface potential of the sample (on the order of  $\pm 2$  V) is applied to the tip, it does not vibrate. During scanning, a difference between the DC bias potential applied to the tip and the potential of the surface will create DC electric fields that interact

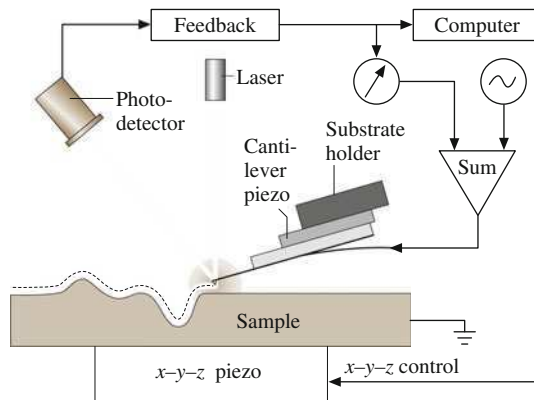


**Fig. 12.7** Schematic of lift mode used to make surface potential measurement. The topography is collected in tapping mode in the primary scan. The cantilever piezo is deactivated. Using topography information of the primary scan, the cantilever is scanned across the surface at a constant height above the sample. An oscillating voltage at the resonant frequency is applied to the tip, and a feedback loop adjusts the DC bias of the tip to maintain the cantilever amplitude at zero. The output of the feedback loop is recorded by the computer and becomes the surface potential map

with the oscillating charges (as a result of the AC potential), causing the cantilever to oscillate at its resonant frequency, as in tapping mode. However, a feedback loop is used to adjust the DC bias on the tip to exactly cancel the electric field, and thus the vibrations of the cantilever. The required bias voltage follows the localized potential of the surface. The surface potential is obtained by reversing the sign of the bias potential provided by the electronics [80, 81]. Surface and subsurface changes of structure and/or chemistry can cause changes in the measured potential of a surface. Thus, mapping of the surface potential after sliding can be used for detecting wear precursors and studying the early stages of localized wear.

### 12.1.5 *In Situ Characterization of Local Deformation Studies*

In situ characterization of local deformation of materials can be carried out by performing tensile, bending or compression experiments inside an AFM and by observing nanoscale changes during the deformation experiment [17]. In these experiments, small deformation stages are used to deform the samples inside an AFM. In tensile testing of the polymeric films carried out by Bobji and Bhushan [73, 74] and Tambe and Bhushan [75] a tensile stage was used (Fig. 12.8). The stage with a left-right combination lead screw (which helps to move the slider in the opposite direction) was used to stretch the sample to minimize the movement of the scanning area, which was kept close to the center of the tensile specimen. One end of the sample was mounted on the slider via a force sensor to monitor the tensile load. The samples were stretched for various strains using a stepper motor and the

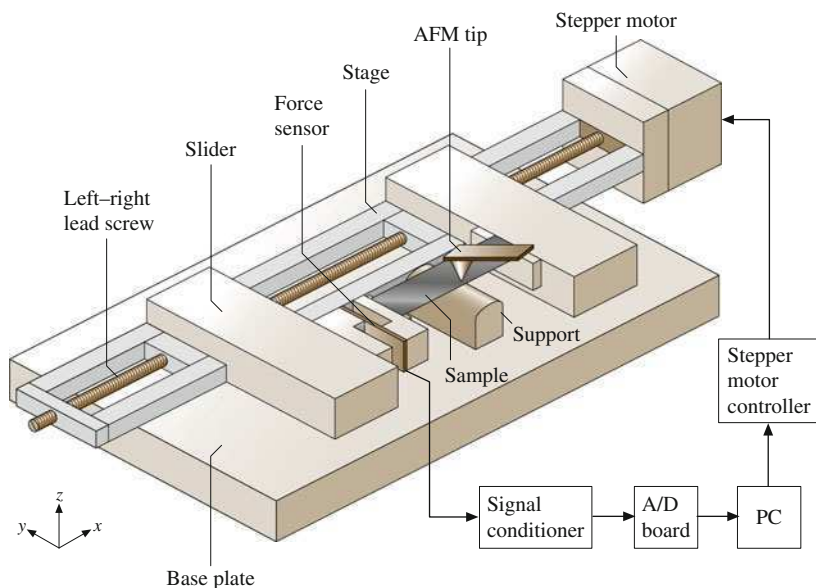


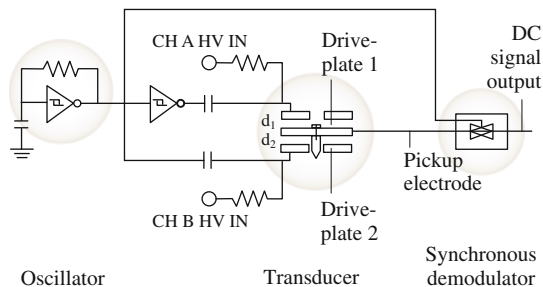
**Fig. 12.8** Schematic of the tensile stage to conduct in situ tensile testing of polymeric films in an AFM

same control area at different strains was imaged. In order to better locate the control area for imaging, a set of four markers was created at the corners of a  $30 \times 30 \mu\text{m}$  square at the center of the sample by scratching the sample with a sharp silicon tip. The scratching depth was controlled such that it did not affect the cracking behavior of the coating. A minimum displacement of  $1.6 \mu\text{m}$  could be obtained. This corresponded to a strain increment of  $8 \times 10^{-3}\%$  for a sample length of 38 mm. The maximum travel was about 100 mm. The resolution of the force sensor was 10 mN with a capacity of 45 N. During stretching, a stress-strain curve was obtained during the experiment to study any correlation between the degree of plastic strain and propensity for cracking.

### 12.1.6 Nanoindentation Measurements

For nanoindentation hardness measurements the scan size is set to zero, and then a normal load is applied to make the indents using the diamond tip (Sect. 12.1.5). During this procedure, the tip is continuously pressed against the sample surface for about 2 s at various indentation loads. The sample surface is scanned before and after the scratching, wear or indentation to obtain the initial and final surface topography, at a low normal load of  $\approx 0.3 \mu\text{N}$  using the same diamond tip. An area larger than the indentation region is scanned to observe the indentation marks.

**Fig. 12.9** Schematic of a nano/picoindentation system with three-plate transducer with electrostatic actuation hardware and capacitance sensor (after [61])



Nanohardness is calculated by dividing the indentation load by the projected residual area of the indents [62].

Direct imaging of the indent allows one to quantify piling up of ductile material around the indenter. However, it becomes difficult to identify the boundary of the indentation mark with great accuracy. This makes the direct measurement of contact area somewhat inaccurate. A technique with the dual capability of depth sensing as well as in situ imaging, which is most appropriate in nanomechanical property studies, is used for accurate measurement of hardness with shallow depths [5, 13, 61]. This nano/picoindentation system is used to make load–displacement measurements and subsequently carry out in situ imaging of the indent, if required. The indentation system, shown in Fig. 12.9, consists of a three-plate transducer with electrostatic actuation hardware used for direct application of a normal load and a capacitive sensor used for measurement of vertical displacement. The AFM head is replaced with this transducer assembly while the specimen is mounted on the PZT scanner, which remains stationary during indentation experiments. The transducer consists of a three-plate (Be–Cu) capacitive structure, and the tip is mounted on the center plate. The upper and lower plates serve as drive electrodes, and the load is applied by applying an appropriate voltage to the drive electrodes. Vertical displacement of the tip (indentation depth) is measured by measuring the displacement of the center plate relative to the two outer electrodes using a capacitance technique. Indent area and consequently the hardness value can be obtained from the load–displacement data. The Young’s modulus of elasticity is obtained from the slope of the unloading curve.

### 12.1.7 Localized Surface Elasticity and Viscoelasticity Mapping

#### Localized Surface Elasticity

Indentation experiments provide a single point measurement of the Young’s modulus of elasticity calculated from the slope of the indentation curve during unloading. Localized surface elasticity maps can be obtained using dynamic force

microscopy, in which an oscillating tip is scanned over the sample surface in contact under steady and oscillating load. Lower-frequency operation modes in the kHz range, such as force modulation mode [64, 66] or pulsed force mode [82], are well suited for soft samples such as polymers. However, if the tip-sample contact stiffness becomes significantly higher than the cantilever stiffness, the sensitivity of these techniques strongly decreases. In this case, the sensitivity of the measurement of stiff materials can be improved by using high-frequency operation modes in the MHz range with a lateral motion, such as acoustic (ultrasonic) force microscopy, referred to as atomic force acoustic microscopy (AFAM) or contact resonance spectroscopy [67, 68, 83]. Inclusion of vibration frequencies other than only the first cantilever flexural or torsional resonant frequency also allows additional information to be obtained.

In the negative lift mode force modulation technique, during primary scanning height data is recorded in tapping mode as described earlier. During interleave scanning, the entire cantilever-tip assembly is moved up and down at the force modulation holder's bimorph resonant frequency ( $\approx 24$  kHz) at some amplitude, here referred to as the force modulation amplitude, and the  $z$ -direction feedback control for the sample  $x$ - $y$ - $z$  piezo is deactivated (Fig. 12.10a) [64, 66, 69]. During this scanning, height information from the primary scan is used to maintain a constant lift scan height. This eliminates the influence of height on the measured signals during the interleave scan. Lift scan height is the mean tip-sample distance between the tip and sample during the interleave scan. The lift scan height is set such that the tip is in constant contact with the sample, i.e., a constant static load is applied. (A higher lift scan height gives a closer mean tip-sample distance.) In addition, the tip motion caused by the bimorph vibration results in a modulating periodic force. The sample surface resists the oscillations of the tip to a greater or lesser extent depending upon the sample's stiffness. The computer records amplitude (which is a function of the elastic stiffness of the material). Contact analyses can be used to obtain a quantitative measure of localized elasticity of soft surfaces [66]. Etched single-crystal silicon cantilevers with integrated tips (DI force modulation etched Si probe or FESP) with a radius of 25–50 nm, a stiffness of 1–5 N/m, and a natural frequency of 60–100 kHz are commonly used for the measurements. Scanning is normally set to a rate of 0.5 Hz along the fast axis.

In the AFAM technique [67, 68, 83], the cantilever-tip assembly is moved either in the normal or lateral mode, and the contact stiffness is evaluated by comparing the resonant frequency of the cantilever in contact with the sample surface with those of the free vibrations of the cantilever. Several free resonant frequencies are measured. Based on the shift of the measured frequencies, the contact stiffness is determined by solving the characteristic equation for the tip vibrating in contact with the sample surface. The elastic modulus is calculated from contact stiffness using Hertz analysis for a spherical tip indenting a plane. Contact stiffness is equal to  $8 \times \text{contact radius} \times \text{reduced shear modulus in shear mode}$ .

In the lateral mode using the AFAM technique, the sample is glued onto cylindrical pieces of aluminum which serve as ultrasonic delay lines coupled to an ultrasonic shear wave transducer (Fig. 12.10b) [46, 67, 68]. The transducer is

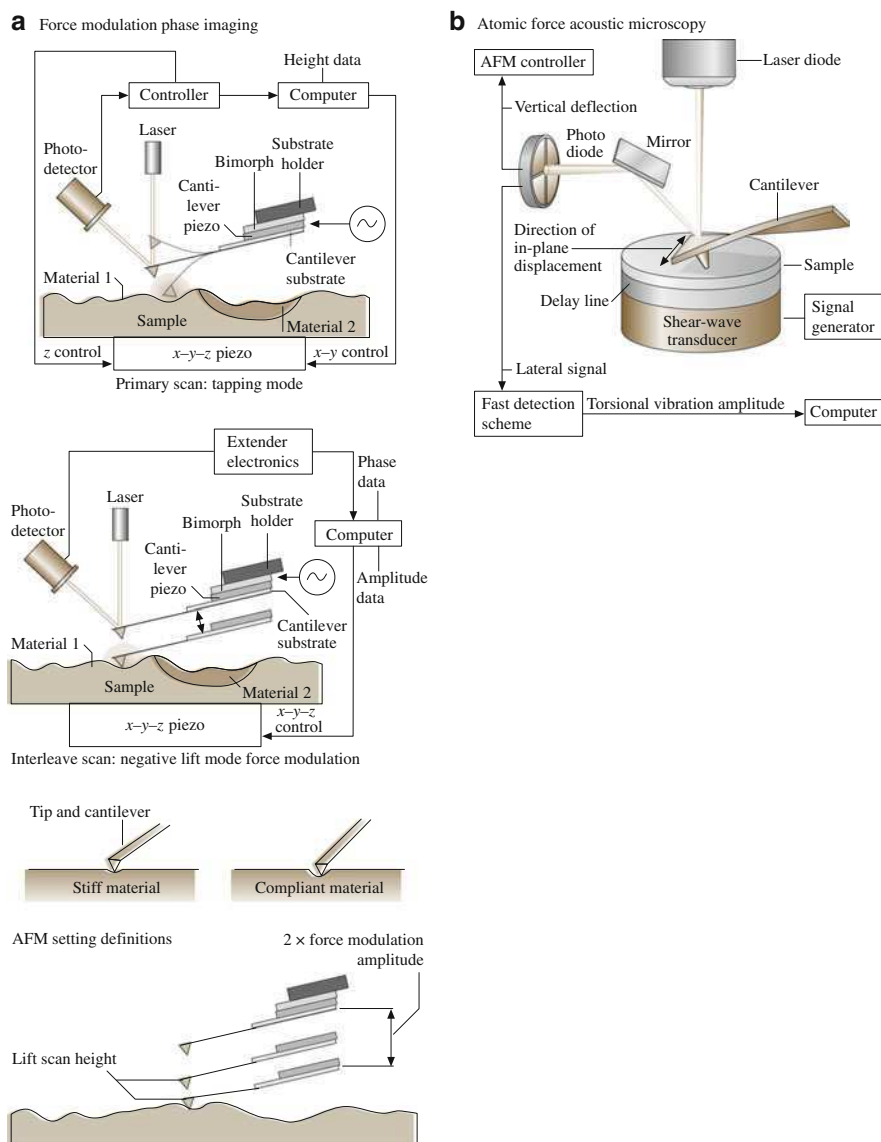


**Fig. 12.10 (a)** Schematic of force modulation mode used to obtain amplitude (stiffness), and definitions of force modulation amplitude and lift scan height. During primary scanning, height data is recorded in tapping mode. During interleave scanning, the entire cantilever–tip assembly is vibrated at the bimorph’s resonant frequency and the  $z$ -direction feedback control for the sample  $x$ – $y$ – $z$  piezo is deactivated. During this scanning, height information from the primary scan is used to maintain a constant lift scan height. The computer records amplitude (which is a function of material stiffness) during the interleave scan. **(b)** Schematic of an AFM incorporating a shear wave transducer that generates in-plane lateral sample surface vibrations. Because of the forces between the tip and the surface, torsional vibrations of the cantilever are excited [46]. The shift in contact resonant frequency is a measure of the contact stiffness

driven with frequency sweeps to generate in-plane lateral sample surface vibrations. These couple to the cantilever via the tip-sample contact. To measure torsional vibrations of the cantilever at frequencies up to 3 MHz, the original electronic circuit of the lateral channel of the AFM (using a low-pass filter with limited bandwidth to a few hundred kHz) was replaced by a high-speed scheme which bypasses the low-pass filter. The high-frequency signal was fed to a lock-in amplifier, digitized using a fast analog-to-digital (A/D) card, and fed into a broadband amplifier followed by a root-mean-square (RMS)-to-DC converter, and read by a computer. Etched single-crystal silicon cantilevers (normal stiffness of 3.8–40 N/m) integrated tips are used.

## Viscoelastic Mapping

Another form of dynamic force microscopy, phase-contrast microscopy, is used to detect the contrast in viscoelastic (viscous energy dissipation) properties of different materials across the surface [65, 69–72, 84, 85]. In these techniques, both deflection amplitude and phase angle contrasts are measured, which are measures of the relative stiffness and viscoelastic properties, respectively. Two phase measurement techniques – tapping mode and torsional resonance (TR) mode – have been developed. We describe them next.

In the tapping mode (TM) technique, as described earlier, the cantilever-tip assembly is sinusoidally vibrated at its resonant frequency, and the sample  $x$ - $y$ - $z$  piezo is adjusted using feedback control in the  $z$ -direction to maintain a constant setpoint (Fig. 12.3) [69, 70]. The feedback signal to the  $z$ -direction sample piezo (to keep the setpoint constant) is a measure of surface roughness. The extender electronics is used to measure the phase angle lag between the cantilever piezo drive signal and the cantilever response during sample engagement. As illustrated in Fig. 12.3, the phase angle lag (at least partially) is a function of the viscoelastic properties of the sample material. A range of tapping amplitudes and setpoints can be used for measurements. Commercially an etched single-crystal silicon tip (DI TESP) used for tapping mode, with a radius of 5–10 nm, a stiffness of 20–100 N/m, and a natural frequency of 350–400 kHz, is normally used. Scanning is normally set to a rate of 1 Hz along the fast axis.

In the TR mode, a tip is vibrated in the torsional mode at high frequency at the resonant frequency of the cantilever beam. An etched single-crystal silicon cantilever with integrated tip (DI FESP) with a radius of  $\approx 5$ –10 nm, normal stiffness of 1–5 N/m, torsional stiffness of  $\approx 30$  times normal stiffness, and torsional natural frequency of 800 kHz is normally used. A major difference between the TM and TR modes is the directionality of the applied oscillation – a normal (compressive) amplitude exerted for the TM and a torsional amplitude for the TR mode. The TR mode is expected to provide good contrast in the tribological and mechanical properties of the near-surface region as compared with the TM. Two of the reasons are as follows:

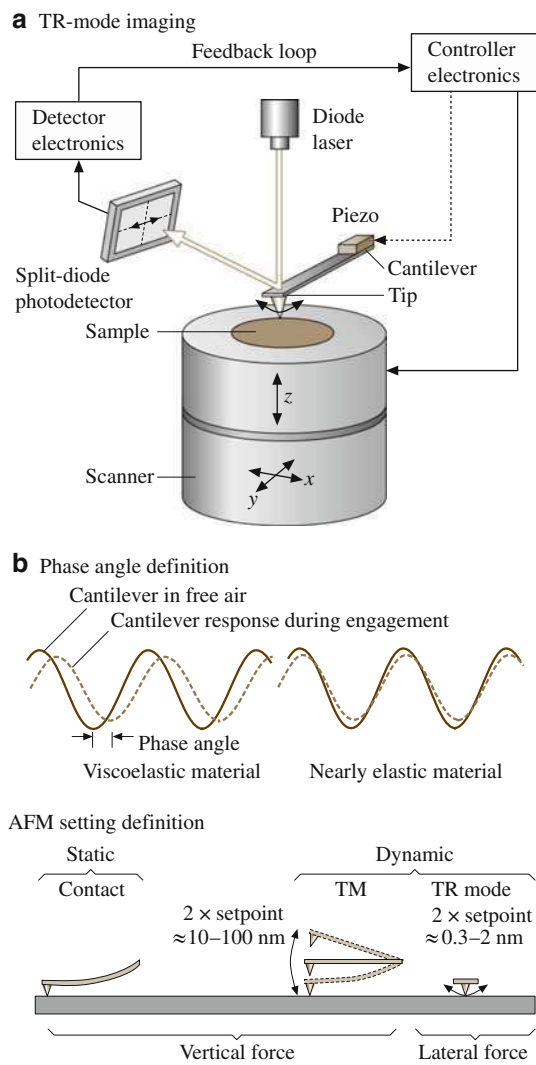
1. In the TM, the interaction is dominated by the vertical properties of the sample, so the tip spends a small fraction of its time in the near-field interaction with the sample. Furthermore, the distance between the tip and the sample changes during the measurements, which changes interaction time and forces, and affects measured data. In the TR mode, the distance remains nearly constant.
2. The lateral stiffness of a cantilever is typically about two orders of magnitude larger than the normal (flexural) stiffness. Therefore, in the TM, if the sample is relatively rigid, much of the deformation occurs in the cantilever beam, whereas in the TR mode, much of the deformation occurs in the sample. A few comments on the special applications of the TR mode are made next. Since most of the deformation occurs in the sample, the TR mode can be used to measure stiff and hard samples. Furthermore, properties of thin films can be measured more readily with the TR mode. For both the TM and TR modes, if the cantilever is driven to vibrate at frequencies above resonance, it would have less motion (high apparent stiffness), leading to higher sample deformation and better contrast. It should be further noted that the TM exerts a compressive force, whereas the TR mode exerts a torsional force, therefore normal and shear properties are measured in the TM and TR modes, respectively.

In the TR mode, the torsional vibration of the cantilever beam is achieved using a specially designed cantilever holder. It is equipped with a piezo system mounted in a cantilever holder, in which two piezos vibrate out of phase with respect to each other. A tuning process prior to scanning is used to select the torsional vibration frequency. The piezo system excites torsional vibration at the cantilever's resonant frequency. The torsional vibration amplitude of the tip (TR amplitude) is detected by the lateral segments of the split-diode photodetector (Fig. 12.11) [71]. The TR mode measures surface roughness and phase angle as follows. During the measurement, the cantilever-tip assembly is first vibrated at its resonance at some amplitude dependent upon the excitation voltage, before the tip engages the sample. Next, the tip engages the sample at some setpoint. A feedback system coupled to a piezo stage is used to keep a constant TR amplitude during scanning. This is done by controlling the vertical position of the sample using a piezo moving in the  $z$ -direction, which changes the degree of tip interaction. The displacement of the sample  $z$  piezo gives a roughness image of the sample. A phase-angle image can be obtained by measuring the phase lag of the cantilever vibration response in the torsional mode during engagement with respect to the cantilever vibration response in free air before engagement. The control feedback of the TR mode is similar to that of tapping, except that the torsional resonance amplitude replaces the flexural resonance amplitude [71].

Chen and Bhushan [72] used a variation to the approach just described (referred to as mode I here). They performed measurements at constant normal cantilever deflection (constant load) (mode II) instead of using the constant setpoint in the Kasai et al. [71] approach. Their approach overcomes the meniscus adhesion problem present in mode I and reveals true surface properties.



**Fig. 12.11** Schematic of torsional resonance mode shown *at the top*. Two examples of the phase-angle response are shown *in the middle*. One is for materials exhibiting viscoelastic (a) and the other nearly elastic properties (b). Three AFM settings are compared *at the bottom*: contact, tapping mode (TM), and TR modes. The TR mode is a dynamic approach with a laterally vibrating cantilever tip that can interact with the surface more intensively than other modes. Therefore, more detailed near-surface information is available



Song and Bhushan [86] presented a forced torsional vibration model for a tip–cantilever assembly under viscoelastic tip–sample interaction. This model provides the relationship of torsional amplitude and phase shift with lateral contact stiffness and viscosity which can be used to extract in-plane interfacial mechanical properties.

Various operating modes of AFM used for surface roughness, localized surface elasticity, viscoelastic mapping, and friction force measurements (to be discussed later) are summarized in Table 12.2.

**Table 12.2** Summary of various operating modes of AFM for surface roughness, stiffness, phase angle, and friction

Operating mode	Direction of cantilever vibration	Vibration frequency of cantilever (kHz)	Vibration amplitude (nm)	Feedback control	Data obtained
Contact	N/A				
Tapping	Vertical	350–400	10–100	Constant normal load Setpoint (constant tip amplitude)	Surface height, friction Surface height, phase angle (normal viscoelasticity)
Force modulation	Vertical	10–20 (bimorph)	10–100	Constant normal load	Surface height, amplitude (normal stiffness)
Lateral	Lateral (AAFM)	100–3,000 (sample)	$\approx 5$ (sample)	Constant normal load	Shift in contact resonance (normal stiffness, friction)
TR mode I	Torsional	$\approx 800$	0.3–2	Setpoint (constant tip amplitude)	Surface height, phase angle (lateral viscoelasticity)
TR mode II	Torsional	$\approx 800$	0.3–2	Constant normal load	Surface height, amplitude, and phase angle (lateral stiffness and lateral viscoelasticity)
TR mode III	Torsional	$> 800$ in contact	0.3–2	Constant normal load	Shift in contact resonance (friction)

### 12.1.8 Boundary Lubrication Measurements

To study nanoscale boundary lubrication properties, adhesive forces are measured in the force calibration mode, as previously described. The adhesive forces are also calculated from the horizontal intercept of friction versus normal load curves at a zero value of friction force. For friction measurements, the samples are typically scanned using a  $\text{Si}_3\text{N}_4$  tip over an area of  $2 \times 2 \mu\text{m}^2$  at normal load ranging from 5 to 130 nN. The samples are generally scanned at a rate of 0.5 Hz, resulting in a scanning speed of  $2 \mu\text{m/s}$ . Velocity effects on friction are studied by changing the scan frequency from 0.1 to 60 Hz while the scan size is maintained at  $2 \times 2 \mu\text{m}^2$ , which allows velocity to vary from 0.4 to  $240 \mu\text{m/s}$ . To study durability properties, the friction force and coefficient of friction are monitored during scanning at normal load of 70 nN and scanning speed of  $0.8 \mu\text{m/s}$ , for a desired number of cycles [51, 52, 54].

## 12.2 Surface Imaging, Friction, and Adhesion

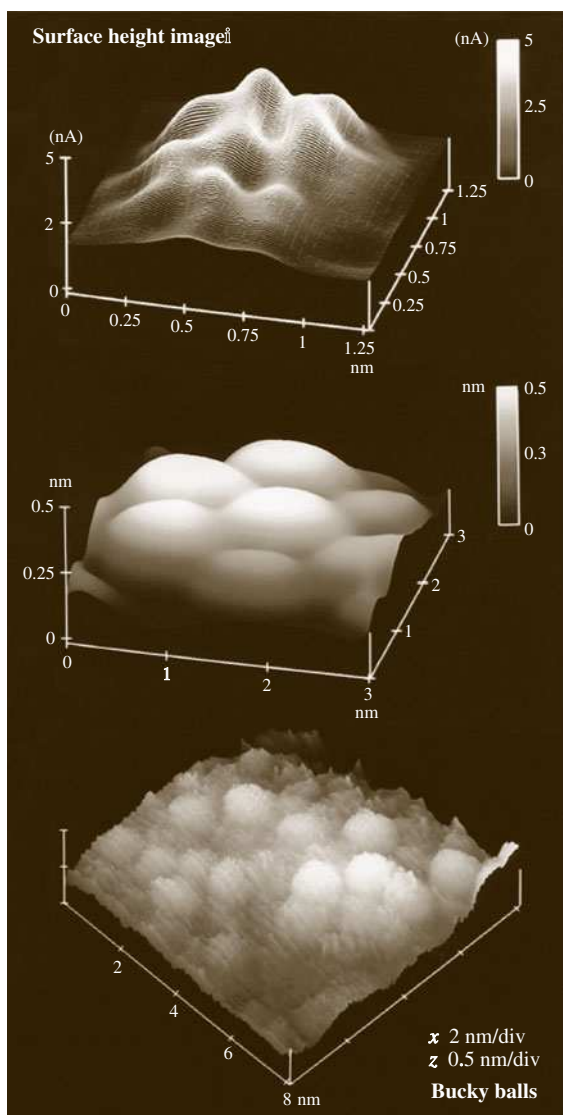
### 12.2.1 Atomic-Scale Imaging and Friction

Surface height imaging down to atomic resolution of electrically conducting surfaces can be carried out using an STM. An AFM can also be used for surface height imaging and roughness characterization down to the nanoscale. Figure 12.12 shows a sequence of STM images at various scan sizes of solvent-deposited  $\text{C}_{60}$  film on 200 nm-thick gold-coated freshly cleaved mica [87]. The film consists of clusters of  $\text{C}_{60}$  molecules of 8 nm diameter. The  $\text{C}_{60}$  molecules within a cluster appear to pack into a hexagonal array with a spacing of  $\approx 1$  nm, however, they do not follow any long-range order. The measured cage diameter of the  $\text{C}_{60}$  molecule is  $\approx 0.7$  nm, very close to the projected diameter of 0.71 nm.

In an AFM measurement during surface imaging, the tip comes into intimate contact with the sample surface and leads to surface deformation with finite tip-sample contact area (typically a few atoms). The finite size of the contact area prevents the imaging of individual point defects, and only the periodicity of the atomic lattice can be imaged. Figure 12.13a shows the topography image of a freshly cleaved surface of highly oriented pyrolytic graphite (HOPG) [39]. The periodicity of the graphite is clearly observed.

To study friction mechanisms on an atomic scale, a freshly cleaved HOPG has been studied by Mate et al. [36] and Ruan and Bhushan [39]. Figure 12.14a shows the atomic-scale friction force map (raw data) and Fig. 12.13a shows the friction force maps after two-dimensional (2-D) spectrum filtering with high-frequency noise truncated [39]. Figure 12.14a also shows a line plot of the friction force profile along some crystallographic direction. The actual shape of the friction profile depends upon the spatial location of the axis of tip motion. Note that a portion

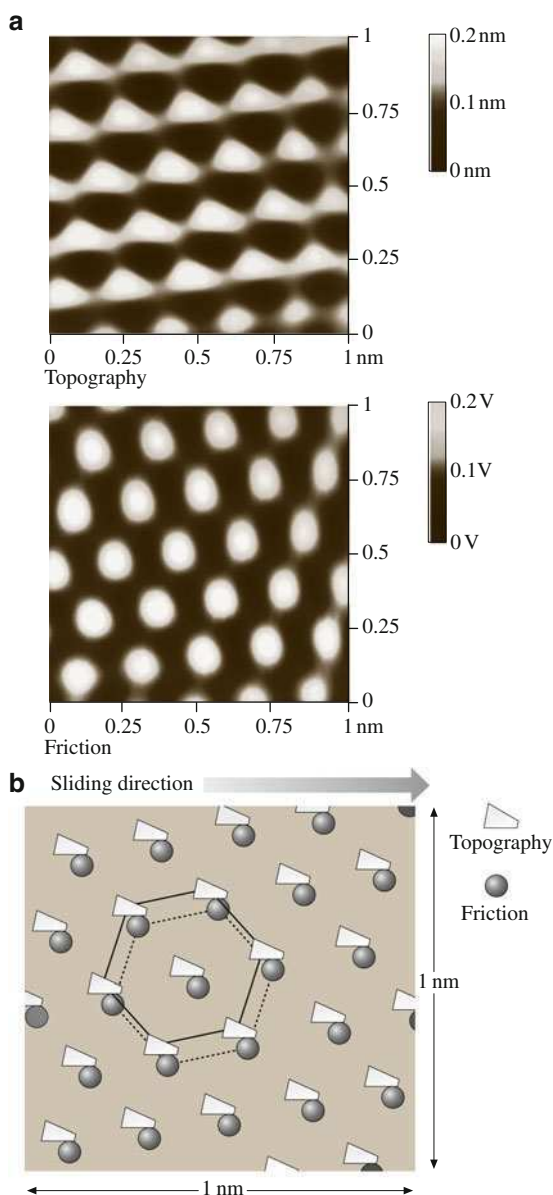
**Fig. 12.12** STM images of solvent-deposited  $C_{60}$  film on a gold-coated freshly cleaved mica at various scan sizes (after [87])



of the atomic-scale lateral force is conservative. Mate et al. [36] and Ruan and Bhushan [39] reported that the average friction force increased linearly with normal load and was reversible with load. Friction profiles were similar during sliding of the tip in either direction.

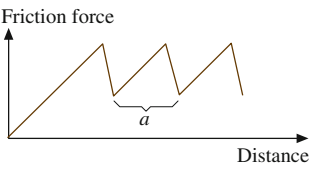
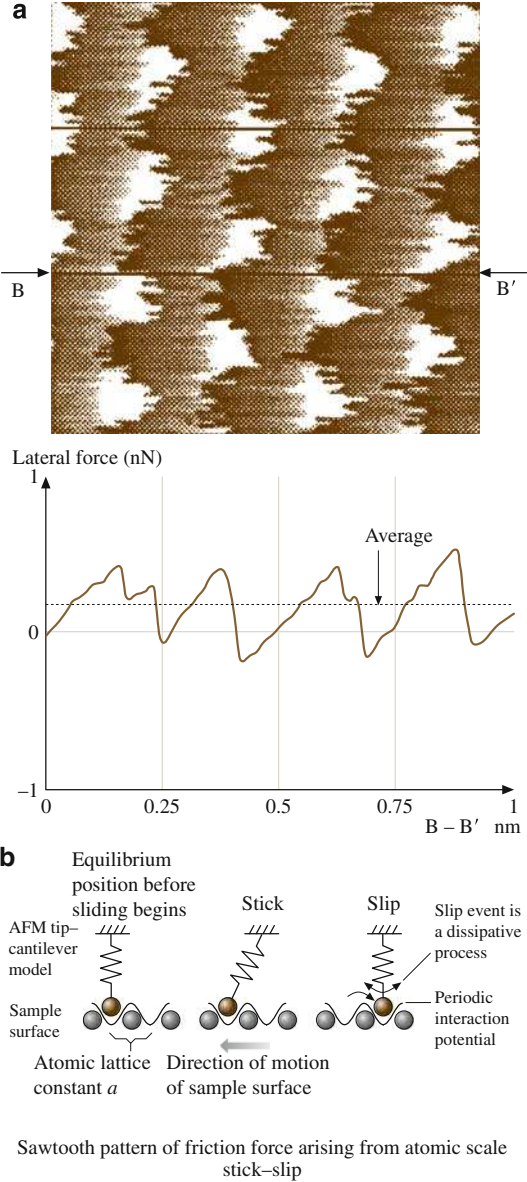
During scanning, the tip moves discontinuously over the sample surface and jumps with discrete steps from one potential minimum (well) to the next. This leads to a sawtooth-like pattern for the lateral motion (force) with periodicity of the lattice constant. This motion is called stick-slip movement of the tip [6, 11, 29,

**Fig. 12.13** (a) Gray-scale plots of surface topography and friction force maps (2-D spectrum filtered), measured simultaneously, of a  $1\text{ nm} \times 1\text{ nm}$  area of freshly cleaved HOPG, showing the atomic-scale variation of topography and friction, and (b) schematic of superimposed topography and friction maps from (a); the symbols correspond to maxima. Note the spatial shift between the two plots (after [38])



[36, 39]. The observed friction force includes two components – conservative and periodic, and nonconservative and constant. If the relative motion of the sample and tip were simply that of two rigid collections of atoms, the effective force would be a conservative force oscillating about zero. Slow reversible elastic deformation would also contribute to conservative force. The origin of the nonconservative

**Fig. 12.14** (a) Gray-scale plot of the friction force map (raw data) of a  $1 \times 1 \text{ nm}^2$  area of freshly cleaved HOPG, showing atomic-scale variation of the friction force. High points are shown by lighter color. Also shown is a line plot of the friction force profile along the line indicated by arrows. The normal load was 25 nN and the cantilever normal stiffness was 0.4 N/m [39]. (b) Schematic of a model for a tip atom sliding on an atomically flat periodic surface. The schematic shows the tip jumping from one potential minimum to another, resulting in stick-slip behavior



direction-dependent force component could be phonon generation, viscous dissipation or plastic deformation.

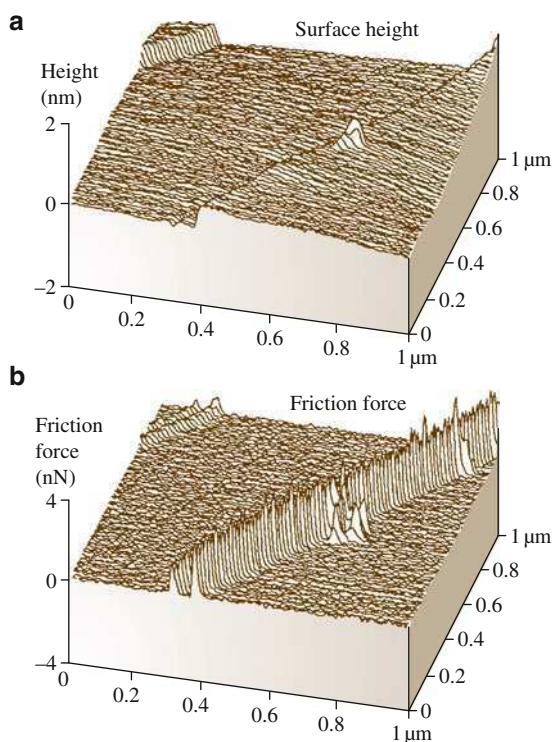
Stick–slip on the atomic scale, discussed above, is the result of the energy barrier required to be overcome for jumping over the atomic corrugations on the sample surface. It corresponds to the energy required for the jump of the tip from a stable equilibrium position on the surface into a neighboring position. The perfect atomic regularity of the surface guarantees the periodicity of the lateral force signal, independent of the actual atomic structure of the tip apex. A few atoms (based on the magnitude of the friction force,  $< 10$ ) on a tip sliding over an array of atoms on the sample are expected to go through the stick–slip. For simplicity, Fig. 12.14b shows a simplified model for one atom on a tip with a one-dimensional spring–mass system. As the sample surface slides against the AFM tip, the tip remains *stuck* initially until it can overcome the energy (potential) barrier, which is illustrated by a sinusoidal interaction potential as experienced by the tip. After some motion, there is enough energy stored in the spring, which leads to *slip* into the neighboring stable equilibrium position. During the slip and before attaining stable equilibrium, stored energy is converted into vibrational energy of the surface atoms in the range of  $10^{13}$  Hz (phonon generation) and decays within the range of  $10^{-11}$  s into heat. (A wave of atoms vibrating in concert are termed a phonon.) The stick–slip phenomenon, resulting from irreversible atomic jumps, can be modeled theoretically with classical mechanical models [88, 89]. The Tomanek–Zhong–Thomas model [89] is the starting point for determining friction force during atomic-scale stick–slip. The AFM model describes the total potential as the sum of the potential acting on the tip due to interaction with the sample and the elastic energy stored in the cantilever. Thermally activated stick–slip behavior can explain the velocity effects on friction, to be presented later.

Finally, based on Fig. 12.13a, the atomic-scale friction force of HOPG exhibited the same periodicity as that of the corresponding topography, but the peaks in friction and those in topography are displaced relative to each other (Fig. 12.13b). A Fourier expansion of the interatomic potential was used by Ruan and Bhushan [39] to calculate the conservative interatomic forces between atoms of the FFM tip and those of the graphite surface. Maxima in the interatomic forces in the normal and lateral directions do not occur at the same location, which explains the observed shift between the peaks in the lateral force and those in the corresponding topography.

### 12.2.2 Microscale Friction

Local variations in the microscale friction of cleaved graphite are observed (Fig. 12.15). Microscale friction is defined as the friction measured with a scan size equal to or larger than  $1 \times 1 \mu\text{m}$ . These arise from structural changes that occur during the cleaving process [40]. The cleaved HOPG surface is largely atomically smooth but exhibits line-shaped regions in which the coefficient of friction is more than an order of magnitude larger. Transmission electron microscopy indicates that

**Fig. 12.15** (a) Surface roughness and (b) friction force maps at normal load of 42 nN for a freshly cleaved HOPG surface against an  $\text{Si}_3\text{N}_4$  FFM tip. Friction in the line-shaped region is over an order of magnitude larger than in the smooth areas (after [39])

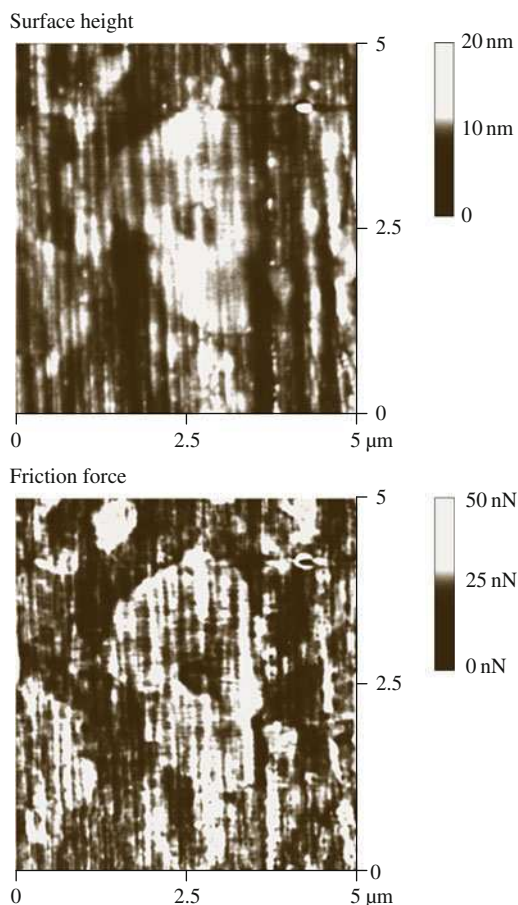


the line-shaped regions consist of graphite planes of different orientation, as well as of amorphous carbon. Differences in friction have also been observed for multi-phase ceramic materials [57]. Figure 12.16 shows surface roughness and friction force maps of  $\text{Al}_2\text{O}_3$ -TiC (70–30 wt%). TiC grains have a Knoop hardness of  $\approx 2800 \text{ kg/mm}^2$  and  $\text{Al}_2\text{O}_3$  has  $2,100 \text{ kg/mm}^2$ , therefore TiC grains do not polish as much and therefore have a slightly higher elevation ( $\approx 2\text{--}3 \text{ nm}$  higher than that of  $\text{Al}_2\text{O}_3$  grains). TiC grains exhibit higher friction force than  $\text{Al}_2\text{O}_3$  grains. The coefficients of friction of TiC and  $\text{Al}_2\text{O}_3$  grains are 0.034 and 0.026, respectively, and the coefficient of friction of the  $\text{Al}_2\text{O}_3$ -TiC composite is 0.03. Local variation in friction force also arises from the scratches present on the  $\text{Al}_2\text{O}_3$ -TiC surface. Meyer et al. [90] also used FFM to measure structural variations of organic mono- and multilayer films. All of these measurements suggest that the FFM can be used for structural mapping of the surfaces. FFM measurements can also be used to map chemical variations, as indicated by the use of the FFM with a modified probe tip to map the spatial arrangement of chemical functional groups in mixed organic monolayer films [91]. Here, sample regions that had stronger interactions with the functionalized probe tip exhibited larger friction.

Local variations in the microscale friction of nominally rough surfaces of homogeneous material can be significant, and are seen to depend on the local surface slope rather than the surface height distribution (Fig. 12.17). This dependence was



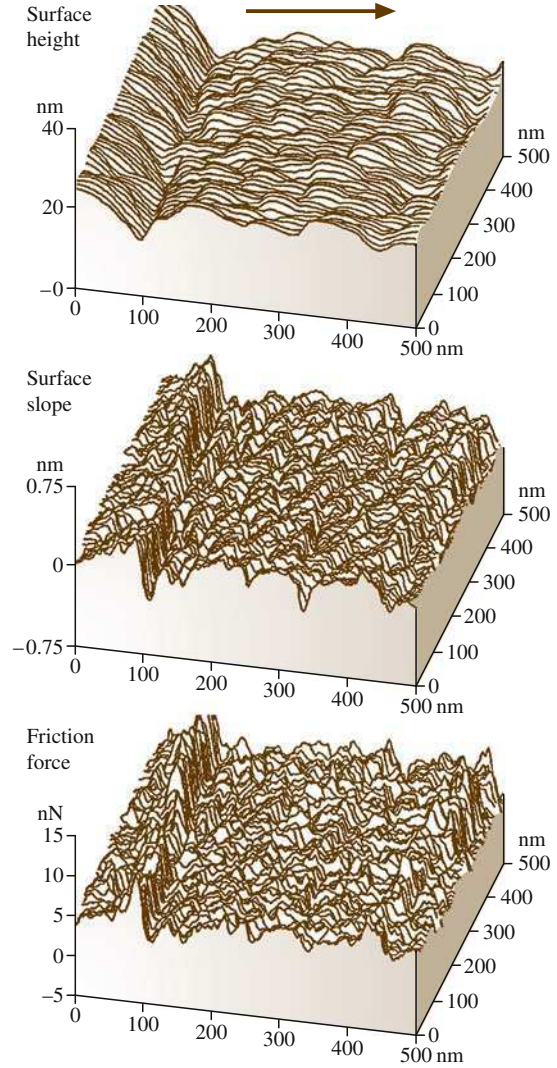
**Fig. 12.16** Gray-scale surface roughness ( $\sigma = 0.80$  nm) and friction force maps (mean = 7.0 nN,  $\sigma = 0.90$  nN) for  $\text{Al}_2\text{O}_3$ -TiC (70–30 wt%) at normal load of 138 nN (after [57])



first reported by Bhushan and Ruan [37], Bhushan et al. [41], and Bhushan [78] and later discussed in more detail by Koinkar and Bhushan [92] and Sundararajan and Bhushan [93]. In order to elegantly show any correlation between local values of friction and surface roughness, surface roughness and friction force maps of a gold-coated ruler with somewhat rectangular grids and a silicon grid with square pits were obtained (Fig. 12.18) [93]. Figures show the surface roughness map, the slopes of the roughness map taken along the sliding direction (surface slope map), and the friction force map for various samples. There is a strong correlation between the surface slopes and friction forces. For example, in Fig. 12.18, the friction force is high locally at the edge of the grids and pits with a positive slope and is low at the edges with negative slope.

We now examine the mechanism of microscale friction, which may explain the resemblance between the slope of surface roughness maps and the corresponding friction force maps [5, 6, 13, 39, 40, 41, 49, 92, 93]. There are three dominant

**Fig. 12.17** Surface roughness map ( $\sigma = 4.4$  nm), surface slope map taken in the sample sliding direction (the *horizontal axis*; mean = 0.023,  $\sigma = 0.197$ ), and friction force map (mean = 6.2 nN,  $\sigma = 2.1$  nN) for a lubricated thin-film magnetic rigid disk for normal load of 160 nN (after [41])



mechanisms of friction: adhesive, ratchet, and plowing [11, 17]. To first order, we may assume these to be additive. The adhesive mechanism cannot explain the local variation in friction. Next we consider the ratchet mechanism. We consider a small tip sliding over an asperity making an angle  $\theta$  with the horizontal plane (Fig. 12.19). The normal (to the general surface) force  $W$  applied by the tip to the sample surface is constant. The friction force  $F$  on the sample would be a constant for a smooth surface if the friction mechanism does not change. For a rough surface shown in Fig. 12.19, if the adhesive mechanism does not change during sliding, the local value of the coefficient of friction remains constant,

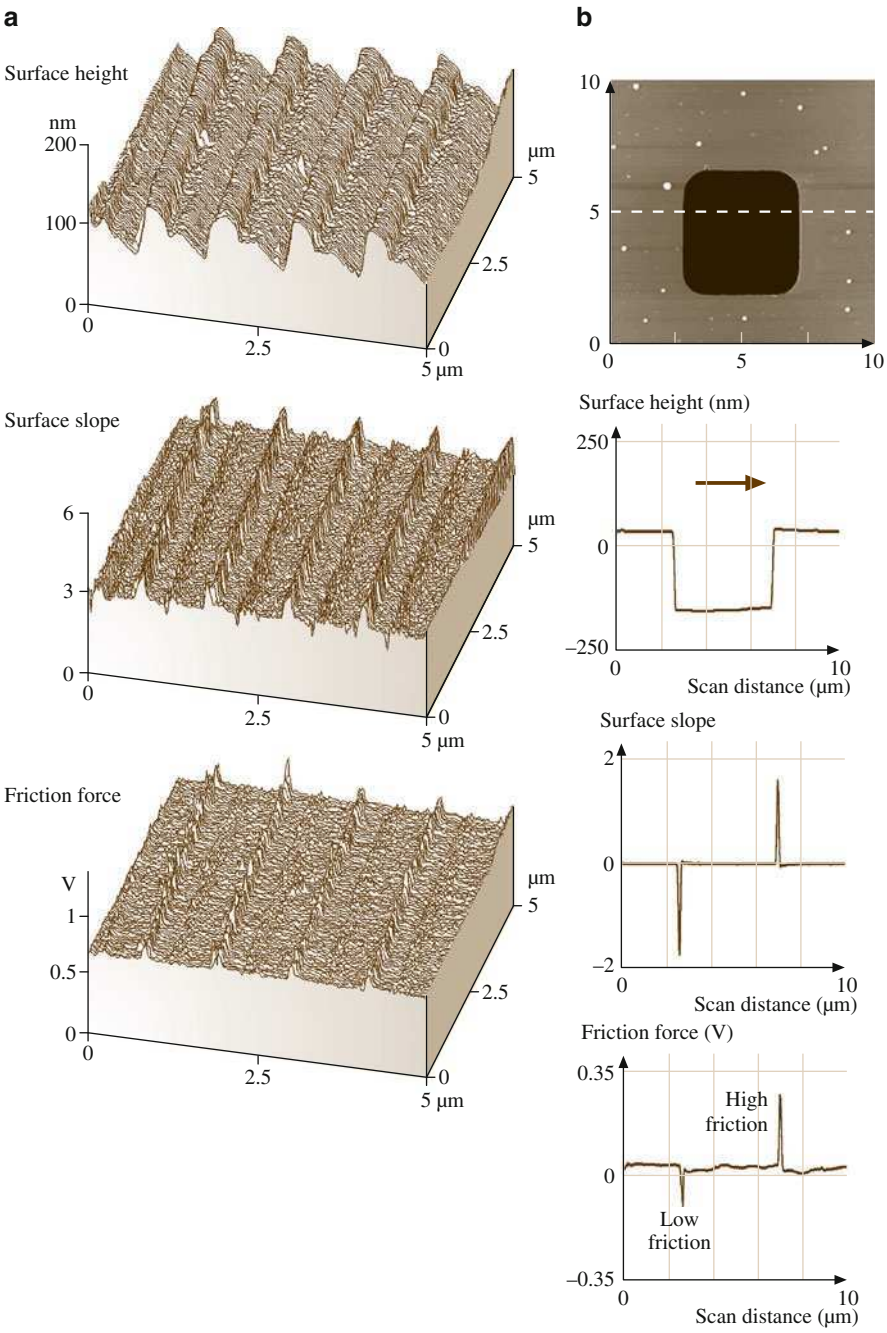


**Fig. 12.18** Surface roughness map, surface slope map taken in the sample sliding direction (*the horizontal axis*), and friction force map for (a) a gold-coated ruler (with somewhat rectangular grids with a pitch of 1  $\mu\text{m}$  and a ruling step height of about 70 nm) at normal load of 25 nN, and (b) a silicon grid (with 5  $\mu\text{m}$  square pits of depth 180 nm and pitch 10  $\mu\text{m}$ ) (after [93])

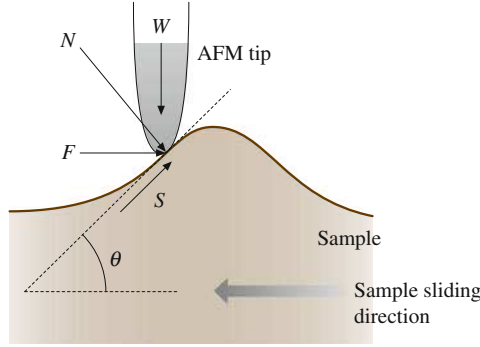


**Fig. 12.19** Schematic illustration showing the effect of an asperity (making an angle  $\theta$  with the horizontal plane) on the surface in contact with the tip on local friction in the presence of the adhesive friction mechanism.  $W$  and  $F$  are the normal and friction forces, respectively, and  $S$  and  $N$  are the force components along and perpendicular to the local surface of the sample at the contact point, respectively

$$\mu_0 = S/N, \quad (12.1)$$

where  $S$  is the local friction force and  $N$  is the local normal force. However, the friction and normal forces are measured with respect to global horizontal and normal axes, respectively. The measured local coefficient of friction  $\mu_1$  in the ascending part is

$$\mu_1 = \frac{F}{W} = \frac{(\mu_0 + \tan \theta)}{(1 - \mu_0 \tan \theta)} \propto \mu_0 + \tan \theta \quad (12.2)$$

for small  $\mu_0 \tan \theta$ ,

indicating that in the ascending part of the asperity one may simply add the friction force and the asperity slope to one another. Similarly, on the right-hand side (descending part) of the asperity,

$$\mu_2 = \frac{(\mu_0 - \tan \theta)}{(1 + \mu_0 \tan \theta)} \propto \mu_0 - \tan \theta, \quad (12.3)$$

for small  $\mu_0 \tan \theta$ .

For a symmetrical asperity, the average coefficient of friction experienced by the FFM tip traveling across the whole asperity is

$$\begin{aligned} \mu_{\text{ave}} &= \frac{(\mu_1 + \mu_2)}{2} \\ &= \mu_0 \frac{(1 + \tan^2 \theta)}{(1 - \mu_0^2 \tan^2 \theta)} \propto \mu_0 (1 + \tan^2 \theta), \end{aligned} \quad (12.4)$$

for small  $\mu_0 \tan \theta$ .

Finally, we consider the plowing component of friction with the tip sliding in either direction, which is [11, 17]

$$\mu_p \propto \tan \theta. \quad (12.5)$$

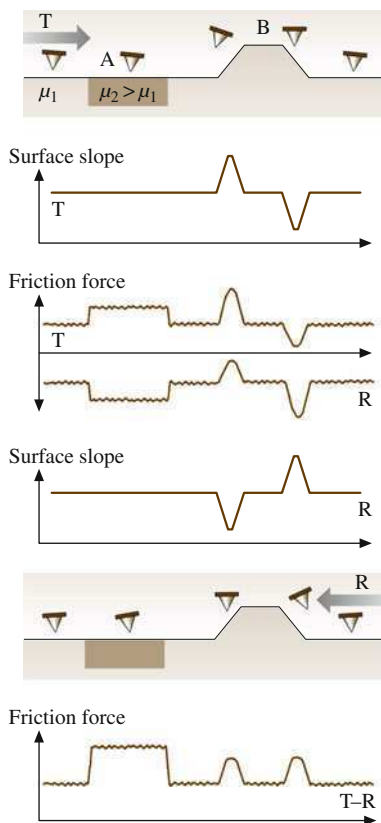
Because in FFM measurements we notice little damage of the sample surface, the contribution from plowing is expected to be small, and the ratchet mechanism is believed to be the dominant mechanism for the local variations in the friction force map. With the tip sliding over the leading (ascending) edge of an asperity, the surface slope is positive; it is negative during sliding over the trailing (descending) edge of an asperity. Thus, measured friction is high at the leading edge of asperities and low at the trailing edge. In addition to the slope effect, the collision of the tip when encountering an asperity with a positive slope produces additional torsion of the cantilever beam leading to higher measured friction force. When encountering an asperity with the same negative slope, however, there is no collision effect and hence no effect on torsion. This effect also contributes to the difference in friction forces when the tip scans up and down on the same topography feature. The ratchet mechanism and the collision effects thus semiquantitatively explain the correlation between the slopes of the roughness maps and friction force maps observed in Figs. 12.17 and 12.18. We note that, in the ratchet mechanism, the FFM tip is assumed to be small compared with the size of asperities. This is valid since the typical radius of curvature of the tips is  $\approx 10\text{--}50$  nm. The radii of curvature of the asperities of the samples measured here (the asperities that produce most of the friction variation) are found to be typically  $\approx 100\text{--}200$  nm, which is larger than that of the FFM tip [94]. It is important to note that the measured local values of friction and normal forces are measured with respect to global (and not local) horizontal and vertical axes, which are believed to be relevant in applications.

### 12.2.3 Directionality Effect on Microfriction

During friction measurements, the friction force data from both the forward (trace) and backward (retrace) scans are useful in understanding the origins of the observed friction forces. Magnitudes of material-induced effects are independent of the scanning direction whereas topography-induced effects are different between forward and backward scanning directions. Since the sign of the friction force changes as the scanning direction is reversed (because of the reversal of torque applied to the end of the tip), addition of the friction force data of the forward and backward scan eliminates the material-induced effects while topography-induced effects remain. Subtraction of the data between forward and backward scans does not eliminate either effect (Fig. 12.20) [93].

Owing to the reversal of the sign of the retrace (R) friction force with respect to the trace (T) data, the friction force variations due to topography are in the same direction (peaks in the trace correspond to peaks in the retrace). However, the

**Fig. 12.20** Schematic of friction forces expected when a tip traverses a sample composed of different materials with sharp changes in topography. A schematic of the surface slope is also shown



magnitudes of the peaks in the trace and retrace at a given location are different. The increase in the friction force experienced by the tip when scanning up a sharp change in topography is greater than the decrease in the friction force experienced when scanning down the same topography change, partly because of the collision effects discussed earlier. Asperities on engineering surfaces are asymmetrical, which also affects the magnitude of the friction force in the two directions. Asymmetry in the tip shape may also have an effect on the directionality of friction. We will note later that the magnitude of the surface slopes are virtually identical, therefore the tip shape asymmetry should not have much effect.

Figure 12.21 shows surface height and friction force data for a gold ruler and a silicon grid in the trace and retrace directions. Subtraction of the two sets of friction data yields a residual peak because of the differences in the magnitudes of the friction forces in the two directions. This effect is observed at all locations of significant changes in topography.

In order to facilitate comparison of the effect of directionality on friction, it is important to take into account the change of sign of the surface slope and friction force in the trace and retrace directions. Figure 12.22 shows surface height, surface

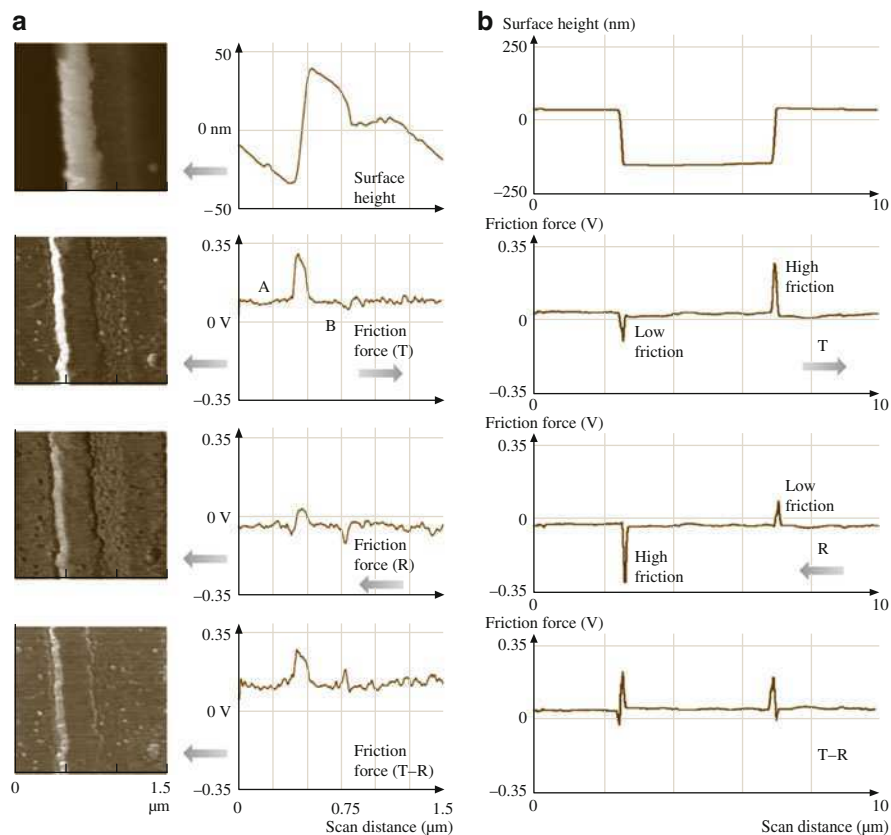


**Fig. 12.21** (a) Gray-scale images and two-dimensional profiles of surface height and friction forces across a single ruling of the gold-coated ruler, and (b) two-dimensional profiles of surface height and friction forces across a silicon grid pit. Friction force data in trace and retrace directions, and subtracted force data are presented

slope, and friction force data for two samples in the trace and retrace directions. The correlations between the surface slope and friction forces are clear. The third column in the figure shows the retrace slope and friction data with an inverted sign ( $-\text{retrace}$ ). Now we can compare trace data with  $-\text{retrace}$  data. It is clear that the friction experienced by the tip is dependent upon the scanning direction because of the surface topography. In addition to the effect of topographical changes discussed earlier, during surface-finishing processes, material can be transferred preferentially onto one side of the asperities, which also causes asymmetry and direction dependence. Reduction of local variations and in the directionality of friction properties requires careful optimization of surface roughness distributions and surface-finishing processes.

The directionality as a result of the effect of surface asperities will also be manifested in macroscopic friction data; i.e., the coefficient of friction may be different



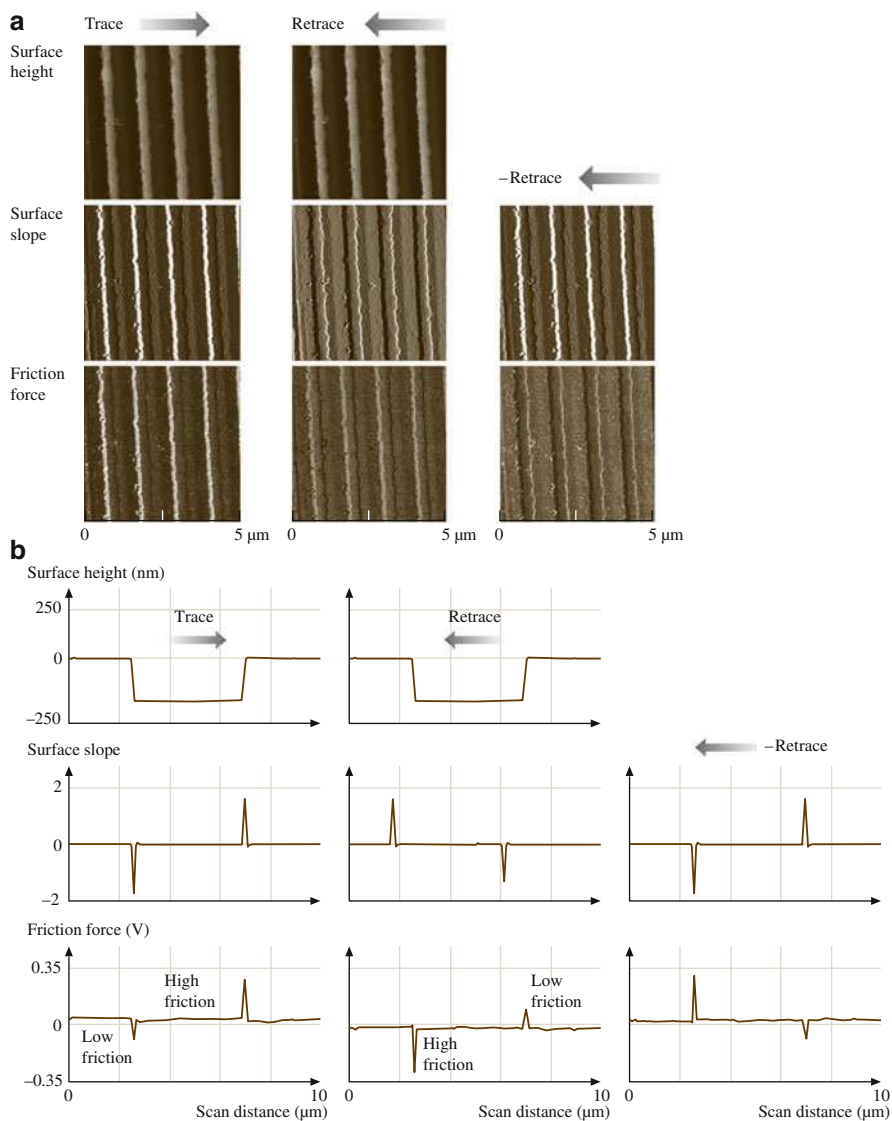


**Fig. 12.22** (a) Gray-scale images of surface heights, surface slopes, and friction forces for scans across a gold-coated ruling, and (b) two-dimensional profiles of surface heights, surface slopes, and friction forces for scans across a silicon grid pit. Arrows indicate the tip sliding direction (after [93])

in one sliding direction than the other. The asymmetrical shape of the asperities accentuates this effect. Frictional directionality can also exist in materials with particles having a preferred orientation. The directionality effect in friction on a macroscale is observed in some magnetic tapes. In a macroscale test, a 12.7 mm-wide polymeric magnetic tape was wrapped over an aluminum drum and slid in a



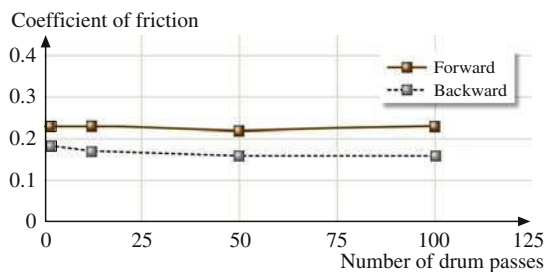


**Fig. 12.23** Coefficient of macroscale friction as a function of drum passes for a polymeric magnetic tape sliding over an aluminum drum in a reciprocating mode in both directions. Normal load = 0.5 N over 12.7 mm-wide tape, sliding speed = 60 mm/s (after [78])

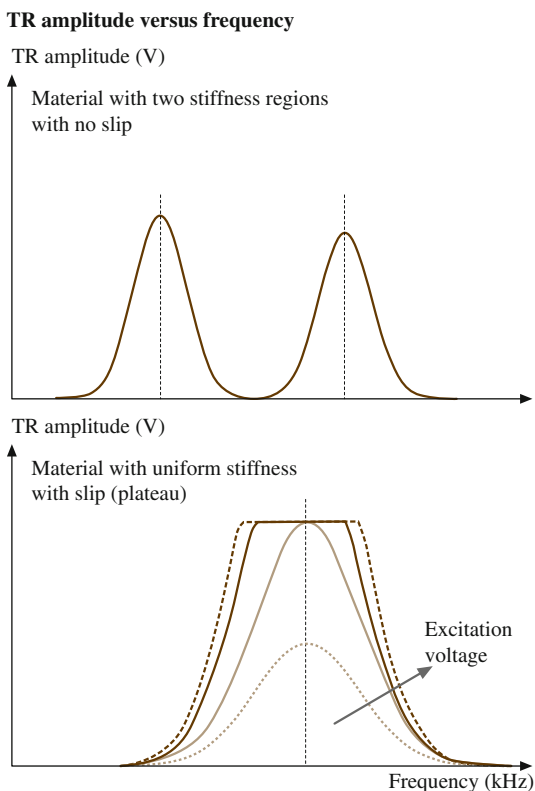
reciprocating motion with a normal load of 0.5 N and a sliding speed of  $\approx 60$  mm/s [4]. The coefficient of friction as a function of sliding distance in either direction is shown in Fig. 12.23. We note that the coefficient of friction on a macroscale for this tape is different in different directions. Directionality in friction is sometimes observed on the macroscale; on the microscale this is the norm [5, 15]. On the macroscale, the effect of surface asperities is usually averaged out over a large number of contacting asperities.

### 12.2.4 Surface-Roughness-Independent Microscale Friction

As just reported, the friction contrast in conventional friction measurements is based on interactions dependent upon interfacial material properties superimposed by roughness-induced lateral forces, and the cantilever twist is dependent on the sliding direction because of the local surface slope. Hence it is difficult to separate friction-induced from roughness-induced cantilever twist in the image. To obtain roughness-independent friction, lateral or torsional modulation techniques are used, in which the tip is oscillated in-plane with a small amplitude at a constant normal load, and change in the shape and magnitude of the cantilever resonance is used as a measure of the friction force [44, 49, 95]. These techniques also allow measurements over a very small region (a few nm to a few  $\mu\text{m}$ ).

Scherer et al. [45] and Reinstädler et al. [46, 47] used the lateral mode for friction measurements (Fig. 12.10b) whereas Bhushan and Kasai [49] used the TR mode for these measurements (Fig. 12.11). Before engagement, the cantilever is driven into torsional motion of the cantilever–tip assembly with a given normal vibration amplitude (the vibration amplitude in free air). After engagement, the vibration amplitude decreases due to the interaction between the tip and the sample, the vibration frequency increases, and phase shift occurs. During scanning, the normal load is kept constant, and the vibration amplitude of the cantilever is measured at the contact frequency.

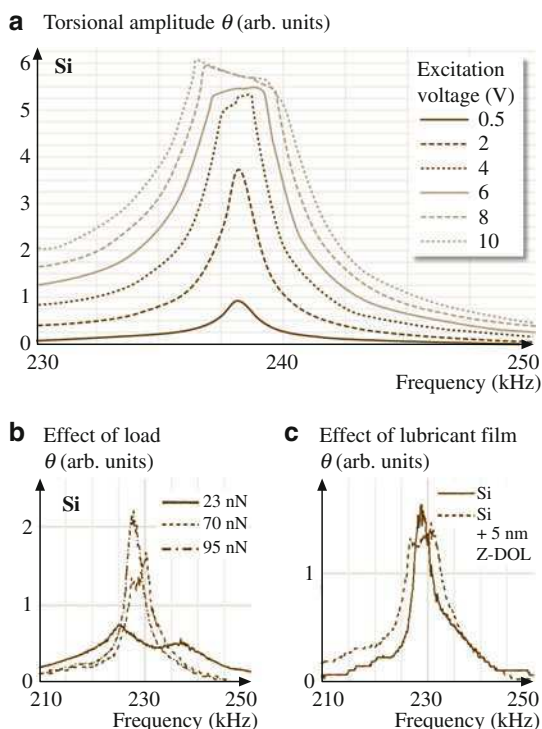
**Fig. 12.24** Schematic showing frequency profiles of the TR amplitude for materials with two phases and a single phase. The maximum TR amplitude at the contact resonant frequency of the resonance curve with a flattened top, resulting from slip, can be used for friction force measurement



As mentioned earlier, the shift in contact resonant frequency in both the lateral and TR modes is a measure of contact stiffness, as shown schematically in Fig. 12.24. At an excitation voltage above a certain value, as a result of microslip at the interface, a flattening of the resonant frequency spectra occurs (Fig. 12.22). At low excitation voltage, the AFM tip sticks to the sample surface and follows the motion like an elastic contact with viscous damping, in which case the resonance curve is Lorentzian with a well-defined maximum. The excitation voltage should be high enough to initiate microslip. The maximum torsional amplitude at a given resonance frequency is a function of the friction force and sample stiffness, so the technique is not valid for inhomogeneous samples. If the torsional stiffness of the cantilever is very high compared with the sample stiffness, the technique should work.

Reinstädler et al. [46] performed lateral-mode experiments on bare Si and Si lubricated with 5 nm-thick chemically bonded perfluoropolyether (Z-DOL) lubricant film. Figure 12.25a shows the amplitude of the cantilever torsional vibration as a function of frequency on a bare silicon sample. The frequency sweep was adjusted such that a contact resonant frequency was covered. The different curves correspond to different excitation voltages applied to the shear wave transducer. At low amplitudes, the shape of the resonance curve is Lorentzian. Above a critical

**Fig. 12.25** Torsional vibration amplitude of the cantilever as a function of excitation frequency. **(a)** Measurement on bare silicon. The different curves correspond to increasing excitation voltages applied to the transducer, and hence increasing surface amplitudes. **(b)** Measurement on silicon lubricated with a 5 nm-thick Z-DOL layer. Curves for three different static loads are shown. The transducer was excited with 5 V of amplitude. **(c)** Measurement with a static load of 70 nN and 7 V excitation amplitude. The two curves correspond to bare silicon and lubricated silicon (after [46])



excitation amplitude of the transducer (excitation voltage = 4 V, corresponding to  $\approx 0.2$  nm lateral surface amplitude as measured by interferometry), the resonance curve flattens out, and the frequency range of the flattened part increases further with the excitation amplitude. Here, the static force applied was 47 nN and the adhesion force was 15 nN. The resonance behavior of the tip–cantilever system in contact with the lubricated silicon sample (Fig. 12.25b) was similar to that with the bare silicon sample. By increasing the static load, the critical amplitude for the appearance of the flattening increases. Deviations from the Lorentzian resonance curve became visible at static loads  $< 95$  nN. As shown in Fig. 12.25c, the resonance curve obtained at the same normal load of 70 nN and the same excitation voltage (7 V) is more flattened on the lubricated sample than on the bare silicon, which led us to conclude that the critical amplitude is lower on the lubricated sample than on the bare sample. These experiments clearly demonstrate that torsional vibration of an AFM cantilever at ultrasonic frequencies leads to stick–slip phenomena and sliding friction. Above a critical vibration amplitude, sliding friction sets in.

Bhushan and Kasai [49] performed friction measurements on a silicon ruler and demonstrated that friction data in TR mode is essentially independent of surface roughness and sliding direction. Figure 12.26a shows surface height and friction force maps on a silicon ruler obtained using the TR-mode and contact-mode techniques. A comparison is made between the TR-mode and contact-mode friction



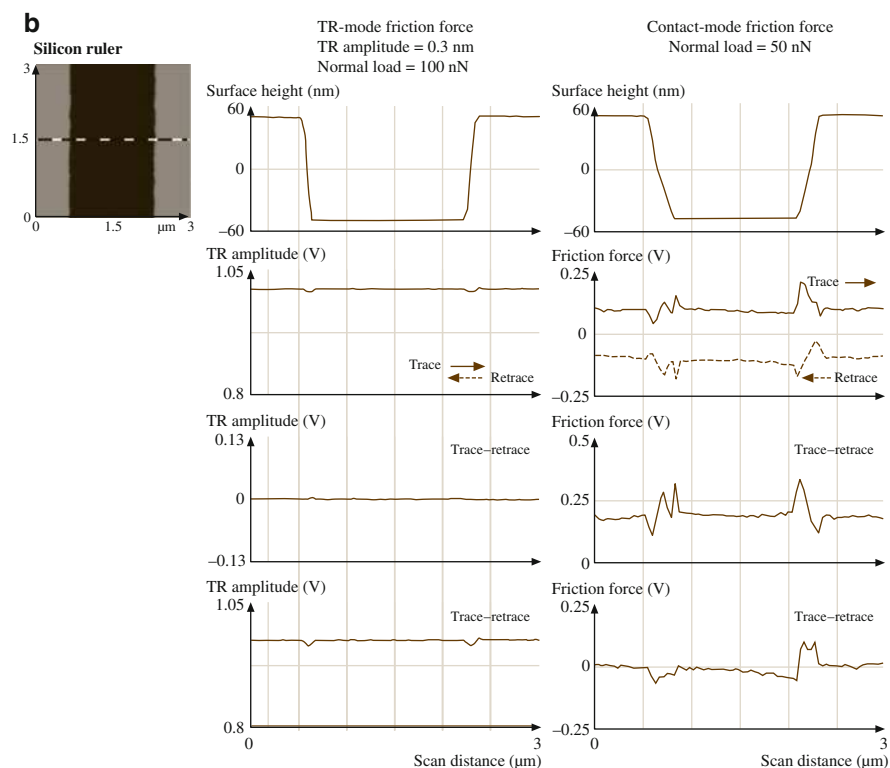


**Fig. 12.26** (a) Comparison between the TR-mode friction and contact-mode friction maps together with line scans, on a silicon ruler. TR-mode surface height and contact-mode surface height images are also shown. (b) Comparison of line scans of TR-mode friction and contact-mode friction on a selected pitch of the silicon ruler (after [49])

force maps. For easy comparison, the line scan profiles near the central area are shown on top of the gray scale maps. The vertical scales of the friction force profiles in the two graphs are selected to cover the same range of friction force so that direct comparison can be made, i.e., 0.25 V at full scale for the TR mode corresponds to 0.5 V for the contact mode in these measurements. As expected, for the trace scan, small downward peaks in the TR-mode map and large upward and downward peaks in the contact-mode map are observed. The positions of these peaks coincide with those of the surface slope; therefore, the peaks in the friction signals are attributed to a topography-induced effect. For the retrace scan, the peak pattern for the TR mode stays similar, but for the contact mode the pattern becomes reversed.

The subtraction image for the TR mode shows almost flat contrast, since the trace and retrace friction data profiles are almost identical. For the contact mode, the subtraction image shows that the topography-induced contribution still exists. As stated earlier, the addition image of the TR mode and the addition image of the contact mode enhance the topography-induced effect, as observed in the figure.

A closer look at the silicon ruler images at one pitch was taken, and the associated images are shown in Fig. 12.26b. The surface-height profiles in the TR mode and contact mode are somewhat different. The TR mode shows sharper edges than those in contact mode. The ratios of the change in amplitude at the steps to the change in the mean amplitude in the TR mode and in the contact mode are a measure of topography effects. The ratio in the contact mode ( $\approx 85\%$ ) is about seven times larger than that in the TR mode ( $\approx 12\%$ ).

### 12.2.5 *Velocity Dependence of Micro/Nanoscale Friction*

AFM/FFM experiments can generally be conducted at relative velocities as high as  $\approx 100\text{--}250\text{ }\mu\text{m/s}$ . To simulate applications, it is of interest to conduct friction experiments at higher velocities (up to 1 m/s). Furthermore, high-velocity experiments would be useful to study the velocity dependence of friction and wear. One approach has been to mount samples on a shear wave transducer (an ultrasonic transducer) and then drive it at very high frequencies (in the MHz range), as reported earlier (Fig. 12.10) [44–48, 95, 97]. The coefficient of friction on the nanoscale is estimated based on the contact resonant frequency and requires the solution of the characteristic equations for the tip vibrating in contact with the sample surface. The approach is complex and depends upon various assumptions.

An alternative approach is to utilize piezo stages with large amplitude ( $\approx 10\text{--}100\text{ }\mu\text{m}$ ) and relatively low resonance frequency (a few kHz) and measure the friction force on the microscale directly using the FFM signal without any analysis with the assumptions used in the previous approaches based on shear wave transducers. A commercial AFM setup modified with this approach can yield sliding velocities up to 200 mm/s [50, 97]. In the high-velocity piezo stage shown in Fig. 12.27a, the single-axis piezo stage is oriented such that the scanning axis is perpendicular to the long axis of the AFM cantilever (which corresponds to the  $90^\circ$  scan angle mode of the commercial AFM). The displacement is monitored using an integrated capacitive feedback sensor, located diametrically opposite to the piezo crystal. The capacitive change, corresponding to the stage displacement, gives a measure of the amount of displacement and can be used as feedback to the piezo controller for better guidance and tracking accuracy during scanning. The closed-loop position control of the piezoelectric-driven stages using capacitive feedback sensors provides linearity of motion better than 0.01% with nanometer resolution and stable drift-free motion [50]. In the ultrahigh-velocity piezo stage shown in Fig. 12.27a, a rectangular monolithic piezoceramic plate (the stator) with two excitation electrodes is resonated using a 12 V power supply. Depending on the desired direction of the motion, the left or right electrode is excited to produce high-frequency eigenmode oscillations up to 200 kHz. Simultaneous eigenmodes result in quasielliptical motion. An alumina friction tip (pusher) attached to the plate pushes a slider with a glued friction bar which rests on a set of bearings. Through its contact with the friction bar, the piezoceramic plate provides microimpulses and

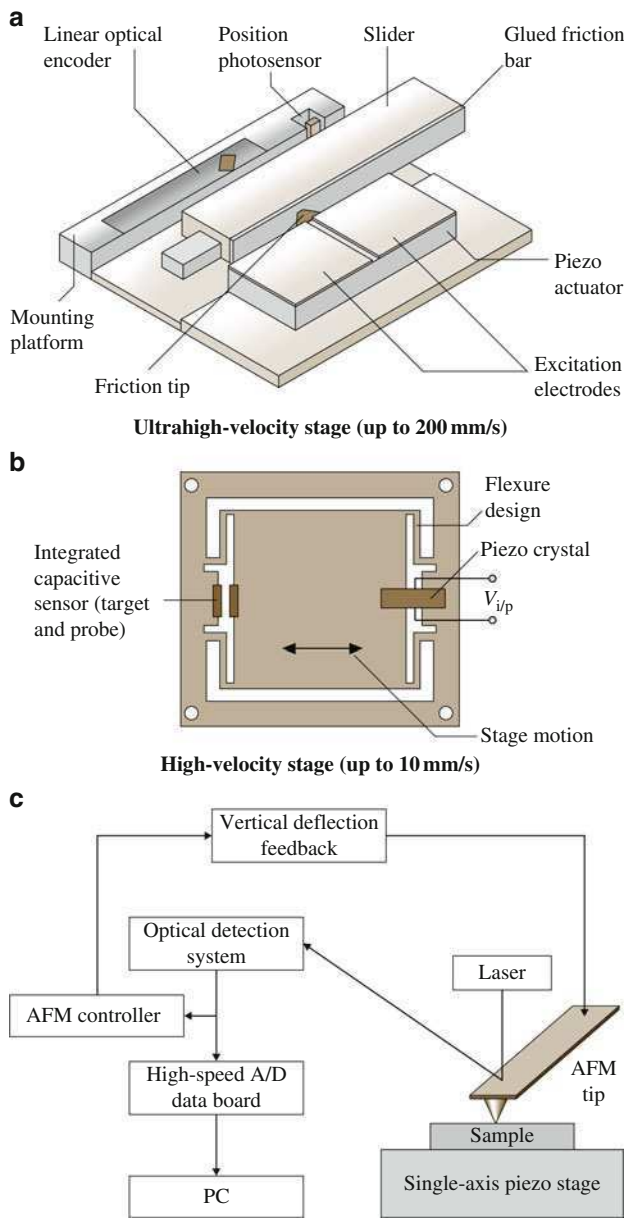


**Fig. 12.27** Schematics of (a) an ultrahigh-velocity piezo stage and (b) a high-velocity piezo stage, and (c) a block diagram of the high-speed data collection and processing system used for friction force measurement (after [50, 96])

drives the slider forward or backward. While the longitudinal oscillation component provides the energy as the driving force, the transverse component serves to change the pressure of the friction tip against the friction bar. The transverse oscillation energy determines the maximum frictional force and hence the holding and driving force of the stage. An optical position reference photosensor is located approximately in the middle of the range of travel and is used to reference the absolute position of the stage within 1  $\mu\text{m}$  repeatability. During motion, the increments of the linear scale from a home (reference) position point are converted to determine position using a linear optical encoder.

A block diagram of the high-speed data collection and processing system used for the friction force measurement is shown in Fig. 12.27b. During the experiments, the AFM cantilever is held stationary by maintaining a scan size of zero. The mounted sample is scanned below the AFM tip by moving stages, and the normal and torsional deflections of the tip are recorded by a photodiode detector. The raw deflection signals from the optical detection system are directly routed to a high-speed data-acquisition A/D board. Raw friction data is acquired at a high sampling rate of up to 80 kilosamples/s.

The velocity dependence of friction for Si(100), diamond-like carbon (DLC), self-assembled monolayer, and perfluoropolyether lubricant films has been studied by Tambe and Bhushan [50, 98–101] and Tao and Bhushan [96, 102]. The friction force as a function of velocity for Si(100) and DLC (deposited by filtered cathodic arc) is shown in Fig. 12.28 on a logarithm velocity scale (middle column). The solid lines in the figure represent the results for a scan length of 1,000  $\mu\text{m}$  with velocity ranging from 1,000 to  $2 \times 10^5$   $\mu\text{m/s}$  using the ultrahigh-velocity stage. The dotted lines represent results for a 25  $\mu\text{m}$  scan length with velocity ranging from 5 to 500  $\mu\text{m/s}$  using the high-velocity stage. To show the friction force dependence on velocity in the lower range clearly, the test results with velocity varying from 5 to 500  $\mu\text{m/s}$  for 25  $\mu\text{m}$  are shown on a magnified scale in the left column of Fig. 12.28.

On the Si(100) sample, the friction force decreased with velocity at low velocities ( $v < 10$   $\mu\text{m/s}$ ) and then increased linearly with  $\log(v)$  for the 25  $\mu\text{m}$  scan length. For the 1,000  $\mu\text{m}$  scan length, the friction force increased linearly with  $\log(v)$  when the velocity was  $< 2 \times 10^4$   $\mu\text{m/s}$ . When the velocity was  $> 2 \times 10^4$   $\mu\text{m/s}$ , the friction force increased linearly with velocity. For DLC, the friction force increased linearly with  $\log(v)$  from 5 to 500  $\mu\text{m/s}$  for the 25  $\mu\text{m}$  scan length. For the 1000  $\mu\text{m}$  scan length, the friction force increased with velocity until about  $2 \times 10^4$   $\mu\text{m/s}$ , where the friction force reaches a maximum, after which the friction force decreased with velocity.

For different samples, the change in the friction force with velocity involves different mechanisms due to the sample surface conditions. The silicon surface is hydrophilic whereas the DLC surface is nearly hydrophobic. Under ambient conditions, a thin water film is condensed on a hydrophilic sample surface. On a hydrophobic surface, with high contact angle, it is difficult for a water film to form on the sample surface, and the effect of the water film on the adhesive force and friction force can be neglected.



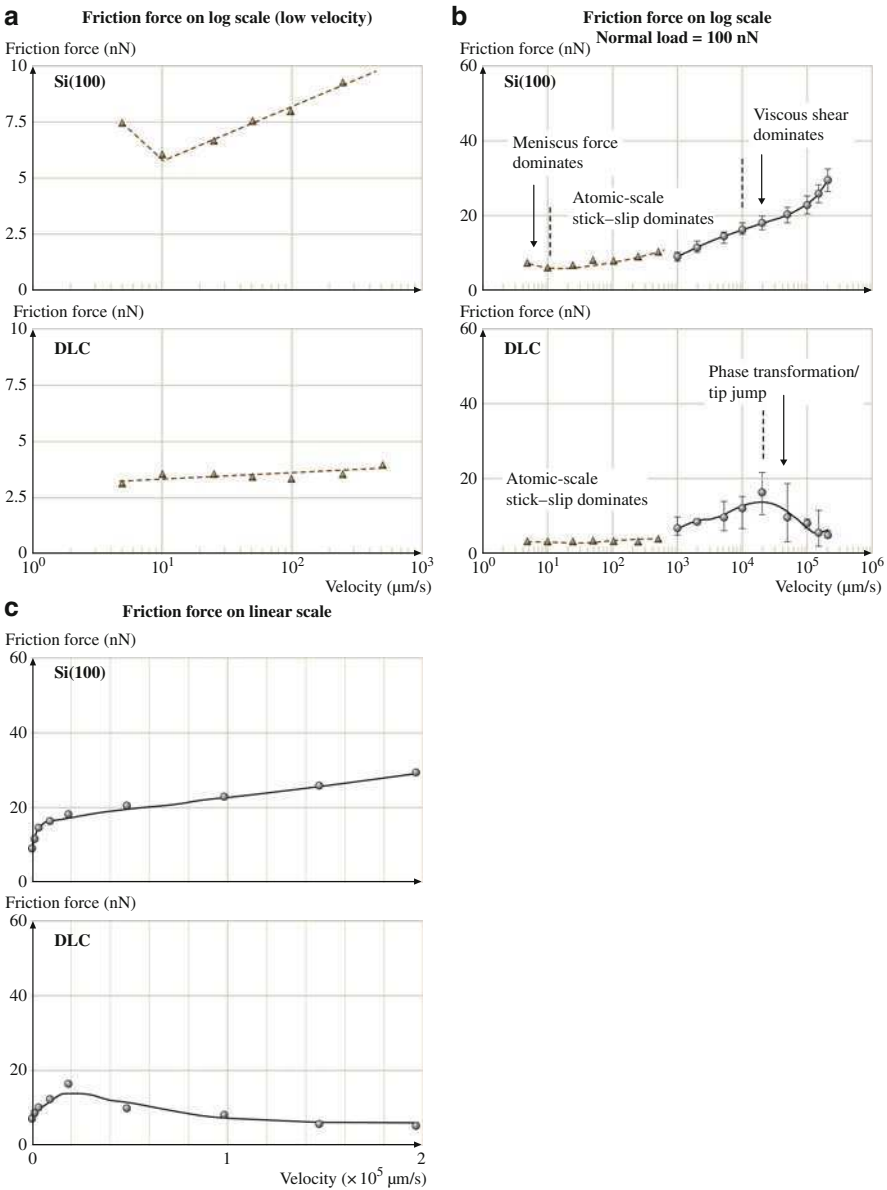


**Fig. 12.28** Friction force as a function of sliding velocity obtained with a 25  $\mu\text{m}$  scan length using a high-velocity stage (*dotted line*) and with a 1000  $\mu\text{m}$  scan length using an ultrahigh-velocity stage (*solid line*). In (a) and (b), velocity is plotted on a logarithmic scale. (a) Lower range of the velocity (1–500  $\mu\text{m/s}$ ). (c) Data at the higher range of velocity on a linear scale (after [102])

On the silicon surface, when the velocity is  $< 10 \mu\text{m/s}$ , the friction force decreased with velocity. This can be explained as follows. The water meniscus bridges develop as a function of time around the tip until reaching the equilibrium condition, being the dominant contributor to the friction force [5, 6, 11, 13, 19]. The motion of the tip results in continuous breaking and reforming of the meniscus bridges. As the tip sliding velocity exceeds a critical velocity ( $10 \mu\text{m/s}$ ), there is not sufficient time for the menisci to reform, and the meniscus force will not play a dominant role any more. Between  $10$  and  $2 \times 10^4 \mu\text{m/s}$ , the friction increases linearly with  $\log(v)$  for both  $25$  and  $1,000 \mu\text{m}$  scan lengths. This logarithmic dependence can be explained by atomic-scale stick-slip [99, 102]. At velocity  $> 2 \times 10^5 \mu\text{m/s}$ , the friction increases linearly with velocity, a trend that can be explained by viscous shear (see the friction force plotted as a function of velocity on a linear magnified scale in the right column of Fig. 12.28).

To explain the atomic-scale stick-slip mechanism of friction, the motion of the tip is expressed by a spring-mass model [103] as

$$m\ddot{x}_t = -\eta\dot{x}_t - k(x_M - x_t) - F, \quad (12.6)$$

where  $m$  is the effective mass of the system,  $\eta$  is the viscous damping coefficient,  $k$  is the spring constant of the cantilever,  $x_M = v_M t$  is the equilibrium position of the cantilever,  $x_t$  is the position of the tip, and  $F$  is the external force. The lateral force is expressed as  $F_l = k(x_M - x_t)$ , and the friction force  $F_{\text{fric}}$  is the lateral force averaged over time.

For velocities  $< 2 \times 10^4 \mu\text{m/s}$ , the damping part ( $\eta\dot{x}_t$ ) in (12.6) is comparatively low, and atomic-scale stick-slip is dominant. To investigate the stick-slip, Tomlinson [88] assumed a periodic surface with potential

$$V(x) = V_0 \left( 1 - \cos \frac{2\pi x}{a} \right), \quad (12.7)$$

where  $V_0$  is the surface barrier potential height and  $a$  is the lattice constant of the surface. Then the force  $F$  in (12.6) can be expressed as

$$F = V'(x) = \frac{2\pi V_0}{a} \sin \left( \frac{2\pi x}{a} \right). \quad (12.8)$$

Based on the Tomlinson model, and taking into account the effect of thermal activation, or the elastic energy stored in the cantilever during sliding, Gnecco et al. [104] derived the relationship between the friction force and velocity, which is expressed as

$$F_{\text{stick-slip}} = F_0 + c \ln v, \quad (12.9)$$

where  $F_0$  and  $c$  are constants.

When the tip slides at high velocities on a solid surface covered by a viscous film such as a water film, the friction force ( $F_{\text{fric}}$ ) is related to the velocity and viscosity of the film by [11]

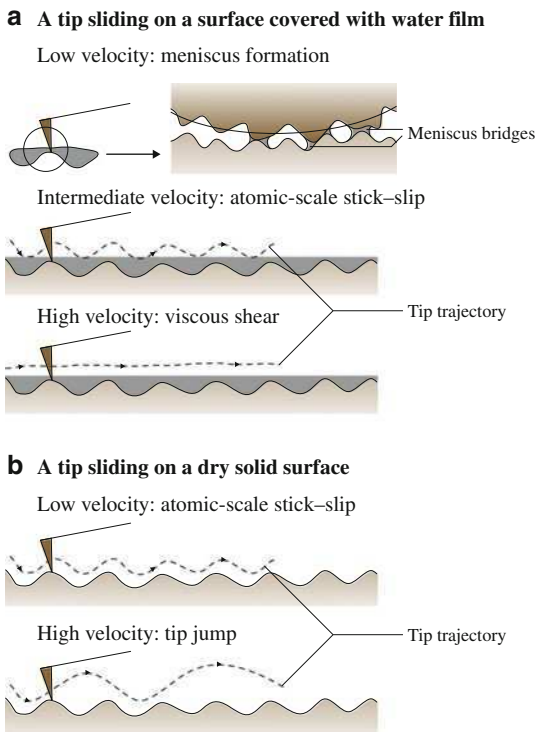
$$F_{\text{fric}} = \mu N + \eta \dot{\gamma} A \approx \mu N + \frac{\eta v A}{d}, \quad (12.10)$$

where  $\mu$  is the coefficient of friction between the dry sliding bodies,  $N$  is the applied load,  $\tau$  is the shear stress,  $A$  is the real contact area,  $\eta$  is the viscosity of the film,  $\dot{\gamma}$  is the velocity gradient,  $v$  is the sliding velocity, and  $d$  is the thickness of the film. Based on (12.10), the relationship between the friction force and the sliding velocity is linear when sliding on a viscous coating. The relationship is consistent with the conclusion by Helman et al. [105] about the linear relationship between the friction force and the sliding velocity ( $F_{\text{fric}} \approx \eta v_M$ ) at high sliding velocities for a spring–mass model in (12.6), which simulates the AFM tip sliding on a viscous liquid.

The sliding of the tip on a hydrophilic surface with a water film at low, intermediate, and high velocities is illustrated schematically in Fig. 12.29a. It should be noted that the stick–slip mechanism considered by Gnecco et al. [104] was based on the investigation on a dry surface. In this study, although the water was condensed on the Si(100) surface, the water film on the surface would not have significant effect on energy dissipation due to surface variation at relatively low velocities. Thus the linear relationship between friction and  $\log(v)$  could be maintained. When the velocity increases above a certain value, the tip would lose direct contact with the sample surface and shear the water film. At velocities  $> 2 \times 10^4 \mu\text{m/s}$ , the asperity deformation from the high-velocity impact could be another mechanism, as proposed by Tambe and Bhushan [99].

For the DLC film, since the surface is nearly hydrophobic, a uniform water film would not form on the surface. When sliding at a velocity lower than  $1,000 \mu\text{m/s}$ , the friction force increased linearly with  $\log(v)$ , which could also be explained by atomic-scale stick–slip. At velocities  $> 1,000 \mu\text{m/s}$ , the friction force increased with velocity until the local maximum at the velocity of  $2 \times 10^4 \mu\text{m/s}$ , then decreased with velocity. The decreasing trend in friction at higher velocities could be due to tip jump during sliding, as illustrated in Fig. 12.29b. Tip jump results in the reduction of the lateral force during sliding. Variation of friction force with distance, indicative of tip jump, was observed from the lateral force signal (not shown). When damping is low and velocity is high, the tip could jump several periodical cycles or several peaks [106]. At a given low damping coefficient, the slip results in a low transient lateral force, as discussed by Fusco and Fasolino [106]. Thus the average lateral force (friction force) over the scan length is low. The tip jump could also cause high-velocity impact of asperities on the DLC surface, resulting in the phase transformation of DLC from  $\text{sp}^3$  to  $\text{sp}^2$ , as explained by Tambe and Bhushan [99]. The layer of  $\text{sp}^2$  phase can act as a lubricant and reduce the interfacial friction.

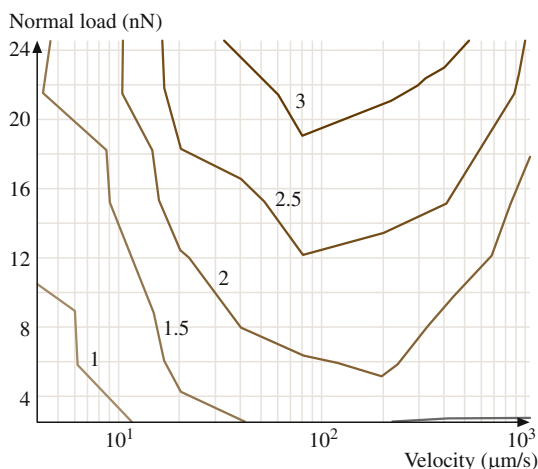
**Fig. 12.29** Schematics of a tip sliding at different velocities on (a) a water-covered surface, and (b) a dry surface (after [102])



### 12.2.6 Nanoscale Friction and Wear Mapping

Contrary to classical friction laws postulated by Amontons and Coulomb centuries ago, nanoscale friction force is found to be strongly dependent on the normal load and sliding velocity. Many materials, coatings, and lubricants that have wide applications show reversals in friction behavior corresponding to transitions between different friction mechanisms [50, 98–100, 108]. Most of the analytical models developed for explaining nanoscale friction behavior have remained limited in their focus and have left investigators short-handed when trying to explain friction behavior spanning multiple regimes. Nanoscale friction maps provide fundamental insights into friction behavior. They help to identify and classify the dominant friction mechanisms as well as to determine the critical operating parameters that influence transitions between different mechanisms [99, 100]. Figure 12.30 shows a nanoscale friction map for DLC with friction mapped as a function of normal load and sliding velocity [107]. The contours represent lines of constant friction force. The friction force is seen to increase with normal load as well as velocity. The increase in friction force with velocity is the result of atomic-scale stick-slip. This is a result of thermal activation of the irreversible jumps of the AFM tip that arise from overcoming the energy barrier between adjacent atomic

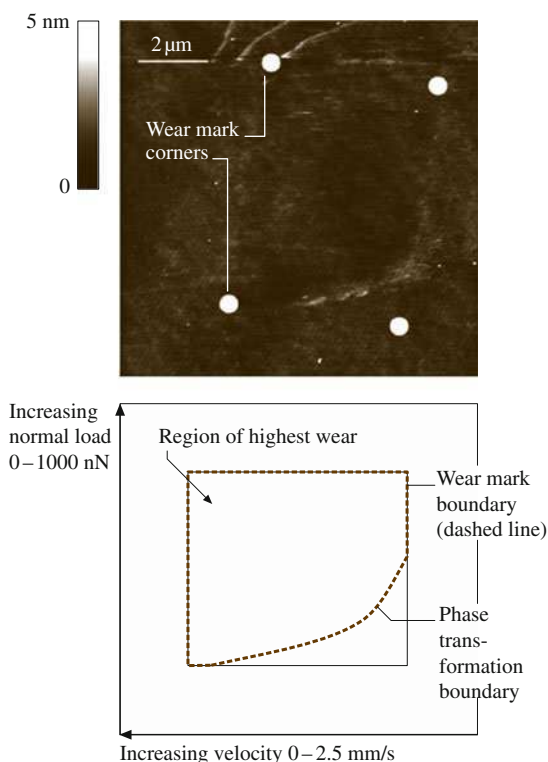
**Fig. 12.30** Contour map showing the dependence of friction force on normal load and sliding velocity for DLC (after [107])



positions, as described earlier. The concentric contour lines corresponding to constant friction force predict a peak point, i.e., a point where the friction force reaches a maxima and beyond which any further increase in normal load or sliding velocity results in a decrease in friction force. This characteristic behavior for DLC is the result of phase transformation of DLC into a graphite-like phase by the  $sp^3$ -to- $sp^2$  phase transition, as described earlier. During the AFM experiments, the  $Si_3N_4$  tip gives rise to contact pressures in the range of 1.8–4.4 GPa for DLC for normal loads of 10–150 nN [109]. A combination of the high contact pressures that are encountered on the nanoscale and the high frictional energy dissipation arising from the asperity impacts at the tip-sample interface due to the high sliding velocities accelerates the phase-transition process whereby a low-shear-strength graphite-like layer is formed at the sliding interface.

Similar to friction mapping, one way of exploring the broader wear patterns is to construct wear mechanism maps that summarize data and models for wear, thereby showing mechanisms for any given set of conditions [108, 110–112]. Wear of sliding surfaces can occur by one or more wear mechanisms, including adhesive, abrasive, fatigue, impact, corrosive, and fretting [6, 11]. Tambe and Bhushan [109, 112] performed AFM experiments to develop nanoscale wear maps. Figure 12.31 shows a nanowear map generated for a DLC sample by simultaneously varying the normal load and sliding velocity over the entire scan area. The wear map was generated for a normal load range of 0–1,000 nN and sliding velocity range of 0–2.5 mm/s. Wear debris, believed to result from the  $sp^3$ -to- $sp^2$  DLC phase transition, was seen to form only for a high value of the product of sliding velocity and normal load, i.e., only beyond a certain threshold of friction energy dissipation [109, 112]. Hence the wear region exhibits a transition line, indicating that for low velocities and low normal loads there is no phase transformation. For clarity, the wear mark corners are indicated by white dots in the AFM image (top) and the two zones of interest over the entire wear mark are illustrated schematically in Fig. 12.31a (top).

**Fig. 12.31** Nanowear map (AFM image and schematic) illustrating the effect of sliding velocity and normal load on the wear of DLC resulting from phase transformation. *Curved area* shows debris lining and is indicative of the minimum frictional energy needed for phase transformation. For clarity, the wear mark corners are indicated by *white dots* in the AFM image and the various zones of interest over the entire wear mark are schematically illustrated (after [112])



Nanoscale friction and wear mapping are novel techniques for investigating friction and wear behavior on the nanoscale over a range of operating parameters. By simultaneously varying the sliding velocity and normal load over a large range of values, nanoscale friction and wear behavior can be mapped, and the transitions between different wear mechanisms can be investigated. These maps help identify and demarcate critical operating parameters for different wear mechanisms and are very important tools in the process of design and selection of materials/coatings.

### 12.2.7 Adhesion and Friction in Wet Environments

#### Experimental Observations

Relative humidity affects adhesion and friction for dry and lubricated surfaces [18, 43, 113]. Figure 12.32 shows the variation of single-point adhesive force measurements as a function of tip radius on a Si(100) sample for several humidities. The adhesive force data are also plotted as a function of relative humidity for several tip radii. The general trend at humidities up to the ambient is that

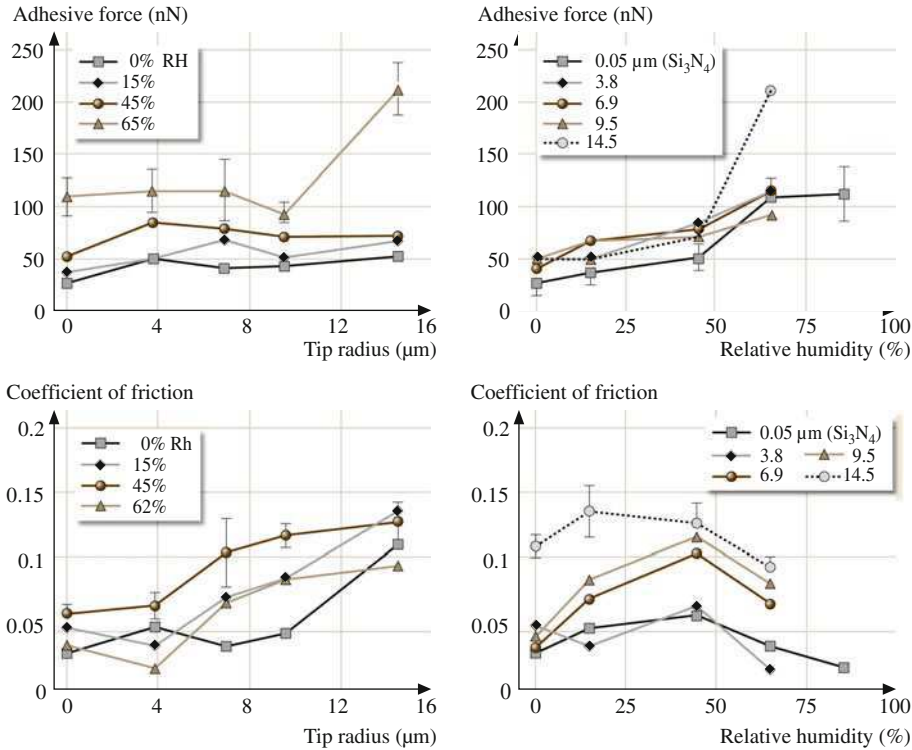


**Fig. 12.32** Adhesive force and coefficient of friction as a function of tip radius at several humidities and as a function of relative humidity at several tip radii on Si(100) (after [43])

a 50 nm-radius Si<sub>3</sub>N<sub>4</sub> tip exhibits a lower adhesive force compared with other microtips of larger radii; in the latter case, values are similar. Thus, for the microtips there is no appreciable variation in adhesive force with tip radius at given humidity up to ambient. The adhesive force increases with the relative humidity for all tips.

Sources of adhesive force between a tip and a sample surface are van der Waals attraction and meniscus formation [6, 11, 18]. The relative magnitudes of the forces from these two sources are dependent upon various factors, including the distance between the tip and the sample surface, their surface roughness, their hydrophobicity, and the relative humidity [114]. For most rough surfaces, the meniscus contribution dominates at moderate to high humidities, due to capillary condensation of water vapor from the environment. If enough liquid is present to form a meniscus bridge, the meniscus force should increase with increasing tip radius (proportional to the tip radius for a spherical tip). In addition, an increase in tip radius results in increased contact area, leading to higher values of the van der Waals forces. However, if nanoasperities on the tip and sample are considered, then the number of contacting and near-contacting asperities forming meniscus bridges increases with increasing humidity, leading to an increase in the meniscus forces. These explain the trends observed in Fig. 12.32. From the data, the tip radius has

little effect on the adhesive forces at low humidities but increases with tip radius at high humidity. The adhesive force also increases with increasing humidity for all tips. This observation suggests that the thickness of the liquid film at low humidity is insufficient to form continuous meniscus bridges to affect the adhesive forces in the case of all tips.

Figure 12.32 also shows the variation in the coefficient of friction as a function of tip radius at a given humidity, and as a function of relative humidity for a given tip radius for Si(100). It can be observed that for 0% relative humidity (RH), the coefficient of friction is about the same for all the tip radii except the largest one, which shows a higher value. At all other humidities, the trend consistently shows that the coefficient of friction increases with tip radius. An increase in friction with tip radius at low to moderate humidities arises from increased contact area (higher van der Waals forces) and the higher values of the shear forces required for the larger contact area. At high humidities, similar to the adhesive force data, an increase with tip radius occurs because of both contact area and meniscus effects. Although AFM/FFM measurements are able to measure the combined effect of the contribution of van der Waals and meniscus forces towards friction force or adhesive force, it is difficult to measure their individual contributions separately. It can be seen that, for all tips, the coefficient of friction increases with humidity up to about ambient, beyond which it starts to decrease. The initial increase in the coefficient of friction with humidity arises from the fact that the thickness of the water film increases with increasing humidity, which results in a larger number of nanoasperities forming meniscus bridges and higher friction (larger shear force). The same trend is expected for microtips beyond 65% RH. This is attributed to the fact that, at higher humidity, the adsorbed water film on the surface acts as a lubricant between the two surfaces. Thus the interface is changed at higher humidities, resulting in lower shear strength and hence lower friction force and coefficient of friction.

### Adhesion and Friction Force Expressions for a Single-Asperity Contact

We now obtain the expressions for the adhesive force and coefficient of friction for a single-asperity contact with a meniscus formed at the interface (Fig. 12.33).

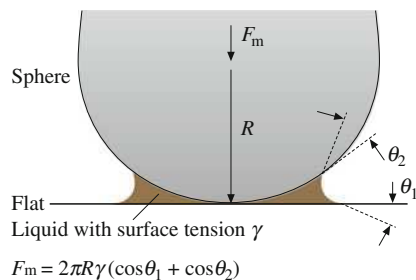


**Fig. 12.33** Meniscus formation from a liquid condensate at the interface for a sphere in contact with a plane surface



For a spherical asperity of radius  $R$  in contact with a flat, smooth surface with composite modulus of elasticity  $E^*$  and in the presence of a liquid with a concave meniscus, the attractive meniscus force (adhesive force), designated as  $F_m$  or  $W_{ad}$ , is given by [7, 11]

$$W_{ad} = 2\pi R\gamma(\cos \theta_1 + \cos \theta_2), \quad (12.11)$$

where  $\gamma$  is the surface tension of the liquid and  $\theta_1$  and  $\theta_2$  are the contact angles of the liquid with surfaces 1 and 2, respectively. For an elastic contact for both extrinsic ( $W$ ) and intrinsic ( $W_{ad}$ ) normal load, the friction force is given by

$$F_e = \pi\tau \left( \frac{3(W + W_{ad})R}{4E^*} \right)^{\frac{2}{3}}, \quad (12.12)$$

where  $W$  is the external load and  $\tau$  is the average shear strength of the contacts. (Surface energy effects are not considered here.) Note that adhesive force increases linearly with increasing tip radius, and the friction force increases with tip radius as  $R^{2/3}$  and with normal load as  $(W + W_{ad})^{2/3}$ . Experimental data in support of the  $W^{2/3}$  dependence on the friction force can be found in various references [115]. The coefficient of friction  $\mu_e$  is obtained from (12.12) as

$$\mu_e = \frac{F_e}{(W + W_{ad})} = \pi\tau \left( \frac{3R}{4E^*} \right)^{\frac{2}{3}} \frac{1}{(W + W_{ad})^{\frac{1}{3}}}. \quad (12.13)$$

In the plastic contact regime [7], the coefficient of friction  $\mu_p$  is obtained as

$$\mu_p = \frac{F_p}{(W + W_{ad})} = \frac{\tau}{H_s}, \quad (12.14)$$

where  $H_s$  is the hardness of the softer material. Note that, in the plastic contact regime, the coefficient of friction is independent of the external load, adhesive contributions, and surface geometry.

For comparison, for multiple-asperity contacts in the elastic contact regime, the total adhesive force  $W_{ad}$  is the summation of the adhesive forces at  $n$  individual contacts,

$$W_{ad} = \sum_{i=1}^n (W_{ad})_i \quad (12.15)$$

and

$$\mu_e \approx \frac{3.2\tau}{E^* \left( \frac{\sigma_p}{R_p} \right)^{\frac{1}{2}} + \left( \frac{W_{ad}}{W} \right)},$$

where  $\sigma_p$  and  $R_p$  are the standard deviation of the summit heights and the average summit radius, respectively. Note that the coefficient of friction depends upon the surface roughness. In the plastic contact regime, the expression for  $\mu_p$  in (12.14) does not change.

The sources of the adhesive force in a wet contact in AFM experiments performed in an ambient environment include mainly attractive meniscus force due to capillary condensation of water vapor from the environment. The meniscus force for a single contact increases with an increase in tip radius. A sharp AFM tip in contact with a smooth surface at low loads (on the order of a few nN) for most materials can be simulated as a single-asperity contact. At higher loads, for rough and soft surfaces, multiple contacts would occur. Furthermore, at low loads (nN range) for most materials the local deformation would be primarily elastic. Assuming that the shear strength of contacts does not change, the adhesive force for smooth and hard surfaces at low normal load (on the order of a few nN) (for a single-asperity contact in the elastic contact regime) would increase with increasing tip radius, and the coefficient of friction would decrease with increasing total normal load as  $(W + W_{ad})^{-1/3}$  and would increase with increasing tip radius as  $R^{2/3}$ . In this case, the Amontons law of friction, which states that the coefficient of friction is independent of normal load and independent of apparent area of contact, does not hold. For a single-asperity plastic contact and multiple-asperity plastic contacts, neither the normal load nor the tip radius comes into play in the calculation of the coefficient of friction. In the case of multiple-asperity contacts, the number of contacts increases with increasing normal load; therefore the adhesive force increases with increasing load.

In the data presented earlier in this section, the effect of tip radius and humidity on the adhesive forces and coefficient of friction is investigated for experiments with Si(100) surface at loads in the range 10–100 nN. The multiple-asperity elastic-contact regime is relevant for this study involving large tip radii. An increase in humidity generally results in an increase in the number of meniscus bridges, which would increase the adhesive force. As suggested earlier, this increase in humidity may also decrease the shear strength of contacts. A combination of an increase in adhesive force and a decrease in shear strength would affect the coefficient of friction. An increase in tip radius would increase the meniscus force (adhesive force). A substantial increase in the tip radius may also increase the interatomic forces. These effects influence the coefficient of friction with increasing tip radius.

### ***12.2.8 Separation Distance Dependence of Meniscus and van der Waals Forces***

When two surfaces are in close proximity, sources of adhesive forces are weak van der Waals attraction and meniscus formation. The relative magnitudes of the forces from these two sources are dependent upon various factors, including the

interplanar separation, their surface roughness, their hydrophobicity, and the relative humidity (liquid volume) [114]. The meniscus contribution dominates at moderate to high humidities, whereas van der Waals forces dominate at asperities a few nm apart. In some micro/nanocomponents, it is important to know the relative contribution of these two sources as a function of interplanar separation in order to design an interface for low adhesion. For example, if two ultrasMOOTH surfaces come into close proximity, with an interplanar separation on the order of 1 nm, van der Waals forces may dominate, and their magnitude may be reduced by creating bumps on one of the interfaces. This analysis is also of interest in AFM studies to understand the distance dependence of adhesive forces as the tip goes in and out of contact.

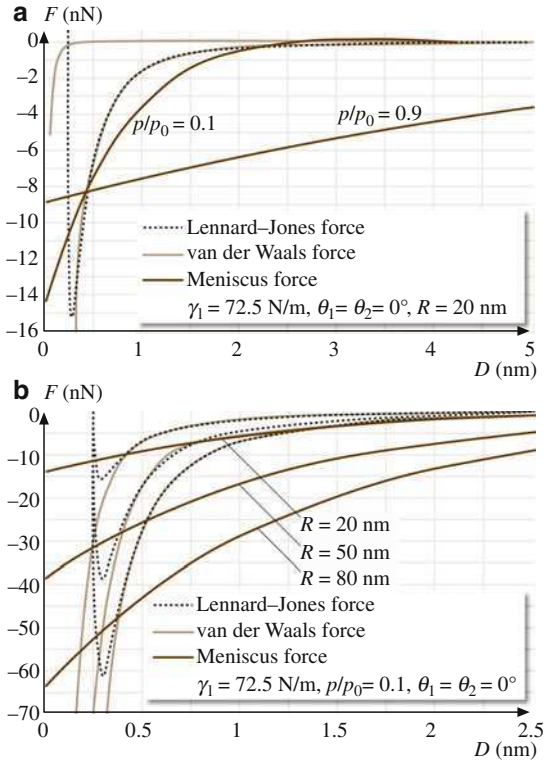
Stifter et al. [114] modeled the contact of a parabolic-shaped tip and a flat, smooth sample surface. The tip may represent a surface asperity on an interface or an AFM tip in an AFM experiment. They calculated van der Waals and meniscus forces as a function of various parameters, namely tip geometry, tip-sample starting distance, relative humidity, surface tension, and contact angle. They compared the meniscus forces with van der Waals forces to understand their relative importance under various operating conditions.

The interaction force between the tip and sample under dry conditions is the Lennard-Jones force derived from the Lennard-Jones potential. The Lennard-Jones potential is composed of two interactions – the van der Waals attraction and Pauli repulsion. van der Waals forces are significant because they are always present. For a parabolic tip above a half-plane with a separation  $D$  between the tip and plane, the Lennard-Jones potential is obtained by integrating the atomic potential over the volume of the tip and sample. It is given as [114]

$$V(D) = \frac{c}{12} \left( -\frac{A}{D} + \frac{B}{210D^7} \right), \quad (12.16)$$

where  $c$  is the width of the parabolic tip (= the diameter in the case of a spherical tip), and  $A$  and  $B$  are two potential parameters, where  $A$  is Hamaker constant. Equation (12.16) provides expressions for attractive and repulsive parts. The calculations were made for Lennard-Jones force (total) and van der Waals force (attractive part) for two Hamaker constants:  $0.04 \times 10^{-19}$  J (representative of polymers) and  $3.0 \times 10^{-19}$  J (representative of ceramics), and meniscus force for a water film ( $\gamma_\ell = 72.5$  N/m). Figure 12.34 shows various forces as a function of separation distance. The effect of two relative humidities and three tip radii, which affect meniscus forces, was also studied. The two dashed curves indicate the spread of possible van der Waals forces for the two Hamaker constants. The figure shows that meniscus forces exhibit weaker distance dependence. The meniscus forces can be stronger or weaker than the van der Waals forces for distances smaller than  $\approx 0.5$  nm. For longer distances, the meniscus forces are stronger than the van der Waals forces. van der Waals forces must be considered for a tip-sample distance up to a few nm ( $D < 5$  nm). The meniscus forces operate up to breakage of the meniscus in the range from 5 to 20 nm [114].

**Fig. 12.34** Relative contribution of meniscus, van der Waals, and Lennard–Jones forces ( $F$ ) as a function of separation distance ( $D$ ) and at (a) two values of relative humidity ( $p/p_0$ ) for tip radius of 20 nm and Hamaker constants of  $0.04 \times 10^{-19}$  and  $3.0 \times 10^{-19}$  J, and (b) three tip radii ( $R$ ) and Hamaker constant of  $3.0 \times 10^{-19}$  J (after [114])



### 12.2.9 Scale Dependence in Friction

Table 12.3 presents adhesive force and coefficient of friction data obtained on the nanoscale and microscale [38, 98, 116, 117]. Adhesive force and coefficient of friction values on the nanoscale are about half to one order of magnitude lower than that on the microscale. Scale dependence is clearly observed in this data. As a further evidence of scale dependence, Table 12.4 shows the coefficient of friction measured for Si(100), HOPG, natural diamond, and DLC on the nanoscale and microscale. It is clearly observed that friction values are scale dependent.

To estimate the scale length, the apparent contact radius at test loads was calculated and is presented in the table. Mean apparent pressures are also calculated and presented. For nanoscale AFM experiments, it is assumed that an AFM tip coming into contact with a flat surface represents a single-asperity elastic contact, and Hertz analysis was used for the calculations. In the microscale experiments, a ball coming into contact with a flat surface represents multiple-asperity contacts due to the roughness, and the contact pressure of the asperity contacts is higher than the apparent pressure. For the calculation of a characteristic scale length for

**Table 12.3** Micro- and nanoscale values of adhesive force and coefficient of friction in micro- and nanoscale measurements (after [116])

Sample	Adhesive force		Coefficient of friction	
	Microscale <sup>a</sup> ( $\mu\text{N}$ )	Nanoscale <sup>b</sup> (nN)	Microscale <sup>a</sup>	Nanoscale <sup>b</sup>
Si(100)	685	52	0.47	0.06
DLC	325	44	0.19	0.03
Z-DOL	315	35	0.23	0.04
HDT	180	14	0.15	0.006

<sup>a</sup>Versus 500  $\mu\text{m}$  radius Si(100) ball<sup>b</sup>Versus 50 nm radius  $\text{Si}_3\text{N}_4$  tip

multiple-asperity contacts, which is equal to the apparent length of contact, Hertz analysis was also used. This analysis provides an upper limit on apparent radius and lower limit on the mean contact pressure.

There are several factors responsible for the differences in the coefficients of friction at the micro- and nanoscale. Among these are the contributions from wear and contaminant particles, the transition from elasticity to plasticity, and the meniscus effect. The contribution of wear and contaminant particles is more significant at the macro/microscale because of the larger number of trapped particles, referred to as the third-body contribution. It can be argued that for nanoscale AFM experiments the asperity contacts are predominantly elastic (with average real pressure being less than the hardness of the softer material), and adhesion is the main contributor to the friction, whereas for microscale experiments the asperity contacts are predominantly plastic, and deformation is an important factor. It will be shown later that hardness has a scale effect; it increases with decreasing scale and is responsible for less deformation on a smaller scale. The meniscus effect results in an increase of friction with increasing tip radius (Fig. 12.32). Therefore, the third-body contribution, the scale-dependent hardness, and other properties transition from elastic contacts in nanoscale contacts to plastic deformation in microscale contacts, and the meniscus contribution plays an important role [118, 125, 126].

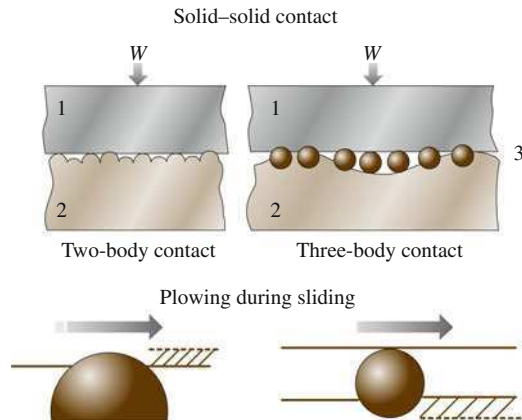
Friction is a complex phenomenon, which involves asperity interactions involving adhesion and deformation (plowing). Adhesion and plastic deformation imply energy dissipation, which is responsible for friction (Fig. 12.35) [6, 11]. A contact between two bodies takes place on high asperities, and the real area of contact ( $A_r$ ) is a small fraction of the apparent area of contact. During the contact of two asperities, a lateral force may be required for asperities of a given slope to climb against each other. This mechanism is known as the ratchet mechanism, and it also contributes to the friction. Wear and contaminant particles present at the interface, referred as the *third body*, also contribute to the friction (Fig. 12.35). In addition, during contact, even at low humidity, a meniscus is formed (Fig. 12.33). Generally any liquid that wets or has a small contact angle on surfaces will condense from vapor into cracks and pores on surfaces as bulk liquid and in the form of annular-shaped capillary condensate in the contact zone. A quantitative theory of scale effects in friction should consider the effect of scale on physical properties relevant to various contributions.

**Table 12.4** Micro- and nanoscale values of the coefficient of friction, typical physical properties of specimen, and calculated apparent contact radii and apparent contact pressures at loads used in micro- and nanoscale measurements. For calculation purposes it is assumed that contacts on micro- and nanoscale are single-asperity elastic contacts (after [118])

Sample	Coefficient of friction		Elastic modulus (GPa)	Poisson's ratio	Hardness (GPa)	Apparent contact radius at test load for		Mean apparent pressure at test load for	
	Microscale	Nanoscale				Microscale (μm) (upper limit)	Nanoscale (nm)	Microscale (GPa) (lower limit)	Nanoscale (GPa)
Si(100) wafer	0.47 <sup>a</sup>	0.06 <sup>b</sup>	130 <sup>c,d</sup>	0.28 <sup>d</sup>	9–10 <sup>c,d</sup>	0.8–2.2 <sup>a</sup>	1.6–3.4 <sup>b</sup>	0.05–0.13 <sup>a</sup>	1.3–2.8 <sup>b</sup>
Graphite (HOPG)	0.1 <sup>e</sup>	0.006 <sup>b</sup>	9–15 <sup>f</sup> (9)	– (0.25)	0.01 <sup>g</sup>	62 <sup>e</sup>	3.4–7.4 <sup>b</sup>	0.082 <sup>e</sup>	0.27–0.58 <sup>b</sup>
Natural diamond	0.2 <sup>e</sup>	0.05 <sup>b</sup>	1140 <sup>h</sup>	0.07 <sup>h</sup>	80–104 <sup>f,h</sup>	21 <sup>e</sup>	1.1–2.5 <sup>b</sup>	0.74 <sup>e</sup>	2.5–5.3 <sup>b</sup>
DLC film	0.19 <sup>a</sup>	0.03 <sup>i</sup>	280 <sup>j</sup>	0.25 <sup>j</sup>	20–30 <sup>j</sup>	0.7–2.0 <sup>a</sup>	1.3–2.9 <sup>i</sup>	0.06–0.16 <sup>a</sup>	1.8–3.8 <sup>i</sup>

<sup>a</sup>500 μm-radius Si(100) ball at 100–2000 μN and 720 μm/s in dry air [116]  
<sup>b</sup>50 nm-radius Si<sub>3</sub>N<sub>4</sub> tip at load range from 10–100 nN and 0.5 nm/s, in dry air [38]  
<sup>c</sup>[120]  
<sup>d</sup>[120]  
<sup>e</sup>3 mm-radius Si<sub>3</sub>N<sub>4</sub> ball (elastic modulus 310 GPa, Poisson's ratio 0.22 [110]) at 1 N and 800 μm/s [38]  
<sup>f</sup>[119]  
<sup>g</sup>[124]  
<sup>h</sup>[122]  
<sup>i</sup>50 nm-radius Si<sub>3</sub>N<sub>4</sub> tip at load range from 10–100 nN in dry air [116]  
<sup>j</sup>[123]

**Fig. 12.35** Schematic of two-body and three-body dry contacts of rough surfaces



According to the adhesion and deformation model of friction, the coefficient of dry friction  $\mu$  is the sum of an adhesion component  $\mu_a$  and a deformation (plowing) component  $\mu_d$ . The latter, in the presence of particles, is the sum of an asperity-summit deformation component  $\mu_{ds}$  and a particle-deformation component  $\mu_{dp}$ , so that the total coefficient of friction is [125]

$$\begin{aligned}\mu &= \mu_a + \mu_{ds} + \mu_{dp} = \frac{F_a + F_{ds} + F_{dp}}{W} \\ &= \frac{A_{ra}\tau_a + A_{ds}\tau_{ds} + A_{dp}\tau_{dp}}{W},\end{aligned}\quad (12.17)$$

where  $W$  is the normal load,  $F$  is the friction force, and  $A_{ra}$ ,  $A_{ds}$ , and  $A_{dp}$  are the real areas of contact during adhesion, two-body deformation, and with particles, respectively;  $\tau$  is the shear strength. The subscripts “a”, “ds”, and “dp” correspond to adhesion, summit deformation, and particle deformation, respectively.

The adhesional component of friction depends on the real area of contact and adhesion shear strength. The real area of contact is scale dependent due to the scale dependence of the surface roughness (for elastic and plastic contacts) and due to the scale dependence of hardness (for plastic contacts) [125]. We limit the analysis here to multiple-asperity contacts. For this case, the scale  $L$  is defined as the apparent size of the contact between the two bodies. (For completeness, for single-asperity contact, the scale is defined as the contact diameter.) It is suggested by Bhushan and Nosonovsky [127] that, for many materials, dislocation-assisted sliding (micro-slip) is the main mechanism responsible for the shear strength. They considered dislocation-assisted sliding based on the assumption that contributing dislocations are located in a subsurface volume. The thickness of this volume is limited by the distance which dislocations can climb  $\ell_s$  (a material parameter) and by the radius of contact  $a$ . They showed that  $\tau_a$  is scale dependent. Based on this, the adhesional

components of the coefficient of friction in the case of elastic contact  $\mu_{ae}$  and in the case of plastic contact  $\mu_{ap}$  are given by [127]

$$\mu_{ae} = \frac{\mu_{ae0}}{\sqrt{\ell + \left(\frac{\ell_s}{a_0}\right)}} \left(\frac{L}{L_{\ell c}}\right)^{m-n} \times \sqrt{1 + \left(\frac{L_s}{L}\right)^m}, \quad L < L_{\ell c}, \quad (12.18)$$

$$\mu_{ap} = \mu_{ap0} \sqrt{\frac{1 + \left(\frac{\ell_d}{a_0}\right)}{1 + \left(\frac{\ell_s}{a_0}\right)}} \sqrt{\frac{1 + \left(\frac{L_s}{L}\right)^m}{1 + \left(\frac{\ell_d}{L}\right)^m}}, \quad L < L_{\ell c}, \quad (12.19)$$

where  $\mu_{ae0}$  and  $\mu_{ap0}$  are the values of the coefficient of friction at the macroscale ( $L \geq L_{\ell c}$ ),  $m$  and  $n$  are indices that characterize the scale dependence of surface parameters,  $\bar{a}_0$  is the macroscale value of the mean contact radius,  $L_{\ell c}$  is the long-wavelength limit for scale dependence of the contact parameters,  $\ell_s$  and  $\ell_d$  are material-specific characteristic length parameters, and  $L_s$  and  $L_d$  are length parameters related to  $\ell_s$  and  $\ell_d$ . The scale dependence of the adhesional component of the coefficient of friction is presented in Fig. 12.36, based on (12.18) and (12.19).

Based on the assumption that multiple asperities of two rough surfaces in contact have a conical shape, the two-body deformation component of friction can be determined as [6, 11]

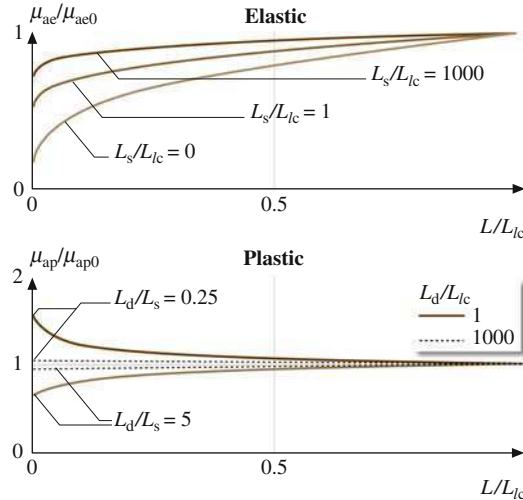


**Fig. 12.36** Normalized results for the adhesional component of the coefficient of friction, as a function of  $L/L_{\ell c}$  for multiple-asperity contact. Data are presented for  $m = 0.5$ ,  $n = 0.2$ . For multiple-asperity plastic contact, data are presented for two values of  $L_d/L_{\ell c}$  (after [125])



$$\mu_{ds} = \frac{2 \tan \theta_r}{\pi}, \quad (12.20)$$

where  $\theta_r$  is the roughness angle (or attack angle) of a conical asperity. Mechanical properties affect the real area of contact and shear strength, and these cancel out in (12.16) [125]. Based on a statistical analysis of a random Gaussian surface [125]

$$\mu_{ds} = \frac{2\sigma_0}{\pi\beta_0^*} \left( \frac{L}{L_{\ell c}} \right)^{n-m} = \mu_{ds0} \left( \frac{L}{L_{\ell c}} \right)^{n-m}, \quad L < L_{\ell c}, \quad (12.21)$$

where  $\mu_{ds0}$  is the value of the coefficient of the summit-deformation component of the coefficient of friction at the macroscale ( $L \geq L_{\ell c}$ ), and  $\sigma_0$  and  $\beta_0^*$  are macro-scale values of the standard deviation of surface height and correlation length, respectively, for a Gaussian surface. The scale dependence for the two-body deformation component of the coefficient of friction is presented in Fig. 12.37 (top curve) for  $m = 0.5$  and  $n = 0.2$ , based on (12.21). The coefficient of friction increases with decreasing scale, according to (12.21). This effect is a consequence of increasing average slope or roughness angle.

For three-body deformation, it is assumed that wear and contaminant particles at the borders of the contact region are likely to leave the contact region, while the particles in the center are likely to stay (Fig. 12.38). The plowing three-body deformation is plastic and, assuming that particles are harder than the bodies, the shear strength  $\tau_{dp}$  is equal to the shear yield strength of the softer body  $\tau_Y$ ,

**Fig. 12.37** Normalized results for the two-body deformation component of the coefficient of friction, and the number of trapped particles divided by the total number of particles and three-body deformation component of the coefficient of friction, normalized by the macroscale value for the log-normal distribution of debris size, where  $\alpha$  is the probability of a particle in the border zone leaving the contact region. Various constants given in the figure correspond to the log-normal distribution (after [125])

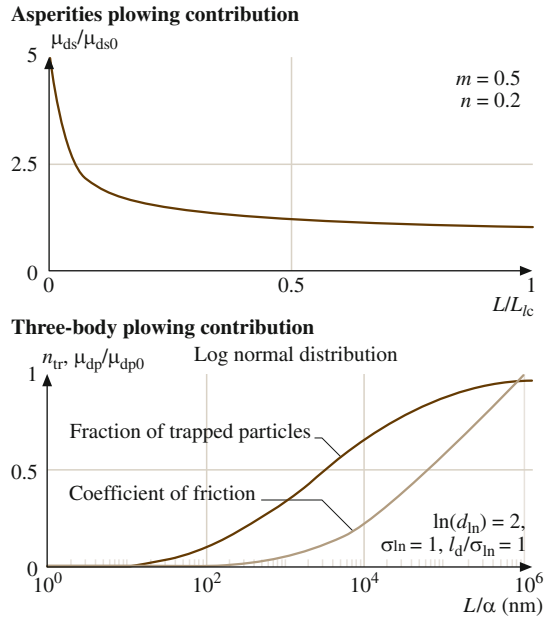
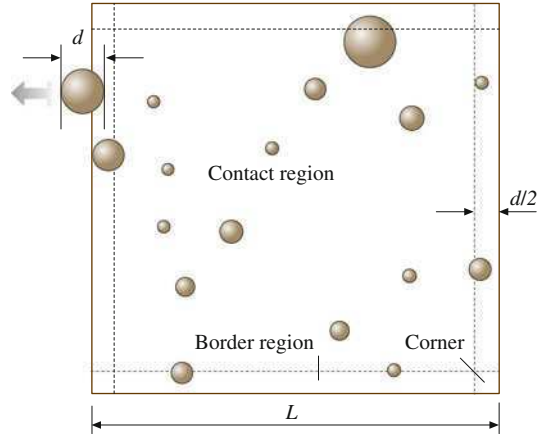


**Fig. 12.38** Schematic of debris in the contact zone and its border region. A particle of diameter  $d$  in the border region of  $d/2$  is likely to leave the contact zone (after [125])



and the three-body deformation component of the coefficient of friction is given by [126]

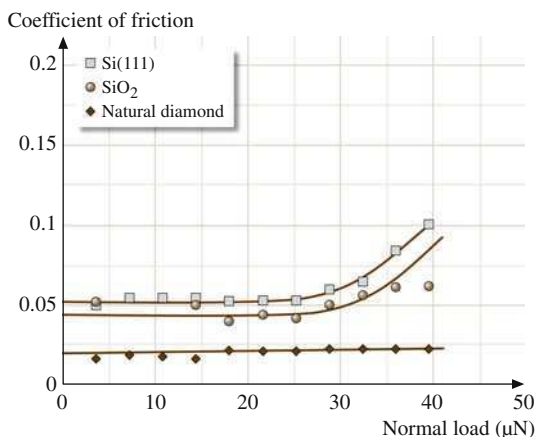
$$\mu_{dp} = \mu_{dp0} n_{tr} \frac{\bar{d}^2}{d_0^2} \frac{\sqrt{1 + \frac{2\ell_d}{d}}}{\sqrt{1 + \frac{2\ell_d}{d_0}}}, \quad (12.22)$$

where  $\bar{d}$  is the mean particle diameter,  $\bar{d}_0$  is the macroscale value of the mean particle diameter,  $n_{tr}$  is the number of trapped particles divided by the total number of particles, and  $\mu_{dp0}$  is the macroscale ( $L \rightarrow \infty$ ,  $n_{tr} \rightarrow 1$ ) value of the third-body deformation component of the coefficient of friction. The scale dependence of  $\mu_{dp}$  is shown in Fig. 12.37 (bottom curve) based on (12.22). Based on scale effect predictions presented in Figs. 12.36 and 12.37, the trends in the experimental results presented in Table 12.3 can be explained.

The scale dependence of meniscus effects in friction, wear, and interface temperature can be analyzed in a similar way [126].

To demonstrate the load dependence of friction at the nano/microscale, the coefficient of friction as a function of normal load is presented in Fig. 12.39. The coefficient of friction was measured by Bhushan and Kulkarni [42] for a  $\text{Si}_3\text{N}_4$  tip versus Si,  $\text{SiO}_2$ , and natural diamond using an AFM. They reported that, for low loads, the coefficient of friction is independent of load and then increases with increasing load after a certain load. It is noted that the critical load values for Si and  $\text{SiO}_2$  correspond to stresses equal to their hardness values, which suggests that the transition to plasticity plays a role in this effect. The friction values at higher loads for Si and  $\text{SiO}_2$  approach the macroscale values.

**Fig. 12.39** Coefficient of friction as a function of normal load for Si(111), SiO<sub>2</sub> coating, and natural diamond. Inflections in the curves for silicon and SiO<sub>2</sub> correspond to contact stresses equal to the hardnesses of these materials (after [42])



## 12.3 Wear, Scratching, Local Deformation, and Fabrication/Machining

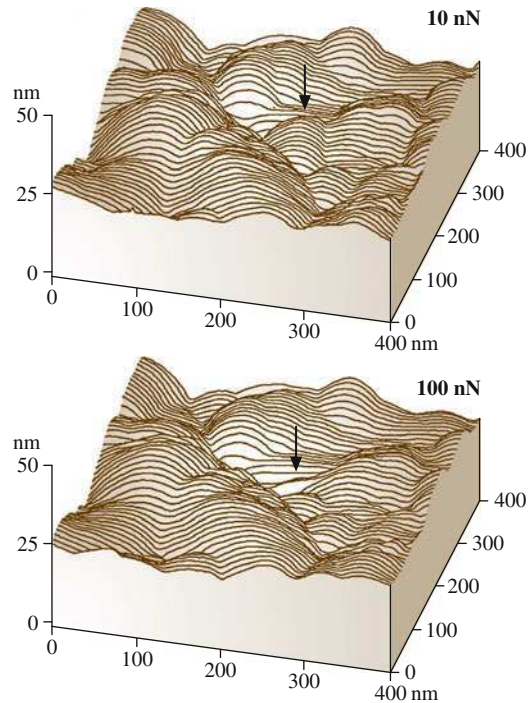
### 12.3.1 Nanoscale Wear

Bhushan and Ruan [37] conducted nanoscale wear tests on polymeric magnetic tapes using conventional silicon nitride tips at two different loads of 10 and 100 nN (Fig. 12.40). For a low normal load of 10 nN, measurements were made twice. There was no discernible difference between consecutive measurements for this load. However, as the load was increased from 10 to 100 nN, topographical changes were observed during subsequent scanning at normal load of 10 nN; material was pushed in the sliding direction of the AFM tip relative to the sample. The material movement is believed to occur as a result of plastic deformation of the tape surface. Thus, deformation and movement of the soft materials on a nanoscale can be observed.

### 12.3.2 Microscale Scratching

The AFM can be used to investigate how surface materials can be moved or removed on micro- to nanoscales, for example, in scratching and wear [5, 29] (where these things are undesirable) and nanofabrication/nanomachining (where they are desirable). Figure 12.41a shows microscratches made on Si(111) at various loads with a scanning velocity of 2 μm/s after ten cycles [41]. As expected, the scratch depth increases linearly with load. Such microscratching measurements can be used to study failure mechanisms on the microscale and to evaluate the mechanical integrity (scratch resistance) of ultrathin films at low loads.

**Fig. 12.40** Surface roughness maps of a polymeric magnetic tape at applied normal loads of 10 and 100 nN. Location of the change in surface topography as a result of nanowear is indicated by arrows (after [37])



To study the effect of scanning velocity, unidirectional scratches 5  $\mu\text{m}$  in length were generated at scanning velocities ranging from 1 to 100  $\mu\text{m/s}$  at various normal loads ranging from 40 to 140  $\mu\text{N}$ . No effect of scanning velocity was observed for a given normal load. For representative scratch profiles at 80  $\mu\text{N}$  (Fig. 12.41b). This may be because of a small effect of frictional heating with the change in scanning velocity used here. Furthermore, for a small change in interface temperature, there is a large underlying volume to dissipate the heat generated during scratching.

Scratching can be performed under ramped loading to determine the scratch resistance of materials and coatings. The coefficient of friction is measured during scratching, and the load at which the coefficient of friction increases rapidly is known as the critical load, which is a measure of scratch resistance. In addition, postscratch imaging can be performed in situ with the AFM in tapping mode to study failure mechanisms. Figure 12.42 shows data from a scratch test on Si(100) with scratch length of 25  $\mu\text{m}$  and scratching velocity of 0.5  $\mu\text{m/s}$ . At the beginning of the scratch, the coefficient of friction is 0.04, a typical value for silicon. At about 35  $\mu\text{N}$  (indicated by the arrow in the figure), there is a sharp increase in the coefficient of friction, which indicates the critical load. Beyond the critical load, the coefficient of friction continues to increase steadily. In the postscratch image, we note that, at the critical load, a clear groove starts to form. This implies that Si(100) was damaged by plowing at the critical load, associated with plastic flow of the material. At and after the critical load, small and uniform debris is observed, and

**Fig. 12.41** Surface plots of (a) Si(111) scratched for ten cycles at various loads and scanning velocity of 2  $\mu\text{m/s}$ . Note that  $x$ - and  $y$ -axes are in  $\mu\text{m}$  and  $z$ -axis is in nm, and (b) Si(100) scratched in one unidirectional scan cycle at normal force of 80  $\mu\text{N}$  and different scanning velocities

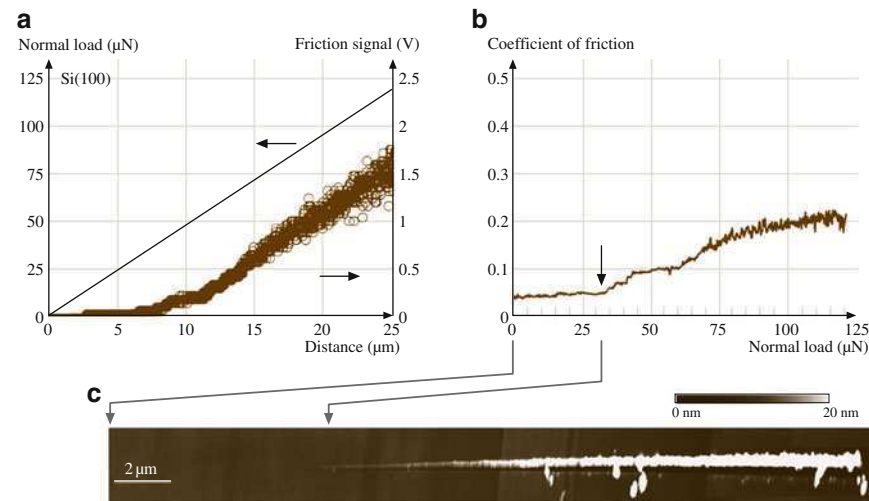
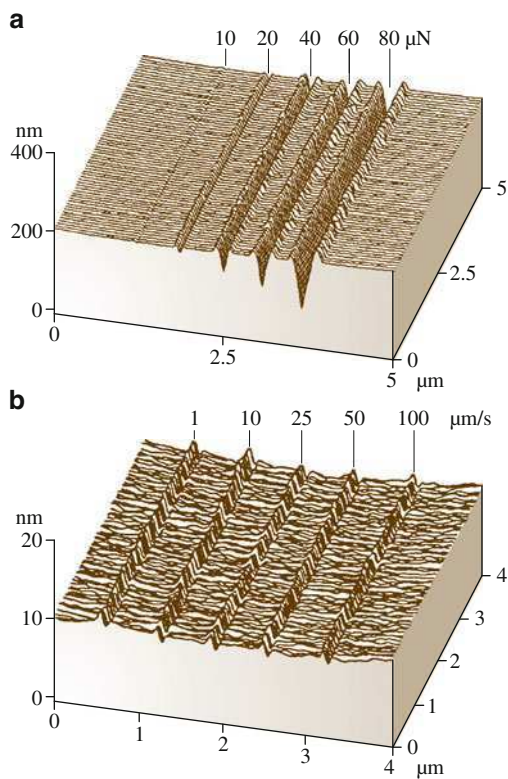


**Fig. 12.42** (a) Applied normal load and friction signal measured during a microscratch experiment on Si(100) as a function of scratch distance, and (b) friction data plotted in the form of the coefficient of friction as a function of normal load. (c) AFM surface height image of a scratch obtained in tapping mode (after [59])

the amount of debris increases with increasing normal load. Sundararajan and Bhushan [59] have also used this technique to measure the scratch resistance of diamond-like carbon coatings with thickness of 3.5–20 nm.

### 12.3.3 Microscale Wear

By scanning the sample in two dimensions with the AFM, wear scars are generated on the surface. Figure 12.43 shows the effect of normal load on wear depth on Si(100). We note that wear depth is very small for normal load  $< 20 \mu\text{N}$  [128, 129]. A normal load of  $20 \mu\text{N}$  corresponds to contact stresses comparable to the hardness of silicon. Primarily, elastic deformation at loads below  $20 \mu\text{N}$  is responsible for the low wear [42].

A typical wear mark of size  $2 \mu\text{m} \times 2 \mu\text{m}$  generated at normal load of  $40 \mu\text{N}$  for one scan cycle and imaged using AFM with scan size  $4 \mu\text{m} \times 4 \mu\text{m}$  at  $300 \text{ nN}$  load is shown in Fig. 12.44a [128]. The inverted map of wear marks shown in Fig. 12.44b indicates uniform material removal at the bottom of the wear mark. An AFM image of the wear mark shows debris at the edges, probably swiped during AFM scanning. This indicates that the debris is loose (not sticky) and can be removed during AFM scanning.

Next we examined the mechanism of material removal on the microscale in AFM wear experiments [43, 128, 129]. Figure 12.45 shows a secondary-electron image of the wear mark and associated wear particles. The specimen used for the scanning electron microscope (SEM) was not scanned with the AFM after initial wear, in order to retain wear debris in the wear region. Wear debris is clearly observed. In the SEM micrographs, the wear debris appears to be agglomerated because of the high surface energy of the fine particles. Particles appear to be a mixture of rounded and so-called cutting type (feather-like or ribbon-like material). Zhao and Bhushan [129] reported an increase in the number and size of cutting-type particles with increasing normal load. The presence of cutting-type particles indicates that the material is removed primarily by plastic deformation.

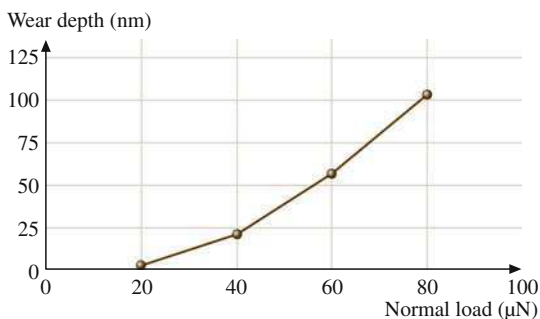


**Fig. 12.43** Wear depth as a function of normal load for Si(100) after one cycle (after [129])

**Fig. 12.44** (a) Typical gray-scale and (b) inverted AFM images of a wear mark created using a diamond tip at normal load of 40  $\mu\text{N}$  and one scan cycle on Si(100) surface

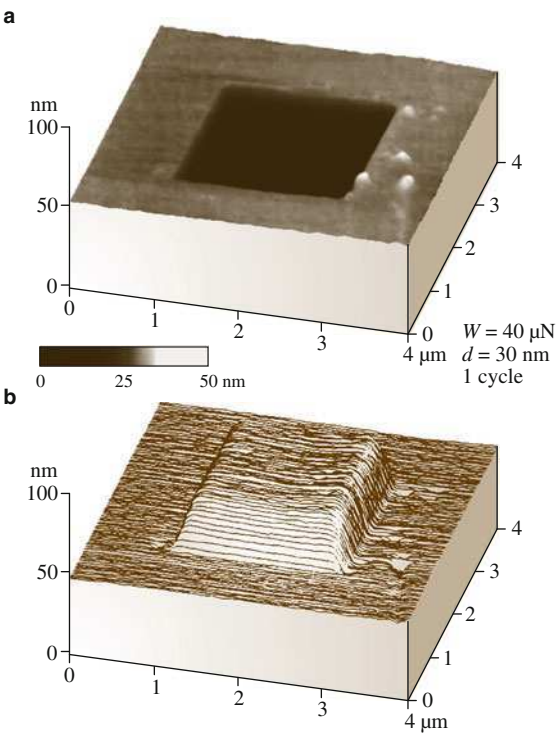
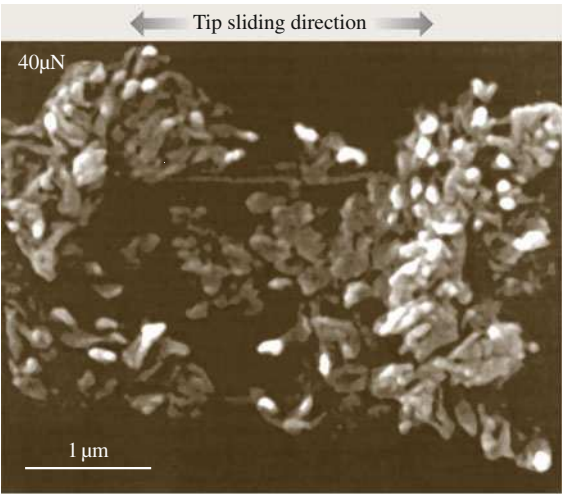


**Fig. 12.45** Secondary-electron image of the wear mark and debris for Si(100) produced at normal load of 40  $\mu\text{N}$  and one scan cycle



To better understand the material removal mechanisms, Zhao and Bhushan [129] used transmission electron microscopy (TEM). The TEM micrograph of the worn region and associated diffraction pattern are shown in Fig. 12.46a,b. The bend



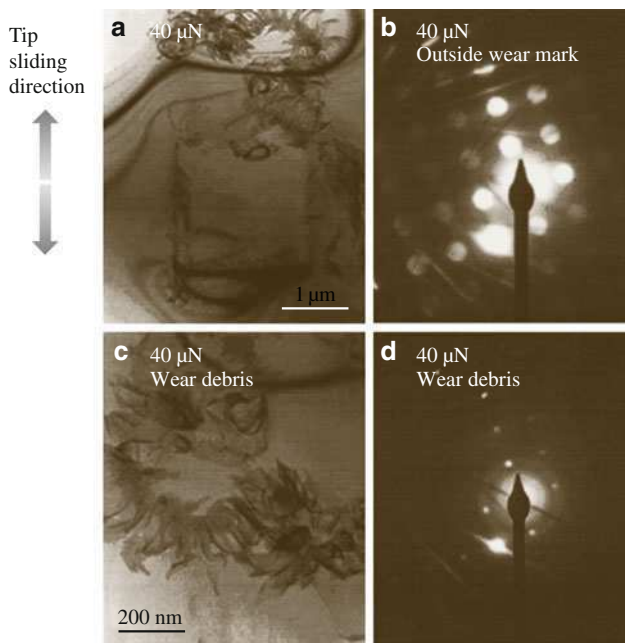
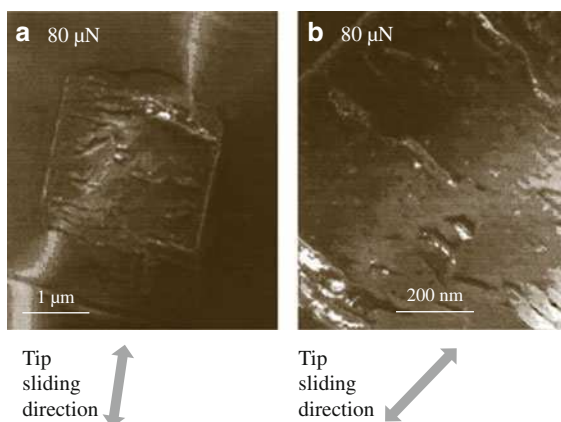


**Fig. 12.46** Bright-field TEM micrographs (a) and diffraction patterns (b), of the wear mark (a, b) and wear debris (c, d) on Si(100) produced at normal load of 40  $\mu\text{N}$  and one scan cycle. *Bend contours* around and inside wear mark are observed

contours are observed to pass through the wear mark in the micrograph. The bend contours around and inside the wear mark are indicative of a strain field, which in the absence of applied stresses can be interpreted as plastic deformation and/or elastic residual stresses. Often, localized plastic deformation during loading would lead to residual stresses during unloading; therefore, bend contours reflect a mix of elastic and plastic strains. The wear debris is observed outside the wear mark. The enlarged view of the wear debris in Fig. 12.46c shows that much of the debris is ribbon-like, indicating that material is removed by a cutting process via plastic deformation, which is consistent with the SEM observations. The diffraction pattern from inside the wear mark is similar to that of virgin silicon, showing no evidence of any phase transformation (amorphization) during wear. A selected-area diffraction pattern of the wear debris shows some diffuse rings, which indicates the existence of amorphous material in the wear debris, confirmed as silicon oxide products from chemical analysis. It is known that plastic deformation occurs by generation and propagation of dislocations. No dislocation activity or cracking was observed at 40  $\mu\text{N}$ . However, dislocation arrays could be observed at 80  $\mu\text{N}$ . Figure 12.47 shows TEM micrographs of the worn region at 80  $\mu\text{N}$ ; for better observation of the worn surface, wear debris was moved out of the wear mark by using AFM with a large-area scan at 300 nN after the wear test. The existence of dislocation arrays confirms that material removal occurs by plastic deformation.



**Fig. 12.47** (a) Bright-field and (b) weak-beam TEM micrographs of a wear mark produced in Si(100) at normal load of  $80\ \mu\text{N}$  and one scan cycle, showing bend contours and dislocations (after [129])

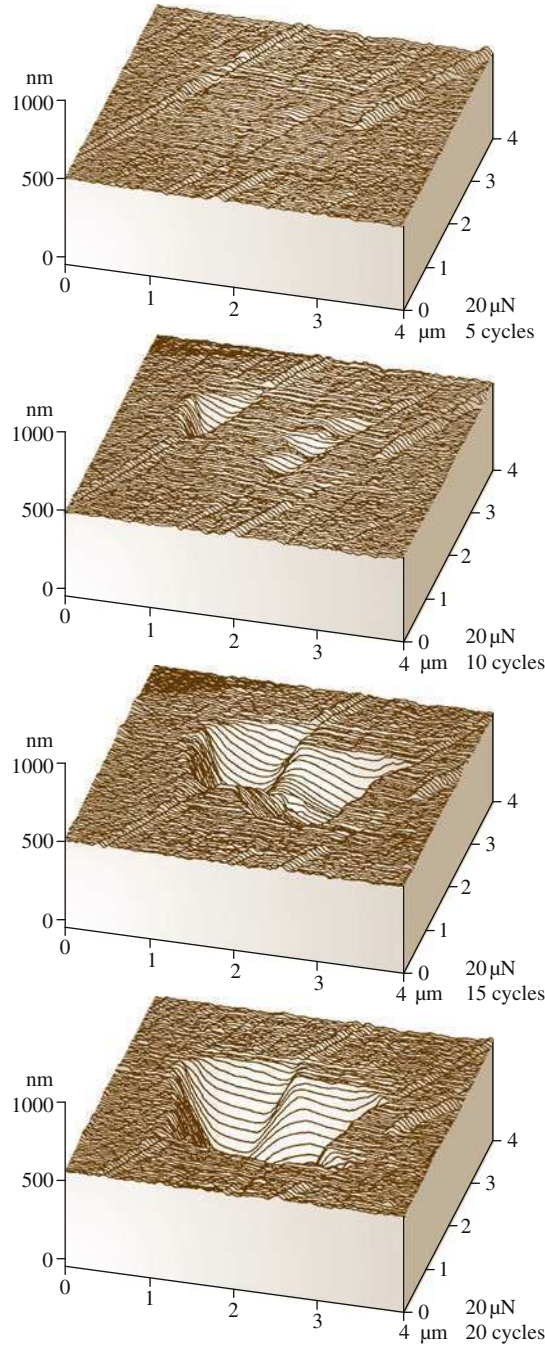


This corroborates the observations made in scratch tests at ramped load in the previous section. It is concluded that the material on the microscale at high loads is removed by plastic deformation with a small contribution from elastic fracture [129].

To understand wear mechanisms, evolution of wear can be studied using AFM. Figure 12.48 shows the evolution of wear marks of a DLC-coated disk sample. The data illustrate how the microwear profile for a load of  $20\ \mu\text{N}$  develops as a function of the number of scanning cycles [41]. Wear is not uniform, but is initiated at the nanoscratches. Surface defects (with high surface energy) present at the nanoscratches act as initiation sites for wear. Coating deposition also may not be uniform on and near nanoscratches, which may lead to coating delamination. Thus, scratch-free surfaces will be relatively resistant to wear.

Wear precursors (precursors to measurable wear) can be studied by making surface potential measurements [79–81]. The contact potential difference, or simply the surface potential between two surfaces, depends on a variety of parameters such as the electronic work function, adsorption, and oxide layers. The surface potential map of an interface gives a measure of changes in the work function, which is sensitive to both physical and chemical conditions of the surfaces including structural and chemical changes. Before material is actually removed in a wear process, the surface experiences stresses that result in surface and subsurface changes of structure and/or chemistry. These can cause changes in the measured potential of a surface. An AFM tip allows mapping of surface potential with nanoscale resolution. Surface height and change in surface potential maps of a polished single-crystal aluminum (100) sample, abraded using a diamond tip at loads of  $1$  and  $9\ \mu\text{N}$ , are shown in Fig. 12.49a. (Note that the sign of the change in surface potential is reversed here from that in [79].) It is evident that both abraded regions show a large potential contrast ( $\approx 0.17\ \text{V}$ ) with respect to the nonabraded area. The black region in the lower right-hand part of the topography scan shows a step that was created during the polishing phase. There is no potential contrast between the high and low region of the sample, indicating that the technique is independent of surface height. Figure 12.49b shows a close-up scan of the upper

**Fig. 12.48** Surface plots of a diamond-like-carbon-coated thin-film disk showing the worn region; the normal load and number of test cycles are indicated (after [41])



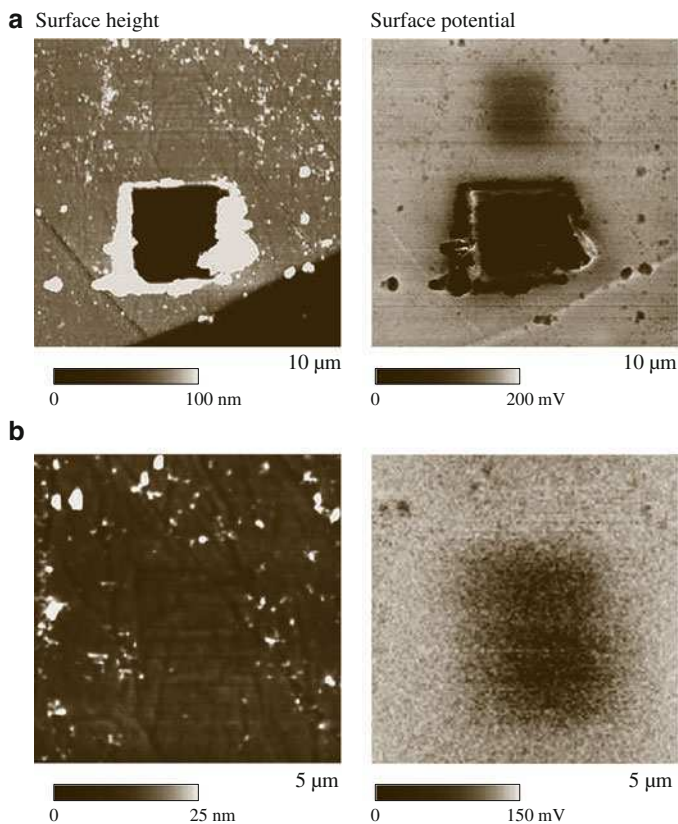


**Fig. 12.49** (a) Surface height and change in surface potential maps of wear regions generated at 1  $\mu\text{N}$  (a) and 9  $\mu\text{N}$  (b) on a single-crystal aluminum sample showing bright contrast in the surface potential map on the worn regions. (b) Close-up of the upper (low-load) wear region (after [79])

(low-load) wear region in Fig. 12.49a. Notice that, while there is no detectable change in the surface topography, there is nonetheless a large change in the potential of the surface in the worn region. Indeed, the wear mark of Fig. 12.49b might not be visible at all in the topography map were it not for the noted absence of wear debris generated nearby and then swept off during the low-load scan. Thus, even in the case of zero wear (no measurable deformation of the surface using AFM), there can be a significant change in the surface potential inside the wear mark, which is useful for the study of wear precursors. It is believed that the removal of the thin contaminant layer including the natural oxide layer gives rise to the initial change in surface potential. The structural changes that precede generation of wear debris and/or measurable wear scars occur under ultralow loads in the top few nanometers of the sample, and are primarily responsible for the subsequent changes in surface potential.

### 12.3.4 *In Situ Characterization of Local Deformation*

In situ surface characterization of local deformation of materials and thin films is carried out using a tensile stage inside an AFM. Failure mechanisms of coated polymeric thin films under tensile load were studied by Bobji and Bhushan [73, 74]. The specimens were strained at a rate of  $4 \times 10^{-3}\%$  per s, and AFM images were captured at different strains up to  $\approx 10\%$  to monitor the generation and propagation of cracks and deformation bands.

Bobji and Bhushan [73, 74] studied three magnetic tapes of thickness ranging from 7 to 8.5  $\mu\text{m}$ . One of these had an acicular-shaped metal particle (MP) coating and the other two had metal-evaporated (ME) coating with and without a thin diamond-like carbon (DLC) overcoat on a polymeric substrate, all of which had a particulate back-coating [15]. They also studied the polyethylene terephthalate (PET) substrate with 6  $\mu\text{m}$  thickness. They reported that cracking of the coatings started at  $\approx 1\%$  strain for all tapes, much before the substrate started to yield at  $\approx 2\%$  strain. Figure 12.50 shows topographical images of the MP tape at

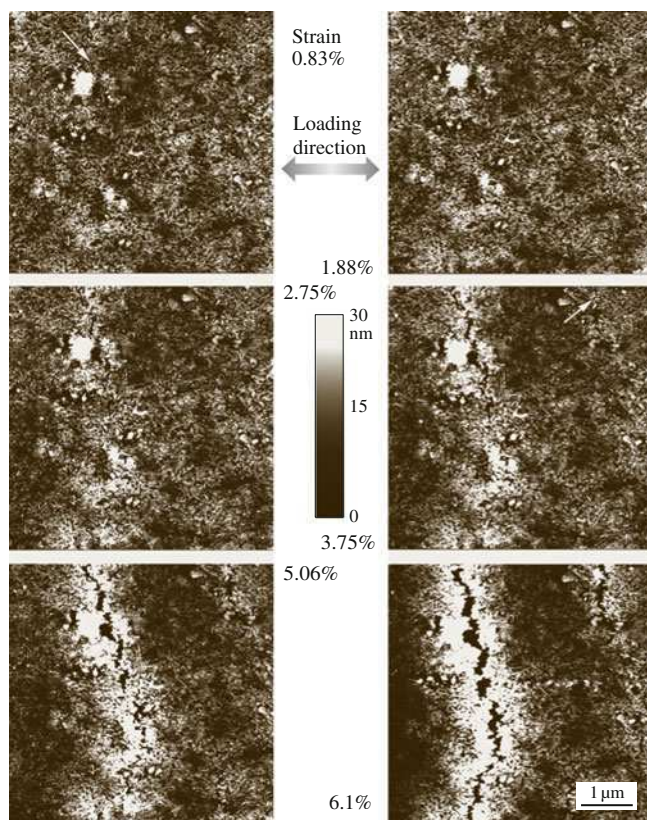


**Fig. 12.50** Topographical images of MP magnetic tape at different strains (after [73])

different strains. At 0.83% strain, a crack can be seen, originating at the marked point. As the tape is stretched further along this direction, as shown in Fig. 12.50, the crack propagates along the shorter boundary of the ellipsoidal particle. However, the general direction of the crack propagation remains perpendicular to the direction of stretching. The length, width, and depth of the cracks increase with strain, and at the same time newer cracks keep nucleating and propagate with reduced crack spacing. At 3.75% strain, another crack can be seen nucleating. This crack continues to grow parallel to the first one. When the tape is unloaded after stretching up to a strain of  $\approx 2\%$ , i.e., within the elastic limit of the substrate, the cracks close perfectly, and it is impossible to determine the difference from the unstrained tape.

Figure 12.51 shows topographical images of the three magnetic tapes and the PET substrate after being strained to 3.75%, which is well beyond the elastic limit of the substrate. The MP tape develops numerous short cracks perpendicular to the direction of loading. In tapes with metallic coating, the cracks extend throughout the tape width. In the ME tape with the DLC coating, there is a bulge in the coating around the primary cracks that are initiated when the substrate is still elastic, like crack A in the figure. The white band on the right-hand side of the figure is the bulge of another crack. Secondary cracks, such as B and C, are generated at higher strains and are straighter compared with the primary cracks. In ME tape with a Co-O film on a PET substrate, with a thickness ratio of 0.03, both with and without DLC coating,

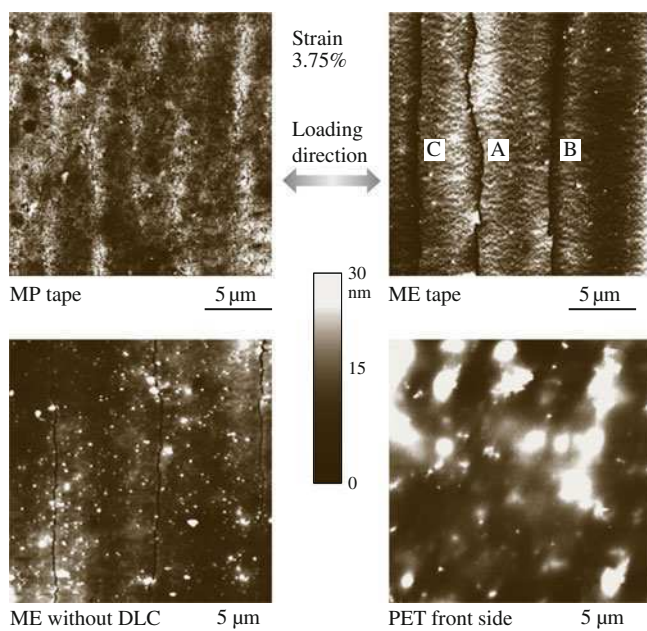


**Fig. 12.51** Comparison of crack morphologies at 3.75% strain in three magnetic tapes and PET substrate. Cracks B and C, nucleated at higher strains, are more linear than crack A (after [74])



no difference is observed in the rate of growth between primary and secondary cracks. Failure is cohesive with no bulging of the coating. This seems to suggest that the DLC coating has residual stresses that relax when the coating cracks, causing delamination. Since the stresses are already relaxed, the secondary crack does not result in delamination. The presence of the residual stress is confirmed by the fact that a free-standing ME tape curls up (in a cylindrical form with its axis perpendicular to the tape length) with a radius of curvature of  $\approx 6$  mm, whereas the ME tape without the DLC does not curl. The magnetic coating side of the PET substrate is much smoother at smaller scan lengths. However, in  $20\text{ }\mu\text{m}$  scans it has a lot of bulges, which appear as white spots in the figure. These spots change shape even while scanning the samples in tapping mode at very low contact forces.

The variation of average crack width and average crack spacing with strain is plotted in Fig. 12.52. The crack width is measured at a spot along a given crack

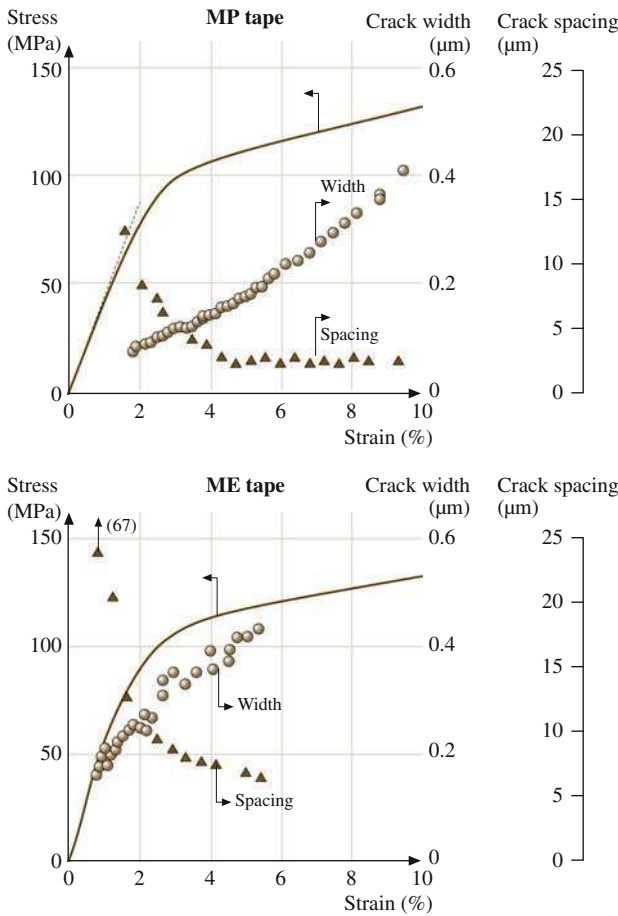


**Fig. 12.52** Variation of stress, crack width, and crack spacing with strain in two magnetic tapes (after [73])

over a distance of 1  $\mu\text{m}$  in the 5  $\mu\text{m}$  scan image at different strains. The crack spacing is obtained by averaging the intercrack distance measured in five separate 50  $\mu\text{m}$  scans at each strain. It can be seen that the cracks nucleate at a strain of about 0.7 – 1.0%, well within the elastic limit of the substrate. There is a definite change in the slope of the load–displacement curve at the strain where cracks nucleate, and the slope after that is closer to the slope of the elastic portion of the substrate. This would mean that most of the load is supported by the substrate once the coating fails by cracking.

Fatigue experiments can be performed by applying a cyclic stress amplitude with a certain mean stress [75]. Fatigue life was determined by the first occurrence of cracks. Experiments were performed at various constant mean stresses and with a range of cyclic stress amplitudes for each mean stress value for various magnetic tapes. Number of cycles to failure was plotted as a function of stress state to obtain a so-called  $S$ – $N$  (stress–life) diagram. As the stress is decreased, there is a stress value for which no failure occurs. This stress is termed the endurance limit or simply the fatigue limit. Figure 12.53 shows the  $S$ – $N$  curves for an ME tape and an

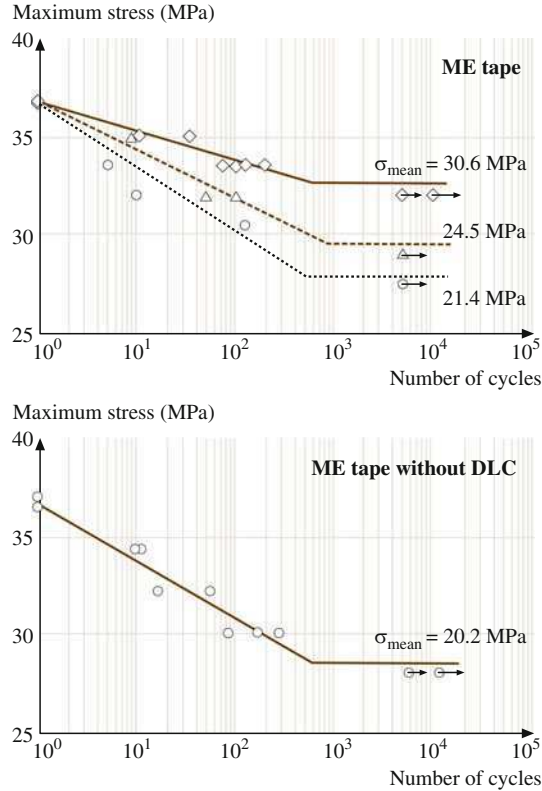


**Fig. 12.53**  $S$ – $N$  curve for two magnetic tapes with maximum stress plotted on the *ordinate* and number of cycles to failure on the *abscissa*. The data points marked with *arrows* indicate tests for which no failure (cracking) was observed in the scan area, even after a large number of cycles (10,000)

ME tape without DLC. For the ME tape, the endurance limit is seen to go down with decreasing mean stress. This is consistent with the literature, and is because for lower mean stress the corresponding stress amplitude is relatively high and this causes failure. The endurance limit is found to be almost the same for all three mean stresses. In the case of ME tape without DLC as well, the critical number of cycles is found to be in the same range.

In situ surface characterization of unstretched and stretched films has been used to measure the Poisson's ratio of polymeric thin films by Bhushan et al. [130]. Uniaxial tension is applied by the tensile stage. Surface height profiles obtained from the AFM images of unstretched and stretched samples are used to monitor the changes in displacements of the polymer films in the longitudinal and lateral directions simultaneously.

### 12.3.5 Nanofabrication/Nanomachining

An AFM can be used for nanofabrication/nanomachining by extending the micro-scale scratching operation [5, 14, 41, 78]. Figure 12.54 shows two examples of nanofabrication. The patterns were created on a single-crystal Si(100) wafer by scratching the sample surface with a diamond tip at specified locations and scratching angles. Each line is scribed manually at normal load of 15  $\mu\text{N}$  and writing speed of 0.5  $\mu\text{m/s}$ . The separation between lines is  $\approx 50$  nm, and the variation in line width is due to the tip asymmetry. Nanofabrication parameters – normal load, scanning speed, and tip geometry – can be controlled precisely to control the depth and length of the devices.

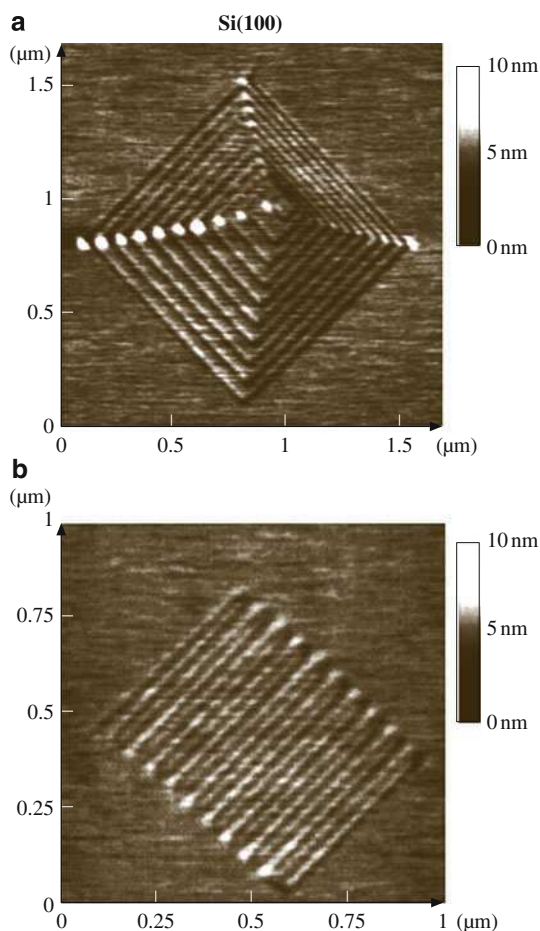
Nanofabrication using mechanical scratching has several advantages over other techniques. Better control over the applied normal load, scan size, and scanning speed can be used for nanofabrication of devices. Using the technique, nanofabrication can be performed on any engineering surface. Use of chemical etching or reactions is not required, and this dry nanofabrication process can be used where the use of chemicals and electric field is prohibited. One disadvantage of this technique is the formation of debris during scratching. At light loads, debris formation is not a problem compared with during high-load scratching. However, debris can be easily removed from the scan area at light loads during scanning.

## 12.4 Indentation

Mechanical properties on relevant scales are needed for the analysis of friction and wear mechanisms. Mechanical properties, such as hardness and Young's modulus of elasticity, can be determined on micro- to picoscales using the AFM [37, 41, 56, 62] and a depth-sensing indentation system used in conjunction with an AFM [42, 131–133].



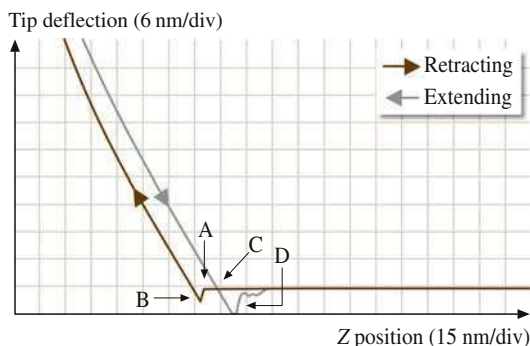
**Fig. 12.54** (a) Trim and (b) spiral patterns generated by scratching a Si(100) surface using a diamond tip at normal load of 15  $\mu\text{N}$  and writing speed of 0.5  $\mu\text{m/s}$



### 12.4.1 Picoindentation

Indentability on the scale of subnanometers of soft samples can be studied in the force calibration mode (Fig. 12.6) by monitoring the slope of cantilever deflection as a function of sample traveling distance after the tip is engaged and the sample is pushed against the tip. For a rigid sample, cantilever deflection equals the sample traveling distance, but the former quantity is smaller if the tip indents the sample. In an example for a polymeric magnetic tape shown in Fig. 12.55, the line in the left portion of the figure is curved with a slope of  $< 1$  shortly after the sample touches the tip, which suggests that the tip has indented the sample [37]. Later, the slope is unity, suggesting that the tip no longer indents the sample. This observation indicates that the tape surface is soft (polymer rich) locally but hard (as a result of magnetic particles) underneath. Since the curves in extending and retracting

**Fig. 12.55** Tip deflection (normal load) as a function of  $z$  (separation distance) for a polymeric magnetic tape (after [37])



modes are identical, the indentation is elastic up to the maximum load of  $\approx 22$  nN used in the measurements.

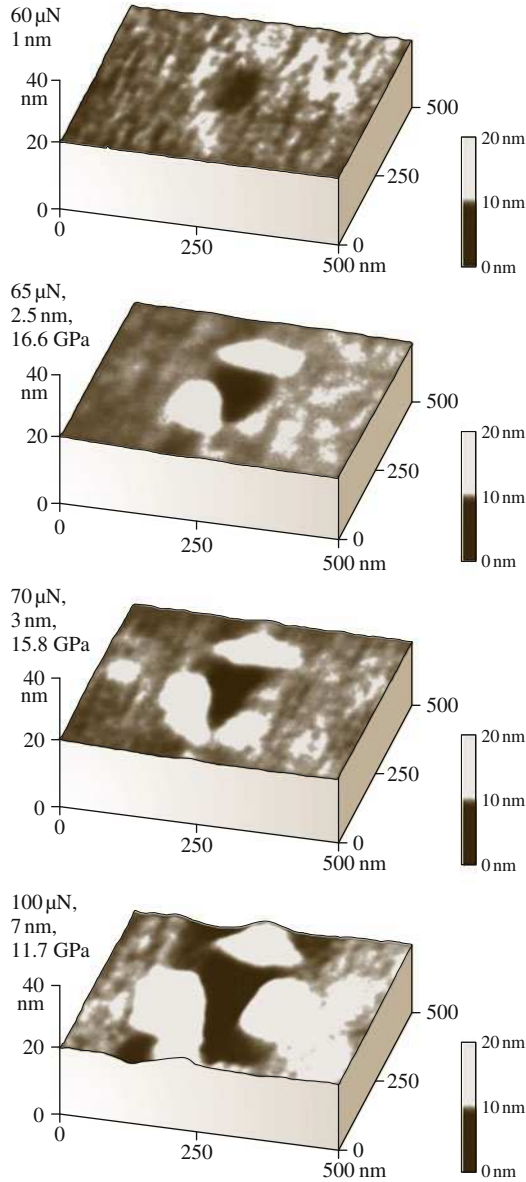
Detection of the transfer of material on a nanoscale is possible with the AFM. Indentation of  $C_{60}$ -rich fullerene films with an AFM tip has been shown [60] to result in the transfer of fullerene molecules to the AFM tip, as indicated by discontinuities in the cantilever deflection as a function of sample traveling distance in subsequent indentation studies.

### 12.4.2 Nanoscale Indentation

The indentation hardness of surface films with indentation depth as small as  $\approx 1$  nm can be measured using an AFM [14, 61, 62]. Figure 12.56 shows gray scale plots of indentation marks made on Si(111) at normal loads of 60, 65, 70, and 100  $\mu$ N. Triangular indents can be clearly observed with very shallow depths. At normal load of 60  $\mu$ N, indents are observed, and the depth of penetration is  $\approx 1$  nm. As the normal load is increased, the indents become clearer, and indentation depth increases. For the case of hardness measurements at shallow depths on the same order as variations in surface roughness, it is desirable to subtract the original (unindented) map from the indent map for an accurate measurement of the indentation size and depth [41].

To make accurate measurements of hardness at shallow depths, a depth-sensing nano/picoindentation system (Fig. 12.9) is used [61]. Figure 12.57 shows load-displacement curves at different peak loads for Si(100). Loading/unloading curves often exhibit sharp discontinuities, particularly at high loads. Discontinuities, also referred to as pop-ins, occurring during the initial loading part of the curve, mark a sharp transition from pure elastic loading to plastic deformation of the specimen surface, thus corresponding to an initial yield point. The sharp discontinuities in the unloading part of the curves are believed to be due to the formation of lateral cracks which form at the base of the median crack, which results in the surface of the

**Fig. 12.56** Gray-scale plots of indentation marks on a Si (111) sample at various indentation loads. Loads, indentation depths, and hardness values are listed in the figure (after [62])



specimen being thrust upward. Load–displacement data at residual depths as low as  $\approx 1$  nm can be obtained. The indentation hardness of surface films has been measured for various materials at a range of loads, including Si(100) up to a peak load of 500  $\mu\text{N}$  and Al(100) up to a peak load of 2,000  $\mu\text{N}$  by Bhushan et al. [61] and Kulkarni and Bhushan [131–133]. The hardnesses of single-crystal silicon and single-crystal aluminum at shallow depths on the order of a few nm (i.e., on the

**Fig. 12.57** Load–displacement curves at various peak loads for Si (100). Inset shows magnified curve for peak load 50  $\mu\text{N}$  (after [61])

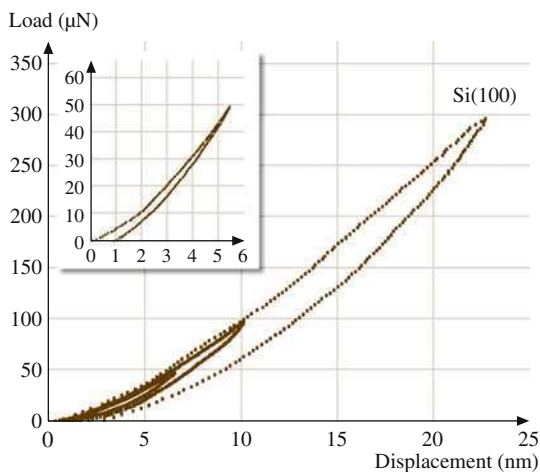
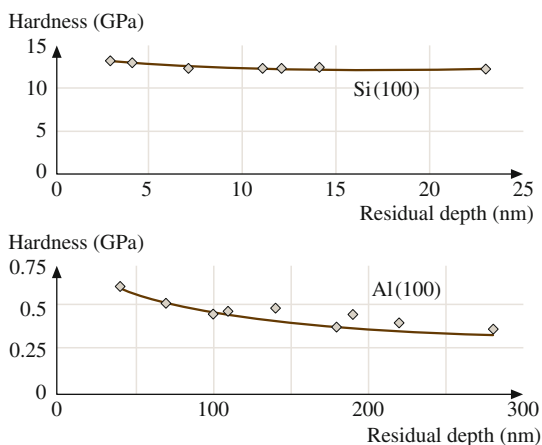


**Fig. 12.58** Indentation hardness as a function of residual indentation depth for Si(100) (after [61]) and Al(100) (after [131])



nanoscale) are found to be higher than at depths on the order of a few hundred nm (i.e., on the microscale) (Fig. 12.58). Microhardness has also been reported to be higher than that on the millimeter scale by several investigators. The data reported to date show that hardness exhibits scale (size) effects.

During loading, generation and propagation of dislocations is responsible for plastic deformation. A strain gradient plasticity theory has been developed for micro/nanoscale deformations, based on randomly created, statistically stored, and geometrically necessary dislocations [134, 135]. Large strain gradients inherent to small indentations lead to accumulation of geometrically necessary dislocations located in a certain subsurface volume for strain compatibility reasons, which cause enhanced hardening. The large strain gradients in small indentations require these dislocations to account for the large slope at the indented surface. These are

a function of strain gradient, whereas statistically, stored dislocations are a function of strain. Based on this theory, scale-dependent hardness is given as

$$H = H_0 \sqrt{1 + \frac{\ell_d}{a}}, \quad (12.23)$$

where  $H_0$  is the hardness in the absence of strain gradient or macrohardness,  $\ell_d$  is the material-specific characteristic length parameter, and  $a$  is the contact radius. In addition to the role of strain gradient plasticity theory, an increase in hardness with decreasing indentation depth can possibly be rationalized on the basis that, as the volume of deformed material decreases, there is a lower probability of encountering material defects.

Bhushan and Koinkar [56] have used AFM measurements to show that ion implantation of silicon surfaces increases their hardness and thus their wear resistance. Formation of surface alloy films with improved mechanical properties by ion implantation is of growing technological importance as a means of improving the mechanical properties of materials. Hardness of 20 nm-thick DLC films have been measured by Kulkarni and Bhushan [133].

The creep and strain-rate effects (viscoelastic effects) of ceramics can be studied using a depth-sensing indentation system. Bhushan et al. [61] and Kulkarni and Bhushan [131–133] have reported that ceramics (single-crystal silicon and diamond-like carbon) exhibit significant plasticity and creep on a nanoscale. Figure 12.59a shows load–displacement curves for single-crystal silicon at various peak loads held for 180 s. To demonstrate the creep effects, the load–displacement curves for 500  $\mu\text{N}$  peak load held for 0 and 30 s are also shown in the inset. Note that significant creep occurs at room temperature. Nanoindenter experiments conducted by Li et al. [136] exhibited significant creep only at high temperatures (greater than or equal to 0.25 times the melting point of silicon). The mechanism of dislocation glide plasticity is believed to dominate the indentation creep process on the macro-scale. To study the strain-rate sensitivity of silicon, data at two different (constant) rates of loading are presented in Fig. 12.59b. Note that a change in the loading rate by a factor of about five results in a significant change in the load–displacement data. The viscoelastic effects observed here for silicon at ambient temperature could arise from the size effects mentioned earlier. Most likely, creep and strain rate experiments are being conducted on the hydrated films present on the silicon surface in the ambient environment, and these films are expected to be viscoelastic.

### 12.4.3 Localized Surface Elasticity and Viscoelasticity Mapping

The Young's modulus of elasticity can be calculated from the slope of the indentation curve during unloading. However, these measurements provide a single-point measurement. By using the force modulation technique, it is possible to obtain localized elasticity maps of soft and compliant materials of near-surface

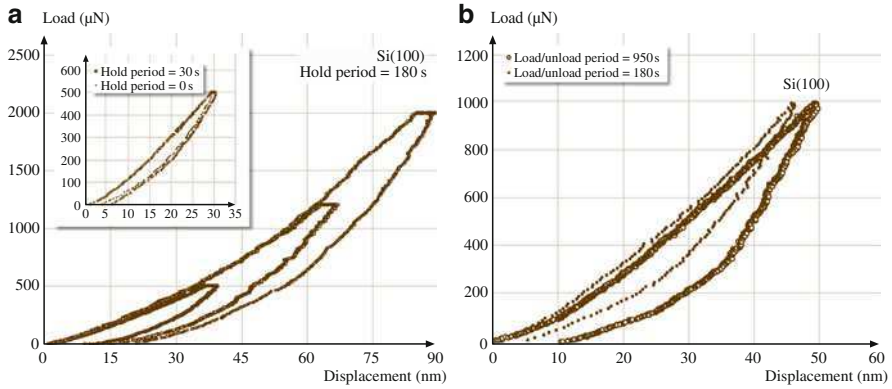


**Fig. 12.59** (a) Creep behavior and (b) strain-rate sensitivity of Si(100) (after [61])

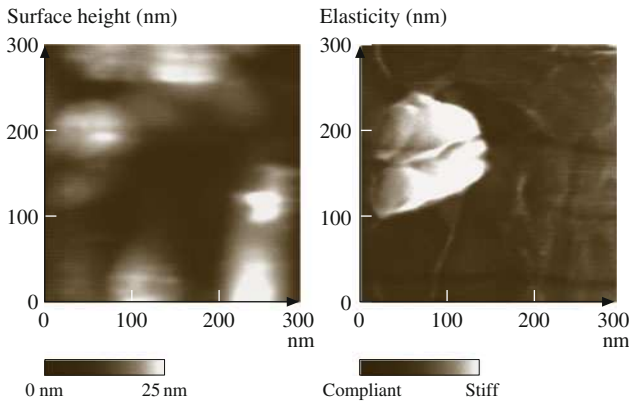


**Fig. 12.60** Surface height and elasticity maps on a polymeric magnetic tape ( $\sigma = 6.7$  nm and  $P-V = 32$  nm;  $\sigma$  and  $P-V$  refer to the standard deviation of surface height and the peak-to-valley distance, respectively). The gray scale on the elasticity map is arbitrary (after [66])

regions with nanoscale lateral resolution. This technique has been successfully used for polymeric magnetic tapes, which consist of magnetic and nonmagnetic ceramic particles in a polymeric matrix. Elasticity maps of a tape can be used to identify the relative distribution of hard magnetic and nonmagnetic ceramic particles on the tape surface, which has an effect on friction and stiction at the head–tape interface [15]. Figure 12.60 shows surface height and elasticity maps on a polymeric magnetic tape [66]. The elasticity image reveals sharp variations in surface elasticity due to the composite nature of the film. As can be clearly seen, regions of high elasticity do not always correspond to high or low topography. Based on a Hertzian elastic-contact analysis, the static indentation depth of these samples during the force modulation scan is estimated to be about 1 nm. We conclude that the observed contrast is influenced most strongly by material properties in the top few nanometers, independent of the composite structure beneath the surface layer.

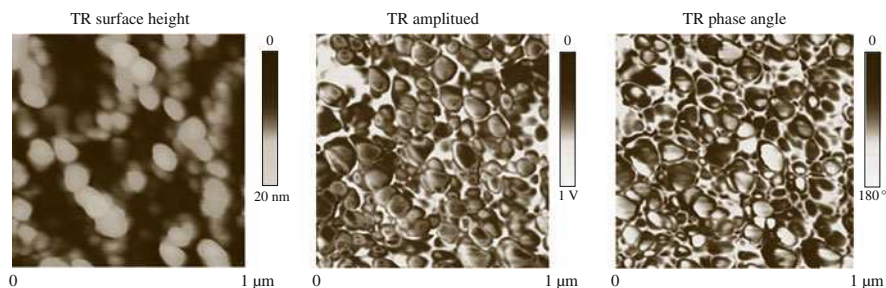


**Fig. 12.61** Images of an MP tape obtained with TR mode II (constant deflection). TR mode II amplitude and phase-angle images have the largest contrast among tapping, TR mode I, and TR mode II techniques (after [72])

By using phase-contrast microscopy, it is possible to obtain phase-contrast maps or the contrast in viscoelastic properties of near-surface regions with nanoscale lateral resolution. This technique has been successfully used for polymeric films and magnetic tapes that consist of ceramic particles in a polymeric matrix [69–72].

Figure 12.61 shows typical surface height, TR amplitude, and TR phase-angle images for a MP tape using TR mode II, described earlier. The TR amplitude image provides contrast in lateral stiffness, and the TR phase-angle image provides contrast in viscoelastic properties. In the TR amplitude and phase-angle images, the distribution of magnetic particles can be clearly seen, and with better contrast than in the TR surface height image. MP tape samples show a granular structure with elliptically shaped magnetic particle aggregates (50–100 nm in diameter). Studies by Scott and Bhushan [69], Bhushan and Qi [70], and Kasai et al. [71] have indicated that the phase shift can be related to the energy dissipation through the viscoelastic deformation process between the tip and the sample. Recent theoretical analysis has established a quantitative correlation between the lateral surface properties (stiffness and viscoelasticity) of materials and the amplitude/phase-angle shift in TR measurements [86]. The contrast in the TR amplitude and phase-angle images is due to the in-plane (lateral) heterogeneity of the surface. Based on the TR amplitude and phase-angle images, mapping of the lateral surface properties (lateral stiffness and viscoelasticity) of materials can be obtained.

## 12.5 Boundary Lubrication

### 12.5.1 Perfluoropolyether Lubricants

The classic approach to lubrication uses freely supported multimolecular layers of liquid lubricants [6, 11, 15, 137]. The liquid lubricants are sometimes chemically bonded to improve their wear resistance [6, 11, 15]. Partially chemically bonded, molecularly thick perfluoropolyether (PFPE) films are used for lubrication of



magnetic storage media because of their thermal stability and extremely low vapor pressure [15]). Chemically bonded lubricants are considered as potential candidate lubricants for MEMS/NEMS. Molecularly thick PFPEs are well suited to this application because of the following properties: low surface tension and low contact angle, which allow easy spreading on surfaces and provide hydrophobic properties; chemical and thermal stability, which minimizes degradation during use; low vapor pressure, which provides low outgassing; high adhesion to substrate via organic functional bonds; and good lubricity, which reduces contact surface wear.

For boundary lubrication studies, friction, adhesion, and durability experiments have been performed on virgin Si(100) surfaces and silicon surfaces lubricated with various PFPE lubricants [51, 52, 54, 138–141]. More recently, there has been interest in selected ionic liquids for lubrication [142–144]. They possess efficient heat transfer properties. They are also electrically conducting, which is of interest in various MEMS/NEMS applications. Results of the following two PFPE lubricants will be presented here: Z-15 (with  $-\text{CF}_3$  nonpolar end groups),  $\text{CF}_3 - \text{O} - (\text{CF}_2 - \text{CF}_2 - \text{O})_m - (\text{CF}_2 - \text{O})_n - \text{CF}_3$  ( $m/n \approx 2/3$ ) and Z-DOL (with  $-\text{OH}$  polar end groups),  $\text{HO} - \text{CH}_2 - \text{CF}_2 - \text{O} - (\text{CF}_2 - \text{CF}_2 - \text{O})_m - (\text{CF}_2 - \text{O})_n - \text{CF}_2 - \text{CH}_2 - \text{OH}$  ( $m/n \approx 2/3$ ). Z-DOL film was thermally bonded at  $150^\circ\text{C}$  for 30 min, and the unbonded fraction was removed by a solvent (referred to as fully bonded herein) [15]. The thicknesses of Z-15 and Z-DOL films were 2.8 and 2.3 nm, respectively. Lubricant chain diameters of these molecules are  $\approx 0.6$  nm, and molecularly thick films generally lie flat on surfaces with high coverage.

The adhesive forces of Si(100), Z-15, and Z-DOL (fully bonded) measured by force calibration plot and plots of friction force versus normal load are summarized in Fig. 12.62 [54]. The data obtained by these two methods are in good agreement. Figure 12.62 shows that the presence of mobile Z-15 lubricant film increases the adhesive force as compared with Si(100) due to meniscus formation. In contrast, the presence of the solid-like phase of the Z-DOL (fully bonded) film reduces the adhesive force as compared with Si(100), because of the absence of mobile liquid. The schematic in Fig. 12.65b (bottom) shows the relative size and sources of the meniscus. It is well known that the native oxide layer ( $\text{SiO}_2$ ) on the top of Si (100) wafer exhibits hydrophilic properties, and some water molecules can be adsorbed on this surface. The condensed water will form a meniscus as the tip approaches the sample surface. The larger adhesive force in Z-15 is not only caused by the Z-15 meniscus alone; the nonpolarized Z-15 liquid does not have good wettability and strong bonding with Si(100). Consequently, in the ambient environment, condensed water molecules from the environment will permeate through the liquid Z-15 lubricant film and compete with the lubricant molecules present on the substrate. The interaction of the liquid lubricant with the substrate is weakened, and a boundary layer of the liquid lubricant forms puddles [51, 52]. This dewetting allows water molecules to be adsorbed onto the Si(100) surface along with Z-15 molecules, and both of them can form meniscus as the tip approaches the surface. Thus the dewetting of liquid Z-15 film results in a higher adhesive force and poorer



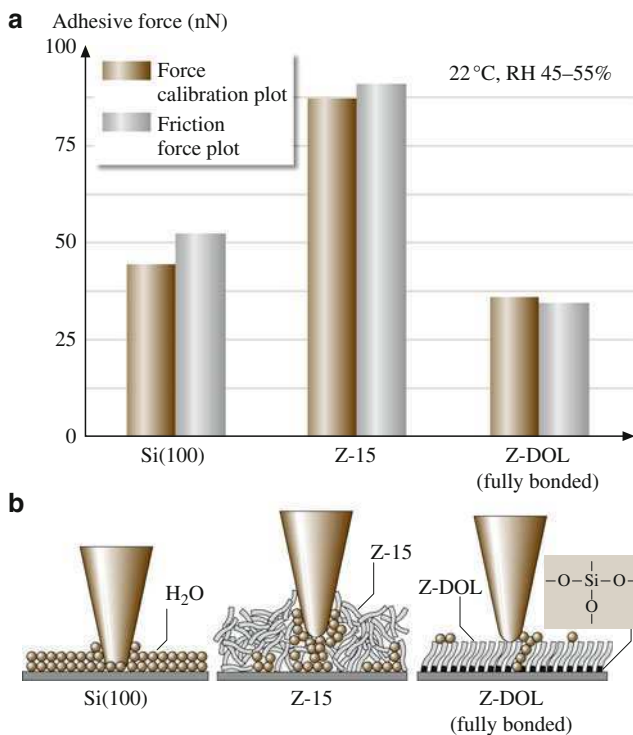


**Fig. 12.62** Summary of the adhesive forces of Si(100) and Z-15 and Z-DOL (fully bonded) films measured by force calibration plots and plots of friction force versus normal load in ambient air (**a**). (**b**) Schematic showing the effect of meniscus formed between the AFM tip and the surface sample on the adhesive and friction forces (after [54])

lubrication performance. In addition, the Z-15 film is soft compared with the solid Si(100) surface, and penetration of the tip into the film occurs when pushing the tip down. This results in a large area of the tip being wetted by the liquid to form the meniscus at the tip–liquid (mixture of Z-15 and water) interface. It should also be noted that Z-15 has a higher viscosity compared with water; therefore Z-15 film provides greater resistance to motion and higher coefficient of friction. In the case of Z-DOL (fully bonded) film, both of the active groups of Z-DOL molecules are mostly bonded onto the Si(100) substrate, thus the Z-DOL (fully bonded) film has low free surface energy and cannot be readily displaced by water molecules or readily adsorb water molecules. Thus, the use of Z-DOL (fully bonded) can reduce the adhesive force.

To study the effect of velocity on friction and adhesion, the variation of friction force, adhesive force, and coefficient of friction of Si(100), Z-15, and Z-DOL (fully bonded) as a function of velocity is summarized in Fig. 12.63 [54]. The results indicates that, for silicon wafer, the friction force decreases logarithmically with increasing velocity. For Z-15, the friction force decreases with increasing velocity

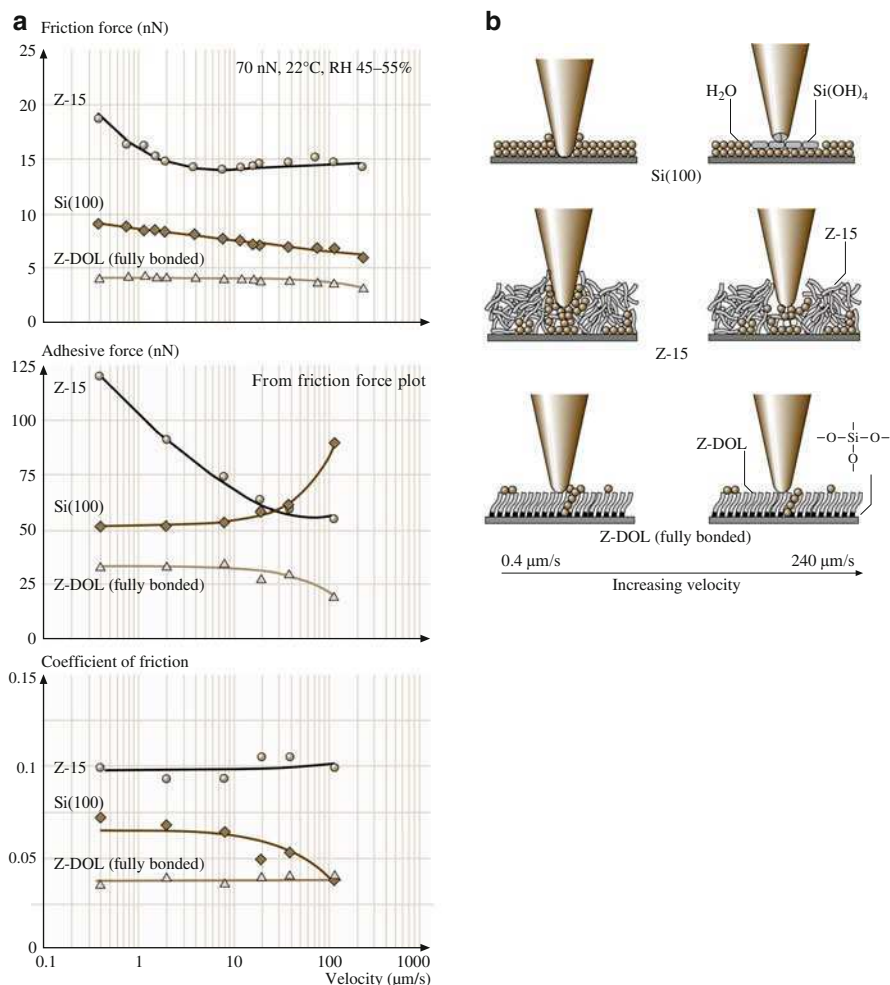


**Fig. 12.63** The influence of velocity on the friction force, adhesive force, and coefficient of friction of Si(100) and Z-15 and Z-DOL (fully bonded) films at 70 nN in ambient air (**a**). (**b**) Schematic showing the change of surface composition (by tribochemical reaction) and formation of meniscus while increasing velocity (after [54])

up to 10  $\mu\text{m/s}$ , after which it remains almost constant. The velocity has a very small effect on the friction force of Z-DOL (fully bonded); it reduced slightly only at very high velocity. Figure 12.63 also indicates that the adhesive force of Si(100) is increased when the velocity is  $> 10 \mu\text{m/s}$ . The adhesive force of Z-15 is reduced dramatically with a velocity increase up to 20  $\mu\text{m/s}$ , after which it is reduced slightly, and the adhesive force of Z-DOL (fully bonded) is also decreased at high velocity. In the tested range of velocity, only the coefficient of friction of Si(100) decreases with velocity, while the coefficients of friction of Z-15 and Z-DOL (fully

bonded) remain almost constant. This implies that the friction mechanisms of Z-15 and Z-DOL (fully bonded) do not change with velocity.

The mechanisms of the effect of velocity on adhesion and friction can be explained based on the schematics shown in Fig. 12.63b (right) [54]. For Si(100), tribochemical reaction plays a major role. Although, at high velocity, the meniscus is broken and does not have enough time to rebuild, the contact stresses and high velocity lead to tribochemical reactions of the Si(100) wafer (which has  $\text{SiO}_2$  native oxide) and the  $\text{Si}_3\text{N}_4$  tip with water molecules to form  $\text{Si}(\text{OH})_4$ . The  $\text{Si}(\text{OH})_4$  is removed and continuously replenished during sliding. The  $\text{Si}(\text{OH})_4$  layer between the tip and the Si(100) surface is known to be of low shear strength and causes a decrease in friction force and coefficient of friction [11, 17]. The Si–OH chemical bonds between the tip and the Si(100) surface induce a large adhesive force. For Z-15 film, at high velocity, the meniscus formed by condensed water and Z-15 molecules is broken and does not have enough time to rebuild, therefore the adhesive force and consequently the friction force is reduced. The friction mechanism for the Z-15 film is still shearing of the same viscous liquid even in the high velocity range, thus the coefficient of friction of Z-15 does not change with velocity. For the Z-DOL (fully bonded) film, the surface can adsorb a few water molecules under ambient conditions, and at high velocity these molecules are displaced, which is responsible for the slight decrease in friction force and adhesive force. Koinkar and Bhushan [51, 52] have suggested that, in the case of samples with mobile films such as condensed water and Z-15 films, alignment of liquid molecules (shear thinning) is responsible for the drop in friction force with increasing scanning velocity. This could be another reason for the decrease in friction force with velocity for the Si(100) and Z-15 film in this study.

To study the effect of relative humidity on friction and adhesion, the variation of friction force, adhesive force, and coefficient of friction of Si(100), Z-15, and Z-DOL (fully bonded) as a function of relative humidity is shown in Fig. 12.64 [54], showing that, for Si(100) and Z-15 film, the friction force increases with relative humidity up to 45% and then shows a slight decrease with further increase in relative humidity. Z-DOL (fully bonded) has a smaller friction force than Si(100) and Z-15 over the whole testing range, and its friction force shows a relative apparent increase when the relative humidity is higher than 45%. For Si(100), Z-15, and Z-DOL (fully bonded), the adhesive forces increase with relative humidity, and their coefficients of friction increase with relative humidity up to 45%, after which they decrease with further increase of relative humidity. It is also observed that the effect of humidity on Si(100) really depends on the history of the Si(100) sample. As the surface of the Si(100) wafer readily adsorbs water in air, without any pretreatment the Si(100) used in our study almost reaches its saturated stage of adsorbed water, which is responsible for the smaller effect with increasing relative humidity. However, if the Si(100) wafer is thermally treated by baking at 150 °C for 1 h, a larger effect is observed.

The schematic in Fig. 12.64b (right) shows that, for Si(100), because of its high free surface energy, it can adsorb more water molecules with increasing relative humidity [54]. As discussed earlier, for Z-15 film in the humid environment, the water condensed from the humid environment competes with the lubricant film

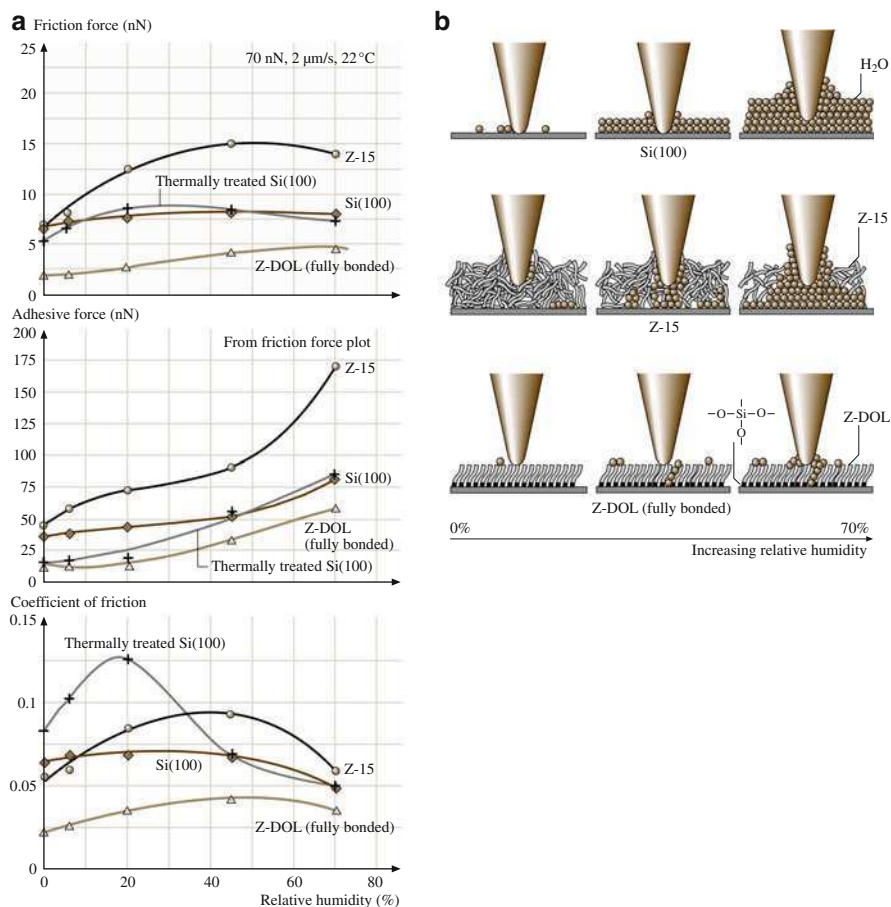


**Fig. 12.64** Influence of relative humidity on the friction force, adhesive force, and coefficient of friction of Si(100) and Z-15 and Z-DOL (fully bonded) films at 70 nN, 2  $\mu\text{m/s}$ , and in 22  $^{\circ}\text{C}$  air **(a)**. **(b)** Schematic showing the change of meniscus while increasing the relative humidity. In this figure, the thermally treated Si(100) represents the Si(100) wafer baked at 150  $^{\circ}\text{C}$  for 1 h in an oven (in order to remove adsorbed water) just before it was placed in the 0% RH chamber (after [54])

present on the sample surface, and interaction of the liquid lubricant film with the silicon substrate is weakened and a boundary layer of the liquid lubricant forms puddles. This dewetting allows water molecules to be adsorbed on the Si(100) substrate mixed with Z-15 molecules [51, 52]. Obviously, more water molecules can be adsorbed on the Z-15 surface with increasing relative humidity. The greater amount of adsorbed water molecules in the case of Si(100), along with the lubricant molecules in the case of the Z-15 film, form a larger meniscus, which leads to an increase of friction force, adhesive force, and coefficient of friction for Si(100) and Z-15 with humidity, although at very high humidity of 70% large quantities of adsorbed water can form a continuous water layer that separate the tip and sample

surface and acts as a kind of lubricant, which causes a decrease in the friction force and coefficient of friction. For Z-DOL (fully bonded) film, because of its hydrophobic surface properties, water molecules can be adsorbed at humidity above 45%, causing an increase in the adhesive force and friction force.

To study the effect of temperature on friction and adhesion, the variation of friction force, adhesive force, and coefficient of friction of Si(100), Z-15, and Z-DOL (fully bonded) with temperature is summarized in Fig. 12.65 [54].

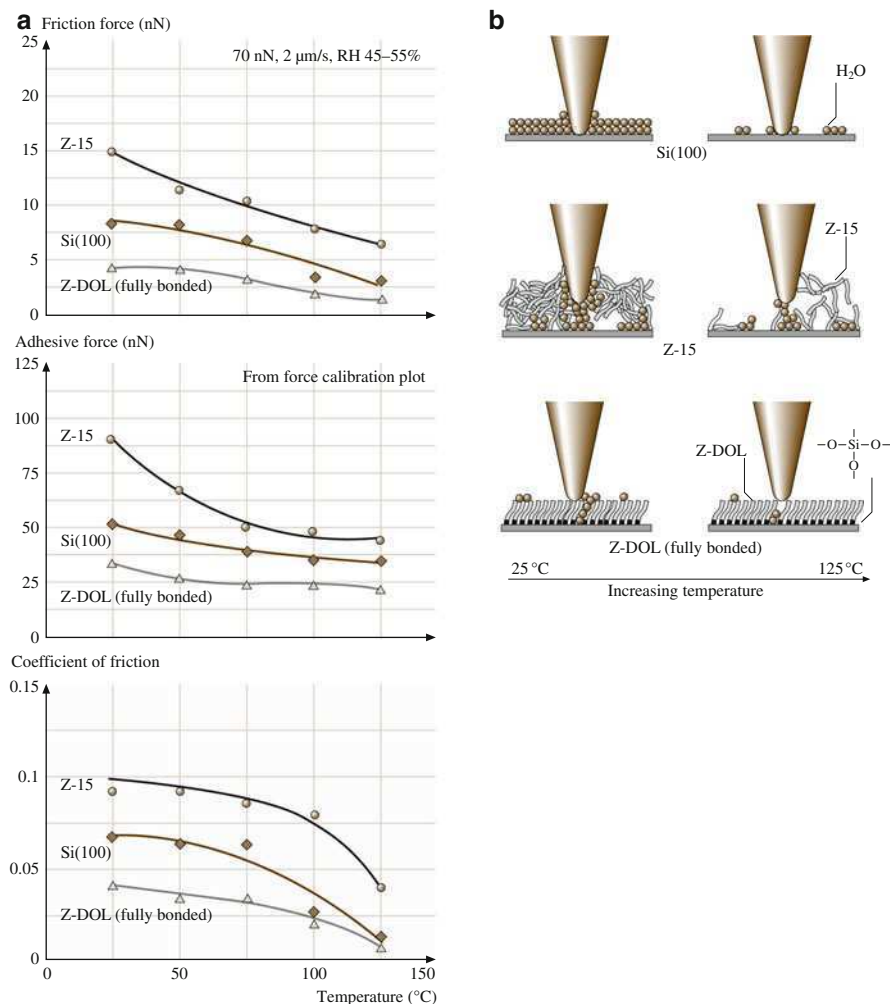


**Fig. 12.65** The influence of temperature on the friction force, adhesive force, and coefficient of friction of Si(100) and Z-15 and Z-DOL (fully bonded) films at 70 nN, 2  $\mu\text{m/s}$ , and in RH 40–50% air (a). (b) Schematic showing that, at high temperature, desorption of water decreases the adhesive forces. The reduced viscosity of Z-15 leads to the decrease of the coefficient of friction. High temperature facilitates the orientation of molecules in Z-DOL (fully bonded) film, which results in lower coefficient of friction (after [54])

The results shows that increasing temperature causes a decrease of friction force, adhesive force, and coefficient of friction for Si(100), Z-15, and Z-DOL (fully bonded). The schematic in Fig. 12.65b (right) indicates that, at high temperature, desorption of water leads to decrease of the friction force, adhesive forces, and coefficient of friction for all of the samples. For the Z-15 film, the reduction of viscosity at high temperature also contributes to the decrease of friction force and coefficient of friction. In the case of Z-DOL (fully bonded) film, molecules are easily oriented at high temperature, which may be partly responsible for the low friction force and coefficient of friction.

To summarize, the influence of velocity, relative humidity, and temperature on the friction force of mobile Z-15 film is presented in Fig. 12.66 [54]. The changing trends are also addressed in this figure.

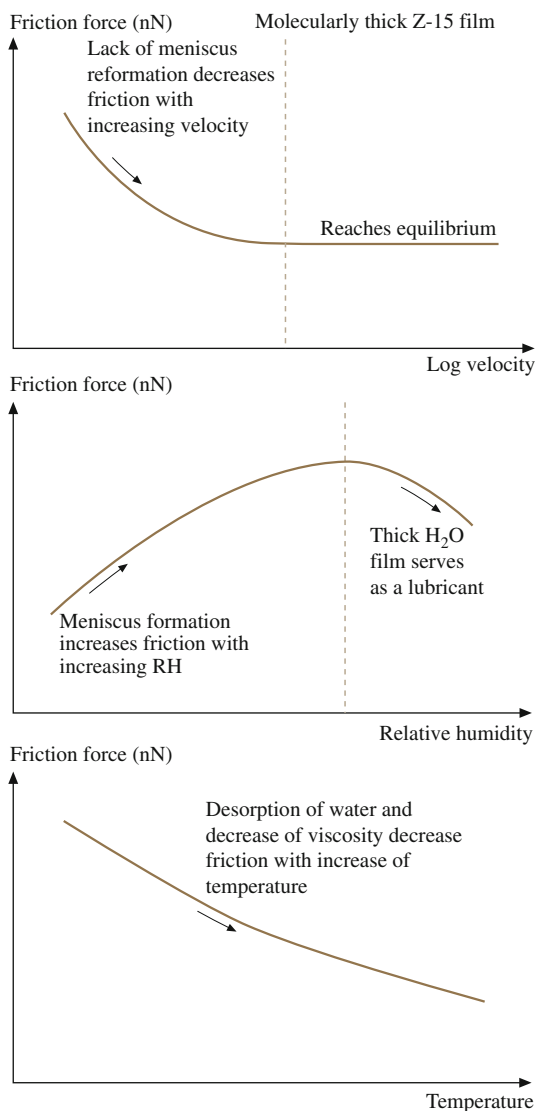
To study the durability of lubricant films at the nanoscale, the friction of Si(100), Z-15, and Z-DOL (fully bonded) as a function of the number of scanning cycles is shown in Fig. 12.67 [54]. As observed earlier, the friction force for Z-15 is higher than that for Si(100), with the lowest values for Z-DOL (fully bonded). During cycling, the friction force and coefficient of friction for Si(100) show a slight decrease during the first few cycles, then remain constant. This is related to the removal of the native oxide. In the case of the Z-15 film, the friction force and coefficient of friction show an increase during the first few cycles and then approach higher, stable values. This is believed to be caused by the attachment of Z-15 molecules to the tip. After several scans, the molecular interaction reaches an equilibrium, and after that the friction force and coefficient of friction remain constant. In the case of Z-DOL (fully bonded) film, the friction force and coefficient of friction start out low and remain low during the entire test for 100 cycles. This suggests that Z-DOL (fully bonded) molecules do not get attached or displaced as readily as those of Z-15.

## 12.5.2 Self-Assembled Monolayers

For lubrication of MEMS/NEMS, another effective approach involves the deposition of organized and dense molecular layers of long-chain molecules. Two common methods to produce monolayers and thin films are Langmuir–Blodgett (LB) deposition and self-assembled monolayers (SAMs) by chemical grafting of molecules. LB films are physically bonded to the substrate by weak van der Waals attraction, while SAMs are chemically bonded via covalent bonds to the substrate. Because of the choice of chain length and terminal linking group that SAMs offer, they hold great promise for boundary lubrication of MEMS/NEMS. A number of studies have been conducted to study the tribological properties of various SAMs deposited on Si, Al, and Cu substrates [20, 53, 55, 145–158].

Bhushan and Liu [53] studied the effect of film compliance on adhesion and friction. They used hexadecane thiol (HDT), 1, 1'-biphenyl-4-thiol (BPT), and cross-linked BPT (BPTC) solvent-deposited on Au(111) substrate (Fig. 12.68a).

**Fig. 12.66** Schematic showing the change of friction force of molecularly thick Z-15 films with log velocity, relative humidity, and temperature. The changing trends are also addressed in this figure (after [54])



The average values and standard deviation of the adhesive force and coefficient of friction are presented in Fig. 12.68b. Based on these data, the adhesive force and coefficient of friction of SAMs are lower than those of the corresponding substrates. Among the tested films, HDT exhibited the lowest values. Based on stiffness measurements of various SAMs, HDT was the most compliant, followed by BPT and BPTC. Based on friction and stiffness measurements, SAMs with high-compliance long carbon chains exhibit low friction; chain compliance is desirable for low friction. The friction mechanism of SAMs is explained by a so-called *molecular*

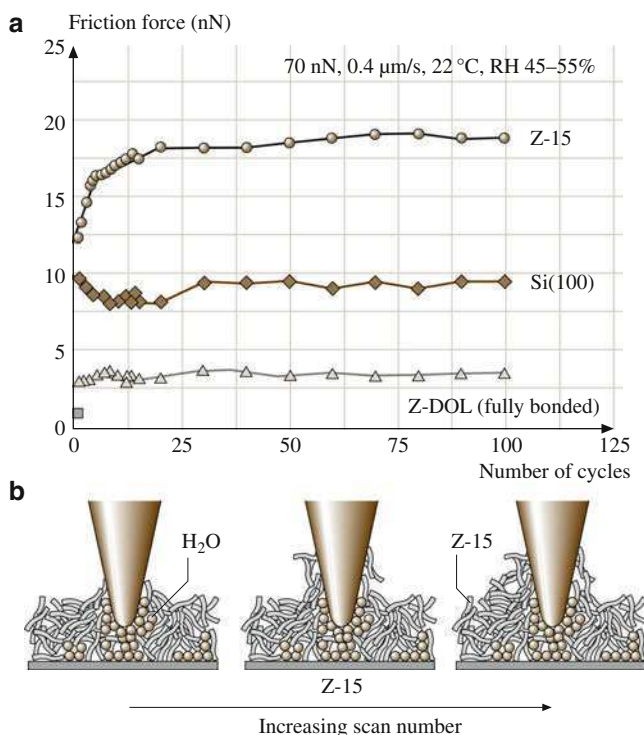


**Fig. 12.67** Friction force versus number of sliding cycles for Si(100) and Z-15 and Z-DOL (fully bonded) films at 70 nN, 0.8  $\mu\text{m/s}$ , and in ambient air (a). (b) Schematic showing that some liquid Z-15 molecules can be attached to the tip. The molecular interaction between the molecules attached to the tip and the Z-15 molecules in the film results in an increase of the friction force with multiple scans (after [54])

*spring* model (Fig. 12.69). According to this model, the chemically adsorbed self-assembled molecules on a substrate are just like assembled molecular springs anchored to the substrate. An asperity sliding on the surface of SAMs is like a tip sliding on the top of *molecular springs* or a *brush*. The molecular spring assembly has compliant features and can experience orientation and compression under load. The orientation of the molecular springs or brush under a normal load reduces the shearing force at the interface, which in turn reduces the friction force. The orientation is determined by the spring constant of a single molecule as well as the interaction between the neighboring molecules, which can be reflected by the packing density or packing energy. It should be noted that the orientation can lead to conformational defects along the molecular chains, which lead to energy dissipation.

An elegant way to demonstrate the influence of molecular stiffness on friction is to investigate SAMs with different structures on the same wafer. For this purpose, a micropatterned SAM was prepared. First biphenyldimethylchlorosilane (BDCS) was deposited on silicon by a typical self-assembly method [147]. Then the film was partially cross-linked using a mask technique using low-energy electron



**Fig. 12.68** (a) Schematics of structures of hexadecane thiol and biphenylthiol SAMs on Au(111) substrates, and (b) adhesive force and coefficient of friction of Au(111) substrate and various SAMs

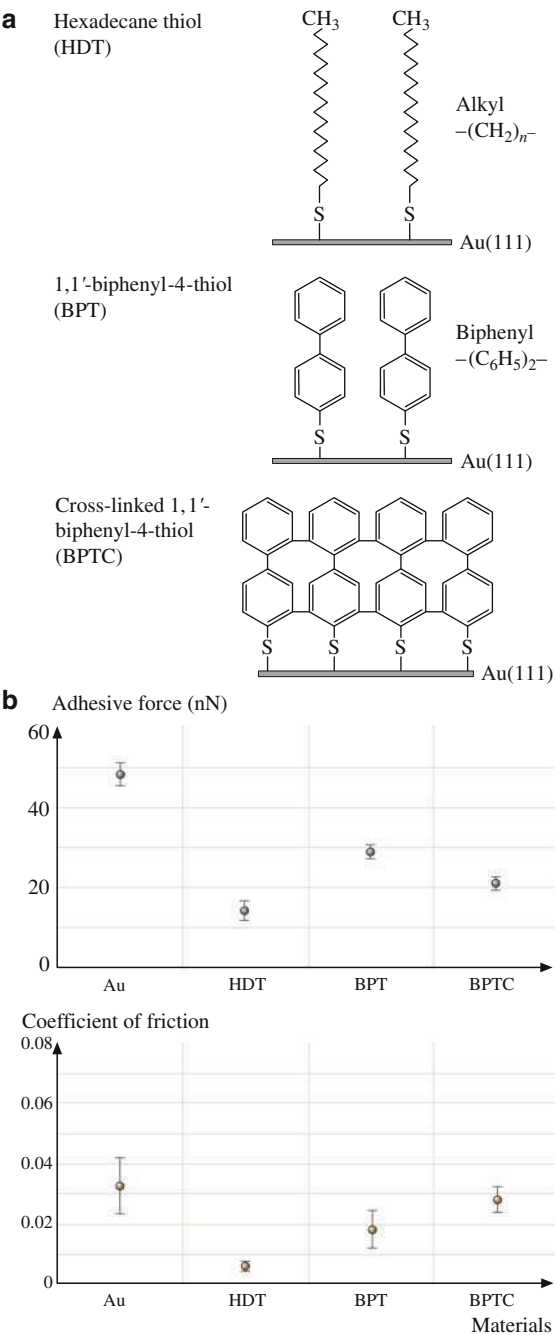


**Fig. 12.69** Molecular spring model of SAMs. In this figure,  $\alpha_1 < \alpha_2$ , which is caused by further orientation under the normal load applied by an asperity tip (after [53])

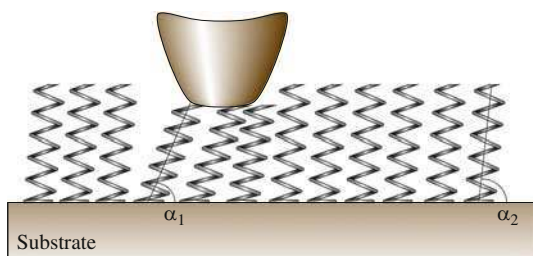
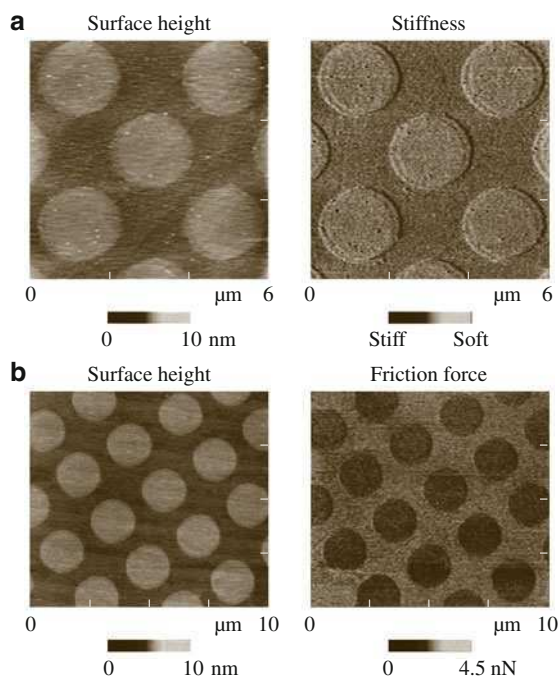
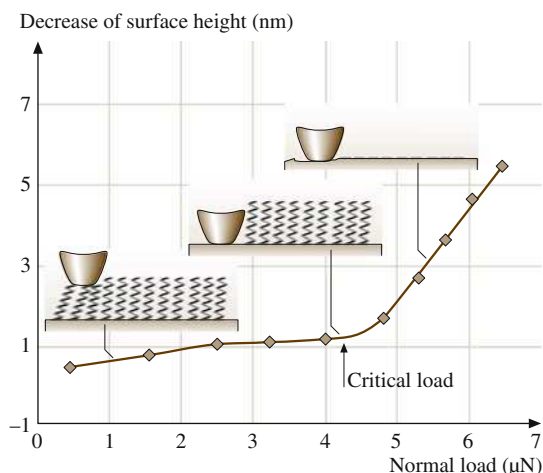


**Fig. 12.70** (a) AFM gray-scale surface height and stiffness images, and (b) AFM gray-scale surface height and friction force images of micropatterned BDCS (after [147])



irradiation. Finally micropatterned BDCS films were realized, which had both as-deposited and cross-linked coating regions on the same wafer. The local stiffness properties of this micropatterned sample were investigated by the force-modulation AFM technique [66]. The variation in the deflection amplitude provides a measure of the relative local stiffness of the surface. Surface height, stiffness, and friction images of the micropatterned biphenyldimethylchlorosilane (BDCS) specimen were obtained and are presented in Fig. 12.70 [147]. The circular areas correspond to the as-deposited film, and the remaining area to the cross-linked film. Figure 12.70a indicates that cross-linking caused by the low-energy electron irradiation leads to  $\approx 0.5$  nm decrease of the surface height of the BDCS film. The corresponding stiffness images indicate that the cross-linked area has higher

**Fig. 12.71** Illustration of the wear mechanism of SAMs with increasing normal load (after [147])



stiffness than the as-deposited area. Figure 12.70b indicates that the as-deposited area (higher surface height) has a lower friction force. Obviously, these data from the micropatterned sample prove that the local stiffness of SAMs influences their friction performance. Higher stiffness leads to larger friction force. These results provide strong proof of the suggested molecular spring model.

SAMs with high-compliance long carbon chains also exhibit the best wear resistance [53, 147]. In wear experiments, curves of wear depth as a function of normal load show a critical normal load, at which the film wears rapidly. A representative curve is shown in Fig. 12.71. Below the critical normal load, SAMs undergo orientation; at the critical load SAMs wear away from the substrate due to relatively weak interface bond strengths, while above the critical normal load severe wear takes place on the substrate.

### 12.5.3 Liquid Film Thickness Measurements

Liquid film thickness mapping of ultrathin films (on the order of 2 nm) can be obtained using friction force microscopy [51] and adhesive force mapping [113]. Figure 12.72 shows gray scale plots of the surface topography and friction force obtained simultaneously for unbonded Demnum S-100-type PFPE lubricant film on silicon. Demnum-type PFPE lubricant (Demnum, Daikin, Japan) chains have  $-\text{CF}_2 - \text{CH}_2 - \text{OH}$  (a reactive end group) on one end, whereas Z-DOL chains have hydroxyl groups on both ends, as described earlier. The friction force plot shows well-distinguished low- and high-friction regions roughly corresponding to high and low regions in the surface topography (thick and thin lubricant regions). A uniformly lubricated sample does not show such a variation in the friction. Friction force imaging can thus be used to measure the lubricant uniformity on

**Fig. 12.72** Gray-scale plots of the surface topography and friction force obtained simultaneously for unbonded Demnum-type perfluoropolyether lubricant film on silicon (after [51])

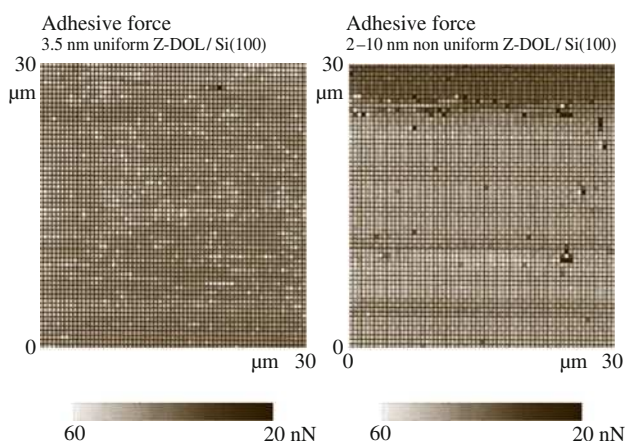
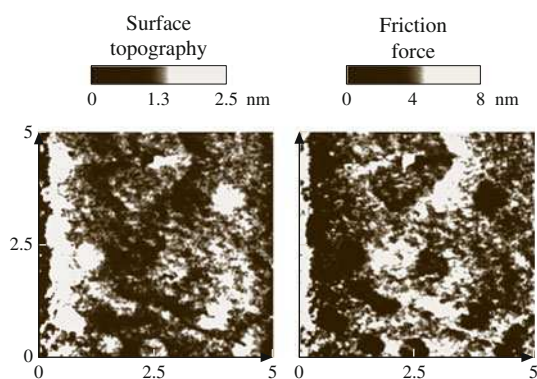
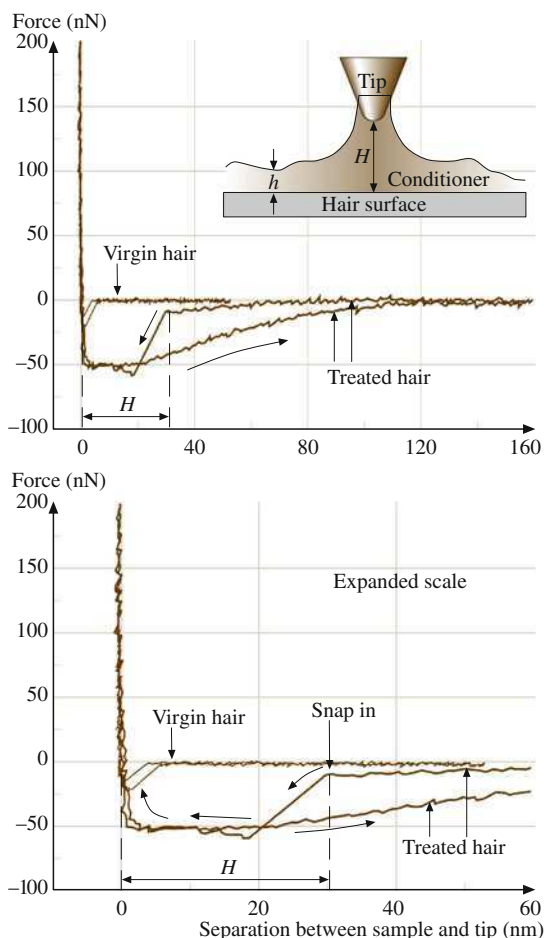


**Fig. 12.73** Gray-scale plots of the adhesive force distribution of a uniformly coated, 3.5 nm-thick unbonded Z-DOL film on silicon and 3–10 nm-thick unbonded Z-DOL film on silicon that was deliberately coated nonuniformly by vibrating the sample during the coating process (after [113])

the sample surface, which cannot be identified by surface topography alone. Figure 12.73 shows the gray scale plots of the adhesive force distribution for silicon samples coated uniformly and nonuniformly with Z-DOL-type PFPE lubricant. It can be clearly seen that there exists a region which has adhesive force distinctly different from the other region for the nonuniformly coated sample. This implies that the liquid film thickness is nonuniform, giving rise to a difference in the meniscus forces.

Quantitative measurements of liquid film thickness of thin lubricant films (on the order of a few nm) with nanometer lateral resolution can be made by using AFM [5, 13, 72, 94]. The liquid film thickness is obtained by measuring the force on the tip as it approaches, contacts, and pushes through the liquid film and ultimately contacts the substrate. The distance between the sharp snap-in (owing to the formation of a liquid meniscus and van der Waals forces between the film and

**Fig. 12.74** Forces between the tip and the hair surface as a function of tip–sample separation for virgin and conditioner-treated hair. A schematic of the measurement of localized conditioner thickness is shown in the *inset at the top*. An expanded-scale view of the force curve for small separations is shown at the *bottom* (after [72])



the tip) at the liquid surface and the hard repulsion at the substrate surface is a measure of the liquid film thickness. Figure 12.74 shows a plot of the forces between the tip and virgin hair or hair treated with conditioner. The hair sample was first brought into contact with the tip and then pulled away at a velocity of 400 nm/s. The zero tip–sample separation is defined to be the position where the force on the tip is zero, and the tip is not in contact with the sample. As the tip approaches the sample, a negative force exists, which indicates an attractive force. The treated hair surface shows a much longer range of interaction with the tip compared with the very short range of interaction between the virgin hair surface and the tip. Typically, the tip suddenly snaps into contact with the conditioner layer at a finite separation  $H$  ( $\approx 30$  nm), which is proportional to the conditioner thickness  $h$ . As the tip contacts the substrate, the tip travels with the sample. When the sample is withdrawn, the forces on the tip slowly decrease to zero once the liquid meniscus is drawn out from the hair surface. It should be noted that the

distance  $H$  between the sharp snap-in at the liquid surface and the hard wall contact with the substrate is not the real conditioner thickness  $h$ . Due to the interaction of the liquid with the tip at some spacing distance,  $H$  tends to be thicker than the actual film thickness, but can still provide an estimate and upper limit for the actual film thickness.

## 12.6 Conclusion

For most solid–solid interfaces of technological relevance, contact occurs at multiple asperities. A sharp AFM/FFM tip sliding on a surface simulates just one such contact. However, asperities come in all shapes and sizes. The effect of the radius of a single asperity (tip) on the friction/adhesion performance can be studied using tips of different radii. AFM/FFM is used to study various tribological phenomena, which include surface roughness, adhesion, friction, scratching, wear, indentation, detection of material transfer, and boundary lubrication. Measurement of atomic-scale friction of a freshly cleaved highly oriented pyrolytic graphite exhibits the same periodicity as that of the corresponding topography. However, the peaks in friction and those in the corresponding topography are displaced relative to each other. Variations in atomic-scale friction and the observed displacement can be explained by the variation in interatomic forces in the normal and lateral directions. The relevant friction mechanism is atomic-scale stick–slip. Local variations in microscale friction occur and are found to correspond to the local slopes, suggesting that a ratchet mechanism and collision effects are responsible for this variation. Directionality in the friction is observed on both micro- and macroscales, which results from the surface roughness and surface preparation. Anisotropy in surface roughness accentuates this effect. The friction contrast in conventional frictional measurements is based on interactions dependent upon interfacial material properties superimposed by roughness-induced lateral forces. To obtain roughness-independent friction, lateral or torsional modulation techniques can be used. These techniques also allow measurements over a small region. AFM/FFM experiments are generally conducted at relative velocities up to  $\approx 200 \mu\text{m/s}$ . High-velocity experiments can be performed by either mounting a sample on a shear wave transducer driven at very high frequencies or mounting a sample on a high-velocity piezo stage. By using these techniques, friction and wear experiments can be performed at a range of sliding velocities as well as normal loads, and the data have been used to develop nanoscale friction and wear maps. Relevant friction mechanisms are different for different ranges of sliding velocities and normal loads.

The adhesion and friction in wet environment depends on the tip radius, surface roughness, and relative humidity. Superhydrophobic surfaces can be designed by roughness optimization.

Nanoscale friction is generally found to be smaller than microscale friction. There are several factors responsible for these differences, including wear and contaminant particles, transition from elasticity to plasticity, scale-dependent

roughness and mechanical properties, and meniscus effects. Nanoscale friction values increase with an increase in the normal load above a certain critical load (pressure), approaching the macroscale friction. The critical contact pressure corresponds to the hardness of the softer of the two contacting materials.

The wear rate on the microscale for single-crystal silicon is negligible below 20  $\mu\text{N}$ , and much higher and approximately constant at higher loads. Elastic deformation at low loads is responsible for negligible wear. Most of the wear debris is loose. SEM and TEM studies of the wear region suggest that the material on the microscale is removed by plastic deformation, with a small contribution from elastic fracture; this observation corroborates with the scratch data. Evolution of wear has also been studied using AFM. Wear is found to be initiated at nanoscratches. For a sliding interface requiring near-zero friction and wear, contact stresses should be below the hardness of the softer material to minimize plastic deformation, and surfaces should be free of nanoscratches. Further, wear precursors can be detected at early stages of wear by using surface potential measurements. It is found that, even in the case of zero wear (no measurable deformation of the surface using AFM), there can be a significant change in the surface potential inside the wear mark, which is useful for the study of wear precursors. Detection of material transfer on a nanoscale is possible with AFM.

In situ surface characterization of the local deformation of materials and thin coatings can be carried out using a tensile stage inside an AFM. An AFM can also be used for nanofabrication/nanomachining.

A modified AFM can be used to obtain load–displacement curves and for measurement of nanoindentation hardness and Young's modulus of elasticity, with depth of indentation as low as 1 nm. Hardness of ceramics on nanoscales is found to be higher than that on the microscale. Ceramics exhibit significant plasticity and creep on a nanoscale. By using the force-modulation technique, localized surface elasticity maps of composite materials with penetration depth as low as 1 nm can be obtained. By using phase-contrast microscopy in tapping or torsional mode, it is possible to get phase-contrast maps or the contrast in viscoelastic properties of near-surface regions. Scratching and indentation on nanoscales are powerful ways to screen for adhesion and resistance to deformation of ultrathin films.

Boundary lubrication studies and measurement of lubricant film thickness with lateral resolution on the nanoscale can be conducted using AFM. Chemically bonded lubricant films and self-assembled monolayers are superior in terms of friction and wear resistance. For chemically bonded lubricant films, the adsorption of water, the formation of meniscus and its change during sliding, and surface properties play an important role in the adhesion, friction, and durability of these films. Sliding velocity, relative humidity, and temperature affect adhesion and friction. For SAMs, the friction mechanism is explained by a so-called *molecular spring* model. Films with high-compliance long carbon chains exhibit low friction and wear. Also perfluoroalkylsilane SAMs on Si appear to be more hydrophobic with lower adhesion than alkylsilane SAMs on Si.

Investigations of adhesion, friction, wear, scratching, and indentation on the nanoscale using AFM can provide insights into the failure mechanisms of materials. Coefficients of friction, wear rates, and mechanical properties such as hardness have been found to be different on the nanoscale than on the macroscale; generally, coefficients of friction and wear rates on micro- and nanoscales are smaller, whereas hardness is greater. Therefore, micro/nanotribological studies may help to define the regimes for ultralow friction and near-zero wear. These studies also provide insight into the atomic origins of adhesion, friction, wear, and lubrication mechanisms.

## References

1. I.L. Singer, H.M. Pollock (Eds.), *Fundamentals of Friction: Macroscopic and Microscopic Processes*, NATO ASI Ser. E, Vol. 220 (Kluwer, Dordrecht, 1992)
2. H.J. Güntherodt, D. Anselmetti, *Forces in Scanning Probe Methods*, NATO ASI Ser. E, Vol. 286 (Kluwer, Dordrecht, 1995)
3. B.N.J. Persson, E. Tosatti, *Physics of Sliding Friction*, NATO ASI Ser. E, Vol. 311 (Kluwer, Dordrecht, 1996)
4. B. Bhushan, *Micro/Nanotribology and its Applications*, NATO ASI Ser. E, Vol. 330 (Kluwer, Dordrecht, 1997)
5. B. Bhushan, *Handbook of Micro/Nanotribology*, 2nd edn. (CRC, Boca Raton, 1999)
6. B. Bhushan, *Principles and Applications of Tribology* (Wiley, New York, 1999)
7. B. Bhushan, Nanoscale tribophysics and tribomechanics. *Wear* **225–229**, 465–492 (1999)
8. B. Bhushan, *Modern Tribology Handbook, Vol. 1: Principles of Tribology* (CRC, Boca Raton, 2001)
9. B. Bhushan, *Fundamentals of Tribology and Bridging the Gap Between the Macro- and Micro/ Nanoscales*, NATO Sci. Ser. II, Vol. 10 (Kluwer, Dordrecht, 2001)
10. B. Bhushan, Nano- to microscale wear and mechanical characterization studies using scanning probe microscopy. *Wear* **251**, 1105–1123 (2001)
11. B. Bhushan, *Introduction to Tribology* (Wiley, New York, 2002)
12. B. Bhushan, Nanotribology and nanomechanics. *Wear* **259**, 1507–1531 (2005)
13. B. Bhushan, *Nanotribology and Nanomechanics – An Introduction*, 2nd edn. (Springer, Berlin, 2008)
14. B. Bhushan, J.N. Israelachvili, U. Landman, Nanotribology: Friction, wear and lubrication at the atomic scale. *Nature* **374**, 607–616 (1995)
15. B. Bhushan, *Tribology and Mechanics of Magnetic Storage Devices*, 2nd edn. (Springer, New York, 1996)
16. B. Bhushan, *Tribology Issues and Opportunities in MEMS* (Kluwer, Dordrecht, 1998)
17. B. Bhushan, Wear and mechanical characterisation on micro- to picoscales using AFM. *Int. Mater. Rev.* **44**, 105–117 (1999)
18. B. Bhushan, Adhesion and stiction, Mechanisms, measurement techniques, and methods for reduction (invited). *J. Vac. Sci. Technol. B* **21**, 2262–2296 (2003)
19. B. Bhushan, Nanotribology, nanomechanics and nanomaterials characterization. *Philos. Trans. R. Soc. A* **366**, 1351–1381 (2008)
20. B. Bhushan, A.V. Kulkarni, V.N. Koinkar, M. Boehm, L. Odoni, C. Martelet, M. Belin, Microtribological characterization of self-assembled and Langmuir–Blodgett monolayers by atomic and friction force microscopy. *Langmuir* **11**, 3189–3198 (1995)
21. B. Bhushan, H. Fuchs, S. Hosaka (Eds.), *Applied Scanning Probe Methods* (Springer, Berlin, 2004)



22. B. Bhushan, H. Fuchs, S. Kawata (Eds.), *Applied Scanning Probe Methods V – Scanning Probe Microscopy Techniques* (Springer, Berlin, 2007)
23. B. Bhushan, H. Fuchs, M. Tomitori (Eds.), *Applied Scanning Probe Methods VIII – Scanning Probe Microscopy Techniques* (Springer, Berlin, 2008)
24. B. Bhushan, H. Fuchs, M. Tomitori (Eds.), *Applied Scanning Probe Methods IX – Characterization* (Springer, Berlin, 2008)
25. B. Bhushan, H. Fuchs, M. Tomitori (Eds.), *Applied Scanning Probe Methods X – Biomimetics and Industrial Applications* (Springer, Berlin, 2008)
26. B. Bhushan, H. Fuchs (Eds.), *Applied Scanning Probe Methods II – Scanning Probe Microscopy Techniques* (Springer, Berlin, 2006)
27. B. Bhushan, H. Fuchs (Eds.), *Applied Scanning Probe Methods III – Characterization* (Springer, Berlin, 2006)
28. B. Bhushan, H. Fuchs (Eds.), *Applied Scanning Probe Methods IV – Industrial Applications* (Springer, Berlin, 2006)
29. B. Bhushan, H. Fuchs (Eds.), *Applied Scanning Probe Methods VII – Biomimetics and Industrial Applications* (Springer, Berlin, 2007)
30. B. Bhushan, H. Fuchs (Eds.), *Applied Scanning Probe Methods XI – Scanning Probe Microscopy Techniques* (Springer, Berlin, 2009)
31. B. Bhushan, H. Fuchs (Eds.), *Applied Scanning Probe Methods XII – Characterization* (Springer, Berlin, 2009)
32. B. Bhushan, H. Fuchs (Eds.), *Applied Scanning Probe Methods XIII – Biomimetics and Industrial Applications* (Springer, Berlin, 2009)
33. B. Bhushan, S. Kawata (Eds.), *Applied Scanning Probe Methods VI – Characterization* (Springer, Berlin, 2007)
34. G. Binnig, C.F. Quate, C. Gerber, Atomic force microscopy. *Phys. Rev. Lett.* **56**, 930–933 (1986)
35. G. Binnig, C. Gerber, E. Stoll, T.R. Albrecht, C.F. Quate, Atomic resolution with atomic force microscope. *Europhys. Lett.* **3**, 1281–1286 (1987)
36. C.M. Mate, G.M. McClelland, R. Erlandsson, S. Chiang, Atomic-scale friction of a tungsten tip on a graphite surface. *Phys. Rev. Lett.* **59**, 1942–1945 (1987)
37. B. Bhushan, J. Ruan, Atomic-scale friction measurements using friction force microscopy: Part II – Application to magnetic media. *ASME J. Tribol.* **116**, 389–396 (1994)
38. J. Ruan, B. Bhushan, Atomic-scale friction measurements using friction force microscopy: Part I – General principles and new measurement techniques. *ASME J. Tribol.* **116**, 378–388 (1994)
39. J. Ruan, B. Bhushan, Atomic-scale and microscale friction of graphite and diamond using friction force microscopy. *J. Appl. Phys.* **76**, 5022–5035 (1994)
40. J. Ruan, B. Bhushan, Frictional behavior of highly oriented pyrolytic graphite. *J. Appl. Phys.* **76**, 8117–8120 (1994)
41. B. Bhushan, V.N. Koinkar, J. Ruan, Microtribology of magnetic media, *Proc. Inst. Mech. Eng. J: J. Eng. Tribol.* **208**, 17–29 (1994)
42. B. Bhushan, A.V. Kulkarni, Effect of normal load on microscale friction measurements. *Thin Solid Films* **278**, 49–56 (1996)
43. B. Bhushan, S. Sundararajan, Micro/nanoscale friction and wear mechanisms of thin films using atomic force and friction force microscopy. *Acta Mater.* **46**, 3793–3804 (1998)
44. V. Scherer, W. Arnold, B. Bhushan, Active friction control using ultrasonic vibration. In, *Tribology Issues and Opportunities in MEMS*, ed. by B. Bhushan (Kluwer, Dordrecht, 1998), pp. 463–469
45. V. Scherer, W. Arnold, B. Bhushan, Lateral force microscopy using acoustic friction force microscopy. *Surf. Interface Anal.* **27**, 578–587 (1999)
46. M. Reinstädter, U. Rabe, V. Scherer, U. Hartmann, A. Goldade, B. Bhushan, W. Arnold, On the nanoscale measurement of friction using atomic force microscope cantilever torsional resonances. *Appl. Phys. Lett.* **82**, 2604–2606 (2003)

47. M. Reinstädter, U. Rabe, A. Goldade, B. Bhushan, W. Arnold, Investigating ultra-thin lubricant layers using resonant friction force microscopy. *Tribol. Int.* **38**, 533–541 (2005)
48. M. Reinstädter, T. Kasai, U. Rabe, B. Bhushan, W. Arnold, Imaging and measurement of elasticity and friction using the TR mode. *J. Phys. D* **38**, R269–R282 (2005)
49. B. Bhushan, T. Kasai, A surface topography independent friction measurement technique using torsional resonance mode in an AFM. *Nanotechnology* **15**, 923–935 (2004)
50. N.S. Tambe, B. Bhushan, A new atomic force microscopy based technique for studying nanoscale friction at high sliding velocities. *J. Phys. D: Appl. Phys.* **38**, 764–773 (2005)
51. V.N. Koinkar, B. Bhushan, Micro/nanoscale studies of boundary layers of liquid lubricants formagnetic disks. *J. Appl. Phys.* **79**, 8071–8075 (1996)
52. V.N. Koinkar, B. Bhushan, Microtribological studies of unlubricated and lubricated surfaces using atomic force/friction force microscopy. *J. Vac. Sci. Technol.* **14**, 2378–2391 (1996)
53. B. Bhushan, H. Liu, Nanotribological properties and mechanisms of alkylthiol and biphenyl thiol self-assembled monolayers studied by AFM. *Phys. Rev. B* **63**, 245412-1–245412-11 (2001)
54. H. Liu, B. Bhushan, Nanotribological characterization of molecularly thick lubricant films for applications to MEMS/NEMS by AFM. *Ultramicroscopy* **97**, 321–340 (2003)
55. B. Bhushan, T. Kasai, G. Kulik, L. Barbieri, P. Hoffmann, AFM study of perfluorosilane and alkylsilane self-assembled monolayers for antistiction in MEMS/NEMS. *Ultramicroscopy* **105**, 176–188 (2005)
56. B. Bhushan, V.N. Koinkar, Tribological studies of silicon for magnetic recording applications. *J. Appl. Phys.* **75**, 5741–5746 (1994)
57. V.N. Koinkar, B. Bhushan, Microtribological studies of  $\text{Al}_2\text{O}_3$ -TiC, polycrystalline and single-crystal Mn-Zn ferrite and SiC head slider materials. *Wear* **202**, 110–122 (1996)
58. V.N. Koinkar, B. Bhushan, Microtribological properties of hard amorphous carbon protective coatings for thin film magnetic disks and heads. *J. Eng. Tribol.* **211**, 365–372 (1997)
59. S. Sundararajan, B. Bhushan, Development of a continuous microscratch technique in an atomic force microscope and its application to study scratch resistance of ultra-thin hard amorphous carbon coatings. *J. Mater. Res.* **16**, 75–84 (2001)
60. J. Ruan, B. Bhushan, Nanoindentation studies of fullerene films using atomic force microscopy. *J. Mater. Res.* **8**, 3019–3022 (1993)
61. B. Bhushan, A.V. Kulkarni, W. Bonin, J.T. Wyrobek, Nano/picoindentation measurement using a capacitance transducer system in atomic force microscopy. *Philos. Mag.* **74**, 1117–1128 (1996)
62. B. Bhushan, V.N. Koinkar, Nanoindentation hardness measurements using atomic force microscopy. *Appl. Phys. Lett.* **64**, 1653–1655 (1994)
63. B. Bhushan, X. Li, Nanomechanical characterisation of solid surfaces and thin films. *Int. Mater. Rev.* **48**, 125–164 (2003)
64. P. Maivald, H.J. Butt, S.A.C. Gould, C.B. Prater, B. Drake, J.A. Gurley, V.B. Elings, P.K. Hansma, Using force modulation to image surface elasticities with the atomic force microscope. *Nanotechnology* **2**, 103–106 (1991)
65. B. Anczykowski, D. Kruger, K.L. Babcock, H. Fuchs, Basic properties of dynamic force microscopy with the scanning force microscope in experiment and simulation. *Ultramicroscopy* **66**, 251–259 (1996)
66. D. DeVecchio, B. Bhushan, Localized surface elasticity measurements using an atomic force microscope. *Rev. Sci. Instrum.* **68**, 4498–4505 (1997)
67. V. Scherer, B. Bhushan, U. Rabe, W. Arnold, Local elasticity and lubrication measurements using atomic force and friction force microscopy at ultrasonic frequencies, *IEEE Trans. Magn.* **33**, 4077–4079 (1997)
68. S. Amelio, A.V. Goldade, U. Rabe, V. Scherer, B. Bhushan, W. Arnold, Measurements of elastic properties of ultra-thin diamond-like carbon coatings using atomic force acoustic microscopy. *Thin Solid Films* **392**, 75–84 (2001)

69. W.W. Scott, B. Bhushan, Use of phase imaging in atomic force microscopy for measurement of viscoelastic contrast in polymer nanocomposites and molecularly-thick lubricant films. *Ultramicroscopy* **97**, 151–169 (2003)
70. B. Bhushan, J. Qi, Phase contrast imaging of nanocomposites and molecularly thick lubricant films in magnetic media. *Nanotechnology* **14**, 886–895 (2003)
71. T. Kasai, B. Bhushan, L. Huang, C. Su, Topography and phase imaging using the torsional resonance mode. *Nanotechnology* **15**, 731–742 (2004)
72. N. Chen, B. Bhushan, Morphological, nanomechanical and cellular structural characterization of human hair and conditioner distribution using torsional resonance mode in an AFM. *J. Microsc.* **220**, 96–112 (2005)
73. M.S. Bobji, B. Bhushan, Atomic force microscopic study of the micro-cracking of magnetic thin films under tension. *Scr. Mater.* **44**, 37–42 (2001)
74. M.S. Bobji, B. Bhushan, In-situ microscopic surface characterization studies of polymeric thin films during tensile deformation using atomic force microscopy. *J. Mater. Res.* **16**, 844–855 (2001)
75. N. Tambe, B. Bhushan, In situ study of nanocracking of multilayered magnetic tapes under monotonic and fatigue loading using an AFM. *Ultramicroscopy* **100**, 359–373 (2004)
76. M. Palacio, B. Bhushan, Normal and lateral force calibration techniques for AFM cantilevers. *Crit. Rev. Solid State Mater. Sci.* **35**, 73–104 (2010)
77. B. Bhushan, T. Kasai, C.V. Nguyen, M. Meyyappan, Multiwalled carbon nanotube AFM probes for surface characterization of micro/nanostructures. *Microsyst. Technol.* **10**, 633–639 (2004)
78. B. Bhushan, Micro/nanotribology and Its applications to magnetic storage devices and MEMS. *Tribol. Int.* **28**, 85–95 (1995)
79. D. DeVecchio, B. Bhushan, Use of a nanoscale Kelvin probe for detecting wear precursors. *Rev. Sci. Instrum.* **69**, 3618–3624 (1998)
80. B. Bhushan, A.V. Goldade, Measurements and analysis of surface potential change during wear of single crystal silicon (100) at ultralow loads using Kelvin probe microscopy. *Appl. Surf. Sci.* **157**, 373–381 (2000)
81. B. Bhushan, A.V. Goldade, Kelvin probe microscopy measurements of surface potential change under wear at low loads. *Wear* **244**, 104–117 (2000)
82. H.U. Krottil, T. Stifter, H. Waschipky, K. Weishaupt, S. Hild, O. Marti, Pulse force mode: A new method for the investigation of surface properties. *Surf. Interface Anal.* **27**, 336–340 (1999)
83. U. Rabe, K. Janser, W. Arnold, Vibrations of free and surface-coupled atomic force microscope cantilevers: Theory and experiment. *Rev. Sci. Instrum.* **67**, 3281–3293 (1996)
84. J. Tamayo, R. Garcia, Deformation, contact time, and phase contrast in tapping mode scanning force microscopy. *Langmuir* **12**, 4430–4435 (1996)
85. R. Garcia, J. Tamayo, M. Calleja, F. Garcia, Phase contrast in tapping-mode scanning force microscopy. *Appl. Phys. A* **66**, 309–312 (1998)
86. Y. Song, B. Bhushan, Quantitative extraction of inplane surface properties using torsional resonance mode in atomic force microscopy. *J. Appl. Phys.* **87**, 083533 (2005)
87. B. Bhushan, J. Ruan, B.K. Gupta, A scanning tunnelling microscopy study of fullerene films. *J. Phys. D: Appl. Phys.* **26**, 1319–1322 (1993)
88. G.A. Tomlinson, A molecular theory of friction. *Philos. Mag. Ser. 7*, 905–939 (1929)
89. D. Tomanek, W. Zhong, H. Thomas, Calculation of an atomically modulated friction force in atomic force microscopy. *Europhys. Lett.* **15**, 887–892 (1991)
90. E. Meyer, R. Overney, R. Lüthi, D. Brodbeck, L. Howald, J. Frommer, H.J. Güntherodt, O. Wolter, M. Fujihira, T. Takano, Y. Gotoh, Friction force microscopy of mixed Langmuir–Blodgett films. *Thin Solid Films* **220**, 132–137 (1992)
91. C.D. Frisbie, L.F. Rozsnyai, A. Noy, M.S. Wrighton, C.M. Lieber, Functional group imaging by chemical force microscopy. *Science* **265**, 2071–2074 (1994)
92. V.N. Koinkar, B. Bhushan, Effect of scan size and surface roughness on microscale friction measurements. *J. Appl. Phys.* **81**, 2472–2479 (1997)

93. S. Sundararajan, B. Bhushan, Topography-induced contributions to friction forces measured using an atomic force/friction force microscope. *J. Appl. Phys.* **88**, 4825–4831 (2000)
94. B. Bhushan, G.S. Blackman, Atomic force microscopy of magnetic rigid disks and sliders and its applications to tribology. *ASME J. Tribol.* **113**, 452–458 (1991)
95. K. Yamanaka, E. Tomita, Lateral force modulation atomic force microscope for selective imaging of friction forces. *Jpn. J. Appl. Phys.* **34**, 2879–2882 (1995)
96. O. Marti, H.-U. Krottil, Dynamic friction measurement with the scanning force microscope. In, *Fundamentals of Tribology and Bridging the Gap Between the Macro- and Micro/Nanoscales*, NATO Sci. Ser. II, Vol. 10, ed. by B. Bhushan (Kluwer, Dordrecht, 2001), pp. 121–135
97. Z. Tao, B. Bhushan, A new technique for studying nanoscale friction at sliding velocities up to 200 mm/s using atomic force microscope. *Rev. Sci. Instrum.* **71**, 103705 (2006)
98. N.S. Tambe, B. Bhushan, Scale dependence of micro/nano-friction and adhesion of MEMS/NEMS materials, coatings and lubricants. *Nanotechnology* **15**, 1561–1570 (2004)
99. N.S. Tambe, B. Bhushan, Friction model for the velocity dependence of nanoscale friction. *Nanotechnology* **16**, 2309–2324 (2005)
100. N.S. Tambe, B. Bhushan, Durability studies of micro/nanoelectromechanical system materials, coatings, and lubricants at high sliding velocities (up to 10 mm/s) using a modified atomic force microscope. *J. Vac. Sci. Technol. A* **23**, 830–835 (2005)
101. N.S. Tambe, B. Bhushan, Identifying materials with low friction and adhesion for nanotechnology applications. *Appl. Phys. Lett.* **86**, 061906-1–061906-3 (2005)
102. Z. Tao, B. Bhushan, Velocity dependence and rest time effect in nanoscale friction of ultrathin films at high sliding velocities. *J. Vac. Sci. Technol. A* **25**, 1267–1274 (2007)
103. O. Zwörner, H. Hölscher, U.D. Schwarz, R. Wiesendanger: The velocity dependence of frictional forces in point-contact friction. *Appl. Phys. A* **66**, S263–S267 (1998)
104. E. Gnecco, R. Bennewitz, T. Gyalog, C. Loppacher, M. Bammerlin, E. Meyer, H.J. Güntherodt, Velocity dependence of atomic friction. *Phys. Rev. Lett.* **84**, 1172–1175 (2000)
105. J.S. Helman, W. Baltensperger, J.A. Holyst, Simple-model for dry friction. *Phys. Rev. B* **49**, 3831–3838 (1994)
106. C. Fusco, A. Fasolino, Velocity dependence of atomic-scale friction: A comparative study of the one- and two-dimensional Tomlinson model. *Phys. Rev. B* **71**, 045413 (2005)
107. N.S. Tambe, B. Bhushan, Nanoscale friction mapping. *Appl. Phys. Lett.* **86**, 193102-1–193102-3 (2005)
108. N.S. Tambe, B. Bhushan, Nanoscale friction and wear maps. *Philos. Trans. R. Soc. A* **366**, 1405–1424 (2008)
109. N.S. Tambe, B. Bhushan, Nanoscale frictioninduced phase transformation of diamond-like carbon. *Scr. Mater.* **52**, 751–755 (2005)
110. S.C. Lim, M.F. Ashby, Wear mechanism maps. *Acta Metall.* **35**, 1–24 (1987)
111. S.C. Lim, M.F. Ashby, J.H. Brunton, Wear-rate transitions and their relationship to wear mechanisms. *Acta Metall.* **35**, 1343–1348 (1987)
112. N.S. Tambe, B. Bhushan, Nanowear mapping, A novel atomic force microscopy based approach for studying nanoscale wear at high sliding velocities. *Tribol. Lett.* **20**, 83–90 (2005)
113. B. Bhushan, C. Dandavate, Thin-film friction and adhesion studies using atomic force microscope. *J. Appl. Phys.* **87**, 1201–1210 (2000)
114. T. Stifter, O. Marti, B. Bhushan, Theoretical investigation of the distance dependence of capillary and van der Waals forces in scanning probe microscopy. *Phys. Rev. B* **62**, 13667–13673 (2000)
115. U.D. Schwarz, O. Zwörner, P. Köster, R. Wiesendanger, Friction force spectroscopy in the lowload regime with well-defined tips. In, *Micro/Nanotribology and Its Applications*, ed. by B. Bhushan (Kluwer, Dordrecht, 1997), pp. 233–238
116. B. Bhushan, H. Liu, S.M. Hsu, Adhesion and friction studies of silicon and hydrophobic and low friction films and investigation of scale effects. *ASME J. Tribol.* **126**, 583–590 (2004)

117. H. Liu, B. Bhushan, Adhesion and friction studies of microelectromechanical systems/nanoelectromechanical systems materials using a novel microtriboapparatus. *J. Vac. Sci. Technol. A* **21**, 1528–1538 (2003)
118. M. Nosonovsky, B. Bhushan, Scale effects in dry friction during multiple-asperity contact. *ASME J. Tribol.* **127**, 37–46 (2005)
119. B. Bhushan, B.K. Gupta, *Handbook of Tribology: Materials, Coatings and Surface Treatments* (McGraw-Hill, New York, 1991), reprinted by Krieger, Malabar (1997)
120. B. Bhushan, S. Venkatesan, Mechanical and tribological properties of silicon for micro-mechanical applications: A review. *Adv. Info. Storage Syst.* **5**, 211–239 (1993)
121. Anonymous, *Properties of Silicon*, EMIS Data Reviews Series No. 4. INSPEC, Institution of Electrical Engineers, London. See also Anonymous, MEMS Materials Database, <http://www.memsnet.org/material/> (2002)
122. J.E. Field (Ed.), *The Properties of Natural and Synthetic Diamond* (Academic, London, 1992)
123. B. Bhushan, Chemical, mechanical and tribological characterization of ultra-thin and hard amorphous carbon coatings as thin as 3.5 nm: Recent developments. *Diam. Relat. Mater.* **8**, 1985–2015 (1999)
124. Anonymous, *The Industrial Graphite Engineering Handbook* (National Carbon Company, New York, 1959)
125. B. Bhushan, M. Nosonovsky, Comprehensive model for scale effects in friction due to adhesion and two- and three-body deformation (plowing). *Acta Mater.* **52**, 2461–2474 (2004)
126. B. Bhushan, M. Nosonovsky, Scale effects in dry and wet friction, wear, and interface temperature. *Nanotechnology* **15**, 749–761 (2004)
127. B. Bhushan, M. Nosonovsky, Scale effects in friction using strain gradient plasticity and dislocation-assisted sliding (microslip). *Acta Mater.* **51**, 4331–4345 (2003)
128. V.N. Koinkar, B. Bhushan, Scanning and transmission electron microscopies of single-crystal silicon microworn/machined using atomic force microscopy. *J. Mater. Res.* **12**, 3219–3224 (1997)
129. X. Zhao, B. Bhushan, Material removal mechanism of single-crystal silicon on nanoscale and at ultralow loads. *Wear* **223**, 66–78 (1998)
130. B. Bhushan, P.S. Mokashi, T. Ma, A new technique to measure Poisson's ratio of ultrathin polymeric films using atomic force microscopy. *Rev. Sci. Instrum.* **74**, 1043–1047 (2003)
131. A.V. Kulkarni, B. Bhushan, Nanoscale mechanical property measurements using modified atomic force microscopy. *Thin Solid Films* **290/291**, 206–210 (1996)
132. A.V. Kulkarni, B. Bhushan, Nano/picoindentation measurements on single-crystal aluminum using modified atomic force microscopy. *Mater. Lett.* **29**, 221–227 (1996)
133. A.V. Kulkarni, B. Bhushan, Nanoindentation measurement of amorphous carbon coatings. *J. Mater. Res.* **12**, 2707–2714 (1997)
134. N.A. Fleck, G.M. Muller, M.F. Ashby, J.W. Hutchinson, Strain gradient plasticity: Theory and experiment. *Acta Metall. Mater.* **42**, 475–487 (1994)
135. W.D. Nix, H. Gao, Indentation size effects in crystalline materials: A law for strain gradient plasticity. *J. Mech. Phys. Solids* **46**, 411–425 (1998)
136. W.B. Li, J.L. Henshall, R.M. Hooper, K.E. Easterling, The mechanism of indentation creep. *Acta Metall. Mater.* **39**, 3099–3110 (1991)
137. F.P. Bowden, D. Tabor, *The Friction and Lubrication of Solids* (Clarendon, Oxford, 1950)
138. Z. Tao, B. Bhushan, Bonding, degradation, and environmental effects on novel perfluoropolyether lubricants. *Wear* **259**, 1352–1361 (2005)
139. B. Bhushan, M. Cichomski, Z. Tao, N.T. Tran, T. Ethen, C. Merton, R.E. Jewett, Nanotribological characterization and lubricant degradation studies of metal-film magnetic tapes using novel lubricants. *ASME J. Tribol.* **129**, 621–627 (2007)
140. M. Palacio, B. Bhushan, Surface potential and resistance measurements for detecting wear of chemically-bonded and unbonded molecularly-thick perfluoropolyether lubricant films using atomic force microscopy. *J. Colloid Interface Sci.* **315**, 261–269 (2007)

141. M. Palacio, B. Bhushan, Wear detection of candidate MEMS/NEMS lubricant films using atomic force microscopy-based surface potential measurements. *Scr. Mater.* **57**, 821–824 (2007)
142. B. Bhushan, M. Palacio, B. Kinzig, AFM-based nanotribological and electrical characterization of ultrathin wear-resistant ionic liquid films. *J. Colloid Interface Sci.* **317**, 275–287 (2008)
143. M. Palacio, B. Bhushan, Ultrathin wear-resistant ionic liquid films for novel MEMS/NEMS applications. *Adv. Mater.* **20**, 1194–1198 (2008)
144. M. Palacio, B. Bhushan, Molecularly thick dicationic ionic liquid films for nanolubrication. *J. Vac. Sci. Technol. A* **27**(4), 986–995 (2009)
145. B. Bhushan, D. Hansford, K.K. Lee, Surface modification of silicon and polymethylsiloxane surfaces with vapor-phase-deposited ultrathin fluorosilane films for biomedical nanodevices. *J. Vac. Sci. Technol. A* **24**, 1197–1202 (2006)
146. H. Liu, B. Bhushan, W. Eck, V. Stadler, Investigation of the adhesion, friction, and wear properties of biphenyl thiol self-assembled monolayers by atomic force microscopy. *J. Vac. Sci. Technol. A* **19**, 1234–1240 (2001)
147. H. Liu, B. Bhushan, Investigation of nanotribological properties of self-assembled monolayers with alkyl and biphenyl spacer chains. *Ultramicroscopy* **91**, 185–202 (2002)
148. T. Kasai, B. Bhushan, G. Kulik, L. Barbieri, P. Hoffman, Micro-/nanotribological study of perfluorosilane SAMs for antistiction and low wear. *J. Vac. Sci. Technol. B* **23**, 995–1003 (2005)
149. K.K. Lee, B. Bhushan, D. Hansford, Nanotribological characterization of fluoropolymer thin films for biomedical micro-/nanoelectromechanical systems applications. *J. Vac. Sci. Technol. A* **23**, 804–810 (2005)
150. N.S. Tambe, B. Bhushan, Nanotribological characterization of self assembled monolayers deposited on silicon and aluminum substrates. *Nanotechnology* **16**, 1549–1558 (2005)
151. Z. Tao, B. Bhushan, Degradation mechanisms and environmental effects on perfluoropolyether, self-assembled monolayers, and diamondlike carbon films. *Langmuir* **21**, 2391–2399 (2005)
152. E. Hoque, J.A. DeRose, P. Hoffmann, H.J. Mathieu, B. Bhushan, M. Cichomski, Phosphonate self-assembled monolayers on aluminum surfaces. *J. Chem. Phys.* **124**, 174710 (2006)
153. E. Hoque, J.A. DeRose, G. Kulik, P. Hoffmann, H.J. Mathieu, B. Bhushan, Alkylphosphonate modified aluminum oxide surfaces. *J. Phys. Chem. B* **110**, 10855–10861 (2006)
154. E. Hoque, J.A. DeRose, P. Hoffmann, B. Bhushan, H.J. Mathieu, Alkylperfluorosilane self-assembled monolayers on aluminum: A comparison with alkylphosphonate self-assembled monolayers. *J. Phys. Chem. C* **111**, 3956–3962 (2007)
155. E. Hoque, J.A. DeRose, P. Hoffmann, B. Bhushan, H.J. Mathieu, Chemical stability of nonwetting, low adhesion self-assembled monolayer films formed by perfluoroalkylsilazation of copper. *J. Chem. Phys.* **126**, 114706 (2007)
156. E. Hoque, J.A. DeRose, B. Bhushan, H.J. Mathieu, Self-assembled monolayers on aluminum and copper oxide surfaces: Surface and interface characteristics, nanotribological properties, and chemical stability. In, *Applied Scanning Probe Methods IX – Characterization*, ed. by B. Bhushan, H. Fuchs, M. Tomitori (Springer, Berlin, 2008), pp. 235–281
157. E. Hoque, J.A. DeRose, B. Bhushan, K.W. Hipps, Low adhesion, non-wetting phosphonate self-assembled monolayer films formed on copper oxide surfaces. *Ultramicroscopy* **109**(8), 1015–1022 (2009)
158. J.A. DeRose, E. Hoque, B. Bhushan, H.J. Mathieu, Characterization of perfluorodecanote self-assembled monolayers on aluminum and comparison of stability with phosphonate and siloxy self-assembled monolayers. *Surf. Sci.* **602**, 1360–1367 (2008)

# Chapter 13

## Surface Forces and Nanorheology of Molecularly Thin Films

Marina Ruths and Jacob N. Israelachvili

**Abstract** In this chapter, we describe the static and dynamic normal forces that occur between surfaces in vacuum or liquids and the different modes of friction that can be observed between: (1) bare surfaces in contact (dry or interfacial friction), (2) surfaces separated by a thin liquid film (lubricated friction), and (3) surfaces coated with organic monolayers (boundary friction).

Experimental methods suitable for measuring normal surface forces, adhesion and friction (lateral or shear) forces of different magnitude at the molecular level are described. We explain the molecular origin of van der Waals, electrostatic, solvation and polymer-mediated interactions, and basic models for the contact mechanics of adhesive and nonadhesive elastically deforming bodies. The effects of interaction forces, molecular shape, surface structure and roughness on adhesion and friction are discussed.

Simple models for the contributions of the adhesion force and external load to interfacial friction are illustrated with experimental data on both unlubricated and lubricated systems, as measured with the surface forces apparatus. We discuss rate-dependent adhesion (adhesion hysteresis) and how this is related to friction. Some examples of the transition from wearless friction to friction with wear are shown.

Lubrication in different lubricant thickness regimes is described together with explanations of nanorheological concepts. The occurrence of and transitions between smooth and stick–slip sliding in various types of dry (unlubricated and solid boundary lubricated) and liquid lubricated systems are discussed based on recent experimental results and models for stick–slip involving memory distance and dilatancy.

### 13.1 Introduction: Types of Surface Forces

In this chapter, we discuss the most important types of surface forces and the relevant equations for the force and friction laws. Several different attractive and repulsive forces operate between surfaces and particles. Some forces occur in vacuum, for example, attractive van der Waals and repulsive hard-core interactions. Other types of forces can arise only when the interacting surfaces are separated by another condensed phase, which is usually a liquid. The most common types of surface forces and their main characteristics are listed in Table 13.1.

**Table 13.1** Types of surface forces in vacuum versus in liquid (colloidal forces). Note: (v) applies only to interactions in vacuum, (s) applies only to interactions in solution (or to surfaces separated by a liquid), and (v & s) applies to interactions occurring both in vacuum and in solution

Type of force	Subclasses or alternative names	Main characteristics
<b>Attractive forces</b>		
van der Waals	Debye induced dipole force (v & s) London dispersion force (v & s) Casimir force (v & s)	Ubiquitous, occurs both in vacuum and in liquids
Electrostatic	Ionic bond (v) Coulombic force (v & s) Hydrogen bond (v) Charge-exchange interaction (v & s) Acid–base interaction (s) “Harpooning” interaction (v)	Strong, long-range, arises in polar solvents; requires surface charging or charge-separation mechanism
Ion correlation	van der Waals force of polarizable ions (s)	Requires mobile charges on surfaces in a polar solvent
Quantum mechanical	Covalent bond (v) Metallic bond (v) Exchange interaction (v)	Strong, short-range, responsible for contact binding of crystalline surfaces
Solvation	Oscillatory force (s) Depletion force (s)	Mainly entropic in origin, the oscillatory force alternates between attraction and repulsion
Hydrophobic	Attractive hydration force (s)	Strong, apparently long-range; origin not yet understood
Specific binding	“Lock-and-key” or complementary binding (v & s) Receptor–ligand interaction (s) Antibody–antigen interaction (s)	Subtle combination of different non-covalent forces giving rise to highly specific binding; main recognition mechanism of biological systems
<b>Repulsive forces</b>		
van der Waals	van der Waals disjoining pressure (s)	Arises only between dissimilar bodies interacting in a medium
Electrostatic	Coulombic force (v & s)	Arises only for certain constrained surface charge distributions
Quantum mechanical	Hard-core or steric repulsion (v) Born repulsion (v)	Short-range, stabilizing attractive covalent and ionic binding forces, effectively determine molecular size and shape
Solvation	Oscillatory solvation force (s) Structural force (s) Hydration force (s)	Monotonically repulsive forces, believed to arise when solvent molecules bind strongly to surfaces
Entropic	Osmotic repulsion (s) Double-layer force (s) Thermal fluctuation force (s) Steric polymer repulsion (s) Undulation force (s) Protrusion force (s)	Due to confinement of molecular or ionic species; requires mechanism that keeps trapped species between the surfaces
<b>Dynamic interactions</b>		
Non-equilibrium	Hydrodynamic forces (s) Viscous forces (s) Friction forces (v & s) Lubrication forces (s)	Energy-dissipating forces occurring during relative motion of surfaces or bodies



In *vacuum*, the two main long-range interactions are the attractive van der Waals and electrostatic (Coulomb) forces. At smaller surface separations (corresponding to molecular contact at surface separations of  $D \approx 0.2$  nm), additional attractive interactions can be found such as covalent or metallic bonding forces. These attractive forces are stabilized by the hard-core repulsion. Together they determine the surface and interfacial energies of planar surfaces, as well as the strengths of materials and adhesive junctions. Adhesion forces are often strong enough to elastically or plastically deform bodies or particles when they come into contact.

In *vapors* (e.g., atmospheric air containing water and organic molecules), solid surfaces in, or close to, contact will generally have a surface layer of chemisorbed or physisorbed molecules, or a capillary condensed liquid bridge between them. A surface layer usually causes the adhesion to decrease, but in the case of capillary condensation, the additional Laplace pressure or attractive *capillary* force may make the adhesion between the surfaces stronger than in an inert gas or vacuum.

When totally immersed in a *liquid*, the force between particles or surfaces is completely modified from that in vacuum or air (vapor). The van der Waals attraction is generally reduced, but other forces can now arise that can qualitatively change both the range and even the sign of the interaction. The attractive force in such a system can be either stronger or weaker than in the absence of the intervening liquid. For example, the overall attraction can be stronger in the case of two hydrophobic surfaces separated by water, but weaker for two hydrophilic surfaces. Depending on the different forces that may be operating simultaneously in solution, the overall force law is not generally monotonically attractive even at long range; it can be repulsive, or the force can change sign at some finite surface separation. In such cases, the potential-energy minimum, which determines the adhesion force or energy, does not occur at the true molecular contact between the surfaces, but at some small distance further out.

The forces between surfaces in a liquid medium can be particularly complex at *short range*, i.e., at surface separations below a few nanometers or 4–10 molecular diameters. This is partly because, with increasing confinement, a liquid ceases to behave as a structureless continuum with bulk properties; instead, the size and shape of its molecules begin to determine the overall interaction. In addition, the surfaces themselves can no longer be treated as inert and structureless walls (i.e., mathematically flat) and their physical and chemical properties at the atomic scale must now be taken into account. The force laws will then depend on whether the surfaces are amorphous or crystalline (and whether the lattices of crystalline surfaces are matched or not), rough or smooth, rigid or soft (fluidlike), and hydrophobic or hydrophilic.

It is also important to distinguish between *static* (i.e., equilibrium) interactions and *dynamic* (i.e., nonequilibrium) forces such as viscous and friction forces. For example, certain liquid films confined between two contacting surfaces may take a surprisingly long time to equilibrate, as may the surfaces themselves, so that the short-range and adhesion forces appear to be time-dependent, resulting in “aging” effects.

## 13.2 Methods Used to Study Surface Forces

### 13.2.1 Force Laws

The full force law  $F(D)$  between two surfaces, i.e., the force  $F$  as a function of surface separation  $D$ , can be measured in a number of ways [1–5]. The simplest is to move the base of a spring by a known amount  $\Delta D_0$ . Figure 13.1 illustrates this method when applied to the interaction of two magnets. However, the method is also applicable at the microscopic or molecular level, and it forms the basis of all direct force-measuring apparatuses such as the surface forces apparatus (SFA; [2, 7]) and the atomic force microscope (AFM; [8–10]). If there is a detectable force between the surfaces, this will cause the force-measuring spring to deflect by  $\Delta D_s$ , while the surface separation changes by  $\Delta D$ . These three displacements are related by

$$\Delta D_s = \Delta D_0 - \Delta D. \quad (13.1)$$

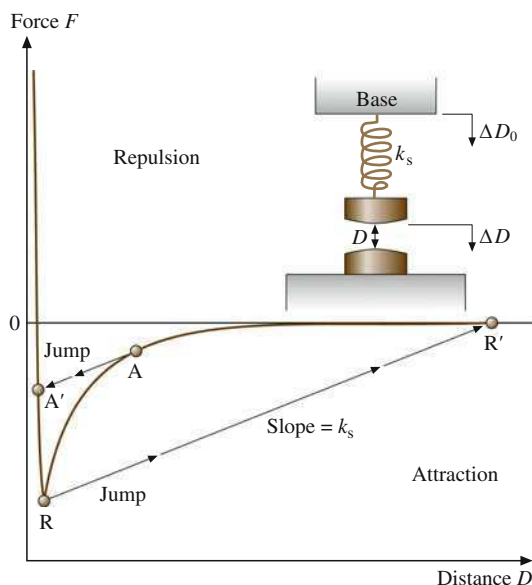


**Fig. 13.1** Schematic attractive force law between two macroscopic objects such as two magnets, or between two microscopic objects such as the van der Waals force between a metal tip and a surface. On lowering the base supporting the spring, the latter will expand or contract such that, at any equilibrium separation  $D$ , the attractive force balances the elastic spring restoring force. If the gradient of the attractive force  $dF/dD$  exceeds the gradient of the spring's restoring force (defined by the spring constant  $k_s$ ), the upper surface will jump from  $A$  into contact at  $A'$  ( $A$  for “advancing”). On separating the surfaces by raising the base, the two surfaces will jump apart from  $R$  to  $R'$  ( $R$  for “receding”). The distance  $R-R'$  multiplied by  $k_s$  gives the adhesion force, i.e., the value of  $F$  at the point  $R$  (after [6] with permission)

The difference in force,  $\Delta F$ , between the initial and final separations is given by

$$\Delta F = k_s \Delta D_s, \quad (13.2)$$

where  $k_s$  is the spring constant. The equations above provide the basis for measurements of the force difference between any two surface separations. For example, if a force-measuring apparatus with a known  $k_s$  can measure  $D$  (and thus  $\Delta D$ ),  $\Delta D_0$ , and  $\Delta D_s$ , the force difference  $\Delta F$  can be measured between a large initial or reference separation  $D$ , where the force is zero ( $F = 0$ ), and another separation  $D - \Delta D$ . By working one's way in increasing increments of  $\Delta D = \Delta D_0 - \Delta D_s$ , the full force law  $F(D)$  can be constructed over any desired distance regime.

In order to measure an equilibrium force law, it is essential to establish that the two surfaces have stopped moving before the displacements are measured. When displacements are measured while two surfaces are still in relative motion, one also measures a viscous or frictional contribution to the total force. Such dynamic force measurements have enabled the viscosities of liquids near surfaces and in thin films to be accurately determined [11–13].

In practice, it is difficult to measure the forces between two perfectly flat surfaces, because of the stringent requirement of perfect alignment for making reliable measurements at distances of a few tenths of a nanometer. It is far easier to measure the forces between curved surfaces, e.g., two spheres, a sphere and a flat surface, or two crossed cylinders. Furthermore, the force  $F(D)$  measured between two curved surfaces can be directly related to the energy per unit area  $E(D)$  between two flat surfaces at the same separation  $D$  by the so-called Derjaguin approximation [14]

$$E(D) = \frac{F(D)}{2\pi R}, \quad (13.3)$$

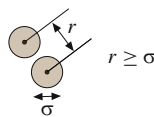
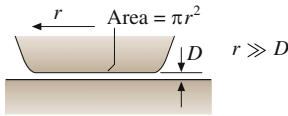
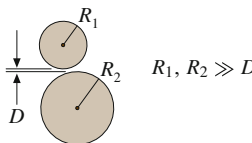
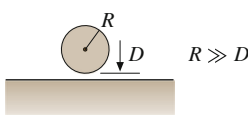
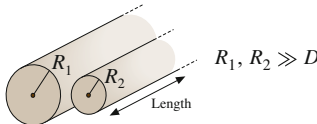
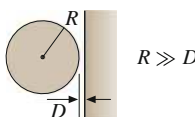
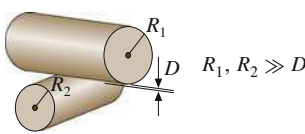
where  $R$  is the radius of the sphere (for a sphere and a flat surface) or the radii of the cylinders (for two crossed cylinders, cf. Table 13.2).

### 13.2.2 Adhesion Forces

The most direct way to measure the adhesion of two solid surfaces (such as two spheres or a sphere on a flat) is to suspend one of them on a spring and measure the adhesion or “pull-off” force needed to separate the two bodies, using the deflection of the spring. If  $k_s$  is the stiffness of the force-measuring spring and  $\Delta D$  is the distance the two surfaces jump apart when they separate, then the adhesion force  $F_{\text{ad}}$  is given by

$$F_{\text{ad}} = F_{\text{max}} = k_s \Delta D, \quad (13.4)$$

**Table 13.2** Van der Waals interaction energy and force between macroscopic bodies of different geometries. A negative force ( $A_H$  positive) implies attraction, a positive force means repulsion ( $A_H$  negative) (after [15], with permission)

Geometry of bodies with surfaces $D$ apart ( $D \ll R$ )		van der Waals interaction	
		Energy $E$	Force $F$
Two atoms or small molecules		$\frac{-C_{vdW}}{r^6}$	$\frac{-6C_{vdW}}{r^7}$
Two flat surfaces (per unit area)		$\frac{-A_H}{12\pi D^2}$	$\frac{-A_H}{6\pi D^3}$
Two spheres or macromolecules of radii $R_1$ and $R_2$		$\frac{-A_H}{6D} \left( \frac{R_1 R_2}{R_1 + R_2} \right)$	$\frac{-A_H}{6D^2} \left( \frac{R_1 R_2}{R_1 + R_2} \right)$
Sphere or macromolecule of radius $R$ near a flat surface		$\frac{-A_H R}{6D}$	$\frac{-A_H R}{6D^2}$
Two parallel cylinders or rods of radii $R_1$ and $R_2$ (per unit length)		$\frac{-A_H}{12\sqrt{2}D^{3/2}} \left( \frac{R_1 R_2}{R_1 + R_2} \right)^{1/2}$	$\frac{-A_H}{8\sqrt{2}D^{5/2}} \left( \frac{R_1 R_2}{R_1 + R_2} \right)^{1/2}$
Cylinder of radius $R$ near a flat surface (per unit length)		$\frac{-A_H \sqrt{R}}{12\sqrt{2}D^{3/2}}$	$\frac{-A_H \sqrt{R}}{8\sqrt{2}D^{5/2}}$
Two cylinders or filaments of radii $R_1$ and $R_2$ crossed at $90^\circ$		$\frac{-A_H \sqrt{R_1 R_2}}{6D}$	$\frac{-A_H \sqrt{R_1 R_2}}{6D^2}$

where we note that, in liquids, the maximum or minimum in the force may occur at some nonzero surface separation (Fig. 13.7). From  $F_{\text{ad}}$  and a known surface geometry, and assuming that the surfaces were everywhere in molecular contact, one may also calculate the surface or interfacial energy  $\gamma$ . For an elastically deformable sphere of radius  $R$  on a flat surface, or for two crossed cylinders of radius  $R$ , we have [3, 16]

$$\gamma = \frac{F_{\text{ad}}}{3\pi R}, \quad (13.5)$$

while for two spheres of radii  $R_1$  and  $R_2$

$$\gamma = \frac{F_{\text{ad}}}{3\pi} \left( \frac{1}{R_1} + \frac{1}{R_2} \right), \quad (13.6)$$

where  $\gamma$  is in units of  $\text{J m}^{-2}$  (Sect. 13.5.2).

### 13.2.3 The SFA and AFM

In a typical force-measuring experiment, at least two of the above displacement parameters –  $\Delta D_0$ ,  $\Delta D$ , and  $\Delta D_s$  – are directly or indirectly measured, and from these the third displacement and the resulting force law  $F(D)$  are deduced using (13.1) and (13.2) together with a measured value of  $k_s$ . For example, in SFA experiments,  $\Delta D_0$  is changed by expanding or contracting a piezoelectric crystal by a known amount or by moving the base of the spring with sensitive motor-driven mechanical stages. The resulting change in surface separation  $\Delta D$  is measured optically, and the spring deflection  $\Delta D_s$  can then be obtained according to (13.1). In AFM experiments,  $\Delta D_0$  and  $\Delta D_s$  are measured using a combination of piezoelectric, optical, capacitance or magnetic techniques, from which the change in surface separation  $\Delta D$  is deduced. Once a force law is established, the geometry of the two surfaces (e.g., their radii) must also be known before the results can be compared with theory or with other experiments.

The SFA (Fig. 13.2) is used for measurements of adhesion and force laws between two curved molecularly smooth surfaces immersed in liquids or controlled vapors [3, 7, 17]. The surface separation is measured by multiple-beam interferometry with an accuracy of  $\pm 0.1$  nm. From the shape of the interference fringes one also obtains the radius of the surfaces  $R$  and any surface deformation that arises during an interaction [18–20]. The resolution in the lateral direction is about 1  $\mu\text{m}$ . The surface separation can be independently controlled to within 0.1 nm, and the force sensitivity is about  $10^{-8}$  N. For a typical surface radius of  $R \approx 1$  cm,  $\gamma$  values can be measured to an accuracy of about  $10^{-3}$   $\text{mJ m}^{-2}$ .

Several different materials have been used to form the surfaces in the SFA, including mica [21, 22], silica [23], sapphire [24], and polymer sheets [25]. These

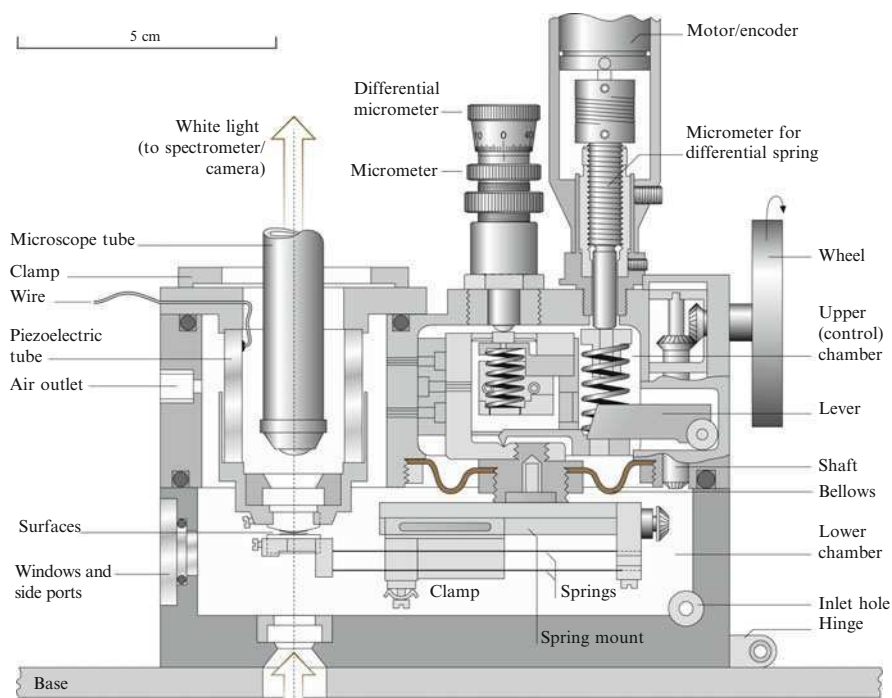


**Fig. 13.2** A surface forces apparatus (SFA) where the intermolecular forces between two macroscopic, cylindrical surfaces of local radius  $R$  can be directly measured as a function of surface separation over a large distance regime from tenths of a nanometer to micrometers. Local or transient surface deformations can be detected optically. Various attachments for moving one surface laterally with respect to the other have been developed for friction measurements in different regimes of sliding velocity and sliding distance (after [17] with permission)

materials can also be used as supporting substrates in experiments on the forces between adsorbed or chemically bound polymer layers [13, 26–31], surfactant and lipid monolayers and bilayers [32–35], and metal and metal oxide layers [36–43]. The range of liquids and vapors that can be used is almost endless, and have thus far included aqueous solutions, organic liquids and solvents, polymer melts, various petroleum oils and lubricant liquids, dyes, and liquid crystals.

Friction attachments for the SFA [44–49] allow for the two surfaces to be sheared laterally past each other at varying sliding speeds or oscillating frequencies, while simultaneously measuring both the transverse (frictional or shear) force and the normal force (load) between them. The ranges of friction forces and sliding speeds that can be studied with such methods are currently  $10^{-7} - 10^{-1}$  N and  $10^{-13} - 10^{-2}$  ms $^{-1}$ , respectively [50]. The externally applied load  $L$  can be varied continuously, and both positive and negative loads can be applied. The distance between the surfaces  $D$  their true molecular contact area, their elastic (or viscoelastic or elastohydrodynamic) deformation, and their lateral motion can all be monitored simultaneously by recording the moving interference-fringe

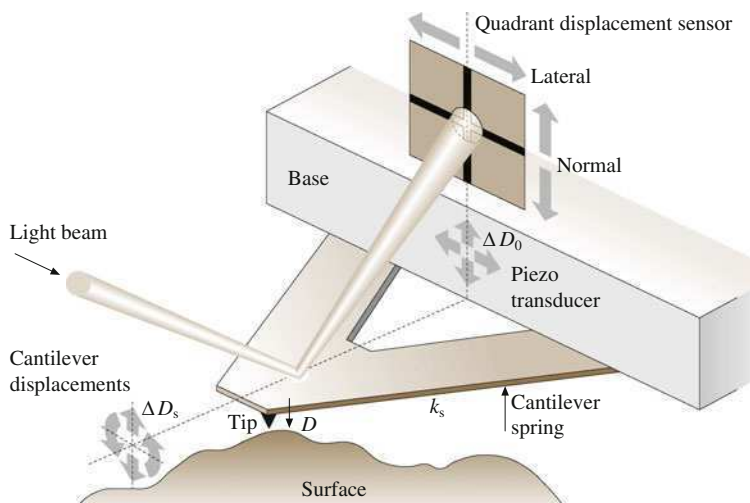


**Fig. 13.3** Schematic drawing of an atomic force microscope (AFM) tip supported on a triangular cantilever interacting with an arbitrary solid surface. The normal force and topology are measured by monitoring the calibrated deflection of the cantilever as the tip is moved across the surface by means of a piezoelectric transducer. Various designs have been developed that move either the sample or the cantilever during the scan. Friction forces can be measured from the torsion of the cantilever when the scanning is in the direction perpendicular to its long axis (after [15] with permission)

pattern. Equipment for dynamic measurements of normal forces has also been developed. Such measurements give information on the viscosity of the medium and the location of the shear or slip planes relative to the surfaces [11–13, 51, 52].

In the atomic force microscope (Fig. 13.3), the force is measured by monitoring the deflection of a soft cantilever supporting a submicroscopic tip ( $R \approx 10 - 200 \text{ nm}$ ) as this interacts with a flat, macroscopic surface [8, 53, 54]. The measurements can be done in a vapor or liquid. The normal (bending) spring stiffness of the cantilever can be as small as  $0.01 \text{ N m}^{-1}$ , allowing measurements of normal forces as small as  $1 \text{ pN}$  ( $10^{-12} \text{ N}$ ), which corresponds to the bond strength of single molecules [55–58]. Distances can be inferred with an accuracy of about  $1 \text{ nm}$ , and changes in distance can be measured to about  $0.1 \text{ nm}$ . Since the contact area can be small when using sharp tips, different interaction regimes can be resolved on samples with a heterogeneous composition on lateral scales of a few nanometers. Height differences and the roughness of the sample can be measured directly from the cantilever deflection or, alternatively, by using a feedback system to raise or lower the sample so that the deflection (the normal force) is kept constant during a scan over the area of interest. Weak interaction forces and larger (microscopic) interaction areas can be investigated by replacing the tip with a micrometer-sized sphere to form a “colloidal probe” [9].

The atomic force microscope can also be used for friction measurements (lateral force microscopy, LFM, or friction force microscopy, FFM) by monitoring

the torsion of the cantilever as the sample is scanned in the direction perpendicular to the long axis of the cantilever [10, 54, 59, 60]. Typically, the stiffness of the cantilever to lateral bending is much larger than to bending in the normal direction and to torsion, so that these signals are decoupled and height and friction can be detected simultaneously. The torsional spring constant can be as low as  $0.1 \text{ N m}^{-1}$ , giving a lateral (friction) force sensitivity of  $10^{-11} \text{ N}$ .

Rapid technical developments have facilitated the calibrations of the normal [61, 62] and lateral spring constants [60, 63–65], as well as in situ measurements of the macroscopic tip radius [66, 67]. Cantilevers of different shapes with a large range of spring constants, tip radii, and surface treatments (inorganic or organic coatings) are commercially available. The flat surface, and also the particle in the colloidal probe technique, can be any material of interest. However, remaining difficulties with this technique are that the distance between the tip and the substrate  $D$  and the deformations of the tip and sample, are not directly measurable. Another important difference between the AFM/LFM and SFA techniques is the different size of the contact area, and the related observation that, even when a cantilever with a very low spring constant is used in the AFM, the pressure in the contact zone is typically much higher than in the SFA. Hydrodynamic effects in liquids also affect the measurements of normal forces differently on certain time scales [68–71].

### 13.2.4 *Some Other Force-Measuring Techniques*

A large number of other techniques are available for the measurements of the normal forces between solid or fluid surfaces [4, 15]. The techniques discussed in this section are not used for lateral (friction) force measurements, but are commonly used to study normal forces, particularly in biological systems.

Micropipette aspiration is used to measure the forces between cells or vesicles, or between a cell or vesicle and another surface [72–74]. The cell or vesicle is held by suction at the tip of a glass micropipette and deforms elastically in response to the net interactions with another surface and to the applied suction. The shape of the deformed surface (cell membrane) is measured and used to deduce the force between the surfaces and the membrane tension [73]. The membrane tension, and thus the stiffness of the cell or vesicle, is regulated by applying different hydrostatic pressures. Forces can be measured in the range of  $0.1 \text{ pN}$  to  $1 \text{ nN}$ , and the distance resolution is a few nanometers. The interactions between a colloidal particle and another surface can be studied by attaching the particle to the cell membrane [75].

In the osmotic stress technique, pressures are measured between colloidal particles in aqueous solution, membranes or bilayers, or other ordered colloidal structures (viruses, DNA). The separation between the particle surfaces and the magnitude of membrane undulations are measured by x-ray or neutron scattering techniques. This is combined with a measurement of the osmotic pressure of the solution [76–79]. The technique has been used to measure repulsive forces, such as



Derjaguin–Landau–Verwey–Overbeek (DLVO) interactions, steric forces, and hydration forces [80]. The sensitivity in pressure is  $0.1 \text{ mN m}^{-2}$ , and distances can be resolved to  $0.1 \text{ nm}$ .

The optical tweezers technique is based on the trapping of dielectric particles at the center of a focused laser beam by restoring forces arising from radiation pressure and light-intensity gradients [81, 82]. The forces experienced by particles as they are moved toward or away from one another can be measured with a sensitivity in the pN range. Small biological molecules are typically attached to a larger bead of a material with suitable refractive properties. Recent development allows determinations of position with nanometer resolution [83], which makes this technique useful for studying the forces during the extension of single molecules.

In total internal reflection microscopy (TIRM), the potential energy between a micrometer-sized colloidal particle and a flat surface in aqueous solution is deduced from the average equilibrium height of the particle above the surface, measured from the intensity of scattered light. The average height ( $D \approx 10 - 100 \text{ nm}$ ) results from a balance of gravitational force, radiation pressure from a laser beam focused at the particle from below, and intermolecular forces [84]. The technique is particularly suitable for measuring weak forces (sensitivity ca.  $10^{-14} \text{ N}$ ), but is more difficult to use for systems with strong interactions. A related technique is reflection interference contrast microscopy (RICM), where optical interference is used to also monitor changes in the shape of the approaching colloidal particle or vesicle [85].

An estimate of bond strengths can be obtained from the hydrodynamic shear force exerted by a fluid on particles or cells attached to a substrate [86, 87]. At a critical force, the bonds are broken and the particle or cell will be detached and move with the velocity of the fluid. This method requires knowledge of the contact area and the flow-velocity profile of the fluid. Furthermore, a uniform stress distribution in the contact area is generally assumed. At low bond density, this technique can be used to determine the strength of single bonds ( $1 \text{ pN}$ ).

## 13.3 Normal Forces Between Dry (Unlubricated) Surfaces

### 13.3.1 *Van der Waals Forces in Vacuum and Inert Vapors*

Forces between macroscopic bodies (such as colloidal particles) across vacuum arise from interactions between the constituent atoms or molecules of each body across the gap separating them. These intermolecular interactions are electromagnetic forces between permanent or induced dipoles (van der Waals forces), and between ions (electrostatic forces). In this section, we describe the van der Waals forces, which occur between all atoms and molecules and between all macroscopic bodies [2].

The interaction between two permanent dipoles with a fixed relative orientation can be attractive or repulsive. For the specific case of two freely rotating permanent dipoles in a liquid or vapor (orientational or Keesom interaction), and

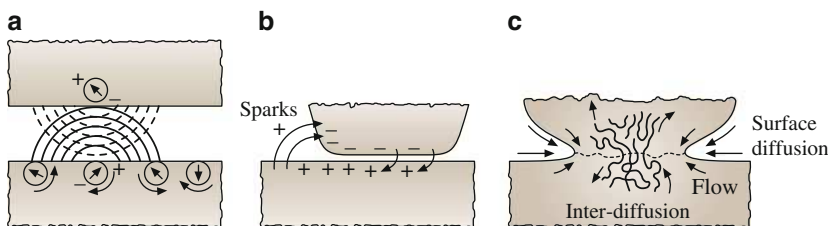


**Fig. 13.4** Schematic representation of (a) van der Waals interaction (dipole–induced dipole interaction), (b) charge exchange, which acts to increase adhesion and friction forces, and (c) sintering between two surfaces

for a permanent dipole and an induced dipole in an atom or polar or nonpolar molecule (induction or Debye interaction), the interaction is on average always attractive. The third type of van der Waals interaction, the fluctuation or London dispersion interaction, arises from instantaneous polarization of one nonpolar or polar molecule due to fluctuations in the charge distribution of a neighboring nonpolar or polar molecule (Fig. 13.4a). Correlation between these fluctuating induced dipole moments gives an attraction that is present between any two molecules or surfaces across vacuum. At very small separations, the interaction will ultimately be repulsive as the electron clouds of atoms and molecules begin to overlap. The total interaction is thus a combination of a short-range repulsion and a relatively long-range attraction.

Except for in highly polar materials such as water, London dispersion interactions give the largest contribution (70–100%) to the van der Waals attraction. The interaction energy of the van der Waals force between atoms or molecules depends on the separation  $r$  as

$$E(D) = \frac{-C_{\text{vdW}}}{r^6}, \quad (13.7)$$

where the constant  $C_{\text{vdW}}$  depends on the dipole moments and polarizabilities of the molecules. At large separations ( $>10$  nm), the London interaction is weakened by a randomizing effect caused by the rapid fluctuations. That is, the induced temporary dipole moment of one molecule may have changed during the time needed for the transmission of the electromagnetic wave (photon) generated by its fluctuating charge density to another molecule and the return of the photon generated by the induced fluctuation in this second molecule. This phenomenon is called retardation and causes the interaction energy to decay as  $r^{-7}$  at large separations [88].

Dispersion interactions are to a first approximation additive, and their contribution to the interaction energy between two macroscopic bodies (such as colloidal particles) across vacuum can be found by summing the pairwise interactions [89]. The interaction is generally described in terms of the Hamaker constant,  $A_H$ . Another approach is to treat the interacting bodies and an intervening medium as continuous phases and determine the strength of the interaction from bulk dielectric properties of the materials [90, 91]. Unlike the pairwise summation, this method

takes into account the screening of the interactions between molecules inside the bodies by the molecules closer to the surfaces and the effects of the intervening medium. For the interaction between material 1 and material 3 across material 2, the nonretarded Hamaker constant given by the Lifshitz theory is approximately [2]

$$A_{H,123} = A_{H,v=0} + A_{H,v>0} \approx \frac{3}{4}k_B T \left( \frac{\varepsilon_1 - \varepsilon_2}{\varepsilon_1 + \varepsilon_2} \right) \left( \frac{\varepsilon_3 - \varepsilon_2}{\varepsilon_3 + \varepsilon_2} \right) + \frac{3h\nu_e}{8\sqrt{2}} \times \frac{(n_1^2 - n_2^2)(n_3^2 - n_2^2)}{\sqrt{(n_1^2 + n_2^2)}\sqrt{(n_3^2 + n_2^2)}\left(\sqrt{(n_1^2 + n_2^2)} + \sqrt{(n_3^2 + n_2^2)}\right)}, \quad (13.8)$$

where the first term ( $v = 0$ ) represents the permanent dipole and dipole-induced dipole interactions and the second ( $v > 0$ ) the London (dispersion) interaction.  $\varepsilon_i$  and  $n_i$  are the static dielectric constants and refractive indexes of the materials, respectively.  $\nu_e$  is the frequency of the lowest electron transition (around  $3 \times 10^{15} \text{ s}^{-1}$ ). Either one of the materials 1, 2, or 3 in (13.8) can be vacuum or air ( $\varepsilon = n = 1$ ).  $A_H$  is typically  $10^{-20} - 10^{-19} \text{ J}$  (the higher values are found for metals) for interactions between solids and liquids across vacuum or air.

The interaction energy between two macroscopic bodies is dependent on the geometry and is always attractive between two bodies of the same material [ $A_H$  positive, see (13.8)]. The van der Waals interaction energy and force laws ( $F = -dE(D)/dD$ ) for some common geometries are given in Table 13.2. Because of the retardation effect, the equations in Table 13.2 will lead to an overestimation of the dispersion force at large separations. It is, however, apparent that the interaction energy between macroscopic bodies decays more slowly with separation (i.e., has a longer range) than between two molecules.

For inert nonpolar surfaces, e.g., consisting of hydrocarbons or van der Waals solids and liquids, the Lifshitz theory has been found to apply even at molecular contact, where it can be used to predict the surface energies (surface tensions) of such solids and liquids. For example, for hydrocarbon surfaces,  $A_H = 5 \times 10^{-20} \text{ J}$ . Inserting this value into the equation for two flat surfaces (Table 13.2) and using a “cut-off” distance of  $D_0 \approx 0.165 \text{ nm}$  as an effective separation when the surfaces are in contact [2], we obtain for the surface energy  $\gamma$  (which is defined as half the interaction energy)

$$\gamma = \frac{E}{2} = \frac{A_H}{24\pi D_0^2} \approx 24 \text{ mJ m}^{-2}, \quad (13.9)$$

a value that is typical for hydrocarbon solids and liquids [92].

If the adhesion force is measured between two crossed-cylindrical surfaces of  $R=1 \text{ cm}$  (a geometry equivalent to a sphere with  $R=1 \text{ cm}$  interacting with a flat surface, cf. Table 13.2) using an SFA, we expect the adhesion force to be (Table 13.2)  $F = A_H R / (6D_0^2) = 4\pi R\gamma \approx 3.0 \text{ mN}$ . Using a spring constant of  $k_s = 100 \text{ N m}^{-1}$ , such an adhesive force will cause the two surfaces to jump apart

by  $\Delta D = F/k_s = 30 \mu\text{m}$ , which can be accurately measured. (For elastic bodies that deform in adhesive contact,  $R$  changes during the interaction and the measured adhesion force is 25% lower, see Sect. 13.5.2). Surface energies of solids can thus be directly measured with the SFA and, in principle, with the AFM if the contact geometry can be quantified. The measured values are in good agreement with calculated values based on the known surface energies  $\gamma$  of the materials, and for nonpolar low-energy solids they are well accounted for by the Lifshitz theory [2].

### 13.3.2 Charge-Exchange Interactions

Electrostatic interactions are present between ions (Coulomb interactions), between ions and permanent dipoles, and between ions and nonpolar molecules in which a charge induces a dipole moment. The interaction energy between ions or between a charge and a fixed permanent dipole can be attractive or repulsive. For an induced dipole or a freely rotating permanent dipole in vacuum or air, the interaction energy with a charge is always attractive.

Spontaneous charge transfer may occur between two dissimilar materials in contact [93–97]. The phenomenon, called contact electrification, is especially prominent in contact between a metal and a material with low conductivity (including organic liquids) [95, 97], but is also observed, for example, between two different polymer layers. It is believed that when two different materials are in static contact, charge transfer might occur due to quantum tunneling of electrons or, in some cases, transfer of surface ions. The charging is generally seen to be stronger with increasing difference in work function (or electron affinity) between the two materials [95, 97]. During separation, rolling or sliding of one body over the other, the surfaces experience both charge transition from one surface to the other and charge transfer (conductance) along each surface (Fig. 13.4b). The latter process is typically slower, and, as a result, charges remain on the surfaces as they are separated in vacuum or dry nitrogen gas. The charging gives rise to a strong adhesion with adhesion energies of over  $1000 \text{ mJ m}^{-2}$ , similar to fracture or cohesion energies of the solid bodies themselves [93, 94, 98]. Upon separating the surfaces further apart, a strong, long-range electrostatic attraction is observed. The charging can be decreased through discharges across the gap between the surfaces (which requires a high charging) or through conduction in the solids. The discharge may give rise to triboluminescence [99], but can also cause sparks that may ignite combustible materials [100]. It has been suggested that charge-exchange interactions are particularly important in rolling friction between dry surfaces (which can simplistically be thought of as an adhesion–separation process), where the distance dependence of forces acting normally to the surfaces plays a larger role than in sliding friction. In the case of sliding friction, charge transfer is also observed between identical materials [98, 101]. Mechanisms such as bond formation and breakage (polymer scission), slip at the wall between a flowing liquid and a solid [102], or material transfer and the creation of wear particles have been

suggested. However, friction electrification or triboelectrification also occurs during wearless sliding, i.e., when the surfaces are not damaged. Other explanations such as the creation or translation of defects on or near the surface have been put forward [98]. Attempts have been made to correlate the amount of charging with the normal force or load and with the polarizability of the sliding materials [96, 103]. Recent experiments on the sliding friction between metal–insulator surfaces indicate that stick–slip would be accompanied by charge-transfer events [104, 105].

Photoinduced charge transfer, or harpooning, involves the transfer of an electron between an atom in a molecular beam or at a solid surface (typically an alkali or transition metal) to an atom or molecule in a gas (typically a halide) to form a negatively charged molecular ion in a highly excited vibrational state. This transfer process can occur at atomic distances of 0.5–0.7 nm, which is far from molecular contact. The formed molecular ion is attracted to the surface and chemisorbs onto it. Photoinduced charge-transfer processes also occur in the photosynthesis in green plants and in photoelectrochemical cells (solar cells) at the junction between two semiconductors or between a semiconductor and an electrolyte solution [106].

### 13.3.3 *Sintering and Cold Welding*

When macroscopic particles in a powder or in a suspension come into molecular contact, they can bond together to form a network or solid body with very different density and shear strength compared to the powder (a typical example is porcelain). The rate of bonding is dependent on the surface energy (causing a stress at the edge of the contact) and the atomic mobility (diffusion rate) of the contacting materials. To increase the diffusion rate, objects formed from powders are heated to about one half of the melting temperature of the components in a process called sintering, which can be done in various atmospheres or in a liquid.

In the sintering process, the surface energy of the system is lowered due to the reduction of total surface area (Fig. 13.4c). In metal and ceramic systems, the most important mechanism is solid-state diffusion, initially surface diffusion. As the surface area decreases and the grain boundaries increase at the contacts, grain boundary diffusion and diffusion through the crystal lattice become more important [107]. The grain boundaries will eventually migrate, so that larger particles are formed (coarsening). Mass can also be transferred through evaporation and condensation, and through viscous and plastic flow. In liquid-phase sintering, the materials can melt, which increases the mass transport. Amorphous materials like polymers and glasses do not have real grain boundaries and sinter by viscous flow [108].

Some of these mechanisms (surface diffusion and evaporation–condensation) reduce the surface area and increase the grain size (coarsening) without densification, in contrast to bulk transport mechanisms such as grain-boundary diffusion and plastic and viscous flow. As the material becomes denser, elongated pores collapse to form smaller, spherical pores with a lower surface energy. Models for sintering typically consider the size and growth rate of the grain boundary (the “neck”)

formed between two spherical particles. At a high stage of densification, the sintering stress  $\sigma$  at the curved neck between two particles is given by [108]

$$\sigma = \frac{2\gamma_{ss}}{G} + \frac{2\gamma_{sv}}{r_p}, \quad (13.10)$$

where  $\gamma_{ss}$  is the solid–solid grain boundary energy,  $\gamma_{sv}$  is the solid–vapor surface energy,  $G$  is the grain size, and  $r_p$  is the radius of the pore.

A related phenomenon is cold welding, which is the spontaneous formation of strong junctions between clean (unoxidized) metal surfaces with a mutual solubility when they are brought into contact, with or without an applied pressure. The plastic deformations accompanying the formation and breaking of such contacts on a molecular scale during motion of one surface normally (Fig. 13.10c,d) or laterally (shearing) with respect to the other have been studied both experimentally [109, 110] and theoretically [111–116]. The breaking of a cold-welded contact is generally associated with damage or deformation of the surface structure.

## 13.4 Normal Forces Between Surfaces in Liquids

### 13.4.1 *Van der Waals Forces in Liquids*

The dispersion interaction in a medium will be significantly lower than in vacuum, since the attractive interaction between two solute molecules in a medium (solvent) involves displacement and reorientation of the nearest-neighbor solvent molecules. Even though the surrounding medium may change the dipole moment and polarizability from that in vacuum, the interaction between two identical molecules remains attractive in a binary mixture. The extension of the interactions to the case of two macroscopic bodies is the same as described in Sect. 13.3.1. Typically, the Hamaker constants for interactions in a medium are an order of magnitude lower than in vacuum. Between macroscopic surfaces in liquids, van der Waals forces become important at distances below 10–15 nm and may at these distances start to dominate interactions of different origin that have been observed at larger separations.

Figure 13.5 shows the measured van der Waals forces between two crossed-cylindrical mica surfaces in water and various salt solutions. Good agreement is obtained between experiment and theory. At larger surface separations, above about 5 nm, the measured forces fall off more rapidly than  $D^{-2}$ . This retardation effect (Sect. 13.3.1) is also predicted by the Lifshitz theory and is due to the time needed for propagation of the induced dipole moments over large distances.

From Fig. 13.5, we may conclude that, at separations above about 2 nm, or 8 molecular diameters of water, the *continuum* Lifshitz theory is valid. This would

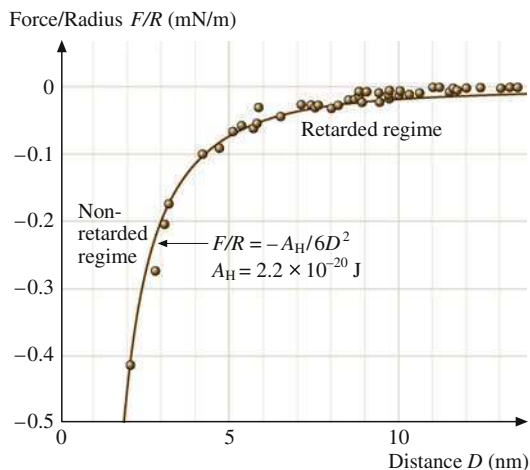


**Fig. 13.5** Attractive van der Waals force  $F$  between two curved mica surfaces of radius  $R \approx 1$  cm measured in water and various aqueous electrolyte solutions. The electrostatic interaction has been subtracted from the total measured force. The measured nonretarded Hamaker constant is  $A_H = 2.2 \times 10^{-20}$  J. Retardation effects are apparent at distances larger than 5 nm, as expected theoretically (after [2], © 1991, with permission from Elsevier Science)

mean that water films as thin as 2 nm may be expected to have bulklike properties, at least as far as their interaction forces are concerned. Similar results have been obtained with other liquids, where in general continuum properties are manifested, both as regards their interactions and other properties such as viscosity, at a film thickness larger than 5 or 10 molecular diameters. In the absence of a solvent (in vacuum), the agreement of measured van der Waals forces with the continuum Lifshitz theory is generally good at all separations down to molecular contact ( $D = D_0$ ).

Van der Waals interactions in a system of three or more different materials (13.8) can be attractive or repulsive, depending on their dielectric properties. Numerous experimental studies show the attractive van der Waals forces in various systems [2], and repulsive van der Waals forces have also been measured directly [117, 118]. A practical consequence of the repulsive interaction obtained across a medium with intermediate dielectric properties is that the van der Waals forces will give rise to preferential, nonspecific adsorption of molecules with an intermediate dielectric constant. This is commonly seen as adsorption of vapors or solutes to a solid surface. It is also possible to diminish the attractive interaction between dispersed colloidal particles by adsorption of a thin layer of material with dielectric properties close to those of the surrounding medium (matching of refractive index), or by adsorption of a polymer that gives a steric repulsive force that keeps the particles separated at a distance where the magnitude of the van der Waals attraction is negligible. Thermal motion will then keep the particles dispersed.

### 13.4.2 Electrostatic and Ion Correlation Forces

Most surfaces in contact with a highly polar liquid (such as water) acquire a surface charge, either by dissociation of ions from the surface into the solution or by preferential adsorption of certain ions from the solution. The surface charge is balanced by a layer of oppositely charged ions (counterions) in the solution at some small distance from the surface [2]. In dilute solution, this distance is the Debye length  $\kappa^{-1}$  which is purely a property of the electrolyte *solution*. The Debye length falls with increasing ionic strength (i.e., with the molar concentration  $M_i$  and valency  $z_i$ ) of the ions in solution

$$\kappa^{-1} = \left( \frac{\epsilon \epsilon_0 k_B T}{e^2 N_A \sum_i z_i^2 M_i} \right)^{1/2}, \quad (13.11)$$

where  $e$  is the electronic charge. For example, for 1:1 electrolytes at 25 °C,  $\kappa^{-1} = 0.304 \text{ nm} / \sqrt{M_{1:1}}$ , where  $M_i$  is given in M ( $\text{mol dm}^{-3}$ ).  $\kappa^{-1}$  is thus about 10 nm in a 1 mM NaCl solution and 0.3 nm in a 1M solution. In totally pure water at pH 7, where  $M_i = 10^{-7} \text{ M}$ ,  $\kappa^{-1}$  is 960 nm, or about 1  $\mu\text{m}$ . The Debye length also relates the surface charge density  $\sigma$  of a surface to the electrostatic surface potential  $\psi_0$  via the Grahame equation, which for 1:1 electrolytes can be expressed as

$$\sigma = \sqrt{8\epsilon \epsilon_0 k_B T} \sinh\left(\frac{e\psi_0}{2k_B T}\right) \times \sqrt{M_{1:1} N_A}. \quad (13.12)$$

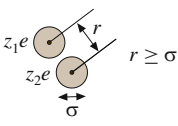
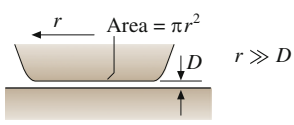
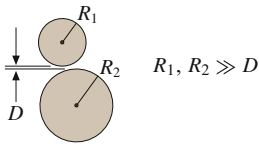
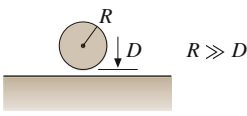
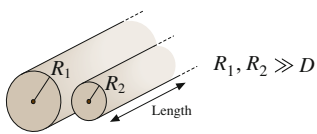
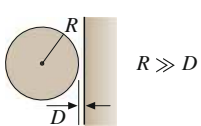
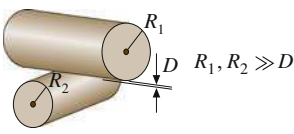
Since the Debye length is a measure of the thickness of the diffuse atmosphere of counterions near a charged surface, it also determines the range of the electrostatic “double-layer” interaction between two charged surfaces. The electrostatic double-layer interaction is an entropic effect that arises upon decreasing the thickness of the liquid film containing the dissolved ions. Because of the attractive force between the dissolved ions and opposite charges on the surfaces, the ions stay between the surfaces, but an osmotic repulsion arises as their concentration increases. The long-range electrostatic interaction energy at large separations (weak overlap) between two similarly charged molecules or surfaces is typically repulsive and is roughly an exponentially decaying function of  $D$

$$E(D) \approx + C_{\text{ES}} e^{-\kappa D}, \quad (13.13)$$

where  $C_{\text{ES}}$  is a constant that depends on the geometry of the interacting surfaces, on their surface charge density, and the solution conditions (Table 13.3). We see that the Debye length is the decay length of the interaction energy between two surfaces (and of the mean potential away from one surface).  $C_{\text{ES}}$  can be determined by solving the so-called Poisson–Boltzmann equation or by using other theories [119–123]. The equations in Table 13.3 are expressed in terms of a constant  $Z$  defined as



**Table 13.3** Electrical double-layer interaction energy  $E(D)$  and force ( $F = -dE/dD$ ) between macroscopic bodies. The interaction energy and force for bodies of different geometries is based on the Poisson–Boltzmann equation (a continuum, mean-field theory). Equation (13.14) gives the interaction constant  $Z$  (in terms of the surface potential  $\psi_0$ ) for the interaction between similarly charged (ionized) surfaces in aqueous solutions of monovalent electrolyte. It can also be expressed in terms of the surface charge density  $\sigma$  by applying the Grahame equation (13.12) (after [15], with permission)

Geometry of bodies with surfaces $D$ apart ( $D \ll R$ )	Electric double-layer interaction	
	Energy $E$	Force $F$
Two ions or small molecules 	$\frac{+z_1 z_2 e^2}{4\pi\epsilon_0 r} \frac{e^{-\kappa(r-\sigma)}}{(1+\kappa\sigma)}$	$\frac{+z_1 z_2 e^2}{4\pi\epsilon_0 r^2} \frac{(1+\kappa r)}{(1+\kappa\sigma)} e^{-\kappa(r-\sigma)}$
Two flat surfaces (per unit area) 	$(\kappa/2\pi) Z e^{-\kappa D}$	$\left(\frac{\kappa^2}{2\pi}\right) Z e^{-\kappa D}$
Two spheres or macromolecules of radii $R_1$ and $R_2$ 	$\left(\frac{R_1 R_2}{R_1 + R_2}\right) Z e^{-\kappa D}$	$\kappa \left(\frac{R_1 R_2}{R_1 + R_2}\right) Z e^{-\kappa D}$
Sphere or macromolecule of radius $R$ near a flat surface 	$R Z e^{-\kappa D}$	$\kappa R Z e^{-\kappa D}$
Two parallel cylinders or rods of radii $R_1$ and $R_2$ (per unit length) 	$\frac{\kappa^{1/2}}{\sqrt{2\pi}} \left(\frac{R_1 R_2}{R_1 + R_2}\right)^{1/2} Z^{-\kappa D}$	$\frac{\kappa^{3/2}}{\sqrt{2\pi}} \left(\frac{R_1 R_2}{R_1 + R_2}\right)^{1/2} Z e^{-\kappa D}$
Cylinder of radius $R$ near a flat surface (per unit length) 	$k^{1/2} \sqrt{\frac{R}{2\pi}} Z e^{-\kappa D}$	$k^{3/2} \sqrt{\frac{R}{2\pi}} Z e^{-\kappa D}$
Two cylinders or filaments of radii $R_1$ and $R_2$ crossed at $90^\circ$ 	$\sqrt{R_1 R_2} Z e^{-\kappa D}$	$\kappa \sqrt{R_1 R_2} Z e^{-\kappa D}$

$$Z = 64\pi\epsilon\epsilon_0 \left(\frac{k_B T}{e}\right)^2 \tanh^2 \left(\frac{ze\psi_0}{4k_B T}\right), \quad (13.14)$$

which depends only on the properties of the *surfaces*.

The above approximate expressions are accurate only for surface separations larger than about one Debye length. At smaller separations one must use numerical solutions of the Poisson–Boltzmann equation to obtain the exact interaction potential, for which there are no simple expressions. In the limit of small  $D$ , it can be shown that the interaction energy depends on whether the surfaces remain at constant potential  $\psi_0$  (as assumed in the above equations) or at constant charge  $\sigma$  (when the repulsion exceeds that predicted by the above equations), or somewhere between these limits. In the “constant charge limit” the total *number* of counterions in the compressed film does not change as  $D$  is decreased, whereas at constant potential, the *concentration* of counterions is constant. The limiting pressure (or force per unit area) at constant charge is the osmotic pressure of the confined ions

$$\begin{aligned} F &= k_B T \times \text{ion number density} \\ &= 2\sigma k_B T / (zeD), \quad \text{for } D \ll \kappa^{-1}. \end{aligned} \quad (13.15)$$

That is, as  $D \rightarrow 0$  the double-layer pressure at constant surface charge becomes infinitely repulsive and independent of the salt concentration (at constant potential the force instead becomes a constant at small  $D$ ). However, at small separations, the van der Waals attraction (which goes as  $D^{-2}$  between two spheres or as  $D^{-3}$  between two planar surfaces, see Table 13.2) wins out over the double-layer repulsion, unless some other short-range interaction becomes dominant (Sect. 13.4.4). This is the theoretical prediction that forms the basis of the so-called Derjaguin–Landau–Verwey–Overbeek (DLVO) theory [119, 124], illustrated in Fig. 13.6.

Because of the different distance dependence of the van der Waals and electrostatic interactions, the total force law, as described by the DLVO theory, can show several minima and maxima. Typically, the depth of the outer (secondary) minimum is a few  $k_B T$ , which is enough to cause reversible flocculation of particles from an aqueous dispersion. If the force barrier between the secondary and primary minimum is lowered, for example, by increasing the electrolyte concentration, particles can be irreversibly coagulated in the primary minimum. In practice, other forces (described in the following sections) often appear at very small separations, so that the full force law between two surfaces or colloidal particles in solution can be more complex than might be expected from the DLVO theory.

There are situations when the double-layer interaction can be attractive at short range even between surfaces of similar charge, especially in systems with charge regulation due to dissociation of chargeable groups on the surfaces [123, 125]; ion condensation [126], which may lower the effective surface charge density in systems containing di- and trivalent counterions; or ion correlation, which is an additional van der Waals-like attraction due to mobile and therefore highly polarizable counterions located at the surface [127]. The ion correlation (or charge

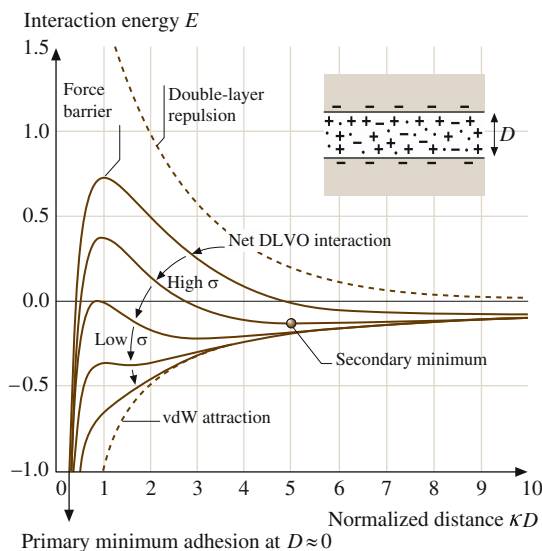


**Fig. 13.6** Schematic plots of the DLVO interaction potential energy  $E$  between two flat, charged surfaces [or, according to the Derjaguin approximation, (13.3), the force  $F$  between two curved surfaces] as a function of the surface separation normalized by the Debye length  $\kappa^{-1}$ . The van der Waals attraction (inverse power-law dependence on  $D$ ) together with the repulsive electrostatic “double-layer” force (roughly exponential) at different surface charge  $\sigma$  (or potential, see (13.12)) determine the net interaction potential in aqueous electrolyte solution (after [15] with permission)

fluctuation) force becomes significant at separations below 4 nm and increases with the surface charge density  $\sigma$  and the valency  $z$  of the counterions. Computer simulations have shown that, at high charge density and for monovalent counterions, the ion correlation force can reduce the effective double-layer repulsion by 10–15 %. With divalent counterions, the ion correlation force was found to exceed the double-layer repulsion and the total force then became attractive at a separation below 2 nm even in dilute electrolyte solution [128]. Experimentally, such short-range attractive forces have been found between charged bilayers [129, 130] and also in other systems [131].

### 13.4.3 Solvation and Structural Forces

When a liquid is confined within a restricted space, for example, a very thin film between two surfaces, it ceases to behave as a structureless continuum. At small surface separations (below about 10 molecular diameters), the van der Waals force between two surfaces or even two solute molecules in a liquid (solvent) is no longer a smoothly varying attraction. Instead, there arises an additional “solvation” force that generally oscillates between attraction and repulsion with distance, with a

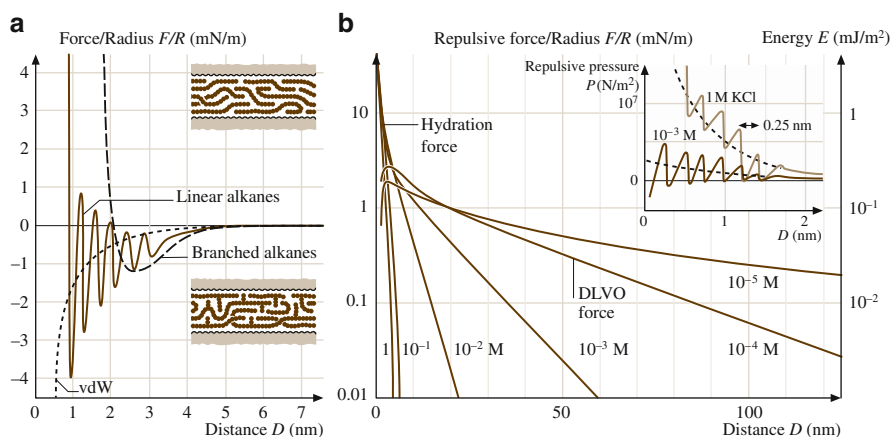


**Fig. 13.7** (a) Solid curve: Forces measured between two mica surfaces across saturated linear chain alkanes such as *n*-tetradecane and *n*-hexadecane [133,134]. The 0.4 nm periodicity of the oscillations indicates that the molecules are preferentially oriented parallel to the surfaces, as shown schematically in the upper insert. The theoretical continuum van der Waals attraction is shown as a dotted curve. Dashed curve: Smooth, nonoscillatory force law exhibited by irregularly shaped alkanes (such as 2-methyloctadecane) that cannot order into well-defined layers (lower insert) (after [134,135]). Similar nonoscillatory forces are also observed between “rough” surfaces, even when these interact across a saturated linear chain liquid. This is because the irregularly shaped surfaces (rather than the liquid) now prevent the liquid molecules from ordering in the gap. (b) Forces measured between charged mica surfaces in KCl solutions of varying concentrations [21]. In dilute solutions ( $10^{-5}$  and  $10^{-4}$  M), the measured forces are excellently described by the DLVO theory, based on exact solutions to the nonlinear Poisson–Boltzmann equation for the electrostatic forces and the Lifshitz theory for the van der Waals forces (using a Hamaker constant of  $A_H = 2.2 \times 10^{-20}$  J). At higher concentrations, as more hydrated  $K^+$  cations adsorb onto the negatively charged surfaces, an additional hydration force appears superimposed on the DLVO interaction at distances below 3–4 nm. This force has both an oscillatory and a monotonic component. Insert: Short-range hydration forces between mica surfaces shown as pressure versus distance. The lower and upper curves show surfaces 40 and 95% saturated with  $K^+$  ions. At larger separations, the forces are in good agreement with the DLVO theory (after [2], © 1991, with permission from Elsevier Science)

periodicity equal to some mean dimension  $\sigma$  of the liquid molecules [132]. Figure 13.7a shows the force law between two smooth mica surfaces across the hydrocarbon liquid tetradecane, whose inert, chainlike molecules have a width of  $\sigma \approx 0.4$  nm.

The short-range oscillatory force law is related to the “density distribution function” and “potential of mean force” characteristic of intermolecular interactions in liquids. These forces arise from the confining effects that the two surfaces have on liquid molecules, forcing them to order into quasi-discrete layers. Such layers are energetically or entropically favored and correspond to the minima in the free energy, whereas fractional layers are disfavored (energy maxima). This effect is quite general and arises in all simple liquids when they are confined between two smooth, rigid surfaces, both flat and curved. Oscillatory forces do not require any attractive liquid–liquid or liquid–wall interaction, only two hard walls confining

molecules whose shape is not too irregular and that are free to exchange with molecules in a bulk liquid reservoir. In the absence of any attractive pressure between the molecules, the bulk liquid density could be maintained by an external hydrostatic pressure – in real liquids attractive van der Waals forces play the role of such an external pressure.

Oscillatory forces are now well understood theoretically, at least for simple liquids, and a number of theoretical studies and computer simulations of various confined liquids (including water) that interact via some form of Lennard–Jones potential have invariably led to an oscillatory solvation force at surface separations below a few molecular diameters [136–144]. In a first approximation, the oscillatory force law may be described by an exponentially decaying cosine function of the form

$$E \approx E_0 \cos(2\pi D/\sigma) e^{-D/\sigma}, \quad (13.16)$$

where both theory and experiments show that the oscillatory period and the characteristic decay length of the envelope are close to  $\sigma$ .

Once the solvation zones of the two surfaces overlap, the mean liquid density in the gap is no longer the same as in the bulk liquid. Since the van der Waals interaction depends on the optical properties of the liquid, which in turn depends on the density, the van der Waals and the oscillatory solvation forces are not strictly additive. It is more correct to think of the solvation force as *the* van der Waals force at small separations with the molecular properties and density variations of the medium taken into account. It is also important to appreciate that solvation forces do not arise simply because liquid molecules tend to structure into semi-ordered layers at surfaces. They arise because of the disruption or *change* of this ordering during the approach of a second surface. The two effects are related; the greater the tendency toward structuring at an isolated surface the greater the solvation force between two such surfaces, but there is a real distinction between the two phenomena that should be borne in mind.

Oscillatory forces lead to different adhesion values depending on the energy minimum from which two surfaces are being separated. For an interaction energy described by (13.16), “quantized” adhesion energies will be  $E_0$  at  $D = 0$  (primary minimum),  $E_0/e$  at  $D = \sigma$ ,  $E_0/e^2$  at  $D = 2\sigma$ , etc.  $E_0$  can be thought of as a depletion force (Sect. 13.4.5) that is approximately given by the osmotic limit  $E_0 \approx -k_B T/\sigma^2$ , which can exceed the contribution to the adhesion energy in contact from the van der Waals forces (at  $D_0 \approx 0.15$ – $0.20$  nm, as discussed in Sect. 13.3.1, keeping in mind that the Lifshitz theory fails to describe the force law at *intermediate* distances). Such multivalued adhesion forces have been observed in a number of systems, including the interactions of fibers.

Measurements of oscillatory forces between different surfaces across both aqueous and nonaqueous liquids have revealed their richness of properties [145–149], for example, their great sensitivity to the shape and rigidity of the solvent molecules, to the presence of other components, and to the structure of the confining surfaces (Sects. 13.5.3 and 13.9). In particular, the oscillations can be smeared out if the molecules are irregularly shaped (e.g., branched) and therefore

unable to pack into ordered layers, or when the interacting surfaces are rough or fluidlike (Sect. 13.4.6).

It is easy to understand how oscillatory forces arise between two flat, plane parallel surfaces. Between two curved surfaces, e.g., two spheres, one might imagine the molecular ordering and oscillatory forces to be smeared out in the same way that they are smeared out between two randomly rough surfaces (Sect. 13.5.3); however, this is not the case. Ordering can occur as long as the curvature or roughness is itself regular or uniform, i.e., not random. This is due to the Derjaguin approximation (13.3). If the energy between two flat surfaces is given by a decaying oscillatory function (for example, a cosine function as in (13.16)), then the force (and energy) between two curved surfaces will also be an oscillatory function of distance with some phase shift. Likewise, two surfaces with regularly curved regions will also retain their oscillatory force profile, albeit modified, as long as the corrugations are truly regular, i.e., periodic. On the other hand, surface roughness, even on the nanometer scale, can smear out oscillations if the roughness is random and the confined molecules are smaller than the size of the surface asperities [150, 151]. If an organic liquid contains small amounts of water, the expected oscillatory force can be replaced by a strongly attractive capillary force (Sect. 13.5.1).

#### 13.4.4 Hydration and Hydrophobic Forces

The forces occurring in water and electrolyte solutions are more complex than those occurring in nonpolar liquids. According to continuum theories, the attractive van der Waals force is always expected to win over the repulsive electrostatic “double-layer” force at small surface separations (Fig. 13.6). However, certain surfaces (usually oxide or hydroxide surfaces such as clays or silica) swell spontaneously or repel each other in aqueous solution, even at high salt concentrations. Yet in all these systems one would expect the surfaces or particles to remain in strong adhesive contact or coagulate in a primary minimum if the only forces operating were DLVO forces.

There are many other aqueous systems in which the DLVO theory fails and where there is an additional short-range force that is not oscillatory but monotonic. Between hydrophilic surfaces this force is exponentially repulsive and is commonly referred to as the *hydration*, or *structural*, force. The origin and nature of this force has long been controversial, especially in the colloidal and biological literature. Repulsive hydration forces are believed to arise from strongly hydrogen-bonding surface groups, such as hydrated ions or hydroxyl (–OH) groups, which modify the hydrogen-bonding network of liquid water adjacent to them. Because this network is quite extensive in range [152], the resulting interaction force is also of relatively long range.

Repulsive hydration forces were first extensively studied between clay surfaces [153]. More recently, they have been measured in detail between mica and silica

surfaces [21–23, 154], where they have been found to decay exponentially with decay lengths of about 1 nm. Their effective range is 3–5 nm, which is about twice the range of the oscillatory solvation force in water. Empirically, the hydration repulsion between two hydrophilic surfaces appears to follow the simple equation

$$E = E_0 e^{-D/\lambda_0}, \quad (13.17)$$

where  $\lambda_0 \approx 0.6$ –1.1 nm for 1:1 electrolytes and  $E_0 = 3$ –30 mJ m<sup>-2</sup> depending on the hydration (hydrophilicity) of the surfaces, higher  $E_0$  values generally being associated with lower  $\lambda_0$  values.

The interactions between molecularly smooth mica surfaces in dilute electrolyte solutions obey the DLVO theory (Fig. 13.7b). However, at higher salt concentrations, specific to each electrolyte, hydrated cations bind to the negatively charged surfaces and give rise to a repulsive hydration force [21, 22]. This is believed to be due to the energy needed to dehydrate the bound cations, which presumably retain some of their water of hydration on binding. This conclusion was arrived at after noting that the strength and range of the hydration forces increase with the known hydration numbers of the electrolyte cations in the order: Mg<sup>2+</sup> > Ca<sup>2+</sup> > Li<sup>+</sup> ~ Na<sup>+</sup> > K<sup>+</sup> > Cs<sup>+</sup>. Similar trends are observed with other negatively charged colloidal surfaces.

While the hydration force between two mica surfaces is overall repulsive below a distance of 4 nm, it is not always monotonic below about 1.5 nm but exhibits oscillations of mean periodicity of  $0.25 \pm 0.03$  nm, roughly equal to the diameter of the water molecule. This is shown in the insert in Fig. 13.7b, where we may note that the first three minima at  $D = 0, 0.28$ , and  $0.56$  nm occur at negative energies, a result that rationalizes observations on certain colloidal systems. For example, clay platelets such as montmorillonite often repel each other increasingly strongly as they come closer together, but they are also known to stack into stable aggregates with water interlayers of typical thickness 0.25 and 0.55 nm between them [155, 156], suggestive of a turnabout in the force law from a monotonic repulsion to discretized attraction. In chemistry we would refer to such structures as stable hydrates of fixed stoichiometry, whereas in physics we may think of them as experiencing an oscillatory force.

Both surface force and clay swelling experiments have shown that hydration forces can be modified or “regulated” by exchanging ions of different hydration on surfaces, an effect that has important practical applications in controlling the stability of colloidal dispersions. It has long been known that colloidal particles can be precipitated (coagulated or flocculated) by increasing the electrolyte concentration, an effect that was traditionally attributed to the reduced screening of the electrostatic double-layer repulsion between the particles due to the reduced Debye length. However, there are many examples where colloids are stabilized at high salt concentrations, not at low concentrations. This effect is now recognized as being due to the increased hydration repulsion experienced by certain surfaces when they bind highly hydrated ions at higher salt concentrations. Hydration regulation of adhesion and interparticle forces is an important practical method for controlling various processes such as clay swelling

[155, 156], ceramic processing and rheology [157, 158], material fracture [157], and colloidal particle and bubble coalescence [159].

Water appears to be unique in having a solvation (hydration) force that exhibits both a monotonic and an oscillatory component. Between hydrophilic surfaces the monotonic component is repulsive (Fig. 13.7b), but between hydrophobic surfaces it is attractive and the final adhesion is much greater than expected from the Lifshitz theory.

A hydrophobic surface is one that is inert to water in the sense that it cannot bind to water molecules via ionic or hydrogen bonds. Hydrocarbons and fluorocarbons are hydrophobic, as is air, and the strongly attractive hydrophobic force has many important manifestations and consequences such as the low solubility or miscibility of water and oil molecules, micellization, protein folding, strong adhesion and rapid coagulation of hydrophobic surfaces, nonwetting of water on hydrophobic surfaces, and hydrophobic particle attachment to rising air bubbles (the basic principle of froth flotation).

In recent years, there has been a steady accumulation of experimental data on the force laws between various hydrophobic surfaces in aqueous solution [160–178]. These studies have found that the force law between two macroscopic hydrophobic surfaces is of surprisingly long range, decaying exponentially with a characteristic decay length of 1–2 nm in the separation range of 0–10 nm, and then more gradually further out. The hydrophobic force can be far stronger than the van der Waals attraction, especially between hydrocarbon surfaces in water, for which the Hamaker constant is quite small. The magnitude of the hydrophobic attraction has been found to decrease with the decreasing hydrophobicity (increasing hydrophilicity) of lecithin lipid bilayer surfaces [32] and silanated surfaces [168], whereas examples of the opposite trend have been shown for some Langmuir–Blodgett-deposited monolayers [179]. An apparent correlation has been found between high stability of the hydrophobic surface (as measured by its contact angle hysteresis) and the absence of a long-range part of the attractive force [180].

For two surfaces in water the purely hydrophobic interaction energy (ignoring DLVO and oscillatory forces) in the range 0–10 nm is given by

$$E = -2\gamma e^{-D/\lambda_0}, \quad (13.18)$$

where typically  $\lambda_0 = 1\text{--}2$  nm, and  $\gamma = 10\text{--}50$  mJ m<sup>-2</sup>. The higher value corresponds to the interfacial energy of a pure hydrocarbon–water interface.

At a separation below 10 nm, the hydrophobic force appears to be insensitive or only weakly sensitive to changes in the type and concentration of electrolyte ions in the solution. The absence of a “screening” effect by ions attests to the nonelectrostatic origin of this interaction. In contrast, some experiments have shown that, at separations greater than 10 nm, the attraction does depend on the intervening electrolyte, and that in dilute solutions, or solutions containing divalent ions, it can continue to exceed the van der Waals attraction out to separations of 80 nm [165, 181]. Recent research suggests that the interactions at very long range might not be a “hydrophobic” force since they are influenced by the presence of dissolved gas in



the solution [176, 177], the stability of the hydrophobic surface [178, 180], and, on some types of surfaces, bridging submicroscopic bubbles [172–174].

The long-range nature of the hydrophobic interaction has a number of important consequences. It accounts for the rapid coagulation of hydrophobic particles in water and may also account for the rapid folding of proteins. It also explains the ease with which water films rupture on hydrophobic surfaces. In this case, the van der Waals force across the water film is repulsive and therefore favors wetting, but this is more than offset by the attractive hydrophobic interaction acting between the two hydrophobic phases across water. Hydrophobic forces are increasingly being implicated in the adhesion and fusion of biological membranes and cells. It is known that both osmotic and electric-field stresses enhance membrane fusion, an effect that may be due to the concomitant increase in the hydrophobic area exposed between two adjacent surfaces.

From the previous discussion we can infer that hydration and hydrophobic forces are not of a simple nature. These interactions are probably the most important, yet the least understood of all the forces in aqueous solutions. The unusual properties of water and the nature of the surfaces (including their homogeneity and stability) appear to be equally important. Some particle surfaces can have their hydration forces regulated, for example, by ion exchange. Others appear to be intrinsically hydrophilic (e.g., silica) and cannot be coagulated by changing the ionic condition, but can be rendered hydrophobic by chemically modifying their surface groups. For example, on heating silica to above 600 °C, two adjacent surface silanol (–OH) groups release a water molecule and form a hydrophobic siloxane (–O–) group, whence the repulsive hydration force changes into an attractive hydrophobic force.

How do these exponentially decaying repulsive or attractive forces arise? Theoretical work and computer simulations [138, 140, 182, 183] suggest that the solvation forces in water should be purely oscillatory, whereas other theoretical studies [184–191] suggest a monotonically exponential repulsion or attraction, possibly superimposed on an oscillatory force. The latter is consistent with experimental findings, as shown in the inset to Fig. 13.7b, where it appears that the oscillatory force is simply additive with the monotonic hydration and DLVO forces, suggesting that these arise from essentially different mechanisms. It has been suggested that for a sufficiently solvophilic surface, there could be “hydration”-like forces also in nonaqueous systems [190].

It is probable that the short-range hydration force between all smooth, rigid, or crystalline surfaces (e.g., mineral surfaces such as mica) has an oscillatory component. This may or may not be superimposed on a monotonic force due to image interactions [186], dipole–dipole interactions [191], and/or structural or hydrogen-bonding interactions [184, 185].

Like the repulsive hydration force, the origin of the hydrophobic force is still unknown. Luzar et al. [188] carried out a Monte Carlo simulation of the interaction between two hydrophobic surfaces across water at separations below 1.5 nm. They obtained a decaying oscillatory force superimposed on a monotonically attractive curve. In more recent computational and experimental work [192–195], it has been suggested that hydrophobic surfaces generate a depleted region of water around

them, and that a long-range attractive force due to depletion arises between two such surfaces. Such a difference in density might also cause boundary slip of water at hydrophobic surfaces [51, 196, 197].

It is questionable whether the hydration or hydrophobic force should be viewed as an ordinary type of solvation or structural force that reflects the packing of water molecules. The energy (or entropy) associated with the hydrogen-bonding network, which extends over a much larger region of space than the molecular correlations, is probably at the root of the long-range interactions of water. The situation in water appears to be governed by much more than the molecular packing effects that dominate the interactions in simpler liquids.

### 13.4.5 *Polymer-Mediated Forces*

Polymers or macromolecules are chainlike molecules consisting of many identical segments (monomers or repeating units) held together by covalent bonds. The size of a polymer coil in solution or in the melt is determined by a balance between van der Waals attraction (and hydrogen bonding, if present) between polymer segments, and the entropy of mixing, which causes the polymer coil to expand. In polymer melts above the glass transition temperature, and at certain conditions in solution, the attraction between polymer segments is exactly balanced by the entropy effect. The polymer solution will then behave virtually ideally, and the density distribution of segments in the coil is Gaussian. This is called the theta ( $\theta$ ) condition, and it occurs at the theta or Flory temperature for a particular combination of polymer and solvent or solvent mixture. At lower temperatures (in a poor or bad solvent), the polymer–polymer interactions dominate over the entropic, and the coil will shrink or precipitate. At higher temperatures (good solvent conditions), the polymer coil will be expanded.

High-molecular-weight polymers form large coils, which significantly affect the properties of a solution even when the total mass of polymer is very low. The radius of the polymer coil is proportional to the segment length  $a$  and the number of segments  $n$ . At theta conditions, the hydrodynamic radius of the polymer coil (the root-mean-square separation of the ends of one polymer chain) is theoretically given by  $R_h = a n^{1/2}$ , and the unperturbed radius of gyration (the average root-mean-square distance of a segment from the center of mass of the molecule) is  $R_g = a (n/6)^{1/2}$ . In a good solvent the perturbed size of the polymer coil, the Flory radius  $R_F$ , is proportional to  $n^{3/5}$ .

Polymers interact with surfaces mainly through van der Waals and electrostatic interactions. The physisorption of polymers containing only one type of segment is reversible and highly dynamic, but the rate of exchange of adsorbed chains with free chains in the solution is low, since the polymer remains bound to the surface as long as one segment along the chain is adsorbed. The adsorption energy per segment is on the order of  $k_B T$ . In a good solvent, the conformation of a polymer on a surface is very different from the coil conformation in bulk solution. Polymers

adsorb in “trains”, separated by “loops” extending into solution and dangling “tails” (the ends of the chain). Compared to adsorption at lower temperatures, good solvent conditions favor more of the polymer chain being in the solvent, where it can attain its optimum conformation. As a result, the extension of the polymer is longer, even though the total amount of adsorbed polymer is lower. In a good solvent, the polymer chains can also be effectively repelled from a surface, if the loss in conformational entropy close to the surface is not compensated for by a gain in enthalpy from adsorption of segments. In this case, there will be a layer of solution (thickness  $\approx R_g$ ) close to the surfaces that is depleted of polymer.

The interaction forces between two surfaces across a polymer solution will depend on whether the polymer adsorbs onto the surfaces or is repelled from them, and also on whether the interaction occurs at “true” or “restricted” thermodynamic equilibrium. At true or full equilibrium, the polymer between the surfaces can equilibrate (exchange) with polymer in the bulk solution at all surface separations. Some theories [198, 199] predict that, at full equilibrium, the polymer chains would move from the confined gap into the bulk solution where they could attain entropically more favorable conformations, and that a monotonic attraction at all distances would result from bridging and depletion interactions (which will be discussed below). Other theories suggest that the interaction at small separations would be ultimately repulsive, since some polymer chains would remain in the gap due to their attractive interactions with many sites on the surface (enthalpic) – more sites would be available to the remaining polymer chains if some others desorbed and diffused out from the gap [73, 200–202].

At restricted equilibrium, the polymer is kinetically trapped, and the adsorbed amount is thus constant as the surfaces are brought toward each other, but the chains can still rearrange on the surfaces and in the gap. Experimentally, the true equilibrium situation is very difficult to attain, and most experiments are done at restricted equilibrium conditions. Even the equilibration of conformations assumed in theoretical models for restricted equilibrium conditions can be so slow that this condition is difficult to reach experimentally.

In systems of adsorbing polymer, bridging of chains from one surface to the other can give rise to a long-range attraction, since the bridging chains would gain conformational entropy if the surfaces were closer together. In poor solvents, both bridging and intersegment interactions contribute to an attraction [27]. However, regardless of solvent and equilibrium conditions, a strong repulsion due to the osmotic interactions is seen at small surface separations in systems of adsorbing polymers at restricted equilibrium.

In systems containing high concentrations of nonadsorbing polymer, the difference in solute concentration in the bulk and between the surfaces at separations smaller than the approximate polymer coil diameter ( $2R_g$ , i.e., when the polymer has been squeezed out from the gap between the surfaces) may give rise to an attractive osmotic force (the “depletion attraction”) [203–208]. In addition, if the polymer coils become initially compressed as the surfaces approach each other, this can give rise to a repulsion (“depletion stabilization”) at large separations [206]. For a system of two cylindrical surfaces of radius  $R$ , the maximum depletion force  $F_{\text{dep}}$

is expected to occur when the surfaces are in contact and is given by multiplying the depletion (osmotic) pressure,  $P_{\text{dep}} = \rho k_B T$ , by the contact area  $\pi r^2$ , where  $r$  is given by the chord theorem:  $r^2 = (2R - R_g)R_g \approx 2RR_g$  [2]

$$F_{\text{dep}}/R = -2\pi R_g \rho k_B T, \quad (13.19)$$

where  $\rho$  is the number density of the polymer in the bulk solution.

If a part of the polymer (typically an end group) is different from the rest of the chain, this part may preferentially adsorb to the surface. End-adsorbed polymer is attached to the surface at only one point, and the extension of the chain is dependent on the grafting density, i.e., the average distance  $s$  between adsorbed end groups on the surface (Fig. 13.8). One distinguishes between different regions of increasing

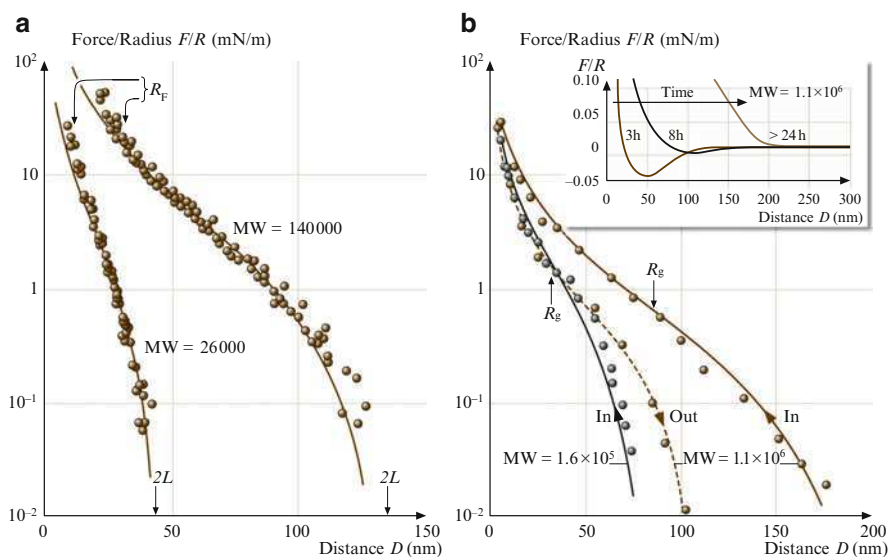


**Fig. 13.8** Experimentally determined forces in systems of two interacting polymer layers: (a) Polystyrene brush layers grafted via an adsorbing chain-end group onto mica surfaces in toluene (a good solvent for polystyrene). *Left curve*:  $MW = 26,000$  g/mol,  $R_F = 12$  nm. *Right curve*:  $MW = 14,000$  g/mol,  $R_F = 32$  nm. Both force curves were reversible on approach and separation. The *solid curves* are theoretical fits using the Alexander-de Gennes theory with the following measured parameters: spacing between attachments sites:  $s = 8.5$  nm, brush thickness:  $L = 22.5$  and  $65$  nm, respectively (adapted from [209]). (b) Polyethylene oxide layers physisorbed onto mica from  $150 \mu\text{g/ml}$  solution in aqueous  $0.1 \text{ M KNO}_3$  (a good solvent for polyethylene oxide). *Main figure*: Equilibrium forces at full coverage after  $\sim 16$  h adsorption time. *Left curve*:  $MW = 160,000$  g/mol,  $R_g = 32$  nm. *Right curve*:  $MW = 1,100,000$  g/mol,  $R_g = 86$  nm. Note the hysteresis (irreversibility) on approach and separation for this *physisorbed* layer, in contrast to the absence of hysteresis with *grafted* chains in case (a). The *solid curves* are based on a modified form of the Alexander-de Gennes theory. *Insert in (b)*: evolution of the forces with the time allowed for the higher MW polymer to adsorb from solution. Note the gradual reduction in the attractive bridging component (adapted from [210–212], after [2], © 1991, with permission from Elsevier Science)

overlap of the chains (stretching) called pancake, mushroom, and brush regimes [213]. In the mushroom regime, where the coverage is sufficiently low that there is no overlap between neighboring chains, the thickness of the adsorbed layer is proportional to  $n^{1/2}$  (i.e., to  $R_g$ ) at theta conditions and to  $n^{3/5}$  in a good solvent.

Several models [213–218] have been developed for the extension and interactions between two brushes (strongly stretched grafted chains). They are based on a balance between osmotic pressure within the brush layers (uncompressed and compressed) and the elastic energy of the chains and differ mainly in the assumptions of the segment density profile, which can be a step function or parabolic. At high coverage (in the brush regime), where the chains will avoid overlapping each other, the thickness of the layer is proportional to  $n$ .

Experimental work on both monodisperse [28, 29, 209, 219] and polydisperse [31, 220] systems at different solvent conditions has confirmed the expected range and magnitude of the repulsive interactions resulting from compression of densely packed grafted layers.

### 13.4.6 Thermal Fluctuation Forces

If a surface is not rigid but very soft or even fluidlike, this can act to smear out any oscillatory solvation force. This is because the thermal fluctuations of such interfaces make them dynamically “rough” at any instant, even though they may be perfectly smooth on a time average. The types of surfaces that fall into this category are fluidlike amphiphilic surfaces of micelles, bilayers, emulsions, soap films, etc., but also solid colloidal particle surfaces that are coated with surfactant monolayers, as occurs in lubricating oils, paints, toners, etc.

These thermal fluctuation forces (also called entropic or steric forces) are usually short range and repulsive and are very effective at stabilizing the attractive van der Waals forces at some small but finite separation. This can reduce the adhesion energy or force by up to three orders of magnitude. It is mainly for this reason that fluidlike micelles and bilayers, biological membranes, emulsion droplets, or gas bubbles adhere to each other only very weakly.

Because of their short range it was, and still is, commonly believed that these forces arise from water ordering or “structuring” effects at surfaces, and that they reflect some unique or characteristic property of water. However, it is now known that these repulsive forces also exist in other liquids [221, 222]. Moreover, they appear to become stronger with increasing temperature, which is unlikely if the force originated from molecular ordering effects at surfaces. Recent experiments, theory, and computer simulations [223–226] have shown that these repulsive forces have an entropic origin arising from the osmotic repulsion between exposed thermally mobile surface groups once these overlap in a liquid. These phenomena include undulating and peristaltic forces between membranes or bilayers, and, on the molecular scale, protrusion and head-group overlap forces where the interactions are also influenced by hydration forces.

## 13.5 Adhesion and Capillary Forces

### 13.5.1 Capillary Forces

When considering the adhesion of two solid surfaces or particles in air or in a liquid, it is easy to overlook or underestimate the important role of capillary forces, i.e., forces arising from the Laplace pressure of curved menisci formed by condensation of a liquid between and around two adhering surfaces (Fig. 13.9).

The adhesion force between a nondeformable spherical particle of radius  $R$  and a flat surface in an inert atmosphere (Fig. 13.9a) is

$$F_{\text{ad}} = 4\pi R\gamma_{\text{SV}}. \quad (13.20)$$

But in an atmosphere containing a condensable vapor, the expression above is replaced by

$$F_{\text{ad}} = 4\pi R(\gamma_{\text{LV}} \cos \theta + \gamma_{\text{SL}}), \quad (13.21)$$

where the first term is due to the Laplace pressure of the meniscus and the second is due to the direct adhesion of the two contacting solids within the liquid. Note that the above equation does not contain the radius of curvature  $r$  of the liquid meniscus (Fig. 13.9b). This is because for smaller  $r$  the Laplace pressure  $\gamma_{\text{LV}}/r$  increases, but the area over which it acts decreases by the same amount, so the two effects cancel out. Experiments with inert liquids, such as hydrocarbons, condensing between two

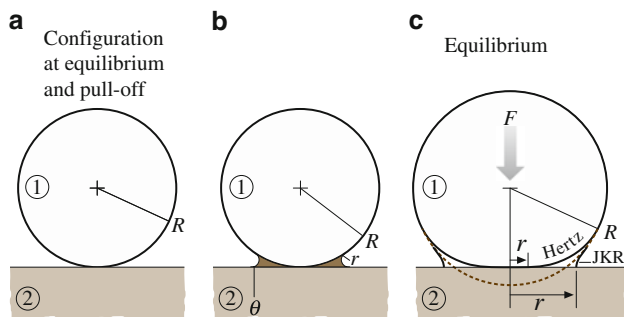


**Fig. 13.9** Adhesion and capillary forces: (a) a nondeforming sphere on a rigid, flat surface in an inert atmosphere and (b) in a vapor that can “capillary condense” around the contact zone. At equilibrium, the concave radius  $r$  of the liquid meniscus is given by the Kelvin equation. For a concave meniscus to form, the contact angle  $\theta$  has to be less than  $90^\circ$ . In the case of hydrophobic surfaces surrounded by water, a vapor cavity can form between the surfaces. As long as the surfaces are perfectly smooth, the contribution of the meniscus to the adhesion force is independent of  $r$  (after [6] with permission). (c) Elastically deformable sphere on a rigid flat surface in the absence (Hertz) and presence (JKR) of adhesion ((a) and (c) after [2], © 1991, with permission from Elsevier Science)

mica surfaces indicate that (13.21) is valid for values of  $r$  as small as 1–2 nm, corresponding to vapor pressures as low as 40% of saturation [148, 227, 228]. Capillary condensation also occurs in binary liquid systems, e.g., when water dissolved in hydrocarbon liquids condenses around two contacting hydrophilic surfaces or when a vapor cavity forms in water around two hydrophobic surfaces. In the case of water condensing from vapor or from oil, it also appears that the bulk value of  $\gamma_{LV}$  is applicable for meniscus radii as small as 2 nm.

The capillary condensation of liquids, especially water, from vapor can have additional effects on the physical state of the contact zone. For example, if the surfaces contain ions, these will diffuse and build up within the liquid bridge, thereby changing the chemical composition of the contact zone, as well as influencing the adhesion. In the case of surfaces covered with surfactant or polymer molecules (amphiphilic surfaces), the molecules can turn over on exposure to humid air, so that the surface nonpolar groups become replaced by polar groups, which renders the surfaces hydrophilic. When two such surfaces come into contact, water will condense around the contact zone and the adhesion force will also be affected – generally increasing well above the value expected for inert hydrophobic surfaces. It is apparent that adhesion in vapor or a solvent is often largely determined by capillary forces arising from the condensation of liquid that may be present only in very small quantities, e.g., 10–20% of saturation in the vapor, or 20 ppm in the solvent.

### 13.5.2 Adhesion Mechanics

Two bodies in contact deform as a result of surface forces and/or applied normal forces. For the simplest case of two interacting elastic spheres (a model that is easily extended to an elastic sphere interacting with an undeformable surface, or vice versa) and in the absence of attractive surface forces, the vertical central displacement (compression) was derived by *Hertz* [229] (Fig. 13.9c). In this model, the displacement and the contact area are equal to zero when no external force (load) is applied, i.e., at the points of contact and of separation. The contact area  $A$  increases with normal force or load as  $L^{2/3}$ .

In systems where attractive surface forces are present between the surfaces, the deformations are more complicated. Modern theories of the adhesion mechanics of two contacting solid surfaces are based on the Johnson–Kendall–Roberts (JKR) theory [6, 230], or on the Derjaguin–Muller–Toporov (DMT) theory [231–233]. The JKR theory is applicable to easily deformable, large bodies with high surface energy, whereas the DMT theory better describes very small and hard bodies with low surface energy [234]. The intermediate regime has also been described [235].

In the JKR theory, two spheres of radii  $R_1$  and  $R_2$ , bulk elastic modulus  $K$ , and surface energy  $\gamma$  will flatten due to attractive surface forces when in contact at no external load. The contact area will increase under an external load  $L$  or normal

force  $F$ , such that at mechanical equilibrium the radius of the contact area  $r$  is given by

$$r^3 = \frac{R}{K} \left[ F + 6\pi R\gamma + \sqrt{12\pi R\gamma F + (6\pi R\gamma)^2} \right], \quad (13.22)$$

where  $R = R_1 R_2 / (R_1 + R_2)$ . In the absence of surface energy  $\gamma$  equation (13.22) is reduced to the expression for the radius of the contact area in the Hertz model. Another important result of the JKR theory gives the adhesion force or “pull-off” force

$$F_{\text{ad}} = -3\pi R\gamma_S, \quad (13.23)$$

where the surface energy  $\gamma_S$  is defined through  $W = 2\gamma_S$ , where  $W$  is the reversible work of adhesion. Note that, according to the JKR theory, a finite elastic modulus  $K$  while having an effect on the load–area curve, has no effect on the adhesion force, an interesting and unexpected result that has nevertheless been verified experimentally [16, 236–238].

Equations (13.22) and (13.23) provide the framework for analyzing results of adhesion measurements (Fig. 13.10) of contacting solids, known as contact mechanics [230, 239], and for studying the effects of surface conditions and time on adhesion energy hysteresis (Sect. 13.5.4).

The JKR theory has been extended [240, 241] to consider rigid or elastic substrates separated by thin compliant layers of very different elastic moduli, a situation commonly encountered in SFA and AFM experiments. The deformation of the system is then strongly dependant on the ratio of  $r$  to the thickness of the confined layer. At small  $r$  (low  $L$ ), the deformation occurs mostly in the thin confined layer, whereas at large  $r$  (large  $L$ ), it occurs mainly in the substrates. Because of the changing distribution of traction across the contact, the adhesion force in a layered system is also modified from that of isotropic systems (13.23) so that it is no longer independent of the elastic moduli.

### 13.5.3 *Effects of Surface Structure, Roughness, and Lattice Mismatch*

In a contact between two rough surfaces, the real area of contact varies with the applied load in a different manner than between smooth surfaces [242, 243]. For nonadhering surfaces exhibiting an exponential distribution of *elastically* deforming asperities (spherical caps of equal radius), it has been shown that the contact area for rough surfaces increases approximately linearly with the applied normal force (load)  $L$  instead of as  $L^{2/3}$  for smooth surfaces [242]. It has also been shown that for *plastically* deforming metal microcontacts the real contact area increases with load as  $A \propto L$  [244, 245]. In systems with attractive surface forces, there is a competition between this attraction and repulsive forces arising from compression



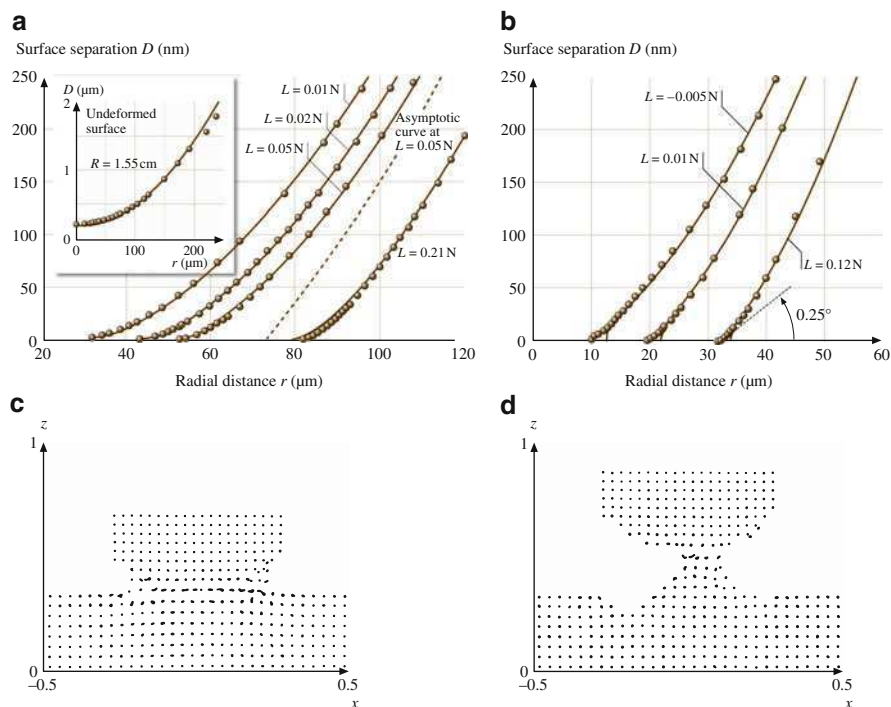


**Fig. 13.10** Experimental and computer simulation data on contact mechanics for ideal Hertz and JKR contacts. **(a)** Measured profiles of surfaces in nonadhesive contact (*circles*) compared with Hertz profiles (*continuous curves*). The system was mica surfaces in a concentrated KCl solution in which they do not adhere. When not in contact, the surface shape is accurately described by a sphere of radius  $R = 1.55\text{ cm}$  (*insert*). The applied loads were 0.01, 0.02, 0.05, and 0.21 N. The last profile was measured in a different region of the surfaces where the local radius of curvature was 1.45 cm. The Hertz profiles correspond to central displacements of  $\delta = 66.5, 124, 173$ , and 441 nm. The *dashed line* shows the shape of the undeformed sphere corresponding to the curve at a load of 0.05 N; it fits the experimental points at larger distances (not shown). **(b)** Surface profiles measured with adhesive contact (mica surfaces adhering in dry nitrogen gas) at applied loads of  $-0.005, 0.01$ , and  $0.12\text{ N}$ . The *continuous lines* are JKR profiles obtained by adjusting the central displacement in each case to get the best fit to points at larger distances. The values are  $\delta = -4.2, 75.6$ , and  $256\text{ nm}$ . Note that the scales of this figure exaggerate the apparent angle at the junction of the surfaces. This angle, which is insensitive to load, is only about  $0.25^\circ$ . **(c,d)** Molecular dynamics simulation illustrating the formation of a connective neck between an Ni tip (topmost eight layers) and an Au substrate. The figures show the atomic configuration in a slice through the system at indentation **(c)** and during separation **(d)**. Note the crystalline structure of the neck. Distances are given in units of  $x$  and  $z$ , where  $x = 1$  and  $z = 1$  correspond to  $6.12\text{ nm}$  (**(a,b)** after [236], © 1987, with permission from Elsevier Science, **(c,d)** after [112], with kind permission from Kluwer Academic Publishers)

of high asperities. As a result, the adhesion in such systems can be very low, especially if the surfaces are not easily deformed [246, 248]. The opposite is possible for soft (viscoelastic) surfaces where the real (molecular) contact area might be larger than for two perfectly smooth surfaces [249]. The size of the real

contact area at a given normal force is also an important issue in studies of nanoscale friction, both of single-asperity contacts (Sect. 13.7) and of contacts between rough surfaces (Sect. 13.9.2).

Adhesion forces may also vary depending on the commensurability of the crystallographic lattices of the interacting surfaces. *McGuiggan* and *Israelachvili* [250] measured the adhesion between two mica surfaces as a function of the orientation (twist angle) of their surface lattices. The forces were measured in air, water, and an aqueous salt solution where oscillatory structural forces were present. In humid air, the adhesion was found to be relatively independent of the twist angle  $\theta$  due to the adsorption of a 0.4 nm thick amorphous layer of organics and water at the interface. In contrast, in water, sharp adhesion peaks (energy minima) occurred at  $\theta = 0, \pm 60, \pm 120$  and  $180^\circ$ , corresponding to the “coincidence” angles of the surface lattices (Fig. 13.11). As little as  $\pm 1^\circ$  away from these peaks, the energy decreased by 50%. In aqueous KCl solution, due to potassium ion adsorption the water between the surfaces becomes ordered, resulting in an oscillatory force profile where the adhesive minima occur at discrete separations of about 0.25 nm, corresponding to integral numbers of water layers. The whole interaction potential was now found to depend on the orientation of the surface lattices, and the effect extended at least four molecular layers.

It has also been appreciated that the structure of the confining surfaces is just as important as the nature of the liquid for determining the solvation forces [111, 150, 151, 252–256]. Between two surfaces that are completely flat but “unstructured”, the liquid molecules will order into layers, but there will be no lateral ordering

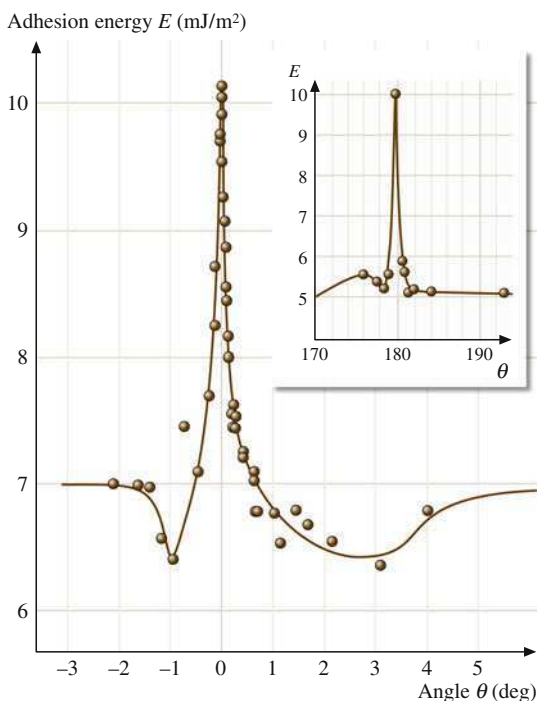


**Fig. 13.11** Adhesion energy for two mica surfaces in contact in water (in the primary minimum of an oscillatory force curve) as a function of the mismatch angle  $\theta$  about  $\theta = 0$  and  $180^\circ$  between the mica surface lattices (after [240] with permission)

within the layers. In other words, there will be positional ordering normal but not parallel to the surfaces. If the surfaces have a crystalline (periodic) lattice, this may induce ordering parallel to the surfaces, as well, and the oscillatory force then also depends on the structure of the surface lattices. Further, if the two lattices have different dimensions (“mismatched” or “incommensurate” lattices), or if the lattices are similar but are not in register relative to each other, the oscillatory force law is further modified [250, 257] and the tribological properties of the film are also influenced, as discussed in Sect. 13.9 [257, 258].

As shown by the experiments, these effects can alter the magnitude of the adhesive minima found at a given separation within the last 1 or 2 nm of a thin film by a factor of two. The force barriers (maxima) may also depend on orientation. This could be even more important than the effects on the minima. A high barrier could prevent two surfaces from coming closer together into a much deeper adhesive well. Thus the maxima can effectively contribute to determining not only the final separation of two surfaces, but also their final adhesion. Such considerations should be particularly important for determining the thickness and strength of intergranular spaces in ceramics, the adhesion forces between colloidal particles in concentrated electrolyte solution, and the forces between two surfaces in a crack containing capillary condensed water.

For surfaces that are *randomly* rough, oscillatory forces become smoothed out and disappear altogether, to be replaced by a purely monotonic solvation force [134, 150, 151]. This occurs even if the liquid molecules themselves are perfectly capable of ordering into layers. The situation of *symmetric* liquid molecules confined between *rough* surfaces is therefore not unlike that of *asymmetric* molecules between *smooth* surfaces (Sect. 13.4.3 and Fig. 13.7a). To summarize, for there to be an oscillatory solvation force, the liquid molecules must be able to be correlated over a reasonably long range. This requires that both the liquid molecules and the surfaces have a high degree of order or symmetry. If either is missing, so will the oscillations. Depending on the size of the molecules to be confined, a roughness of only a few tenths of a nanometer is often sufficient to eliminate any oscillatory component of the force law [43, 150].

### 13.5.4 Nonequilibrium and Rate-Dependent Interactions: Adhesion Hysteresis

Under ideal conditions the adhesion energy is a well-defined thermodynamic quantity. It is normally denoted by  $E$  or  $W$  (the work of adhesion) or  $\gamma$  (the surface tension, where  $W = 2\gamma$ ) and gives the reversible work done on bringing two surfaces together or the work needed to separate two surfaces from contact. Under ideal, equilibrium conditions these two quantities are the same, but under most realistic conditions they are not; the work needed to separate two surfaces is always greater than that originally gained by bringing them together. An understanding of the molecular mechanisms underlying this phenomenon is essential for understanding

many adhesion phenomena, energy dissipation during loading–unloading cycles, contact angle hysteresis, and the molecular mechanisms associated with many frictional processes.

It is wrong to think that hysteresis arises because of some imperfection in the system such as rough or chemically heterogeneous surfaces, or because the supporting material is viscoelastic. Adhesion hysteresis can arise even between perfectly smooth and chemically homogenous surfaces supported by perfectly elastic materials. It can be responsible for such phenomena as rolling friction and elastoplastic adhesive contacts [239, 259–262] during loading–unloading and adhesion–decohesion cycles.

Adhesion hysteresis may be thought of as being due to mechanical effects such as instabilities, or chemical effects such as interdiffusion, interdigitation, molecular reorientations and exchange processes occurring at an interface after contact, as illustrated in Fig. 13.12. Such processes induce roughness and chemical heterogeneity even though initially (and after separation and reequilibration) both surfaces are perfectly smooth and chemically homogeneous. In general, if the energy change, or work done, on separating two surfaces from adhesive contact is not fully recoverable on bringing the two surfaces back into contact again, the adhesion hysteresis may be expressed as

$$W_{\text{Receding}} > W_{\text{Advancing}}$$

or

$$\Delta W = (W_{\text{R}} - W_{\text{A}}) > 0, \quad (13.24)$$

where  $W_{\text{R}}$  and  $W_{\text{A}}$  are the adhesion or surface energies for receding (separating) and advancing (approaching) two solid surfaces, respectively.

Hysteresis effects are also commonly observed in wetting/dewetting phenomena [267]. For example, when a liquid spreads and then retracts from a surface the advancing contact angle  $\theta_{\text{A}}$  is generally larger than the receding angle  $\theta_{\text{R}}$ . Since the contact angle  $\theta$  is related to the liquid–vapor surface tension  $\gamma_{\text{L}}$  and the solid–liquid adhesion energy  $W$  by the Dupré equation

$$(1 + \cos \theta)\gamma_{\text{L}} = W, \quad (13.25)$$

we see that *wetting hysteresis* or *contact angle hysteresis* ( $\theta_{\text{A}} > \theta_{\text{R}}$ ) actually implies adhesion hysteresis,  $W_{\text{R}} > W_{\text{A}}$ , as given by (13.24).

Energy-dissipating processes such as adhesion and contact angle hysteresis arise because of practical constraints of the *finite time* of measurements and the *finite elasticity* of materials. This prevents many loading–unloading or approach–separation cycles from being thermodynamically reversible, even though they would be if carried out infinitely slowly. By thermodynamically irreversible one simply means that one cannot go through the approach–separation cycle via a continuous series of equilibrium states, because some of these are connected via

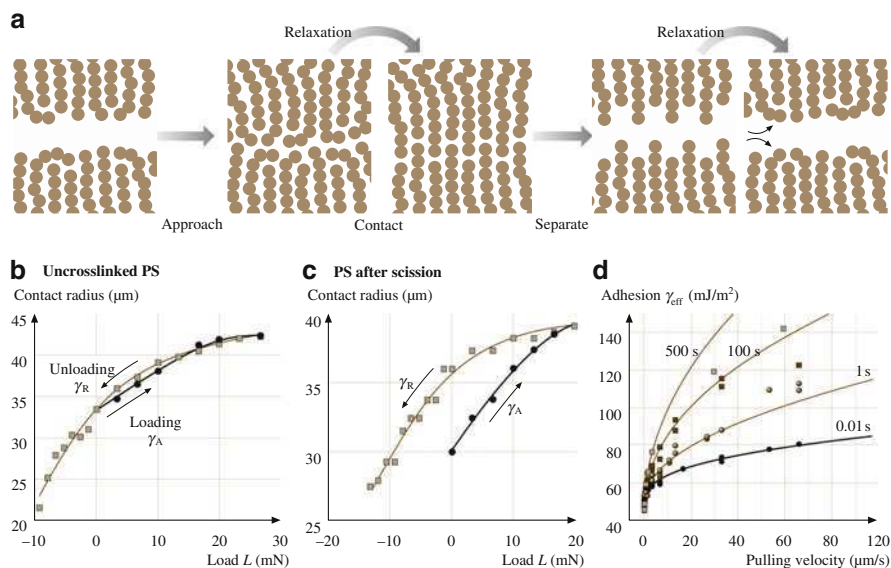


**Fig. 13.12** (a) Schematic representation of interpenetrating chains. (b, c) JKR plots (contact radius  $r$  as a function of applied load  $L$ ) showing small adhesion hysteresis for uncrosslinked polystyrene and larger adhesion hysteresis after chain scission at the surfaces after 18 h irradiation with ultraviolet light in an oxygen atmosphere. The adhesion hysteresis continues to increase with the irradiation time. (b) Rate-dependent adhesion of hexadecyl trimethyl ammonium bromide (CTAB) surfactant monolayers. The solid curves [263] are fits to experimental data on CTAB adhesion after different contact times [264] using an approximate analytical solution for a JKR model, including crack tip dissipation. Due to the limited range of validity of the approximation, the fits rely on the part of the experimental data with low effective adhesion energy only. From the fits one can determine the thermodynamic adhesion energy, the characteristic dissipation velocity, and the intrinsic dissipation exponent of the model (a) after [265], © 1993 American Chemical Society, (b,c) after [266], © 2002 American Association for the Advancement of Science, (d) after [263], © 2000 American Chemical Society)

spontaneous – and therefore thermodynamically irreversible – instabilities or transitions where energy is liberated and therefore “lost” via heat or phonon release [268]. This is an area of much current interest and activity, especially regarding the fundamental molecular origins of adhesion and friction in polymer and surfactant systems, and the relationships between them [239, 260, 263, 264, 266, 269–272].

### 13.6 Introduction: Different Modes of Friction and the Limits of Continuum Models

Most frictional processes occur with the sliding surfaces becoming damaged in one form or another [259]. This may be referred to as “normal” friction. In the case of brittle materials, the damaged surfaces slide past each other while separated by

relatively large, micrometer-sized wear particles. With more ductile surfaces, the damage remains localized to nanometer-sized, plastically deformed asperities. Some features of the friction between damaged surfaces will be described in Sect. 13.7.4.

There are also situations in which sliding can occur between two perfectly smooth, undamaged surfaces. This may be referred to as “interfacial” sliding or “boundary” friction and is the focus of the following sections. The term “boundary lubrication” is more commonly used to denote the friction of surfaces that contain a thin protective lubricating layer such as a surfactant monolayer, but here we shall use the term more broadly to include any molecularly thin solid, liquid, surfactant, or polymer film.

Experiments have shown that, as a liquid film becomes progressively thinner, its physical properties change, at first quantitatively and then qualitatively [45, 48, 273–276]. The quantitative changes are manifested by an increased viscosity, non-Newtonian flow behavior, and the replacement of normal melting by a glass transition, but the film remains recognizable as a liquid (Fig. 13.13). In tribology, this regime is commonly known as the “mixed lubrication” regime, where the rheological properties of a film are intermediate between the bulk and boundary properties. One may also refer to it as the “intermediate” regime (Table 13.4).

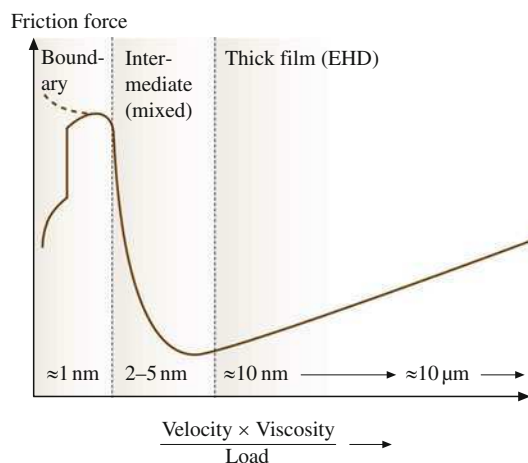


**Fig. 13.13** Stribeck curve: an empirical curve giving the trend generally observed in the friction forces or friction coefficients as a function of sliding velocity, the bulk viscosity of the lubricating fluid, and the applied load (normal force). The three friction/lubrication regimes are known as the boundary lubrication regime (Sect. 13.7), the intermediate or mixed lubrication regime (Sect. 13.8.2), and thick film or elastohydrodynamic (EHD) lubrication regime (Sect. 13.8.1). The film thicknesses believed to correspond to each of these regimes are also shown. For thick films, the friction force is purely viscous, e.g., Couette flow at low shear rates, but may become complicated at higher shear rates where EHD deformations of surfaces can occur during sliding (after [6], with permission)

**Table 13.4** The three main tribological regimes characterizing the changing properties of liquids subjected to increasing confinement between two solid surfaces<sup>a</sup>. Based on work by Granick [273], Hu and Granick [274], and others [39,265,277] on the dynamic properties of short chain molecules such as alkanes and polymer melts confined between surfaces

Regime	Conditions for getting into this regime	Static/equilibrium properties <sup>b</sup>	Dynamic properties <sup>c</sup>
Bulk	<ul style="list-style-type: none"> <li>• Thick films (<math>&gt; 10</math> molecular diameters, <math>\gg R_g</math> for polymers)</li> <li>• Low or zero loads</li> <li>• High shear rates</li> </ul>	Bulk (continuum) properties: <ul style="list-style-type: none"> <li>• Bulk liquid density</li> <li>• No long-range order</li> </ul>	Bulk (continuum) properties: <ul style="list-style-type: none"> <li>• Newtonian viscosity</li> <li>• Fast relaxation times</li> <li>• No glass temperature</li> <li>• No yield point</li> <li>• Elastohydrodynamic lubrication</li> </ul>
Intermediate mixed	<ul style="list-style-type: none"> <li>• Intermediately thick films (4–10 molecular diameters, <math>\sim R_g</math> for polymers)</li> <li>• Low loads or pressure</li> </ul>	Modified fluid properties include: <ul style="list-style-type: none"> <li>• Modified positional and orientational order<sup>a</sup></li> <li>• Medium- to long-range molecular correlations</li> <li>• Highly entangled states</li> </ul>	Modified rheological properties include: <ul style="list-style-type: none"> <li>• Non-Newtonian flow</li> <li>• Glassy states</li> <li>• Long relaxation times</li> <li>• Mixed lubrication</li> </ul>
Boundary	<ul style="list-style-type: none"> <li>• Molecularly thin films (<math>&lt; 4</math> molecular diameters)</li> <li>• High loads or pressure</li> <li>• Low shear rates</li> <li>• Smooth surfaces or asperities</li> </ul>	Onset of nonfluidlike properties: <ul style="list-style-type: none"> <li>• Liquidlike to solidlike phase transitions</li> <li>• Appearance of new liquid-crystalline states</li> <li>• Epitaxially induced long-range ordering</li> </ul>	Onset of tribological properties: <ul style="list-style-type: none"> <li>• No flow until yield point or critical shear stress reached</li> <li>• Solidlike film behavior characterized by defect diffusion, dislocation motion, shear melting</li> <li>• Boundary lubrication</li> </ul>

<sup>a</sup>Confinement can lead to an increased or decreased order in a film, depending both on the surface lattice structure and the geometry of the confining cavity

<sup>b</sup>In each regime both the static and dynamic properties change. The static properties include the film density, the density distribution function, the potential of mean force, and various positional and orientational order parameters

<sup>c</sup>Dynamic properties include viscosity, viscoelastic constants, and tribological yieldpoints such as the friction coefficient and critical shear stress

For even thinner films, the changes in behavior are more dramatic, resulting in a qualitative change in properties. Thus first-order phase transitions can now occur to solid or liquid-crystalline phases [47, 255, 263, 277, 278–281], whose properties can no longer be characterized even qualitatively in terms of bulk or continuum liquid properties such as viscosity. These films now exhibit yield points (characteristic of fracture in solids) and their molecular diffusion and relaxation times can be ten orders of magnitude longer than in the bulk liquid or even in films that are just slightly thicker. The three friction regimes are summarized in Table 13.4.

### 13.7 Relationship Between Adhesion and Friction Between Dry (Unlubricated and Solid Boundary Lubricated) Surfaces

#### 13.7.1 *Amontons' Law and Deviations from It Due to Adhesion: The Cobblestone Model*

Early theories and mechanisms for the dependence of friction on the applied normal force or load  $L$  were developed by da Vinci et al. [282]. For the macroscopic objects investigated, the friction was found to be directly proportional to the load, with no dependence on the contact area. This is described by the so-called Amontons' law

$$F = \mu L, \quad (13.26)$$

where  $F$  is the shear or friction force and  $\mu$  is a constant defined as the coefficient of friction. This friction law has a broad range of applicability and is still the principal means of quantitatively describing the friction between surfaces. However, particularly in the case of adhering surfaces, Amontons' law does not adequately describe the friction behavior with load, because of the finite friction force measured at zero and even negative applied loads.

When a lateral force, or shear stress, is applied to two surfaces in adhesive contact, the surfaces initially remain “pinned” to each other until some critical shear force is reached. At this point, the surfaces begin to slide past each other either smoothly or in jerks. The frictional force needed to initiate sliding from rest is known as the *static* friction force, denoted by  $F_s$ , while the force needed to maintain smooth sliding is referred to as the *kinetic* or *dynamic* friction force, denoted by  $F_k$ . In general,  $F_s > F_k$ . Two sliding surfaces may also move in regular jerks, known as stick–slip sliding, which is discussed in more detail in Sect. 13.8.3. Such friction forces cannot be described by models used for thick films that are viscous (Sect. 13.8.1) and, therefore, shear as soon as the smallest shear force is applied.

In Sects. 13.7 and 13.8 we will be concerned mainly with single-asperity contacts. Experimentally, it has been found that during both smooth and stick–slip sliding at small film thicknesses the local geometry of the contact zone remains largely unchanged from the static geometry [46]. In an adhesive contact, the contact area as a function of load is thus generally well described by the JKR equation, (13.22). The friction force between two molecularly smooth surfaces sliding in *adhesive* contact is not simply proportional to the applied load  $L$  as might be expected from Amontons' law. There is an additional adhesion contribution that is proportional to the area of contact,  $A$ . Thus, in general, the interfacial friction force of dry, unlubricated surfaces sliding smoothly past each other in adhesive contact is given by

$$F = F_k = S_c A + \mu L, \quad (13.27)$$



where  $S_c$  is the “critical shear stress” (assumed to be constant),  $A = \pi r^2$  is the contact area of radius  $r$  given by (13.22), and  $\mu$  is the coefficient of friction. For low loads we have

$$\begin{aligned} F &= S_c A = S_c \pi r^2 \\ &= S_c \pi \left[ \frac{R}{K} \left( L + 6\pi R\gamma + \sqrt{12\pi R\gamma L + (6\pi R\gamma)^2} \right) \right]^{2/3} \end{aligned} \quad (13.28)$$

whereas for high loads (or high  $\mu$ ), or when  $\gamma$  is very low [283–287], (13.27) reduces to Amontons’ law:  $F = \mu L$ . Depending on whether the friction force in (13.27) is dominated by the first or second term, one may refer to the friction as *adhesion-controlled* or *load-controlled*, respectively.

The following friction model, first proposed by Tabor [288] and developed further by Sutcliffe et al. [289], McClelland [290], and Homola et al. [46], has been quite successful at explaining the interfacial and boundary friction of two solid crystalline surfaces sliding past each other in the absence of wear. The surfaces may be unlubricated, or they may be separated by a monolayer or more of some boundary lubricant or liquid molecules. In this model, the values of the critical shear stress  $S_c$ , and the coefficient of friction  $\mu$ , in (13.27) are calculated in terms of the energy needed to overcome the attractive intermolecular forces and compressive externally applied load as one surface is raised and then slid across the molecular-sized asperities of the other.

This model (variously referred to as the *interlocking asperity model*, *Coulomb friction*, or the *cobblestone model*) is similar to pushing a cart over a road of cobblestones where the cartwheels (which represent the molecules of the upper surface or film) must be made to roll over the cobblestones (representing the molecules of the lower surface) before the cart can move. In the case of the cart, the downward force of gravity replaces the attractive intermolecular forces between two material surfaces. When at rest, the cartwheels find grooves between the cobblestones where they sit in potential-energy minima, and so the cart is at some stable mechanical equilibrium. A certain lateral force (the “push”) is required to raise the cartwheels against the force of gravity in order to initiate motion. Motion will continue as long as the cart is pushed, and rapidly stops once it is no longer pushed. Energy is dissipated by the liberation of heat (phonons, acoustic waves, etc.) every time a wheel hits the next cobblestone. The cobblestone model is not unlike the *Coulomb* and *interlocking asperity* models of friction [282] except that it is being applied at the molecular level and for a situation where the external load is augmented by attractive intermolecular forces.

There are thus two contributions to the force pulling two surfaces together: the externally applied load or pressure, and the (internal) attractive intermolecular forces that determine the adhesion between the two surfaces. Each of these contributions affects the friction force in a different way, which we will discuss in more detail below.

### 13.7.2 Adhesion Force and Load Contribution to Interfacial Friction

#### Adhesion Force Contribution

Consider the case of two surfaces sliding past each other, as shown in Fig. 13.14a. When the two surfaces are initially in adhesive contact, the surface molecules will adjust themselves to fit snugly together [292], in an analogous manner to the self-positioning of the cartwheels on the cobblestone road. A small tangential force applied to one surface will therefore not result in the sliding of that surface relative to the other. The attractive van der Waals forces between the surfaces must first be overcome by having the surfaces separate by a small amount. To initiate motion, let the separation between the two surfaces increase by a small amount  $\Delta D$ , while the lateral distance moved is  $\Delta\sigma$ . These two values will be related via the geometry of the two surface lattices. The energy put into the system by the force  $F$  acting over a lateral distance  $\Delta\sigma$  is

$$\text{Input energy: } F \times \Delta\sigma. \quad (13.29)$$

This energy may be equated with the change in interfacial or surface energy associated with separating the surfaces by  $\Delta D$ , i.e., from the equilibrium separation  $D = D_0$  to  $D = (D_0 + \Delta D)$ . Since  $\gamma \propto D^{-2}$  for two flat surfaces (Sect. 13.3.1, Table 13.2), the energy cost may be approximated by

$$\text{Surface energy change} \times \text{area} : 2\gamma A \left[ 1 - \frac{D_0^2}{(D_0 + \Delta D)^2} \right] \approx 4\gamma A \left( \frac{\Delta D}{D_0} \right), \quad (13.30)$$

where  $\gamma$  is the surface energy,  $A$  the contact area, and  $D_0$  the surface separation at equilibrium. During steady-state sliding (kinetic friction), not all of this energy will be “lost” or absorbed by the lattice every time the surface molecules move by one lattice spacing: some fraction will be reflected during each impact of the “cart-wheel” molecules [290]. Assuming that a fraction  $\varepsilon$  of the above surface energy is “lost” every time the surfaces move across the characteristic length  $\Delta\sigma$  (Fig. 13.14a), we obtain after equating (13.29) and (13.30)

$$S_c = \frac{F}{A} = \frac{4\gamma\varepsilon\Delta D}{D_0\Delta\sigma}. \quad (13.31)$$

For a typical hydrocarbon or a van der Waals surface,  $\gamma \approx 25 \text{ mJ m}^{-2}$ . Other typical values would be:  $\Delta D \approx 0.05 \text{ nm}$ ,  $D_0 \approx 0.2 \text{ nm}$ ,  $\Delta\sigma \approx 0.1 \text{ nm}$ , and  $\varepsilon \approx 0.1 - 0.5$ . Using the above parameters, (13.31) predicts  $S_c \approx (2.5 - 12.5) \times 10^7 \text{ N m}^{-2}$  for

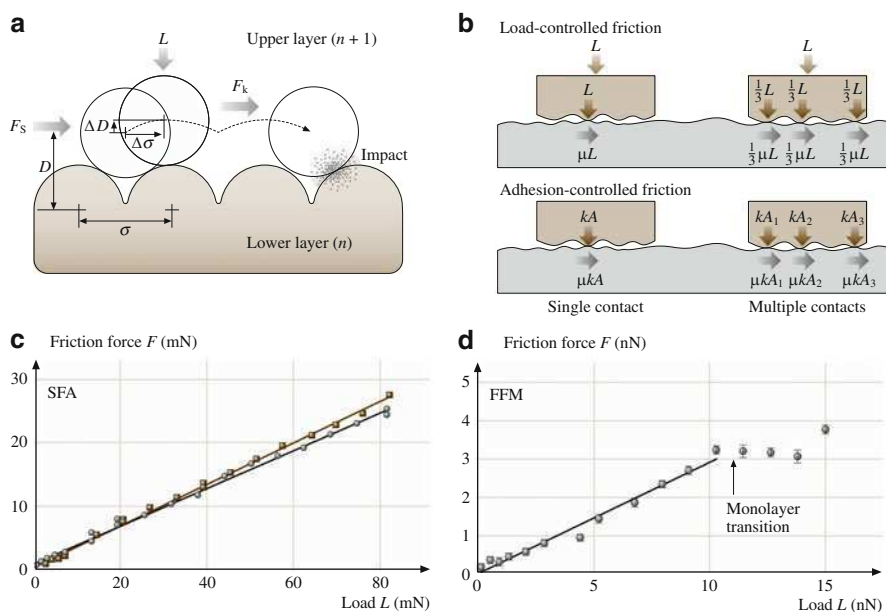


**Fig. 13.14** (a) Schematic illustration of how one molecularly smooth surface moves over another when a lateral force  $F$  is applied (the “cobblestone model”). As the upper surface moves laterally by some fraction of the lattice dimension  $\Delta\sigma$ , it must also move up by some fraction of an atomic or molecular dimension  $\Delta D$  before it can slide across the lower surface. On impact, some fraction  $\varepsilon$  of the kinetic energy is “transmitted” to the lower surface, the rest being “reflected” back to the colliding molecule (upper surface) (after [291], with permission). (b) Difference in the local distribution of the total applied external load or normal adhesive force between load-controlled nonadhering surfaces and adhesion-controlled surfaces. In the former case, the total friction force  $F$  is given either by  $F = \mu L$  for one contact point (left side) or by  $F = \frac{1}{3}\mu L + \frac{1}{3}\mu L + \frac{1}{3}\mu L = \mu L$  for three contact points (right side). Thus the load-controlled friction is always proportional to the applied load, independently of the number of contacts and of their geometry. In the case of adhering surfaces, the effective “internal” load is given by  $kA$ , where  $A$  is the real local contact area, which is proportional to the number of intermolecular bonds being made and broken across each single contact point. The total friction force is now given by  $F = \mu kA$  for one contact point (left side), and  $F = \mu(kA_1 + kA_2 + kA_3) = \mu kA_{\text{tot}}$  for three contact points (right side). Thus, for adhesion-controlled friction, the friction is proportional to the real contact area, at least when no additional external load is applied to the system (after [287], with permission, © 2004 American Chemical Society). (c,d) Friction force between benzyltrichlorosilane monolayers chemically bound to glass or Si, measured in ethanol ( $\gamma < 1 \text{ mJ/m}^2$ ). (c) SFA measurements where both glass surfaces were covered with a monolayer. Circles and squares show two different experiments: one with  $R = 2.6 \text{ cm}$ ,  $v = 0.15 \text{ }\mu\text{m/s}$ , giving  $\mu = 0.33 \pm 0.01$ ; the other with  $R = 1.6 \text{ cm}$ ,  $v = 0.5 \text{ }\mu\text{m/s}$ , giving  $\mu = 0.30 \pm 0.01$ . (d) Friction force microscopy (FFM) measurements of a monolayer-functionalized Si tip ( $R = 11 \text{ nm}$ ) sliding on a monolayer-covered glass surface at  $v = 0.15 \text{ }\mu\text{m/s}$ , giving  $\mu = 0.30 \pm 0.01$ . Note the different scales in (c) and (d) (after [286], with permission, © 2003 American Chemical Society)

van der Waals surfaces. This range of values compares very well with typical experimental values of  $2 \times 10^7 \text{ N m}^{-2}$  for hydrocarbon or mica surfaces sliding in air (Fig. 13.16) or separated by one molecular layer of cyclohexane [46].

The above model suggests that all interfaces, whether dry or lubricated, dilate just before they shear or slip. This is a small but important effect: the dilation provides the crucial extra space needed for the molecules to slide across each other or flow. This dilation is known to occur in macroscopic systems [293, 294] and for nanoscopic systems it has been computed by Thompson and Robbins [255] and Zaloj et al. [295] and measured by Dhinojwala et al. [296].

This model may be extended, at least semiquantitatively, to lubricated sliding, where a thin liquid film is present between the surfaces. With an increase in the number of liquid layers between the surfaces,  $D_0$  increases while  $\Delta D$  decreases, hence the friction force decreases. This is precisely what is observed, but with more than one liquid layer between two surfaces the situation becomes too complex to analyze analytically (actually, even with one or no interfacial layers, the calculation of the fraction of energy dissipated per molecular collision  $\varepsilon$  is not a simple matter). Furthermore, even in systems as simple as linear alkanes, interdigitation and interdiffusion have been found to contribute strongly to the properties of the system [143, 297]. Sophisticated modeling based on computer simulations is now required, as discussed in the following section.

### Relation Between Boundary Friction and Adhesion Energy Hysteresis

While the above equations suggest that there is a direct correlation between friction and adhesion, this is not the case. The correlation is really between friction and adhesion hysteresis, described in Sect. 13.5.4. In the case of friction, this subtle point is hidden in the factor  $\varepsilon$ , which is a measure of the amount of energy absorbed (dissipated, transferred, or “lost”) by the lower surface when it is impacted by a molecule from the upper surface. If  $\varepsilon = 0$ , all the energy is reflected, and there will be no kinetic friction force or any adhesion hysteresis, but the absolute magnitude of the adhesion force or energy will remain finite and unchanged. This is illustrated in Figs. 13.17 and 13.19.

The following simple model shows how adhesion hysteresis and friction may be quantitatively related. Let  $\Delta\gamma = \gamma_R - \gamma_A$  be the adhesion energy hysteresis per unit area, as measured during a typical loading–unloading cycle (Figs. 13.17a and 13.19c, d). Now consider the same two surfaces sliding past each other and assume that frictional energy dissipation occurs through the same mechanism as adhesion energy dissipation, and that both occur over the same characteristic molecular length scale  $\sigma$ . Thus, when the two surfaces (of contact area  $A = \pi r^2$ ) move a distance  $\sigma$ , equating the frictional energy ( $F \times \sigma$ ) to the dissipated adhesion energy ( $A \times \Delta\gamma$ ), we obtain

$$\text{Friction force: } = \frac{A \times \Delta\gamma}{\sigma} = \frac{\pi r^2}{\sigma} (\gamma_R - \gamma_A), \quad (13.32)$$

or

$$\text{Critical shear stress: } S_c = F/A = \Delta\gamma/\sigma, \quad (13.33)$$

which is the desired expression and has been found to give order-of-magnitude agreement between measured friction forces and adhesion energy hysteresis [261]. If we equate (13.33) with (13.31), since  $4\Delta D/(D_0\Delta\sigma) \approx 1/\sigma$ , we obtain the intuitive relation

$$\varepsilon = \frac{\Delta\gamma}{\gamma}. \quad (13.34)$$

### External Load Contribution to Interfacial Friction

When there is no interfacial adhesion,  $S_c$  is zero. Thus, in the absence of any adhesive forces between two surfaces, the only “attractive” force that needs to be overcome for sliding to occur is the externally applied load or pressure, as shown in Fig. 13.14b.

For a preliminary discussion of this question, it is instructive to compare the magnitudes of the *externally* applied pressure to the *internal* van der Waals pressure between two smooth surfaces. The internal van der Waals pressure between two flat surfaces is given (Table 13.2) by  $P = A_H/6\pi D_0^3 \approx 1 \text{ GPa}$  ( $10^4 \text{ atm}$ ), using a typical Hamaker constant of  $A_H = 10^{-19} \text{ J}$ , and assuming  $D_0 \approx 2 \text{ nm}$  for the equilibrium interatomic spacing. This implies that we should not expect the externally applied load to affect the interfacial friction force  $F$ , as defined by (13.27), until the externally applied pressure  $L/A$  begins to exceed  $\sim 100 \text{ MPa}$  ( $10^3 \text{ atm}$ ). This is in agreement with experimental data [298] where the effect of load became dominant at pressures in excess of  $10^3 \text{ atm}$ .

For a more general semiquantitative analysis, again consider the cobblestone model used to derive (13.31), but now include an additional contribution to the surface-energy change of (13.30) due to the work done against the external load or pressure,  $L\Delta D = P_{\text{ext}}\Delta D$  (this is equivalent to the work done against gravity in the case of a cart being pushed over cobblestones). Thus

$$S_c = \frac{F}{A} = \frac{4\gamma\varepsilon\Delta D}{D_0\Delta\sigma} + \frac{P_{\text{ext}}\varepsilon\Delta D}{\Delta\sigma}, \quad (13.35)$$

which gives the more general relation

$$S_c = F/A = C_1 + C_2 P_{\text{ext}}, \quad (13.36)$$

where  $P_{\text{ext}} = L/A$  and  $C_1$  and  $C_2$  are characteristic of the surfaces and sliding conditions. The constant  $C_1 = 4\gamma\varepsilon\Delta D/(D_0\Delta\sigma)$  depends on the mutual adhesion of the two surfaces, while both  $C_1$  and  $C_2 = \varepsilon\Delta D/\Delta\sigma$  depend on the topography or atomic bumpiness of the surface groups (Fig. 13.14a). The smoother the surface groups the smaller the ratio  $\Delta D/\Delta\sigma$  and hence the lower the value of  $C_2$ . In addition, both  $C_1$  and  $C_2$  depend on  $\varepsilon$  (the fraction of energy dissipated per collision), which

depends on the relative masses of the shearing molecules, the sliding velocity, the temperature, and the characteristic molecular relaxation processes of the surfaces. This is by far the most difficult parameter to compute, and yet it is the most important since it represents the energy-transfer mechanism in any friction process, and since  $\varepsilon$  can vary between 1 and 0, it determines whether a particular friction force will be large or close to zero. Molecular simulations offer the best way to understand and predict the magnitude of  $\varepsilon$ , but the complex multibody nature of the problem makes simple conclusions difficult to draw [299–302]. Some of the basic physics of the energy transfer and dissipation of the molecular collisions can be drawn from simplified models such as a 1-D three-body system [268].

Finally, the above equation may also be expressed in terms of the friction force  $F$

$$F = S_c A = C_1 A + C_2 L. \quad (13.37)$$

Equations similar to (13.36) and (13.37) were previously derived by Derjaguin [303, 304] and by Briscoe and Evans [305], where the constants  $C_1$  and  $C_2$  were interpreted somewhat differently than in this model.

In the absence of any attractive interfacial force, we have  $C_1 \approx 0$ , and the second term in (13.36) and (13.37) should dominate (Fig. 13.15). Such situations typically arise when surfaces repel each other across the lubricating liquid film. In such cases, the total frictional force should be low and should increase *linearly* with the external load according to

$$F = C_2 L. \quad (13.38)$$

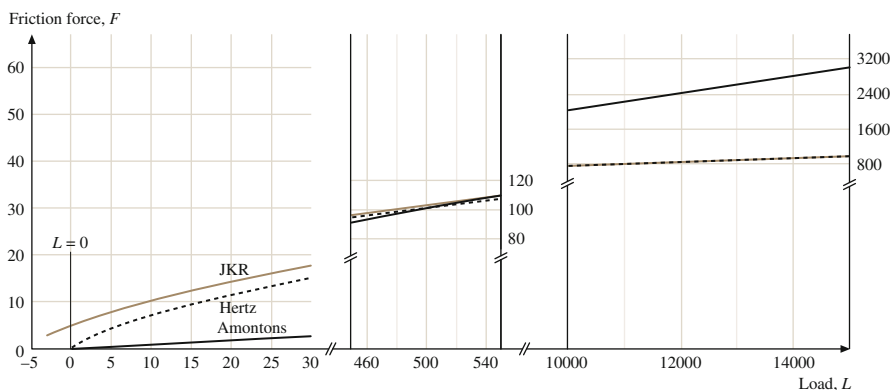


**Fig. 13.15** Friction as a function of load for smooth surfaces. At low loads, the friction is dominated by the  $C_1 A$  term of (13.38). The adhesion contribution (JKR curve) is most prominent near zero load where the Hertzian and Amontons' contributions to the friction are minimal. As the load increases, the adhesion contribution becomes smaller as the JKR and Hertz curves converge. In this range of loads, the linear  $C_2 L$  contribution surpasses the area contribution to the friction. At much higher loads the explicit load dependence of the friction dominates the interactions, and the observed behavior approaches Amontons' law. It is interesting to note that for smooth surfaces the pressure over the contact area does not increase as rapidly as the load. This is because as the load is increased, the surfaces deform to increase the surface area and thus moderate the contact pressure (after [306], with permission of Kluwer Academic Publishers)

An example of such lubricated sliding occurs when two mica surfaces slide in water or in salt solution (Fig. 13.20a), where the short-range “hydration” forces between the surfaces are repulsive. Thus, for sliding in 0.5 M KCl it was found that  $C_2 = 0.015$  [283]. Another case where repulsive surfaces eliminate the adhesive contribution to friction is for polymer chains attached to surfaces at one end and swollen by a good solvent [219]. For this class of systems,  $C_2 < 0.001$  for a finite range of polymer layer compressions (normal loads  $L$ ). The low friction between the surfaces in this regime is attributed to the entropic repulsion between the opposing brush layers with a minimum of entanglement between the two layers. However, with higher normal loads, the brush layers become compressed and begin to entangle, which results in higher friction [307].

It is important to note that (13.38) has exactly the same form as Amontons’ Law

$$F = \mu L, \quad (13.39)$$

where  $\mu$  is the coefficient of friction.

Figure 13.14c shows the kinetic friction force measured with both SFA and FFM (friction force microscopy, using AFM) on a system where both surfaces were covered with a chemically bound benzyltrichlorosilane monolayer [286]. When immersed in ethanol, the adhesion in this system is low, and very different contact areas and loads give a linear dependence of  $F$  on  $L$  with the same friction coefficients, and  $F \rightarrow 0$  as  $L \rightarrow 0$ . In the FFM measurements (Fig. 13.14d), the plateau in the data at higher loads suggest a transition in the monolayers, similar to previous observations on other monolayer systems. The pressure in the contact region in the SFA is much lower than in the FFM, and no transitions in the friction forces or in the thickness of the confined monolayers were observed in the SFA experiments (and no damage to the monolayers or the underlying substrates was observed during the experiments, indicating that the friction was “wearless”). Despite the difference of more than six orders of magnitude in the contact radii, pressure, loads, and friction forces, the measured friction coefficients are practically the same.

At the molecular level a thermodynamic analog of the Coulomb or cobblestone models (Sect. 13.7.1) based on the “contact value theorem” [3, 283, 306] can explain why  $F \propto L$  also holds at the microscopic or molecular level. In this analysis we consider the surface molecular groups as being momentarily compressed and decompressed as the surfaces move along. Under irreversible conditions, which always occur when a cycle is completed in a finite amount of time, the energy “lost” in the compression–decompression cycle is dissipated as heat. For two nonadhering surfaces, the stabilizing pressure  $P_i$  acting locally between any two elemental contact points  $i$  of the surfaces may be expressed by the contact value theorem [2]

$$P_i = \rho_i k_B T = k_B T / V_i, \quad (13.40)$$

where  $\rho_i = V_i^{-1}$  is the local number density (per unit volume) or activity of the interacting entities, be they molecules, atoms, ions or the electron clouds of atoms. This equation is essentially the osmotic or entropic pressure of a gas of

confined molecules. As one surface moves across the other, local regions become compressed and decompressed by a volume  $\Delta V_i$ . The work done per cycle can be written as  $\varepsilon P_i \Delta V_i$ , where  $\varepsilon$  ( $\varepsilon \leq 1$ ) is the fraction of energy per cycle “lost” as heat, as defined earlier. The energy balance shows that, for each compression–decompression cycle, the dissipated energy is related to the friction force by

$$F_i x_i = \varepsilon P_i \Delta V_i, \quad (13.41)$$

where  $x_i$  is the lateral distance moved per cycle, which can be the distance between asperities or the distance between surface lattice sites. The pressure at each contact junction can be expressed in terms of the local normal load  $L_i$  and local area of contact  $A_i$  as  $P_i = L_i/A_i$ . The volume change over a cycle can thus be expressed as  $\Delta V_i = A_i z_i$ , where  $z_i$  is the vertical distance of confinement. Inserting these into (13.41), we get

$$F_i = \varepsilon L_i (z_i/x_i), \quad (13.42)$$

which is independent of the local contact area  $A_i$ . The total friction force is thus

$$\begin{aligned} F &= \sum F_i = \sum \varepsilon L_i (z_i/x_i) \\ &= \varepsilon \langle z_i/x_i \rangle \sum L_i = \mu L, \end{aligned} \quad (13.43)$$

where it is assumed that on average the local values of  $L_i$  and  $P_i$  are independent of the local *slope*  $z_i/x_i$ . Therefore, the friction coefficient  $\mu$  is a function only of the average surface topography and the sliding velocity, but is independent of the local (real) or macroscopic (apparent) contact areas.

While this analysis explains nonadhering surfaces, there is still an additional explicit contact area contribution for the case of adhering surfaces, as in (13.37). The distinction between the two cases arises because the initial assumption of the contact value theorem (13.40) is incomplete for adhering systems. A more appropriate starting equation would reflect the full intermolecular interaction potential, including the attractive interactions, in addition to the purely repulsive contributions of (13.40), much as the van der Waals equation of state modifies the ideal gas law.

### 13.7.3 Examples of Experimentally Observed Friction of Dry Surfaces

Numerous model systems have been studied with a surface forces apparatus (SFA) modified for friction experiments (Sect. 13.2.3). The apparatus allows for control of load (normal force) and sliding speed, and simultaneous measurement of surface separation, surface shape, true (molecular) area of contact between



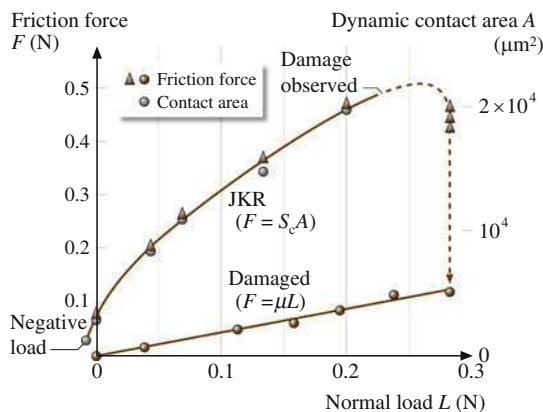


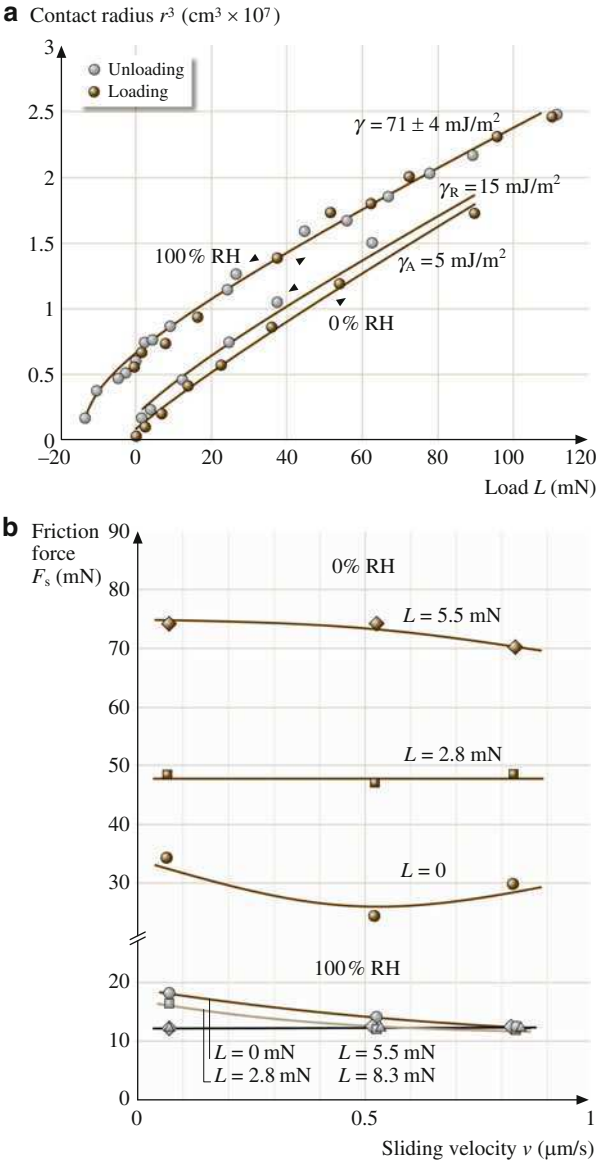
**Fig. 13.16** Friction force  $F$  and contact area  $A$  versus load  $L$  for two mica surfaces sliding in adhesive contact in dry air. The contact area is well described by the JKR theory, (13.22), even during sliding, and the friction force is found to be directly proportional to this area, (13.28). The vertical dashed line and arrow show the transition from interfacial to normal friction with the onset of wear (lower curve). The sliding velocity is  $0.2 \mu\text{m s}^{-1}$  (after [46], with permission, © 1989 American Society of Mechanical Engineers)

smooth surfaces, and friction forces. A variety of both unlubricated and solid- and liquid-lubricated surfaces have been studied both as smooth single-asperity contacts and after they have been roughened by shear-induced damage.

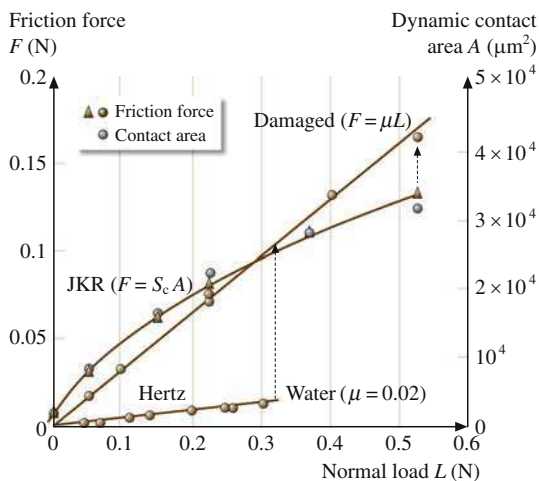
Figure 13.16 shows the contact area  $A$  and friction force  $F$ , both plotted against the applied load  $L$  in an experiment in which two molecularly smooth surfaces of mica in adhesive contact were slid past each other in an atmosphere of dry nitrogen gas. This is an example of the low-load adhesion-controlled limit, which is excellently described by (13.28). In a number of different experiments,  $S_c$  was measured to be  $2.5 \times 10^7 \text{ N m}^{-2}$  and to be independent of the sliding velocity [46, 308]. Note that there is a friction force even at negative loads, where the surfaces are still sliding in adhesive contact.

Figure 13.17 shows the correlation between adhesion hysteresis and friction for two surfaces consisting of silica films deposited on mica substrates [42]. The friction between undamaged hydrophobic silica surfaces showed stick-slip both at dry conditions and at 100% relative humidity. Similar to the mica surfaces in Figs. 13.16, 13.18, and 13.20a, the friction of damaged silica surfaces obeyed Amontons' law with a friction coefficient of 0.25–0.3 both at dry conditions and at 55% relative humidity.

The high friction force of unlubricated sliding can often be reduced by treating the solid surface with a boundary layer of some other solid material that exhibits lower friction, such as a surfactant monolayer, or by ensuring that during sliding a thin liquid film remains between the surfaces (as will be discussed in Sect. 13.8). The effectiveness of a solid boundary lubricant layer on reducing the forces of friction is illustrated in Fig. 13.18. Comparing this with the friction of the unlubricated/untreated surfaces (Fig. 13.16) shows that the critical shear stress has been reduced by a factor of about ten: from  $2.5 \times 10^7$  to  $3.5 \times 10^6 \text{ N m}^{-2}$ . At much



**Fig. 13.17** (a) Contact radius  $r$  versus externally applied load  $L$  for loading and unloading of two hydrophilic silica surfaces exposed to dry and humid atmospheres. Note that, while the adhesion is higher in humid air, the *hysteresis* in the adhesion is higher in dry air. (b) Effect of velocity on the static friction force  $F_s$  for hydrophobic (heat-treated electron-beam-evaporated) silica in dry and humid air. The effects of humidity, load, and sliding velocity on the friction forces, as well as the stick–slip friction of the hydrophobic surfaces, are qualitatively consistent with a “friction” phase diagram representation as in Fig. 13.28 (after [42], © 1994, with permission from Elsevier Science)



**Fig. 13.18** Sliding of mica surfaces, each coated with a 2.5 nm thick monolayer of calcium stearate surfactant, in the absence of damage (obeying JKR-type boundary friction) and in the presence of damage (obeying Amontons-type normal friction). Note that both for this system and for the bare mica in Figs. 13.16 and 13.20a, the friction force obeys Amontons' law with a friction coefficient of  $\mu \approx 0.3$  after damage occurs. At much higher applied loads, the undamaged surfaces also follow Amontons-type sliding, but for a different reason: the dependence on adhesion becomes smaller. *Lower line:* interfacial sliding with a monolayer of water between the mica surfaces (load-controlled friction, Fig. 13.20a), shown for comparison (after [308], © 1990, with permission from Elsevier Science)

higher applied loads or pressures, the friction force is proportional to the load, rather than the area of contact [298], as expected from (13.27).

*Yamada and Israelachvili* [309] studied the adhesion and friction of fluorocarbon surfaces (surfactant-coated boundary lubricant layers), which were compared to those of hydrocarbon surfaces. They concluded that well-ordered fluorocarbon surfaces have high friction, in spite of their lower adhesion energy (in agreement with previous findings). The low friction coefficient of Teflon (polytetrafluoroethylene, PTFE) must, therefore, be due to some effect other than low adhesion. For example, the softness of PTFE, which allows material to flow at the interface, which thus behaves like a fluid lubricant. On a related issue, *Luengo et al.* [310] found that  $C_{60}$  surfaces also exhibited low adhesion but high friction. In both cases the high friction appears to arise from the bulky surface groups – fluorocarbon compared to hydrocarbon groups in the former, large fullerene spheres in the latter. Apparently, the fact that  $C_{60}$  molecules rotate *in their lattice* does not make them a good lubricant: the molecules of the opposing surface must still climb over them in order to slide, and this requires energy that is independent of whether the surface molecules are fixed or freely rotating. Larger particles such as  $\sim 25$  nm sized nanoparticles (also known as “inorganic fullerenes”) do appear to produce low friction by behaving like molecular ball bearings, but the potential of this promising new class of solid lubricant has still to be explored [311].

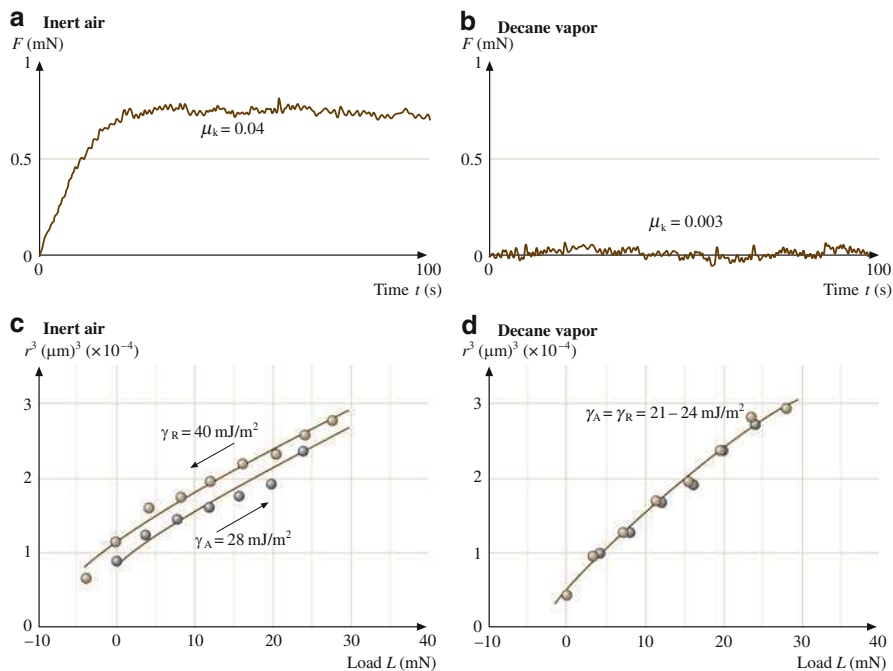


**Fig. 13.19** *Top*: friction traces for two fluidlike calcium alkylbenzene sulfonate monolayer-coated surfaces at 25 °C showing that the friction force is much higher between dry monolayers (a) than between monolayers whose fluidity has been enhanced by hydrocarbon penetration from vapor (b). *Bottom*: Contact radius versus load ( $r^3$  versus  $L$ ) data measured for the same two surfaces as above and fitted to the JKR equation (13.22), shown by the solid curves. For dry monolayers (c) the adhesion energy on unloading ( $\gamma_R = 40 \text{ mJ m}^{-2}$ ) is greater than that on loading ( $\gamma_A = 28 \text{ mJ m}^{-2}$ ), which is indicative of an adhesion energy hysteresis of  $\Delta\gamma = \gamma_R - \gamma_A = 12 \text{ mJ m}^{-2}$ . For monolayers exposed to saturated decane vapor (d) their adhesion hysteresis is zero ( $\gamma_A = \gamma_R$ ), and both the loading and unloading data are well fitted by the thermodynamic value of the surface energy of fluid hydrocarbon chains,  $\gamma = 24 \text{ mJ m}^{-2}$  (after [265], with permission, © 1993 American Chemical Society)

Figure 13.19 illustrates the relationship between adhesion hysteresis and friction for surfactant-coated surfaces under different conditions. This effect, however, is much more general and has been shown to hold for other surfaces as well [42, 266, 291, 312].

Direct comparisons between absolute adhesion energies and friction forces show little correlation. In some cases, higher adhesion energies for the same system under different conditions correspond to lower friction forces. For example, for hydrophilic silica surfaces (Fig. 13.17) it was found that with increasing relative humidity the adhesion energy *increases*, but the adhesion energy hysteresis measured in a loading–unloading cycle *decreases*, as does the friction force [42]. For hydrophobic silica surfaces under dry conditions, the friction at load  $L = 5.5 \text{ mN}$  was  $F = 75 \text{ mN}$ . For the same sample, the adhesion energy hysteresis

was  $\Delta\gamma = 10 \text{ mJ m}^{-2}$ , with a contact area of  $A \approx 10^{-8} \text{ m}^2$  at the same load. Assuming a value for the characteristic distance  $\sigma$  on the order of one lattice spacing,  $\sigma \approx 1 \text{ nm}$ , and inserting these values into (13.32), the friction force is predicted to be  $F \approx 100 \text{ mN}$  for the kinetic friction force, which is close to the measured value of  $75 \text{ mN}$ . Alternatively, we may conclude that the dissipation factor is  $\varepsilon = 0.75$ , i.e., that almost all the energy is dissipated as heat at each molecular collision.

A liquid lubricant film (Sect. 13.8.3) is usually much more effective at lowering the friction of two surfaces than a solid boundary lubricant layer. However, to use a liquid lubricant successfully, it must “wet” the surfaces, that is, it should have a high affinity for the surfaces, so that not all the liquid molecules become squeezed out when the surfaces come close together, even under a large compressive load. Another important requirement is that the liquid film remains a liquid under tribological conditions, i.e., that it does not epitaxially solidify between the surfaces.

Effective lubrication usually requires that the lubricant be injected between the surfaces, but in some cases the liquid can be made to condense from the vapor. This is illustrated in Fig. 13.20a for two untreated mica surfaces sliding with a thin layer of water between them. A monomolecular film of water (of thickness  $0.25 \text{ nm}$  per surface) has reduced  $S_c$  from its value for dry surfaces (Fig. 13.16) by a factor of more than 30, which may be compared with the factor of ten attained with the boundary lubricant layer (of thickness  $2.5 \text{ nm}$  per surface) in Fig. 13.18. Water appears to have unusual lubricating properties and usually gives wearless friction with no stick–slip [313].

The effectiveness of a water film only  $0.25 \text{ nm}$  thick to lower the friction force by more than an order of magnitude is attributed to the “hydrophilicity” of the mica surface (mica is “wetted” by water) and to the existence of a strongly repulsive short-range hydration force between such surfaces in aqueous solutions, which effectively removes the adhesion-controlled contribution to the friction force [283]. It is also interesting that a  $0.25 \text{ nm}$  thick water film between two mica surfaces is sufficient to bring the coefficient of friction down to  $0.01$ – $0.02$ , a value that corresponds to the unusually low friction of ice. Clearly, a single monolayer of water can be a very good lubricant – much better than most other monomolecular liquid films – for reasons that will be discussed in Sect. 13.9. A linear dependence of  $F$  on  $L$  has also been observed for mica surfaces separated by certain hydrocarbon liquids [277, 285]. Figure 13.20b shows the kinetic friction forces measured at a high velocity across thin films of squalane, a branched hydrocarbon liquid ( $\text{C}_{30}\text{H}_{62}$ ), which is a model for lubricating oils. Very low adhesive forces are measured between mica surfaces across this liquid [285] and the film thickness decreased monotonically with load. The friction force at a given load was found to be velocity-dependent, whereas the contact area was not [285].

Dry polymer layers (Fig. 13.21) typically show a high initial static friction (“stiction”) as sliding commences from rest in adhesive contact. The development of the friction force after a change in sliding direction, a gradual transition from stick–slip to smooth sliding, is shown in Fig. 13.21. A correlation between adhesion hysteresis and friction similar to that observed for silica surfaces in Fig. 13.17 can be seen for dry polymer layers below their glass-transition temperature. As shown in

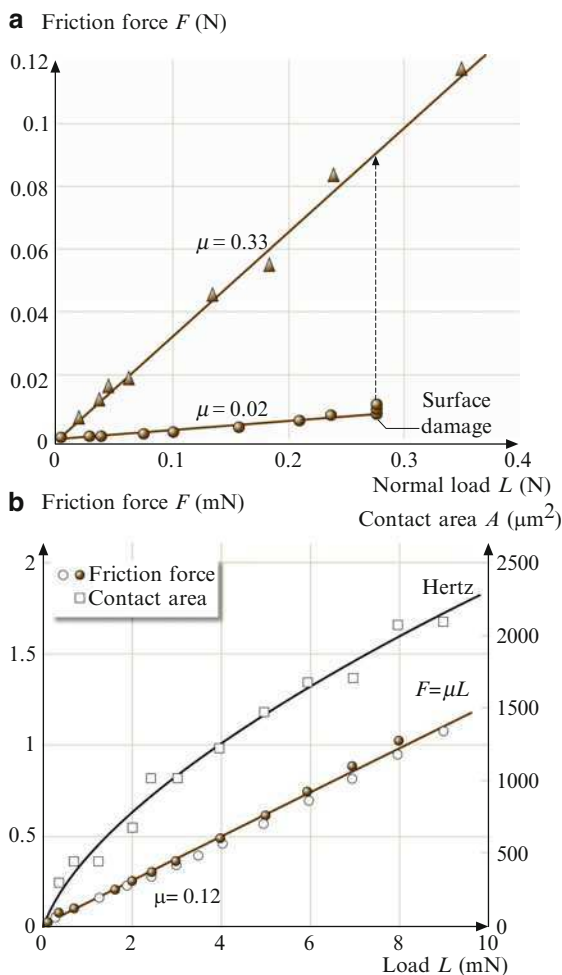


**Fig. 13.20** Load-controlled friction. **(a)** Two mica surfaces sliding past each other while immersed in a 0.01 M KCl salt solution (nonadhesive conditions). The water film is molecularly thin, 0.25 to 0.5 nm thick, and the interfacial friction force is very low:  $S_c \approx 5 \times 10^5 \text{ N m}^{-2}$ ,  $\mu \approx 0.02$  (before damage occurs). After the surfaces have become damaged, the friction coefficient is about 0.3 (after [308], © 1990, with permission from Elsevier Science). **(b)** Steady-state friction force and contact area measured on a confined squalane film between two undamaged mica surfaces at  $v = 0.6 \mu\text{m/s}$  in the smooth sliding regime (no stick-slip). Open circles show  $F$  obtained on loading (increasing  $L$ ), solid circles show unloading. Both data sets are straight lines passing through the origin, as shown by the brown line ( $\mu = 0.12$ ). The black curve is a fit of the Hertz equation (Sect. 13.5.2 and [3]) to the  $A$  versus  $L$  data (open squares) using  $K = 10^{10} \text{ N/m}^2$ ,  $R = 2 \text{ cm}$ . The thickness  $D$  varies monotonically from  $D = 2.5$  to  $1.7 \text{ nm}$  as the load increases from  $L = 0$  to  $10 \text{ mN}$  (adapted from [285], © 2003 American Physical Society)

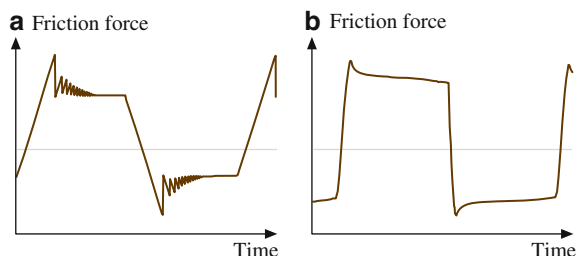


**Fig. 13.21** Typical friction traces showing how the friction force varies with the sliding time for two symmetric, glassy polymer films under dry conditions. Qualitative features that are common to both polystyrene and polyvinyl benzyl chloride: (a) Decaying stick-slip motion is observed until smooth sliding is attained if the motion continues for a sufficiently long distance. (b) Smooth sliding observed at sufficiently high speeds. Similar observations have been made by Berthoud et al. [314] in measurements on polymethyl methacrylate (after [266], with permission, © 2002 American Association for the Advancement of Science)

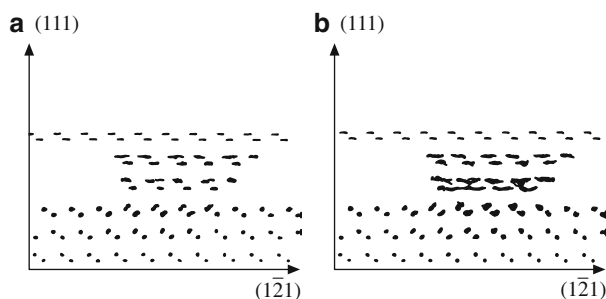


**Fig. 13.22** Computer simulation of the sliding of two contacting Si surfaces (a tip and a flat surface). Shown are particle trajectories in a constant-force simulation,  $F_{z, \text{external}} = -2.15 \times 10^{-8}$  N, viewed along the  $((10\bar{1}))$  direction just before (a) and after (b) a stick-slip event for a large, initially ordered, dynamic tip (after [112] with permission of Kluwer Academic Publishers)

Fig. 13.12b,c, the adhesion hysteresis for polystyrene surfaces can be increased by irradiation to induce scission of chains, and it has been found that the steady-state friction force (kinetic friction) shows a similar increase with irradiation time [266].

Figure 13.22 shows an example of a computer simulation of the sliding of two unlubricated silicon surfaces (modeled as a tip sliding over a planar surface) [112]. The sliding proceeds through a series of stick-slip events, and information on the friction force and the local order of the initially crystalline surfaces can be obtained. Similar studies for cold-welding systems [112] have demonstrated the occurrence of shear or friction damage within the sliding surface (tip) as the lowest layer of it adheres to the bottom surface. Recent computer simulations have addressed many of the phenomena seen experimentally, including the differences between adhesive and nonadhesive systems, the issue of the dependence of the observed friction on the real contact area (a parameter that is difficult to define or measure at the nanoscale), and the molecular origin of friction responses that follow Amontons' law [287, 302, 315–317].

### 13.7.4 *Transition from Interfacial to Normal Friction with Wear*

Frictional damage can have many causes, such as adhesive tearing at high loads or overheating at high sliding speeds. Once damage occurs, there is a transition from “interfacial” to “normal” or load-controlled friction as the surfaces become forced apart by the torn-out asperities (wear particles). For low loads, the friction changes from obeying  $F = S_c A$  to obeying Amontons’ law,  $F = \mu L$ , as shown in Figs. 13.16 and 13.18, and sliding now proceeds smoothly with the surfaces separated by a 10–100 nm forest of wear debris (in this case, mica flakes). The wear particles keep the surfaces apart over an area that is much greater than their size, so that even one submicroscopic particle or asperity can cause a significant reduction in the area of contact and, therefore, in the friction [308]. For this type of frictional sliding, one can no longer talk of the molecular contact area of the two surfaces, although the macroscopic or “apparent” area is still a useful parameter.

One remarkable feature of the transition from interfacial to normal friction of brittle surfaces is that, while the strength of interfacial friction, as reflected in the values of  $S_c$ , is very dependent on the type of surface and on the liquid film between the surfaces, this is not the case once the transition to normal friction has occurred. At the onset of damage, the material properties of the underlying substrates control the friction. In Figs. 13.16, 13.18, and 13.20a the friction for the damaged surfaces is that of any damaged mica–mica system,  $\mu \approx 0.3$ , *independent of the initial surface coatings or liquid films between the surfaces*. A similar friction coefficient was found for damaged silica surfaces [42].

In order to modify the frictional behavior of such brittle materials practically, it is important to use coatings that will both alter the interfacial tribological character and remain intact and protect the surfaces from damage during sliding. Berman et al. [318] found that the friction of a strongly bound octadecyl phosphonic acid monolayer on alumina surfaces was higher than for untreated, undamaged  $\alpha$ -alumina surfaces, but the bare surfaces easily became damaged upon sliding, resulting in an ultimately higher friction system with greater wear rates than the more robust monolayer-coated surfaces.

Clearly, the mechanism and factors that determine *normal* friction are quite different from those that govern *interfacial* friction (Sects. 13.7.1 and 13.7.2). This effect is not general and may only apply to brittle materials. For example, the friction of ductile surfaces is totally different and involves the continuous plastic deformation of contacting surface asperities during sliding, rather than the rolling of two surfaces on hard wear particles [259]. Furthermore, in the case of ductile surfaces, water and other surface-active components do have an effect on the friction coefficients under “normal” sliding conditions.



## 13.8 Liquid Lubricated Surfaces

### 13.8.1 Viscous Forces and Friction of Thick Films: Continuum Regime

Experimentally, it is usually difficult to unambiguously establish which type of sliding mode is occurring, but an empirical criterion, based on the Stribeck curve (Fig. 13.13), is often used as an indicator. This curve shows how the friction force or the coefficient of friction is expected to vary with sliding speed, depending on which type of friction regime is operating. For thick liquid lubricant films whose behavior can be described by bulk (continuum) properties, the friction forces are essentially the hydrodynamic or viscous drag forces. For example, for two plane parallel surfaces of area  $A$  separated by a distance  $D$  and moving laterally relative to each other with velocity  $v$ , if the intervening liquid is *Newtonian*, i.e., if its viscosity  $\eta$  is independent of the shear rate, the frictional force experienced by the surfaces is given by

$$F = \frac{\eta A v}{D}, \quad (13.44)$$

where the shear rate  $\dot{\gamma}$  is defined by

$$\dot{\gamma} = \frac{v}{D}. \quad (13.45)$$

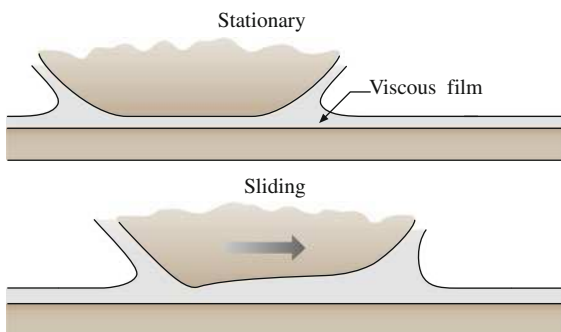
At higher shear rates, two additional effects often come into play. First, certain properties of liquids may change at high  $\dot{\gamma}$  values. In particular, the effective viscosity may become non-Newtonian, one form given by

$$\eta \propto \dot{\gamma}^n, \quad (13.46)$$

where  $n = 0$  (i.e.,  $\eta_{\text{eff}} = \text{constant}$ ) for Newtonian fluids,  $n > 0$  for shear-thickening (dilatant) fluids, and  $n < 0$  for shear-thinning (pseudoplastic) fluids (the latter become less viscous, i.e., flow more easily, with increasing shear rate). An additional effect on  $\eta$  can arise from the higher local stresses (pressures) experienced by the liquid film as  $\dot{\gamma}$  increases. Since the viscosity is generally also sensitive to the pressure (usually increasing with  $P$ ), this effect also acts to increase  $\eta_{\text{eff}}$  and thus the friction force.

A second effect that occurs at high shear rates is surface deformation, arising from the large hydrodynamic forces acting on the sliding surfaces. For example, Fig. 13.23 shows how two surfaces deform elastically when the sliding speed increases to a high value. These deformations alter the hydrodynamic friction forces, and this type of friction is often referred to as *elastohydrodynamic lubrication* (EHD or EHL), as mentioned in Table 13.4.

**Fig. 13.23** *Top:* Stationary surfaces (one more deformable and one rigid) separated by a thick liquid film. *Bottom:* Elastohydrodynamic deformation of the upper surface during sliding (after [6], with permission)



How thin can a liquid film be before its dynamic, e.g., viscous flow, behavior ceases to be described by bulk properties and continuum models? Concerning the static properties, we have already seen in Sect. 13.4.3 that films composed of simple liquids display continuum behavior down to thicknesses of 4–10 molecular diameters. Similar effects have been found to apply to the dynamic properties, such as the viscosity, of simple liquids in thin films. Concerning viscosity measurements, a number of dynamic techniques were recently developed [11–13, 44, 52, 319, 320] for directly measuring the viscosity as a function of film thickness and shear rate across very thin liquid films between two surfaces. By comparing the results with theoretical predictions of fluid flow in thin films, one can determine the effective positions of the shear planes and the onset of non-Newtonian behavior in very thin films.

The results show that, for simple liquids including linear chain molecules such as alkanes, the viscosity in thin films is the same, within 10%, as the bulk even for films as thin as 10 molecular diameters (or segment widths) [11–13, 319, 320]. This implies that the shear plane is effectively located within one molecular diameter of the solid–liquid interface, and these conclusions were found to remain valid even at the highest shear rates studied (of  $\sim 2 \times 10^5 \text{ s}^{-1}$ ). With water between two mica or silica surfaces [23, 313, 319–321] this has been found to be the case (to within  $\pm 10\%$ ) down to surface separations as small as 2 nm, implying that the shear planes must also be within a few tenths of a nanometer of the solid–liquid interfaces. These results appear to be independent of the existence of electrostatic “double-layer” or “hydration” forces. For the case of the simple liquid toluene confined between surfaces with adsorbed layers of  $\text{C}_{60}$  molecules, this type of viscosity measurement has shown that the traditional no-slip assumption for flow at a solid interface does not always hold [322]. The  $\text{C}_{60}$  layer at the mica–toluene interface results in a “full-slip” boundary, which dramatically lowers the viscous drag or effective viscosity for regular Couette or Poiseuille flow.

With polymeric liquids (polymer melts) such as polydimethylsiloxanes (PDMS) and polybutadienes (PBD), or with polystyrene (PS) adsorbed onto surfaces from solution, the far-field viscosity is again equal to the bulk value, but with the nonslip plane (hydrodynamic layer thickness) being located at  $D = 1\text{--}2 R_g$  away from each surface [11, 48], or at  $D = L$  or less for polymer brush layers of thickness  $L$  per

surface [13, 323]. In contrast, the same technique was used to show that, for nonadsorbing polymers in solution, there is actually a depletion layer of nearly pure solvent that exists at the surfaces that affects the confined solution flow properties [321]. These effects are observed from near contact to surface separations in excess of 200 nm.

Further experiments with surfaces closer than a few molecular diameters ( $D < 2\text{--}4$  nm for simple liquids, or  $D < 2\text{--}4 R_g$  for polymer fluids) indicate that large deviations occur for thinner films, described below. One important conclusion from these studies is, therefore, that the dynamic properties of simple liquids, including water, near an *isolated* surface are similar to those of the bulk liquid *already within the first layer of molecules adjacent to the surface*, only changing when another surface approaches the first. In other words, the viscosity and position of the shear plane near a surface are not simply a property of that surface, but of how far that surface is from another surface. The reason for this is that, when two surfaces are close together, the constraining effects on the liquid molecules between them are much more severe than when there is only one surface. Another obvious consequence of the above is that one should not make measurements on a single, isolated solid–liquid interface and then draw conclusions about the state of the liquid or its interactions in a thin film *between* two surfaces.

### 13.8.2 Friction of Intermediate Thickness Films

For liquid films in the thickness range between 4 and 10 molecular diameters, the properties can be significantly different from those of bulk films. Still, the fluids remain recognizable as fluids; in other words, they do not undergo a phase transition into a solid or liquid-crystalline phase. This regime has recently been studied by Granick et al. [45, 273–276], who used a friction attachment [44, 45] to the SFA where a sinusoidal input signal to a piezoelectric device makes the two surfaces slide back and forth laterally past each other at small amplitudes. This method provides information on the real and imaginary parts (elastic and dissipative components, respectively) of the shear modulus of thin films at different shear rates and film thickness. Granick [273] and Hu et al. [276] found that films of simple liquids become non-Newtonian in the 2.5–5 nm regime (about 10 molecular diameters, Fig. 13.24). Polymer melts become non-Newtonian at much larger film thicknesses, depending on their molecular weight [48].

Klein and Kumacheva [47, 280, 325] studied the interaction forces and friction of small quasi-spherical liquid molecules such as cyclohexane between molecularly smooth mica surfaces. They concluded that surface epitaxial effects can cause the liquid film to solidify already at six molecular diameters, resulting in a sudden (discontinuous) jump to high friction at low shear rates. Such dynamic first-order transitions, however, may depend on the shear rate.

A generalized friction map (Fig. 13.24c,d) has been proposed by Luengo et al. [324] that illustrates the changes in  $\eta_{\text{eff}}$  from bulk Newtonian behavior

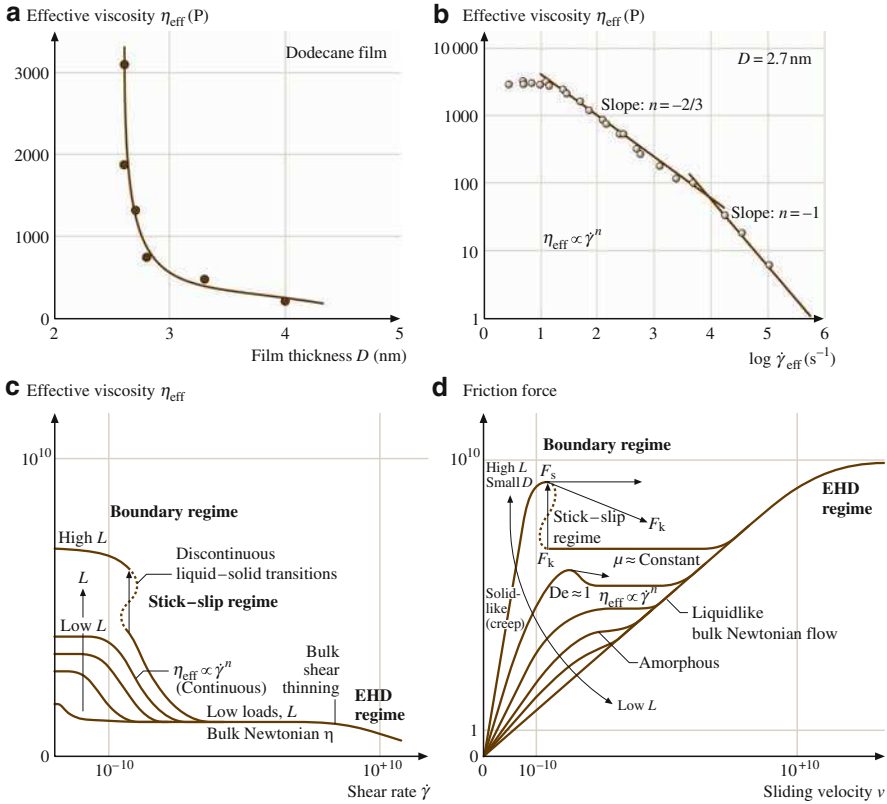


**Fig. 13.24** Typical rheological behavior of liquid films in the mixed lubrication regime. **(a)** Increase in effective viscosity of dodecane film between two mica surfaces with decreasing film thickness. At distances larger than 4–5 nm, the effective viscosity  $\eta_{\text{eff}}$  approaches the bulk value  $\eta_{\text{bulk}}$  and does not depend on the shear rate  $\dot{\gamma}$  (after [273], © 1991 American Association for the Advancement of Science.). **(b)** Non-Newtonian variation of  $\eta_{\text{eff}}$  with shear rate of a 2.7 nm thick dodecane film at a net normal pressure of 0.12 MPa and at 28 °C. The effective viscosity decays as a power law, as in (13.46). In this example,  $n = 0$  at the lowest  $\dot{\gamma}$  and changes to  $n = -2/3$  and  $-1$  at higher  $\dot{\gamma}$ . For films of bulk thickness, dodecane is a low-viscosity Newtonian fluid ( $n = 0$ ). **(c)** Proposed general friction map of effective viscosity  $\eta_{\text{eff}}$  (arbitrary units) as a function of effective shear rate  $\dot{\gamma}$  (arbitrary units) on logarithmic scales. Three main classes of behavior emerge: (1) Thick films: elastohydrodynamic sliding. At  $L = 0$ , approximating bulk conditions,  $\eta_{\text{eff}}$  is independent of shear rate except when shear thinning might occur at sufficiently large  $\dot{\gamma}$ . (2) Boundary layer films, intermediate regime. A Newtonian regime is again observed ( $\eta_{\text{eff}} = \text{constant}$ ,  $n = 0$  in (13.46)) at low loads and low shear rates, but  $\eta_{\text{eff}}$  is much higher than the bulk value. As the shear rate  $\dot{\gamma}$  increases beyond  $\dot{\gamma}_{\text{min}}$ , the effective viscosity starts to drop with a power-law dependence on the shear rate **(b)**, with  $n$  in the range  $-1/2$  to  $-1$  most commonly observed. As the shear rate  $\dot{\gamma}$  increases still more, beyond  $\dot{\gamma}_{\text{max}}$ , a second Newtonian plateau is encountered. (3) Boundary layer films, high load. The  $\eta_{\text{eff}}$  continues to grow with load and to be Newtonian provided that the shear rate is sufficiently low. Transition to sliding at high velocity is discontinuous ( $n < -1$ ) and usually of the stick-slip variety. **(d)** Proposed friction map of friction force as a function of sliding velocity in various tribological regimes. With increasing load, Newtonian flow in the elastohydrodynamic (EHD) regimes crosses into the boundary regime of

**Table 13.5** Effect of molecular shape and short-range forces on tribological properties for molecularly thin liquid films between two shearing mica surfaces at 20°C

Liquid	Short-range force	Type of friction	Friction coefficient	Bulk liquid viscosity (cP)
<b>Organic (water-free)</b>				
Cyclohexane	Oscillatory	Quantized stick-slip	$\gg 1$	0.6
OMCTS <sup>a</sup>	Oscillatory	Quantized stick-slip	$\gg 1$	2.3
Octane	Oscillatory	Quantized stick-slip	1.5	0.5
Tetradecane	Oscillatory	stick-slip	1.0	2.3
Octadecane (branched)	$\leftrightarrow$ smooth	$\leftrightarrow$ smooth		
	Oscillatory	stick-slip	0.3	5.5
	$\leftrightarrow$ smooth	$\leftrightarrow$ smooth		
PDMS <sup>a</sup>	Oscillatory	Smooth	0.4	50
( $M = 3,700 \text{ g mol}^{-1}$ , melt)	$\leftrightarrow$ smooth			
PBD <sup>a</sup> ( $M = 3,500 \text{ g mol}^{-1}$ , branched)	Smooth	Smooth	0.03	800
<b>Water</b>				
Water (KCl solution)	Smooth	Smooth	0.01–0.03	1.0

<sup>a</sup>OMCTS Octamethylcyclotetrasiloxane, PDMS Polydimethylsiloxane, PBD Polybutadiene

( $n = 0$ ,  $\eta_{\text{eff}} = \eta_{\text{bulk}}$ ) through the transition regime where  $n$  reaches a minimum of  $-1$  with decreasing shear rate to the solidlike creep regime at very low  $\dot{\gamma}$  where  $n$  returns to 0. A number of results from experimental, theoretical, and computer simulation work have shown values of  $n$  from  $-1/2$  to  $-1$  for this transition regime for a variety of systems and assumptions [273, 274, 299, 326–332].

The intermediate regime appears to extend over a narrow range of film thickness, from about 4 to 10 molecular diameters or polymer radii of gyration. Thinner films begin to adopt boundary or interfacial friction properties (described below, see also Table 13.5). Note that the intermediate regime is actually a very narrow one when defined in terms of film thickness, for example, varying from about  $D = 2$  to 4 nm for hexadecane films [273].

**Fig. 13.24** (continued) lubrication. Note that even EHD lubrication changes, at the highest velocities, to limiting shear stress response. At the highest loads ( $L$ ) and smallest film thickness ( $D$ ), the friction force goes through a maximum (the static friction  $F_s$ ) followed by a regime where the friction coefficient ( $\mu$ ) is roughly constant with increasing velocity (meaning that the kinetic friction,  $F_k$ , is roughly constant). Non-Newtonian shear thinning is observed at somewhat smaller load and larger film thickness; the friction force passes through a maximum at the point where  $De = 1$ .  $De$  – the Deborah number – is the point at which the applied shear rate exceeds the natural relaxation time of the boundary layer film. The velocity axis from  $10^{-10}$  to  $10^{10}$  (arbitrary units) indicates a large span. (Panels (b–d) after [324], © 1996, with permission from Elsevier Science)

A fluid's effective viscosity  $\eta_{\text{eff}}$  in the intermediate regime is usually higher than in the bulk, but  $\eta_{\text{eff}}$  usually *decreases* with increasing sliding velocity,  $v$  (known as *shear thinning*). When two surfaces slide in the intermediate regime, the motion tends to thicken the film (dilatancy). This sends the system into the bulk EHD regime where, as indicated by (13.44), the friction force now *increases* with velocity. This initial decrease, followed by an increase, in the frictional forces of many lubricant systems is the basis for the empirical Stribeck curve of Fig. 13.13. In the transition from bulk to boundary behavior there is first a quantitative change in the material properties (viscosity and elasticity), which can be continuous, to discontinuous qualitative changes that result in yield stresses and nonliquidlike behavior.

The rest of this section is devoted to friction in the boundary regime. Boundary friction may be thought of as applying to the case where a lubricant film is present, but where this film is of molecular dimensions – a few molecular layers or less.

### 13.8.3 *Boundary Lubrication of Molecularly Thin Films: Nanorheology*

When a liquid is confined between two surfaces or within any narrow space whose dimensions are less than 4–10 molecular diameters, both the static (equilibrium) and dynamic properties of the liquid, such as its compressibility and viscosity, can no longer be described even qualitatively in terms of the bulk properties. The molecules confined within such molecularly thin films become ordered into layers (“out-of-plane” ordering), and within each layer they can also have lateral order (“in-plane” ordering). Such films may be thought of as behaving more like a liquid crystal or a solid than a liquid.

As described in Sect. 13.4.3, the measured *normal* forces between two solid surfaces across molecularly thin films exhibit exponentially decaying oscillations, varying between attraction and repulsion with a periodicity equal to some molecular dimension of the solvent molecules. Thus most liquid films can sustain a finite normal stress, and the adhesion force between two surfaces across such films is “quantized”, depending on the thickness (or number of liquid layers) between the surfaces. The structuring of molecules in thin films and the oscillatory forces it gives rise to are now reasonably well understood, both experimentally and theoretically, at least for simple liquids.

Work has also recently been done on the dynamic, e.g., viscous or shear, forces associated with molecularly thin films. Both experiments [39, 47, 257, 277, 280, 281, 333, 334] and theory [254, 255, 326, 335] indicate that, even when two surfaces are in steady-state sliding, they still prefer to remain in one of their stable potential-energy minima, i.e., a sheared film of liquid can retain its basic layered structure. Thus even during motion the film does not become totally liquidlike. Indeed, if there is some “in-plane” ordering within a film, it will exhibit a yield point before it begins to flow. Such films can therefore sustain a finite shear stress,

in addition to a finite normal stress. The value of the yield stress depends on the number of layers comprising the film and represents another “quantized” property of molecularly thin films [254].

The dynamic properties of a liquid film undergoing shear are very complex. Depending on whether the film is more liquidlike or solidlike, the motion will be smooth or of the stick–slip type illustrated schematically in Fig. 13.25. During sliding, transitions can occur between  $n$  layers and  $(n - 1)$  or  $(n + 1)$  layers (Fig. 13.27). The details of the motion depend critically on the externally applied load, the temperature, the sliding velocity, the twist angle between the two surface lattices, and the sliding direction relative to the lattices.

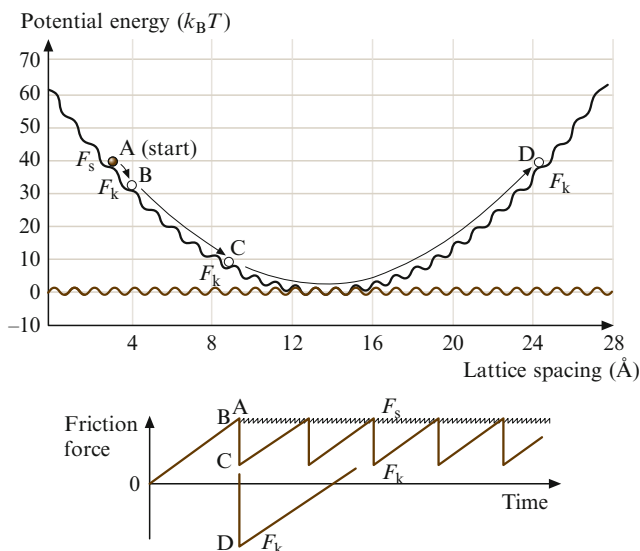


**Fig. 13.25** Simple schematic illustration of the most common molecular mechanism leading from smooth to stick–slip sliding in terms of the efficiency of the energy transfer from mechanical to kinetic to phonons. The potential energy of the corrugated surface lattice is shown by the horizontal sine wave. Let the depth of each minimum be  $\varepsilon$  which is typically  $> k_B T$ . At equilibrium, a molecule will “sit” at one of these minima. When the molecule is connected to a horizontal spring, a smooth parabolic curve must be added to the horizontal curve. If this spring is now pushed or pulled laterally at a constant velocity  $v$ , the sine curve will move like a wave along the parabola carrying the molecule up with it (towards point A). When the point of inflection at A is reached the molecule will drop and acquire a kinetic energy greater than  $\varepsilon$  even before it reaches the next lattice site. This energy can be “released” at the next lattice site (i.e., on the first collision), in which case the processes will now be repeated – each time the molecule reaches point A it will fall to point B. This type of motion will give rise to periodic changes in temperature at the interface, as predicted by computer simulations [336]. The stick–slip here will have a magnitude of the lattice dimension and, except for AFM measurements that can detect such small atomic-scale jumps [60,337], the measured macro- and microscopic friction forces will be smooth and independent of  $v$ . If the energy dissipation (or “transfer”) mechanism is less than 100% efficient on each collision, the molecule will move further before it stops. In this case the stick–slip amplitude can be large (point C), and the kinetic friction  $F_k$  can even be negative in the case of an overshoot (point D) (after [287], with permission, © 2004 American Chemical Society)

## Smooth and Stick–Slip Sliding

Recent advances in friction-measuring techniques have enabled the interfacial friction of molecularly thin films to be measured with great accuracy. Some of these advances have involved the surface forces apparatus technique [39, 45–48, 274, 277, 280, 281, 285, 286, 296, 297, 308, 313, 333, 334, 338] while others have involved the atomic force microscope [10, 59, 60, 284, 290, 339, 340]. In addition, computer simulations [111, 151, 254, 255, 287, 295, 299–302, 315–317, 335, 336, 341] have become sufficiently sophisticated to enable fairly complex tribological systems to be studied. All these advances are necessary if one is to probe such subtle effects as smooth or stick–slip friction, transient and memory effects, and ultralow friction mechanisms at the molecular level.

The theoretical models presented in this section will be concerned with a situation commonly observed experimentally: stick–slip occurs between a static state with high friction and a low-friction kinetic state, and a transition from this sliding regime to smooth sliding can be induced by an increase in velocity. Experimental data on various systems showing this behavior are shown in Figs. 13.27, 13.30b, and 13.31a. Recent studies on adhesive systems have revealed the possibility of other dynamic responses such as inverted stick–slip between two kinetic states of higher and lower friction and with a transition from smooth sliding to stick–slip with increasing velocity, as shown in Fig. 13.30c [342]. Similar friction responses have also been seen in computer simulations [343].

With the added insights provided by computer simulations, a number of distinct molecular processes have been identified during smooth and stick–slip sliding in model systems for the more familiar static-to-kinetic stick–slip and transition from stick–slip to smooth sliding. These are shown schematically in Fig. 13.26 for the case of spherical liquid molecules between two solid crystalline surfaces. The following regimes may be identified:

*Surfaces at rest* (Fig. 13.26a): even with no externally applied load, solvent–surface epitaxial interactions can cause the liquid molecules in the film to attain a solidlike state. Thus at rest the surfaces are stuck to each other through the film.

*Sticking regime (frozen, solidlike film)* (Fig. 13.26b): a progressively increasing lateral shear stress is applied. The solidlike film responds elastically with a small lateral displacement and a small increase or dilatancy in film thickness (less than a lattice spacing or molecular dimension  $\sigma$ ). In this regime the film retains its frozen, solidlike state: all the strains are elastic and reversible, and the surfaces remain effectively stuck to each other. However, slow creep may occur over long time periods.

*Slipping and sliding regimes (molten, liquidlike film)* (Fig. 13.26c–c''): when the applied shear stress or force has reached a certain critical value, the static friction force  $F_s$  the film suddenly melts (known as “shear melting”) or rearranges to allow for wall slip or slip within the film to occur at which point the two surfaces begin to slip rapidly past each other. If the applied stress is kept at a high value, the upper surface will continue to slide indefinitely.

*Refreezing regime (resolidification of film)* (Fig. 13.26d): In many practical cases, the rapid slip of the upper surface relieves some of the applied force, which



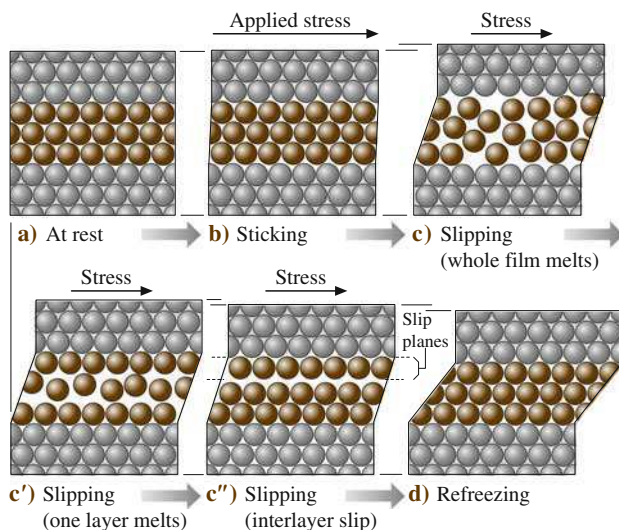


**Fig. 13.26** Idealized schematic illustration of molecular rearrangements occurring in a molecularly thin film of spherical or simple chain molecules between two solid surfaces during shear. Depending on the system, a number of different molecular configurations within the film are possible during slipping and sliding, shown here as stages (c) total disorder as the whole film melts; (c') partial disorder; and (c'') order persists even during sliding with slip occurring at a single slip plane either within the film or at the walls. A dilation is predicted in the direction normal to the surfaces (after [278], with permission)

eventually falls below another critical value, the *kinetic* friction force  $F_k$ , at which point the film resolidifies and the whole stick–slip cycle is repeated. On the other hand, if the slip rate is smaller than the rate at which the external stress is applied, the surfaces will continue to slide smoothly in the kinetic state and there will be no more stick–slip. The critical velocity at which stick–slip disappears is discussed in more detail in Sect. 13.8.3.

Experiments with linear chain (alkane) molecules show that the film thickness remains quantized during sliding, so that the structure of such films is probably more like that of a nematic liquid crystal where the liquid molecules have become shear-aligned in some direction, enabling shear motion to occur while retaining some order within the film [344]. Experiments on the friction of two molecularly smooth mica surfaces separated by three molecular layers of the liquid octamethylcyclotetrasiloxane (OMCTS, Fig. 13.27) show how the friction increases to higher values in a quantized way when the number of layers falls from  $n = 3$  to  $n = 2$  and then to  $n = 1$ .

Computer simulations for simple spherical molecules [255] further indicate that during slip the film thickness is roughly 15% higher than at rest (i.e., the film density falls), and that the order parameter within the film drops from 0.85 to about 0.25. Such dilatancy has been investigated both experimentally [296] and in further computer simulations [295]. The changes in thickness and in the order parameter are consistent with a disorganized state for the whole film during the slip [335], as

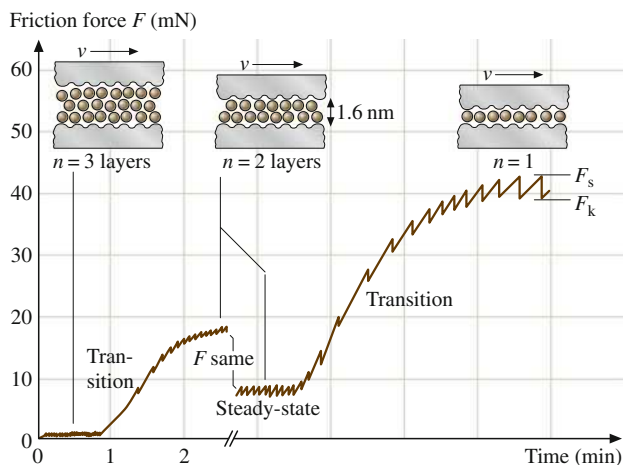


**Fig. 13.27** Measured change in friction during interlayer transitions of the silicone liquid octamethylcyclotetrasiloxane (OMCTS), an inert liquid whose quasi-spherical molecules have a diameter of 0.8 nm. In this system, the shear stress  $S_c = F/A$  was found to be constant as long as the number of layers,  $n$ , remained constant. Qualitatively similar results have been obtained with other quasi-spherical molecules such as cyclohexane [333]. The shear stresses are only weakly dependent on the sliding velocity  $v$ . However, for sliding velocities above some critical value,  $v_c$ , the stick-slip disappears and sliding proceeds smoothly at the kinetic value (after [277], with permission)

illustrated schematically in Fig. 13.26c. At this stage, we can only speculate on other possible configurations of molecules in the slipping and sliding regimes. This probably depends on the shapes of the molecules (e.g., whether they are spherical or linear or branched), on the atomic structure of the surfaces, on the sliding velocity, etc. [345]. Figure 13.26c-c'' shows three possible sliding modes wherein the shearing film either totally melts, or where the molecules retain their layered structure and where slip occurs between two or more layers. Other sliding modes, for example, involving the movement of dislocations or disclinations are also possible, and it is unlikely that one single mechanism applies in all cases.

Both friction and adhesion hysteresis vary nonlinearly with temperature, often peaking at some particular temperature  $T_0$ . The temperature dependence of these forces can, therefore, be represented on a friction phase diagram such as the one shown in Fig. 13.28. Experiments have shown that  $T_0$ , and the whole bell-shaped curve, are shifted along the temperature axis (as well as in the vertical direction) in a systematic way when the load, sliding velocity, etc., are varied. These shifts also appear to be highly correlated with one another, for example, an increase in temperature produces effects that are similar to *decreasing* the sliding speed or load.

Such effects are also commonly observed in other energy-dissipating phenomena such as polymer viscoelasticity [346], and it is likely that a similar physical mechanism is at the heart of all such phenomena. A possible molecular process underlying the energy dissipation of chain molecules during boundary-layer sliding is illustrated in Fig. 13.29, which shows the three main dynamic phase states of boundary monolayers.

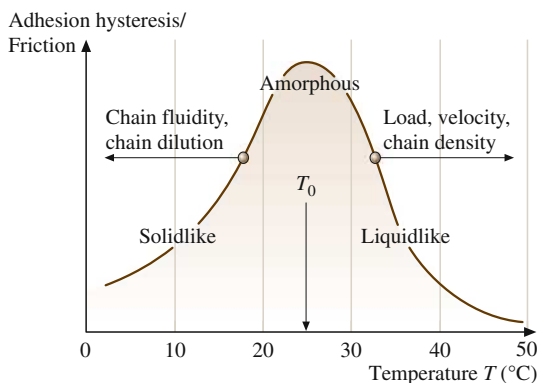


**Fig. 13.28** Schematic friction phase diagram representing the trends observed in the boundary friction of a variety of different surfactant monolayers. The characteristic bell-shaped curve also correlates with the adhesion energy hysteresis of the monolayers. The *arrows* indicate the direction in which the whole curve is dragged when the load, velocity, etc., is increased (after [291], with permission)

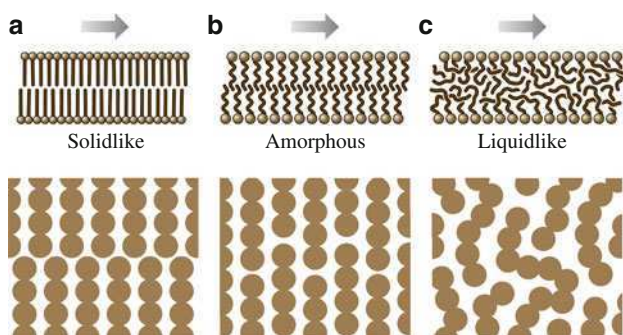


**Fig. 13.29** Different dynamic phase states of boundary monolayers during adhesive contact and/or frictional sliding. Solidlike (a) and liquidlike monolayers (c) exhibit low adhesion hysteresis and friction. Increasing the temperature generally shifts a system from the left to the right. Changing the load, sliding velocity, or other experimental conditions can also change the dynamic phase state of surface layers, as shown in Fig. 13.28 (after [291], with permission)

In contrast to the characteristic relaxation time associated with fluid lubricants, it has been established that for unlubricated (dry, solid, rough) surfaces, there is a characteristic memory distance that must be exceeded before the system loses all memory of its initial state (original surface topography). The underlying mechanism for a characteristic distance was first used to successfully explain rock mechanics and earthquake faults [347] and, more recently, the tribological behavior of unlubricated surfaces of ceramics, paper and elastomeric polymers [314, 348]. Recent experiments [285, 344, 345, 349] suggest that fluid lubricants composed of complex branched-chained or polymer molecules may also have characteristic distances (in addition to characteristic relaxation times) associated with their tribological behavior – the characteristic distance being the total sliding distance that must be exceeded before the system reaches its steady-state tribological conditions (Sect. 13.8.3).

## Abrupt Versus Continuous Transitions Between Smooth and Stick–Slip Sliding

An understanding of stick–slip is of great practical importance in tribology [350], since these spikes are the major cause of damage and wear of moving parts. Stick–slip motion is a very common phenomenon and is also the cause of sound generation (the sound of a violin string, a squeaking door, or the chatter of machinery), sensory perception (taste texture and feel), earthquakes, granular flow, nonuniform fluid flow such as the spurting flow of polymeric liquids, etc. In the previous section, the stick–slip motion arising from freezing–melting transitions in thin interfacial films was described. There are other mechanisms that can give rise to stick–slip friction, which will now be considered. However, before proceeding with this, it is important to clarify exactly what one is measuring during a friction experiment.

Most tribological systems and experiments can be described in terms of an equivalent mechanical circuit with certain characteristics. The friction force  $F_0$ , which is generated at the surfaces, is generally measured as  $F$  at some other place in the setup. The mechanical coupling between the two may be described in terms of a simple elastic stiffness or compliance  $K$  or as more complex nonelastic coefficients, depending on the system. The distinction between  $F$  and  $F_0$  is important because, in almost all practical cases, the applied, measured, or detected force  $F$  is *not* the same as the “real” or “intrinsic” friction force  $F_0$  generated at the surfaces.  $F$  and  $F_0$  are coupled in a way that depends on the mechanical construction of the system, for example, the axle of a car wheel that connects it to the engine. This coupling can be modeled as an elastic spring of stiffness  $K$  and mass  $m$ . This is the simplest type of mechanical coupling and is also the same as in SFA- and AFM-type experiments. More complicated real systems can be reduced to a system of springs and dashpots, as described by Peachey et al. [351] and Luengo et al. [48].

We now consider four different models of stick–slip friction, where the mechanical couplings are assumed to be of the simple elastic spring type. The first three mechanisms may be considered traditional or classical mechanisms or models [350], the fourth is essentially the same as the freezing–melting phase-transition model described in Sect. 13.8.3.

### Rough Surfaces or Surface Topology Model

Rapid slips can occur whenever an asperity on one surface goes over the top of an asperity on the other surface. The extent of the slip will depend on asperity heights and slopes, on the speed of sliding, and on the elastic compliance of the surfaces and the moving stage. As in all cases of stick–slip motion, the driving velocity  $v$  may be constant, but the resulting motion at the surfaces  $v_0$  will display large slips. This type of stick–slip has been described by Rabinowicz [350]. It will not be of much concern here since it is essentially a noise-type fluctuation, resulting from surface imperfections rather than from the intrinsic interaction between two surfaces. Actually, at the atomic level, the regular atomic-scale corrugations of surfaces

can lead to periodic stick–slip motion of the type shown here. This is what is sometimes measured by AFM tips [10, 59, 60, 290, 339, 340].

### Distance-Dependent or Creep Model

Another theory of stick–slip, observed in solid-on-solid sliding, is one that involves a characteristic *distance*, but also a characteristic time  $\tau_s$  this being the characteristic time required for two asperities to increase their adhesion strength after coming into contact. Originally proposed by Rabinowicz [350, 352], this model suggests that two rough macroscopic surfaces adhere through their microscopic asperities of a characteristic length. During shearing, each surface must first creep this distance (the size of the contacting junctions) after which the surfaces continue to slide, but with a lower (kinetic) friction force than the original (static) value. The reason for the decrease in the friction force is that even though, on average, new asperity junctions should form as rapidly as the old ones break, the time-dependent adhesion and friction of the new ones will be lower than the old ones.

The friction force, therefore, remains high during the creep stage of the slip. However, once the surfaces have moved the characteristic distance, the friction rapidly drops to the kinetic value. For any system where the kinetic friction is less than the static force (or one that has a negative slope over some part of its curve of  $F_0$  versus  $v_0$ ) will exhibit regular stick–slip sliding motion for certain values of  $K$ ,  $m$ , and driving velocity  $v$ .

This type of friction has been observed in a variety of dry (unlubricated) systems such as paper-on-paper [353, 354] and steel-on-steel [352, 355, 356]. This model is also used extensively in geologic systems to analyze rock-on-rock sliding [357, 358]. While originally described for adhering macroscopic asperity junctions, the distance-dependent model may also apply to molecularly smooth surfaces. For example, for polymer lubricant films, the characteristic length would now be the chain–chain entanglement length, which could be much larger in a confined geometry than in the bulk.

### Velocity-Dependent Friction Model

In contrast to the two friction models mentioned above, which apply mainly to unlubricated, solid-on-solid contacts, the stick–slip of surfaces with thin liquid films between them is better described by other mechanisms. The velocity-dependent friction model is the most studied mechanism of stick–slip and, until recently, was considered to be the only cause of intrinsic stick–slip. If a friction force decreases with increasing sliding velocity, as occurs with boundary films exhibiting shear thinning, the force ( $F_s$ ) needed to initiate motion will be higher than the force ( $F_k$ ) needed to maintain motion.

A decreasing intrinsic friction force  $F_0$  with sliding velocity  $v_0$  results in the sliding surface or stage moving in a periodic fashion, where during each cycle rapid acceleration is followed by rapid deceleration. As long as the drive continues to move at a fixed velocity  $v$ , the surfaces will continue to move in a periodic fashion

punctuated by abrupt stops and starts whose frequency and amplitude depend not only on the function  $F_0(v_0)$ , but also on the stiffness  $K$  and mass  $m$  of the moving stage, and on the starting conditions at  $t = 0$ .

More precisely, the motion of the sliding surface or stage can be determined by solving the following differential equation:

$$\begin{aligned} m\ddot{x} &= (F_0 - F) = F_0 - (x_0 - x)K \quad \text{or} \\ m\ddot{x} + (x_0 - x)K - F_0 &= 0, \end{aligned} \tag{13.47}$$

where  $F_0 = F_0(x_0, v_0, t)$  is the intrinsic or “real” friction force at the shearing surfaces,  $F$  is the force on the spring (the externally applied or measured force), and  $(F_0 - F)$  is the force on the stage. To solve (13.47) fully, one must also know the initial (starting) conditions at  $t = 0$ , and the driving or steady-state conditions at finite  $t$ . Commonly, the driving condition is:  $x = 0$  for  $t < 0$  and  $x = vt$  for  $t > 0$ , where  $v = \text{constant}$ . In other systems, the appropriate driving condition may be  $F = \text{constant}$ .

Various, mainly phenomenological, forms for  $F_0 = F_0(x_0, v_0, t)$  have been proposed to explain various kinds of stick–slip phenomena. These models generally assume a particular functional form for the friction as a function of velocity only,  $F_0 = F_0(v_0)$ , and they may also contain a number of mechanically coupled elements comprising the stage [359, 360]. One version is a two-state model characterized by two friction forces,  $F_s$  and  $F_k$ , which is a simplified version of the phase transitions model described below. More complicated versions can have a rich  $F$ – $v$  spectrum, as proposed by Persson [361]. Unless the experimental data is very detailed and extensive, these models cannot generally distinguish between different types of mechanisms. Neither do they address the basic question of the *origin* of the friction force, since this is assumed to begin with.

Experimental data has been used to calculate the friction force as a function of velocity *within* an individual stick–slip cycle [362]. For a macroscopic granular material confined between solid surfaces, the data shows a velocity-weakening friction force during the first half of the slip. However, the data also shows a hysteresis loop in the friction–velocity plot, with a different behavior in the deceleration half of the slip phase. Similar results were observed for a 1–2 nm liquid lubricant film between mica surfaces [345]. These results indicate that a purely velocity-dependent friction law is insufficient to describe such systems, and an additional element such as the *state* of the confined material must be considered.

### Phase Transitions Model

In recent molecular dynamics computer simulations it has been found that thin interfacial films undergo first-order phase transitions between solid-like and liquid-like states during sliding [255, 364], as illustrated in Fig. 13.30. It has been suggested that this is responsible for the observed stick–slip behavior of simple isotropic liquids between two solid crystalline surfaces. With this interpretation, stick–slip is seen to arise because of the abrupt change in the flow properties of a

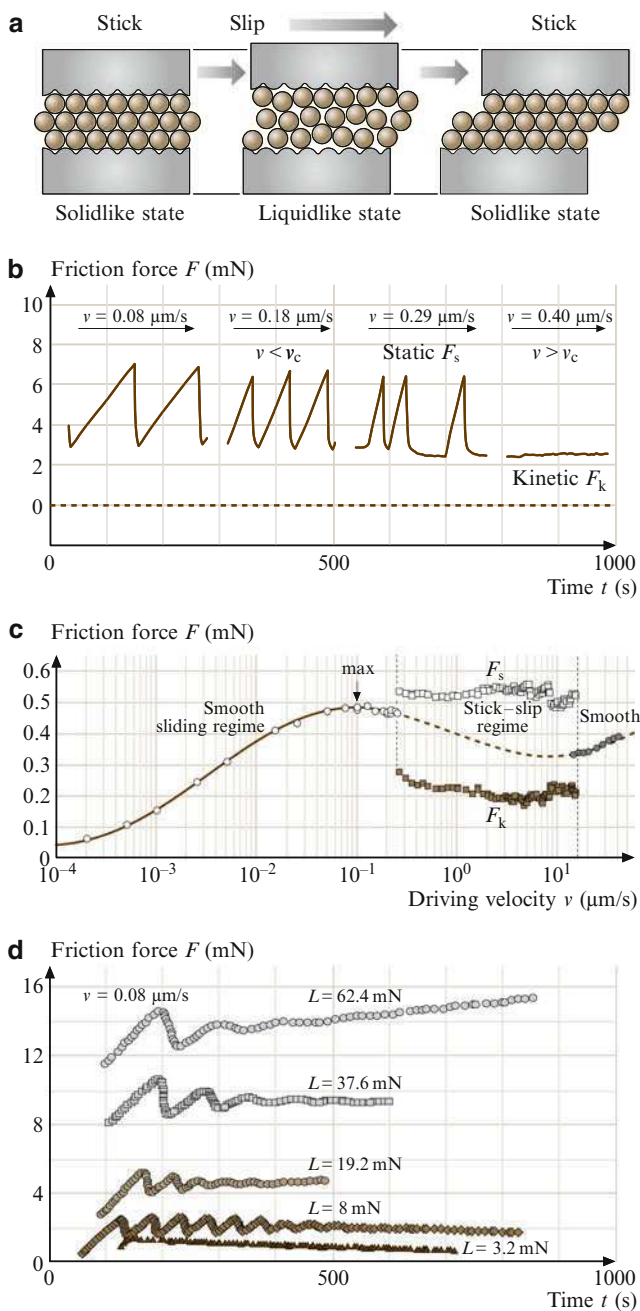


**Fig. 13.30** (a) “Phase transitions” model of stick–slip where a thin liquid film alternately freezes and melts as it shears, shown here for 22 spherical molecules confined between two solid crystalline surfaces. In contrast to the velocity-dependent friction model, the intrinsic friction force is assumed to change abruptly (at the transitions), rather than smooth or continuously. The



film at a transition [278, 279, 326], rather than the gradual or continuous change, as occurs in the previous example. Other computer simulations indicate that it is the stick–slip that induces a disorder (“shear melting”) in the film, not the other way around [365].

An interpretation of the well-known phenomenon of decreasing coefficient of friction with increasing sliding velocity has been proposed by *Thompson* and *Robbins* [255] based on their computer simulation. This postulates that it is not the friction that changes with sliding speed  $v$ , but rather the time various parts of the system spend in the sticking and sliding modes. In other words, at any instant during sliding, the friction at any local region is always  $F_s$  or  $F_k$ , corresponding to the “static” or “kinetic” values. The measured frictional force, however, is the sum of all these discrete values averaged over the whole contact area. Since as  $v$  increases each local region spends more time in the sliding regime ( $F_k$ ) and less in the sticking regime ( $F_s$ ), the overall friction coefficient falls. One may note that this interpretation reverses the traditional way that stick–slip has been explained. Rather than invoking a decreasing friction with velocity to explain stick–slip, it is now the more fundamental stick–slip phenomenon that is producing the apparent decrease in the friction force with increasing sliding velocity. This approach has been studied

---

**Fig. 13.30** (continued) resulting stick–slip is also different, for example, the peaks are sharper and the stick–slip disappears above some critical velocity  $v_c$ . Note that, while the slip displacement is here shown to be only two lattice spacings, in most practical situations it is much larger, and that freezing and melting transitions at surfaces or in thin films may not be the same as freezing or melting transitions between the bulk solid and liquid phases. **(b)** Exact reproduction of a chart-recorder trace of the friction force for hexadecane between two untreated mica surfaces at increasing sliding velocity  $v$ , plotted as a function of time. In general, with increasing sliding speed, the stick–slip spikes increase in frequency and decrease in magnitude. As the critical sliding velocity  $v_c$  is approached, the spikes become erratic, eventually disappearing altogether at  $v = v_c$ . At higher sliding velocities the sliding continues smoothly in the kinetic state. Such friction traces are fairly typical for simple liquid lubricants and dry boundary lubricant systems (Fig. 13.31a) and may be referred to as the “conventional” type of static–kinetic friction (in contrast to panel **(c)**). Experimental conditions: contact area  $A = 4 \times 10^{-9} \text{ m}^2$ , load  $L = 10 \text{ mN}$ , film thickness  $D = 0.4 - 0.8 \text{ nm}$ ,  $v = 0.08 - 0.4 \mu\text{m s}^{-1}$ ,  $v_c \approx 0.3 \mu\text{m s}^{-1}$ , atmosphere: dry  $\text{N}_2$  gas,  $T = 18^\circ\text{C}$  ((a, b) after [363] with permission, © 1993 American Chemical Society). **(c)** Transition from smooth sliding to “inverted” stick–slip and to a second smooth-sliding regime with increasing driving velocity during shear of two adsorbed surfactant monolayers in aqueous solution at a load of  $L = 4.5 \text{ mN}$  and  $T = 20^\circ\text{C}$ . The smooth sliding (*open circles*) to inverted stick–slip (*squares*) transition occurs at  $v_c \sim 0.3 \mu\text{m/s}$ . Prior to the transition, the kinetic stress levels off at after a logarithmic dependence on velocity. The quasi-smooth regime persists up to the transition at  $v_c$ . At high driving velocities (*filled circles*), a new transition to a smooth sliding regime is observed between 14 and 17  $\mu\text{m/s}$  (after [342] with permission). **(d)** Friction response of a thin squalane (a branched hydrocarbon) film at different loads and a constant sliding velocity  $v = 0.085 \mu\text{m s}^{-1}$ , slightly above the critical velocity for this system at low loads. Initially, with increasing load, the stick–slip amplitude and the mean friction force decrease with sliding time or sliding distance. However, at high loads or pressures, the mean friction force increases with time, and the stick–slip takes on a more symmetrical, sinusoidal shape. At all loads investigated, the stick–slip component gradually decayed as the friction proceeded towards smooth sliding (after [285] with permission, © 2003 American Physical Society)



analytically by Carlson and Batista [366], with a comprehensive rate- and state-dependent friction force law. This model includes an analytic description of the freezing–melting transitions of a film, resulting in a friction force that is a function of sliding velocity in a natural way. This model predicts a full range of stick–slip behavior observed experimentally.

An example of the rate- and state-dependent model is observed when shearing thin films of OMCTS between mica surfaces [367, 368]. In this case, the static friction between the surfaces is dependent on the time that the surfaces are at rest with respect to each other, while the intrinsic kinetic friction  $F_{k,0}$  is relatively constant over the range of velocities. At slow driving velocities, the system responds with stick–slip sliding with the surfaces reaching maximum static friction before each slip event, and the amplitude of the stick–slip,  $F_s - F_k$ , is relatively constant. As the driving velocity increases, the static friction decreases as the time at relative rest becomes shorter with respect to the characteristic time of the lubricant film. As the static friction decreases with increasing drive velocity, it eventually equals the intrinsic kinetic friction  $F_{k,0}$ , which defines the critical velocity  $v_c$ , above which the surfaces slide smoothly without the jerky stick–slip motion.

The above classifications of stick–slip are not exclusive, and molecular mechanisms of real systems may exhibit aspects of different models simultaneously. They do, however, provide a convenient classification of existing models and indicate which experimental parameters should be varied to test the different models.

### Critical Velocity for Stick–Slip

For any given set of conditions, stick–slip disappears above some critical sliding velocity  $v_c$ , above which the motion continues smoothly in the liquidlike or kinetic state [265, 285, 342, 345, 363]. The critical velocity is well described by two simple equations. Both are based on the phase transition model, and both include some parameter associated with the inertia of the measuring instrument. The first equation is based on both experiments and simple theoretical modeling [363]

$$v_c \approx \frac{(F_s - F_k)}{5K\tau_0}, \quad (13.48)$$

where  $\tau_0$  is the *characteristic nucleation time* or freezing time of the film. For example, inserting the following typically measured values for a  $\sim 1$  nm thick hexadecane film between mica:  $(F_s - F_k) \approx 5$  mN, spring constant  $K \approx 500$  N m $^{-1}$ , and nucleation time [363]  $\tau_0 \approx 5$  s, we obtain  $v_c \approx 0.4$   $\mu\text{m s}^{-1}$ , which is close to typically measured values (Fig. 13.31b).

The second equation is based on computer simulations [364]:

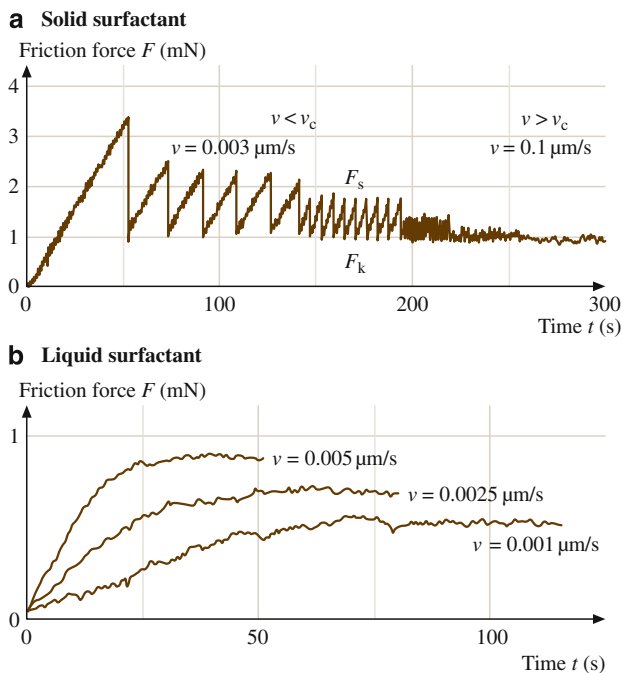


**Fig. 13.31** (a) Exact reproduction of chart-recorder trace for the friction of closely packed surfactant monolayers (1- $\alpha$ -dimirystoyl-phosphatidyl-ethanolamine, DMPE) on mica (dry boundary friction) showing qualitatively similar behavior to that obtained with a liquid hexadecane film (Fig. 13.30b). In this case,  $L = 0$ ,  $v_c \approx 0.1 \mu\text{m s}^{-1}$ , atmosphere: dry  $\text{N}_2$  gas,  $T = 25^\circ\text{C}$ . (b) Sliding typical of liquidlike monolayers, here shown for calcium alkylbenzene sulfonate in dry  $\text{N}_2$  gas at  $T = 25^\circ\text{C}$  and  $L = 0$  (after [265], with permission, © 1993 American Chemical Society)

$$v_c \approx 0.1 \sqrt{\frac{F_s \sigma}{m}}, \quad (13.49)$$

where  $\sigma$  is a molecular dimension and  $m$  is the mass of the stage. Again, inserting typical experimental values into this equation, viz.,  $m \approx 20 \text{ g}$ ,  $\sigma \approx 0.5 \text{ nm}$ , and  $(F_s - F_k) \approx 5 \text{ mN}$  as before, we obtain  $v_c \approx 0.3 \mu\text{m s}^{-1}$ , which is also close to measured values.

Stick-slip also disappears above some critical temperature  $T_c$ , which is not the same as the melting temperature of the bulk fluid [285]. Certain correlations have been found between  $v_c$  and  $T_c$  and between various other tribological parameters that appear to be consistent with the principle of time-temperature superposition (Sect. 13.8.3), similar to that occurring in viscoelastic polymer fluids [346, 369, 370].

Recent work on the coupling between the mechanical resonances of the sliding system and molecular-scale relaxations [295, 338, 341, 371] has resulted in a better understanding of a phenomenon previously noted in various

engineering applications: the vibration of one of the sliding surfaces perpendicularly to the sliding direction can lead to a significant reduction of the friction. At certain oscillation amplitudes and a frequency higher than the molecular-scale relaxation frequency, stick-slip friction can be eliminated and replaced by an ultralow kinetic-friction state.

## 13.9 Effects of Nanoscale Texture on Friction

The above scenario is already quite complicated, and yet this is the situation for the simplest type of experimental system. The factors that appear to determine the critical velocity  $v_c$  depend on the type of liquid between the surfaces, as well as on the surface lattice structure.

### 13.9.1 *Role of the Shape of Confined Molecules*

Small spherical molecules such as cyclohexane and OMCTS have been found to have very high  $v_c$ , which indicates that these molecules can rearrange relatively quickly in thin films. Chain molecules and especially branched-chain molecules have been found to have much lower  $v_c$ , which is to be expected, and such liquids tend to slide smoothly or with erratic stick-slip [345], rather than in a stick-slip fashion (Table 13.5). With highly asymmetric molecules, such as multiply branched isoparaffins and polymer melts, no regular spikes or stick-slip behavior occurs at any speed, since these molecules can never order themselves sufficiently to solidify. Examples of such liquids are some perfluoropolyethers and polydimethylsiloxanes (PDMS).

Recent computer simulations [144, 151, 287, 315, 372] of the structure, interaction forces, and tribological behavior of chain molecules between two shearing surfaces indicate that both linear *and* singly or doubly branched-chain molecules order between two flat surfaces by aligning into discrete layers parallel to the surfaces. However, in the case of the weakly branched molecules, the expected oscillatory forces do not appear because of a complex cancelation of entropic and enthalpic contributions to the interaction free energy, which results in a monotonically smooth interaction, exhibiting a weak energy minimum rather than the oscillatory force profile that is characteristic of linear molecules. During sliding, however, these molecules can be induced to further align, which can result in a transition from smooth to stick-slip sliding.

Table 13.5 shows the trends observed with some organic and polymeric liquids between smooth mica surfaces. Also listed are the bulk viscosities of the liquids. From the data of Table 13.5 it appears that there is a direct correlation between the shapes of molecules and their coefficient of friction or effectiveness as lubricants (at least at low shear rates). Small spherical or chain molecules have high friction

with stick–slip, because they can pack into ordered solidlike layers. In contrast, longer chained and irregularly shaped molecules remain in an entangled, disordered, fluidlike state even in very thin films, and these give low friction and smoother sliding. It is probably for this reason that irregularly shaped branched chain molecules are usually better lubricants. It is interesting to note that the friction coefficient generally decreases as the bulk viscosity of the liquids *increases*. This unexpected trend occurs because the factors that are conducive to low friction are generally conducive to high viscosity. Thus molecules with side groups such as branched alkanes and polymer melts usually have higher bulk viscosities than their linear homologues for obvious reasons. However, in thin films the linear molecules have higher shear stresses, because of their ability to become ordered. The only exception to the above correlations is water, which has been found to exhibit both low viscosity *and* low friction (Fig. 13.20a, and Sect. 13.7.3). In addition, the presence of water can drastically lower the friction and eliminate the stick–slip of hydrocarbon liquids when the sliding surfaces are hydrophilic.

If an “effective” viscosity,  $\eta_{\text{eff}}$ , were to be calculated for the liquids of Table 13.5, the values would be many orders of magnitude higher than those of the bulk liquids. This can be demonstrated by the following simple calculation based on the usual equation for Couette flow (13.44):

$$\eta_{\text{eff}} = F_k D / A v, \quad (13.50)$$

where  $F_k$  is the kinetic friction force,  $D$  is the film thickness,  $A$  the contact area, and  $v$  the sliding velocity. Using typical values for experiments with hexadecane [363]:  $F_k = 5 \text{ mN}$ ,  $D = 1 \text{ nm}$ ,  $A = 3 \times 10^{-9} \text{ m}^2$  and  $v = 1 \mu\text{m s}^{-1}$ , one gets  $\eta_{\text{eff}} \approx 2000 \text{ N s m}^{-2}$ , or 20000 P, which is  $\approx 10^6$  times higher than the bulk viscosity,  $\eta_{\text{bulk}}$ , of the liquid. It is instructive to consider that this very high effective viscosity nevertheless still produces a low friction force or friction coefficient  $\mu$  of about 0.25. It is interesting to speculate that, if a 1 nm film were to exhibit bulk viscous behavior, the friction coefficient under the same sliding conditions would be as low as 0.000001. While such a low value has never been reported for any tribological system, one may consider it a theoretical lower limit that could conceivably be attained under certain experimental conditions.

### 13.9.2 Effects of Surface Structure

Various studies [45, 273–275, 284–286] have shown that confinement and load generally increase the effective viscosity and/or relaxation times of molecules, suggestive of an increased glassiness or solidlike behavior (Figs. 13.32 and 13.33). This is in marked contrast to studies of liquids in small confining capillaries where the opposite effects have been observed [373, 374]. The reason for this is probably because the two modes of confinement are different. In the former case

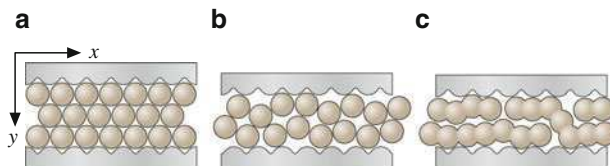


**Fig. 13.32** Schematic view of interfacial film composed of spherical molecules under a compressive pressure between two solid crystalline surfaces. **(a)** If the two surface lattices are free to move in the  $x$ - $y$ - $z$  directions, so as to attain the lowest energy state, they could equilibrate at values of  $x$ ,  $y$ , and  $z$ , which induce the trapped molecules to become “epitaxially” ordered into a “solidlike” film. **(b)** Similar view of trapped molecules between two solid surfaces that are not free to adjust their positions, for example, as occurs in capillary pores or in brittle cracks. **(c)** Similar to **(a)**, but with chain molecules replacing the spherical molecules in the gap. These may not be able to order as easily as do spherical molecules even if  $x$ ,  $y$ , and  $z$  can adjust, resulting in a situation that is more akin to **(b)** (after [363] with permission, © 1993 American Chemical Society)

(confinement of molecules between two structured solid surfaces), there is generally little opposition to any lateral or vertical displacement of the two surface lattices relative to each other. This means that the two lattices can shift in the  $x$ - $y$ - $z$  planes (Fig. 13.32a) to accommodate the trapped molecules in the most crystallographically commensurate or epitaxial way, which would favor an ordered, solidlike state. In contrast, the walls of capillaries are rigid and cannot easily move or adjust to accommodate the confined molecules (Fig. 13.32b), which will therefore be forced into a more disordered, liquidlike state (unless the capillary wall geometry and lattice are *exactly* commensurate with the liquid molecules, as occurs in certain zeolites [374]).

Experiments have demonstrated the effects of surface lattice mismatch on the friction between surfaces [257, 258, 375]. Similar to the effects of lattice mismatch on adhesion (Fig. 13.11), the static friction of a confined liquid film is maximum when the lattices of the confining surfaces are aligned. For OMCTS confined between mica surfaces [258] the static friction was found to vary by more than a factor of 4, while for bare mica surfaces the variation was by a factor of 3.5 [375]. In contrast to the sharp variations in adhesion energy over small twist angles, the variations in friction as a function of twist angle were much broader both in magnitude and angular spread. Similar variations in friction as a function of twist or misfit angles have also been observed in computer simulations [376].

Robbins and coworkers [315] computed the friction forces of two clean crystalline surfaces as a function of the angle between their surface lattices. They found that, for all nonzero angles (finite “twist” angles), the friction forces fell to zero due to incommensurability effects. They further found that submonolayer amounts of organic or other impurities trapped between two incommensurate surfaces can generate a finite friction force. They therefore concluded that any finite friction force measured between incommensurate surfaces is probably due to such “third-body” effects.

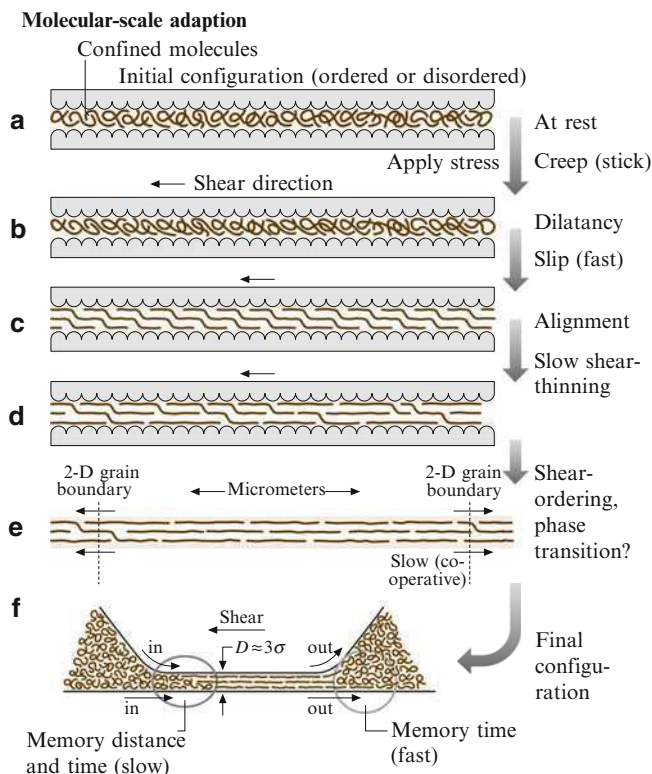


**Fig. 13.33** Schematic representation of the film under shear. (a) The lubricant molecules are just confined, but not oriented in any particular direction. Because of the need to shear, the film dilates (b). The molecules disentangle (c) and get oriented in a certain direction related to the shear direction (d). (e) Slowly evolving domains grow inside the contact region. These macroscopic domains are responsible for the long relaxation times. (f) At the steady-state, a continuous gradient of confinement time and molecular order is established in the contact region, which is different for molecules adsorbed on the upper and lower surfaces. Molecules entering into the contact are not oriented or ordered. The required sliding distance to modify their state defines a characteristic distance. Molecules leaving the contact region need some (short) characteristic time to regain their bulk, unconfined configuration (after [344], with permission, © 2000 American Chemical Society)

The reason why surface texture (lattice structure, roughness, granularity, topography, etc.) has a larger effect on the lateral (shear or friction) forces between two surfaces than on their normal (adhesion) forces is because friction is proportional to the adhesion hysteresis (Sect. 13.7.2), which can be low even when the adhesion force is high. It is also important to recognize that a system might be defined by more than one length scale. Some systems have well-defined dimensions or size (e.g., a perfect lattice, monodisperse nanoparticles), while others have different lateral and vertical dimensions and macroscopic curvature [248]. Furthermore, the morphology or texture of many systems, such as asperities that are randomly distributed over a surface, affects adhesion and tribological properties [243, 248, 287, 317, 377–379].

With rough surfaces, i.e., those that have *random* protrusions rather than being periodically structured, we expect a smearing out of the correlated intermolecular interactions that are involved in film freezing and melting (and in phase transitions in general). This should effectively eliminate the highly regular stick–slip and may also affect the location of the slipping planes [151, 287, 314, 348]. The stick–slip friction of “real” surfaces, which are generally rough, may, therefore, be quite different from those of perfectly smooth surfaces composed of the same material. We should note, however, that even between rough surfaces, most of the contacts occur between the tips of microscopic asperities, which may be smooth over their microscopic contact area [380].

## References

1. K.B. Lodge, Techniques for the measurement of forces between solids. *Adv. Colloid Interface Sci.* **19**, 27–73 (1983)
2. J.N. Israelachvili, *Intermolecular and Surface Forces*, 2nd edn. (Academic, London, 1991)
3. P.F. Luckham, B.A.L. de Costello, Recent developments in the measurement of interparticle forces. *Adv. Colloid Interface Sci.* **44**, 183–240 (1993)
4. P.M. Claesson, T. Ederth, V. Bergeron, M.W. Rutland, Techniques for measuring surface forces. *Adv. Colloid Interface Sci.* **67**, 119–183 (1996)
5. V.S.J. Craig, An historical review of surface force measurement techniques, *Colloids Surf. A* **129/130**, 75–94 (1997)
6. J.N. Israelachvili, Surface Forces and Microrheology of Molecularly Thin Liquid Films. In: *Handbook of Micro/Nanotribology*, ed. by B. Bhushan (CRC, Boca Raton, FL 1995), pp. 267–319
7. J.N. Israelachvili, G.E. Adams, Measurements of forces between two mica surfaces in aqueous electrolyte solutions in the range 0–100 nm. *J. Chem. Soc. Faraday Trans. I* **74**, 975–1001 (1978)
8. G. Binnig, C.F. Quate, C. Gerber, Atomic force microscope. *Phys. Rev. Lett.* **56**, 930–933 (1986)
9. W.A. Ducker, T.J. Senden, R.M. Pashley, Direct measurement of colloidal forces using an atomic force microscope. *Nature* **353**, 239–241 (1991)
10. E. Meyer, R.M. Overney, K. Dransfeld, T. Gyalog, *Nanoscience: Friction and Rheology on the Nanometer Scale* (World Scientific, Singapore, 1998)
11. J.N. Israelachvili, Measurements of the viscosity of thin fluid films between two surfaces with and without adsorbed polymers. *Colloid Polym. Sci.* **264**, 1060–1065 (1986)
12. J.P. Montfort, G. Hadzioannou, Equilibrium and dynamic behavior of thin films of a perfluorinated polyether. *J. Chem. Phys.* **88**, 7187–7196 (1988)
13. A. Dhinojwala, S. Granick, Surface forces in the tapping mode, Solvent permeability and hydrodynamic thickness of adsorbed polymer brushes. *Macromolecules* **30**, 1079–1085 (1997)
14. B.V. Derjaguin, Untersuchungen über die Reibung und Adhäsion, IV. Theorie des Anhaftens kleiner Teilchen. *Kolloid Z.* **69**, 155–164 (1934)
15. D. Leckband, J. Israelachvili, Intermolecular forces in biology. *Quart. Rev. Biophys.* **34**, 105–267 (2001)
16. K.L. Johnson, K. Kendall, A.D. Roberts, Surface energy and the contact of elastic solids. *Proc. R. Soc. Lond. A* **324**, 301–313 (1971)
17. J.N. Israelachvili, P.M. McGuigan, Adhesion and short-range forces between surfaces. Part 1: New apparatus for surface force measurements. *J. Mater. Res.* **5**, 2223–2231 (1990)

18. J.N. Israelachvili, Thin film studies using multiple-beam interferometry. *J. Colloid Interface Sci.* **44**, 259–272 (1973)
19. Y.L. Chen, T. Kuhl, J. Israelachvili, Mechanism of cavitation damage in thin liquid films: Collapse damage vs. inception damage. *Wear* **153**, 31–51 (1992)
20. M. Heuberger, G. Luengo, J. Israelachvili, Topographic information from multiple beam interferometry in the surface forces apparatus. *Langmuir* **13**, 3839–3848 (1997)
21. R.M. Pashley, DLVO and hydration forces between mica surfaces in  $\text{Li}^+$ ,  $\text{Na}^+$ ,  $\text{K}^+$ , and  $\text{Cs}^+$  electrolyte solutions: A correlation of double-layer and hydration forces with surface cation exchange properties. *J. Colloid Interface Sci.* **83**, 531–546 (1981)
22. R.M. Pashley, Hydration forces between mica surfaces in electrolyte solution. *Adv. Colloid Interface Sci.* **16**, 57–62 (1982)
23. R.G. Horn, D.T. Smith, W. Haller, Surface forces and viscosity of water measured between silica sheets. *Chem. Phys. Lett.* **162**, 404–408 (1989)
24. R.G. Horn, D.R. Clarke, M.T. Clarkson, Direct measurements of surface forces between sapphire crystals in aqueous solutions. *J. Mater. Res.* **3**, 413–416 (1988)
25. W.W. Merrill, A.V. Pocius, B.V. Thakker, M. Tirrell, Direct measurement of molecular level adhesion forces between biaxially oriented solid polymer films. *Langmuir* **7**, 1975–1980 (1991)
26. J. Klein, Forces between mica surfaces bearing adsorbed macromolecules in liquid media. *J. Chem. Soc. Faraday Trans. I* **79**, 99–118 (1983)
27. S.S. Patel, M. Tirrell, Measurement of forces between surfaces in polymer fluids. *Annu. Rev. Phys. Chem.* **40**, 597–635 (1989)
28. H. Watanabe, M. Tirrell, Measurements of forces in symmetric and asymmetric interactions between diblock copolymer layers adsorbed on mica. *Macromolecules* **26**, 6455–6466 (1993)
29. T.L. Kuhl, D.E. Leckband, D.D. Lasic, J.N. Israelachvili, Modulation and modeling of interaction forces between lipid bilayers exposing terminally grafted polymer chains. In: *Stealth Liposomes*, ed. by D. Lasic, F. Martin (CRC, Boca Raton, 1995), pp. 73–91
30. J. Klein, Shear, friction, and lubrication forces between polymer-bearing surfaces. *Annu. Rev. Mater. Sci.* **26**, 581–612 (1996)
31. M. Ruths, D. Johannsmann, J. R  he, W. Knoll, Repulsive forces and relaxation on compression of entangled, polydisperse polystyrene brushes. *Macromolecules* **33**, 3860–3870 (2000)
32. C.A. Helm, J.N. Israelachvili, P.M. McGuiggan, Molecular mechanisms and forces involved in the adhesion and fusion of amphiphilic bilayers. *Science* **246**, 919–922 (1989)
33. Y.L. Chen, C.A. Helm, J.N. Israelachvili, Molecular mechanisms associated with adhesion and contact angle hysteresis of monolayer surfaces. *J. Phys. Chem.* **95**, 10736–10747 (1991)
34. D.E. Leckband, J.N. Israelachvili, F.-J. Schmitt, W. Knoll, Long-range attraction and molecular rearrangements in receptor–ligand interactions. *Science* **255**, 1419–1421 (1992)
35. J. Peanasky, H.M. Schneider, S. Granick, C.R. Kessel, Self-assembled monolayers on mica for experiments utilizing the surface forces apparatus. *Langmuir* **11**, 953–962 (1995)
36. C.J. Coakley, D. Tabor, Direct measurement of van der Waals forces between solids in air. *J. Phys. D* **11**, L77–L82 (1978)
37. J.L. Parker, H.K. Christenson, Measurements of the forces between a metal surface and mica across liquids. *J. Chem. Phys.* **88**, 8013–8014 (1988)
38. C.P. Smith, M. Maeda, L. Atanasoska, H.S. White, D.J. McClure, Ultrathin platinum films on mica and the measurement of forces at the platinum/water interface. *J. Phys. Chem.* **92**, 199–205 (1988)
39. S.J. Hirz, A.M. Homola, G. Hadzioannou, C.W. Frank, Effect of substrate on shearing properties of ultrathin polymer films. *Langmuir* **8**, 328–333 (1992)
40. J.M. Levins, T.K. Vanderlick, Reduction of the roughness of silver films by the controlled application of surface forces. *J. Phys. Chem.* **96**, 10405–10411 (1992)



41. S. Steinberg, W. Ducker, G. Vigil, C. Hyukjin, C. Frank, M.Z. Tseng, D.R. Clarke, J.N. Israelachvili, Van der Waals epitaxial growth of  $\alpha$ -alumina nanocrystals on mica. *Science* **260**, 656–659 (1993)
42. G. Vigil, Z. Xu, S. Steinberg, J. Israelachvili, Interactions of silica surfaces. *J. Colloid Interface Sci.* **165**, 367–385 (1994)
43. M. Ruths, M. Heuberger, V. Scheumann, J. Hu, W. Knoll, Confinement-induced film thickness transitions in liquid crystals between two alkanethiol monolayers on gold. *Langmuir* **17**, 6213–6219 (2001)
44. J. Van Alsten, S. Granick, Molecular tribometry of ultrathin liquid films. *Phys. Rev. Lett.* **61**, 2570–2573 (1988)
45. J. Van Alsten, S. Granick, Shear rheology in a confined geometry: Polysiloxane melts. *Macromolecules* **23**, 4856–4862 (1990)
46. A.M. Homola, J.N. Israelachvili, M.L. Gee, P.M. McGuiggan, Measurements of and relation between the adhesion and friction of two surfaces separated by molecularly thin liquid films. *J. Tribol.* **111**, 675–682 (1989)
47. J. Klein, E. Kumacheva, Simple liquids confined to molecularly thin layers. I. Confinement-induced liquid-to-solid phase transitions. *J. Chem. Phys.* **108**, 6996–7009 (1998)
48. G. Luengo, F.-J. Schmitt, R. Hill, J. Israelachvili, Thin film rheology and tribology of confined polymer melts: Contrasts with bulk properties. *Macromolecules* **30**, 2482–2494 (1997)
49. L. Qian, G. Luengo, D. Douillet, M. Charlot, X. Dollat, E. Perez: New two-dimensional friction force apparatus design for measuring shear forces at the nanometer scale. *Rev. Sci. Instrum.* **72**, 4171–4177 (2001)
50. E. Kumacheva, Interfacial friction measurements in surface force apparatus. *Prog. Surf. Sci.* **58**, 75–120 (1998)
51. F. Restagno, J. Crassous, E. Charlaix, C. Cottin-Bizonne, M. Monchanin, A new surface forces apparatus for nanorheology. *Rev. Sci. Instrum.* **73**, 2292–2297 (2002)
52. C. Cottin-Bizonne, B. Cross, A. Steinberger, E. Charlaix, Boundary slip on smooth hydrophobic surfaces: Intrinsic effects and possible artifacts. *Phys. Rev. Lett.* **94**, 056102–1–056102–4 (2005)
53. A.L. Weisenhorn, P.K. Hansma, T.R. Albrecht, C.F. Quate, Forces in atomic force microscopy in air and water. *Appl. Phys. Lett.* **54**, 2651–2653 (1989)
54. G. Meyer, N.M. Amer, Simultaneous measurement of lateral and normal forces with an optical-beam-deflection atomic force microscope. *Appl. Phys. Lett.* **57**, 2089–2091 (1990)
55. E.L. Florin, V.T. Moy, H.E. Gaub, Adhesion forces between individual ligand–receptor pairs. *Science* **264**, 415–417 (1994)
56. G.U. Lee, D.A. Kidwell, R.J. Colton, Sensing discrete streptavidin–biotin interactions with atomic force microscopy. *Langmuir* **10**, 354–357 (1994)
57. H. Skulason, C.D. Frisbie, Detection of discrete interactions upon rupture of Au microcontacts to self-assembled monolayers terminated with  $-S(CO)CH_3$  or  $-SH$ . *J. Am. Chem. Soc.* **122**, 9750–9760 (2000)
58. M. Carrion-Vazquez, A.F. Oberhauser, S.B. Fowler, P.E. Marszalek, S.E. Broedel, J. Clarke, J.M. Fernandez, Mechanical and chemical unfolding of a single protein: A comparison. *Proc. Natl. Acad. Sci. USA* **96**, 3694–3699 (1999)
59. C.M. Mate, G.M. McClelland, R. Erlandsson, S. Chiang, Atomic-scale friction of a tungsten tip on a graphite surface. *Phys. Rev. Lett.* **59**, 1942–1945 (1987)
60. R.W. Carpick, M. Salmeron, Scratching the surface: Fundamental investigations of tribology with atomic force microscopy. *Chem. Rev.* **97**, 1163–1194 (1997)
61. J.P. Cleveland, S. Manne, D. Bocek, P.K. Hansma, A nondestructive method for determining the spring constant of cantilevers for scanning force microscopy. *Rev. Sci. Instrum.* **64**, 403–405 (1993)
62. J.E. Sader, J.W.M. Chon, P. Mulvaney, Calibration of rectangular atomic force microscope cantilevers. *Rev. Sci. Instrum.* **70**, 3967–3969 (1999)

63. Y. Liu, T. Wu, D.F. Evans, Lateral force microscopy study on the shear properties of self-assembled monolayers of dialkylammonium surfactant on mica. *Langmuir* **10**, 2241–2245 (1994)
64. A. Feiler, P. Attard, I. Larson, Calibration of the torsional spring constant and the lateral photodiode response of frictional force microscopes. *Rev. Sci. Instrum.* **71**, 2746–2750 (2000)
65. C.P. Green, H. Lioe, J.P. Cleveland, R. Proksch, P. Mulvaney, J.E. Sader, Normal and torsional spring constants of atomic force microscope cantilevers. *Rev. Sci. Instrum.* **75**, 1988–1996 (2004)
66. C. Neto, V.S.J. Craig, Colloid probe characterization: Radius and roughness determination. *Langmuir* **17**, 2097–2099 (2001)
67. G.M. Sacha, A. Verdager, J. Martinez, J.J. Saenz, D.F. Ogletree, M. Salmeron, Effective tip radius in electrostatic force microscopy. *Appl. Phys. Lett.* **86**, 123101–1–123101–3 (2005)
68. R.G. Horn, J.N. Israelachvili, Molecular organization and viscosity of a thin film of molten polymer between two surfaces as probed by force measurements. *Macromolecules* **21**, 2836–2841 (1988)
69. R.G. Horn, S.J. Hirz, G. Hadziioannou, C.W. Frank, J.M. Catala, A reevaluation of forces measured across thin polymer films: Nonequilibrium and pinning effects. *J. Chem. Phys.* **90**, 6767–6774 (1989)
70. O.I. Vinogradova, H.-J. Butt, G.E. Yakubov, F. Feuillebois, Dynamic effects on force measurements. I. Viscous drag on the atomic force microscope cantilever. *Rev. Sci. Instrum.* **72**, 2330–2339 (2001)
71. V.S.J. Craig, C. Neto, In situ calibration of colloid probe cantilevers in force microscopy: Hydrodynamic drag on a sphere approaching a wall. *Langmuir* **17**, 6018–6022 (2001)
72. E. Evans, D. Needham, Physical properties of surfactant bilayer membranes: Thermal transitions, elasticity, rigidity, cohesion, and colloidal interactions. *J. Phys. Chem.* **91**, 4219–4228 (1987)
73. E. Evans, D. Needham, Attraction between lipid bilayer membranes in concentrated solutions of nonadsorbing polymers: Comparison of mean-field theory with measurements of adhesion energy. *Macromolecules* **21**, 1822–1831 (1988)
74. S.E. Chesla, P. Selvaraj, C. Zhu, Measuring two-dimensional receptor-ligand binding kinetics by micropipette. *Biophys. J.* **75**, 1553–1572 (1998)
75. E. Evans, K. Ritchie, R. Merkel, Sensitive force technique to probe molecular adhesion and structural linkages at biological interfaces. *Biophys. J.* **68**, 2580–2587 (1995)
76. D.M. LeNeveu, R.P. Rand, V.A. Parsegian, Measurements of forces between lecithin bilayers. *Nature* **259**, 601–603 (1976)
77. A. Homola, A.A. Robertson, A compression method for measuring forces between colloidal particles. *J. Colloid Interface Sci.* **54**, 286–297 (1976)
78. V.A. Parsegian, N. Fuller, R.P. Rand, Measured work of deformation and repulsion of lecithin bilayers. *Proc. Natl. Acad. Sci. USA* **76**, 2750–2754 (1979)
79. R.P. Rand, V.A. Parsegian, Hydration forces between phospholipid bilayers. *Biochim. Biophys. Acta* **988**, 351–376 (1989)
80. S. Leikin, V.A. Parsegian, D.C. Rau, R.P. Rand, Hydration forces. *Annu. Rev. Phys. Chem.* **44**, 369–395 (1993)
81. S. Chu, J.E. Bjorkholm, A. Ashkin, A. Cable, Experimental observation of optically trapped atoms. *Phys. Rev. Lett.* **57**, 314–317 (1986)
82. A. Ashkin, Optical trapping and manipulation of neutral particles using lasers. *Proc. Natl. Acad. Sci. USA* **94**, 4853–4860 (1997)
83. K. Visscher, S.P. Gross, S.M. Block, Construction of multiple-beam optical traps with nanometer-resolution positioning sensing. *IEEE J. Sel. Top. Quantum Electron.* **2**, 1066–1076 (1996)
84. D.C. Prieve, N.A. Frej, Total internal reflection microscopy: A quantitative tool for the measurement of colloidal forces. *Langmuir* **6**, 396–403 (1990)

85. J. Rädler, E. Sackmann, On the measurement of weak repulsive and frictional colloidal forces by reflection interference contrast microscopy. *Langmuir* **8**, 848–853 (1992)
86. P. Bongrand, C. Capo, J.-L. Mege, A.-M. Benoliel, Use of hydrodynamic flows to study cell adhesion. In: *Physical Basis of Cell–Cell Adhesion*, ed. by P. Bongrand (CRC, Boca Raton, 1988), pp. 125–156
87. G. Kaplanski, C. Farnarier, O. Tissot, A. Pierres, A.-M. Benoliel, A.-C. Alessi, S. Kaplanski, P. Bongrand, Granulocyte–endothelium initial adhesion: Analysis of transient binding events mediated by E-selectin in a laminar shear flow. *Biophys. J.* **64**, 1922–1933 (1993)
88. H.B.G. Casimir, D. Polder, The influence of retardation on the London–van der Waals forces. *Phys. Rev.* **73**, 360–372 (1948)
89. H.C. Hamaker, The London–van der Waals attraction between spherical particles. *Physica* **4**, 1058–1072 (1937)
90. E.M. Lifshitz, The theory of molecular attraction forces between solid bodies. *Sov. Phys. JETP* **2**, 73–83 (1956)
91. I.E. Dzyaloshinskii, E.M. Lifshitz, L.P. Pitaevskii, The general theory of van der Waals forces. *Adv. Phys.* **10**, 165–209 (1961)
92. H.W. Fox, W.A. Zisman, The spreading of liquids on low-energy surfaces. III. Hydrocarbon surfaces. *J. Colloid Sci.* **7**, 428–442 (1952)
93. B.V. Derjaguin, V.P. Smilga, Electrostatic component of the rolling friction force moment. *Wear* **7**, 270–281 (1964)
94. R.G. Horn, D.T. Smith, Contact electrification and adhesion between dissimilar materials. *Science* **256**, 362–364 (1992)
95. W.R. Harper, *Contact and frictional electrification* (Laplacian, Morgan Hill, 1998)
96. J.A. Wiles, B.A. Grzybowski, A. Winkleman, G.M. Whitesides, A tool for studying contact electrification in systems comprising metals and insulating polymers. *Anal. Chem.* **75**, 4859–4867 (2003)
97. J. Lowell, A.C. Rose-Innes, Contact electrification. *Adv. Phys.* **29**, 947–1023 (1980)
98. C. Guerret-Piecourt, S. Bec, F. Segualt, D. Juve, D. Treheux, A. Tonck, Adhesion forces due to nano-triboelectrification between similar materials. *Eur. Phys. J. Appl. Phys.* **28**, 65–72 (2004)
99. T. Miura, N. Hirokawa, K. Enokido, I. Arakawa, Spatially resolved spectroscopy of gas discharge during sliding friction between diamond and quartz in N<sub>2</sub> gas. *Appl. Surf. Sci.* **235**, 114–118 (2004)
100. T.E. Fischer, Tribochemistry. *Annu. Rev. Mater. Sci.* **18**, 303–323 (1988)
101. J. Lowell, W.S. Truscott, Triboelectrification of identical insulators. I. An experimental investigation. *J. Phys. D Appl. Phys.* **19**, 1273–1280 (1986)
102. L. Perez-Trejo, J. Perez-Gonzalez, L. de Vargas, E. Moreno, Triboelectrification of molten linear low-density polyethylene under continuous extrusion. *Wear* **257**, 329–337 (2004)
103. K. Ohara, T. Tonouchi, S. Uchiyama, Frictional electrification of thin films deposited by the Langmuir–Blodgett method. *J. Phys. D Appl. Phys.* **23**, 1092–1096 (1990)
104. R. Budakian, S.J. Putterman, Correlation between charge transfer and stick–slip friction at a metal–insulator interface. *Phys. Rev. Lett.* **85**, 1000–1003 (2000)
105. J.V. Wasem, P. Upadhyaya, S.C. Langford, J.T. Dickinson, Transient current generation during wear of high-density polyethylene by a stainless steel stylus. *J. Appl. Phys.* **93**, 719–730 (2003)
106. M. Grätzel, Photoelectrochemical cells. *Nature* **414**, 338–344 (2001)
107. X. Xu, Y. Liu, R.M. German, Reconciliation of sintering theory with sintering practice. *Adv. Powder Metall. Part. Mater.* **5**, 67–78 (2000)
108. R.M. German, *Sintering Theory and Practice* (Wiley, New York, 1996)
109. R. Budakian, S.J. Putterman, Time scales for cold welding and the origins of stick–slip friction. *Phys. Rev. B* **65**, 235429–1–235429–5 (2002)
110. D.H. Buckley, Influence of various physical properties of metals on their friction and wear behavior in vacuum. *Met. Eng. Quart.* **7**, 44–53 (1967)

111. U. Landman, W.D. Luedtke, N.A. Burnham, R.J. Colton, Atomistic mechanisms and dynamics of adhesion, nanoindentation, and fracture. *Science* **248**, 454–461 (1990)
112. U. Landman, W.D. Luedtke, E.M. Ringer, Molecular dynamics simulations of adhesive contact formation and friction. *NATO Sci. Ser. E* **220**, 463–510 (1992)
113. W.D. Luedtke, U. Landman, Solid and liquid junctions. *Comput. Mater. Sci.* **1**, 1–24 (1992)
114. U. Landman, W.D. Luedtke, Interfacial junctions and cavitation. *MRS Bulletin* **18**, 36–44 (1993)
115. B. Bhushan, J.N. Israelachvili, U. Landman, Nanotribology: Friction, wear and lubrication at the atomic scale. *Nature* **374**, 607–616 (1995)
116. M.R. Sørensen, K.W. Jacobsen, P. Stoltze, Simulations of atomic-scale sliding friction. *Phys. Rev. B* **53**, 2101–2113 (1996)
117. A. Meurk, P.F. Luckham, L. Bergström, Direct measurement of repulsive and attractive van der Waals forces between inorganic materials. *Langmuir* **13**, 3896–3899 (1997)
118. S.-W. Lee, W.M. Sigmund, AFM study of repulsive van der Waals forces between Teflon AF thin film and silica or alumina. *Colloids Surf. A* **204**, 43–50 (2002)
119. E.J.W. Verwey, J.T.G. Overbeek, *Theory of the Stability of Lyophobic Colloids*, 1st edn. (Elsevier, Amsterdam, 1948)
120. D.Y.C. Chan, R.M. Pashley, L.R. White, A simple algorithm for the calculation of the electrostatic repulsion between identical charged surfaces in electrolyte. *J. Colloid Interface Sci.* **77**, 283–285 (1980)
121. J.E. Sader, S.L. Carnie, D.Y.C. Chan, Accurate analytic formulas for the double-layer interaction between spheres. *J. Colloid Interface Sci.* **171**, 46–54 (1995)
122. D. Harries, Solving the Poisson–Boltzmann equation for two parallel cylinders. *Langmuir* **14**, 3149–3152 (1998)
123. P. Attard, Recent advances in the electric double layer in colloid science. *Curr. Opin. Colloid Interface Sci.* **6**, 366–371 (2001)
124. B. Derjaguin, L. Landau, Theory of the stability of strongly charged lyophobic sols and of the adhesion of strongly charged particles in solutions of electrolytes. *Acta Physicochim. URSS* **14**, 633–662 (1941)
125. D. Chan, T.W. Healy, L.R. White, Electrical double layer interactions under regulation by surface ionization equilibria – dissimilar amphoteric surfaces. *J. Chem. Soc. Faraday Trans. 1* **72**, 2844–2865 (1976)
126. G.S. Manning, Limiting laws and counterion condensation in polyelectrolyte solutions. I. Colligative properties. *J. Chem. Phys.* **51**, 924–933 (1969)
127. L. Guldbrand, V. Jönsson, H. Wennerström, P. Linse, Electrical double-layer forces: A Monte Carlo study. *J. Chem. Phys.* **80**, 2221–2228 (1984)
128. H. Wennerström, B. Jönsson, P. Linse, The cell model for polyelectrolyte systems. Exact statistical mechanical relations, Monte Carlo simulations, and the Poisson–Boltzmann approximation. *J. Chem. Phys.* **76**, 4665–4670 (1982)
129. J. Marra, Effects of counterion specificity on the interactions between quaternary ammonium surfactants in monolayers and bilayers. *J. Phys. Chem.* **90**, 2145–2150 (1986)
130. J. Marra, Direct measurement of the interaction between phosphatidylglycerol bilayers in aqueous-electrolyte solutions. *Biophys. J.* **50**, 815–825 (1986)
131. B. Jönsson, H. Wennerström, Ion–ion correlations in liquid dispersions. *J. Adhes.* **80**, 339–364 (2004)
132. R.G. Horn, J.N. Israelachvili, Direct measurement of structural forces between two surfaces in a nonpolar liquid. *J. Chem. Phys.* **75**, 1400–1411 (1981)
133. H.K. Christenson, D.W.R. Gruen, R.G. Horn, J.N. Israelachvili, Structuring in liquid alkanes between solid surfaces: Force measurements and mean-field theory. *J. Chem. Phys.* **87**, 1834–1841 (1987)
134. M.L. Gee, J.N. Israelachvili, Interactions of surfactant monolayers across hydrocarbon liquids. *J. Chem. Soc. Faraday Trans.* **86**, 4049–4058 (1990)

135. J.N. Israelachvili, S.J. Kott, M.L. Gee, T.A. Witten, Forces between mica surfaces across hydrocarbon liquids: Effects of branching and polydispersity. *Macromolecules* **22**, 4247–4253 (1989)
136. I.K. Snook, W. van Megen, Solvation forces in simple dense fluids I. *J. Chem. Phys.* **72**, 2907–2913 (1980)
137. W.J. van Megen, I.K. Snook, Solvation forces in simple dense fluids II. Effect of chemical potential. *J. Chem. Phys.* **74**, 1409–1411 (1981)
138. R. Kjellander, S. Marcelja, Perturbation of hydrogen bonding in water near polar surfaces. *Chem. Phys. Lett.* **120**, 393–396 (1985)
139. P. Tarazona, L. Vicente, A model for the density oscillations in liquids between solid walls. *Mol. Phys.* **56**, 557–572 (1985)
140. D. Henderson, M. Lozada-Cassou, A simple theory for the force between spheres immersed in a fluid. *J. Colloid Interface Sci.* **114**, 180–183 (1986)
141. J.E. Curry, J.H. Cushman, Structure in confined fluids: Phase separation of binary simple liquid mixtures. *Tribol. Lett.* **4**, 129–136 (1998)
142. M. Schoen, T. Gruhn, D.J. Diestler, Solvation forces in thin films confined between macroscopically curved substrates. *J. Chem. Phys.* **109**, 301–311 (1998)
143. F. Porcheron, B. Rousseau, M. Schoen, A.H. Fuchs, Structure and solvation forces in confined alkane films. *Phys. Chem. Chem. Phys.* **3**, 1155–1159 (2001)
144. J. Gao, W.D. Luedtke, U. Landman, Layering transitions and dynamics of confined liquid films. *Phys. Rev. Lett.* **79**, 705–708 (1997)
145. H.K. Christenson, Forces between solid surfaces in a binary mixture of non-polar liquids. *Chem. Phys. Lett.* **118**, 455–458 (1985)
146. H.K. Christenson, R.G. Horn, Solvation forces measured in non-aqueous liquids. *Chem. Scr.* **25**, 37–41 (1985)
147. J. Israelachvili, Solvation forces and liquid structure, as probed by direct force measurements. *Acc. Chem. Res.* **20**, 415–421 (1987)
148. H.K. Christenson, Non-DLVO forces between surfaces – solvation, hydration and capillary effects. *J. Disp. Sci. Technol.* **9**, 171–206 (1988)
149. V. Franz, H.-J. Butt, Confined liquids: Solvation forces in liquid alcohols between solid surfaces. *J. Phys. Chem. B* **106**, 1703–1708 (2002)
150. L.J.D. Frink, F. van Swol, Solvation forces between rough surfaces. *J. Chem. Phys.* **108**, 5588–5598 (1998)
151. J. Gao, W.D. Luedtke, U. Landman, Structures, solvation forces and shear of molecular films in a rough nano-confinement. *Tribol. Lett.* **9**, 3–13 (2000)
152. H.E. Stanley, J. Teixeira, Interpretation of the unusual behavior of H<sub>2</sub>O and D<sub>2</sub>O at low temperatures: Tests of a percolation model. *J. Chem. Phys.* **73**, 3404–3422 (1980)
153. H. van Olphen, *An Introduction to Clay Colloid Chemistry*, 2nd edn. (Wiley, New York, 1977), Chap. 10
154. N. Alcantar, J. Israelachvili, J. Boles, Forces and ionic transport between mica surfaces: Implications for pressure solution, *Geochim. Cosmochim. Acta* **67**, 1289–1304 (2003)
155. U. Del Pennino, E. Mazzega, S. Valeri, A. Alietti, M.F. Brigatti, L. Poppi, Interlayer water and swelling properties of monoionic montmorillonites. *J. Colloid Interface Sci.* **84**, 301–309 (1981)
156. B.E. Viani, P.F. Low, C.B. Roth, Direct measurement of the relation between interlayer force and interlayer distance in the swelling of montmorillonite. *J. Colloid Interface Sci.* **96**, 229–244 (1983)
157. R.G. Horn, Surface forces and their action in ceramic materials. *J. Am. Ceram. Soc.* **73**, 1117–1135 (1990)
158. B.V. Velamakanni, J.C. Chang, F.F. Lange, D.S. Pearson, New method for efficient colloidal particle packing via modulation of repulsive lubricating hydration forces. *Langmuir* **6**, 1323–1325 (1990)

159. R.R. Lessard, S.A. Zieminski, Bubble coalescence and gas transfer in aqueous electrolytic solutions. *Ind. Eng. Chem. Fundam.* **10**, 260–269 (1971)
160. J. Israelachvili, R. Pashley, The hydrophobic interaction is long range, decaying exponentially with distance. *Nature* **300**, 341–342 (1982)
161. R.M. Pashley, P.M. McGuiggan, B.W. Ninham, D.F. Evans, Attractive forces between uncharged hydrophobic surfaces: Direct measurements in aqueous solutions. *Science* **229**, 1088–1089 (1985)
162. P.M. Claesson, C.E. Blom, P.C. Herder, B.W. Ninham, Interactions between water-stable hydrophobic Langmuir–Blodgett monolayers on mica. *J. Colloid Interface Sci.* **114**, 234–242 (1986)
163. Y.I. Rabinovich, B.V. Derjaguin, Interaction of hydrophobized filaments in aqueous electrolyte solutions. *Colloids Surf.* **30**, 243–251 (1988)
164. J.L. Parker, D.L. Cho, P.M. Claesson, Plasma modification of mica: Forces between fluorocarbon surfaces in water and a nonpolar liquid. *J. Phys. Chem.* **93**, 6121–6125 (1989)
165. H.K. Christenson, J. Fang, B.W. Ninham, J.L. Parker, Effect of divalent electrolyte on the hydrophobic attraction. *J. Phys. Chem.* **94**, 8004–8006 (1990)
166. K. Kurihara, S. Kato, T. Kunitake, Very strong long range attractive forces between stable hydrophobic monolayers of a polymerized ammonium surfactant. *Chem. Lett.* **19**, 1555–1558 (1990)
167. Y.H. Tsao, D.F. Evans, H. Wennerstrom, Long-range attractive force between hydrophobic surfaces observed by atomic force microscopy. *Science* **262**, 547–550 (1993)
168. Y.I. Rabinovich, R.-H. Yoon, Use of atomic force microscope for the measurements of hydrophobic forces between silanated silica plate and glass sphere. *Langmuir* **10**, 1903–1909 (1994)
169. V.S.J. Craig, B.W. Ninham, R.M. Pashley, Study of the long-range hydrophobic attraction in concentrated salt solutions and its implications for electrostatic models. *Langmuir* **14**, 3326–3332 (1998)
170. P. Kékicheff, O. Spalla, Long-range electrostatic attraction between similar, charge-neutral walls. *Phys. Rev. Lett.* **75**, 1851–1854 (1995)
171. H.K. Christenson, P.M. Claesson, Direct measurements of the force between hydrophobic surfaces in water. *Adv. Colloid Interface Sci.* **91**, 391–436 (2001)
172. P. Attard, Nanobubbles and the hydrophobic attraction. *Adv. Colloid Interface Sci.* **104**, 75–91 (2003)
173. J.L. Parker, P.M. Claesson, P. Attard, Bubbles, cavities, and the long-ranged attraction between hydrophobic surfaces. *J. Phys. Chem.* **98**, 8468–8480 (1994)
174. T. Ederth, B. Liedberg, Influence of wetting properties on the long-range “hydrophobic” interaction between self-assembled alkylthiolate monolayers. *Langmuir* **16**, 2177–2184 (2000)
175. S. Ohnishi, V.V. Yaminsky, H.K. Christenson, Measurements of the force between fluorocarbon monolayer surfaces in air and water. *Langmuir* **16**, 8360–8367 (2000)
176. Q. Lin, E.E. Meyer, M. Tadmor, J.N. Israelachvili, T.L. Kuhl, Measurement of the long- and short-range hydrophobic attraction between surfactant-coated surfaces. *Langmuir* **21**, 251–255 (2005)
177. E.E. Meyer, Q. Lin, J.N. Israelachvili, Effects of dissolved gas on the hydrophobic attraction between surfactant-coated surfaces. *Langmuir* **21**, 256–259 (2005)
178. E.E. Meyer, Q. Lin, T. Hassenkam, E. Oroudjev, J. Israelachvili, Origin of the long-range attraction between surfactant-coated surfaces. *Proc. Natl. Acad. Sci. USA* **102**, 6839–6842 (2005)
179. M. Hato, Attractive forces between surfaces of controlled “hydrophobicity” across water, A possible range of “hydrophobic interactions” between macroscopic hydrophobic surfaces across water. *J. Phys. Chem.* **100**, 18530–18538 (1996)
180. H.K. Christenson, V.V. Yaminsky, Is long-range hydrophobic attraction related to the mobility of hydrophobic surface groups?. *Colloids Surf. A* **129–130**, 67–74 (1997)

181. H.K. Christenson, P.M. Claesson, J. Berg, P.C. Herder, Forces between fluorocarbon surfactant monolayers: Salt effects on the hydrophobic interaction. *J. Phys. Chem.* **93**, 1472–1478 (1989)
182. N.I. Christou, J.S. Whitehouse, D. Nicholson, N.G. Parsonage, A Monte Carlo study of fluid water in contact with structureless walls. *Faraday Symp. Chem. Soc.* **16**, 139–149 (1981)
183. B. Jönsson, Monte Carlo simulations of liquid water between two rigid walls. *Chem. Phys. Lett.* **82**, 520–525 (1981)
184. S. Marcelja, D.J. Mitchell, B.W. Ninham, M.J. Sculley, Role of solvent structure in solution theory. *J. Chem. Soc. Faraday Trans. II* **73**, 630–648 (1977)
185. D.W.R. Gruen, S. Marcelja, Spatially varying polarization in water: A model for the electric double layer and the hydration force. *J. Chem. Soc. Faraday Trans. 2* **79**, 225–242 (1983)
186. B. Jönsson, H. Wennerström, Image-charge forces in phospholipid bilayer systems. *J. Chem. Soc. Faraday Trans. 2* **79**, 19–35 (1983)
187. D. Schiby, E. Ruckenstein, The role of the polarization layers in hydration forces. *Chem. Phys. Lett.* **95**, 435–438 (1983)
188. A. Luzar, D. Bratko, L. Blum, Monte Carlo simulation of hydrophobic interaction. *J. Chem. Phys.* **86**, 2955–2959 (1987)
189. P. Attard, M.T. Batchelor, A mechanism for the hydration force demonstrated in a model system. *Chem. Phys. Lett.* **149**, 206–211 (1988)
190. J. Forsman, C.E. Woodward, B. Jönsson, Repulsive hydration forces and attractive hydrophobic forces in a unified picture. *J. Colloid Interface Sci.* **195**, 264–266 (1997)
191. E. Ruckenstein, M. Manciu, The coupling between the hydration and double layer interactions. *Langmuir* **18**, 7584–7593 (2002)
192. K. Leung, A. Luzar, Dynamics of capillary evaporation. II. Free energy barriers. *J. Chem. Phys.* **113**, 5845–5852 (2000)
193. D. Bratko, R.A. Curtis, H.W. Blanch, J.M. Prausnitz, Interaction between hydrophobic surfaces with metastable intervening liquid. *J. Chem. Phys.* **115**, 3873–3877 (2001)
194. J.R. Grigera, S.G. Kalko, J. Fischbarg, Wall–water interface. A molecular dynamics study. *Langmuir* **12**, 154–158 (1996)
195. M. Mao, J. Zhang, R.-H. Yoon, W.A. Ducker, Is there a thin film of air at the interface between water and smooth hydrophobic solids?. *Langmuir* **20**, 1843–1849 (2004), Erratum: *Langmuir* **20**, 4310 (2004)
196. Y. Zhu, S. Granick, Rate-dependent slip of Newtonian liquid at smooth surfaces. *Phys. Rev. Lett.* **87**, 096105–1–096105–4 (2001)
197. D. Andrienko, B. Dunweg, O.I. Vinogradova, Boundary slip as a result of a prewetting transition. *J. Chem. Phys.* **119**, 13106–13112 (2003)
198. P.G. de Gennes, Polymers at an interface. 2. Interaction between two plates carrying adsorbed polymer layers. *Macromolecules* **15**, 492–500 (1982)
199. J.M.H.M. Scheutjens, G.J. Fleer, Interaction between two adsorbed polymer layers. *Macromolecules* **18**, 1882–1900 (1985)
200. E.A. Evans, Force between surfaces that confine a polymer solution: Derivation from self-consistent field theories. *Macromolecules* **22**, 2277–2286 (1989)
201. H.J. Ploehn, Compression of polymer interphases. *Macromolecules* **27**, 1627–1636 (1994)
202. J. Ennis, B. Jönsson, Interactions between surfaces in the presence of ideal adsorbing block copolymers. *J. Phys. Chem. B* **103**, 2248–2255 (1999)
203. S. Asakura, F. Oosawa, Interaction between particles suspended in solutions of macromolecules. *J. Polym. Sci.* **33**, 183–192 (1958)
204. J.F. Joanny, L. Leibler, P.G. de Gennes, Effects of polymer solutions on colloid stability. *J. Polym. Sci. Polym. Phys.* **17**, 1073–1084 (1979)
205. B. Vincent, P.F. Luckham, F.A. Waite, The effect of free polymer on the stability of sterically stabilized dispersions. *J. Colloid Interface Sci.* **73**, 508–521 (1980)
206. R.I. Feigin, D.H. Napper, Stabilization of colloids by free polymer. *J. Colloid Interface Sci.* **74**, 567–571 (1980)

207. P.G. de Gennes, Polymer solutions near an interface. 1. Adsorption and depletion layers. *Macromolecules* **14**, 1637–1644 (1981)
208. G.J. Fleer, R. Tuinier, Concentration and solvency effects on polymer depletion and the resulting pair interaction of colloidal particles in a solution of non-adsorbing polymer. *Polym. Prepr.* **46**, 366 (2005)
209. H.J. Taunton, C. Toprakcioglu, L.J. Fetters, J. Klein, Interactions between surfaces bearing end-adsorbed chains in a good solvent. *Macromolecules* **23**, 571–580 (1990)
210. J. Klein, P. Luckham, Forces between two adsorbed poly(ethylene oxide) layers immersed in a good aqueous solvent. *Nature* **300**, 429–431 (1982)
211. J. Klein, P.F. Luckham, Long-range attractive forces between two mica surfaces in an aqueous polymer solution. *Nature* **308**, 836–837 (1984)
212. P.F. Luckham, J. Klein, Forces between mica surfaces bearing adsorbed homopolymers in good solvents. *J. Chem. Soc. Faraday Trans.* **86**, 1363–1368 (1990)
213. P.G. de Gennes, Polymers at an interface; a simplified view. *Adv. Colloid Interface Sci.* **27**, 189–209 (1987)
214. S. Alexander, Adsorption of chain molecules with a polar head. A scaling description. *J. Phys.* **38**, 983–987 (1977)
215. P.G. de Gennes, Conformations of polymers attached to an interface. *Macromolecules* **13**, 1069–1075 (1980)
216. S.T. Milner, T.A. Witten, M.E. Cates, Theory of the grafted polymer brush. *Macromolecules* **21**, 2610–2619 (1988)
217. S.T. Milner, T.A. Witten, M.E. Cates, Effects of polydispersity in the end-grafted polymer brush. *Macromolecules* **22**, 853–861 (1989)
218. E.B. Zhulina, O.V. Borisov, V.A. Priamitsyn, Theory of steric stabilization of colloid dispersions by grafted polymers. *J. Colloid Interface Sci.* **137**, 495–511 (1990)
219. J. Klein, E. Kumacheva, D. Mahalu, D. Perahia, L.J. Fetters, Reduction of frictional forces between solid surfaces bearing polymer brushes. *Nature* **370**, 634–636 (1994)
220. D. Goodman, J.N. Kizhakkedathu, D.E. Brooks, Evaluation of an atomic force microscopy pull-off method for measuring molecular weight and polydispersity of polymer brushes: Effect of grafting density. *Langmuir* **20**, 6238–6245 (2004)
221. T.J. McIntosh, A.D. Magid, S.A. Simon, Range of the solvation pressure between lipid membranes: Dependence on the packing density of solvent molecules. *Biochemistry* **28**, 7904–7912 (1989)
222. P.K.T. Persson, B.A. Bergenstähl, Repulsive forces in lecithin glycol lamellar phases. *Biophys. J.* **47**, 743–746 (1985)
223. J.N. Israelachvili, H. Wennerström, Hydration or steric forces between amphiphilic surfaces?. *Langmuir* **6**, 873–876 (1990)
224. J.N. Israelachvili, H. Wennerström, Entropic forces between amphiphilic surfaces in liquids. *J. Phys. Chem.* **96**, 520–531 (1992)
225. M.K. Granfeldt, S.J. Miklavic, A simulation study of flexible zwitterionic monolayers. Interlayer interaction and headgroup conformation. *J. Phys. Chem.* **95**, 6351–6360 (1991)
226. G. Pabst, J. Katsaras, V.A. Raghunathan, Enhancement of steric repulsion with temperature in oriented lipid multilayers. *Phys. Rev. Lett.* **88**, 128101–1–128101–4 (2002)
227. L.R. Fisher, J.N. Israelachvili, Direct measurements of the effect of meniscus forces on adhesion: A study of the applicability of macroscopic thermodynamics to microscopic liquid interfaces. *Colloids Surf.* **3**, 303–319 (1981)
228. H.K. Christenson, Adhesion between surfaces in unsaturated vapors – A reexamination of the influence of meniscus curvature and surface forces. *J. Colloid Interface Sci.* **121**, 170–178 (1988)
229. H. Hertz, Über die Berührung fester elastischer Körper. *J. Reine Angew. Math.* **92**, 156–171 (1881)
230. H.M. Pollock, D. Maugis, M. Barquins, The force of adhesion between solid surfaces in contact. *Appl. Phys. Lett.* **33**, 798–799 (1978)



231. B.V. Derjaguin, V.M. Muller, Y.P. Toporov, Effect of contact deformations on the adhesion of particles. *J. Colloid Interface Sci.* **53**, 314–326 (1975)
232. V.M. Muller, V.S. Yushchenko, B.V. Derjaguin, On the influence of molecular forces on the deformation of an elastic sphere and its sticking to a rigid plane. *J. Colloid Interface Sci.* **77**, 91–101 (1980)
233. V.M. Muller, B.V. Derjaguin, Y.P. Toporov, On 2 methods of calculation of the force of sticking of an elastic sphere to a rigid plane. *Colloids Surf.* **7**, 251–259 (1983)
234. D. Tabor, Surface forces and surface interactions. *J. Colloid Interface Sci.* **58**, 2–13 (1977)
235. D. Maugis, Adhesion of spheres, The JKR–DMT transition using a Dugdale model. *J. Colloid Interface Sci.* **150**, 243–269 (1992)
236. R.G. Horn, J.N. Israelachvili, F. Pribac, Measurement of the deformation and adhesion of solids in contact. *J. Colloid Interface Sci.* **115**, 480–492 (1987)
237. V. Mangipudi, M. Tirrell, A.V. Pocius, Direct measurement of molecular level adhesion between poly(ethylene terephthalate) and polyethylene films: Determination of surface and interfacial energies. *J. Adhes. Sci. Technol.* **8**, 1251–1270 (1994)
238. H.K. Christenson, Surface deformations in direct force measurements. *Langmuir* **12**, 1404–1405 (1996)
239. M. Barquins, D. Maugis, Fracture mechanics and the adherence of viscoelastic bodies. *J. Phys. D Appl. Phys.* **11**, 1989–2023 (1978)
240. I. Sridhar, K.L. Johnson, N.A. Fleck, Adhesion mechanics of the surface force apparatus. *J. Phys. D Appl. Phys.* **30**, 1710–1719 (1997)
241. I. Sridhar, Z.W. Zheng, K.L. Johnson, A detailed analysis of adhesion mechanics between a compliant elastic coating and a spherical probe. *J. Phys. D Appl. Phys.* **37**, 2886–2895 (2004)
242. J.A. Greenwood, J.B.P. Williamson, Contact of nominally flat surfaces. *Proc. R. Soc. Lond. A* **295**, 300–319 (1966)
243. B.N.J. Persson, Elastoplastic contact between randomly rough surfaces. *Phys. Rev. Lett.* **87**, 116101–1–116101–4 (2001)
244. F.P. Bowden, D. Tabor, *An Introduction to Tribology* (Anchor/Doubleday, Garden City, 1973)
245. D. Maugis, H.M. Pollock, Surface forces, deformation and adherence at metal microcontacts. *Acta Metall.* **32**, 1323–1334 (1984)
246. K.N.G. Fuller, D. Tabor, The effect of surface roughness on the adhesion of elastic solids. *Proc. R. Soc. Lond. A* **345**, 327–342 (1975)
247. D. Maugis, On the contact and adhesion of rough surfaces. *J. Adhes. Sci. Technol.* **10**, 161–175 (1996)
248. B.N.J. Persson, E. Tosatti, The effect of surface roughness on the adhesion of elastic solids. *J. Chem. Phys.* **115**, 5597–5610 (2001)
249. H.-C. Kim, T.P. Russell, Contact of elastic solids with rough surfaces. *J. Polym. Sci. Polym. Phys.* **39**, 1848–1854 (2001)
250. P.M. McGuiggan, J.N. Israelachvili, Adhesion and short-range forces between surfaces. Part II: Effects of surface lattice mismatch. *J. Mater. Res.* **5**, 2232–2243 (1990)
251. P.M. McGuiggan, J. Israelachvili, Measurements of the effects of angular lattice mismatch on the adhesion energy between two mica surfaces in water. *Mater. Res. Soc. Symp. Proc.* **138**, 349–360 (1989)
252. C.L. Rhykerd Jr., M. Schoen, D.J. Diestler, J.H. Cushman, Epitaxy in simple classical fluids in micropores and near-solid surfaces. *Nature* **330**, 461–463 (1987)
253. M. Schoen, D.J. Diestler, J.H. Cushman, Fluids in micropores. I. Structure of a simple classical fluid in a slit-pore. *J. Chem. Phys.* **87**, 5464–5476 (1987)
254. M. Schoen, C.L. Rhykerd Jr., D.J. Diestler, J.H. Cushman, Shear forces in molecularly thin films. *Science* **245**, 1223–1225 (1989)
255. P.A. Thompson, M.O. Robbins, Origin of stick–slip motion in boundary lubrication. *Science* **250**, 792–794 (1990)

256. K.K. Han, J.H. Cushman, D.J. Diestler, Grand canonical Monte Carlo simulations of a Stockmayer fluid in a slit micropore. *Mol. Phys.* **79**, 537–545 (1993)
257. M. Ruths, S. Granick, Influence of alignment of crystalline confining surfaces on static forces and shear in a liquid crystal, 4'-n-pentyl-4-cyanobiphenyl (5CB). *Langmuir* **16**, 8368–8376 (2000)
258. A.D. Berman, Dynamics of molecules at surfaces. Ph.D. Thesis (University of California, Santa Barbara, 1996)
259. F.P. Bowden, D. Tabor, *The Friction and Lubrication of Solids* (Clarendon, London, 1971)
260. J.A. Greenwood, K.L. Johnson, The mechanics of adhesion of viscoelastic solids. *Philos. Mag. A* **43**, 697–711 (1981)
261. D. Maugis, Subcritical crack growth, surface energy, fracture toughness, stick-slip and embrittlement. *J. Mater. Sci.* **20**, 3041–3073 (1985)
262. F. Michel, M.E.R. Shanahan, Kinetics of the JKR experiment. *C. R. Acad. Sci. II* **310**, 17–20 (1990)
263. E. Barthel, S. Roux, Velocity dependent adherence: An analytical approach for the JKR and DMT models. *Langmuir* **16**, 8134–8138 (2000)
264. M. Ruths, S. Granick, Rate-dependent adhesion between polymer and surfactant monolayers on elastic substrates. *Langmuir* **14**, 1804–1814 (1998)
265. H. Yoshizawa, Y.L. Chen, J. Israelachvili, Fundamental mechanisms of interfacial friction. I: Relation between adhesion and friction. *J. Phys. Chem.* **97**, 4128–4140 (1993)
266. N. Maeda, N. Chen, M. Tirrell, J.N. Israelachvili, Adhesion and friction mechanisms of polymer-on-polymer surfaces. *Science* **297**, 379–382 (2002)
267. C.A. Miller, P. Neogi, *Interfacial Phenomena: Equilibrium and Dynamic Effects* (Dekker, New York, 1985)
268. J. Israelachvili, A. Berman, Irreversibility, energy dissipation, and time effects in intermolecular and surface interactions. *Israel J. Chem.* **35**, 85–91 (1995)
269. A.N. Gent, A.J. Kinloch, Adhesion of viscoelastic materials to rigid substrates. III. Energy criterion for failure. *J. Polym. Sci. A-2* **9**, 659–668 (1971)
270. A.N. Gent, Adhesion and strength of viscoelastic solids. Is there a relationship between adhesion and bulk properties?. *Langmuir* **12**, 4492–4496 (1996)
271. H.R. Brown, The adhesion between polymers. *Annu. Rev. Mater. Sci.* **21**, 463–489 (1991)
272. M. Deruelle, M. Tirrell, Y. Marciano, H. Hervet, L. Léger, Adhesion energy between polymer networks and solid surfaces modified by polymer attachment. *Faraday Discuss.* **98**, 55–65 (1995)
273. S. Granick, Motions and relaxations of confined liquids. *Science* **253**, 1374–1379 (1991)
274. H.W. Hu, S. Granick, Viscoelastic dynamics of confined polymer melts. *Science* **258**, 1339–1342 (1992)
275. J. Van Alsten, S. Granick, The origin of static friction in ultrathin liquid films. *Langmuir* **6**, 876–880 (1990)
276. H.-W. Hu, G.A. Carson, S. Granick, Relaxation time of confined liquids under shear. *Phys. Rev. Lett.* **66**, 2758–2761 (1991)
277. M.L. Gee, P.M. McGuigan, J.N. Israelachvili, A.M. Homola, Liquid to solidlike transitions of molecularly thin films under shear. *J. Chem. Phys.* **93**, 1895–1906 (1990)
278. J. Israelachvili, M. Gee, P. McGuigan, P. Thompson, M. Robbins, Melting-freezing transitions in molecularly thin liquid films during shear, Fall Meet. Mater. Res. Soc., Boston, ed. by J.M. Drake, J. Klafter, R. Kopelman (MRS, Pittsburgh, 1990), pp. 3–6
279. J. Israelachvili, P. McGuigan, M. Gee, A. Homola, M. Robbins, P. Thompson, Liquid dynamics in molecularly thin films. *J. Phys. Condens. Matter* **2**, SA89–SA98 (1990)
280. J. Klein, E. Kumacheva, Confinement-induced phase transitions in simple liquids. *Science* **269**, 816–819 (1995)
281. A.L. Demirel, S. Granick, Glasslike transition of a confined simple fluid. *Phys. Rev. Lett.* **77**, 2261–2264 (1996)

282. D. Dowson, *History of Tribology*, 2nd edn. (Professional Engineering Publishing, London, 1998)
283. A. Berman, C. Drummond, J. Israelachvili, Amontons' law at the molecular level. *Tribol. Lett.* **4**, 95–101 (1998)
284. M. Ruths, Boundary friction of aromatic self-assembled monolayers, Comparison of systems with one or both sliding surfaces covered with a thiol monolayer. *Langmuir* **19**, 6788–6795 (2003)
285. D. Gourdon, J.N. Israelachvili, Transitions between smooth and complex stick-slip sliding of surfaces. *Phys. Rev. E* **68**, 021602–1–021602–10 (2003)
286. M. Ruths, N.A. Alcantar, J.N. Israelachvili, Boundary friction of aromatic silane self-assembled monolayers measured with the surface forces apparatus and friction force microscopy. *J. Phys. Chem. B* **107**, 11149–11157 (2003)
287. J. Gao, W.D. Luedtke, D. Gourdon, M. Ruths, J.N. Israelachvili, U. Landman, Frictional forces and Amontons' law: From the molecular to the macroscopic scale. *J. Phys. Chem. B* **108**, 3410–3425 (2004)
288. D. Tabor, The role of surface and intermolecular forces in thin film lubrication. *Tribol. Ser.* **7**, 651–682 (1982)
289. M.J. Sutcliffe, S.R. Taylor, A. Cameron, Molecular asperity theory of boundary friction. *Wear* **51**, 181–192 (1978)
290. G.M. McClelland, Friction at weakly interacting interfaces. In, *Adhesion and Friction*, ed. by M. Grunze, H.J. Kreuzer (Springer, Berlin, Heidelberg, 1989), pp. 1–16
291. D.H. Buckley, The metal-to-metal interface and its effect on adhesion and friction. *J. Colloid Interface Sci.* **58**, 36–53 (1977)
292. J.N. Israelachvili, Y.-L. Chen, H. Yoshizawa, Relationship between adhesion and friction forces. *J. Adhes. Sci. Technol.* **8**, 1231–1249 (1994)
293. J.-C. Géminard, W. Losert, J.P. Gollub, Frictional mechanics of wet granular material. *Phys. Rev. E* **59**, 5881–5890 (1999)
294. R.G. Cain, N.W. Page, S. Biggs, Microscopic and macroscopic aspects of stick–slip motion in granular shear. *Phys. Rev. E* **64**, 016413–1–016413–8 (2001)
295. V. Zaloj, M. Urbakh, J. Klafter, Modifying friction by manipulating normal response to lateral motion. *Phys. Rev. Lett.* **82**, 4823–4826 (1999)
296. A. Dhinojwala, S.C. Bae, S. Granick, Shear-induced dilation of confined liquid films. *Tribol. Lett.* **9**, 55–62 (2000)
297. L.M. Qian, G. Luengo, E. Perez, Thermally activated lubrication with alkanes: The effect of chain length. *Europhys. Lett.* **61**, 268–274 (2003)
298. B.J. Briscoe, D.C.B. Evans, D. Tabor, The influence of contact pressure and saponification on the sliding behavior of steric acid monolayers. *J. Colloid Interface Sci.* **61**, 9–13 (1977)
299. M. Urbakh, L. Daikhin, J. Klafter, Dynamics of confined liquids under shear. *Phys. Rev. E* **51**, 2137–2141 (1995)
300. M.G. Rozman, M. Urbakh, J. Klafter, Origin of stick–slip motion in a driven two-wave potential. *Phys. Rev. E* **54**, 6485–6494 (1996)
301. M.G. Rozman, M. Urbakh, J. Klafter, Stick–slip dynamics as a probe of frictional forces. *Europhys. Lett.* **39**, 183–188 (1997)
302. M. Urbakh, J. Klafter, D. Gourdon, J. Israelachvili, The nonlinear nature of friction. *Nature* **430**, 525–528 (2004)
303. B.V. Derjaguin, Molekulartheorie der äußeren Reibung. *Z. Phys.* **88**, 661–675 (1934)
304. B.V. Derjaguin, Mechanical properties of the boundary lubrication layer. *Wear* **128**, 19–27 (1988)
305. B.J. Briscoe, D.C.B. Evans, The shear properties of Langmuir–Blodgett layers. *Proc. R. Soc. Lond. A* **380**, 389–407 (1982)
306. A. Berman, J. Israelachvili, Control and minimization of friction via surface modification. *NATO ASI Ser. E Appl. Sci.* **330**, 317–329 (1997)

307. P.F. Luckham, S. Manimaaran, Investigating adsorbed polymer layer behaviour using dynamic surface force apparatuses – A review. *Adv. Colloid Interface Sci.* **73**, 1–46 (1997)
308. A.M. Homola, J.N. Israelachvili, P.M. McGuiggan, M.L. Gee, Fundamental experimental studies in tribology: The transition from “interfacial” friction of undamaged molecularly smooth surfaces to “normal” friction with wear. *Wear* **136**, 65–83 (1990)
309. S. Yamada, J. Israelachvili, Friction and adhesion hysteresis of fluorocarbon surfactant monolayer-coated surfaces measured with the surface forces apparatus. *J. Phys. Chem. B* **102**, 234–244 (1998)
310. G. Luengo, S.E. Campbell, V.I. Srdanov, F. Wudl, J.N. Israelachvili, Direct measurement of the adhesion and friction of smooth C<sub>60</sub> surfaces. *Chem. Mater.* **9**, 1166–1171 (1997)
311. L. Rapoport, Y. Bilik, Y. Feldman, M. Homyonfer, S.R. Cohen, R. Tenne, Hollow nanoparticles of WS<sub>2</sub> as potential solid-state lubricants. *Nature* **387**, 791–793 (1997)
312. J. Israelachvili, Y.-L. Chen, H. Yoshizawa, Relationship between adhesion and friction forces. In: *Fundamentals of Adhesion and Interfaces*, ed. by D.S. Rimai, L.P. DeMejo, K.L. Mittal (VSP, Utrecht, 1995), pp. 261–279
313. U. Raviv, S. Perkin, P. Laurat, J. Klein, Fluidity of water confined down to subnanometer films. *Langmuir* **20**, 5322–5332 (2004)
314. P. Berthoud, T. Baumberger, C. G’Sell, J.M. Hiver, Physical analysis of the state- and rate-dependent friction law: Static friction. *Phys. Rev. B* **59**, 14313–14327 (1999)
315. G. He, M. Müser, M. Robbins, Adsorbed layers and the origin of static friction. *Science* **284**, 1650–1652 (1999)
316. M.H. Müser, L. Wenning, M.O. Robbins, Simple microscopic theory of Amontons’s laws for static friction. *Phys. Rev. Lett.* **86**, 1295–1298 (2001)
317. B. Luan, M.O. Robbins, The breakdown of continuum models for mechanical contacts. *Nature* **435**, 929–932 (2005)
318. A. Berman, S. Steinberg, S. Campbell, A. Ulman, J. Israelachvili, Controlled microtribology of a metal oxide surface. *Tribol. Lett.* **4**, 43–48 (1998)
319. D.Y.C. Chan, R.G. Horn, The drainage of thin liquid films between solid surfaces. *J. Chem. Phys.* **83**, 5311–5324 (1985)
320. J.N. Israelachvili, S.J. Kott, Shear properties and structure of simple liquids in molecularly thin films: The transition from bulk (continuum) to molecular behavior with decreasing film thickness. *J. Colloid Interface Sci.* **129**, 461–467 (1989)
321. T.L. Kuhl, A.D. Berman, S.W. Hui, J.N. Israelachvili, Part 1: Direct measurement of depletion attraction and thin film viscosity between lipid bilayers in aqueous polyethylene glycol solutions. *Macromolecules* **31**, 8250–8257 (1998)
322. S.E. Campbell, G. Luengo, V.I. Srdanov, F. Wudl, J.N. Israelachvili, Very low viscosity at the solid–liquid interface induced by adsorbed C<sub>60</sub> monolayers. *Nature* **382**, 520–522 (1996)
323. J. Klein, Y. Kamiyama, H. Yoshizawa, J.N. Israelachvili, G.H. Fredrickson, P. Pincus, L.J. Fetters, Lubrication forces between surfaces bearing polymer brushes. *Macromolecules* **26**, 5552–5560 (1993)
324. G. Luengo, J. Israelachvili, A. Dhinojwala, S. Granick, Generalized effects in confined fluids: New friction map for boundary lubrication. *Wear* **200**, 328–335 (1996), Erratum: *Wear* **205** 246 (1997)
325. E. Kumacheva, J. Klein, Simple liquids confined to molecularly thin layers. II. Shear and frictional behavior of solidified films. *J. Chem. Phys.* **108**, 7010–7022 (1998)
326. P.A. Thompson, G.S. Grest, M.O. Robbins, Phase transitions and universal dynamics in confined films. *Phys. Rev. Lett.* **68**, 3448–3451 (1992)
327. Y. Rabin, I. Hersht, Thin liquid layers in shear: Non-Newtonian effects. *Physica A* **200**, 708–712 (1993)
328. P.A. Thompson, M.O. Robbins, G.S. Grest, Structure and shear response in nanometer-thick films. *Israel J. Chem.* **35**, 93–106 (1995)

329. M. Urbakh, L. Daikhin, J. Klafter, Sheared liquids in the nanoscale range. *J. Chem. Phys.* **103**, 10707–10713 (1995)
330. A. Subbotin, A. Semenov, E. Manias, G. Hadzioannou, G. ten Brinke, Rheology of confined polymer melts under shear flow: Strong adsorption limit. *Macromolecules* **28**, 1511–1515 (1995)
331. A. Subbotin, A. Semenov, E. Manias, G. Hadzioannou, G. ten Brinke, Rheology of confined polymer melts under shear flow: Weak adsorption limit. *Macromolecules* **28**, 3901–3903 (1995)
332. J. Huh, A. Balazs, Behavior of confined telechelic chains under shear. *J. Chem. Phys.* **113**, 2025–2031 (2000)
333. J.N. Israelachvili, P.M. McGuiggan, A.M. Homola, Dynamic properties of molecularly thin liquid films. *Science* **240**, 189–191 (1988)
334. A.M. Homola, H.V. Nguyen, G. Hadzioannou, Influence of monomer architecture on the shear properties of molecularly thin polymer melts. *J. Chem. Phys.* **94**, 2346–2351 (1991)
335. M. Schoen, S. Hess, D.J. Diestler, Rheological properties of confined thin films. *Phys. Rev. E* **52**, 2587–2602 (1995)
336. H. Xie, K. Song, D.J. Mann, W.L. Hase, Temperature gradients and frictional energy dissipation in the sliding of hydroxylated  $\alpha$ -alumina surfaces. *Phys. Chem. Chem. Phys.* **4**, 5377–5385 (2002)
337. U. Landman, W.D. Luedtke, A. Nitzan, Dynamics of tip-substrate interactions in atomic force microscopy. *Surf. Sci.* **210**, L177–L184 (1989)
338. M. Heuberger, C. Drummond, J. Israelachvili, Coupling of normal and transverse motions during frictional sliding. *J. Phys. Chem. B* **102**, 5038–5041 (1998)
339. G.M. McClelland, S.R. Cohen, *Chemistry and Physics of Solid Surfaces VIII* (Springer, Heidelberg, 1990), pp. 419–445
340. E. Gnecco, R. Bennewitz, T. Gyalog, E. Meyer, Friction experiments on the nanometre scale. *J. Phys. Condens. Matter* **13**, R619–R642 (2001)
341. J. Gao, W.D. Luedtke, U. Landman, Friction control in thin-film lubrication. *J. Phys. Chem. B* **102**, 5033–5037 (1998)
342. C. Drummond, J. Elezgaray, P. Richetti, Behavior of adhesive boundary lubricated surfaces under shear: A new dynamic transition. *Europhys. Lett.* **58**, 503–509 (2002)
343. A.E. Filippov, J. Klafter, M. Urbakh, Inverted stick–slip friction: What is the mechanism?. *J. Chem. Phys.* **116**, 6871–6874 (2002)
344. C. Drummond, J. Israelachvili, Dynamic behavior of confined branched hydrocarbon lubricant fluids under shear. *Macromolecules* **33**, 4910–4920 (2000)
345. C. Drummond, J. Israelachvili, Dynamic phase transitions in confined lubricant fluids under shear. *Phys. Rev. E* **63**, 041506–1–041506–11 (2001)
346. J.D. Ferry, *Viscoelastic Properties of Polymers*, 3rd edn. (Wiley, New York, 1980)
347. A. Ruina, Slip instability and state variable friction laws. *J. Geophys. Res.* **88**, 10359–10370 (1983)
348. T. Baumberger, P. Berthoud, C. Caroli, Physical analysis of the state- and rate-dependent friction law. II. Dynamic friction. *Phys. Rev. B* **60**, 3928–3939 (1999)
349. J. Israelachvili, S. Giasson, T. Kuhl, C. Drummond, A. Berman, G. Luengo, J.-M. Pan, M. Heuberger, W. Ducker, N. Alcantar, Some fundamental differences in the adhesion and friction of rough versus smooth surfaces. *Tribol. Ser.* **38**, 3–12 (2000)
350. E. Rabinowicz, *Friction and Wear of Materials*, 2nd edn. (Wiley, New York, 1995), Chap. 4
351. J. Peachey, J. Van Alsten, S. Granick, Design of an apparatus to measure the shear response of ultrathin liquid films. *Rev. Sci. Instrum.* **62**, 463–473 (1991)
352. E. Rabinowicz, The intrinsic variables affecting the stick–slip process. *Proc. Phys. Soc.* **71**, 668–675 (1958)
353. T. Baumberger, F. Heslot, B. Perrin, Crossover from creep to inertial motion in friction dynamics. *Nature* **367**, 544–546 (1994)

354. F. Heslot, T. Baumberger, B. Perrin, B. Caroli, C. Caroli, Creep, stick-slip, and dry-friction dynamics: Experiments and a heuristic model. *Phys. Rev. E* **49**, 4973–4988 (1994)
355. J. Sampson, F. Morgan, D. Reed, M. Muskat, Friction behavior during the slip portion of the stick-slip process. *J. Appl. Phys.* **14**, 689–700 (1943)
356. F. Heymann, E. Rabinowicz, B. Rightmire, Friction apparatus for very low-speed sliding studies. *Rev. Sci. Instrum.* **26**, 56–58 (1954)
357. J.H. Dieterich, Time-dependent friction and the mechanics of stick-slip. *Pure Appl. Geophys.* **116**, 790–806 (1978)
358. J.H. Dieterich, Modeling of rock friction. 1. Experimental results and constitutive equations. *J. Geophys. Res.* **84**, 2162–2168 (1979)
359. G.A. Tomlinson, A molecular theory of friction. *Philos. Mag.* **7**, 905–939 (1929)
360. J.M. Carlson, J.S. Langer, Mechanical model of an earthquake fault. *Phys. Rev. A* **40**, 6470–6484 (1989)
361. B.N.J. Persson, Theory of friction: The role of elasticity in boundary lubrication. *Phys. Rev. B* **50**, 4771–4786 (1994)
362. S. Nasuno, A. Kudrolli, J.P. Gollub, Friction in granular layers: Hysteresis and precursors. *Phys. Rev. Lett.* **79**, 949–952 (1997)
363. H. Yoshizawa, J. Israelachvili, Fundamental mechanisms of interfacial friction. 2: Stick-slip friction of spherical and chain molecules. *J. Phys. Chem.* **97**, 11300–11313 (1993)
364. M.O. Robbins, P.A. Thompson, Critical velocity of stick-slip motion. *Science* **253**, 916 (1991)
365. P. Bordarier, M. Schoen, A. Fuchs, Stick-slip phase transitions in confined solidlike films from an equilibrium perspective. *Phys. Rev. E* **57**, 1621–1635 (1998)
366. J.M. Carlson, A.A. Batista, Constitutive relation for the friction between lubricated surfaces. *Phys. Rev. E* **53**, 4153–4165 (1996)
367. A.D. Berman, W.A. Ducker, J.N. Israelachvili, Origin and characterization of different stick-slip friction mechanisms. *Langmuir* **12**, 4559–4563 (1996)
368. A.D. Berman, W.A. Ducker, J.N. Israelachvili, Experimental and theoretical investigations of stick-slip friction mechanisms. *NATO ASI Ser. E Appl. Sci.* **311**, 51–67 (1996)
369. K.G. McLaren, D. Tabor, Viscoelastic properties and the friction of solids. Friction of polymers and influence of speed and temperature. *Nature* **197**, 856–858 (1963)
370. K.A. Grosch, Viscoelastic properties and friction of solids. Relation between friction and viscoelastic properties of rubber. *Nature* **197**, 858–859 (1963)
371. L. Bureau, T. Baumberger, C. Caroli, Shear response of a frictional interface to a normal load modulation. *Phys. Rev. E* **62**, 6810–6820 (2000)
372. J.P. Gao, W.D. Luedtke, U. Landman, Structure and solvation forces in confined films: Linear and branched alkanes. *J. Chem. Phys.* **106**, 4309–4318 (1997)
373. J. Warnock, D.D. Awschalom, M.W. Shafer, Orientational behavior of molecular liquids in restricted geometries. *Phys. Rev. B* **34**, 475–478 (1986)
374. D.D. Awschalom, J. Warnock, Supercooled liquids and solids in porous glass. *Phys. Rev. B* **35**, 6779–6785 (1987)
375. M. Hirano, K. Shinjo, R. Kaneko, Y. Murata, Anisotropy of frictional forces in muscovite mica. *Phys. Rev. Lett.* **67**, 2642–2645 (1991)
376. T. Gyalog, H. Thomas, Friction between atomically flat surfaces. *Europhys. Lett.* **37**, 195–200 (1997)
377. B.N.J. Persson, F. Bucher, B. Chiaia, Elastic contact between randomly rough surfaces: comparison of theory with numerical results. *Phys. Rev. B* **65**, 184106–1–184106–7 (2002)
378. S. Hyun, L. Pei, J.-F. Molinari, M.O. Robbins, Finite-element analysis of contact between elastic self-affine surfaces. *Phys. Rev. E* **70**, 026117–1–026117–12 (2004)
379. J. Israelachvili, N. Maeda, K.J. Rosenberg, M. Akbulut, Effects of sub-ångstrom (pico-scale) structure of surfaces on adhesion, friction and bulk mechanical properties. *J. Mater. Res.* **20**, 1952–1972 (2005)
380. T.R. Thomas, *Rough Surfaces*, 2nd edn. (Imperial College Press, London, 1999)

# Chapter 14

## Interfacial Forces and Spectroscopic Study of Confined Fluids

Y. Elaine Zhu, Ashis Mukhopadhyay, and Steve Granick

**Abstract** In this chapter we discuss three specific issues which are relevant for liquids in intimate contact with solid surfaces. (1) Studies of the hydrodynamic flow of simple and complex fluids within ultra-narrow channels show the effects of flow rate, surface roughness and fluid–surface interaction on the determination of the boundary condition. We draw attention to the importance of the microscopic particulars to the discovery of what boundary condition is appropriate for solving continuum equations and the potential to capitalize on *slip at the wall* for purposes of materials engineering. (2) We address the long-standing question of the structure of aqueous films near a hydrophobic surface. When water was confined between adjoining hydrophobic and hydrophilic surfaces (a Janus interface), giant fluctuations in shear responses were observed, which implies some kind of flickering, fluctuating complex at the water–hydrophobic interface. (3) Finally we discuss recent experiments that augment friction studies by measurement of diffusion, using fluorescence correlation spectroscopy (FCS). Here spatially resolved measurements showed that translation diffusion slows exponentially with increasing mechanical pressure from the edges of a Hertzian contact toward the center, accompanied by increasingly heterogeneous dynamical responses. This dynamical probe of how liquids order in molecularly thin films fails to support the hypothesis that shear produces a melting transition.

### 14.1 Introduction

Confinement of fluids, ranging from water, hydrocarbon oil, polymer melts and solutions, to DNA, protein and other bio-macromolecules, can strongly affect the structures and dynamics of the fluid molecules, particularly when the thickness of fluid films becomes comparable to the length scale of the molecular dimension. Phase transitions, such as solidification or glass transition, can be induced, and confinement can not only result in structural changes in terms of molecular

orientation and packing, but changes of dynamical processes, such as molecular translational as well as rotational diffusion. These questions about confined fluid structure and dynamics involve deep scientific puzzles. On the applied side, they also pertain directly to the understanding of many fundamental issues in nature and technology, including various applications in adhesion, colloidal stabilization, lubrication, micro/nanofluidics, and micro/nano-electromechanical systems (MEMS/NEMS) devices, among others.

The techniques that have been used to study confined fluids are mainly surface forces apparatus (SFA) [1–4] and recently atomic force microscopy (AFM) and its derivatives [5, 6]. SFA, which was originally designed to directly measure the van der Waals and Derjaguin–Landau–Verwey–Overbeek (DLVO) forces in simple liquids and in colloidal systems, was later modified by several groups to study the frictional forces of molecularly thin films confined between rigid surfaces [2–4]. AFM is an alternative method to study surface force, friction, adhesion and lubrication of thin film. With these two techniques many new phenomena about confined fluids, such as layering structure, solidification, stick–slip motion, etc. have been experimentally observed and interpreted.

The previous Chap. 9 reviewed the advances in the studies of surface forces, adhesion and shear interaction of confined liquids. In this chapter, we review recent studies on some specific interfacial forces of thin liquid films by using modified SFA devices and the results from an integrated experimental platform, which enables direct fluorescence-based observation of the dynamics of individual molecules under confinement.

This chapter is organized as follows. This introductory section is followed by a discussion of the validity of the no-slip boundary for fluid molecules moving past a solid surface, determined by measuring the hydrodynamic force in flow geometry. A specific interfacial force – the long-range hydrophobic interaction – and its related hydrophobic effect on the behavior of water molecules near a hydrophobic interface are discussed in Sect. 14.3. In Sects. 14.4–14.6, recent developments in combining ultrafast spectroscopy with the SFA to investigate the dynamic behavior of individual confined molecules, instead of their ensemble-averaged behavior, are reviewed.

## 14.2 Hydrodynamic Force of Fluids Flowing in Micro- to Nanofluidics: A Question About No-Slip Boundary Condition

Viscous flow is familiar and useful, yet the underlying physics is surprisingly subtle and complex. A tenet of textbook continuum fluid dynamics is the *no-slip* boundary condition, which means that fluid molecules immediately adjacent to the surface of a solid move with exactly the same velocity as that solid. It stands at the bedrock



of our understanding of the flow of simple low-viscosity fluids and comprises a springboard for much sophisticated calculation. While it is true that at some level of detail this continuum description must fail and demand description at the molecular level, it is tremendously successful as the basis for continuum-based calculations. This section is adapted from discussions in some previous primary accounts [7–9].

As expressed in a prominent fluid dynamics textbook [10]:

In other words there is no relative motion between the fluid and the solid. This fact may seem surprising but it is undoubtedly true. No matter how smooth the solid surface or how small the viscosity of the fluid, the particles immediately adjacent to the surface do not move relative to it. It is perhaps not without interest that Newton's term for viscosity was 'defectus lubricitatis' – 'lack of slipperiness'. Even for a fluid that does not 'wet' the surface this rule is not violated.

Feynman noted in his lectures that the no-slip boundary condition explains why large particles are easy to remove by blowing past a surface, but small particles are not.

However, for many years it was observed that the *no-slip* boundary condition is not intuitively obviously and has been controversial for centuries. A pantheon of great scientists – among them, Bernoulli, Coulomb, Navier, Poisson, Stokes, Taylor, Debye, de Gennes – has worried about it. The compelling rational arguments – for and against – were divided by the pragmatic observation that predictions agree with experiments. The possibility of slip was discussed until recently, in mainstream literature, only in the context of the flow of polymer melts [11, 12], though over the years persistent doubts were expressed [13]. *No-slip* contrasts with *slip* characteristic of highly viscous polymers [11, 12], monolayers of gas condensed on vibrated solids [14], superfluid helium [15], moving contact lines of liquid droplets on solids [16], and kinetic friction of liquid films less than 5–10 molecular dimensions thick [17, 18]. However, experimental capability and technical needs have changed – especially so with the emerging interest in microfluidics and microelectromechanical system (MEMS)-based devices.

The situation has changed but the enormous and enduring success of the no-slip assumption for modeling must be emphasized. It works beautifully provided that certain assumptions are met: a single-component fluid, a wetted surface, and low levels of shear stress. Then careful experiments imply that the fluid comes to rest within 1–2 molecular diameters of the surface [19–21]. But the necessary assumptions are more restrictive, and their applicability is more susceptible to intentional control than is widely appreciated. Generally, one may argue from the fact that fluid molecules are ("obviously") stuck to walls by intermolecular forces. The traditional explanation is that, since most surfaces are rough, the viscous dissipation as fluid flows past surface irregularities brings it to rest, regardless of how weakly or strongly molecules are attracted to the surface [7, 8, 22–24]. This has been challenged by accumulating evidence that, if molecularly smooth surfaces are wet only partially, hydrodynamic models work better when one uses instead *partial slip* boundary conditions [13, 21, 25–30]. Then the main issue would be whether the fluid molecules attract the surface or the fluid more strongly [9, 13, 27–34].

### 14.2.1 *How to Quantify the Amount of Slip*

To know what boundary condition is appropriate in solving continuum equations requires inquiry into microscopic particulars. Attention is drawn to unresolved topics of investigation and to the potential to purposively capitalize on *slip at the wall* for purposes of materials engineering.

The formal idea of a *slip length* is common. *Slip* signifies that, in the continuum model of flow, the fluid velocity at the surface is finite (the slip velocity,  $v_s$ ) and increases linearly with distance normal to it. The slip velocity is assumed to be proportional to the shear stress at the surface,  $\sigma_s$  in the relation:

$$\eta v_s = b \sigma_s, \quad (14.1)$$

where  $\eta$  is the viscosity and  $b$ , the slip length, is the notional distance inside the surface at which the velocity equals zero, if the velocity profile is extrapolated inside the surface until it reaches zero. In much of the literature the slip length has been assumed to be a constant that characterizes the material response of a given fluid–surface pair, but evidence of additional dependence on velocity is discussed below.

It is unreasonable to expect this continuum description to yield microscopic information. One example of this was already given – the appearance of no-slip conditions when the microscopic reason is that flow irregularities pin the fluid to the wall [7, 8, 22–24]. Another example is apparent slip when a low-viscosity component in the fluid facilitates flow because it segregates near the surface [35, 36]. When conventional continuum mechanics contends with situations that are more complex than the model allows, one should resist the temptation to interpret literally the parameters in which the continuum mechanics model is couched. These examples emphasize instances where the notions of *stick* and *slip* are numerical conveniences not to be interpreted literally in terms of molecular mechanism. The appearance of slip owing to surface segregation of a low-viscosity component is illustrated in Fig. 14.1.

### 14.2.2 *The Mechanisms that Control Slip in Low-Viscosity Fluids*

Partial slip of so-called Newtonian fluids such as alkanes and water is predicted by an increasing number of computer simulations [25–27, 37–39] and, in the laboratory when forces are measured, systematic deviations from the predictions based on *stick* are found [7–9, 28–34, 40, 41]. Some sense of urgency comes from potential practical applications. Typical magnitudes of the slip length reported in the literature are submicron, so small that the practical consequences of slip would be minimal for flow in channels whose size is macroscopic. But if the channel size is very small, there are potential ramifications for microfluidics.

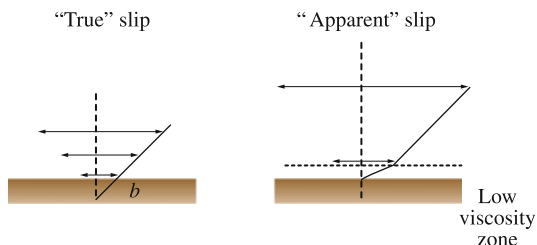


**Fig. 14.1** Schematic illustration of the distinction between true slip (*left*) and apparent slip (*right*) in oscillatory flow, although for both cases the velocity of the moving fluid extrapolates to zero at a notional distance inside the wall and is finite where it crosses the wall. For true slip, this is literally so. It may also happen that a low-viscosity component in the fluid facilitates flow because it segregates near the surface. The velocity gradient is then larger nearest the surface because the viscosity is smaller. When specific real systems are investigated, structural and chemical materials analysis at the microscopic scale are needed to distinguish between these possibilities. After [7] with permission

The simulations must be believed because they are buttressed by direct measurements. In the past, all laboratory reports of slip were based on comparing mechanical measurements of force to fluid mechanics models and hence were indirect inferences. Recently, optical methods were introduced to measure fluid velocity directly. For example, Léger and coworkers photobleached tracer fluorescent dyes and from the time rate of fluorescence recovery, measured in attenuated total reflection in order to focus on the region within an optical wavelength of the surface, the velocity of flow near the surface was inferred [28]. They reported slip of hexadecane near an oleophobic surface provided that it was smooth, but not when it was rough. Tretheway and Meinhart used laser particle image velocimetry of tracer latex particles to infer the velocity of water flow in microchannels [34]. They reported slip when the surface was hydrophobic but stick when it was hydrophilic. Callahan and coworkers demonstrated the feasibility of using nuclear magnetic resonance (NMR) velocity imaging, though this method has been used to date only for multicomponent fluids [42].

An important hint about the mechanism comes from the repeated observation that the amount of slip depends on the flow rate, in measurements using not only the surface forces apparatus (SFA) [8, 9, 31, 32] but also atomic force microscopy (AFM) [29, 41]. The main idea of all of these experiments is that two solids of mean radius of curvature  $R$ , at spacing  $D$ , experience a hydrodynamic force,  $F_H$  as they approach one another (or retreat from one another) in a liquid medium, thereby squeezing fluid out of (or into) the intervening gap. This force  $F_H$  is proportional to the rate at which the spacing changes,  $dD/dt$  (where  $t$  denotes time), is proportional to the viscosity,  $\eta$  (assumed to be constant), and is inversely proportional to  $D$ . The no-slip boundary condition combined with the Navier–Stokes equations gives to first order the following expression, known as the Reynolds equation:

$$F_H = f \frac{6\pi R^2 \eta}{D} \frac{dD}{dt} . \quad (14.2)$$

Higher-order solutions of the Navier–Stokes equations confirm that the lowest-order term is enough. The deviation of the dimensionless number  $f^*$  from unity quantifies the deviation from the classical no-slip prediction. The classical prediction is analogous when the surface spacing is vibrated. In that case a sinusoidal oscillatory drive generates an oscillatory hydrodynamic force whose peak we denote as  $F_{H, \text{peak}}$ . The peak velocity of vibration is  $v_{\text{peak}} = d \cdot \omega$ , where  $d$  is the vibration amplitude and  $\omega$  the angular frequency of vibration. Studies show that, when the frequency and amplitude of oscillatory flow are varied, results depend on their product,  $v_{\text{peak}}$  and the deviations from (14.2) depend on  $v_{\text{peak}}/D$ . This ratio, the flow rate, is the ratio suggested by the form of (14.2).

Without necessarily assigning physical meaning to this quantity, it can be used as an alternative expression of the same data. Mathematical manipulation [43] shows that  $f^*$  and the slip length,  $b$  are related as:

$$f^* = 2 \frac{D}{6b} \left[ \left( 1 + \frac{D}{6b} \right) \ln \left( 1 + \frac{6b}{D} \right) - 1 \right]. \quad (14.3)$$

### 14.2.3 Experimental

The slippery question was studied experimentally by testing the limits of ideas about interfacial force and surface roughness. Figure 14.2 sketches the experimental strategy and shows AFM (atomic force microscopy) images of some of the surfaces studied. Three strategies were used to vary surface roughness systematically. The first was based on using collapsed polymers. Narrow-distribution samples of diblock copolymers of polystyrene ( $M_w = 55,400$ ) and polyvinylpyridine ( $M_w = 28,200$ ), PS/PVP, were allowed to adsorb for a limited time from dilute ( $5 \times 10^3 \mu\text{g/ml}$ ) toluene solution onto freshly cleaved muscovite mica. They appeared to aggregate during the drying process. The remaining bare regions of mica were then coated with an organic monolayer of condensed octadecyltriethoxysilane (OTE) [44]. The contact angles against water and tetradecane were stable in time, which shows that the liquids did not penetrate them. AFM images in Fig. 14.2 quantify the roughness. To produce larger roughness values, mica was coated with condensed octadecyltrichlorosilane (OTS) after first saturating the cyclohexane deposition solution with  $\text{H}_2\text{O}$  to encourage partial polymerization in solution before surface attachment. In the third method, self-assembled monolayers of alkane thiols were formed on silver whose roughness was controlled by a direct-current (DC) bias applied during sputter deposition. The silver was coated with octadecanethiol deposited from ethanol solution and placed in opposition with a molecularly smooth OTE surface.

According to (14.2), the *stick* prediction ( $f^* = 1$ ) corresponds to a horizontal line and one observes in Fig. 14.3 that deviations from this prediction decreased systematically as the surface roughness increased. In addition, deviations from the

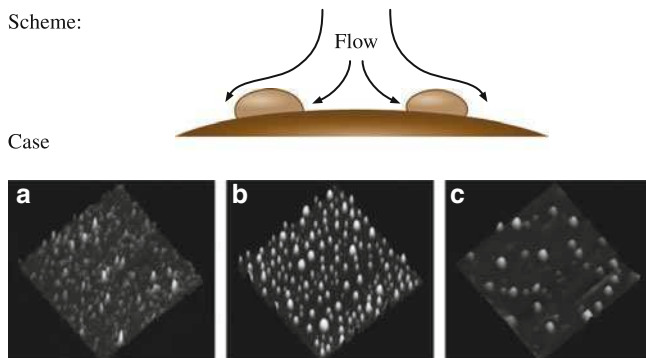


**Fig. 14.2** (a–c) The scheme of flow over a rough surface is shown schematically in the top portion. In the bottom panel, AFM images are shown of the following case: (a) self-assembled OTS layers; (b) PS/PVP-OTE layers (surface coverage  $\approx 80\%$ ); (c) PS/PVP-OTE layers (surface coverage  $\approx 20\%$ ). Each AFM image concerns an area  $3\ \mu\text{m} \times 3\ \mu\text{m}$ . After [8] with permission

predictions of the no-slip boundary condition are alternatively often represented as the *slip length* discussed above, the fictitious distance inside the solid at which the no-slip flow boundary condition would hold; the equivalent representation of this data in terms of the slip length is included in Fig. 14.3. While it was known previously that a very large amount of roughness is sufficient to generate *no-slip* [22–24], an experimental study in which roughness was varied systematically [7, 8] succeeded in quantifying how much actual roughness was needed in an actual system. The critical level of 6 nm considerably exceeded the size of the fluid molecules. As methods are known to achieve greater smoothness in MEMS devices, and potentially in microfluidic devices, this offers the promise of practical applications.

Observation of rate-dependent slip suggests that fluid is pinned up to some critical shear stress, beyond which it slips. However, some laboratories report slip *regardless* of flow rate [27, 29, 32–39]. Perhaps, the essential difference is that the magnitude of shear stress is larger in the latter experiments [45]. But in cases where slip is rate dependent, this affords a potential strategy by which to effect purposeful mixing in a microfluidic device. The idea would be simply to make some patches on the surface hydrophobic and other patches hydrophilic, so that when flow was slow enough it would be smooth, but when it was fast enough, mixing would result from jerkiness at the hydrophobic patches.

While it is true that slip at smooth surfaces is predicted based on computer simulations [25–27, 37–39], the shear rate of molecular dynamics (MD) simulations so much exceeds shear rate in those laboratory experiments that the direct connection to experiment is not evident. To quantify the influence of surface roughness, Fig. 14.4 considers the limit up to which predictions based on the classical no-slip boundary condition still described the data in Fig. 14.3. Since the no-slip boundary condition still held, it was valid [7–9] to calculate the shear rate and shear stress by known equations.

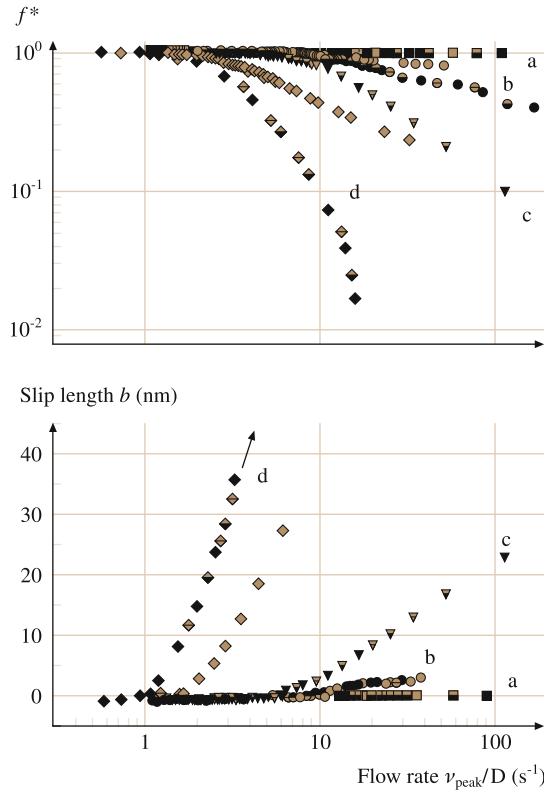


**Fig. 14.3**  $f^*$  as a function of logarithmic flow rate  $v_{\text{peak}}/D$  (top panel) where  $f^*$  is defined in (14.2), and the equivalent slip length (bottom panel), for deionized water (filled symbols) and tetradecane (open symbols) between surfaces of different levels of rms surface roughness, specifically: 6 nm (case a; squares), 3.5 nm (case b; circles), 2 nm (case c; down triangles), 1.2 nm (case d; hexagons), 0.6 nm (case e, upper triangles) and molecularly-smooth (case f; diamonds). The data, taken at different amplitudes in the range of 0.3–1.5 nm and frequencies in the range 6.3–250 rad/s, are mostly not distinguished in order to avoid clutter. To illustrate the similarly successful collapse at these rough surfaces, data taken at the two frequencies 6.3 rad/s (cross filled symbols) and 31 rad/s (semi-filled symbols) for water are included explicitly. After [8] with permission

The data show that deviations from the no-slip prediction began at very low levels of hydrodynamic stress – on the order of only 1–10 Pa. Beyond this point, in some sense the moving fluid was depinned from the surface.

*Slip* need not necessarily be predicated on having surfaces coated with self-assembled monolayers to render them partially wetted, though this was the case in most of the studies cited so far. The no-slip boundary condition switches to partial slip when the fluid contains a small amount of adsorbing surfactant [30, 32].

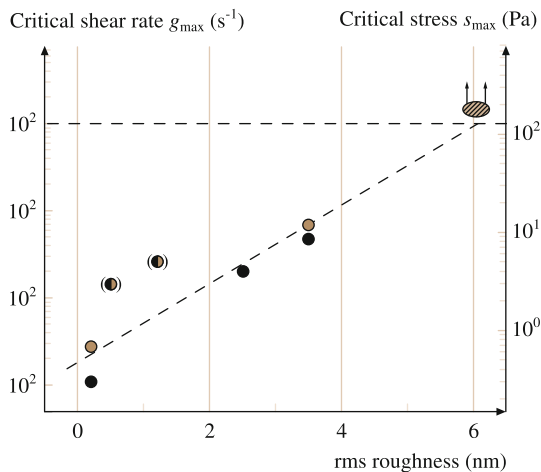


**Fig. 14.4** Illustration that deviations from the traditional no-slip boundary condition depend systematically on surface roughness. Here the critical shear rate for onset of slip (*left ordinate*) and critical shear stress (*right ordinate*) are plotted semilogarithmically against rms surface roughness for flow of deionized water (*solid symbols*) and tetradecane (*open symbols* and *semi-filled symbols* as identified in [32]). The data in parentheses indicate the asymmetric situation – one surface was rough and the opposed surface was atomically smooth, as discussed in [32]. Maximum shear rate and shear stress on the crossed cylinders were calculated using known relations

based on continuum hydrodynamics from [13, 42]. Specifically,  $\gamma_{\max} = A \sqrt{\frac{R}{D} \frac{v_{\text{peak}}}{D}}$  and  $\sigma_{\text{peak}} = 1.378 \eta R^{1/2} \frac{v_{\text{peak}}}{D^{3/2}}$ . After [7] with permission

#### 14.2.4 Slip Can Be Modulated by Dissolved Gas

When experimental observations deviate from expectations based on the *stick* boundary condition, there are at least two alternative scenarios with microscopic interpretations. One might argue that the fluid viscosity depends on distance from the wall, but for Newtonian fluids this would not be realistic. Why then do experimental data appear to undergo shear thinning with increasing values of the parameter  $v_{\text{peak}}/D$ , if it is unreasonable to suppose that the viscosity really diminished? Inspection shows that the data for smooth surfaces at high flow rates are consistent with a two-layer-fluid model in which a layer  $<1$  nm thick, but with viscosity 10–20 times *less* than the bulk fluid, adjoins each solid surface [9]. A possible mechanism to explain its genesis was proposed by de Gennes [46], who conjectured that shear may induce nucleation of vapor bubbles; once the nucleation barrier is exceeded the bubbles grow to cover the surface, and flow of liquid is over this thin gas film rather than the solid surface itself. Indeed, it is likely that incomplete air removal from the solid surfaces can profoundly influence findings in these situations

where surface roughness is so low. This has been identified by recent research as a likely source of the misnamed *long-range hydrophobic attraction* [47, 48]; gases also appear to influence the sedimentation rate of small particles in liquid [49].

Accordingly, similar experiments were performed, in which the surface forces apparatus was used to measure hydrodynamic forces of Newtonian fluids that had been purged with various gases. Dissolved gas strongly influences hydrodynamic forces, in spite of the fact that gas solubility is low.

Figure 14.5 (top panel) illustrates experiments in which a simple nonpolar fluid (tetradecane) was placed between a wetted mica surface on one side, and a partially wetted methyl-terminated surface on the other, using methods described in detail elsewhere [8, 9]. The surface–surface spacing of 10–100 nm substantially exceeded the size of the fluid molecules. The spacings were vibrated with small amplitude at these spacings where the fluid responded as a continuum, and the magnitude of hydrodynamic force was measured as a function of the ratio  $v_{\text{peak}}/D$  suggested by (14.2). The experiments showed that, whereas textbook behavior [10] was nearly followed when the tetradecane had been saturated with carbon dioxide gas, massive deviations from this prediction were found when the tetradecane was saturated with argon. This makes it seem likely that argon segregated to the solid walls, creating a low-viscosity boundary layer, in this way greasing the flow of fluid past that surface. Presumably, the amount of segregation is a material property of the fluid, the chemical makeup of the surface, and the chemical identity of the dissolved gas. In this example, the fact that argon possesses low solubility in tetradecane may have made it more prone to segregate to the surfaces.

Indeed, when a solid wall is hydrophobic and immersed in water, the ideas of Chandler and coworkers [50] suggest that thermodynamics may assist the formation of a vapor phase near the wall. Recent force measurements support this idea [51, 52].

### 14.2.5 Slip Past Wetted Surfaces

The influence of dissolved gas (just discussed) casts doubt on a traditional assumption of work in this field, which is that slip arises because fluid–fluid intermolecular interactions are stronger than those between fluid and surface, i.e. that the surface must be wetted only partially. Yet for several years, there have been prominent counterexamples [28, 41]. Recent experiments show that dissolved gases can mediate apparent slip even for solid surfaces that are fully wetted by the flowing fluid.

Figure 14.5 (bottom panel) summarizes experiments in which deionized water was placed between wetted surfaces of mica and the surface–surface spacing of 10–100 nm was vibrated with small amplitude in the manner described previously [7–9, 31–34]. Hydrodynamic force is plotted against the ratio,  $v_{\text{peak}}/D$ . It is obvious that the prediction based on (14.2), a straight line on the log–log plot with a slope of unity, was violated systematically when the hydrodynamic force reached a critical



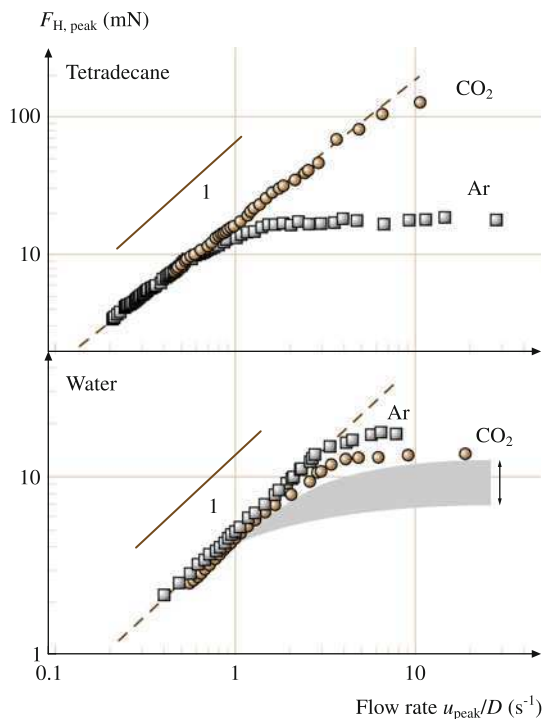


**Fig. 14.5** Illustration that the onset of slip depends on dissolved gas, when simple Newtonian fluids flow past atomically smooth surfaces, either wetted or partially wetted. On log–log scales, the hydrodynamic force  $F_{H, \text{peak}}$  is plotted against reduced flow rate,  $u_{\text{peak}}/D$ , such that a straight line of slope unity would indicate the *no-slip* condition assumed by (14.1). The vibration frequency is 9 Hz. *Top panel*: tetradecane flowing between the asymmetric case of a wetted mica surface on one side, a partially wetted surface of methyl-terminated self-assembled monolayer on the other side, prepared as described elsewhere [33]. *Filled symbols*, tetradecane saturated with carbon dioxide; *open symbols*, tetradecane saturated with argon. *Bottom panel*: deionized water flowing between mica surfaces that are wetted by this fluid. The hatched region of the graph shows the range of irreproducible results obtained when the gas dissolved in the water was not controlled. *Filled symbols*, water saturated with carbon dioxide; *open symbols*, water saturated with argon. After [7] with permission

level. An intriguing point is that initial findings were found to be irreproducible (they varied within the range marked by the hatched lines in the graph) but became reproducible when the water was first deliberately saturated with gas. One observes that water saturated with argon appeared to *slip* at a slightly higher level of shear stress than water saturated with carbon dioxide, and that in both cases the limiting hydrodynamic force was larger than when the nature of the dissolved gas was not controlled.

This rich and complex sensitivity to the detailed materials chemistry of the system disappears, unfortunately, when surfaces are so rough that the *stick*

boundary condition is produced trivially by the influence of surface roughness [7, 8, 22–24]. Therefore for scientific and practical reasons alike, these issues of flow past nearly smooth surfaces comprise fertile ground for future work.

### 14.2.6 *The Purposeful Generation of Slip*

Inspired by these ideas to design new engineering structures, one might strive to “grease” the flow of liquids past solid surfaces by altering the boundary condition. One strategy is to make the surfaces ultra-smooth [7–9]. Another (also mentioned already) is to add processing aids that segregate to the surface [30, 32, 36]. A third way is to purposefully use multicomponent fluids to generate concentration gradients and differential wetting to generate slip, as can occur even if there is no velocity gradient in the fluid [38]. These methods could potentially be used in nanomotors or nanopumps.

Alternatively, one may seek to maximize contact with air, which is exceedingly solvophobic. Readers will have noticed that water ubiquitously beads up on the leaves of plants. Some plants can display a contact angle that approaches  $180^\circ$ , even though water at a smooth surface of the same chemical makeup displays a much lower contact angle. A beautiful recent series of experiments from the Kao Corporation in Japan provided insight into why [53] – the surfaces are rough on many length scales [54, 55] and trap air beneath them. Readers will have noticed that, if one tilts a leaf, a drop of water on it rolls smoothly, because it rides mainly on a cushion of air, whose effect will be further discussed in the next section. It is the principle of an ingenious method introduced recently to lower the viscous drag when fluids [56] are caused to flow through pipes whose diameter is macroscopic. Of course, given a long enough period of time it is likely that the trapped gas would dissolve into the flowing fluid, but perhaps this effect could be enhanced by placing air nozzles along the walls of the tube and replenishing the trapped gas with a stream of inlet air.

A final method by which flow of a Newtonian fluid past surfaces may be facilitated is to *ciliate* the surfaces by coating with chain molecules – polymers, proteins, or sugars. Recent experiments using a surface forces apparatus (SFA) suggest a similar (but less dramatic) rate-dependent slip in this case also [31]. This is possibly related to fluid flow in biological organs whose surfaces are also extensively ciliated, such as blood vessels and the kidney [57].

### 14.2.7 *Outlook*

The textbook presentation of engineering fluid mechanics is often of a subject thoroughly understood, but recent experiments and simulations using smooth surfaces show behavior that is richer and more complex than had been supposed. The correct boundary condition appears to depend on physical chemical properties of the solid–liquid interface that are susceptible to rational control.

### 14.3 Hydrophobic Interaction and Water at a Hydrophobicity Interface

The role of water in physical situations from biology to geology is almost universally thought to be important but the details are disputed [1, 48, 50–52, 58–72]. For example, as concerns proteins, the side-chains of roughly half the amino acids are polar while the other half are hydrophobic; the non-mixing of the two is a major mechanism steering the folding of proteins and other self-assembly processes. As a second example, it is an everyday occurrence to observe beading-up of raindrops, on raincoats or leaves of plants. Moreover, it is observed theoretically and experimentally that, when the gap between two hydrophobic surfaces becomes critically small, water is ejected spontaneously [50, 51, 70–72] whereas water films confined between symmetric hydrophilic surfaces are stable [1]. Despite its importance, water exhibits many anomalous behaviors when compared to other fluids. Particularly, it presents some even more puzzling behaviors near hydrophobic surfaces. This section is adapted from discussions in several primary accounts published previously [51, 52].

In its liquid form, water consists of an ever-changing three-dimensional network of hydrogen bonds. Hydrophobic surfaces cannot form hydrogen bonds, and the hydrogen-bonding network must be disrupted. So what happens when water is compelled to be close to a hydrophobic surface? Energetically, it is expected that the system forms as many hydrogen bonds as possible, resulting in a preferential ordering of the water. Entropically, it is expected that the system orients randomly and thus samples the maximum number of states. Which of these two competing interactions dominates? What effect does the competition have on the dynamic and equilibrium properties of the system? The answers to these questions are still hotly debated. To help resolve this debate, static and dynamic interaction of water confined to a hydrophobic surface is studied by SFA.

#### 14.3.1 *Experimental*

The atomically smooth clay surfaces used in this study, muscovite mica (hydrophilic) and muscovite mica blanketed with a methyl-terminated organic self-assembled monolayer (hydrophobic), allowed the surface separation to be measured, by multiple beam interferometry, with a resolution of  $\pm 2\text{--}5$  Å. Surfaces were brought to the spacings described below using a surface forces apparatus modified for dynamic oscillatory shear [44, 73]. A droplet of water was placed between the two surfaces oriented in a crossed cylinder geometry. Piezoelectric bimorphs were used to produce and detect controlled shear motions. The deionized water was previously passed through a purification system, Barnstead Nanopure II (control experiments with water containing dissolved salt were similar). In experiments using degassed water, the water was either first boiled, then cooled in a sealed container, or vacuumed for 5–10 h in an oven at room temperature. The temperature of measurements was 25°C.

In order to determine firmly that findings did not depend on details of surface preparation, three methods were used to render one surface hydrophobic. In order of increasing complexity, these were: (a) atomically smooth mica coated with a self-assembled monolayer of condensed octadecyltriethoxysilane (OTE), using methods described previously [44]; (b) mica coated using Langmuir–Blodgett methods with a monolayer of condensed octadecyltriethoxysilane; and (c) a thin film of silver sputtered onto atomically smooth mica, then coated with a self-assembled thiol monolayer. In method (a), the monolayer quality was improved by distilling the OTE before self-assembly. In method (b), OTE was spread onto aqueous HCl ( $\text{pH} = 2.5$ ), 0.5 h was allowed for hydrolysis, the film was slowly compressed to the surface pressure  $\pi = 20 \text{ mN/m}$  (3–4 h), and the close-packed film was transferred onto mica by the Langmuir–Blodgett technique at a creep-up speed of 2 mm/min. Finally the transferred films were vacuum baked at  $120^\circ\text{C}$  for 2 h. In method (c), 650 Å of silver were sputtered at 120 V (1 Å/s) onto mica that was held at room temperature, and then octadecanethiol was deposited from 0.5 mM ethanol solution. In this case, AFM (atomic force microscopy; Nanoscope II) showed the rms (root mean square) roughness to be 0.5 nm. All three methods led to the same conclusions, summarized below.

### 14.3.2 *Hydrophobic Interaction*

A puzzling aspect of the hydrophobic attraction is that its intensity and range appear to be qualitatively different as concerns extended surfaces of large area, and small molecules of modest size [50, 60, 67, 74]. One difference is fundamental: the hydrogen-bond network of water is believed for theoretical reasons to be less disrupted near a single alkane molecule than near an extended surface [50, 60, 67, 74]. A second difference is phenomenological: direct measurement shows attractive forces between extended surfaces starting at separations too large to be reasonably explained by disruption of the hydrogen-bond network. This conclusion comes from 20 years of research using the surface forces apparatus (SFA) and, more recently, atomic force microscopy (AFM). The onset of attraction,  $\approx 10 \text{ nm}$  in the first experiments [69, 75–78], soon increased by nearly an order of magnitude [79–81] and has been reported, in the most recent work, to begin at separations as large as 500 nm [71]. This has engendered much speculation because it is unreasonably large compared to the size of the water molecule ( $\approx 0.25 \text{ nm}$ ). The range of interaction decreases if the system (water and the hydrophobic surfaces) are carefully degassed [48, 82–86]. Water in usual laboratory experiments is not degassed, however, so it is relevant to understand the origin of long-range attraction in that environment. A recent review summarizes the experimental and theoretical situation [81].

In the course of experiments intended to probe the predicted slip of water over hydrophobic surfaces [9, 45] (see the previous section), weakening of the long-range

hydrophobic force to the point of vanishing was observed when the solid surfaces experienced low-level vibrations around a mean static separation.

The attraction recorded during the approach of OTE surfaces with a droplet of deionized water in between is plotted in Fig. 14.6 as a function of surface–surface separation ( $D$ ).  $D = 0$  here refers to a monolayer–monolayer contact in air. In water, the surfaces jumped into adhesive contact at  $0 \pm 2$  Å. This *jump in* was very slow to develop, however. The pull-off force to separate the surfaces from contact at rest (113 mN/m in Fig. 14.6) implies, from the Johnson–Kendall–Roberts (JKR) theory [76], the surface energy of about 12 mJ/m<sup>2</sup> (and up to about 30% less than this when oscillations were applied). The onset of attraction at 650 nm for the hydrophobic surfaces at rest is somewhat larger than in any past study of which we are aware. However, we emphasize that the level of pull-off force was consistent with the prior findings of other groups using other systems [1, 60–72].

These observations clearly imply some kind of rate-dependent process. As shown in Fig. 14.7, the force  $F$  diminished with increasing velocity and its magnitude at a given  $D$  appeared in every instance to extrapolate smoothly to zero. The possible role of hydrodynamic forces was considered but discarded as a possible explanation. Similar results (not shown) were also obtained when the surfaces were vibrated parallel to one another rather than in the normal direction. Some

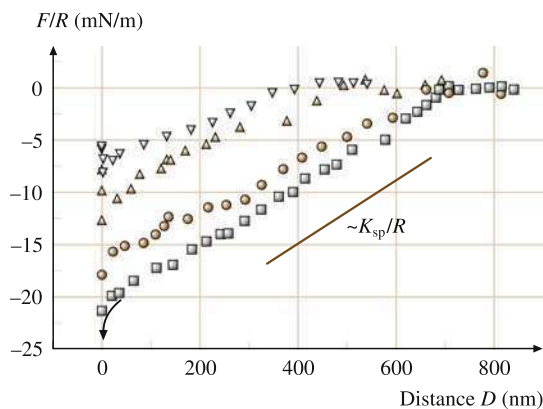
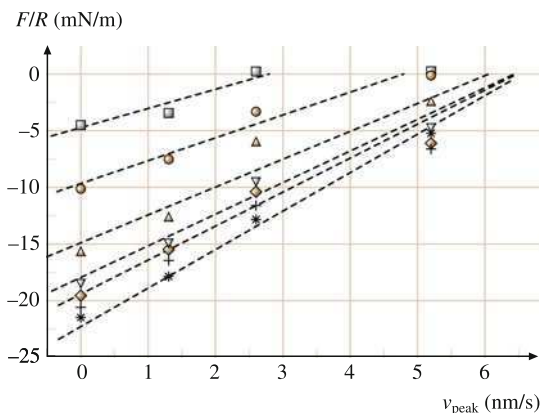


**Fig. 14.6** Force–distance profiles of deionized water between hydrophobic surfaces (OTE monolayers on mica). Force  $F$ , normalized by the mean radius of curvature ( $R \approx 2$  cm) of the crossed cylinders, is plotted against surface separation. Forces were measured during approach from static deflection of the force-measuring spring, while simultaneously applying small-amplitude harmonic oscillations in the normal direction with peak velocity  $v_{\text{peak}} = d \times 2\pi f$  where  $d$  denotes displacement amplitude and  $f$  denotes frequency. This velocity was zero (*solid squares*), 7.6 nm/s ( $d = 1.6$  nm,  $f = 0.76$  Hz; *circles*), 26 nm/s ( $d = 3.2$  nm,  $f = 1.3$  Hz; *up triangles*), 52 nm/s ( $d = 3.2$  nm,  $f = 2.6$  Hz; *down triangles*). The pull-off adhesion forces (“jump out”), measured at rest and with oscillation, are indicated by the respective *semi-filled symbols*. The approach data follow the straight line with slope  $K_{\text{sp}}/R$  (*drawn separately as a guide to the eye*), indicating that they represented a spring instability (“jump in”) such that the gradient of the attractive force exceeded the spring constant ( $K_{\text{sp}}$ ), 930 N/m. After [51] with permission

**Fig. 14.7** The attractive force ( $F/R$ ) at seven different surface separations ( $D$ ) is plotted against peak velocity. The film thickness was  $D = 720$  nm (squares), 540 nm (circles), 228 nm (up triangles), 116 nm (down triangles), 63 nm (diamonds), 17 nm (crosses), 5 nm (stars). After [51] with permission



precedence is found in a recent AFM study that reported weakened hydrophobic adhesion force with increasing approach rate [85].

These observations remove some of the discrepancy between the range of hydrophobic forces between extended surfaces of macroscopic size [1, 60–72] and the range that is expected theoretically [50, 60, 67, 74]. A tentative explanation is based on the frequent suggestion that the long-range hydrophobic attraction between extended surfaces stems from the action of microscopic or submicron-sized bubbles that arise either from spontaneous cavitation or the presence of adventitious air droplets that form bridges between the opposed surfaces [48, 81, 83–86]. The experiments reported here show that this effect required time to develop. Hydrophobic attraction at long range was softened to the point of vanishing when the solid surfaces were not stationary.

### 14.3.3 Hydrophobicity at a Janus Interface

Due to the strong propensity to repel water completely out of two hydrophobic surfaces, it is then interesting to consider the antisymmetric situation, a hydrophilic surface on one side (A) and a hydrophobic surface (B) on the other. The surface A prevents water from being expelled, to successfully retain a stabilized aqueous thin film at intimately close contact. The surface B introduces the hydrophobic effect. This Janus situation is shown in the cartoon of Fig. 14.8.

Similar to the force between two OTE surfaces, long-range attraction was also observed at the Janus interface, as shown in the inset of Fig. 14.8. The opposed surfaces ultimately sprang into contact from  $D \approx 5$  nm and upon pulling the surfaces apart, an attractive minimum was observed at  $D = 5.4$  nm. The surfaces could be squeezed to a lower thickness,  $D \approx 2.0$  nm. Knowing that the linear dimension of a water molecule is  $\approx 0.25$  nm [1], the thickness of the resulting aqueous films amounted to the order of 5–20 water molecules, although (see below) it is not clear that molecules were distributed evenly across this space. Below we discuss shear results.

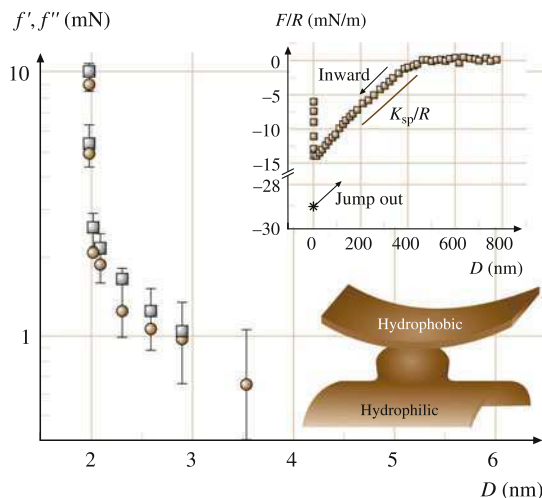


**Fig. 14.8** Deionized water confined between a hydrophilic surface on one side and a hydrophobic surface on the other (*cartoon*). The cartoon is not to scale because the gap thickness is nanometers at closest approach and the droplet size ( $\approx 2$  mm on a side) vastly exceeds the contact zone ( $\approx 10$   $\mu\text{m}$  on a side). The main figure shows the time-averaged viscous (*circles*) and elastic (*squares*) shear forces measured at 1.3 Hz and 0.3-nm deflection, plotted semilogarithmically against surface separation for deionized water confined between OTE deposited onto mica using the Langmuir–Blodgett (LB) technique (shear impulses were applied to this hydrophobic surface). The *inset* shows the static force–distance relations. Force, normalized by the mean radius of curvature ( $R \approx 2$  cm) of the crossed cylinders, is plotted against the thickness of the water film ( $D = 0$  refers to contact in air). The pull-off adhesion at  $D \approx 5.4$  nm is indicated by a *star*. The *straight line* with slope  $K_{sp}/R$  indicates the onset of a spring instability where the gradient of attractive force exceeds the spring constant ( $K_{sp}$ ), 930 N/m. Following this *jump* into contact, films of stable thickness resulted, whose thickness could be varied in the range  $D = 1$ –4 nm with application of compressive force. After [52] with permission

In the shear measurements, the sinusoidal shear deformations were gentle – the significance of the resulting linear response being that the act of measurement did not perturb their equilibrium structure (linear responses were verified from the absence of harmonics in the time dependence of shear motion). Using techniques that are well known in rheology, from the phase lag and amplitude during oscillatory excitation the responses to shear excitation were decomposed into one in-phase component (the elastic force,  $f'$ ) and one out-of-phase component (the viscous force,  $f''$ ) [87]. Figure 14.8 (main portion) illustrates responses at a single frequency and variable thickness. The shear forces stiffened by more than one order of magnitude as the films were squeezed. It is noteworthy that, when molecularly thin aqueous films are confined between clay surfaces that are symmetrically hydrophilic, deviations from the response of bulk water appear only at smaller separations [88]; evidently the physical origin is different here. Moreover, at each separation the elastic and viscous forces were nearly identical. The equality of elastic and viscous forces proved to be general, not an accident of the shear frequency chosen. Again this contrasts with recent studies of molecularly thin water

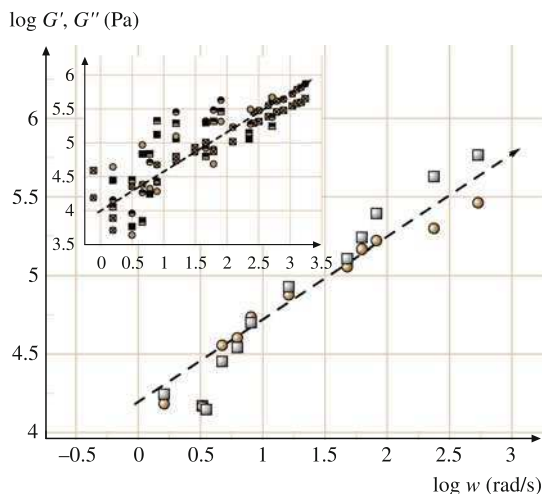
films between surfaces that are symmetrically hydrophilic [88]. The magnitudes of the shear moduli in Fig. 14.8 are “soft” – something like those of agar or jelly. They were considerably softer than for molecularly thin aqueous films between symmetrically hydrophilic surfaces. This again emphasizes the different physical origin of shear forces in the present Janus situation.

Figure 14.9 illustrates the unusual result that the shear forces scaled in magnitude with the *same* power law, the square root of excitation frequency. This behavior, which is intermediate between solid and liquid, is often associated in other systems with dynamical heterogeneity [89, 90]. By known arguments it indicates a broad distribution of relaxation times rather than any single dominant one [87]. The slope of  $1/2$  is required mathematically by the Kramers–Kronig relations if  $G'(\omega) = G''(\omega)$  [87]; its observation lends credibility to the measurements. Figure 14.9 (main panel) illustrates this scaling for an experiment in which data were averaged over a long time. The inset shows that the same was observed using other methods to prepare a hydrophobic surface. In all of these instances,  $\omega^{1/2}$  scaling was observed regardless of the method of rendering the surface hydrophobic. But to observe clean  $\omega^{1/2}$  scaling required extensive time averaging – see later.

In repeated measurements at the same frequency, we observed giant fluctuations ( $\pm 30$ – $40\%$ ) around a definite mean, as illustrated in Fig. 14.10, although water confined between symmetric hydrophilic–hydrophilic surfaces (bottom panel) did not display this. It is extraordinary that fluctuations did not average out over the large contact area ( $\approx 10\ \mu\text{m}$  on a side) that far exceeded any molecular size. The structural implication is that the confined water film comprised some kind of fluctuating complex – seeking momentarily to dewet the hydrophobic side by a thermal fluctuation in one direction, but unable to because of the nearby hydrophilic side; seeking next to dewet the hydrophobic side by a thwarted fluctuation in another direction; and so on. Apparently, nearby hydrophobic and hydrophilic surfaces may produce a quintessential instance of competing terms in the free energy, to satisfy which there may be many metastable states that are equally bad (or almost equally bad) compromises [91, 92]. This suggests the physical picture of flickering capillary-type waves, sketched hypothetically in Fig. 14.11. These proposed long-wavelength capillary fluctuations would differ profoundly from those at the free liquid–gas interface because they would be constricted by the nearby solid surface.

The power spectrum is the decomposition of the traces into their Fourier components whose squared amplitudes are plotted, on log–log scales, against Fourier frequency in Fig. 14.11. In the power spectrum one observes, provided the Fourier frequency is sufficiently low, a high level of “white” frequency-independent noise. But the amplitude began to decrease beyond a threshold Fourier frequency ( $f \approx 0.001\ \text{Hz}$ ), about  $10^3$  times less than the drive frequency. Other experiments (not shown) showed the same threshold Fourier frequency when the drive frequency was raised from 1.3 to 80 Hz, and therefore it appears to be a characteristic feature of the system. It defines a characteristic time for rearrangement of some kind of structure,  $\approx 10^3/2\pi\text{s}$ ; we tentatively identify this with the lifetime of bubbles or vapor (see below). The subsequent decay of the power spectrum as roughly  $1/f^2$  suggests that these fluctuations reflect discrete entities,





**Fig. 14.9** The frequency dependence of the momentum transfer between the moving surface (hydrophobic) and the aqueous film with an adjoining hydrophilic surface is plotted on log-log scales. Time-averaged quantities are plotted. On the *right-hand ordinate* scale are the viscous,  $g''$  (circles), and elastic,  $g'$  (squares) spring constants. The equivalent loss moduli,  $G''_{\text{eff}}$  (circles), and elastic moduli,  $G'_{\text{eff}}$  (squares), are on the *left-hand ordinate*. All measurements were made just after the jump into contact shown in Fig. 14.6, i.e. at nearly the same compressive pressure  $\approx 3$  MPa. The main panel, representing LB-deposited OTE, shows  $\omega^{1/2}$  scaling after long-time averaging, 0.5–1 h per datum. The *inset* shows comparisons with using other methods to produce a hydrophobic surface. In those experiments the thickness was generally  $D = 1.5$ – $1.6$  nm but occasionally as large as  $2.5$  nm when dealing with octadecanethiol monolayers. Symbols in the *inset* show data averaged over only 5–10 min with hydrophobic surfaces prepared with (a) a self-assembled monolayer of OTE (*half-filled symbols*), (b) Langmuir–Blodgett deposition of OTE (*crossed symbols*), or (c) deposition of octadecanethiol on Ag (*open symbols*). As in the main figure, circles denote viscous forces, squares denote elastic forces. Scatter in this data reflects shorter averaging times than in the main part of this figure (Fig. 14.8). After [52] with permission

as smooth variations would decay more rapidly. Noise again appeared to become “white” but with an amplitude  $10^4$  times smaller at a Fourier frequency of  $f > 0.1$  Hz but the physical origin of this is not evident at this time.

The possible role of dissolved gas is clear in the context of our proposed physical explanation. Indeed, submicron-sized bubbles resulting from dissolved air have been proposed to explain the anomalously long range of the hydrophobic attraction observed between extended surfaces [48, 51, 70–72]. To test this idea, we performed control experiments using degassed water. The power spectrum, shown in Fig. 14.12, was nearly the same. Although we cannot exclude that a small amount of residual dissolved gas was responsible, this method of degassing is reported to remove long-range hydrophobic attraction [71], whereas the comparison in Fig. 14.12 shows the consequence in the present situation to be minor. We conclude that the effects reported in this chapter do not appear to stem from the presence of dissolved gas.

From recent theoretical analysis of the hydrophobic interaction the expectation of dewetting emerges – it is predicted that an ultrathin gas gap, with a thickness

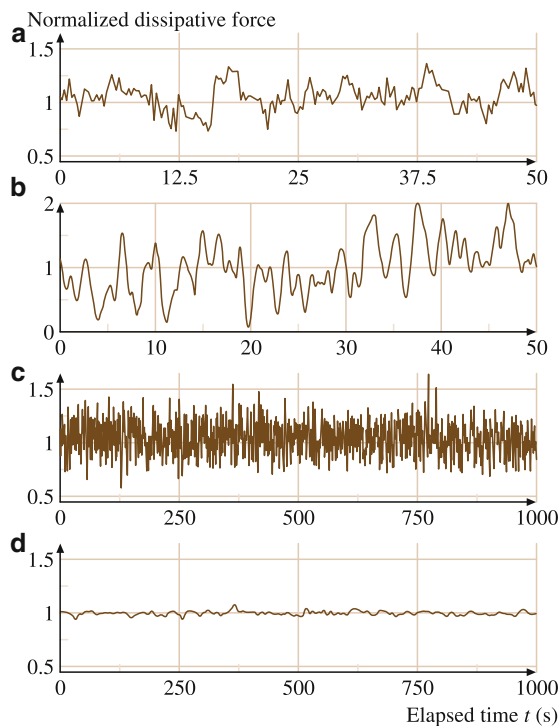


**Fig. 14.10 (a–d)** The prominence of fluctuations for water confined in a Janus interface is illustrated. In panels (a)–(c), the viscous forces, normalized to the mean (at 1.3 Hz), are plotted against time elapsed. In panel (a), the surfaces were first wetted with ethanol to remove adsorbed gas, then flushed with degassed, deionized water. In panel (b), the ethanol rinse was omitted. Panel (c) shows a long-time trace for data taken under the same conditions as for panel (b). Panel (d) illustrates that water confined between symmetric hydrophilic–hydrophilic surfaces (panel (d)) did not display noisy responses. Confined ethanol films likewise failed to display noisy responses (not shown). After [52] with permission

on the order of 1 nm, forms spontaneously when an extended hydrophobic surface is immersed in water [50, 61, 67]. The resulting capillary-wave spectrum does not appear to have yet been considered theoretically, but for the related case of the free water–vapor interface, measurements confirm that capillary waves with a broad spectrum of wavelengths up to micrometers in size contribute to its width [93]. On physical grounds, the thin gas gap suggested by our measurements should also be expected to possess soft modes with fluctuations whose wavelength ranges from small to large. From this perspective, we then expect that the experimental geometry of a Janus-type water film, selected for experimental convenience, was incidental to the main physical effect.

This has evident connections to understanding the long-standing question of the structure of aqueous films near a hydrophobic surface and may have a bearing on understanding the structure of water films near the patchy hydrophilic–hydrophobic surfaces that are so ubiquitous in proteins.

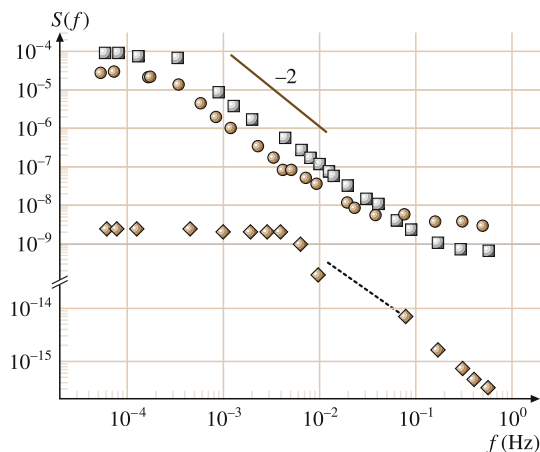
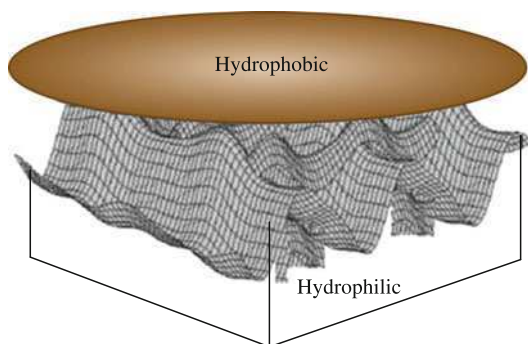


**Fig. 14.11** The power spectrum for deionized water and the hydrophobized surface comprised of OTE deposited by the LB technique (*squares*); degassed deionized water and the hydrophobized surface comprised of an octadecanethiol monolayer (*circles*); and water containing 25 mM NaCl confined between symmetric hydrophilic–hydrophilic surfaces (*diamonds*). To calculate the power spectra the time elapsed was at least  $10^5$  s (the complete time series is not shown). The power-law exponent is close to  $-2$ . After [52] with permission

**Fig. 14.12** Schematic illustration of the capillary waves of water meeting the hydrophobic surface with a flickering vapor phase in between



## 14.4 Ultrafast Spectroscopic Study of Confined Fluids: Combining Ultra-Fast Spectroscopy with Force Apparatus

The surface forces apparatus (SFA) modified to measure interfacial rheology has been used widely in last few years to study the viscoelasticity of molecularly thin fluid films [1–4, 94–98]. A recent application of this technique is described in Sect. 14.3. Though the force-based techniques are powerful and sensitive, they are indirect. The observation of structure-related transitions, e.g., oscillatory forces [1], confinement-induced solidification [4, 94, 95], and stick–slip motion in SFA

experiments [17, 96, 97] have not been directly verified experimentally using an independent technique.

The power of scattering, microscopy and spectroscopic techniques in the studies of confined fluids has been of speculative interest for a long time. However, there are only a few reported successes, primarily because of technical difficulties of combining these forms of techniques with SFA. Neutron and X-ray diffraction methods are very powerful for direct determination of structures at the nanoscale. Recently developed X-ray surface forces apparatus permits simultaneous X-ray diffraction and direct normal and lateral forces measurements of complex fluids under shear and confinement [98]. Safinya et al. have investigated the structure of thin liquid crystal films under confinement using this apparatus [99]. The deep penetrating power of neutrons and the ability to substitute hydrogen with deuterium in many liquid systems can be exploited to measure the molecular density and orientation of confined fluids by using neutron diffraction [100]. The structure of end-grafted polymer brush layers have been investigated in this manner. Successful utilization of this method requires one to devise an apparatus that can keep single-crystal substrates of quartz or sapphire with areas up to tens of square centimeters parallel at controlled and well-defined separations [101]. So far, both neutron and X-ray confinement cells are limited to confining gaps ranging from several hundred angstroms to millimeters and are not capable of studying ultrathin ( $\approx$ nm) liquid films. This intermediate length scale is more suited to study complex fluids, e.g., long polymer chains, colloidal particles and biological cells, where self-organized structures of larger scale come into play. For simple fluids, the difficulty arises because, as the film thickness decreases, the total number of scatterers decreases and the signal-to-noise ratio presents severe limitations. It is difficult to distinguish with sufficient confidence the structure of a molecularly thin fluid film from that of the thicker solids that envelop it. Synchrotron X-ray sources, such as the advanced photon source at Argonne National Laboratory have sufficient flux for experiments of extremely confined liquid films possible. Recent X-ray reflectivity experiments have confirmed the expected layering in the direction perpendicular to the confining surfaces [102], but questions about in-plane order and responses to external fields remain conjectural.

The interaction of light with matter – for example Raman and infrared – has impressive potential, but the problem is to distinguish the signal (the fluid monolayer) from all the noise (the sliding surfaces and the solids beneath them). The micro-rheometer developed by Dhinojwala et al. can readily be combined with spectroscopy (Fourier-transform infrared spectroscopy and dielectric spectroscopy) or scattering (X-ray and neutron) techniques [103]. It uses two parallel optically flat windows plates whose separation can be controlled from a few tens of nm to tens of  $\mu$ m, but is more suited to thicker (0.1–10  $\mu$ m) films. It has been used for in situ study of shear-induced molecular orientation of nematic liquid crystals by using Fourier-transform infrared time-resolved spectroscopy (FTIR-TRS) synchronized with the shear motion [104]. By replacing one of the plates with a prism, recently it has been shown that this rheometer can be combined with the surface-sensitive technique of infrared-visible sum-frequency generation (SFG) in the total internal reflection

(TIR) geometry [105]. This combination can be used to probe the orientation, alignment and relaxation modes of organic molecules at the buried interface in a condition of flow or shear. Some years back it was shown that SFG can be combined with the surface forces apparatus to study nanometer-thick films of self-assembled monolayer confined between atomically smooth mica surfaces [106], but implementation of this approach to other experimental situations, such as confined fluids still presents significant challenges.

Another problematic issue arises in interpreting experiments that measure mechanical properties, such as the SFA or AFM. The measurement generates a single number, the force, but although the surface separations are molecular, the areas of interaction are macroscopic. So this force is the result of the average response of a large collection of molecules. Recent advances in optical spectroscopy and microscopy have made it possible not only to detect and image single molecules, but to conduct spectroscopic measurements and monitor dynamic processes as well at the level of single (or a handful of) molecules [107, 108]. These studies illustrate their utility to dissect the distributions around the average for processes such as diffusion or chemical reactions. In many of these experiments, a fluorescent molecule is doped into the sample, which acts as a probe of its local environment [109]. Monitoring motions of the probe over time and in the presence of external fields can offer insights into changes in this local environment within which the dye molecule is embedded. However, to integrate force measurements using SFA with concurrent measurements using fluorescence spectroscopy required significant modification of the usual methods [110]. In the following we discuss the challenges of combining SFA with single-molecule-sensitive spectroscopy techniques. This section is adapted from discussions in several primary accounts published previously [109, 110].

### 14.4.1 Challenges

One of the major difficulties is to detect and collect fluorescence efficiently and to separate it from background noise. Background originates from many sources: Raman and Rayleigh scattering, fluorescence owing to impurities in the solvent, and from the substrates, which includes the lens, glue and mica (the glue attaches a cleaved mica sheet onto the supporting cylindrical lens in SFA experiments). Typical background counts can far exceed those from a dilute concentration of fluorophore molecules doped inside the sample of interest.

Another type of challenge comes from the limited photochemical lifetime of a fluorophore. A common fluorophore photobleaches irreversibly after emitting a finite number of photons ( $10^5$ – $10^6$ ). This problem becomes severe in ultrathin films, where the dynamics can become slower and a dye molecule resides for a long time within the laser focus.

A third difficulty is the necessity to perform spectroscopy at the same time as multiple-beam interferometry (MBI) to determine the film thickness. Traditionally

a silver coating of thickness  $\approx 63$  nm is used at the back side of mica for the purpose of MBI, but the high reflectivity of silver from the infrared to UV regime excludes this possibility here.

The final challenge is to incorporate the SFA and the needed optics. As the signal must be as large as possible, the maximum possible amount of fluorescence from the fluorophore of interest should be detected for a successful experiment. A high numerical aperture (N.A.) objective is desirable but such objectives have a very small working distance ( $\approx 1\text{--}2$  mm). This requires significant modification of the traditional SFA in order to make it possible to focus the laser beam on the sample.

We recently succeeded in implementing the technique of fluorescence correlation spectroscopy (FCS), which can measure the translational diffusion with surface forces measurement and friction studies within the SFA [111]. The scientific objective of building this integrated platform was to answer questions such as: how is the rate of molecular probe diffusion, within a confined fluid, related to the stress relaxation time? Is there significant collective molecular motion or dynamical heterogeneity? What happens to the molecules during the stick–slip motion? The principle of the FCS technique and the experimental set-up of the combined platform are described below.

#### 14.4.2 Principles of FCS Measurement

Fluorescence correlation spectroscopy (FCS) is an experimental method to extract information on dynamical processes from the fluctuation of fluorescence intensity [112]. The technique has enjoyed widespread application recently in the field of chemical biology because of its ability to access to a multitude of parameters with biological relevance [113, 114]. The fluctuation of fluorescence, when dye molecules are dilute, can in principle result from diffusion, aggregation, or chemical reaction. Compared to other techniques for studying diffusion problems, such as quasi-elastic light scattering (QELS), fluorescence recovery after photobleaching (FRAP), and laser-induced transient grating spectroscopy, FCS presents the unique capability of measuring extremely dilute systems with high spatial resolution (down to the optical diffraction limit). On the average there can be as few as 1–5 dye molecules within the  $\approx 1$  fl volume element of the focused laser beam. However, these dye molecules move in and out due to Brownian motion, causing intensity fluctuations which can be observed as low-frequency noise on the mean fluorescence signal (Fig. 14.13). By inspecting the autocorrelation function of this fluctuation,

$$G(\tau) \equiv \langle \delta I(t) \delta I(t + \tau) \rangle / \langle \delta I(t) \rangle^2, \quad (14.4)$$

(here  $I$  denotes fluorescence intensity and  $t$  is the time variable), and by choosing a suitable model to analyze it, the rate of dynamic process is obtained [112]. If the primary reason for fluctuation is translational diffusion, and assuming that the

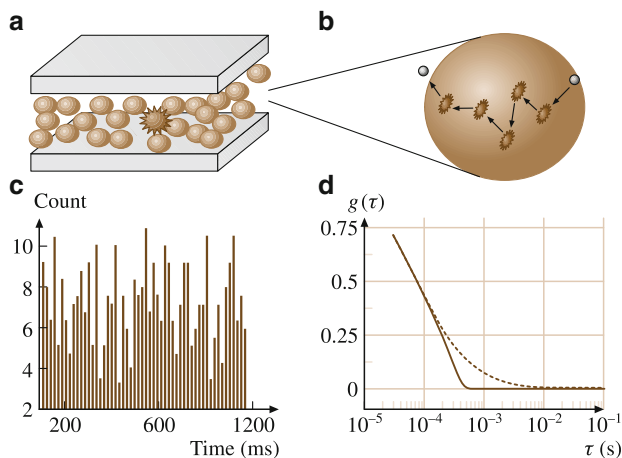


**Fig. 14.13 (a–d)** Schematic illustration of the utility of fluorescence correlation spectroscopy in a confined geometry: (a) A fluorescent molecule is doped within an ultrathin film of fluids (e.g., simple alkanes, polymers, colloidal particles) confined between two solid surfaces. Photon emission counts can fluctuate with time (c) resulting from the diffusion of fluorophores through the laser focus (b). From the autocorrelation function of this fluctuation  $G(\tau)$ , the rate of dynamic process can be obtained (d). Calculated  $G(\tau)$  for pure Brownian diffusion (*dashed curve*) and flow superimposed with diffusion (*solid curve*) are shown

fluorescence characteristics of the diffusing molecules do not change while traversing the laser volume, one can use Fick's second law to calculate the translational diffusion coefficient ( $D$ ) from the autocorrelation function by using the relation [115],

$$G(\tau) = G(0) / (1 + 8D\tau/\omega_0^2) . \quad (14.5)$$

This result follows from the convolution of the concentration correlation with the spatial profile of the laser focus, which has been assumed to be a two-dimensional Gaussian of width  $\omega_0$ . The magnitude of the autocorrelation function at time zero,  $G(0)$ , is related to the average number of fluorophores ( $N$ ) in the observation volume by the relation [116]

$$G(0) = 1/(2\sqrt{2}N) . \quad (14.6)$$

Molecular mobilities can be measured over a wide range of characteristic time constants from  $\approx 10^{-3}$  to  $10^3$  ms by using this technique.

Fluctuation analysis is best performed if the system under observation is restricted to very small ensembles and if the background is efficiently suppressed. These can be accomplished by a combination of very low sample concentrations

( $\approx$ nanomolar) with extremely small measurements volumes ( $\approx$ femtoliter). The excitation of the fluorophores can be performed either with two photons using a pulsed laser or with one photon using continuous-wave lasers [115]. In one-photon FCS, spatial resolution is obtained with a confocal set-up, in which a small pinhole inserted into the image plane can reject the out-of-focus fluorescence. For two-photon excitation on the other hand, simultaneous (within  $\approx 10^{-15}$  s) absorption of two lower-energy photons of approximately twice the wavelength is required for a transition to the excited state. Mode-locked lasers providing short pulses ( $\approx 10^{-13}$  s) with a high repetition rate ( $10^8$  Hz) can provide sufficient photon flux densities for two-photon processes. As the excitation probability is proportional to the mean square of the intensity, it results in inherent depth discrimination. Additionally, two-photon excitation improves the signal-to-background ratio considerably. As the most prominent scattering came from the incident light, which is well separated in wavelength from the induced fluorescence, this makes it easy to separate the fluorescence emission from the excitation light and the scattered light. However, the photobleaching rates with two-photon excitation are significantly enhanced with respect to one-photon excitation at comparable photon-emission yields [117].

### 14.4.3 *Experimental Set-Up*

A schematic diagram of the method of combing fluorescence correlation spectroscopy with the surface forces apparatus is shown in Fig. 14.12. The FCS portion of the set-up consists of three major parts: light source, microscope and data acquisition [110]. A femtosecond Ti:sapphire laser, which typically generates laser pulses with full width at half maximum (FWHM) of 100 fs at a repetition rate of 80 MHz can be used for the two-photon excitation of the fluorophores. An inverted microscope serves as the operational platform for the whole experiment. The excitation light is focused onto the sample with an objective lens of high N.A. and the emitted light is collected through the same objective and is detected by a photomultiplier tube (PMT) or avalanche photodiode (APD). The photon counting output is recorded by an integrated FCS data-acquisition board and data analysis can be performed with commercial or home-written software. By introducing the laser beam through the objective lens, a small excitation volume ( $\approx 1$  fl) is generated within the sample. The lateral dimension of the excitation spot is about  $\approx 0.5$   $\mu\text{m}$ , which can be determined by a calibration experiment using widely used dyes, such as fluorescein, whose diffusion coefficient in water is known to be  $\approx 300$   $\mu\text{m}^2/\text{s}$ . The excitation power at the sample needs to be less than 1 mW to avoid photobleaching and heating effects of the sample.

The modified surface forces apparatus sat directly on the microscope stage. The traditional crossed-cylindrical geometry produced a circular contact of parallel plates when the crossed cylinders were squeezed together such that they flattened at the apex. Using an inchworm motor, separation of the surfaces can be controlled from nanometers to millimeters. To determine the separation between the surfaces, the traditional silver sheets for interferometric measurements of surface spacing in



the SFA need to be replaced by multilayer dielectric coatings [118]. These multilayers can be produced by successive evaporation of layers (typically 13 or 15) of  $\text{TiO}_x$  and  $\text{Al}_2\text{O}_3$  by electron-beam evaporation. The optical thickness of each layer was approximately  $\lambda/4$  ( $\lambda \approx 650$  nm), as determined by the optical monitor within the coating chamber. The thickness of each coating determines the windows of reflectivity and translucency. This approach can produce high reflectivity in the region 600–700 nm, as well as translucent windows in the region  $\approx 800$  nm (to allow fluorescence excitation) and 400–550 nm (to detect fluorescence). The reflectivity as a function of wavelength is shown in Fig. 14.13 for the bare mica surface and for surfaces with different numbers of multilayers.

The same set-up (Fig. 14.14) with some modification can be used to probe molecular rotational diffusion. In the ground state fluorophores are all randomly oriented. When excited by polarized light, only those fluorophores that have their dipole moments oriented along the electric vector of the incident light are preferentially excited. So the excited-state population is not randomly oriented, instead there is a larger number of excited molecules having their transition moments oriented along the polarization direction of the incident light. This anisotropy of orientation can be determined by measuring the intensity of light polarized parallel to the incident light and perpendicular to the incident light. This preferential anisotropy at time zero decays due to the rotational diffusion of the dye molecule, following an exponential law with a *characteristic rotation time* ( $\tau$ ). As the typical rotational time ranges from picoseconds to nanoseconds, the dynamics on much smaller length scales, that of only one or two nm, can be investigated by this

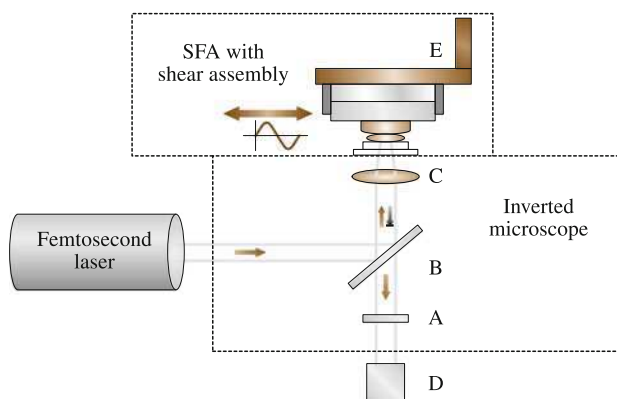


**Fig. 14.14** Schematic diagram of the assembly used to perform fluorescence correlation spectroscopy within a surface forces apparatus equipped for shear experiments. A miniaturized surface forces apparatus sits on a microscope stage. A femtosecond pulsed laser excites fluorescent dye molecules within a molecularly thin liquid film contained between two opposed surfaces of muscovite mica. Colored filter (A) to remove the residual excitation light ( $\lambda = 800$  nm) from the fluorescence light (400–550 nm) which is collected by the single-photon counting module (D). Dichroic mirror (B) and the objective lens (C) used to focus and collect the light. An inchworm motor (E) controls the separation of the surfaces from nanometers up to several micrometers

method. Translational diffusion experiments by FCS, on the other hand, (as discussed in the following sections) involves a large distance – the probe molecules travel hundreds of nm into and out of the laser spot – to produce a signal. Therefore, it is more sensitive to the *global* environment of the molecules.

## 14.5 Contrasting Friction with Diffusion in Molecularly Thin Films

In FCS experiments, the magnitude of the fluctuation autocorrelation function scales inversely with the number of fluorescent molecules in the observation volume (14.6). Large fluorophore concentrations more than micromolar are not efficient in FCS, because  $G(0)$  eventually becomes too small for fluctuation analysis. Typical dye concentration for confined fluid experiments is kept at 50 nM. A key point for these experiments is to find systems in which adsorption of the fluorophore would not complicate the situation. In other words, the fluids themselves, not the fluorophores, should be attracted preferentially to the confining solid surfaces [111]. This point can be verified by scanning the laser focus vertically from within the mica, through the surface, into the bulk fluids, and observing that there is no jump in fluorescence counts as the surface is crossed. Finally, one needs to be sensitive to the concern that, when using fluorophores to probe local micro-environments, micro-environments might be perturbed by their presence. Therefore, it is essential to perform normal and shear force experiments with and without the presence of dye molecules to verify that these are not affected. This section is adapted from discussions in several primary accounts published previously [111].

In SFA experiments, a drop of the fluid for study is placed between the two mica sheets, oriented as crossed cylinders so that in projection the geometry is as a sphere against a flat (Fig. 14.15). In the study of surface forces, it is well known that, as surfaces separated by fluid are brought together, fluid drains smoothly until a thickness of 5–10 molecular dimensions, at which point the fluid supports stress owing to packing of molecules at the surface [1]. When rounded surfaces of this kind are pressed together, separated by fluid, the curved surfaces flatten at the apex to form parallel plates. The resulting inhomogeneous pressure distribution over the contact region is well known in the field of tribology. It is approximately *Hertzian*; zero at the edges of the contact zone and, at the center,  $3/2$  the mean value [119]. The Hertzian model is generally a good approximation in the absence of strongly attractive forces.

Figure 14.16 shows results for two different fluid systems: (a) propane diol containing  $\approx 50$  nM rhodamine 123, and (b) octamethylcyclotetrasiloxane (OMCTS), containing  $\approx 50$  nM coumarin. Propane diol is a low-viscosity fluid ( $\approx 0.4$  Poise) with a glass-transition temperature far below room temperature ( $T_g = -105^\circ\text{C}$ ). The OMCTS molecule is ring-shaped; it is the cyclic tetramer of dimethylsiloxane. It has a viscosity much like water ( $\approx 0.002$  Poise) and possesses the intriguing feature that it crystallizes at 1 atm near room temperature ( $T_m = 17^\circ\text{C}$ ), thus enhancing the possibility that a confinement-induced elevation of the melting

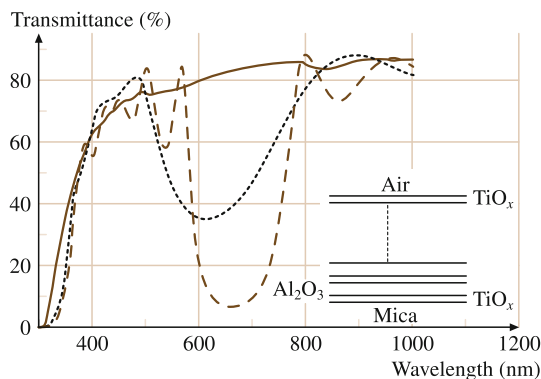


**Fig. 14.15** Optical transmittance of mica coated with a multilayer dielectric, showing the feasibility of performing optical spectroscopies in the region 400–600 nm while also measuring surface–surface separation by multiple beam interferometry in the region 650–750 nm. Bare mica (*solid line*), mica coated with seven layers of coating (*dotted line*) and with 13 layers of coating (*dash-dot line*). The window of optical transmission is adjustable through variations of multilayer dielectric. (*Inset*) The schematic diagram of the dielectric coating, composed of alternate layers of  $\text{TiO}_x$  and  $\text{Al}_2\text{O}_3$

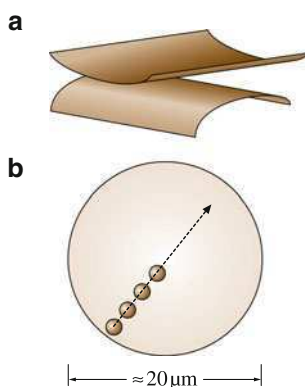


**Fig. 14.16** (a–b) Experimental scheme. (a) Crossed-cylinder configuration. Droplets of fluids were placed between crossed cylinders of mica as a drop and force is applied in the normal direction, causing the formation of a circular area of flattened contact. (b) Fluorescence correlation spectroscopy (FCS) is performed after compressing the films with a mean normal pressure of 2–3 MPa. The sequence of smaller circles illustrate that the focus of the laser beam (diameter  $\approx 0.5 \mu\text{m}$ ) was scanned across the contact (radius  $\approx 10 \mu\text{m}$ ), enabling spatially resolved measurements. After [111] with permission

temperature might be detected. There is a long tradition of considering it to constitute a model system when studying friction and surface-induced structure of nonpolar confined fluids because numerous computer simulations designed to model lubrication have concerned particles of spherical shape [2, 95, 120]. As the typical size of the contact area is  $\approx 50 \mu\text{m}$  and the size of the laser spot is  $\approx 0.5 \mu\text{m}$ ,

it is possible to scan the laser focus laterally, as sketched in Fig. 14.14. From time series of fluctuations of the fluorescence intensity, the intensity–intensity autocorrelation function can be calculated and is plotted against logarithmic time lag. From Fig. 14.16 it is obvious that the characteristic diffusion time increased with increasing proximity to the center of the contact. Their physical meaning is to describe the time to diffuse through the spot of calibrated diameter,  $\approx 0.5\ \mu\text{m}$ , at which the interrogatory laser beam was focused. The time scale of these processes, which can be estimated as the time at which the autocorrelation function decayed to one half of its initial value, slowed for example from 2 ms (rhodamine 123 in bulk propane diol) to 800 ms (the slowest curve shown in Fig. 14.16a).

For quantitative analysis, one can fit these curves to the standard model for two-dimensional Fickian diffusion and assume a single diffusion process; the imperfect fits towards the center of the contact zone are discussed below. Figure 14.17 shows  $D/D_{\text{bulk}}$ , the relative diffusion coefficient, plotted against position within the contact on semi-logarithmic scales; the logarithmic scale is needed because the dependence was so strong. Equivalently, assuming a Hertzian contact-pressure distribution,  $D/D_{\text{bulk}}$  is plotted against relative pressure within the contact in Fig. 14.17 (inset). A separate control experiment in which the bulk pressure was varied showed the diffusion in propane diol slowed by a much smaller amount, a factor of only 1.5, when the pressure was raised to 7 MPa. Evidently the findings described in this report are significantly larger than those produced by compressibility of the bulk fluid under isotropic pressure, and a different sort of explanation is needed.

Postulating that  $D_{\text{eff}}$  was proportional to a Boltzmann factor in energy ( $\Delta E/kT$ , where  $E$  is the energy,  $k$  the Boltzmann constant, and  $T$  the absolute temperature, which was constant),  $\Delta E$  can be regarded as the net differential normal pressure,  $\Delta p$ , times an activation volume,  $\Delta V_{\text{act}}$ . Figure 14.17 (inset) shows that the data are consistent with the implied exponential decrease of  $D_{\text{eff}}$  with  $p$ , in spite of the fact that  $p$  is mechanical pressure squeezing the confined fluid, not the usual isotropic pressure. From the slope in Fig. 14.17, one deduces that  $\Delta V_{\text{act}} = 15 - 20\ \text{nm}^3$ . It is intriguingly close to the activation volume obtained some years ago from independent friction measurements [122]. In the bulk, by contrast, the activation volume for diffusion is only  $\approx 0.2\ \text{nm}^3$ , the size of a fluid molecule. This analysis highlights one of the key conclusions that diffusion appeared to involve cooperative rearrangements of many molecules. But this concept assumes a single reaction coordinate and a fully equilibrated homogeneous system. Therefore, it may not seem physically meaningful to identify the deduced activation volume with the lateral size of cooperatively rearranging regions within the confined films.

The inflections in the intensity–intensity autocorrelation functions of Fig. 14.18 are quantitatively reproducible on different days with fresh samples. They refer to the same data-acquisition time,  $\approx 45\ \text{min}$ . Near the edges of the contact this time is enough to produce an autocorrelation curve that conformed well to expectations for a diffusion process with a single diffusion rate. But in the same system, at the same film thickness, at the same temperature, and in the same experiment, the autocorrelation curves deviated from this expectation more and more, the higher the local mechanical pressure. The results suggest that the system became increasingly

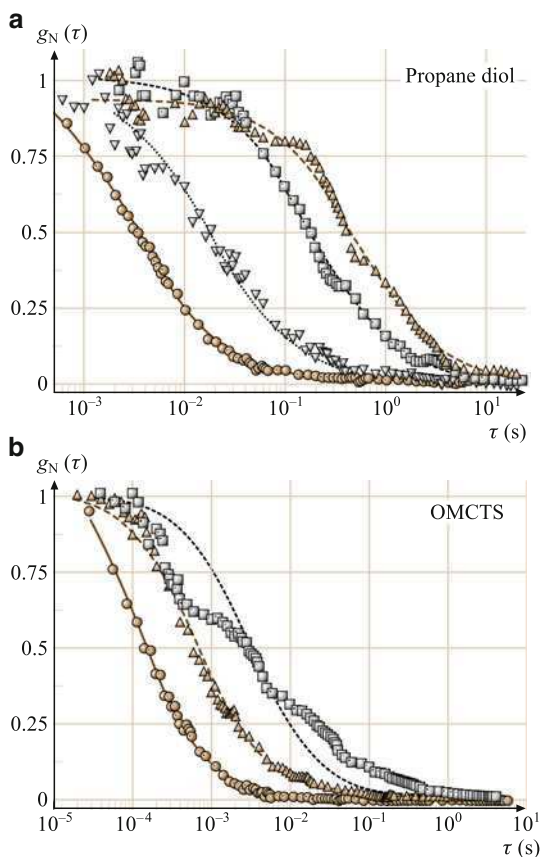
**Fig. 14.17 (a–b)**

Quantification of the effective diffusion coefficients ( $D_{\text{eff}}$ ) inferred from the raw data in the previous figure. (a) The ratio,  $D_{\text{eff}}/D_{\text{bulk}}$ , is plotted against focus position,  $a/r$ .

(b) The ratio,  $D_{\text{eff}}/D_{\text{bulk}}$ , is plotted against relative pressure squeezing the surfaces together,

$P_r \equiv P/P_{\text{max}}$  ( $P_{\text{max}} \approx 4$  MPa) assuming a Hertzian pressure distribution. *Open circles* (main figures) denote rhodamine 123 in 1,2-propane diol ( $D_{\text{bulk}} \approx 8 \mu\text{m}^2/\text{s}$ ).

*Filled circles (insets)* denote coumarin 153 in OMCTS ( $D_{\text{bulk}} \approx 190 \mu\text{m}^2/\text{s}$ ). After [121] with permission



heterogeneous with increasing pressure, so much so that the spatial resolution of this experiment sampled zones of slightly different dynamical response. Molecules diffused at one rate through a certain micro-environment, then entered another. Physically, this signifies some kind of long-lived but quantitatively reproducible heterogeneity, which becomes increasingly intense when moving from the edges of the contact towards the center. To make this more precise, it is worth remembering that molecules in confined fluid films are known to organize into layers parallel to the confining surfaces, in which local density differs. In this scenario, the multiple processes suggested in the autocorrelation curves signify that translational diffusion rates differed in these layers. For example, for OMCTS the slowest curve in Fig. 14.18b can be decomposed into sub-processes with  $D_{\text{eff}} = 0.1, 0.7, 2.9$ , and  $40 \mu\text{m}^2/\text{s}$ , the average being  $5.5 \mu\text{m}^2/\text{s}$  because the slowest two processes had the smallest amplitude and contributed least. This interpretation is consistent with the observation that the heterogeneity was more pronounced for OMCTS than for 1,2-propane diol, which is not expected to organize so definitively into distinct layers. From another perspective, these data are qualitatively reminiscent of the ‘cage’ slowing down observed in

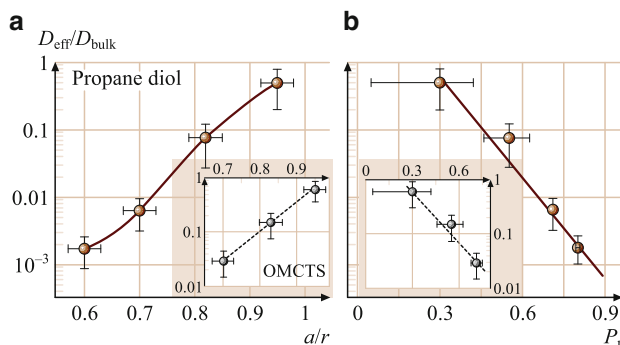


**Fig. 14.18** (a–b) Fluorescence autocorrelation functions, normalized to unity, are plotted against logarithmic time for rhodamine 123 in 1,2-propane diol (a) and coumarin 153 in OMCTS (b). The focus was at distance  $a$  from the center of the contact and the ratio  $x \equiv a/r$  was considered, where  $r$  is the contact radius. In panel (a),  $x \approx 0.95$  (circles),  $0.82$  (down triangles),  $0.7$  (squares), and  $0.6$  (up triangles). In panel (b),  $x \approx 0.95$  (circles),  $0.8$  (up triangles), and  $0.7$  (squares). Lines through the autocorrelation curves are the least-squares fit to a single Fickian diffusion process. After [111] with permission

autocorrelation curves from dynamic light scattering (DLS) studies of colloidal glasses – some kind of incipient but incomplete solidification [123]. From the available data it is difficult so far to assess the relative importance of these two scenarios, but one conclusion is firm: the scale of heterogeneity must have been impressively large, when one considers that these heterogeneities did not average out in spite of the long averaging time and the fact that the laser beam spot ( $\approx 500$ -nm diameter) exceeded the size of the diffusing molecules by so much.

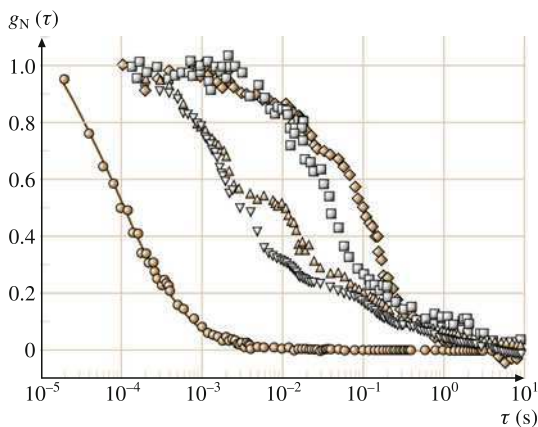
Concerning the question of how the diffusion of individual molecules is related to friction, these results suggest that the slit-averaged retardation of diffusion is much less than the confinement-induced enhancement of effective viscosity, which is known to be at least 6–7 orders of magnitude [94, 95]. However, the generality of the observation has been cast into doubt recently by mechanical experiments, which showed that the solidity of molecularly thin films using mica as substrates depends on a particular method of surface preparation [124]. Mica recleaved immediately before an experiment to minimize potential exposure to airborne contaminants, is reported to produce very low friction [125]. These results are consistent with the spectroscopy experiments, with molecular dynamics simulation and dielectric measurements, none of which had observed divergence of relaxation times, or confinement induced solidification.

## 14.6 Diffusion of Confined Molecules During Shear

In most previous friction experiments using the traditional mica cleaving procedure, static friction (a mechanically solid state) was found to give way, under

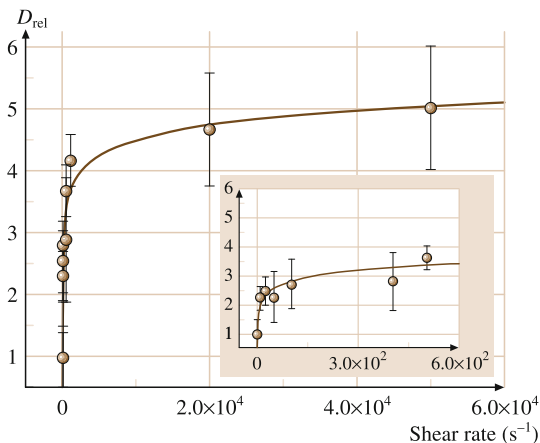
sliding, to kinetic friction (a mechanically molten state) [126]. The transition from mechanical *solidity* to *fluidity* has been interpreted to suggest a shear-induced phase transition. The premise was that, if the hypothesis of shear-melting held, shear should induce considerable quickening of the intensity–intensity autocorrelation function time scale of the dye molecule. Shear forces in SFA experiments are generated by sliding the top cylindrical lens, which is suspended from the upper portion of the apparatus by two piezoelectric bimorphs, mounted symmetrically to the two ends of the mount (Fig. 14.14). Shear forces were generated by one of the piezoelectric bimorphs (the “sender”), and the response of the device induced a voltage across the right-hand bimorph (the “receiver”). A typical frequency range is 0.1–256 Hz, with shear displacement amplitude of 0.1–10  $\mu\text{m}$ . These forces were usually sinusoidal in time but sometimes were a triangular ramp of constant slope, for better comparison with nanotribology measurements and simulations that employed a constant sliding velocity. The triangular ramp produced nearly constant velocity except for a slight acceleration to prevent stick–slip. This section is adapted from discussions in several primary accounts published previously [121].

Figure 14.19 shows representative autocorrelation curves of the fluorescence fluctuations. In Fig. 14.20, the ratio of  $D_{\text{eff}}$  during sliding to  $D_{\text{eff}}$  at rest is plotted against the shear rate; the main figure shows the entire range of shear rate and the inset magnifies the regime of small shear rate. One sees that shear speeded up this measure of the time scale of the autocorrelation function by less than a factor of 5 in



**Fig. 14.19** Illustrative fluorescence intensity–intensity autocorrelation functions,  $g_N(\tau)$ , normalized to unity at short time and plotted against logarithmic time lag  $\tau$ . The thickness of the liquid film was  $3.0 \pm 0.4$  nm relative to air, corresponding to  $\approx 3$ –4 molecular layers. The curves compare diffusion at rest in the unconfined bulk (circles;  $D = 180 \mu\text{m}^2/\text{s}$ ) and at two radial positions (“a”) within the contact zone of radius  $r \approx 25 \mu\text{m}$ ;  $a/r = 0.7$  (triangles) and  $a/r = 0.5$  (squares). These data are taken at rest (open symbols) and while sliding (filled symbols) at shear rates of  $10^4$  and  $10^2 \text{ s}^{-1}$ , respectively. Sliding was performed at 1–256 Hz such that it was unidirectional for half the period then reversed direction, and so on repetitively; for the data shown here, it was 256 and 32 Hz, respectively. Lines through the data for the bulk are fits to a single diffusion process. After [111] with permission

**Fig. 14.20** The ratio ( $\lambda$ ) of the effective diffusion coefficient during sliding (defined in text) to that at rest, plotted against peak shear rate. The data represent the average of more than 30 experiments, with error bars indicated. The *inset* shows the low-shear part of this data. After [121] with permission



every case [121]. The significance is that this affords a direct (negative) test of the common hypothesis that the transition from rest to sliding reflects shear melting that is analogous to the melting transition of a solid. The reason that the autocorrelation functions were unaffected by motion is believed to be that the fluid undergoes partial slip when the moving surface is smooth; the same conclusion follows from friction measurements in similar systems.

Taken together, these ultrafast spectroscopy experiments show that these complex molecularly thin systems retain a high degree of fluidity at the molecular level. While it is true that the structure factor of in-plane correlation is predicted from computer simulations to be enhanced relative to the bulk and that the activation volume for diffusion exceeds that in the bulk liquid by about three orders of magnitude, indicating a higher degree of order than in the bulk fluid, shear does not appear to substantially modify the degree of fluidity inferred by direct measurements of the diffusion of individual molecules. An agenda for future investigation will be to understand better the relationship between the mechanical friction response, which is an ensemble average, and measurements such as those presented here, which refer to the motion of individual molecules.

## 14.7 Summary

We have reviewed some recent advances in the experimental study of confined fluids. Some important questions involving thin liquid films with broad applications from biology to tribology have been addressed with complementary approaches. Surface and interfacial forces of liquids in intimate contact with surfaces can be directly measured by SFA, AFM and other force-based techniques. Meanwhile, scattering, microscopic and spectroscopic techniques combined with the surface forces apparatus have been developed to provide unique experimental platforms in



order to understand the structure, the phase behavior, and the dynamical responses of fluids confined between surfaces whose spacing becomes comparable to the correlation length of short-range packing, the size of supramolecular structures, and/or the size of the molecules. Taking all the efforts together, the study of fluid molecules in close proximity to surfaces and under confinement gets us to the nitty-gritty of the beauty and distinction of the nano-world and nanotechnology.

**Acknowledgement** Y. Elaine Zhu gratefully acknowledges the financial support from the US Department of Energy, Division of Materials Science (Grant No. DE-FG02-07ER46390) and the National Science Foundation (Grant No. CBET-0651408 and CBET-0730813). Ashis Mukhopadhyay acknowledges the supports of the American Chemical Society Petroleum Research fund (PRF No. 44953-G5) and National Science Foundation (Grant No. DMR-0605900). Steve Granick appreciates financial support from the NSF (Surface Engineering program) and also from the NSF (Polymers Program, Grant No. DMR-0605947).

## References

1. J.N. Israelachvili, *Intermolecular and Surface Forces*, 2nd edn. (Academic, New York, 1991)
2. B. Bhushan, J.N. Israelachvili, U. Landman, Nanotribology – Friction, wear and lubrication at the atomic-scale. *Nature* **374**, 607–616 (1995)
3. J.M. Drake, J. Klafter, P.E. Levitz, R.M. Overney, M. Urbakh, *Dynamics in Small Confining Systems V* (Materials Research Society, Warrendale, 2000)
4. S. Granick, Soft matter in a tight spot. *Phys. Today* **52**, 26–31 (1999)
5. C.M. Mate, G.M. McClelland, R. Erlandsson, S. Chiang, Atomic-scale friction of a tungsten tip on a graphite surface. *Phys. Rev. Lett.* **59**, 1942–1945 (1987)
6. G. Meyer, N.M. Amer, Simultaneous measurement of lateral and normal forces with an optical-beam-deflection atomic force microscope. *Appl. Phys. Lett.* **57**, 2089–2091 (1990)
7. S. Granick, Y. Zhu, H. Lee, Slippery questions about complex fluids flowing past solids. *Nat. Mater.* **2**, 221–227 (2003)
8. Y. Zhu, S. Granick, Limits of the hydrodynamic no-slip boundary condition. *Phys. Rev. Lett.* **88**, 106102 (2002)
9. Y. Zhu, S. Granick, Rate-dependent slip of Newtonian liquid at smooth surfaces. *Phys. Rev. Lett.* **87**, 096105 (2001)
10. B.S. Massey, *Mechanics of Fluids*, 6th edn. (Chapman Hall, London, 1989)
11. P.-G. de Gennes, Viscometric flows of tangled polymers. *C. R. Acad. Sci. B. Phys.* **288**, 219 (1979)
12. L. Léger, E. Raphael, H. Hervet, Surface-anchored polymer chains: Their role in adhesion and friction. *Adv. Polym. Sci.* **138**, 185–225 (1999)
13. O.I. Vinogradova, Slippage of water over hydrophobic surfaces. *Int. J. Miner. Process.* **56**, 31–60 (1999)
14. C. Mak, J. Krim, Quartz-crystal microbalance studies of the velocity dependence of interfacial friction. *Phys. Rev. B* **58**, 5157–5179 (1998)
15. S.M. Tholen, J.M. Parpia, Slip and the effect of He-4 at the He-3–silicon interface. *Phys. Rev. Lett.* **67**, 334–337 (1991)
16. C. Huh, L.E. Scriven, Hydrodynamic model of steady movement of a solid/liquid/fluid contact line. *J. Colloid Interface Sci.* **35**, 85–101 (1971)
17. G. Reiter, A.L. Demirel, S. Granick, From static to kinetic friction in confined liquid-films. *Science* **263**, 1741–1744 (1994)

18. G. Reiter, A.L. Demirel, J.S. Peanasky, L. Cai, S. Granick, Stick to slip transition and adhesion of lubricated surfaces in moving contact. *J. Chem. Phys.* **101**, 2606–2615 (1994)
19. N.V. Churaev, V.D. Sobolev, A.N. Somov, Slippage of liquids over lyophobic solid surfaces. *J. Colloid Interface Sci.* **97**, 574–581 (1984)
20. D.Y.C. Chan, R.G. Horn, The drainage of thin liquid films between solid surfaces. *J. Chem. Phys.* **83**, 5311–5324 (1985)
21. J.N. Israelachvili, Measurement of the viscosity of liquids in very thin films. *J. Colloid Interface Sci.* **110**, 263–271 (1986)
22. J.F. Nye, A calculation on the sliding of ice over a wavy surface using a Newtonian viscous approximation. *Proc. R. Soc. A* **311**, 445–467 (1969)
23. S. Richardson, On the no-slip boundary condition. *J. Fluid Mech.* **59**, 707–719 (1973)
24. K.M. Jansons, Determination of the macroscopic (partial) slip boundary condition for a viscous flow over a randomly rough surface with a perfect slip microscopic boundary condition. *Phys. Fluids* **31**, 15–17 (1988)
25. P.A. Thompson, M.O. Robbins, Shear flow near solids: epitaxial order and flow boundary condition. *Phys. Rev. A* **41**, 6830–6839 (1990)
26. P.A. Thompson, S. Troian, A general boundary condition for liquid flow at solid surfaces. *Nature* **389**, 360–362 (1997)
27. J.-L. Barrat, L. Bocquet, Large slip effect at a nonwetting fluid–solid interface. *Phys. Rev. Lett.* **82**, 4671–4674 (1999)
28. R. Pit, H. Hervet, L. Liger, Direct experimental evidence of slip in hexadecane–solid interfaces. *Phys. Rev. Lett.* **85**, 980–983 (2000)
29. V.S.J. Craig, C. Neto, D.R.M. Williams, Shear-dependent boundary slip in aqueous Newtonian liquid. *Phys. Rev. Lett.* **87**, 54504 (2001)
30. O.A. Kiseleva, V.D. Sobolev, N.V. Churaev, Slippage of the aqueous solutions of cetyltrimethylammonium bromide during flow in thin quartz capillaries. *Colloid J.* **61**, 263–264 (1999)
31. Y. Zhu, S. Granick, Apparent slip of Newtonian fluids past adsorbed polymer layers. *Macromolecules* **36**, 4658–4663 (2002)
32. Y. Zhu, S. Granick, The no slip boundary condition switches to partial slip when the fluid contains surfactant. *Langmuir* **18**, 10058–10063 (2002)
33. J. Baudry, E. Charlaix, A. Tonck, D. Mazuyer, Experimental evidence of a large slip effect at a nonwetting fluid–solid interface. *Langmuir* **17**, 5232–5236 (2002)
34. D.C. Tretheway, C.D. Meinhart, Apparent fluid slip at hydrophobic microchannel walls. *Phys. Fluids* **14**, L9–L12 (2002)
35. H.A. Barnes, A review of the slip (wall depletion) of polymer solutions, emulsions and particle suspensions in viscometers: Its cause, character, and cure. *J. Nonnewton. Fluid Mech.* **56**, 221–251 (1995)
36. E.C. Achilleos, G. Georgiou, S.G. Hatzikiriakos, Role of processing aids in the extrusion of molten polymers. *J. Vinyl Additive Technol.* **8**, 7–24 (2002)
37. H. Brenner, V. Ganesan, Molecular wall effects: Are conditions at a boundary ‘boundary conditions’? *Phys. Rev. E* **61**, 6879–6897 (2000)
38. J. Gao, W.D. Luedtke, U. Landman, Structures, solvation forces and shear of molecular films in a rough nano-confinement. *Tribol. Lett.* **9**, 3–134 (2000)
39. C. Denniston, M.O. Robbins, Molecular and continuum boundary conditions for a miscible binary fluid. *Phys. Rev. Lett.* **87**, 178302 (2001)
40. S.E. Campbell, G. Luengo, V.I. Srdanov, F. Wudl, J.N. Israelachvili, Very low viscosity at the solid–liquid interface induced by adsorbed C-60 monolayers. *Nature* **382**, 520–522 (1996)
41. E. Bonaccorso, M. Kappl, H.-J. Butt, Hydrodynamic force measurements: Boundary slip of water on hydrophilic surfaces and electrokinetic effects. *Phys. Rev. Lett.* **88**, 076103 (2002)

42. M.M. Britton, P.T. Callaghan, Two-phase shear band structures at uniform stress. *Phys. Rev. Lett.* **78**, 4930–4933 (1997)
43. O.I. Vinogradova, Drainage of a thin liquid-film confined between hydrophobic surfaces. *Langmuir* **11**, 2213–2220 (1995)
44. J.S. Peanasky, H.M. Schneider, S. Granick, C.R. Kessel, Self-assembled monolayers on mica for experiments utilizing the surface forces apparatus. *Langmuir* **11**, 953–962 (1995)
45. H.A. Spikes, The half-wetted bearing. Part 2: Potential application to low load contacts. *Proc. Inst. Mech. Eng. Part J* **217**, 15–26 (2003)
46. P.-G. de Gennes, On fluid/wall slippage. *Langmuir* **18**, 3413–3414 (2002)
47. J.W.G. Tyrrell, P. Attard, Atomic force microscope images of nanobubbles on a hydrophobic surface and corresponding force–separation data. *Langmuir* **18**, 160–167 (2002)
48. N. Ishida, T. Inoue, N. Miyahara, K. Higashitani, Nano bubbles on a hydrophobic surface in water observed by tapping-mode atomic force microscopy. *Langmuir* **16**, 6377–6380 (2000)
49. U.C. Boehnke, T. Remmler, H. Motschmann, S. Wurlitzer, J. Hauwede, T.M. Fischer, Partial air wetting on solvophobic surfaces in polar liquids. *J. Colloid Interface Sci.* **211**, 243–251 (1999)
50. K. Lum, D. Chandler, J.D. Weeks, Hydrophobicity at small and large length scales. *J. Phys. Chem. B* **103**, 4570–4577 (1999)
51. X. Zhang, Y. Zhu, S. Granick, Softened hydrophobic attraction between macroscopic surfaces in relative motion. *J. Am. Chem. Soc.* **123**, 6736–6737 (2001)
52. X. Zhang, Y. Zhu, S. Granick, Hydrophobicity at a Janus Interface. *Science* **295**, 663–666 (2002)
53. T. Onda, S. Shibuichi, N. Satoh, K. Tsuji, Super-water-repellent fractal surfaces. *Langmuir* **12**, 2125–2127 (1996)
54. J. Bico, C. Marzolin, D. Quiri, Pearl drops. *Europhys. Lett.* **47**, 220–226 (1999)
55. S. Herminghaus, Roughness-induced non-wetting. *Europhys. Lett.* **52**, 165–170 (2000)
56. K. Watanabe, Y. Udagawa, H. Udagawa, Drag reduction of Newtonian fluid in a circular pipe with a highly water-repellent wall. *J. Fluid Mech.* **381**, 225–238 (1999)
57. D.W. Bechert, M. Bruse, W. Hage, R. Meyer, Fluid mechanics of biological surfaces and their technological application. *Naturwissenschaften* **87**, 157–171 (2000)
58. W. Kauzmann, Some forces in the interpretation of protein denaturation. *Adv. Protein Chem.* **14**, 1 (1959)
59. C. Tanford, *The Hydrophobic Effect – Formation of Micelles and Biological Membranes* (Wiley-Interscience, New York, 1973). 1973
60. F.H. Stillinger, Structure in aqueous solutions of nonpolar solutes from the standpoint of scaled-particle theory. *J. Solution Chem.* **2**, 141 (1973)
61. E. Ruckenstein, P. Rajora, On the no-slip boundary-condition of hydrodynamics. *J. Colloid Interface Sci.* **96**, 488–491 (1983)
62. L.R. Pratt, D. Chandler, Theory of hydrophobic effect. *J. Chem. Phys.* **67**, 3683–3704 (1977)
63. A. Ben-Naim, *Hydrophobic Interaction* (Kluwer, New York, 1980)
64. A. Wallqvist, B.J. Berne, Computer-simulation of hydrophobic hydration forces stacked plates at short-range. *J. Phys. Chem.* **99**, 2893–2899 (1995)
65. G. Hummer, S. Garde, A.E. Garcia, A. Pohorille, L.R. Pratt, An information theory model of hydrophobic interactions. *Proc. Natl. Acad. Sci. U.S.A.* **93**, 8951–8955 (1996)
66. Y.K. Cheng, P.J. Rossky, The effect of vicinal polar and charged groups on hydrophobic hydration. *Biopolymers* **50**, 742–750 (1999)
67. D.M. Huang, D. Chandler, Temperature and length scale dependence of hydrophobic effects and their possible implications for protein folding. *Proc. Natl. Acad. Sci. U.S.A.* **97**, 8324–8327 (2000)
68. G. Hummer, S. Garde, A.E. Garcia, L.R. Pratt, New perspectives on hydrophobic effects. *Chem. Phys.* **258**, 349–370 (2000)
69. D. Bratko, R.A. Curtis, H.W. Blanch, J.M. Prausnitz, Interaction between hydrophobic surfaces with metastable intervening liquid. *J. Chem. Phys.* **115**, 3873–3877 (2001)

70. Y.-H. Tsao, D.F. Evans, H. Wennerstvm, Long-range attractive force between hydrophobic surfaces observed by atomic force microscopy. *Science* **262**, 547–550 (1993)
71. R.F. Considine, C.J. Drummond, Long-range force of attraction between solvophobic surfaces in water and organic liquids containing dissolved air. *Langmuir* **16**, 631–635 (2000)
72. J.W.G. Tyrrell, P. Attard, Images of nanobubbles on hydrophobic surfaces and their interactions. *Phys. Rev. Lett.* **87**, 176104 (2001)
73. J. Peachey, J. Van Alsten, S. Granick, Design of an apparatus to measure the shear response of ultrathin liquid-films. *Rev. Sci. Instrum.* **62**, 463–473 (1991)
74. C.Y. Lee, J.A. McCammon, P.J. Rossky, The structure of liquid water at an extended hydrophobic surface. *J. Chem. Phys.* **80**, 4448–4455 (1984)
75. J.N. Israelachvili, R.M. Pashley, The hydrophobic interaction is long-range, decaying exponentially with distance. *Nature* **300**, 341–342 (1982)
76. J.N. Israelachvili, R.M. Pashley, Measure of the hydrophobic interaction between 2 hydrophobic surfaces in aqueous-electrolyte solutions. *J. Colloid Interface Sci.* **98**, 500–514 (1984)
77. R.M. Pashley, P.M. McGuiggan, B.W. Ninham, D.F. Evans, Attractive forces between uncharged hydrophobic surfaces-direct measurement in aqueous-solution. *Science* **229**, 1088–1089 (1985)
78. P.M. Claesson, C.E. Blom, P.C. Herder, B.W. Ninham, Interactions between water-stable hydrophobic Langmuir–Blodgett monolayers on mica. *J. Colloid Interface Sci.* **114**, 234–242 (1986)
79. P.M. Claesson, H.K. Christenson, Very long-range attractive forces between uncharged hydrocarbon and fluorocarbon surfaces in water. *J. Phys. Chem.* **92**, 1650–1655 (1988)
80. H.K. Christenson, P.M. Claesson, J. Berg, P.C. Herder, Forces between fluorocarbon surfactant monolayers – Salt effects on the hydrophobic interact. *J. Phys. Chem.* **93**, 1472–1478 (1989)
81. O. Spalla, Long-range attraction between surfaces: Existence and amplitude? *Curr. Opin. Colloid Interface Sci.* **5**, 5–12 (2000)
82. J. Wood, R. Sharma, How long is the long-range hydrophobic attraction? *Langmuir* **11**, 4797–4802 (1995)
83. J.L. Parker, P.M. Claesson, P. Attard, Bubbles, cavities, and the long-range attraction between hydrophobic surfaces. *J. Phys. Chem.* **98**, 8468–8480 (1994)
84. A. Carambassis, L.C. Jonker, P. Attard, M.W. Rutland, Forces measured between hydrophobic surfaces due to a submicroscopic bridging bubble. *Phys. Rev. Lett.* **80**, 5357–5360 (1998)
85. V.S.J. Craig, B.W. Ninham, R.M. Pashley, Direct measurement of hydrophobic forces: A study of dissolved gas, approach rate, and neutron irradiation. *Langmuir* **15**, 1562–1569 (1999)
86. R.F. Considine, R.A. Hayes, R.G. Horn, Forces measured between latex spheres in aqueous electrolyte: Non-DLVO behavior and sensitivity to dissolved gas. *Langmuir* **15**, 1657–1659 (1999)
87. J.D. Ferry, *Viscoelastic Properties of Polymers*, 3rd edn. (Wiley, New York, 1982)
88. Y. Zhu, S. Granick, Viscosity of interfacial water. *Phys. Rev. Lett.* **87**, 096104 (2001)
89. H.H. Winter, F. Chambon, Analysis of linear viscoelasticity of a cross-linking polymer at the gel point. *J. Rheol.* **30**, 367–382 (1986)
90. R. Yamamoto, A. Onuki, Dynamics of highly supercooled liquids: Heterogeneity, rheology, and diffusion. *Phys. Rev. E* **58**, 3515–3529 (1998)
91. A.O. Parry, R. Evans, Influence of wetting on phase-equilibria – A novel mechanism for critical-point shifts in films. *Phys. Rev. Lett.* **64**, 439–442 (1990)
92. K. Binder, D.P. Landau, A.M. Ferrenberg, Thin ising films with completing walls – A Monte Carlo study. *Phys. Rev. E* **51**, 2823–2838 (1995)
93. D.K. Schwartz, M.L. Schlossman, E.H. Kawamoto, G.J. Kellog, P.S. Perhan, B.M. Ocko, Thermal diffuse X-ray-scattering studies of the water–vapor interface. *Phys. Rev. A* **41**, 5687–5690 (2000)
94. S. Granick, Motions and relaxations of confined liquids. *Science* **253**, 1374–1379 (1991)

95. J. Klein, E. Kumacheva, Simple liquids confined to molecularly thin layers. I. Confinement-induced liquid-to-solid phase transitions. *J. Chem. Phys.* **108**, 6996–7009 (1998)
96. E. Kumacheva, J. Klein, Simple liquids confined to molecularly thin layers. II. Shear and frictional behavior of solidified films. *J. Chem. Phys.* **108**, 7010–7022 (1998)
97. C. Drummond, J. Israelachvili, Dynamic phase transitions in confined lubricant fluids under shear. *Phys. Rev. E* **63**, 041506 (2001)
98. Y. Golan, M. Seitz, C. Luo, A. Martin-Herranz, M. Yasa, Y.L. Li, C.R. Safinya, J. Israelachvili, The X-ray surface forces apparatus for simultaneous X-ray diffraction and direct normal and lateral force measurements. *Rev. Sci. Instrum.* **73**, 2486–248 (2002)
99. Y. Golan, A. Martin-Herranz, Y. Li, C.R. Safinya, J. Israelachvili, Direct observation of shear-induced orientational phase coexistence in a lyotropic system using a modified X-ray surface forces apparatus. *Phys. Rev. Lett.* **86**, 1263–1266 (2001)
100. S.M. Baker, G. Smith, R. Pynn, P. Butler, J. Hayter, W. Hamilton, L. Magid, Shear cell for the study of liquid–solid interfaces by neutron scattering. *Rev. Sci. Instrum.* **65**, 412–416 (1994)
101. T.L. Kuhl, G.S. Smith, J.N. Israelachvili, J. Majewski, W. Hamilton, Neutron confinement cell for investigating complex fluids. *Rev. Sci. Instrum.* **72**, 1715–1720 (2001)
102. O.H. Seeck, H. Kim, D.R. Lee, D. Shu, I.D. Kaendler, J.K. Basu, S.K. Sinha, Observation of thickness quantization in liquid films confined to molecular dimension. *Europhys. Lett.* **60**, 376–382 (2002)
103. A. Dhinojwala, S. Granick, Micron-gap rheo-optics with parallel plates. *J. Chem. Phys.* **107**, 8664–8667 (1998)
104. I. Soga, A. Dhinojwala, S. Granick, Optorheological studies of sheared confined fluids with mesoscopic thickness. *Langmuir* **4**, 1156–1161 (1998)
105. S. Mamedov, A.D. Schwab, A. Dhinojwala, A device for surface study of confined micron thin films in a total internal reflection geometry. *Rev. Sci. Instrum.* **73**, 2321–2324 (2002)
106. P. Frantz, F. Wolf, X.D. Xiao, Y. Chen, S. Bosch, M. Salmeron, Design of surface forces apparatus for tribology studies combined with nonlinear optical spectroscopy. *Rev. Sci. Instrum.* **68**, 2499–2504 (1997)
107. X.S. Xie, J.K. Trautman, Optical studies of single molecules at room temperature. *Annu. Rev. Phys. Chem.* **49**, 441–480 (1998)
108. W.E. Moerner, M. Orritt, Illuminating single molecules. *Science* **283**, 670–1676 (1999)
109. L.A. Deschenes, D.A. Vanden Bout, Single molecule studies of heterogeneous dynamics in polymer melts near the glass transition. *Science* **292**, 255–258 (2001)
110. A. Mukhopadhyay, S. Granick, An integrated platform for surface force measurements and fluorescence correlation spectroscopy. *Rev. Sci. Instrum.* **74**, 3067–3072 (2003)
111. A. Mukhopadhyay, J. Zhao, S.C. Bae, S. Granick, Contrasting friction and diffusion in molecularly-thin films. *Phys. Rev. Lett.* **89**, 136103 (2002)
112. K.M. Berland, P.T.C. So, E. Gratton, 2-Photon fluorescence correlation spectroscopy – Method and application to the intracellular environment. *Biophys. J.* **68**, 694–701 (1995)
113. U. Kettling, A. Koltermann, P. Schwille, M. Eigen, Real-time enzyme kinetics monitored by dual-color fluorescence cross-correlation spectroscopy. *Proc. Natl. Acad. Sci. U.S.A.* **95**, 1416–1420 (1998)
114. A.M. Lieto, R.C. Cush, N.L. Thompson, Ligand-receptor kinetics measured by total internal reflection with fluorescence correlation spectroscopy. *Biophys. J.* **85**, 3294–3302 (2003)
115. P. Schwille, U. Haupts, S. Maiti, W.W. Webb, Molecular dynamics in living cells observed by fluorescence correlation spectroscopy with one- and two-photon excitation. *Biophys. J.* **77**, 2251–2265 (1999)
116. W.W. Webb, Fluorescence correlation spectroscopy: inception, biophysical experimentations, and prospectus. *Appl. Opt.* **40**, 3969–3983 (2001)
117. P.S. Dittrich, P. Schwill, Photobleaching and stabilization of fluorophores used for single-molecule analysis with one- and two-photon excitation. *Appl. Phys. B* **73**, 829–837 (2001)
118. M. Born, E. Wolf, *Principles of Optics* (Cambridge University Press, Cambridge, 1999), p. 7

119. I. Sridhar, K.L. Johnson, N.A. Fleck, Adhesion mechanics of the surface force apparatus. *J. Appl. Phys. D* **30**, 1710–1719 (1997)
120. Y. Zhu, S. Granick, Reassessment of solidification in fluids confined between mica sheets. *Langmuir* **19**, 8148–8151 (2003)
121. A. Mukhopadhyay, S.C. Bae, J. Zhao, S. Granick, How confined lubricants diffuse during shear. *Phys. Rev. Lett.* **93**, 236105 (2004)
122. H.-W. Hu, G. Carson, S. Granick, Relaxation-time of confined liquids under shear. *Phys. Rev. Lett.* **66**, 2758–2761 (1991)
123. K.N. Pham, A.M. Puertas, J. Bergenholtz, S.U. Egelhaaf, A. Moussaid, P.N. Pusey, B. Schofield, M.E. Cates, M. Fuchs, W.C.K. Poon, Multiple glassy states in a simple model system. *Science* **296**, 104–106 (2002)
124. Z.Q. Lin, S. Granick, Platinum nanoparticles at mica surfaces. *Langmuir* **19**, 7061–7070 (2003)
125. Y. Zhu, S. Granick, Superlubricity: A paradox about confined fluids resolved. *Phys. Rev. Lett.* **93**, 096101 (2004)
126. M. Urbakh, J. Klafter, D. Gourdon, J. Israelachvili, The nonlinear nature of friction. *Nature* **430**, 525–528 (2004)

## Chapter 15

# Friction and Wear on the Atomic Scale

Enrico Gnecco, Roland Bennewitz, Oliver Pfeiffer, Anisoara Socoliuc,  
and Ernst Meyer

**Abstract** Friction has long been the subject of research: the empirical da Vinci–Amontons friction laws have been common knowledge for centuries. Macroscopic experiments performed by the school of *Bowden* and *Tabor* revealed that macroscopic friction can be related to the collective action of small asperities. Over the last 15 years, experiments performed with the atomic force microscope have provided new insights into the physics of single asperities sliding over surfaces. This development, together with the results from complementary experiments using surface force apparatus and the quartz microbalance, have led to the new field of *nanotribology*. At the same time, increasing computing power has permitted the simulation of processes that occur during sliding contact involving several hundreds of atoms. It has become clear that atomic processes cannot be neglected when interpreting nanotribology experiments. Even on well-defined surfaces, experiments have revealed that atomic structure is directly linked to friction force. This chapter will describe friction force microscopy experiments that reveal, more or less directly, atomic processes during sliding contact.

We will begin by introducing friction force microscopy, including the calibration of cantilever force sensors and special aspects of the ultrahigh vacuum environment. The empirical Tomlinson model often used to describe atomic stick-slip results is therefore presented in detail. We review experimental results regarding atomic friction, including thermal activation, velocity dependence and temperature dependence. The geometry of the contact is crucial to the interpretation of experimental results, such as the calculation of the lateral contact stiffness, as we shall see. The onset of wear on the atomic scale has recently been studied experimentally and it is described here. In order to compare results, we present molecular dynamics simulations that are directly related to atomic friction experiments. The chapter ends with a discussion of dissipation measurements performed in noncontact force microscopy, which may become an important complementary tool for the study of mechanical dissipation in nanoscopic devices.

## 15.1 Friction Force Microscopy in Ultrahigh Vacuum

The *friction force microscope* (FFM, also called the lateral force microscope, LFM) exploits the interaction of a sharp tip sliding on a surface in order to quantify dissipative processes down to the atomic scale (Fig. 15.1).

### 15.1.1 Friction Force Microscopy

The relative motion of tip and surface is realized by a *scanner* created from piezoelectric elements, which moves the surface perpendicularly to the tip with a certain periodicity. The scanner can be also extended or retracted in order to vary the normal force  $F_N$  that is applied to the surface. This force is responsible for the deflection of the *cantilever* that supports the tip. If the normal force  $F_N$  increases while scanning due to the local slope of the surface, the scanner is retracted by a feedback loop. On the other hand, if  $F_N$  decreases, the surface is brought closer to the tip by extending the scanner. In this way, the surface topography can be determined line-by-line from the vertical displacement of the scanner. Accurate control of such vertical movement is made possible by a light beam reflected from the rear of the lever into a photodetector. When the cantilever bends, the light spot on the detector moves up or down and causes the photocurrent to vary, when in turn triggers a corresponding change in the normal force  $F_N$  applied.

The relative sliding of tip and surface is usually also accompanied by *friction*. A lateral force  $F_L$ , which acts in the opposite direction to the scan velocity  $v$  hinders

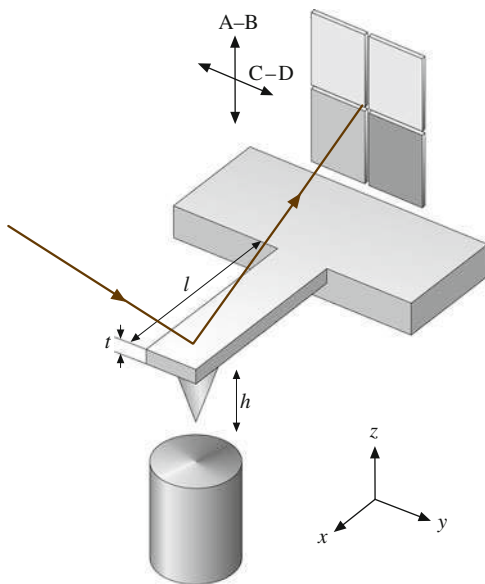


**Fig. 15.1** Schematic diagram of a beam-deflection friction force microscope



the motion of the tip. This force causes torsion in the cantilever, which can be observed along with the topography if the photodetector can detect not only the normal deflection but also the lateral movement of the lever while scanning. In practice this is achieved using a four-quadrant photodetectors, as shown in Fig. 15.1. We should note that friction forces also cause lateral bending of the cantilever, but this effect is negligible if the thickness of the lever is much less than the width.

The FFM was first used by Mate et al. in 1987 to study the friction associated with atomic features [1] (just one year after Binnig et al. introduced the atomic force microscope [2]). In their experiment, Mate used a tungsten wire and a slightly different technique to that described above to detect lateral forces (nonfiber interferometry). Optical beam deflection was introduced later by Marti et al. and Meyer et al. [3, 4]. Other methods of measuring the forces between tip and surface include capacitance detection [5], dual fiber interferometry [6] and piezolevers [7]. In the first method, two plates close to the cantilever reveal the capacitance while scanning. The second technique uses two optical fibers to detect the cantilever deflection along two orthogonal directions aligned  $45^\circ$  with respect to the surface normal. Finally, in the third method, cantilevers with two Wheatstone bridges at their bases reveal normal and lateral forces, which are respectively proportional to the sum and the difference of both bridge signals.

### 15.1.2 Force Calibration

Force calibration is relatively simple if rectangular cantilevers are used. Due to possible discrepancies with the geometric values provided by manufacturers, one should use optical and electron microscopes to determine the width, thickness and length of the cantilever ( $w$ ,  $t$ ,  $l$ ), the tip height  $h$  and the position of the tip with respect to the cantilever. The thickness of the cantilever can also be determined from the resonance frequency of the lever  $f_0$  using the relation [8]

$$t = \frac{2\sqrt{12}\pi}{1.875^2} \sqrt{\frac{\rho}{E}} f_0 l^2. \quad (15.1)$$

Here  $\rho$  is the density of the cantilever and  $E$  is its Young's modulus. The normal spring constant ( $c_N$ ) and the lateral spring constant ( $c_L$ ) of the lever are given by

$$c_N = \frac{Ewt^3}{4l^3}, \quad c_L = \frac{Gwt^3}{3h^2l}, \quad (15.2)$$

where  $G$  is the shear modulus. Figure 15.2 shows some SEM images of rectangular silicon cantilevers used for FFM. In the case of silicon,  $\rho = 2.33 \times 10^3 \text{ kg/m}^3$ ,  $E = 1.69 \times 10^{11} \text{ N/m}^2$  and  $G = 0.5 \times 10^{11} \text{ N/m}^2$ . Thus, for the cantilever shown in Fig. 15.2,  $c_N = 1.9 \text{ N/m}$  and  $c_L = 675 \text{ N/m}$ .

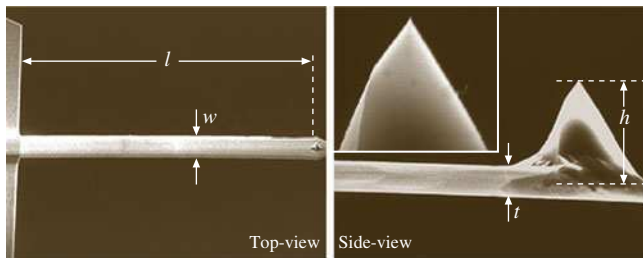
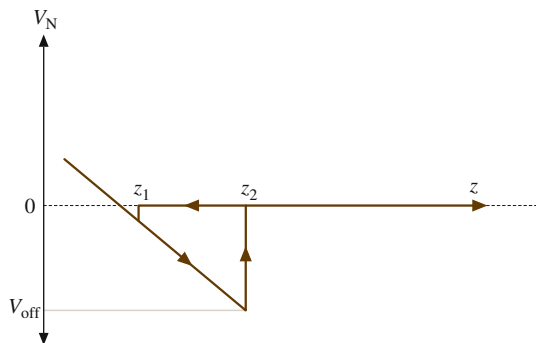


**Fig. 15.2** SEM images of a rectangular cantilever. The relevant dimensions are  $l = 445 \mu\text{m}$ ,  $w = 43 \mu\text{m}$ ,  $t = 4.5 \mu\text{m}$ ,  $h = 14.75 \mu\text{m}$ . Note that  $h$  is given by the sum of the tip height and half of the cantilever thickness (after [9])

**Fig. 15.3** Sketch of a typical force versus distance curve



The next force calibration step consists of measuring the sensitivity of the photodetector  $S_z$  (nm/V). For beam-deflection FFMs, the sensitivity  $S_z$  can be determined by force versus distance curves measured on hard surfaces (such as  $\text{Al}_2\text{O}_3$ ), where elastic deformations are negligible and the vertical movement of the scanner equals the deflection of the cantilever. A typical relation between the difference between the vertical signals on the four-quadrant detector  $V_N$  and the distance from the surface ( $z$ ) is sketched in Fig. 15.3. When the tip is approached, no signal is revealed until the tip jumps into contact at  $z = z_1$ . Further extension or retraction of the scanner results in elastic behavior until the tip jumps out of contact again at a distance  $z_2 > z_1$ . The slope of the elastic part of the curve gives the required sensitivity  $S_z$ .

The normal and lateral forces are related to the voltage  $V_N$ , and the difference between the horizontal signals  $V_L$  as follows

$$F_N = c_N S_z V_N, \quad F_L = \frac{3}{2} c_L \frac{h}{l} S_z V_L. \quad (15.3)$$

It is assumed here that the light beam is positioned above the probing tip.

The normal spring constant  $c_N$  can also be calibrated using other methods. Cleveland et al. [10] attached tungsten spheres to the tip, which changes the resonance frequency  $f_0$  according to the formula

$$f_0 = \frac{1}{2\pi} \sqrt{\frac{c_N}{M + m^*}}. \quad (15.4)$$

$M$  is the mass of the added object, and  $m^*$  is an effective mass of the cantilever, which depends on its geometry [10]. The spring constant can be extrapolated from the frequency shifts corresponding to the different masses attached.

As an alternative, Hutter et al. observed that the spring constant  $c_N$  can be related to the area of the power spectrum of the thermal fluctuations of the cantilever  $P$  [11]. The correct relation is  $c_N = 4k_B T / (3P)$ , where  $k_B \approx 1.38 \times 10^{-23}$  J/K is Boltzmann's constant and  $T$  is the temperature [12].

Cantilevers with different shapes require finite element analysis, although analytical formulas can be derived in a few cases. For V-shaped cantilevers, Neumeister et al. derived the following approximation for the lateral spring constant  $c_L$  [13]

$$c_L = \frac{Et^3}{3(1+\nu)h^2} \times \left( \frac{1}{\tan \alpha} \ln \frac{w}{d \sin \alpha} + \frac{L \cos \alpha}{w} - \frac{3 \sin 2\alpha}{8} \right)^{-1}. \quad (15.5)$$

The geometrical quantities  $L$ ,  $w$ ,  $\alpha$ ,  $d$ ,  $t$  and  $h$  are defined in Fig. 15.4. The expression for the normal constant is more complex and can be found in the cited reference.

Surfaces with well-defined profiles permit an alternative in situ calibration of lateral forces [14]. We present a slightly modified version of the method [15]. Figure 15.5 shows a commercial grating formed by alternate faces with opposite inclinations with respect to the scan direction. When the tip slides on the inclined

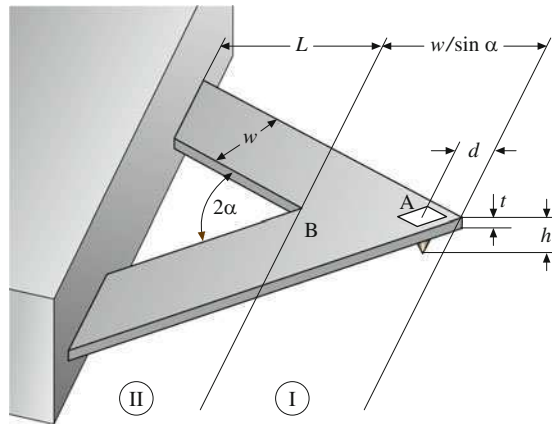


**Fig. 15.4** Geometry of a V-shaped cantilever (after [13])

**Fig. 15.5** Silicon grating formed by alternated faces angled at  $\pm 55^\circ$  from the surface (© Silicon-MDT Ltd., Moscow)

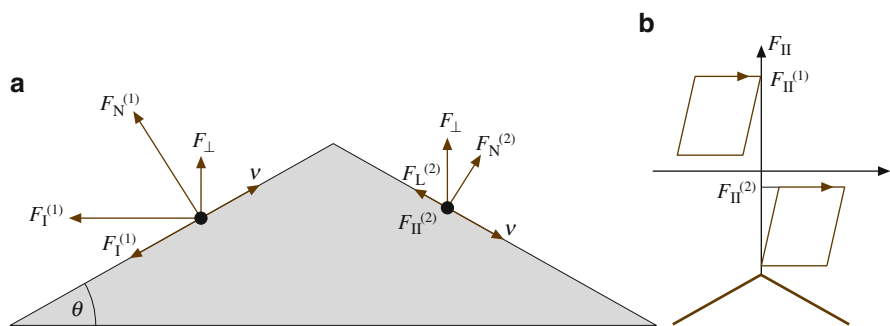
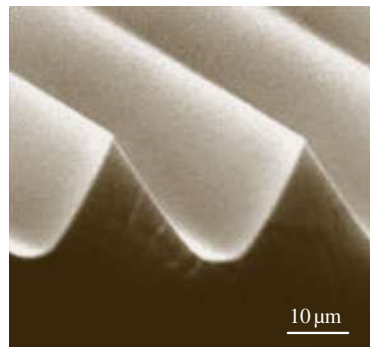


**Fig. 15.6** (a) Forces acting on a FFM tip sliding on the grating shown in Fig. 15.5; (b) friction loops acquired on the two faces

planes, the normal force  $F_N$  and the lateral force  $F_L$  with respect to the surface are different from the two components  $F_\perp$  and  $F_\parallel$ , which are separated by the photodiode (Fig. 15.6a).

If the linear relation  $F_L = \mu F_N$  holds (Sect. 15.5), the component  $F_\parallel$  can be expressed in terms of  $F_\perp$

$$F_\parallel = \frac{\mu + \tan \theta}{1 - \mu \tan \theta} F_\perp. \quad (15.6)$$

The component  $F_\perp$  is kept constant by the feedback loop. The sum of and the difference between the  $F_\parallel$  values for the two planes (1) and (2) are given by

$$\begin{aligned} F_+ &\equiv F_\parallel^{(1)} + F_\parallel^{(2)} = \frac{2\mu(1 + \tan^2 \theta)}{1 - \mu^2 \tan^2 \theta} F_\perp, \\ F_- &\equiv F_\parallel^{(1)} - F_\parallel^{(2)} = \frac{2(1 + \mu^2) \tan \theta}{1 - \mu^2 \tan^2 \theta} F_\perp. \end{aligned} \quad (15.7)$$

The values of  $F_+$  and  $F_-$  (in volts) can be measured by scanning the profile back and forth (Fig. 15.6b). If  $F_+$  and  $F_-$  are recorded with different values of  $F_\perp$ , one can determine the conversion ratio between volts and nanonewtons as well as the coefficient of friction  $\mu$ .

An accurate error analysis of lateral force calibration was provided by Schwarz et al., who revealed the importance of the cantilever oscillations induced by the feedback loop and the so-called *pull-off force* (Sect. 15.5) in friction measurements, aside from the geometrical positioning of the cantilevers and laser beams [16]. Other sources of error (in-plane deformation and cantilever tilt) have been recently discussed by Sader and coworkers [17, 18].

An adequate estimation of the radius of curvature of the tip  $R$  is also important for some applications (Sect. 15.5.2). This quantity can be evaluated with a scanning electron microscope. This allows well-defined structures such as step sites [19, 20] or whiskers [21] to be imaged. Images of these high aspect ratio structures are convolutions with the tip structure. A deconvolution algorithm that allows for the extraction of the probe tip's radius of curvature was suggested by Villarrubia [22].

### 15.1.3 The Ultrahigh Vacuum Environment

Atomic friction studies require well-defined surfaces and – whenever possible – tips. For the surfaces, established methods of surface science performed in ultrahigh vacuum (UHV) can be employed. Ionic crystals such as NaCl have become standard materials for friction force microscopy on the atomic scale. Atomically clean and flat surfaces can be prepared by cleavage in UHV. The crystal has to be heated to  $\approx 150^\circ\text{C}$  for 1 h in order to remove charge after the cleavage process. Metal surfaces can be cleaned and flattened by cycles of sputtering with argon ions and annealing. Even surfaces prepared in air or liquids, such as self-assembled molecular monolayers, can be transferred into the vacuum and studied after careful heating procedures that remove water layers.

Tip preparation in UHV is more difficult. Most force sensors for friction studies have silicon nitride or pure silicon tips. Tips can be cleaned and oxide layers removed by sputtering with argon ions. However, the sharpness of the tip is normally reduced by sputtering. As an alternative, tips can be etched in fluoric acid directly before transfer to the UHV. The significance of tip preparation is limited by the fact that the chemical and geometrical structure of the tip can undergo significant changes when sliding over the surface.

Using the friction force microscope in UHV conditions requires some additional effort. First of all, only materials with low vapor pressures can be used, which excludes most plastics and lubricants. Beam-deflection force microscopes employ either a light source in the vacuum chamber or an optical fiber guiding the light into the chamber. The positioning of the light beam on the cantilever and the reflected beam on the position-sensitive detector is achieved by motorized mirrors [23] or

by moving the light source or detector [24]. Furthermore, a motorized sample approach must be realized.

The quality of the force sensor's electrical signal can seriously deteriorate when it is transferred out of the vacuum chamber. Low noise and high bandwidth can be preserved using a preamplifier in the vacuum. Again, the choice of materials for printing and devices is limited by the need for low vapor pressure. Stronger heating of the electrical circuitry in vacuum, therefore, may be needed.

### 15.1.4 A Typical Microscope Operated in UHV

A typical AFM used in UHV is shown in Fig. 15.7. The housing (1) contains the light source and a set of lenses that focus the light onto the cantilever. Alternatively, the light can be guided via an optical fiber into the vacuum. By using light emitting diodes with low coherency it is possible to avoid interference effects often found in instruments that use a laser as the light source. A plane mirror fixed on the spherical rotor of a first stepping motor (2) can be rotated around vertical and horizontal axes in order to guide the light beam onto the rear of the cantilever, which is mounted on a removable carrier plate (3). The light is reflected off the cantilever toward a second motorized mirror (4) that guides the beam to the center of the quadrant photodiode (5), where the light is then converted into four photocurrents. Four preamplifiers in close vicinity to the photodiode allow low-noise measurements with a bandwidth of 3 MHz.

The two motors with spherical rotors, used to realign the light path after the cantilever has been exchanged, work as *inertial stepping motors*: the sphere rests on

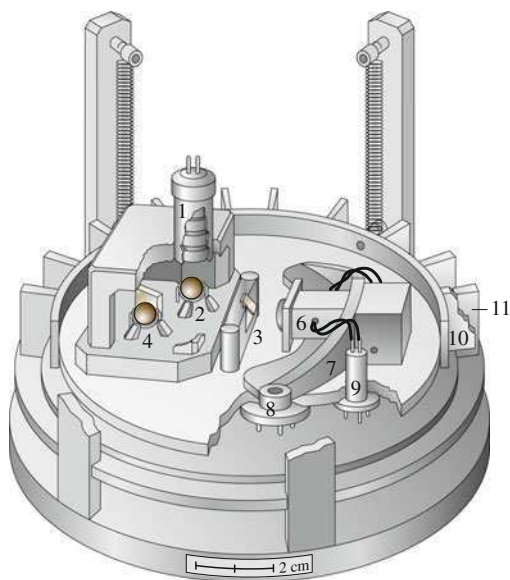


**Fig. 15.7** Schematic view of the UHV-AFM realized at the University of Basel (after [23]) (1 – light source, 2, 4 – mirrors, 3 – cantilever holders, 5 – photodetector, 6 – scanner, 7 – slider, 8 – driving piezo, 9 – fixed post, 10, 11 – eddy current damping)

three piezoelectric legs that can be moved in small amounts tangentially to the sphere. Each step of the motor consists of the slow forward motion of two legs followed by an abrupt jump backwards. During the slow forward motion, the sphere follows the legs due to friction, whereas it cannot follow the sudden jump due to its inertia. A series of these tiny steps rotates the sphere macroscopically.

The sample, which is also placed on an exchangeable carrier plate, is mounted at the end of a tube scanner (6), which can move the sample in three dimensions over several micrometers. The whole scanning head (7) is the slider of a third inertial stepping motor for coarse positioning of the sample. It rests with its flat and polished bottom on three supports. Two of them are symmetrically placed piezoelectric legs (8), whereas the third central support is passive. The slider (7) can be moved in two dimensions and rotated about a vertical axis by several millimeters (rotation is achieved by antiparallel operation of the two legs). The slider is held down by two magnets, close to the active supports, and its travel is limited by two fixed posts (9) that also serve as cable attachments. The whole platform is suspended by four springs. A ring of radial copper lamellae (10), floating between a ring of permanent magnets (11) on the base flange, acts to efficiently damp eddy currents.

## 15.2 The Tomlinson Model

In Sect. 15.3, we show that the FFM can reveal friction forces down to the atomic scale, which are characterized by a typical sawtooth pattern. This phenomenon can be seen as a consequence of a *stick-slip* mechanism, discussed by Tomlinson in 1929 [25].

### 15.2.1 One-Dimensional Tomlinson Model

In the Tomlinson model, the motion of the tip is influenced by both the interaction with the atomic lattice of the surface and the elastic deformations of the cantilever. The shape of the tip-surface potential  $V(r)$  depends on several factors, such as the chemical composition of the materials in contact and the atomic arrangement at the tip end. For the sake of simplicity, we will start the analysis in the one-dimensional case considering a sinusoidal profile with an atomic lattice periodicity  $a$  and a peak-to-peak amplitude  $E_0$ . In Sect. 15.5, we will show how the elasticity of the cantilever and the contact area can be described in a unique framework by introducing an effective lateral spring constant  $k_{\text{eff}}$ . If the cantilever moves with a constant velocity  $v$  along the  $x$ -direction, the total energy of the system is

$$E_{\text{tot}}(x, t) = -\frac{E_0}{2} \cos \frac{2\pi x}{a} + \frac{1}{2} k_{\text{eff}} (vt - x)^2. \quad (15.8)$$

**Fig. 15.8** Energy profile experienced by the FFM tip (black circle) at  $t = 0$  (dotted line) and  $t = t^*$  (continuous line)

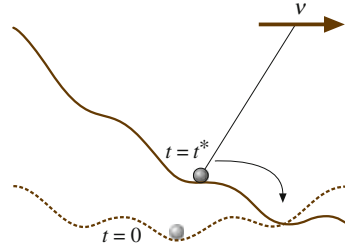


Figure 15.8 shows the energy profile  $E_{\text{tot}}(x, t)$  at two different instants. When  $t = 0$ , the tip is localized in the absolute minimum of  $E_{\text{tot}}$ . This minimum increases with time due to the cantilever motion, until the tip position becomes unstable when  $t = t^*$ .

At a given time  $t$ , the position of the tip can be determined by equating the first derivative of  $E_{\text{tot}}(x, t)$  with respect to  $x$  to zero

$$\frac{\partial E_{\text{tot}}}{\partial x} = \frac{\pi E_0}{a} \sin \frac{2\pi x}{a} - k_{\text{eff}}(vt - x) = 0. \quad (15.9)$$

The critical position  $x^*$  corresponding to  $t = t^*$  is determined by equating the second derivative  $\partial^2 E_{\text{tot}}(x, t)/\partial x^2$  to zero, which gives

$$x^* = \frac{a}{4} \arccos \left( -\frac{1}{\gamma} \right), \quad \gamma = \frac{2\pi^2 E_0}{k_{\text{eff}} a^2}. \quad (15.10)$$

The coefficient  $\gamma$  compares the strength of the interaction between the tip and the surface with the stiffness of the system. When  $t = t^*$  the tip suddenly *jumps* into the next minimum of the potential profile. The lateral force  $F^* = k_{\text{eff}}(vt - x^*)$  that induces the jump can be evaluated from (15.9) and (15.10)

$$F^* = \frac{k_{\text{eff}} a}{2\pi} \sqrt{\gamma^2 - 1}. \quad (15.11)$$

Thus the stick-slip is observed only if  $\gamma > 1$ : when the system is not too stiff or when the tip-surface interaction is strong enough. Figure 15.9 shows the lateral force  $F_L$  as a function of the cantilever position  $X$ . When the cantilever is moved to the right, the lower part of the curve in Fig. 15.9 is obtained. If, at a certain point, the cantilever's direction of motion is suddenly inverted, the force has the profile shown in the upper part of the curve. The area of the *friction loop* obtained by scanning back and forth gives the total energy dissipated.

On the other hand, when  $\gamma < 1$ , the stick-slip is suppressed. The tip slides in a continuous way on the surface and the lateral force oscillates between negative



and positive values. Instabilities vanish in this regime, which leads to the disappearance of lateral force hysteresis and correspondingly negligible dissipation losses.

### 15.2.2 Two-Dimensional Tomlinson Model

In two dimensions, the energy of our system is given by

$$E_{\text{tot}}(\mathbf{r}, t) = U(\mathbf{r}) + \frac{k_{\text{eff}}}{2} (\mathbf{v}t - \mathbf{r})^2, \quad (15.12)$$

where  $\mathbf{r} \equiv (x, y)$  and  $\mathbf{v}$  is arbitrarily oriented on the surface (note that  $\mathbf{v} \neq d\mathbf{r}/dt!$ ). Figure 15.10 shows the total energy corresponding to a periodic potential of the form

$$U(x, y, t) = -\frac{E_0}{2} \left( \cos \frac{2\pi x}{a} + \cos \frac{2\pi y}{a} \right) + E_1 \cos \frac{2\pi x}{a} \cos \frac{2\pi y}{a}. \quad (15.13)$$

The equilibrium condition becomes

$$\nabla E_{\text{tot}}(\mathbf{r}, t) = \nabla U(\mathbf{r}) + k_{\text{eff}}(\mathbf{r} - \mathbf{v}t) = 0. \quad (15.14)$$

**Fig. 15.9** Friction loop obtained by scanning back and forth in the 1-D Tomlinson model. The effective spring constant  $k_{\text{eff}}$  is the slope of the sticking part of the loop (if  $\gamma \gg 1$ )

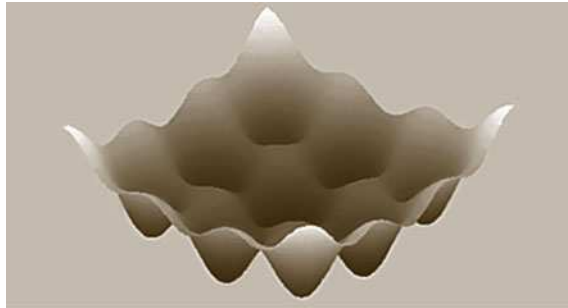
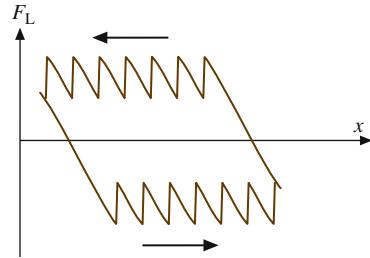
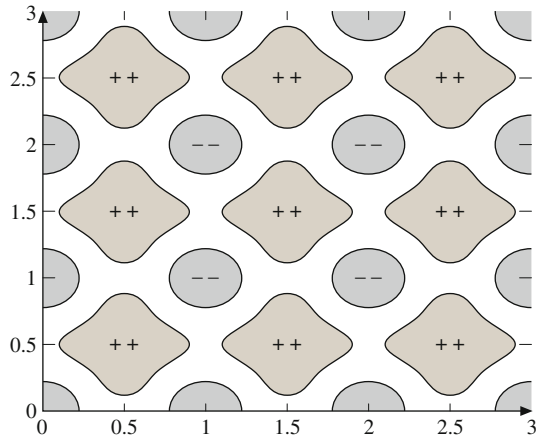


**Fig. 15.10** Energy landscape experienced by the FFM tip in 2-D

**Fig. 15.11** Regions on the tip plane labeled according to the signs of the eigenvalues of the Hessian matrix (after [26])



The stability of the equilibrium can be described by introducing the Hessian matrix

$$H = \begin{pmatrix} \frac{\partial^2 U}{\partial x^2} + k_{\text{eff}} & \frac{\partial^2 U}{\partial x \partial y} \\ \frac{\partial^2 U}{\partial y \partial x} & \frac{\partial^2 U}{\partial y^2} + k_{\text{eff}} \end{pmatrix}. \quad (15.15)$$

When both eigenvalues  $\lambda_{1,2}$  of the Hessian are positive, the position of the tip is stable. Figure 15.11 shows these regions for a potential of the form (15.13). The tip follows the cantilever adiabatically as long as it remains in the (++)-region. When the tip is dragged to the border of the region, it suddenly jumps into the next (++)-region. A comparison between a theoretical friction map deduced from the 2-D Tomlinson model and an experimental map acquired by UHV-FFM is given in the next section.

### 15.2.3 Friction Between Atomically Flat Surfaces

So far we have implicitly assumed that the tip is terminated by only one atom. It is also instructive to consider the case of a periodic surface sliding on another periodic surface. In the Frenkel–Kontorova–Tomlinson (FKT) model, the atoms of one surface are harmonically coupled with their nearest neighbors. We will restrict ourselves to the case of quadratic symmetries, with lattice constants  $a_1$  and  $a_2$  for the upper and lower surfaces, respectively (Fig. 15.12). In this context, the role of *commensurability* is essential. It is well known that any real number  $z$  can be represented as a continued fraction

$$z = N_0 + \frac{1}{N_1 + \frac{1}{N_2 + \dots}}. \quad (15.16)$$

**Fig. 15.12** The FKT model in 2-D (after [27])

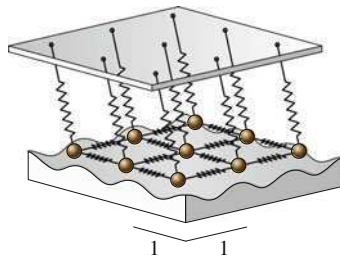
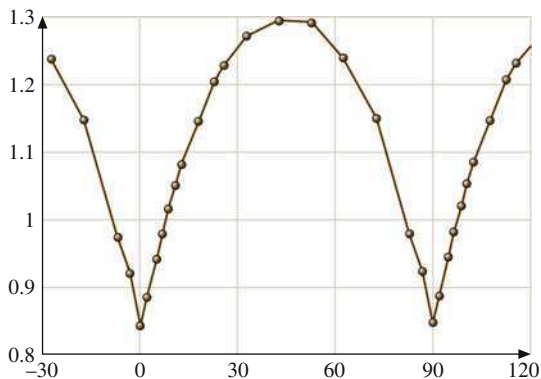


**Fig. 15.13** Friction as a function of the sliding angle  $\varphi$  in the 2-D FKT model (after [27])



The sequence that converges most slowly is obtained when all  $N_i = 1$ , which corresponds to the *golden mean*  $\bar{z} = (\sqrt{5} - 1)/2$ . In 1-D, Weiss and Elmer predicted that friction should decrease with decreasing commensurability, the minimum friction being reached when  $a_1/a_2 = \bar{z}$  [28].

In 2-D, Gyalog and Thomas studied the case  $a_1 = a_2$ , with a misalignment between the two lattices given by an angle  $\theta$  [27]. When the sliding direction changes, friction also varies from a minimum value (corresponding to the sliding angle  $\varphi = \theta/2$ ) to a maximum value (which is reached when  $\varphi = \theta/2 + \pi/4$ ; see Fig. 15.13). The misfit angle  $\theta$  is related to the commensurability. Since the misfit angles that give rise to commensurate structure form a dense subset, the dependence of friction on  $\theta$  should be discontinuous. The numerical simulations performed by Gyalog are in agreement with this conclusion. The role of intrabulk elastic forces has been considered in a scaling study by Müser [29], where the symmetry of the surfaces and the dimensionalities of interface and solids have been found to play a crucial role.

### 15.3 Friction Experiments on the Atomic Scale

Figure 15.14 shows the first atomic-scale friction map, as observed by Mate. The periodicity of the lateral force is the same as that of the atomic lattice of graphite. The series of friction loops in Fig. 15.15 reveals the stick–slip effect discussed in

**Fig. 15.14** First atomic friction map acquired on graphite with a normal force  $F_N = 56 \mu\text{N}$ . Frame size: 2 nm (after [1])

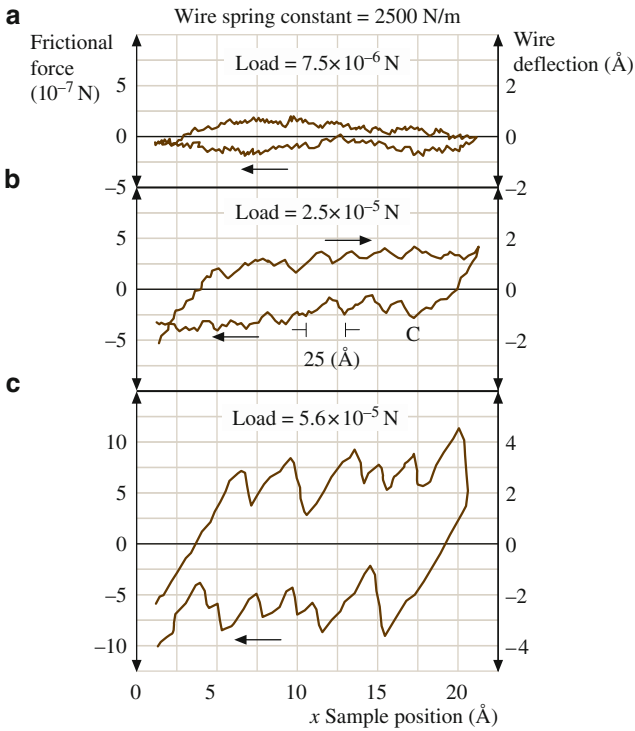
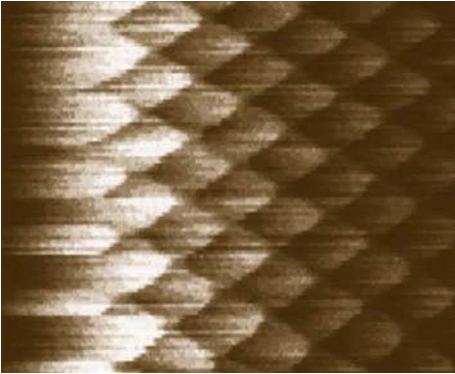
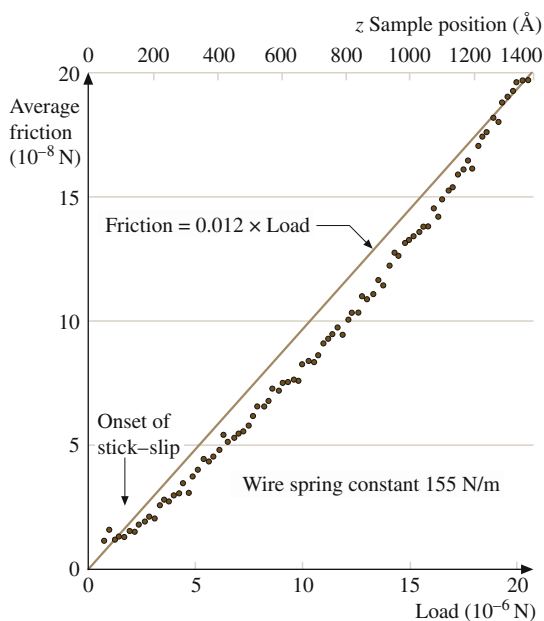


**Fig. 15.15** Friction loops on graphite acquired with (a)  $F_N = 7.5 \mu\text{N}$ , (b)  $24 \mu\text{N}$  and (c)  $75 \mu\text{N}$  (after [1])

the previous section. The applied loads are in the range of tens of  $\mu\text{N}$ . According to the continuum models discussed in Sect. 15.5, these values correspond to contact diameters of 100 nm. A possible explanation for the atomic features observed at such high loads is that graphite flakes may have detached from the surface and adhered to the tip [30]. Another explanation is that the contact between tip and

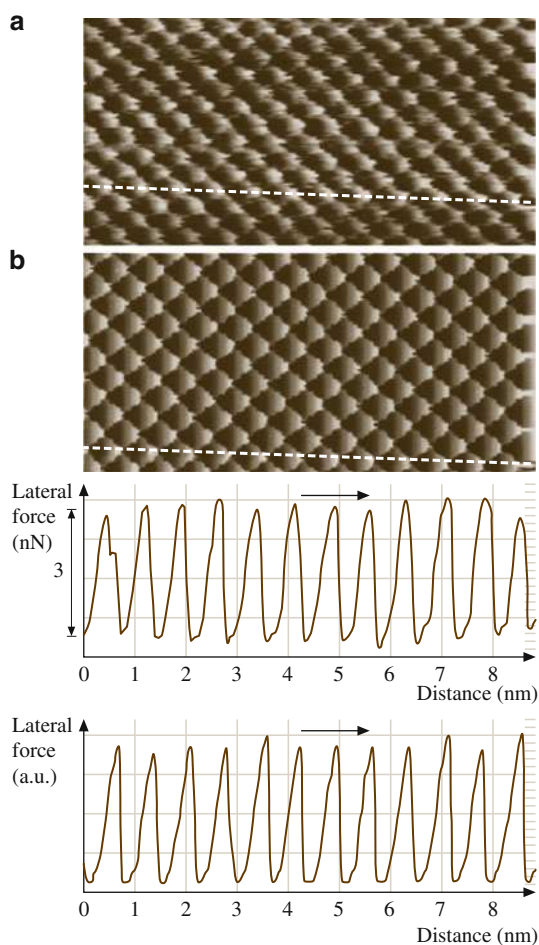
**Fig. 15.16** Load dependence of friction on graphite (after [1])



surface consisted of few nm-scale asperities and that the corrugation was not entirely averaged out while sliding. The load dependence of friction as found by Mate is rather linear, with a small friction coefficient  $\mu = 0.01$  (Fig. 15.16).

The UHV environment reduces the influence of contaminants on the surface and leads to more precise and reproducible results. Meyer et al. [31] obtained a series of interesting results on ionic crystals using the UHV-FFM apparatus described in Sect. 15.1.4. By applying subnanonewton loads to a NaCl surface, Socoliuc et al. observed the transition from stick-slip to continuous sliding discussed in Sect. 15.2.1 [32]. In another experiment, the same group observed that the transition could also be induced dynamically by superimposed oscillations of the applied load at the contact resonance [33]. In Fig. 15.17, a friction map recorded on KBr(100) is compared with a theoretical map obtained with the 2-D Tomlinson model. The periodicity  $a = 0.47$  nm corresponds to the spacing between equally charged ions. No individual defects were observed. One possible reason is that the contact realized by the FFM tip is always formed by many atoms, which superimpose and average their effects. Molecular dynamics (MD) calculations (Sect. 15.7) show that even single-atom contact may cause rather large stresses in the sample, which lead to the motion of defects far away from the contact area. However, this seems to be not the case when ultrathin films of ionic crystals are epitaxially grown on a different species. Indeed, high resolution FFM images of stable defects across a KBr/NaCl interface have been recently reported by Maier and coworkers [35]. The duration of slip events was the main topic of another study on KBr [36]. Here, the broad time distribution experimentally observed was attributed to the atomistic structure of the contact area, in agreement with a multispring model of the tip-surface interface.

**Fig. 15.17** (a) Measured and (b) theoretical friction map on KBr(100) (after [34])



Lüthi et al. [37] even detected atomic-scale friction on a reconstructed Si(111)- $7 \times 7$  surface. However, uncoated Si tips and tips coated with Pt, Au, Ag, Cr and Pt/C damaged the sample irreversibly, and the observation of atomic features was achieved only after coating the tips with polytetrafluoroethylene (PTFE), which has lubricant properties and does not react with the dangling bonds of Si(111)- $7 \times 7$  (Fig. 15.18).

Friction has been resolved on the atomic scale even on metallic surfaces in UHV. In Fig. 15.19 reproducible stick-slip process on Cu(111) is shown. Current measurements performed at the same time suggested that the AFM tip was covered by copper atoms. More recently, the Cu(100) surface has also revealed regular atomic stick-slip [39], despite previous theoretical and experimental observations suggested that the atomic packing of this surface is prone to be worn off by the tip. Sliding on the (100) surface of copper produced irregular patterns, although atomic features were recognized even in this case [38]. Molecular dynamics suggests that

**Fig. 15.18** (a) Topography and (b) friction image of Si(111)  $7 \times 7$  measured with a PTFE-coated Si tip (after [37])

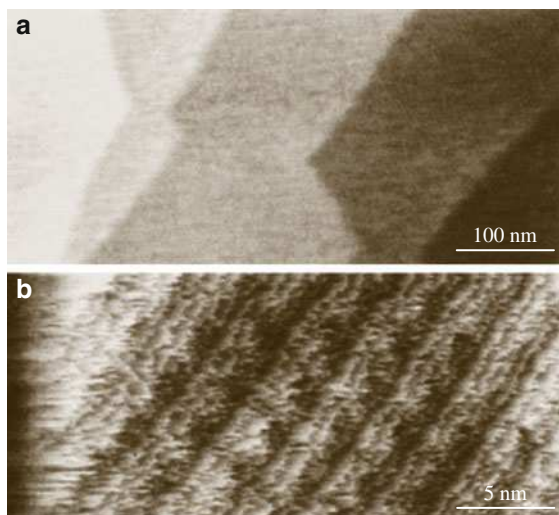
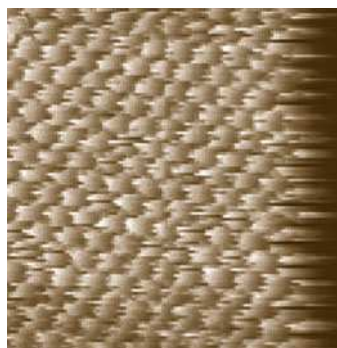


**Fig. 15.19** Friction images of Cu(111). Frame size: 3 nm (after [38])



wear should occur more easily on the Cu(100) surface than on the close-packed Cu(111) (Sect. 15.7). This conclusion was achieved by adopting copper tips in computer simulations. The assumption that the FFM tip used in the experiments was covered by copper is supported by current measurements performed at the same time.

Atomic stick-slip on diamond was observed by Germann et al. with an apposite diamond tip prepared by chemical vapor deposition [40] and, a few years later, by van der Oetelaar et al. [41] with standard silicon tips. The values of friction vary dramatically depending on the presence or absence of hydrogen on the surface.

Fujisawa et al. [42] measured friction on mica and on MoS<sub>2</sub> with a 2-D FFM apparatus that could also reveal forces perpendicular to the scan direction. The features in Fig. 15.20 correspond to a zigzag tip walk, which is predicted by the 2-D Tomlinson model [43]. Two-dimensional stick-slip on NaF was detected with normal forces <14 nN, whereas loads of up to 10  $\mu$ N could be applied to layered materials. The contact between tip and NaF was thus formed by one or a few atoms.

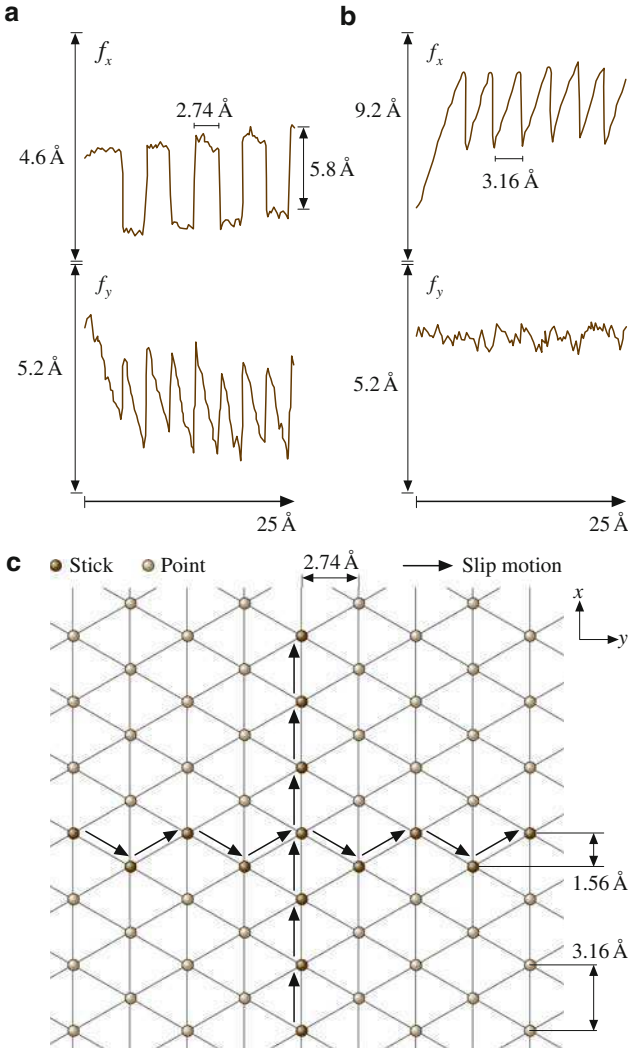


**Fig. 15.20** (a) Friction force on  $\text{MoS}_2$  acquired by scanning along the cantilever and (b) across the cantilever. (c) Motion of the tip on the sample (after [42])

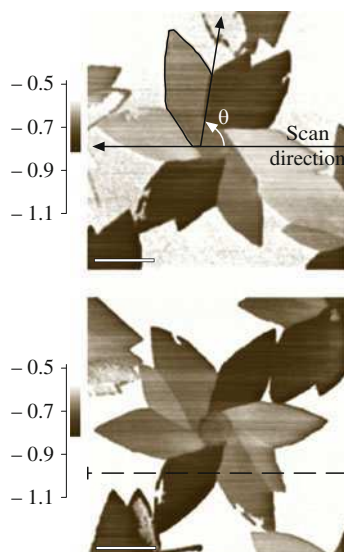
A zigzag walk on mica was also observed by *Kawakatsu et al.* using an original 2-D FFM with two laser beams and two quadrant photodetectors [44].

### 15.3.1 Anisotropy of Friction

The importance of the misfit angle in the reciprocal sliding of two flat surfaces was first observed experimentally by *Hirano et al.* in the contact of two mica sheets [45].



**Fig. 15.21** Friction images of a thiolipid monolayer on a mica surface. In (b) the sample is rotated by  $70^\circ$  with respect to (a) (after [50])



The friction increased when the two surfaces formed commensurate structures, in agreement with the discussion in Sect. 15.2.3. In more recent measurements with a monocrystalline tungsten tip on Si(001), Hirano et al. observed *superlubricity* in the incommensurate case [46].

Overney et al. [47] studied the effects of friction anisotropy on a bilayer lipid film. In this case, different molecular alignments resulted in significant variations in the friction. Other measurements of friction anisotropy on single crystals of stearic acid were reported by Takano and Fujihira [48]. An impressive confirmation of this effect recently came from a dedicated force microscope developed by Frenken and coworkers, the Tribolover, which allows quantitative tracking of the scanning force in three dimensions [49]. With this instrument, a flake from a graphite surface was picked up and the lateral forces between the flake and the surface were measured at different angles of rotation. Stick-slip and energy dissipation were only clearly revealed at rotation angles of  $0$  and  $60^\circ$ , when the two lattices are in registry.

Liley et al. [50] observed flower-shaped islands of a lipid monolayer on mica, which consisted of domains with different molecular orientations (Fig. 15.21). The angular dependence of friction reflects the tilt direction of the alkyl chains of the monolayer, as revealed by other techniques.

Lüthi et al. [51] used the FFM tip to move  $C_{60}$  islands, which slide on sodium chloride in UHV without disruption (Fig. 15.22). In this experiment the friction was found to be independent of the sliding direction. This was not the case in other experiments performed by Sheehan and Lieber, who observed that the misfit angle is relevant when  $MoO_3$  islands are dragged on the  $MoS_2$  surface [52]. In these experiments, sliding was possible only along low index directions. The weak

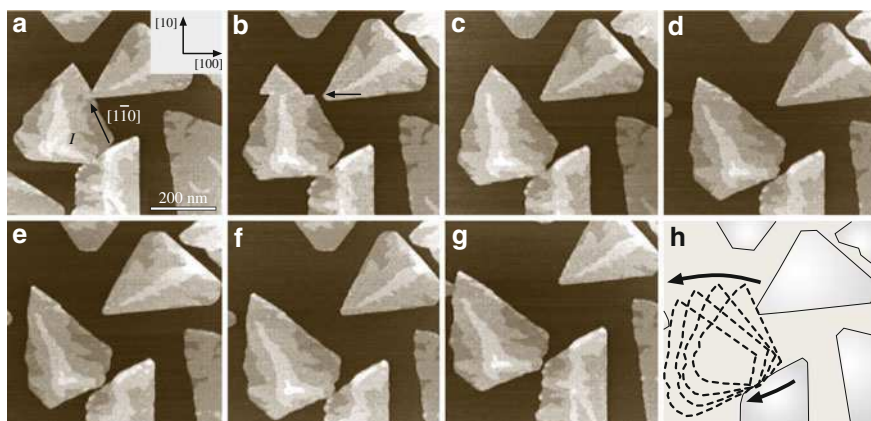
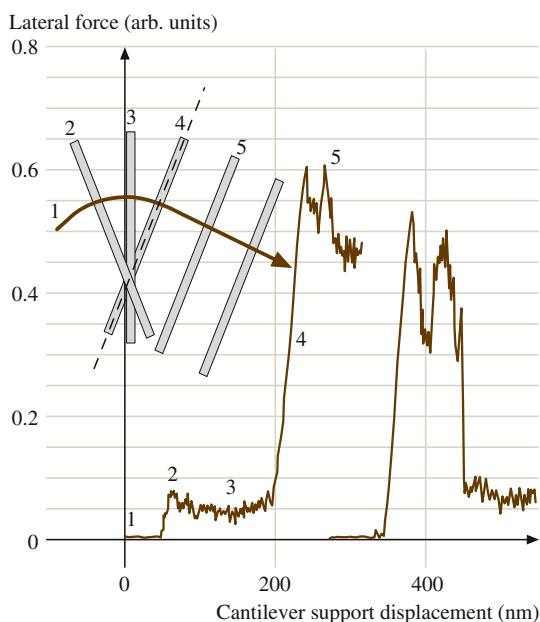


**Fig. 15.22** (a–g) Sequence of topography images of C<sub>60</sub> islands on NaCl(100) (after [51]). (h) Overview of the roto-translational motion of the island

**Fig. 15.23** Friction force experienced as a carbon nanotube is rotated into (*left trace*) and out of (*right trace*) commensurate contact (after [53])



orientation dependence found by Lüthi et al. [51] is probably due to the large mismatch of C<sub>60</sub> on NaCl.

A recent example of friction anisotropy is related to carbon nanotubes. Falvo et al. [53] manipulated nanotubes on graphite using a FFM tip (Fig. 15.23). A dramatic increase in the lateral force was found in directions corresponding to

commensurate contact. At the same time, the nanotube motion changed from sliding/rotating to stick-roll.

15.4 Thermal Effects on Atomic Friction

Although the Tomlinson model gives a good interpretation of the basic mechanism of the atomic stick–slip discussed in Sect. 15.2, it cannot explain some minor features observed in the atomic friction. For example, Fig. 15.24 shows a friction loop acquired on NaCl(100). The peaks in the sawtooth profile have different heights, which is in contrast to the result in Fig. 15.9. Another effect is observed if the scan velocity  $v$  is varied: the mean friction force increases with the logarithm of  $v$  (Fig. 15.25). This effect cannot be interpreted within the mechanical approach in Sect. 15.2 without further assumptions.

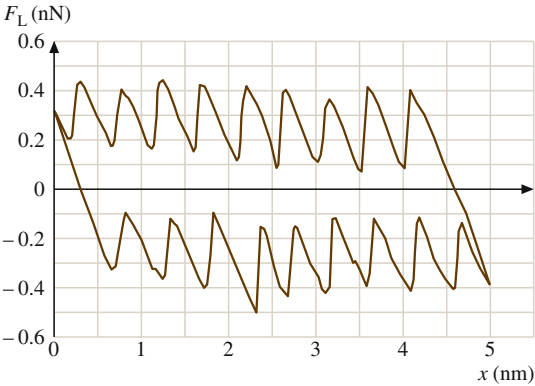


**Fig. 15.24** Friction loop on NaCl(100) (after [54])

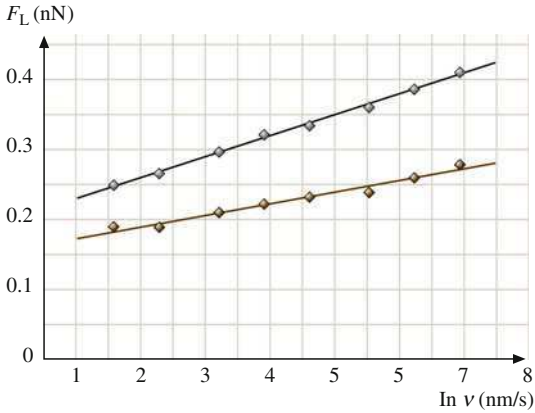


**Fig. 15.25** Mean friction force vs. scanning velocity on NaCl(100) at  $F_N = 0.44$  nN (+) and  $F_N = 0.65$  nN (x) (after [54])

### 15.4.1 The Tomlinson Model at Finite Temperature

Let us focus again on the energy profile discussed in Sect. 15.2.1. For the sake of simplicity, we will assume that  $\gamma \gg 1$ . At a given time  $t < t^*$ , the tip jump is prevented by the energy barrier  $\Delta E = E(x_{\max}, t) - E(x_{\min}, t)$ , where  $x_{\max}$  corresponds to the first maximum observed in the energy profile and  $x_{\min}$  is the actual position of the tip (Fig. 15.26). The quantity  $\Delta E$  decreases with time or, equivalently, with the frictional force  $F_L$  until it vanishes when  $F_L = F^*$  (Fig. 15.27). Close to the critical point, the energy barrier can be written approximately as

$$\Delta E = \lambda(\tilde{F} - F_L), \quad (15.17)$$

where  $\tilde{F}$  is close to the critical value  $F^* = \pi E_0/a$ .

At finite temperature  $T$ , the lateral force required to induce a jump is lower than  $F^*$ . To estimate the most probable value of  $F_L$  at this point, we first consider the probability  $p$  that the tip does *not* jump. The probability  $p$  changes with time  $t$  according to the master equation

$$\frac{dp(t)}{dt} = -f_0 \exp\left(-\frac{\Delta E(t)}{k_B T}\right) p(t), \quad (15.18)$$

**Fig. 15.26** Energy barrier that hinders the tip jump in the Tomlinson model

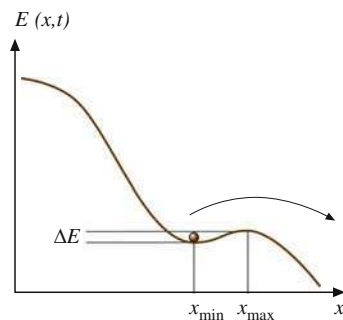
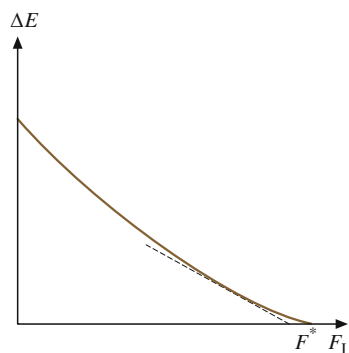


**Fig. 15.27** Energy barrier  $\Delta E$  as a function of the lateral force  $F_L$ . The dashed line close to the critical value corresponds to the linear approximation (15.17)



where  $f_0$  is a characteristic frequency of the system. The physical meaning of this frequency is discussed in Sect. 15.4.2. We should note that the probability of a reverse jump is neglected, since in this case the energy barrier that must be overcome is much higher than  $\Delta E$ . If time is replaced by the corresponding lateral force, the master equation becomes

$$\frac{dp(F_L)}{dF_L} = -f_0 \exp\left(-\frac{\Delta E(F_L)}{k_B T}\right) \left(\frac{dF_L}{dt}\right)^{-1} p(F_L). \quad (15.19)$$

At this point, we substitute

$$\frac{dF_L}{dt} = \frac{dF_L}{dX} \frac{dX}{dt} = k_{\text{eff}} v \quad (15.20)$$

and use the approximation (15.17). The maximum probability transition condition  $d^2 p(F)/dF^2 = 0$  then yields

$$F_L(v) = F^* - \frac{K_B T}{\lambda} \ln \frac{v_c}{v} \quad (15.21)$$

with

$$v_c = \frac{f_0 k_B T}{k_{\text{eff}} \lambda}. \quad (15.22)$$

Thus, the lateral force depends logarithmically on the sliding velocity, as observed experimentally. However, approximation (15.17) does not hold when the tip jump occurs very close to the critical point  $x = x^*$ , which is the case at high velocities. In this instance, the factor  $(dF_L/dt)^{-1}$  in (15.19) is small and, consequently, the probability  $p(t)$  does not change significantly until it suddenly approaches 1 when  $t \rightarrow t^*$ . Thus friction is constant at high velocities, in agreement with the classical Coulomb's law of friction [31].

Sang et al. [55] observed that the energy barrier close to the critical point is better approximated by a relation like

$$\Delta E = \mu(F^* - F_L)^{3/2}. \quad (15.23)$$

The same analysis performed using approximation (15.23) instead of (15.17) leads to the expression [56]

$$\frac{\mu(F^* - F_L)^{3/2}}{k_B T} = \ln \frac{v_c}{v} - \sqrt{1 - \frac{F^*}{F_L}}, \quad (15.24)$$

where the critical velocity  $v_c$  is now

$$v_c = \frac{\pi\sqrt{2}}{2} \frac{f_0 k_B T}{k_{\text{eff}} a}. \quad (15.25)$$

The velocity  $v_c$  discriminates between two different regimes. If  $v \ll v_c$ , the second logarithm in (15.24) can be neglected, which leads to the logarithmic dependence

$$F_L(v) = F^* - \left( \frac{k_B T}{\mu} \right)^{2/3} \left( \ln \frac{v_c}{v} \right)^{2/3}. \quad (15.26)$$

In the opposite case,  $v \gg v_c$ , the term on the left in (15.23) is negligible and

$$F_L(v) = F^* \left[ 1 - \left( \frac{v_c}{v} \right)^2 \right]. \quad (15.27)$$

In such a case, the lateral force  $F_L$  tends to  $F^*$ , as expected.

In a recent work, Reimann et al. distinguished between the dissipation that occurs in the tip apex and that in the substrate volume in contact with the tip [57]. After the initial logarithmic increase, the velocity dependence of friction changes in different ways, depending on the relative contribution of the tip apex to the total dissipation. A *friction plateau* is only predicted when  $\theta \approx 0.5$  over a limited velocity range. At lower or higher values of  $\theta$ , friction is expected to increase, or, respectively, decrease beyond the critical velocity  $v_c$ .

The thermally activated Tomlinson model has been recently extended to two dimensions by Fasolino and coworkers [58].

### 15.4.2 Velocity Dependence of Friction

The velocity dependence of friction was only recently studied by FFM. Zwörner et al. observed that friction between silicon tips and diamond, graphite or amorphous carbon is constant with scan velocities of a few  $\mu\text{m/s}$  [62]. The friction decreased when  $v$  was reduced below 1  $\mu\text{m/s}$ . In their experiment on lipid films on mica (Sect. 15.3.1), Gourdon et al. [60] explored a range of velocities from 0.01 to 50  $\mu\text{m/s}$  and found a critical velocity  $v_c = 3.5 \mu\text{m/s}$  that discriminates between an increasing friction and a constant friction regime (Fig. 15.28). Although these results were not explained by thermal activation, we argue that the previous theoretical discussion gives the correct interpretative key. A clear observation of a logarithmic dependence of friction on the micrometer scale was reported by Bouhacina et al., who studied friction on triethoxysilane molecules and polymers grafted on silica with sliding velocities of up to  $v = 300 \mu\text{m/s}$  [61]. The result was

**Fig. 15.28** Velocity dependence of friction on mica and on lipid films with different orientations (arms 4 and 5) and in a fluid phase (after [60])

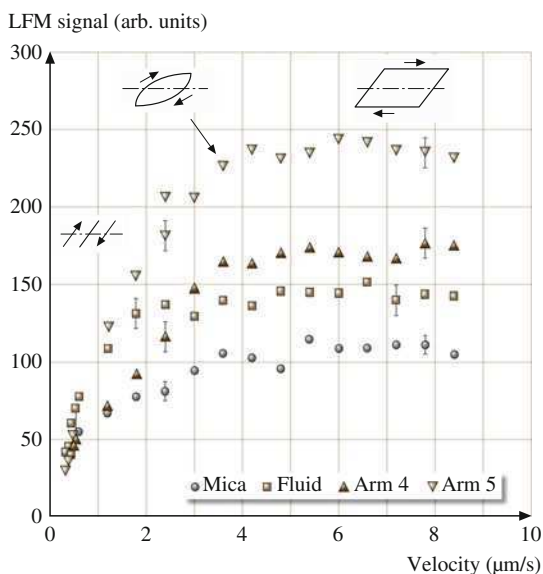
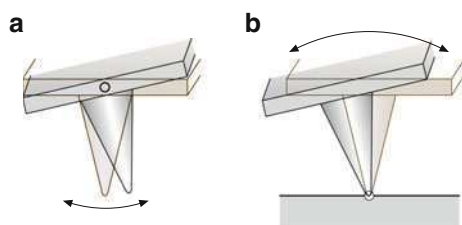


**Fig. 15.29** Torsional modes of cantilever oscillation (a) when the tip is free and (b) when the tip is in contact with a surface (after [65])



explained with a thermally activated Eyring model, which does not differ significantly from the model discussed in the previous subsection [62, 63].

The first measurements on the atomic scale were performed by Bennewitz et al. on copper and sodium chloride [54, 64]; in both cases a logarithmic dependence of friction was revealed up to  $v < 1 \mu\text{m/s}$  (Fig. 15.25), in agreement with (15.21). Higher values of velocities were not explored, due to the limited range of the scan frequencies possible with FFM on the atomic scale. The same limitation does not allow a clear distinction between (15.21) and (15.26) when interpreting the experimental results.

At this point we would like to discuss the physical meaning of the characteristic frequency  $f_0$ . With a lattice constant  $a$  of a few angstroms and an effective spring constant  $k_{\text{eff}} \approx 1 \text{ N/m}$ , which are typical of FFM experiments, (15.25) gives a value of a few hundred kHz for  $f_0$ . This is the characteristic range in which the torsional eigenfrequencies of the cantilevers are located in both contact and noncontact modes (Fig. 15.29). Future work may clarify whether or not  $f_0$  must be identified with these frequencies.

To conclude this section, we should emphasize that the increase in friction with increasing velocity is ultimately related to the materials and the environment in which the measurements are realized. In a humid environment, Riedo et al. observed that the surface wettability plays an important role [66]. Friction *decreases* with increasing velocity on hydrophilic surfaces, and the rate of this decrease depends drastically on humidity. A logarithmic increase is again found on partially hydrophobic surfaces (Fig. 15.30). These results were interpreted

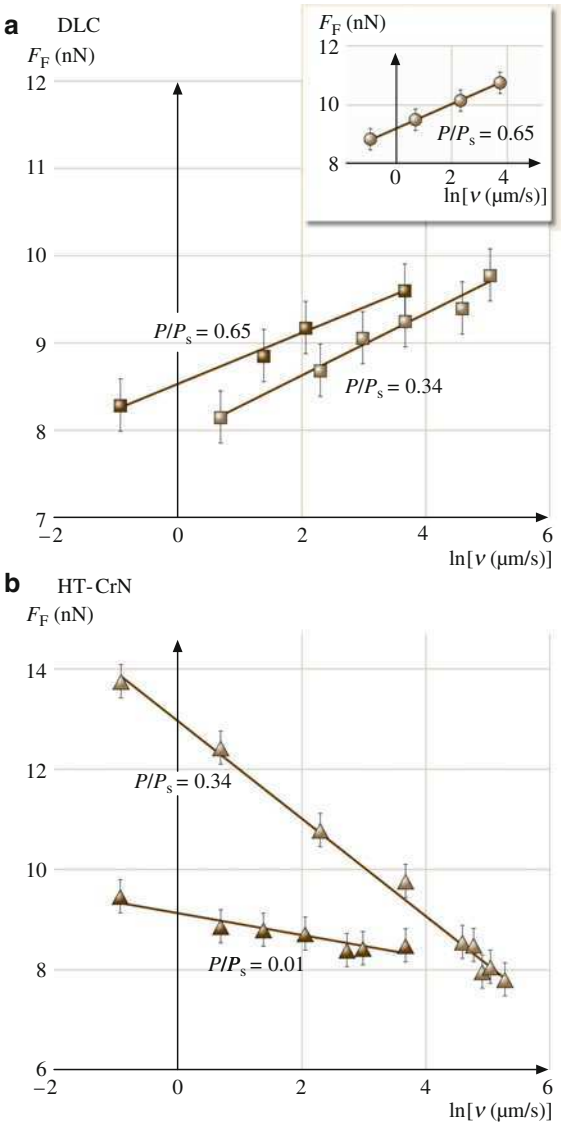
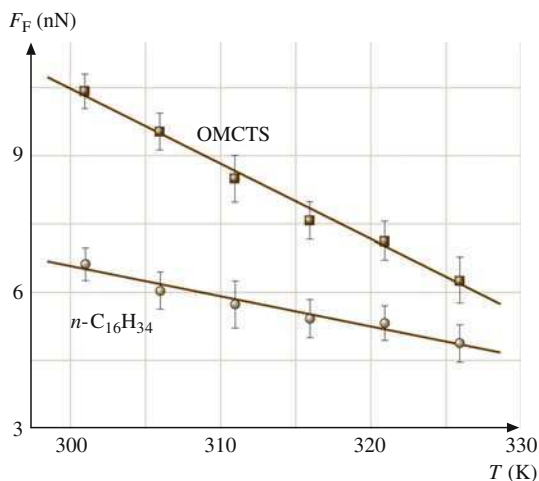


**Fig. 15.30** Friction versus sliding velocity (a) on hydrophobic surfaces and (b) on hydrophilic surfaces (after [66])



**Fig. 15.31** Temperature dependence of friction on *n*-hexadecane and octamethylcyclotetrasiloxane (after [67])



considering the thermally activated nucleation of water bridges between tip and sample asperities, as discussed in the cited reference.

### 15.4.3 Temperature Dependence of Friction

Thus far we have used thermal activation to explain the velocity dependence of friction. The same mechanism also predicts that friction should change with temperature. The master equation (15.18) shows that the probability of a tip jump is reduced at low temperatures  $T$  until it vanishes when  $T = 0$ . Within this limit case, thermal activation is excluded, and the lateral force  $F_L$  is equal to  $F^*$ , independent of the scanning velocity  $v$ .

Only few experimental studies focused on the temperature dependence of friction, none of them revealing atomic-scale features. A linear decrease of friction with temperature was observed on silicon surfaces covered by organic molecules in a limited range of temperatures [67]. On bare Si(111) in UHV a peak of friction was found  $\approx 100$  K, the origin of which remained unexplained [68]. In a recent FFM study on graphite Zhao et al. [69] found a significant dependence of friction on  $1/T$  over a wide temperature range (140–750 K), supporting the hypothesis of thermal activation of the stick-slip process.

## 15.5 Geometry Effects in Nanocontacts

Friction is ultimately related to the real shape of the contact between the sliding surfaces. On the macroscopic scale, the contact between two bodies is studied within the context of continuum mechanics, which is based on the elasticity theory

developed by Hertz in the nineteenth century. Various FFM experiments have shown that continuum mechanics is still valid down to contact areas just a few nanometers in size. Only when contact is reduced to few atoms does the continuum frame become unsuitable, and other approaches like molecular dynamics become necessary. This section will deal with continuum mechanics theory; molecular dynamics will be discussed in Sect. 15.7.

### 15.5.1 Continuum Mechanics of Single Asperities

The lateral force  $F_L$  between two surfaces in reciprocal motion depends on the size of the real area of contact,  $A$ , which can be a few orders of magnitude smaller than the apparent area of contact. The simplest assumption is that friction is proportional to  $A$ ; the proportionality factor is called the *shear strength*  $\sigma$  [70]

$$F_L = \sigma A. \quad (15.28)$$

For plastic deformation, the asperities are compressed until the pressure  $p$  equals a certain yield value  $p^*$ . The resulting contact area is thus  $A = F_N/p^*$ , and the well-known Amontons' law is obtained:  $F_L = \mu F_N$ , where  $\mu = \sigma/p^*$  is the *coefficient of friction*. The same idea can be extended to contacts formed by many asperities, and it leads again to Amontons' law. The simplicity of this analysis explains why most friction processes were related to plastic deformation for a long time. Such a mechanism, however, should provoke quick disruption of surfaces, which is not observed in practice.

Elastic deformation can be easily studied in the case of a sphere of radius  $R$  pressed against a flat surface. In this case, the contact area is

$$A(F_N) = \pi \left( \frac{R}{K} \right)^{2/3} F_N^{2/3}, \quad (15.29)$$

where  $K = 3E^*/4$  and  $E^*$  is an effective Young's modulus, related to the Young's moduli ( $E_1$  and  $E_2$ ) and the Poisson numbers ( $\nu_1$  and  $\nu_2$ ) of sphere and plane, by the following relation [71]

$$\frac{1}{E^*} = \frac{1 - \nu_1^2}{E_1} + \frac{1 - \nu_2^2}{E_2}. \quad (15.30)$$

The result  $A \propto F_N^{2/3}$  contrasts with Amontons' law. However, a linear relation between  $F_L$  and  $F_N$  can be obtained for contacts formed from several asperities in particular cases. For example, the area of contact between a flat surface and a set of asperities with an exponential height distribution and the same radius of curvature  $R$  depends linearly on the normal force  $F_N$  [72]. The same conclusion holds approximately even for a Gaussian height distribution. However, the hypothesis that the radii of curvature are the same for all asperities is not realistic. A general model was

recently proposed by Persson, who analytically derived the proportionality between contact area and load for a large variety of elastoplastic contacts formed by surfaces with arbitrary roughnesses [73]. However, this discussion is not straightforward and goes beyond the purposes of this section.

Further effects are observed if adhesive forces between the asperities are taken into account. If the range of action of these forces is smaller than the elastic deformation, (15.29) is extended to the Johnson–Kendall–Roberts (JKR) relation

$$A(F_N) = \pi \left( \frac{R}{K} \right)^{2/3} \times \left( F_N + 3\pi\gamma R + \sqrt{6\pi\gamma R F_N + (3\pi\gamma R)^2} \right)^{2/3}, \quad (15.31)$$

where  $\gamma$  is the surface tension of the sphere and plane [74]. The real contact area at zero load is finite and the sphere can be detached only by pulling it away with a certain force. This is also true in the opposite case, in which the range of action of adhesive forces is larger than the elastic deformation. In this case, the relation between contact area and load takes the simple form

$$A(F_N) = \pi \left( \frac{R}{K} \right)^{2/3} (F_N - F_{\text{off}})^{2/3}, \quad (15.32)$$

where  $F_{\text{off}}$  is the negative load required to break the contact. The Hertz-plus-offset relation (15.32) can be derived from the Derjaguin–Muller–Toporov (DMT) model [75]. To discriminate between the JKR or DMT models, Tabor introduced a nondimensional parameter

$$\Phi = \left( \frac{9R\gamma^2}{4K^2 z_0^3} \right)^{1/3}, \quad (15.33)$$

where  $z_0$  is the equilibrium distance during contact. The JKR model can be applied if  $\Phi > 5$ ; the DMT model holds when  $\Phi < 0.1$  [76]. For intermediate values of  $\Phi$ , the Maugis–Dugdale model [77] could reasonably explain experimental results (Sect. 15.5.3).

### 15.5.2 Dependence of Friction on Load

The FFM tip represents a single asperity sliding on a surface. The previous discussion suggests a nonlinear dependence of friction on the applied load, provided that continuum mechanics is applicable. Schwarz et al. observed the Hertz-plus-offset relation (15.32) on graphite, diamond, amorphous carbon and  $C_{60}$  in an argon atmosphere (Fig. 15.32). In their measurements, they used well-defined spherical tips with radii of curvature of tens of nanometers, obtained by contaminating silicon tips with amorphous carbon in a transmission electron microscope. In order to

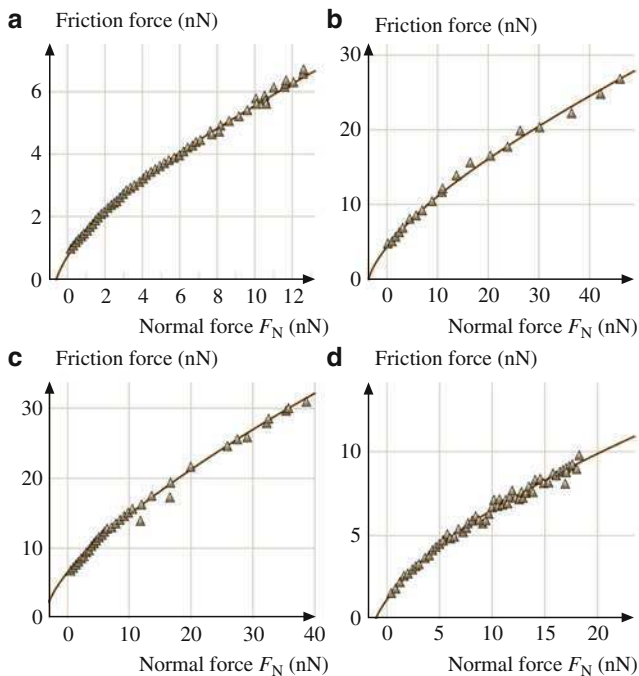


**Fig. 15.32** Friction versus load curve on amorphous carbon in argon atmosphere. Curves (a)–(d) refer to tips with different radii of curvature (after [78])

compare the tribological behavior of different materials, Schwarz et al. suggested the introduction of an effective coefficient of friction  $\tilde{C}$  which is independent of the tip curvature [78].

Meyer et al., Carpick et al., and Polaczyc et al. performed friction measurements in UHV in agreement with JKR theory [19, 79, 80]. Different materials were considered (ionic crystals, mica and metals) in these experiments. In order to correlate the lateral and normal forces with improved statistics, Meyer et al. applied an original 2-D histogram technique (Fig. 15.33). Carpick et al. extended the JKR relation (15.32) to include nonspherical tips. In the case of an axisymmetric tip profile  $z \propto r^{2n}$  ( $n > 1$ ), it can be proven analytically that the increase in the friction becomes less pronounced with increasing  $n$  (Fig. 15.34).

### 15.5.3 Estimation of the Contact Area

In contrast to other tribological instruments, such as the surface force apparatus [81], the contact area cannot be measured directly by FFM. Indirect methods are provided by contact stiffness measurements. The contact between the FFM tip and

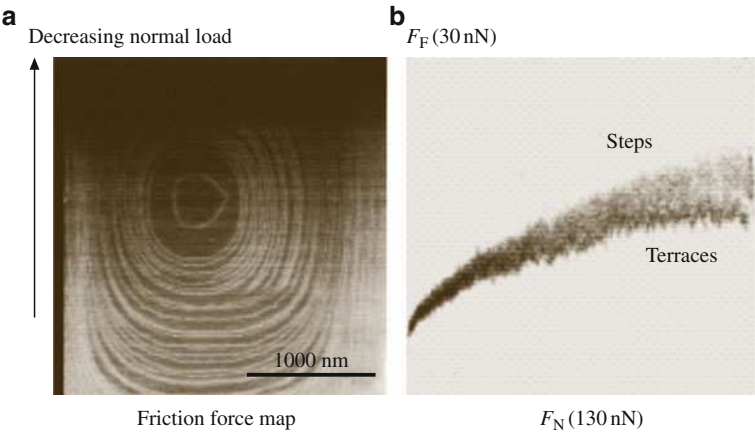


**Fig. 15.33** (a) Friction force map on NaCl(100). The load is decreased from 140 to 0 nN (jump-off point) during imaging. (b) 2-D histogram of (a) (after [19])

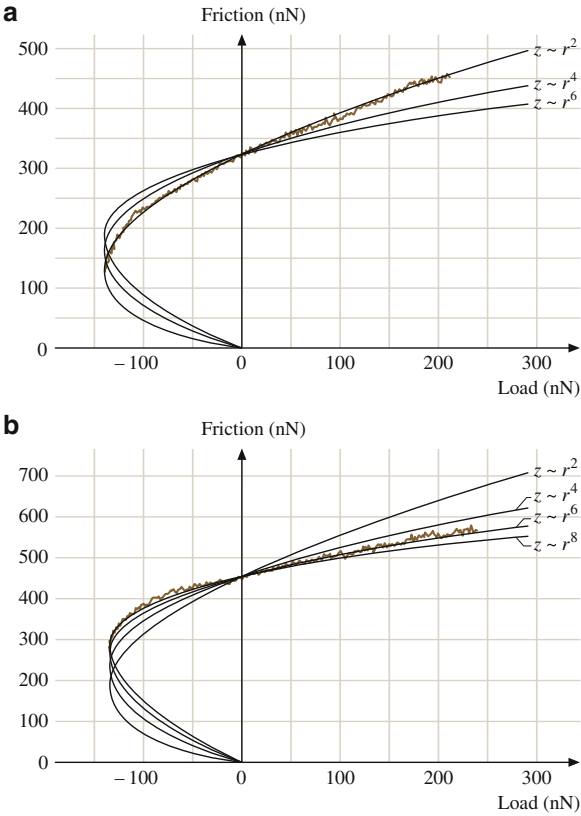
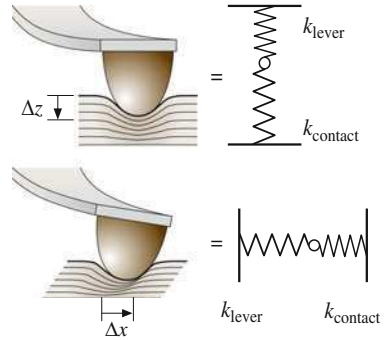


**Fig. 15.34** Friction versus load curves (a) for a spherical tip and (b) for a blunted tip. The solid curves are determined using the JKR theory (after [79])

**Fig. 15.35** Sketch of normal and lateral stiffness of the contact between tip and surface (after [83])



the sample can be modeled by a series of two springs (Fig. 15.35). The effective constant  $k_{\text{eff}}^z$  of the series is given by

$$\frac{1}{k_{\text{eff}}^z} = \frac{1}{k_{\text{contact}}^z} + \frac{1}{c_N}, \quad (15.34)$$

where  $c_N$  is the normal spring constant of the cantilever and  $k_{\text{contact}}^z$  is the normal stiffness of the contact. This quantity is related to the radius of the contact area ( $a$ ) by the simple relation

$$k_{\text{contact}}^z = 2aE^*, \quad (15.35)$$

where  $E^*$  is the effective Young's modulus introduced previously [82]. Typical values of  $k_{\text{contact}}^z$  are an order of magnitude larger than  $c_N$ , however, and practical application of (15.34) is not possible.

Carpick et al. independently suggested an alternative method [83, 84]. According to various models, the *lateral* contact stiffness of the contact between a sphere and a flat surface is [85]

$$k_{\text{contact}}^x = 8aG^*, \quad (15.36)$$

where the effective shear stress  $G^*$  is defined by

$$\frac{1}{G^*} = \frac{2 - \nu_1^2}{G_1} + \frac{2 - \nu_2^2}{G_2}. \quad (15.37)$$

$G_1, G_2$  are the shear moduli of the sphere and the plane, respectively. The contact between the FFM tip and the sample can again be modeled by a series of springs (Fig. 15.35). The effective constant  $k_{\text{eff}}^x$  of the series is given by

$$\frac{1}{k_{\text{eff}}^x} = \frac{1}{k_{\text{contact}}^x} + \frac{1}{k_{\text{tip}}^x} + \frac{1}{c_L}, \quad (15.38)$$

where  $c_L$  is the lateral spring constant of the cantilever and  $k_{\text{contact}}^x$  is the lateral stiffness of the contact. As suggested by Lantz, (15.38) also includes the lateral stiffness of the tip  $k_{\text{tip}}^x$  which can be comparable to the lateral spring constant. The effective spring constant  $k_{\text{eff}}^x$  is simply given by the slope  $dF_L/dx$  of the friction loop (Sect. 15.2.1). Once  $k_{\text{contact}}^x$  is determined, the contact radius  $a$  is easily estimated by (15.36).

The lateral stiffness method was applied to contacts between silicon nitride and muscovite mica in air and between NbSe<sub>2</sub> and graphite in UHV. The dependences of both the spring constant  $k_{\text{eff}}^x$  and the lateral force  $F_L$  on the load  $F_N$  were explained within the same models (JKR and Maugis–Dugdale, respectively), which confirms that friction is proportional to the contact area for the range of loads applied (up to  $F_N = 40$  nN in both experiments).

Enachescu et al. estimated the contact area by measuring the contact conductance on diamond as a function of the applied load [86, 87]. Their experimental data were fitted with the DMT model, which was also used to explain the dependence of friction on load. Since the contact conductance is proportional to the contact area, the validity of the hypothesis (15.28) was confirmed again.

## 15.6 Wear on the Atomic Scale

If the normal force  $F_N$  applied by the FFM exceeds a critical value, which depends on the tip shape and on the material under investigation, the surface topography is permanently modified. In some cases wear is exploited to create patterns with well-defined shapes. Here we will focus on the mechanisms that act at the nanometer scale, where recent experiments have demonstrated the unique ability of the FFM to both scratch and image surfaces down to the atomic scale.

### 15.6.1 Abrasive Wear on the Atomic Scale

Lüthi et al. observed the appearance of wear at very low loads, i.e.  $F_N = 3$  nN, for ionic crystals [34]. Atomically resolved images of the damage produced by scratching the FFM tip area on potassium bromide were obtained by Gnecco et al. [88]. In Fig. 15.36, a small mound that has piled up at the end of a groove on KBr(100) is shown at different magnifications. The groove was created a few minutes before imaging by repeatedly scanning with the normal force  $F_N = 21$  nN. The image shows a lateral force map acquired with a load of  $\approx 1$  nN; no atomic features were observed in the corresponding topographic signal. Figure 15.36a, b shows that the debris extracted from the groove recrystallized with the same atomic arrangement of the undamaged surface, which suggests that the wear process occurred in a similar way to epitaxial growth, assisted by the microscope tip.

**Fig. 15.36** Lateral force images acquired at the end of a groove scratched 256 times with a normal force  $F_N = 21$  nN. Frame sizes: (a) 39 nm, (b) 25 nm

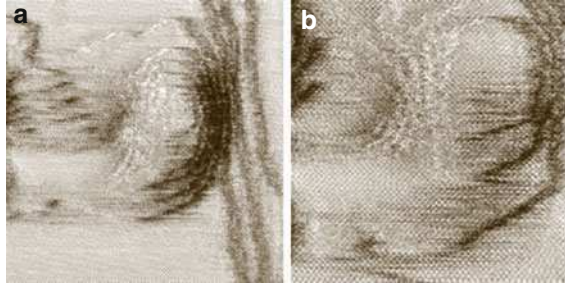


**Fig. 15.37** Friction loops acquired while scratching the KBr surface on 5 nm long lines with different loads  $F_N = 5.7\text{--}22.8$  nN (after [88])

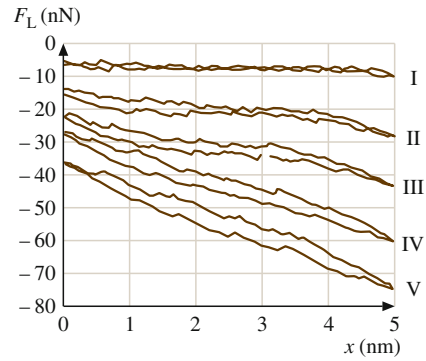
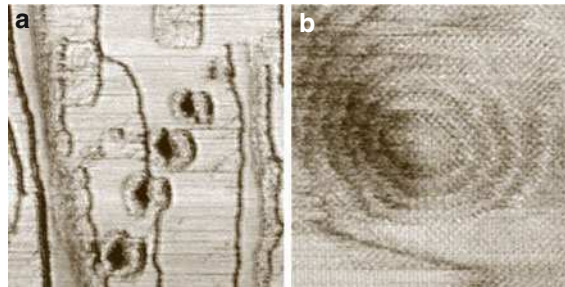


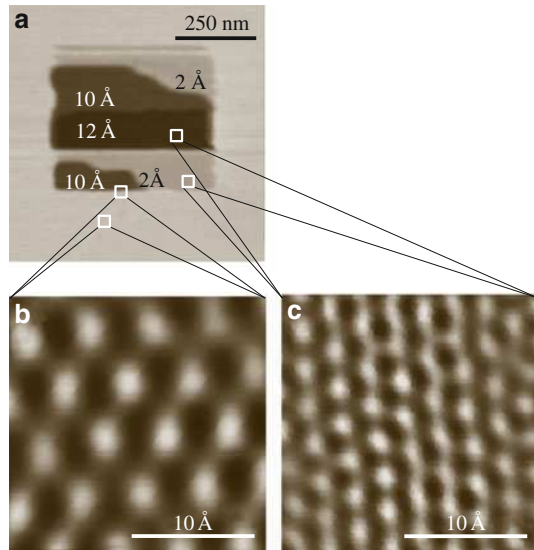
**Fig. 15.38** (a) Lateral force images of the pits produced with  $F_N = 5.7\text{--}22.8$  nN. Frame size: 150 nm; (b) Detailed image of the fourth pit from the top with pseudo-atomic resolution. Frame size: 20 nm



Although it is not that easy to understand how wear is initiated and how the tip transports the debris, important indications are given by the profile of the lateral force  $F_L$  recorded while scratching. Figure 15.37 shows some friction loops acquired when the tip was scanned laterally on areas of size  $5 \times 5 \text{ nm}^2$ . The mean lateral force multiplied by the scanned length gives the total energy dissipated in the process. The tip movement produces the pits shown in Fig. 15.38a. Thanks to the pseudo-atomic resolution obtained by FFM (Fig. 15.38b), the number of removed atoms can be determined from lateral force images, which allow us to estimate that 70% of the dissipated energy went into wearless friction [88].



**Fig. 15.39** (a) Topography image of an area scratched on muscovite mica with  $F_N = 230$  nN; (b, c) Fourier-filtered images of different regions (after [89])



Figures 15.37 and 15.38 clearly show that the damage increases with increasing load. On the other hand, changing the scan velocity  $v$  between 25 and 100 nm/s did not produce any significant variation in the wear process.

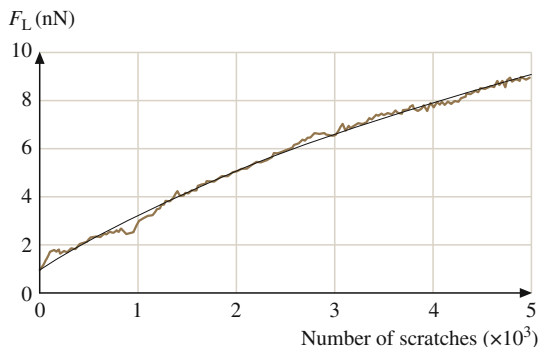
In a recent study on KBr films on Cu(100) Filleter et al. [41] reported significant wear at intrinsic step edges of the films, where atomic coordination is lower. In contrast, low friction and no wear were observed across metal steps covered by KBr, which indicates a stabilizing effect of the alkali halide coating on the metal surface. A different kind of wear was observed on layered materials. Kopta et al. [89] removed layers from a muscovite mica surface by scratching with normal force  $F_N = 230$  nN (Fig. 15.39a). Fourier-filtered images acquired on very small areas revealed the different periodicities of the underlying layers, which reflect the complex structure of the muscovite mica (Fig. 15.39b, c).

### 15.6.2 Contribution of Wear to Friction

The mean lateral force detected while scratching a KBr(100) surface with a fixed load  $F_N = 11$  nN is shown in Fig. 15.40. A rather continuous increase in *friction* with the number of scratches  $N$  is observed, which can be approximated with the following exponential law

$$F_L = F_0 e^{-N/N_0} + F_\infty (1 - e^{-N/N_0}). \quad (15.39)$$

**Fig. 15.40** Mean value of the lateral force during repeated scratching with  $F_N = 11$  nN on a 500 nm line (after [88])



Equation (15.39) is easily interpreted by assuming that friction is proportional to contact area  $A(N)$ , and that time evolution of  $A(N)$  can be described by

$$\frac{dA}{dN} = \frac{A_\infty - A(N)}{N_0}. \quad (15.40)$$

Here  $A_\infty$  is the limit area in which the applied load can be balanced without scratching.

To interpret their experiment on mica, Kopta et al. assumed that wear is initiated by atomic defects. When the defects accumulate beyond a critical concentration, they grow to form the scars shown in Fig. 15.39. Such a process was once again related to thermal activation. The number of defects created in the contact area  $A(F_N)$  is

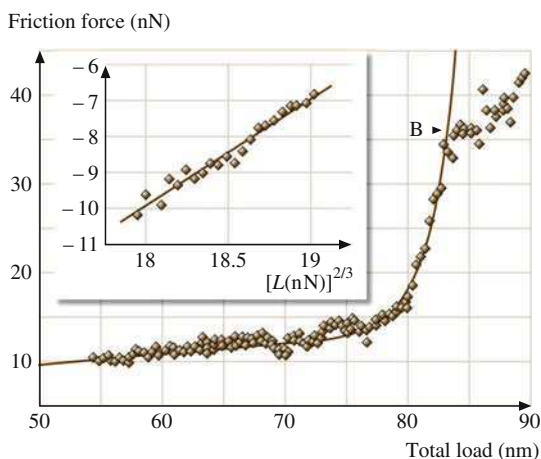
$$N_{\text{def}}(F_N) = t_{\text{res}} n_0 A(F_N) f_0 \exp\left(-\frac{\Delta E}{k_B T}\right), \quad (15.41)$$

where  $t_{\text{res}}$  is the residence time of the tip,  $n_0$  is the surface density of atoms, and  $f_0$  is the frequency of attempts to overcome the energy barrier  $\Delta E$  to break a Si–O bond, which depends on the applied load. When the defect density reaches a critical value, a hole is nucleated. The friction force during the creation of a hole was also estimated via thermal activation by Kopta et al., who derived the formula

$$F_L = c(F_N - F_{\text{off}})^{\frac{2}{3}} + \gamma F_N^{\frac{2}{3}} \exp\left(B_0 F_N^{\frac{2}{3}}\right). \quad (15.42)$$

The first term on the right gives the wearless dependence of friction in the Hertz-plus-offset model (Sect. 15.5.1); the second term is the contribution of the defect production. The agreement between (15.42) and experiment can be observed in Fig. 15.41.

**Fig. 15.41** Friction versus load curve during the creation of a hole in the muscovite mica (after [89])



## 15.7 Molecular Dynamics Simulations of Atomic Friction and Wear

Section 15.5 mentioned that small sliding contacts can be modeled by continuum mechanics. This modeling has several limitations. The first and most obvious is that continuum mechanics cannot account for atomic-scale processes like atomic stick-slip. While this limit can be overcome by semiclassical descriptions like the Tomlinson model, one definite limit is the determination of contact stiffness for contacts with a radius of a few nanometers. Interpreting experimental results with the methods introduced in Sect. 15.5.3 regularly yields contact radii of atomic or even smaller size, in clear contradiction to the minimal contact size given by adhesion forces. Macroscopic quantities such as shear modulus or pressure fail to describe the mechanical behavior of these contacts. Microscopic modeling that includes the atomic structure of the contact is therefore required. This is usually achieved through a *molecular dynamics* (MD) simulation of the contact. In such simulations, the sliding contact is set up by boundaries of fixed atoms in relative motion and the atoms of the contact, which are allowed to relax their positions according to interactions between each pair of atoms. Methods of computer simulation used in tribology are discussed elsewhere in this book. In this section we will discuss simulations that can be directly compared to experimental results showing atomic friction processes. The major outcome of the simulations beyond the inclusion of the atomic structure is the importance of including displacement of atoms in order to correctly predict forces. Then we present simulation studies that include wear of the tip or the surface.

### 15.7.1 *Molecular Dynamics Simulations of Friction Processes*

The first experiments that exhibited the features of atomic friction were performed on layered materials, often graphite. A theoretical study of forces between an atomically sharp diamond tip and the graphite surface has been reported by Tang et al. [90]. The authors found that the forces were significantly dependent on distance. The strongest contrasts appeared at different distances for normal and lateral forces due to the strong displacement of surface atoms. The order of magnitude found in this study was one nanonewton, much less than in most experimental reports, which indicated that contact areas of far larger dimensions were realized in such experiments. Tang et al. determined that the distance dependence of the forces could even change the symmetrical appearance of the lateral forces observed. The experimental situation has also been studied in numerical simulations using a simplified one-atom potential for the tip–surface interaction but including the spring potential of the probing force sensor [43]. The motivation for these studies was the observation of a hexagonal pattern in the friction force, while the surface atoms of graphite are ordered in a honeycomb structure. The simulations revealed how the jump path of the tip under lateral force is dependent on the force constant of the probing force sensor.

Surfaces of ionic crystals have become model systems for studies in atomic friction. Atomic stick–slip behavior has been observed by several groups with a lateral force modulation of the order of 1 nN. Pioneering work in atomistic simulation of sliding contacts has been done by Landman et al. The first ionic system studied was a  $\text{CaF}_2$  tip sliding over a  $\text{CaF}_2(111)$  surface [91]. In MD calculations with controlled temperature, the tip was first moved toward the surface up to the point at which an attractive normal force of  $-3$  nN acted on the tip. Then the tip was moved laterally, and the lateral force determined. An oscillation with a periodicity corresponding to the atomic periodicity of the surface and with an amplitude decreasing from 8 nN was found. Inspection of the atomic positions revealed a wear process from shear cleavage of the tip. This transfer of atoms between tip and surface plays a crucial role in atomic friction studies, as was shown by Shluger et al. [92]. These authors simulated a  $\text{MgO}$  tip scanning laterally over a  $\text{LiF}(100)$  surface. Initially an irregular oscillation of the system's energy is found together with transfer of atoms between surface and tip. After a while, the tip apex structure is changed by adsorption of Li and F ions in such a way that nondestructive sliding with perfectly regular energy oscillations correlating with the periodicity of the surface was observed. The authors called this effect self-lubrication and speculate that, in general, dynamic self-organization of the surface material on the tip might promote the observation of periodic forces. In a less costly molecular mechanics study, in which the forces were calculated for each fixed tip–sample configuration, Tang et al. produced lateral and normal force maps for a diamond tip over a  $\text{NaCl}(100)$  surface, including such defects as vacancies and a step [93]. As with the studies mentioned before, they found that significant atomic force contrast can be expected for tip–sample distances of  $< 0.35$  nm, while distances  $< 0.15$  nm

result in destructive forces. For the idealized conditions of scanning at constant height in this regime, the authors predict that even atomic-sized defects could be imaged. Experimentally, these conditions cannot be stabilized in the static modes used so far in lateral force measurements. However, dynamic modes of force microscopy have given atomic resolution of defects within the distance regime of 0.2 and 0.4 nm [94]. Recent experimental progress in atomic friction studies of surfaces of ionic crystals include the velocity dependence of lateral forces and atomic-scale wear processes. Such phenomena are not yet accessible by MD studies: the experimental scanning timescale is too far from the atomic relaxation timescales that govern MD simulations. Furthermore, the number of freely transferable atoms that can be included in a simulation is simply limited by meaningful calculation time.

Landman et al. also simulated a system of high reactivity, namely a silicon tip sliding over a silicon surface [95]. A clear stick-slip variation in the lateral force was observed for this situation. Strong atom displacements created an interstitial atom under the influence of the tip, which was annealed as the tip moved on. Permanent damage was predicted, however, when the tip enters the repulsive force regime. Although the simulated Si(111) surface is not experimentally accessible, it should be mentioned that the tip had to be passivated by a Teflon layer on the Si(111)- $7 \times 7$  reconstructed surface before nondestructive contact mode measurements became possible (Sect. 15.3). It is worth noting that the simulations for the Cu(111) surface revealed a linear relation between contact area and mean lateral force, similar to classical macroscopic laws.

Wear processes are predicted by several MD studies of metallic sliding over metallic surfaces, which will be discussed in the following section. For a (111)-terminated copper tip sliding over a Cu(111) surface, however, Sørensen et al. found that nondestructive sliding is possible while the lateral force exhibits the sawtooth-like shape characteristic of atomic stick-slip (Fig. 15.42). In contrast, a Cu(100) surface would be disordered by a sliding contact (Fig. 15.43).

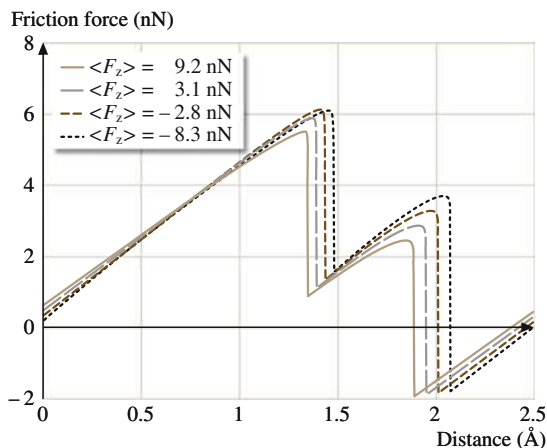
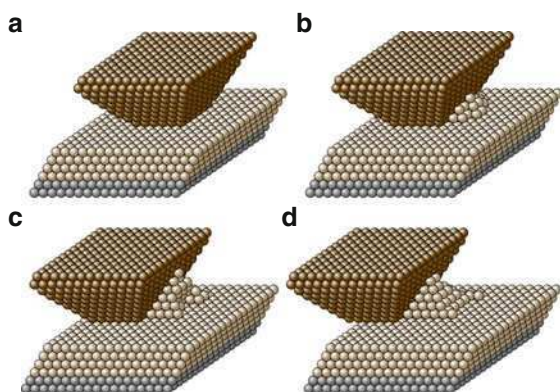


**Fig. 15.42** Lateral force acting on a Cu(111) tip in matching contact with a Cu(111) substrate as a function of the sliding distance at different loads (after [96])

**Fig. 15.43** Snapshot of a Cu(100) tip on a Cu(100) substrate during sliding. (a) Starting configuration; (b–d) snapshots after two, four, and six slips (after [96])



### 15.7.2 Molecular Dynamics Simulations of Abrasive Wear

The long timescales characteristic of wear processes and the large amount of material involved make any attempt to simulate these mechanisms on a computer a tremendous challenge. Despite this, MD can provide useful insights on the mechanisms of removal and deposition of single atoms by the FFM tip, which is not the kind of information directly observable experimentally. Complex processes like abrasive wear and nanolithography can be investigated only within approximate classical mechanics.

The observation made by Livshits and Shluger, that the FFM tip undergoes a process of self-lubrication when scanning ionic surfaces (Sect. 15.7.1), proves that friction and wear are strictly related phenomena. In their MD simulations on copper, Sørensen et al. considered not only ordered (111)- and (100)-terminated tips, but also amorphous structures obtained by *heating* the tip to high temperatures [96]. The lateral motion of the neck thus formed revealed stick–slip behavior due to combined sliding and stretching, as well as ruptures, accompanied by deposition of debris on the surface (Fig. 15.44).

To our knowledge, only a few examples of abrasive wear simulations on the atomic scale have been reported. Buldum and Ciraci, for instance, studied nanoindentation and sliding of a sharp Ni(111) tip on Cu(110) and a blunt Ni(001) tip on Cu(100) [97]. In the case of the sharp tip, quasiperiodic variations of the lateral force were observed, due to stick–slip involving phase transition. One layer of the asperity was deformed to match the substrate during the first slip and then two asperity layers merged into one in a structural transition during the second slip. In the case of the blunt tip, the stick–slip was less regular.

Different results have been reported in which the tip is harder than the underlying sample. Komanduri et al. considered an infinitely hard Ni indenter scratching single crystal aluminum at extremely low depths (Fig. 15.45) [98]. A linear relation between friction and load was found, with a high coefficient of friction  $\mu = 0.6$ , independent of the scratch depth. Nanolithography simulations were recently

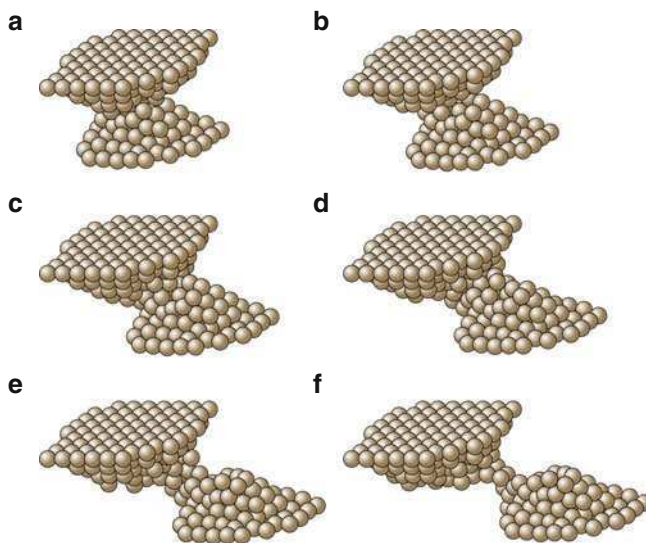
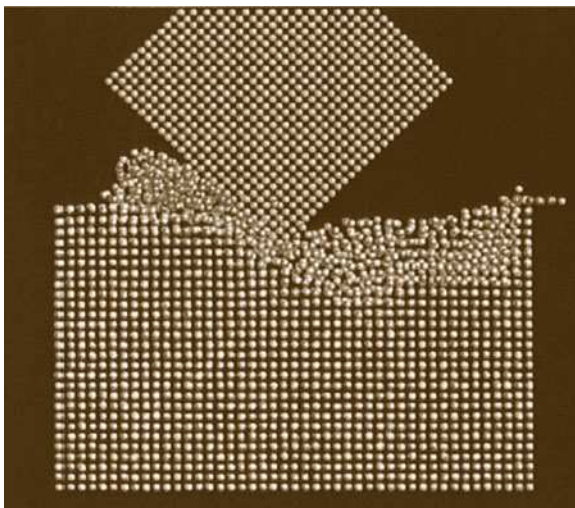


**Fig. 15.44** Snapshot of a Cu(100) neck during shearing starting from configuration (a). The upper substrate was displaced 4.2 Å between subsequent pictures (after [96])

**Fig. 15.45** MD simulation of a scratch realized with an infinitely hard tool (after [98])



performed by Fang et al. [99], who investigated the role of the displacement of the FFM tip along the direction of slow motion between a scan line and the next one. They found a certain correlation with FFM experiments on silicon films coated with aluminum.



## 15.8 Energy Dissipation in Noncontact Atomic Force Microscopy

Historically, the measurement of energy dissipation induced by tip–sample interaction has been the domain of friction force microscopy, where the sharp AFM tip slides over a sample that it is in gentle contact with. The origins of dissipation in friction are related to phonon excitation, electronic excitation and irreversible changes of the surface. In a typical stick–slip experiment, the energy dissipated in a single atomic slip event is of the order of 1 eV.

However, the lateral resolution of force microscopy in the contact mode is limited by a minimum contact area of several atoms due to adhesion between tip and sample.

This problem has been overcome in noncontact dynamic force microscopy. In the dynamic mode, the tip oscillates with a constant amplitude  $A$  of typically 1–20 nm at the eigenfrequency  $f$  of the cantilever, which shifts by  $\Delta f$  due to interaction forces between tip and sample. This technique is described in detail in Part B of this book.

Dissipation also occurs in the noncontact mode of force microscopy, where the atomic structure of tip and sample are reliably preserved. In this dynamic mode, the damping of the cantilever oscillation can be deduced from the excitation amplitude  $A_{\text{exc}}$  required to maintain the constant tip oscillation amplitude on resonance.

Compared to friction force microscopy, the interpretation of noncontact AFM (NC-AFM) experiments is complicated due to the perpendicular oscillation of the tip, typically with an amplitude that is large compared to the minimum tip–sample separation. Another problem is to relate the measured damping of the cantilever to the different origins of dissipation.

In all dynamic force microscopy measurements, a power dissipation  $P_0$  caused by internal friction of the freely oscillating cantilever is observed, which is proportional to the eigenfrequency  $\omega_0$  and to the square of the amplitude  $A$  and is inversely proportional to the known  $Q$  value of the cantilever. When the tip–sample distance is reduced, the tip interacts with the sample and therefore additional damping of the oscillation is encountered. This extra dissipation  $P_{\text{ts}}$  caused by the tip–sample interaction can be calculated from the excitation signal  $A_{\text{exc}}$  [100].

The observed energy losses per oscillation cycle (100 meV) [101] are roughly similar to the 1 eV energy loss in the contact slip process. When estimating the contact area in the contact mode for a few atoms, the energy dissipation per atom that can be associated with a bond being broken and reformed is also  $\approx 100$  meV.

The idea of relating the additional damping of the tip oscillation to dissipative tip–sample interactions has recently attracted much attention [102]. The origins of this additional dissipation are manifold: one may distinguish between apparent energy dissipation (for example from inharmonic cantilever motion, artefacts from the phase controller, or slow fluctuations round the steady state solution [102, 103]), velocity-dependent dissipation (for example electric and magnetic-field-mediated



Joule dissipation [104, 105]) and hysteresis-related dissipation (due to atomic instabilities [106, 107] or hysteresis due to adhesion [108]).

Forces and dissipation can be measured by recording  $\Delta f$  and  $A_{\text{exc}}$  simultaneously during a typical AFM experiment. Many experiments show true atomic contrast in topography (controlled by  $\Delta f$ ) and in the dissipation signal  $A_{\text{exc}}$  [109]; however, the origin of the atomic energy dissipation process is still not completely resolved.

To prove that the observed atomic-scale variation in the damping is indeed due to atomic-scale energy dissipation and not an artefact of the distance feedback, Loppacher et al. [101] carried out a NC-AFM experiment on Si(111)- $7 \times 7$  at constant height (with distance feedback stopped). Frequency-shift and dissipation exhibit atomic-scale contrast, demonstrating true atomic-scale variations in force and dissipation.

Strong atomic-scale dissipation contrast at step edges has been demonstrated in a few experiments (NaCl on Cu [94] or measurements on KBr [110]). In Fig. 15.46, ultrathin NaCl islands grown on Cu(111) are shown. As shown in Fig. 15.46a, the island edges have a higher contrast than the NaCl terrace and they show atomically resolved corrugation. The strongly enhanced contrast of the step edges and kink sites could be attributed to a slower decay of the electric field and to easier relaxation of the positions of the ions at these locations. The dissipation image shown in Fig. 15.46b was recorded at the same time. To establish a direct spatial correspondence between the excitation and the topography signal, the match between topography and  $A_{\text{exc}}$  has been studied on many images. Sometimes the topography and  $A_{\text{exc}}$  are in phase, sometimes they are shifted a little bit, and sometimes  $A_{\text{exc}}$  is at a minimum when topography is at a maximum. The local contrast formation thus depends strongly on the atomic tip structure. In fact, the strong dependence of the dissipation contrast on the atomic state of the tip apex is impressively confirmed by the tip change observed in the experimental images shown in Fig. 15.46b. The dissipation contrast is seriously enhanced, while the topography contrast remains almost unchanged. The dissipation clearly depends

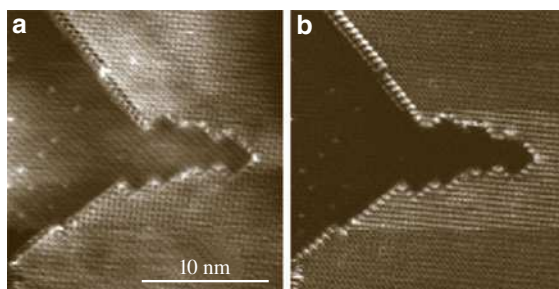


**Fig. 15.46** (a) Topography and (b)  $A_{\text{exc}}$  images of a NaCl island on Cu(111). The tip changes after 1/4 of the scan, thereby changing the contrast in the topography and enhancing the contrast in  $A_{\text{exc}}$ . After 2/3 of the scan, the contrast from the *lower part* of the image is reproduced, indicating that the tip change was reversible (after [94])

strongly on the state of the tip and exhibits more short-range character than the frequency shift.

More directly related to friction measurements, where the tip is sliding in contact with the sample, are NC-AFM experiments, where the tip is oscillating parallel to the surface. Stowe et al. [111] oriented cantilever beams with in-plane tips perpendicular to the surface, so that the tip motion was approximately parallel to the surface. The noncontact damping of the lever was used to measure localized electrical Joule dissipation. They were able to image the dopant density for n- and p-type silicon samples with 150 nm spatial resolution. A dependence of  $U_{ts}^2$  on the tip-sample voltage was found for the dissipation, as proposed by Denk and Pohl [104] for electric field Joule dissipation.

Stipe et al. [112] measured the noncontact friction between a Au(111) surface and a gold-coated tip with the same setup. They observed the same  $U_{ts}^2$  dependence of the bias voltage and a distance dependence that follows the power law  $1/d^n$ , where  $n$  is between 1.3 and 3 [112, 113]. A substantial electric-field is present even when the external bias voltage is zero. The presence of inhomogeneous tip-sample electric fields is difficult to avoid, even under the best experimental conditions. Although this dissipation is electrical in origin, the detailed mechanism is not totally clear. The most straightforward mechanism is to assume that inhomogeneous fields emanating from the tip and the sample induce surface charges in the nearby metallic sample. When the tip moves, currents are induced, causing ohmic dissipation [104, 111]. But in metals with good electrical conductivity, ohmic dissipation is insufficient to account for the observed effect [114]. Thus the tip-sample electric field must have an additional effect, such as driving the motions of adsorbates and surface defects.

When exciting the torsional oscillation of commercial, rectangular AFM cantilevers, the tip is oscillating approximately parallel to the surface. In this mode, it was possible to measure lateral forces acting on the tip at step edges and near impurities quantitatively [65]. Enhanced energy dissipation was also observed at the impurities. When the tip is moved further toward the sample, contact formation transforms the nearly free torsional oscillation of the cantilever into a different mode, with the tip-sample contact acting as a hinge. When this contact is formed, a rapid increase in the power required to maintain a constant tip oscillation amplitude and a positive frequency shift are found. The onsets of the simultaneously recorded damping and positive frequency shift are sharp and essentially coincide. It is assumed that these changes indicate the formation of a tip-sample contact. Two recent studies [115, 116] report on the use of the torsional eigenmode to measure the elastic properties of the tip-sample contact, where the tip is in contact with the sample and the shear stiffness depends on the normal load.

Kawagishi et al. [117] scanned with lateral amplitudes of the order of 10 pm to 3 nm; their imaging technique showed up contrast between graphite terraces, silicon and silicon dioxide, graphite and mica. Torsional self-excitation showed nanometric features of self-assembled monolayer islands due to different lateral dissipations.

Giessibl et al. [118] recently established true atomic resolution of both conservative and dissipative forces by lateral force microscopy. The interaction between a single tip atom oscillated parallel to an Si(111)- $7 \times 7$  surface was measured. A dissipation energy of up to 4 eV per oscillation cycle was found, which is explained by the plucking action of one atom onto the other, as described by Tomlinson in 1929 [25].

A detailed review of dissipation phenomena in noncontact force microscopy has been given by Hug [119].

## 15.9 Conclusion

Over the last 15 years, two instrumental developments have stimulated scientific activities in the field of nanotribology. On the one hand, the invention and development of friction force microscopy has allowed us to quantitatively study single-asperity friction. As we have discussed in this chapter, atomic processes are observed using forces of  $\approx 1$  nN (forces related to single chemical bonds). On the other hand, the enormous increase in achievable computing power has provided the basis for molecular dynamics simulations of systems containing several hundreds of atoms. These methods allow the development of the atomic structure in a sliding contact to be analyzed and the forces to be predicted.

The most prominent observation of atomic friction is stick-slip behavior with the periodicity of the surface atomic lattice. Semiclassical models can explain experimental findings, including the velocity dependence, which is a consequence of the thermal activation of slip events. Classical continuum mechanics can also describe the load dependence of friction in contacts with an extension of several tens of nanometers. However, when we try to apply continuum mechanics to contacts formed at just ten atoms, obviously wrong numbers result (for the contact radius for instance). Only comparison with atomistic simulations can provide a full, meaningful picture of the physical parameters of such sliding contacts. These simulations predict a close connection between wear and friction, in particular the transfer of atoms between surface and tip, which in some cases can even lower the friction in a process of self-lubrication.

First experiments have succeeded in studying the onset of wear with atomic resolution. Research into microscopic wear processes will certainly grow in importance as nanostructures are produced and their mechanical properties exploited. Simulations of such processes involving the transfer of thousands of atoms will become feasible with further increases in computing power. Another aspect of nanotribology is the expansion of atomic friction experiments toward surfaces with well-defined roughnesses. In general, the problem of bridging the gap between single-asperity experiments on well-defined surfaces and macroscopic friction should be approached, both experimentally and via modeling.

## References

1. C.M. Mate, G.M. McClelland, R. Erlandsson, S. Chiang, Atomic-scale friction of a tungsten tip on a graphite surface. *Phys. Rev. Lett.* **59**, 1942–1945 (1987)
2. G. Binnig, C.F. Quate, C. Gerber, Atomic force microscope. *Phys. Rev. Lett.* **56**, 930–933 (1986)
3. O. Marti, J. Colchero, J. Mlynek, Combined scanning force and friction microscopy of mica. *Nanotechnology* **1**, 141–144 (1990)
4. G. Meyer, N. Amer, Simultaneous measurement of lateral and normal forces with an optical-beam-deflection atomic force microscope. *Appl. Phys. Lett.* **57**, 2089–2091 (1990)
5. G. Neubauer, S.R. Cohen, G.M. McClelland, D.E. Horn, C.M. Mate, Force microscopy with a bidirectional capacitance sensor. *Rev. Sci. Instrum.* **61**, 2296–2308 (1990)
6. G.M. McClelland, J.N. Glosli, Friction at the atomic scale. In: *NATO ASI Series E*, Vol. 220, ed. by L. Singer, H.M. Pollock (Kluwer, Dordrecht, 1992), pp. 405–425
7. R. Linnemann, T. Gotszalk, I.W. Rangelow, P. Dumania, E. Oesterschulze, Atomic force microscopy and lateral force microscopy using piezoresistive cantilevers. *J. Vac. Sci. Technol. B* **14**, 856–860 (1996)
8. M. Nonnenmacher, J. Greschner, O. Wolter, R. Kassing, Scanning force microscopy with micromachined silicon sensors. *J. Vac. Sci. Technol. B* **9**, 1358–1362 (1991)
9. R. Lüthi, Untersuchungen zur Nanotribologie und zur Auflösungsgrenze im Ultrahochvakuum mittels Rasterkraftmikroskopie. Ph.D. Thesis (University of Basel, Basel 1996)
10. J. Cleveland, S. Manne, D. Bocek, P.K. Hansma, A nondestructive method for determining the spring constant of cantilevers for scanning force microscopy. *Rev. Sci. Instrum.* **64**, 403–405 (1993)
11. J.L. Hutter, J. Bechhoefer, Calibration of atomic-force microscope tips. *Rev. Sci. Instrum.* **64**, 1868–1873 (1993)
12. H.J. Butt, M. Jaschke, Calculation of thermal noise in atomic-force microscopy. *Nanotechnology* **6**, 1–7 (1995)
13. J.M. Neumeister, W.A. Ducker, Lateral, normal, and longitudinal spring constants of atomic-force microscopy cantilevers. *Rev. Sci. Instrum.* **65**, 2527–2531 (1994)
14. D.F. Ogletree, R.W. Carpick, M. Salmeron, Calibration of frictional forces in atomic force microscopy. *Rev. Sci. Instrum.* **67**, 3298–3306 (1996)
15. E. Gnecco, AFM study of friction phenomena on the nanometer scale. Ph.D. Thesis (University of Genova, Genova, 2001)
16. U.D. Schwarz, P. Köster, R. Wiesendanger, Quantitative analysis of lateral force microscopy experiments. *Rev. Sci. Instrum.* **67**, 2560–2567 (1996)
17. J.E. Sader, C.P. Green, In-plane deformation of cantilever plates with applications to lateral force microscopy. *Rev. Sci. Instrum.* **75**, 878–883 (2004)
18. S.A. Edwards, W.A. Ducker, J.E. Sader, Influence of atomic force microscope cantilever tilt and induced torque on force measurements. *J. Appl. Phys.* **103**, 064513 (2008)
19. E. Meyer, R. Lüthi, L. Howald, M. Bammerlin, M. Guggisberg, H.-J. Güntherodt, Site-specific friction force spectroscopy. *J. Vac. Sci. Technol. B* **14**, 1285–1288 (1996)
20. S.S. Sheiko, M. Möller, E.M.C.M. Reuvekamp, H.W. Zandberger, Calibration and evaluation of scanning-force microscopy probes. *Phys. Rev. B* **48**, 5675 (1993)
21. F. Atamny, A. Baiker, Direct imaging of the tip shape by AFM. *Surf. Sci.* **323**, L314 (1995)
22. J.S. Villarrubia, Algorithms for scanned probe microscope image simulation, surface reconstruction, and tip estimation. *J. Res. Natl. Inst. Stand. Technol.* **102**, 425–454 (1997)
23. L. Howald, E. Meyer, R. Lüthi, H. Haefke, R. Overney, H. Rudin, H.-J. Güntherodt, Multifunctional probe microscope for facile operation in ultrahigh vacuum. *Appl. Phys. Lett.* **63**, 117–119 (1993)
24. Q. Dai, R. Vollmer, R.W. Carpick, D.F. Ogletree, M. Salmeron, A variable temperature ultrahigh vacuum atomic force microscope. *Rev. Sci. Instrum.* **66**, 5266–5271 (1995)
25. G.A. Tomlinson, A molecular theory of friction. *Philos. Mag. Ser. 7*, 905 (1929)

26. T. Gyalog, M. Bammerlin, R. Lüthi, E. Meyer, H. Thomas, Mechanism of atomic friction. *Europhys. Lett.* **31**, 269–274 (1995)
27. T. Gyalog, H. Thomas, Friction between atomically flat surfaces. *Europhys. Lett.* **37**, 195–200 (1997)
28. M. Weiss, F.J. Elmer, Dry friction in the Frenkel–Kontorova–Tomlinson model: Static properties. *Phys. Rev. B* **53**, 7539–7549 (1996)
29. M.H. Müser, Structural lubricity: Role of dimension and symmetry. *Europhys. Lett.* **66**, 97 (2004)
30. J.B. Pethica, Comment on “Interatomic forces in scanning tunneling microscopy, Giant corrugations of the graphite surface”. *Phys. Rev. Lett.* **57**, 3235 (1986)
31. E. Meyer, R.M. Overney, K. Dransfeld, T. Gyalog, *Nanoscience, Friction and Rheology on the Nanometer Scale* (World Scientific, Singapore, 1998)
32. A. Socoliuc, R. Bennewitz, E. Gnecco, E. Meyer, Transition from stick-slip to continuous sliding in atomic friction: Entering a new regime of ultralow friction. *Phys. Rev. Lett.* **92**, 134301 (2004)
33. A. Socoliuc, E. Gnecco, S. Maier, O. Pfeiffer, A. Baratoff, R. Bennewitz, E. Meyer, Atomic-scale control of friction by actuation of nanometer-sized contacts. *Science* **313**, 207–210 (2006)
34. R. Lüthi, E. Meyer, M. Bammerlin, L. Howald, H. Haefke, T. Lehmann, C. Loppacher, H.-J. Güntherodt, T. Gyalog, H. Thomas, Friction on the atomic scale: An ultrahigh vacuum atomic force microscopy study on ionic crystals. *J. Vac. Sci. Technol. B* **14**, 1280–1284 (1996)
35. S. Maier, E. Gnecco, A. Baratoff, R. Bennewitz, E. Meyer, Atomic scale friction modulated by a buried interface. *Phys. Rev. B* (2008), in press
36. S. Maier, Y. Sang, T. Filleter, M. Grant, R. Bennewitz, E. Gnecco, E. Meyer, Fluctuations and jump dynamics in atomic friction experiments. *Phys. Rev. B* **72**, 245418 (2008)
37. L. Howald, R. Lüthi, E. Meyer, H.-J. Güntherodt, Atomic-force microscopy on the Si(111)  $7 \times 7$  surface. *Phys. Rev. B* **51**, 5484–5487 (1995)
38. R. Bennewitz, E. Gnecco, T. Gyalog, E. Meyer, Atomic friction studies on well-defined surfaces. *Tribol. Lett.* **10**, 51–56 (2001)
39. T. Filleter, W. Paul, R. Bennewitz, Atomic structure and friction of ultrathin films of KBr on Cu(100). *Phys. Rev. B* **77**, 035430 (2008)
40. G.J. Germann, S.R. Cohen, G. Neubauer, G.M. McClelland, H. Seki, Atomic-scale friction of a diamond tip on diamond (100) and (111) surfaces. *J. Appl. Phys.* **73**, 163–167 (1993)
41. R.J.A. van den Oetelaar, C.F.J. Flipse, Atomic-scale friction on diamond(111) studied by ultrahigh vacuum atomic force microscopy. *Surf. Sci.* **384**, L828–L835 (1997)
42. S. Fujisawa, E. Kishi, Y. Sugawara, S. Morita, Atomic-scale friction observed with a two-dimensional frictional-force microscope. *Phys. Rev. B* **51**, 7849–7857 (1995)
43. N. Sasaki, M. Kobayashi, M. Tsukada, Atomic-scale friction image of graphite in atomic-force microscopy. *Phys. Rev. B* **54**, 2138–2149 (1996)
44. H. Kawakatsu, T. Saito, Scanning force microscopy with two optical levers for detection of deformations of the cantilever. *J. Vac. Sci. Technol. B* **14**, 872–876 (1996)
45. M. Hirano, K. Shinjo, R. Kaneko, Y. Murata, Anisotropy of frictional forces in muscovite mica. *Phys. Rev. Lett.* **67**, 2642–2645 (1991)
46. M. Hirano, K. Shinjo, R. Kaneko, Y. Murata, Observation of superlubricity by scanning tunneling microscopy. *Phys. Rev. Lett.* **78**, 1448–1451 (1997)
47. R.M. Overney, H. Takano, M. Fujihira, W. Paulus, H. Ringsdorf, Anisotropy in friction and molecular stick-slip motion. *Phys. Rev. Lett.* **72**, 3546–3549 (1994)
48. H. Takano, M. Fujihira, Study of molecular scale friction on stearic acid crystals by friction force microscopy. *J. Vac. Sci. Technol. B* **14**, 1272–1275 (1996)
49. M. Dienwiebel, G. Verhoeven, N. Pradeep, J. Frenken, J. Heimberg, H. Zandbergen, Superlubricity of graphite. *Phys. Rev. Lett.* **92**, 126101 (2004)

50. M. Liley, D. Gourdon, D. Stamou, U. Meseth, T.M. Fischer, C. Lautz, H. Stahlberg, H. Vogel, N.A. Burnham, C. Duschl, Friction anisotropy and asymmetry of a compliant monolayer induced by a small molecular tilt. *Science* **280**, 273–275 (1998)
51. R. Lüthi, E. Meyer, H. Haefke, L. Howald, W. Gutmannsbauer, H.-J. Güntherodt, Sled-type motion on the nanometer scale: Determination of dissipation and cohesive energies of C<sub>60</sub>. *Science* **266**, 1979–1981 (1994)
52. P.E. Sheehan, C.M. Lieber, Nanotribology and nanofabrication of MoO<sub>3</sub> structures by atomic force microscopy. *Science* **272**, 1158–1161 (1996)
53. M.R. Falvo, J. Steele, R.M. Taylor, R. Superfine, Evidence of commensurate contact and rolling motion: AFM manipulation studies of carbon nanotubes on HOPG. *Tribol. Lett.* **9**, 73–76 (2000)
54. E. Gnecco, R. Bennewitz, T. Gyalog, C. Loppacher, M. Bammerlin, E. Meyer, H.-J. Güntherodt, Velocity dependence of atomic friction. *Phys. Rev. Lett.* **84**, 1172–1175 (2000)
55. Y. Sang, M. Dubé, M. Grant, Thermal effects on atomic friction. *Phys. Rev. Lett.* **87**, 174301 (2001)
56. E. Riedo, E. Gnecco, R. Bennewitz, E. Meyer, H. Brune, Interaction potential and hopping dynamics governing sliding friction. *Phys. Rev. Lett.* **91**, 084502 (2003)
57. P. Reimann, M. Evstigneev, Nonmonotonic velocity dependence of atomic friction. *Phys. Rev. Lett.* **93**, 230802 (2004)
58. C. Fusco, A. Fasolino, Velocity dependence of atomic-scale friction: A comparative study of the one- and two-dimensional Tomlinson model. *Phys. Rev. B* **71**, 45413 (2005)
59. O. Zwörner, H. Hölscher, U.D. Schwarz, R. Wiesendanger, The velocity dependence of frictional forces in point-contact friction. *Appl. Phys. A* **66**, 263–267 (1998)
60. D. Gourdon, N.A. Burnham, A. Kulik, E. Dupas, F. Oulevey, G. Gremaud, D. Stamou, M. Liley, Z. Dienes, H. Vogel, C. Duschl, The dependence of friction anisotropies on the molecular organization of LB films as observed by AFM. *Tribol. Lett.* **3**, 317–324 (1997)
61. T. Bouhacina, J.P. Aimé, S. Gauthier, D. Michel, V. Heroguez, Tribological behavior of a polymer grafted on silanized silica probed with a nanotip. *Phys. Rev. B* **56**, 7694–7703 (1997)
62. H.J. Eyring, The activated complex in chemical reactions. *J. Chem. Phys.* **3**, 107 (1937)
63. J.N. Glosli, G.M. McClelland, Molecular dynamics study of sliding friction of ordered organic monolayers. *Phys. Rev. Lett.* **70**, 1960–1963 (1993)
64. R. Bennewitz, T. Gyalog, M. Guggisberg, M. Bammerlin, E. Meyer, H.-J. Güntherodt, Atomic-scale stick-slip processes on Cu(111). *Phys. Rev. B* **60**, R11301–R11304 (1999)
65. O. Pfeiffer, R. Bennewitz, A. Baratoff, E. Meyer, P. Grütter, Lateral-force measurements in dynamic force microscopy. *Phys. Rev. B* **65**, 161403 (2002)
66. E. Riedo, F. Lévy, H. Brune, Kinetics of capillary condensation in nanoscopic sliding friction. *Phys. Rev. Lett.* **88**, 185505 (2002)
67. M. He, A.S. Blum, G. Overney, R.M. Overney, Effect of interfacial liquid structuring on the coherence length in nanolubrication. *Phys. Rev. Lett.* **88**, 154302 (2002)
68. A. Schirmeisen, L. Jansen, H. Hölscher, H. Fuchs, Temperature dependence of point contact friction on silicon. *Appl. Phys. Lett.* **88**, 123108 (2006)
69. X. Zhao, M. Hamilton, W.G. Sawyer, S.S. Perry, Thermally activated friction. *Tribol. Lett.* **27**, 113–117 (2007)
70. F.P. Bowden, F.P. Tabor, *The Friction and Lubrication of Solids* (Oxford University Press, Oxford, 1950)
71. L.D. Landau, E.M. Lifshitz, *Introduction to Theoretical Physics* (Nauka, Moscow, 1998), Vol. 7
72. J.A. Greenwood, J.B.P. Williamson, Contact of nominally flat surfaces. *Proc. R. Soc. Lond. A* **295**, 300 (1966)
73. B.N.J. Persson, Elastoplastic contact between randomly rough surfaces. *Phys. Rev. Lett.* **87**, 116101 (2001)

74. K.L. Johnson, K. Kendall, A.D. Roberts, Surface energy and contact of elastic solids. *Proc. R. Soc. Lond. A* **324**, 301 (1971)
75. B.V. Derjaguin, V.M. Muller, Y.P. Toporov, Effect of contact deformations on adhesion of particles. *J. Colloid Interface Sci.* **53**, 314–326 (1975)
76. D. Tabor, Surface forces and surface interactions. *J. Colloid Interface Sci.* **58**, 2–13 (1977)
77. D. Maugis, Adhesion of spheres, the JKR-DMT transition using a Dugdale model. *J. Colloid Interface Sci.* **150**, 243–269 (1992)
78. U.D. Schwarz, O. Zwörner, P. Köster, R. Wiesendanger, Quantitative analysis of the frictional properties of solid materials at low loads. *Phys. Rev. B* **56**, 6987–6996 (1997)
79. R.W. Carpick, N. Agrait, D.F. Ogletree, M. Salmeron, Measurement of interfacial shear (friction) with an ultrahigh vacuum atomic force microscope. *J. Vac. Sci. Technol. B* **14**, 1289–1295 (1996)
80. C. Polaczyk, T. Schneider, J. Schöfer, E. Santner, Microtribological behavior of Au(001) studied by AFM/FFM. *Surf. Sci.* **402**, 454–458 (1998)
81. J.N. Israelachvili, D. Tabor, Measurement of van der Waals dispersion forces in range 1.5 to 130 nm. *Proc. R. Soc. Lond. A* **331**, 19 (1972)
82. S.P. Jarvis, A. Oral, T.P. Weihs, J.B. Pethica, A novel force microscope and point-contact probe. *Rev. Sci. Instrum.* **64**, 3515–3520 (1993)
83. R.W. Carpick, D.F. Ogletree, M. Salmeron, Lateral stiffness: A new nanomechanical measurement for the determination of shear strengths with friction force microscopy. *Appl. Phys. Lett.* **70**, 1548–1550 (1997)
84. M.A. Lantz, S.J. O'Shea, M.E. Welland, K.L. Johnson, Atomic-force-microscope study of contact area and friction on NbSe<sub>2</sub>. *Phys. Rev. B* **55**, 10776–10785 (1997)
85. K.L. Johnson, *Contact Mechanics* (Cambridge University Press, Cambridge 1985)
86. M. Enachescu, R.J.A. van den Oetelaar, R.W. Carpick, D.F. Ogletree, C.F.J. Flipse, M. Salmeron, Atomic force microscopy study of an ideally hard contact: the diamond (111)/tungsten carbide interface. *Phys. Rev. Lett.* **81**, 1877–1880 (1998)
87. M. Enachescu, R.J.A. van den Oetelaar, R.W. Carpick, D.F. Ogletree, C.F.J. Flipse, M. Salmeron, Observation of proportionality between friction and contact area at the nanometer scale. *Tribol. Lett.* **7**, 73–78 (1999)
88. E. Gnecco, R. Bennewitz, E. Meyer, Abrasive wear on the atomic scale. *Phys. Rev. Lett.* **88**, 215501 (2002)
89. S. Kopta, M. Salmeron, The atomic scale origin of wear on mica and its contribution to friction. *J. Chem. Phys.* **113**, 8249–8252 (2000)
90. H. Tang, C. Joachim, J. Devillers, Interpretation of AFM images – the graphite surface with a diamond tip. *Surf. Sci.* **291**, 439–450 (1993)
91. U. Landman, W.D. Luedtke, E.M. Ringer, Atomistic mechanisms of adhesive contact formation and interfacial processes. *Wear* **153**, 3–30 (1992)
92. A.I. Livshits, A.L. Shluger, Self-lubrication in scanning force microscope image formation on ionic surfaces. *Phys. Rev. B* **56**, 12482–12489 (1997)
93. H. Tang, X. Bouju, C. Joachim, C. Girard, J. Devillers, Theoretical study of the atomic-force microscopy imaging process on the NaCl(100) surface. *J. Chem. Phys.* **108**, 359–367 (1998)
94. R. Bennewitz, A.S. Foster, L.N. Kantorovich, M. Bammerlin, C. Loppacher, S. Schär, M. Guggisberg, E. Meyer, A.L. Shluger, Atomically resolved edges and kinks of NaCl islands on Cu(111): Experiment and theory. *Phys. Rev. B* **62**, 2074–2084 (2000)
95. U. Landman, W.D. Luetke, M.W. Ribarsky, Structural and dynamical consequences of interactions in interfacial systems. *J. Vac. Sci. Technol. A* **7**, 2829–2839 (1989)
96. M.R. Sørensen, K.W. Jacobsen, P. Stoltze, Simulations of atomic-scale sliding friction. *Phys. Rev. B* **53**, 2101–2113 (1996)
97. A. Buldum, C. Ciraci, Contact, nanoindentation and sliding friction. *Phys. Rev. B* **57**, 2468–2476 (1998)
98. R. Komanduri, N. Chandrasekaran, L.M. Raff, Molecular dynamics simulation of atomic-scale friction. *Phys. Rev. B* **61**, 14007–14019 (2000)

99. T.H. Fang, C.I. Weng, J.G. Chang, Molecular dynamics simulation of a nanolithography process using atomic force microscopy. *Surf. Sci.* **501**, 138–147 (2002)
100. B. Gotsmann, C. Seidel, B. Anczykowski, H. Fuchs, Conservative and dissipative tip–sample interaction forces probed with dynamic AFM. *Phys. Rev. B* **60**, 11051–11061 (1999)
101. C. Loppacher, R. Bennewitz, O. Pfeiffer, M. Guggisberg, M. Bammerlin, S. Schär, V. Barwich, A. Baratoff, E. Meyer, Experimental aspects of dissipation force microscopy. *Phys. Rev. B* **62**, 13674–13679 (2000)
102. M. Gauthier, M. Tsukada, Theory of noncontact dissipation force microscopy. *Phys. Rev. B* **60**, 11716–11722 (1999)
103. J.P. Aimé, R. Boisgard, L. Nony, G. Couturier, Nonlinear dynamic behavior of an oscillating tip–microlever system and contrast at the atomic scale. *Phys. Rev. Lett.* **82**, 3388–3391 (1999)
104. W. Denk, D.W. Pohl, Local electrical dissipation imaged by scanning force microscopy. *Appl. Phys. Lett.* **59**, 2171–2173 (1991)
105. S. Hirsekorn, U. Rabe, A. Boub, W. Arnold, On the contrast in eddy current microscopy using atomic force microscopes. *Surf. Interf. Anal.* **27**, 474–481 (1999)
106. U. Dürig, Atomic-Scale Metal Adhesion. In: *Forces in Scanning Probe Methods*, NATO ASI Ser. E, Vol. 286, ed. by H.J. Güntherodt, D. Anselmetti, E. Meyer (Kluwer, Dordrecht, 1995) pp. 191–234
107. N. Sasaki, M. Tsukada, Effect of microscopic nonconservative process on noncontact atomic force microscopy. *Jpn. J. Appl. Phys.* **39**, L1334–L1337 (2000)
108. B. Gotsmann, H. Fuchs, The measurement of hysteretic forces by dynamic AFM. *Appl. Phys. A* **72**, 55–58 (2001)
109. M. Guggisberg, M. Bammerlin, A. Baratoff, R. Lüthi, C. Loppacher, F.M. Battiston, J. Lü, R. Bennewitz, E. Meyer, H.J. Güntherodt, Dynamic force microscopy across steps on the Si (111)-(7 × 7) surface. *Surf. Sci.* **461**, 255–265 (2000)
110. R. Bennewitz, S. Schär, V. Barwich, O. Pfeiffer, E. Meyer, F. Krok, B. Such, J. Kolodziej, M. Szymonski, Atomic-resolution images of radiation damage in KBr. *Surf. Sci.* **474**, 197–202 (2001)
111. T.D. Stowe, T.W. Kenny, J. Thomson, D. Rugar, Silicon dopant imaging by dissipation force microscopy. *Appl. Phys. Lett.* **75**, 2785–2787 (1999)
112. B.C. Stipe, H.J. Mamin, T.D. Stowe, T.W. Kenny, D. Rugar, Noncontact friction and force fluctuations between closely spaced bodies. *Phys. Rev. Lett.* **87**, 96801 (2001)
113. B. Gotsmann, H. Fuchs, Dynamic force spectroscopy of conservative and dissipative forces in an Al–Au(111) tip–sample system. *Phys. Rev. Lett.* **86**, 2597–2600 (2001)
114. B.N.J. Persson, A.I. Volokitin, Comment on “Brownian motion of microscopic solids under the action of fluctuating electromagnetic fields”. *Phys. Rev. Lett.* **84**, 3504 (2000)
115. K. Yamanaka, A. Noguchi, T. Tsuji, T. Koike, T. Goto, Quantitative material characterization by ultrasonic AFM. *Surf. Interface Anal.* **27**, 600–606 (1999)
116. T. Drobek, R.W. Stark, W.M. Heckl, Determination of shear stiffness based on thermal noise analysis in atomic force microscopy: Passive overtone microscopy. *Phys. Rev. B* **64**, 045401 (2001)
117. T. Kawagishi, A. Kato, Y. Hoshi, H. Kawakatsu, Mapping of lateral vibration of the tip in atomic force microscopy at the torsional resonance of the cantilever. *Ultramicroscopy* **91**, 37–48 (2002)
118. F.J. Giessibl, M. Herz, J. Mannhart, Friction traced to the single atom. *Proc. Natl. Acad. Sci. USA* **99**, 12006–12010 (2002)
119. H.-J. Hug, A. Baratoff, Measurement of dissipation induced by tip–sample interactions. In: *Noncontact Atomic Force Microscopy*, ed. by S. Morita, R. Wiesendanger, E. Meyer (Springer, Berlin, 2002), p. 395



# Chapter 16

## Scale Effect in Mechanical Properties and Tribology

Bharat Bhushan and Michael Nosonovsky

**Abstract** A model, which explains scale effects in mechanical properties and tribology is presented. Mechanical properties are scale dependent based on the strain gradient plasticity and the effect of dislocation-assisted sliding. Both single asperity and multiple asperity contacts are considered. The relevant scaling length is the nominal contact length – contact diameter for a single-asperity contact, and scan length for multiple-asperity contacts. For multiple asperity contacts, based on an empirical power-rule for scale dependence of roughness, contact parameters are calculated. The effect of load on the contact parameters and the coefficient of friction is also considered. During sliding, adhesion and two- and three-body deformation, as well as ratchet mechanism, contribute to the dry friction force. These components of the friction force depend on the relevant real areas of contact (dependent on roughness and mechanical properties), average asperity slope, number of trapped particles, and shear strength during sliding. Scale dependence of the components of the coefficient of friction is studied. A scale dependent transition index, which is responsible for transition from predominantly elastic adhesion to plastic deformation has been proposed. Scale dependence of the wet friction, wear, and interface temperature has been also analyzed. The proposed model is used to explain the trends in the experimental data for various materials at nanoscale and microscale, which indicate that nanoscale values of coefficient of friction are lower than the microscale values due to an increase of the three-body deformation and transition from elastic adhesive contact to plastic deformation.

### 16.1 Nomenclature

$a, \bar{a}, \bar{a}_0, a_{\max}, \bar{a}_{\max}$ : Contact radius, mean contact radius, macroscale value of mean contact radius, maximum contact radius, mean value of maximum contact radius

$A_a, A_r, A_{ra}, A_{re}, A_{re0}, A_{rp}, A_{rp0}, A_{ds}, A_{dp}$ : Apparent area of contact, real area of contact, real area of contact during adhesion, real area of elastic contact, macroscale value of real area of elastic contact, real area of plastic contact, macroscale value

of real area of plastic contact, real area of contact during asperity summit deformation, area of contact with particles

$b$ : Burgers vector

$c$ : Constant, specified by crystal structure

$C_0$ : Constant required for normalization of  $p(d)$

$d, d_e, d_n, d_{ln}, \bar{d}, d_0$ : Particle diameter, minimum for exponential distribution, mean for normal distribution, exponential of mean of  $\ln(d)$  for log-normal distribution, mean trapped particles diameter, macroscale value of mean trapped particles diameter

$D$ : Interface zone thickness

$E_1, E_2, E^*$ : Elastic moduli of contacting bodies, effective elastic modulus

$F, F_a, F_d, F_{ac}, F_{ap}, F_a, F_{ds}, F_{dp}, F_m, F_{m0}$ : Friction force, friction force due to adhesion, friction force due to deformation, friction force during elastic adhesional contact, plastic adhesional contact, summit deformation, particles deformation respectively, meniscus force for wet contact, macroscale value of meniscus force

$G$ : Elastic shear modulus

$h$ : Indentation depth

$h_f$ : Liquid film thickness

$H, H_0$ : Hardness, hardness in absence of strain gradient

$k, k_0$ : Wear coefficient, macroscale value of wear coefficient

$l_s, l_d$ : Material-specific characteristic length parameters

$L, L_{lwl}, L_{lc}, L_s, L_d$ : Length of the nominal contact zone, long wavelength limit for roughness parameters, long wavelength limit for contact parameters, length parameters related to  $l_s$  and  $l_d$

$L_p$ : Peclet number

$m, n$ : Indices of exponents for scale-dependence of  $\sigma$  and  $\beta^*$

$n_{tr}$ : Number of trapped particles divided by the total number of particles

$p_a, p_{ac}$ : Apparent pressure, critical apparent pressure

$p(d), p_{tr}(d)$ : Probability density function for particle size distribution, probability density function for trapped particle size distribution

$P(d)$ : Cumulative probability distribution for particle size

$R, R_p, \bar{R}_p, \bar{R}_{p0}$ : Effective radius of summit tips, radius of summit tip, mean radius of summit tips, macroscale value of the mean radius of summit tips

$R(\tau)$ : Autocorrelation function

$s$ : Spacing between slip steps on the indentation surface

$s_d$ : Separation distance between reference planes of two surfaces in contact

$N, N_0$ : Total number of contacts, macroscale value of total number of contacts

$T, T_0$ : Maximum flash temperature rise, macroscale value of temperature rise

$x$ : Sliding distance

$v$ : Volume of worn material

$V$ : Sliding velocity

$W$ : Normal load

- $z, z_{\min}, z_{\max}$ : Random variable, minimum and maximum value of  $z$   
 $\alpha$ : Probability for a particle in the border zone to leave the contact region  
 $\beta^*, \beta_0^*$ : Correlation length, macroscale value of correlation length  
 $\gamma$ : Surface tension  
 $\Gamma$ : Gamma function  
 $\varepsilon$ : Strain  
 $\eta$ : Density of particles per apparent area of contact  
 $\eta_{\text{int}}, \eta_{\text{cr}}$ : Density of dislocation lines per interface area, critical density of dislocation lines per interface area  
 $\kappa$ : Curvature  
 $\kappa_t$ : Thermal diffusivity  
 $\theta$ : Contact angle between the liquid and surface  
 $\theta_i$ : Indentation angle  
 $\theta_r$ : Roughness angle  
 $\mu, \mu_a, \mu_{ae}, \mu_{ae0}, \mu_{ap}, \mu_{ap0}, \mu_d, \mu_{ds}, \mu_{ds0}, \mu_{dp}, \mu_{dp0}, \mu_r, \mu_{r0}, \mu_{re}, \mu_{re0}, \mu_{rp}, \mu_{rp0}, \mu_{wet}$ : Coefficient of friction, coefficient of adhesional friction, coefficient of adhesional elastic friction, macroscale value of coefficient of adhesional elastic friction, coefficient of adhesional plastic friction, macroscale value of coefficient of adhesional plastic friction, coefficient of deformation friction, coefficient of summits deformation friction, macroscale value of coefficient of summits deformation friction, coefficient of particles deformation friction, macroscale value of coefficient of particles deformation friction, ratchet component of the coefficient of friction, macroscale value of ratchet component of the coefficient of friction, ratchet component of the coefficient of elastic friction, macroscale value of ratchet component of the coefficient of elastic friction, ratchet component of the coefficient of plastic friction, macroscale value of ratchet component of the coefficient of plastic friction, and coefficient of wet friction  
 $\nu_1, \nu_2$ : Poisson's ratios of contacting bodies  
 $\rho c_p$ : Volumetric specific heat  
 $\sigma, \sigma_0, \sigma_e, \sigma_n, \sigma_{\ln}$ : Standard deviation of rough surface profile height, macroscale value of standard deviation of rough surface profile height, standard deviation for the exponential distribution, standard deviation for the normal distributions, standard deviation for  $\ln(d)$  of the log normal distribution  
 $\rho, \rho_G, \rho_S$ : Total density of dislocation lines per volume, density of GND per volume, density of SSD per volume  
 $\phi, \phi_0$ : Transition index, macroscale value of transition index  
 $\tau, \tau_0$ : Spatial parameter, value at which the autocorrelation function decays  
 $\tau_a, \tau_{a0}, \tau_Y, \tau_{Y0}, \tau_{ds}, \tau_{ds0}, \tau_{dp}, \tau_{dp0}, \tau_p$ : Adhesional shear strength during sliding, macroscale value of adhesional shear strength, shear yield strength, shear yield strength in absence of strain gradient, shear strength during summits deformation, macroscale value of shear strength during summits deformation, shear strength during particles deformation, macroscale value of shear strength during particles deformation, Peierls stress.

## 16.2 Introduction

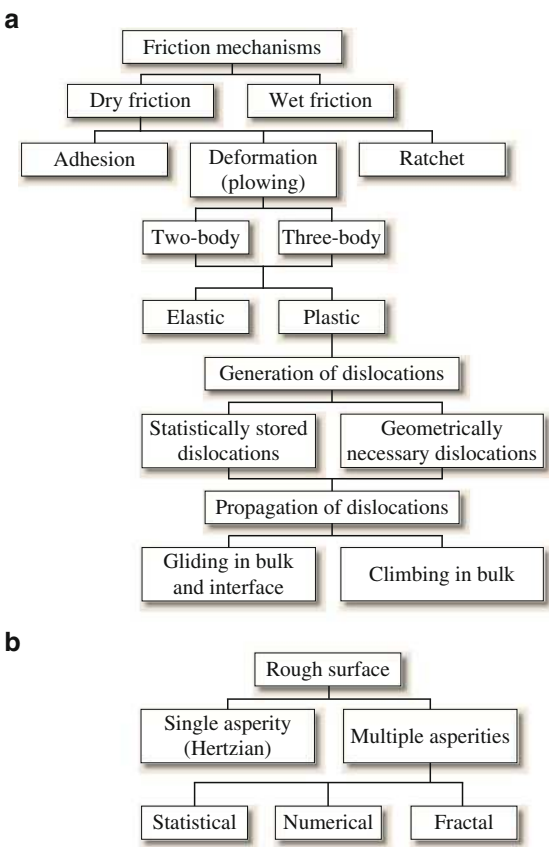
Microscale and nanoscale measurements of tribological properties, which became possible due to the development of the surface force apparatus (SFA), atomic force microscope (AFM), and friction force microscope (FFM) demonstrate scale dependence of adhesion, friction, and wear as well as mechanical properties including hardness [1–4]. Advances of micro-/nanoelectromechanical systems (MEMS/NEMS) technology in the past decade make understanding of scale effects in adhesion, friction, and wear especially important, since surface to volume ratio grows with miniaturization and surface phenomena dominate. Dimensions of MEMS/NEMS devices range from  $\approx 1$  mm to few nm.

Experimental studies of scale dependence of tribological phenomena have been conducted recently. AFM experiments provide data on nanoscale [5, 6, 7, 8, 9, 10] whereas microtriboapparatus [11, 12] and SFA [13] provide data on microscale. Experimental data indicate that wear mechanisms and wear rates are different at macro- and micro-/nanoscales [14, 15]. During sliding, the effect of operating conditions such as load and velocity on friction and wear are frequently manifestations of the effect of temperature rise on the variable under study. The overall interface temperature rise is a cumulative result of numerous flash temperature rises at individual asperity contacts. The temperature rise at each contact is expected to be scale dependent, since it depends on contact size, which is scale dependent.

Friction is a complex phenomenon, which involves asperity interactions involving adhesion and deformation (plowing) (Fig. 16.1). Adhesion and plastic deformation imply energy dissipation, which is responsible for friction. A contact between two bodies takes place on high asperities, and the real area of contact ( $A_r$ ) is a small fraction of the apparent area of contact [16]. During contact of two asperities, a lateral force may be required for asperities of a given slope to climb against each other. This mechanism is known as ratchet mechanism, and it also contributes to the friction. Wear and contaminant particles present at the interface, referred as the *third body*, also contribute to friction (Fig. 16.2a). In addition, during contact, even at low humidity, a meniscus is formed. Generally, any liquid that wets or has a small contact angle on surfaces will condense from vapor into cracks and pores on surfaces as bulk liquid and in the form of annular-shaped capillary condensate in the contact zone. Figure 16.2b shows a random rough surface in contact with a smooth surface with a continuous liquid film on the smooth surface. The presence of the liquid film of the condensate or preexisting film of the liquid can significantly increase the adhesion between the solid bodies [16]. The effect of meniscus is scale-dependent.

A quantitative theory of scale effects in friction should consider scale effect on physical properties relevant to these contributions. However, conventional theories of contact and friction lack characteristic length parameters, which would be responsible for scale effects. The linear elasticity and conventional plasticity theories are scale-invariant and do not include any material length scales. A strain gradient plasticity theory has been developed, for microscale deformations, by Fleck et al. [17], Nix and Gao [18] and Hutchinson [19]. Their theory predicts a

**Fig. 16.1** (a) A block diagram showing friction mechanisms and generation and propagation of dislocations during sliding, (b) a block diagram of rough contact models

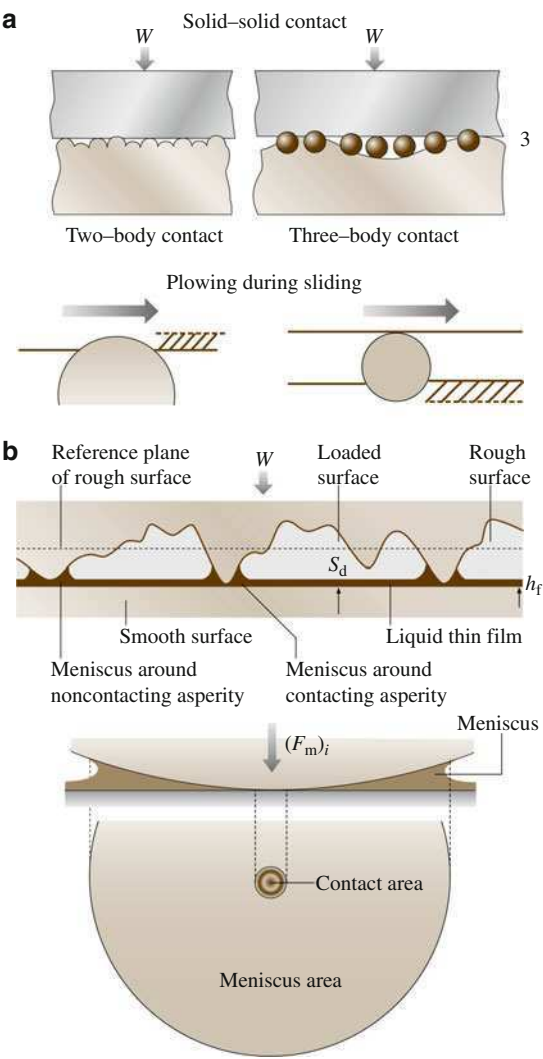


dependence of mechanical properties on the strain gradient, which is scale dependent: the smaller is the size of the deformed region, the greater is the gradient of plastic strain, and, the greater is the yield strength and hardness.

A comprehensive model of scale effect in friction including adhesion, two- and three-body deformations and the ratchet mechanism, has recently been proposed by Bhushan and Nosonovsky [20, 21, 22] and Nosonovsky and Bhushan [23]. The model for adhesional friction during single and multiple asperity contact was developed by Bhushan and Nosonovsky [20] and is based on the strain gradient plasticity and dislocation assisted sliding (gliding dislocations at the interface or microslip). The model for the two-body and three-body deformation was proposed by Bhushan and Nosonovsky [21] and for the ratchet mechanism by Nosonovsky and Bhushan [23]. The model has been extended for wet contacts, wear and interface temperature by Bhushan and Nosonovsky [22]. The detailed model is presented in this chapter.

The chapter is organized as follows. In the next section of this chapter, the scale effect in mechanical properties is considered, including yield strength

**Fig. 16.2** Schematics of (a) two-bodies and three-bodies during dry contact of rough surfaces, (b) formation of menisci during wet contact



and hardness based on the strain gradient plasticity and shear strength at the interface based on the dislocation assisted sliding (microslip). In the fourth section, scale effect in surface roughness and contact parameters is considered, including the real area of contact, number of contacts, and mean size of contact. Load dependence of contact parameters is also studied in this section. In the fifth section, scale effect in friction is considered, including adhesion, two- and three-body deformation, ratchet mechanism, meniscus analysis, total value of the coefficient of friction and comparison with the experimental data. In the sixth and seventh sections, scale effects in wear and interface temperature are analyzed, respectively.

### 16.3 Scale Effect in Mechanical Properties

In this section, scale dependence of hardness and shear strength at the interface is considered. A strain gradient plasticity theory has been developed, for microscale deformations, by Fleck et al. [17], Nix and Gao [18], Hutchinson [19], and others, which is based on statistically stored and geometrically necessary dislocations (to be described later). Their theory predicts a dependence of mechanical properties on the strain gradient, which is scale dependent: the smaller is the size of the deformed region, the greater is the gradient of plastic strain, and, the greater is the yield strength and hardness. Gao et al. [24] and Huang et al. [25] proposed a mechanism-based strain gradient (MSG) plasticity theory, which is based on a multiscale framework, linking the microscale (10–100 nm) notion of statistically stored and geometrically necessary dislocations to the mesoscale (1–10  $\mu\text{m}$ ) notion of plastic strain and strain gradient. Bazant [26] analyzed scale effect based on the MSG plasticity theory in the limit of small scale, and found that corresponding nominal stresses in geometrically similar structures of different sizes depend on the size according to a power exponent law.

It was recently suggested also, that relative motion of two contacting bodies during sliding takes place due to dislocation-assisted sliding (microslip), which results in scale-dependent shear strength at the interface [20]. Scale effects in mechanical properties (yield strength, hardness, and shear strength at the interface) based on the strain gradient plasticity and dislocation-assisted sliding models are considered in this section.

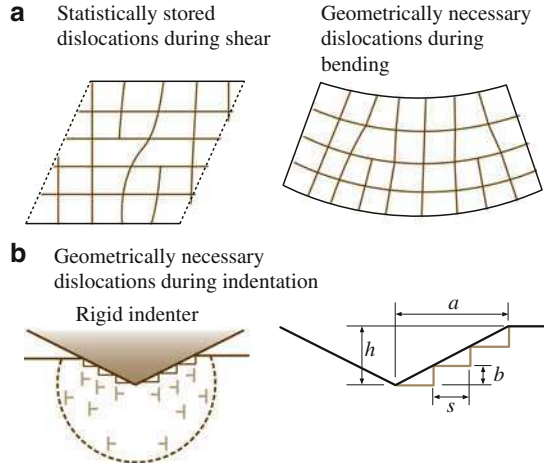
#### 16.3.1 Yield Strength and Hardness

Plastic deformation occurs during asperity contacts because a small real area of contact results in high contact stresses, which are often beyond the limits of the elasticity. As stated earlier, during loading, generation and propagation of dislocations is responsible for plastic deformation. Because dislocation motion is irreversible, plastic deformation provides a mechanism for energy dissipation during friction. The strain gradient plasticity theories [17, 18, 19] consider two types of dislocations: randomly created statistically stored dislocations (SSD) and geometrically necessary dislocations (GND). The GND are required for strain compatibility reasons. Randomly created SSD during shear and GND during bending are presented in Fig. 16.3a. The density of the GND (total length of dislocation lines per volume) during bending is proportional to the curvature  $\kappa$  and to the strain gradient

$$\rho_G = \frac{\kappa}{b} = \frac{1}{b} \frac{\partial \varepsilon}{\partial z} \propto \nabla \varepsilon, \quad (16.1)$$

where  $\varepsilon$  is strain,  $b$  is the Burgers vector, and  $\nabla \varepsilon$  is the strain gradient.

**Fig. 16.3** (a) Illustration of statistically stored dislocations during shear and geometrically necessary dislocations during bending, (b) geometrically necessary dislocations during indentation



The GND during indentation (Fig. 16.3b) are located in a certain sub-surface volume. The large strain gradients in small indentations require GND to account for the large slope at the indented surface. SSD, not shown here, also would be created and would contribute to deformation resistance, and are function of strain rather than strain gradient. According to Nix and Gao [18], we assume that indentation is accommodated by circular loops of GND with Burgers vector normal to the plane of the surface. If we think of the individual dislocation loops being spaced equally along the surface of the indentation, then the surface slope

$$\tan \theta_i = \frac{h}{a} = \frac{b}{s}, \quad (16.2)$$

where  $\theta_i$  is the angle between the surface of the conical indenter and the plane of the surface,  $a$  is the contact radius,  $h$  is the indentation depth,  $b$  is the Burgers vector, and  $s$  is the spacing between individual slip steps on the indentation surface (Fig. 16.3b). They reported that for geometrical (strain compatibility) considerations, the density of the GND is

$$\rho_G = \frac{3}{2bh} \tan^2 \theta_i = \frac{3}{2b} \left( \frac{\tan \theta_i}{a} \right) = \frac{3}{2b} \nabla \epsilon. \quad (16.3)$$

Thus  $\rho_G$  is proportional to strain gradient (scale dependent) whereas the density of SSD,  $\rho_S$  is dependent upon the average strain in the indentation, which is related to the slope of the indenter ( $\tan \theta_i$ ). Based on experimental observations,  $\rho_S$  is approximately proportional to strain [17].

According to the Taylor model of plasticity [30], dislocations are emitted from Frank–Read sources. Due to interaction with each other, the dislocations may become stuck in what is called the Taylor network, but when externally



applied stress reaches the order of Peierls stress for the dislocations, they start to move and the plastic yield is initiated. The magnitude of the Peierls stress  $\tau_p$  is proportional to the dislocation's Burgers vector  $b$  divided by a distance between dislocation lines  $s$  [27, 28]

$$\tau_p = Gb/(2\pi s), \quad (16.4)$$

where  $G$  is the elastic shear modulus. An approximate relation of the shear yield strength  $\tau_Y$  to the dislocations density at a moment when yield is initiated is given by [27]

$$\tau_{Y0} = cGb/s = cGb\sqrt{\rho}, \quad (16.5)$$

where  $c$  is a constant on the order of unity, specified by the crystal structure and  $\rho$  is the total length of dislocation lines per volume, which is a complicated function of strain  $\varepsilon$  and strain gradient  $(\nabla\varepsilon)$

$$\rho = \rho_S(\varepsilon) + \rho_G(\nabla\varepsilon). \quad (16.6)$$

The shear yield strength  $\tau_Y$  can be written now as a function of SSD and GND densities [30]

$$\tau_Y = cGb\sqrt{\rho_S + \rho_G} = \tau_{Y0}\sqrt{1 + (\rho_G/\rho_S)}, \quad (16.7)$$

where

$$\tau_{Y0} = cGb\sqrt{\rho_S} \quad (16.8)$$

is the shear yield strength value in the limit of small  $\rho_G/\rho_S$  ratio (large scale) that would arise from the SSD, in the absence of GND. Note that the ratio of the two densities is defined by the problem geometry and is scale dependent. Based on the relationships for  $\rho_G$  (16.3) and  $\rho_S$ , the ratio  $\rho_G/\rho_S$  is inversely proportional to  $a$  and (16.7) reduces to

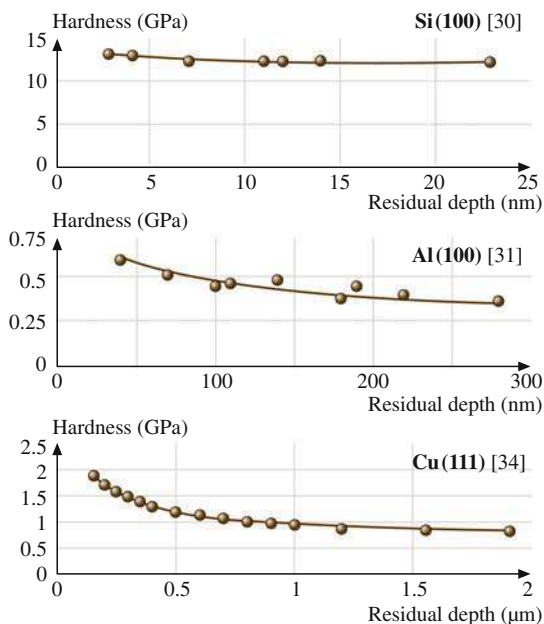
$$\tau_Y = \tau_{Y0}\sqrt{1 + (l_d/a)}, \quad (16.9)$$

where  $l_d$  is a plastic deformation length that characterizes depth dependence on shear yield strength. According to Hutchinson [19], this length is physically related to an average distance a dislocation travels, which was experimentally determined to be between 0.2 and 5  $\mu\text{m}$  for copper and nickel. Note that  $l_d$  is a function of the material and the asperity geometry and is dependent on SSD.

Using von Mises yield criterion, hardness  $H = 3\sqrt{3}\tau_Y$ . From (16.9) the hardness is also scale-dependent [18]

$$H = H_0\sqrt{1 + (l_d/a)}, \quad (16.10)$$

**Fig. 16.4** Indentation hardness as a function of residual indentation depth for Si(100) [30], Al(100) [31], Cu(111) [32]



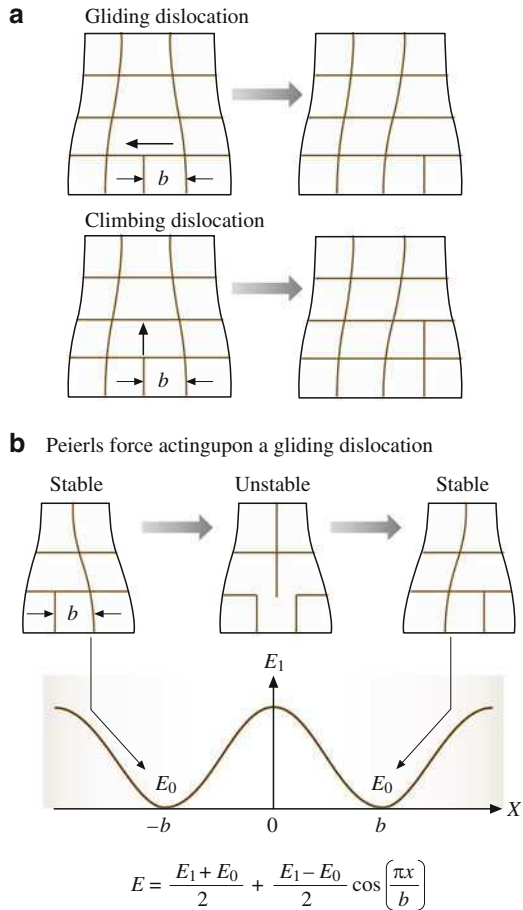
where  $H_0$  is hardness in absence of strain gradient. Equation (16.9) provides dependence of the resistance force to deformation upon the scale in a general case of plastic deformation [20].

Scale dependence of yield strength and hardness has been well established experimentally. Bhushan and Koinkar [29] and Bhushan et al. [30] measured hardness of single-crystal silicon(100) up to a peak load of 500  $\mu\text{N}$ . Kulkarni and Bhushan [31] measured hardness of single crystal aluminum(100) up to 2000  $\mu\text{N}$  and Nix and Gao [18] presented data for single crystal copper; using a three-sided pyramidal (Berkovich) diamond tip. The hardness on nanoscale is found to be higher than on microscale (Fig. 16.4). Similar results have been reported in other tests, including indentation tests for other materials [32, 33, 34], torsion and tension experiments on copper wires [17, 19], and bending experiments on silicon and silica beams [35].

### 16.3.2 Shear Strength at the Interface

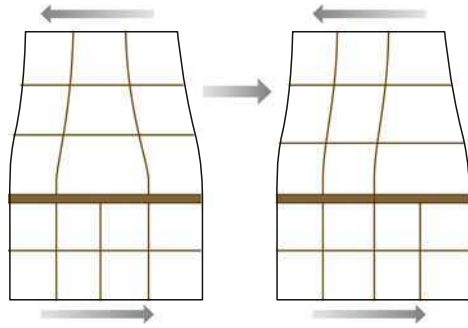
Mechanism of slip involves motion of large number of dislocations, which is responsible for plastic deformation during sliding. Dislocations are generated and stored in the body and propagate under load. There are two modes of possible line (or edge) dislocation motion: gliding, when dislocation moves in the direction of its Burgers vector  $b$  by a unit step of its magnitude, and climbing, when dislocation moves in a direction, perpendicular to its Burgers vector (Fig. 16.5a). Motion of

**Fig. 16.5** (a) Schematics of gliding and climbing dislocations motion by a unit step of Burgers vector  $b$ . (b) Origin of the periodic force acting upon a gliding dislocation (Peierls force). Gliding dislocation passes locations of high and low potential energy



dislocations can take place in the bulk of the body or at the interface. Due to periodicity of the lattice, a gliding dislocation experiences a periodic force, known as the Peierls force [31]. The Peierls force is responsible for keeping the dislocation at a central position between symmetric lattice lines and it opposes dislocation's gliding (Fig. 16.5b). Therefore, an external force should be applied to overcome Peierls force resistance against dislocation's motion. Weertman [36] showed that a dislocation or a group of dislocations can glide uniformly along an interface between two bodies of different elastic properties. In continuum elasticity formulation, this motion is equivalent to a propagating interface slip pulse, however the physical nature of this deformation is plastic, because dislocation motion is irreversible. The local plastic deformation can occur at the interface due to concentration of dislocations even in the predominantly elastic contacts. Gliding of a dislocation along the interface results in a relative displacement of the bodies for a distance equal to the Burgers vector of the dislocation, whereas a propagating set

**Fig. 16.6** Schematic showing microslip due to gliding dislocations at the interface



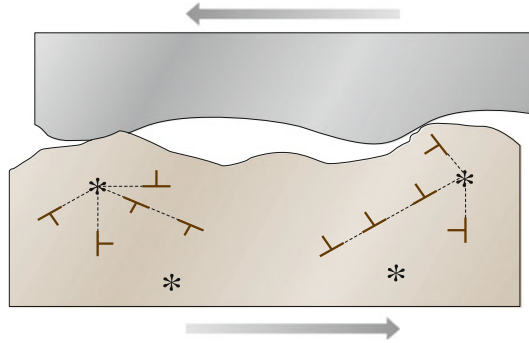
of dislocations effectively results in dislocation-assisted sliding, or microslip (Fig. 16.6).

Several types of microslip are known in the tribology literature [16], the dislocation-assisted sliding is one type of microslip, which propagates along the interface. Conventional mechanism of sliding is considered to be concurrent slip with simultaneous breaking of all adhesive bonds. Based on Johnson [37] and Bhushan and Nosonovsky [20], for contact sizes on the order of few nm to few  $\mu\text{m}$ , dislocation-assisted sliding is more energetically profitable than a concurrent slip. Their argument is based on the fact that experimental measurements with the SFA demonstrated that, for mica, frictional stress is of the same order as Peierls stress, which is required for gliding of dislocations.

Polonsky and Keer [38] considered the preexisting dislocation sources and carried out a numerical microcontact simulation based on contact plastic deformation representation in terms of discrete dislocations. They found that when the asperity size decreases and becomes comparable with the characteristic length of materials microstructure (distance between dislocation sources), resistance to plastic deformation increases, which supports conclusions drawn from strain gradient plasticity. Deshpande et al. [39] conducted discrete plasticity modeling of cracks in single crystals and considered dislocation nucleation from Frank–Read sources distributed randomly in the material. Pre-existing sources of dislocations, considered by all of these authors, are believed to be a more realistic reason for increasing number of dislocations during loading, rather than newly nucleated dislocations [30]. In general, dislocations are emitted under loads from preexisting sources and propagate along slip lines (Fig. 16.7). As shown in the figure, in regions of higher loads, number of emitted dislocations is higher. Their approach was limited to numerical analysis of special cases.

Bhushan and Nosonovsky [20] considered a sliding contact between two bodies. Slip along the contact interface is an important special case of plastic deformation. The local dislocation-assisted microslip can exist even if the contact is predominantly elastic due to concentration of dislocations at the interface. Due to these dislocations, the stress at which yield occurs at the interface is lower than shear yield strength in the bulk. This means that average shear strength at the interface is lower than in the bulk.

**Fig. 16.7** Generation of dislocations from sources (\*) during plowing due to plastic deformation



An assumption that all dislocations produced by externally applied forces are distributed randomly throughout the volume would result in vanishing small probability for a dislocation to be exactly at the interface. However, many traveling (gliding and climbing) dislocations will be stuck at the interface as soon as they reach it. As a result of this, a certain number of dislocations will be located at the interface. In order to account for a finite dislocation density at the interface, Bhushan and Nosonovsky [20] assumed, that the interface zone has a finite thickness  $D$ . Dislocations within the interface zone may reach the contact surface due to climbing and contribute into the microslip. In the case of a small contact radius  $a$ , compared to interface zone thickness  $D$ , which is scale dependent, and is approximately equal to  $a$ . However, in the case of a large contact radius, the interface zone thickness is approximately equal to the average distance dislocations can climb  $l_s$ . An illustration of this is provided in Fig. 16.8. The depth of the subsurface volume, from which dislocations have a high chance to reach the interface is limited by  $l_s$  and by  $a$ , respectively, for the two cases considered here. Based on these geometrical considerations, an approximate relation can be written as

$$D = \frac{al_s}{l_s + a}. \quad (16.11)$$

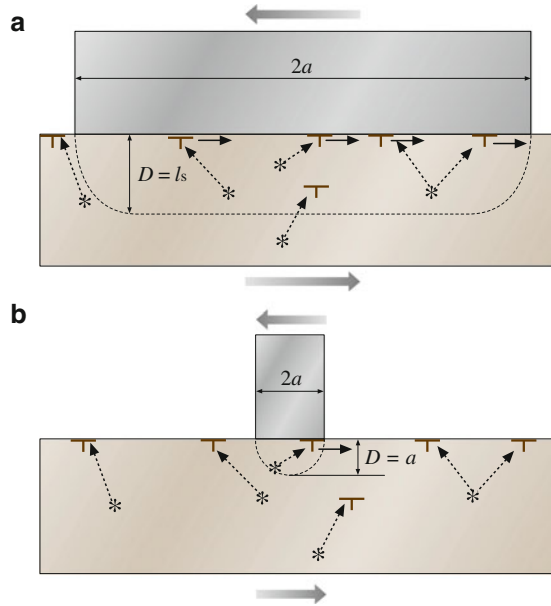
The interface density of dislocations (total length of dislocation lines per interface area) is related to the volume density as

$$\eta_{\text{int}} = \rho D = \rho \left( \frac{al_s}{l_s + a} \right). \quad (16.12)$$

During sliding, dislocations must be generated at the interface with a certain critical density  $\eta_{\text{int}} = \eta_{\text{cr}}$ . The corresponding shear strength during sliding can be written following (16.9) as

$$\tau_a = \tau_{a0} \sqrt{1 + (l_s/a)}, \quad (16.13)$$

**Fig. 16.8** Gliding dislocations at the interface generated from sources (\*). Only dislocations generated within the interface zone can reach the interface. **(a)** For a large contact radius  $a$ , thickness of this zone  $D$  is approximately equal to an average distance dislocations climb  $l_s$ . **(b)** For small contact radius  $a$ , the thickness of the interface zone is approximately equal to  $a$



where

$$\tau_{a0} = cGb\sqrt{\frac{\eta_{cr}}{l_s}} \quad (16.14)$$

is the shear strength during sliding in the limit of  $a \gg l_s$ .

Equation (16.13) gives scale-dependence of the shear strength at the interface and is based on the following assumptions. First, it is assumed that only dislocations in the interface zone of thickness  $D$ , given by (16.11), contribute into sliding. Second, it is assumed, that a critical density of dislocations at the interface  $\eta_{cr}$  is required for sliding. Third, the shear strength is equal to the Peierls stress, which is related to the volume density of the dislocations  $\rho = \eta/D$  according to (16.4), with the typical distance between dislocations  $s = 1/\sqrt{\rho}$ . It is noted, that proposed scaling rule for the dislocation assisted sliding mechanism (16.13) has a similar form to that for the yield strength (16.9), since both results are consequences of scale dependent generation and propagation of dislocations under load [20].

## 16.4 Scale Effect in Surface Roughness and Contact Parameters

During multiple-asperity contact, scale dependence of surface roughness is a factor which contributes to scale dependence of the real area of contact. Roughness parameters are known to be scale dependent [16], which results, during the contact

of two bodies, in scale dependence of the real area of contact, number of contacts and mean contact size. The contact parameters also depend on the normal load, and the load dependence is similar to the scale dependence [23]. Both effects are analyzed in this section.

### 16.4.1 Scale Dependence of Roughness and Contact Parameters

A random rough surface with Gaussian height distribution is characterized by the standard deviation of surface height  $\sigma$  and the correlation length  $\beta^*$  [16]. The correlation length is a measure of how quickly a random event decays and it is equal to the length, over which the autocorrelation function drops to a small fraction of the value at the origin. The correlation length can be considered as a distance, at which two points on a surface have just reached the condition where they can be regarded as being statistically independent. Thus,  $\sigma$  is a measure of height distribution and  $\beta^*$  is a measure of spatial distribution.

A surface is composed of a large number of length scales of roughness that are superimposed on each other. According to AFM measurements on glass-ceramic disk surface, both  $\sigma$  and  $\beta^*$  initially increase with the scan size and then approach a constant value, at certain scan size (Fig. 16.9). This result suggests that disk roughness has a long wavelength limit,  $L_{lwl}$ , which is equal to the scan size at which the roughness values approach a constant value [16]. It can be assumed that  $\sigma$  and  $\beta^*$  depend on the scan size according to an empirical power rule

$$\begin{aligned}\sigma &= \sigma_0 \left( \frac{L}{L_{lwl}} \right)^n, & L < L_{lwl}, \\ \beta^* &= \beta_0^* \left( \frac{L}{L_{lwl}} \right)^m, & L < L_{lwl},\end{aligned}\quad (16.15)$$

where  $n$  and  $m$  are indices of corresponding exponents and  $\sigma_0$  and  $\beta_0^*$  are macro-scale values [20]. Based on the data, presented in Fig. 16.9, it is noted that for

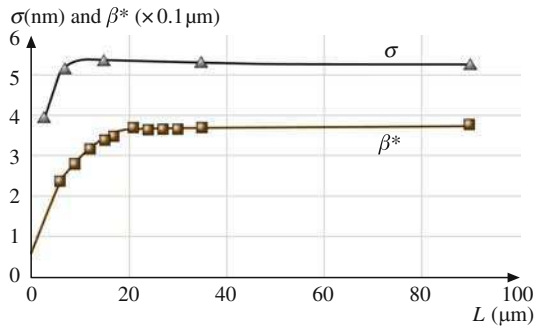


**Fig. 16.9** Roughness parameters as a function of scan size for a glass-ceramic disk measured using AFM [16]

glass-ceramic disk, long-wavelength limit for  $\sigma$  and  $\beta^*$  is  $\approx 17$  and  $23 \mu\text{m}$ , respectively. The difference is expected to be due to measurement errors. An average value  $L_{\text{lw}} = 20 \mu\text{m}$  is taken here for calculations. The values of the indices are found as  $m = 0.5$ ,  $n = 0.2$ , and the macroscale values are  $\sigma_0 = 5.3 \text{ nm}$ ,  $\beta_0^* = 0.37 \mu\text{m}$  [23].

For two random surfaces in contact, the length of the nominal contact size  $L$  defines the characteristic length scale of the problem. The contact problem can be simplified by considering a rough surface with composite roughness parameters in contact with a flat surface. The composite roughness parameters  $\sigma$  and  $\beta^*$  can be obtained based on individual values for the two surfaces [16]. For Gaussian surfaces, the contact parameters of interest, to be discussed later, are the real area of contact  $A_r$ , number of contacts  $N$ , and mean contact radius  $\bar{a}$ . The long wavelength limit for scale dependence of the contact parameters  $L_{\text{lc}}$ , which is not necessarily equal to that of the roughness  $L_{\text{lw}}$  will be used for normalization of length parameters. The scale dependence of the contact parameters exists if  $L < L_{\text{lc}}$  [23].

The mean of surface height distribution corresponds to so-called reference plane of the surface. Separation  $s_d$  is a distance between reference planes of two surfaces in contact, normalized by  $\sigma$ . For a given  $s_d$  and statistical distribution of surface heights, the total real area of contact ( $A_r$ ), number of contacts ( $N$ ), and elastic normal load  $W_e$  can be found, using statistical analysis of contacts. The real area of contact, number of contacts and elastic normal load are related to the separation distance  $s_d$  [40]

$$\begin{aligned} A_r &\propto F_A(s_d), \\ N &\propto \frac{1}{(\beta^*)^2} F_N(s_d), \\ W_e &\propto \frac{E^* \sigma}{\beta^*} F_W(s_d), \end{aligned} \quad (16.16)$$

where  $F_A(s_d)$ ,  $F_N(s_d)$ , and  $F_W(s_d)$ , are integral functions defined by *Onions* and *Archard* [40]. It should be noted, that  $A_r$  and  $N$  as functions of  $s_d$  are prescribed by the contact geometry ( $\sigma$ ,  $\beta^*$ ) and do not depend on whether the contact is elastic or plastic. Based on *Onions* and *Archard* data, it is observed that the ratio  $F_W/F_A$  is almost constant for moderate  $s_d < 1.4$  and increases slightly for  $s_d > 1.4$ . The ratio  $F_A/F_N$  decreases rapidly with  $s_d$  and becomes almost constant for  $s_d > 2.0$ . For moderate loads, the contact is expected to occur on the upper parts of the asperities ( $s_d > 2.0$ ), and a linear proportionality of  $F_A(s_d)$ ,  $F_N(s_d)$ , and  $F_W(s_d)$  can be assumed [20].

Based on (16.16) and the observation that  $F_W/F_A$  is almost constant, for moderate loads,  $A_{\text{re}}$  (the real area of elastic contact),  $N$ , and  $\bar{a}$  are related to the roughness, based on the parameter  $L_{\text{lc}}$ , as

$$A_{\text{re}} \propto \frac{\beta^*}{\sigma E^*} W = A_{\text{re}0} \left( \frac{L}{L_{\text{lc}}} \right)^{m-n}, \quad L < L_{\text{lc}}, \quad (16.17)$$



$$N \propto \frac{W}{\beta^* \sigma E^*} = N_0 \left( \frac{L}{L_{lc}} \right)^{-m-n}, \quad L < L_{lc}, \quad (16.18)$$

$$\bar{a} \propto \beta^* = \sqrt{\frac{A_r}{N}} = \bar{a}_0 \left( \frac{L}{L_{lc}} \right)^m, \quad L < L_{lc}. \quad (16.19)$$

The mean radius of summit tips  $\bar{R}_p$  is given, according to Whitehouse and Archard [41]

$$\bar{R}_p \propto \frac{(\beta^*)^2}{\sigma} = \bar{R}_{p0} \left( \frac{L}{L_{lw1}} \right)^{2m-n}, \quad L < L_{lw1}, \quad (16.20)$$

where  $\bar{a}_0$ ,  $N_0$  and  $\bar{R}_{p0}$  are macroscale values,  $E^*$  is the effective elastic modulus of contacting bodies [22], which is related to the elastic moduli  $E_1$ ,  $E_2$  and Poisson's ratios  $\nu_1$ ,  $\nu_2$  of the two bodies as  $1/E^* = (1 - \nu_1^2)/E_1 + (1 - \nu_2^2)/E_2$  and which is known to be scale independent, and variables with the subscript 0 are corresponding macroscale values (for  $L \geq L_{lc}$ ).

Dependence of the real area of plastic contact  $A_{rp}$  on the load is given by

$$A_{rp} = \frac{W}{H}, \quad (16.21)$$

where  $H$  is hardness. According to the strain gradient plasticity model [17, 18], the yield strength  $\tau_Y$  is given by (16.9) and hardness  $H$  is given by (16.10). In the case of plastic contact, the mean contact radius can be determined from (16.19), which is based on the contact geometry and independent of load [20]. Assuming the contact radius as its mean value from (16.19) based on elastic analysis, and combining (16.10), (16.19) and (16.21), the real area of plastic contact is given as

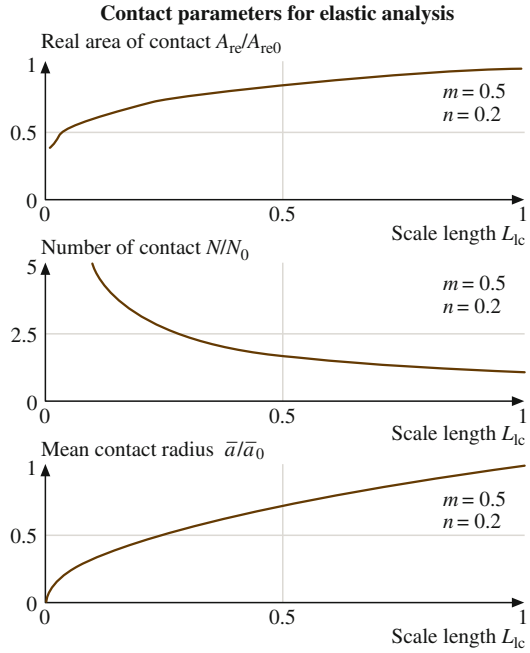
$$\begin{aligned} A_{rp} &= \frac{W}{H_0 \sqrt{1 + (l_d/\bar{a})}} \\ &= \frac{W}{H_0 \sqrt{1 + (L_d/L)^{\bar{m}}}}, \quad L < L_{lc}, \end{aligned} \quad (16.22)$$

where  $L_d$  is a characteristic length parameter related to  $l_d$ ,  $\bar{a}$ , and  $L_{lc}$  [20]

$$L_d = L_{lc} \left( \frac{l_d}{\bar{a}_0} \right)^{1/m}. \quad (16.23)$$

The scale dependence of  $A_{re}$ ,  $N$ , and  $\bar{a}$  is presented in Fig. 16.10.

**Fig. 16.10** Scale length dependence of normalized contact parameters ( $m = 0.5$ ,  $n = 0.2$ ) (a) real area of contact, (b) number of contacts, and (c) mean contact radius



### 16.4.2 Dependence of Contact Parameters on Load

The effect of short and long wavelength details of rough surfaces on contact parameters also depends on the normal load. For low loads, the ratio of real to apparent areas of contact  $A_r/A_a$ , is small, contact spots are small, and long wavelength details are irrelevant. For higher  $A_r/A_a$ , long wavelength details become important, whereas small wavelength details of the surface geometry become irrelevant. The effect of increased load is similar to the effect of increased scale length [23].

In the preceding subsections, it was assumed that the roughness parameters are scale-dependent for  $L < L_{lwl}$ , whereas the contact parameters are scale-dependent for  $L < L_{lc}$ . The upper limit of scale dependence for the contact parameters  $L_{lc}$  depends on the normal load, and it is reasonable to assume that  $L_{lc}$  is a function of  $A_r/A_a$ , and the contact parameters are scale-dependent when  $A_r/A_a$  is below a certain critical value. It is convenient to consider the apparent pressure  $p_a$ , which is equal to the normal load divided by the apparent area of contact [23].

For elastic contact, based on (16.15) and (16.17), this condition can be written as

$$\frac{A_{re}}{A_a} \propto \frac{\beta^* p_a}{\sigma} = p_a \frac{\beta_0^*}{\sigma_0} \left( \frac{L}{L_{lwl}} \right)^{m-n} < p_{ac}, \quad (16.24)$$

where  $p_{ac}$  is a critical apparent pressure, below which the scale dependence occurs [23]. From (16.24) one can find

$$L < L_{lwl} \left( \frac{\beta_0^* p_a}{\sigma_0 p_{ac}} \right)^{1/(n-m)}. \quad (16.25)$$

The right-hand expression in (16.24) is defined as  $L_{lc}$

$$L_{lc} = L_{lwl} \left( \frac{\beta_0^* p_a}{\sigma_0 p_{ac}} \right)^{1/(n-m)}. \quad (16.26)$$

For plastic contact, based on (16.22)

$$\frac{A_{rp}}{A_a} \propto \frac{p_a}{\sqrt{1 + (L_d/L)^m}} < p_{ac}. \quad (16.27)$$

In a similar manner to the elastic case, (16.27) yields [23]

$$L_{lc} = L_d \left[ \left( \frac{p_a}{p_{ac}} \right)^2 - 1 \right]^{-1/m}. \quad (16.28)$$

Load dependence of the long wavelength limit for contact parameters,  $L_{lc}$  is presented in Fig. 16.11 for an elastic contact based on (16.28), and for a plastic

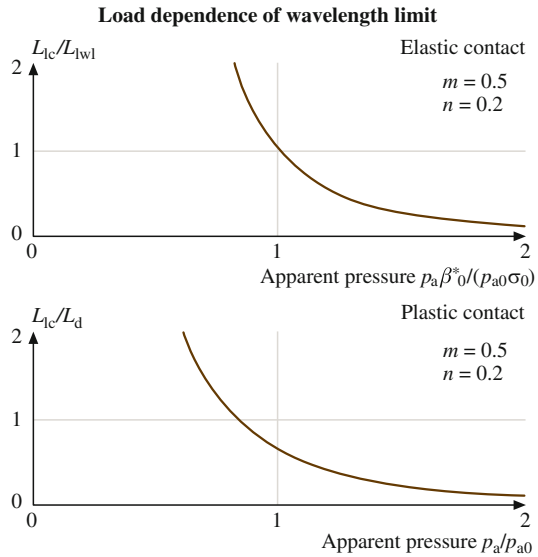


**Fig. 16.11** Dependence of the normalized long wavelength limit for contact parameters on load (normalized apparent pressure) for elastic and plastic contacts ( $m = 0.5$ ,  $n = 0.2$ )

contact based on (16.28), for  $m = 0.5$ ,  $n = 0.2$  [23]. The load (apparent pressure) is normalized by  $\beta_0^*/(p_{ac}\sigma_0)$  for the elastic contact and by  $p_{ac}$  for the plastic contact. In the case of elastic contact, it is observed, that the long wavelength limit decreases with increasing load. For a problem, characterized by a given scale length  $L$ , increase of load will result in decrease of  $L_{lc}$  and, eventually, the condition  $L < L_{lc}$  will be violated; thus the contact parameters, including the coefficient of friction, will reach the macroscale values. Decrease of  $L_{lc}$  with increasing load is also observed in the case of plastic contact, the data presented for  $p_a/p_{ac} > 1$ .

## 16.5 Scale Effect in Friction

According to the adhesion and deformation model of friction [16], the coefficient of dry friction  $\mu$  can be presented as a sum of adhesion component  $\mu_a$  and deformation (plowing) component  $\mu_d$ . The later, in the presence of particles, is a sum of asperity summits deformation component  $\mu_{ds}$  and particles deformation component  $\mu_{dp}$ , so that the total coefficient of friction is [21]

$$\mu = \mu_a + \mu_{ds} + \mu_{dp} = \frac{F_a + F_{ds} + F_{dp}}{W} = \frac{A_{ra}\tau_a + A_{ds}\tau_{ds} + A_{dp}\tau_{dp}}{W}, \quad (16.29)$$

where  $W$  is the normal load,  $F$  is the friction force,  $A_{ra}$ ,  $A_{ds}$ ,  $A_{dp}$  are the real areas of contact during adhesion, two body deformation and with particles, respectively, and  $\tau$  is the shear strength. The subscripts a, ds, and dp correspond to adhesion, summit deformation and particle deformation.

In the presence of meniscus, the friction force is given by

$$F = \mu(W + F_m), \quad (16.30)$$

where  $F_m$  is the meniscus force [16]. The coefficient of friction in the presence of the meniscus force,  $\mu_{wet}$ , is calculated using only the applied normal load, as normally measured in the experiments [22]

$$\begin{aligned} \mu_{wet} &= \mu \left( 1 + \frac{F_m}{W} \right) \\ &= \frac{A_{ra}\tau_a + A_{ds}\tau_{ds} + A_{dp}\tau_{dp}}{W} \left( 1 + \frac{F_m}{W} \right). \end{aligned} \quad (16.31)$$

Equation (16.31) shows that  $\mu_{wet} > \mu$ , because  $F_m$  is not taken into account for calculation of the normal load in the wet contact.

It was shown by Greenwood and Williamson [42] and by subsequent modifications of their model, that for contacting surfaces with common statistical distributions of asperity heights, the real area of contact is almost linearly proportional to the normal load. This linear dependence, along with (16.29), result in

linear dependence of the friction force on the normal load, or coefficient of friction being independent of the normal load. For a review of the numerical analysis of rough surface contacts, see Bhushan [43, 44] and Bhushan and Peng [45]. The statistical and numerical theories of contact involve roughness parameters – e.g. the standard deviation of asperity heights and the correlation length [16]. The roughness parameters are scale dependent. In contrast to this, the theory of self-similar (fractal) surfaces solid contact developed by Majumdar and Bhushan [46] does not include length parameters and are scale-invariant in principle. The shear strength of the contacts in (16.29) is also scale dependent. In addition to the adhesional contribution to friction, elastic and plastic deformation on nano- to macroscale contributes to friction [16]. The deformations are also scale dependent.

### 16.5.1 Adhesional Friction

The adhesional component of friction depends on the real area of contact and adhesion shear strength. Here we derive expressions for scale dependence of adhesional friction during single-asperity and multiple-asperity contacts.

#### Single-Asperity Contact

The scale length during single-asperity contact is the nominal contact length, which is equal to the contact diameter  $2a$ . In the case of predominantly elastic contacts, the real area of contact  $A_{re}$  depends on the load according to the Hertz analysis [47]

$$A_{re} = \pi a^2, \quad (16.32)$$

and

$$a = \left( \frac{3WR}{4E^*} \right)^{1/3}, \quad (16.33)$$

where  $R$  is effective radius of curvature of summit tips, and  $E^*$  is the effective elastic modulus of the two bodies. In the case of predominantly plastic contact, the real area of contact  $A_{rp}$  is given by (16.21), whereas the hardness is given by (16.10).

Combining (16.10), (16.13), (16.29), and (16.32), the adhesional component of the coefficient of friction can be determined for the predominantly elastic contact as

$$\mu_{ae} = \mu_{ae0} \sqrt{1 + (l_s/a)} \quad (16.34)$$

and for the predominantly plastic contact as

$$\mu_{ap} = \mu_{ap0} \sqrt{\frac{1 + (l_s/a)}{1 + (l_d/a)}}, \quad (16.35)$$

where  $\mu_{ae0}$  and  $\mu_{ap0}$  are corresponding values at the macroscale [20].

The scale dependence of adhesional friction in single-asperity contact is presented in Fig. 16.12a. In the case of single asperity elastic contact, the coefficient of friction increases with decreasing scale (contact diameter), because of an increase in the adhesion strength, according to (16.34). In the case of single asperity plastic

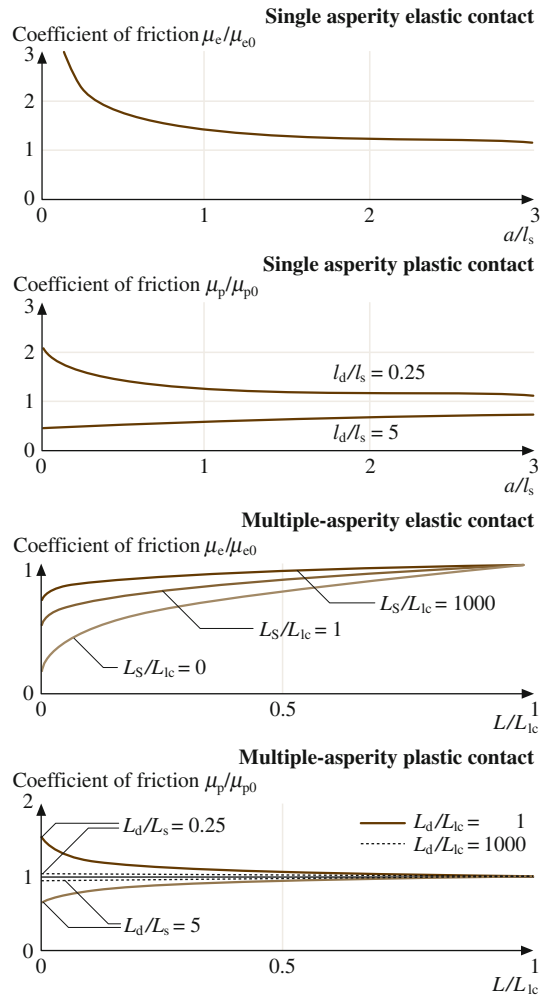


**Fig. 16.12** Normalized results for the adhesional component of the coefficient of friction, as a function of scale ( $a/l_s$  for single asperity contact and  $L/L_{lc}$  for multi-asperity contact). In the case of single asperity plastic contact, data are presented for two values of  $l_d/l_s$ . In the case of multi-asperity elastic contact, data are presented for three values of  $L_s/L_{lc}$ . For multi-asperity plastic contact, data are presented for two values of  $L_d/L_s$ .

contact, the coefficient of friction can increase or decrease with decreasing scale, because of an increased hardness or increase in adhesional strength. The competition of these two factors is governed by  $l_d/l_s$ , according to (16.35). There is no direct way to measure  $l_d$  and  $l_s$ . We will see later, from experimental data, that the coefficient of friction tends to decrease with decreasing scale, therefore, it must be assumed that  $l_d/l_s > 1$  for the data reported in the paper [20].

### Multiple-Asperity Contact

The adhesional component of friction depends on the real area of contact and adhesion shear strength. Scale dependence of the real area of contact was considered in the preceding section. Here we derive expressions for scale-dependence of the shear strength at the interface during adhesional friction. It is suggested by Bhushan and Nosonovsky [20] that, for many materials, dislocation-assisted sliding (microslip) is the main mechanism, which is responsible for the shear strength. They considered dislocation assisted sliding based on the assumption, that contributing dislocations are located in a subsurface volume. The thickness of this volume is limited by the distance which dislocations can climb  $l_s$  (material parameter) and by the radius of contact  $a$ . They showed that  $\tau_a$  is scale dependent according to (16.13). Assuming the contact radii equal to the mean value given by (16.19)

$$\tau_a = \tau_{a0} \sqrt{1 + (L_s/L)^m}, \quad L < L_{lc}, \quad (16.36)$$

where

$$L_s = L_{lc} \left( \frac{l_s}{\bar{a}_0} \right)^{1/m}. \quad (16.37)$$

In the case of absence of the microslip (e.g., for an amorphous material), it should be assumed in (16.34–16.36),  $L_s = l_s = 0$ .

Based on (16.9, 16.17, 16.24, 16.29, 16.36, 16.37), the adhesional component of the coefficient of friction in the case of elastic contact  $\mu_{ac}$  and in the case of plastic contact  $\mu_{ap}$ , is given as [20]

$$\begin{aligned} \mu_{ac} &= \frac{\tau_a A_{re}}{W} = \frac{\tau_{a0} A_{re0}}{W} \left( \frac{L}{L_{lc}} \right)^{m-n} \sqrt{1 + (L_s/L)^m} = \frac{\mu_{ac0}}{\sqrt{1 + (l_s/\bar{a}_0)}} \left( \frac{L}{L_{lc}} \right)^{m-n} \\ &\quad \times \sqrt{1 + (L_s/L)^m}, \quad L < L_{lc}; \end{aligned} \quad (16.38)$$

$$\mu_{ap} = \frac{\tau_{a0}}{H_0} \sqrt{\frac{1 + (L_s/L)^m}{1 + (L_d/L)^m}} = \mu_{ap0} \sqrt{\frac{1 + (l_d/\bar{a}_0)}{1 + (l_s/\bar{a}_0)}} \sqrt{\frac{1 + (L_s/L)^m}{1 + (L_d/L)^m}}, \quad L < L_{lc}, \quad (16.39)$$

where  $\mu_{ae0}$  and  $\mu_{ap0}$  are values of the coefficient of friction at macroscale ( $L \geq L_{lc}$ ).

The scale dependence of adhesional friction in multiple-asperity elastic contact is presented in Fig. 16.12b, which is based on (16.38), for various values of  $L_s/L_{lc}$ . The change of scale length  $L$  affects the coefficient of friction in two different ways: through the change of  $A_{re}$  (16.17) and  $\tau_a$  (16.36) below  $L_{lc}$ . Further,  $\tau_a$  is controlled by the ratio  $L_s/L$ . Based on (16.36), for small ratio of  $L_s/L_{lc}$ , scale effects on  $\tau_a$  is insignificant for  $L/L_{lc} > 0$ . As it is seen from Fig. 16.12b by comparison of the curve with  $L_s/L_{lc} = 0$  (insignificant scale effect on  $\tau_a$ ),  $L_s/L_{lc} = 1$ , and  $L_s/L_{lc} = 1000$  (significant scale effect on  $\tau_a$ ), the results for the normalized coefficient of friction are close, thus, the main contribution to the scaling effect is due to change of  $A_{re}$ . In the case of multiple-asperity plastic contact, the results, based on (16.39), are presented in Fig. 16.12b for  $L_d/L_s = 0.25$ ,  $L_d/L_s = 5$  and  $L_d/L_{lc} = 1$  and  $L_d/L_{lc} = 1,000$ . The change of scale affects the coefficient of friction through the change of  $A_{rp}$  (16.34), which is controlled by  $L_d$ , and  $\tau_a$  (16.36), which is controlled by  $L_s$ . It can be observed from Fig. 16.12b, that for  $L_d > L_s$ , the change of  $A_{rp}$  prevails over the change of  $\tau_a$ , with decreasing scale, and the coefficient of friction decreases. For  $L_d < L_s$ , the change of  $\tau_a$  prevails, with decreasing scale, and the coefficient of friction increases [20]. Expressions for the coefficient of adhesional friction are presented in Table 16.1.

## 16.5.2 Two-Body Deformation

Based on the assumption that multiple asperities of two rough surfaces in contact have conical shape, the two-body deformation component of friction can be determined as

$$\mu_{ds} = \frac{2 \tan \theta_r}{\pi}, \quad (16.40)$$

where  $\theta_r$  is the roughness angle (or attack angle) of a conical asperity [16, 48]. Mechanical properties affect the real area of contact and shear strength and these cancel out in (16.29).

The roughness angle is scale-dependent and is related to the roughness parameters [41]. Based on statistical analysis of a random Gaussian surface,

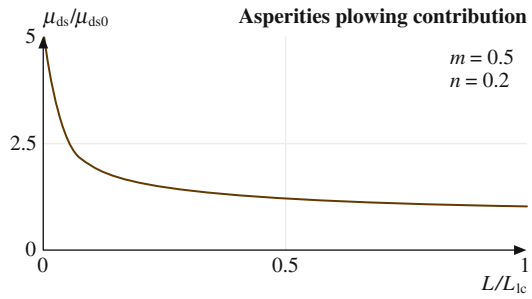
$$\tan \theta_r \propto \frac{\sigma}{\beta^*}. \quad (16.41)$$

**Table 16.1** Scaling factors for the coefficient of adhesional friction [20]

Single asperity elastic contact	Single asperity plastic contact	Multiple-asperity elastic contact	Multiple-asperity plastic contact
$\mu_e = \mu_{e0} \sqrt{1 + (l_s/a)}$	$\mu_e = \mu_{e0} \sqrt{\frac{1 + (l_s/a)}{1 + (l_d/a)}}$	$\mu_e = \mu_{e0} C_E L^{m-n}$ $\times \sqrt{1 + (L_s/L)^m}$	$\mu_p = \mu_{p0} C_P \sqrt{\frac{1 + (L_s/L)^m}{1 + (l_d/L)^m}}$



**Fig. 16.13** Normalized results for the two-body deformation component of the coefficient of friction



From (16.40) it can be interpreted that stretching the rough surface in the vertical direction (increasing vertical scale parameter  $\sigma$ ) increases  $\tan \theta_r$ , and stretching in the horizontal direction (increasing vertical scale parameter  $\beta^*$ ) decreases  $\tan \theta_r$ .

Using (16.40) and (16.41), the scale dependence of the two-body deformation component of the coefficient of friction is given as [21]

$$\mu_{ds} = \frac{2\sigma_0}{\pi\beta^*} \left( \frac{L}{L_{lc}} \right)^{n-m} = \mu_{ds0} \left( \frac{L}{L_{lc}} \right)^{n-m}, \quad L < L_{lc}, \quad (16.42)$$

where  $\mu_{ds0}$  is the value of the coefficient of summits deformation component of the coefficient of friction at macroscale ( $L \geq L_{lc}$ ).

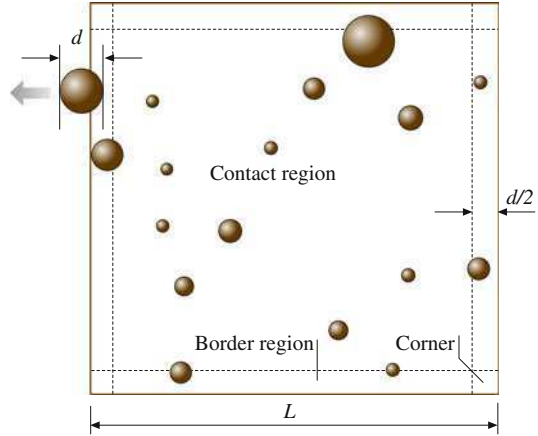
The scale dependence for the two-body deformation component of the coefficient of friction is presented in Fig. 16.13 for  $m = 0.5$ ,  $n = 0.2$ . The coefficient of friction increases with decreasing scale, according to (16.42). This effect is a consequence of increasing average slope or roughness angle.

### 16.5.3 Three-Body Deformation Friction

In this sections of the paper, size distribution of particles will be idealized according to the exponential, normal, and log normal density functions, since these distributions are the most common in nature and industrial applications (See Appendix). The probability for a particle of a given size to be trapped at the interface depends on the size of the contact region. Particles at the edge of the region of contact are likely to leave the contact area, whereas those in the middle are likely to be trapped. The ratio of the edge region area to the total apparent area of contact increases with decreasing scale size. Therefore, the probability for a particle to be trapped decreases, as well as the three-body component of the coefficient of friction [21].

Let us consider a square region of contact of two rough surfaces with a length  $L$  (relevant scale length), with the density of debris of  $\eta$  particles per unit area (Fig. 16.14). We assume that the particles have the spherical form and that  $p(d)$  is the probability density function of particles size. It is also assumed that, for

**Fig. 16.14** Schematics of debris at the contact zone and at its border region. A particle of diameter  $d$  in the border region of  $d/2$  is likely to leave the contact zone



a given diameter, particles at the border region of the contact zone of the width  $d/2$  are likely to leave the contact zone, with a certain probability  $\alpha$ , whereas particles at the center of the contact region are likely to be trapped. It should be noted, that particles in the corners of the contact region can leave in two different directions, therefore, for them the probability to leave is  $2\alpha$ . The total nominal contact area is equal to  $L^2$ , the area of the border region, without the corners, is equal to  $4(L - d)d/2$ , and the area of the corners is equal to  $d^2$ .

The probability density of size distribution for the trapped particles  $p_{tr}(d)$  can be calculated by multiplying  $p(d)$  by one minus the probability of a particle with diameter  $d$  to leave; the later is equal to the ratio of the border region area, multiplied by a corresponding probability of the particle to leave, divided by the total contact area [21]

$$p_{tr}(d) = p(d) \left( 1 - \frac{2\alpha(L - d)d + 2\alpha d^2}{L^2} \right) = p(d) \left( 1 - \frac{2\alpha d}{L} \right), \quad d < \frac{L}{2\alpha}. \quad (16.43)$$

The ratio of the number of trapped particles to the total number of particles, average radius of a trapped particle  $\bar{d}$ , and average square of trapped particles  $\overline{d^2}$ , as functions of  $L$ , can be calculated as

$$\begin{aligned} n_{tr} &= \frac{\int_0^{L/2} p_{tr}(d) dd}{\int_0^\infty p(d) dd} = \frac{\int_0^{L/2} p(d) \left( 1 - \frac{2\alpha d}{L} \right) dd}{\int_0^\infty p(d) dd}, \\ \bar{d} &= \frac{\int_0^{L/2} d p_{tr}(d) dd}{\int_0^{L/2} p_{tr}(d) dd}, \\ \overline{d^2} &= \frac{\int_0^{L/2} d^2 p_{tr}(d) dd}{\int_0^{L/2} p_{tr}(d) dd}. \end{aligned} \quad (16.44)$$

Let us assume an exponential distribution of particles' size (16.A7) with  $d_e = 0$ . Substituting (16.A7) into (16.44) and integrating yields for the ratio of trapped particles [21]

$$\begin{aligned} n_{tr} &= \frac{\int_0^{L/(2\alpha)} \frac{1}{\sigma_e} \exp\left(-\frac{d}{\sigma_e}\right) \left(1 - \frac{2\alpha d}{L}\right) dd}{\int_0^\infty \frac{1}{\sigma_e} \exp\left(-\frac{d}{\sigma_e}\right) dd} = \exp\left(-\frac{d}{\sigma_e}\right) \frac{\sigma_e - L/(2\alpha) + d}{L/(2\alpha)} \Big|_0^{L/(2\alpha)} \\ &= \frac{2\alpha\sigma_e}{L} \left[ \exp\left(-\frac{L}{2\alpha\sigma_e}\right) - 1 \right] + 1, \end{aligned} \quad (16.45)$$

whereas the mean diameter of the trapped particles is

$$\bar{d} = \frac{\int_0^{L/(2\alpha)} d \exp\left(-\frac{d}{\sigma_e}\right) \left(1 - \frac{2\alpha d}{L}\right) dd}{\int_0^{L/(2\alpha)} \exp\left(-\frac{d}{\sigma_e}\right) \left(1 - \frac{2\alpha d}{L}\right) dd} = \sigma_e \frac{\exp\left(-\frac{L}{2\alpha\sigma_e}\right) \left(1 + \frac{4\alpha\sigma_e}{L}\right) + 1 - \frac{4\alpha\sigma_e}{L}}{\frac{2\alpha\sigma_e}{L} \left[ \exp\left(-\frac{L}{2\alpha\sigma_e}\right) - 1 \right] + 1} \quad (16.46)$$

and the mean square radius of the trapped particles is

$$\begin{aligned} \overline{d^2} &= \frac{\int_0^{L/(2\alpha)} d^2 \exp\left(-\frac{d}{\sigma_e}\right) \left(1 - \frac{2\alpha d}{L}\right) dd}{\int_0^{L/(2\alpha)} \exp\left(-\frac{d}{\sigma_e}\right) \left(1 - \frac{2\alpha d}{L}\right) dd} \\ &= \sigma_e^2 \frac{\exp\left(-\frac{L}{2\alpha\sigma_e}\right) \left(\frac{L}{2\alpha\sigma_e} + 4 + \frac{12\alpha\sigma_e}{L}\right) + 2 - \frac{12\alpha\sigma_e}{L}}{\frac{2\alpha\sigma_e}{L} \left( \exp\left(-\frac{L}{2\alpha\sigma_e}\right) - 1 \right) + 1}. \end{aligned} \quad (16.47)$$

For the normal and log normal distributions, similar calculations can be conducted numerically.

The area, supported by particles can be found as the number of trapped particles  $\eta L^2 n_{tr}$  multiplied by average particle contact area

$$A_{dp} = \eta L^2 n_{tr} \frac{\pi \overline{d^2}}{4}, \quad (16.48)$$

where  $\overline{d^2}$  is mean square of particle diameter,  $\eta$  is particle density per apparent area of contact ( $L^2$ ) and  $n_{tr}$  is a number of trapped particles divided by the total number of particles [21].

The plowing deformation is plastic and, assuming that particles are harder than the bodies, the shear strength  $\tau_{dp}$  is equal to the shear yield strength of the softer body  $\tau_Y$  which is given by the (16.9) with  $a = \bar{d}/2$ . Combining (16.29) with (16.9) and (16.48)

$$\begin{aligned}\mu_{dp} &= \frac{A_{dp}\tau_{dp}}{W} = \eta \frac{L^2}{W} \frac{\pi \bar{d}^2}{4} n_{tr} \tau_{Y0} \sqrt{1 + 2l_d/\bar{d}} \\ &= \mu_{dp0} n_{tr} \frac{\bar{d}^2}{d_0^2} \frac{\sqrt{1 + 2l_d/\bar{d}}}{\sqrt{1 + 2l_d/d_0}},\end{aligned}\quad (16.49)$$

where  $\bar{d}$  is mean particle diameter,  $\bar{d}_0$  is the macroscale value of mean particle diameter, and  $\mu_{dp0}$  is macroscale ( $L \rightarrow \infty$ ,  $n_{tr} \rightarrow 1$ ) value of the third-body deformation component of the coefficient of friction given as

$$\mu_{dp0} = \eta \frac{L^2}{W} \frac{\pi \bar{d}_0^2}{4} \tau_{Y0} \sqrt{1 + 2l_d/\bar{d}_0}. \quad (16.50)$$

Scale dependence of the three-body deformation component of the coefficient of friction is presented in Fig. 16.15, based on (16.49). The number of trapped

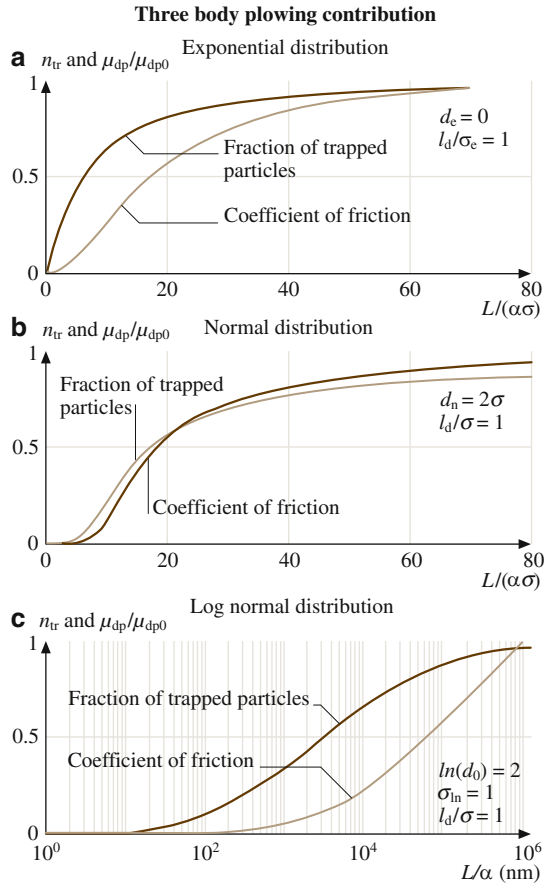


**Fig. 16.15** The number of trapped particles divided by the total number of particles and three-body deformation component of the coefficient of friction, normalized by the macroscale value, for three different distributions of debris size: (a) exponential, (b) normal, and (c) log-normal distributions

particles divided by the total number of particles, as well as the three-body deformation component of the coefficient of friction, are presented as a function of scale size divided by  $\alpha$  for the exponential, normal, and log normal distributions. The dependence of  $\mu_d/\mu_{d0}$  is shown as a function of  $L/(\alpha\sigma_e)$  for the exponential distribution and normal distribution, for  $d_n = d_e = 2\sigma_e$  and  $l_d/\sigma_e = 1$ , whereas for the log normal distribution the results are presented as a function of  $L/\alpha$ , for  $(\ln d_{ln}) = 2$ ,  $\sigma_{ln} = 1$ , and  $l_d/\sigma_{ln} = 1$ . This component of the coefficient of friction decreases for all of the three distributions. The results are shown for  $l_d/\sigma_{ln} = 1$ , however, variation of  $l_d/\sigma_{ln}$  in the range between 0.1 and 10 does not change significantly the shape of the curve. The decrease of the three-body deformation friction force with decreasing scale results with this component being small at the nanoscale.

#### 16.5.4 Ratchet Mechanism

Surface roughness can have an appreciable influence on friction during adhesion. If one of the contacting surfaces has asperities of much smaller lateral size, such that a small tip slides over an asperity, having the average angle  $\theta_r$  (so called ratchet mechanism), the corresponding component of the coefficient of friction is given by

$$\mu_r = \mu_a \tan^2 \theta_r, \quad (16.51)$$

where  $\mu_r$  is the ratchet mechanism component of friction [16]. Combining (16.15, 16.41, 16.38, 16.39) yields for the scale dependence of the ratchet component of the coefficient of friction in the case of elastic  $\mu_{re}$  and plastic contact  $\mu_{rp}$

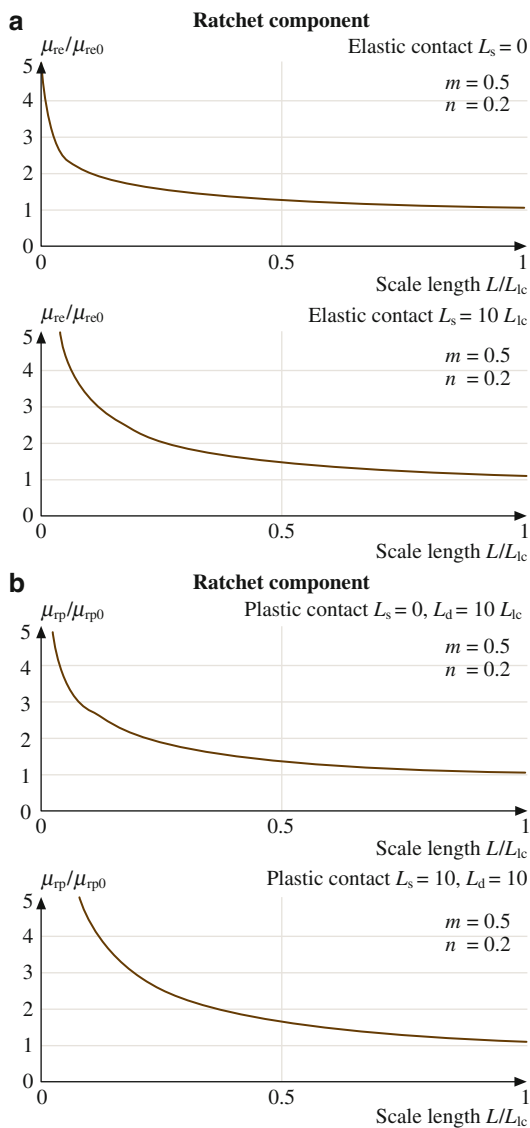
$$\begin{aligned} \mu_{re} &= \mu_{ae} \left[ \frac{2\sigma_0}{\pi\beta_0^*} \left( \frac{L}{L_{lc}} \right)^{n-m} \right]^2 = \frac{\mu_{re0}}{\sqrt{1 + (l_s/\bar{a}_0)}} \left( \frac{L}{L_{lc}} \right)^{n-m} \\ &\times \sqrt{1 + (L_s/L)^m}, \quad L < L_{lc}, \end{aligned} \quad (16.52)$$

$$\begin{aligned} \mu_{rp} &= \mu_{ap} \left[ \frac{2\sigma_0}{\pi\beta_0^*} \left( \frac{L}{L_{lc}} \right)^{n-m} \right]^2 = \mu_{rp0} \left( \frac{L}{L_{lc}} \right)^{2(n-m)} \sqrt{\frac{1 + (l_d/\bar{a}_0)}{1 + (l_s/\bar{a}_0)}} \\ &\times \sqrt{\frac{1 + (L_s/L)^m}{1 + (L_d/L)^m}}, \quad L < L_{lc}, \end{aligned} \quad (16.53)$$

where  $\mu_{re0}$  and  $\mu_{rp0}$  are the macroscale values of the ratchet component of the coefficient of friction for elastic and plastic contact correspondingly [23].

Scale dependence of the ratchet component of the coefficient of friction, normalized by the macroscale value, is presented in Fig. 16.16, for scale independent

**Fig. 16.16** Normalized results for the ratchet component of the coefficient of friction, as a function of scale, for scale independent ( $L_s = 0$ ) and scale dependent ( $L_s = 10L_{lc}$ ) shear strength ( $m = 0.5$ ,  $n = 0.2$ ). **(a)** contact, **(b)** plastic contact ( $L_d = 10L_{lc}$ )



adhesional shear strength,  $\tau_a = \text{const}$ , ( $L_s = 0$ ) and for scale dependent  $\tau_a$  ( $L_s = 10L_d$ ), based on (16.51) and (16.53). The ratchet component during adhesional elastic friction  $\mu_{re}$  is presented in Fig. 16.16a. It is observed, that, with decreasing scale,  $\mu_{re}$  increases. The ratchet component during adhesional plastic friction  $\mu_{rp}$  is presented in Fig. 16.16b. It is observed, that, for  $L_s = 0$ , with decreasing scale,  $\mu_{rp}$  increases [23].

### 16.5.5 Meniscus Analysis

During contact, if a liquid is introduced at the point of asperity contact, the surface tension results in a pressure difference across a meniscus surface, referred to as capillary pressure or Laplace pressure. The attractive force for a sphere in contact with a plane surface is proportional to the sphere radius  $R_p$ , for a sphere close to a surface with separation  $s$  or for a sphere close to a surface with continuous liquid film [16]

$$F_m \propto R_p. \quad (16.54)$$

The case of multiple-asperity contact is shown in Fig. 16.1b. Note, that both contacting and near-contacting asperities wetted by the liquid film contribute to the total meniscus force. A statistical approach can be used to model the contact. In general, given the interplanar separation  $s_d$ , the mean peak radius  $\bar{R}_p$ , the thickness of liquid film  $h_f$ , the surface tension  $\gamma$ , liquid contact angle between the liquid and surface  $\theta$ , and the total number of summits in the nominal contact area  $N$ ,

$$F_m = 2\pi\bar{R}_p\gamma(1 + \cos\theta)N. \quad (16.55)$$

In (16.54),  $\gamma$  and  $\theta$  are material properties, which are not expected to depend on scale, whereas  $\bar{R}_p$  and  $N$  depend on surface topography, and are scale-dependent, according to (16.18) and (16.20).

$$F_m \propto \bar{R}_p N = F_{m0} \left( \frac{L}{L_{lwl}} \right)^{m-2n}, \quad L < L_{lwl}, \quad (16.56)$$

where  $F_{m0}$  is the macroscale value of the meniscus force ( $L \geq L_{lwl}$ ).

Scale dependence of the meniscus force is presented in Fig. 16.17, based on (16.56) for  $m = 0.5$ ,  $n = 0.2$ . It may be observed that, depending on the value of  $D$ , the meniscus force may increase or decrease with decreasing scale size.

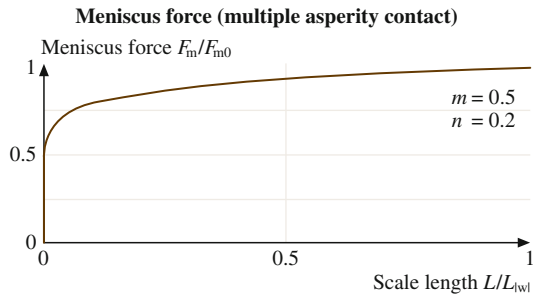


**Fig. 16.17** Meniscus force for  $m = 0.5$ ,  $n = 0.2$

### 16.5.6 Total Value of Coefficient of Friction and Transition from Elastic to Plastic Regime

During transition from elastic to plastic regime, contribution of each of the three components of the coefficient of friction in (16.29) changes. In the elastic regime, the dominant contribution is expected to be adhesion involving elastic deformation, and in the plastic regime the dominant contribution is expected to be deformation. Therefore, in order to study transition from elastic to plastic regime, the ratios of deformation to adhesion component should be considered. The expression for the total value of the coefficient of friction, which includes meniscus force contribution, based on (16.29) and (16.31) can be rewritten as [21]

$$\mu_{\text{wet}} = \mu_a \left( 1 + \frac{\mu_{\text{ds}}}{\mu_a} + \frac{\mu_{\text{dp}}}{\mu_a} \right) \left( 1 + \frac{F_m}{W} \right). \quad (16.57)$$

The ratchet mechanism component is ignored here since it is present only in special cases. Results in the preceding subsection provide us with data about the adhesion and two-body and three-body deformation components of the coefficient of friction, normalized by their values at the macroscale. However, that analysis does not provide any information about their relation to each other or about transition from the elastic to plastic regime. In order to analyze the transition from pure adhesion involving elastic deformation to plastic deformation, a transition index  $\phi$  can be considered [21]. The transition index is equal to the ratio of average pressure in the elastic regime (normal load per real area of elastic contact) to hardness or simply the ratio of the real area of plastic contact divided by the real area of elastic contact

$$\phi = \frac{W}{A_{\text{re}} H} = \frac{A_{\text{rp}}}{A_{\text{re}}}. \quad (16.58)$$

Using (16.17) and (16.22), the scale-dependence of  $\phi$  is

$$\phi = \frac{W}{A_{\text{re}0} (L/L_{\text{lc}})^{m-n} H_0 \sqrt{1 + (L_s/L)^m}} = \phi_0 \frac{\sqrt{1 + (l_s/\bar{a})(L/L_{\text{lc}})^{n-m}}}{\sqrt{1 + (L_s/L)^m}}, \quad L < L_{\text{lc}}, \quad (16.59)$$

where  $\phi_0$  is the macroscale value of the transition index [21].

With a low value of  $\phi$  close to zero, the contacts are mostly elastic and only adhesion contributes to the coefficient of friction involving elastic deformation. Whereas with increasing  $\phi$  approaching unity, the contacts become predominantly plastic and deformation becomes a dominant contributor. It can be argued that  $A_{\text{ds}}/A_{\text{re}}$  and  $A_{\text{dp}}/A_{\text{re}}$  will also be a direct function of  $\phi$ , and in the paper these will be assumed to have linear relationship.



Next, the ratio of adhesion and deformation components of the coefficient of friction in terms of  $\phi$  is obtained. In this relationship,  $\tau_{ds}$  and  $\tau_{dp}$  are equal to the shear yield strength, which is proportional to hardness and can be obtained from (16.9), using (16.19) and (16.36)

$$\frac{\mu_{ds}}{\mu_{ae}} = \frac{A_{ds}\tau_{ds}}{A_{re}\tau_a} \propto \phi \frac{\tau_{ds}}{\tau_a} = \phi \frac{\tau_{ds0}\sqrt{1+(L_d/L)^m}}{\tau_{a0}\sqrt{1+(L_s/L)^m}}, \quad L < L_{lc}, \quad (16.60)$$

$$\frac{\mu_{dp}}{\mu_{ae}} = \frac{A_{dp}\tau_{dp}}{A_{re}\tau_a} \propto \phi \frac{\tau_{dp}}{\tau_a} = \phi \frac{\tau_{Y0}\sqrt{1+2l_d/d}}{\tau_{a0}\sqrt{1+(L_s/L)^m}}, \quad L < L_{lc}, \quad (16.61)$$

The sum of adhesion and deformation components [21]

$$\begin{aligned} \mu_{wet} = \mu_{ae} & \left[ 1 + \phi \left( \frac{\tau_{ds0}\sqrt{1+(L_d/L)^m}}{\tau_{a0}\sqrt{1+(L_s/L)^m}} + \frac{\tau_{Y0}\sqrt{1+2l_d/d}}{\tau_{a0}\sqrt{1+(L_s/L)^m}} \right) \right] \\ & \times \left[ 1 + \frac{F_{m0}}{W} \left( \frac{L}{L_{lwl}} \right)^{m-2n} \right], \quad L < L_{lc}. \end{aligned} \quad (16.62)$$

Note that  $\phi$  itself is a complicated function of  $L$ , according to (16.59).

Scale dependence of the transition index, normalized by the macroscale value, is presented in Fig. 16.18, based on (16.59). It is observed that, for  $L_s = 0$ , the transition index decreases with increasing scale. For  $L_s = 10 L_{lc}$ , the same trend is observed for  $m > 2n$ , but, in the case  $m < 2n$ ,  $\phi$  decreases. An increase of the transition index means that the ratio of plastic to elastic real areas of contact increases. With decreasing scale, the mean radius of contact decreases, causing

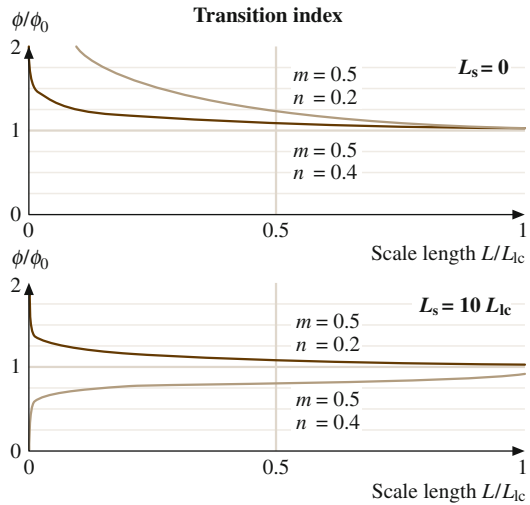
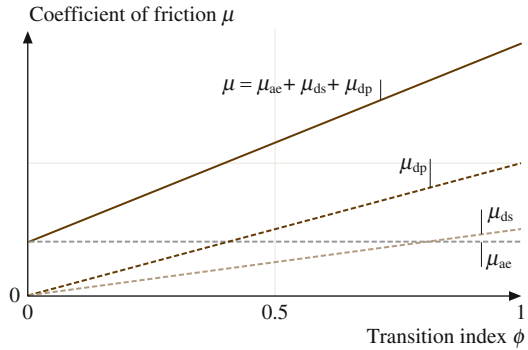


**Fig. 16.18** The transition index as a function of scale. Presented for  $m = 0.5$ ,  $n = 0.2$  and  $m = 0.5$ ,  $n = 0.4$

**Fig. 16.19** The coefficient of friction (dry contact) as a function of the transition index for given scale length  $L$ . With increasing  $\phi$  and onset of plastic deformation, both  $\mu_{ds}$  and  $\mu_{dp}$  grow, as a result of this, the total coefficient of friction  $\mu$  grows as well



hardness enhancement and decrease of the plastic area of contact. Based on this, the model may predict an increase or decrease of the transition index, depending on whether elastic or plastic area decreases faster.

The dependence of the coefficient of friction on  $\phi$  is illustrated in Fig. 16.19, based on (16.62). It is assumed in the figure that the slope for the dependence of  $\mu_{dp}$  on  $\phi$  is greater than the slope for the dependence of  $\mu_{ds}$  on  $\phi$ . For  $\phi$  close to zero, the contact is predominantly elastic, whereas for  $\phi$  approaching unity the contact is predominantly plastic.

### 16.5.7 Comparison with the Experimental Data

Experimental data on friction at micro- and nanoscale are presented in this subsection and compared with the model. First, a single-asperity predominantly elastic contact is considered [20], then transition to plastic deformation involving multiple asperity contacts is analyzed [23].

#### Single-Asperity Predominantly-Elastic Contact

Nanoscale dependence of friction force upon the normal load was studied for Pt-coated AFM tip versus mica in ultra-high vacuum (UHV) by Carpick et al. [7], for Si tip versus diamond and amorphous carbon by Schwarz et al. [8] and for  $\text{Si}_3\text{N}_4$  tip on Si,  $\text{SiO}_2$ , and diamond by Bhushan and Kulkarni [6] (Fig. 16.20a). Homola et al. [13] conducted SFA experiments with mica rolls with a single contact zone (before onset of wear) (Fig. 16.21b). Contacts relevant in these experiments can be considered as single-asperity, predominantly elastic in all of these cases. For a single-asperity elastic contact of radius  $a$ , expression for  $\mu$  is given by (16.17). For the limit of a small contact radius  $a \ll l_s$ , the (16.13) combined with the Hertzian dependence of the contact area upon the normal load (16.33) yields

$$F_e \approx \pi a^2 \tau_0 \sqrt{l_s/a}^{3/2} \propto W^{1/2}. \quad (16.63)$$

**Fig. 16.20** Summary of (a) AFM data (*upper*: Pt-coated tip on mica in UHV [7], *middle*: Si tip on DLC and diamond in UHV [8], *lower*: Si<sub>3</sub>N<sub>4</sub> tip on various materials [6]) and (b) SFA data (on mica versus mica in dry air [13]) for friction force as a function of normal load

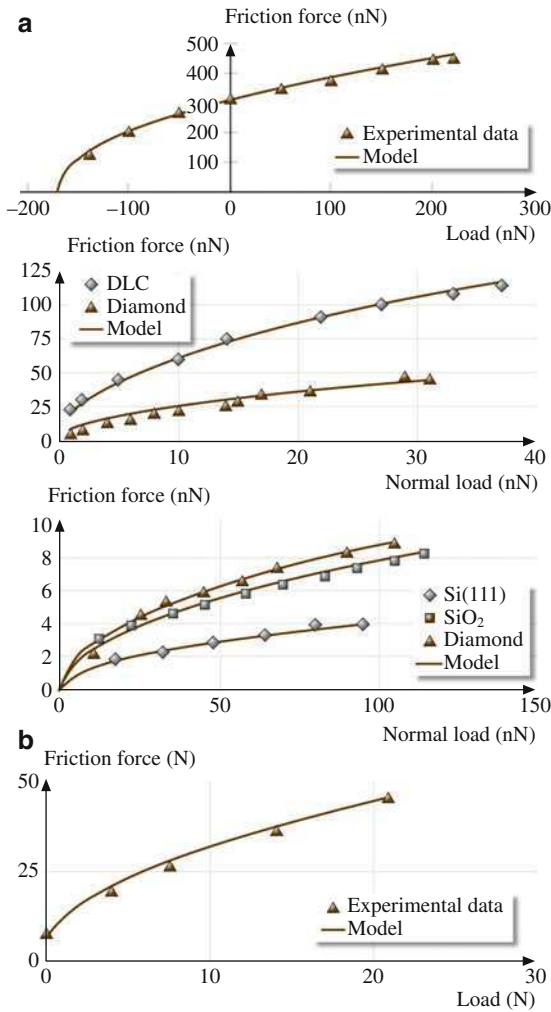
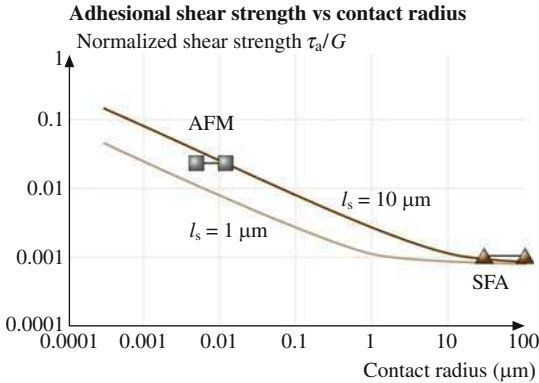


**Fig. 16.21** Shear stress as a function of contact radius. Microscale and nanoscale data compared with the model for  $l_s = 1 \mu\text{m}$  and  $l_s = 10 \mu\text{m}$



If an adhesive pull-off force  $W_0$  is large, (16.63) can be modified as

$$F_e = C_0 \sqrt{W + W_0}, \quad (16.64)$$

where  $C_0$  is a constant. Friction force increases with square root of the normal load, opposed to the two third exponent in scale independent analysis.

The results in Fig. 16.20 demonstrate a reasonable agreement of the experimental data with the model. The platinum-coated tip versus mica [7] has a relatively high pull-off force and the data fit with  $C_0 = 23.7 \text{ (nN)}^{1/2}$  and  $W_0 = 170 \text{ nN}$ . For the silicon tip versus amorphous carbon and natural diamond, the fit is given by  $C_0 = 8.0, 19.3 \text{ (nN)}^{1/2}$  and small  $W_0$ . For the virgin Si(111), SiO<sub>2</sub>, and natural diamond sliding versus Si<sub>3</sub>N<sub>4</sub> tip [8], the fit is given by  $C_0 = 0.40, 0.76, 0.86 \text{ (nN)}^{1/2}$  for Si(111), SiO<sub>2</sub>, and diamond, respectively and small  $W_0$ . For two mica rolls [13], the fit is given by  $C_0 = 10 \text{ N}^{1/2}$  and  $W_0 = 0.5 \text{ N}$  [20].

AFM experiments provide data on nanoscale, whereas SFA experiments provide data on microscale. Next we study scale dependence on the shear strength based on these data. In the AFM measurements by Carpick et al. [7], the average shear strength during sliding for Pt–mica interface was reported as 0.86 GPa, whereas the pull-off contact radius was reported as 7 nm. In the SFA measurements by Homola et al. [13], the average shear strength during sliding for mica–mica interface was reported as 25 MPa, whereas the contact area during high loads was on the order of  $10^{-8} \text{ m}^2$ , which corresponds to a contact radius on the order 100  $\mu\text{m}$ . To normalize shear strength, we need shear modulus. The shear modulus for mica is  $G_{\text{mica}} = 25.7 \text{ GPa}$  [49] and for Pt is  $G_{\text{Pt}} = 63.7 \text{ GPa}$  [50]. For mica–Pt interface, the effective shear modulus is

$$G = 2G_{\text{mica}}G_{\text{Pt}}/(G_{\text{mica}} + G_{\text{Pt}}) = 36.6. \quad (16.65)$$

This yields the value of the shear stress normalized by the shear modulus  $\tau_a/G = 2.35 \times 10^{-2}$  for Carpick et al. [7] AFM data and  $9.73 \times 10^{-4}$  for the SFA data. These values are presented in the Fig. 16.21 together with the values predicted by the model for assumed values of  $l_s = 1$  and 10  $\mu\text{m}$ . It can be seen that the model (16.13) provides an explanation of adhesional shear strength increase with a scale decrease [20].

### Transition to Predominantly Plastic Deformation Involving Multiple Asperity Contacts

Next, we analyze the effect of transition from predominantly elastic adhesion to predominantly plastic deformation involving multiple asperity contacts [23]. The data on nano- and microscale friction for various materials, are presented in Table 16.2, based on Ruan and Bhushan [5], Liu and Bhushan [11], and Bhushan et al. [12], for Si(100), graphite (HOPG), natural diamond, and diamond-like

**Table 16.2** Micro- and nanoscale values of the coefficient of friction, typical physical properties of specimens, and calculated apparent contact radii and apparent contact pressures at loads used in micro- and nanoscale measurements. For calculation purposes it is assumed that contacts on micro- and nanoscale are single-asperity elastic contacts [23]

Specimen	Coefficient of friction		Elastic modulus (GPa)	Poisson's ratio	Hardness (GPa)	Apparent contact radius at test load for		Mean apparent pressure at test load for	
	Nanoscale					Microscale (μm)	Nanoscale (nm)	Microscale (GPa)	Nanoscale (GPa)
	Microscale	Nanoscale							
Si(100) wafer	0.47 <sup>a</sup>	0.06 <sup>b</sup>	130 <sup>c,d</sup>	0.28 <sup>d</sup>	9–10 <sup>c,d</sup>	0.8–2.2	1.6–3.4	0.05–0.13 <sup>a</sup>	1.3–2.8 <sup>b</sup>
Graphite (HOPG)	0.1 <sup>e</sup>	0.006 <sup>b</sup>	9–15 <sup>f</sup> (9)	– (0.25)	0.01 <sup>g</sup>	62	3.4–7.4	0.082 <sup>e</sup>	0.27–0.58 <sup>b</sup>
Natural diamond	0.2 <sup>e</sup>	0.05 <sup>b</sup>	1140 <sup>h</sup>	0.07 <sup>h</sup>	80–104 <sup>f,h</sup>	21	1.1–2.5	0.74 <sup>e</sup>	2.5–5.3 <sup>b</sup>
DLC film	0.19 <sup>a</sup>	0.03 <sup>i</sup>	280 <sup>j</sup>	0.25 <sup>j</sup>	20–30 <sup>j</sup>	0.7–2.0	1.3–2.9	0.06–0.16 <sup>a</sup>	1.8–3.8 <sup>i</sup>

<sup>a</sup>500  $\mu\text{m}$  radius Si(100) ball at 100–2,000  $\mu\text{N}$  and 720  $\mu\text{m/s}$  in dry air [12]

<sup>b</sup>50 nm radius Si<sub>3</sub>N<sub>4</sub> tip at load range from 10–100 nN and 0.5 nm/s, in dry air [5]

<sup>c</sup>[51]

<sup>d</sup>[52]

<sup>e</sup>3 mm radius Si<sub>3</sub>N<sub>4</sub> ball (elastic modulus 310 GPa, Poisson's ratio 0.22 [50]), at 1 N and 800  $\mu\text{m/s}$  [5]

<sup>f</sup>[50]

<sup>g</sup>[55]

<sup>h</sup>[53]

<sup>i</sup>50 nm radius Si<sub>3</sub>N<sub>4</sub> tip at load range from 10–100 nN in dry air [12]

<sup>j</sup>[54]

carbon (DLC). There are several factors responsible for the differences in the coefficients of friction at micro- and nanoscale. Among them are the contributions from ratchet mechanism, meniscus effect, wear and contamination particles, and transition from elasticity to plasticity. The ratchet mechanism and meniscus effect result in an increase of friction with decreasing scale and cannot explain the decrease of friction found in the experiments. The contribution of wear and contamination particles is more significant at macro/microscale because of larger number of trapped particles (Fig. 16.15). It can be argued, that for the nanoscale AFM experiments the contacts are predominantly elastic and adhesion is the main contribution to the friction, whereas for the microscale experiments the contacts are predominantly plastic and deformation is an important factor. Therefore, transition from elastic contacts in nanoscale contacts to plastic deformation in microscale contacts is an important effect [23].

According to (16.29), the friction force depends on the shear strength and a relevant real area of contact. For calculation of contact radii and contact pressures, the elastic modulus, Poisson's ratio, and hardness for various samples, are required and presented in Table 16.2 [50, 51, 52, 53, 54, 55]. In the nanoscale AFM experiments a sharp tip was slid against a flat sample. The apparent contact size and mean contact pressures are calculated based on the assumption, that the contacts are single asperity, elastic contacts (contact pressures are small compared to hardness). Based on the Hertz equation [47], for spherical asperity of radius  $R$  in contact with a flat surface, with an effective elastic modulus  $E^*$ , under normal load  $W$ , the contact radius  $a$  and mean apparent contact pressure  $p_a$  are given by

$$a = \left( \frac{3WR}{4E^*} \right)^{1/3}, \quad (16.66)$$

$$p_a = \frac{W}{\pi a^2}. \quad (16.67)$$

The surface energy effect [16] was neglected in (16.66) and (16.67), because the experimental value of the normal adhesion force was small, compared to  $W$  [5]. The calculated values of  $a$  and  $p_a$  for the relevant normal load are presented in Table 16.2 [23].

In the microscale experiments, a ball was slid against a nominally flat surface. The contact in this case is multiple-asperity contact due to the roughness, and the contact pressure of the asperity contacts is higher than the apparent pressure. For calculation of a characteristic scale length for the multiple asperity contacts, which is equal to the apparent length of contact, (16.66) was also used. Apparent radius and mean apparent contact pressure for microscale contacts at relevant load ranges are also presented in Table 16.2 [23].

A quantitative estimate of the effect of the shear strength and the real area of contact on friction is presented in Table 16.3. The friction force at mean load (average of maximum and minimum loads) is shown, based on the experimental data presented in Table 16.2. For microscale data, the real area of contact was

**Table 16.3** Mean friction force, the real area of contact and lower limit of shear strength [23]

Specimen	Friction force at mean load <sup>a</sup>		Upper limit of real area of contact at mean load		Lower limit of mean shear strength (GPa)	
	Microscale (mN)	Nanoscale (nN)	Microscale <sup>b</sup> (μm <sup>2</sup> )	Nanoscale <sup>c</sup> (nm <sup>2</sup> )	Microscale <sup>d</sup>	Nanoscale <sup>d</sup>
Si(100) wafer	0.49	3.3	0.11	19	4.5	0.17
Graphite (HOPG)	100	0.33	10 <sup>5</sup>	92	0.001	0.004
Natural diamond	200	2.7	10.9	10	18.4	0.27
DLC film	0.2	1.7	0.042	14	4.8	0.12

<sup>a</sup>Based on the data from Table 16.2. Mean load at microscale is 1050 μN for Si(100) and DLC film and 1 N for HOPG and natural diamond, and 55 nN for all samples at nanoscale

<sup>b</sup>For plastic contact, based on hardness values from Table 16.2. Scale-dependent hardness value will be higher at relevant scale, presented values of the real area of contact are an upper estimate

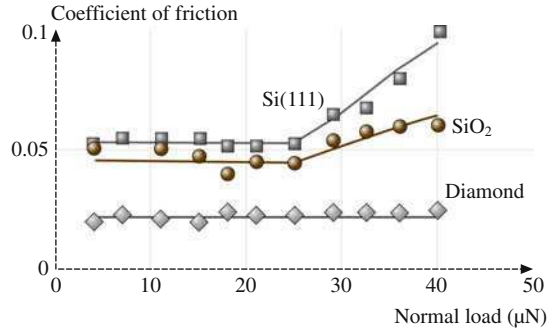
<sup>c</sup>Upper limit for the real area is given by the apparent area of contact calculated based on the radius of contact data from Table 16.2

<sup>d</sup>Lower limit for the mean shear strength is obtained by dividing the friction force by the upper limit of the real area of contact

estimated based on the assumption that the contacts are plastic and based on (16.33) for mean loads given in Table 16.2. For nanoscale data, the apparent area of contact was on the order of several square nanometers, and it was assumed that the real area of contact is comparable with the mean apparent area of contact, which can be calculated for the mean apparent contact radius, given in Table 16.2. The estimate provides with the upper limit of the real area of contact. The lower limit of the shear strength is calculated as friction force, divided by the upper limit of the real area of contact, and presented in Table 16.3 [23]. Based on the data in Table 16.3, for Si (100), natural diamond and DLC film, the microscale value of shear strength is about two orders of magnitude higher, than the nanoscale value, which indicates, that transition from adhesion to deformation mechanism of friction and the third-body effect are responsible for an increase of friction at microscale. For graphite, this effect is less pronounced due to molecularly smooth structure of the graphite surface [23].

Based on data available in the literature [6], load dependence of friction at nano-/microscale as a function of normal load is presented in Fig. 16.22. Coefficient of friction was measured for Si<sub>3</sub>N<sub>4</sub> tip versus Si, SiO<sub>2</sub>, and natural diamond using an AFM. They reported that for low loads the coefficient of friction is independent of load and increases with increasing load after a certain load. It is noted that the critical value of loads for Si and SiO<sub>2</sub> corresponds to stresses equal to their hardness values, which suggests that transition to plasticity plays a role in this effect. The friction values at higher loads for Si and SiO<sub>2</sub> approach to that of macroscale values. This result is consistent with predictions of the model for plastic contact (Fig. 16.11), which states that, with increasing normal load, the long wavelength limit for the contact parameters decreases. This decrease results in violation of the condition  $L < L_{lc}$ , and the contact parameters and the coefficient of friction reach

**Fig. 16.22** Coefficient of friction as a function of normal load [6]



the macroscale values, as was discussed earlier. It must be noted, that the values of  $m = 0.5$  and  $n = 0.2$  are taken based on available data for the glass-ceramic disk (Fig. 16.9), these parameters depend on material and on surface preparation and may be different for Si, SiO<sub>2</sub>, and natural diamond, however, no experimental data on scale dependence of roughness parameters for the materials of interest are available.

## 16.6 Scale Effect in Wear

The amount of wear during adhesive or abrasive wear involving plastic deformation is proportional to the load and sliding distance  $x$ , divided by hardness [16]

$$v = k_0 \frac{W_x}{H}, \quad (16.68)$$

where  $v$  is volume of worn material and  $k_0$  is a nondimensional wear coefficient. Using (16.10) and (16.19), the relationships can be obtained for scale dependence of the coefficient of wear in the case of the fractal surface and power-law dependence of roughness parameters

$$v = k \frac{W_x}{H_0} \quad (16.69)$$

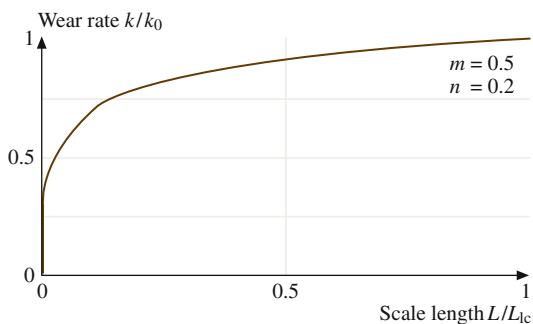
and

$$k = \frac{k_0}{\sqrt{1 + (l_d/\bar{a})}} = \frac{k_0}{\sqrt{1 + (L_d/L)^m}}, \quad L < L_{lw1}, \quad (16.70)$$

where  $k$  is scale-dependent wear coefficient, and  $k_0$  corresponds to the macroscale limit of the value of  $k$  [22].



**Fig. 16.23** The wear coefficient as a function of scale, presented for  $m = 0.5$ ,  $n = 0.2$



Scale dependence of the wear coefficient is presented in Fig. 16.23 for  $m = 0.5$  and  $n = 0.2$ , based on (16.70). It is observed, that the wear coefficient decreases with decreasing scale; this is due to the fact that the hardness increases with decreasing mean contact size.

## 16.7 Scale Effect in Interface Temperature

Frictional sliding is a dissipative process, and frictional energy is dissipated as heat over asperity contacts. Therefore, a high amount of heat per unit area is generated during sliding. A contact is formed and destroyed as one asperity passes the other at a given velocity. When an asperity comes into contact with another asperity, the real area of contact starts to grow, when the asperities are directly above each other, the area is at maximum, as they move away from each other, the area starts to get smaller. There are number of contacts at a given time during sliding. For each individual asperity contact, a flash temperature rise can be calculated. High temperature rise affects mechanical and physical properties of contacting bodies.

For thermal analysis, a dimensionless Peclet number is used

$$L_p = \frac{6Va_{\max}}{16\kappa_t}, \quad (16.71)$$

where  $V$  is sliding velocity,  $a_{\max}$  is maximum radius of contact for a given contact spot, and  $\kappa_t$  is thermal diffusivity. This parameter indicates whether the sliding is high-speed or low-speed. If  $L_p > 10$ , the contact falls into the category of high speed; if  $L_p < 0.5$ , it falls into the category of low speed; if  $0.5 \leq L_p \leq 10$ , a transition regime should be considered [16]. For high  $L_p$ , there is not enough time for the heat to flow to the sides during the lifetime of the contact and the heat flows only in the direction, perpendicular to the sliding surface. Based on the numerical calculations for flash temperature rise of as asperity contact for adhesional contact [16], the following relation holds for the maximum temperature rise  $T$ , normalized by the rate at which heat is generated  $q$ , divided by the volumetric specific heat  $\rho c_p$

$$\begin{aligned}\frac{T\rho c_p V}{q} &= 0.95 \left( \frac{2Va_{\max}}{\kappa_t} \right)^{1/2}, & L_p > 10 \\ &= 0.33 \left( \frac{2Va_{\max}}{\kappa_t} \right), & L_p < 0.5.\end{aligned}\quad (16.72)$$

The rate at which heat generated per time per unit area depends on the coefficient of friction  $\mu$ , sliding velocity  $V$ , apparent normal pressure  $p_a$ , and ratio of the apparent to real areas of contact ( $A_a/A_r$ )

$$q = \mu p_a V \frac{A_a}{A_r}. \quad (16.73)$$

Based on (16.72) and (16.73),

$$\begin{aligned}\frac{T\rho c_p}{p_a} &= 0.95 \frac{A_c}{A_a} \mu \left( \frac{2Va_{\max}}{\kappa_t} \right)^{1/2}, & L_p > 10 \\ &= 0.33 \frac{A_r}{A_a} \mu \left( \frac{2Va_{\max}}{\kappa_t} \right), & L_p < 0.5.\end{aligned}\quad (16.74)$$

For a multiple asperity contact, mean temperature in terms of average of maximum contact size can be written as

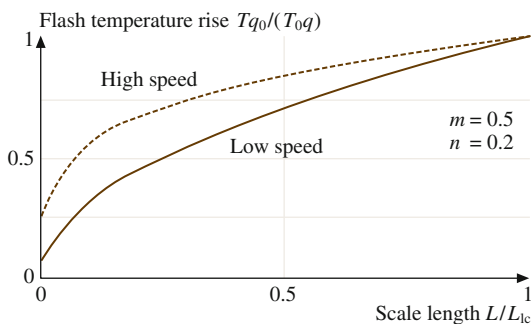
$$\begin{aligned}\frac{\bar{T}\rho c_p}{p_a} &= 0.95 \frac{A_r}{A_a} \mu \left( \frac{2V\bar{a}_{\max}}{\kappa_t} \right)^{1/2}, & L_p > 10 \\ &= 0.33 \frac{A_r}{A_a} \mu \left( \frac{2V\bar{a}_{\max}}{\kappa_t} \right), & L_p < 0.5.\end{aligned}\quad (16.75)$$

In (16.75)  $\bar{a}_{\max}$ ,  $\mu$  and  $A_a/A_r$  are scale dependent parameters. During adhesion contact, the maximum radius  $\bar{a}_{\max}$  is proportional to the contact radius  $\bar{a}$ , and the scale dependence for  $\bar{a}_{\max}$  is given by (16.19), for  $\mu$  by (16.38–16.39), and for  $A_{re}$  and  $A_{rp}$  by (16.17) and (16.21). The scale dependence of  $q$ , involving  $\mu$  and  $A_r$ , and  $\bar{a}_{\max}$  in (16.72) can be considered separately and then combined. For the sake of simplicity, we only consider the scale dependence of  $\bar{a}_{\max}$ . For the empirical rule dependence of surface roughness parameters and the fractal model, in the case of high and low velocity, (16.75) yields [22]

$$\begin{aligned}\frac{\bar{T}\rho c_p V}{q} &= 0.95 \left( \frac{2VC_A L^m}{\kappa} \right)^{1/2}, & L < L_{lw1}, L_p > 10 \\ &= 0.33 \left( \frac{2VC_A L^m}{\kappa} \right), & L < L_{lw1}, L_p < 0.5.\end{aligned}\quad (16.76)$$

Scale dependence for the ratio of the flash temperature rise to the amount of heat generated per unit time per unit area, for a given sliding velocity, as a function of

**Fig. 16.24** Ratio of the flash temperature rise to the amount of heat generated per unit time per unit area, for a given sliding velocity, as a function of scale. Presented for  $m = 0.5$ ,  $n = 0.2$



scale, is presented in Fig. 16.24, based on (16.76), for the high-speed and low-speed cases. For the empirical rule dependence of roughness parameters, the results are shown for  $m = 0.5$ ,  $n = 0.2$ .

## 16.8 Closure

A model, which explains scale effects in mechanical properties (yield strength, hardness, and shear strength at the interface) and tribology (surface roughness, contact parameters, friction, wear, and interface temperature), has been presented in this chapter.

Both mechanical properties and roughness parameters are scale-dependent. According to the strain gradient plasticity, the scale dependence of the so-called geometrically necessary dislocations causes enhanced yield strength and hardness with decreasing scale. The shear strength at the interface is scale dependent due to the effect of dislocation-assisted sliding. An empirical rule for scale dependence of the roughness parameters has been proposed, namely, it was assumed, that the standard deviation of surface height and autocorrelation length depend on scale according to a power law when scale is less than the long wavelength limit value.

Both single asperity and multiple asperity contacts were considered. For multiple asperity contacts, based on the empirical power-rule for scale dependence of roughness, contact parameters were calculated. The effect of load on the contact parameters was also studied. The effect of increasing load is similar to that of increasing scale because it results in increased relevance of longer wavelength details of roughness of surfaces in contact.

During sliding, adhesion and two- and three-body deformation, as well as ratchet mechanism, contribute to the friction force. These components of the friction force depend on the relevant real areas of contact (dependent on roughness, mechanical properties, and load), average asperity slope, number of trapped particles, and relevant shear strength during sliding. The relevant scaling length is the nominal

contact length – contact diameter ( $2a$ ) for a single-asperity contact, only considered in adhesion, and scan length ( $L$ ) for multiple-asperity contacts, considered in adhesion and deformation.

For the adhesional component of the coefficient of friction, the shear yield strength and hardness increase with decreasing scale. In the case of elastic contact, the real area of contact is scale independent for single-asperity contact, and may increase or decrease depending on roughness parameters, for multiple-asperity contact. In the case of plastic contact, enhanced hardness results in a decrease in the real area of contact. The adhesional shear strength at the interface may remain constant or increase with decreasing scale, due to dislocation-assisted sliding (or microslip). The model predicts that the adhesional component of the coefficient of friction may increase or decrease with scale, depending on the material parameters and roughness. The coefficient of friction during two-body deformation and the ratchet component depend on the average slope of the rough surface. The average slope increases with scale due to scale dependence of the roughness parameters. As a result, the two-body deformation component of the coefficient of friction increases with decreasing scale. The three-body component of the coefficient of friction depends on the concentrations of particles, trapped at the interface, which decreases with decreasing scale.

The transition index, which is responsible for transition from predominantly elastic adhesional friction to plastic deformation was proposed and was found to change with scale, due to scale dependence of roughness parameters. For the transition index close to zero, the contact is predominantly elastic and the dominant contribution to friction is adhesion involving elastic deformation. The increase of the transition index leads to an increase in plastic deformation with increasing contribution of the deformation component of friction, which results in larger value of the total coefficient of friction.

In presence of the meniscus force, the measured value of the coefficient of friction is greater than the value of the coefficient of dry friction. The difference is especially important for small loads, when the normal load is comparable with the meniscus force. The meniscus force depends on peak radii and may either increase or decrease with scale, depending on the surface parameters.

The wear coefficient and the ratio of the maximum flash temperature rise to the amount of heat generated per unit time per unit area, for a given sliding velocity, as a function of scale, decrease with decreasing scale due to decrease in the mean contact size.

The proposed model is used to explain the trends in the experimental data for various materials at nanoscale and microscale, which indicate that nanoscale values of coefficient of friction are lower than the microscale values (Tables 16.2 and 16.3). The two factors responsible for this trend are the increase of the three-body deformation and transition from elastic adhesive contact to plastic deformation. Experimental data show that the coefficient of friction increases with increasing load after a certain load and reaches the macroscale value. This is due to the onset of plastic deformation with increasing load and the effect of load on contact parameters, which affect the coefficient of friction.

## 16.9 Statistics of Particle Size Distribution

### 16.9.1 Statistical Models of Particle Size Distribution

Particle size analysis is an important field for different areas of engineering, environmental, and biomedical studies. In general, size distribution of particles depends on how the particles were formed and sorted. Several statistical distributions, which govern distribution of random variables including particle size, have been suggested (Fig. 16.25), [56, 57, 58, 59, 60]. Statistical distributions commonly used are either the probability density (or frequency) function (PDF)  $p(z)$  or cumulative distribution function (CDF)  $P(h)$ .  $P(h)$  associated with random variable  $z(x)$ , which can take any value between  $-\infty$  and  $+\infty$  or  $z_{\min}$  and  $z_{\max}$ , is defined as the probability of the event  $z(x) \leq z'$  and is written as [61]

$$P(z) = \text{Prob}(z \leq z') \quad (16.77)$$

with  $P(-\infty) = 0$  and  $P(\infty) = 1$ .

The PDF is the slope of the CDF given by its derivative

$$p(z) = \frac{dP(z)}{dz} \quad (16.78)$$

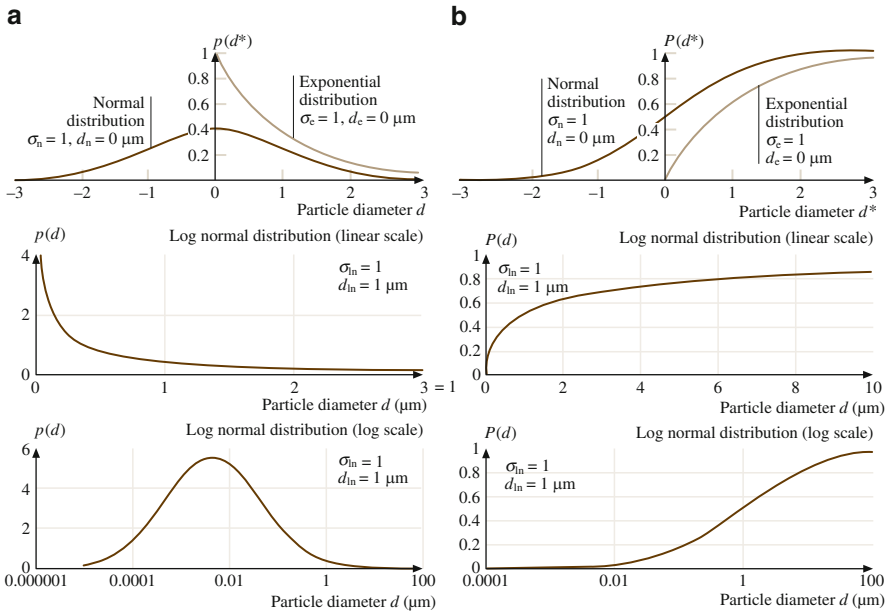


**Fig. 16.25** Common statistical distributions of particle size. (a) Probability density distributions. (b) Cumulative distributions

or

$$P(z \leq z') = P(z') = \int_{-\infty}^{z'} p(z) dz. \quad (16.79)$$

Furthermore, the total area under the probability density function must be unity; that is, it is certain that the value of  $z$  at any  $x$  must fall somewhere between plus and minus infinity or  $z_{\min}$  and  $z_{\max}$ . The definition of  $p(z)$  is phrased as that the random variable  $z(x)$  is distributed as  $p(z)$ .

The probability density (or frequency) function,  $p(d)$ , in the exponential form is the simplest distribution mathematically

$$p(d) = \frac{1}{\sigma_e} \exp\left(-\frac{d - d_e}{\sigma_e}\right), \quad d \geq d_0, \quad (16.80)$$

where  $d$  is particle diameter,  $\sigma_e$  is standard deviation, and  $d_e$  is minimum value (for this distribution). For convenience, the density function can be normalized by  $\sigma_e$  in terms of a normalized variable  $d^*$  equal to  $(d - d_e)/\sigma_e$

$$p(d^*) = \exp(-d^*), \quad d^* \geq 0, \quad (16.81)$$

which has zero minimum and unity standard deviation. The cumulative distribution function  $P(d')$  is given as

$$P(d') = P(d^* \leq d') = 1 - \exp(-d'). \quad (16.82)$$

The Gaussian or normal distribution is used to represent data for a wide collection of random physical phenomena in practice such as surface roughness. The probability density and cumulative distribution functions are given as

$$p(d) = \frac{1}{\sqrt{2\pi}\sigma_n} \exp\left(-\frac{(d - d_n)^2}{2\sigma_n^2}\right), \quad -\infty < d < \infty, -\infty < d_n < \infty, \sigma_e > 0, \quad (16.83)$$

where  $d_n$  is the mean value. The integral of  $p(d)$  in the interval  $-\infty < d < \infty$  is equal to 1. In terms of the normalized variables, (16.82) reduces to

$$p(d^*) = \frac{1}{\sqrt{2\pi}} \exp\left(-\frac{d^{*2}}{2}\right) \quad (16.84)$$

and

$$\begin{aligned} p(d') &= P(d^* \leq d') \\ &= \frac{1}{\sqrt{2\pi}} \int_{-\infty}^{d'} \exp[-(d^*)^2/2] dd^* = \text{erf}(d'), \end{aligned} \quad (16.85)$$

where  $\text{erf}(d')$  is called the *error function* and its values are listed in most statistical handbooks. The pdf is bell-shaped and the CDF is S-shaped.

For particle size distribution, of interest here, the diameter cannot be less than zero. For this condition, (16.83) must be modified by using a constant on the right side

$$p(d) = \frac{C_0}{\sqrt{2\pi}\sigma_e} \exp\left(-\frac{(d-d_n)^2}{2\sigma_e^2}\right), \quad 0 \leq d < \infty, \quad (16.86)$$

where

$$C_0 = \left[ \frac{1}{\sqrt{2\pi}} \int_{-d_0/\sigma}^{\infty} \exp\left(-\frac{t^2}{2}\right) dt \right]^{-1}.$$

The constant is calculated by integrating  $p(d)$  in the interval  $0 \leq d \leq \infty$  and equating to one

$$\int_0^{\infty} p(d) dd = 1. \quad (16.87)$$

The log-normal distribution is commonly used to describe particle size distribution. A variable  $d$  is log-normally distributed if  $\ln d$  is normally distributed. Log-normal probability density function for variable  $d$ , for which  $\ln(d)$  has a Gaussian distribution with a mean  $\ln(d)_{\ln}$  and standard deviation  $\sigma_{\ln}$ , is given as

$$p(d) = \frac{1}{\sqrt{2\pi}\sigma_{\ln}} \left(\frac{1}{d}\right) \exp\left\{-\frac{[\ln(d/d_{\ln})]^2}{2\sigma_{\ln}^2}\right\}, \quad 0 < d < \infty. \quad (16.88)$$

The mean of the log-normal distribution is  $\exp(\ln d_{\ln} + \sigma_{\ln}^2/2)$ , the standard deviation is  $\exp(2 \ln d_{\ln} + \sigma_{\ln}^2) \times [\exp(\sigma_{\ln}^2) - 1]$ , the skewness is  $[\exp(\sigma_{\ln}^2) + 2][\exp(\sigma_{\ln}^2) - 1]^{1/2}$ , and kurtosis is  $\exp[4(\sigma_{\ln}^2)] + 2 \exp[3(\sigma_{\ln}^2)] + 3 \exp[2(\sigma_{\ln}^2)] - 3$  [58]. The case where  $d_{\ln} = 0$  is called the standard log-normal distribution. The density function can be normalized by  $\sigma_{\ln}$  in terms of a normalized variable  $d^* = (\ln d - d_{\ln})/\sigma_{\ln}$

$$p(d^*) = \frac{1}{\sqrt{2\pi}} \left( \frac{1}{d^*} \right) \exp \left( -\frac{(d^*)^2}{2} \right) \quad (16.89)$$

and

$$P(d') = P(d^* \leq d') = \frac{1}{2} \left[ 1 + \operatorname{erf} \left( \frac{d'}{\sqrt{2}} \right) \right]. \quad (16.90)$$

The log-normal distribution of particle size occurs when the dispersion is attained by comminution (milling, grinding, crushing). The size distribution of pulverized silica, granite, calcite, limestone, quartz, soda, ash, alumina, clay, as well as of wear particles is often governed by the log-normal distribution [62]. A size distribution is usually presented either as probability density or frequency  $p(d)$ , or as cumulative percent (percent of particles greater than given size)  $P(d)$ , or as cumulative mass versus particle size. All these presentations are interrelated [62].

### 16.9.2 Typical Particle Size Distribution Data

Typical experimental data for size distributions of atmospheric (dust), sand, and abrasive diamond particles are presented in Fig. 16.26a. It can be seen, that the atmospheric particles [63] follow the normal distribution function. The dune sand is low in heavy mineral content, so the curve is concaved downward. Micaceous dune sand is sorted by gravity slide on a sharp mountain slope and appears to follow log-normal distribution, as many distributions of sediments, which are sorted by gravity. Whereas beach sand distribution curve is concaved upward, due to richness in smaller size component [62]. The abrasive diamond particles follow the log-normal distribution [64].

Size distribution of wear particles has been studied actively since 1970s, when the ferrography was introduced [69, 70]. The data for wear particles is presented in Fig. 16.26b. Xuan et al. [65] studied the size distribution of submicrometer particles during sliding of steel–steel using a Falex 3, pin-on-disk machine, using a laser particle counter for various sliding distances. They found a distribution, which is close to the log-normal function. Mizumoto and Kato [66] studied size distribution of particles generated during pin-on-disk test, for diamond, sapphire, silicon carbide, and tungsten carbide pins versus steel disk, using a laser particle counter. They found that the probability density function is exponential for particles greater than 1  $\mu\text{m}$  diameter, however for smaller particles a linear law was assumed. Shanbhag et al. [67] studied wear particles for ultrahigh molecular weight polyethylene (UHMWPE) versus titanium in biomedical applications (total knee replacement) using a scanning electron microscope. They found that the distribution is close to that of the normal distribution. Numerous data for wear particles are presented by Anderson [71]. Hunt [68] discusses various techniques of debris measurement and



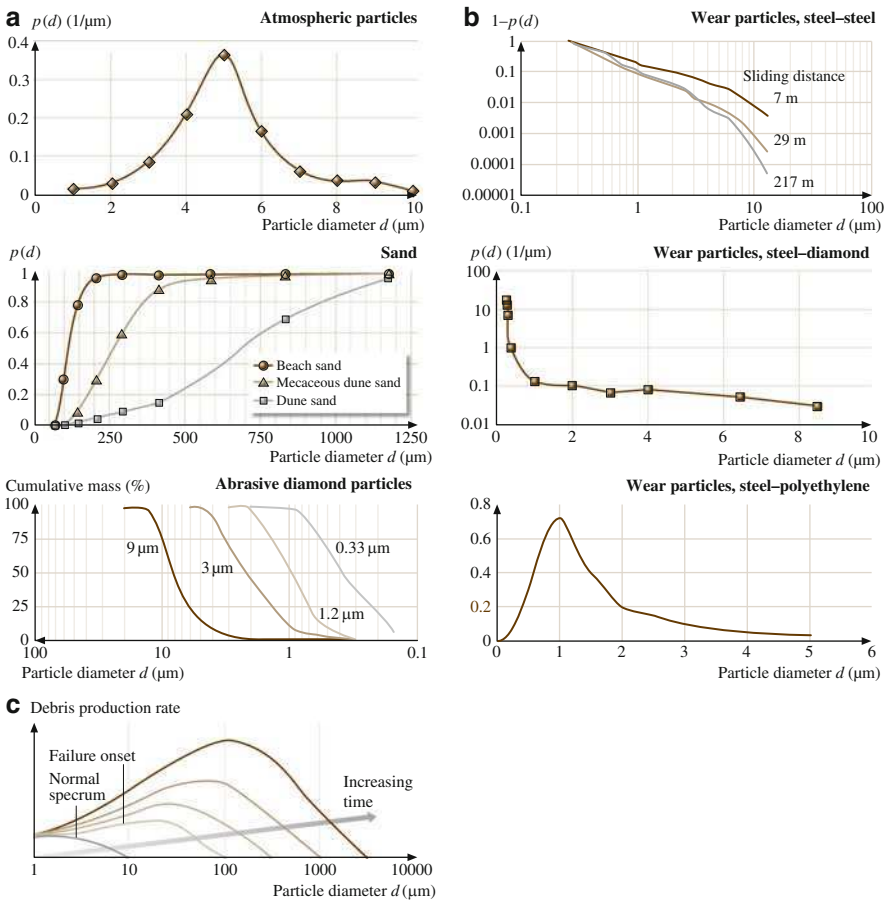


**Fig. 16.26** (a) Experimental data for atmospheric [63], sand [62], and abrasive diamond [64] particle size distribution. (b) Experimental data for wear particle size distribution (steel–steel [65], steel–diamond [66], steel–polyethylene [67]). (c) Change with time of wear debris production rate during lubricated sliding as a function of particle size [68]

analysis in lubricants. A typical change in wear debris generation rate, which occurs with time, is presented in Fig. 16.26c. Change in the size distribution of wear particles in lubricant indicates an onset of mechanical failure.

## References

1. B. Bhushan, *Handbook of Micro/Nanotribology*, 2nd edn. (CRC, Boca Raton, 1999)
2. B. Bhushan, Nanoscale tribophysics and tribomechanics, *Wear* **225–229**, 465–492 (1999)
3. B. Bhushan, *Springer Handbook of Nanotechnology* (Springer, Berlin, 2004)

4. B. Bhushan, J.N. Israelachvili, U. Landman, Nanotribology: Friction, wear and lubrication at the atomic scale, *Nature* **374**, 607–616 (1995)
5. J. Ruan, B. Bhushan, Atomic-scale friction measurements using friction force microscopy: Part I – General principles and new measurement technique, *ASME J. Tribol.* **116**, 378–388 (1994)
6. B. Bhushan, A.V. Kulkarni, Effect of normal load on microscale friction measurements, *Thin Solid Films* **278**, 49–56 (1996), Erratum: **293**, 333
7. R.W. Carpick, N. Agrait, D.F. Ogletree, M. Salmeron, Measurement of interfacial shear (friction) with an ultrahigh vacuum atomic force microscope, *J. Vac. Sci. Technol. B* **14**, 1289–1295 (1996)
8. U.D. Schwarz, O. Zwörner, P. Köster, R. Wiesendanger, Quantitative analysis of the frictional properties of solid materials at low loads. 1. Carbon compounds, *Phys. Rev. B* **56**, 6987–6996 (1997)
9. B. Bhushan, S. Sundararajan, Micro/nanoscale friction and wear mechanisms of thin films using atomic force and friction force microscopy, *Acta Mater.* **46**, 3793–3804 (1998)
10. B. Bhushan, C. Dandavate, Thin-film friction and adhesion studies using atomic force microscopy, *J. Appl. Phys.* **87**, 1201–1210 (2000)
11. H. Liu, B. Bhushan, Adhesion and friction studies of microelectromechanical systems/nanoelectromechanical systems materials using a novel microtriboapparatus, *J. Vac. Sci. Technol. A* **21**, 1538 (2003)
12. B. Bhushan, H. Liu, S.M. Hsu, Adhesion and friction studies of silicon and hydrophobic and low friction films and investigation of scale effects, *ASME J. Tribol.* **126**, 583–590 (2004)
13. A.W. Homola, J.N. Israelachvili, P.M. McGuiggan, M.L. Gee, Fundamental experimental studies in tribology: The transition from interfacial friction of undamaged molecularly smooth surfaces to normal friction with wear, *Wear* **136**, 65–83 (1990)
14. V.N. Koinkar, B. Bhushan, Scanning and transmission electron microscopies of single-crystal silicon microworn/machined using atomic force microscopy, *J. Mater. Res.* **12**, 3219–3224 (1997)
15. X. Zhao, B. Bhushan, Material removal mechanisms of single-crystal silicon on nanoscale and at ultralow loads, *Wear* **223**, 66–78 (1998)
16. B. Bhushan, *Introduction to Tribology* (Wiley, New York, 2002)
17. N.A. Fleck, G.M. Muller, M.F. Ashby, J.W. Hutchinson, Strain gradient plasticity: Theory and experiment, *Acta Metall. Mater.* **42**, 475–487 (1994)
18. W.D. Nix, H. Gao, Indentation size effects in crystalline materials: A law for strain gradient plasticity, *J. Mech. Phys. Solids* **46**, 411–425 (1998)
19. J.W. Hutchinson, Plasticity at the micron scale, *Int. J. Solids Struct.* **37**, 225–238 (2000)
20. B. Bhushan, M. Nosonovsky, Scale effects in friction using strain gradient plasticity and dislocation-assisted sliding (microslip), *Acta Mater.* **51**, 4331–4345 (2003)
21. B. Bhushan, M. Nosonovsky, Comprehensive model for scale effects in friction due to adhesion and two- and three-body deformation (plowing), *Acta Mater.* **52**, 2461–2474 (2004)
22. B. Bhushan, M. Nosonovsky, Scale effects in dry and wet friction, wear, and interface temperature, *Nanotechnology* **15**, 749–761 (2004)
23. M. Nosonovsky, B. Bhushan, Scale effect in dry friction during multiple asperity contact, *ASME J. Tribol.* **127**, 37–46 (2005)
24. H. Gao, Y. Huang, W.D. Nix, J.W. Hutchinson, Mechanism-based strain-gradient plasticity – I. theory, *J. Mech. Phys. Solids* **47**, 1239–1263 (1999)
25. Y. Huang, H. Gao, W.D. Nix, J.W. Hutchinson, Mechanism-based strain-gradient plasticity – II. analysis, *J. Mech. Phys. Solids* **48**, 99–128 (2000)
26. Z.P. Bazant, Scaling of dislocation-based strain-gradient plasticity, *J. Mech. Phys. Solids* **50**, 435–448 (2002)
27. J. Friedel, *Dislocations* (Pergamon, New York, 1964)
28. J. Weertman, J.R. Weertman, *Elementary Dislocations Theory* (MacMillan, New York, 1966)

29. B. Bhushan, A.V. Koinkar, Nanoindentation hardness measurements using atomic force microscopy, *Appl. Phys. Lett.* **64**, 1653–1655 (1994)
30. B. Bhushan, A.V. Kulkarni, W. Bonin, J.T. Wyrobek, Nano/picoindentation measurement using a capacitive transducer system in atomic force microscopy, *Philos. Mag.* **74**, 1117–1128 (1996)
31. A.V. Kulkarni, B. Bhushan, Nanoscale mechanical property measurements using modified atomic force microscopy, *Thin Solid Films* **290/291**, 206–210 (1996)
32. K.W. McElhaney, J.J. Vlassak, W.D. Nix, Determination of indenter tip geometry and indentation contact area of depth-sensing indentation experiments, *J. Mater. Res.* **13**, 1300–1306 (1998)
33. N. Gane, J.M. Cox, The micro-hardness of metals at very low loads, *Philos. Mag.* **22**, 881–891 (1970)
34. M.A. Stelmashenko, M.G. Walls, L.M. Brown, Y.V. Miman, Microindentation on W and Mo oriented single crystal an SEM study, *Acta Metall. Mater.* **41**, 2855–2865 (1993)
35. S. Sundararajan, B. Bhushan, Development of AFM-based techniques to measure mechanical properties of nanoscale structures, *Sens. Actuators A* **101**, 338–351 (2002)
36. J.J. Weertman, Dislocations moving uniformly on the interface between isotropic media of different elastic properties, *J. Mech. Phys. Solids* **11**, 197–204 (1963)
37. K.L. Johnson, Adhesion and friction between a smooth elastic spherical asperity and a plane surface, *Proc. R. Soc. Lond. A* **453**, 163–179 (1997)
38. I.A. Polonsky, L.M. Keer, Scale effects of elastic-plastic behavior of microscopic asperity contact, *ASME J. Tribol.* **118**, 335–340 (1996)
39. V.S. Deshpande, A. Needleman, E. Van der Giessen, Discrete dislocation plasticity modeling of short cracks in single crystals, *Acta Mater.* **51**, 1–15 (2003)
40. R.A. Onions, J.F. Archard, The contact of surfaces having a random structure, *J. Phys. D* **6**, 289–304 (1973)
41. D.J. Whitehouse, J.F. Archard, The properties of random surfaces of significance in their contact, *Proc. R. Soc. Lond. A* **316**, 97–121 (1970)
42. J.A. Greenwood, J.B.P. Williamson, Contact of nominally flat surfaces, *Proc. R. Soc. Lond. A* **295**, 300–319 (1966)
43. B. Bhushan, Contact mechanics of rough surfaces in tribology: Single asperity contact, *Appl. Mech. Rev.* **49**, 275–298 (1996)
44. B. Bhushan, Contact mechanics of rough surfaces in tribology: Multiple asperities contact, *Tribol. Lett.* **4**, 1–35 (1998)
45. B. Bhushan, W. Peng, Contact modeling of multilayered rough surfaces, *Appl. Mech. Rev.* **55**, 435–480 (2002)
46. A. Majumdar, B. Bhushan, Fractal model of elastic-plastic contact between rough surfaces, *ASME J. Tribol.* **113**, 1–11 (1991)
47. K.L. Johnson, *Contact Mechanics* (Clarendon, Oxford, 1985)
48. E. Rabinowicz, *Friction and Wear of Materials*, 2nd edn. (Wiley, New York, 1995)
49. H.R. Clauser (Ed.), *The Encyclopedia of Engineering Materials and Processes* (Reinhold, London, 1963)
50. B. Bhushan, B.K. Gupta, *Handbook of Tribology: Materials, Coatings, and Surface Treatments* (McGraw-Hill, New York, 1991; Krieger, Malabar, New York, 1997)
51. B. Bhushan, S. Venkatesan, Mechanical and tribological properties of silicon for micromechanical applications: A review, *Adv. Inf. Storage Syst.* **5**, 211–239 (1993)
52. INSPEC, *Properties of Silicon*, EMIS Data Rev. Ser., Vol. 4 (INSPEC Institution of Electrical Engineers, London, 2002), see also, MEMS Materials Database, <http://www.memsnet.org/material/>
53. J.E. Field (Ed.), *The Properties of Natural and Synthetic Diamond* (Academic, London, 1992)
54. B. Bhushan, Chemical, mechanical and tribological characterization of ultra-thin and hard amorphous carbon coatings as thin as 3.5 nm: Recent developments, *Diam. Relat. Mater.* **8**, 1985–2015 (1999)

55. National Carbon Comp., *The Industrial Graphite Engineering Handbook* (National Carbon Company, New York, 1959)
56. C. Bernhardt, *Particle Size Analysis* (Chapman Hall, London, 1994)
57. J.L. Devoro, *Probability and Statistics for Engineering and the Sciences* (Duxbury, New York, 1995)
58. B.S. Everitt, *The Cambridge Dictionary of Statistics* (Cambridge university Press, Cambridge, 1998)
59. D. Zwillinger, S. Kokoska, *CRC Standard Probability and Statistics Tables and Formulas* (CRC, Boca Raton, 2000)
60. S. Wolfram, *The Mathematica Book*, 5th edn. (Wolfram Media, Champaign, 2003)
61. J.S. Bendet, A.G. Piersol, *Engineering Applications of Correlation and Spectral Analysis*, 2nd edn. (Wiley, New York, 1986)
62. G. Herdan, *Small Particle Statistics* (Butterworth, London, 1960)
63. R.D. Cadle, *Particle Size – Theory and Industrial Applications* (Reinhold, New York, 1965)
64. Y. Xie, B. Bhushan, Effect of particle size, polishing pad and contact pressure in free abrasive polishing, *Wear* **200**, 281–295 (1996)
65. J.L. Xuan, H.S. Cheng, R.J. Miller, Generation of submicrometer particles in dry sliding, *ASME J. Tribol.* **112**, 664–691 (1990)
66. M. Mizumoto, K. Kato, *Wear Particles: From the Cradle to the Grave*, ed. by D. Dowson, C. M. Taylor, T.H.C. Childs, M. Godet, G. Dalmaz (Elsevier, Amsterdam, 1992), pp. 523–530
67. A.S. Shanbhag, H.O. Bailey, D.S. Hwang, C.W. Cha, N.G. Eror, H.E. Rubash, Quantitative analysis of ultrahigh molecular weight polyethylene (UHMWPE) wear debris associated with total knee replacements, *J. Biomed. Mater. Res.* **53**, 100–110 (2000)
68. T.M. Hunt, *Handbook of Wear Debris Analysis and Particle Detection in Liquids* (Elsevier Applied Science, London, 1993)
69. W.W. Seifert, V.C. Westcott, A method for the study of wear particles in lubricating oil, *Wear* **21**, 27–42 (1972)
70. D. Scott, V.C. Westcott, Predictive maintenance by ferrography, *Wear* **44**, 173–182 (1977)
71. D.P. Anderson, *Wear Particle Atlas*, 2nd edn. (Spectro Inc. Industrial Tribology Systems, Littleton, 1991)

**Part IV**  
**Molecularly-Thick Films for Lubrication**

# Chapter 17

## Nanotribology of Ultrathin and Hard Amorphous Carbon Films

**Bharat Bhushan**

**Abstract** One of the best materials to use in applications that require very low wear and reduced friction is diamond, especially in the form of a diamond coating. Unfortunately, true diamond coatings can only be deposited at high temperatures and on selected substrates, and they require surface finishing. However, hard amorphous carbon – commonly known as diamond-like carbon or a DLC coating – has similar mechanical, thermal and optical properties to those of diamond. It can also be deposited at a wide range of thicknesses using a variety of deposition processes on various substrates at or near room temperature. The coatings reproduce the topography of the substrate, removing the need for finishing. The friction and wear properties of some DLC coatings make them very attractive for some tribological applications. The most significant current industrial application of DLC coatings is in magnetic storage devices.

In this chapter, the state-of-the-art in the chemical, mechanical and tribological characterization of ultrathin amorphous carbon coatings is presented.

EELS and Raman spectroscopies can be used to characterize amorphous carbon coatings chemically. The prevailing atomic arrangement in the DLC coatings is amorphous or quasi-amorphous, with small diamond ( $sp^3$ ), graphite ( $sp^2$ ) and other unidentifiable micro- or nanocrystallites. Most DLC coatings, except for those produced using a filtered cathodic arc, contain from a few to about 50 at.% hydrogen. Sometimes hydrogen is deliberately incorporated into the sputtered and ion-plated coatings in order to tailor their properties.

Amorphous carbon coatings deposited by different techniques exhibit different mechanical and tribological properties. Thin coatings deposited by filtered cathodic arc, ion beam and ECR-CVD hold much promise for tribological applications. Coatings of 5 nm or even less provide wear protection. A nanoindenter can be used to measure DLC coating hardness, elastic modulus, fracture toughness and fatigue life. Microscratch and microwear tests can be performed on the coatings using either a nanoindenter or an AFM, and along with accelerated wear testing, can be used to screen potential industrial coatings. For the examples shown in this chapter, the trends observed in such tests were similar to those found in functional tests.

Carbon exists in both crystalline and amorphous forms and exhibits both metallic and nonmetallic characteristics [1–3]. Forms of crystalline carbon include graphite, diamond, and a family of fullerenes (Fig. 17.1). The graphite and diamond are infinite periodic network solids with a planar structure, whereas the fullerenes are a molecular form of pure carbon with a finite network and a nonplanar structure. Graphite has a hexagonal, layered structure with weak interlayer bonding forces and it exhibits excellent lubrication properties. The graphite crystal may be visualized as infinite parallel layers of hexagons stacked 0.34 nm apart with an interatomic distance of 0.1415 nm between the carbon atoms in the basal plane. Each atom lying in the basal planes is trigonally coordinated and closely packed with strong  $\sigma$  (covalent) bonds to its three carbon neighbors via hybrid  $sp^2$  orbitals. The fourth electron lies in a  $p_z$  orbital lying normal to the  $\sigma$  bonding plane and forms a weak  $\pi$  bond by overlapping side-to-side with a  $p_z$  orbital of an adjacent atom to which the carbon is attached by a  $\sigma$  bond. The layers (basal planes) themselves are relatively far apart and the forces that bond them are weak van der Waals forces. These layers can align themselves parallel to the direction of the relative motion and slide over one another with relative ease, meaning low friction. Strong

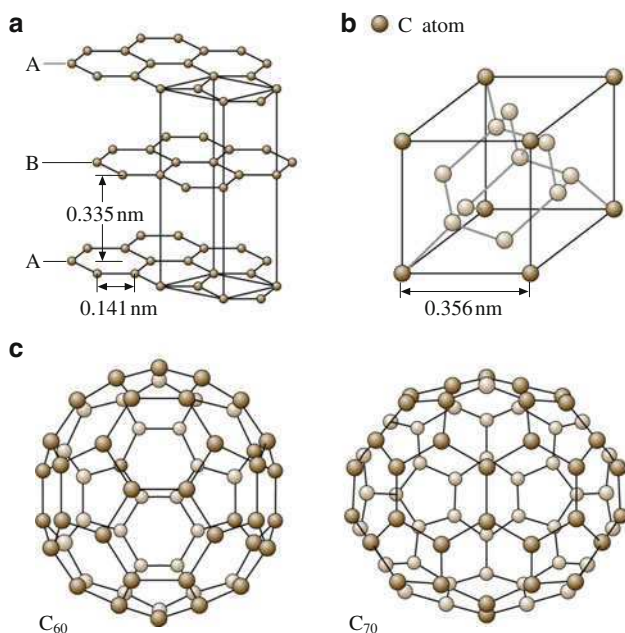


**Fig. 17.1** The structures of the three known forms of crystalline carbon: (a) hexagonal structure of graphite, (b) modified face-centered cubic (fcc) structure (two interpenetrating fcc lattices displaced by a quarter of the cube diagonal) of diamond (each atom is bonded to four others that form the corners of a tetrahedron), and (c) the structures of the two most common fullerenes: a soccer ball  $C_{60}$  and a rugby ball  $C_{70}$  molecules

interatomic bonding and packing in each layer is thought to help reduce wear. The operating environment has a significant influence on the lubrication – low friction and low wear – properties of graphite. It lubricates better in a humid environment than a dry one, due to the adsorption of water vapor and other gases from the environment, which further weakens the interlayer bonding forces and results in easy shear and transfer of the crystallite platelets to the mating surface. Thus, transfer plays an important role in controlling friction and wear. Graphite oxidizes at high operating temperatures and can be used up to about 430°C.

One of the most well-known fullerene molecules is C<sub>60</sub>, commonly known as buckyballs. Since these C<sub>60</sub> molecules are very stable and do not require additional atoms to satisfy chemical bonding requirements, they are expected to have low adhesion to the mating surface and low surface energy. Since the C<sub>60</sub> molecule, which has a perfect spherical symmetry, bonds only weakly to other molecules, C<sub>60</sub> clusters readily become detached, similar to other layered lattice structures, and either get transferred to the mating surface by mechanical compaction or are present as loose wear particles that may roll like tiny ball bearings in a sliding contact, resulting in low friction and wear. The wear particles are expected to be harder than as-deposited C<sub>60</sub> molecules, because of their phase transformation at the high-asperity contact pressures present in a sliding interface. The low surface energy, the spherical shapes of C<sub>60</sub> molecules, the weak intermolecular bonding, and the high load bearing capacity offer vast potential for various mechanical and tribological applications. Sublimed C<sub>60</sub> coatings and fullerene particles used as an additive to mineral oils and greases have been reported to be good solid lubricants comparable to graphite and MoS<sub>2</sub> [4–6].

Diamond crystallizes in a modified face-centered cubic (fcc) structure with an interatomic distance of 0.154 nm. The diamond cubic lattice consists of two interpenetrating fcc lattices displaced by a quarter of the cube diagonal. Each carbon atom is tetrahedrally coordinated, making strong  $\sigma$  (covalent) bonds to its four carbon neighbors using the hybrid  $sp^3$  atomic orbitals, which accounts for it having the highest hardness (80–104 GPa) and thermal conductivity (900–2,100 W/(m K), on the order of five times that of copper) of any known solid, as well as high electrical resistivity and optical transmission and a large optical band gap. It is relatively chemically inert, and it exhibits poor adhesion with other solids, enhancing its low friction and wear properties. Its high thermal conductivity permits the dissipation of frictional heat during sliding and it protects the interface, and the dangling carbon bonds on the surface react with the environment to form hydrocarbons that act as good lubrication films. These are some of the reasons for the low friction and wear of the diamond. Diamond and its coatings find many industrial applications: tribological applications (low friction and wear), optical applications (exceptional optical transmission, high abrasion resistance), and thermal management or heat sink applications (high thermal conductivity). Diamond can be used at high temperatures; it starts to graphitize at about 1,000°C in ambient air and at about 1,400°C in vacuum. Diamond is an attractive material for cutting tools, abrasives for grinding wheels and lapping compounds, and other extreme wear applications.



Natural diamond – particularly in large quantities – is very expensive, and so diamond coatings – a low-cost alternative – are attractive. True diamond coatings are deposited by chemical vapor deposition (CVD) processes at high substrate temperatures (on the order of 800°C). They adhere best on silicon substrate and require an interlayer for other substrates. One major hindrance to the widespread use of true diamond films in tribological, optical and thermal management applications is their surface roughness. Growth of the diamond phase on a nondiamond substrate is initiated by nucleation at either randomly seeded sites or at thermally favored sites, due to statistical thermal fluctuations at the substrate surface. Depending on the growth temperature and pressure conditions, certain favored crystal orientations dominate the competitive growth process. As a result, the films grown are polycrystalline in nature with a relatively large grain size ( $>1\mu\text{m}$ ) and they terminate in very rough surfaces, with RMS roughnesses ranging from a few tenths of a micrometer to tens of micrometers. Techniques for polishing these films have been developed. It has been reported that laser polished films exhibit friction and wear properties almost comparable to those of bulk polished diamond [7, 8].

Amorphous carbon has no long-range order, and the short-range order of the carbon atoms in it can have one or more of three bonding configurations:  $sp^3$  (diamond),  $sp^2$  (graphite), or  $sp^1$  (with two electrons forming strong  $\sigma$  bonds, and the remaining two electrons left in orthogonal  $p_y$  and  $p_z$  orbitals, that form weak  $\pi$  bonds). Short-range order controls the properties of amorphous materials and coatings. Hard amorphous carbon (a-C) coatings, commonly known as diamond-like carbon or DLC (implying high hardness) coatings, are a class of coatings that are mostly metastable amorphous materials, but that include a micro- or nanocrystalline phase. The coatings are random networks of covalently bonded carbon in hybridized tetragonal ( $sp^3$ ) and trigonal ( $sp^2$ ) local coordination with some of the bonds terminated by hydrogen. These coatings have been successfully deposited by a variety of vacuum deposition techniques on a variety of substrates at or near room temperature. These coatings generally reproduce substrate topography and do not require any post-finishing. However, these coatings mostly adhere best on silicon substrates. The best adhesion is obtained on substrates that form carbides, such as Si, Fe and Ti. Based on depth profile analyses (using Auger and XPS) of DLC coatings deposited on silicon substrates, it has been reported that a substantial amount of silicon carbide (on the order of 5–10 nm in thickness) is present at the carbon–silicon interface, giving good adhesion and hardness [9]. For good adhesion of DLC coatings to other substrates, in most cases, an interlayer of silicon is required in most cases, except for coatings deposited by a cathodic arc.

There is significant interest in DLC coatings due to their unique combination of desirable properties. These properties include high hardness and wear resistance, chemical inertness to both acids and alkalis, lack of magnetic response, and an optical band gap ranging from zero to a few eV, depending upon the deposition conditions. These are used in a wide range of applications, including tribological, optical, electronic and biomedical applications [1, 10, 11]. The high hardness, good

friction and wear properties, versatility in deposition and substrates, and no requirement for post-deposition finishing make them very attractive for tribological applications. Two primary examples include overcoats for magnetic media (thin film disks and ME tapes) and MR-type magnetic heads for magnetic storage devices (Fig. 17.2) [12–20], and the emerging field of microelectromechanical systems (Fig. 17.3) [21–24]. The largest industrial application of the family of amorphous carbon coatings, typically deposited by DC/RF magnetron sputtering, plasma-enhanced chemical vapor deposition or ion beam deposition techniques, is in magnetic storage devices. These are employed to protect magnetic coatings on thin film rigid disks and metal evaporated tapes and the thin film head structure of a read/write disk head against wear and corrosion (Fig. 17.2). Thicknesses ranging from 3 to 10 nm are employed to maintain low physical spacing between the magnetic element of a read/write head and the magnetic layer of the storage media. Mechanical properties affect friction wear and therefore need to be optimized. In 1998, Gillette introduced Mach 3 razor blades with ultrathin DLC coatings, which could potentially become a very large industrial application. DLC coatings are also used in other commercial applications such as the glass windows of supermarket laser barcode scanners and sunglasses. These coatings are actively pursued in microelectromechanical systems (MEMS) components [23].

In this chapter, a state-of-the-art review of recent developments in the field of chemical, mechanical, and tribological characterization of ultrathin amorphous carbon coatings is presented. An overview of the most commonly used deposition techniques is provided, followed by typical chemical and mechanical characterization data and typical tribological data from both coupon-level testing and functional testing.

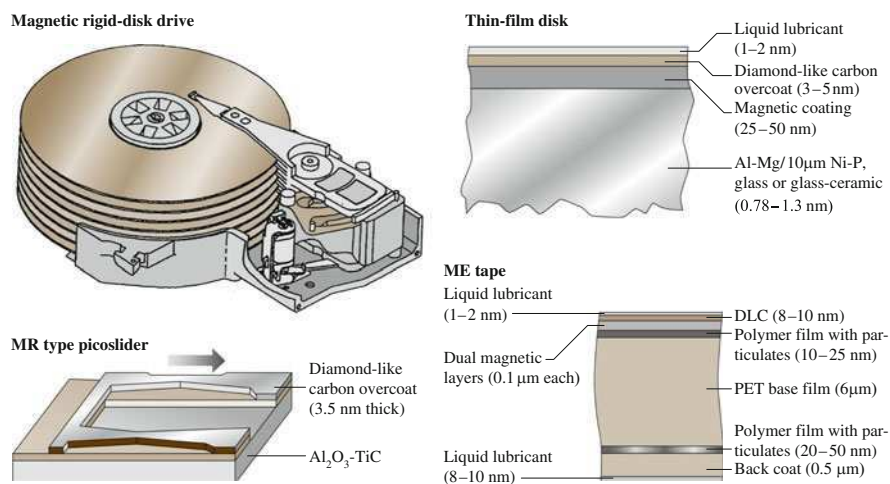


**Fig. 17.2** Schematic of a magnetic rigid-disk drive and MR type picoslider, and cross-sectional schematics of a magnetic thin film rigid disk and a metal evaporated (ME) tape

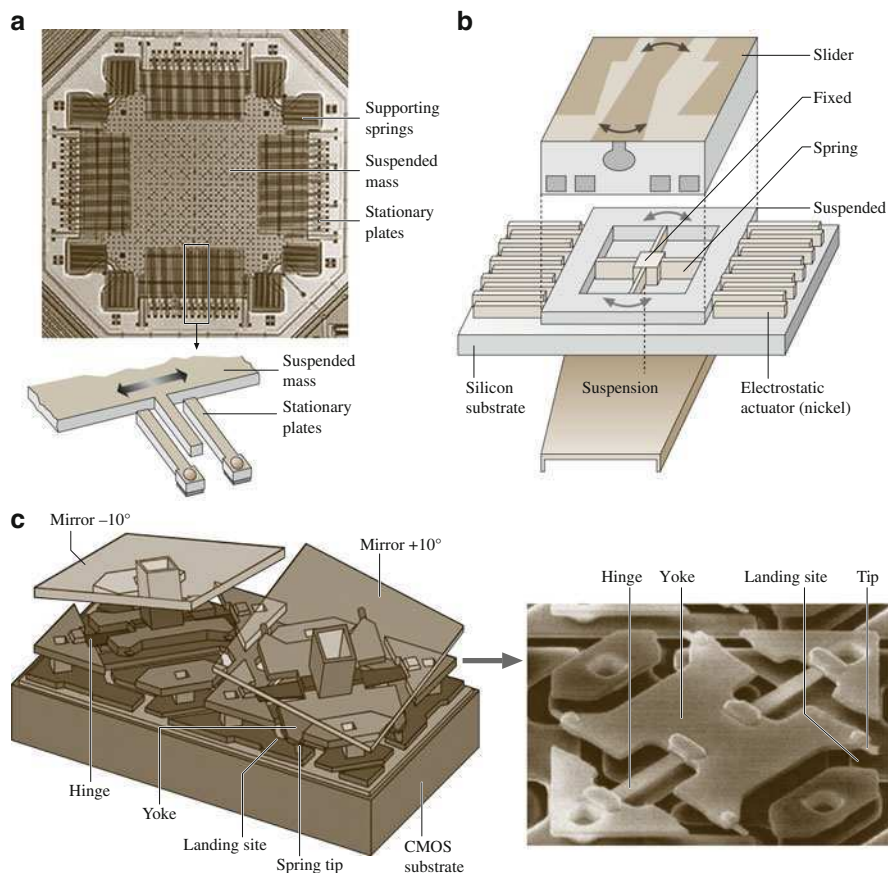


**Fig. 17.3** Schematics of (a) a capacitive-type silicon accelerometer for automotive sensory applications, (b) digital micrometer devices for high-projection displays, and (c) a polysilicon rotary microactuator for a magnetic disk drives

## 17.1 Description of Common Deposition Techniques

The first hard amorphous carbon coatings were deposited by a beam of carbon ions produced in an argon plasma on room temperature substrates, as reported by Aisenberg and Chabot [25]. Subsequent confirmation by Spencer et al. [26] led to the explosive growth of this field. Following this first work, several alternative techniques were developed. Amorphous carbon coatings have been prepared by a variety of deposition techniques and precursors, including evaporation, DC, RF or ion beam sputtering, RF or DC plasma-enhanced chemical vapor deposition (PECVD), electron cyclotron resonance chemical vapor deposition (ECR-CVD), direct ion beam deposition, pulsed laser vaporization and vacuum arc, from a variety of carbon-bearing solids or gaseous source materials [1,27]. Coatings with both graphitic and

diamond-like properties have been produced. Evaporation and ion plating techniques have been used to produce coatings with graphitic properties (low hardness, high electrical conductivity, very low friction, and so on, and all of the techniques have been used to produce coatings with diamond-like properties.

The structure and properties of a coating are dependent upon the deposition technique and parameters. High-energy surface bombardment has been used to produce harder and denser coatings. It is reported that the  $sp^3/sp^2$  fraction decreases in the order: cathodic arc deposition, pulsed laser vaporization, direct ion beam deposition, plasma-enhanced chemical vapor deposition, ion beam sputtering, DC/RF sputtering [12, 28, 29]. A common feature of these techniques is that the deposition is energetic; in other words the carbon species arrive with an energy significantly greater than that represented by the substrate temperature. The resultant coatings are amorphous in structure, with hydrogen contents of up to 50%, and display a high degree of  $sp^3$  character. From the results of previous investigations, it has been proposed that deposition of  $sp^3$ -bonded carbon requires that the depositing species have kinetic energies on the order of 100 eV or higher, well above those obtained in thermal processes like evaporation (0–0.1 eV). The species must then be quenched into the metastable configuration via rapid energy removal. Excess energy, such as that provided by substrate heating, is detrimental to the achievement of a high  $sp^3$  fraction. In general, the higher the fraction of  $sp^3$ -bonded carbon atoms in the amorphous network, the greater the hardness [29–36]. The mechanical and tribological properties of a carbon coating depend on the  $sp^3/sp^2$ -bonded carbon ratio, the amount of hydrogen in the coating, and the adhesion of the coating to the substrate, which are influenced by the precursor material, the kinetic energy of the carbon species prior to deposition, the deposition rate, the substrate temperature, the substrate biasing, and the substrate itself [29, 33, 35, 37–46]. The kinetic energies and deposition rates involved in selected deposition processes used in the deposition of DLC coatings are compared in Table 17.1 [1,28].

In the studies by Gupta and Bhushan [12, 47], Li and Bhushan [48, 49], and Sundararajan and Bhushan [50], DLC coatings typically ranging in thickness from 3.5 to 20 nm were deposited on single-crystal silicon, magnetic Ni-Zn ferrite, and  $Al_2O_3$ -TiC substrates (surface roughness  $\approx 1$ –3 nm RMS) by filtered cathodic arc (FCA) deposition, (direct) ion beam deposition (IBD), electron cyclotron resonance chemical vapor deposition (ECR-CVD), plasma-enhanced chemical vapor deposition (PECVD), and DC/RF planar magnetron sputtering (SP) deposition techniques [51]. In this chapter, we will limit the presentation of data to coatings deposited by FCA, IBD, ECR-CVD and SP deposition techniques.

### 17.1.1 Filtered Cathodic Arc Deposition

When the filtered cathodic arc deposition technique is used to create carbon coatings [29, 52–59], a vacuum arc plasma source is used to form the carbon film. In the FCA technique used by Gupta and Bhushan [12], energetic carbon ions are

**Table 17.1** Summary of common deposition techniques, the kinetic energies of the depositing species and deposition rates

Deposition technique	Process	Kinetic energy (eV)	Deposition rate (nm/s)
Filtered cathodic arc (FCA)	Energetic carbon ions produced by a vacuum arc discharge between a graphite cathode and a grounded anode	100–2,500	0.1–1
Direct ion beam (IB)	Carbon ions produced from methane gas in an ion source and accelerated toward a substrate	50–500	0.1–1
Plasma-enhanced chemical vapor deposition (PECVD)	Hydrocarbon species produced by plasma decomposition of a hydrocarbon gas (such as acetylene) are accelerated toward a DC-biased substrate	1–30	1–10
Electron cyclotron resonance plasma chemical vapor deposition (ECR-CVD)	Hydrocarbon ions produced by the plasma decomposition of ethylene gas in the presence of a plasma at the electron cyclotron resonance condition are accelerated toward a RF-biased substrate	1–50	1–10
DC/RF sputtering	Sputtering of graphite target by argon ion plasma	1–10	1–10

produced by a vacuum arc discharge between a planar graphite cathode and a grounded anode (Fig. 17.4a). The cathode is a 6 mm diameter high-density graphite disk mounted on a water-cooled copper block. The arc is driven at an arc current of 200 A, with an arc duration of 5 ms and an arc repetition rate of 1 Hz. The plasma beam is guided by a magnetic field that transports current between the electrodes to form tiny, rapidly moving spots on the cathode surface. The source is coupled to a 90° bent magnetic filter to remove the macroparticles produced concurrently with the plasma in the cathode spots. The ion current density at the substrate is in the range of 10–50 mA/cm<sup>2</sup>. The base pressure is less than 10<sup>−4</sup> Pa. A much higher plasma density is achieved using a powerful arc discharge than using electron beam evaporation with auxiliary discharge. In the discharge process, the cathodic material suffers a complicated transition from the solid phase to an expanding, nonequilibrium plasma via liquid and dense equilibrium nonideal plasma phases [58]. The carbon ions in the vacuum arc plasma have a direct kinetic energy of 20–30 eV. The high voltage pulses are applied to the substrate which is mounted on a water-cooled sample holder, and ions are accelerated through the sheath and arrive at the substrate with an additional energy given by the potential difference between the plasma and the substrate. The substrate holder is pulsed-biased to a voltage of up to −2 kV with a pulse duration of 1 μs. The negative biasing of −2 kV corresponds to a kinetic energy of 2 keV for the carbon ions. The use of a pulsed bias instead of a DC bias enables much higher voltages to be applied and it permits a surface potential to be created on nonconducting films. The ion energy is varied during

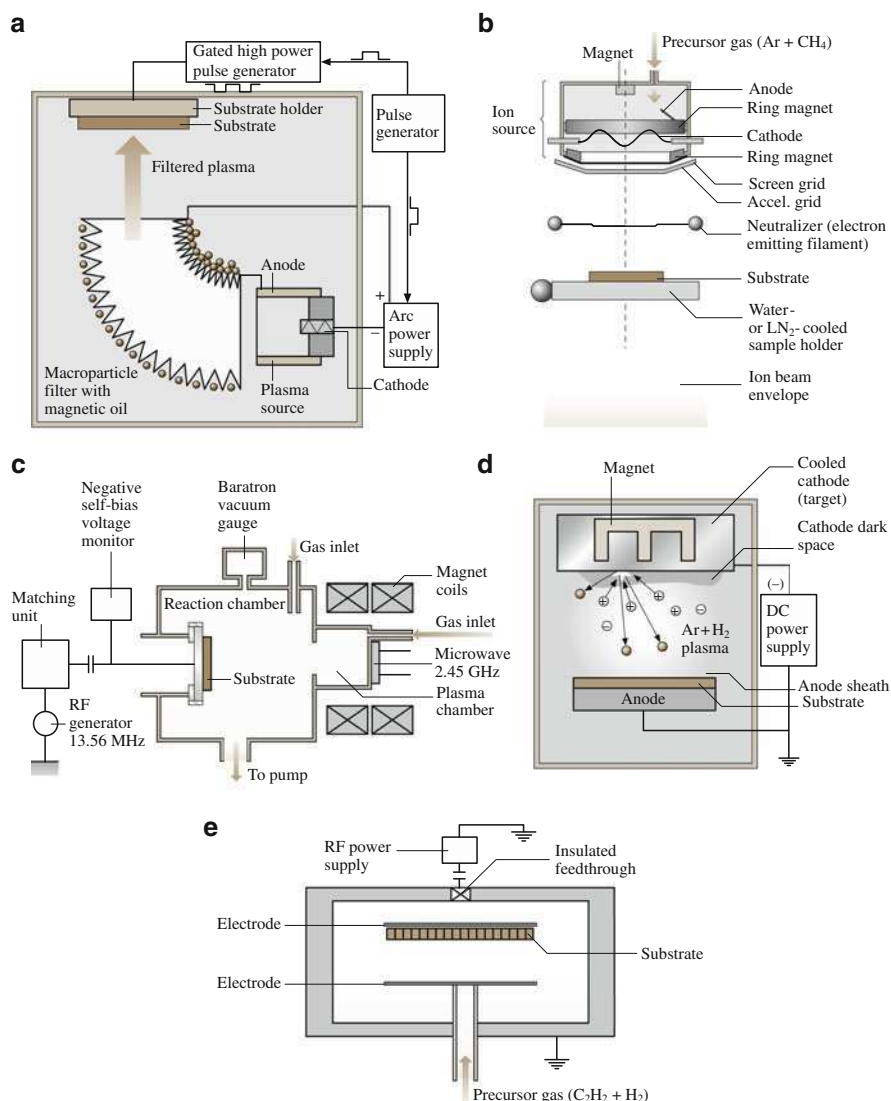


**Fig. 17.4** Schematic diagrams of deposition by (a) filtered cathodic arc deposition, (b) ion beam deposition, (c) electron cyclotron resonance chemical vapor deposition (ECR-CVD), (d) DC planar magnetron sputtering, and (e) plasma-enhanced chemical vapor deposition (PECVD)

the deposition. For the first 10% of the deposition, the substrates are pulsed-biased to  $-2$  keV with a pulse duty cycle of 25%, so for 25% of the time the energy is 2 keV and for the remaining 75% it is 20 eV, which is the *natural* energy of carbon ions in a vacuum discharge. For the last 90% of the deposition, the pulsed-biased voltage is reduced to  $-200$  eV with a pulsed bias duty cycle of 25%, so the energy is 200 eV for 25% and 20 eV for 75% of the deposition. The high energy at the

beginning leads to good intermixing and adhesion of the films, whereas the lower energy at the later stage leads to hard films. Under the conditions described, the deposition rate at the substrate is about 0.1 nm/s, which is slow. Compared with most gaseous plasma, the cathodic arc plasma is almost fully ionized, and the ionized carbon atoms have high kinetic energies which promotes the formation of a high fraction of  $sp^3$ -bonded carbon ions, which in turn results in high hardness and higher interfacial adhesion. Cuomo et al. [42] have reported, based on electron energy loss spectroscopy (EELS) analysis, that the  $sp^3$ -bonded carbon fraction of a cathodic arc coating is 83% compared to 38% for ion beam sputtered carbon. These coatings are reported to be *nonhydrogenated*.

This technique does not require an adhesion underlayer for nonsilicon substrates. However, adhesion of the DLC coatings on the electrically insulating substrate is poor, as negative pulsed biasing forms an electrical sheath that accelerates depositing ions to the substrate and enhances the adhesion of the coating to the substrate with associated ion implantation. It is difficult to build potential on an insulating substrate, and lack of biasing results in poor adhesion.

### 17.1.2 Ion Beam Deposition

In the direct ion beam deposition of a carbon coating [60–64], as used by Gupta and Bhushan [12], the carbon coating is deposited from an accelerated carbon ion beam. The sample is precleaned by ion etching. In the case of nonsilicon substrates, a 2–3 nm thick amorphous silicon adhesion layer is deposited by ion beam sputtering using an ion beam containing a mixture of methane and argon at 200 V. For the carbon deposition, the chamber is pumped to about  $10^{-4}$  Pa, and methane gas is fed through the cylindrical ion source and ionized by energetic electrons produced by a hot-wire filament (Fig. 17.4b). Ionized species then pass through a grid with a bias voltage of about 50 eV, where they gain a high acceleration energy and reach a hot-wire filament, emitting thermionic electrons that neutralize the incoming ions. The discharging of ions is important when insulating ceramics are used as substrates. The species are then deposited on a water-cooled substrate. Operating conditions are adjusted to give an ion beam with an acceleration energy of about 200 eV and a current density of about 1 mA/cm<sup>2</sup>. At these operating conditions, the deposition rate is about 0.1 nm/s, which is slow. Incidentally, tough and soft coatings are deposited at a high acceleration energy of about 400 eV and at a deposition rate of about 1 nm/s. The ion beam-deposited carbon coatings are reported to be hydrogenated (30–40at.% hydrogen).

### 17.1.3 Electron Cyclotron Resonance Chemical Vapor Deposition

The lack of electrodes in the ECR-CVD technique and its ability to create high densities of charged and excited species at low pressures ( $\leq 10^{-4}$  Torr) make it



attractive for coating deposition [65]. In the ECR-CVD carbon deposition process described by Suzuki and Okada [66] and used by Li and Bhushan [48, 49] and Sundararajan and Bhushan [50], microwave power is generated by a magnetron operating in continuous mode at a frequency of 2.45 GHz (Fig. 17.4c). The plasma chamber functions as a microwave cavity resonator. The magnetic coils arranged around the plasma chamber generate a magnetic field of 875 G, necessary for electron cyclotron resonance. The substrate is placed on a stage that is connected capacitively to a 13.56 MHz RF generator. The process gas is introduced into the plasma chamber and the hydrocarbon ions generated are accelerated by a negative self-bias voltage, which is generated by applying RF power to the substrate. Both the substrate stage and the plasma chamber are water-cooled. The process gas used is 100% ethylene and its flow rate is held constant at 100 sccm. The microwave power is 100–900 W. The RF power is 30–120 W. The pressure during deposition is kept close to the optimum value of  $5.5 \times 10^{-3}$  Torr. Before the deposition, the substrates are cleaned using Ar ions generated in the ECR plasma chamber.

#### ***17.1.4 Sputtering Deposition***

In DC planar magnetron carbon sputtering [13, 33, 37, 40, 67–71], the carbon coating is deposited by the sputtering of a graphite target with Ar ion plasma. In the glow discharge, positive ions from the plasma strike the target with sufficient energy to dislodge the atoms by momentum transfer, which are intercepted by the substrate. An  $\approx 5$  nm thick amorphous silicon adhesion layer is initially deposited by sputtering if the deposition is to be carried out on a nonsilicon surface. In the process used by Gupta and Bhushan [12], the coating is deposited by the sputtering of a 200 mm diameter graphite target with Ar ion plasma at 300 W power and a pressure of about 0.5 Pa (6 mTorr) (Fig. 17.4d). Plasma is generated by applying a DC potential between the substrate and a target. Bhushan et al. [35] reported that the sputtered carbon coating contains about 35 at.% hydrogen. The hydrogen comes from the hydrocarbon contaminants present in the deposition chamber. In order to produce a hydrogenated carbon coating with a larger concentration of hydrogen, the deposition is carried out in Ar and hydrogen plasma.

#### ***17.1.5 Plasma-Enhanced Chemical Vapor Deposition***

In the RF-PECVD deposition of carbon, as used by Gupta and Bhushan [12], the carbon coating is deposited by adsorbing hydrocarbon free radicals onto the substrate and then via chemical bonding to other atoms on the surface. The hydrocarbon species are produced by the RF plasma decomposition of hydrocarbon precursors such as acetylene ( $C_2H_2$ ), Fig. 17.4e [27, 69, 72–75]. Instead of requiring thermal energy, as in thermal CVD, the energetic electrons in the plasma (at



a pressure of  $1\text{--}5 \times 10^2$  Pa, and typically less than 10 Pa) can activate almost any reaction among the gases in the glow discharge at relatively a low substrate temperature of  $100\text{--}600^\circ\text{C}$  (typically less than  $300^\circ\text{C}$ ). To deposit the coating on nonsilicon substrates, an amorphous silicon adhesion layer about 4 nm thick is first deposited under similar conditions from a gas mixture of 1% silane in argon in order to improve adhesion [76]. In the process used by Gupta and Bhushan [12], the plasma is sustained in a parallel-plate geometry by a capacitive discharge at 13.56 MHz, at a surface power density of around  $100\text{ mW/cm}^2$ . The deposition is performed at a flow rate on the order of 6 sccm and a pressure on the order of 4 Pa (30 mTorr) on a cathode-mounted substrate maintained at a substrate temperature of  $180^\circ\text{C}$ . The cathode bias is held fixed at about  $-120\text{ V}$  with an external DC power supply attached to the substrate (powered electrode). The carbon coatings deposited by PECVD usually contain hydrogen at levels of up to 50% [35, 77].

## 17.2 Chemical and Physical Coating Characterization

The chemical structures and properties of amorphous carbon coatings depend on the deposition conditions employed when they are formed. It is important to understand the relationship between the chemical structure of a coating and its properties since it allows useful deposition parameters to be defined. Amorphous carbon films are metastable phases formed when carbon particles are condensed on a substrate. The prevailing atomic arrangement in the DLC coatings is amorphous or quasi-amorphous, with small diamond ( $sp^3$ ), graphite ( $sp^2$ ) and other unidentifiable micro- or nanocrystallites. The coating is dependent upon the deposition process and the deposition conditions used because these influence the  $sp^3/sp^2$  ratio and the proportion of hydrogen in the coating. The  $sp^3/sp^2$  ratios of DLC coatings typically range from 50% to close to 100%, and hardness increases with the  $sp^3/sp^2$  ratio. Most DLC coatings, except those produced by a filtered cathodic arc, contain from a few to about 50% *at.* hydrogen. Sometimes hydrogen and nitrogen are deliberately added to produce hydrogenated (a-C:H) and nitrogenated amorphous carbon (a-C:N) coatings, respectively. Hydrogen helps to stabilize  $sp^3$  sites (most of the carbon atoms attached to hydrogen have a tetrahedral structure), so the  $sp^3/sp^2$  ratio for hydrogenated carbon is higher [30]. The optimum  $sp^3/sp^2$  ratio for a random covalent network composed of  $sp^3$  and  $sp^2$  carbon sites ( $N_{sp^2}$  and  $N_{sp^3}$ ) and hydrogen is [30]

$$\frac{N_{sp^3}}{N_{sp^2}} = \frac{6X_H - 1}{8 - 13X_H}, \quad (17.1)$$

where  $X_H$  is the atomic fraction of hydrogen. The hydrogenated carbon has a larger optical band gap, higher electrical resistivity (semiconductor), and a lower optical absorption or high optical transmission. Hydrogenated coatings have lower

densities, probably because of the reduced cross-linking due to hydrogen incorporation. However, the hardness decreases with increasing hydrogen, even though the proportion of  $sp^3$  sites increases (that is, as the local bonding environment becomes more diamondlike) [78, 79]. It is speculated that the high hydrogen content introduces frequent terminations in the otherwise strong 3-D network, and hydrogen increases the soft polymeric component of the structure more than it enhances the cross-linking  $sp^3$  fraction.

A number of investigations have been performed to identify the microstructure of amorphous carbon films using a variety of techniques, such as Raman spectroscopy, EELS, nuclear magnetic resonance, optical measurements, transmission electron microscopy, and x-ray photoelectron spectroscopy [33]. The structure of diamondlike amorphous carbon is amorphous or quasi-amorphous, with small graphitic ( $sp^2$ ), tetrahedrally coordinated ( $sp^3$ ) and other types of nanocrystallites (typically on the order of a couple of nm in size, randomly oriented) [33, 80, 81]. These studies indicate that the chemical structure and physical properties of the coatings are quite variable, depending on the deposition techniques and film growth conditions. It is clear that both  $sp^2$ - and  $sp^3$ -bonded atomic sites are incorporated in diamondlike amorphous carbon coatings and that the physical and chemical properties of the coatings depend strongly on their chemical bonding and microstructures. Systematic studies have been conducted to carry out chemical characterization and to investigate how the physical and chemical properties of amorphous carbon coatings vary as a function of deposition conditions [33, 35, 40]. EELS and Raman spectroscopy are commonly used to characterize the chemical bonding and microstructure. The hydrogen concentration in the coating is obtained via forward recoil spectrometry (FRS). A variety of physical properties relevant to tribological performance are measured.

In order to give the reader a feel for typical data obtained when characterizing amorphous carbon coatings and their relationships to physical properties, we present data on several sputtered coatings, RF-PECVD amorphous carbon and microwave-PECVD (MPECVD) diamond coatings [33, 35, 40]. The sputtered coatings were DC magnetron sputtered at a chamber pressure of 10 mTorr under sputtering power densities of 0.1 and 2.1 W/cm<sup>2</sup> (labeled as coatings W1 and W2, respectively) in a pure Ar plasma. These coatings were prepared at a power density of 2.1 W/cm<sup>2</sup> with various hydrogen fractions (0.5, 1, 3, 5, 7 and 10%) of Ar/H; the gas mixtures were labeled as H1, H2, H3, H4, H5, and H6, respectively.

### 17.2.1 EELS and Raman Spectroscopy

EELS and Raman spectra of four sputtered (W1, W2, H1, and H3) carbon samples and one PECVD carbon sample were obtained. Figure 17.5 shows the EELS spectra of these carbon coatings. EELS spectra (up to 50 eV) for bulk diamond and polycrystalline graphite are also shown in Fig. 17.5. One prominent peak is seen

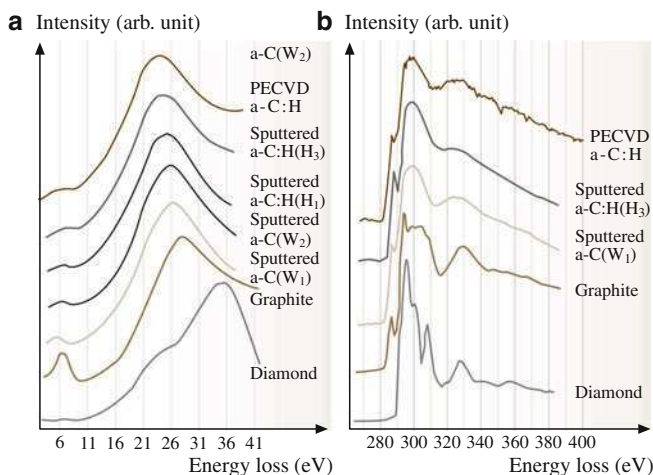


**Fig. 17.5** (a) Low-energy and (b) high-energy EELS of DLC coatings produced by the DC magnetron sputtering and RF-PECVD techniques. Data for bulk diamond and polycrystalline graphite are included for comparison [35]

at 35 eV in diamond, while two peaks are seen at 27 eV and 6.5 eV in graphite, which are called the  $(\pi + \sigma)$  and  $(\pi)$  peaks, respectively. These peaks are produced by the loss of transmitted electron energy to plasmon oscillations of the valence electrons. The  $\pi + \sigma$  peak in each coating is positioned at a lower energy region than that of graphite. The  $\pi$  peaks in the W series and PECVD samples also occur at a lower energy region than that of the graphite. However, the  $\pi$  peaks in the H-series are comparable to or higher than those of graphite (Table 17.2). The plasmon oscillation frequency is proportional to the square root of the corresponding electron density to a first approximation. Therefore, the samples in the H-series most likely have a higher density of  $\pi$  electrons than the other samples.

Amorphous carbon coatings contain (mainly) a mixture of  $sp^2$ - and  $sp^3$ -bonds, even though there is some evidence for the presence of  $sp$ -bonds as well [82]. The PECVD coatings and the H-series coatings in this study have almost the same mass density (as seen in Table 17.4, discussed in more detail later), but the former have a lower concentration of hydrogen (18.1%) than the H-series (35–39%) (as seen in Table 17.3, also discussed in more detail later). The relatively low-energy positions of the  $\pi$  peaks of the PECVD coatings compared to those of the H-series indicates that the PECVD coatings contain a higher fraction of  $sp^3$ -bonds than the sputtered hydrogenated carbon coatings (H-series).

Figure 17.5b shows EELS spectra associated with the inner-shell (K-shell) ionization. Again, the spectra for diamond and polycrystalline graphite are included for comparison. Sharp peaks are observed at 285.5 eV and 292.5 eV in graphite, while no peak is seen at 285.5 eV in diamond. The general features of the K-shell EELS spectra for the sputtered and PECVD carbon samples resemble those of graphite, but with the higher energy features smeared. The peak at 285.5 eV in the

**Table 17.2** Experimental results from EELS and Raman spectroscopy [35]

Sample	EELS peak position		Raman peak position		Raman FWHM <sup>a</sup>		$I_D/I_G$ <sup>d</sup>
	$\pi$ (eV)	$\pi + \sigma$ (eV)	G-band <sup>b</sup> (cm <sup>-1</sup> )	D-band <sup>c</sup> (cm <sup>-1</sup> )	G-band (cm <sup>-1</sup> )	D-band (cm <sup>-1</sup> )	
Sputtered a-C coating (W1)	5.0	24.6	1,541	1,368	105	254	2.0
Sputtered a-C coating (W2)	6.1	24.7	1,560	1,379	147	394	5.3
Sputtered a-C:H coating (H1)	6.3	23.3	1,542	1,334	95	187	1.6
Sputtered a-C:H coating (H3)	6.7	22.4	e	e	e	e	e
PECVD a-C:H coating	5.8	24.0	1,533	1,341	157	427	1.5
Diamond coating	–	–	1,525 <sup>f</sup>	1,333 <sup>g</sup>	–	8 <sup>g</sup>	–
Graphite (for reference)	6.4	27.0	1,580	1,358	37	47	0.7
Diamond (for reference)	–	37.0	–	1,332 <sup>g</sup>	–	2 <sup>g</sup>	–

<sup>a</sup>Full width at half maximum<sup>b</sup>Peak associated with  $sp^2$  graphite carbon<sup>c</sup>Peak associated with  $sp^2$  disordered carbon (not  $sp^3$ -bonded carbon)<sup>d</sup>Intensity ratio of the D-band to the G-band<sup>e</sup>Fluorescence<sup>f</sup>Includes D- and G-band, signal too weak to analyze<sup>g</sup>Peak position and width for diamond phonon**Table 17.3** Experimental results of FRS analysis [35]

Sample	Ar/H ratio	C (at.% ± 0.5)	H (at.% ± 0.5)	Ar (at.% ± 0.5)	O (at.% ± 0.5)
Sputtered a-C coating (W2)	100/0	90.5	9.3	0.2	–
Sputtered a-C:H coating (H2)	99/1	63.9	35.5	0.6	–
Sputtered a-C:H coating (H3)	97/3	56.1	36.5	–	7.4
Sputtered a-C:H coating (H4)	95/5	53.4	39.4	–	7.2
Sputtered a-C:H coating (H5)	93/7	58.2	35.4	0.2	6.2
Sputtered a-C:H coating (H6)	90/10	57.3	35.5	–	7.2
PECVD a-C:H coating	99.5% CH <sub>4</sub>	81.9	18.1	–	–
Diamond coating	H <sub>2</sub> -1 mol % CH <sub>4</sub>	94.0	6.0	–	–

sputtered and PECVD coatings also indicates the presence of  $sp^2$ -bonded atomic sites in the coatings. All of these spectra peak at 292.5 eV, similar to the spectra of graphite, but the peak in graphite is sharper.

Raman spectra from samples W1, W2, H1 and PECVD are shown in Fig. 17.6. Raman spectra could not be observed in specimens H2 and H3 due to high fluorescence signals. The Raman spectra of single-crystal diamond and polycrystalline graphite are also shown for comparison in Fig. 17.6. The results from the spectral fits are summarized in Table 17.2. We will focus on the position of the

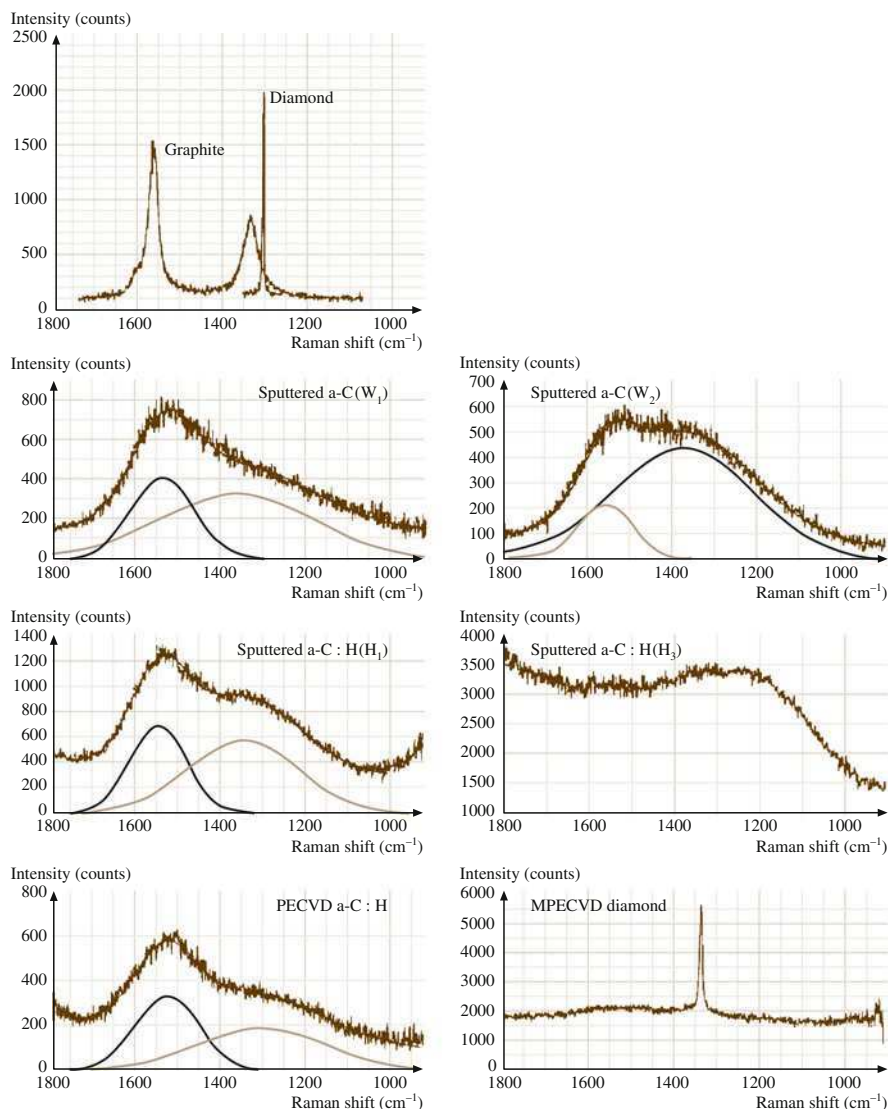


**Fig. 17.6** Raman spectra of the DLC coatings produced by DC magnetron sputtering and RF-PECVD techniques and a diamond film produced by the MPE-CVD technique. Data for bulk diamond and microcrystalline graphite are included for comparison [35]

G-band, which has been shown to be related to the fraction of  $sp^3$ -bonded sites. Increasing the power density in the amorphous carbon coatings (W1 and W2) results in a higher G-band frequency, implying a smaller fraction of  $sp^3$ -bonding in W2 than in W1. H1 and PEVCD have even lower G-band positions than W1, implying an even higher fraction of  $sp^3$ -bonding, which is presumably caused by the incorporation of H atoms into the lattice. The high hardness of H3 might be attributed to efficient  $sp^3$  cross-linking of small  $sp^2$ -ordered domains.

The Raman spectrum of a MPECVD diamond coating is shown in Fig. 17.6. The Raman peak of diamond is at  $1,333\text{ cm}^{-1}$ , with a line width of  $7.9\text{ cm}^{-1}$ . There is a small broad peak at around  $1,525\text{ cm}^{-1}$ , which is attributed to a small amount of a-C:H. This impurity peak is not intense enough to be able to separate the G- and D-bands. The diamond peak frequency is very close to that of natural diamond ( $1,332.5\text{ cm}^{-1}$ , see Fig. 17.6), indicating that the coating is not under stress [83]. The large line width compared to that of natural diamond ( $2\text{ cm}^{-1}$ ) indicates that the microcrystallites probably have a high concentration of defects [84].

## 17.2.2 Hydrogen Concentrations

A FRS analysis of six sputtered (W2, H2, H3, H4, H5, and H6) coatings, one PECVD coating, and one diamond coating was performed. Figure 17.7 shows an overlay of the spectra from the six sputtered samples. Similar spectra were obtained from the PECVD and the diamond films. Table 17.3 shows the H and C fractions as well as the amount of impurities (Ar and O) in the films in atomic %. Most apparent is the large fraction of H in the sputtered films. Regardless of how much  $\text{H}_2$  is in the Ar sputtering gas, the H content of the coatings is about the same,  $\approx 35\text{ at.}\%$ .

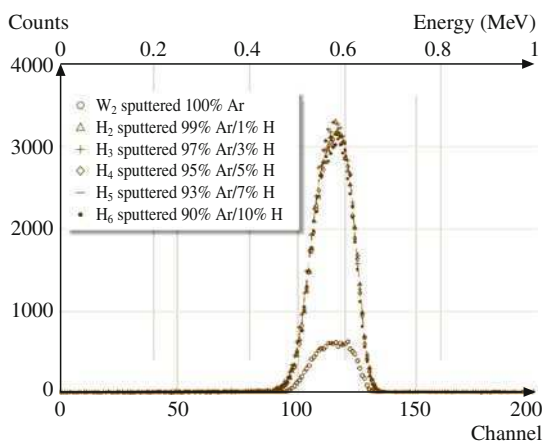


**Fig. 17.7** FRS spectra for six DLC coatings produced by DC magnetron sputtering [35]

Interestingly, there is still  $\approx 10\%$  H present in the coating sputtered in pure Ar (W2). It is interesting to note that Ar is present only in coatings grown using Ar carrier gas with a low ( $<1\%$ ) H content. The presence of O in the coatings combined with the fact that the coatings were prepared approximately nine months before the FRS analysis caused suspicion that they had absorbed water vapor, and that this may be the cause of the H peak in specimen W2.

All samples were annealed for 24 h at  $250^\circ\text{C}$  in a flowing He furnace and then reanalyzed. Surprisingly, the H contents of all coatings measured increased slightly, even though the O content decreased, and W2 still had a substantial amount of  $\text{H}_2$ . This slight increase in H concentration is not understood. However, the fact that the H concentration did not decrease with the oxygen as a result of annealing suggests that high H concentration is not due to adsorbed water vapor. The PECVD film has more H ( $\approx 18\%$ ) than the sputtered films initially, but after annealing it has the same fraction as specimen W2, the film sputtered in pure Ar. The diamond film has the smallest amount of hydrogen, as seen in Table 17.3.

### 17.2.3 Physical Properties

The physical properties of the four sputtered (W1, W2, H1, and H3) coatings, one PECVD coating, one diamond coating, and bulk diamond and graphite are presented in Table 17.4. The hydrogenated carbon and the diamond coatings have very high resistivity compared to unhydrogenated carbon coatings. It appears that

**Table 17.4** Experimental results of physical properties [35]

Sample	Mass density ( $\text{g}/\text{cm}^3$ )	Nano-hardness (GPa)	Elastic modulus (GPa)	Electrical resistivity ( $\Omega\text{ cm}$ )	Compressive residual stress (GPa)
Sputtered a-C coating (W1)	2.1	15	141	1,300	0.55
Sputtered a-C:H coating (W2)	1.8	14	136	0.61	0.57
Sputtered a-C:H coating (H1)	—	14	96	—	$> 2$
Sputtered a-C:H coating (H3)	1.7	7	35	$> 10^6$	0.3
PECVD a-C:H coating	1.6–1.8	33–35	$\approx 200$	$> 10^6$	1.5–3.0
Diamond coating	—	40–75	370–430	—	—
Graphite (for reference)	2.267	Soft	9–15	$5 \times 10^{-5a}$ , $4 \times 10^{-3b}$	0
Diamond (for reference)	3.515	70–102	900–1,050	$10^7$ – $10^{20}$	0

<sup>a</sup>Parallel to layer planes

<sup>b</sup>Perpendicular to layer planes

unhydrogenated carbon coatings have higher densities than hydrogenated carbon coatings, although both groups are less dense than graphite. The density depends upon the deposition technique and the deposition parameters. It appears that unhydrogenated sputtered coatings deposited at low power exhibit the highest density. The nanohardness of hydrogenated carbon is somewhat lower than that of unhydrogenated carbon. PECVD coatings are significantly harder than sputtered coatings. The nanohardness and modulus of elasticity of a diamond coating is very high compared to that of a DLC coating, even though the hydrogen contents are similar. The compressive residual stresses of the PECVD coatings are substantially higher than those of sputtered coatings, which is consistent with the results for the hardness.

Figure 17.8a shows the effect of hydrogen in the plasma on the residual stresses and the nanohardness for the sputtered coatings W2 and H1 to H6. The coatings made with a hydrogen flow of between 0.5 and 1.0% delaminate very quickly, even when they are only a few tens of nm thick. In pure Ar and at  $H_2$  flows that are greater than 1%, the coatings appear to be more adhesive. The tendency of some coatings to delaminate can be caused by intrinsic stress in the coating, which is measured by substrate bending. All of the coatings in the figure are in compressive stress. The maximum stress occurs between 0 and 1%  $H_2$  flow, but the stress cannot be quantified in this range because the coatings instantly delaminate upon exposure to air. At higher hydrogen concentrations the stress gradually

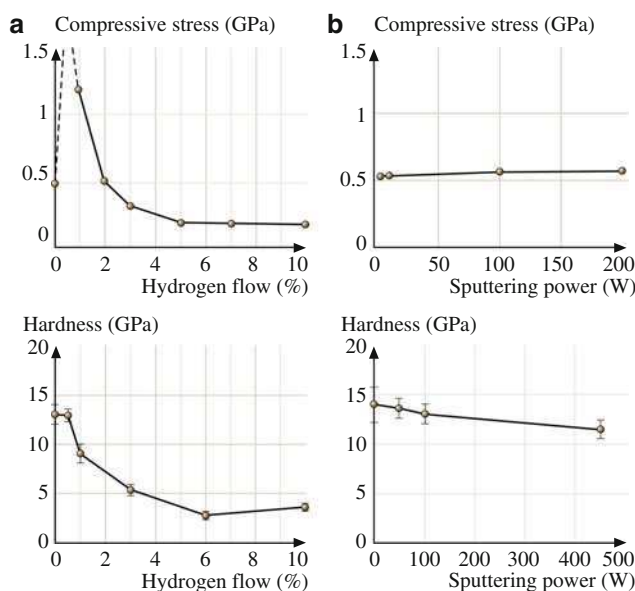


**Fig. 17.8** Residual compressive stresses and nanohardness (a) as a function of hydrogen flow rate, where the sputtering power is 100 W and the target diameter is 75 mm (power density =  $2.1 \text{ W/cm}^2$ ), and (b) as a function of sputtering power over a 75 mm diameter target with no hydrogen added to the plasma [40]



diminishes. A generally decreasing trend is observed for the hardness of the coatings as the hydrogen content is increased. The hardness decreases slightly, going from 0% H<sub>2</sub> to 0.5% H<sub>2</sub>, and then decreases sharply. These results are probably lower than the true values because of local delamination around the indentation point. This is especially likely for the 0.5% and 1.0% coatings, where delamination is visually apparent, but may also be true to a lesser extent for the other coatings. Such an adjustment would bring the hardness profile into closer correlation with the stress profile. Weissmantel et al. [68] and Scharff et al. [85] observed a downturn in hardness for high bias and a low hydrocarbon gas pressure for ion-plated carbon coating, and, therefore, presumably low hydrogen content in support of the above contention.

Figure 17.8b shows the effect of sputtering power (with no hydrogen added to the plasma) on the residual stresses and nanohardness for various sputtered coatings. As the power decreases, the compressive stress does not seem to change while the nanohardness slowly increases. The rate of change becomes more rapid at very low power levels.

The addition of H<sub>2</sub> during sputtering of the carbon coatings increases the H concentration in the coating. Hydrogen causes the character of the C–C bonds to shift from  $sp^2$  to  $sp^3$ , and a rise in the number of C–H bonds, which ultimately relieves stress and produces a softer *polymerlike* material. Low power deposition, like the presence of hydrogen, appears to stabilize the formation of  $sp^3$  C–C bonds, increasing hardness. These coatings relieve stress and lead to better adhesion. Increasing the temperature during deposition at high power density results in graphitization of the coating material, producing a decrease in hardness with an increase in power density. Unfortunately, low power also means impractically low deposition rates.

#### 17.2.4 Summary

Based on analyses of EELS and Raman data, it is clear that all DLC coatings have both  $sp^2$  and  $sp^3$  bonding characteristics. The  $sp^2/sp^3$  bonding ratio depends upon the deposition technique and parameters used. DLC coatings deposited by sputtering and PECVD contain significant concentrations of hydrogen, while diamond coatings contain only small amounts of hydrogen impurities. Sputtered coatings with no deliberate addition of hydrogen in the plasma contain a significant amount of hydrogen. Regardless of how much hydrogen is in the Ar sputtering gas, the hydrogen content of the coatings increases initially but then does not increase further.

Hydrogen flow and sputtering power density affect the mechanical properties of these coatings. Maximum compressive residual stress and hardness occur between 0 and 1% hydrogen flow, resulting in rapid delamination. Low sputtering power moderately increases hardness and also relieves residual stress.

## 17.3 Micromechanical and Tribological Coating Characterization

### 17.3.1 *Micromechanical Characterization*

Common mechanical characterizations include measurements of hardness and elastic modulus, fracture toughness, fatigue life, and scratch and wear testing. Nanoindentation and atomic force microscopy (AFM) are used for the mechanical characterization of ultrathin films.

Hardness and elastic modulus are calculated from the load displacement data obtained by nanoindentation at loads of typically 0.2–10 mN using a commercially available nanoindenter [23, 86]. This instrument monitors and records the dynamic load and displacement of the three-sided pyramidal diamond (Berkovich) indenter during indentation. For fracture toughness measurements of ultrathin films 100 nm to a few  $\mu\text{m}$  thick, a nanoindentation-based technique is used in which through-thickness cracking in the coating is detected from a discontinuity observed in the load–displacement curve, and the energy released during the cracking is obtained from the curve [87–89]. Based on the energy released, fracture mechanics analysis is then used to calculate the fracture toughness. An indenter with a cube-corner tip geometry is preferred because the through-thickness cracking of hard films can be accomplished at lower loads. In fatigue measurement, a conical diamond indenter with a tip radius of about 1  $\mu\text{m}$  is used and load cycles with sinusoidal shapes are applied [90, 91]. The fatigue behavior of a coating is studied by monitoring the change in contact stiffness, which is sensitive to damage formation.

### Hardness and Elastic Modulus

For materials that undergo plastic deformation, high hardness and elastic modulus are generally needed for low friction and wear, whereas for brittle materials, high fracture toughness is needed [2, 3, 21]. The DLC coatings used for many applications are hard and brittle, and values of hardness and fracture toughness need to be optimized.

Representative load–displacement plots of indentations made at 0.2 mN peak indentation load on 100 nm thick DLC coatings deposited by the four deposition techniques on a single-crystal silicon substrate are compared in Fig. 17.9. The indentation depths at the peak load range from about 18 to 26 nm, smaller than that of the coating thickness. Many of the coatings exhibit a discontinuity or pop-in marks in the loading curve, which indicate a sudden penetration of the tip into the sample. A nonuniform penetration of the tip into a thin coating possibly results from formation of cracks in the coating, formation of cracks at the coating–substrate interface, or debonding or delamination of the coating from the substrate.

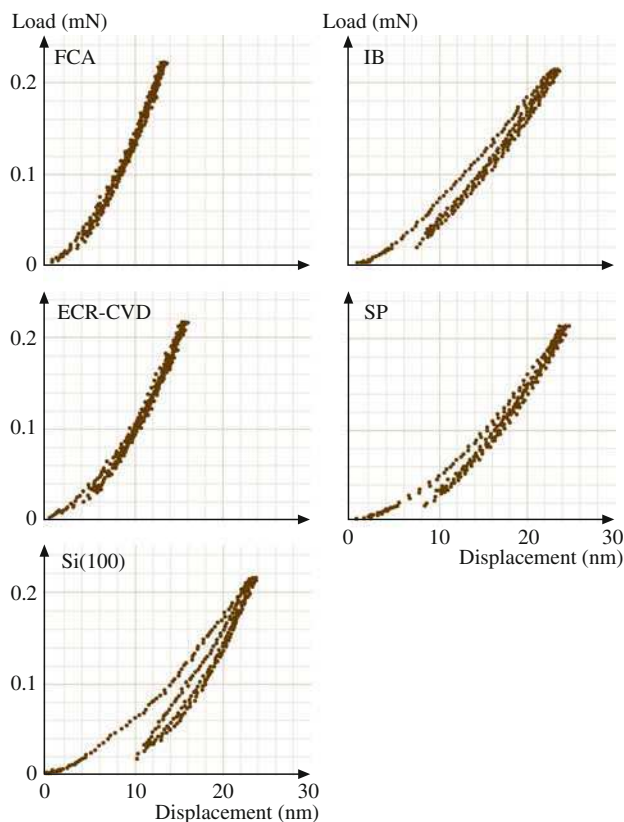


**Fig. 17.9** Load versus displacement plots for various 100 nm thick amorphous carbon coatings on single-crystal silicon substrate and bare substrate

The hardness and elastic modulus values for a peak load of 0.2 mN on the various coatings and single-crystal silicon substrate are summarized in Table 17.5 and Fig. 17.10 [47, 49, 89, 90]. Typical values for the peak and residual indentation depths range from 18 to 26 nm and 6 to 12 nm, respectively. The FCA coating exhibits the greatest hardness of 24 GPa and the highest elastic modulus of 280 GPa of the various coatings, followed by the ECR-CVD, IB and SP coatings. Hardness and elastic modulus have been known to vary over a wide range with the  $sp^3$ -to- $sp^2$  bonding ratio, which depends on the kinetic energy of the carbon species and the amount of hydrogen [6, 30, 47, 92, 93]. The high hardness and elastic modulus of the FCA coatings are attributed to the high kinetic energy of the carbon species involved in the FCA deposition [12, 47]. Anders et al. [57] also reported a high hardness, measured by nanoindentation, of about 45 GPa for cathodic arc carbon coatings. They observed a change in hardness from 25 to 45 GPa with a pulsed bias voltage and bias duty cycle. The high hardness of cathodic arc carbon was attributed to the high percentage (more than 50%) of  $sp^3$  bonding. Savvides and

**Table 17.5** Hardness, elastic modulus, fracture toughness, fatigue life, critical load during scratch, coefficient of friction during accelerated wear testing and residual stress for various DLC coatings on single-crystal silicon substrate

Coating	Hardness <sup>a</sup> [48] (GPa)	Elastic modulus <sup>a</sup> [48] (GPa)	Fracture toughness <sup>a</sup> [89] (MPa m <sup>1/2</sup> )	Fatigue life <sup>b</sup> $N_f^d \times 10^4$ [90]	Critical load during scratch <sup>b</sup> [48] (mN)	Coefficient of friction during accelerated wear testing <sup>b</sup> [48]	Compressive residual stress <sup>c</sup> [47] (GPa)
Cathodic arc carbon coating (a-C)	24	280	11.8	2.0	3.8	0.18	12.5
Ion beam carbon coating (a-C:H)	19	140	4.3	0.8	2.3	0.18	1.5
ECR-CVD carbon coating (a-C:H)	22	180	6.4	1.2	5.3	0.22	0.6
DC sputtered carbon coating (a-C:H)	15	140	2.8	0.2	1.1	0.32	2.0
Bulk graphite (for comparison)	Very soft	9–15	–	–	–	–	–
Diamond (for comparison)	80–104	900–1,050	–	–	–	–	–
Si(100) substrate	11	220	0.75	–	0.6	0.55	0.02

<sup>a</sup>Measured on 100 nm thick coatings

<sup>b</sup>Measured on 20 nm thick coatings

<sup>c</sup>Measured on 400 nm thick coatings

<sup>d</sup> $N_f$  was obtained for a mean load of 10  $\mu$ N and a load amplitude of 8  $\mu$ N

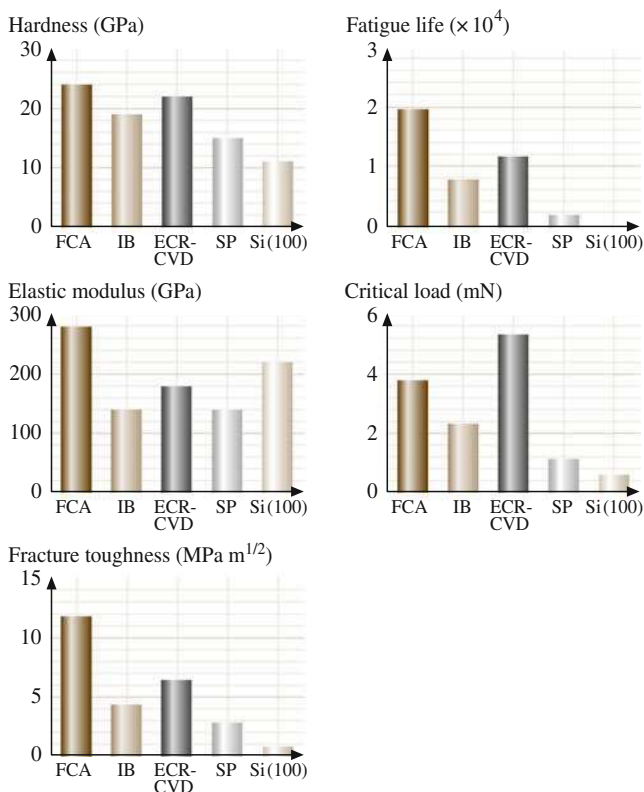


**Fig. 17.10** Bar charts summarizing data for various coatings and single-crystal silicon substrate. Hardnesses, elastic moduli, and fracture toughnesses were measured on 100 nm thick coatings, and fatigue lifetimes and critical loads during scratch were measured on 20 nm thick coatings

Bell [94] reported an increase in hardness from 12 to 30 GPa and an increase in elastic modulus from 62 to 213 GPa with an increase in the  $sp^3$ -to- $sp^2$  bonding ratio, from 3 to 6, for a C:H coating deposited by low-energy ion-assisted unbalanced magnetron sputtering of a graphite target in an Ar- $H_2$  mixture.

Bhushan et al. [35] reported hardnesses of about 15 and 35 GPa and elastic moduli of about 140 and 200 GPa, measured by nanoindentation, for a-C:H coatings deposited by DC magnetron sputtering and RF-plasma-enhanced chemical vapor deposition techniques, respectively. The high hardness of RF-PECVD a-C:H coatings is attributed to a higher concentration of  $sp^3$  bonding than in a sputtered hydrogenated a-C:H coating. Hydrogen is believed to play a crucial role in the bonding configuration of carbon atoms by helping to stabilize the tetrahedral coordination ( $sp^3$  bonding) of carbon species. Jansen et al. [78] suggested that the incorporation of hydrogen efficiently passivates the dangling bonds and saturates the graphitic bonding to some extent. However, a large concentration of hydrogen in the plasma in sputter deposition is undesirable. Cho et al. [33] and

Rubin et al. [40] observed that the hardness decreased from 15 to 3 GPa with increased hydrogen content. Bhushan and Doerner [95] reported a hardness of about 10–20 GPa and an elastic modulus of about 170 GPa, measured by nanoindentation, for 100 nm thick DC magnetron sputtered a-C:H on the silicon substrate.

Residual stresses measured using a well-known curvature measurement technique are also presented in Table 17.5. The DLC coatings are under significant compressive internal stresses. Very high compressive stresses in FCA coatings are believed to be partly responsible for their high hardness. However, high stresses result in coating delamination and buckling. For this reason, the coatings that are thicker than about 1  $\mu\text{m}$  have a tendency to delaminate from the substrates.

## Fracture Toughness

Representative load–displacement curves of indentations on 400 nm thick cathodic arc carbon coating on silicon for various peak loads are shown in Fig. 17.11. Steps are found in all of the curves, as shown by arrows in Fig. 17.11a. In the 30 mN SEM micrograph, in addition to several radial cracks, ring-like through-thickness cracking is observed with small lips of material overhanging the edge of indentation. The steps at about 23 mN in the loading curves of indentations made with 30 and 100 mN peak indentation loads result from the ring-like through-thickness cracking. The step at 175 mN in the loading curve of the indentation made with 200 mN peak indentation load is caused by spalling and second ring-like through-thickness cracking.

According to Li et al. [87], the fracture process progresses in three stages: (1) ring-like through-thickness cracks form around the indenter due to high stresses in the contact area, (2) delamination and buckling occur around the contact area at the coating–substrate interface due to high lateral pressure, and (3) second ring-like through-thickness cracks and spalling are generated by high bending stresses at the edges of the buckled coating (Fig. 17.12a). In the first stage, if the coating under the indenter is separated from the bulk coating via the first ring-like through-thickness cracking, a corresponding step will be present in the loading curve. If discontinuous cracks form and the coating under the indenter is not separated from the remaining coating, no step appears in the loading curve, because the coating still supports the indenter and the indenter cannot suddenly advance into the material. In the second stage, for the coating used in the present study, the advances of the indenter during the radial cracking delamination, and buckling are not big enough to form steps in the loading curve, because the coating around the indenter still supports the indenter, but they generate discontinuities that change the slope of the loading curve with increasing indentation load. In the third stage, the stress concentration at the end of the interfacial crack cannot be relaxed by the propagation of the interfacial crack. With an increase in indentation depth, the height of the bulged coating increases. When the height reaches a critical value, the bending stresses caused by the bulged coating around the indenter will result in second ring-like through-thickness crack formation and spalling at the edge of the buckled coating,

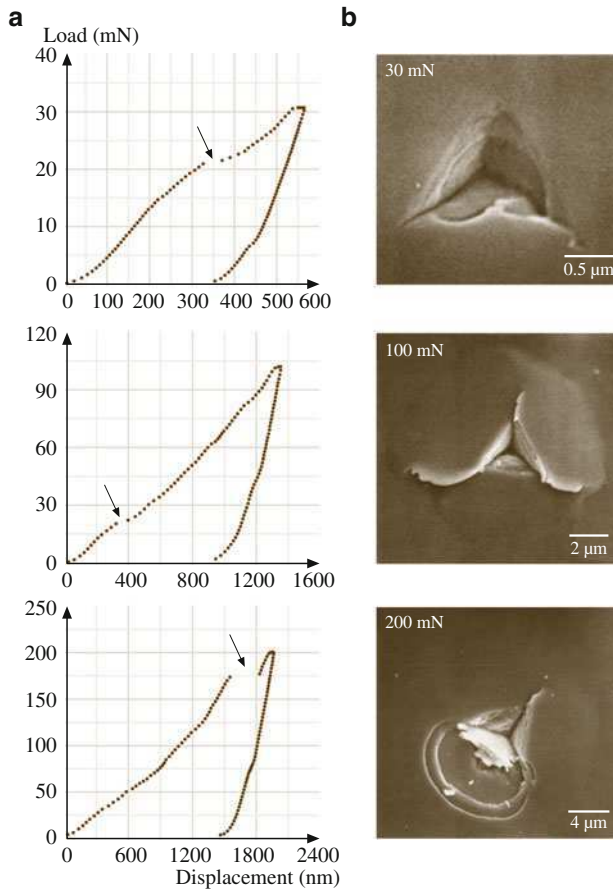
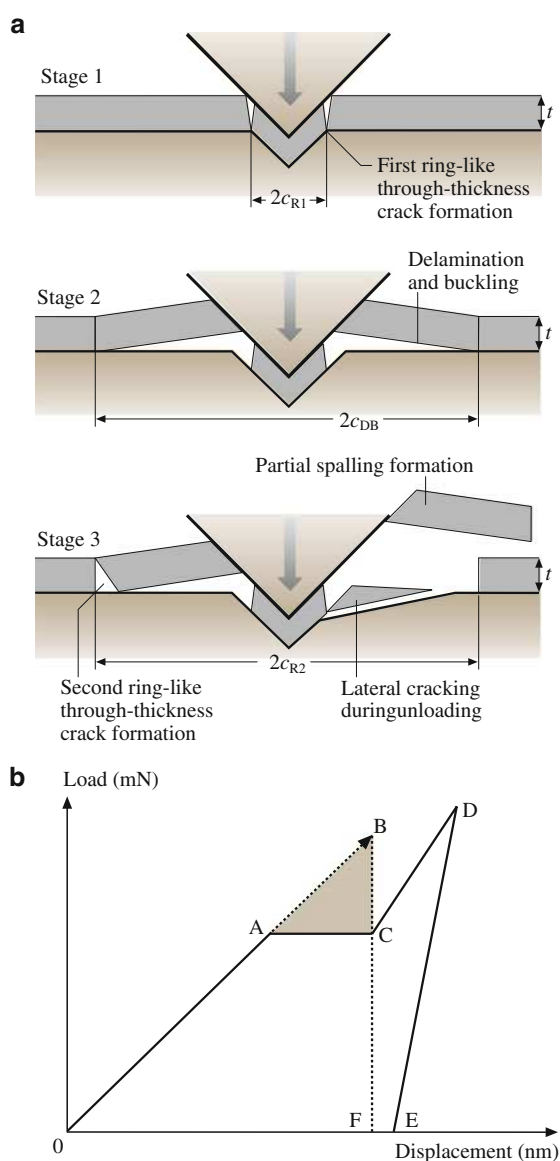


**Fig. 17.11** (a) Load–displacement curves of indentations made with 30, 100, and 200 mN peak indentation loads using the cube corner indenter, and (b) SEM micrographs of indentations on a 400 nm thick cathodic arc carbon coating on silicon. *Arrows* indicate steps during the loading portion of the load–displacement curve [87]

as shown in Fig. 17.12a, which leads to a step in the loading curve. This is a single event and it results in the separation of the part of the coating around the indenter from the bulk coating via cracking through coatings. The step in the loading curve results (completely) from the coating cracking and not from the interfacial cracking or the substrate cracking.

The area under the load–displacement curve is the work performed by the indenter during the elastic–plastic deformation of the coating/substrate system. The strain energy release in the first/second ring-like cracking and spalling can be calculated from the corresponding steps in the loading curve. Figure 17.12b shows a modeled load–displacement curve. OACD is the loading curve and DE is the unloading curve. The first ring-like through-thickness crack should be considered.

**Fig. 17.12** (a) Schematic of various stages in nanoindentation fracture for the coating/substrate system, and (b) schematic of a load–displacement curve showing a step during the loading cycle and the associated energy release



It should be emphasized that the edge of the buckled coating is far from the indenter and, therefore, it does not matter if the indentation depth exceeds the coating thickness, or if deformation of the substrate occurs around the indenter when we measure the fracture toughness of the coating from the energy released during the second ring-like through-thickness cracking (spalling). Suppose that the second ring-like through-thickness cracking occurs at AC. Now, let us consider the loading curve 0AC. If the second ring-like through-thickness crack does not occur, 0A will



extend to 0B to reach the same displacement as 0C. This means that crack formation changes the loading curve 0AB into 0AC. For point B, the elastic–plastic energy stored in the coating/substrate system should be 0BF. For point C, the elastic–plastic energy stored in the coating/substrate system should be 0ACF. Therefore, the energy difference before and after the crack generation is the area of ABC, so this energy stored in ABC will be released as strain energy, creating the ring-like through-thickness crack. According to the theoretical analysis by Li et al. [87], the fracture toughness of a thin film can be written as

$$K_{Ic} = \left[ \left( \frac{E}{(1 - \nu^2)2\pi C_R} \right) \left( \frac{U}{t} \right) \right]^{1/2}, \quad (17.2)$$

where  $E$  is the elastic modulus,  $\nu$  is the Poisson ratio,  $2\pi C_R$  is the crack length in the coating plane,  $t$  is the coating thickness, and  $U$  is the strain energy difference before and after cracking.

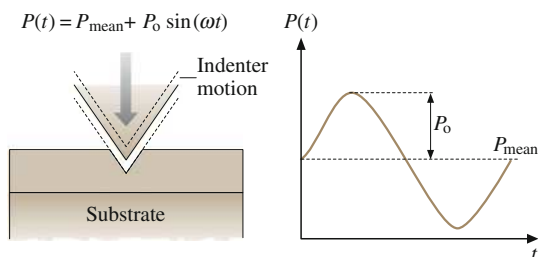
The fracture toughness of the coatings can be calculated using (17.2). The loading curve is extrapolated along the tangential direction of the loading curve from the starting point of the step up to reach the same displacement as the step. The area between the extrapolated line and the step is the estimated strain energy difference before and after cracking.  $C_R$  is measured from SEM micrographs or AFM images of indentations. The second ring-like crack is where the spalling occurs. For example, for the 400 nm thick cathodic arc carbon coating data presented in Fig. 17.11, the  $U$  value of 7.1 nN m is assessed from the steps in Fig. 17.11a at peak indentation loads of 200 mN. For a  $C_R$  value of 7.0  $\mu\text{m}$ , from Fig. 17.11b, with  $E = 300$  GPa (measured using a nanoindenter and an assumed value of 0.25 for  $\nu$ ), fracture toughness values are calculated as 10.9 MPa  $\sqrt{\text{m}}$  [87, 88]. The fracture toughness and related data for various 100 nm thick DLC coatings are presented in Fig. 17.10 and Table 17.5.

## Nanofatigue

Delayed fracture resulting from extended service is called fatigue [96]. Fatigue fracturing progresses through a material via changes within the material at the tip of a crack, where there is a high stress intensity. There are several situations: cyclic fatigue, stress corrosion and static fatigue. Cyclic fatigue results from cyclic loading of machine components. In a low-flying slider in a magnetic head-disk interface, isolated asperity contacts occur during use and the fatigue failure occurs in the multilayered thin film structure of the magnetic disk [13]. Impact occurs in many MEMS components and the failure mode is cyclic fatigue. Asperity contacts can be simulated using a sharp diamond tip in oscillating contact with the component.

Figure 17.13 shows the schematic of a fatigue test on a coating/substrate system using a continuous stiffness measurement (CSM) technique. Load cycles are applied to the coating, resulting in cyclic stress.  $P$  is the cyclic load,  $P_{\text{mean}}$  is the

**Fig. 17.13** Schematic of a fatigue test on a coating/substrate system using the continuous stiffness measurement technique



mean load,  $P_0$  is the oscillation load amplitude, and  $\omega$  is the oscillation frequency. The following results can be obtained: (1) endurance limit (the maximum load below which there is no coating failure for a preset number of cycles); (2) number of cycles at which the coating failure occurs; and (3) changes in contact stiffness (measured using the unloading slope of each cycle), which can be used to monitor the propagation of interfacial cracks during a cyclic fatigue process.

Figure 17.14a shows the contact stiffness as a function of the number of cycles for 20 nm thick FCA coatings cyclically deformed by various oscillation load amplitudes with a mean load of 10  $\mu\text{N}$  at a frequency of 45 Hz. At 4  $\mu\text{N}$  load amplitude, no change in contact stiffness was found for all coatings. This indicates that 4  $\mu\text{N}$  load amplitude is not high enough to damage the coatings. At 6  $\mu\text{N}$  load amplitude, an abrupt decrease in contact stiffness was found after a certain number of cycles for each coating, indicating that fatigue damage had occurred. With increasing load amplitude, the number of cycles to failure  $N_f$  decreases for all coatings. Load amplitude versus  $N_f$ , a so-called S–N curve, is plotted in Fig. 17.14b. The critical load amplitude below which no fatigue damage occurs (an endurance limit), was identified for each coating. This critical load amplitude, together with the mean load, are of critical importance to the design of head-disk interfaces or MEMS/NEMS device interfaces.

To compare the fatigue lives of the different coatings studied, the contact stiffness is shown as a function of the number of cycles for 20 nm thick FCA, IB, ECR-CVD and SP coatings cyclically deformed by an oscillation load amplitude of 8  $\mu\text{N}$  with a mean load of 10  $\mu\text{N}$  at a frequency of 45 Hz in Fig. 17.14c. The FCA coating has the largest  $N_f$ , followed by the ECR-CVD, IB and SP coatings. In addition, after  $N_f$ , the contact stiffness of the FCA coating shows a slower decrease than the other coatings. This indicates that the FCA coating was less damaged than the others after  $N_f$ . The fatigue behaviors of FCA and ECR-CVD coatings of different thicknesses are compared in Fig. 17.14d. For both coatings,  $N_f$  decreases with decreasing coating thickness. At 10 nm, FCA and ECR-CVD have almost the same fatigue life. At 5 nm, the ECR-CVD coating shows a slightly longer fatigue life than the FCA coating. This indicates that the microstructure and residual stresses are not uniform across the thickness direction, even for nanometer-thick DLC coatings. Thinner coatings are more influenced by interfacial stresses than thicker coatings.

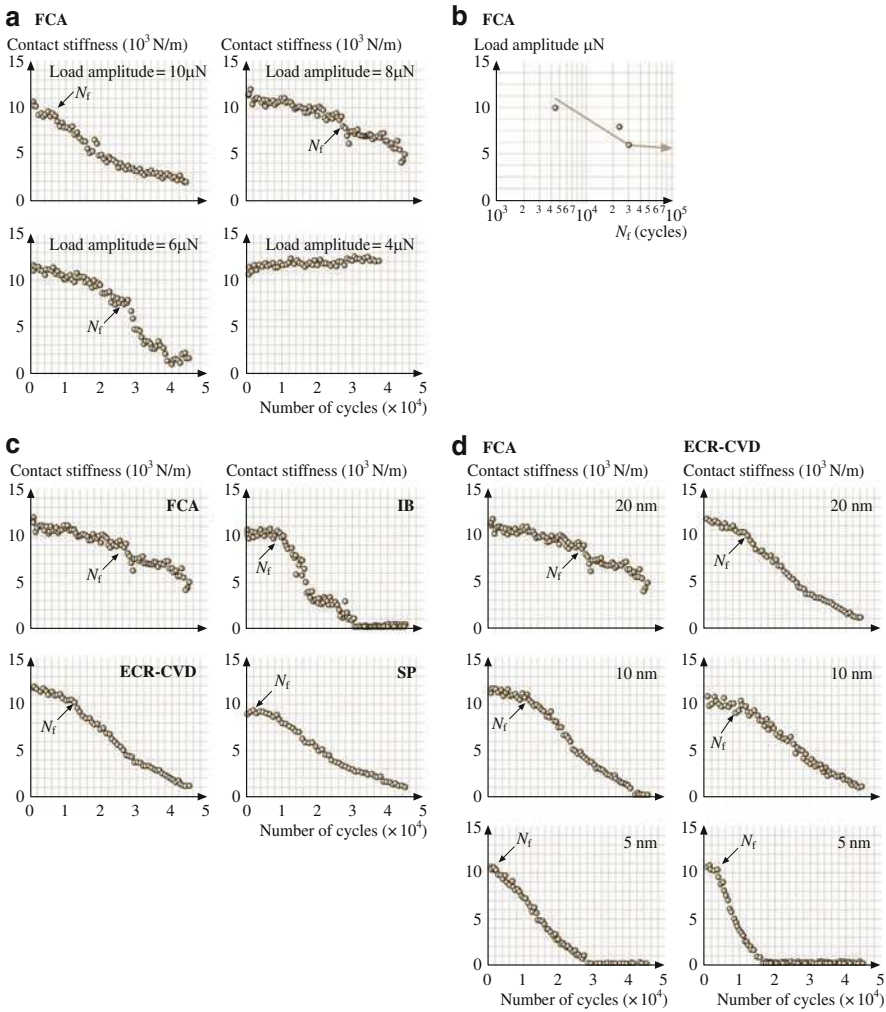
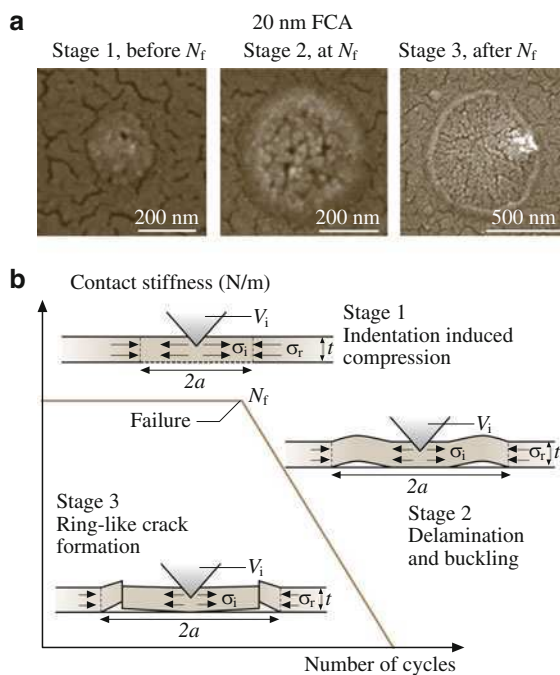


**Fig. 17.14** (a) Contact stiffness as a function of the number of cycles for 20 nm thick FCA coatings cyclically deformed by various oscillation load amplitudes with a mean load of 10  $\mu$ N at a frequency of 45 Hz; (b) plot of load amplitude versus  $N_f$ ; (c) contact stiffness as a function of the number of cycles for four different 20 nm thick coatings with a mean load of 10  $\mu$ N and a load amplitude of 8  $\mu$ N at a frequency of 45 Hz; and (d) contact stiffness as a function of the number of cycles for two coatings of different thicknesses at a mean load of 10  $\mu$ N and a load amplitude of 8  $\mu$ N at a frequency of 45 Hz

Figure 17.15a shows high-magnification SEM images of 20 nm thick FCA coatings before, at, and after  $N_f$ . In the SEM images, the net-like structure is the gold film coated on the DLC coating, which should be ignored when analyzing the indentation fatigue damage. Before  $N_f$ , no delamination or buckling was found except for the residual indentation mark at magnifications of up to  $1,200,000 \times$  using SEM.

**Fig. 17.15** (a) High-magnification SEM images of a coating before, at, and after  $N_f$ , and (b) schematic of various stages of indentation fatigue damage for a coating/substrate system [90]



This suggests that only plastic deformation occurred before  $N_f$ . At  $N_f$ , the coating around the indenter bulged upwards, indicating delamination and buckling. Therefore, it is believed that the decrease in contact stiffness at  $N_f$  results from delamination and buckling of the coating from the substrate. After  $N_f$ , the buckled coating was broken down around the edge of the buckled area, forming a ring-like crack. The remaining coating overhung at the edge of the buckled area. It is noted that the indentation size increases with the number of cycles. This indicates that deformation, delamination and buckling as well as ring-like crack formation occurred over a period of time.

The schematic in Fig. 17.15b shows various stages of indentation fatigue damage for a coating/substrate system. Based on this study, three stages of indentation fatigue damage appear to exist: (1) indentation-induced compression; (2) delamination and buckling; (3) ring-like crack formation at the edge of the buckled coating. The deposition process often induces residual stresses in coatings. The model shown in Fig. 17.15b considers a coating with uniform biaxial residual compression  $\sigma_r$ . In the first stage, indentation induces elastic/plastic deformation, exerting a pressure (acting outward) on the coating around the indenter. Interfacial defects like voids and impurities act as original cracks. These cracks propagate and link up as the indentation compressive stress increases. At this stage, the coating, which is under the indenter and above the interfacial crack (with a crack length of  $2a$ ), still maintains a solid contact with the substrate; the substrate still fully supports the coating. Therefore, this interfacial crack does not lead to an abrupt

decrease in contact stiffness, but gives rise to a slight decrease in contact stiffness, as shown in Fig. 17.14. The coating above the interfacial crack is treated as a rigidly clamped disk. We assume that the crack radius  $a$  is large compared with the coating thickness  $t$ . Since the coating thickness ranges from 5 to 20 nm, this assumption is easily satisfied in this study (the radius of the delaminated and buckled area, shown in Fig. 17.15a, is on the order of 100 nm). The compressive stress caused by indentation is given as [97]

$$\sigma_i = \frac{E}{(1 - \nu)} \varepsilon_i = \frac{EV_i}{2\pi t a^2 (1 - \nu)}, \quad (17.3)$$

where  $\nu$  and  $E$  are the Poisson ratio and elastic modulus of the coating,  $V_i$  is the indentation volume,  $t$  is the coating thickness, and  $a$  is the crack radius. As the number of cycles increases, so does the indentation volume  $V_i$ . Therefore, the indentation compressive stress  $\sigma_i$  increases accordingly. In the second stage, buckling occurs during the unloading segment of the fatigue testing cycle when the sum of the indentation compressive stress  $\sigma_i$  and the residual stress  $\sigma_r$  exceed the critical buckling stress  $\sigma_b$  for the delaminated circular section, as given by [98]

$$\sigma_b = \frac{\mu^2 E}{12(1 - \nu^2)} \left(\frac{t}{a}\right)^2, \quad (17.4)$$

where the constant  $\mu$  equals 42.67 for a circular clamped plate with a constrained center point and 14.68 when the center is unconstrained. The buckled coating acts as a cantilever. In this case, the indenter indents a cantilever rather than a coating/substrate system. This ultrathin coating cantilever has much less contact stiffness than the coating/substrate system. Therefore, the contact stiffness shows an abrupt decrease at  $N_f$ . In the third stage, with more cycles, the delaminated and buckled size increases, resulting in a further decrease in contact stiffness since the cantilever beam length increases. On the other hand, a high bending stress acts at the edge of the buckled coating. The larger the buckled size, the higher the bending stress. The cyclic bending stress causes fatigue damage at the end of the buckled coating, forming a ring-like crack. The coating under the indenter is separated from the bulk coating (caused by the ring-like crack at the edge of the buckled coating) and the substrate (caused by the delamination and buckling in the second stage). Therefore, the coating under the indenter is not constrained; it is free to move with the indenter during fatigue testing. At this point, the sharp nature of the indenter is lost, because the coating under the indenter gets stuck on the indenter. The indentation fatigue experiment results in the contact of a (relatively) huge blunt tip with the substrate. This results in a low contact stiffness value.

Compressive residual stresses result in delamination and buckling. A coating with a higher adhesion strength and a lower compressive residual stress is required for a higher fatigue life. Interfacial defects should be avoided in the coating deposition process. We know that ring-like crack formation occurs in the coating.

Formation of fatigue cracks in the coating depends upon the hardness and the fracture toughness. Cracks are more difficult to form and propagate in the coating with higher strength and fracture toughness.

It is now accepted that long fatigue life in a coating/substrate almost always involves *living with a crack*, that the threshold or limit condition is associated with the nonpropagation of existing cracks or defects, even though these cracks may be undetectable [96]. For all of the coatings studied at 4  $\mu\text{N}$ , the contact stiffness does not change much. This indicates that delamination and buckling did not occur within the number of cycles tested in this study. This is probably because the indentation-induced compressive stress was not high enough to allow the cracks to propagate and link up under the indenter, or the sum of the indentation compressive stress  $\sigma_i$  and the residual stress  $\sigma_r$  did not exceed the critical buckling stress  $\sigma_b$ .

Figure 17.10 and Table 17.5 summarize the hardnesses, elastic moduli, fracture toughnesses, and fatigue lifetimes of all of the coatings studied. A good correlation exists between the fatigue life and other mechanical properties. Higher mechanical properties result in a longer fatigue life. The mechanical properties of DLC coatings are controlled by the  $sp^3$ -to- $sp^2$  ratio. An  $sp^3$ -bonded carbon exhibits the outstanding properties of diamond [51]. Higher kinetic energy during deposition will result in a larger fraction of  $sp^3$ -bonded carbon in an amorphous network. Thus, the higher kinetic energy for the FCA could be responsible for its enhanced carbon structure and mechanical properties [48–50, 99]. Higher adhesion strength between the FCA coating and substrate makes the FCA coating more difficult to delaminate from the substrate.

### 17.3.2 Microscratch and Microwear Studies

For microscratch studies, a conical diamond indenter (that has a tip radius of about 1  $\mu\text{m}$  and a cone angle of  $60^\circ$  for example) is drawn over the sample surface, and the load is ramped up (typically from 2 to 25 mN) until substantial damage occurs. The coefficient of friction is monitored during scratching. Scratch-induced coating damage, specifically fracture or delamination, can be monitored by in situ friction force measurements and using optical and SEM imaging of the scratches after tests. A gradual increase in friction is associated with plowing, and an abrupt increase in friction is associated with fracture or catastrophic failure [100]. The load corresponding to an abrupt increase in friction or an increase in friction above a certain value (typically  $2 \times$  the initial value) provides a measure of the scratch resistance or the adhesive strength of a coating, and is called the *critical load*. The depths of scratches are measured with increasing scratch length or normal load using an AFM, typically with an area of  $10 \times 10 \mu\text{m}^2$  [48, 49, 101].

Microscratch and microwear studies are also conducted using an AFM [23, 50, 99, 102, 103]. A square pyramidal diamond tip (tip radius  $\approx 100 \text{ nm}$ ) or a three-sided pyramidal diamond (Berkovich) tip with an apex angle of  $60^\circ$  and a tip radius of about 100 nm, mounted on a platinum-coated, rectangular stainless steel

cantilever of stiffness of about 40 N/m, is scanned orthogonal to the long axis of the cantilever to generate scratch and wear marks. During the scratch test, the normal load is either kept constant or is increased (typically from 0 to 100  $\mu\text{N}$ ) until damage occurs. Topographical images of the scratch are obtained in situ with the AFM at a low load. By scanning the sample during scratching, wear experiments can be conducted. Wear is monitored as a function of the number of cycles at a constant load. Normal loads (10–80  $\mu\text{N}$ ) are typically used.

## Microscratch

Scratch tests conducted with a sharp diamond tip simulate a sharp asperity contact. In a scratch test, the cracking or delamination of a hard coating is signaled by a sudden increase in the coefficient of friction [23]. The load associated with this event is called the *critical load*.

Wu [104], Bhushan et al. [70], Gupta and Bhushan [12,47], and Li and Bhushan [48, 49, 101] have used a nanoindenter to perform microscratch (mechanical durability) studies of various carbon coatings. The coefficient of friction profiles as a function of increasing normal load as well as AFM surface height maps of regions over scratches at the respective critical loads (indicated by the arrows in the friction profiles and AFM images) observed for coatings with different thicknesses and single-crystal silicon substrate using a conical tip are compared in Figs. 17.16 and 17.17. Bhushan and Koinkar [102], Koinkar and Bhushan [103], Bhushan [23], and Sundararajan and Bhushan [50, 99] used an AFM to perform microscratch studies. Data obtained for coatings with different thicknesses and silicon substrate using a Berkovich tip are compared in Figs. 17.18 and 17.19. Critical loads for various coatings tested using a nanoindenter and AFM are summarized in Fig. 17.20. Selected data for 20 nm thick coatings obtained using nanoindenter are also presented in Fig. 17.10 and Table 17.5.

It is clear that a well-defined critical load exists for each coating. The AFM images clearly show that below the critical loads the coatings were plowed by the scratch tip, associated with the plastic flow of materials. At and after the critical loads, debris (chips) or buckling was observed on the sides of the scratches. Delamination or buckling can be observed around or after the critical loads, which suggests that the damage starts from delamination and buckling. For the 3.5 and 5 nm thick FCA coatings, before the critical loads small debris is observed on the sides of the scratches. This suggests that the thinner FCA coatings are not so durable. It is obvious that, for a given deposition method, the critical loads increase with increasing coating thickness. This indicates that the critical load is determined not only by the strength of adhesion to the substrate, but also by the coating thickness. We note that more debris generated on the thicker coatings than thinner coatings. A thicker coating is more difficult to break; the broken coating chips (debris) seen for a thicker coating are larger than those for the thinner coatings. The different residual stresses of coatings of different thicknesses may also affect the size of the debris. The AFM image shows that the silicon substrate was damaged by



plowing, associated with the plastic flow of material. At and after the critical load, a small amount of uniform debris is observed and the amount of debris increases with increasing normal load.

Since the damage mechanism at the critical load appears to be the onset of plowing, harder coatings with more fracture toughness will therefore require a higher load for deformation and hence a higher critical load. Figure 17.21 gives critical loads of various coatings, obtained with AFM tests, as a function of the coating hardness and fracture toughness (from Table 17.5). It can be seen that, in general, increasing coating hardness and fracture toughness results in a higher critical load. The only exceptions are the FCA coatings at 5 and 3.5 nm thickness, which show the lowest critical loads despite their high hardness and fracture toughness. The brittleness of the thinner FCA coatings may be one reason for their low critical loads. The mechanical properties of coatings that are less than 10 nm thick are not known. The FCA process may result in coatings with low hardness at low thickness due to differences in coating stoichiometry and structure compared to coatings of higher thickness. Also, at these thicknesses stresses at the coating–substrate interface may affect coating adhesion and load-carrying capacity.

Based on the experimental results, a schematic of the scratch damage mechanisms encountered for the DLC coatings used in this study is shown in Fig. 17.22.

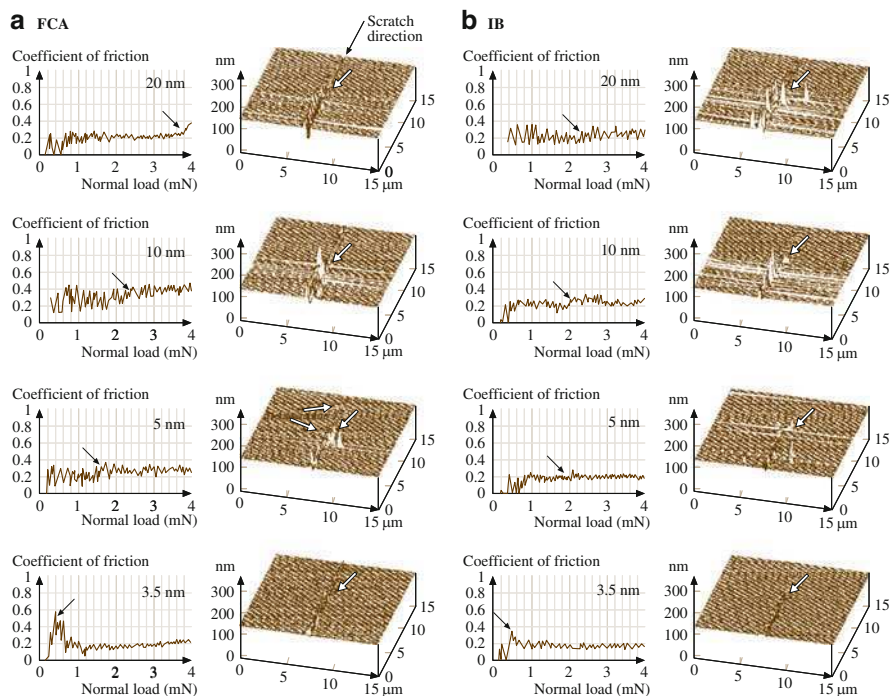
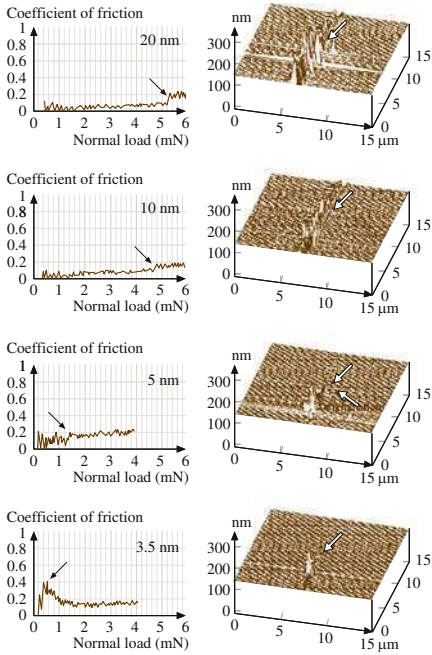


Fig. 17.16 (continued)



**c** ECR-CVD



**d** SP

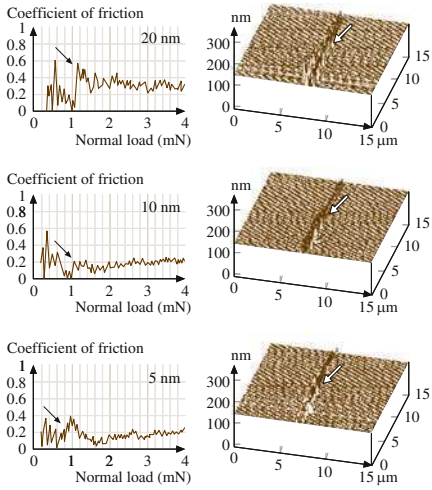


**Fig. 17.16** Coefficient of friction profiles as a function of normal load, as well as corresponding AFM surface height maps of regions over scratches at the respective critical loads (indicated by the arrows in the friction profiles and AFM images), for coatings of different thicknesses deposited by various deposition techniques: (a) FCA, (b) IB, (c) ECR-CVD, (d) SP

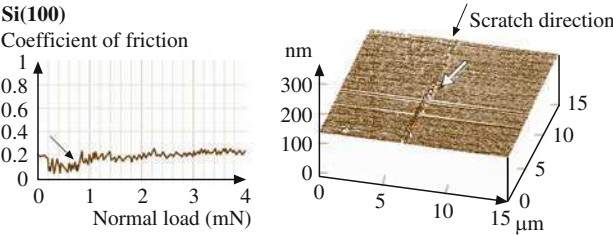


**Fig. 17.17** Coefficient of friction profiles as a function of normal load as well as corresponding AFM surface height maps of regions over scratches at the respective critical loads (indicated by the arrows in the friction profiles and AFM images) for Si(100)

Below the critical load, if a coating has a good combination of strength and fracture toughness, plowing associated with the plastic flow of materials is responsible for the coating damage (Fig. 17.22a). However, if the coating has a low fracture toughness, cracking could occur during plowing, resulting in the formation of

small amounts of debris (Fig. 17.22b). When the normal load is increased to the critical load, delamination or buckling will occur at the coating–substrate interface (Fig. 17.22c). A further increase in normal load will result in coating breakdown via through-coating thickness cracking, as shown in Fig. 17.22d. Therefore, adhesion strength plays a crucial role in the determination of critical load. If a coating adheres strongly to the substrate, the coating is more difficult to delaminate, which will result in a higher critical load. The interfacial and residual stresses of a coating may also greatly affect the delamination and buckling [1]. A coating with higher interfacial and residual stresses is more easily delaminated and buckled, which will result in a low critical load. It was reported earlier that FCA coatings have higher residual stresses than other coatings [47]. Interfacial stresses play an increasingly important role as the coating gets thinner. A large mismatch in elastic modulus between the FCA coating and the silicon substrate may cause large interfacial stresses. This may be why thinner FCA coatings show lower critical loads than thicker FCA coatings, even though the FCA coatings have higher hardness and elastic moduli. The brittleness of thinner FCA coatings may be another reason for the lower critical loads. The strength and fracture toughness of a coating also affect the critical load. Greater strength and fracture toughness will make the coating more difficult to break after delamination and buckling. The high scratch resistance/adhesion of FCA coatings is attributed to the atomic intermixing that occurs at the coating–substrate interface due to the high kinetic energy (2 keV) of the plasma formed during the cathodic arc deposition process [57]. This atomic intermixing provides a graded compositional transition between the coating and the

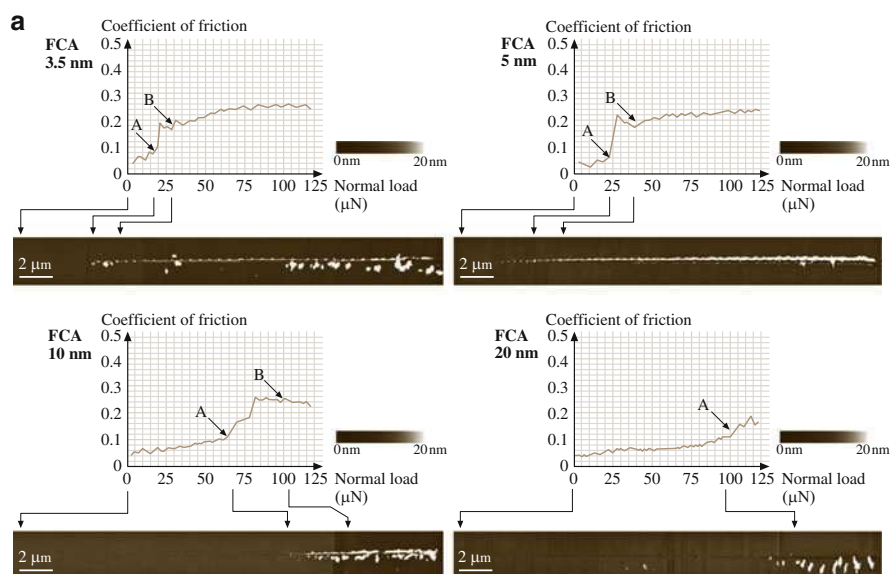
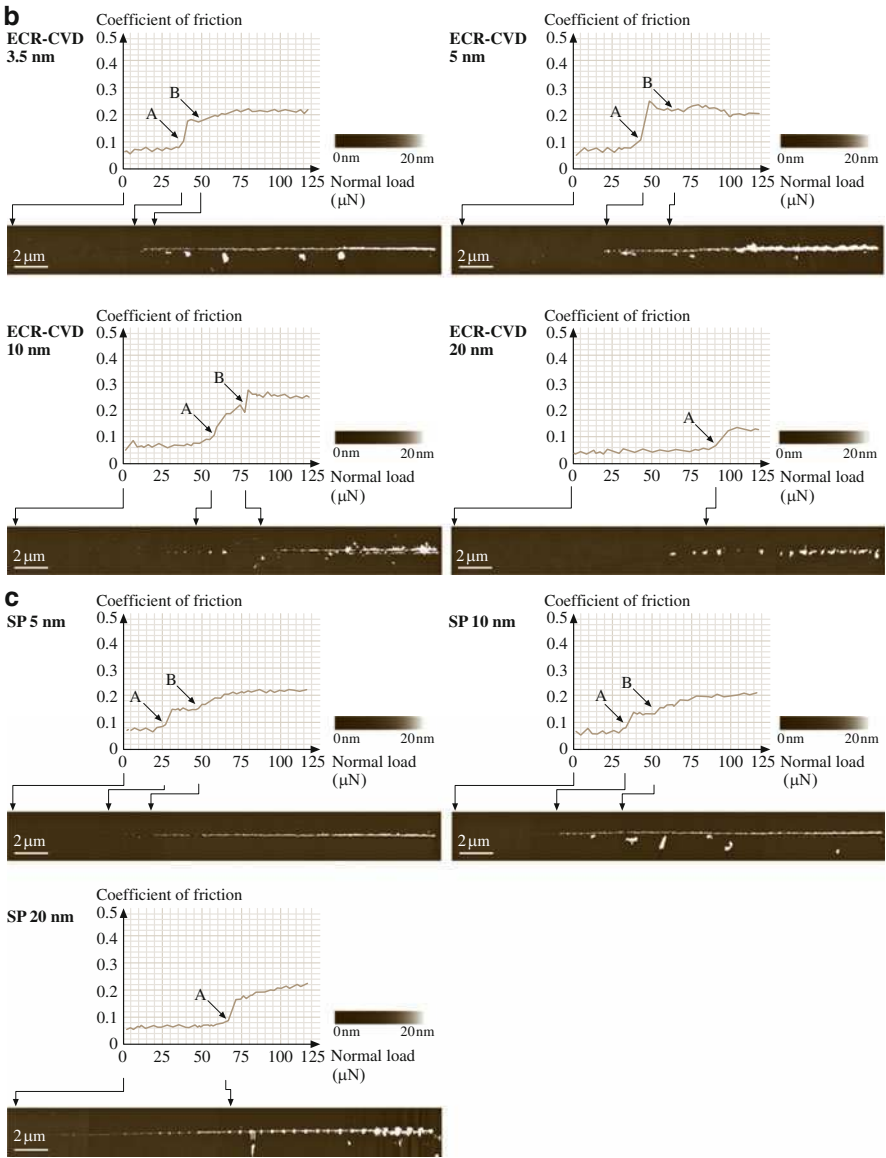


Fig. 17.18 (continued)



**Fig. 17.18** Coefficient of friction profiles during scratch as a function of normal load and corresponding AFM surface height maps for (a) FCA, (b) ECR-CVD, and (c) SP coatings [99]

substrate material. In all other coatings used in this study, the kinetic energy of the plasma is insufficient for atomic intermixing.

Gupta and Bhushan [12, 47] and Li and Bhushan [48, 49] measured the scratch resistances of DLC coatings deposited on  $\text{Al}_2\text{O}_3\text{-TiC}$ , Ni-Zn ferrite and single-crystal

**Fig. 17.19** Coefficient of friction profiles during scratch as a function of normal load and corresponding AFM surface height maps for Si(100) [99]

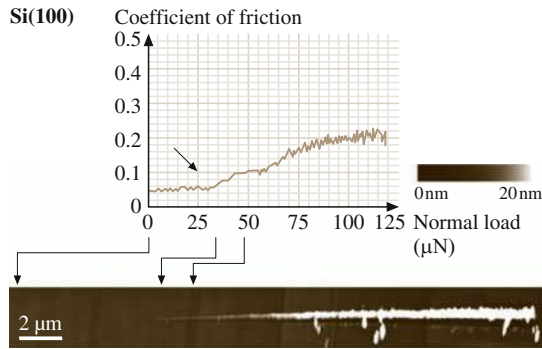
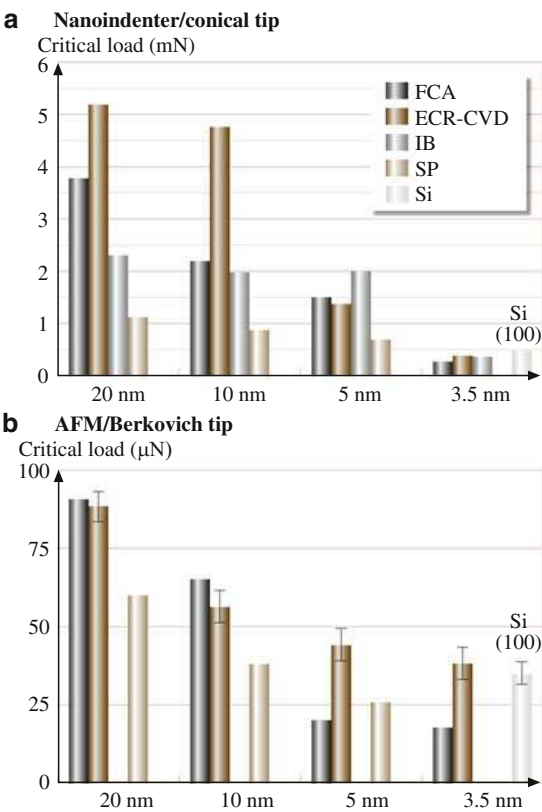
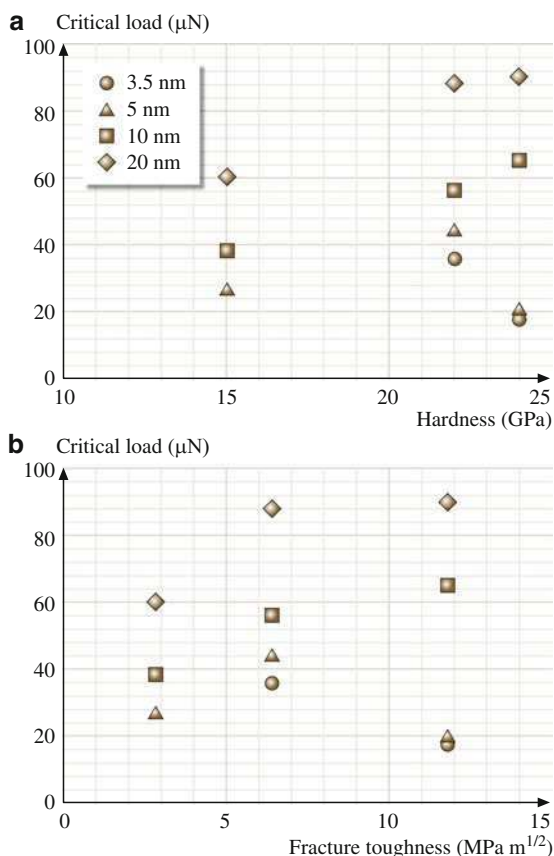


**Fig. 17.20** Critical loads estimated from the coefficient of friction profiles from (a) nanoindenter and (b) AFM tests for various coatings of different thicknesses and Si(100) substrate



silicon substrates. An interlayer of silicon is required to adhere the DLC coating to other substrates, except in the case of cathodic arc-deposited coatings. The best adhesion with cathodic arc carbon coating is obtained on electrically conducting substrates such as  $\text{Al}_2\text{O}_3\text{-TiC}$  and silicon rather than Ni-Zn ferrite.

**Fig. 17.21** Measured critical loads estimated from the coefficient of friction profiles from AFM tests as a function of (a) coating hardness and (b) fracture toughness. Coating hardness and fracture toughness values were obtained using a nanoindenter on 100 nm thick coatings (Table 17.5)

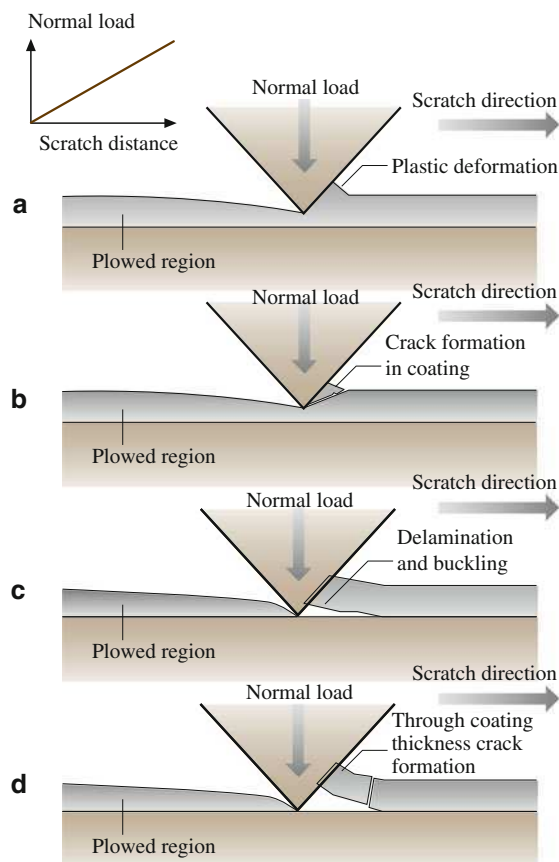


## Microwear

Microwear studies can be conducted using an AFM [23]. For microwear studies, a three-sided pyramidal single-crystal natural diamond tip with an apex angle of about  $80^\circ$  and a tip radius of about 100 nm is used at relatively high loads of 1–150  $\mu\text{N}$ . The diamond tip is mounted on a stainless steel cantilever beam with a normal stiffness of about 30 N/m. The sample is generally scanned in a direction orthogonal to the long axis of the cantilever beam (typically at a rate of 0.5 Hz). The tip is mounted on the beam such that one of its edges is orthogonal to the beam axis. In wear studies, an area of  $2 \times 2 \mu\text{m}^2$  is typically scanned for a selected number of cycles.

Microwear studies of various types of DLC coatings have been conducted [50, 102, 103]. Figure 17.23a shows a wear mark on uncoated Si(100). Wear occurs uniformly and material is removed layer-by-layer via plowing from the first cycle, resulting in constant friction force during the wear (Fig. 17.24a). Figure 17.23b shows AFM images of the wear marks on 10 nm thick coatings. It is clear that the

**Fig. 17.22** Schematic of scratch damage mechanisms for DLC coatings: (a) plowing associated with the plastic flow of materials, (b) plowing associated with the formation of small debris, (c) delamination and buckling at the critical load, and (d) breakdown via through-coating thickness cracking at and after the critical load [48]



coatings wear nonuniformly. Coating failure is sudden and accompanied by a sudden rise in the friction force (Fig. 17.24b). Figure 17.24 shows the wear depth of Si(100) substrate and various DLC coatings at two different loads. FCA- and ECR-CVD-deposited 20 nm thick coatings show excellent wear resistance up to 80  $\mu\text{N}$ , the load that is required for the IB 20 nm coating to fail. In these tests, *failure* of a coating occurs when the wear depth exceeds the quoted coating thickness. The SP 20 nm coating fails at a much lower load of 35  $\mu\text{N}$ . At 60  $\mu\text{N}$ , the coating hardly provides any protection. Moving on to the 10 nm coatings, the ECR-CVD coating requires about 45 cycles at 60  $\mu\text{N}$  to fail, whereas the IB and FCA, coatings fail at 45  $\mu\text{N}$ . The FCA coating exhibits slight roughening in the wear track after the first few cycles, which leads to an increase in the friction force. The SP coating continues to exhibit poor resistance, failing at 20  $\mu\text{N}$ . For the 5 nm coatings, the load required to make the coatings fail continues to decrease, but IB and ECR-CVD still provide adequate protection compared to bare Si(100) in that order, with the silicon failing at 35  $\mu\text{N}$ , the FCA coating at 25  $\mu\text{N}$  and the SP coating at 20  $\mu\text{N}$ . Almost all of the 20, 10, and 5 nm coatings provide better wear

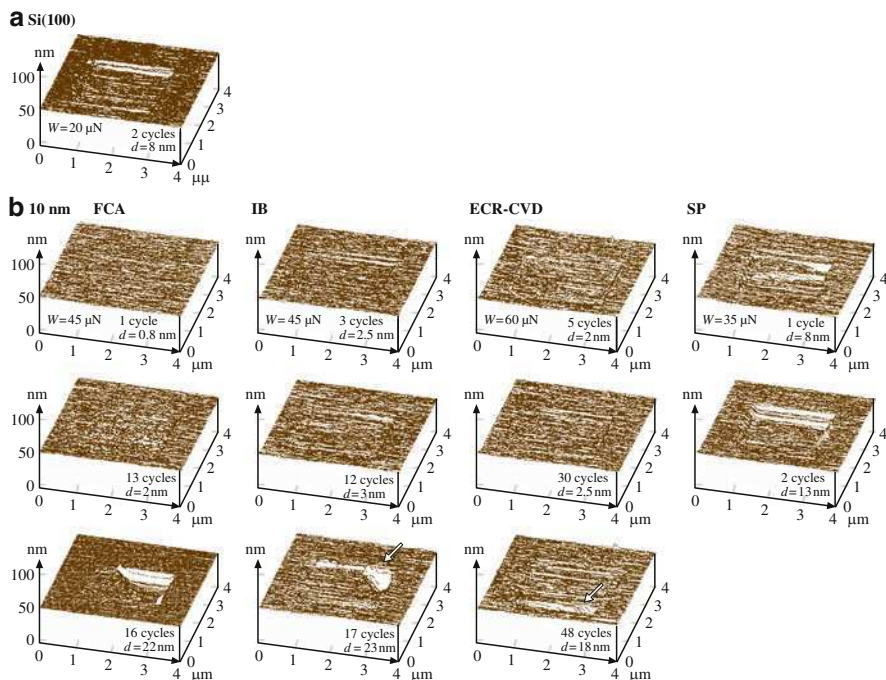


**Fig. 17.23** AFM images of wear marks on (a) bare Si(100), and (b) various 10 nm thick DLC coatings [50]

resistance than bare silicon. At 3.5 nm, FCA coating provides no wear resistance, failing almost instantly at 20  $\mu\text{N}$ . The IB and ECR-CVD coatings show good wear resistance at 20  $\mu\text{N}$  compared to bare Si(100). However, IB only lasts about ten cycles and ECR-CVD about three cycles at 25  $\mu\text{N}$ .

The wear tests highlight the differences between the coatings more vividly than the scratch tests. At higher thicknesses (10 and 20 nm), the ECR-CVD and FCA coatings appear to show the best wear resistance. This is probably due to the greater hardness of the coatings (Table 17.5). At 5 nm, the IB coating appears to be the best. FCA coatings show poorer wear resistance with decreasing coating thickness. This suggests that the trends in hardness seen in Table 17.5 no longer hold at low thicknesses. SP coatings show consistently poor wear resistance at all thicknesses. The 3.5 nm IB coating does provide reasonable wear protection at low loads.

### 17.3.3 Macroscale Tribological Characterization

So far, we have presented data on mechanical characterization and microscratch and microwear studies using a nanoindenter and an AFM. Mechanical properties affect the tribological performance of a coating, and microwear studies simulate a

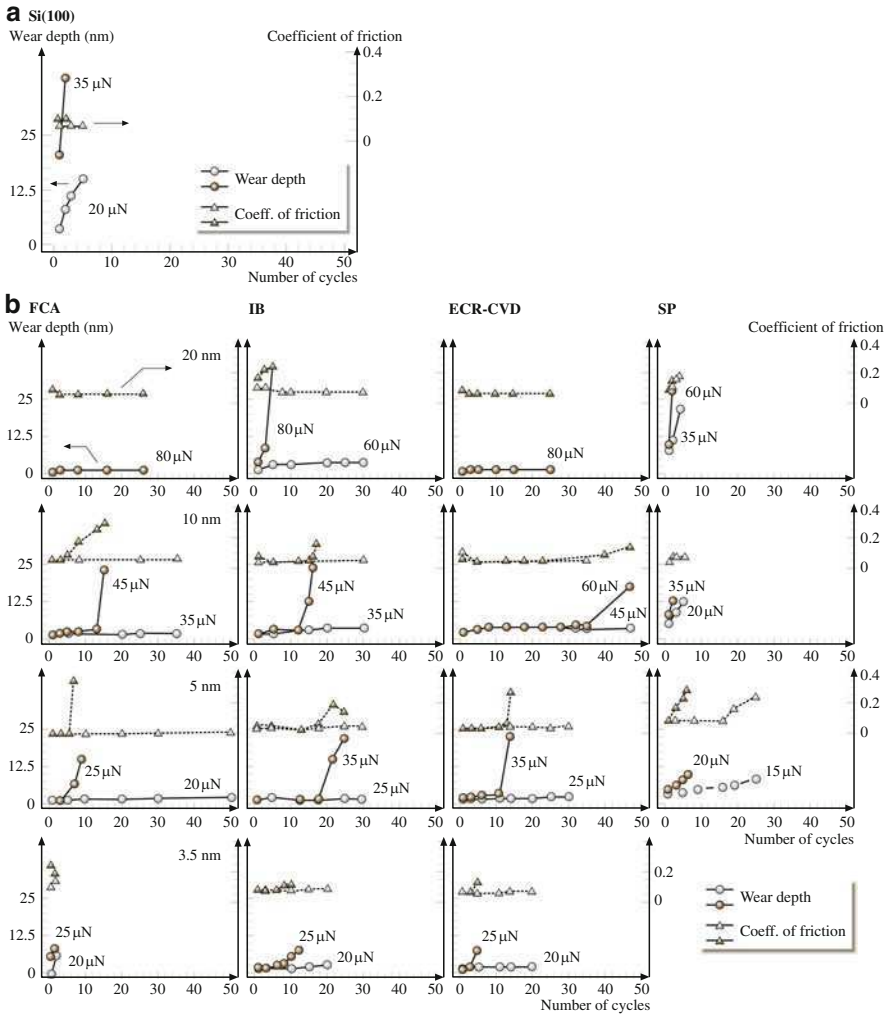


**Fig. 17.24** Wear data for (a) bare Si(100) and (b) various DLC coatings. Coating thickness is constant along each row in (b). Both the wear depth and the coefficient of friction during wear are plotted for a given cycle [50]

single asperity contact, which helps us to understand the wear process. These studies are useful when screening various candidate coatings, and also aid our understanding of the relationships between deposition conditions and properties of the samples. In the next step, macroscale friction and wear tests need to be conducted to measure the tribological performance of the coating.

Macroscale accelerated friction and wear tests have been conducted to screen a large number of candidates, as have functional tests on selected candidates. An accelerated test is designed to accelerate the wear process such that it does not



change the failure mechanism. The accelerated friction and wear tests are generally conducted using a ball-on-flat tribometer under reciprocating motion [70]. Typically, a diamond tip with a tip radius of 20  $\mu\text{m}$  or a sapphire ball with a diameter of 3 mm and a surface finish of about 2 nm RMS is slid against the coated substrates at selected loads. The coefficient of friction is monitored during the tests.

Functional tests are conducted using an actual machine running at close to the actual operating conditions for which the coatings have been developed. The tests are generally accelerated somewhat to fail the interface in a short time.

### Accelerated Friction and Wear Tests

Li and Bhushan [48] conducted accelerated friction and wear tests on DLC coatings deposited by various deposition techniques using a ball-on-flat tribometer. The average coefficient of friction values observed are presented in Table 17.5. Optical micrographs of wear tracks and debris formed on all samples when slid against a sapphire ball after a sliding distance of 5 nm are presented in Fig. 17.25. The normal load used for the 20 and 10 nm thick coatings was 200 mN, and the normal load used for the 5 and 3.5 nm thick coatings and the silicon substrate was 150 mN.

Among the 20 nm thick coatings, the SP coating exhibits a higher coefficient of friction (about 0.3) than for the other coatings coefficient of friction (all of which were about 0.2). The optical micrographs show that the SP coating has a larger wear track and more debris than the IB coating. No wear track or debris were found on the 20 nm thick FCA and ECR-CVD coatings. The optical micrographs of 10 nm thick coatings show that the SP coating was severely damaged, showing a large wear track with scratches and lots of debris. The FCA and ECR-CVD coatings show smaller wear tracks and less debris than the IB coatings. The 5 nm and 3.5 nm thick coatings and the silicon substrate show even larger wear tracks and more debris than the 10 nm thick coatings.

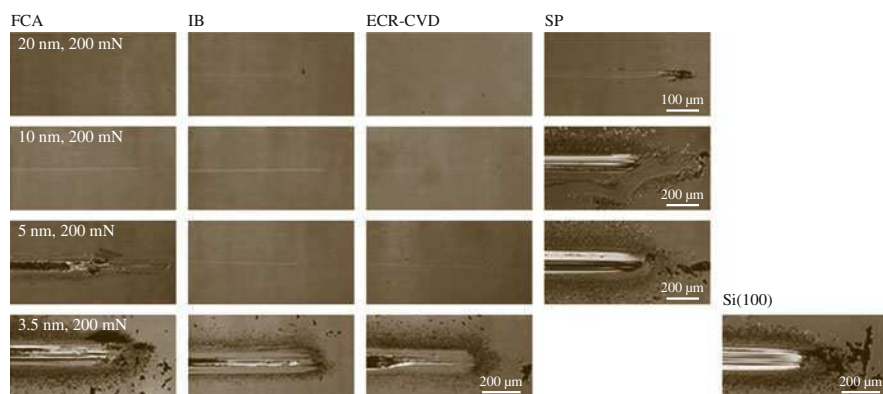
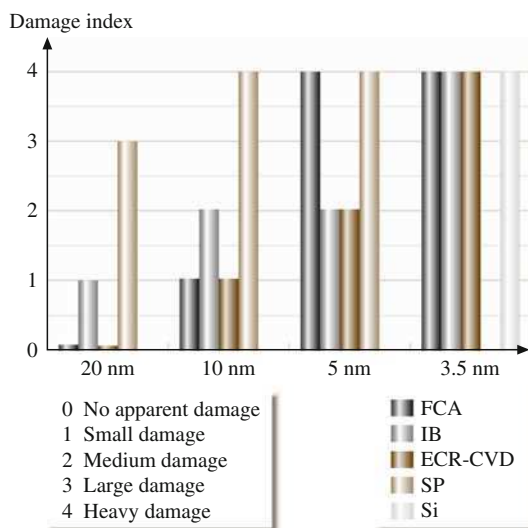


**Fig. 17.25** Optical micrographs of wear tracks and debris formed on various coatings of different thicknesses and silicon substrate when slid against a sapphire ball after a sliding distance of 5 nm. The end of the wear track is on the right-hand side of the image

**Fig. 17.26** Bar chart of the wear damage indices for various coatings of different thicknesses and Si(100) substrate based on optical examination of the wear tracks and debris



For the 5 nm thick coatings, the wear tracks and debris of the IB and ECR-CVD coatings are comparable. The bad wear resistance of the 5 nm thick FCA coating is in good agreement with the low critical scratch load, which may be due to the higher interfacial and residual stresses as well as the brittleness of the coating.

At 3.5 nm, all of the coatings exhibit wear. The FCA coating provides no wear resistance, failing instantly like the silicon substrate. Large block-like debris is observed on the sides of the wear track of the FCA coating. This indicates that large region delamination and buckling occurs during sliding, resulting in large block-like debris. This block-like debris, in turn, scratches the coating, making the damage to the coating even more severe. The IB and ECR-CVD coatings are able to provide some protection against wear at 3.5 nm.

In order to better evaluate the wear resistance of various coatings, based on an optical examination of the wear tracks and debris after tests, a bar chart of the wear damage index for various coatings of different thicknesses and an uncoated silicon substrate is presented in Fig. 17.26. Among the 20 and 10 nm thick coatings, the SP coatings show the worst damage, followed by FCA/ECR-CVD. At 5 nm, the FCA and SP coatings show the worst damage, followed by the IB and ECR-CVD coatings. All of the 3.5 nm thick coatings show the same heavy damage as the uncoated silicon substrate.

The wear damage mechanisms of the thick and thin DLC coatings studied are believed to be as illustrated in Fig. 17.27. In the early stages of sliding, deformation zone, Hertzian and wear fatigue cracks that have formed beneath the surface extend within the coating upon subsequent sliding [1]. Formation of fatigue cracks depends on the hardness and subsequent cycles. These are controlled by the  $sp^3$ -to- $sp^2$  ratio. For thicker coatings, the cracks generally do not penetrate the coating. For a thinner coating, the cracks easily propagate down to the interface aided by the interfacial

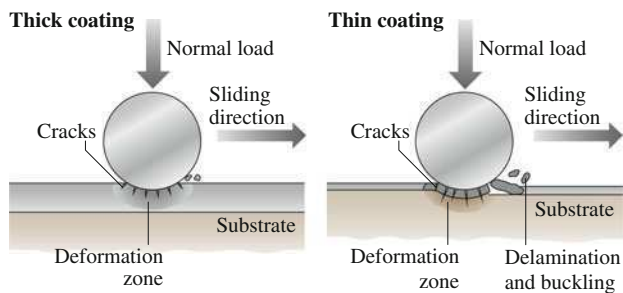


**Fig. 17.27** Schematic of wear damage mechanisms for thick and thin DLC coatings [48]

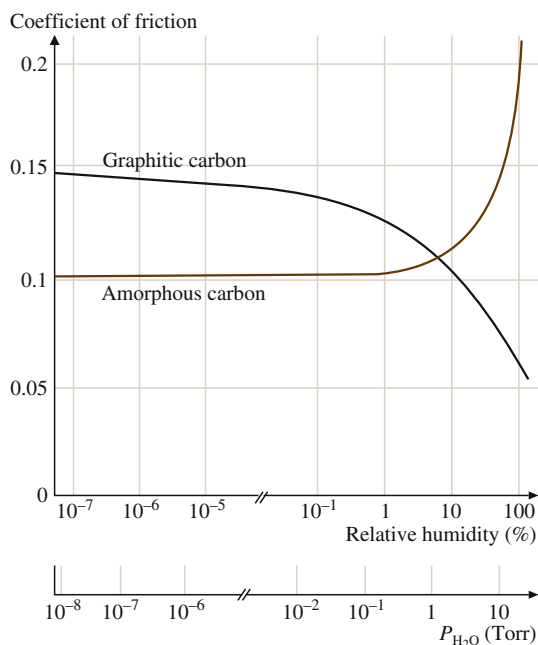
stresses and get diverted along the interface just enough to cause local delamination of the coating. When this happens, the coating experiences excessive plowing. At this point, the coating fails catastrophically, resulting in a sudden rise in the coefficient of friction. All 3.5 nm thick coatings failed much quicker than the thicker coatings. It appears that these thin coatings have very low load-carrying capacities and so the substrate undergoes deformation almost immediately. This generates stresses at the interface that weaken the coating adhesion and lead to delamination of the coating. Another reason may be that the thickness is insufficient to produce a coating that has the DLC structure. Instead, the bulk may be made up of a matrix characteristic of the interface region where atomic mixing occurs with the substrate and/or any interlayer used. This would also result in poor wear resistance and silicon-like behavior of the coating, especially for FCA coatings, which show the worst performance at 3.5 nm. SP coatings show the worst wear performance at any thickness (Fig. 17.25). This may be due to their poor mechanical properties, such as lower hardness and scratch resistance, compared to the other coatings.

Comparison of Figs. 17.20 and 17.26 shows a very good correlation between the wear damage and critical scratch loads. Less wear damage corresponds to a higher critical scratch load. Based on the data, thicker coatings do show better scratch and wear resistance than thinner coatings. This is probably due to the better load-carrying capacities of the thick coatings compared to the thinner ones. For a given coating thickness, increased hardness and fracture toughness and better adhesion strength are believed to be responsible for the superior wear performance.

### Effect of Environment

The friction and wear performance of an amorphous carbon coating is known to be strongly dependent on the water vapor content and partial gas pressure in the test environment. The friction data for an amorphous carbon film on a silicon substrate sliding against steel are presented as a function of the partial pressure of water vapor in Fig. 17.28 [1, 13, 69, 105, 106]. Friction increases dramatically above a relative humidity of about 40%. At high relative humidity, condensed water vapor forms

**Fig. 17.28** Coefficient of friction as a function of relative humidity and water vapor partial pressure for a RF-plasma deposited amorphous carbon coating and a bulk graphitic carbon coating sliding against a steel ball



meniscus bridges at the contacting asperities, and the menisci result in an intrinsic attractive force that is responsible for an increase in the friction. For completeness, data on the coefficient of friction of bulk graphitic carbon are also presented in Fig. 17.28. Note that the friction decreases with increased relative humidity [107]. Graphitic carbon has a layered crystal lattice structure. Graphite absorbs polar gases (such as  $H_2O$ ,  $O_2$ ,  $CO_2$ ,  $NH_3$ ) at the edges of the crystallites, which weakens the interlayer bonding forces facilitating interlayer slip and results in lower friction [1].

A number of tests have been conducted in controlled environments in order to better study the effects of environmental factors on carbon-coated magnetic disks. Marchon et al. [108] conducted tests in alternating environments of oxygen and nitrogen gases (Fig. 17.29). The coefficient of friction increases as soon as oxygen is added to the test environment, whereas in a nitrogen environment the coefficient of friction reduces slightly. Tribochemical oxidation of the DLC coating in the oxidizing environment is responsible for an increase in the coefficient of friction, implying wear. Dugger et al. [109], Strom et al. [110], Bhushan and Ruan [111] and Bhushan et al. [71] conducted tests with DLC-coated magnetic disks (with about 2 nm thick perfluoropolyether lubricant film) in contact with  $Al_2O_3$ -TiC sliders in different gaseous environments, including a high vacuum of  $2 \times 10^{-7}$  Torr (Fig. 17.30). The wear lives are the shortest in high vacuum and the longest in atmospheres of mostly nitrogen and argon with the following order (from best to worst): argon or nitrogen, Ar +  $H_2O$ , ambient, Ar +  $O_2$ , Ar +  $H_2O$ , vacuum. From this sequence of wear performance, we can see that having oxygen and water in an operating environment worsens the wear performance of the coating, but having a

**Fig. 17.29** Coefficient of friction as a function of sliding distance for a ceramic slider against a magnetic disk coated with a 20 nm thick DC magnetron sputtered DLC coating, measured at a speed of 0.06 m/s for a load of 10 g. The environment was alternated between oxygen and nitrogen gases [108]

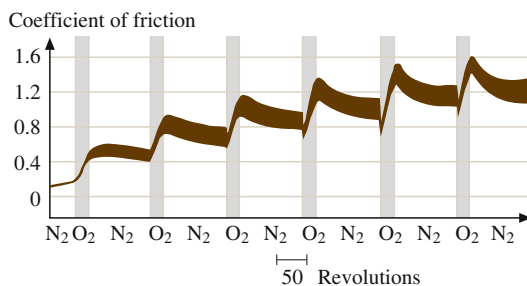
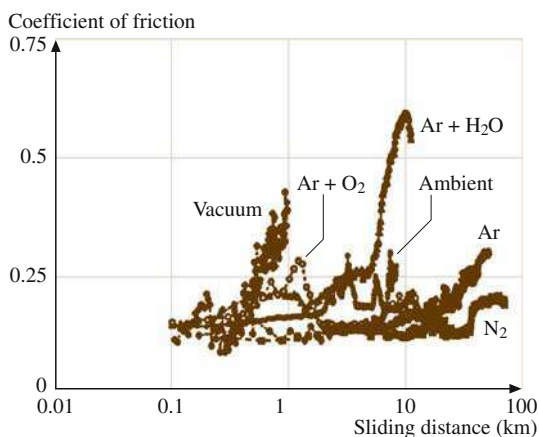


**Fig. 17.30** Durability, measured by sliding a  $\text{Al}_2\text{O}_3$ -TiC magnetic slider against a magnetic disk coated with a 20 nm thick DC sputtered amorphous carbon coating and 2 nm thick perfluoropolyether film, measured at a speed of 0.75 m/s and for a load of 10 g. Vacuum refers to  $2 \times 10^{-7}$  Torr [71]



vacuum is even worse. Indeed, failure mechanisms differ in different environments. In high vacuum, intimate contact between the disk and the slider surface results in significant wear. In ambient air,  $\text{Ar} + \text{O}_2$  and  $\text{Ar} + \text{H}_2\text{O}$ , tribochemical oxidation of the carbon overcoat is responsible for interface failure. For experiments performed in pure argon and nitrogen, mechanical shearing of the asperities causes the formation of debris, which is responsible for the formation of scratch marks on the carbon surface, which were observed with an optical microscope [71].

## Functional Tests

Magnetic thin film heads made with  $\text{Al}_2\text{O}_3$ -TiC substrate are used in magnetic storage applications [13]. A multilayered thin film pole-tip structure present on the head surface wears more rapidly than the much harder  $\text{Al}_2\text{O}_3$ -TiC substrate. Pole-tip recession (PTR) is a serious concern in magnetic storage [15–19, 112]. Two of the diamond-like carbon coatings with superior mechanical properties – ion beam and cathodic arc carbon coatings – were deposited on the air-bearing surfaces of

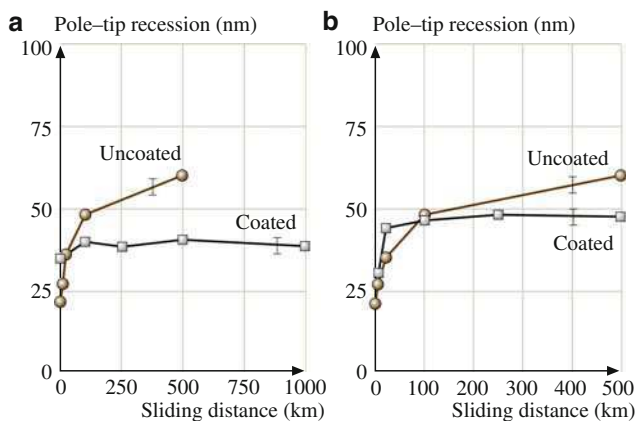


**Fig. 17.31** Pole-tip recession as a function of sliding distance, measured with an AFM, for (a) uncoated and 20 nm thick ion beam carbon coated, and (b) uncoated and 20 nm thick cathodic arc carbon coated  $\text{Al}_2\text{O}_3$ -TiC heads run against MP tapes [15]

$\text{Al}_2\text{O}_3$ -TiC head sliders [15]. Functional tests were conducted by running a metal particle (MP) tape in a computer tape drive. The average PTR as a function of sliding distance is presented in Fig. 17.31. We note that the PTR increases for the uncoated head, whereas there is a slight increase in PTR for the coated heads during early sliding followed by little change. Thus, the coatings provide protection.

The micromechanical as well as the accelerated and functional tribological data presented here clearly suggest that there is a good correlation between the scratch resistance and wear resistance measured using accelerated tests and functional tests. Thus, scratch tests can be successfully used to screen coatings for wear applications.

### 17.3.4 Coating Continuity Analysis

Ultrathin (less than 10 nm) coatings may not uniformly coat the sample surface. In other words, the coating may be discontinuous and deposited in the form of islands on the microscale. Therefore, one possible reason for poor wear protection and the nonuniform failure of thin coatings may be poor coverage of the substrate. Coating continuity can be studied using surface analytical techniques such as Auger and/or XPS analyses. Any discontinuity in coating thickness that is less than the sampling depth of the instrument result in the local detection of the substrate species [49, 50, 102].

The results from an XPS analysis of  $1.3 \text{ mm}^2$  regions (single point measurement with spot diameter of  $1,300 \text{ }\mu\text{m}$ ) on various coatings deposited on Si(100) substrates are shown in Fig. 17.32. The sampling depth is about 2–3 nm. The poor SP coatings and the poor 5 nm and 3.5 nm FCA coatings ( ) show much lower carbon

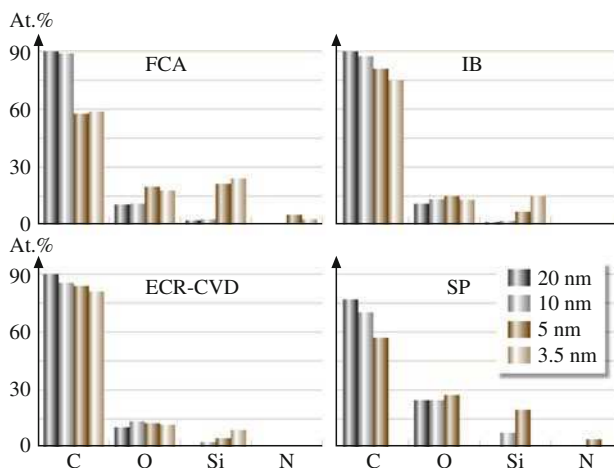


**Fig. 17.32** Quantified XPS data for various DLC coatings on Si(100) substrate [50]. Atomic concentrations are shown

contents (atomic concentrations of  $<75\%$  and  $<60\%$  respectively) than the IB and ECR-CVD coatings. Silicon is detected in all of the 5 nm coatings. From the data it is hard to infer whether the Si is from the substrate or from exposed regions due to discontinuous coating. Based on the sampling depth, any Si detected in 3.5 nm coatings would likely be from the substrate. The other interesting observation is that all poor coatings (all SP and FCA 5 and 3.5 nm coatings) have almost twice the oxygen content of the other coatings. Any oxygen present may be due to leaks in the deposition chamber, and it is present as silicon oxides.

AES measurements averaged over a scan area of  $900\ \mu\text{m}^2$  were conducted on FCA and SP 5 nm coatings at six different regions on each sample. Very little silicon was detected on this scale, and the detected peaks were characteristic of oxides. The oxygen levels were comparable to those seen for good coatings via XPS. These results contrast with the XPS measurements performed at a larger scale, suggesting that the coatings only possess discontinuities at isolated areas and that the 5 nm coatings are generally continuous on the microscale. Figure 17.33 shows representative XPS and AES spectra of selected samples.

## 17.4 Closure

Diamond material and its smooth coatings are used for very low wear and relatively low friction. Major limitations of the true diamond coatings are that they need to be deposited at high temperatures, can only be deposited on selected substrates, and require surface finishing. Hard amorphous carbon (a-C) or commonly known as DLC coatings exhibit mechanical, thermal and optical properties close to that of

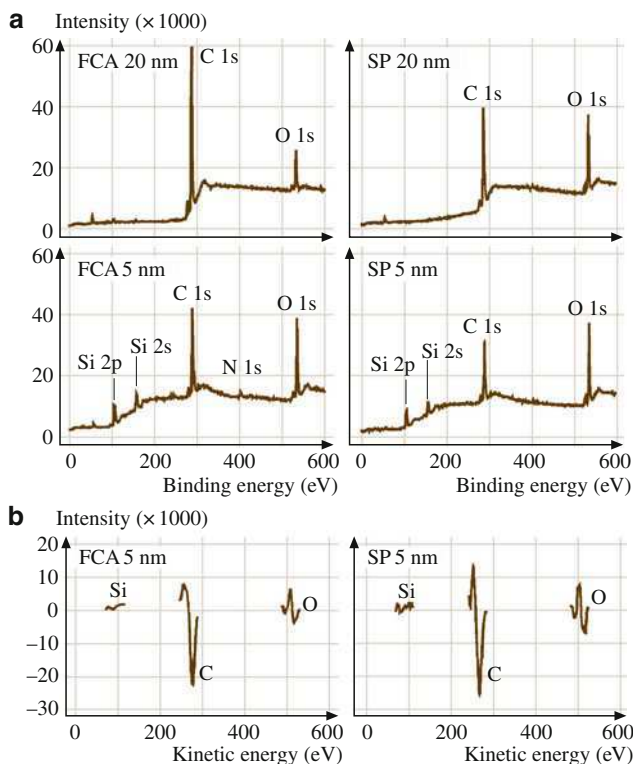


**Fig. 17.33** (a) XPS spectra for 5 nm and 20 nm thick FCA and SP coatings on Si(100) substrate, and (b) AES spectra for FCA and SP coatings of 5 nm thickness on Si(100) substrate [50]

diamond. These can be deposited with a large range of thicknesses by using a variety of deposition processes, on variety of substrates at or near room temperature. The coatings reproduce substrate topography avoiding the need of post finishing. Friction and wear properties of some DLC coatings can be very attractive for tribological applications. The largest industrial application of these coatings is in magnetic storage devices. They are expected to be used in MEMS/NEMS.

EELS and Raman spectroscopies can be successfully used for chemical characterization of amorphous carbon coatings. The prevailing atomic arrangement in the DLC coatings is amorphous or quasi-amorphous with small diamond ( $sp^3$ ), graphite ( $sp^2$ ) and other unidentifiable micro- or nanocrystallites. Most DLC coatings except those produced by filtered cathodic arc contain from a few to about 50 at.% hydrogen. Sometimes hydrogen is deliberately incorporated in the sputtered and ion plated coatings to tailor their properties.

Amorphous carbon coatings deposited by various techniques exhibit different mechanical and tribological properties. The nanoindenter can be successfully used for measurement of hardness, elastic modulus, fracture toughness, and fatigue life. Microscratch and microwear experiments can be performed using either



a nanoindenter or an AFM. Thin coatings deposited by filtered cathodic arc, ion beam and ECR-CVD hold a promise for tribological applications. Coatings as thin as 5 nm or even thinner in thickness provide wear protection. Microscratch, microwear, and accelerated wear testing, if simulated properly can be successfully used to screen coating candidates for industrial applications. In the examples shown in this chapter, trends observed in the microscratch, microwear, and accelerated macrofriction wear tests are similar to that found in functional tests.

## References

1. B. Bhushan, B.K. Gupta, *Handbook of Tribology: Materials, Coatings, and Surface Treatments* (Krieger, Malabar, 1997)
2. B. Bhushan, *Principles and Applications of Tribology* (Wiley, New York, 1999)
3. B. Bhushan, *Introduction to Tribology* (Wiley, New York, 2002)
4. B. Bhushan, B.K. Gupta, G.W. VanCleeef, C. Capp, J.V. Coe: Fullerene (C<sub>60</sub>) films for solid lubrication. *Tribol. Trans.* **36**, 573–580 (1993)
5. B.K. Gupta, B. Bhushan, C. Capp, J.V. Coe, Material characterization and effect of purity and ion implantation on the friction and wear of sublimed fullerene films. *J. Mater. Res.* **9**, 2823–2838 (1994)
6. B.K. Gupta, B. Bhushan, Fullerene particles as an additive to liquid lubricants and greases for low friction and wear. *Lubr. Eng.* **50**, 524–528 (1994)
7. B. Bhushan, V.V. Subramaniam, A. Malshe, B.K. Gupta, J. Ruan, Tribological properties of polished diamond films. *J. Appl. Phys.* **74**, 4174–4180 (1993)
8. B. Bhushan, B.K. Gupta, V.V. Subramaniam, Polishing of diamond films, *Diam. Films Technol.* **4**, 71–97 (1994)
9. P. Sander, U. Kaiser, M. Altebockwinkel, L. Wiedmann, A. Benninghoven, R.E. Sah, P. Koidl, Depth profile analysis of hydrogenated carbon layers on silicon by x-ray photoelectron spectroscopy, auger electron spectroscopy, electron energy-loss spectroscopy, and secondary ion mass spectrometry. *J. Vac. Sci. Technol. A* **5**, 1470–1473 (1987)
10. A. Matthews, S.S. Eskildsen, Engineering applications for diamond-like carbon. *Diam. Relat. Mater.* **3**, 902–911 (1994)
11. A.H. Lettington, Applications of diamond-like carbon thin films. *Carbon* **36**, 555–560 (1998)
12. B.K. Gupta, B. Bhushan, Mechanical and tribological properties of hard carbon coatings for magnetic recording heads. *Wear* **190**, 110–122 (1995)
13. B. Bhushan, *Tribology and Mechanics of Magnetic Storage Devices*, 2nd edn. (Springer, Heidelberg, 1996)
14. B. Bhushan, *Mechanics and Reliability of Flexible Magnetic Media*, 2nd edn. (Springer, Heidelberg, 2000)
15. B. Bhushan, S.T. Patton, R. Sundaram, S. Dey, Pole tip recession studies of hard carbon-coated thin-film tape heads. *J. Appl. Phys.* **79**, 5916–5918 (1996)
16. J. Xu, B. Bhushan, Pole tip recession studies of thin-film rigid disk head sliders II: Effects of air bearing surface and pole tip region designs and carbon coating. *Wear* **219**, 30–41 (1998)
17. W.W. Scott, B. Bhushan, Corrosion and wear studies of uncoated and ultra-thin DLC coated magnetic tape-write heads and magnetic tapes. *Wear* **243**, 31–42 (2000)
18. W.W. Scott, B. Bhushan, Loose debris and head stain generation and pole tip recession in modern tape drives. *J. Inf. Storage Proc. Syst.* **2**, 221–254 (2000)
19. W.W. Scott, B. Bhushan, A.V. Lakshmikumaran, Ultrathin diamond-like carbon coatings used for reduction of pole tip recession in magnetic tape heads. *J. Appl. Phys.* **87**, 6182–6184 (2000)

20. B. Bhushan, Macro- and microtribology of magnetic storage devices. In *Modern Tribology Handbook*, ed. by B. Bhushan (CRC, Boca Raton, 2001) pp.1413–1513
21. B. Bhushan, Nanotribology and nanomechanics of MEMS devices. *Proc. 9th Annu. Workshop Micro Electro Mech. Syst.* (IEEE, New York, 1996) pp.91–98
22. B. Bhushan (Ed.), *Tribology Issues and Opportunities in MEMS* (Kluwer, Dordrecht, 1998)
23. B. Bhushan: *Handbook of Micro/Nanotribology*, 2nd edn. (CRC, Boca Raton 1999)
24. B. Bhushan, Macro- and microtribology of MEMS materials. In *Modern Tribology Handbook*, ed. by B. Bhushan (CRC, Boca Raton, 2001) pp.1515–1548
25. S. Aisenberg, R. Chabot, Ion beam deposition of thin films of diamond-like carbon. *J. Appl. Phys.* **49**, 2953–2958 (1971)
26. E.G. Spencer, P.H. Schmidt, D.C. Joy, F.J. Sansalone, Ion beam deposited polycrystalline diamond-like films. *Appl. Phys. Lett.* **29**, 118–120 (1976)
27. A. Grill, B.S. Meyerson, Development and status of diamondlike carbon. In *Synthetic Diamond: Emerging CVD Science and Technology*, ed. by K.E. Spear, J.P. Dismukes (Wiley, New York, 1994) pp.91–141
28. Y. Catherine, Preparation techniques for diamond-like carbon. In *Diamond and Diamond-Like Films and Coatings*, ed. by R.E. Clausing, L.L. Horton, J.C. Angus, P. Koidl (Plenum, New York, 1991), pp.193–227
29. J.J. Cuomo, D.L. Pappas, J. Bruley, J.P. Doyle, K.L. Seagner, Vapor deposition processes for amorphous carbon films with  $sp^3$  fractions approaching diamond. *J. Appl. Phys.* **70**, 1706–1711 (1991)
30. J.C. Angus, C.C. Hayman, Low pressure metastable growth of diamond and diamondlike phase. *Science* **241**, 913–921 (1988)
31. J.C. Angus, F. Jensen, Dense diamondlike hydrocarbons as random covalent networks. *J. Vac. Sci. Technol. A* **6**, 1778–1782 (1988)
32. D.C. Green, D.R. McKenzie, P.B. Lukins, The microstructure of carbon thin films. *Mater. Sci. Forum* **52/53**, 103–124 (1989)
33. N.H. Cho, K.M. Krishnan, D.K. Veirs, M.D. Rubin, C.B. Hopper, B. Bhushan, D.B. Bogy, Chemical structure and physical properties of diamond-like amorphous carbon films prepared by magnetron sputtering. *J. Mater. Res.* **5**, 2543–2554 (1990)
34. J.C. Angus, Diamond and diamondlike films, *Thin Solid Films* **216**, 126–133 (1992)
35. B. Bhushan, A.J. Kellock, N.H. Cho, J.W. Ager III, Characterization of chemical bonding and physical characteristics of diamond-like amorphous carbon and diamond films. *J. Mater. Res.* **7**, 404–410 (1992)
36. J. Robertson, Properties of diamond-like carbon. *Surf. Coat. Technol.* **50**, 185–203 (1992)
37. N. Savvides, B. Window, Diamondlike amorphous carbon films prepared by magnetron sputtering of graphite, *J. Vac. Sci. Technol. A* **3**, 2386–2390 (1985)
38. J.C. Angus, P. Koidl, S. Domitz, Carbon thin films. In, *Plasma Deposited Thin Films*, ed. by J. Mort, F. Jensen (CRC, Boca Raton, 1986) pp.89–127
39. J. Robertson, Amorphous carbon, *Adv. Phys.* **35**, 317–374 (1986)
40. M. Rubin, C.B. Hooper, N.H. Cho, B. Bhushan, Optical and mechanical properties of DC sputtered carbon films. *J. Mater. Res.* **5**, 2538–2542 (1990)
41. G.J. Varentop, M. Kawasaki, R.M. Nix, I.G. Brown, M. Salmeron, G.A. Somorjai, Formation of hydrogenated amorphous carbon films of controlled hardness from a methane plasma. *Phys. Rev. B* **41**, 3200–3210 (1990)
42. J.J. Cuomo, D.L. Pappas, R. Lossy, J.P. Doyle, J. Bruley, G.W. Di Bello, W. Krakow, Energetic carbon deposition at oblique angles. *J. Vac. Sci. Technol. A* **10**, 3414–3418 (1992)
43. D.L. Pappas, K.L. Saenger, J. Bruley, W. Krakow, J.J. Cuomo, Pulsed laser deposition of diamondlike carbon films. *J. Appl. Phys.* **71**, 5675–5684 (1992)
44. H.J. Scheibe, B. Schultrich, DLC film deposition by laser-arc and study of properties. *Thin Solid Films* **246**, 92–102 (1994)
45. C. Donnet, A. Grill, Friction control of diamond-like carbon coatings. *Surf. Coat. Technol.* **94/95**, 456 (1997)

46. A. Grill, Tribological properties of diamondlike carbon and related materials. *Surf. Coat. Technol.* **94/95**, 507 (1997)
47. B.K. Gupta, B. Bhushan, Micromechanical properties of amorphous carbon coatings deposited by different deposition techniques. *Thin Solid Films* **270**, 391–398 (1995)
48. X. Li, B. Bhushan, Micro/nanomechanical and tribological characterization of ultra-thin amorphous carbon coatings. *J. Mater. Res.* **14**, 2328–2337 (1999)
49. X. Li, B. Bhushan, Mechanical and tribological studies of ultra-thin hard carbon overcoats for magnetic recording heads. *Z. Metallkd.* **90**, 820–830 (1999)
50. S. Sundararajan, B. Bhushan, Micro/nanotribology of ultra-thin hard amorphous carbon coatings using atomic force/friction force microscopy. *Wear* **225–229**, 678–689 (1999)
51. B. Bhushan, Chemical, mechanical, and tribological characterization of ultra-thin and hard amorphous carbon coatings as thin as 3.5nm: Recent developments. *Diam. Relat. Mater.* **8**, 1985–2015 (1999)
52. I.I. Aksenov, V.E. Strel'Nitskii, Wear resistance of diamond-like carbon coatings. *Surf. Coat. Technol.* **47**, 252–256 (1991)
53. D.R. McKenzie, D. Muller, B.A. Pailthorpe, Z.H. Wang, E. Kravtchinskaja, D. Segal, P.B. Lukins, P.J. Martin, G. Amarutunga, P.H. Gaskell, A. Saeed, Properties of tetrahedral amorphous carbon prepared by vacuum arc deposition. *Diam. Relat. Mater.* **1**, 51–59 (1991)
54. R. Lossy, D.L. Pappas, R.A. Roy, J.J. Cuomo, Filtered arc deposition of amorphous diamond. *Appl. Phys. Lett.* **61**, 171–173 (1992)
55. I.G. Brown, A. Anders, S. Anders, M.R. Dickinson, I.C. Ivanov, R.A. MacGill, X.Y. Yao, K.M. Yu, Plasma synthesis of metallic and composite thin films with atomically mixed substrate bonding. *Nucl. Instrum. Methods. B* **80/81**, 1281–1287 (1993)
56. P.J. Fallon, V.S. Veerasamy, C.A. Davis, J. Robertson, G.A.J. Amarutunga, W.I. Milne, J. Koskinen, Properties of filtered-ion-beam-deposited diamond-like carbon as a function of ion energy. *Phys. Rev. B* **48**, 4777–4782 (1993)
57. S. Anders, A. Anders, I.G. Brown, B. Wei, K. Komvopoulos, J.W. Ager III, K.M. Yu: Effect of vacuum arc deposition parameters on the properties of amorphous carbon thin films, *Surf. Coat. Technol.* **68/69**, 388–393 (1994)
58. S. Anders, A. Anders, I.G. Brown, M.R. Dickinson, R.A. MacGill, Metal plasma immersion ion implantation and deposition using arc plasma sources. *J. Vac. Sci. Technol. B* **12**, 815–820 (1994)
59. S. Anders, A. Anders, I.G. Brown, Transport of vacuum arc plasma through magnetic macroparticle filters. *Plasma Sources Sci.* **4**, 1–12 (1995)
60. D.M. Swec, M.J. Mirtich, B.A. Banks, *Ion Beam and Plasma Methods of Producing Diamondlike Carbon Films* (NASA, Cleveland, 1989). Report No. NASA TM102301
61. A. Erdemir, M. Switala, R. Wei, P. Wilbur, A tribological investigation of the graphite-to-diamond-like behavior of amorphous carbon films ion beam deposited on ceramic substrates. *Surf. Coat. Technol.* **50**, 17–23 (1991)
62. A. Erdemir, F.A. Nicols, X.Z. Pan, R. Wei, P.J. Wilbur, Friction and wear performance of ion-beam deposited diamond-like carbon films on steel substrates. *Diam. Relat. Mater.* **3**, 119–125 (1993)
63. R. Wei, P.J. Wilbur, M.J. Liston, Effects of diamond-like hydrocarbon films on rolling contact fatigue of bearing steels. *Diam. Relat. Mater.* **2**, 898–903 (1993)
64. A. Erdemir, C. Donnet, Tribology of diamond, diamond-like carbon, and related films. In *Modern Tribology Handbook*, ed. by B. Bhushan (CRC, Boca Raton, 2001), pp.871–908
65. J. Asmussen, Electron cyclotron resonance microwave discharges for etching and thin-film deposition. *J. Vac. Sci. Technol. A* **7**, 883–893 (1989)
66. J. Suzuki, S. Okada, Deposition of diamondlike carbon films using electron cyclotron resonance plasma chemical vapor deposition from ethylene gas. *Jpn. J. Appl. Phys.* **34**, L1218–L1220 (1995)
67. B.A. Banks, S.K. Rutledge, Ion beam sputter deposited diamond like films. *J. Vac. Sci. Technol.* **21**, 807–814 (1982)

68. C. Weissmantel, K. Bewilogua, K. Breuer, D. Dietrich, U. Ebersbach, H.J. Erler, B. Rau, G. Reisse, Preparation and properties of hard i-C and i-BN coatings. *Thin Solid Films* **96**, 31–44 (1982)
69. H. Dimigen, H. Hubsch, Applying low-friction wear-resistant thin solid films by physical vapor deposition. *Philips Tech. Rev.* **41**, 186–197 (1983)
70. B. Bhushan, B.K. Gupta, M.H. Azarian, Nanoindentation, microscratch, friction and wear studies for contact recording applications. *Wear* **181–183**, 743–758 (1995)
71. B. Bhushan, L. Yang, C. Gao, S. Suri, R.A. Miller, B. Marchon, Friction and wear studies of magnetic thin-film rigid disks with glass-ceramic, glass and aluminum-magnesium substrates. *Wear* **190**, 44–59 (1995)
72. L. Holland, S.M. Ojha, Deposition of hard and insulating carbonaceous films of an RF target in butane plasma. *Thin Solid Films* **38**, L17–L19 (1976)
73. L.P. Andersson, A review of recent work on hard i-C films. *Thin Solid Films* **86**, 193–200 (1981)
74. A. Bubenzer, B. Dischler, B. Brandt, P. Koidl, RF plasma deposited amorphous hydrogenated hard carbon thin films, preparation, properties and applications. *J. Appl. Phys.* **54**, 4590–4594 (1983)
75. A. Grill, B.S. Meyerson, V.V. Patel, Diamond-like carbon films by RF plasma-assisted chemical vapor deposition from acetylene. *IBM J. Res. Dev.* **34**, 849–857 (1990)
76. A. Grill, B.S. Meyerson, V.V. Patel, Interface modification for improving the adhesion of a-C:H to metals. *J. Mater. Res.* **3**, 214 (1988)
77. A. Grill, V.V. Patel, B.S. Meyerson, Optical and tribological properties of heat-treated diamond-like carbon. *J. Mater. Res.* **5**, 2531–2537 (1990)
78. F. Jansen, M. Machonkin, S. Kaplan, S. Hark, The effect of hydrogenation on the properties of ion beam sputter deposited amorphous carbon. *J. Vac. Sci. Technol. A* **3**, 605–609 (1985)
79. S. Kaplan, F. Jansen, M. Machonkin, Characterization of amorphous carbon-hydrogen films by solid-state nuclear magnetic resonance. *Appl. Phys. Lett.* **47**, 750–753 (1985)
80. H.C. Tsai, D.B. Bogy, M.K. Kundmann, D.K. Veirs, M.R. Hilton, S.T. Mayer, Structure and properties of sputtered carbon overcoats on rigid magnetic media disks. *J. Vac. Sci. Technol. A* **6**, 2307–2315 (1988)
81. B. Marchon, M. Salmeron, W. Siekhaus, Observation of graphitic and amorphous structures on the surface of hard carbon films by scanning tunneling microscopy. *Phys. Rev. B* **39**, 12907–12910 (1989)
82. B. Dischler, A. Bubenzer, P. Koidl, Hard carbon coatings with low optical absorption. *Appl. Phys. Lett.* **42**, 636–638 (1983)
83. D.S. Knight, W.B. White, Characterization of diamond films by Raman spectroscopy. *J. Mater. Res.* **4**, 385–393 (1989)
84. J.W. Ager III, D.K. Veirs, C.M. Rosenblatt, Spatially resolved Raman studies of diamond films grown by chemical vapor deposition. *Phys. Rev. B* **43**, 6491–6499 (1991)
85. W. Scharff, K. Hammer, O. Stenzel, J. Ullman, M. Vogel, T. Frauenheim, B. Eibisch, S. Roth, S. Schulze, I. Muhling, Preparation of amorphous i-C films by ion-assisted methods. *Thin Solid Films* **171**, 157–169 (1989)
86. B. Bhushan, X. Li, Nanomechanical characterization of solid surfaces and thin films. *Int. Mater. Rev.* **48**, 125–164 (2003)
87. X. Li, D. Diao, B. Bhushan, Fracture mechanisms of thin amorphous carbon films in nanoindentation. *Acta Mater.* **45**, 4453–4461 (1997)
88. X. Li, B. Bhushan, Measurement of fracture toughness of ultra-thin amorphous carbon films. *Thin Solid Films* **315**, 214–221 (1998)
89. X. Li, B. Bhushan, Evaluation of fracture toughness of ultra-thin amorphous carbon coatings deposited by different deposition techniques. *Thin Solid Films* **355/356**, 330–336 (1999)
90. X. Li, B. Bhushan, Development of a nanoscale fatigue measurement technique and its application to ultrathin amorphous carbon coatings. *Scr. Mater.* **47**, 473–479 (2002)
91. X. Li, B. Bhushan, Nanofatigue studies of ultrathin hard carbon overcoats used in magnetic storage devices. *J. Appl. Phys.* **91**, 8334–8336 (2002)

92. J. Robertson, Deposition of diamond-like carbon. *Philos. Trans. R. Soc. Lond. A* **342**, 277–286 (1993)
93. S.J. Bull, Tribology of carbon coatings: DLC, diamond and beyond. *Diam. Relat. Mater.* **4**, 827–836 (1995)
94. N. Savvides, T.J. Bell, Microhardness and Young's modulus of diamond and diamondlike carbon films. *J. Appl. Phys.* **72**, 2791–2796 (1992)
95. B. Bhushan, M.F. Doerner, Role of mechanical properties and surface texture in the real area of contact of magnetic rigid disks. *ASME J. Tribol.* **111**, 452–458 (1989)
96. S. Suresh, *Fatigue of Materials* (Cambridge University Press, Cambridge, 1991)
97. D.B. Marshall, A.G. Evans, Measurement of adherence of residual stresses in thin films by indentation. I. Mechanics of interface delamination. *J. Appl. Phys.* **15**, 2632–2638 (1984)
98. A.G. Evans, J.W. Hutchinson, On the mechanics of delamination and spalling in compressed films. *Int. J. Solids Struct.* **20**, 455–466 (1984)
99. S. Sundararajan, B. Bhushan, Development of a continuous microscratch technique in an atomic force microscope and its application to study scratch resistance of ultrathin hard amorphous carbon coatings. *J. Mater. Res.* **16**, 437–445 (2001)
100. B. Bhushan, B.K. Gupta, Micromechanical characterization of Ni-P coated aluminum-magnesium, glass and glass-ceramic substrates and finished magnetic thin-film rigid disks. *Adv. Inf. Storage Syst.* **6**, 193–208 (1995)
101. X. Li, B. Bhushan, Micromechanical and tribological characterization of hard amorphous carbon coatings as thin as 5 nm for magnetic recording heads. *Wear* **220**, 51–58 (1998)
102. B. Bhushan, V.N. Koinkar, Microscale mechanical and tribological characterization of hard amorphous coatings as thin as 5 nm for magnetic disks. *Surf. Coat. Technol.* **76/77**, 655–669 (1995)
103. V.N. Koinkar, B. Bhushan, Microtribological properties of hard amorphous carbon protective coatings for thin-film magnetic disks and heads. *Proc. Inst. Mech. Eng. J* **211**, 365–372 (1997)
104. T.W. Wu, Microscratch and load relaxation tests for ultra-thin films. *J. Mater. Res.* **6**, 407–426 (1991)
105. R. Memming, H.J. Tolle, P.E. Wierenga, Properties of polymeric layers of hydrogenated amorphous carbon produced by plasma-activated chemical vapor deposition: tribological and mechanical properties. *Thin Solid Films* **143**, 31–41 (1986)
106. C. Donnet, T. Le Mogne, L. Ponsonnet, M. Belin, A. Grill, V. Patel, The respective role of oxygen and water vapor on the tribology of hydrogenated diamond-like carbon coatings. *Tribol. Lett.* **4**, 259 (1998)
107. F.P. Bowden, J.E. Young, Friction of diamond, graphite and carbon and the influence of surface films. *Proc. R. Soc. Lond. A* **208**, 444–455 (1951)
108. B. Marchon, N. Heiman, M.R. Khan, Evidence for tribochemical wear on amorphous carbon thin films. *IEEE Trans. Magn.* **26**, 168–170 (1990)
109. M.T. Dugger, Y.W. Chung, B. Bhushan, W. Rothschild, Friction, wear, and interfacial chemistry in thin film magnetic rigid disk files. *ASME J. Tribol.* **112**, 238–245 (1990)
110. B.D. Strom, D.B. Bogy, C.S. Bhatia, B. Bhushan, Tribochemical effects of various gases and water vapor on thin film magnetic disks with carbon overcoats. *ASME J. Tribol.* **113**, 689–693 (1991)
111. B. Bhushan, J. Ruan, Tribological performance of thin film amorphous carbon overcoats for magnetic recording rigid disks in various environments. *Surf. Coat. Technol.* **68/69**, 644–650 (1994)
112. B. Bhushan, G.S.A.M. Theunissen, X. Li, Tribological studies of chromium oxide films for magnetic recording applications. *Thin Solid Films* **311**, 67–80 (1997)

# Chapter 18

## Self-Assembled Monolayers for Nanotribology and Surface Protection

**Bharat Bhushan**

**Abstract** Reliability of various micro- and nanodevices requiring relative motion as well as magnetic storage devices requires the use of hydrophobic and lubricating films to minimize adhesion, stiction, friction, and wear. In various applications, surfaces need to be protected from exposure to the operating environment, and hydrophobic films are of interest. The surface films should be molecularly thick, well-organized, chemically bonded to the substrate, and insensitive to environment. Ordered molecular assemblies with high hydrophobicity can be engineered using chemical grafting of various polymer molecules with suitable functional head groups, spacer chains, and nonpolar surface terminal groups.

In this chapter, we focus on self-assembled monolayers (SAMs) with high hydrophobicity and good nanotribological properties. SAMs are produced by various organic precursors. We first present a primer to organic chemistry, followed by an overview of selected SAMs with various substrates, spacer chains, and terminal groups in the molecular chains and an overview of nanotribological properties of SAMs. The contact angle, adhesion, friction, and wear properties of SAMs having various spacer chains with different surface terminal and head groups (hexadecane thiol, biphenyl thiol, perfluoroalkylsilane, alkylsilane, perfluoroalkylphosphonate, and alkylphosphonate) on various substrates (Au, Si, and Al) are surveyed. Chemical degradation mechanisms and environmental effects are studied. Based on the contact angle and nanotribological properties of various SAM films by atomic force microscopy (AFM) it is found that perfluoroalkylsilane and perfluorophosphonate SAMs exhibit attractive hydrophobic and tribological properties.

### 18.1 Background

Reliability of various micro- and nanodevices, also commonly referred to as micro-/nanoelectromechanical systems (MEMS/NEMS) and bioMEMS/bioNEMS, requiring relative motion, as well as magnetic storage devices (which include magnetic rigid disk and tape drives) requires the use of hydrophobic and lubricating films to minimize adhesion, stiction, friction, and wear [1–10]. In various applications,

surfaces need to be protected from exposure to the operating environment. For example, in various biomedical applications, such as biosensors and implantable biomedical devices, undesirable protein adsorption, biofouling, and biocompatibility are some of the major issues [5, 7]. In micro- and nanofluidic-based sensors, the fluid drag in micro- and nanochannels can be reduced by using hydrophobic coatings. Selected hydrophobic films are needed for these applications.

### 18.1.1 Need for Hydrophobic Surfaces for Nanotribology

The source of the liquid film at the interface can be a preexisting film of liquid and/or capillary condensates of water vapor from the environment. If the liquid wets the surface ( $0 \leq \theta < 90^\circ$ , where  $\theta$  is the contact angle between the liquid–vapor interface and the liquid–solid interface for a liquid droplet sitting on a solid surface (Fig. 18.1a)), the liquid surface is constrained to lie parallel to the surface [11–13], and the complete liquid surface is therefore concave in shape (Fig. 18.1b). Direct measurement of contact angle is most widely made from sessile drops. The angle is generally measured by aligning a tangent with the drop profile at the point of contact with the solid surface using a telescope equipped with a goniometer eyepiece. Surface tension results in a pressure difference across any meniscus surface, referred to as capillary pressure or Laplace pressure, which is negative for a concave meniscus [14, 15]. The negative Laplace pressure results in an intrinsic attractive (adhesive) force which depends on the interface roughness (the local

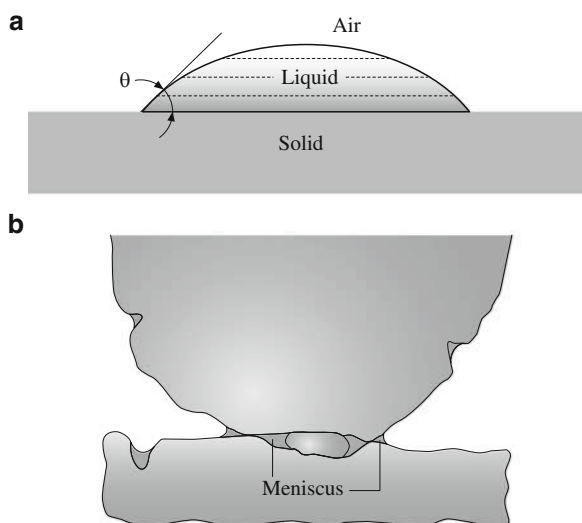


**Fig. 18.1** (a) Schematic of a sessile drop on a solid surface and the definition of contact angle. (b) Formation of meniscus bridges as a result of liquid present at an interface

geometry of interacting asperities and number of asperities), the surface tension, and the contact angle. During normal separation, this intrinsic force needs to be overcome [16]. During sliding, frictional effects need to be overcome, not only because of external load but also because of intrinsic adhesive force. A measured value of high static friction force contributed largely by liquid-mediated adhesion (meniscus contribution) is generally referred to as *stiction*. It becomes a major concern in micro- and nanodevices operating at ultralow loads, as the liquid-mediated adhesive force may be on the same order as the external load. The effect of liquid-mediated adhesion can be minimized by increasing surface roughness and/or the use of a liquid with low surface tension with film thickness on the order of the surface roughness, as well as its chemical bonding to the substrate [14–21]. The formation of menisci and/or condensation of water vapor from the environment at the interface can be minimized by the use of hydrophobic (water-fearing) coatings. Surfaces can be made superhydrophobic by the introduction of controlled roughness on the surfaces to take advantage of the so-called lotus effect [22, 23].

### 18.1.2 Surface Films for Nanotribology and Surface Protection

Surfaces can be treated or coated with a liquid with relatively low surface tension or certain solid films to make them hydrophobic and/or to control adhesion, stiction, friction, and wear.

The classic approach to lubrication uses freely supported multimolecular layers of liquid lubricants [2, 4, 6, 14, 15, 20, 24–27]. Boundary lubricant films are formed by physisorption, chemisorption or chemical reaction. The physisorbed films can be either monomolecularly or polymolecularly thick. Chemisorbed films are monomolecular, but stoichiometric films formed by chemical reaction can be multilayers. In general, the stability and durability of surface films decrease in the following order: chemically reacted films > chemisorbed films > physisorbed films. A good boundary lubricant should have a high degree of interaction between its molecules and the sliding surface. As a general rule, liquids will have a more desirable performance when they are polar and thus able to grip onto solid surfaces (or be adsorbed). Polar lubricants contain reactive functional end groups. Boundary lubrication properties are also dependent upon the molecular conformation and lubricant spreading. It should be noted that liquid films with thickness on the order of a few nm may be discontinuous and may deposit in island form with nonuniform thickness and lateral resolution on the nm scale.

Solid films are also commonly used for controlling hydrophobicity and/or adhesion, stiction, friction, and wear. Hydrophobic films have nonpolar surface terminal groups (to be described later) which repel water. These films have low surface energy (15–30 dyn/cm) and high contact angle ( $\theta \geq 90^\circ$ ) which minimize wetting (e.g., [25, 28, 29]). Multimolecularly thick (few tenths of nm) films of conventional solid lubricants have been studied. Hansma et al. [30] reported the deposition of multimolecularly thick, highly oriented polytetrafluoroethylene



(PTFE) films from the melt or vapor phase or from solution by a mechanical deposition technique by dragging the polymer at controlled temperature, pressure, and speed against a smooth glass substrate. Scandella et al. [31] reported that the coefficient of nanoscale friction of MoS<sub>2</sub> platelets on mica, obtained by the exfoliation of lithium intercalated MoS<sub>2</sub> in water, was a factor of 1.4 less than that of mica itself. However, MoS<sub>2</sub> is reactive to water, and its friction and wear properties degrade with increasing humidity [14, 15]. Amorphous diamond-like carbon (DLC) coatings can be produced with extremely high hardness and are used commercially as wear-resistant coatings [32, 33]. They are widely used in magnetic storage devices [2]. Doping of the DLC matrix with elements such as hydrogen, nitrogen, oxygen, silicon, and fluorine influences their hydrophobicity and tribological properties [32, 34, 35]. Nitrogen and oxygen reduce the contact angle (or increase the surface energy) due to the strong polarity formed when these elements bond to carbon. On the other hand, silicon and fluorine increase the contact angle to 70–100° (or reduce the surface energy to 20–40 dyn/cm), making them hydrophobic [36, 37]. Nanocomposite coatings with a diamond-like carbon (a-C:H) network and a glasslike a-Si:O network are generally deposited using a plasma-enhanced chemical vapor deposition (PECVD) technique in which plasma is formed from a siloxane precursor using a hot filament. For fluorinated DLC, CF<sub>4</sub> is added as the fluorocarbon source to an acetylene plasma. In addition, fluorination of DLC can be achieved by postdeposition treatment of DLC coatings in CF<sub>4</sub> plasma. Silicon- and fluorine-containing DLC coatings mainly reduce their polarity due to the loss of sp<sup>2</sup> bonded carbon (due to the polarization potential of the involved  $\pi$  electrons) and dangling bonds of the DLC network. As silicon and fluorine are unable to form double bonds, they force carbon into a sp<sup>3</sup> bonding state [37]. Friction and wear properties of both silicon-containing and fluorinated DLC coatings have been reported to be superior to those of conventional DLC coatings [38, 39]. However, DLC coatings require a line-of-sight deposition process which prevents deposition on complex geometries. Furthermore, it has been reported that some self-assembled monolayers (SAMs) are superior to DLC coatings in terms of their hydrophobicity and tribological performance [40, 41].

Organized and dense molecular-scale layers of, preferably long-chain, organic molecules are known to be superior lubricants on both macro- and micro-/nanoscales as compared with freely supported multimolecular layers [4, 6]. Common techniques to produce molecular scale organized layers are Langmuir–Blodgett (LB) deposition and chemical grafting of organic molecules to realize SAMs [28, 29]. In the LB technique, organic molecules from suitable amphiphilic molecules are first organized at the air–water interface and then physisorbed on a solid surface to form mono- or multimolecular layers [42]. In the case of SAMs the functional groups of molecules chemisorb onto a solid surface, which results in the spontaneous formation of robust, highly ordered, oriented, dense monolayers [29]. In both cases, the organic molecules used have well-distinguished amphiphilic properties (a hydrophilic functional head and a hydrophobic aliphatic tail) so that adsorption of such molecules on an active inorganic substrate leads to their firm attachment to the surface. Direct organization of SAMs on the solid surfaces allows coating in

inaccessible areas. The weak adhesion of classical LB films to the substrate surface restricts their lifetime during sliding, whereas certain SAMs can be very durable. As a result, SAMs are of great interest in tribological applications.

Much research into the application of SAMs has been carried out using the so-called soft lithographic technique [43, 44]. This is a nonphotolithographic technique. Photolithography is based on a projection-printing system used for projection of an image from a mask to a thin-film photoresist; its resolution is limited by optical diffraction limits. In soft lithography, an elastomeric stamp or mold is used to generate micropatterns of SAMs by either contact printing (known as microcontact printing,  $\mu$ CP [45]), by embossing (nanoimprint lithography) [46] or by replica molding [47], thereby circumventing the diffraction limits of photolithography. The stamps are generally cast from photolithographically generated patterned masters, and the stamp material is generally polydimethylsiloxane (PDMS). In  $\mu$ CP, the ink is a SAM precursor to produce nm-thick resists with lines thinner than 100 nm. Soft lithography requires little capital investment.  $\mu$ CP and embossing techniques may be used to produce microdevices which are substantially cheaper and more flexible in terms of the choice of material for construction than with conventional photolithography (e.g., SAMs and non-SAM entities for  $\mu$ CP and elastomers for embossing).

The largest industrial application for SAMs is in digital micromirror devices (DMD) used in optical projection displays [48, 49]. The chip set of a DMD consists of half a million to more than two million independently controlled reflective aluminum alloy micromirrors of about  $12\ \mu\text{m}^2$ . These micromirrors switch forward and backward at a frequency on the order of 5–7 kHz with a rotation of  $\pm 12^\circ$  with respect to the horizontal plane; the movement is limited by a mechanical stop. Mechanical contact leads to stiction and wear in contacting surfaces. A SAM of vapor-deposited perfluorinated *n*-alkanoic acid ( $\text{C}_n\text{F}_{2n-1}\text{O}_2\text{H}$ ) [e.g., perfluorodecanoic acid (PFDA),  $\text{CF}_3(\text{CF}_2)_8\text{COOH}$ ] is used to coat contacting surfaces to make them hydrophobic in order to minimize meniscus formation. Furthermore, the entire DMD chip set is hermetically sealed in order to prevent particulate contamination and excessive condensation of water at the contacting surfaces. A so-called *getter* strip of PFDA is included inside the hermetically sealed enclosure containing the chip, which acts as a reservoir in order to maintain a PFDA vapor within the package. Degradation mechanisms of SAMs leading to stiction have been studied by Liu and Bhushan [50, 51]. Nanotribological studies of various SAMs on Al substrates have been carried out by Tambe and Bhushan [52], Bhushan et al. [53], Hoque et al. [54–56], and DeRose et al. [57].

There are various other micro-/nanodevices which require SAMs for hydrophobicity in order to minimize meniscus formation. Examples include micromotors, microgears, microvalves, microswitches, mirror-based optical switches, and atomic force microscopy probes [5–7]. Nanotribological studies on Si substrates have been carried out by Bhushan et al. [58–60], Kasai et al. [61], Lee et al. [62], Tambe and Bhushan [52], and Tao and Bhushan [63, 64]. SAM deposition on Cu surfaces is also being explored for corrosion inhibition for micro-/nanoelectronics and/or heat-exchange surfaces, exploiting dropwise condensation [65–67].

Other industrial applications for SAMs are in the areas of biochemical and optical sensors, devices for use as drug-delivery vehicles, and in the construction of electronic components [68–71]. Biochemical sensors require highly sensitive organic layers with tailored biological properties that can be incorporated into electronic, optical or electrochemical devices. Self-assembled microscopic vesicles are being developed to ferry potentially life-saving drugs to cancer patients. By assembling organic, metal, and phosphonate molecules (complexes of phosphorous and oxygen atoms) into conductive materials, these can be produced as self-made sandwiches for use as electronic components. Several applications have been proposed based on silicon, glass or polymer nanochannels, including cell immunoisolation chambers, DNA separation devices, and biocapsules for drug delivery [5, 6].

SAMs are also being considered for protection of surfaces from exposure to the operating environment. They are being developed to reduce corrosion and oxidation of Cu in heat exchangers [65–67]. They are being developed to minimize undesirable protein adsorption and biofouling, and improve biocompatibility in biosensors and implantable biomedical devices [52, 53, 58–63, 72, 73]. These films can also be used to reduce fluid drag in micro-/nanochannels.

### ***18.1.3 Scope of the Chapter***

An overview of molecularly thick layers of liquid lubricants and conventional solid lubricants can be found in various references, such as works by Bhushan [2, 4, 6, 14, 15, 18, 32], Bhushan and Zhao [20], and Liu [27]. In this chapter, we focus on SAMs for high hydrophobicity, and low adhesion, friction, and wear. SAMs are produced by various organic precursors. We first present a primer to organic chemistry followed by an overview on suitable substrates, spacer chains, and end groups in molecular chains, an overview on contact angle, adhesion, friction, and wear properties of various SAMs, and some concluding remarks.

## **18.2 A Primer to Organic Chemistry**

All organic compounds contain the carbon (C) atom. Carbon, in combination with hydrogen, oxygen, nitrogen, sulfur, and phosphor, results in a large number of organic compounds. The atomic number of carbon is 6, and its electron structure is  $1s^2 2s^2 2p^2$ . Two stable isotopes of carbon,  $^{12}\text{C}$  and  $^{13}\text{C}$ , exist. With four electrons in its outer shell, carbon forms four covalent bonds, with each bond resulting from two atoms sharing a pair of electrons. The number of electron pairs that two atoms share determines whether or not the bond is single or multiple. In a single bond, only one pair of electrons is shared by the atoms. Carbon can also form multiple bonds by sharing two or three pairs of electrons between the atoms. For example, the double bond formed by sharing two electron pairs is stronger than a single bond, and it is

shorter than a single bond. An organic compound is classified as saturated if it contains only single bonds and as unsaturated if the molecules possess one or more multiple carbon–carbon bonds.

### 18.2.1 Electronegativity/Polarity

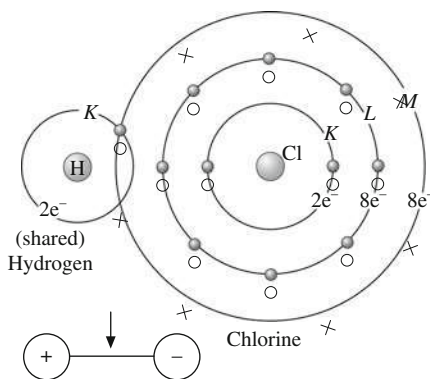
When two different kinds of atoms share a pair of electrons, a bond is formed in which electrons are shared unequally; one atom assumes a partial positive charge and the other a negative charge with respect to each other. This difference in charge occurs because the two atoms exert unequal attraction on the pair of shared electrons. The attractive force that an atom of an element has for shared electrons in a molecule or polyatomic ion is known as its electronegativity. Elements differ in their electronegativities. A scale of relative electronegatives, in which the most electronegative element, fluorine, is assigned a value of 4.0, was developed by Pauling. Relative electronegativities of the elements in the Periodic Table can be found in most undergraduate chemistry textbooks [74]. The relative electronegativity of nonmetals is high compared with that of metals. The relative electronegativity of selected elements of interest with high values is presented in Table 18.1.

The polarity of a bond is determined by the difference in electronegativity values of the atoms forming the bond. If the electronegativities are the same the bond is nonpolar, and the electrons are shared equally. In this type of bond, there is no separation of positive and negative charge between atoms. If the atoms have greatly different electronegativities the bond is very polar. A dipole is a molecule that is electrically asymmetrical, causing it to be oppositely charged at two points. As an example, in HCl both hydrogen and chlorine need one electron to form stable electron configurations. They share a pair of electrons. Chlorine is more electronegative and therefore has a greater attraction for the shared electrons than does hydrogen. As a result, the pair of electrons is displaced towards the chlorine atom, giving it a partial negative charge and leaving the hydrogen atom with a partial positive charge (Fig. 18.2). However, the entire HCl molecule is electrically neutral. The hydrogen atom with a partial positive charge (exposed proton on one end) can be easily attracted to the negative charge of other molecules and this is

**Table 18.1** Relative electronegativity of selected elements

Element	Relative electronegativity
F	4.0
O	3.5
N	3.0
Cl	3.0
C	2.5
S	2.5
P	2.1
H	2.1

**Fig. 18.2** Schematic representation of the formation of a polar HCl molecule



responsible for the polarity of the molecule. A partial charge is usually indicated by  $\delta$ , and the electronic structure of HCl is given as



Similar to the HCl molecule, HF is polar, and both behave as a small dipole. On the other hand, methane ( $\text{CH}_4$ ), carbon tetrachloride ( $\text{CCl}_4$ ), and carbon dioxide ( $\text{CO}_2$ ) are nonpolar. In  $\text{CH}_4$  and  $\text{CCl}_4$ , the four C–H and C–Cl polar bonds are identical, and because these bonds emanate from the center to the corners of a tetrahedron in the molecule, the effects of their polarities cancel one another.  $\text{CO}_2$  ( $\text{O}=\text{C}=\text{O}$ ) is nonpolar because the C–O dipoles cancel each other by acting in opposite direction. Water ( $\text{H}-\text{O}-\text{H}$ ) is a polar molecule. If the atoms in water were linear as in  $\text{CO}_2$ , the two O–H dipoles would cancel each other, and the molecule would be nonpolar. However, water has a bent structure with an angle of  $105^\circ$  between the two bonds, which is responsible for water being a polar molecule.


## 18.2.2 Classification and Structure of Organic Compounds

Table 18.2 presents selected organic compounds grouped into classes.

### Hydrocarbons

Hydrocarbons are compounds that are composed entirely of carbon and hydrogen atoms bonded to each other by covalent bonds. Saturated hydrocarbons (alkanes) contain single bonds. Unsaturated hydrocarbons that contain  $\text{C}=\text{C}$  bonds are called alkenes, and ones with triple bonds are called alkynes. Unsaturated hydrocarbons that contain aromatic rings, e.g., benzene rings, are called aromatic hydrocarbons.

**Table 18.2** Names and formulas of selected hydrocarbons

Name	Formula
<b>Saturated hydrocarbons</b>	
Straight-chain alkanes	$C_nH_{2n+2}$
e.g., methane	$CH_4$
ethane	$C_2H_6$ or $CH_3CH_3$
Alkyl groups	$C_nH_{2n+1}$
e.g., methyl	$-CH_3$
ethyl	$-CH_2CH_3$
<b>Unsaturated hydrocarbons</b>	
Alkenes	$(CH_2)_n$
e.g., ethene	$C_2H_4$ or $CH_2=CH_2$
propene	$C_3H_6$ or $CH_3CH=CH_2$
Alkynes e.g., acetylene	$HC \equiv CH$
Aromatic hydrocarbons e.g., benzene	$C_6H_5OH$ or 

### Saturated Hydrocarbons: Alkanes

The alkanes, also known as paraffins, are saturated hydrocarbons, straight- or branched-chain hydrocarbons with only single covalent bonds between the carbon atoms. The general molecular formula for the alkanes is  $C_nH_{2n+2}$ , where  $n$  is the number of carbon atoms in the molecule. Each carbon atom is connected to four other atoms by four single covalent bonds. These bonds are separated by angles of  $109.5^\circ$  (the angle between lines from the center of a regular tetrahedron to its corners). Alkane molecules contain only carbon-carbon and carbon-hydrogen bonds, which are symmetrically directed towards the corners of a tetrahedron. Therefore alkane molecules are essentially nonpolar.

Common alkyl groups have the general formula  $C_nH_{2n+1}$  (one hydrogen atom fewer than the corresponding alkane). The missing H atom may be detached from any carbon in the alkane. The name of the group is formed from the name of the corresponding alkane by replacing -ane with -yl ending. Some examples are shown in Table 18.2.

### Unsaturated Hydrocarbons

Unsaturated hydrocarbons consist of three families of compounds that contain fewer hydrogen atoms than the alkane with the corresponding number of carbon atoms, and contain multiple bonds between carbon atoms. These include alkenes (with  $C=C$  bonds), alkynes (with  $C \equiv C$  bonds), and aromatic compounds (with benzene rings which are arranged in a six-membered ring with one hydrogen atom bonded to each carbon atom). Some examples are shown in Table 18.2.

### Alcohols, Ethers, Phenols, and Thiols

Organic molecules with certain functional groups are synthesized for desirable properties. Alcohols, ethers, and phenols are derived from the structure of water by replacing the hydrogen atoms of water with alkyl groups (R) or aromatic (Ar) rings. For example, phenol is a class of compounds that has a hydroxy group attached to an aromatic ring (benzene ring). Organic compounds that contain the –SH group are analogs of alcohols, and are known as thiols. Some examples are shown in Table 18.3.

### Aldehydes and Ketones

Both aldehydes and ketones contain the carbonyl group



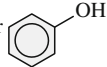
a carbon–oxygen double bond. Aldehydes have at least one hydrogen atom bonded to the carbonyl group, whereas ketones have only alkyl or aromatic group bonded to the carbonyl group. The general formula for the saturated homologous series of aldehydes and ketones is  $\text{C}_n\text{H}_{2n}\text{O}$ . Some examples are shown in Table 18.4.

### Carboxyl Acids and Esters

The functional group of the carboxylic acids is known as a carboxyl group, represented as –COOH. Carboxylic acids can be either aliphatic ( $\text{RCOOH}$ ) or aromatic ( $\text{ArCOOH}$ ). The carboxylic acids with even numbers of carbon atoms  $n$  ranging from 4 to about 20 are called fatty acids (e.g.,  $n = 10, 12, 14, 16$ , and 18, called capric acid, lauric acid, myristic acid, palmitic acid, and stearic acid, respectively).

Esters are alcohol derivatives of carboxylic acids. Their general formula is  $\text{RCOOR}'$ , where R may be a hydrogen, alkyl group or aromatic group, and  $\text{R}'$  may be an alkyl group or aromatic group, but not a hydrogen. Esters are found in fats and oils. Some examples are shown in Table 18.5.

**Table 18.3** Names and formulas of selected alcohols, ethers, phenols, and thiols. The letters R and  $\text{R}'$  represent an alkyl group. The R-groups in ethers can be the same or different and can be alkyl or aromatic (Ar) groups

Name	Formula
Alcohols	$\text{R-OH}$
e.g., methanol	$\text{CH}_3\text{OH}$
ethanol	$\text{CH}_3\text{CH}_2\text{OH}$
Ethers	$\text{R-O-R}'$
e.g., dimethyl ether	$\text{CH}_3\text{-O-CH}_3$
diethyl ether	$\text{CH}_3\text{CH}_2\text{-O-CH}_2\text{CH}_3$
Phenols	$\text{C}_6\text{H}_5\text{OH}$ or 
Thiols	$\text{-SH}$
e.g., methanethiol	$\text{CH}_3\text{SH}$

**Table 18.4** Names and formulas of selected aldehydes and ketones. The letters R and R' represent an alkyl group and Ar represents an aromatic group

Name	Formula
Aldehydes	$\text{RCHO}$ or $\begin{array}{c} \text{O} \\ \parallel \\ \text{R}-\text{C}-\text{H} \end{array}$
	$\text{ArCHO}$ or $\begin{array}{c} \text{O} \\ \parallel \\ \text{Ar}-\text{C}-\text{H} \end{array}$
e.g., methanal or formaldehyde	$\text{HCHO}$
ethanol or acetaldehyde	$\text{CH}_3\text{CHO}$
Ketones	$\text{RCOR}'$ or $\begin{array}{c} \text{O} \\ \parallel \\ \text{R}-\text{C}-\text{R}' \end{array}$
	$\text{RCOAr}$ or $\begin{array}{c} \text{O} \\ \parallel \\ \text{R}-\text{C}-\text{Ar} \end{array}$
	$\text{ArCOAr}$ or $\begin{array}{c} \text{O} \\ \parallel \\ \text{Ar}-\text{C}-\text{Ar} \end{array}$
e.g., butanone or methyl ethyl ketone	$\text{CH}_3\text{COCH}_2\text{CH}_3$

**Table 18.5** Names and formulas of selected carboxylic acids and esters

Name	Formula
Carboxylic acid <sup>a</sup>	$\text{RCOOH}$ or $\begin{array}{c} \text{O} \\ \parallel \\ \text{R}-\text{C}-\text{OH} \end{array}$
	$\text{ArCOOH}$ or $\begin{array}{c} \text{O} \\ \parallel \\ \text{Ar}-\text{C}-\text{OH} \end{array}$
e.g., methanoic acid (formic acid)	$\text{HCOOH}$
ethanoic acid (acetic acid)	$\text{CH}_3\text{COOH}$
octadecanoic acid (stearic acid)	$\text{CH}_3(\text{CH}_2)_{16}\text{COOH}$
Esters <sup>b</sup>	$\text{RCOOR}'$ or $\begin{array}{c} \text{O} \\ \parallel \\ \text{R}-\text{C}-\text{O}-\text{R}' \\ \underbrace{\hspace{1cm}} \quad \underbrace{\hspace{1cm}} \\ \text{acid} \quad \text{alcohol} \end{array}$
e.g., methyl propanoate	$\text{CH}_3\text{CH}_2\text{COOCH}_3$

<sup>a</sup>The letter R represents an alkyl group and Ar represents an aromatic group<sup>b</sup>The letter R represents hydrogen, alkyl group or aromatic group and R' represents alkyl group or aromatic group



**Table 18.6** Names and formulas of selected organic nitrogen compounds (amides and amines). The letter R represents an alkyl group or aromatic group

Name	Formula
Amides	$\text{RCONH}_2$ or $\begin{array}{c} \text{O} \\ \parallel \\ \text{R}-\text{C}-\text{NH}_2 \end{array}$
e.g., methanamide (formamide)	$\text{HCONH}_2$
ethanamide (acetamide)	$\text{CH}_3\text{CONH}_2$
Amines	$\text{RNH}_2$ or $\text{R}-\text{N} \begin{array}{l} \nearrow \text{H} \\ \searrow \text{H} \end{array}$
	$\text{R}_2\text{NH}$
	$\text{R}_3\text{N}$
e.g., methylamine	$\text{CH}_3\text{NH}_2$
ethylamine	$\text{CH}_3\text{CH}_2\text{NH}_2$

### *Amides and Amines*

Amides and amines are organic compounds containing nitrogen. Amides are nitrogen derivatives of carboxylic acids. The carbon atom of a carbonyl group is bonded directly to a nitrogen atom of an  $-\text{NH}_2$ ,  $-\text{NHR}$  or  $-\text{NR}_2$  group. The characteristic structure of amide is  $\text{RCONH}_2$ .

An amine is a substituted ammonia molecule which has a general structure of  $\text{RNH}_2$ ,  $\text{R}_2\text{NH}$  or  $\text{R}_3\text{N}$ , where R is an alkyl or aromatic group. Some examples are shown in Table 18.6.

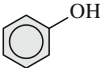
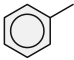
### **18.2.3 Polar and Nonpolar Groups**

Table 18.7 summarizes polar and nonpolar groups commonly used in the construction of hydrophobic and hydrophilic molecules. Table 18.8 lists the relative polarity of selected polar groups [75]. Thiol, silane, carboxylic acid, and alcohol (hydroxyl) groups are the most commonly used polar anchor groups for their attachment to surfaces. Silane anchor groups are commonly used for Si or  $\text{SiO}_2$  surfaces, as  $-\text{Si}-\text{O}-$  bonds are strong. Methyl and trifluoromethyl are commonly used as end groups for hydrophobic film surfaces.

## **18.3 Self-assembled Monolayers: Substrates, Spacer Chains, and End Groups in the Molecular Chains**

SAMs are formed as a result of spontaneous, self-organization of functionalized organic molecules onto the surfaces of appropriate substrates into stable, well-defined structures (Fig. 18.3). The final structure is close to or at thermodynamic

**Table 18.7** Some examples of polar (hydrophilic) and nonpolar (hydrophobic) groups. The letter R represents an alkyl group

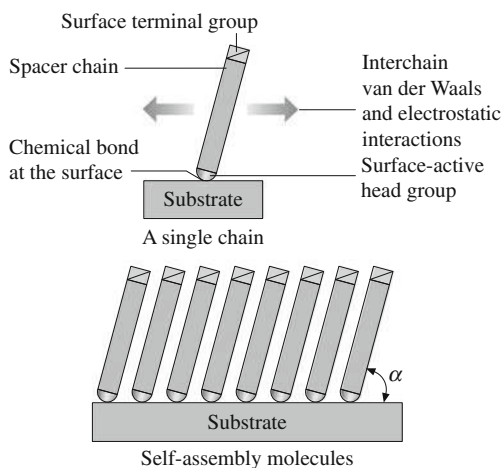
Name	Formula
<b>Polar</b>	
Alcohol (hydroxyl)	-OH
Carboxyl acid	-COOH
Aldehyde	-COH
Ketone	$\begin{array}{c} \text{O} \\ \parallel \\ \text{R}-\text{C}-\text{R} \end{array}$
Ester	-COO-
Carbonyl	$\begin{array}{c} \diagup \\ \text{C}=\text{O} \\ \diagdown \end{array}$
Ether	R-O-R
Amine	-NH <sub>2</sub>
Amide	$\begin{array}{c} \text{O} \\ \parallel \\ -\text{C}-\text{NH}_2 \end{array}$
Phenol	
Thiol	-SH
Trichlorosilane	SiCl <sub>3</sub>
<b>Nonpolar</b>	
Methyl	-CH <sub>3</sub>
Trifluoromethyl	-CF <sub>3</sub>
Aryl (benzene ring)	

**Table 18.8** Organic groups listed in increasing order of polarity

Alkanes
Alkenes
Aromatic hydrocarbons
Ethers
Trichlorosilanes
Aldehydes, ketones, esters, carbonyls
Thiols
Amines
Alcohols, phenols
Amides
Carboxylic acids

equilibrium, and as a result it tends to form spontaneously and rejects defects. SAMs consist of three building groups: a head group that binds strongly to a substrate, a surface terminal (tail or end) group that constitutes the outer surface

**Fig. 18.3** Schematic of a SAM on a surface and the associated forces



of the film, and a spacer chain (backbone chain) that connects the head and surface terminal groups. SAMs are named based on the surface terminal group, followed by the spacer chain and the head group (or type of compound formed at the surface). In order to control hydrophobicity, adhesion, friction, and wear, it should be strongly adherent to the substrate, and the surface terminal group of the organic molecular chain should be nonpolar. For strong attachment of the organic molecules to the substrate, the head group of the molecular chain should contain a polar terminal group, resulting in the exothermic process (energies on the order of tens of kcal/mol), i.e., the apparent pinning of the head group to a specific site on the surface through a chemical bond. Furthermore, the molecular structure and any cross-linking would have a significant effect on their friction and wear performance. The substrate surface should have a high surface energy (hydrophilic), so that there will be a strong tendency for molecules to adsorb onto the surface. The surface should be highly functional with polar groups and dangling bonds (generally unpaired electrons) so that they can react with organic molecules and provide a strong bond. Because of the exothermic head group–substrate interactions, molecules try to occupy every available binding site on the surface, and during this process they generally push together molecules that have already adsorbed. The process results in the formation of ordered molecular assemblies. The interactions between molecular chains are of van der Waals or electrostatic type, with energies on the order of a few kcal/mol ( $< 10$ ), exothermic. The molecular chains in SAMs are not perpendicular to the surface; the tilt angle depends on the anchor group as well as on the substrate and the spacer group. For example, the tilt angle for alkanethiolate on Au is typically about  $30\text{--}35^\circ$  with respect to the substrate normal.

Table 18.9 lists selected systems which have been used for the formation of SAMs [44]. The spacer chain of the SAM is mostly an alkyl chain  $((-\text{CH}_2)_n)$  or made of a derivatized alkyl group. By attaching different terminal groups at the

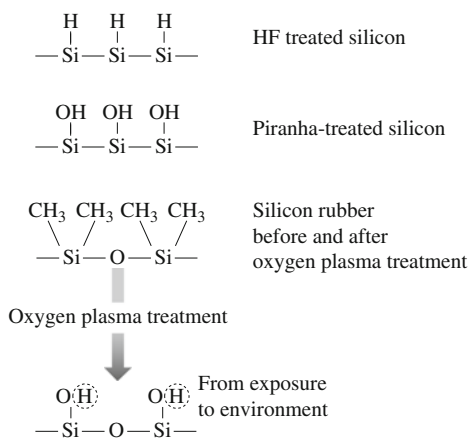
**Table 18.9** Selected substrates and precursors which have commonly been used for formation of SAMs. R represents alkane ( $C_nH_{2n+2}$ ) and Ar represents aromatic hydrocarbon. It consists of various surface active headgroups and mostly with methyl terminal group

Substrate	Precursor	Binding with substrate
Au	RSH (thiol)	RS–Au
Au	ArSH (thiol)	ArS–Au
Au	RSSR' (disulfide)	RS–Au
Au	RSR' (sulfide)	–
Si/SiO <sub>2</sub> , glass	RSiCl <sub>3</sub> (trichlorosilane)	Si–O–Si (siloxane)
Si/Si–H	RCOOH (carboxyl)	R–Si
Metal oxides (e.g., Al <sub>2</sub> O <sub>3</sub> , SnO <sub>2</sub> , TiO <sub>2</sub> )	RCOOH (carboxyl)	RCOO–···–MO <sub>n</sub>

surface, the film surface can be made to attract or repel water. The commonly used surface terminal group of a hydrophobic film with low surface energy, in the case of a single alkyl chain, is a nonpolar methyl ( $-CH_3$ ) or trifluoromethyl ( $-CF_3$ ) group. For a hydrophilic film, the commonly used surface terminal groups are alcohol ( $-OH$ ) or carboxylic acid ( $-COOH$ ) groups. The surface active head groups most commonly used are thiol ( $-SH$ ), silane (e.g., trichlorosilane or  $-SiCl_3$ ), and carboxyl ( $-COOH$ ) groups. The substrates most commonly used are gold, silver, platinum, copper, hydroxylated (activated) surfaces of SiO<sub>2</sub> on Si, Al<sub>2</sub>O<sub>3</sub> on Al, and glass.

As an example substrate, epitaxial Au film on glass, mica or single-crystal silicon, produced by e-beam evaporation, is commonly used because it can be deposited on smooth surfaces as a film which is atomically flat and defect free. Bulk single-crystal Si, sputtered Al film, bulk Al sheets, and copper disks with natural oxide layers have been selected because of their use in the construction of MEMS/NEMS (e.g., digital projection displays) and heat-exchange applications, respectively. The substrate surface should be clean before deposition. For silicon substrates, a concentrated HF solution (typically 49% HF) is commonly used to remove the oxide layer, followed by a rinse with deionized water [60, 62]. Hydrogen passivates the surface by saturating the dangling bonds, which results in a hydrogen-terminated silicon surface with hydrophobic properties. For deposition of multimolecularly thick polymer films with nonpolar ends, hydrophobic substrates may lead to a coated surface with a high contact angle, which is preferred. For SAM deposition, the substrate should be hydrophilic in order to form strong interfacial bonds with their head groups. Hydroxylation of oxide surfaces is carried out to make them hydrophilic. Silicon and other metals get oxidized and get hydroxylated to some degree when exposed to the environment. Bulk silicon, polysilicon film or SiO<sub>2</sub> film surfaces are commonly treated to produce a hydroxylated silica surface by immersion in Piranha solution (a mixture of typically 3:1 v/v 98% H<sub>2</sub>SO<sub>4</sub>:30% H<sub>2</sub>O<sub>2</sub>) at temperatures of  $\approx 90^\circ\text{C}$  for  $\approx 30$  min followed by a rinse in deionized (DI) water [27, 60, 62]. Piranha solution also removes any organic and metallic contaminants, whereas HF would not necessarily remove organics. Oxygen plasma is another technique

**Fig. 18.4** Schematic showing HF-treated silica and the hydroxylation process occurring on a silica and elastomeric surfaces using Piranha solution and oxygen plasma, respectively



used for hydroxylation for  $\text{SiO}_2$  as well as polymer surfaces [59, 61, 64, 73]. For complex silicon geometries or fine structures, such as AFM tips, oxygen plasma may be preferable. Figure 18.4 shows the schematics of surfaces after various surface treatments. Surfaces after piranha or oxygen plasma treatment remain hydrophilic for a few hours to about a day and become hydrophobic when they come into contact with carbon. They can retain hydrophilicity longer in dry nitrogen. To retain hydrophobicity, polymers are generally stored in DI water. Surfaces treated with HF remain hydrophobic for  $\approx 2\text{--}3$  h and can retain hydrophobicity longer in dry nitrogen.

For organic molecules to pack together and provide a better ordering, a substrate for given molecules should be selected such that the cross-sectional diameter of the spacer chains of the molecule is equal to or smaller than the distance between the anchor groups attached to the substrate. For the case of alkanethiol film, the advantage of Au substrate over  $\text{SiO}_2$  substrate is that it results in better ordering because the cross-sectional diameter of the alkane molecule is slightly smaller than the distance between sulfur atoms attached to the Au substrate ( $\approx 0.53$  nm). The thickness of the film can be controlled by varying the length of the hydrocarbon chain, and the surface properties of the film can be modified by the terminal group.

SAMs are usually produced by immersing a substrate in a solution containing the precursor (ligand) that is reactive to the substrate surface or by exposing the substrate to the vapor of the reactive chemical precursors [28]. A schematic of the vapor deposition system is shown in Fig. 18.5 [59, 60, 73]. Samples are placed in the quartz reaction tube. The silane bubbler is used for introducing gas-phase silane into the quartz reaction tube placed in an oven at a controlled temperature. An inert gas flow ( $\text{N}_2$ ) is used as a carrier gas. A byproducts condenser is used for trapping the byproducts and/or nonreacted silanes.

Research on some SAMs has been widely reported. SAMs of long-chain fatty acids  $\text{C}_n\text{H}_{2n+1}\text{COOH}$  or  $(\text{CH}_3)(\text{CH}_2)_n\text{COOH}$  ( $n = 10, 12, 14$  or  $16$ ) on glass or

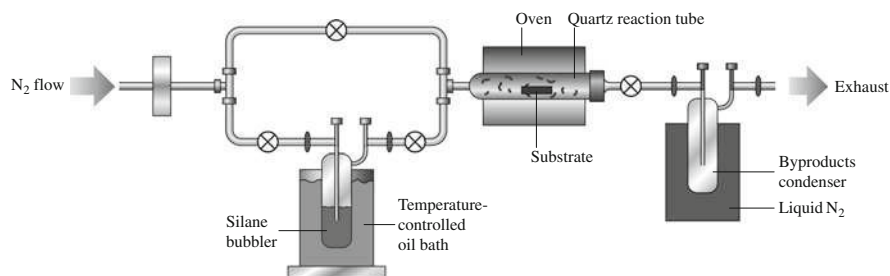
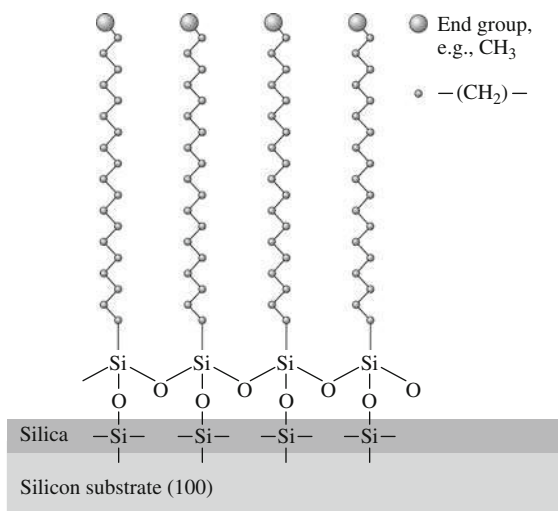


**Fig. 18.5** Schematic showing vapor-phase deposition system for silane SAMs (after [59])

**Fig. 18.6** Schematics of a methyl-terminated, *n*-alkylsiloxane monolayer on Si/SiO<sub>2</sub>



alumina substrates have been widely studied since the 1950s [24, 25, 28, 29, 76]. Probably the most studied SAMs to date are *n*-alkanethiolate (*n*-alkyl and *n*-alkane are used interchangeably) monolayers  $CH_3(CH_2)_nS-$  prepared from the adsorption of alkanethiol  $-(CH_2)_nSH$  solution onto a Au film [44, 77–79, 80, 81] and *n*-alkylsiloxane. *Siloxane* (Si–O–Si) refers to the bond, whereas *silane* ( $Si_nX_{2n+2}$ , which includes a covalently bonded compound containing the elements Si and other atoms or groups such as H and Cl to form  $SiH_4$  and  $SiCl_4$ , respectively) refers to the head group of the precursor. These terms are used interchangeably. Monolayers produced by adsorption of *n*-alkyltrichlorosilane  $-(CH_2)_nSiCl_3$  onto a hydroxylated Si/SiO<sub>2</sub> substrate with siloxane (Si–O–Si) binding (Fig. 18.6) [52, 58–63, 82]. Tambe and Bhushan [52], Bhushan et al. [53], Hoque et al. [54–56, 65–67]. DeRose et al. [57] have produced perfluoroalkylsilane and perfluoroalkylphosphonate on Al and Cu surfaces.

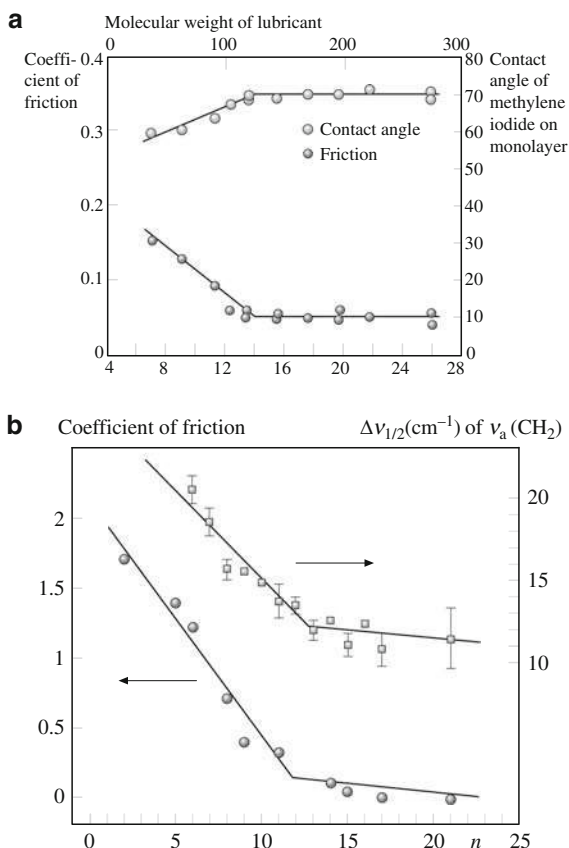
## 18.4 Contact Angle and Nanotribological Properties of SAMs

The basis for the molecular design and tailoring of SAMs should start from complete knowledge of the interrelationships between the molecular structure and contact angle and nanotribological properties of SAMs, as well as deep understanding of the adhesion, friction, and wear mechanisms of SAMs at the molecular level. Friction and wear studies of SAMs have been carried out on macro- and nanoscales. Macroscale tests are conducted using a so-called pin-on-disk tribotester apparatus in which a ball specimen slides against a lubricated flat specimen [14, 15]. Nano-scale tests are conducted using an atomic force/friction force microscope (AFM/FFM) [4, 6, 14, 15]. In AFM/FFM experiments, a sharp tip of a radius ranging from  $\approx 5$  to 50 nm slides against a SAM specimen. A  $\text{Si}_3\text{N}_4$  tip is commonly used for friction studies, and a Si or natural diamond tip is commonly used for scratch, wear, and indentation studies.

In early studies, the effect of chain length of the carbon atoms of fatty-acid monolayers on the coefficient of friction and wear on the macroscale was studied by Bowden and Tabor [24] and Zisman [25]. Zisman [25] reported that, for monolayers deposited on a glass surface sliding against a stainless-steel surface, there is a steady decrease in friction with increasing chain length. At a significantly long chain length, the coefficient of friction reaches a lower limit (Fig. 18.7a). He further reported that monolayers having a chain length below 12 C atoms behave as liquids (poor durability), and those with a chain length of 12–15 C atoms behave like a plastic solid (medium durability), whereas those with a chain length above 15 C atoms behave like a crystalline solid (high durability). Investigations by Ruhe et al. [83] indicated that the lifetime of a alkylsilane monolayer coating on a silicon surface increases greatly with increasing chain length of the alkyl substituent. DePalma and Tillman [84] showed that a monolayer of *n*-octadecyltrichlorosilane ( $n\text{-C}_{18}\text{H}_{37}\text{SiCl}_3$ , OTS) is an effective lubricant on silicon.

With the development of AFM techniques, researchers have successfully characterized the nanotribological properties of self-assembled monolayers [1, 4, 6]. Studies by Bhushan et al. [58] showed that  $\text{C}_{18}$  alkylsiloxane films exhibit the lowest coefficient of friction and can withstand a much higher normal load during sliding as compared with LB films, soft Au films, and hard  $\text{SiO}_2$  coatings. McDermott et al. [85] used AFM to study the effect of the length of alkyl chains on the frictional properties of methyl-terminated *n*-alkylthiolate  $\text{CH}_3(\text{CH}_2)_n\text{S-}$  films chemisorbed on Au(111). They reported that longer-chain monolayers exhibit markedly lower friction and reduced propensity for wear than shorter-chain monolayers (Fig. 18.7b). These results are in good agreement with the macroscale results by Zisman [25]. They also conducted infrared reflection spectroscopy to measure the bandwidth of the methylene stretching mode ( $\nu_{\text{a}}(\text{CH}_2)$ ) which exhibits a qualitative correlation with the packing density of the chains. It was found that the chain structures of monolayers prepared with longer chain lengths are more ordered and more densely packed in comparison with those of monolayers prepared with shorter chain lengths. They further reported that the ability of the longer-chain monolayers

**Fig. 18.7** (a) Effect of chain length (or molecular weight) on the coefficient of macroscale friction of stainless steel sliding on glass lubricated with a monolayer of fatty acid, and contact angle of methyl iodide on condensed monolayers of fatty acid on glass (after [25]). (b) Effect of chain length of methyl-terminated  $n$ -alkanethiolate over Au film  $\text{AuS}(\text{CH}_2)_n\text{CH}_3$  on the coefficient of microscale friction and peak bandwidth at half maximum ( $\Delta\nu_{1/2}$ ) for the bandwidth of the methylene stretching mode ( $\nu_a(\text{CH}_2)$ ) (after [85])



to retain molecular-scale order during shear leads to a lower observed friction. Monolayers having a chain length of more than 12 C atoms, preferably 18 or more, are desirable for tribological applications. (Incidentally, monolayers with 18 C atoms, octadecanethiol films, have been widely studied.)

Xiao et al. [86] and Lio et al. [87] also studied the effect of the length of the alkyl chains on the frictional properties of  $n$ -alkanethiolate films on gold and  $n$ -alkylsilane films on mica. Friction was found to be particularly high with short chains of fewer than eight carbon atoms. Thiols and silanes exhibit similar friction forces for the same  $n$  when  $n > 11$ , while for  $n < 11$ , silanes exhibit higher friction, larger than that for thiols by a factor of about 3 for  $n = 6$ . The increase in friction was attributed to the large number of dissipative modes in the less ordered chains that occurs when going from a thiol to a silane anchor or when decreasing  $n$ . Longer chains ( $n > 11$ ), stabilized by van der Waals attraction, form more compact and rigid layers and act as better lubricants. Schönherr and Vancso [88] also correlated the magnitude of friction with the order of the alkane chains. The disorder



of short-chain hydrocarbon disulfide SAMs was found to result in a significant increase in the magnitude of friction.

Tsukruk and Bliznyuk [89] studied the adhesion and friction between a Si sample and a  $\text{Si}_3\text{N}_4$  tip, in which both surfaces were modified by  $-\text{CH}_3-$ ,  $-\text{NH}_2-$ , and  $-\text{SO}_3\text{H}$ -terminated silane-based SAMs. Various polymer molecules were used for the backbone. They reported a very broad maximum adhesive force in the pH range from 4 to 8, with minimum adhesion at  $\text{pH} > 9$  and  $\text{pH} < 3$  for all of the studied mating surfaces. This observation can be understood by considering a balance of electrostatic and van der Waals interactions between composite surfaces with multiple isoelectric points. The friction coefficient of  $\text{NH}_2/\text{NH}_2$  and  $\text{SO}_3\text{H}/\text{SO}_3\text{H}$  mating SAMs was very high in aqueous solutions. Cappings of  $\text{NH}_2$ -modified surfaces (3-aminopropyltriethoxysilane) with rigid and soft polymer layers resulted in a significant reduction in adhesion to a level lower than that of untreated surface [90]. Fujihira et al. [91] studied the influence of surface terminal groups of SAMs and functional tip on adhesive force. It was found that the adhesive forces measured in air increase in the order:  $\text{CH}_3/\text{CH}_3$ ,  $\text{CH}_3/\text{COOH}$ ,  $\text{COOH}/\text{COOH}$ .

Bhushan and Liu [79], Liu et al. [80], and Liu and Bhushan [81, 92] studied adhesion, friction, and wear properties of alkylthiol and biphenylthiol SAMs on Au (111) films. They explained the friction mechanisms using a molecular spring model in which local stiffness and intermolecular forces govern the friction properties. They studied the influence of relative humidity, temperature, and velocity on adhesion and friction. They also investigated the wear mechanisms of SAMs by a continuous microscratch AFM technique.

Fluorinated carbon (fluorocarbon) molecules are known to have low surface energy and are commonly used for lubrication [14, 15]. Bhushan and Cichomski [73] deposited fluorosilane SAMs on polydimethylsiloxane (PDMS). To make a hydrophobic PDMS surface chemically active, PDMS surface was oxygenated using an oxygen plasma, which introduces silanol groups ( $\text{SiOH}$ ). They reported that SAM-coated PDMS was more hydrophobic, with lower adhesion, friction, and wear. Bhushan et al. [59, 60], Kasai et al. [61], Lee et al. [62], Tambe and Bhushan [52], and Tao and Bhushan [64] studied the adhesion, friction, and wear of methyl- and/or perfluoro-terminated alkylsilanes on silicon. They reported that perfluoroalkylsilane SAMs exhibited lower surface energy, higher contact angle, lower adhesive force, and lower wear as compared with alkylsilanes. Kasai et al. [61] also reported the influence of relative humidity, temperature, and velocity on adhesion and friction. Tao and Bhushan [63] studied degradation mechanisms of alkylsilanes and perfluoroalkylsilane SAMs on Si. They reported that oxygen in the air causes thermal oxidation of SAMs.

Tambe and Bhushan [52], Bhushan et al. [53], Hoque et al. [54, 55], and DeRose et al. [57] studied the nanotribological properties of methyl- and perfluoro-terminated alkylphosphonate, perfluorodecyldimethylchlorosilane, and perfluorodecanoic acid on aluminum, of industrial interest. Hoque et al. [56] and DeRose et al. [57] studied the nanotribological properties of alkylsilanes and perfluoroalkylsilanes on aluminum. Hoque et al. [65–67] studied the nanotribological properties of alkylphosphonate and perfluoroalkylsilane SAMs on copper. The authors found that these



Hexadecane thiol (HDT), 1,1'-biphenyl-4-thiol (BPT), and cross-linked BPT (BPTC) were deposited on Au(111) films on Si(111) substrates by immersing the substrate in a solution containing the precursor (ligand) that is reactive to the substrate surface. Cross-linked BPTC was produced by irradiation of BPT monolayers with low-energy electrons. Perfluoroalkylsilane and alkylsilane SAMs were deposited on Si(100) by exposing the substrate to the vapor of the reactive chemical precursors. Perfluoroalkylphosphonate and alkylphosphonate SAMs were deposited on sputtered Al film on Si substrate as well as bulk Al substrates. Representative data follow.

### **18.4.1 Measurement Techniques**

Experimental techniques used for measurement of the static contact angle, surface energy, adhesion, friction, and wear are described next.

#### **Static Contact Angle and Surface Energy Measurements Using DI Water**

The static contact angle, a measure of water-repellent property, was measured using a Rame–Hart model 100 contact angle goniometer (Mountain Lakes, NJ) [93, 94]. Typically, 10  $\mu\text{L}$  droplets of DI water were used for making contact angle measurements. At least two measurements of the contact angle were made and were found to be reproducible within  $\pm 2^\circ$ . The critical surface tension, a measure of interfacial surface energy, was obtained from the so-called Zisman plot. Contact angles of SAMs with liquids with a range of surface tensions were measured. The cosines of the contact angles were plotted as a function of surface tension of the various  $n$ -alkane liquids (hexadecane, dodecane, undecane, and decane) used. The plot is linear for low-polarizable SAMs. The horizontal intercept of the line passing through  $\cos(\text{contact angle}) = 1$  provides the critical surface tension, which is a measure of the surface energy of the SAM [59].

#### **AFM Adhesion and Friction Measurements**

The adhesion and friction tests were conducted using a commercial AFM system. Square-pyramidal  $\text{Si}_3\text{N}_4$  tips with a 30–50 nm tip radius on gold back-coated triangular  $\text{Si}_3\text{N}_4$  cantilevers with a typical spring constant of 0.58 N/m were used. Adhesion can be calculated using either force calibration plots or from the negative intercepts on plots of friction force versus normal loads. Both methods generally yield similar results. The force calibration plot technique was used in this study. The coefficient of friction was obtained from the slope of plots of friction force versus normal load. Normal loads typically ranged from 5 to 100 nN. Friction

force measurements were generally performed at a scan rate of 1 Hz along the fast scan axis and over a scan size of  $2 \times 2 \mu\text{m}^2$ . The fast scan axis was perpendicular to the longitudinal direction of the cantilever. The friction force was calibrated by the method described in [4, 6].

### **AFM Wear Measurements**

Wear tests were conducted using a diamond tip with a nominal radius of 50 nm and nominal cantilever stiffness of 10 N/m. Wear tests were performed on a  $1 \times 1 \mu\text{m}^2$  scan area at the desired normal load and at a scan rate of 1 Hz. After each wear test, a  $3 \times 3 \mu\text{m}^2$  area was imaged, and the average wear depth was calculated.

### **Effect of Relative Humidity, Temperature, and Sliding Velocity**

The influence of relative humidity on adhesive force, friction force, and wear was studied in an environmentally controlled chamber. Relative humidity was controlled by introducing a mixture of dry and moist air inside the chamber. The temperature was maintained at  $22 \pm 1^\circ\text{C}$ . The sample was kept in the environmental chamber at desired humidity for at least 2 h prior to the tests so that the system could reach equilibrium condition.

In order to study the effect of temperature on adhesion and friction force, the samples were placed on a thermal stage during the measurements. A glass plate was placed under the thermal stage to prevent heat from being transported away. The temperature range studied was from  $20^\circ\text{C}$  to  $110^\circ\text{C}$ . The relative humidity was maintained at  $50 \pm 5\%$  during the temperature effect measurements.

The effect of sliding velocity on friction force was monitored in ambient conditions using a high-velocity piezoelectric stage designed for achieving high relative sliding velocities on a commercial AFM setup [95]. The traveling distance of the sample, i.e., the scan size, was set at  $25 \mu\text{m}$ , while the scan frequency was varied between 0.1 Hz ( $5 \mu\text{m/s}$ ) and 100 Hz ( $5000 \mu\text{m/s}$ ).

### **Chemical Degradation and Environmental Studies**

The chemical degradation experiments were carried out in a high-vacuum tribotest apparatus [96, 97]. The system was equipped with a mass spectrometer so that gaseous emissions from the interface could be monitored in situ during the sliding in high vacuum and other controlled environments. The normal loads and friction forces at the contacting interface were measured using resistive-type strain-gage transducers. For the sliding tests, the coated flat sample was glued onto a flat surface at the end of a rotating shaft. The sample was slid against a Si(100) wafer mounted on the flat surface of a slider integrated with a flexible cantilever used in magnetic rigid disk drives. The sliding speed used was 0.3 m/s, and the

applied pressure was 50 kPa. The environmental effects were investigated in high vacuum ( $2 \times 10^{-7}$  Torr), argon, dry air (less than 2% RH), ambient air (30% RH), and high-humidity air (70% RH).

### 18.4.2 Hexadecane Thiol and Biphenyl Thiol SAMs on Au(111)

Hexadecane thiol on Au(111) film was selected as it is a widely studied film. Biphenyl thiol was selected to study the effect of rigidity on nanotribological performance. Biphenyl thiol film was cross-linked to further increase its stiffness.

#### Surface Roughness, Adhesion, and Friction

Surface height and friction force images of SAMs were recorded simultaneously on an area of  $1 \times 1 \mu\text{m}^2$  by an AFM, and adhesive forces were measured by using the force calibration mode in an AFM [79].

For further analysis, presented later in this chapter, the measured roughness, thickness, tilt angles, and spacer chain lengths of Si(111), Au(111), and various SAMs are listed in Table 18.10 [79]. The roughness of BPT is very close to that of Au(111), but the roughness of BPTC is lower than that of Au(111) and BPT; this is caused by electron irradiation. Table 18.10 indicates that the roughness value of HDT is much higher than the substrate roughness for Au(111). This is caused by local aggregation of organic compounds on the substrates during SAMs deposition. Table 18.10 also indicates that the thickness of biphenyl thiol SAMs are generally smaller than the alkylthiol, because of the shorter spacer chains in biphenyl thiol.

The average values and standard deviation of the adhesive force and coefficient of friction are presented in Fig. 18.9 [79]. Based on the data, the adhesive force and coefficient of friction of SAMs are less than those of their corresponding substrates. Among various films, HDT exhibits the lowest values. The ranking of adhesive

**Table 18.10** The  $R_a$  roughness, thickness, tilt angles, and spacer chain lengths of SAMs

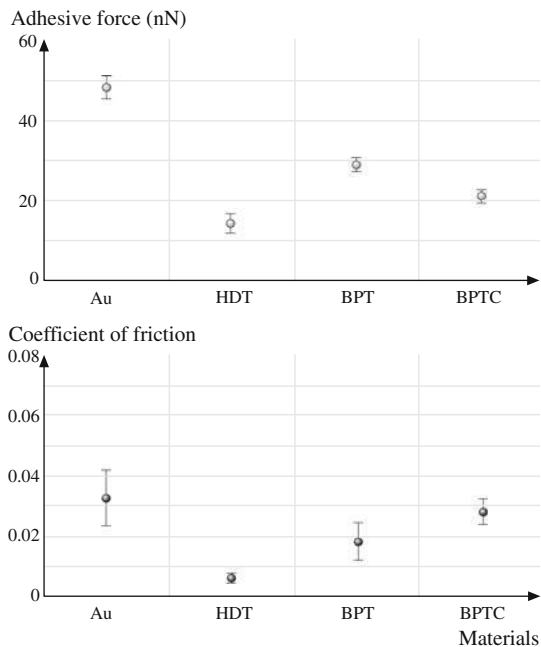
Samples	$R_a$ roughness <sup>a</sup> (nm)	Thickness <sup>b</sup> (nm)	Tilt angle <sup>b</sup> (deg)	Spacer length <sup>c</sup> (nm)
Si(111)	0.07	—	—	—
Au(111)	0.37	—	—	—
HDT	0.92	1.89	30	1.91
BPT	0.36	1.25	15	0.89
BPTC	0.14	1.14	25	0.89

<sup>a</sup>Measured by an AFM with  $1 \times 1 \mu\text{m}^2$  scan size, using  $\text{Si}_3\text{N}_4$  tip under 3.3 nN normal load

<sup>b</sup>The thickness and tilt angles of BPT and BPTC are reported by Geyer et al. [78]. The thickness and tilt angles of HDT are reported by Ulman [29]

<sup>c</sup>The spacer chain lengths of alkylthiols were calculated by the method reported by Miura et al. [98]. The spacer chain lengths of biphenyl thiols were calculated by the data reported by Ratajczak-Sitarz et al. [99]

**Fig. 18.9** Adhesive forces and coefficients of friction of Au(111) and various SAMs



forces  $F_a$  is in the following order:  $F_{a-Au} > F_{a-BPT} > F_{a-BPTC} > F_{a-HDT}$ , and the ranking of the coefficients of friction  $\mu$  is in the following order:  $\mu_{Au} > \mu_{BPTC} > \mu_{BPT} > \mu_{HDT}$ . The ranking of various SAMs for adhesive force and coefficient of friction are similar. This suggests that alkylthiol and biphenyl thiol SAMs can be used as effective molecular lubricants for micro-/nanodevices.

In micro-/nanoscale contact, liquid capillary condensation is one of the sources of adhesion and friction. In the case of a sphere in contact with a flat surface, the attractive Laplace force caused by water capillary forces is [14, 15]

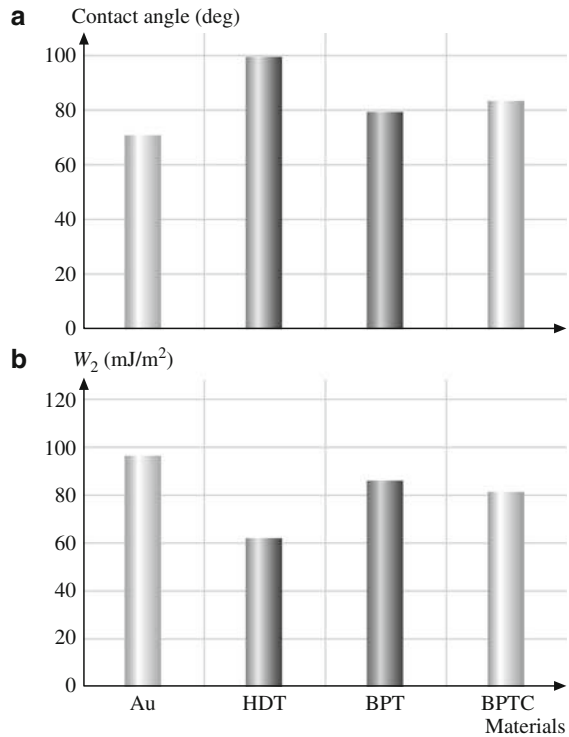
$$F_L = 2\pi R\gamma_{la}(\cos \theta_1 + \cos \theta_2), \quad (18.1)$$

where  $R$  is the radius of the sphere,  $\gamma_{la}$  is the surface tension of the liquid against air, and  $\theta_1$  and  $\theta_2$  are the contact angles between liquid and flat and spherical surfaces, respectively. In an AFM adhesive study, the tip-flat sample contact is just like a sphere in contact with a flat surface, and the liquid is water. Since a single tip was used in the adhesion measurements,  $\cos \theta_2$  can be treated as a constant. Therefore,

$$\begin{aligned} F_L &= 2\pi R\gamma_{la}(1 + \cos \theta_1) - 2\pi R\gamma_{la}(1 - \cos \theta_2) \\ &= 2\pi R\gamma_{la}(1 + \cos \theta_1) - C, \end{aligned} \quad (18.2)$$

where  $C$  is a constant.

**Fig. 18.10** (a) The static contact angle, and (b) work of adhesion of Au(111) and various SAMs. All of the points in this figure represent the mean of six measurements. The uncertainty associated with the average contact angle is within  $\pm 2^\circ$



Based on the following Young–Dupré equation, the work of adhesion  $W_a$  (the work required to pull apart a unit area of solid–liquid interface) can be written as [12]

$$W_a = \gamma_{la}(1 + \cos \theta_1). \quad (18.3)$$

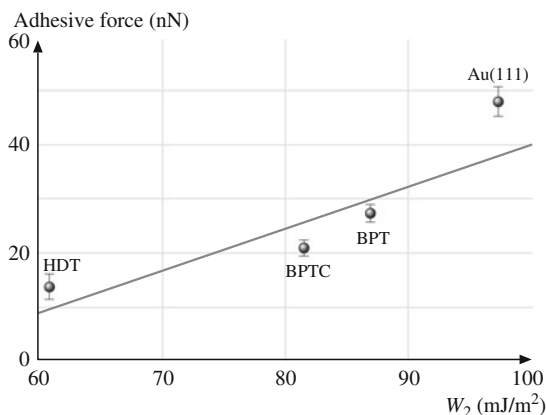
It indicates that  $W_a$  is determined by the contact angle of SAMs, i.e., is influenced by the surface chemistry properties (polarization and hydrophobicity) of SAMs. By substituting (18.3) into (18.2),  $F_L$  can be expressed as

$$F_L = 2\pi R W_a - C. \quad (18.4)$$

When the influence of other factors, such as the van der Waals force, on the adhesive force are very small, the adhesive force  $F_a \approx F_L$ . Thus the adhesive force  $F_a$  should be proportional to the work of adhesion  $W_a$ .

Contact angle is a measure of the wettability of a solid by a liquid and determines the  $W_a$  value [93, 94]. The static contact angles of distilled water on Au(111) and SAMs were measured and are summarized in Fig. 18.10a [79]. For water,  $\gamma_{la} = 72.6 \text{ mJ/m}^2$  at  $22^\circ\text{C}$ , and by using (18.3), the  $W_a$  data are obtained and presented in Fig. 18.10b. The  $W_a$  can be ranked in the following order:  $W_{a-\text{Au}} (97.1) > W_{a-\text{BPT}} (86.8) > W_{a-\text{BPTC}} (82.1) > W_{a-\text{HDT}} (61.4)$ . Except  $W_{a-\text{Au}}$ , this order exactly

**Fig. 18.11** Relationship between the adhesive force and work of adhesion of different specimens



matches the order of adhesion force in Fig. 18.9. The relationship between  $F_a$  and  $W_a$  is summarized in Fig. 18.11 [79]. This indicates that the adhesive force  $F_a$  (nN) increases with the work of adhesion  $W_a$  (mJ/m<sup>2</sup>) according to the following linear relationship

$$F_a = 0.57W_a - 22. \quad (18.5)$$

These experimental results agree well with the modeling prediction presented earlier (18.4). This proves that, on the nanoscale at ambient conditions, the adhesive force of SAMs is mainly influenced by the water capillary force. Though neither HDT nor BPT has polar surface groups, the surface terminal of HDT has a symmetrical structure, which causes a smaller electrostatic attractive force and yields a smaller adhesive force than BPT. It is believed that the easy attachment of Au onto the tip should be one of the reasons that causes the large adhesive force, which does not fit the linear relationship described by (18.5).

### Stiffness, Molecular Spring Model, and Micropatterned SAMs

Next the friction mechanisms of SAMs were examined. Monte Carlo simulation of the mechanical relaxation of  $\text{CH}_3(\text{CH}_2)_{15}\text{SH}$  self-assembled monolayer performed by Siepmann and McDonald [100] indicated that SAMs compress and respond nearly elastically to microindentation by an AFM tip when the load was below a critical normal load. Compression can lead to major changes in the mean molecular tilt (i.e., orientation), but the original structure is recovered as the normal load is removed. Garcia-Parajo et al. [101] also reported compression and relaxation of octadecyltrichlorosilane (OTS) film during loading and unloading.

To study the difference in the stiffness of various films, the stiffness properties were measured by an AFM in force modulation mode [4, 6, 81]. It was reported that



**Fig. 18.12** Normal load versus displacement curves of Au(111) and various SAMs

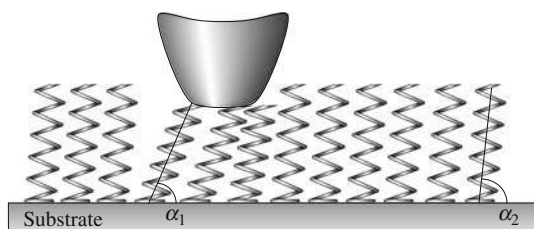
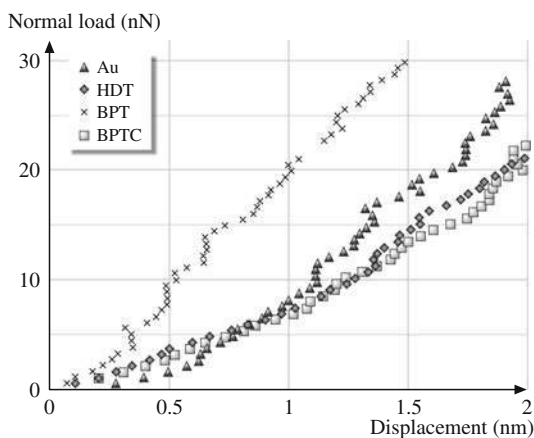


**Fig. 18.13** Molecular spring model of a SAM. In this figure,  $\alpha_1 < \alpha_2$ , which is caused by the orientation under the normal load applied by the AFM tip. The orientation of the molecular springs reduces the shearing force at the interface, which in turn reduces the friction force. The molecular spring constant as well as the intermolecular forces can determine the magnitude of the coefficient of friction of the SAM. In this figure, the size of the tip and molecular springs are not to exact scale (after [79])

BPT was stiffer than HDT. Since BPT has a rigid benzene structure, it is more difficult to compress than HDT. Figure 18.12 shows the variation of the displacement with normal load in indentation mode, clearly indicating that SAMs can be compressed. At a given normal load, SAMs with long carbon chain structure such as HDT are easy to compress as compared with SAMs with rigid benzene ring structure such as BPT, which implies that BPT is more rigid than HDT.

In order to explain the frictional difference of SAMs, based on the friction and stiffness measurements by AFM and the Monte Carlo simulation, a molecular spring model is presented in Fig. 18.13. It is believed that the self-assembled molecules on a substrate are just like assembled molecular springs anchored to the substrates [79]. An AFM tip sliding on the surface of SAMs is like a tip sliding on the top of *molecular springs or brush*. The molecular spring assembly has compliant features and can experience compression and orientation under normal load. The orientation of the molecular springs or brush reduces the shearing force at the interface, which in turn reduces the friction force. The possibility of orientation

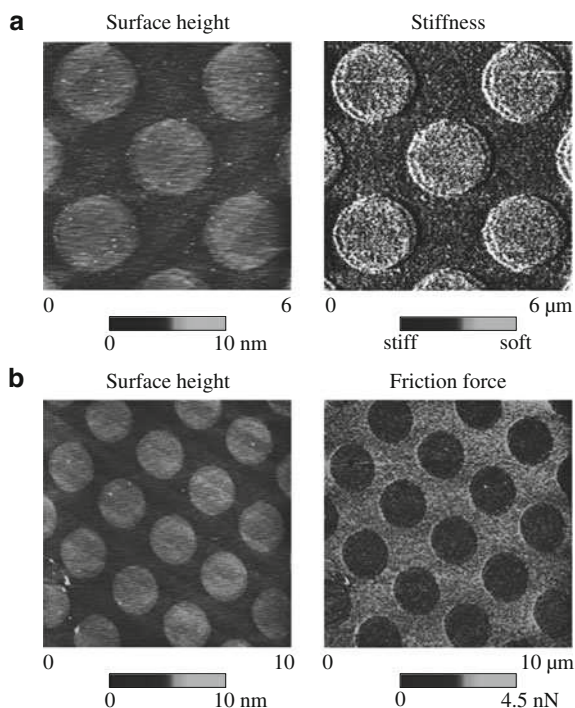
is determined by the spring constant of a single molecule (local stiffness), as well as the interaction between neighboring molecules, which can be reflected by the packing density or packing energy. It should be noted that the orientation can lead to conformational defects along the molecular chains, which leads to energy dissipation. In the study of BPT by AFM, it was found that, after the first several scans, the friction force is significantly reduced, but the surface height does not show any apparent change. This suggests that molecular orientation can be facilitated by initial sliding and is reversible [92].

Based on the stiffness measurements obtained using Fig. 18.12 and the view of the molecular structure in Fig. 18.13, biphenyl is a more rigid structure due to the contribution of two rigid benzene rings. Therefore the spring constant of BPT is larger than that of HDT. The hydrogen ( $H^+$ ) in a biphenyl chain has an electrostatic attractive force with the  $\pi$  electrons in the neighboring benzene ring. Thus the intermolecular force between biphenyl chains is stronger than that for alkyl chains. The larger spring constant of BPT and stronger intermolecular force require a larger external force to allow it to orient, thus causing a higher coefficient of friction. The cross-linking of BPT leads to a larger packing energy for BPTC. Therefore it requires a larger external force to allow BPTC orientation; i.e., the coefficient of BPTC is higher than BPT.

An elegant way to demonstrate the influence of molecular stiffness on friction is to investigate SAMs with different structures on the same wafer. For this purpose, a micropatterned SAM was prepared. First biphenyldimethylchlorosilane (BDCS) was deposited on silicon by a typical self-assembly method [81]. Then the film was partially cross-linked using a mask technique by low-energy electron irradiation. Finally the micropatterned BDCS films were realized, which had the as-deposited and cross-linked coating regions on the same wafer. The local stiffness properties of these micropatterned samples were investigated by force-modulation AFM technique [102]. The variation in the deflection amplitude provides a measure of the relative local stiffness of the surface. Surface height, stiffness, and friction images of the micropatterned biphenyldimethylchlorosilane (BDCS) specimen were obtained and are presented in Fig. 18.14 [81]. The circular areas correspond to the as-deposited film and the remaining area to the cross-linked film. Figure 18.14a indicates that cross-linking caused by the low-energy electron irradiation leads to about a 0.5 nm decrease of the surface height of BDCS films. The corresponding stiffness images indicate that the cross-linked area has a higher stiffness than the as-deposited area. Figure 18.14b indicates that the as-deposited area (area with higher surface height) has a lower friction force. Obviously, these data from the micropatterned sample prove that the local stiffness of SAMs has an influence on their friction performance; higher stiffness leads to larger friction force. These results provide strong proof of the suggested molecular spring model.

In summary, it is found that SAMs exhibit compliance and can experience compression and orientation under normal load. The orientation of SAMs reduces the shear stress at the interface; therefore SAMs can serve as good lubricants. The molecular spring constant (local stiffness), as well as the intermolecular forces, can influence the magnitude of the coefficients of friction of SAMs.

**Fig. 18.14** (a) AFM grayscale surface height and stiffness images, and (b) AFM grayscale surface height and friction force images of micropatterned BDCS (after [81])

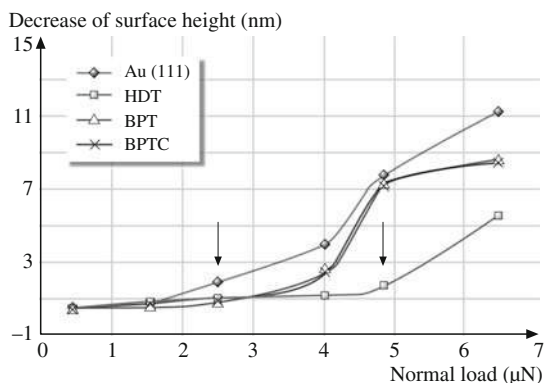


## Wear and Scratch Resistance

Wear resistance was studied on an area of  $1 \times 1 \mu\text{m}^2$ . The variation of wear depth with normal loads is presented in Fig. 18.15 [79]. HDT exhibits the best wear resistance. For all of the tested SAMs, in the curves of wear depth as a function of normal load, there appears a critical normal load, marked by arrows in Fig. 18.15. When the normal load is smaller than this critical normal load, the monolayer shows only a slight height change in the scan areas. When the normal load is higher than this critical value, the height change of the SAM increases dramatically. Relocation and accumulation of BPT molecules have been observed during the initial several scans, which lead to the formation of a larger terrace. Wear studies of a single BPT terrace indicate that the wear life of BPT increases exponentially with terrace size [80, 81].

Scratch resistance of Au(111) and SAMs were studied by a continuous AFM microscratch technique. Figure 18.16a shows coefficient of friction profiles as a function of increasing normal load, and corresponding tapping-mode AFM surface height images of the scratches captured on Au(111) and SAMs [81]. Figure 18.16a indicates that there is an abrupt increase in the coefficient of friction for all of the tested samples. The normal load associated with this event is termed the critical load (indicated by the arrows labeled A). At the initial stages of the scratch, all the

**Fig. 18.15** Wear depth as a function of normal load after one scan cycle



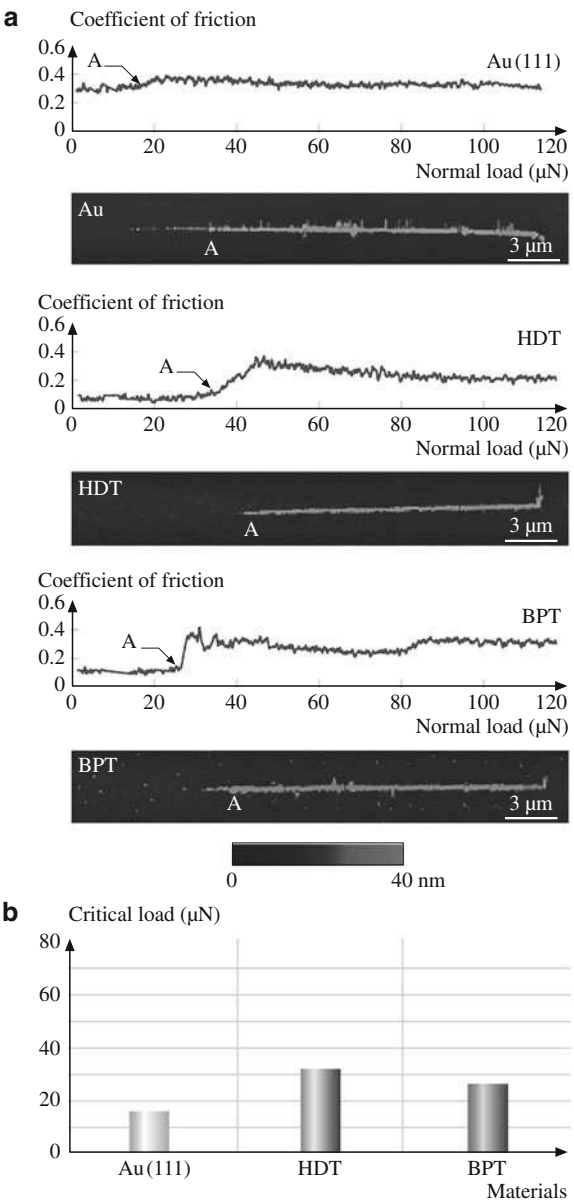
samples exhibit a low coefficient of friction, indicating that the friction force is dominated by the shear component. This is in agreement with analysis of the AFM images, which shows negligible damage on the surfaces prior to the critical load. At the critical load, a clear groove is formed, which is accompanied by the formation of material pileup at the sides of the scratch. This suggests that the initial damage that occurs at the critical load is due to plowing associated with plastic deformation, and this causes the sharp rise in the coefficient of friction. Beyond the critical load, debris can be seen in addition to material pileup at the sides of the scratch. Figure 18.16b summarizes the critical loads for the various samples obtained in this study. It clearly indicates that all SAMs can increase the critical load of the corresponding substrate.

The mechanisms responsible for a sudden drop in decrease in surface height with an increase in load during wear and scratch test need to be understood. Barrena et al. [103] observed that the height of self-assembled alkylsilanes decreases in discrete amounts with normal load. This step-like behavior is due to the discrete molecular tilts, which are dictated by the geometrical requirements of the close packing of molecules. Only certain angles are allowed due to the zigzag arrangement of the C atoms. The relative height of the monolayer under pressure can be calculated by the following equation

$$\left(\frac{h}{L}\right) = \left[1 + \left(\frac{na}{d}\right)^2\right]^{-1/2}, \quad (18.6)$$

where  $L$  is the total length of the molecule,  $h$  is the height of the SAMs in the tilt configuration (monolayer thickness),  $a$  is the distance between alternate C atoms in the molecule,  $d$  is the separation of the molecules, and  $n$  is the step number. Values of  $a$  of 0.25 nm and  $d$  of 0.47 nm are used in the calculation for HDT. The calculated and measured relative heights of HDT are listed in Table 18.11. When the normal loads are smaller than the critical values in Fig. 18.15, the measured relative height values of HDT are very close to the calculated values. This means that HDT underwent step tilting below critical normal loads.

**Fig. 18.16** (a) Coefficient of friction profiles during scratch as a function of normal load and corresponding AFM surface height images. (b) Critical loads estimated from the coefficient of friction profile and AFM images for Au (111), HDT/Au(111), and BPT/Au(111) (after [81])



The residual SAM thickness after wear under critical normal load was measured by profiling the worn film using AFM. The results are listed in Table 18.12. For an alkanethiol monolayer, the relationship between the monolayer thickness  $h$  and intercept length  $L_0$  can be expressed as (Fig. 18.17)

**Table 18.11** Calculated  $[1 + (na/d)^2]^{-1/2}$  and measured  $(h/L)$  relative heights of HDT self-assembled monolayer (after [79])

Steps ( $n$ )	Calculated <sup>a</sup> $[1 + (na/d)^2]^{-1/2}$	Measured $(h/L)$
1	0.883	—
2	0.685	0.674 <sup>b</sup>
3	0.531	0.532 <sup>c</sup>
4	0.425	0.416 <sup>d</sup>
5	0.352	0.354 <sup>e</sup>
6	0.299	—

<sup>a</sup>Calculations are based on the assumption that the molecules tilt in discrete steps ( $n$ ) upon compression with a diamond AFM tip [103]

<sup>b–e</sup>These measured values correspond to the normal loads of 0.50, 1.57, 2.53, and 4.03  $\mu\text{N}$ , respectively

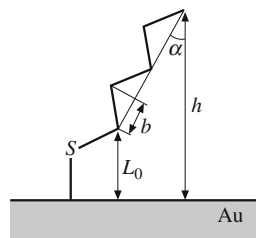
**Table 18.12** Calculated  $L_0$  and measured residual film thickness for SAMs under critical load

	$L_0^a$ (nm)	Residual thickness <sup>b</sup> (nm)
HDT	0.24	0.25
BPT	0.39	0.42
BPTC	0.33	0.38

<sup>a</sup>Calculated by the equation:  $h = b \cos(\alpha)n + L_0$  [98]

<sup>b</sup>Measured by AFM using a diamond tip under critical normal load. The data are mean values of three tests

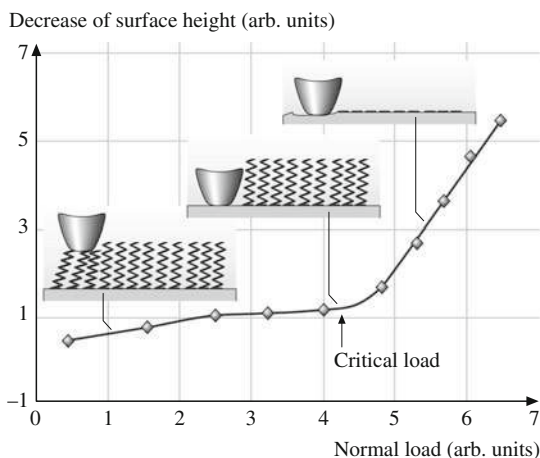
**Fig. 18.17** Illustration of the relationship between the components of the equation  $h = b \cos(\alpha)n + L_0$  (after [79])



$$h = b \cos(\alpha)n + L_0, \quad (18.7)$$

where  $b$  is the length of the projection of the C–C bond onto the main chain axis ( $b = 0.127$  nm for alkanethiol),  $n$  is the chain length defined by  $\text{CH}_3(\text{CH}_2)_n\text{SH}$ , and  $\alpha$  is the tilt angle [98]. For BPT and BPTC, based on the same principle, and using the bond lengths reported in [99], the  $L_0$  values are also calculated (Table 18.12). The results indicate that the measured residual thickness values of SAMs under critical load are very close to the calculated intercept length  $L_0$  values. This means that, under the critical normal load, the  $\text{Si}_3\text{N}_4$  tip approaches the interface, and SAMs wear away from the substrate severely. This is due to the interface chemical adsorption bond strength (S–Au) being generally smaller than the other chemical bond strengths in SAMs spacer chains (Table 18.14, to be introduced later).

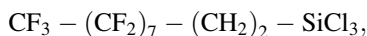
**Fig. 18.18** Illustration of the wear mechanisms of SAMs with increasing normal load (after [81])



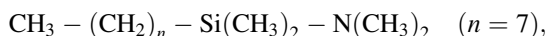
According to the wear and scratch results reported here and the above discussion, the transition of the wear mechanisms of SAMs with increasing normal load is illustrated in Fig. 18.18. Below the critical normal load SAMs undergo step orientation; at the critical load SAMs wear away from the substrate due to the weak interface bond strengths; while above the critical normal load severe wear takes place on the substrate. In order to improve wear resistance, the interface bond must be enhanced; a rigid spacer chain and a hard substrate are also preferred.

#### 18.4.3 *Perfluoroalkylsilane and Alkylsilane SAMs on Si(100) and Perfluoroalkylphosphonate and Alkylphosphonate SAMs on Al*

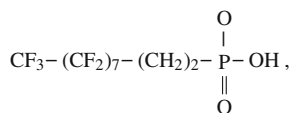
Perfluorodecyltrichlorosilane (PFTS)



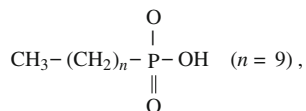
*n*-octyldimethyl(dimethylamino)silane (ODMS)



and *n*-octadecyldimethyl(dimethylamino)silane ( $n = 17$ ) (ODDMS) vapor deposited on Si(100) substrate and perfluorodecylphosphonate (PFDP)



decylphosphonate (DP)



and octadecylphosphonate (ODP) ( $n = 17$ ) by liquid deposition on sputtered Al film on Si substrate were selected. Perfluoro-SAMs were selected because fluorinated films are known to have low surface energy. Two chain lengths of alkylsilanes (with 8 and 18 C atoms) were selected to compare their nanotribological performance with that of the former as well as to study the effect of chain length. Al substrate was selected because of the application of Al micromirrors in digital projection displays. Perfluoroalkylphosphane (with 10 C atoms) and alkylphosphonate SAMs (with 10 and 18 C atoms) on Al were selected.

#### 18.4.3.1 Static Contact Angle and Surface Free Energy Measurements

Static contact angles and surface energy were measured as a measure of hydrophobicity. Figure 18.19 shows a Zisman plot for SAMs deposited on Si and their surface energy values using various liquid alkanes [59]. Critical surface tension, a measure of surface energy values for the two SAMs, are presented in the figure. Zisman analysis for the Si substrate was not available because the liquid alkanes used for the measurement instantly spread on these surfaces. For PFTS, significant reduction in the critical surface tension or surface energy was observed (12.9 mN/m for PFTS/Si) as compared with ODMS (24.7 mN/m for ODMS/Si) and ODDMS (23.9 mN/m for ODDMS/Si). The surface energy for ODMS and ODDMS was comparable. This suggests that the surface was comparably covered by the SAMs without bare substrate appearing.

For comparison, static contact angles were measured for various SAMs on Si and Al substrates. The measured values are compared among the samples in

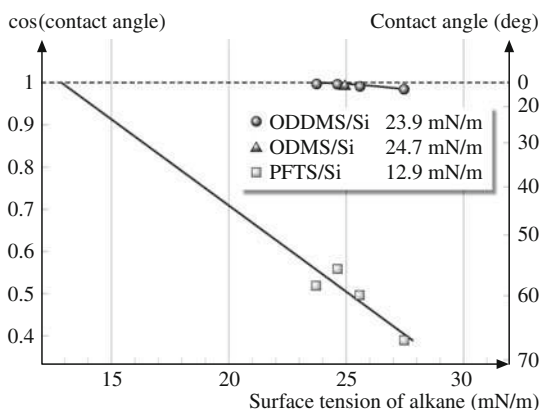


**Fig. 18.19** Zisman plot for PFTS/Si, ODMS/Si, and ODDMS/Si used for calculating the critical surface tension, a measure of surface energy, which is given by the  $x$ -intercept ( $\cos(\text{contact angle}) = 1$ ) of the fitted line to the data



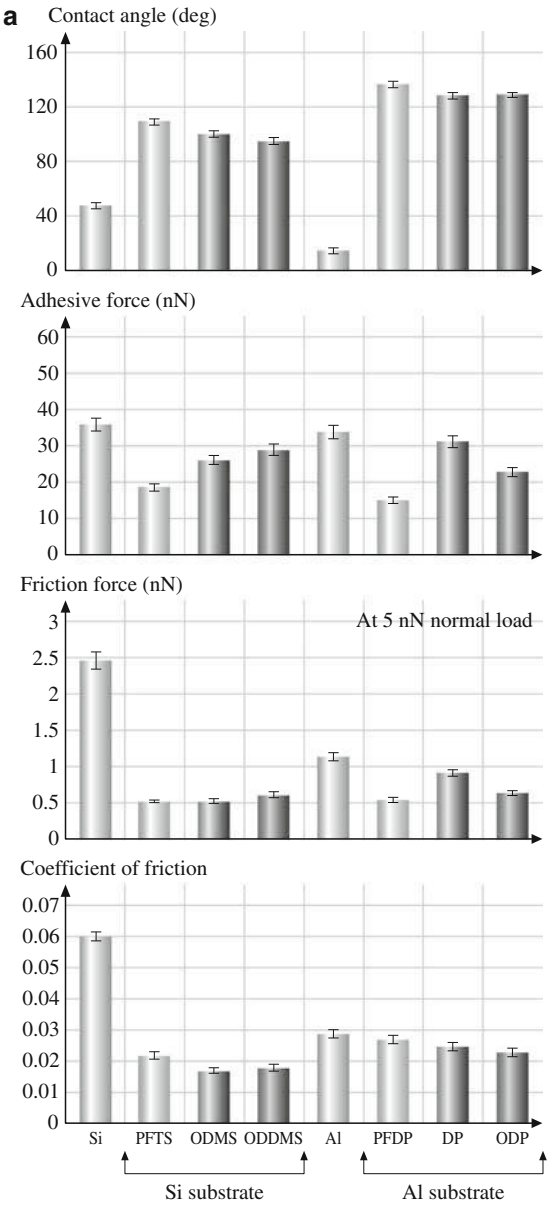
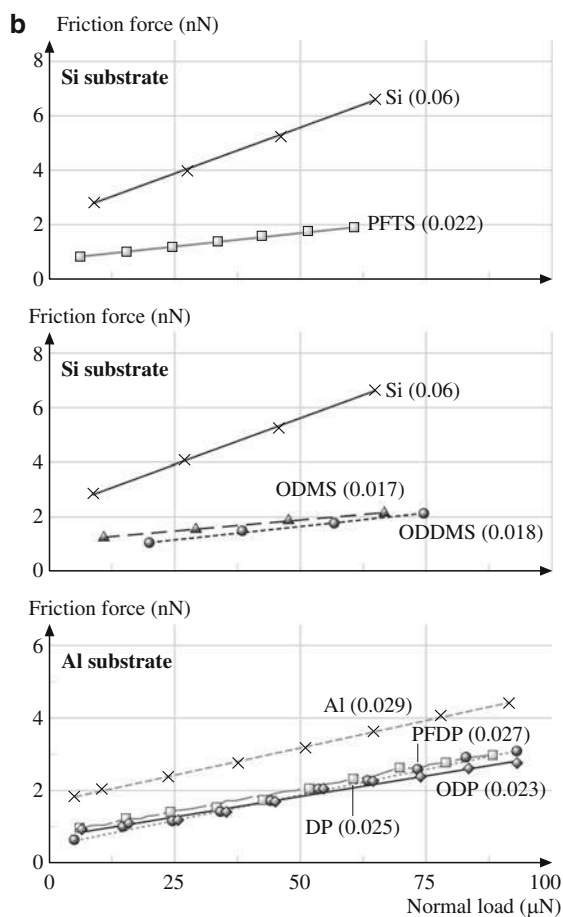


Fig. 18.20 (continued)

Fig. 18.20a [53, 59]. A summary of root-mean-square (RMS) roughness measured by using an AFM, and static contact angles and film thickness measured using an ellipsometer, are summarized in Table 18.13 [53, 61]. Significant improvement in the water-repellent property was observed for perfluorinated SAMs as compared

**Fig. 18.20** (a) The static contact angle, adhesive force, friction force, and coefficient of friction measured using AFM for various SAMs on Si and Al substrates, and (b) friction force versus normal load plots for various SAMs on Si and Al substrates (after [53, 59])



**Table 18.13** A summary of RMS roughness, contact angle, and film thickness of various SAMs

SAM/substrate	Acronym	RMS roughness (nm)	Contact angle (deg)	Film thickness (nm)
Silicon(111) <sup>a</sup>	Si	0.07	48	–
Perfluorodecyltrichlorosilane/Si <sup>a</sup>	PFTS/Si	0.09	112	≈ 1.8
<i>n</i> -Octyldimethyl(dimethylamino) silane/Si <sup>a</sup>	ODMS/Si	0.10	99	≈ 1.9
<i>n</i> -Octadecyldimethyl(dimethylamino) silane/Si <sup>b</sup>	ODDMS/Si	0.10	92	≈ 2.1
Aluminum <sup>b</sup>	Al	32	< 15	–
Perfluorodecylphosphonate	PFDP	34	137	≈ 1.9
Decylphosphonate/Al <sup>b</sup>	DP/Al	31	129	≈ 1.9
Octadecylphosphonate/Al	ODP/Al	36	130	≈ 2.1

<sup>a</sup>Kasai et al. [61]

<sup>b</sup>Bhushan et al. [53]

with bare Si and Al substrates. Static contact angles of alkylsilanes and alkylphosphonates were also higher than corresponding substrates, but lower than corresponding perfluorinated films. The contact angle generally increases with a decrease in surface energy [104], which is consistent with the data obtained. The contact angles can be influenced by the packing density as well as the sample roughness [105]. The higher contact angles for the SAMs deposited on Al substrates than those on Si substrate are probably due to this effect. The  $-\text{CH}_3$  groups in ODMS, ODDMS, DP, and ODP are nonpolar and are known to contribute to the water-repellent property. Perfluorinated SAMs exhibited the highest contact angle among the SAMs tested in this study.

### AFM Adhesion and Friction Measurements Under Ambient Conditions

Figure 18.20a shows the adhesive force, friction force, and the coefficient of friction measured under ambient conditions using an AFM, and Fig. 18.20b shows the friction force versus normal load plots for various SAMs deposited onto Si and Al substrates [53, 59]. Figure 18.21 shows surface height and friction force maps for Si and for PFTS, ODMS, and ODDMS on Si [59].

The bare substrates showed higher adhesive force than the SAMs coatings. ODMS and ODDMS show an adhesive force comparable to that of DP and ODP, despite their lower water contact angles. These SAMs have the same tail groups, and during AFM measurements the AFM tip interacts only with the tail groups, whereas the contact angles can also be influenced by the head groups in these SAMs. This is

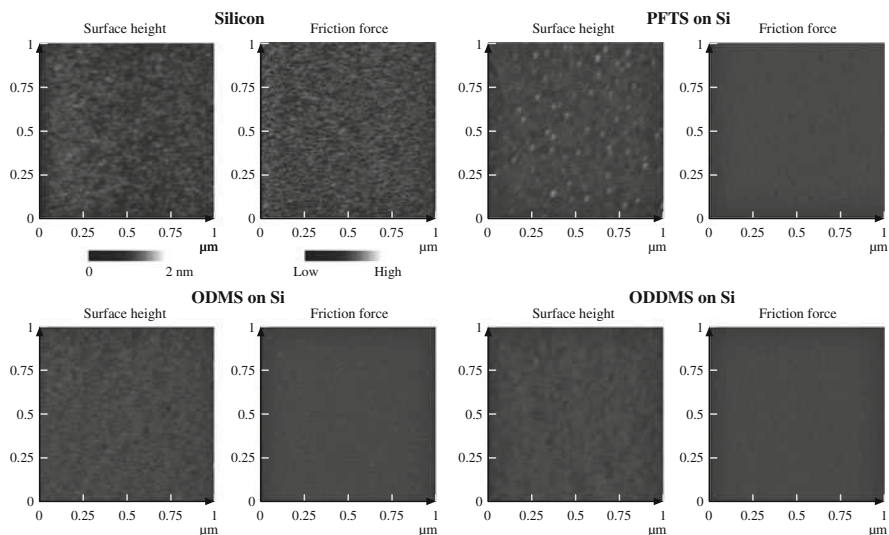


**Fig. 18.21** Surface height and friction force maps for Si, PFTS/Si, ODMS/Si, and ODDMS/Si (after [59])

probably the reason why the adhesive forces for these SAMs are comparable. PFTS and PFDP, which have the highest contact angles, showed the lowest adhesion.

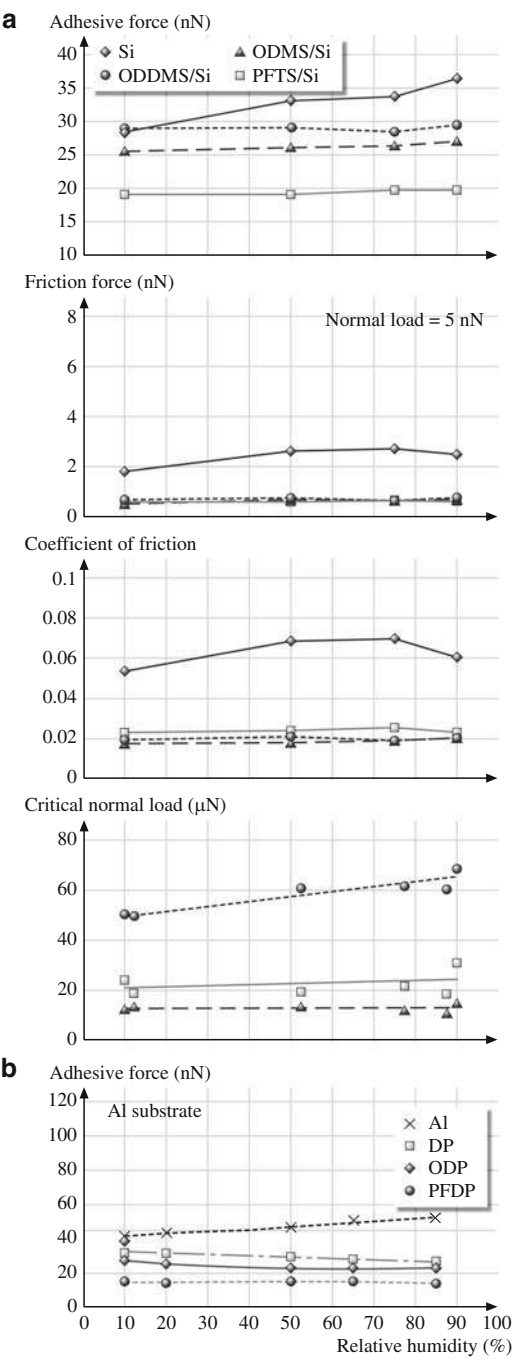
Friction force images of SAMs on Si exhibit more uniform contrast than those of bare Si. The coefficient of friction was higher for the bare substrates as compared with the corresponding SAMs deposited on them. The SAMs deposited on the Si substrate showed lower coefficient of friction than those deposited on the Al substrates. The primary reason for this is believed to be the greater roughness of the Al substrates. The SAMs with fluorocarbon backbone chains were found to have a higher coefficient of friction than those with hydrocarbon backbone chains. This might be attributed to the higher stiffness of the fluorocarbon backbone [53, 61]. For the fluorocarbon backbone chains, it is harder to rotate the backbone structure due to the larger size of the F atoms in comparison with the H atoms [106]. The C–C bonds of hydrocarbon chains can, on the other hand, rotate more freely. We presented earlier a molecular spring or brush model to explain why less compliant SAMs show larger friction. SAMs with a higher spring constant or stiffer backbone structure may need more energy to be elastically deformed during sliding; therefore friction is higher for these SAMs. In terms of the effect of chain length, it has been reported that the coefficient of friction for SAM surfaces decreases with the carbon backbone chain length ( $n$ ) up to 12 C atoms ( $n \approx 12$ ) [85]. This effect of chain length on the coefficient of friction was not obvious in these data.

### **Effect of Relative Humidity, Temperature, and Sliding Velocity on AFM Adhesion and Friction**

The effect of relative humidity on adhesion and friction was studied for various SAMs. Adhesive force, friction force at 5 nN normal load, coefficient of friction, and microwear data are presented in Fig. 18.22 [53, 61]. The result for adhesive force for silicon showed an increase with relative humidity (Fig. 18.22a). This is expected since the surface of silicon is hydrophilic, as shown in Fig. 18.20a. More condensation of water at the tip–sample interface at higher humidity increases the adhesive force due to the capillary effect. On the other hand, the adhesive force for the SAMs showed very weak dependency on humidity. This occurs since the surface of the SAMs is hydrophobic. The adhesive force of ODMS/Si and ODDMS/Si showed a slight increase from 75% to 90% RH. Such an increase was absent for PFTS/Si, possibly because of the hydrophobicity of PFTS/Si. The Al substrate is hydrophilic and hence shows relative humidity dependence (Fig. 18.22b). The PFDP, DP, and ODP SAMs deposited on Al substrates showed almost no change in adhesive force with humidity. The highly hydrophobic nature of these monolayers means that the contribution of water menisci to the overall adhesive force is negligible at all humidities.

The friction force of silicon showed an increase with relative humidity up to about 75% RH and a slight decrease beyond this point (Fig. 18.22a). The initial increase may result from the increase in adhesive force. The decrease in friction force at higher humidity could be attributed to the lubricating effect of the water

**Fig. 18.22** Effect of relative humidity on (a) adhesive force, coefficient of friction, and microwear for various SAMs on (a) Si substrates (after [61]), and (b) adhesive force for various SAMs on Al substrates (after [53])



layer. This effect is more pronounced for the coefficient of friction. Since the adhesive force increased and the coefficient of friction decreased in this range, those effects cancel each other out and the resulting friction force showed only slight changes. On the other hand, the friction force and coefficient of friction of SAMs showed very small changes with relative humidity, like that found for adhesive force. This suggests that the adsorbed water layer on the surface maintained a similar thickness throughout the range of relative humidity tested. The differences among the SAM types were small, within the measurement error, however a closer look at the coefficient of friction for ODMs/Si showed a slight increase from 75% to 90% RH as compared with PFTS/Si, possibly due to the same reason as for the adhesive force increment. The inherent hydrophobicity of SAMs means that they did not show much relative humidity dependence.

Figure 18.23a shows the effect of temperature on adhesive force, friction force at 5 nN normal load, and coefficient of friction for various SAMs on Si substrate [61]. Figure 18.23b shows the effect of temperature on the adhesive force for SAMs on Al [53]. The adhesive force for silicon showed an increase with temperature, from room temperature (RT) to about 55°C, followed by a decrease from 55°C to 75°C, and eventually leveling off from 75°C to 110 °C. The adhesive force increased for Al substrate up to 50°C and then decreased to a stable value for higher temperatures. The initial increase of adhesive force for Si and Al substrates at lower temperatures is not well understood. The observed decrease could be attributed to desorption of water molecules from the surface. After almost full depletion of the water layer, the adhesive force remains constant. The SAMs with hydrocarbon backbones on both Si and Al substrates showed similar behavior as that of the Si and Al substrates, but the initial increase in the adhesive force with temperature was smaller. The SAMs with fluorocarbon backbone chains showed almost no temperature dependence. For the SAMs with hydrocarbon backbone chains, the initial increase in adhesive force is believed to be caused by the melting of the SAM film. The melting point for a linear carbon chain molecule such as  $\text{CH}_3(\text{CH}_2)_{14}\text{CH}_2\text{OH}$  is 50°C [107]. With an increase in temperature, the SAM film softens, thereby increasing the real area of contact and consequently the adhesive force. Once the temperature is higher than the melting point, the lubrication regime is changed from boundary lubrication in a solid SAM to liquid lubrication in the molten SAM [81].

The friction force for silicon showed an increase with temperature followed by a steady decrease. The friction force is highly affected by the change in adhesion. The decrease in friction can result from the depletion of the water layer. The coefficient of friction for silicon remained constant, followed by a decrease starting at about 80°C. For SAMs, the coefficient of friction exhibited a monotonic decrease with temperature. The decrease in friction and coefficient of friction for SAMs possibly results from the decrease in stiffness. As introduced before, the spring model suggests a smaller friction for more compliant SAMs [81]. The difference among the SAM types was not significant. PFTS could maintain its stiffness more than ODMs and ODDMS when temperature was increased [108]; however, this was not pronounced in the results.

**Fig. 18.23** Effect of temperature (a) on adhesive force, friction force, and coefficient of friction for various SAMs on Si substrates (after [61]), and (b) on adhesive force for various SAMs on Al substrates (after [53])

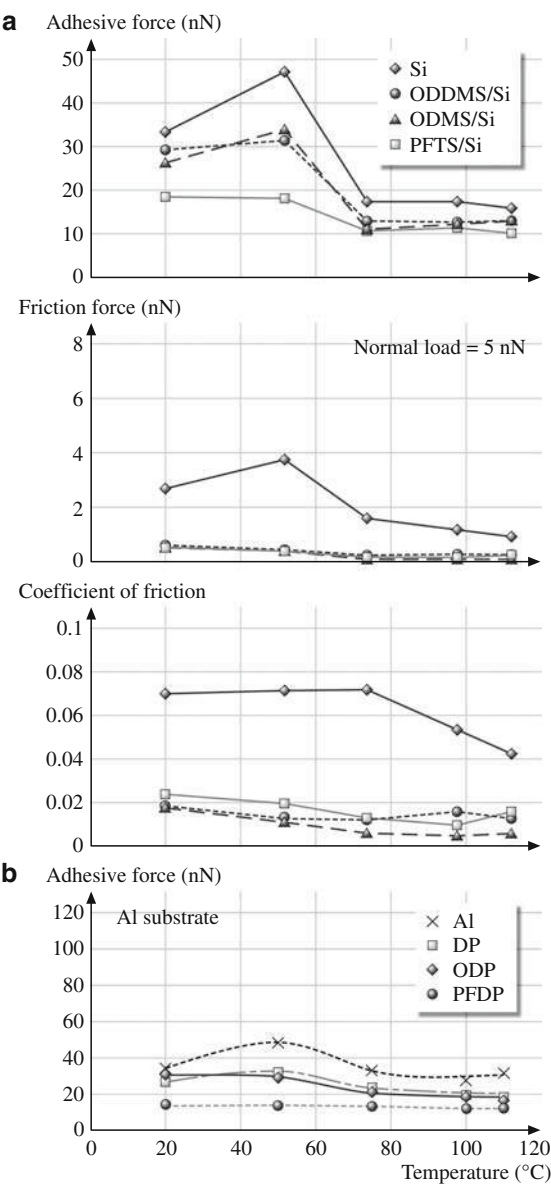
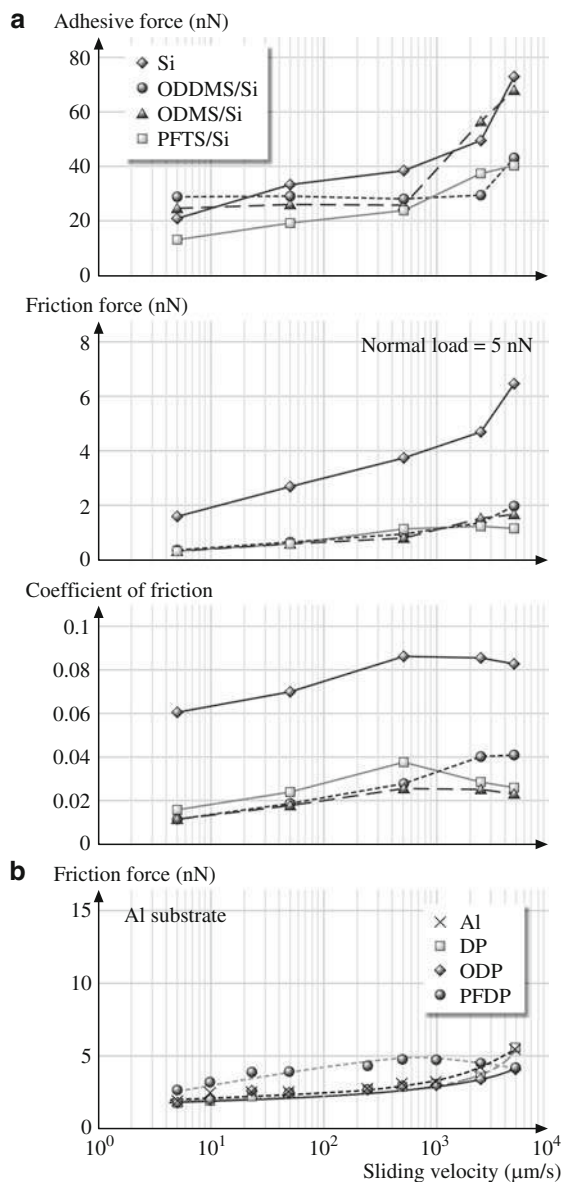


Figure 18.24a shows the effect of sliding velocity on adhesive force, friction force, and coefficient of friction for various SAMs on a Si substrate [61]. The adhesive force for silicon remained rather constant at lower sliding velocity, and then increased rapidly. A similar trend was found for the SAMs. The increase in adhesive force for silicon is believed to be the result of a tribochemical reaction at the tip-sample interface [27] and increase of contact area by mechanical plowing.

**Fig. 18.24** Effect of sliding velocity (**a**) on adhesive force, friction force, and coefficient of friction for various SAMs on Si substrates (after [61]), and (**b**) on friction force for various SAMs on Al substrates (after [53])



For the SAMs, the higher adhesive force at the higher velocity can result from viscous drag of the SAM molecules [109]. SAMs can be detached from the surface and attached to an AFM tip. In addition, another reason may be an increase of contact area, which may be caused by more penetration of the AFM tip into the SAMs. The rate of increase was larger for ODMS than PFTS, presumably because of the higher stiffness and more densely packed structure of PFTS.



The coefficient of friction showed an increase with sliding velocity and reached a plateau for Si, ODMS/Si, and ODDMS/Si. As the sliding speed is increased, the reorientation of the SAMs needs additional work, which might lead to increase in friction. For PFTS, the coefficient of friction decreased at larger sliding velocity, forming a peak. The peak structure may result from the viscoelastic property of SAMs [110].

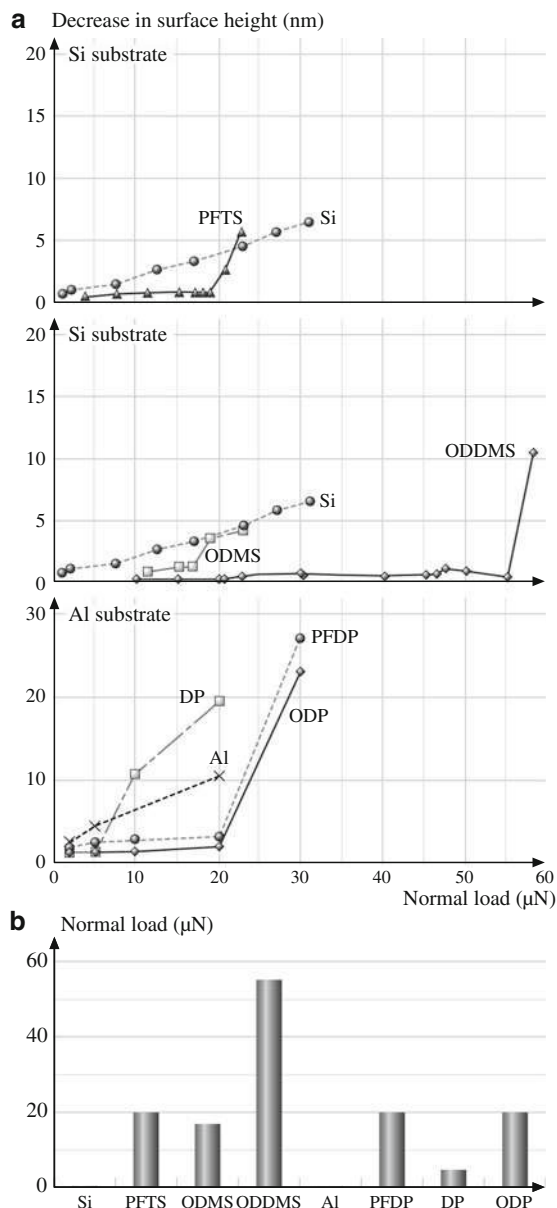
Figure 18.24b shows the effect of sliding velocity on the friction force for various SAMs on Al substrate [53]. The friction force increases slowly at lower sliding velocities for the bare Al substrate and SAMs, followed by a rapid increase at higher sliding velocities, except for PFDP. The increase in friction force at high velocities ( $>1$  mm/s) is the result of asperity impacts and corresponding high frictional energy dissipation at the sliding interface for Al [111]. Tambe and Bhushan [109] extended the *molecular spring* model presented by Bhushan and Liu [79] to explain this velocity-dependent increase in friction force for compliant SAM molecules. Based on this model for the DP and ODP SAMs, the increase in friction force is believed to result from the reorientation of the SAM molecules under the tip load and during tip motion. The reorientation of the SAMs can act as an additional hindrance to tip motion when the AFM tip reverses during scanning and thus result in higher friction. The molecules can consequently become entangled and/or detached from the substrate and attach to the AFM tip.

## AFM Wear Measurements

Figure 18.25a shows the relationship between the decrease in surface height as a function of the normal load during wear tests [53, 61]. As shown in the figure, the SAMs exhibit a critical normal load, beyond which the surface height decreases drastically. Figure 18.25a also shows the wear behavior of the Al and Si substrates. Unlike the SAMs, the substrates show a monotonic decrease in surface height with increasing normal load with wear initiating from the very beginning, i.e., even for low normal loads. Si (Young's modulus of elasticity  $E = 130$  GPa [112, 113], hardness  $H = 11$  GPa [32]) is relatively hard in comparison with Al ( $E = 77$  GPa,  $H = 0.41$  GPa), and hence the decrease in surface height for Al is much larger than that for Si for similar normal loads.

The critical loads corresponding to the sudden failure of SAMs are shown in Fig. 18.25b. Amongst all the SAMs, ODDMS shows the best performance in the wear tests, and this is believed to be because of the effect of the longer chain length. The fluorinated SAMs – PFTS and PFDP – show a higher critical load as compared with ODMS and DP for similar chain length. ODP shows a higher critical load as compared with DP because of its longer chain length. The mechanism of failure of compliant SAMs during wear tests was presented earlier in Fig. 18.18. It is believed that the SAMs fail mostly due to shearing of the molecule at the head group, that is, by means of shearing of the molecules off the substrate. Table 18.14 gives the bond strengths for various intermolecular bonds. The weakest bonds are at the interface, and hence failure is expected to be initiated at the interface.

**Fig. 18.25** (a) Decrease in surface height as a function of normal load after one scan cycle for various SAMs on Si and Al substrates, and (b) comparison of critical loads for failure during wear tests for various SAMs (after [53, 61])



To study the effect of relative humidity, wear tests were performed at various humidities. The bottom of Fig. 18.22a shows critical normal load as a function of relative humidity. The critical normal load showed weak dependency on relative humidity for ODMS/Si and PFTS/Si and was larger for ODMS/Si than PFTS/Si throughout the humidity range. This suggests that water molecules could penetrate

**Table 18.14** Typical bond strengths<sup>a</sup> in SAMs

SAMs	Bond	HDT (kJ/mol)	BPT (kJ/mol)	Bond	PFTS (kJ/mol)	ODMS or ODDMS (kJ/mol)	PFDP (kJ/mol)	DP and ODP (kJ/mol)
Interfacial bonds	S–Au	184 <sup>b</sup>	184 <sup>b</sup>	Si–O	242 <sup>c</sup>	242 <sup>c</sup>	–	–
	S–C	286 <sup>a</sup>	–	–	800 <sup>d</sup>	800 <sup>d</sup>	–	–
	C <sub>6</sub> H <sub>5</sub> –S	–	362 <sup>a</sup>	Si–C	414 <sup>a</sup>	414 <sup>a</sup>	–	–
				Al–O	–	–	511 <sup>a</sup>	511 <sup>a</sup>
				P–C	–	–	513 <sup>a</sup>	513 <sup>a</sup>
				P–O	–	–	599 <sup>a</sup>	599 <sup>a</sup>
Bonds in backbone	C–C	–	–	C–C	–	–	–	–
	CH <sub>2</sub> –CH <sub>2</sub>	326 <sup>e</sup>	–	CH <sub>2</sub> –CH <sub>2</sub>	326 <sup>e</sup>	326 <sup>e</sup>	326 <sup>e</sup>	326 <sup>e</sup>
	CH <sub>3</sub> –CH <sub>2</sub>	≈ 305 <sup>a</sup>	–	CF <sub>2</sub> –CF <sub>2</sub>	≈ 326 <sup>f</sup>	–	≈ 326 <sup>f</sup>	–
	C <sub>6</sub> H <sub>5</sub>	–	Strong	CF <sub>2</sub> –CH <sub>2</sub>	≈ 326 <sup>f</sup>	–	≈ 326 <sup>f</sup>	–
				CF <sub>3</sub> –CF <sub>2</sub>	≈ 326 <sup>f</sup>	–	≈ 326 <sup>f</sup>	–
				CH <sub>3</sub> –CH <sub>2</sub>	–	≈ 305 <sup>a</sup>	–	≈ 305 <sup>a</sup> –

<sup>a</sup>Lide [107]<sup>b</sup>Chemical adsorption bond from Lio et al. [87]<sup>c</sup>Chemical adsorption bond from Hoshino [114]<sup>d</sup>In diatomic molecules<sup>e</sup>Cottrell [115]<sup>f</sup>Due to C–C bond, should be close to that of CH<sub>2</sub>–CH<sub>2</sub>

into the ODDMS, which might work as a lubricant [81, 116]. This effect was absent for PFTS/Si and ODMS/Si.

#### 18.4.4 Chemical Degradation and Environmental Studies

Chemical degradation and environmental studies were carried out for HDT/Au, PFTS/Si, ODMS/Si, and ODDMS/Si films.

##### Chemical Degradation Studies

The coefficient of friction and detected gaseous products for HDT/Au are shown in Fig. 18.26a [63]. A normal pressure of 50 kPa was applied on HDT films. The coefficient of friction increased after a sliding distance of about 10 m. During sliding, (CH<sub>2</sub>)<sub>15</sub>S, C<sub>2</sub>H<sub>3</sub>, CH<sub>3</sub>, CH<sub>2</sub>, and H<sub>2</sub> were detected by mass spectrometer. Partial pressure of HS fragments is of interest as it corresponds to the interface bonds, and it is reported here. Increase of (CH<sub>2</sub>)<sub>15</sub>S was much more than that of other species, due to the breaking of the S–Au bond. Partial pressures of C<sub>2</sub>H<sub>3</sub>, CH<sub>3</sub>, CH<sub>2</sub>, and H<sub>2</sub> were also found to increase during sliding. There was no noticeable change in the partial pressure of HS.

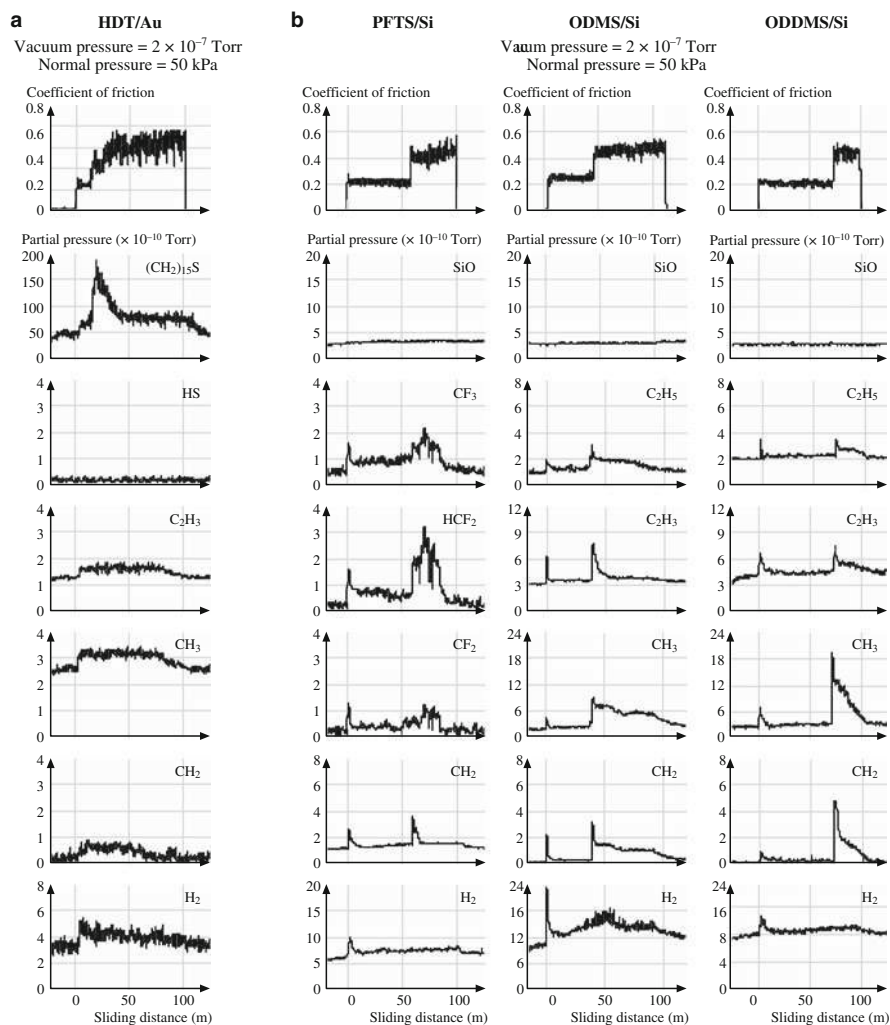


**Fig. 18.26** Coefficients of friction and mass spectra data on (a) HDT/Au (1.9 nm), and (b) PFTS/Si (1.8 nm), ODMS/Si ( $\approx$  1.9 nm), and ODDMS/Si ( $\approx$  2.1 nm) in high vacuum (after [63])

HDT film is deposited on a Au(111) layer. The bond strength of S–Au is 184 kJ/mol (Table 18.9), which is lower than that of the C–C bond (425 kJ/mol), C–H bond (422 kJ/mol), and C–S bond (286 kJ/mol) in the alkyl chain. Since the S–Au bond is the weakest bond in the alkanethiol chain, the whole chain should be sheared away from the substrate. Because the upper atomic mass unit (amu) limit of the mass spectrometer used is 250, we monitored (CH<sub>2</sub>)<sub>15</sub>S (amu = 242), which is the chain with CH<sub>3</sub> sheared. The rate of generation of (CH<sub>2</sub>)<sub>15</sub>S is much larger than that of other species. This suggests that the mechanical shear of the whole alkanethiol chain is the dominant factor causing the failure of the HDT film.

Cleavage of the S–Au bonds has been reported in literature. Based on the bond strength as well as the above studies, mechanical shearing of the C–C bonds and C–H bonds does not likely happen during sliding. The reaction induced by low-energy electrons, generated by triboelectrical emission during the sliding, could be responsible for the degradation of the alkanethiol chain. Thermal desorption of HDT from Au is another possible degradation mechanism of HDT.

The coefficient of friction and generated gaseous products for PFTS/Si, ODMS/Si, and ODDMS/Si are shown in Fig. 18.26b [63]. The coefficients of friction for PFTS/Si, ODMS/Si, and ODDMS/Si increase sharply after a certain sliding distance, which indicates degradation of the film. At the same time, gaseous products of  $\text{CF}_3$ ,  $\text{HCF}_2$ ,  $\text{CF}_2$ ,  $\text{CH}_2$ , and  $\text{H}_2$  were detected for PFTS/Si, and  $\text{C}_2\text{H}_5$ ,  $\text{C}_2\text{H}_3$ ,  $\text{CH}_3$ ,  $\text{CH}_2$ , and  $\text{H}_2$  were detected for ODMS/Si, and ODDMS/Si.

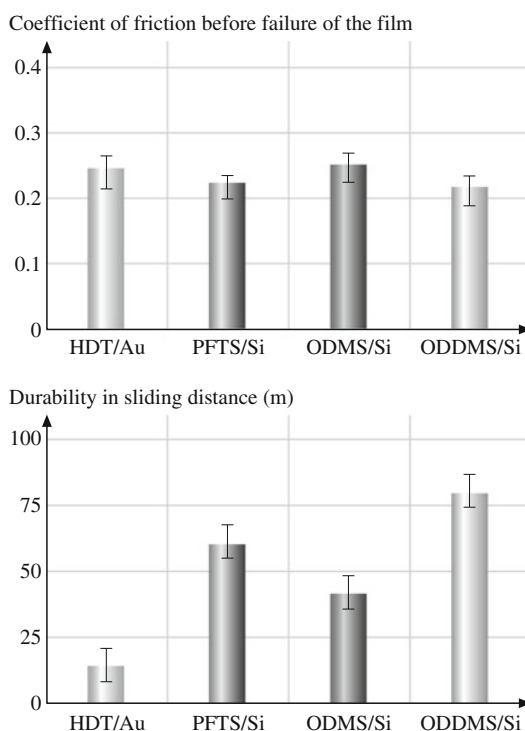
PFTS/Si showed lower friction than ODMS/Si in the tests. ODDMS/Si showed lower friction than both PFTS/Si and ODMS/Si. This is because of the effect of chain length. It has been reported that the coefficient of friction for SAM surfaces decreases with carbon backbone chain length ( $n$ ) when the number of C atoms is less than 12. For chains with more than 12 C atoms, a change in the number of carbon atoms will not influence the coefficient of friction to a noticeable extent.

PFTS/Si showed higher durability than ODMS/Si. For the case of a perfluorinated carbon backbone, it is harder to rotate the backbone structure (due to the different size of F versus H atoms) which implies that this structure is more rigid than a hydrocarbon backbone [106]. Chambers [117] has reported that the C–C bond strength increases when hydrogen is replaced with fluorine. This suggests that the rigid perfluorinated carbon backbone may be responsible for the increased durability. The length of the alkyl chain also influences the desorption energy of alkanes. Based on studies of the adsorption of alkanes on Cu(100), Au(111), Pt (110), and others, the physisorption energy increases with the alkyl chain length [118–120]. Therefore, ODDMS is more durable than ODMS.

During sliding on PFTS films, gaseous products of  $\text{CF}_3$ ,  $\text{HCF}_2$ ,  $\text{CF}_2$ ,  $\text{CH}_2$ , and  $\text{H}_2$  were detected. From the structure of perfluoroalkylsilane, the only source of H on the molecular chain which could cause a partial pressure increase of  $\text{H}_2$  is  $(\text{CH}_2)_2$ , which is located at the bottom of the chain. Since the partial pressure of  $\text{H}_2$  increases immediately after sliding and remains high until the end of sliding, it is probably generated by the low-energy electrons coming from triboelectrical emission. The partial pressure of  $\text{CH}_2$  exhibited a sharp peak at the beginning of sliding and at the moment when friction changes. Meanwhile, the partial pressures of  $\text{CH}_3$ ,  $\text{HSF}_2$ , and  $\text{CF}_2$  increased significantly when the friction increased. For ODMS and ODDMS,  $\text{C}_2\text{H}_5$ ,  $\text{C}_2\text{H}_3$ ,  $\text{CH}_3$ ,  $\text{CH}_2$ , and  $\text{H}_2$  were detected during sliding. The partial pressure of the carbon-related products increase considerably when the friction is increased.  $\text{SiO}_2$ , which is related to the interface bonds, shows no noticeable change during sliding.

Perfluoroalkylsilanes and alkylsilanes are attached to the naturally oxidized silicon by Si–O bonds. The Si–O bond strength varies over a large range (Table 18.14), depending on the forming condition. In the alkylsilane chain, the C–Si bond strength (414 kJ/mol) is slightly lower than the C–C bond strength. Based on Table

**Fig. 18.27** Coefficient of friction and durability comparison of HDT/Au, PFTS/Si, ODMS/Si, and ODDMS/Si in high vacuum. Error bars represent  $\pm 3\sigma$  based on five measurements (after [63])



18.9, interfacial bonds (Si–O) are weaker than the C–C bonds in the backbone. It is believed that cleavage of the films occurs at the interface. We have previously reported evidence of the cleavage of the interfacial bonds using an AFM. To explain the hydrogen, C<sub>1</sub> and C<sub>2</sub> hydrocarbon (in the tests for PFTS/Si, ODMS/Si, and ODDMS/Si) or fluorocarbon (in the tests for PFTS/Si) products, *Kluth* et al. [121] suggested that the alkylsilane (perfluoroalkylsilane as well) chains break and create radicals. The radical could remain on the surface and decompose to generate a shorter radical and an alkene. The radical could repeatedly decompose to ever short radicals and alkenes as long as it remains on the surface.

A summary of the coefficients of friction and durability of all the films in vacuum is presented in Fig. 18.27 [63].

#### 18.4.4.1 Environmental Studies

To study the effect of environment, friction tests on HDT/Au, PFTS/Si, ODMS/Si, and ODDMS/Si were conducted in high vacuum, argon, dry air (less than 2% RH), air with 30% RH, and air with 70% RH (Fig. 18.28) [63]. By comparing the coefficient of friction in different environments, it was found that the friction in argon is the lowest for the SAMs tested. In high vacuum, the intimate contact leads

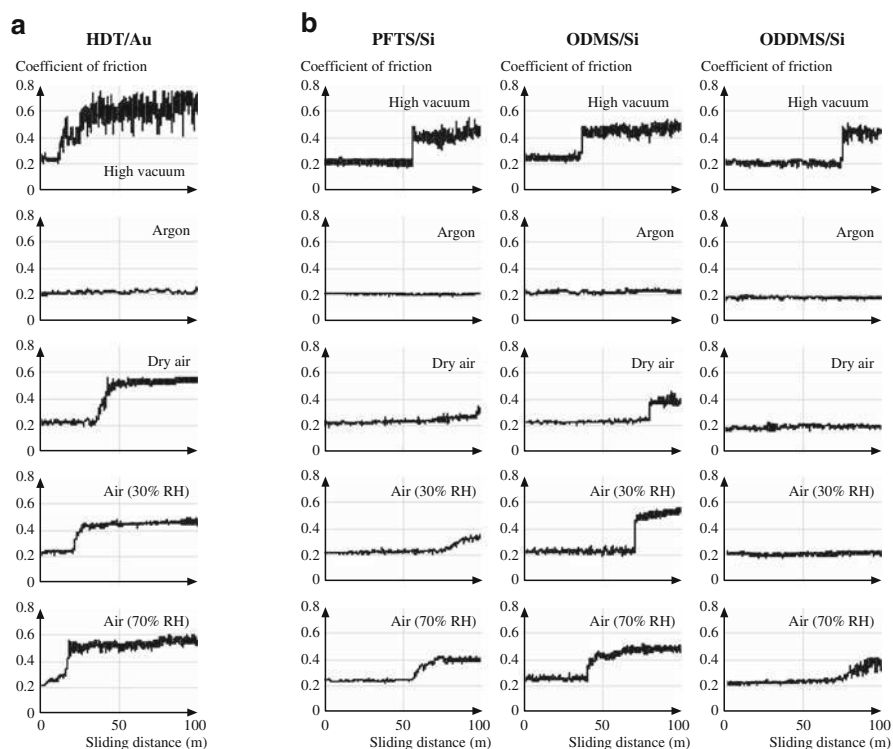
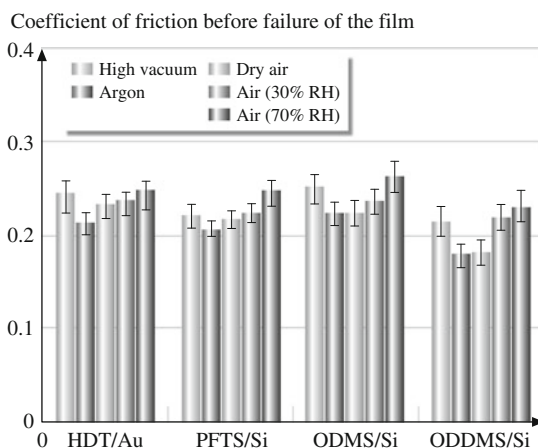


**Fig. 18.28** Coefficient of friction data in high vacuum, argon, and air with different humidity levels of (a) HDT/Au (1.9 nm), and (b) PFTS/Si (1.8 nm), ODMS/Si ( $\approx 1.9$  nm), and ODDMS/Si ( $\approx 2.1$  nm) (after [63])>

to high friction. In dry air, the friction is higher than in the argon. This shows that oxygen has an apparent effect on the performance of SAMs. Kim et al. [122] studied the thermal stability of alkylsiloxane SAMs in air. They found that the alkylsiloxane decomposes at about 200 °C, which is much lower than the decomposition temperature of 470 °C in vacuum reported by Kluth et al. [121]. This difference could be attributed to the oxygen in air. The water contained in air is found to have a significant influence on the friction of SAMs. A study by Tian et al. [116] on the effects of humidity on alkylsilane on mica substrate indicated that water molecules can penetrate the alkylsilane film, which alters their molecular chain ordering and can also detach alkylsilane molecules from the substrate.

A summary of the coefficients of friction before the failure of the lubricant films in various environments is presented in Fig. 18.29 [63]. The data in Fig. 18.29 are average values based on five measurements. To summarize the highlights, friction of the tested lubricant films is high in high vacuum because of the intimate contact between the lubricants and the counterpart surface. Friction of tested lubricant films is lower in argon than in dry air. Friction of SAMs is significantly influenced by water molecules.

**Fig. 18.29** Comparison of coefficient of friction data for HDT/Au, PFTS/Si, ODMS/Si, and ODDMS/Si in high vacuum, argon, and air with different humidity levels. Error bars represent  $\pm 3\sigma$  based on five measurements (after [63])



## 18.5 Summary

Exposure of devices to a humid environment results in condensation of water vapor from the environment. Condensed water or a preexisting film of liquid forms concave meniscus bridges between the hydrophilic mating surfaces. The negative Laplace pressure present in the meniscus results in an adhesive force which depends on the interface roughness, surface tension, and contact angle. The adhesive force can be significant in an interface with ultrasmooth surfaces and it can be on the same order as the external load if the latter is small, such as in micro- and nanodevices. High adhesion also leads to stiction, friction, and wear issues in sliding surfaces. In various applications, surfaces need to be protected from exposure to the operating environment, and hydrophobic films are of interest. Hydrophobic films are also expected to provide low adhesion, stiction, friction, and wear. These films should be molecularly thick, well-organized, chemically bonded to the substrate, and insensitive to environment. Ordered molecular assemblies with high hydrophobicity can be engineered using chemical grafting of various polymer molecules with suitable functional head groups and nonpolar surface terminal groups.

The contact angle, adhesion, friction, and wear properties of various SAMs having alkyl, biphenyl, and perfluoroalkyl spacer chains with different surface terminal groups ( $-\text{CH}_3$  and  $-\text{CF}_3$ ) and head groups ( $-\text{SH}$ ,  $-\text{Si}-\text{O}-$ ,  $-\text{OH}$ , and  $\text{P}-\text{O}-$ ) are presented in this chapter. It is found that the adhesive force varies linearly with the work of adhesion value of SAMs, which indicates that capillary condensation of water plays an important role in the adhesion of SAMs on the nanoscale under ambient conditions. SAMs with high-compliance long carbon spacer chains exhibit the lowest adhesive force and friction force. The friction data can be explained using a molecular spring model, in which the local stiffness and intermolecular force govern frictional performance. The results of the stiffness



**Table 18.15** Summary of nanotribological characterization studies for SAMs on Si and Al substrates

SAMs property		Friction force	Adhesive force	Wear
Substrate	Hard	High	Low	Low
	Soft	Low	Low	High
Chemical structure	Linear chain molecule	High	Low	High
	Ring molecule	High	High	Low
Backbone	Fluorocarbon backbone	Low	Low	Low
	Hydrocarbon backbone	Low	High	High
Chain length	Long backbone chain		High	High
	Short backbone chain		Low	Low

and friction characterization of the micropatterned sample with different structures support this model. Perfluoroalkylsilane and perfluoroalkylphosphonate SAMs exhibit lower surface energy, higher contact angle, and lower adhesive force as compared with alkylsilane and alkylphosphonate SAMs, respectively. The substrate had little effect. The coefficients of friction of various SAMs were comparable.

The influence of relative humidity on adhesion and friction of SAMs is dominated by the thickness of the adsorbed water layer. At higher humidity, water increases friction through increased adhesion by the meniscus effect in the contact zone. With an increase in temperature, in the case of Si(111), desorption of the adsorbed water layer and reduction of the surface tension of water reduces the adhesive force and friction force. A decrease in adhesion and friction with temperature was found for all films. An increase in adhesive force and friction with sliding velocity was found for all films.

PFTS/Si showed better wear resistance than ODMS/Si. ODDMS/Si showed better wear resistance than ODMS/Si due to the effect of chain length. Wear behavior of the SAMs is mostly determined by the molecule–substrate bond strengths. Similar trends were observed for films on Al substrates.

The nanotribological characterization studies of SAMs deposited on Si and Al substrates are summarized in Table 18.15 [52]. SAMs deposited on Si and Al substrates show low friction and low adhesion, both of which are desirable for MEMS/NEMS applications.

Based on studies in high vacuum ( $2 \times 10^{-7}$  Torr), the coefficients of friction of the SAMs are in the following order (from low to high): ODDMS/Si, PFTS/Si, HDT/Au, ODMS/Si. HDT on Au shows lower durability than perfluoroalkylsilane and alkylsilane on Si because of the weak interfacial bond. PFTS/Si has better durability than ODMS/Si. This indicates that fluorination of alkylsilane can improve durability. ODDMS/Si is more durable than ODMS/Si and PFTS/Si because of the effect of chain length. The friction of SAMs in high vacuum is higher than in argon because of intimate contact. Based on studies in argon and air with various relative humidities, oxygen can increase the friction and decrease the durability of SAMs. Water molecules can detach SAM molecules from the substrate, resulting in high friction and low durability.

In summary, based on the contact angle, adhesion, friction, and wear measurements of SAM films by AFM, they exhibit attractive hydrophobic and tribological properties. Fluorinated SAMs appear to exhibit superior performance. SAM films should find many applications, including in micro- and nanodevices requiring good nanotribological properties and surface protection.

## References

1. B. Bhushan, J.N. Israelachvili, U. Landman, Nanotribology, Friction, wear and lubrication at the atomic scale. *Nature* **374**, 607–616 (1995)
2. B. Bhushan, *Tribology and Mechanics of Magnetic Storage Devices*, 2nd edn. (Springer, New York, 1996)
3. B. Bhushan (Ed.), *Tribology Issues and Opportunities in MEMS* (Kluwer, Dordrecht, 1998)
4. B. Bhushan (Ed.), *Handbook of Micro/Nanotribology*, 2nd edn. (CRC, Boca Raton, 1999)
5. B. Bhushan, Nanotribology and nanomechanics of MEMS/NEMS and BioMEMS/BioNEMS materials and devices, *Microelectron. Eng.* **84**, 387–412 (2007)
6. B. Bhushan (Ed.), *Nanotribology and Nanomechanics – An Introduction*, 2nd edn. (Springer, Berlin, 2008)
7. B. Bhushan, Nanotribology and nanomechanics in nano/biotechnology, *Philos. Trans. R. Soc. Lond. Ser. A* **366**, 1499–1537 (2008)
8. K.F. Man, B.H. Stark, R. Ramesham, *A Resource Handbook for MEMS Reliability* (Jet Propulsion Laboratory Press, Pasadena 1998), Rev. A
9. K.F. Man, *MEMS Reliability for Space Applications by Elimination of Potential Failure Modes Through Testing and Analysis* (Jet Propulsion Laboratory Press, Pasadena, 2002)
10. D.M. Tanner, N.F. Smith, L.W. Irwin, W.P. Eaton, K.S. Helgesen, J.J. Clement, W.M. Miller, J.A. Walraven, K.A. Peterson, P. Tangyonyong, M.T. Dugger, S.L. Miller, *MEMS Reliability: Infrastructure, Test Structure, Experiments, and Failure Modes* (Sandia National Laboratories, Albuquerque, 2000), SAND2000-0091
11. A.W. Adamson, *Physical Chemistry of Surfaces*, 5th edn. (Wiley, New York, 1990)
12. J.N. Israelachvili, *Intermolecular and Surface Forces*, 2nd edn. (Academic, London, 1992)
13. M.E. Schrader, G.I. Loeb (Ed.), *Modern Approaches to Wettability* (Plenum, New York, 1992)
14. B. Bhushan, *Principles and Applications of Tribology* (Wiley, New York, 1999)
15. B. Bhushan, *Introduction to Tribology* (Wiley, New York, 2002)
16. S. Cai, B. Bhushan, Meniscus and viscous forces during separation of hydrophilic and hydrophobic surfaces with liquid mediated contacts, *Mater. Sci. Eng. R* **61**, 78–106 (2008)
17. B. Bhushan, Contact mechanics of rough surfaces in tribology: Multiple asperity contact, *Tribol. Lett.* **4**, 1–35 (1998)
18. B. Bhushan (Ed.), *Modern Tribology Handbook* (CRC, Boca Raton, 2001)
19. B. Bhushan, Adhesion and stiction, Mechanisms, measurement techniques, and methods for reduction. *J. Vac. Sci. Technol. B* **21**, 2262–2296 (2003)
20. B. Bhushan, Z. Zhao, Macro- and microscale tribological studies of molecularly-thick boundary layers of perfluoropolyether lubricants for magnetic thin-film rigid disks. *J. Inf. Storage Proc. Syst.* **1**, 1–21 (1999)
21. B. Bhushan, W. Peng, Contact mechanics of multilayered rough surfaces. *Appl. Mech. Rev.* **55**, 435–480 (2002)
22. B. Bhushan, Y.C. Jung, Wetting, adhesion, and friction of superhydrophobic and hydrophilic leaves and fabricated micro-/nanopatterned surfaces. *J. Phys. D* **20**, 225010–1–2250–24 (2008)

23. M. Nosonovsky, B. Bhushan, Roughness-induced superhydrophobicity: A way to design nonadhesive surfaces, *J. Phys. D* **20**, 225009–1–225009–30 (2008)
24. F.P. Bowden, D. Tabor, *The Friction and Lubrication of Solids, Part I* (Clarendon, Oxford, 1950)
25. W.A. Zisman, Friction, durability and wettability properties of monomolecular films on solids. In: *Friction and Wear*, ed. by R. Davies (Elsevier, Amsterdam 1959) pp. 110–148
26. V.N. Koinkar, B. Bhushan, Microtribological studies of unlubricated and lubricated surfaces using atomic force/friction force microscopy. *J. Vac. Sci. Technol. A* **14**, 2378–2391 (1996)
27. H. Liu, B. Bhushan, Nanotribological characterization of molecularly-thick lubricant films for applications to MEMS/NEMS by AFM, *Ultramicroscopy* **97**, 321–340 (2003)
28. A. Ulman, *An Introduction to Ultrathin Organic Films: From Langmuir–Blodgett to Self-Assembly* (Academic, San Diego, 1991)
29. A. Ulman, Formation and structure of self-assembled monolayers. *Chem. Rev.* **96**, 1533–1554 (1996)
30. H. Hansma, F. Motamedi, P. Smith, P. Hansma, J.C. Wittman, Molecular resolution of thin, highly oriented poly (tetrafluoroethylene) films with the atomic force microscope. *Polym. Commun.* **33**, 647–649 (1992)
31. L. Scandella, A. Schumacher, N. Kruse, R. Prins, E. Meyer, R. Luethi, L. Howald, M. Scherge, J.A. Schaefer, Surface modification and mechanical properties of bulk silicon. In: *Tribology Issues and Opportunities in MEMS*, ed. by B. Bhushan (Kluwer, Dordrecht 1998) pp. 529–537
32. B. Bhushan, Chemical, mechanical and tribological characterization of ultra-thin and hard amorphous carbon coatings as thin as 3.5 nm: Recent developments. *Diam. Relat. Mater.* **8**, 1985–2015 (1999)
33. A. Erdemir, C. Donnet, Tribology of diamond, diamond-like carbon, and related films. In: *Modern Tribology Handbook*, Vol. 2, ed. by B. Bhushan (CRC, Boca Raton, 2001) pp. 871–908
34. V.F. Dorfman, Diamond-like nanocomposites (DLN). *Thin Solid Films* **212**, 267–273 (1992)
35. M. Grischke, K. Bewilogua, K. Trojan, H. Dimigan, Application-oriented modification of deposition process for diamond-like-carbon based coatings. *Surf. Coat. Technol.* **74/75**, 739–745 (1995)
36. R.S. Butter, D.R. Waterman, A.H. Lettington, R.T. Ramos, E.J. Fordham, Production and wetting properties of fluorinated diamond-like carbon coatings. *Thin Solid Films* **311**, 107–113 (1997)
37. M. Grischke, A. Hieke, F. Morgenweck, H. Dimigan, Variation of the wettability of DLC coatings by network modification using silicon and oxygen. *Diam. Relat. Mater.* **7**, 454–458 (1998)
38. C. Donnet, J. Fontaine, A. Grill, V. Patel, C. Jahnes, M. Belin, Wear-resistant fluorinated diamond-like carbon films. *Surf. Coat. Technol.* **94-95**, 531–536 (1997)
39. D.J. Kester, C.L. Brodbeck, I.L. Singer, A. Kyriakopoulos, Sliding wear behavior of diamond-like nanocomposite coatings. *Surf. Coat. Technol.* **113**, 268–273 (1999)
40. H. Liu, B. Bhushan, Adhesion and friction studies of microelectromechanical systems/nanoelectromechanical systems materials using a novel microtriboapparatus. *J. Vac. Sci. Technol. A* **21**, 1528–1538 (2003)
41. B. Bhushan, H. Liu, S.M. Hsu, Adhesion and friction studies of silicon and hydrophobic and low friction films and investigation of scale effects. *ASME J. Tribol.* **126**, 583–590 (2004)
42. J.A. Zasadzinski, R. Viswanathan, L. Madsen, J. Garnaes, D.K. Schwartz, Langmuir–Blodgett films. *Science* **263**, 1726–1733 (1994)
43. J. Tian, Y. Xia, G.M. Whitesides, Microcontact printing of SAMs. In: *Thin Films – Self-Assembled Monolayers of Thiols*, Vol. 24, ed. by A. Ulman (Academic, San Diego, 1998) pp. 227–254
44. Y. Xia, G.M. Whitesides, Soft lithography. *Angew. Chem. Int. Ed.* **37**, 550–575 (1998)

45. A. Kumar, G.M. Whitesides, Features of gold having micrometer to centimeter dimensions can be formed through a combination of stamping with an elastomeric stamp and an alkanethiol ink followed by chemical etching. *Appl. Phys. Lett.* **63**, 2002–2004 (1993)
46. S.Y. Chou, P.R. Krauss, P.J. Renstrom, Imprint lithography with 25-nm resolution. *Science* **272**, 85–87 (1996)
47. Y. Xia, E. Kim, X.M. Zhao, J.A. Rogers, M. Prentiss, G.M. Whitesides, Complex optical surfaces formed by replica molding against elastomeric masters. *Science* **273**, 347–349 (1996)
48. L.J. Hornbeck, The DMD projection display chip: A MEMS-based technology. *MRS Bulletin* **26**, 325–328 (2001)
49. M.R. Douglass, Lifetime estimates and unique failure mechanisms of the digital micromirror device (DMD). 1998 Int. Reliab. Phys. Proc., presented at 36th Annu. Int. Reliab. Phys. Symp., Reno (1998)
50. H. Liu, B. Bhushan, Nanotribological characterization of digital micromirror devices using an atomic force microscope. *Ultramicroscopy* **100**, 391–412 (2004)
51. H. Liu, B. Bhushan, Investigation of nanotribological and nanomechanical properties of the digital micromirror device by atomic force microscope. *J. Vac. Sci. Technol. A* **22**, 1388–1396 (2004)
52. N.S. Tambe, B. Bhushan, Nanotribological characterization of self assembled monolayers deposited on silicon and aluminum substrates. *Nanotechnology* **16**, 1549–1558 (2005)
53. B. Bhushan, M. Cichomski, E. Hoque, J.A. DeRose, P. Hoffmann, H.J. Mathieu, Nanotribological characterization of perfluoroalkylphosphonate self-assembled monolayers deposited on aluminum-coated silicon substrates. *Microsyst. Technol.* **12**, 588–596 (2006)
54. E. Hoque, J.A. DeRose, P. Hoffmann, H.J. Mathieu, B. Bhushan, M. Cichomski, Phosphonate self-assembled monolayers on aluminum surfaces. *J. Chem. Phys.* **124**, 174710 (2006)
55. E. Hoque, J.A. DeRose, G. Kulik, P. Hoffmann, H.J. Mathieu, B. Bhushan, Alkylphosphonate modified aluminum oxide surfaces. *J. Phys. Chem. B* **110**, 10855–10861 (2006)
56. E. Hoque, J.A. DeRose, P. Hoffmann, B. Bhushan, H.J. Mathieu, Alkylperfluorosilane self-assembled monolayers on aluminum: A comparison with alkylphosphonate self-assembled monolayers. *J. Phys. Chem. C* **111**, 3956–3962 (2007)
57. J.A. DeRose, E. Hoque, B. Bhushan, H.J. Mathieu, Characterization of perfluorodecanote self-assembled monolayers on aluminum and comparison of stability with phosphonate and siloxy self-assembled monolayers. *Surf. Sci.* **602**, 1360–1367 (2008)
58. B. Bhushan, A.V. Kulkarni, V.N. Koinkar, M. Boehm, L. Odoni, C. Martelet, M. Belin, Microtribological characterization of self-assembled and Langmuir–Blodgett monolayers by atomic and friction force microscopy. *Langmuir* **11**, 3189–3198 (1995)
59. B. Bhushan, T. Kasai, G. Kulik, L. Barbieri, P. Hoffmann, AFM study of perfluorosilane and alkylsilane self-assembled monolayers for anti-stiction in MEMS/NEMS. *Ultramicroscopy* **105**, 176–188 (2005)
60. B. Bhushan, D. Hansford, K.K. Lee, Surface modification of silicon surfaces with vapor phase deposited ultrathin fluorosilane films for biomedical devices. *J. Vac. Sci. Technol. A* **24**, 1197–1202 (2006)
61. T. Kasai, B. Bhushan, G. Kulik, L. Barbieri, P. Hoffmann, Nanotribological study of perfluorosilane SAMs for anti-stiction and low wear. *J. Vac. Sci. Technol. B* **23**, 995–1003 (2005)
62. K.K. Lee, B. Bhushan, D. Hansford, Nanotribological characterization of perfluoropolymer thin films for bioMEMS applications. *J. Vac. Sci. Technol. A* **23**, 804–810 (2005)
63. Z. Tao, B. Bhushan, Degradation mechanisms and environmental effects on perfluoropolyether self assembled monolayers and diamond-like carbon films. *Langmuir* **21**, 2391–2399 (2005)
64. Z. Tao, B. Bhushan, Surface modification of AFM silicon probes for adhesion and wear reduction. *Tribol. Lett.* **21**, 1–16 (2006)

65. E. Hoque, J.A. DeRose, P. Hoffmann, B. Bhushan, H.J. Mathieu, Chemical stability of nonwetting, low adhesion self-assembled monolayer films formed by perfluoroalkylsilazation of copper. *J. Chem. Phys.* **126**, 114706 (2007)
66. E. Hoque, J.A. DeRose, B. Bhushan, H.J. Mathieu, Self-assembled monolayers on aluminum and copper oxide surfaces: Surface and interface characteristics, nanotribological properties, and chemical stability. In: *Applied Scanning Probe Methods IX*, NanoScience and Technology, ed. by B. Bhushan, H. Fuchs, M. Tomitori (Springer, Berlin, 2008) pp. 235–281
67. E. Hoque, J.A. DeRose, B. Bhushan, K.W. Hipps, Low adhesion, nonwetting phosphonate self-assembled monolayer films formed on copper oxide surfaces. *Ultramicroscopy* **109**, 1015–1022 (2009)
68. A. Manz, H. Becker (Eds.), *Microsystem Technology in Chemistry and Life Sciences* (Springer, Heidelberg, 1998)
69. J. Cheng, L.J. Krica (Eds.), *Biochip Technology* (Harwood Academic, New York, 2001)
70. M.J. Heller, A. Guttman (Eds.), *Integrated Microfabricated Biodevices* (Marcel, New York, 2001)
71. A. van den Berg (Ed.), *Lab-on-a-Chip: Chemistry in Miniaturized Synthesis and Analysis Systems* (Elsevier, Amsterdam, 2003)
72. D.R. Tokachichu, B. Bhushan, Bioadhesion of polymers for BioMEMS. *IEEE Trans. Nanotechnol.* **5**, 228–231 (2006)
73. B. Bhushan, M. Cichomski, Nanotribological characterization of vapor phase deposited fluorosilane self-assembled monolayers deposited on polydimethylsiloxane surfaces for biomedical micro-/nanodevices. *J. Vac. Sci. Technol. A* **25**, 1285–1293 (2007)
74. M. Hein, L.R. Best, S. Pattison, S. Arena, *Introduction to General, Organic, and Biochemistry*, 6th edn. (Brooks/Cole, Pacific Grove, 1997)
75. J.R. Mohrig, C.N. Hammond, T.C. Morrill, D.C. Neckers, *Experimental Organic Chemistry* (Freeman, New York, 1998)
76. A. Ulman (Ed.), *Characterization of Organic Thin Films* (Butterworth Heinemann, Boston, 1995)
77. C. Jung, O. Dannenberger, Y. Xu, M. Buck, M. Grunze, Self-assembled monolayers from organosulfur compounds: A comparison between sulfides, disulfides, and thiols, *Langmuir* **14**, 1103–1107 (1998)
78. W. Geyer, V. Stadler, W. Eck, M. Zharnikov, A. Golzhauser, M. Grunze, Electron-induced crosslinking of aromatic self-assembled monolayers: Negative resists for nanolithography. *Appl. Phys. Lett.* **75**, 2401–2403 (1999)
79. B. Bhushan, H. Liu, Nanotribological properties and mechanisms of alkylthiol and biphenyl thiol self-assembled monolayers studied by atomic force microscopy. *Phys. Rev. B* **63**, 245412–1–245412–11 (2001)
80. H. Liu, B. Bhushan, W. Eck, V. Stadler, Investigation of the adhesion, friction, and wear properties of biphenyl thiol self-assembled monolayers by atomic force microscopy. *J. Vac. Sci. Technol. A* **19**, 1234–1240 (2001)
81. H. Liu, B. Bhushan, Investigation of nanotribological properties of alkylthiol and biphenyl thiol self-assembled monolayers. *Ultramicroscopy* **91**, 185–202 (2002)
82. S.R. Wasserman, Y.T. Tao, G.M. Whitesides, Structure and reactivity of alkylsiloxane monolayers formed by reaction of alkylchlorosilanes on silicon substrates. *Langmuir* **5**, 1074–1089 (1989)
83. J. Ruhe, V.J. Novotny, K.K. Kanazawa, T. Clarke, G.B. Street, Structure and tribological properties of ultrathin alkylsilane films chemisorbed to solid surfaces. *Langmuir* **9**, 2383–2388 (1993)
84. V. DePalma, N. Tillman, Friction and wear of self-assembled trichlorosilane monolayer films on silicon. *Langmuir* **5**, 868–872 (1989)
85. M.T. McDermott, J.B.D. Green, M.D. Porter, Scanning force microscopic exploration of the lubrication capabilities of n-alkanethiolate monolayers chemisorbed at gold: Structural basis of microscopic friction and wear. *Langmuir* **13**, 2504–2510 (1997)

86. X. Xiao, J. Hu, D.H. Charych, M. Salmeron, Chain length dependence of the frictional properties of alkylsilane molecules self-assembled on mica studied by atomic force microscopy. *Langmuir* **12**, 235–237 (1996)
87. A. Lio, D.H. Charych, M. Salmeron, Comparative atomic force microscopy study of the chain length dependence of frictional properties of alkanethiol on gold and alkylsilanes on mica. *J. Phys. Chem. B* **101**, 3800–3805 (1997)
88. H. Schönherr, G.J. Vancso, Tribological properties of self-assembled monolayers of fluoro-carbon and hydrocarbon thiols and disulfides on Au(111) studied by scanning force microscopy. *Mater. Sci. Eng. C* **8/9**, 243–249 (1999)
89. V.V. Tsukruk, V.N. Bliznyuk, Adhesive and friction forces between chemically modified silicon and silicon nitride surfaces. *Langmuir* **14**, 446–455 (1998)
90. V.V. Tsukruk, T. Nguyen, M. Lemieux, J. Hazel, W.H. Weber, V.V. Shevchenko, N. Klimenko, E. Sheludko, Tribological properties of modified MEMS surfaces. In: *Tribology Issues and Opportunities in MEMS*, ed. by B. Bhushan (Kluwer, Dordrecht, 1998) pp. 607–614
91. M. Fujihira, Y. Tani, M. Furugori, U. Akiba, Y. Okabe, Chemical force microscopy of self-assembled monolayers on sputtered gold films patterned by phase separation. *Ultramicroscopy* **86**, 63–73 (2001)
92. H. Liu, B. Bhushan, Orientation and relocation of biphenyl thiol self-assembled monolayers. *Ultramicroscopy* **91**, 177–183 (2002)
93. R.J. Good, C.J.V. Oss, *Modern Approaches to Wettability – Theory and Applications* (Plenum, New York 1992)
94. M.H.V.C. Adão, B.J.V. Saramago, A.C. Fernandes, Estimation of the surface properties of styrene-acrylonitrile random copolymers from contact angle measurements. *J. Colloid Interface Sci.* **217**, 94–106 (1999)
95. N.S. Tambe, B. Bhushan, A new atomic force microscopy based technique for studying nanoscale friction at high sliding velocities. *J. Phys. D Appl. Phys.* **38**, 764–773 (2005)
96. B. Bhushan, J. Ruan, Tribological performance of thin film amorphous carbon overcoats for magnetic recording disks in various environments. *Surf. Coat. Technol.* **68/69**, 644–650 (1994)
97. B. Bhushan, L. Yang, C. Gao, S. Suri, R.A. Miller, B. Marchon, Friction and wear studies of magnetic thin film rigid disks with glass-ceramic, glass and aluminum-magnesium substrates. *Wear* **190**, 44–59 (1995)
98. Y.F. Miura, M. Takenga, T. Koini, M. Graupe, N. Garg, R.L. Graham, T.R. Lee, Wettability of self-assembled monolayers generated from CF<sub>3</sub>-terminated alkanethiols on gold. *Langmuir* **14**, 5821–5825 (1998)
99. M. Ratajczak-Sitarz, A. Katrusiak, Z. Kaluski, J. Garbarczyk, 4,4'-Biphenyldithiol, *Acta Crystallogr. C* **43**, 2389–2391 (1987)
100. J.I. Siepmann, I.R. McDonald, Monte Carlo simulation of the mechanical relaxation of a self-assembled monolayer, *Phys. Rev. Lett.* **70**, 453–456 (1993)
101. M. Garcia-Parajo, C. Longo, J. Servat, P. Gorostiza, F. Sanz, Nanotribological properties of octadecyltrichlorosilane self-assembled ultrathin films studied by atomic force microscopy: Contact and tapping modes. *Langmuir* **13**, 2333–2339 (1997)
102. D. DeVecchio, B. Bhushan, Localized surface elasticity measurements using an atomic force microscope. *Rev. Sci. Instrum.* **68**, 4498–4505 (1997)
103. E. Barena, S. Kopta, D.F. Ogletree, D.H. Charych, M. Salmeron, Relationship between friction and molecular structure: Alkylsilane lubricant films under pressure. *Phys. Rev. Lett.* **82**, 2880–2883 (1999)
104. N. Eustathopoulos, M. Nicholas, B. Drevet, *Wettability at High Temperature* (Pergamon, Amsterdam 1999)
105. S. Ren, S. Yang, Y. Zhao, T. Yu, X. Xiao, Preparation and characterization of ultrahydrophobic surface based on a stearic acid self-assembled monolayer over polyethyleneimine thin films. *Surf. Sci.* **546**, 64–74 (2003)

106. E.S. Clark, The molecular conformations of polytetrafluoroethylene: Forms II and IV, *Polymer* **40**, 4659–4665 (1999)
107. D.R. Lide, *CRC Handbook of Chemistry and Physics*, 85th edn. (CRC, Boca Raton, 2004)
108. W.D. Callister, *Materials Science and Engineering*, 4th edn. (Wiley, New York, 1997)
109. N.S. Tambe, B. Bhushan, Friction model for velocity dependence of nanoscale friction, *Nanotechnology* **16**, 2309–2324 (2005)
110. T. Hoshino, Adsorption of atomic and molecular oxygen and desorption of silicon monoxide on Si(111) surfaces. *Phys. Rev. B* **59**, 2332–2340 (1999)
111. T.L. Cottrell, *The Strength of Chemical Bonds*, 2nd edn. (Butterworth, London, 1958)
112. S.C. Clear, P.F. Nealey, The effect of chain density on the frictional behavior of surfaces modified with alkylsilanes and immersed in *n*-alcohols, *J. Chem. Phys.* **114**, 2802–2811 (2001)
113. N.S. Tambe, B. Bhushan, Durability studies of micro/nanoelectromechanical systems materials, coatings and lubricants at high sliding velocities (up to 10 mm/s) using a modified atomic force microscope. *J. Vac. Sci. Technol. A* **23**, 830–835 (2005)
114. Anonymous, *Properties of Silicon*, EMIS Data Rev. Ser., Vol. 4 (INSPEC Institution of Electrical Engineers, London 1988)
115. Anonymous, *MEMS Materials Database* (MEMS and Nanotechnology Clearinghouse, Reston 2002), <http://www.memsnet.org/material/>
116. F. Tian, X. Xiao, M.M.T. Loy, C. Wang, C. Bai, Humidity and temperature effect on frictional properties of mica and alkylsilane monolayer self-assembled on mica. *Langmuir* **15**, 244–249 (1999)
117. R.D. Chambers, *Fluorine in Organic Chemistry* (Wiley, New York, 1973)
118. B.A. Sexton, A.E. Hughes, A comparison of weak molecular adsorption of organic-molecules on clean copper and platinum surfaces. *Surf. Sci.* **140**, 227–248 (1984)
119. L.H. Dubois, B.R. Zegarski, R.G. Nuzzo, Fundamental studies of microscopic wetting on organics surfaces, 2. Interaction of secondary adsorbates with chemically textured organic monolayers. *J. Am. Chem. Soc.* **112**, 570–579 (1990)
120. M.C. McMaster, S.L.M. Schroeder, R.J. Madix, Molecular propane adsorption dynamics on Pt(110)-(1x2). *Surf. Sci.* **297**, 253–271 (1993)
121. G.J. Kluth, M. Sander, M.M. Sung, R. Maboudian, Study of the desorption mechanism of alkylsiloxane self-assembled monolayers through isotopic labeling and high resolution electron energy-loss spectroscopy experiments. *J. Vac. Sci. Technol. A* **16**, 932–936 (1998)
122. H.K. Kim, J.P. Lee, C.R. Park, H.T. Kwak, M.M. Sung, Thermal decomposition of alkylsiloxane self-assembled monolayers in air. *J. Phys. Chem. B* **107**, 4348–4351 (2003)

# Chapter 19

## Nanoscale Boundary Lubrication Studies

**Bharat Bhushan**

**Abstract** Boundary films are formed by physisorption, chemisorption, and chemical reaction. A good boundary lubricant should have a high degree of interaction between its molecules and the solid surface. As a general rule, liquids are good lubricants when they are polar and thus able to grip solid surfaces (or be adsorbed). In this chapter, we focus on various perfluoropolyethers (PFPEs) and ionic liquid films. We present a summary of nanodeformation, molecular conformation, and lubricant spreading studies, followed by an overview of the nanotribological properties of polar and nonpolar PFPEs and ionic liquid films studied by atomic force microscopy (AFM), and chemical degradation studies using a high-vacuum tribotest apparatus. In this chapter, we focus on PFPE and ionic liquid films. We first present a summary of nanodeformation, molecular conformation, and lubricant spreading studies and an overview of nanotribological and electrical studies of commonly used polar and nonpolar PFPE and ionic liquid films using AFM and chemical degradation studies using a high-vacuum tribotest apparatus.

### 19.1 Boundary Films

Boundary films are formed by physisorption, chemisorption, and chemical reaction. With physisorption, no exchange of electrons takes place between the molecules of the adsorbate and those of the adsorbant [1, 2]. The physisorption process typically involves van der Waals forces, which are relatively weak. In chemisorption, there is an actual sharing of electrons or an electron interchange between the chemisorbed species and the solid surface. The solid surface bonds very strongly to the adsorption species through covalent bonds. Chemically reacted films are formed by the chemical reaction of the solid surface with the environment. The physisorbed film can be either monomolecularly or polymolecularly thick. The chemisorbed films are monomolecular, but stoichiometric films formed by chemical reaction can have a large film thickness. In general, the stability and durability of surface films decrease in the following order: chemically reacted films, chemisorbed films, physisorbed films. A good boundary lubricant should have a high degree of interaction between its molecules and the solid surface. As a general rule, liquids are good lubricants when



they are polar and thus able to grip solid surfaces (or be adsorbed). Polar lubricants contain reactive functional groups with low ionization potential or groups having high polarizability [1–3]. Boundary lubrication properties of lubricants are also dependent upon the molecular conformation and lubricant spreading [4–7].

Perfluoropolyether (PFPE) films, self-assembled monolayers (SAMs), and Langmuir–Blodgett (LB) films can be used as boundary lubricants [1–3, 8–15]. PFPE films are exclusively used for the lubrication of rigid magnetic disks and metal-evaporated magnetic tapes to reduce the friction and wear of the head–medium interface [10]. PFPEs are well suited for this application because of the following properties: low surface tension and high contact angle, which allow easy spreading on surfaces and provide hydrophobicity; chemical and thermal stability, which minimize degradation under use; low vapor pressure, which provides low outgassing; high adhesion to substrate via organofunctional bonds; and good lubricity, which reduces the interfacial friction and wear [10–12]. While the structure of the lubricants employed at the head–medium interface has not changed substantially over the past decade, the thickness of the PFPE film used to lubricate the disk has steadily decreased from multilayer thicknesses to the submonolayer thickness regime [12, 14]. Molecularly thick PFPE films are also being considered for lubrication purposes of the evolving microelectromechanical/nanoelectromechanical systems (MEMS/NEMS) industry [16, 17]. It is well known that the properties of molecularly thick liquid films confined to solid surfaces can be dramatically different from those of the corresponding bulk liquid. In order to efficiently develop lubrication systems that meet the requirements of advanced rigid disk drives and MEMS/NEMS industries, the nanotribology of thin films of PFPE lubricants should be fully understood [11, 13, 18, 19]. It is also important to understand lubricant–substrate interfacial interactions and the influence of operating environment on the nanotribological performance of molecularly thick PFPE liquid films. Ionic liquids are considered as potential lubricants [20–22]. They possess efficient heat transfer properties. They are also electrically conducting, which is of interest in various MEMS/NEMS applications such as atomic force microscope probe-based data recording [23–25].

An overview of the nanotribological properties of SAMs and LB films can be found in many references, such as Bhushan [13]. In this chapter, we focus on PFPE and ionic liquid films. We first present a summary of nanodeformation, molecular conformation, and lubricant spreading studies and an overview of nanotribological and electrical studies of commonly used polar and nonpolar PFPE and ionic liquid films using atomic force microscopy (AFM) and chemical degradation studies using a high-vacuum tribotest apparatus.

## 19.2 Nanodeformation, Molecular Conformation, Spreading, and Nanotribological Studies

The molecular structures of two commonly used typical PFPE lubricants (Z-15 and Z-DOL 2000) are shown schematically in Fig. 19.1 (Fomblin, Solvay Solexis Inc., Milan, Italy). Z-15 has nonpolar  $-\text{CF}_3$  end groups, whereas Z-DOL is a polar

**Fig. 19.1** Schematics of the molecular structures of Z-15 and Z-DOL 2000. Z-15 has nonpolar  $-\text{CF}_3$  end groups, whereas Z-DOL is a polar lubricant with hydroxyl ( $-\text{OH}$ ) end groups. In this figure, the  $m/n$  value, shown in Table 19.1, equals 2/3

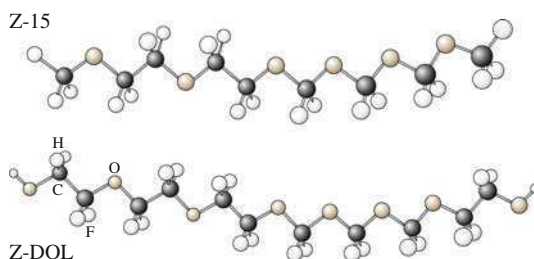


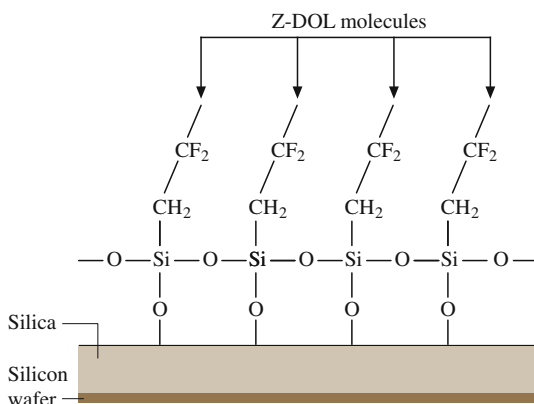
**Table 19.1** Typical properties of Z-15 and Z-DOL (Fomblin Z, Solvay Solexis Inc., Milan)

	Z-15	Z-DOL (2000)
Formula	$\text{CF}_3\text{--O--}(\text{CF}_2\text{--CF}_2\text{--O})_m\text{--}(\text{CF}_2\text{--O})_n\text{--CF}_3^a$	$\text{HO--CH}_2\text{--CF}_2\text{--O--}(\text{CF}_2\text{--CF}_2\text{--O})_m\text{--}(\text{CF}_2\text{--O})_n\text{--CF}_2\text{--CH}_2\text{--OH}^a$
Molecular weight (Da)	9100	2000
Density (ASTM D891) ( $\text{g/cm}^3$ )		
20°C	1.84	1.81
Kinematic viscosity (ASTM D445) (cSt)		
20°C	148	85
38°C	90	34
99°C	25	—
Viscosity index (ASTM D2270)	320	—
Surface tension (ASTM D1331) (dyn/cm)		
20°C	24	24
Vapor pressure (Torr)		
20°C	$1.6 \times 10^{-6}$	$2 \times 10^{-5}$
100°C	$1.7 \times 10^{-5}$	$6 \times 10^{-4}$
Pour point (ASTM D972) (°C)	−80	—
Evaporation weight loss (ASTM D972) (%)		
149°C, 22 h	0.7	—
Oxidative stability (°C)	—	320
Specific heat (cal/(g K))		
38°C	0.21	—

<sup>a</sup> $m/n \approx 2/3$

lubricant with hydroxyl ( $-\text{OH}$ ) end groups. Their typical properties are summarized in Table 19.1, showing that Z-15 and Z-DOL have almost the same density and surface tension, but Z-15 has a larger molecular weight and higher viscosity. Both of them have low surface tension, low vapor pressure, low evaporation weight loss, and good oxidative stability [3, 10]. For nanotribological characterization, a single-crystal Si(100) wafer with native oxide layer has generally been used as a substrate for deposition of molecularly thick lubricant films. Z-15 and Z-DOL films can be directly deposited on the Si(100) wafer by a dip-coating technique. The clean silicon wafer is submerged vertically into a dilute solution of lubricant in

**Fig. 19.2** Schematic of Z-DOL molecules chemically bonded onto a Si(100) substrate surface (which has native oxide) after thermal treatment at 150°C for 30 min

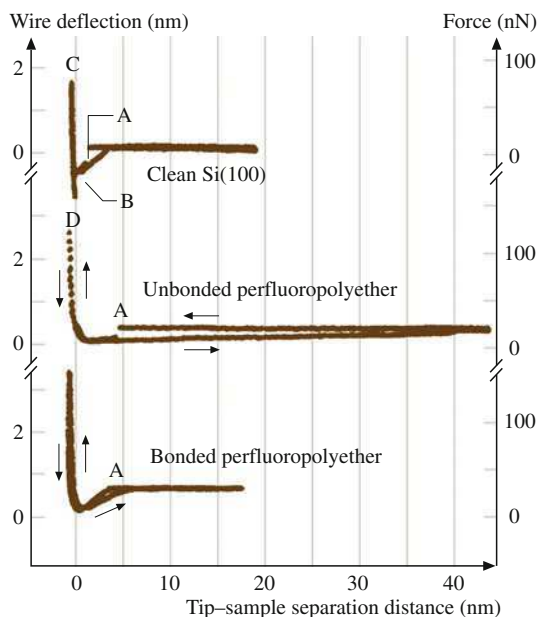


a hydrocarbon solvent (HT-70, Solvay Solexis Inc., Milan, Italy). The silicon wafers are vertically pulled up from the solution with a motorized stage at constant speed for deposition of desired thicknesses of Z-15 and Z-DOL lubricants [12, 14, 26]. The lubricant film thickness obtained in dip-coating is a function of concentration and pulling-up speed, among other factors. The Z-DOL film is bonded to the silicon substrate by heating the as-deposited Z-DOL samples in an oven at 150°C for  $\approx 30$  min. The native oxide layer of Si(100) wafer reacts with the  $\text{—OH}$  groups of the lubricants during thermal treatment [26, 27, 28, 29]. Subsequently, fluorocarbon solvent (FC-72, 3M) washing of the thermally treated specimen removes loosely absorbed species, leaving the chemically bonded phase on the substrate. The chemical bonding between Z-DOL molecules and the silicon substrate is illustrated in Fig. 19.2. The bonded and washed Z-DOL film is referred to as Z-DOL (fully bonded) in this chapter. The as-deposited Z-15 and Z-DOL films are mobile-phase (i.e., liquid-like) lubricants, whereas the Z-DOL (fully bonded) films are fully bonded soft solid-phase (i.e., solid-like) lubricants.

### 19.2.1 Nanodeformation, Molecular Conformation, and Spreading

Nanodeformation behavior of Z-DOL lubricants was studied using an AFM by Blackman et al. [30, 31]. Before bringing a tungsten tip into contact with a molecular overlayer, it was first brought into contact with a bare clean silicon surface (Fig. 19.3). As the sample approaches the tip, the force is initially zero, but at point A the force suddenly becomes attractive (top curve) which increases until point B, where the sample and tip come into intimate contact and the force becomes repulsive. As the sample is retracted, a pull-off force of  $5 \times 10^{-8}$  N (point D) is required to overcome adhesion between the tungsten tip and the silicon surface. When an AFM tip is brought into contact with an unbonded Z-DOL film,

**Fig. 19.3** Wire deflection (normal load) as a function of tip-sample separation distance curves comparing the behavior of clean Si(100) surface with a surface lubricated with free and unbonded PFPE lubricant, and a surface where the PFPE lubricant film was thermally bonded to the surface (after [30])



a sudden jump in adhesive contact is also observed. A much larger pull-off force is required to overcome the adhesion. The adhesion is initiated by the formation of a lubricant meniscus surrounding the tip. This suggests that the unbonded Z-DOL lubricant shows liquid-like behavior. However, when the tip was brought into contact with a lubricant film which was firmly bonded to the surface, the liquid-like behavior disappears. The initial attractive force (point A) is no longer sudden as with the liquid film, but rather gradually increases as the tip penetrates the film.

According to Blackman et al. [30, 31], if the substrate and tip were infinitely hard with no compliance and/or deformation in the tip and sample supports, the line from B to C would be vertical with infinite slope. The tangent to the force-distance curve at a given point is referred to as the stiffness at that point and was determined by fitting a least-squares line through the nearby data points. For silicon, the deformation is reversible (elastic) since the retracting (outgoing) portion of the curve (C to D) follows the extending (ingoing) portion (B to C). For bonded lubricant film, at the point where the slope of the force changes gradually from attractive to repulsive, the stiffness changes gradually, indicating compression of the molecular film. As the load is increased, the slope of the repulsive force eventually approaches that of the bare surface. The bonded film was found to respond elastically up to the highest loads of  $5\ \mu\text{N}$  which could be applied. Thus, bonded lubricant behaves as a soft polymer solid.

Figure 19.4 illustrates two extremes for the conformation on a surface of a linear liquid polymer without any reactive end groups and at submonolayer coverages [4, 6]. At one extreme, the molecules lie flat on the surface, reaching no more than their chain diameter  $\delta$  above the surface. This would be the case if a strong attractive interaction exists between the molecules and the solid. On the other

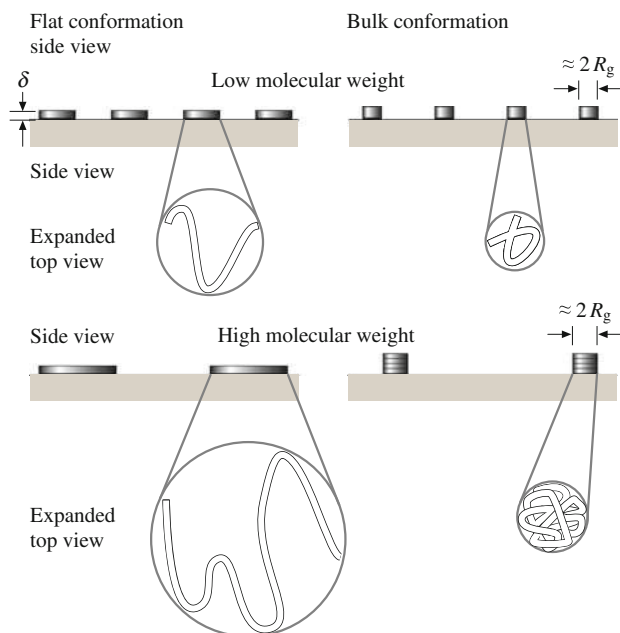


**Fig. 19.4** Schematic representation of two extreme liquid conformations at the surface of the solid for low and high molecular weights at low surface coverage.  $\delta$  is the cross-sectional diameter of the liquid chain and  $R_g$  is the radius of gyration of the molecules in the bulk (after [6])

extreme, when a weak attraction exists between polymer segments and the solid, the molecules adopt conformations close to that of the molecules in the bulk, with microscopic thickness equal to about the radius of gyration  $R_g$ . Mate and Novotny [6] used AFM to study conformation of 0.5–1.3 nm-thick Z-15 molecules on clean Si(100) surfaces. They found that the thickness measured by AFM was thicker than that measured by ellipsometry, with the offset ranging from 3 to 5 nm. They found that the offset was the same for very thin, submonolayer coverages. If the coverage is submonolayer and inadequate to make a liquid film, the relevant thickness is then the height ( $h_e$ ) of the molecules extended above the solid surface. The offset should be equal to  $2h_e$ , assuming that the molecules extend the same height above both the tip and silicon surfaces. They thus concluded that the molecules do not extend  $>1.5$ – $2.5$  nm above a solid or liquid surface, much smaller than the radius of gyration of the lubricants of 3.2–7.3 nm, and similar to the approximate cross-sectional diameter of 0.6–0.7 nm for the linear polymer chain. Consequently, the height that the molecules extend above the surface is considerably less than the diameter of gyration of the molecules and only a few molecular diameters in height, implying that the physisorbed molecules on a solid surface have an extended, flat conformation. They also determined the disjoining pressure of these liquid films based on AFM measurements of the distance needed to break the liquid meniscus that forms between the solid surface and an AFM tip [7]. For a monolayer thickness of  $\approx 0.7$  nm, the disjoining pressure is  $\approx 5$  MPa, indicating strong attractive interaction

between the liquid molecules and the solid surface. The disjoining pressure decreases with increasing film thickness in a manner consistent with a strong attractive van der Waals interaction between the liquid molecules and the solid surface.

Rheological characterization shows that the flow activation energy of PFPE lubricants is weakly dependent on chain length and strongly dependent on the functional end groups [32]. PFPE lubricant films that contain polar end groups have lower mobility than those with nonpolar end groups of similar chain length [33]. The mobility of PFPE also depends on the surface chemical properties of the substrate. The spreading of Z-DOL on an amorphous carbon surface has been studied as a function of hydrogen or nitrogen content in the carbon film, using scanning microellipsometry [34]. The diffusion coefficient data presented in Fig. 19.5 is thickness dependent. It shows that the surface mobility of Z-DOL increased as the hydrogen content increased, but decreased as the nitrogen content increased. The enhancement of Z-DOL surface mobility by hydrogenation may be understood from the fact that the interactions between Z-DOL molecules and the carbon surface can be significantly weakened due to a reduction of the number of high-energy binding sites on the carbon surface. The stronger interactions between Z-DOL molecules and the carbon surface, as the nitrogen content in the carbon coating increases, leads to the lowering of the Z-DOL surface mobility.

Molecularly thick films may be sheared at very high shear rates, on the order of  $10^8$ – $10^9$  s<sup>-1</sup> during sliding, such as during magnetic disk-drive operation. During such shear, lubricant stability is critical to the protection of the interface. For proper lubricant selection, viscosity at high shear rates and associated shear thinning need to be understood. Viscosity measurements of eight different types of PFPE films show that all eight lubricants display Newtonian behavior and that their viscosity remains constant at shear rates up to  $10^7$  s<sup>-1</sup> [35, 36].

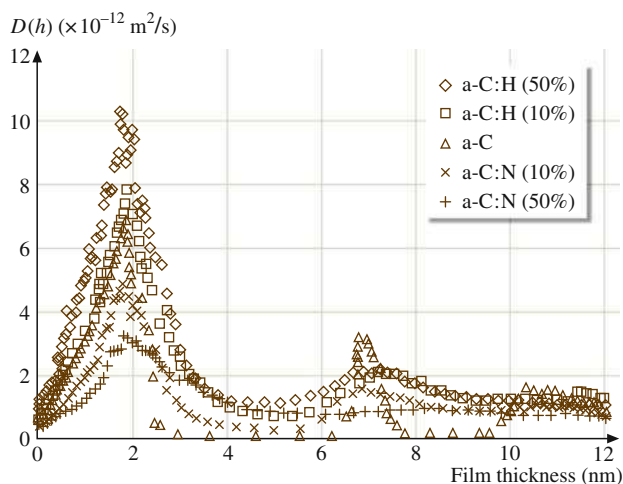


**Fig. 19.5** Diffusion coefficient  $D(h)$  as a function of lubricant film thickness for Z-DOL on different carbon films (after [32])

### 19.2.2 Nanotribological Studies

AFM techniques have been used to investigate the nanotribological performance of PFPEs. Mate [37, 38], O'Shea et al. [39, 40], Bhushan et al. [18, 41], Koinkar and Bhushan [29, 42], Bhushan and Sundararajan [43], Bhushan and Dandavate [44], Liu and Bhushan [26], and Palacio and Bhushan [45, 46] used an AFM to provide insight into how PFPE lubricants function at the molecular level. Mate [37, 38] conducted friction experiments on bonded and unbonded Z-DOL, and found that the coefficient of friction of unbonded Z-DOL is about two times larger than that of bonded Z-DOL [39, 40]. Koinkar and Bhushan [29, 42] and Liu and Bhushan [26] studied the friction and wear performance of a Si(100) sample lubricated with Z-15, Z-DOL, and Z-DOL (fully bonded) lubricants. They found that using Z-DOL (fully bonded) could significantly improve the adhesion, friction, and wear performance of Si(100). They also discussed the lubrication mechanisms on the molecular level. Bhushan and Sundararajan [43] and Bhushan and Dandavate [44] studied the effect of tip radius and relative humidity on the adhesion and friction properties of Si(100) coated with Z-DOL (fully bonded).

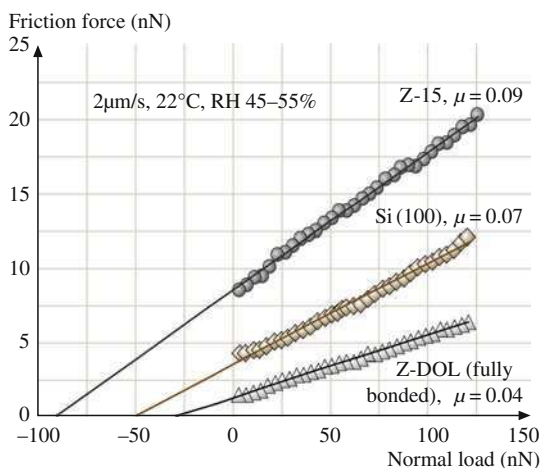
In this section, we review the adhesion, friction, and wear properties of Z-15 and Z-DOL under various operating conditions (rest time, velocity, relative humidity, temperature, and tip radius). The experiments were carried out using a commercial AFM system with pyramidal Si<sub>3</sub>N<sub>4</sub> and diamond tips. An environmentally controlled chamber and a thermal stage were used to perform relative humidity and temperature effect studies.

#### Friction and Adhesion

To investigate the friction properties of Z-15 and Z-DOL (fully bonded) films on Si (100), curves of friction force versus normal load were measured by making friction measurements at increasing normal loads [26]. Representative results for Si(100), Z-15, and Z-DOL (fully bonded) are shown in Fig. 19.6. An approximately linear response of all three samples is observed in the load range of 5–130 nN. The friction force of solid-like Z-DOL (fully bonded) is consistently smaller than that for Si(100), but the friction force of liquid-like Z-15 lubricant is higher than that for Si(100). Sundararajan and Bhushan [47] have studied the static friction force of silicon micromotors lubricated with Z-DOL by AFM. They also found that liquid-like Z-DOL lubricant significantly increased the static friction force; on the contrary a solid-like Z-DOL (fully bonded) coating can dramatically reduce the static friction force. This is in good agreement with the results of Liu and Bhushan [26]. In Fig. 19.6, the nonzero value of the friction force signal at zero external load is due to adhesive forces. It is well known that the following relationship exists between the friction force  $F$  and the external normal load  $W$  [1, 2]

$$F = \mu(W + W_a), \quad (19.1)$$

**Fig. 19.6** Friction force versus normal load curves for Si(100), 2.8 nm-thick Z-15 film, and 2.3 nm-thick Z-DOL (fully bonded) film at 2  $\mu\text{m/s}$ , and in ambient air sliding against a  $\text{Si}_3\text{N}_4$  tip. Based on these curves, coefficient of friction  $\mu$  and adhesion force of  $W_a$  can be calculated (after [26])

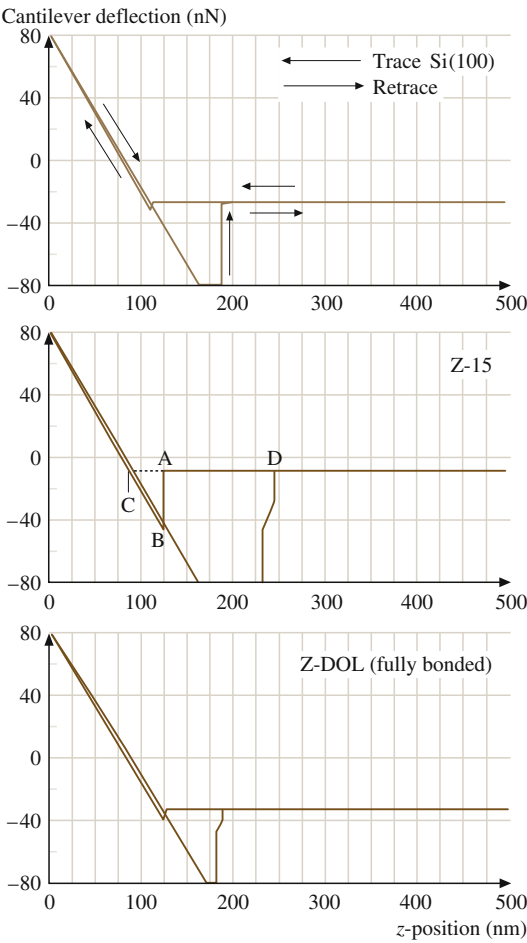


where  $\mu$  is the coefficient of friction and  $W_a$  is the adhesive force. Based on this equation and the data in Fig. 19.6, we can calculate the  $\mu$  and  $W_a$  values. The coefficients of friction for Si(100), Z-15, and Z-DOL are 0.07, 0.09, and 0.04, respectively. Based on (19.1), the adhesive force values are obtained from the horizontal intercepts of the curves of friction force versus normal load, i.e., at zero friction force. Adhesive force values of Si(100), Z-15, and Z-DOL are 52, 91, and 34 nN, respectively.

The adhesive forces of these samples were also measured by using a force calibration plot (FCP) technique to obtain force–distance curves. In this technique, the tip is brought into contact with the sample, and the maximum force needed to pull the tip and sample apart is measured as the adhesive force. Figure 19.7 shows typical FCP curves for Si(100), Z-15, and Z-DOL (fully bonded) [26]. As the tip approaches the sample within a few nanometers (point A), an attractive force exists between the tip and the sample surfaces. The tip is pulled toward the sample, and contact occurs at point B on the graph. The adsorption of water molecules and/or the presence of liquid lubricant molecules on the sample surface can also accelerate this so-called *snap-in*, due to the formation of a meniscus of water and/or liquid lubricant around the tip. From this point on, the tip is in contact with the surface, and as the piezo extends further, the cantilever is further deflected. This is represented by the slope portion of the curve. As the piezo retracts, at point C the tip goes beyond the zero-deflection (flat) line, because of the attractive forces, into the adhesive force regime. At point D, the tip snaps free of the adhesive forces and is again in free air. The adhesive force (pull-off force) is determined by multiplying the cantilever spring constant (0.58 N/m) by the horizontal distance between points C and D, which corresponds to the maximum cantilever deflection toward the samples before the tip is disengaged. Incidentally, the horizontal shift between the loading and unloading curves results from the hysteresis of the PZT tube.



**Fig. 19.7** Typical force calibration plots of Si(100), 2.8 nm-thick Z-15 film, and 2.3 nm-thick Z-DOL (fully bonded) film in ambient air. The adhesive forces can be calculated from the horizontal distance between points C and D, and the cantilever spring constant of 0.58 N/m (after [26])



The adhesive forces of Si(100), Z-15, and Z-DOL (fully bonded) measured by FCP and from plots of friction force versus normal load are summarized in Fig. 19.8 [26]. The results measured by these two methods are in good agreement. Figure 19.8 shows that the presence of a mobile Z-15 lubricant film increases the adhesive force as compared with that of Si(100). In contrast, the presence of a solid-phase Z-DOL (fully bonded) film reduces the adhesive force as compared with that of Si(100). This result is in good agreement with the results of Blackman et al. [30] and Bhushan and Ruan [48]. Sources of adhesive forces between the tip and the sample surfaces are van der Waals attraction and the long-range meniscus force [1, 2, 11, 13]. The relative magnitudes of the forces from these two sources are dependent upon various factors, including the distance between the tip and the sample surface, their surface roughness, their hydrophobicity, and the relative humidity [49]. For most surfaces with some roughness, the contribution of the meniscus force dominates at moderate to high *humidity*.

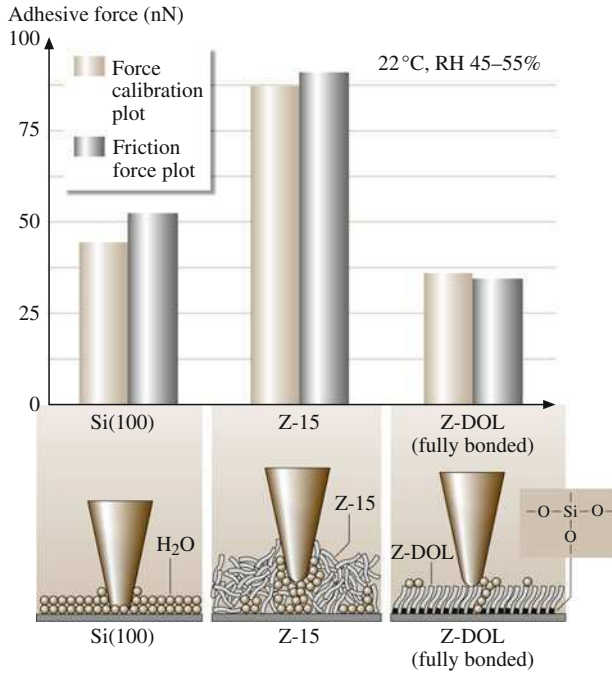


**Fig. 19.8** (a) Summary of the adhesive forces of Si(100), 2.8 nm-thick Z-15 film and 2.3 nm thick Z-DOL (fully bonded) film measured by force calibration plots and plots of friction force versus normal load in ambient air. (b) Schematic showing the effect of meniscus formed between the AFM tip and the sample surface on the adhesive and friction forces (after [26])

The schematic in Fig. 19.8b shows the relative size and source of the meniscus. The native oxide layer (SiO<sub>2</sub>) on the top of the Si(100) wafer exhibits hydrophilic properties, and some water molecules can be adsorbed onto this surface. This condensed water will form a meniscus as the tip approaches the sample surface. In the case of a sphere (such as a single-asperity AFM tip) in contact with a flat surface, the attractive Laplace force  $F_L$  caused by the capillary is

$$F_L = 2\pi R\gamma(\cos \theta_1 + \cos \theta_2), \quad (19.2)$$

where  $R$  is the radius of the sphere,  $\gamma$  is the surface tension of the liquid against air, and  $\theta_1$  and  $\theta_2$  are the contact angles between the liquid and flat or spherical surfaces, respectively [1, 2, 50]. As the surface tension value of Z-15 (24 dyn/cm) is smaller than that of water (72 dyn/cm), the larger adhesive force in Z-15 cannot only be caused by the Z-15 meniscus. The nonpolar Z-15 liquid does not have complete coverage and strong bonding with Si(100). In the ambient environment, the condensed water molecules will permeate through the liquid Z-15 lubricant film and compete with the lubricant molecules present on the substrate. The interaction of the liquid lubricant with the substrate is weakened, and a boundary layer of the

liquid lubricant forms puddles [29, 42]. This dewetting allows water molecules to be adsorbed onto the Si(100) surface as aggregates along with Z-15 molecules, and both of them can form a meniscus while the tip approaches to the surface. In addition, as the Z-15 film is fairly soft compared with the solid Si(100) surface, and penetration of the tip in the film occurs while pushing the tip down, this leads to a large area of the tip involved to form the meniscus at the tip–liquid (water aggregates along with Z-15) interface. These two factors of the liquid-like Z-15 film result in higher adhesive force. It should also be noted that Z-15 has a higher viscosity compared with water; therefore Z-15 film provides higher resistance to sliding motion and results in a larger coefficient of friction. In the case of Z-DOL (fully bonded) film, both active groups of Z-DOL molecules are strongly bonded on the Si(100) substrate through the thermal and washing treatment, thus the Z-DOL (fully bonded) film has a relatively low free surface energy and cannot be readily displaced by water molecules or readily adsorb water molecules. Thus, the use of Z-DOL (fully bonded) can reduce the adhesive force. We further believe that the bonded Z-DOL molecules can be orientated under stress (behaving as a soft polymer solid), which facilitates sliding and reduces the coefficient of friction.

These studies suggest that liquid-like lubricant films, such as Z-15, easily form menisci (by themselves and with adsorbed water molecules), and thus have higher adhesive force and higher friction force, whereas if the lubricant film exists in a solid-like phase, such as Z-DOL (fully bonded) films, they are hydrophobic with low adhesion and friction.

In order to study the uniformity of a lubricant film and its influence on friction and adhesion, friction force mapping and adhesive force mapping of PFPE have been carried out by Koinkar and Bhushan [42] and Bhushan and Dandavate [44], respectively. Figure 19.9 shows gray scale plots of surface topography and friction force images obtained simultaneously for unbonded Demnum-type PFPE lubricant film on silicon [42]. Demnum-type PFPE lubricant (Demnum, Daikin, Japan) chains have  $-\text{CF}_2-\text{CH}_2-\text{OH}$  (a reactive end group) on one end, whereas Z-DOL chains have the hydroxyl groups on both ends, as described earlier [12]. The friction force plot shows well-distinguished low- and high-friction regions, roughly corresponding to high- and low-surface-height regions in the topography image

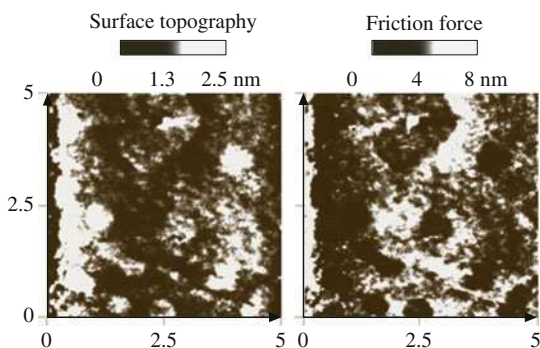


**Fig. 19.9** Gray scale plots of the surface topography and friction force obtained simultaneously for unbonded 2.3 nm-thick Demnum-type PFPE lubricant film on silicon (after [29])

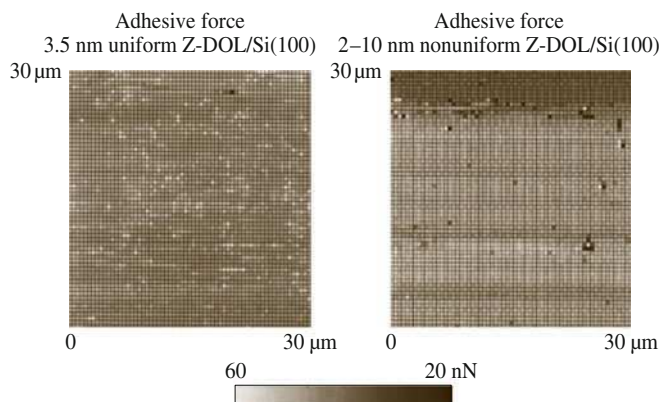


**Fig. 19.10** Gray scale plots of the adhesive force distribution of a uniformly coated, 3.5 nm-thick unbonded Z-DOL film on silicon and 3–10 nm-thick unbonded Z-DOL film on silicon that was deliberately coated nonuniformly by vibrating the sample during the coating process (after [44])

(thick and thin lubricant regions). A uniformly lubricated sample does not show such a variation in the friction. Figure 19.10 shows gray scale plots of the adhesive force distribution for silicon samples coated uniformly and nonuniformly with Z-DOL lubricant. It can be clearly seen that there exists a region which has an adhesive force distinctly different from the other region for the nonuniformly coated sample. This implies that the liquid film thickness is nonuniform, giving rise to a difference in the meniscus forces.

### Rest-Time Effect

It is well known that, in rigid computer disk drives, the stiction force between the head and the disk magnetic medium increases rapidly with increasing rest time [10, 12]. Considering that stiction and friction are major issues that lead to failure of rigid computer disk drives and MEMS, it is very important to determine if this rest-time effect also exists on the nanoscale. First, the rest-time effect on the friction force, adhesive force, and coefficient of Si(100) sliding against a  $\text{Si}_3\text{N}_4$  tip was studied (Fig. 19.11a [26]). It was found that the friction and adhesive forces increase logarithmically up to a certain equilibrium time, after which they remain constant. Figure 19.11a also shows that the rest time does not affect the coefficient of friction. These results suggest that the rest time can result in growth of the meniscus, which causes a higher adhesive force and in turn a higher friction force. However, over the whole testing range the friction mechanisms do not change with the rest time. Similar studies were also performed on Z-15 and Z-DOL (fully bonded) films. The results are summarized in Fig. 19.11b [26]. It is seen that a similar time effect was observed for Z-15 film but not for Z-DOL (fully bonded) film.

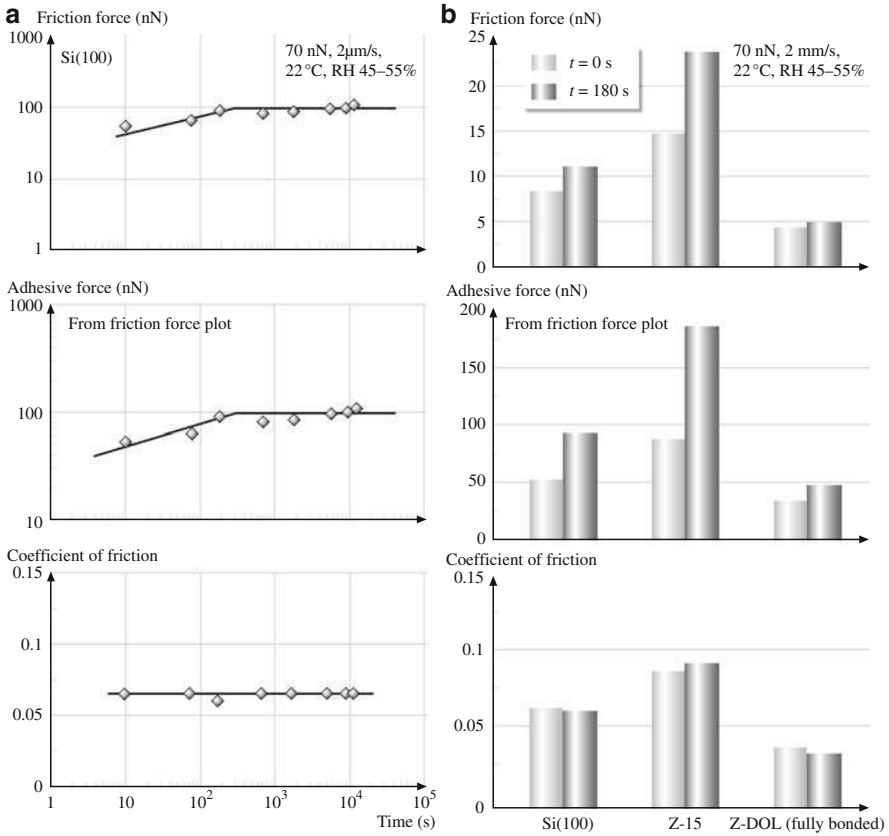
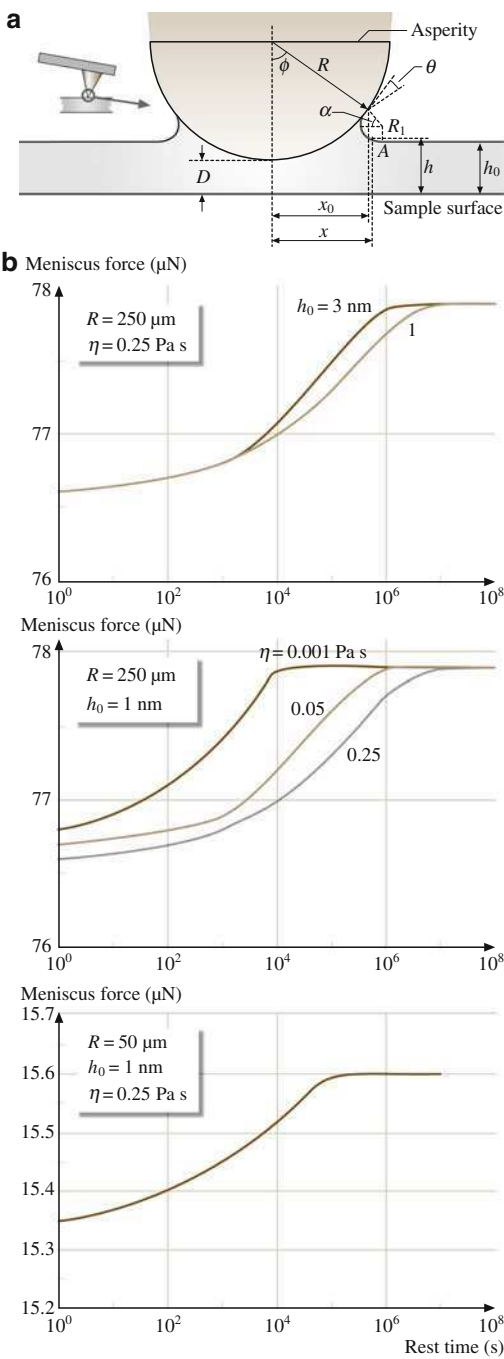


**Fig. 19.11** (a) Rest-time effect on friction force, adhesive force, and coefficient of friction of Si(100). (b) Summary of the rest-time effect on friction force, adhesive force, and coefficient of friction of Si(100), 2.8 nm-thick Z-15 film, and 2.3 nm-thick Z-DOL (fully bonded) film. All of the measurements were carried out at 70 nN, 2  $\mu\text{m/s}$ , and in ambient air (after [26])

An AFM tip in contact with a flat sample surface can be treated as a single-asperity contact. Therefore, a  $\text{Si}_3\text{N}_4$  tip in contact with Si(100) or Z - 15/Si(100) can be modeled as a sphere in contact with a flat surface covered by a layer of liquid (adsorbed water and/or liquid lubricant) (Fig. 19.12a). A meniscus forms around the contacting asperity and grows with time until equilibrium occurs [51]. The meniscus force, which is the product of the meniscus pressure and the meniscus area, depends on the flow of liquid phase toward the contact zone. The flow of the liquid towards the contact zone is governed by the capillary pressure  $P_c$ , which draws liquid into the meniscus, and the disjoining pressure  $\Pi$ , which tends to draw the liquid away from the meniscus. Based on the Young–Laplace equation, the capillary pressure  $P_c$  is

$$P_c = 2\kappa\gamma, \quad (19.3)$$

**Fig. 19.12** (a) Schematic of a single asperity in contact with a smooth flat surface in the presence of a continuous liquid film when  $\phi$  is large. (b) Results of the single-asperity model. Effect of viscosity of the liquid, radius of the asperity, and film thickness is studied with respect to the time-dependent meniscus force (after [51])



where  $2\kappa$  is the mean meniscus curvature ( $= \kappa_1 + \kappa_2$ , where  $\kappa$  and  $\kappa_2$  are the curvatures of the meniscus in the contact plane and perpendicular to the contact plane). Mate and Novotny [6] have shown that the disjoining pressure decreases rapidly with increasing liquid film thickness in a manner consistent with a strong van der Waals attraction. The disjoining pressure  $\Pi$  for these liquid films can be expressed as

$$\Pi = \frac{A}{6\pi h^3}, \quad (19.4)$$

where  $A$  is the Hamaker constant and  $h$  is the liquid film thickness. The driving forces that cause the lubricant flow that result in an increase in the meniscus force are the disjoining pressure gradient due to a gradient in film thickness and the capillary pressure gradient due to the curved liquid–air interface. The driving pressure  $P$  can then be written as

$$P = -2\kappa\gamma - \Pi. \quad (19.5)$$

Based on these three basic relationships, the following differential equation has been derived by Chilamakuri and Bhushan [51] to describe the meniscus at time  $t$

$$2\pi x_0 \left( D + \frac{x_0^2}{2R} - h_0 \right) \frac{dx_0}{dt} = \frac{2\pi h_0^3 \gamma}{3\eta} \frac{(1 + \cos \theta)}{D + a - h_0} - \frac{Ax_0}{3\eta h} \cot \alpha, \quad (19.6)$$

where  $\eta$  is the viscosity of the liquid and  $a$  is given by

$$a = R(1 - \cos \phi) \propto \frac{R\phi^2}{2} \propto \frac{x_0^2}{2R}. \quad (19.7)$$

The differential equation (19.6) was solved numerically using Newton's iteration method. The meniscus force at any time  $t$  less than the equilibrium time is proportional to the meniscus area and the meniscus pressure ( $2\kappa\gamma$ ), and is given by

$$f_m(t) = 2\pi R\gamma(1 + \cos \theta) \left[ \frac{x_0}{(x_0)_{eq}} \right]^2 \left( \frac{\kappa}{\kappa_{eq}} \right), \quad (19.8)$$

where  $(x_0)_{eq}$  is the value of  $x_0$  at the equilibrium time

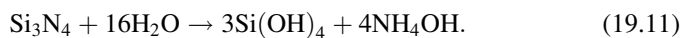
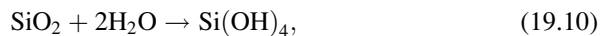
$$[(x_0)_{eq}]^2 = 2R \left[ \frac{-6\pi h_0^3(1 + \cos \theta)}{A} + (h_0 - D) \right]. \quad (19.9)$$

This modeling work (on the microscale) showed that the meniscus force initially increases logarithmically with the rest time up to a certain equilibrium time, after which it remains constant. This equilibrium time decreases with increasing liquid film thickness, decreasing viscosity, and decreasing tip radius (Fig. 19.12b). This early numerical modeling work and the data at the nanoscale in Fig. 19.11a are in good agreement.

## Velocity Effect

To investigate the effect of velocity on friction and adhesion, the friction force versus normal load relationships of Si(100), Z-15, and Z-DOL (fully bonded) at different velocities were measured (Fig. 19.13) [26]. Based on these data, the adhesive force and coefficient of friction values can be calculated by using (19.1). The variation of friction force, adhesive force, and coefficient of friction of Si(100), Z-15, and Z-DOL (fully bonded) as a function of velocity are summarized in Fig. 19.14, indicating that, for Si(100), the friction force decreases logarithmically with increasing velocity. For Z-15, the friction force decreases with increasing velocity up to 10  $\mu\text{m/s}$ , after which it remains almost constant. Velocity has very little effect on the friction force of Z-DOL (fully bonded), which reduces slightly only at very high velocity. Figure 19.14 also indicates that the adhesive force of Si(100) is increased when the velocity is  $> 10 \mu\text{m/s}$ . The adhesive force of Z-15 is reduced dramatically with a velocity increase up to 20  $\mu\text{m/s}$ , after which it is reduced slightly, and the adhesive force of Z-DOL (fully bonded) is also decreased at high velocity. In the tested velocity range, only the coefficient of friction of Si(100) decreases with velocity, whereas the coefficients of friction of Z-15 and Z-DOL (fully bonded) remain almost constant. This implies that the friction mechanisms of Z-15 and Z-DOL (fully bonded) do not change with velocity.

The mechanisms of the effect of velocity on adhesion and friction can be explained based on the schematics shown in Fig. 19.14b. For Si(100), tribochemical reaction plays a major role. Although, at high velocity, the meniscus is broken and does not have enough time to rebuild, the contact stresses and high velocity lead to tribochemical reactions of the Si(100) wafer and  $\text{Si}_3\text{N}_4$  tip, which have native oxide ( $\text{SiO}_2$ ) layers, with water molecules. The following reactions occur:



The  $\text{Si}(\text{OH})_4$  is removed and continuously replenished during sliding. The  $\text{Si}(\text{OH})_4$  layer between the tip and the Si(100) surface is known to have low shear strength and causes a decrease in the friction force and coefficient of friction in the lateral direction [52–56]. The chemical bonds of Si–OH between the tip and the Si(100) surface induce a large adhesive force in the normal direction. For Z-15 film, at high velocity, the meniscus formed by condensed water and Z-15 molecules is broken and does not have enough time to rebuild, therefore the adhesive force and consequently the friction force is reduced. For Z-DOL (fully bonded) film, the surface can adsorb few water molecules under ambient conditions, and at high velocity these molecules are displaced, which is responsible for the slight decrease in friction force and adhesive force. Even in the high velocity range, the friction mechanisms for Z-15 and Z-DOL (fully bonded) films are still shearing of the viscous liquid and molecular orientation, respectively. Thus the coefficients of friction of Z-15 and Z-DOL (fully bonded) do not change with velocity.



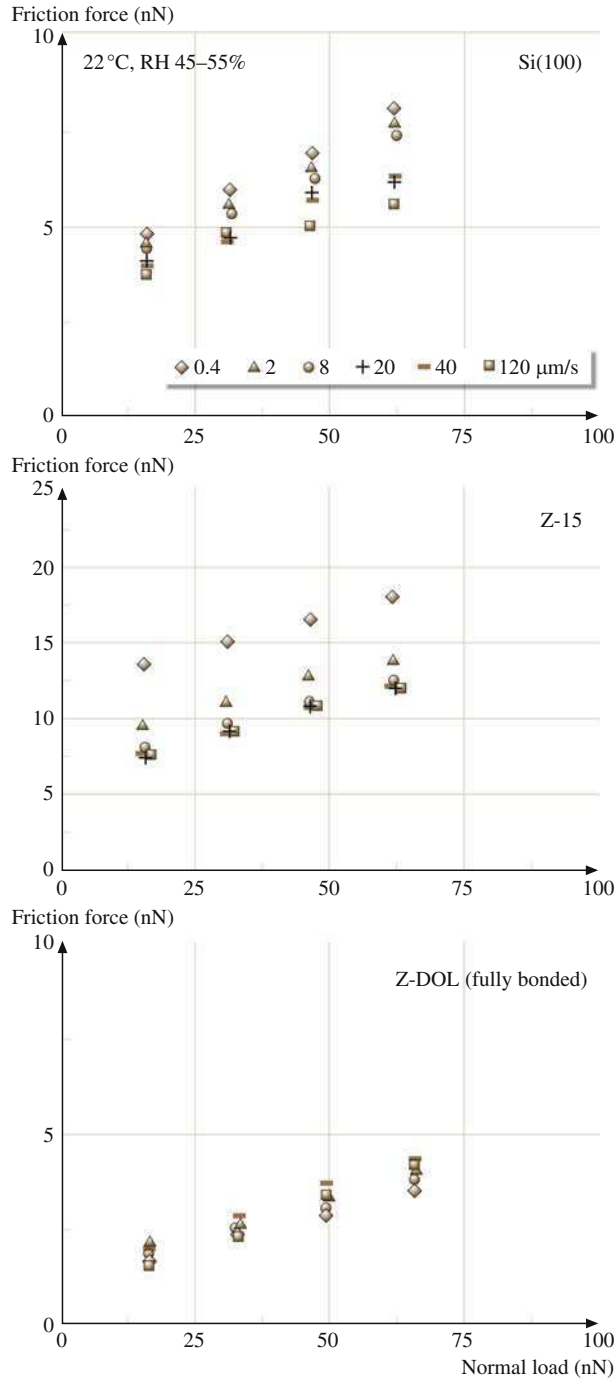


**Fig. 19.13** Friction forces versus normal load data for Si(100), 2.8 nm-thick Z-15 film and 2.3 nm-thick Z-DOL (fully bonded) film at various velocities in ambient air (after [26])

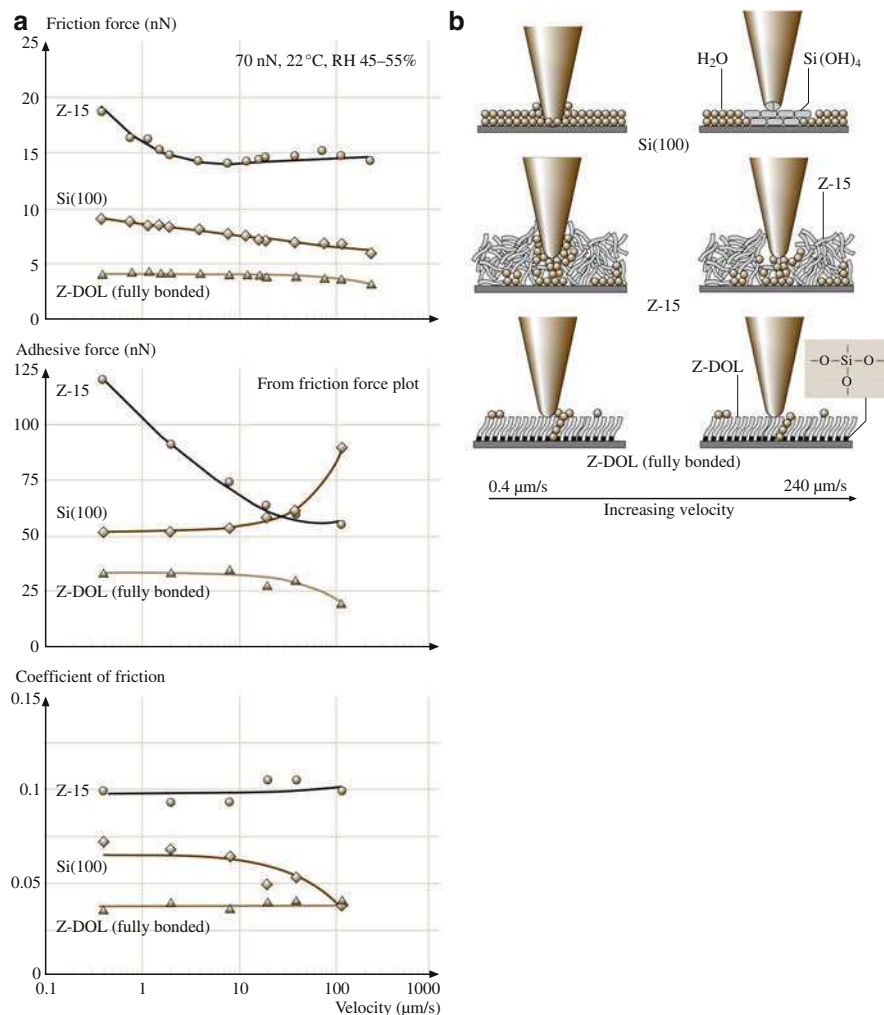


**Fig. 19.14** (a) Influence of velocity on friction force, adhesive force, and coefficient of friction of Si(100), 2.8 nm-thick Z-15 film, and 2.3 nm-thick Z-DOL (fully bonded) film at 70 nN in ambient air. (b) Schematic showing the change of surface composition (by tribochemical reaction) and change of meniscus while increasing the velocity (after [26])

Koinkar and Bhushan [29, 42] have suggested that, in the case of samples with mobile films such as condensed water and Z-15 films, alignment of liquid molecules (shear thinning) is responsible for the drop in friction force with increasing scanning velocity. This could be another reason for the decrease in friction force with velocity for Si(100) and Z-15 film in this study.

## Relative Humidity and Temperature Effect

The influence of relative humidity (RH) on friction and adhesion was studied in an environmentally controlled chamber. The friction force was measured by making measurements at increasing relative humidity; the results are presented in Fig. 19.15 [26], which shows that, for Si(100) and Z-15 film, the friction force increases with increasing relative humidity up to RH 45% and then shows a slight

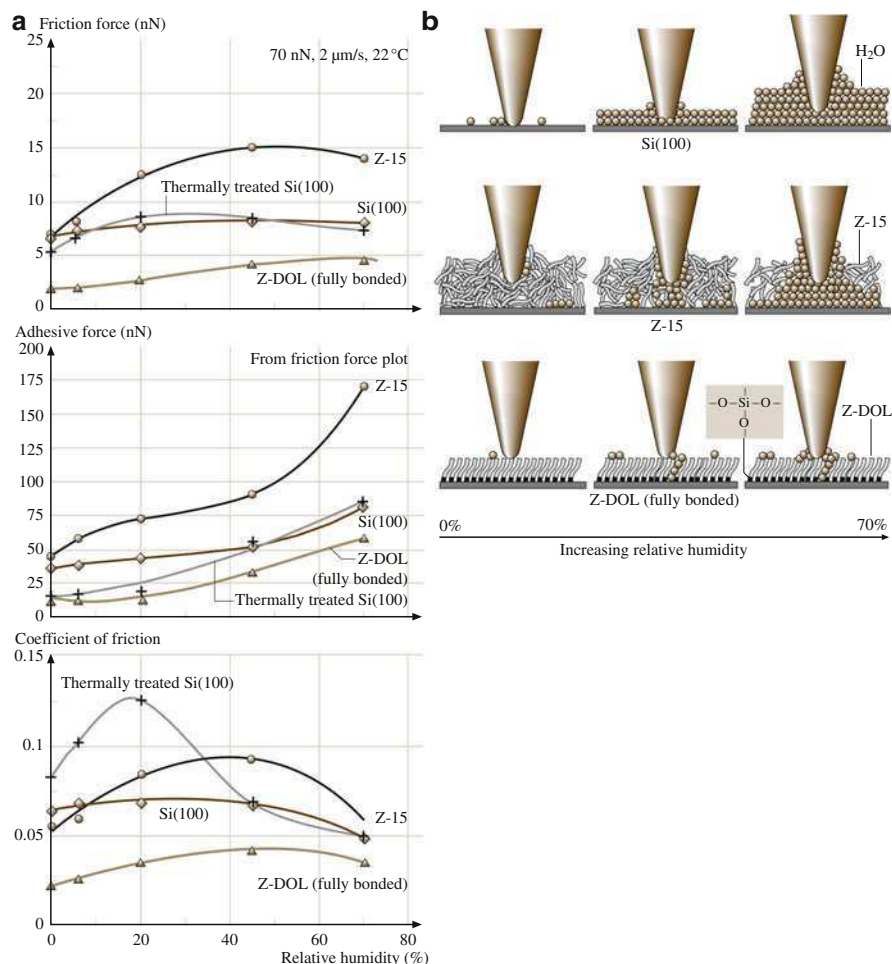


**Fig. 19.15** (a) Influence of relative humidity (RH) on the friction force, adhesive force, and coefficient of friction of Si(100), 2.8 nm-thick Z-15 film, and 2.3 nm-thick Z-DOL (fully bonded) film at 70 nN, 2  $\mu\text{m/s}$ , and in 22°C air. Schematic (b) shows the change of meniscus while increasing the relative humidity. In this figure, the thermally treated Si(100) represents the Si (100) wafer that was baked at 150°C for 1 h in an oven (in order to remove the adsorbed water) just before it was placed in the 0% RH chamber (after [26])

decrease with further increase in relative humidity. Z-DOL (fully bonded) has a smaller friction force than Si(100) and Z-15 over the whole testing range, and its friction force shows a relative apparent increase when the relative humidity is above RH 45%. For Si(100), Z-15, and Z-DOL (fully bonded), the adhesive forces increase with relative humidity, and their coefficients of friction increase with relative humidity up to RH 45%, after which they decrease with further increase of relative humidity. It is also observed that the effect of humidity on Si(100) really depends on the history of the Si(100) sample. As the surface of Si(100) wafer readily adsorbs water from the air, without any pretreatment the Si(100) used in our study almost reaches its saturated stage of adsorbing water, which is responsible for the smaller effect with increasing relative humidity. However, if the Si(100) wafer was thermally treated by baking at 150°C for 1 h, a larger effect was observed.

The schematic in Fig. 19.15b shows that Si(100), because of its high free surface energy, can adsorb more water molecules with increasing relative humidity. As discussed earlier, for Z-15 film in a humid environment, the condensed water from the humid environment competes with the lubricant film present on the sample surface. Obviously, more water molecules also can be adsorbed on Z-15 surface with increasing relative humidity. The increase in adsorbed water molecules in the case of Si(100), along with lubricant molecules in the case of Z-15 film, results in a larger water meniscus, which leads to an increase of friction force, adhesive force, and coefficient of friction of Si(100) and Z-15 with humidity. However, at a very high humidity (RH 70%), large quantities of adsorbed water can form a continuous water layer that separates the tip and sample surface and acts as a kind of lubricant, which causes a decrease in the friction force and coefficient of friction. For Z-DOL (fully bonded) film, because of its hydrophobic surface properties, water molecules can be adsorbed and cause an increase in the adhesive force and friction force only at high humidity ( $\text{RH} \geq 45\%$ ).

The effect of temperature on friction and adhesion was studied using a thermal stage attached to the AFM. The friction force was measured by making measurements at increasing temperature from 22°C to 125°C. The results are presented in Fig. 19.16 [26], which shows that the increasing temperature causes a decrease of friction force, adhesive force, and coefficient of friction of Si(100), Z-15, and Z-DOL (fully bonded). The schematic in Fig. 19.16b indicates that, at high temperature, desorption of water leads to a decrease of friction force, adhesive force, and coefficient of friction for all of the samples. Besides that, the reduction of the surface tension of water also contributes to the decrease of friction and adhesion. For Z-15 film, the reduction of viscosity at high temperature makes an additional contribution to the decrease of friction. In the case of Z-DOL (fully bonded) film, molecules are more easily oriented at high temperature, which may also be responsible for the low friction.

Using a surface force apparatus, Yoshizawa and Israelachvili [57] and Yoshizawa et al. [58] have shown that a change in the velocity or temperature induces phase transformation (from crystalline solid-like, to amorphous, then to liquid-like) in surfactant monolayers, which is responsible for the observed changes in the friction force. Stick-slip is observed in the low-velocity regime of a few  $\mu\text{m/s}$ , and adhesion and friction first increase, followed by a decrease in the temperature range 0–50°C.

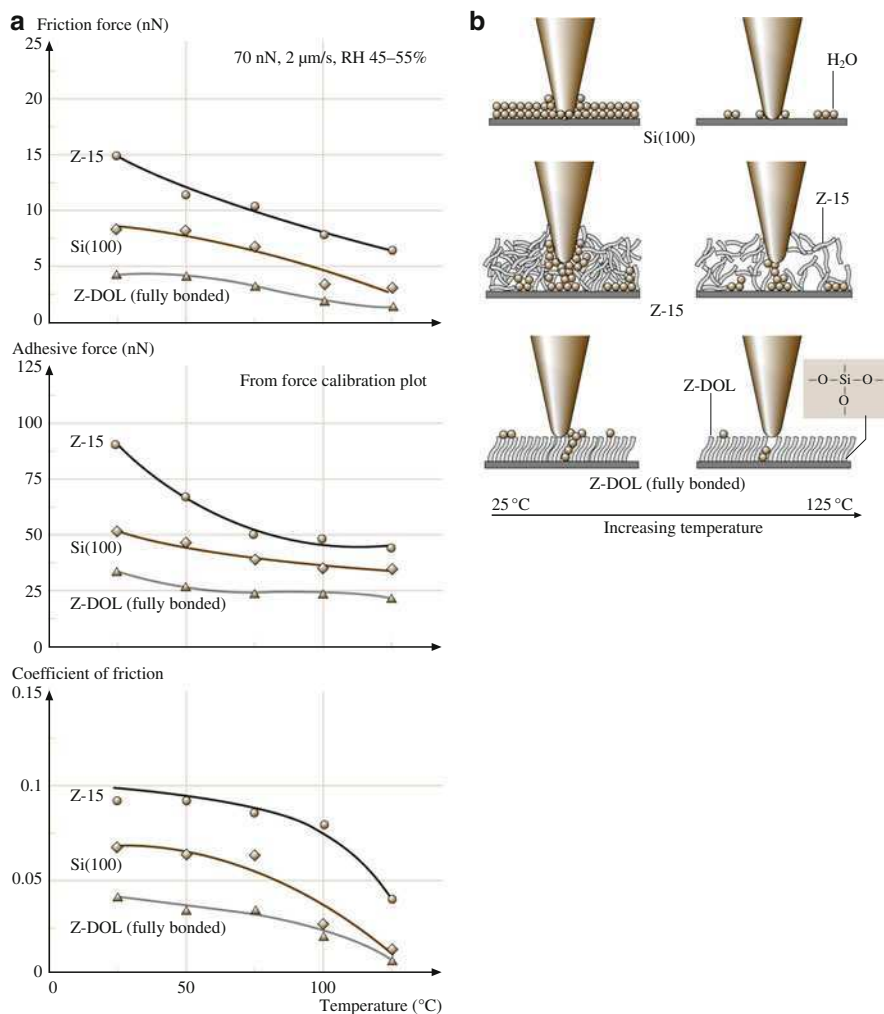
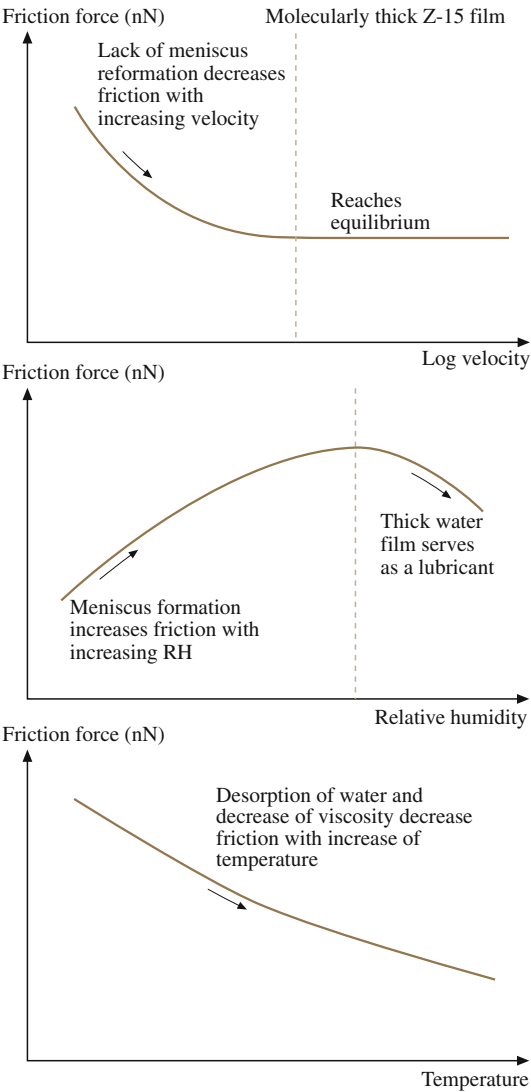


**Fig. 19.16** (a) Influence of temperature on the friction force, adhesive force, and coefficient of friction of Si(100), 2.8 nm-thick Z-15 film, and 2.3 nm-thick Z-DOL (fully bonded) film at 70 nN, at 2  $\mu\text{m/s}$ , and in RH 40–50% air. (b) Schematic showing that, at high temperature, desorption of water decreases the adhesive forces, and the reduced viscosity of Z-15 leads to the decrease of coefficient of friction. High temperature facilitates orientation of molecules in Z-DOL (fully bonded) film, which results in lower coefficient of friction (after [26])

Stick–slip at low velocity, and adhesion and friction curves peaking at some particular temperature (observed in their study), have not been observed in the AFM study. This suggests that the phase transformation may not happen in this study. This is because PFPEs generally have very good thermal stability [3, 10].

As a brief summary, the influence of velocity, relative humidity, and temperature on the friction force of Z-15 film is presented in Fig. 19.17. The changing trends are also addressed in this figure.

**Fig. 19.17** Schematic showing the change of friction force of molecularly thick Z-15 films with log velocity, relative humidity, and temperature (after [26])



**Tip-Radius Effect**

The tip radius and relative humidity affect adhesion and friction for unlubricated and lubricated surfaces [43, 44]. Figure 19.18a shows the variation of single-point adhesive force measurements as a function of tip radius on a Si(100) sample for several humidities. The adhesive force data are also plotted as a function of relative humidity for various tip radii. Figure 19.18a indicates that the tip radius has little effect on the adhesive forces at low humidity, but the adhesive force

increases with tip radius at high humidity. The adhesive force also increases with increasing humidity for all tips. The trend in adhesive forces as a function of tip radii and relative humidity (Fig. 19.18a) can be explained by the presence of meniscus forces, which arise from the capillary condensation of water vapor from the environment. If enough liquid is present to form a meniscus bridge, the

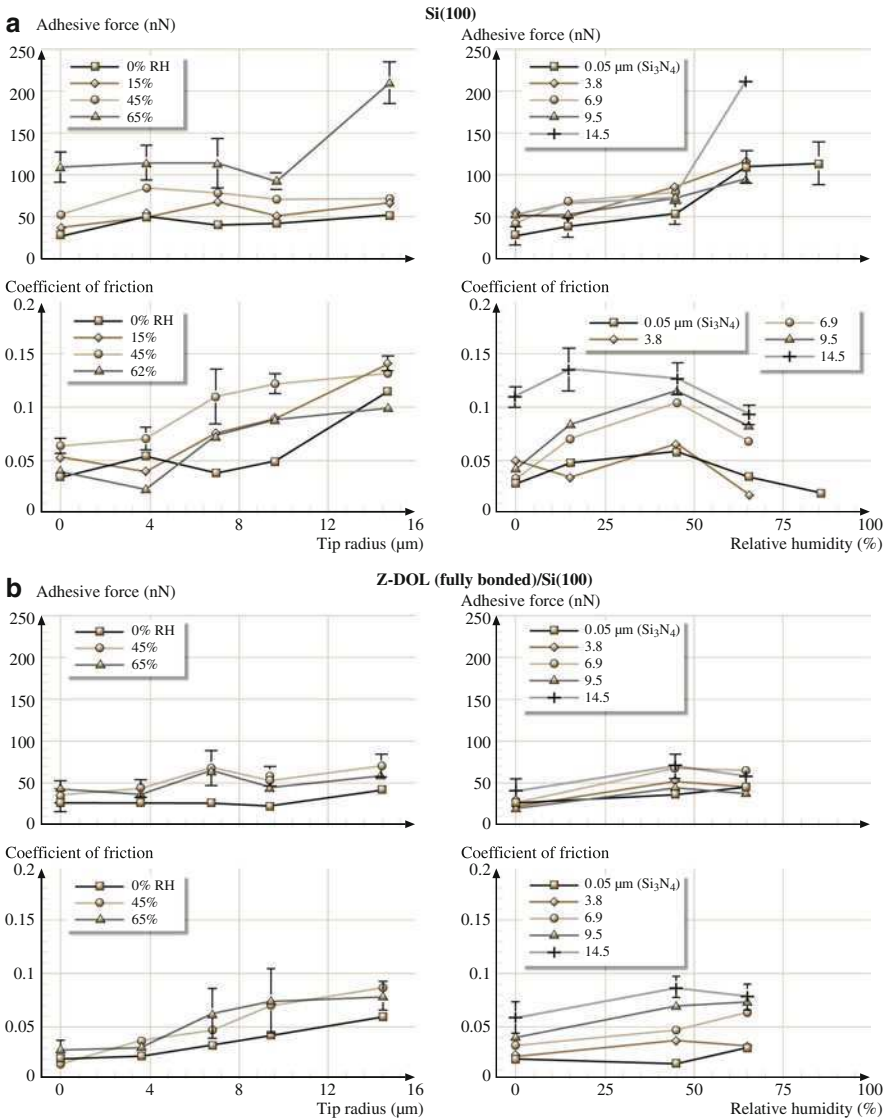


**Fig. 19.18** Adhesive force and coefficient of friction as a function of tip radius at several humidities and as a function of relative humidity at several tip radii on (a) Si(100) and (b) 0.5 nm Z-DOL (fully bonded) films (after [43])

meniscus force should increase with increasing tip radius based on (19.2). This observation suggests that the thickness of the liquid film at low humidity is insufficient to form continuous meniscus bridges to affect adhesive forces in the case of all tips.

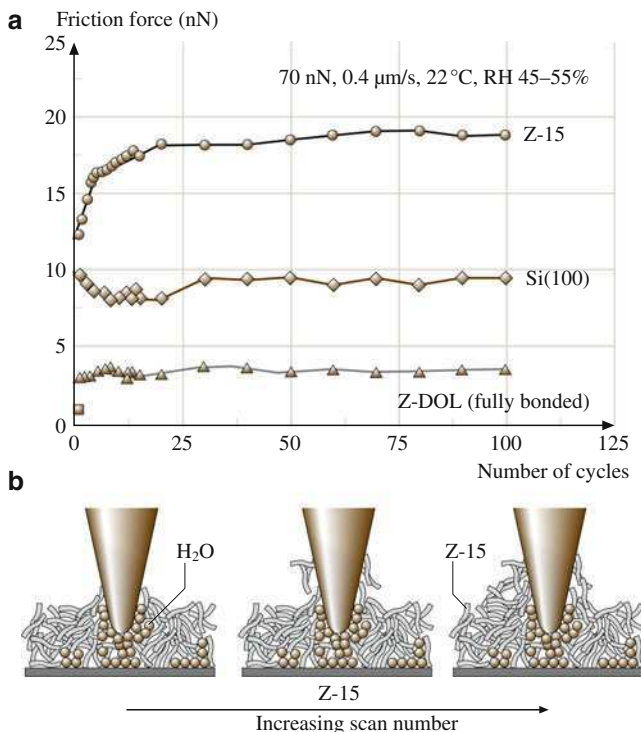
Figure 19.18a also shows the variation of the coefficient of friction as a function of tip radius at a given humidity and as a function of relative humidity for a given tip radius on the Si(100) sample. It can be observed that, for RH 0%, the coefficient of friction is about the same for all the investigated tip radii except the largest one, which shows a higher value. At all other humidities, the trend consistently shows that the coefficient of friction increases with tip radius. An increase in friction with tip radius at low to moderate humidity arises from increased contact area (i.e., higher van der Waals forces) and higher values of shear forces required for the larger contact area. At high humidity, similar to the adhesive force data, an increase with tip radius occurs because of both contact area and meniscus effects. It can be seen that, for all tips, the coefficient of friction increases with humidity up to about RH 45%, beyond which it starts to decrease. This is attributed to the fact that, at higher humidity, the adsorbed water film on the surface acts as a lubricant between the two surfaces [26]. Thus the interface is changed at higher humidity, resulting in lower shear strength and hence lower friction force and coefficient of friction.

Figure 19.18b shows adhesive forces as a function of tip radius and relative humidity on Si(100) coated with a 0.5 nm-thick Z-DOL (fully bonded) film. Adhesive forces for all the tips with the Z-DOL (fully bonded) lubricated sample are much lower than those measured for unlubricated Si(100) (Fig. 19.18a). The data also show that, even at a monolayer thickness of the lubricant, there is very little variation in adhesive forces with tip radius at a given humidity. For a given tip radius, the variation in adhesive forces with relative humidity indicates that these forces increase slightly from RH 0% to RH 45%, but remain more or less the same with further increase in humidity. This is seen even with the largest tip, which indicates that the lubricant is indeed hydrophobic; there is some meniscus formation at humidity above RH 0%, but it is minimal and does not increase appreciably even up to RH 65%. Figure 19.18b also shows the coefficient of friction for various tips at different humidities for the Z-DOL (fully bonded) lubricated sample. Again, all the values obtained with the lubricated sample are much lower than those obtained on unlubricated Si(100) (Fig. 19.18a). The coefficient of friction increases with tip radius for all tested humidities, as was seen on unlubricated Si(100), due to an increase in the contact area. Similar to the adhesive forces, there is an increase in friction from RH 0% to RH 45% due to a contribution from an increased number of menisci bridges. However, there is very little additional water film forming due to the hydrophobicity of the Z-DOL (fully bonded) layer thereafter, and consequentially the coefficient of friction does not change appreciably, even with the largest tip. These findings show that even a monolayer of Z-DOL (fully bonded) offers good hydrophobic performance of the surface.



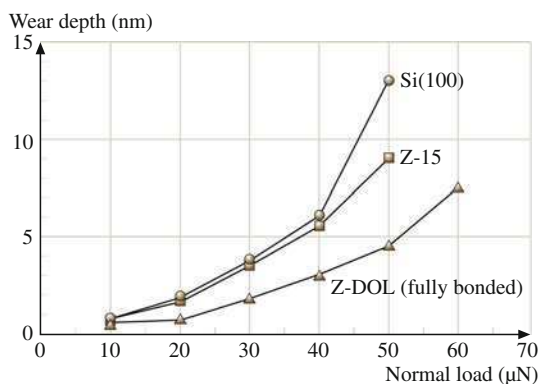
## Wear

To study the durability of lubricant films at the nanoscale, the friction of Si(100), Z-15, and Z-DOL (fully bonded) as a function of number of scanning cycles was measured (Fig. 19.19) [26]. As observed earlier, the friction force of Z-15 is higher than that of Si(100), and Z-DOL (fully bonded) has the lowest value. During cycling, the friction force of Si(100) shows a slight variation during the initial few cycles then remains constant. This is related to the removal of the top adsorbed layer. In the case of Z-15 film, the friction force shows an increase during the initial few cycles and then approaches higher and stable values. This is believed to be caused by the attachment of Z-15 molecules to the tip. The molecular interaction between these molecules attached to the tip and molecules of the film surface is responsible for the increase in friction. However, after several scans, this molecular interaction reaches equilibrium, and thereafter the friction force and coefficient of friction remain constant. In the case of Z-DOL (fully bonded) film, the friction force



**Fig. 19.19** (a) Friction force versus number of sliding cycles for Si(100), 2.8 nm-thick Z-15 film, and 2.3 nm-thick Z-DOL (fully bonded) film at 70 nN, 0.8  $\mu\text{m/s}$ , and in ambient air. (b) Schematic showing that some liquid Z-15 molecules can be attached onto the tip. The molecular interaction between the molecules attached to the tip and the Z-15 molecules in the film results in an increase of the friction force with multiple scans (after [26])

**Fig. 19.20** Wear depth as a function of normal load using a diamond tip for Si(100), 2.9 nm-thick Z-15 film, and 2.3 nm-thick Z-DOL (fully bonded) after one cycle (after [29])



starts out low and remains low during the entire test for 100 cycles. This suggests that Z-DOL (fully bonded) molecules do not become attached or displaced as readily as those of Z-15.

Koinkar and Bhushan [29, 42] conducted wear studies using a diamond tip at high loads. Figure 19.20 shows plots of wear depth as a function of normal force, and Fig. 19.21 shows wear profiles of the worn samples at 40 μN normal load. The 2.3 nm-thick Z-DOL (fully bonded) lubricated sample exhibits better wear resistance than the unlubricated and 2.9 nm-thick Z-15 lubricated silicon samples. The wear resistance of the Z-15 lubricated sample is little better than that of the unlubricated sample. The Z-15 lubricated sample shows debris inside the wear track. Since Z-15 is a liquid lubricant, the debris generated is held by the lubricant, which becomes sticky and moves inside the wear track, causing damage (Fig. 19.20). These results suggest that Z-DOL (fully bonded) exhibits better wear resistance of the substrate as compared with Z-15.

To study the effect of the degree of chemical bonding, durability tests were conducted on both fully bonded and partially bonded Z-DOL films. Durability results for Z-DOL (fully bonded) and Z-DOL bonded and unwashed (partially bonded) (a partially bonded film that contains both bonded and mobile-phase lubricants) with different film thicknesses are shown in Fig. 19.22 [42]. Thicker films, such as Z-DOL (partially bonded) with a thickness of 4.0 nm (bonded/mobile = 2.3 nm/1.7 nm), exhibit behavior similar to that of 2.3 nm-thick Z-DOL (fully bonded) film. Figure 19.22 also indicates that Z-DOL (fully bonded) and Z-DOL (partially bonded) films with thinner film thickness exhibit higher friction values. Comparing 1.0 nm-thick Z-DOL (fully bonded) with 3.0 nm-thick (bonded/mobile = 1.0 nm/2.0 nm) Z-DOL (partially bonded), the Z-DOL (partially bonded) film exhibits lower and stable friction values. This is because the mobile phase on the surface acts as a source of lubricant replenishment. Similar conclusions have also been reported by Ruhe et al. [28], Bhushan and Zhao [14], and Eapen et al. [59]. All of them indicate that using partially bonded Z-DOL films can dramatically reduce friction and improve wear life.

**Fig. 19.21** Wear profiles for Si(100), 2.9 nm-thick Z-15 film, and 2.3 nm-thick Z-DOL (fully bonded) film after wear studies using a diamond tip. Normal force used and wear depths are listed in the figure (after [29])

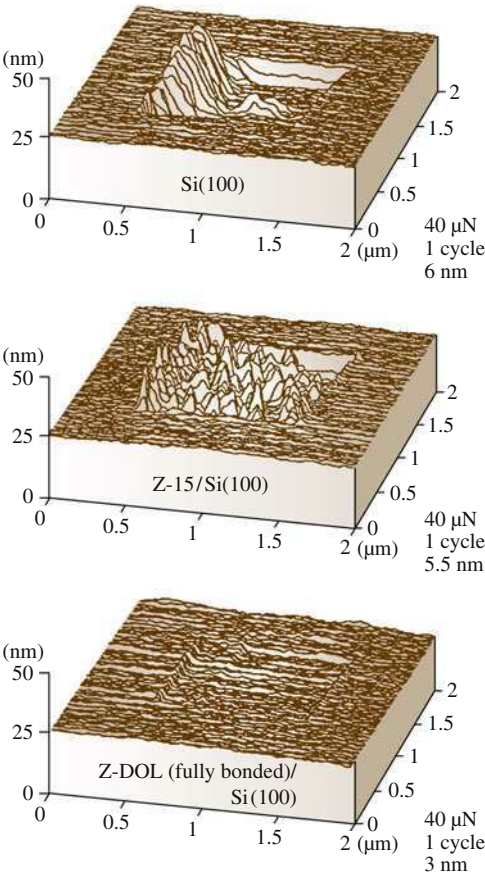
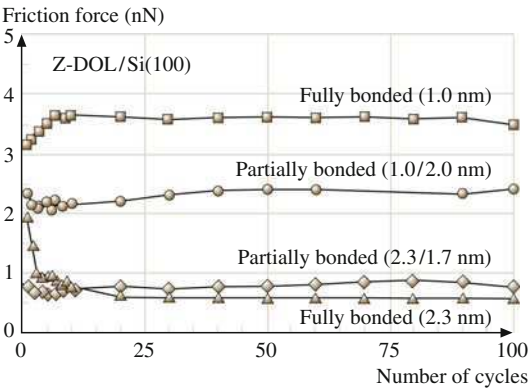


**Fig. 19.22** Friction force as a function of number of cycles using a Si<sub>3</sub>N<sub>4</sub> tip at a normal load of 300 nN for Z-DOL (fully bonded) and Z-DOL (partially bonded) films with different film thicknesses (after [42])



### 19.3 Nanotribological, Electrical, and Chemical Degradations Studies and Environmental Effects in Novel PFPE Lubricant Films

Electrical properties of lubricant films are of interest in various MEMS/NEMS applications. Changes in the surface potential and electrical resistance can be measured during sliding using an AFM [20, 21, 25, 45, 46, 60, 61]. These techniques are also useful for wear detection and for studying the initiation of wear [19, 60]. Palacio and Bhushan [45, 46, 61] carried out nanotribological studies on various novel PFPE lubricant films and monitored the electrical properties as well. Chemical degradation studies and environmental effects on various PFPE lubricant films on a Si(100) wafer and magnetic tapes coated with amorphous (diamond-like) carbon were carried out in a macroscale configuration by Tao and Bhushan [62], Bhushan and Tao [63], and Bhushan et al. [64].

Structure and properties of several novel PFPE lubricants commonly used in the lubrication of magnetic rigid disks – Z-TETRAOL 2000 and A20H-2000 – are presented in Table 19.2 [62]. Z-DOL 2000 is also included for comparison. Z-TETRAOL (Solvay Solexis Inc.) is a derivate of PFPE. The backbone of Z-TETRAOL is the same as that of the conventional PFPE lubricant Z-DOL (Solvay Solexis Inc.) described earlier. The difference between Z-TETRAOL and Z-DOL is that Z-TETRAOL has two hydroxyl groups at each end while Z-DOL has one hydroxyl group at each end. It is believed that the two hydroxyl bonds will lead to stronger interaction with the substrate. However, the Z-TETRAOL lubricant film is less mobile because of its higher viscosity, which may lead to lower durability. A20H (Moresco, Japan) is a PFPE lubricant with a cyclotriphosphazene group at one end and a hydroxyl group at the other end. The backbone of A20H is also the same as that of Z-DOL. Phosphazene lubricants (such as X1-P) have been used as additives in the data-storage industry because they exhibit better durability in high-humidity environments [12, 14]. It is believed that X1-P coats the mating surface and makes it hydrophobic,

**Table 19.2** Chemical structures and selected properties of several PFPE lubricants (data obtained from manufacturers' data sheet)

Lubricant	End group (X <sup>a</sup> )	Molecular weight (amu)	Density ( $\times 10^3$ kg/m <sup>3</sup> at 20 °C)	Kinematic viscosity (mm <sup>2</sup> /s)	Surface tension (mJ/m <sup>2</sup> )	Vapor pressure (Torr)	
						20 °C	100 °C
Z-DOL 2000 <sup>b</sup>	–CF <sub>2</sub> –CH <sub>2</sub> –OH	2000	1.81	85	24	$2 \times 10^{-5}$	$6 \times 10^{-4}$
Z-TETRAOL 2000 <sup>b</sup>	–CF <sub>2</sub> –CH <sub>2</sub> –O–CH <sub>2</sub> –CH(OH)–CH <sub>2</sub> –OH	2300	1.75	2000	–	$5 \times 10^{-7}$	$2 \times 10^{-4}$
A20H-2000 <sup>c</sup>	–CH <sub>2</sub> –OH and –CH <sub>2</sub> –N <sub>3</sub> P <sub>3</sub> (OC <sub>6</sub> H <sub>4</sub> –CF <sub>3</sub> ) <sub>3</sub>	3000	1.7	65	22	–	–

<sup>a</sup>The whole molecular chain: X–CF<sub>2</sub>–O–(CF<sub>2</sub>–CF<sub>2</sub>–O)<sub>m</sub>–(CF<sub>2</sub>–O)<sub>n</sub>–CF<sub>2</sub>–X ( $m/n = 2/3$ )

<sup>b</sup>Solvay Solexis, Inc., Thorofare

<sup>c</sup>Moresco Matsumura Oil Research Corp., Kobe-city, Hyogo, Japan

minimizing stiction and improving durability. Studies have shown that A20H exhibits less thinning or reduced mobility during drive rotation [62]. The durability of these less mobile lubricants could be less than that of the highly mobile Z-DOL + X1 - P systems. A mixture of Z-DOL and A20H is known to provide longer durability and good performance at high humidity.

The lubricants were applied on single-crystal Si(100) with a native oxide layer on the surface using the dip-coating technique by Tao and Bhushan [62] and Palacio and Bhushan [45]. The wafer was ultrasonicated in acetone followed by methanol for 10 min each. This was then followed by soaking in the solvent HFE 7100 (3M, St. Paul, MN), which consists of isomers of methoxynonafluorobutane ( $C_4F_9OCH_3$ ). The cleaned wafer was submerged vertically into a beaker containing a dilute solution of the lubricant in HFE 7100 for 10 min and then pulled out. The lubricated sample used without post thermal treatment is referred to as untreated. Partially bonded samples were prepared by heating at 150°C for 30 min after dip-coating, while the fully bonded samples were heated at 150°C for 30 min and washed in HFE 7100 solvent to remove the mobile fraction. The lubricant-coated silicon samples were then measured with an ellipsometer; the coating thickness was found to be  $\approx 1$ , 3, and 7 nm for the fully bonded, partially bonded, and untreated samples, respectively. A schematic of the bonding of the Z-DOL, Z-TETRAOL, and A20H end groups to the silicon substrate is shown in Fig. 19.23.

### 19.3.1 Nanotribological Studies

Adhesive force and coefficient of friction measurements were made using an AFM; the results are presented in Fig. 19.24 [45]. The lubricant-coated samples have reduce adhesion compared with the uncoated silicon. The adhesive forces measured on the partially bonded lubricant films are higher than the data from their fully bonded counterparts. As discussed earlier, the mobile fraction on the surface of the partially bonded sample facilitates the formation of a meniscus, which increases the tip-surface adhesion. All of the lubricant-coated samples exhibit a reduction in the coefficient of friction relative to the uncoated silicon. The partially bonded samples have a lower coefficient of friction compared with the fully bonded samples, implying that the mobile lubricant molecules in the former facilitate sliding of the tip on the surface. This will be analyzed in more detail in the following subsection in the context of wear, which was monitored using surface potential and resistance measurements.

Palacio and Bhushan [46] studied the effect of relative humidity and temperature on the friction and adhesion of novel PFPE films deposited on magnetic tapes coated with amorphous (diamond-like) carbon. The trends were similar to that reported earlier in Sect. 19.2.2.

**Fig. 19.23** Schematics of Z-DOL, Z-TETRAOL, and A20H molecules bonded onto Si substrate

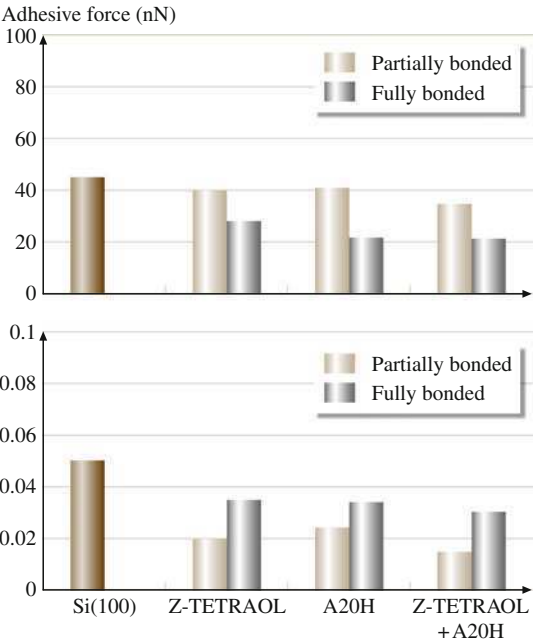
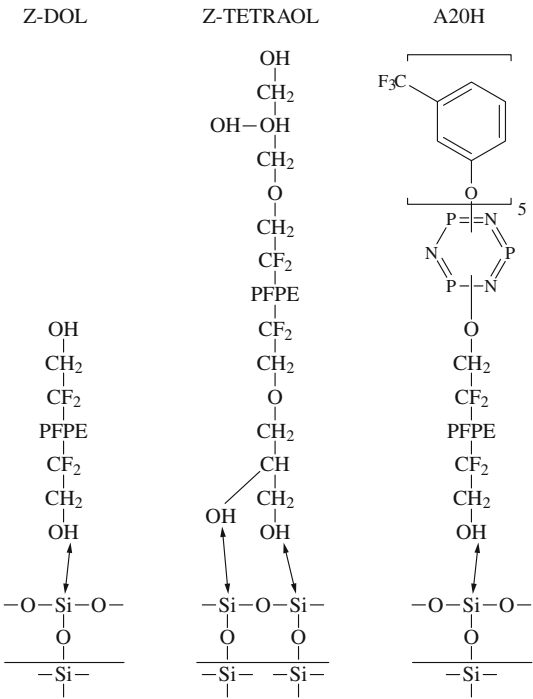


**Fig. 19.24** Summary of the adhesive force and coefficient of friction of Si(100), Z-TETRAOL, A20H, and Z-TETRAOL + A20H films at room temperature (22°C) and ambient air (45–55% RH) (after [45])

### 19.3.2 Wear Detection by Surface Potential Measurements

Wear experiments were performed on the lubricated surfaces using a diamond tip over a  $5 \times 5 \mu\text{m}^2$  region at a load of  $10 \mu\text{N}$  for 20 cycles. Figure 19.25a shows surface height and surface potential images for the fully and partially bonded lubricants [45]. The corresponding images for the uncoated silicon substrate are shown for comparison. It can be seen from these images that debris is generated around the wear region for all coatings tested. More wear debris is observed for the fully bonded samples than for the partially bonded samples. Samples with the fully bonded lubricant have limited wear protection compared with those with partially bonded lubricants because the former has only immobile molecules, while the latter has both immobile and mobile molecules. The mobile fraction of the lubricant can replenish the surface, i.e., it can move to the worn area and protect it after the immobile lubricant molecules have been displaced from the surface after repeated rubbing. Since the partially bonded films are thicker than the fully bonded films, additional wear protection is attributed to a thickness effect.

Figure 19.25b presents a bar chart showing surface potential changes for various samples. The surface potential of the area subjected to the wear test increased, an effect which is more prominent in the fully bonded samples. The partially bonded samples exhibited a smaller change in surface potential, indicating less wear. These findings should be correlated to the result of the wear test on the uncoated silicon sample, where the increase in surface potential is well understood. The Kelvin probe method measures the surface potential difference between the tip and sample, which pertains to differences in the work functions between these two materials. For conducting and semiconducting materials, the mechanism is as follows. The surface potential is altered during physical wear because the Fermi energy level is altered. This is the energy required to remove an electron to a point just outside the material surface. Thermodynamic equilibrium is disrupted with a change in the Fermi level, and can only be restored by the flow of electrons either into or from the area subjected to wear. This mechanism does not apply to materials such as  $\text{SiO}_2$  (naturally present as a thin layer) and the lubricants, which are both insulators. Physical wear on these materials would not cause a change in the surface potential because charge dissipation is poor. Therefore, a considerable surface potential change would be observed only when:

1. The lubricant has been fully removed from the substrate
2. The native  $\text{SiO}_2$  layer has been abraded from the surface
3. Wear has caused subsurface structural changes

However, for insulators such as the lubricant, electrostatic charges are introduced as it comes into contact with a material with a dissimilar electron affinity (the diamond tip) during the wear test. The charges on the insulating lubricant surface have low mobility and would eventually dissipate into the ambient environment. In the presence of debris, the electrostatic charges become localized and may get trapped (as debris particles are mostly isolated), causing an increase in the surface potential of the debris that formed around the worn area.

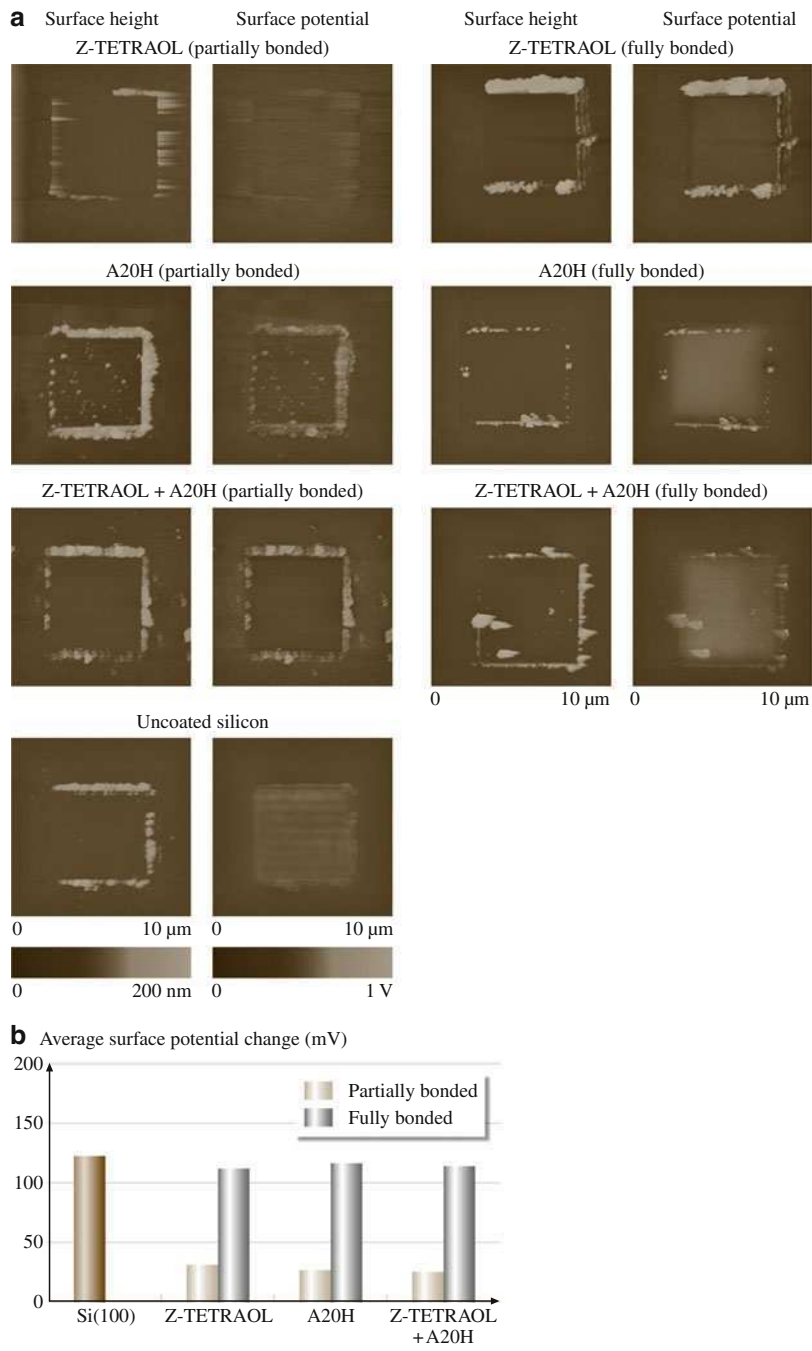


**Fig. 19.25** (a) Surface height and surface potential maps of the coatings under investigation after wear testing. Brighter areas correspond to higher values of both the height and surface potential change. (b) Bar chart showing surface potential change (after [45])



### ***19.3.3 Wear Detection by Electrical Resistance Measurements of Z-TETRAOL and the Effect of Cycling***

For electrical resistance measurements, lubricant films were applied on evaporated Au film deposited on a Si substrate. The silicon wafer used in the experiments is lightly doped, and it was coated with Au so that a metal–metal contact would be attained once the lubricant was removed. PFPE is insulating. Figure 19.26 presents surface height and resistance images for a fully bonded Z-TETRAOL coating on Au by using a scanning spreading resistance microscopy (SSRM) attachment in an AFM. For comparison, another set of tests was conducted on the same sample and the postwear surface potential images were obtained and are shown in the same figure. The Au surface is expected to have a low resistance (corresponding to darker areas in the resistance map), while the lubricant should have high resistance (lighter areas) as it is an insulator. The surface height images show a small amount of wear after one and five cycles. In both cases, the resistance images are featureless, which implies that the lubricant is still present, and the Au is not yet exposed. A surface potential increase is observed, which is attributed to electrostatic charge buildup, but this does not imply full lubricant removal since the resistance of the test area remains unchanged up to this point. After 20 cycles, the contact resistance in the tested area suddenly decreases, which indicates exposure of the underlying Au. The wear debris has the same resistance as the unworn lubricant, indicating that the current flow is influenced by the inherent difference in conductivity between the probe tip and the material it is in contact with.

During the scan of the area subjected to the wear test, the current measured by the SSRM sensor corresponds to the contact resistance between the metal-coated tip and the sample. The spreading resistance of the electric current flowing within the semiconductor sample is not measured because this is only present when there is direct contact between the metal-coated tip and a highly doped semiconductor sample.

Because the lubricant is very soft, some signal instability could occur. This comes about from possible tip contamination by the lubricant as well as plowing of wear debris during the scan. Since this AFM-based resistance measurement is a contact technique, contamination and plowing are more likely to occur compared with the surface potential measurement, which is a tapping technique. However, this technique is of interest because it provides information complementary to the Kelvin probe method in measuring the extent of wear of conducting films and lubricants, which are materials that can potentially be used in MEMS/NEMS devices.

### ***19.3.4 Chemical Degradation and Environmental Studies***

Tao and Bhushan [62] carried out chemical degradation studies in a high-vacuum tribotest apparatus [41, 65]. In this apparatus, a lubricated wafer mounted on a

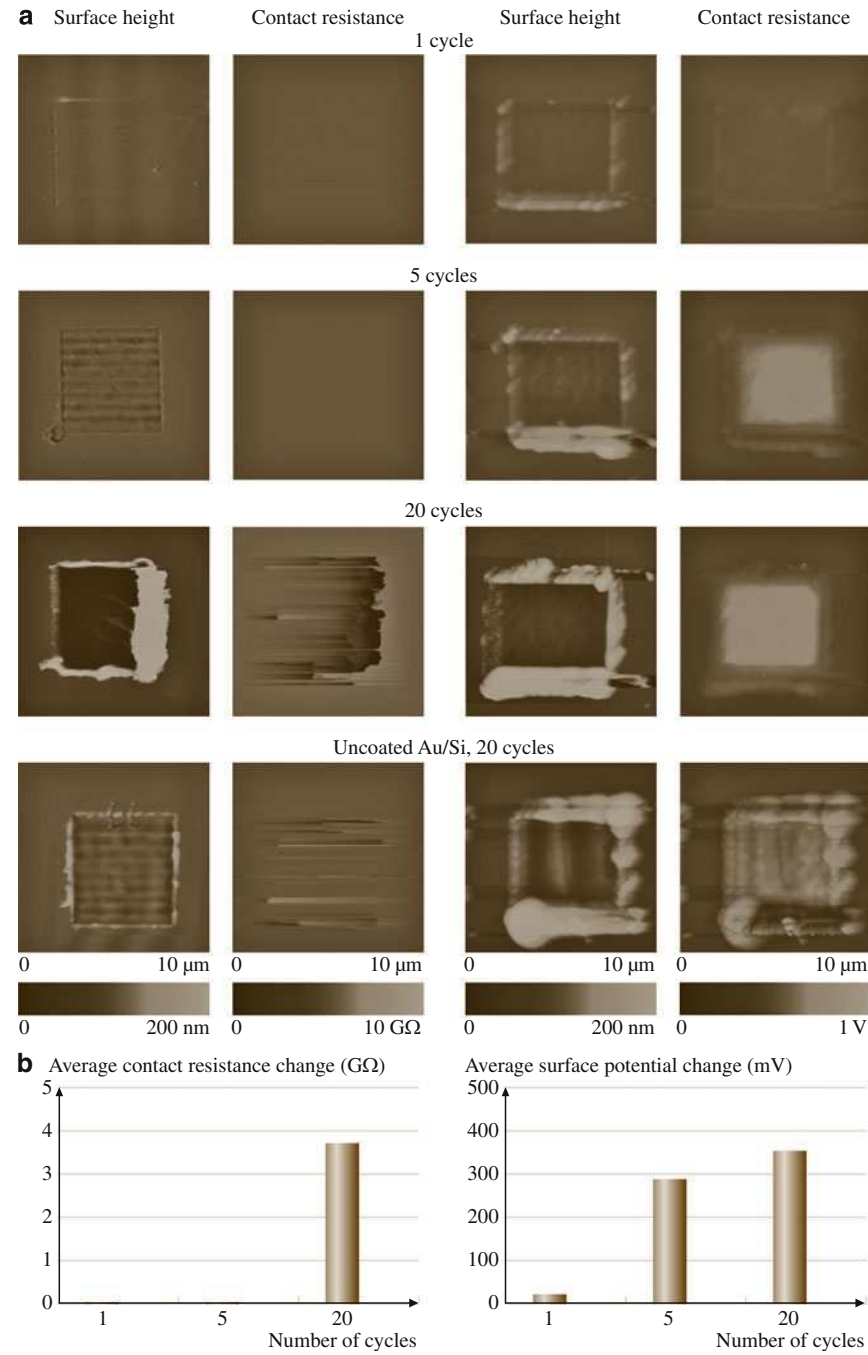


**Fig. 19.26** (a) Surface height, contact resistance, and surface potential maps of fully bonded Z-TETRAOL coating on Au as a function of the number of wear cycles, and (b) bar chart showing contact resistance and surface potential change (after [45])

flexible cantilever beam was slid against an uncoated Si(100) wafer in a macroscale configuration. The system was equipped with a mass spectrometer so that gaseous emissions from the interface could be monitored in situ during sliding in high vacuum and other controlled environments. The normal load and friction force at the contacting interface were measured using resistive-type strain-gage transducers. For the sliding tests, the lubricated Si(100) sample was glued onto a flat surface at the end of a rotating shaft. The sample was slid against a Si(100) wafer mounted on the flat surface of a slider integrated with a flexible cantilever used in magnetic rigid disk drives. The sliding speed was 0.3 m/s and the applied pressure was 150 kPa. The environmental effects were investigated in high vacuum ( $2 \times 10^{-7}$  Torr), argon, dry air (less than 2% RH), ambient air (30% RH), and high-humidity air (70% RH).

### Chemical Degradation Studies

The coefficient of friction and partial pressure of the gaseous products for fully bonded Z-DOL, Z-TETRAOL, A20H, Z – DOL + A20H (30 vol.%), and partially bonded A20H during sliding in high vacuum are shown in Fig. 19.27a–c. The result for untreated Z-DOL is also shown in the figure for comparison.

In the tests, the sharp increase of friction indicates the failure of the lubricant film. Therefore, the durability of the lubricant film can be obtained from the friction curve. Under the normal pressure of 150 kPa, the untreated Z-DOL failed immediately after sliding. The fully bonded Z-DOL began to fail after sliding of  $\approx 40$  m. The fully bonded Z-TETRAOL, began to fail at  $\approx 80$  m. Fully bonded and partially bonded A20H, however, did not fail during the 100 m sliding. The fully bonded Z-DOL + A20H (30 vol.%) failed immediately after sliding. The results show that fully bonded Z-TETRAOL and A20H are more durable than fully bonded Z-DOL, while the untreated Z-DOL is less durable than the bonded films. The PFPE lubricants can be bonded to the applied surface through the hydroxyl group. Z-TETRAOL, with two hydroxyl groups at each end of the molecular chain, can be bonded more tightly onto the silicon surface than Z-DOL. The high durability of A20H, however, is beyond expectations. To further confirm the result, a normal pressure of 200 kPa was applied on partially bonded A20H. At the normal pressure of 200 kPa, the coefficient of friction was found to increase. At the same time, gaseous products were detected (Fig. 19.27c). The final coefficient of friction was  $\approx 0.3$ , which is lower than the values (ap; 0.4) for the other films after failure. This could indicate that the A20H film was only partially worn. The reason for the lower durability of Z-DOL + A20H (30 vol.%) in high vacuum is not clear.

In the tests on Z-DOL and Z-TETRAOL films,  $\text{CF}_2\text{CF}_3$ ,  $\text{CF}_2\text{CFO}$ ,  $\text{CF}_3$ ,  $\text{CF}_2\text{O}$ ,  $\text{HCF}_2$ ,  $\text{CF}_2$ , and  $\text{CFO}$  were found to increase when friction increased. In the test of A20H films,  $\text{C}_6\text{H}_4\text{CF}_3$ ,  $\text{C}_6\text{H}_5\text{CF}_2$ ,  $\text{CF}_3$ ,  $\text{HCF}_2$ ,  $\text{CFO}$ ,  $\text{P}$ , and  $\text{H}_2$  were detected. For Z – DOL + A20H (30 vol.%),  $\text{C}_6\text{H}_4\text{CF}_3$ ,  $\text{C}_6\text{H}_5\text{CF}_2$ ,  $\text{CF}_3$ ,  $\text{HCF}_2$ ,  $\text{CFO}$ ,  $\text{P}$ , and  $\text{H}_2$  were also detected during sliding. Degradation mechanisms for Z-DOL and various

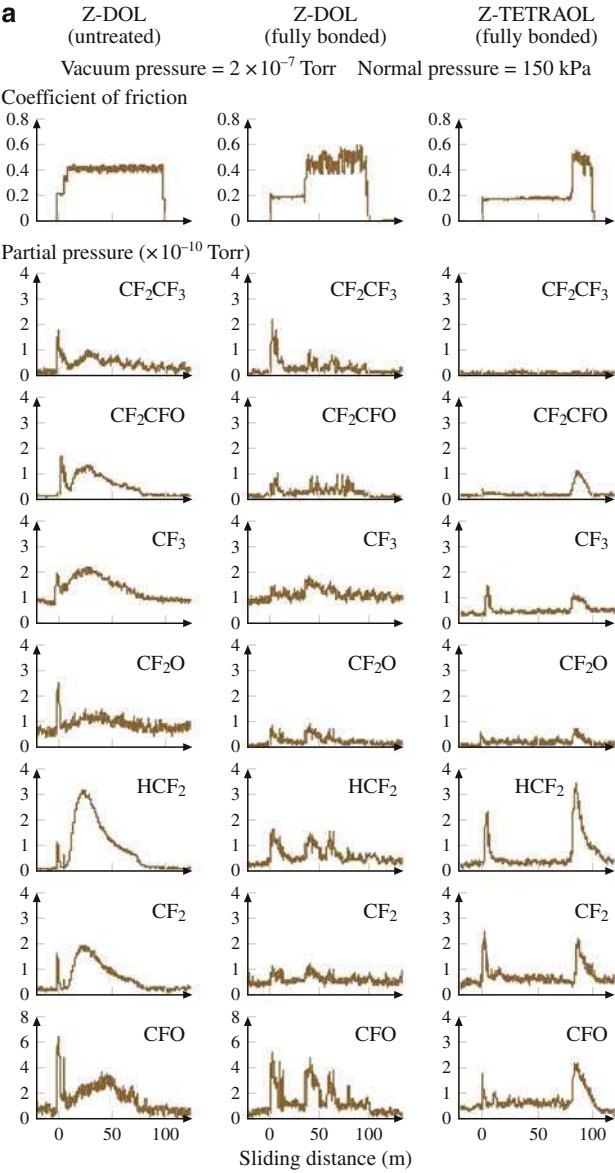
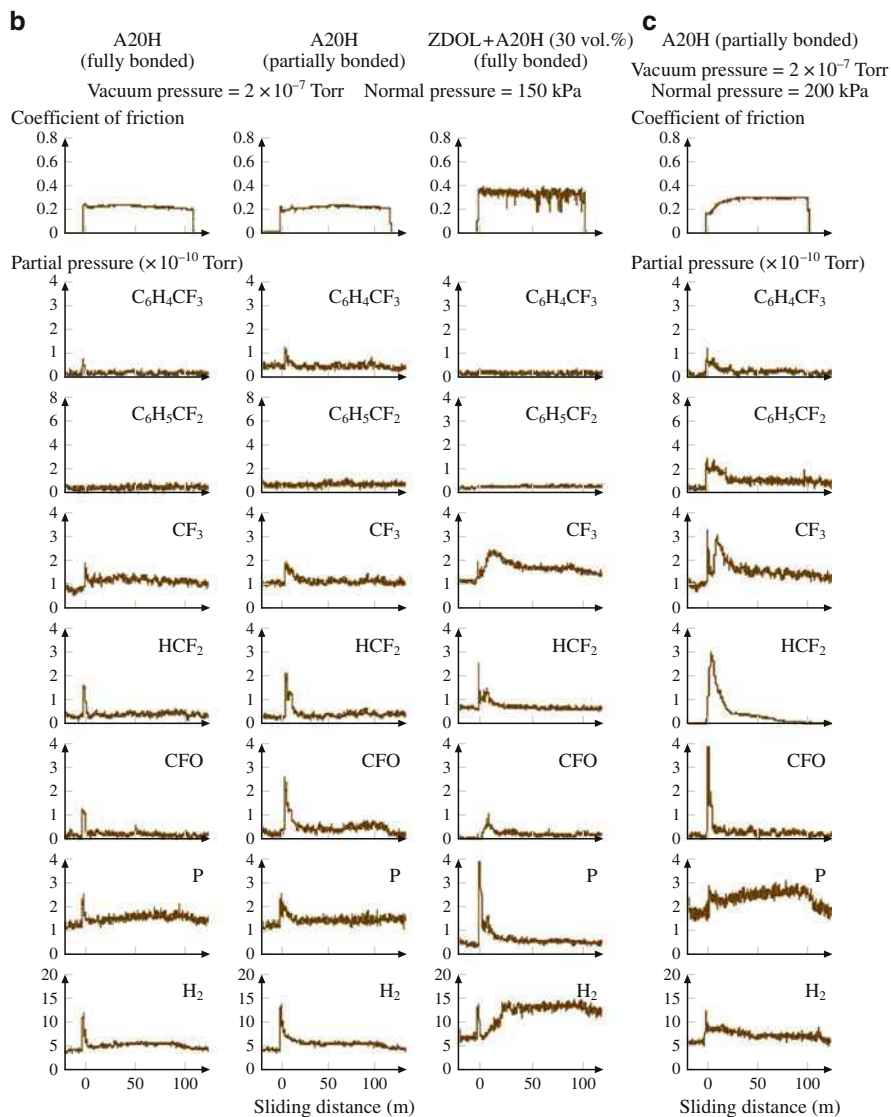


Fig. 19.27 (continued)

model lubricants have been studied by Zhao and Bhushan [66, 67] and Zhao et al. [68]. Based on this work, Z-DOL starts to decompose above 350°C. In the sliding conditions used here, it is not likely that frictional heat could generate such a



**Fig. 19.27** Coefficients of friction and mass spectra data on (a) untreated (2.2 nm) and fully bonded (2.3 nm) Z-DOL, fully bonded Z-TETRAOL (2.6 nm), (b) fully bonded (0.9 nm) and partially bonded (2.3 nm) A20H, and Z – DOL + A20H (2.4 nm) in high vacuum and under 150 kPa normal pressure, (c) partially bonded A20H in high vacuum and under 200 kPa normal pressure (after [62])

high temperature. The possibility of catalytic degradation is very low because of the small contact area. Triboelectrical reaction and mechanical scission are considered to be the dominant mechanisms during the sliding of Si on PFPE films. Electron

emission is known to occur during sliding for both metal and nonmetal surfaces. The interaction of electrons with PFPE molecules could create various radicals such as  $\cdot\text{CF}_2\text{--O--CF}_2\cdot$ ,  $\cdot\text{CF}_2\text{--CF}_2\text{--O--CF}_2\cdot$ , and/or  $\cdot\text{CF}_2\text{--CF}_3$ . These radicals can decompose or react with each other and/or the remaining PFPE molecules. A detailed description of triboelectrical reactions can be found in Zhao et al. [68] and Zhao and Bhushan [67].

Mechanical scission is another mechanism that can cause the degradation of PFPE films. The PFPE molecule has a long linear chain structure. The C–C and C–O bonds in the molecular chain are easily subjected to cleaving by micro-asperities on the rubbing surfaces, which results in decomposition of the lubricant during the sliding process.

A summary of the coefficients of friction and durability of the tested lubricants in high vacuum is shown in Fig. 19.28. The coefficients of friction of fully bonded Z-DOL and Z-TETRAOL are lower than those of untreated Z-DOL and A20H in high vacuum. Z-TETRAOL shows higher durability than Z-DOL, while A20H (both fully bonded and partially bonded) shows even high durability in high vacuum.

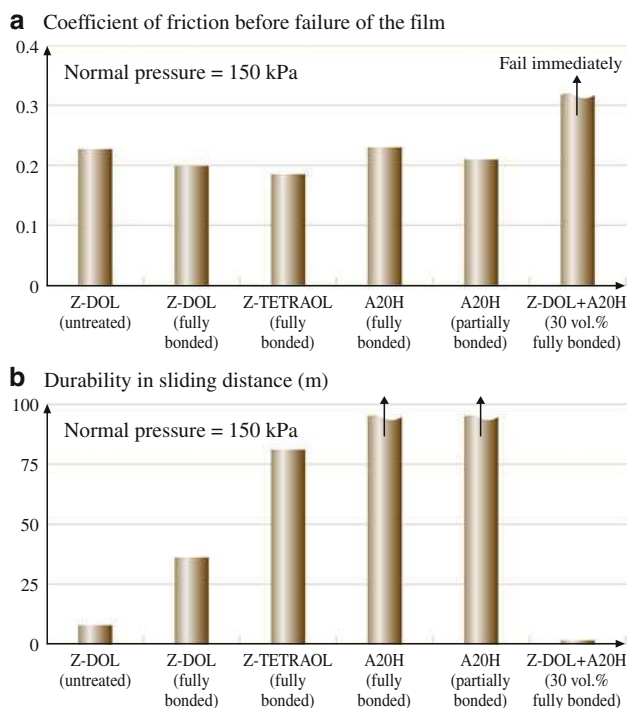


**Fig. 19.28** Coefficient of friction (a) and durability comparison (b) of Z-DOL, Z-TETRAOL, A20H, and Z – DOL + A20H in high vacuum (after [62])

## Environmental Studies

The wear tests were conducted in high vacuum, argon, dry air (<2% RH), air with 30% RH, and air with 70% RH [62]. The normal pressure applied was 150 kPa for all tested films, which was the same as in the degradation tests. Test results are presented in Fig. 19.29. The coefficients of friction show that friction and durability vary with the environment. Z-DOL films fail more rapidly in high vacuum than in other environments. As described in the previous section, there are very few foreign molecules on the contacting surfaces in high vacuum. This enables intimate contact between the lubricant film and the counterpart surface. A tendency for chemical bonding occurs between the lubricant film and the counterpart surface. In argon, the Z-DOL films exhibited lower friction and higher durability than in dry air. The chemical effects of oxygen can influence the friction and durability of the lubricant films [65]. The water molecules at a moderate humidity level (ambient air) can act as a lubricant between the contacting surfaces. However, in a high-humidity environment, the water molecules can penetrate the Z-DOL film and result in a nonuniform distribution of the Z-DOL molecules. The fully bonded Z-DOL film is less influenced by environment than untreated Z-DOL. The reason is that the untreated Z-DOL has more free hydroxyl end groups. The water molecules in the environment can interact with the hydroxyl group of Z-DOL via hydrogen bonding.

Z-TETRAOL is more durable than Z-DOL. Especially, a high-humidity environment does not seem to have negative effects on Z-TETRAOL, although it has one more hydroxyl end group than Z-DOL and may attract more water molecules at high humidity. This could be because the two hydroxyl end groups provides better attachment than for Z-DOL on the surface. The tight bonding reduces the probability of nonuniform distribution of the film. The coefficient of friction of fully bonded Z-TETRAOL is very close to that of fully bonded Z-DOL in argon and air with various humidity levels. In high vacuum, Z-TETRAOL shows a lower coefficient of friction than Z-DOL.

Both fully bonded and partially bonded A20H were very durable in high vacuum. In argon, fully bonded and partially bonded A20H did not fail during the 100 m sliding. In air with various humidity levels, however, the fully bonded A20H failed. The durability is lower compared with Z-DOL. This low durability may be caused by the low thickness of the film, which is only 0.9 nm. For the 2.3 nm-thick partially bonded A20H film, the durability in air with various humidity levels is apparently improved. Especially, at high humidity level, partially bonded A20H exhibits high durability. A20H consists of a phosphazene group that is large in size and protects the surface. Phosphazene lubricant has been used as an additive and is known to have high durability in a high-humidity environment. The coefficient of friction of A20H, however, is higher (5–15%) than that of Z-DOL in various environments.

Z-DOL + A20H (30 vol.%) shows low durability in high vacuum. In argon and air with various humidity levels, however, the film did not fail during the 100 m sliding. The durability of the mixture is higher than that of fully bonded Z-DOL.

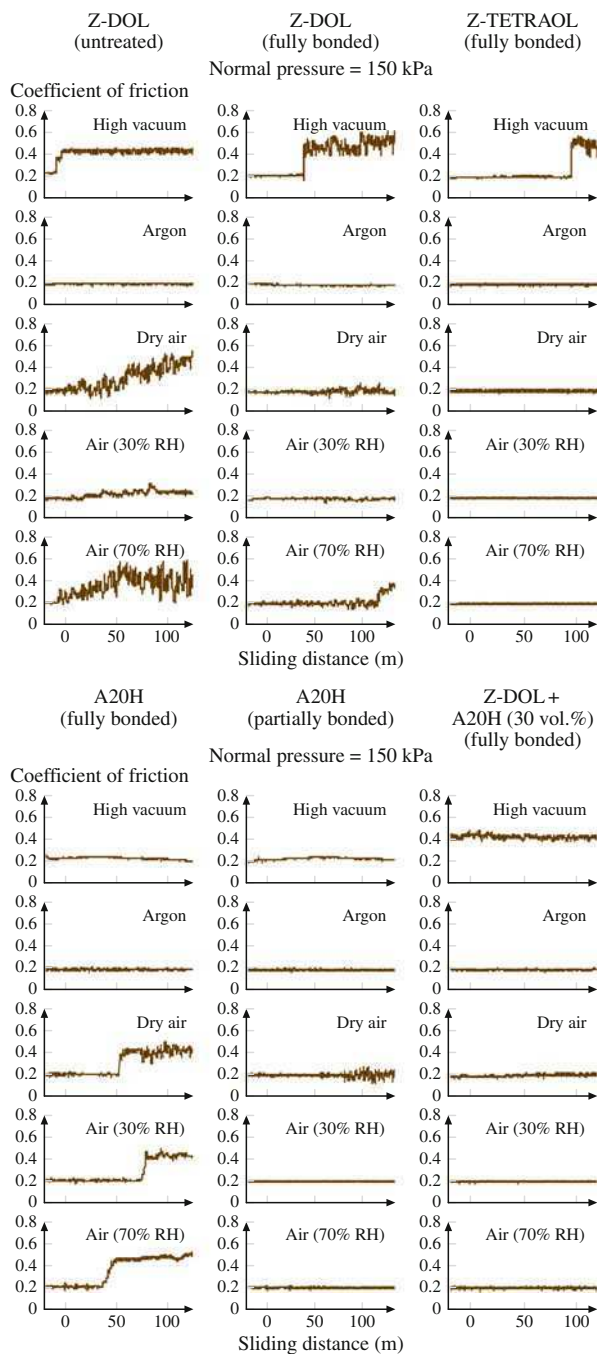


**Fig. 19.29** Coefficient of friction data in high vacuum, argon, and air with different humidity levels of untreated (2.2 nm) and fully bonded (2.3 nm) Z-DOL, fully bonded Z-TETRAOL (2.6 nm), fully bonded (0.9 nm) and partially bonded (2.3 nm) A20H, and Z-DOL + A20H (2.4 nm) (after [62])



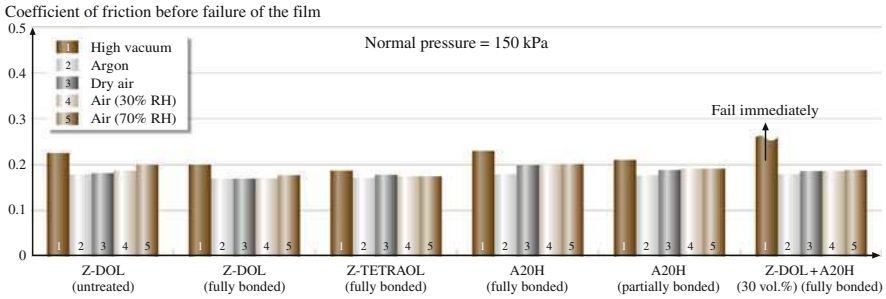


**Fig. 19.30** Comparison of coefficient of friction data for Z-DOL, Z-TETRAOL, A20H, and Z-DOL + A20H in high vacuum, argon, and air with different humidity levels (after [62])

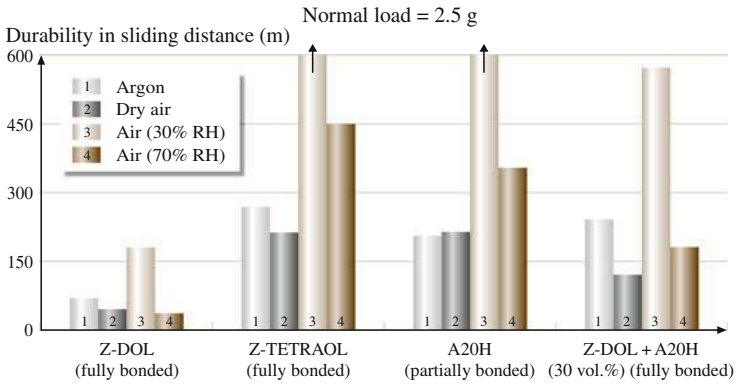


**Fig. 19.31** Durability comparison for Z-DOL, Z-TETRAOL, A20H, and Z-DOL + A20H in argon and air with different humidity levels. A single-crystal Si(100) ball (1 mm in diameter) was used as a slider on the films (after [62])

The coefficient of friction of the mixture is higher than that of Z-DOL while lower than that of A20H.

A summary of the coefficients of friction before the failure of the lubricant films in various environments is presented in Fig. 19.30. To summarize the highlights, Z-TETRAOL exhibits higher durability than Z-DOL. A20H exhibits high durability in high vacuum, in argon, and in air with various humidity levels. The mixture Z-DOL + A20H (vol.%30) shows low durability in high vacuum but high durability in argon and air with various humidity levels.

In order to investigate the durability of the lubricant films further, a single-crystal Si(100) ball (1 mm in diameter,  $5 \times 10^{-7}$  atoms/cm<sup>3</sup> boron doped) was used as a slider on the films to accelerate wear. Tests were performed in argon, dry air, ambient air, and high-humidity air. The applied load on the silicon ball was 2.5 g, and the sliding speed was 0.3 m/s. The sliding distance was up to 600 m. The results are shown in Fig. 19.31. From Fig. 19.31, in all environments, Z-TETRAOL exhibits higher durability than the other films. The durability of A20H is slightly

lower than that of Z-TETRAOL except in ambient air; both are comparable. Tests on Z-TETRAOL and A20H were terminated at 600 m. Z-DOL + A20H shows higher durability than Z-DOL.

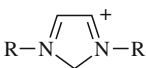
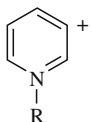
## 19.4 Nanotribological and Electrical Studies of Ionic Liquid Films

An ionic liquid (IL) is a synthetic salt with a melting point  $<100^{\circ}\text{C}$ . A room-temperature ionic liquid is a synthetic molten salt with melting point at or below room temperature. One or both of the ions are organic species. At least one ion has a delocalized charge such that the formation of a stable crystal lattice is prevented, and the ions are held together by strong electrostatic forces. As a result of the poor coordination of the ions, these compounds are liquid below  $100^{\circ}\text{C}$  or even at room temperature [20, 21].

The number of combinations of anions and cations that can be used to produce ionic liquids is in the range of one million. Typical cations include imidazolium, pyridinium, ammonium, phosphonium, and sulfonium, as shown in Table 19.3, where “R” stands for an organic group. Typical anions are tetrafluoroborate ( $\text{BF}_4^-$ ), hexafluorophosphate ( $\text{PF}_6^-$ ), bis(trifluorosulfonyl) imide  $[(\text{CF}_3\text{SO}_2)_2\text{N}]$ , *triflamide*], and toluene-4-sulfonate ( $\text{C}_7\text{H}_7\text{O}_3\text{S}$ , *tosylate*) [69]. Dependent upon the substrate wettability and other functional requirements, a set of cations and anions can be combined. The ionic liquids were initially developed for use as electrolytes in batteries and for electrodeposition. Recent applications have applied these compounds as environmentally friendly solvents for chemical synthesis (*green chemistry*), where these liquids are used as substitutes for conventional organic solvents.

Ionic liquids are considered as potential lubricants. Their strong electrostatic bonding, compared with covalently bonded fluids, leads to very desirable lubrication

**Table 19.3** Typical cations

Imidazolium	
Pyridinium	
Ammonium	$\text{NR}_4^+$
Phosphonium	$\text{PR}_4^+$
Sulfonium	$\text{SR}_3^+$

properties. They also possess desirable properties such as negligible volatility, non-flammability, high thermal stability or high decomposition temperature, efficient heat transfer properties, low melting point, as well as compatibility with lubricant additives. Unlike conventional lubricants that are electrically insulating, ionic liquids can minimize the contact resistance between sliding surfaces because they are conducting, which is needed for various electrical applications [23, 24, 25]. These liquids can also be used to mitigate arcing, which is a cause of electrical breakdown in sliding electrical contacts. In addition, ILs have high thermal conductivity, which helps to dissipate heat during sliding. The use of ionic liquids instead of hydrocarbon-based oils (such as highly reformed mineral oils) has the potential to dramatically reduce air emissions. Perfluoropolyethers (PFPEs) are used in magnetic rigid disk and vacuum grease applications due to their high thermal stability and extremely low vapor pressure. However, from the commercial standpoint, ionic liquids are cheaper than PFPEs by a factor of two or so, providing the motivation for comparing the tribological properties of the former with the latter. ILs are being considered for MEMS/NEMS applications because of their high temperature stability, electrical conductivity, and desirable lubrication properties.

Bhushan et al. [20] evaluated ionic liquids with the hexafluorophosphate anion deposited on Si(100) wafers, and these were found to exhibit improved friction and wear properties compared with conventional lubricants. The films were evaluated as untreated, partially bonded (by heating at 150°C for 30 min after dip-coating), and fully bonded (thermally treated and washed). Ionic liquid containing the octyl sulfate anion has also been developed and is of interest due to its resistance to hydrolysis. Based on experience, anions are observed to affect tribological performance. Table 19.4 lists the physical and thermal properties of a selected ionic liquid and its properties, compared with the PFPE lubricant Z-TETRAOL.

The durability of ionic liquid films on various metal and ceramic substrates has been investigated from the standpoint of film formation (wettability) and film removal (friction and wear), where it was found that certain cations and anions exhibit better wetting, friction reduction, and wear resistance properties [20]. In general, ionic liquids exhibit better wettability on noble-metal and ceramic surfaces than on nonnoble-metal surfaces [69]. The flat imidazolium cation shows poorer wettability compared with bulkier cations such as ammonium and sulfonium. Among salts with the imidazolium cation, the presence of longer organic side-chains leads to reduction of the coefficient of friction. An anion effect is also observed, where oxygen-rich anions show better substrate wettability and lower wear compared with other imidazolium salts. Based on these findings, the ionic liquids of interest are 1-butyl-3-methylimidazolium hexafluorophosphate (BMIM-PF<sub>6</sub>) and 1-butyl-3-methylimidazolium octyl sulfate (BMIM-OctSO<sub>4</sub>). These were studied by Bhushan et al. [20], and the former was found to be superior in terms of tribological performance. The chemical structures of BMIM-PF<sub>6</sub> and Z-TETRAOL are shown in Fig. 19.32 for comparison, and a summary of their properties is presented in Table 19.4.

Some dicationic ILs are thermally stable up to 400°C [74]. The adhesion and friction properties of two dicationic IL films on Si(100) substrate, based on the

**Table 19.4** Physical, thermal, and electrical properties of BMIM-PF<sub>6</sub> and Z-TETRAOL

	<b>1-Butyl-3-methylimidazolium hexafluorophosphate (BMIM-PF<sub>6</sub>)</b>	<b>Z-TETRAOL</b>
Cation	C <sub>8</sub> H <sub>15</sub> N <sub>2</sub> <sup>+</sup>	—
Anion	PF <sub>6</sub> <sup>−</sup>	—
Molecular weight (g/mol)	284 <sup>a</sup>	2,300 <sup>b</sup>
<i>T</i> <sub>melting</sub> (°C)	10 <sup>c</sup>	—
<i>T</i> <sub>decomp</sub> (°C)	300 <sup>c</sup>	≈ 320 <sup>b</sup>
Density (g/cm <sup>3</sup> )	1.37 <sup>a</sup>	1.75 <sup>b</sup>
Kinematic viscosity (mm <sup>2</sup> /s)	281 <sup>a</sup> (20°C) 78.7 <sup>d</sup> (40°C)	2,000 <sup>b</sup> (20°C)
Pour point (°C)	< − 50 <sup>e</sup>	− 67 <sup>b</sup>
Specific heat (J/(g K))	1.44 <sup>f</sup> (25°C)	≈ 0.20 <sup>b</sup> (50°C)
Thermal conductivity at 25°C (W/(m K))	0.15 <sup>g</sup>	≈ 0.09 <sup>b</sup>
Dielectric strength at 25°C (kV/mm)	—	≈ 30 <sup>b</sup>
Volume resistivity (Ω cm)	—	≈ 10 <sup>13b</sup>
Vapor pressure at 20°C (Torr)	<10 <sup>−9</sup>	5 × 10 <sup>−7b</sup>
Wettability on Si	Moderate <sup>c</sup>	—
Water contact angle	95°	102°
Miscibility with isopropanol	Total <sup>a</sup>	—
Miscibility with water	—	—

<sup>a</sup>Merck Ionic Liquids Database, Darmstadt (<http://ilddb.merck.de/ionicliquids/en/startpage.htm>)<sup>b</sup>Z-TETRAOL data sheet, Solvay Solexis Inc., Thorofare<sup>c</sup>Kinzig and Sutor [69]<sup>d</sup>Reich et al. [70]<sup>e</sup>Wang et al. [71]<sup>f</sup>Kabo et al. [72]<sup>g</sup>Frez et al. [73]

imidazolium cation and the bis(trifluoromethanesulfonyl)imide (or *triflamide*) anion, were studied by Palacio and Bhushan [22] and compared with the monocationic IL 1-butyl-3-methyl-1*H*-imidazolium hexafluorophosphate (BMIM-PF<sub>6</sub>). AFM experiments were also performed under various humidity and temperature conditions in order to investigate the effect of the environment on the nanolubrication properties of these ILs. Microscale friction and wear experiments using the ball-on-flat tribometer and wear at ultralow loads using an AFM were carried out. Fourier-transform infrared (FTIR) spectroscopy and x-ray photoelectron spectroscopy (XPS) were used to determine the chemical species that affect intermolecular bonding and also to elucidate the effect of the environment on the IL film surface in the case of FTIR data.

The dicationic ionic liquids used in this study were 1,1'-(pentane-1,5-diyl)bis(3-hydroxyethyl-1*H*-imidazolium-1-yl) di[bis(trifluoromethanesulfonyl)imide] (abbreviated as BHPT) and 1,1'-(3,6,9,12,15-pentaoxapentadecane-1,15-diyl)bis(3-hydroxyethyl-1*H*-imidazolium-1-yl) di[bis(trifluoromethanesulfonyl)imide] (abbreviated as BHPET) [75] deposited on Si(100) wafers. The common name *triflamide* will be used here when referring to the anion. The properties of these dicationic ILs were compared with those of the conventional monocationic ionic liquid 1-butyl-3-methyl-1*H*-imidazolium hexafluorophosphate, abbreviated as BMIM-PF<sub>6</sub>.

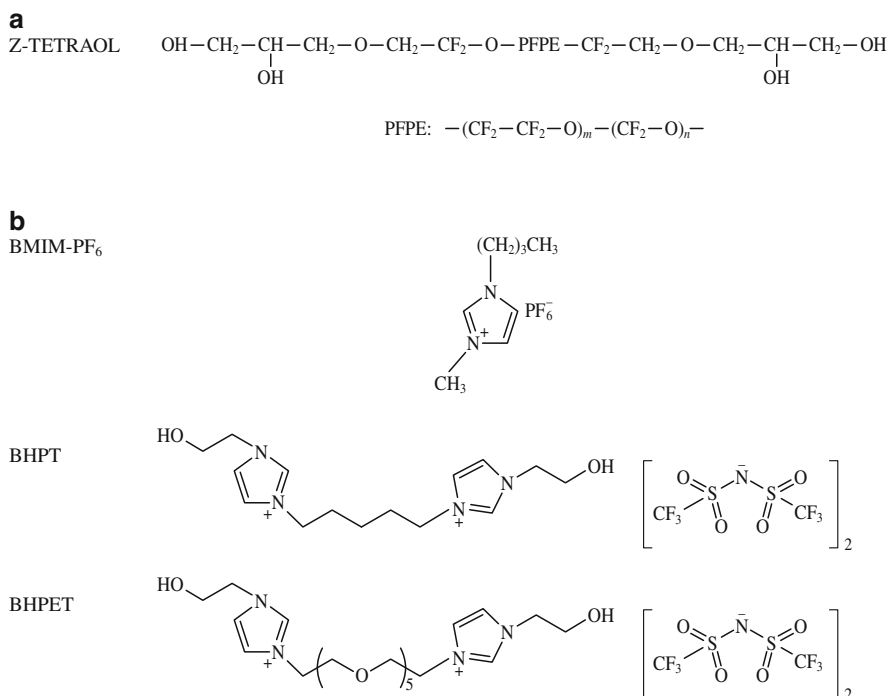


**Fig. 19.32** (a) Chemical structures of the Z-TETRAOL molecule, and (b) chemical structures of the BMIM-PF<sub>6</sub>, BHPT, and BHPET molecules

(Merck, Germany). Their chemical structures are shown in Fig. 19.32b. These compounds have been applied on single-crystal Si(100) (phosphorus doped) with a native oxide layer on the surface using the dip-coating technique. The method and the apparatus used have been described earlier. The films were heat-treated at 150°C for 30 min after dip-coating, such that they were partially bonded [20].

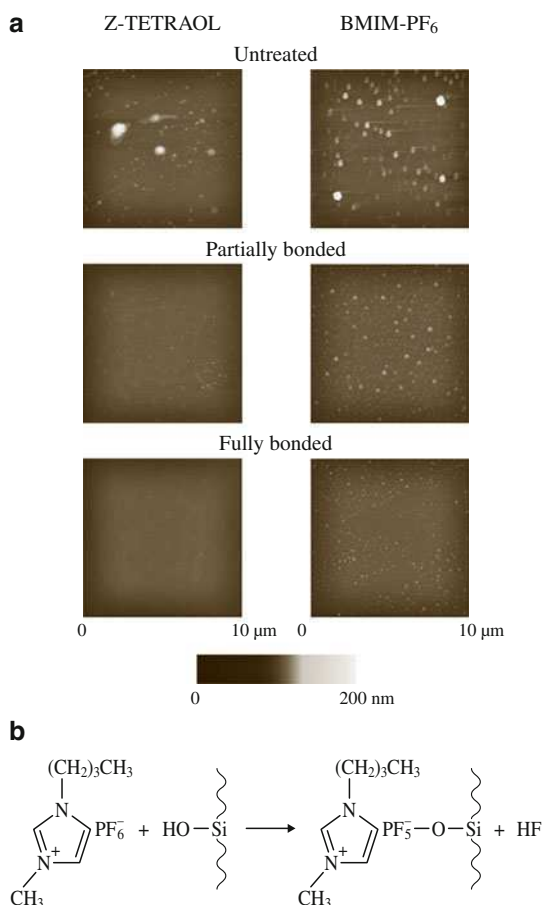
### 19.4.1 Monocationic Liquid Films

In this section, nanotribological data on BMIM-PF<sub>6</sub> and Z-TETRAOL are presented [20, 21, 25, 46].

#### Nanotribological Studies

In Fig. 19.33a, the surface height images for the untreated sample (air dried) are compared with the two chemically bonded samples (partially bonded and fully bonded). Aggregates of varying sizes are observed on the untreated Z-TETRAOL

**Fig. 19.33** (a) Surface height images for untreated, partially bonded, and fully bonded films of BMIM-PF<sub>6</sub> on silicon substrate, and (b) schematic for the attachment of BMIM-PF<sub>6</sub> to the silicon substrate (after [20])



and on the ionic liquid coating. These aggregates could have formed initially during preparation of the dilute solution. For Z-TETRAOL, the long PFPE chains can orient in various configurations (such as coils), leading to aggregate formation [20]. In ionic liquids containing the 1-butyl-3-methylimidazolium cation, it is believed that aggregate formation in solvents that are less polar compared with water aids in minimizing the charge density (charge delocalization) within the ions. These aggregates are subsequently deposited on the silicon surface during the dip-coating procedure. It is observed that the untreated lubricant surface has more prominent aggregates compared with the two chemically bonded samples, implying that the heat treatment promotes bonding to the Si substrate. Without the chemical bonding procedure, the lubricant molecules are less likely to attach to the substrate and would tend to attract each other instead, such that dewetting is more likely. The immobilization of the ionic liquid, which is promoted by thermal treatment, occurs by reaction of the anion with the hydroxyl groups present on the silicon surface, as shown in Fig. 19.33b for BMIM-PF<sub>6</sub>.

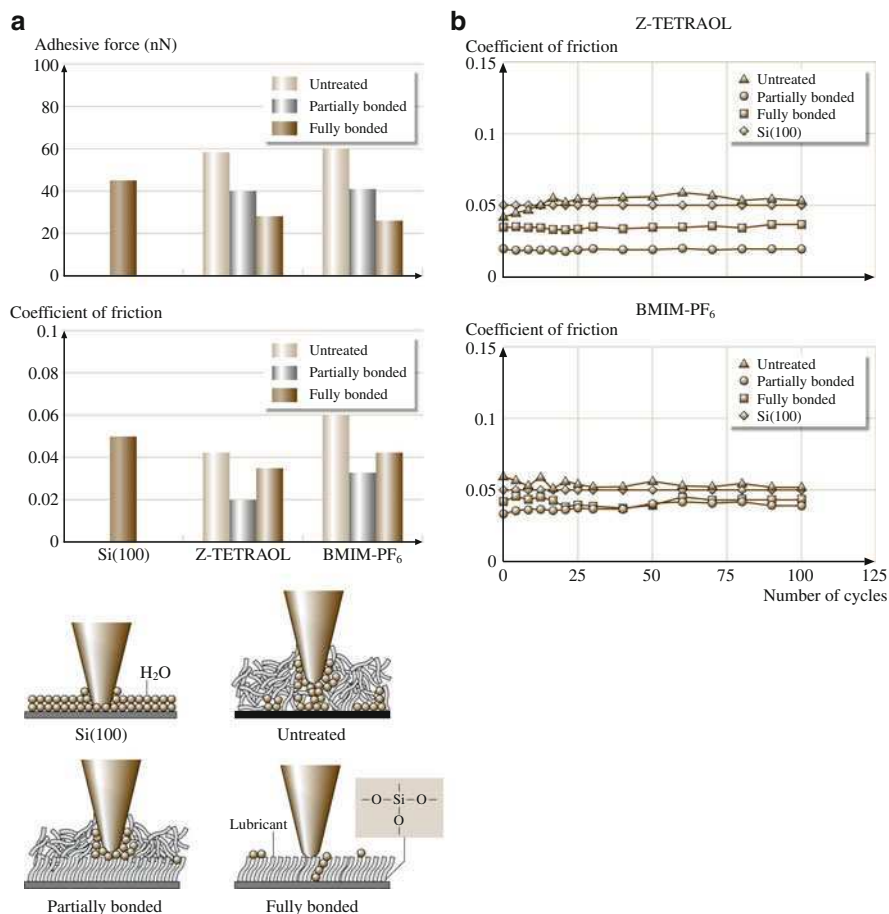


**Fig. 19.34** (a) Summary of the adhesive force and coefficient of friction, and (b) durability data after 100 cycles for BMIM-PF<sub>6</sub> at room temperature (22°C) and ambient air (45–55% RH). Data for uncoated Si and Z-TETRAOL are shown for comparison. Schematics in (a) show the effect of chemical bonding treatment and meniscus formation between the AFM tip and sample surface on the adhesive and friction forces (after [20])

Figure 19.34a shows a summary of the adhesive force and coefficient of friction measurements on the ionic liquid. Z-TETRAOL and Si(100) data are provided for comparison. The adhesive force has been observed to decrease in the following order: untreated > partially bonded > fully bonded. This mobile fraction on the untreated sample facilitates the formation of a meniscus, which increases the tip-sample adhesion. The adhesive force is highest in the untreated coating since it has the greatest amount of the mobile fraction among the three samples. Conversely, the sample with no mobile lubricant fraction available (fully bonded) has the lowest adhesive force.

A different trend is observed in the coefficient of friction ( $\mu$ ) data. Both the fully bonded and partially bonded samples have lower  $\mu$  values compared with the uncoated silicon. Friction forces are lower on the latter, implying that the mobile lubricant fraction present in the partially bonded samples facilitates sliding of the tip on the surface. However,  $\mu$  values for the untreated samples are higher than the data for the heat-treated coatings. Due to the lack of chemical bonding, the interaction of the lubricant with the substrate is weakened and dewetting can occur. Water and lubricant molecules are more likely to form a meniscus as the tip approaches the surface. This provides greater resistance to tip sliding, leading to higher coefficient of friction values. The lower portion of Fig. 19.34a shows a schematic illustrating the role of meniscus formation in the adhesive and friction forces obtained for the uncoated Si and the untreated, partially bonded, and fully bonded lubricant-coated Si surfaces.

Figure 19.34b shows plots of the coefficient of friction as a function of the number of sliding cycles at 70 nN normal load. Only a small rise in the coefficient of friction was observed for both Z-TETRAOL and BMIM-PF<sub>6</sub> surfaces, indicating low surface wear. In the case of untreated Z-TETRAOL, a crossover is observed, where the coefficient of friction increases from its initial value and exceeds the  $\mu$  of silicon after a certain number of cycles. This is attributed to the transfer of lubricant molecules to the AFM tip and the interaction of the transferred molecules with the lubricant still attached to the Si substrate, which will increase the friction force.

In order to compare friction and wear properties on the nanoscale with that on the microscale, conventional ball-on-flat tribometer experiments were conducted on the same samples. Images and profile traces of the wear scars are shown in Fig. 19.35a. The coefficient of friction and number of cycles to failure are summarized in Fig. 19.35b. Ionic liquid shows enhanced durability compared with both the Z-TETRAOL-coated and the uncoated Si. The nanoscale data presented in Fig. 19.34 can be compared with the  $\mu$  values obtained from the ball-on-flat measurements (Fig. 19.35b). The  $\mu$  values of the untreated lubricant samples obtained by using AFM are lower than those obtained from the ball-on-flat tests. This is attributed to the difference in the length scales of the test techniques. An AFM tip simulates a single-asperity contact while the conventional friction test involves the contact of multiple asperities present in the test system [1, 2]. With regards to wear, the interface contact of the AFM and ball-on-flat techniques are different from each other. In an AFM, the contact stress is very high, such that material can be displaced more easily. For the ball-on-flat test, the ball exerts a lower pressure on the surface, and the coating is in a confined geometry. As a consequence, displacement of the coating is not as easy as in AFM, leading to enhanced wear resistance.

### **Wear Detection by Surface Potential and Electrical Resistance Measurements**

Figure 19.36a shows a summary of wear tests and corresponding surface potential measurements on the ionic liquid. A bar plot summarizing the average surface potential change on the tested area is shown in Fig. 19.36b. In all cases, a smaller amount of debris was generated compared with the uncoated silicon surface,



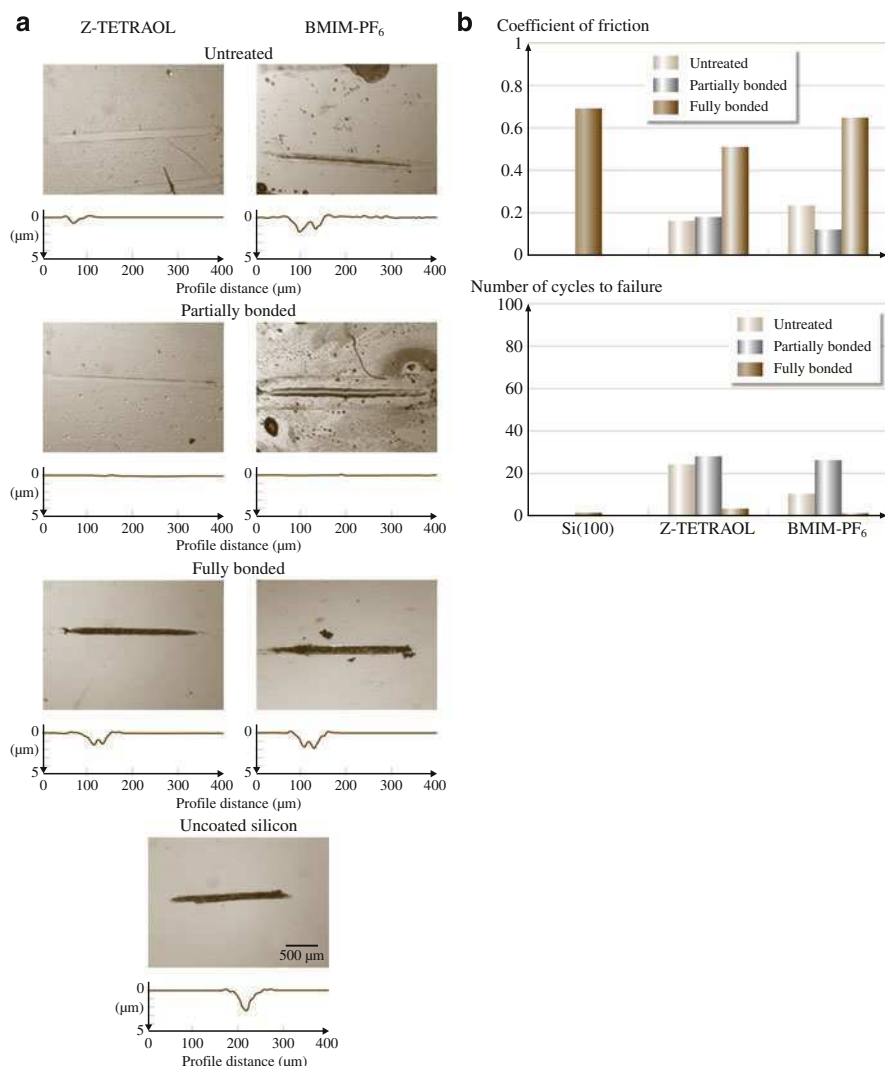


**Fig. 19.35** (a) Optical images and height profiles taken after 20 cycles, and (b) summary of the coefficient of friction and number of cycles to failure in ball-on-flat tests on various BMIM-PF<sub>6</sub> coatings. Data for uncoated Si and Z-TETRAOL are shown for comparison (after [20])

indicating that the ionic liquid provides wear protection. In general, the samples containing the mobile lubricant fraction (i.e., untreated and partially bonded surfaces) exhibit a lower surface potential change compared with the fully bonded sample, which only has immobile lubricant molecules. This is attributed to lubricant replenishment by the mobile fractions, which can occur in the untreated and partially bonded samples [45, 62]. From the bar plot in Fig. 19.36b, it is also observed that the change in surface potential is generally lower in the ionic liquid

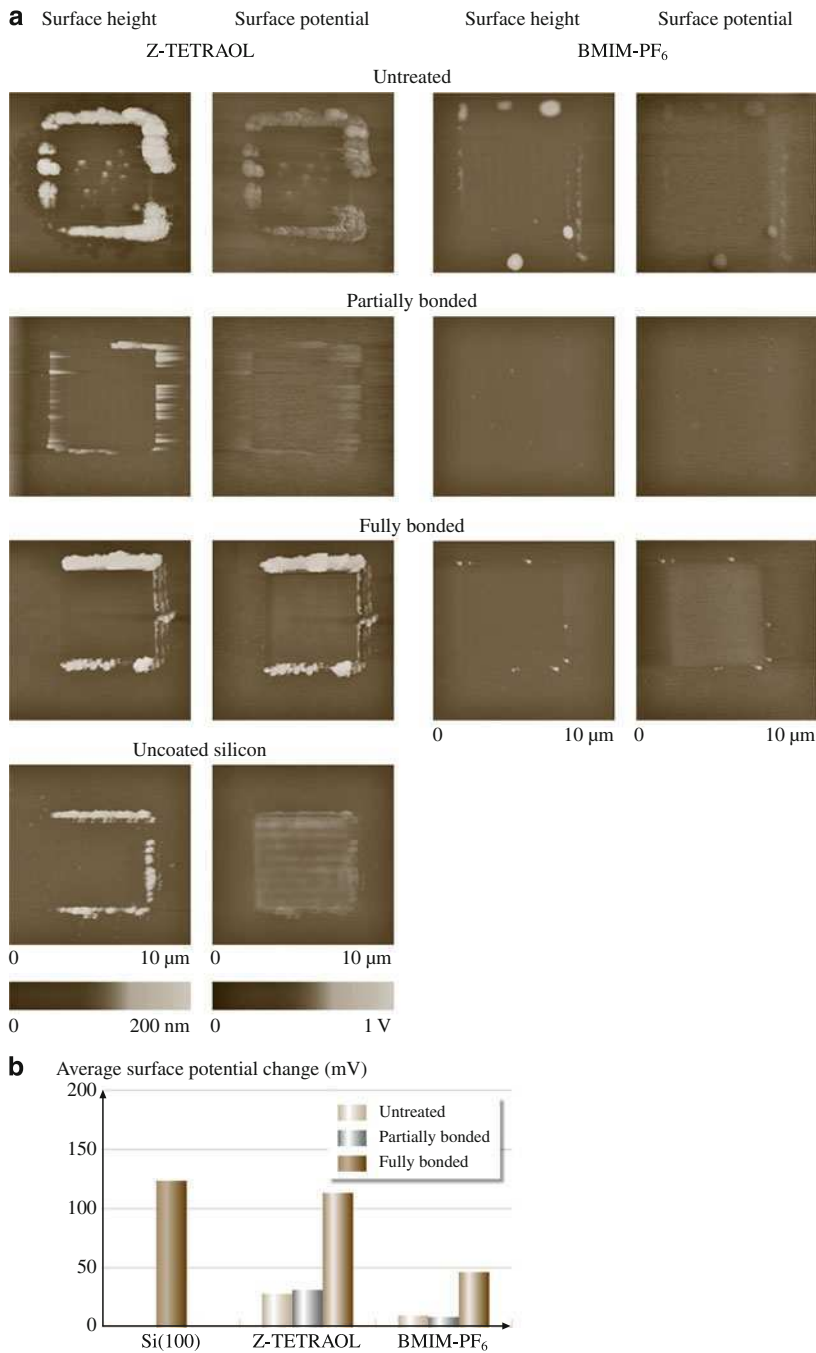


**Fig. 19.36** (a) Surface height and surface potential maps after wear tests, and (b) bar chart showing surface potential change for various BMIM-PF<sub>6</sub> coatings. Data for uncoated Si and Z-TETRAOL are shown for comparison (after [20])

coating compared with the Z-TETRAOL coating and the uncoated silicon. This indicates that any built-up surface charges arising from the wear test were immediately dissipated onto the conducting ionic lubricant coating surface. In the case of Z-TETRAOL and the uncoated silicon, the charges remained trapped in the test area, since both of these materials are insulators. Based on these findings, a considerable surface potential change will be observed on the wear region when:

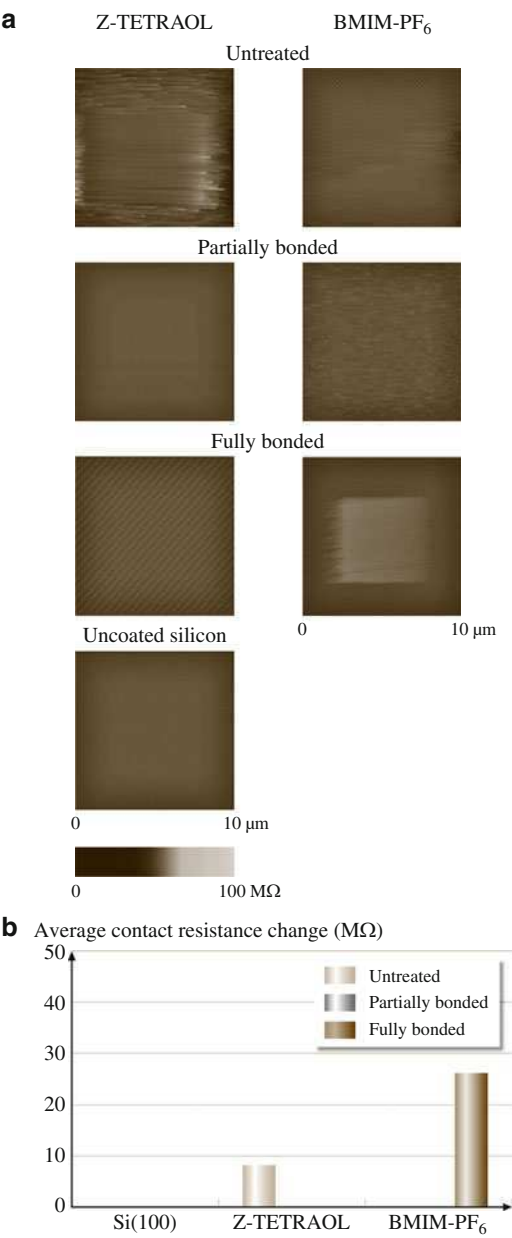
1. The lubricant has been fully removed from the substrate
2. The native  $\text{SiO}_2$  layer has been abraded from the surface
3. Wear has caused subsurface structural changes
4. Charges build up, as they are unable to dissipate into the surrounding material

Contact resistance images for the surfaces subjected to the wear tests are presented in Fig. 19.37a. The average change in the contact resistance of the wear region relative to the untested area is summarized in Fig. 19.37b. The fully bonded BMIM- $\text{PF}_6$  has an appreciable contact resistance increase in the wear region. Since silicon is a semiconductor, it has much higher resistance compared with the surrounding ionic liquid. The resistance increase in the worn area implies that the substrate is exposed after the wear test. Partially bonded films did not get worn off the substrate by the test, as evidenced by the lack of contact resistance change in the tested area. The untreated Z-TETRAOL exhibited an observable resistance change, while BMIM- $\text{PF}_6$  did not. This can be correlated to the durability data in Fig. 19.34b, where the untreated Z-TETRAOL sample exhibited an increase in the friction force with time due to the transfer of lubricant molecules to the tip. Easier lubricant removal means that the diamond tip (in the case of Fig. 19.37) can cause substrate wear much sooner, leading to the observed resistance increase in the tested area. However, the resistance image does not provide a clear contrast between Z-TETRAOL and the newly exposed substrate since both materials have high resistance values.

Microscale contact resistance obtained from ball-on-flat tribometer testing is shown in Fig. 19.38, along with the corresponding coefficient of friction data. For the ionic liquid film, the initial resistance is slightly lower than that of uncoated silicon, confirming their conductive nature. For the Z-TETRAOL samples, the contact resistance is of about the same magnitude as the uncoated silicon. However, for the conducting ionic liquid, an increase in resistance corresponds to an increase in the coefficient of friction, indicating wear of the lubricant and exposure of the silicon substrate, similar to observations on the nanoscale. These results are consistent with the adhesion, friction, and surface potential results with regards to wear detection and wear protection due to the mobile and immobile lubricant fractions.

The durability data and trends for the ionic liquid obtained by using a steel ball are inferior to the results shown in Fig. 19.35, which were measured by using a sapphire ball. In Fig. 19.38, the partially bonded samples still show the best durability, but in this case, Z-TETRAOL has the highest number of cycles to failure (the opposite trend compared with Fig. 19.35b), as indicated by the point where the jump in the coefficient of friction is observed. This can be accounted for by the wetting properties of ionic liquids on different surfaces. It has been observed that

**Fig. 19.37** (a) Nanoscale contact resistance images after wear tests, and (b) *bar chart* showing contact resistance change for various BMIM-PF<sub>6</sub> coatings. Data for uncoated Si and Z-TETRAOL are shown for comparison. Cases without the clear wear scar did not exhibit measurable change (after [20])



ionic liquids have a tendency to wet nonmetal surfaces (e.g., Si<sub>3</sub>N<sub>4</sub>, SiO<sub>2</sub>, glass) better than conventional metal surfaces (such as 440C, M50, and 52100 steel) [20]. For wear tests with a steel ball, less wettability means less lubricant retention at the interface. This material wetting effect is possibly more significant for the ionic

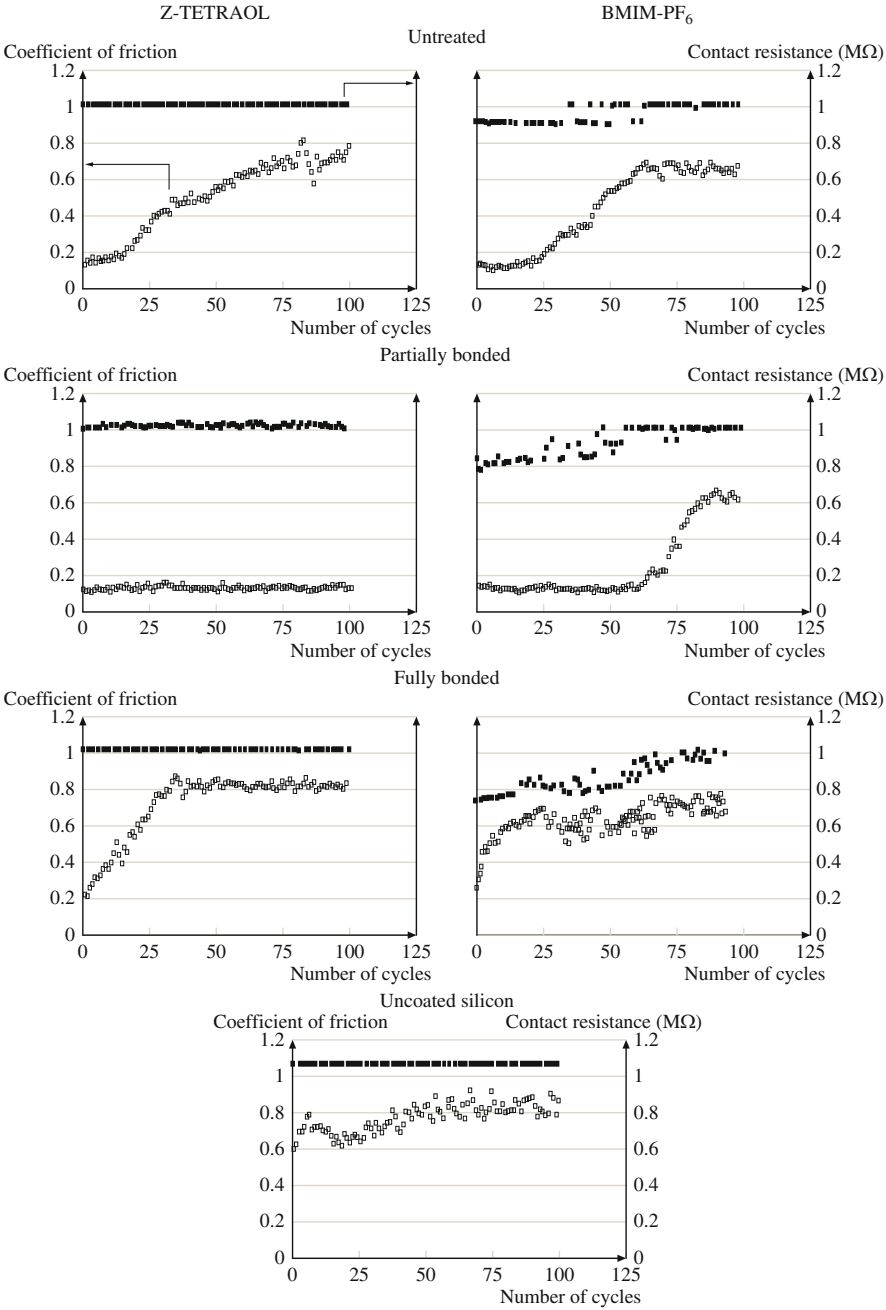


**Fig. 19.38** Microscale contact resistance and coefficient of friction after ball-on-flat tests for 100 cycles on various BMIM-PF<sub>6</sub> coatings. Data for uncoated Si and Z-TETRAOL are shown for comparison (after [20])

liquid than for Z-TETRAOL, but nonetheless the durability of the partially bonded BMIM-PF<sub>6</sub> is still close to its Z-TETRAOL counterpart, such that ILs are still viable lubricants comparable with PFPEs.

### 19.4.2 Dicationic Ionic Liquid Films

In this section, nanotribological data on BHPT and BHPET are presented. Data on BMIM-PF<sub>6</sub> and uncoated Si(100) are also presented for comparison [22].

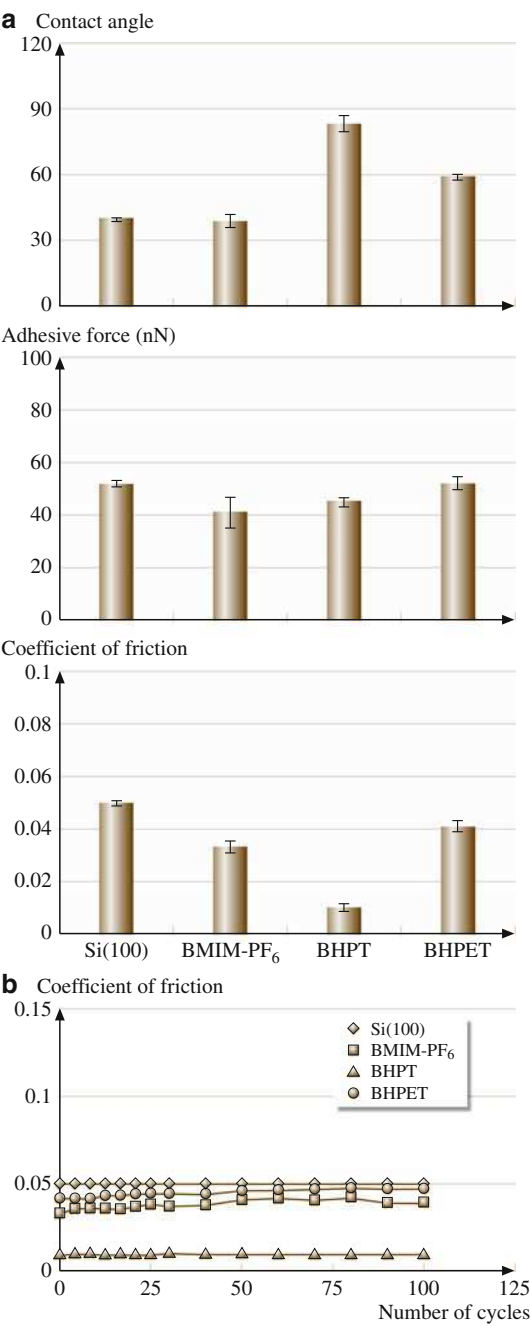
#### Nanotribological Studies

Figure 19.39a shows a summary of the contact angle, adhesive force, and coefficient of friction ( $\mu$ ) measurements for the coated and uncoated samples performed at ambient temperature and humid conditions (22°C and 50% RH, respectively). The data shown in the bar plots are averages of three measurements and the error bars represent  $\pm 1 \sigma$ . BHPT is the least hydrophilic as it has the highest contact angle (81°) among the three IL coatings. This coating also exhibited the greatest reduction in the coefficient of friction relative to the uncoated surface. The high contact angle of BHPT leads to minimal meniscus formation between the tip and surface, leading to a large drop in the nanoscale friction force. In addition, BHPT has a pentyl chain which links the two imidazolium cations. This chain can orient the cation molecules on the substrate, thereby facilitating tip sliding on the film surface. In contrast, the polyether chain of BHPET is susceptible to interactions with water molecules which can promote (instead of minimize) meniscus formation. The BMIM-PF<sub>6</sub> film also exhibited a reduction in the adhesive force and coefficient of friction. This results from the combination of mobile and immobile lubricant fractions. Immobilization of this ionic liquid is possible as a result of the thermal treatment, which promotes the reaction between the hexafluorophosphate anion and the hydroxyl groups present on the silicon substrate surface [20, 22, 76].

Wear tests were conducted by monitoring the change in the friction force on a 2  $\mu\text{m}$  line for 100 cycles. The data shown in Fig. 19.39b are representative of three measurements made for each sample. The focus of this experiment is the wear of the lubricant film on the substrate. The  $\mu$  value of the BHPT film changed minimally during the duration of the experiment, which indicates that the film was not being worn after 100 cycles. On the other hand, the BMIM-PF<sub>6</sub> and BHPET samples exhibited a gradual increase in  $\mu$ , which means that these films could be undergoing some wear and that their interaction with the silicon substrate is weaker compared with that of BHPT.

Figure 19.40 presents a summary of the average contact potential change after the wear tests conducted by creating  $5 \times 5 \mu\text{m}^2$  wear scars with a diamond tip, where the height and surface potential maps were imaged afterwards. The data shown in the bar plot is the average of three measurements and the error bars

**Fig. 19.39** (a) Summary of the contact angle, adhesive force, and coefficient of friction, and (b) durability data after 100 cycles for BMIM-PF<sub>6</sub>, BHPT, and BHPET coatings at room temperature (22°C) and ambient air (45–55% RH). Data for uncoated Si are shown for comparison. The error bars in (a) represent  $\pm 1 \sigma$  based on three measurements performed (after [22])



represent  $\pm 1 \sigma$ . A change in the surface potential in the wear region is observed when the following occur: the lubricant has been fully removed from the substrate, the native SiO<sub>2</sub> layer has been abraded from the surface, wear has caused subsurface

**Fig. 19.40** Bar chart showing average surface potential change for BMIM-PF<sub>6</sub>, BHPT, and BHPET coatings. Data for uncoated Si are shown for comparison. The error bars represent  $\pm 1 \sigma$  based on three measurements performed (after [22])

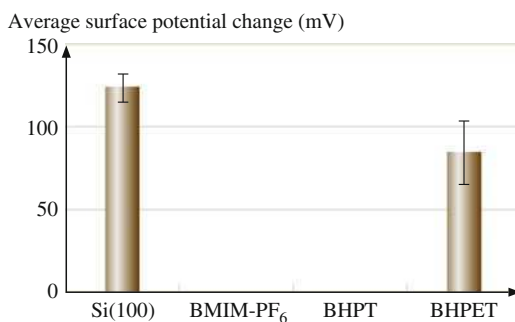
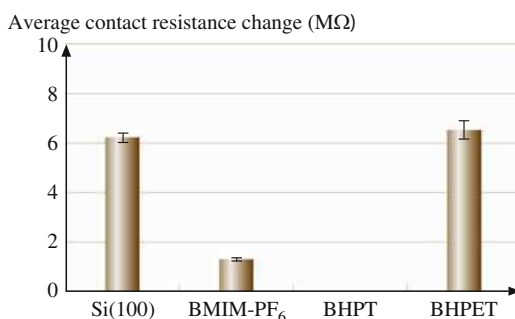


**Fig. 19.41** Bar chart showing average contact resistance change for BMIM-PF<sub>6</sub>, BHPT and BHPET coatings. Data for uncoated Si are shown for comparison. The error bars represent  $\pm 1 \sigma$  based on three measurements performed (after [22])



structural changes, and charges build up, as they are unable to dissipate into the surrounding material [20, 22]. As expected, the uncoated Si exhibited the greatest amount of wear (as evidenced by debris buildup around the edge of the wear test region) and highest increase in the surface potential. The surface potential image for the BHPET film also showed an increase, indicating that the film was worn out after the test. This was not seen on tests with the BMIM-PF<sub>6</sub> and BHPT samples. The surface potential change could be absent in the test area if the lubricant was not removed completely, indicating that these two samples have a stronger interaction with the silicon substrate compared with BHPET.

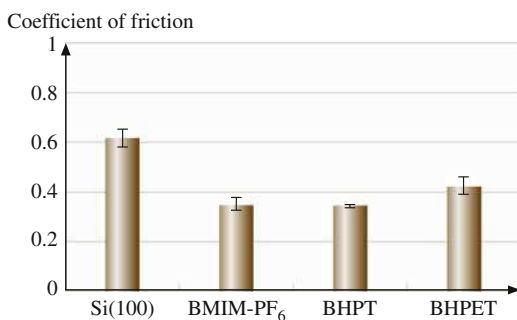
Figure 19.41 presents a summary of the average contact resistance change after the wear test. As in Fig. 19.40, a significant change is observed in the wear region of the Si and BHPET samples. There is also a small amount of localized contact resistance increase in the BMIM-PF<sub>6</sub> sample. These results are consistent with the wear test presented in Fig. 19.39b, where the durability of the films decreases in the order: BHPT > BMIM-PF<sub>6</sub> > BHPET.

## Microscale Friction and Wear

In order to compare friction and wear properties at the microscale and the nanoscale, conventional ball-on-flat tribometer experiments were conducted on the same samples. The coefficient of friction data are summarized in Fig. 19.42. The data shown in the bar plot are averages of three measurements. All of the lubricated



**Fig. 19.42** Summary of the coefficient of friction from ball-on-flat tests on uncoated and coated Si samples. The error bars represent  $\pm 1 \sigma$  based on three measurements performed (after [22])



samples are reported to have less wear scars as a result of the ball having to displace the lubricant before damaging the silicon surface. A reduction in the coefficient of friction arising from application of the lubricant film is observed, consistent with the nanoscale adhesion, friction, and wear results.

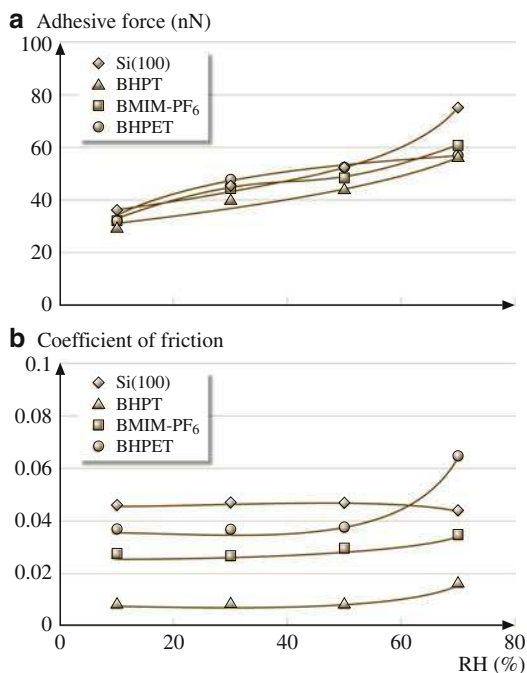
The  $\mu$  values of the lubricant samples obtained by using AFM are lower than the  $\mu$  obtained from the ball-on-flat tests. This is attributed to the difference in the length scales of the test techniques. An AFM tip simulates a single-asperity contact while the conventional friction test involves the contact of multiple asperities present in the test system. With regards to wear, the interface contact of the AFM and ball-on-flat techniques are different from each other such that one cannot expect both tests to show the same trend. On an AFM, the tip stress is very high such that material can be displaced more easily. For a ball-on-flat test, the tip exerts a lower pressure on the surface and the coating is in a confined geometry.

### Relative Humidity and Temperature Effect Measurements

The influence of relative humidity on adhesion and friction is summarized in Fig. 19.43. In general, the adhesive force increases with relative humidity. The condensed water in the humid environment facilitates meniscus formation between the tip and sample and higher adhesive forces. Since Si(100) is hydrophilic, it readily adsorbs water molecules. For the three ionic liquids, an increase in the adhesive force is also due to increased water adsorption. This comes from attractive electrostatic interactions (ion–dipole forces) between the individual ions and water molecules.

Water adsorption affects the coefficient of friction observed as a function of the relative humidity. In Si, the coefficient of friction is uniform at 10–50% RH, then decreases at 70% RH. The adsorbed water at higher humidity can lead to the formation of a continuous water layer separating the tip and sample surface, which can act as a lubricant. Although the adhesive force increases, the reduction in interfacial strength accounts for the slight decrease of the coefficient of friction at the highest range of humidity level examined. However, the presence of more water molecules at higher humidity has the opposite effect on the ionic liquid surfaces,

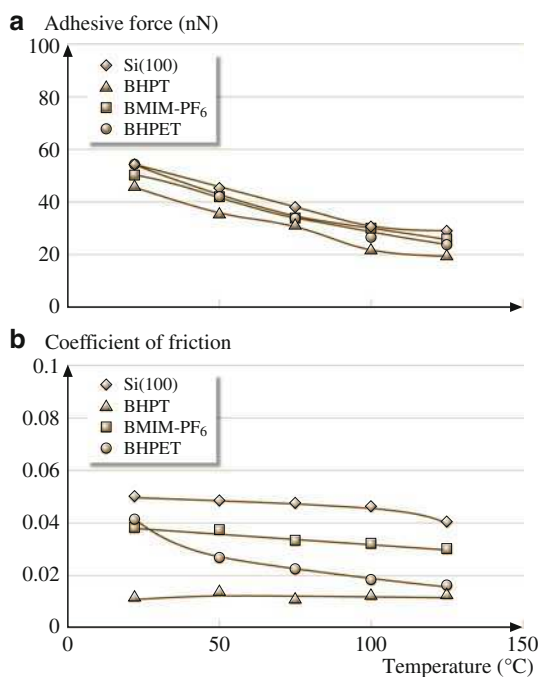
**Fig. 19.43** Influence of relative humidity (RH) on the adhesive force (a) and coefficient of friction (b) for unlubricated and lubricated tapes at 22°C (after [22])



where the coefficient of friction increases with humidity. The attractive ion–dipole forces between the ions and water are amplified at higher humidity because more water molecules are available. A greater attractive force between the tip and the surface leads to greater resistance to sliding and higher coefficient of friction. This is observed for both the monocationic (BMIM-PF<sub>6</sub>) and the dicationic (BHPT and BHPET) ionic liquid-coated surfaces. For BHPET, polar interactions between water and the oxygen atoms in the polyether (C–O–C) chain are possible and increase the adsorption of water to the surface. This could account for the larger rise in the coefficient of friction in the BHPET sample from 50% to 70% RH, compared with BMIM-PF<sub>6</sub> and BHPT.

The effect of temperature on the adhesion and friction properties of the ILs is summarized in Fig. 19.44. The adhesive and friction forces were measured from 22°C to 125°C. As shown in Fig. 19.44, the increase in test temperature leads to a decrease in the adhesive force and the coefficient of friction. The decrease in the adhesive force at higher temperatures is observed in all the samples, while the corresponding drop in the coefficient of friction is seen only for BMIM-PF<sub>6</sub>, BHPET, and the silicon substrate. At higher temperatures, the surface water molecules are desorbed, leading to the decrease in both the adhesive and friction forces. A reduction in the viscosity at higher temperatures can also facilitate the decrease in the friction force [26]. In BHPT, the coefficient of friction was not adversely affected as the test temperature was increased. This implies that, under ambient humidity conditions, the BHPT film does not adsorb a large amount of

**Fig. 19.44** Influence of temperature on the adhesive force (a) and coefficient of friction (b) for uncoated and coated Si samples at 50% RH air (after [22])



water molecules. Moreover, this also implies that the BHPT surface has weak interactions with surface water molecules, such that the friction force during sliding is not greatly affected.

### Fourier-Transform Infrared Spectroscopy

Figure 19.45 presents FTIR spectra obtained for the different ionic-liquid-coated samples, along with the uncoated Si substrate. The observed peaks are labeled with the corresponding chemical bonds. In the case of the Si substrate (with a contact angle of 40°) exposed to water molecules in the ambient, no peaks are observed. C–H stretching vibrations in the coated samples are observed in the 600–800 cm<sup>-1</sup> range. For BHPET, the strong peak at ≈ 1060 cm<sup>-1</sup> corresponds to the C–O–C vibration, which is prominent due to the presence of the polyether chain in its cation. This peak overlaps with the C–O vibration, which is present in BHPT as the terminal primary alcohol (C–OH). In BMIM-PF<sub>6</sub>, a peak appears in this range due to rocking vibrations of the methyl (CH<sub>3</sub>) substituent. The peak at 1,500–1,600 cm<sup>-1</sup> comes from the C=N vibrations, which is common to all three ionic liquids since they are all based on the imidazolium cation. However, it is not observed in BHPT as the C=N vibrations may be weak. The wide peak at 3,600–4,000 cm<sup>-1</sup> corresponds to hydrogen bonding, possibly due to

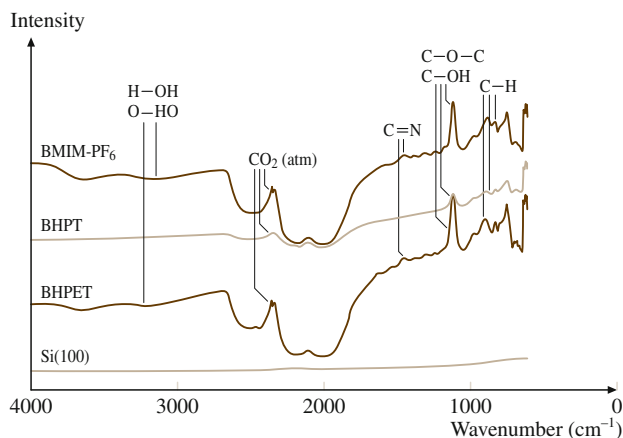


**Fig. 19.45** FTIR spectra of uncoated and coated Si samples. The chemical bonds (or species) are listed above the spectra to indicate the possible bonding modes that correspond to the observed peaks (after [22])

water molecules adsorbed on the surface [22, 77, 78]. This is present in BMIM-PF<sub>6</sub> and in BHPET but not in BHPT. This accounts for the much lower contact angle of BMIM-PF<sub>6</sub> and BHPET (39° and 59°, respectively) compared with BHPT (81°). This implies that the surface of BHPT is more hydrophobic compared with that of either BMIM-PF<sub>6</sub> or BHPET, which is consistent with the observed low coefficient of friction for BHPT [22].

### X-ray Photoelectron Spectroscopy

The XPS survey spectra obtained on the uncoated and coated Si samples are shown in Fig. 19.46a. In the uncoated sample, prominent peaks are observed at 99, 151, and 533 eV, corresponding to the binding energies of Si 2*p*, Si 2*s*, and O 1*s* electrons, respectively. Additional peaks are observed on the three coated samples at 285 and 689 eV, which correspond to C 1*s* and F 1*s* electrons, respectively. Smaller peaks observed at ≈ 1,000 eV on all samples are due to Auger lines (KLL transitions) for oxygen [79].

The high-resolution best-fit XPS spectra are shown in Fig. 19.46b for the Si 2*p*, C 1*s*, O 1*s*, and F 1*s* electrons. The peaks are labeled with the corresponding chemical bonds, which pertain to either the silicon substrate or groups found on the ionic liquid molecule. One noteworthy exception is the presence of peaks at ≈ 292 eV, which confirms the presence of CF<sub>2</sub> on the surface. This indicates the immobilization of the BHPT and BHPET ionic liquids, which occurs by the reaction of the anion with the hydroxyl groups present on the silicon surface [22, 23].

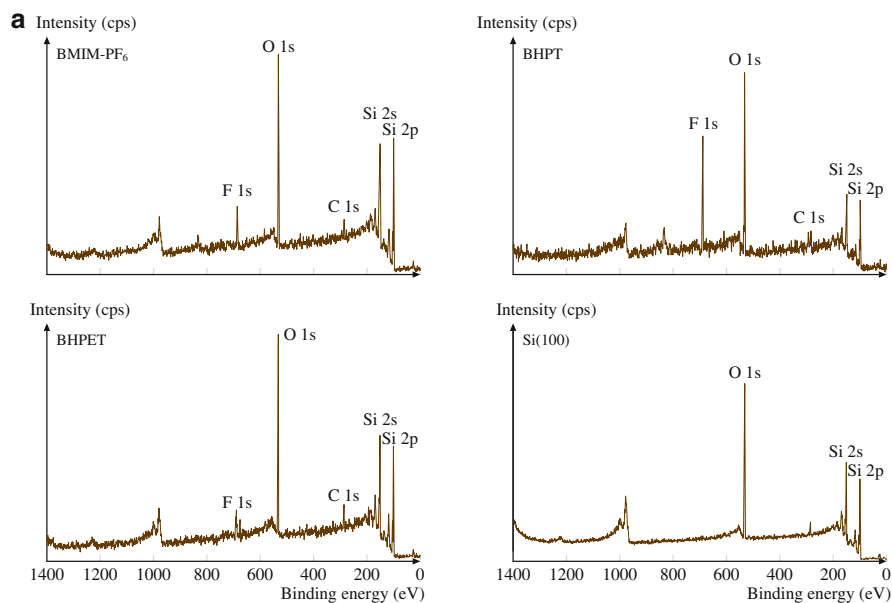
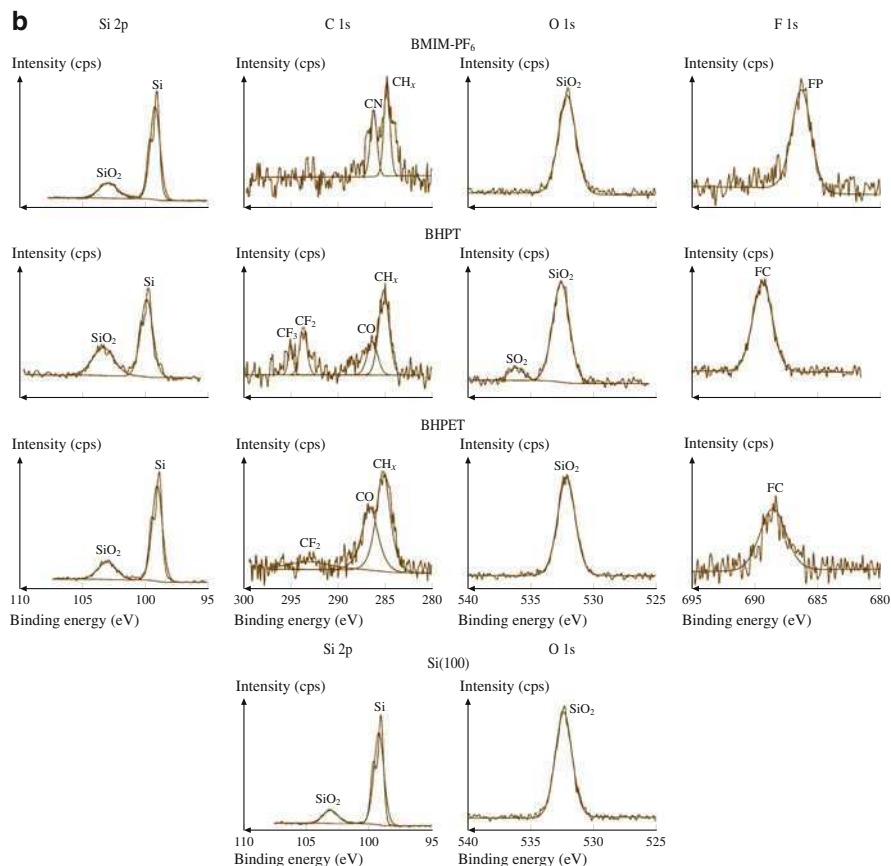


Fig. 19.46 (continued)

### Relationship Between IL Structure and Adhesion, Friction, and Wear Properties

Figure 19.47 presents an interpretation of how the IL cations interact with the silicon substrate. For the monocationic BMIM-PF<sub>6</sub>, only weak interactions between the imidazolium ring and the silicon surface are expected. For the dicationic ionic liquids, multiple cation attachment schemes are possible. In BHPT, the hydroxyl groups attached to the imidazolium cation at the ends of the chain provide a means for strong H-bonding interactions with active sites on the silicon surface. As shown in Fig. 19.47, either one (case 1) or two (case 2) hydroxyl groups can create this bond. The second case is particularly desirable because, if the two hydroxyl groups are bonded (i.e., not exposed to the surface), they are not available to interact with water molecules in the ambient, leading to a reduction in the adhesion and friction forces, as well as enhanced wear resistance [22].

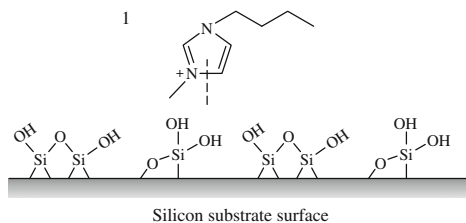
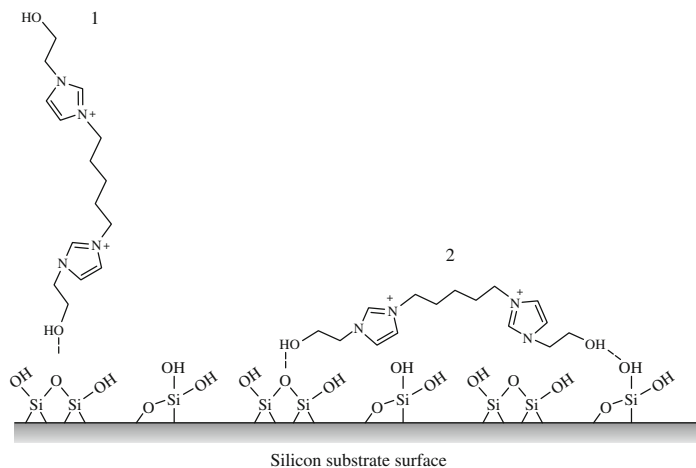
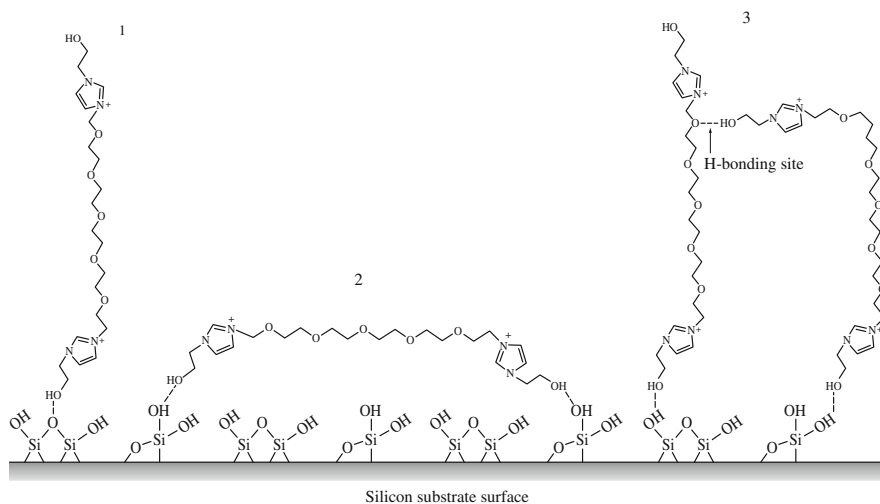
In BHPET, these hydroxyl group attachment schemes are also applicable. However, the additional mechanism of intramolecular hydrogen bonding can also take place (case 3). This is not as desirable as the second case because it depletes the available chain ends with hydroxyl groups which can bond to the silicon surface. The interaction of the lubricant film with the silicon substrate is weakened, and water molecules can displace the lubricant from the substrate. In addition, the polyether chain that links the two cations contains five oxygen atoms in each chain. These oxygen atoms can also form H-bonds with the water molecules in the ambient. This can account for the large difference in the friction properties between BHPET



**Fig. 19.46** (a) XPS spectra of uncoated and coated Si samples. Survey scan from 0 to 1,400 eV provides the surface elemental composition. (b) High-resolution (deconvoluted) XPS spectra for Si 2p, C 1s, O 1s, and F 1s reveal the different binding environments present on the surface (after [22])

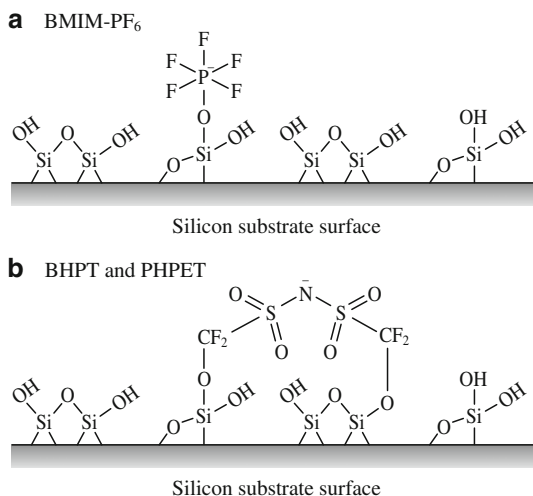
and BHPT. While the application of the BHPT film has lowered the coefficient of friction of the silicon surface, the BHPET film did not have a similar effect due to the molecular interactions described above. This interpretation of lubricant–substrate interaction is corroborated by the adhesion and friction data at varying humidity and temperatures, as well as the FTIR spectra. Both BMIM-PF<sub>6</sub> and BHPT have large peaks in their FTIR spectra that correspond to H-bonds of water molecules, which is consistent with the observed sensitivity of their adhesion and friction to the change in humidity and temperature. Meanwhile, BHPT does not have the aforementioned peak, and its adhesion and friction properties appear to be less sensitive to water molecules compared with the other two ionic liquids [22].

Figure 19.48 shows a schematic of the interaction of the anions with the silicon substrate. As mentioned previously, XPS spectra indicate immobilization of the

**a** BMIM- $\text{PF}_6$ **b** BHPT**c** BHPET

**Fig. 19.47** Schematic for the attachment of the cations of **(a)** BMIM- $\text{PF}_6$ , **(b)** BHPT, and **(c)** BHPET to silicon substrate (after [22])

**Fig. 19.48** Schematic for the attachment of the anions of (a) BMIM-PF<sub>6</sub>, and (b) BHPT and BHPET to silicon substrate (after [22])



ionic liquid, which occurs through the reaction of the anion with the hydroxyl groups on the substrate surface. In BMIM-PF<sub>6</sub>, the O attaches to P, while in BHPT and BHPET (which have the same anion), the O bonds to C. Since the reactions involve the creation of new covalent bonds, this implies that the anions of the investigated ILs are more strongly attached to the substrate compared with the cations, which are chemically adsorbed [22].

Based on the micro- and nanoscale friction and wear measurements, the ionic liquids show strong potential as lubricants for MEMS/NEMS because they have desirable thermal and electrical conductivity as well as desirable tribological properties.

## 19.5 Conclusions

Nanodeformation studies have shown that fully bonded Z-DOL lubricants behave as soft polymer coatings, while the unbonded lubricants behave liquid-like. AFM studies have shown that the physisorbed nonpolar molecules on a solid surface have an extended, flat conformation. The spreading property of PFPE is strongly dependent on the molecular end groups and the substrate chemistry.

Using solid-like Z-DOL (fully bonded) film can reduce the friction and adhesion of Si(100), whereas using liquid-like Z-15 lubricant shows a negative effect. Si(100) and Z-15 films show an apparent time effect. The friction and adhesion forces increase as a result of the growth of meniscus up to an equilibrium time, after which they remain constant. The use of Z-DOL (fully bonded) film can prevent rest-time effects. During sliding at high velocity, the meniscus is broken and does not have enough time to rebuild, which leads to a decrease of the friction force and adhesive force for Z-15 and Z-DOL (fully bonded). The influence of



relative humidity on friction and adhesion is dominated by the amount of adsorbed water molecules. Increasing humidity can either increase friction through increased adhesion by water meniscus or reduce it through an enhanced water-lubricating effect. Increasing temperature leads to desorption of the water layer, decrease of water surface tension, decrease of viscosity, and easier orientation of the Z-DOL (fully bonded) molecules. These changes cause a decrease of the friction force and adhesion at high temperature. During cycling tests, the molecular interaction between Z-15 molecules attached to the tip and the Z-15 molecules on the film surface causes an initial increase of friction. Wear tests show that Z-DOL (fully bonded) can apparently improve the wear resistance of silicon. Partially bonded PFPE film appears to be more durable than fully bonded films. These results suggest that partially/fully bonded films are good lubricants for micro/nanoscale devices operating under various environmental conditions.

The surface potential technique has been shown to be useful in detecting lubricant removal and initiation of substrate wear. The increase in surface potential is attributed to the change in the work function of the silicon after wear and electrostatic charge buildup of debris in the lubricant. Coatings with a mobile lubricant fraction were better able to protect the silicon substrate from wear compared with the fully bonded coating. This enhanced protection is attributed to a lubricant replenishment mechanism. The contact resistance technique provides information complementary to surface potential data in detecting exposure of the substrate after wear and is a promising method for studying conducting lubricants.

Degradation of novel PFPE lubricants – Z-DOL, Z-TETRAOL, A20H, and Z-DOL + A20H (vol.%30) – was studied. The coefficient of friction of Z-TETRAOL is lower than that of Z-DOL and A20H in high vacuum. Fully bonded Z-TETRAOL exhibited higher durability than fully bonded Z-DOL on Si, and both are more durable than untreated Z-DOL. A20H shows very high durability in high vacuum. Environment influences the friction and durability of PFPE films. Generally, PFPE films are less durable in high vacuum than in other environments because of intimate contact between the surfaces. In argon, the PFPE films show low friction and high durability. Water molecules can act as a lubricant for PFPE films at a moderate humidity level while they can penetrate the PFPE films and cause increased friction at a high humidity level. The durability of fully bonded Z-TETRAOL and partially bonded A20H is higher than that of Z-DOL in tested environments. The mixture of Z-DOL + A20H (vol.%30) shows low durability in high vacuum but high durability in argon and air at various humidity levels.

The ionic liquid BMIM-PF<sub>6</sub> exhibits low adhesion, friction, and wear properties comparable to the PFPE lubricant Z-TETRAOL. Based on the surface height, adhesion, and friction data, chemical bonding treatment facilitates attachment of the ionic liquid to the silicon substrate surface, leading to a more uniform coating and lower adhesion force and coefficient of friction. The partially bonded coatings have the lowest coefficient of friction and longest durability as they possess a desirable combination of lubricant bonded to the substrate as well as a mobile fraction which facilitates sliding. In micro- and nanoscale experiments, the ionic liquid exhibits durability comparable to that of the lubricant Z-TETRAOL, which

has high thermal stability and extremely low vapor pressure. The low postwear surface potential change observed on silicon coated with ionic liquid is indicative of enhanced charge dissipation compared with Z-TETRAOL-coated and uncoated surfaces, which are poor conductors. Contact resistance data is consistent with the surface potential data with regards to identifying the role of the mobile and immobile lubricant fractions in protecting the surface from wear.

The dicationic liquid BHPT exhibits superior nanoscale friction and wear resistance properties. This is attributed to the presence of a pentyl chain and hydroxyl groups on both chain ends, which facilitate molecular orientation as well as bonding interactions with the substrate surface. The other dicationic liquid investigated, BHPET, has less desirable adhesion, friction, and wear properties compared with either BHPT or BMIM-PF<sub>6</sub>. Intermolecular hydrogen bonding in BHPET reduces the chain ordering on the substrate surface, which accounts for the observed higher adhesive force and coefficient of friction compared with the other ionic liquids investigated. From the nanoscale wear tests, surface potential, and contact resistance imaging, it was found that the durability of the films decreases in the order: BHPT > BMIM-PF<sub>6</sub> > BHPET. The microscale coefficient of friction is higher than the nanoscale value due to the differences in length scale and configuration of the two test methods.

Nanotribological experiments performed under various humidity and temperature conditions indicate that the adhesive force and coefficient of friction of the ionic liquid films, especially BMIM-PF<sub>6</sub> and BHPET, are highly sensitive to the amount of water molecules present on the surface. This is confirmed by FTIR spectroscopy, where the BMIM-PF<sub>6</sub> and BHPET films show peaks corresponding to hydrogen bonding, mainly resulting from water adsorption and partially from intermolecular interactions. The absence of this peak in BHPT indicates that a much smaller amount of water is adsorbed by this IL, which is consistent with its superior nanotribological properties. The anions are more strongly attached to the substrate compared with the cations. The anions could be covalently bonded, while the cations are chemically adsorbed. XPS analysis confirms the immobilization of the anion onto the silicon substrate.

## References

1. B. Bhushan, *Principles and Applications of Tribology* (Wiley, New York, 1999)
2. B. Bhushan, *Introduction to Tribology* (Wiley, New York, 2002)
3. B. Bhushan, Magnetic recording surfaces, in *Characterization of Tribological Materials*, ed. by W.A. Glaeser (Butterworth Heinemann, Boston, 1993) pp. 116–133
4. V.J. Novotny, I. Hussla, J.M. Turelet, M.R. Philpott, Liquid polymer conformation on solid surfaces, *J. Chem. Phys.* **90**, 5861–5868 (1989)
5. V.J. Novotny, Migration of liquid polymers on solid surfaces, *J. Chem. Phys.* **92**, 3189–3196 (1990)
6. C.M. Mate, V.J. Novotny, Molecular conformation and disjoining pressures of polymeric liquid films, *J. Chem. Phys.* **94**, 8420–8427 (1991)

7. C.M. Mate, Application of disjoining and capillary pressure to liquid lubricant films in magnetic recording, *J. Appl. Phys.* **72**, 3084–3090 (1992)
8. G.G. Roberts, *Langmuir–Blodgett Films* (Plenum, New York, 1990)
9. A. Ulman, *An Introduction to Ultrathin Organic Films* (Academic, Boston, 1991)
10. B. Bhushan, *Tribology and Mechanics of Magnetic Storage Devices*, 2nd edn. (Springer, New York, 1996)
11. B. Bhushan, *Handbook of Micro/Nanotribology*, 2nd edn. (CRC, Boca Raton, 1999)
12. B. Bhushan, Macro- and microtribology of magnetic storage devices, in *Modern Tribology Handbook, Vol. 2: Materials, Coatings, and Industrial Applications*, ed. by B. Bhushan (CRC, Boca Raton, 2001) pp. 1413–1513
13. B. Bhushan, *Nanotribology and Nanomechanics – An Introduction*, 2nd edn. (Springer, Berlin, 2008)
14. B. Bhushan, Z. Zhao, Macroscale and microscale tribological studies of molecularly thick boundary layers of perfluoropolyether lubricants for magnetic thin-film rigid disks, *J. Inf. Storage Proc. Syst.* **1**, 1–21 (1999)
15. E. Hoque, J.A. DeRose, B. Bhushan, H.J. Mathieu, Self-assembled monolayers on aluminum and copper oxide surfaces: surface and interface characteristics, in *Applied Scanning Probe Methods IX*, ed. by B. Bhushan, H. Fuchs, M. Tomitori (Springer, Berlin, 2008) pp. 235–281
16. B. Bhushan, *Tribology Issues and Opportunities in MEMS* (Kluwer, Dordrecht, 1998)
17. B. Bhushan, Nanotribology and nanomechanics in nano/biotechnology, *Philos. Trans. R. Soc. A* **366**, 1499–1537 (2008)
18. B. Bhushan, J.N. Israelachvili, U. Landman, Nanotribology: Friction, wear and lubrication at the atomic scale, *Nature* **374**, 607–616 (1995)
19. B. Bhushan, Nanotribology, nanomechanics and nanomaterials characterization, *Philos. Trans. R. Soc. A* **366**, 1351–1381 (2008)
20. B. Bhushan, M. Palacio, B. Kinzig, AFM-based nanotribological and electrical characterization of ultrathin wear-resistant ionic liquid films, *J. Colloids Inter. Sci.* **317**, 275–287 (2008)
21. M. Palacio, B. Bhushan, Ultrathin wear-resistant ionic liquid films for novel MEMS/NEMS applications, *Adv. Mater.* **20**, 1194–1198 (2008)
22. M. Palacio, B. Bhushan, Molecularly thick dicationic ionic liquid films for nanolubrication, *J. Vac. Sci. Technol. A* **27**(4), 986–995 (2009)
23. B. Bhushan, K. Kwak, The role of lubricants, scanning velocity and operating environment in adhesion, friction and wear of Pt-Ir coated probes for atomic force microscopy probe-based ferroelectric recording technology, *J. Phys. Condens. Matter* **20**, 325240 (2008)
24. B. Bhushan, K. Kwak, M. Palacio, Nanotribology and nanomechanics of AFM probe based data recording technology, *J. Phys. Condens. Matter* **20**, 365207 (2008)
25. M. Palacio, B. Bhushan, Nanotribological and nanomechanical properties of lubricated PZT thin films for ferroelectric data storage applications, *J. Vac. Sci. Technol. A* **26**, 768–776 (2008)
26. H. Liu, B. Bhushan, Nanotribological characterization of molecularly thick lubricant films for applications to MEMS/NEMS by AFM, *Ultramicroscopy* **97**, 321–340 (2003)
27. J. Ruhe, G. Blackman, V.J. Novotny, T. Clarke, G.B. Street, S. Kuan, Thermal attachment of perfluorinated polymers to solid surfaces, *J. Appl. Polym. Sci.* **53**, 825–836 (1994)
28. J. Ruhe, V. Novotny, T. Clarke, G.B. Street, Ultrathin perfluoropolyether films – influence of anchoring and mobility of polymers on the tribological properties, *ASME J. Tribol.* **118**, 663–668 (1996)
29. V.N. Koinkar, B. Bhushan, Microtribological studies of unlubricated and lubricated surfaces using atomic force/friction force microscopy, *J. Vac. Sci. Technol. A* **14**, 2378–2391 (1996)
30. G.S. Blackman, C.M. Mate, M.R. Philpott, Interaction forces of a sharp tungsten tip with molecular films on silicon surface, *Phys. Rev. Lett.* **65**, 2270–2273 (1990)
31. G.S. Blackman, C.M. Mate, M.R. Philpott, Atomic force microscope studies of lubricant films on solid surfaces, *Vacuum* **41**, 1283–1286 (1990)
32. C.A. Kim, H.J. Choi, R.N. Kono, M.S. Jhon, Rheological characterization of perfluoropolyether lubricant, *Polym. Prepr. Am.* **40**, 647–649 (1999)

33. M. Ruths, S. Granick, Rate-dependent adhesion between opposed perfluoropoly(alkylether) layers: Dependence on chain-end functionality and chain length, *J. Phys. Chem. B* **102**, 6056–6063 (1998)
34. X. Ma, J. Gui, K.J. Grannen, L.A. Smoliar, B. Marchon, M.S. Jhon, C.L. Bauer, Spreading of PFPE lubricants on carbon surfaces: Effect of hydrogen and nitrogen content, *Tribol. Lett.* **6**, 9–14 (1999)
35. U. Jonsson, B. Bhushan, Measurement of rheological properties of ultrathin lubricant films at very high shear rates and near-ambient pressure, *J. Appl. Phys.* **78**, 3107–3109 (1995)
36. C. Hahm, B. Bhushan, High shear rate viscosity measurement of perfluoropolyether lubricants for magnetic thin-film rigid disks, *J. Appl. Phys.* **81**, 5384–5386 (1997)
37. C.M. Mate, Atomic-force-microscope study of polymer lubricants on silicon surface, *Phys. Rev. Lett.* **68**, 3323–3326 (1992)
38. C.M. Mate, Nanotribology of lubricated and unlubricated carbon overcoats on magnetic disks studied by friction force microscopy, *Surf. Coat. Technol.* **62**, 373–379 (1993)
39. S.J. O'Shea, M.E. Welland, T. Rayment, Atomic force microscope study of boundary layer lubrication, *Appl. Phys. Lett.* **61**, 2240–2242 (1992)
40. S.J. O'Shea, M.E. Welland, J.B. Pethica, Atomic force microscopy of local compliance at solid–liquid interface, *Chem. Phys. Lett.* **223**, 336–340 (1994)
41. B. Bhushan, L. Yang, C. Gao, S. Suri, R.A. Miller, B. Marchon, Friction and wear studies of magnetic thin-film rigid disks with glass–ceramic, glass, and aluminum–magnesium substrates, *Wear* **190**, 44–59 (1995)
42. V.N. Koinkar, B. Bhushan, Micro/nanoscale studies of boundary layers of liquid lubricants for magnetic disks, *J. Appl. Phys.* **79**, 8071–8075 (1996)
43. B. Bhushan, S. Sundararajan, Micro/nanoscale friction and wear mechanisms of thin films using atomic force and friction force microscopy, *Acta Mater.* **46**, 3793–3804 (1998)
44. B. Bhushan, C. Dandavate, Thin-film friction and adhesion studies using atomic force microscopy, *J. Appl. Phys.* **87**, 1201–1210 (2000)
45. M. Palacio, B. Bhushan, Surface potential and resistance measurements for detecting wear of chemically-bonded and unbonded molecularly thick perfluoropolyether lubricant films using atomic force microscopy, *J. Colloids Inter. Sci.* **315**, 261–269 (2007)
46. M. Palacio, B. Bhushan, Nanotribological properties of novel lubricants for magnetic tapes, *Ultramicroscopy* **109**(8), 980–990 (2009)
47. S. Sundararajan, B. Bhushan, Static friction and surface roughness studies of surface micro-machined electrostatic micromotors using an atomic force/friction force microscope, *J. Vac. Sci. Technol. A* **19**, 1777–1785 (2001)
48. B. Bhushan, J. Ruan, Atomic-scale friction measurements using friction force microscopy: Part II – Application to magnetic media, *ASME J. Tribol.* **116**, 389–396 (1994)
49. T. Stifter, O. Marti, B. Bhushan, Theoretical investigation of the distance dependence of capillary and van der Waals forces in scanning probe microscopy, *Phys. Rev. B* **62**, 13667–13673 (2000)
50. J.N. Israelachvili, *Intermolecular and Surface Forces*, 2nd edn. (Academic, London, 1992)
51. S.K. Chilamakuri, B. Bhushan, A comprehensive kinetic meniscus model for prediction of long-term static friction, *J. Appl. Phys.* **15**, 4649–4656 (1999)
52. H. Ishigaki, I. Kawaguchi, M. Iwasa, Y. Toibana, Friction and wear of hot pressed silicon nitride and other ceramics, *ASME J. Tribol.* **108**, 514–521 (1986)
53. T.E. Fischer, *Tribochemistry*, *Annu. Rev. Mater. Sci.* **18**, 303–323 (1988)
54. K. Mizuhara, S.M. Hsu, Tribochemical reaction of oxygen and water on silicon surfaces, in *Wear Particles*, ed. by D. Dowson (Elsevier, New York, 1992) pp. 323–328
55. S. Danyluk, M. McNallan, D.S. Park, Friction and wear of silicon nitride exposed to moisture at high temperatures, in *Friction and Wear of Ceramics*, ed. by S. Jahanmir (Dekker, New York, 1994) pp. 61–79
56. V.A. Muratov, T.E. Fischer, Tribochemical polishing, *Annu. Rev. Mater. Sci.* **30**, 27–51 (2000)
57. H. Yoshizawa, J.N. Israelachvili, Fundamental mechanisms of interfacial friction – Part II: Stick slip friction of spherical and chain molecules, *J. Phys. Chem.* **97**, 11300–11313 (1993)

58. H. Yoshizawa, Y.L. Chen, J.N. Israelachvili, Fundamental mechanisms of interfacial friction – Part I: Relationship between adhesion and friction, *J. Phys. Chem.* **97**, 4128–4140 (1993)
59. K.C. Eapen, S.T. Patton, J.S. Zabinski, Lubrication of microelectromechanical systems (MEMS) using bound and mobile phase of fomblin Z-DOL, *Tribol. Lett.* **12**, 35–41 (2002)
60. D. DeVecchio, B. Bhushan, Use of a nanoscale Kelvin probe for detecting wear precursors, *Rev. Sci. Instrum.* **69**, 3618–3624 (1998)
61. M. Palacio, B. Bhushan, Wear detection of candidate MEMS/NEMS lubricant films using atomic force microscopy-based surface potential measurements, *Scr. Mater.* **57**, 821–824 (2007)
62. Z. Tao, B. Bhushan, Bonding, degradation, and environmental effects on novel perfluoropolyether lubricants, *Wear* **259**, 1352–1361 (2005)
63. B. Bhushan, Z. Tao, Lubrication of advanced metal evaporated tape using novel perfluoropolyether lubricants, *Microsyst. Technol.* **12**, 579–587 (2006)
64. B. Bhushan, M. Cichomski, Z. Tao, N.T. Tran, T. Ethen, C. Merton, R.E. Jewett, Nanotribological characterization and lubricant degradation studies of metal-film magnetic tapes using novel lubricants, *ASME J. Tribol.* **129**, 621–627 (2007)
65. B. Bhushan, J. Ruan, Tribological performance of thin film amorphous carbon overcoats for magnetic recording disks in various environments, *Surf. Coat. Technol.* **68/69**, 644–650 (1994)
66. X. Zhao, B. Bhushan, Comparison studies on degradation mechanisms of perfluoropolyether lubricants and model lubricants, *Tribol. Lett.* **9**, 187–197 (2000)
67. X. Zhao, B. Bhushan, Studies on degradation mechanisms of lubricants for magnetic thin-film rigid disks, *J. Eng. Tribol.* **215**, 173–188 (2001)
68. X. Zhao, B. Bhushan, C. Kajdas, Lubrication studies of head-disk interfaces in a controlled environment – Part 2: Degradation mechanisms of perfluoropolyether lubricants, *J. Eng. Tribol.* **214**, 547–559 (2000)
69. B.J. Kinzig, P. Sutor, *Ionic Liquids: Novel Lubrication for Air and Space*, Phase I, Final Report for AFOSR/NL (Surfaces Research and Applications Inc., Lenexa, 2005)
70. R.A. Reich, P.A. Stewart, J. Bohaychick, J.A. Urbanski, Base oil properties of ionic liquids, *Lubr. Eng.* **49**, 16–21 (2003)
71. H. Wang, Q. Lu, C. Ye, W. Liu, Z. Cui, Friction and wear behaviors of ionic liquid of alkylimidazolium hexafluorophosphates as lubricants for steel/steel contacts, *Wear* **256**, 44–48 (2004)
72. G.J. Kabo, A.V. Blokhin, Y.U. Paulechka, A.J. Kabo, M.P. Shymanovich, J.W. Magee, Thermodynamic properties of 1-butyl-3-methylimidazolium hexafluorophosphate in the condensed state, *J. Chem. Eng. Data* **49**, 453–461 (2004)
73. C. Frez, G.J. Diebold, C.D. Tran, S. Yu, Determination of thermal diffusivities, thermal conductivities and sound speed of room-temperature ionic liquids by the transient grating technique, *J. Chem. Eng. Data* **51**, 1250–1255 (2006)
74. J.L. Anderson, R. Ding, A. Ellern, D.W. Armstrong, Structure and properties of high stability germinal dicationic ionic liquids, *J. Am. Chem. Soc.* **127**, 593–604 (2005)
75. T. Payagala, J. Huang, Z.S. Breitbart, P.S. Sharma, D.W. Armstrong, Unsymmetrical dicationic ionic liquids: Manipulation of physicochemical properties using specific structural architectures, *Chem. Mater.* **19**, 5848–5850 (2007)
76. M.H. Valkenberg, C. deCastro, W.F. Holderich, Immobilization of ionic liquids on solid supports, *Green Chem.* **4**, 88–93 (2002)
77. R.T. Morrison, R.N. Boyd, *Organic Chemistry*, 6th edn. (Wiley, New York, 1992)
78. L. Zhang, Q. Zhang, J. Li, Electrochemical behaviors and spectral studies of ionic liquid (1-butyl-3-methylimidazolium tetrafluoroborate) based on sol-gel electrode, *J. Electroanal. Chem.* **603**, 243–248 (2007)
79. L.C. Feldman, J.W. Mayer, *Fundamentals of Surface and Thin Film Analysis* (Prentice Hall, Upper Saddle River, 1986)

## **Part V**

# **Biomimetics**

## Chapter 20

# Biomimetics Inspired Surfaces for Superhydrophobicity, Self-cleaning, Low Adhesion, and Drag Reduction

Bharat Bhushan and Yong Chae Jung

**Abstract** Nature has developed materials, objects, and processes that function from the macroscale to the nanoscale. The emerging field of biomimetics allows one to mimic biology or nature to develop nanomaterials, nanodevices, and processes which provide desirable properties. Hierarchical structures with dimensions of features ranging from the macroscale to the nanoscale are extremely common in nature to provide properties of interest. There are a large number of objects including bacteria, plants, land and aquatic animals, and seashells with properties of commercial interest. Certain plant leaves, such as Lotus leaves, are known to be superhydrophobic and self-cleaning due to the hierarchical roughness of their leaf surfaces. The self-cleaning phenomenon is widely known as the “Lotus effect”. These surfaces with high contact angle and low contact angle hysteresis with a self-cleaning effect also exhibit low adhesion and drag reduction for fluid flow. In this article, the theoretical mechanisms of the wetting of rough surfaces are presented followed by the characterization of natural leaf surfaces. The next logical step is to realize superhydrophobic surfaces based on understanding of the leaves. Next, a comprehensive review is presented on artificial superhydrophobic surfaces fabricated using various fabrication techniques and the influence of micro-, nano- and hierarchical structures on superhydrophobicity, self-cleaning, low adhesion, and drag reduction. An aquatic animal, such as a shark, is another model from nature for the reduction of drag in fluid flow. The artificial surfaces from the shark skin have been created, and the influence of structure on drag reduction efficiency is discussed. Furthermore, oleophobic surfaces can be used as a biomimetic coating that prevents contamination of the underwater parts of ships by biological and organic contaminants, including oil. The article discusses the wetting behavior of oil droplets on various superoleophobic surfaces.

**Keywords** Biomimetics · Lotus · Plants · Shark skin · Aquatic animals · Superhydrophobicity · Superoleophobicity · Self Cleaning · Adhesion · Drag

## 20.1 Introduction

Biologically inspired design, adaptation, or derivation from nature is referred to as ‘biomimetics’. It means mimicking biology or nature. Biomimetics is derived from the Greek word biomimesis. The word was coined by polymath Otto Schmitt in 1957, who, in his doctoral research, developed a physical device that mimicked the electrical action of a nerve. Other words used include bionics (coined in 1960 by Jack Steele of Wright–Patterson Air Force Base in Dayton, OH), biomimicry, and biognosis. The field of biomimetics is highly interdisciplinary. It involves the understanding of biological functions, structures, and principles of various objects found in nature by biologists, physicists, chemists, and material scientists, and the design and fabrication of various materials and devices of commercial interest by engineers, material scientists, chemists, and others. The word biomimetics first appeared in Webster’s dictionary in 1974 and is defined as ‘the study of the formation, structure or function of biologically produced substances and materials (as enzymes or silk) and biological mechanisms and processes (as protein synthesis or photosynthesis) especially for the purpose of synthesizing similar products by artificial mechanisms which mimic natural ones’ [1].

Nature has gone through evolution over the 3.8 Gyr since life is estimated to have appeared on the Earth [2]. Nature has evolved objects with high performance using commonly found materials. These function on the macroscale to the nanoscale. The understanding of the functions provided by objects and processes found in nature can guide us to imitate and produce nanomaterials, nanodevices, and processes [1].

There are a large number of objects, including bacteria, plants, land and aquatic animals, and seashells, with properties of commercial interest. Figure 20.1 shows a montage of some examples from nature [1]. Some leaves of water-repellent plants, such as *Nelumbo nucifera* (Lotus), are known to be superhydrophobic and self-cleaning due to hierarchical roughness (microbumps superimposed with a nanostructure) and the presence of a hydrophobic wax coating [1, 4, 10–15]. Water droplets on these surfaces readily sit on the apex of nanostructures because air bubbles fill in the valleys of the structure under the droplet. Therefore, these leaves exhibit considerable superhydrophobicity (Fig. 20.1a). Two strategies used for catching insects by plants for digestion are having sticky surfaces or sliding structures. As an example, for catching insects using sticky surfaces, the glands of the carnivorous plants of the genus *Pinguicula* (butterworts) and *Drosera* (sundew), shown in Fig. 20.1b, secrete adhesives and enzymes to trap and digest small insects, such as mosquitoes and fruit flies [4]. Pond skaters (*Gerris remigis*) have the ability to stand and walk upon a water surface without getting wet (Fig. 20.1c). Even the impact of rain droplets with a size greater than the pond skater’s size does not make it immerse in the water. Gao and Jiang [5] showed that the special hierarchical structure of the pond skater’s legs, which are covered by large numbers of oriented tiny hairs (microsetae) with fine nanogrooves and covered with cuticle wax, makes the leg surfaces superhydrophobic, is responsible for the water resistance, and



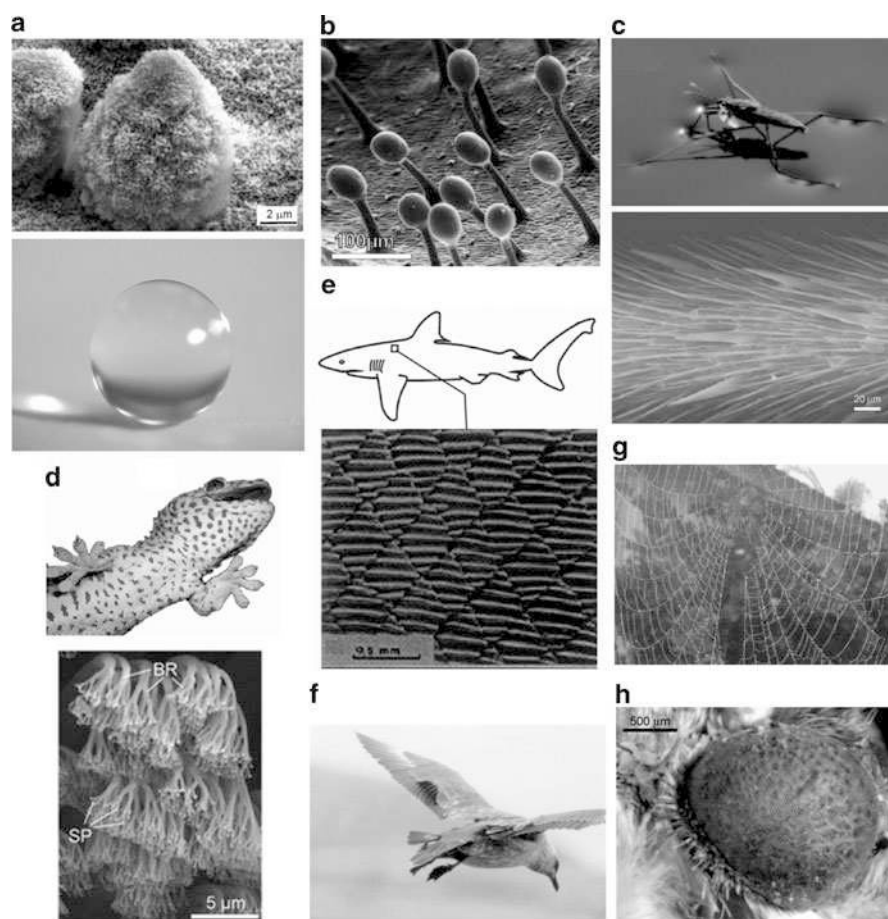


**Fig. 20.1** Montage of some examples from nature: (a) Lotus effect [3], (b) glands of carnivorous plant secrete adhesive to trap insects [4], (c) pond skater walking on water [5], (d) gecko foot exhibiting reversible adhesion [6], (e) scale structure of shark reducing drag [7], (f) wings of a bird in landing approach, (g) spiderweb made of silk material [8], and (h) antireflective moth's eye [9]

enables them to stand and walk quickly on the water surface. A gecko is the largest animal that can produce high (dry) adhesion to support its weight with a high factor of safety. Gecko skin is comprised of a complex hierarchical structure of lamellae, setae, branches, and spatula [6, 16, 17]. The attachment pads on two feet of the Tokay gecko have an area of approximately  $220 \text{ mm}^2$  (Fig. 20.1d). Approximately  $3 \times 10^6$  setae on their toes can produce a clinging ability of approximately 20 N (vertical force required to pull a lizard down a nearly vertical ( $85^\circ$ ) surface) and allow them to climb vertical surfaces at speeds of over 1 m/s, with the capability to attach or detach their toes in milliseconds [17]. Shark skin, which is a model from nature for a low drag surface, is covered by very small individual tooth-like scales

called dermal denticles (little skin teeth), ribbed with longitudinal grooves (aligned parallel to the local flow direction of the water). These grooved scales reduce the formation of vortices present on a smooth surface, resulting in water moving efficiently over their surface [18]. An example of scale structure on the right front of a Galapagos shark (*Carcharhinus galapagensis*) is shown in Fig. 20.1e [7]. Birds consist of several consecutive rows of covering feathers on their wings, which are flexible (Fig. 20.1f). These movable flaps develop the lift. When a bird lands, a few feathers are deployed in front of the leading edges of the wings, which help to reduce the drag on the wings. The spider generates silk fiber and has a sufficient supply of raw material for its silk to span great distances [8, 19]. Spiderweb is a structure built of a one-dimensional fiber (Fig. 20.1g). The fiber is very strong and continuous and is insoluble in water. The web can hold a significant amount of water droplets, and it is resistant to rain, wind, and sunlight [8, 20]. The eyes of moths are antireflective to visible light and consist of hundreds of hexagonally organized nanoscopic pillars, each approximately 200 nm in diameter and height, which result in a very low reflectance for visible light (Fig. 20.1h) [9, 21]. These nanostructures' optical surfaces make the eye surface nearly antireflective in any direction.

This article primarily focuses on water-repellent surfaces such as the Lotus leaf (Fig. 20.1a), which exhibits superhydrophobicity, self-cleaning, low adhesion, and drag reduction. Aquatic animal skin, such as shark skin (Fig. 20.1e), is a model from nature for drag reduction, and is also explored. Furthermore, oleophobic and self-cleaning surfaces inspired from aquatic animals are discussed.

### 20.1.1 Definitions and Applications

The primary parameter that characterizes wetting is the static contact angle, which is defined as the angle that a liquid makes with a solid. The contact angle depends on several factors, such as surface energy, surface roughness, and its cleanliness [22–27]. If the liquid wets the surface (referred to as wetting liquid or hydrophilic surface), the value of the static contact angle is  $0 \leq \theta \leq 90^\circ$ , whereas if the liquid does not wet the surface (referred to as a non-wetting liquid or hydrophobic surface), the value of the contact angle is  $90^\circ < \theta \leq 180^\circ$ . The term hydrophobic/philic, which was originally applied only to water (“hydro-” means “water” in Greek), is often used to describe the contact of a solid surface with any liquid. The term “oleophobic/philic” is used with regard to wetting by oil and organic liquids. The term “amphiphobic/philic” is used for surfaces that are both hydrophobic/philic and oleophobic/philic. Surfaces with high energy, formed by polar molecules, tend to be hydrophilic, whereas those with low energy and built of non-polar molecules tend to be hydrophobic.

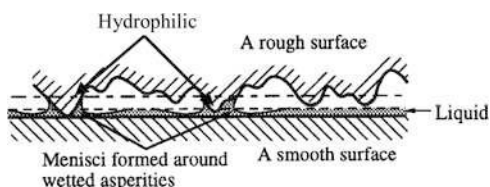
Surfaces with a contact angle of less than  $10^\circ$  are called superhydrophilic, while surfaces with a contact angle between  $150^\circ$  and  $180^\circ$  are called superhydrophobic. In fluid flow, in order to have low drag and for applications requiring the

self-cleaning feature, in addition to the high contact angle, superhydrophobic surfaces should also have very low water contact angle hysteresis. Water droplets roll off (with some slip) on these surfaces and take contaminants with them, providing the self-cleaning ability known as the “Lotus effect”. The contact angle at the front of the droplet (advancing contact angle) is greater than that at the back of the droplet (receding contact angle), resulting in contact angle hysteresis (CAH), which is the difference between the advancing and receding contact angles, representing two stable values. It occurs due to surface roughness and surface heterogeneity. Contact angle hysteresis reflects the irreversibility of the wetting/dewetting cycle. It is a measure of energy dissipation during the flow of a droplet along a solid surface. At a low value of CAH, the droplets may roll in addition to slide, which facilitates removal of contaminant particles. Surfaces with low contact angle hysteresis have a low water roll-off (tilt) angle, which denotes the angle to which a surface must be tilted for roll off of water drops [27–34]. Surfaces with CAH or a low tilting angle of less than  $<10^\circ$  are generally referred to as self-cleaning surfaces. Self-cleaning surfaces are of interest in various applications, including self-cleaning windows, windshields, exterior paints for buildings and navigation ships, utensils, roof tiles, textiles, solar panels, and applications requiring antifouling and a reduction of drag in fluid flow, e.g., in micro/nanochannels.

Superhydrophobic surfaces can also be used for energy conservation and conversion [35–37]. Recent advances in superhydrophobic surfaces make such applications possible. Several concepts can be used. First, the hydrophobic/philic properties of a surface significantly affect the capillary adhesion force that, in turn, affects friction and energy dissipation during the sliding contact of solid surfaces. Selection of a proper superhydrophobic surface allows the reduction of energy dissipation. Second, superhydrophobic and superoleophobic surfaces can be used for fuel economy. Third, the recently discovered effect of reversible superhydrophobicity provides potential for new ways of energy conversion such as the microscale capillary engine.

Wetting may lead to the formation of concave shaped menisci at the interface between hydrophilic solid bodies during static or sliding contact. These menisci develop a negative pressure leading to an intrinsic attractive force which increases adhesion and friction (Fig. 20.2). In some cases, the wet friction force can be greater than the dry friction force, which is usually undesirable [24–26, 38, 39]. On the other hand, high adhesion is desirable in some applications, such as adhesive tapes and adhesion of cells to biomaterial surfaces; therefore, enhanced wetting would be desirable in these applications. Numerous applications, such as magnetic storage

**Fig. 20.2** A schematic diagram of condensed water vapor from the environment forming meniscus bridges at asperity contacts which lead to an intrinsic attractive force



devices and micro/nanoelectromechanical systems (MEMS/NEMS), require surfaces with low adhesion and stiction [26, 38–43]. As the size of these devices decreases, surface forces tend to dominate over the volume forces, and adhesion and stiction constitute a challenging problem for proper operation of these devices. This makes the development of superhydrophobic surfaces with non-adhesive characteristics crucial for many of these emerging applications.

### 20.1.2 Natural Superhydrophobic, Self-cleaning, Low Adhesion, and Drag Reduction Surfaces

In the 1990s, biologists and materials scientists started to study natural superhydrophobic surfaces. Among them are the leaves of water-repellent plants such as *Nelumbo nucifera* (Lotus) and *Colocasia esculenta*, which have high contact angles with water (Fig. 20.3) [1, 4, 10–15]. The leaf surface is very rough due to so-called papillose epidermal cells, which form papillae or microasperities. In addition to the microscale roughness, the surface of the papillae is also rough, with nanoscale asperities composed of three-dimensional epicuticular waxes which are long chain hydrocarbons and hydrophobic. The waxes of Lotus exist as tubules, but on other leaves, waxes exist also in the form of platelets or other morphologies [4, 15]. The hierarchical structure of these leaves has been studied by Burton and Bhushan [13] and Bhushan and Jung [14]. The water droplets on these surfaces readily sit on the

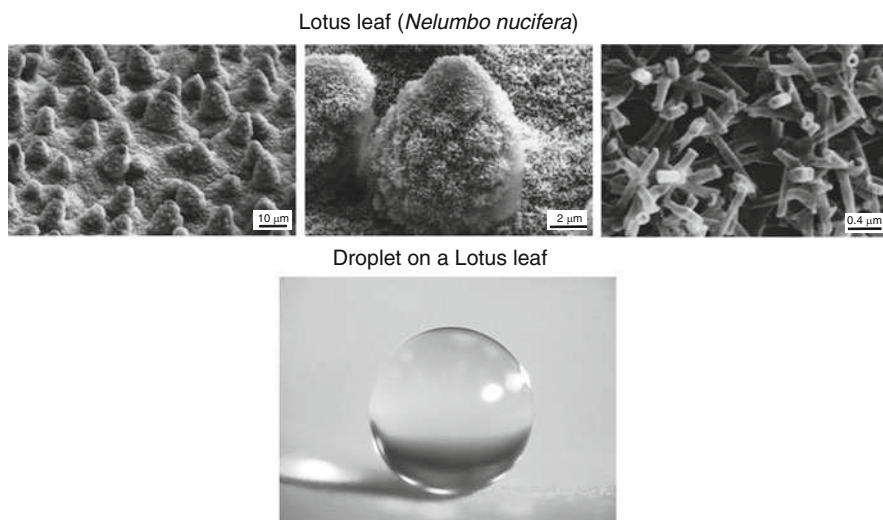


**Fig. 20.3** SEM micrographs (shown at three magnifications) of Lotus (*Nelumbo nucifera*) leaf surface which consists of microstructure formed by papillose epidermal cells covered with 3-D epicuticular wax tubules on surface, which create nanostructure, and image of water droplet sitting on the Lotus leaf [3]

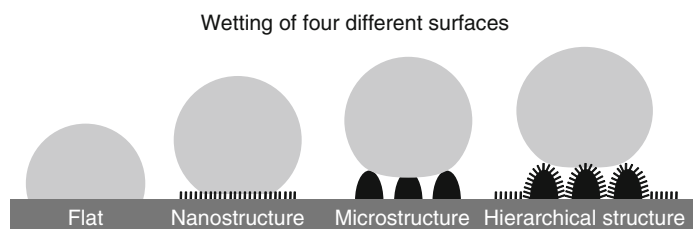


**Fig. 20.4** Schematic and wetting of the four different surfaces. The largest contact area between the droplet and the surface is given in flat and microstructured surfaces, but is reduced in nanostructured surfaces and is minimized in hierarchical structured surfaces

apex of the nanostructures because air bubbles fill in the valleys of the structure under the droplet. Therefore, these leaves exhibit considerable superhydrophobicity. Static contact angle and contact angle hysteresis of a Lotus leaf are about  $164^\circ$  and  $3^\circ$ , respectively [3, 44]. The water droplets on the leaves remove any contaminant particles from their surfaces when they roll off, leading to self-cleaning [10]. It has been reported that all superhydrophobic and self-cleaning leaves consist of an intrinsic hierarchical structure [4, 15]. Hierarchical structure provides air pocket formation, leading to the lowest contact area of an applied water droplet (Fig. 20.4), resulting in the reduction of contact angle hysteresis, tilt angle, and adhesive force [3, 27, 30]. Other examples of biological objects include water striders (*Gerris remigis*) [5] and mosquito (*Culex pipiens*) eyes [45]. Their hierarchical structures are responsible for superhydrophobicity. Duck feathers and butterfly wings also provide superhydrophobicity [1]. Their corrugated surfaces provide air pockets that prevent water from completely touching the surface.

### 20.1.3 Natural Superoleophobic, Self-cleaning, and Drag Reduction Surfaces

A model surface for superoleophobicity and self-cleaning is provided by fish which are known to be well protected from contamination by oil pollution although they are wetted by water [36]. Fish scales have a hierarchical structure consisting of sector-like scales with diameters of 4–5 mm covered by papillae 10–300  $\mu\text{m}$  in length and 30–40  $\mu\text{m}$  in width [46]. Shark skin, which is a model from nature for a low drag surface, is covered by very small individual tooth-like scales called dermal denticles (little skin teeth), ribbed with longitudinal grooves (aligned parallel to the local flow direction of the water). These grooved scales reduce vortices formation present on a smooth surface, resulting in water moving efficiently over their surface [1, 18, 47, 48]. The water surrounding these complex structures can lead to protection from marine fouling and play a role in the defense against adhesion and growth of marine organisms, e.g., bacteria and algae [4, 9]. If oil is present on the surfaces in air or water, surfaces are known to be oleophobic and may provide

self-cleaning and anti-fouling. The many sea animals including fish and shark are known to be oleophobic under water. Superoleophobic surfaces can also reduce significant losses of residual fuel in fuel tanks and pipes [35].

#### ***20.1.4 Roughness-Induced Superhydrophobicity, Self-cleaning, Low Adhesion, and Drag Reduction***

One of the ways to increase the hydrophobic or hydrophilic properties of a surface is to increase surface roughness, so roughness-induced hydrophobicity or hydrophilicity has become the subject of extensive investigations. Wenzel [49] suggested a simple model predicting that the contact angle of a liquid with a rough surface is different from that with a smooth surface. Cassie and Baxter [50] showed that a gaseous phase including water vapor, commonly referred to as “air” in the literature, may be trapped in the cavities of a rough surface, resulting in a composite solid–liquid–air interface, as opposed to the homogeneous solid–liquid interface. These two models describe two possible wetting regimes or states: the homogeneous (Wenzel) and the composite (Cassie–Baxter) regimes. Johnson and Dettre [51] showed that the homogeneous and composite interfaces correspond to the two equilibrium states of a droplet. Many authors have investigated the stability of artificial superhydrophobic surfaces and showed that whether the interface is homogeneous or composite may depend on the history of the system, in particular whether the liquid was applied from the top or condensed at the bottom [52–57]. Extrand [28] pointed out that whether the interface is homogeneous or composite depends on roughness structure and droplet size. It has also been suggested that the hierarchical roughness, composed by superposition of two roughness patterns at different length-scales [27, 31–33, 36, 37, 58–64], and fractal roughness [33, 65] may enhance superhydrophobicity.

Herminghaus [58] showed that certain self-affine profiles may result in superhydrophobic surfaces even for wetting liquids, if the local equilibrium condition for the triple line (line of contact between solid, liquid and air) is satisfied. Nosonovsky and Bhushan [66, 67] pointed out that such configurations, although formally possible, are likely to be unstable. Nosonovsky and Bhushan [67, 68] proposed a probabilistic model for wetting of rough surfaces with a certain probability associated with every equilibrium state. According to their model, the overall contact angle with a two-dimensional rough profile is calculated by assuming that the overall configuration of a droplet occurs as a result of superposition of numerous metastable states. The probability-based concept is consistent with the experimental data [3, 30, 44, 69–78], which suggests that the transition between the composite and homogeneous interfaces is gradual, rather than instant. Nosonovsky and Bhushan [27, 31–33, 61, 63, 64, 79–81] have identified mechanisms which lead to the destabilization of the composite interface, namely the capillary waves, condensation and accumulation of nanodroplets, and surface inhomogeneity. These mechanisms are scale-dependent, with different characteristic length scales.



To effectively resist these scale-dependent mechanisms, a multiscale (hierarchical) roughness is required. High asperities resist the capillary waves, while nanobumps prevent nanodroplets from filling the valleys between asperities and pin the triple line in case of a hydrophilic spot.

Various criteria have been formulated to predict the transitions from a metastable composite state to a wetted state. Extrand [82] formulated the transition criterion referred to as the contact line density criterion, which was obtained by balancing the droplet weight and the surface forces along the contact line. Patankar [56] proposed a transition criterion based on energy balance. There is an energy barrier in going from a higher energy Cassie–Baxter droplet to a lower energy Wenzel droplet. The most probable mechanism is that the decrease in the gravitational potential energy during the transition helps in overcoming the energy barrier. This energy barrier was estimated by considering an intermediate state in which the water fills the grooves below the contact area of a Cassie–Baxter droplet but the liquid–solid contact is yet to be formed at the bottom of the valleys. These criteria were tested on selected experiments from the literature [57, 83–85]. Bhushan et al. [70] and Nosonovsky and Bhushan [62, 63] found that the transition occurs at a critical value of the spacing factor, a non-dimensional parameter which is defined as the diameter of the pillars divided by the pitch distance between them for patterned surfaces and its ratio to the droplet size. Bhushan and Jung [30, 69] and Jung and Bhushan [75–77] proposed the transition criterion based on the pitch distance between the pillars and the curvature of the droplet governed by the Laplace equation, which relates the pressure inside the droplet to its curvature. In addition, the transition can occur by applying external pressure to the droplet, or by the impact of a droplet on the patterned surfaces [55, 77, 78, 81, 86–88].

Contact angle on selected patterned surfaces has been measured to understand how the transition between the Cassie–Baxter regime and Wenzel regime occurs. Evaporation studies are useful in characterizing the wetting behavior because droplets with various sizes can be created to evaluate the transition criterion on a given patterned surface [3, 31, 32, 62, 71, 73–76, 79, 80, 89–92]. It has been reported that the wetting state changes from the Cassie–Baxter to Wenzel state as the droplet becomes smaller than a critical value on patterned surfaces during evaporation. Another important phenomenon related to wetting behavior is the bouncing of droplets. When a droplet hits a surface, it can bounce, spread, or stick. In practical applications of superhydrophobic surfaces, surfaces should maintain their ability to repel penetrating droplets under dynamic conditions. Jung and Bhushan [77] and Nosonovsky and Bhushan [81] showed that the transition can occur by the impact of a droplet on a given patterned surface at a critical velocity with a critical geometric parameter.

An environmental scanning electron microscope (ESEM) can be used to condense or evaporate water droplets on surfaces by adjusting the pressure of the water vapor in the specimen chamber and the temperature of the cooling stage. Transfer of the water droplet has been achieved by a specially designed micro-injector device on wool fibers and then imaged at room temperature in ESEM [93]. Images of water droplets show strong topographic contrast in ESEM such that reliable

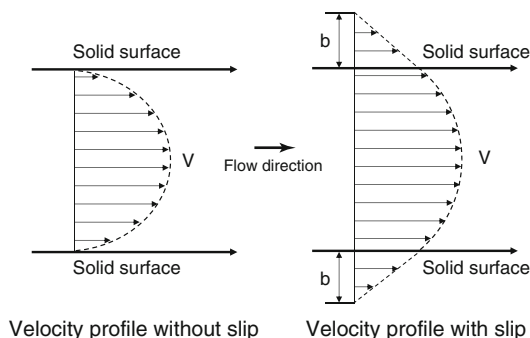
contact angle measurements can be made on the surfaces [94]. Water condensation and evaporation studies on patterned surfaces were carried out by Jung and Bhushan [76] and Nosonovsky and Bhushan [31, 32, 62, 79, 80] where the change of static contact angle and contact angle hysteresis was related with the surface roughness.

It has been demonstrated experimentally that roughness changes contact angle in accordance with the Wenzel model or Cassie–Baxter model, dependent upon whether the surface is hydrophilic or hydrophobic. Yost et al. [95] found that roughness enhances wetting of a copper surface with Sn–Pb eutectic solder, which has a contact angle of  $15\text{--}20^\circ$  for a smooth surface. Shibuichi et al. [65] measured the contact angle of various liquids (mixtures of water and 1,4-dioxane) on alkylketene dimmer (AKD) substrate (contact angle not larger than  $109^\circ$  for a smooth surface). They found that for wetting liquids, the contact angle decreases with increasing roughness, whereas for non-wetting liquids it increases. Semal et al. [96] investigated the effect of surface roughness on contact angle hysteresis by studying a sessile droplet of squalane spreading dynamically on multilayer substrates (behenic acid on glass) and found an increase in microroughness slows the rate of droplet spread. Erbil et al. [97] measured the contact angle of polypropylene (contact angle of  $104^\circ$  for smooth surface) and found that the contact angle increases with increasing roughness. Burton and Bhushan [98] measured contact angle with roughness of patterned surfaces and found that in the case of hydrophilic surfaces, it decreases with increasing roughness, and for hydrophobic surfaces, it increases with increasing roughness. Bhushan and Jung [30, 69], Jung and Bhushan [75–77, 99], Bhushan et al. [3, 70–74], and Koch et al. [44] studied the influence of micro-, nano- and hierarchical structures, created by replication of micropatterns and by self assembly of hydrophobic alkanes and plant wax, on static contact angle, contact angle hysteresis, tilt angle and air pocket formation, adhesive force as well as efficiency of self-cleaning. They showed that for micro-, nano- and hierarchical structures, the introduction of roughness increased the hydrophobicity of the surfaces. A hierarchical structure composed of a microstructure with a superimposed nanostructure of hydrophobic waxes led to superhydrophobicity with static contact angles of  $173^\circ$  and low contact angle hysteresis of  $2^\circ$ . Jung and Bhushan [100] produced mechanically durable carbon nanotubes (CNT) composite hierarchical structures with a static contact angle of  $170^\circ$  and a contact angle hysteresis of  $2^\circ$  by replication of a micropatterned silicon surface using an epoxy resin and by deposition of the CNT composite using a spray method. They showed that the CNT composite structure had high mechanical strength and wear resistance from the uniform distribution and strong bonding of CNT on substrates.

Drag reduction in fluid flow is of interest in micro/nanofluidics based biosensor applications [39]. To reduce pressure drop and volume loss in micro/nanochannels, it is desirable to minimize the drag force in the solid–liquid interface. It is generally assumed that the relative velocity between a solid wall and liquid is zero at the solid–liquid interface, which is so called the no-slip boundary condition (Fig. 20.5 left) [101, 102]. However, this assumption has been widely debated for hydrophobic surfaces, and fluid film exhibits a phenomenon known as slip, which means



**Fig. 20.5** Schematic of velocity profiles of fluid flow without and with boundary slip. The definition of slip length  $b$  characterizes the degree of boundary slip at solid–liquid interface. The arrows represent directions for fluid flow



that the fluid velocity near the solid surface is not equal to the velocity of the solid surface (Fig. 20.5 right) [103–109]. The degree of boundary slip at the solid–liquid interface is characterized by a slip length. Slip length  $b$  is defined as the length of the vertical intercept along the axis orthogonal to the interface when a tangent line is drawn along the velocity profile at the interface (Fig. 20.5 right). Recent experiments with surface force apparatus (SFA) [110–112], atomic force microscopy (AFM) [108, 109, 113], and particle image velocimetry (PIV) [114] techniques have reported slip length on hydrophobic surfaces, and no slip was observed on hydrophilic surfaces [110, 112–116]. Theoretical studies [117–120] and experimental studies [109, 121–123] suggest that the presence of nanobubbles at the solid–liquid interface is responsible for boundary slip on hydrophobic surfaces.

### 20.1.5 Roughness-Induced Superoleophobicity

The surface tension of oil and organic liquids is lower than that of water, so to create a superoleophobic surface, the surface energy of the solid surface in air should be lower than that of oil. For underwater applications, if an oil droplet is placed on a solid surface in water, the solid–water–oil interface exists. The nature of oleophobicity/philicity of an oil droplet in water can be determined from the values of surface energies of various interfaces and contact angles of water and oil in air.

Many superoleophobic surfaces have been developed by modifying the surface chemistry with a coating of extreme low surface energy materials [47, 124–130]. Tuteja et al. [130] showed that surface curvature, in conjunction with chemical composition and roughened texture, can be used for liquids with low surface tension, including alkanes such as decane and octane. Liu et al. [46] performed experiments in a solid–water–oil interface. They found that hydrophilic and oleophilic surfaces (solid–air–water interface and solid–air–oil interface) can switch to an oleophobic surface in water (solid–water–oil interface). As a result, oil contaminants are washed away when immersed in water. This effect can be employed for underwater oleophobicity and self-cleaning that can be used against marine ship

fouling [36]. Jung and Bhushan [47] proposed a model for predicting the oleophobic/philic nature of surfaces and showed how the water and oil droplets in three phase interfaces influence the wetting behavior on micropatterned surfaces with varying pitch values as well as the shark skin replica as an example of aquatic animal.

### ***20.1.6 Scope of the Article***

In this article, numerical models which provide relationships between roughness and contact angle and contact angle hysteresis as well as the Cassie–Baxter and Wenzel regime transition are discussed. The role of microbumps and nanobumps is examined by analyzing the surface characterization of hydrophobic and hydrophilic leaves on the micro- and nanoscale. Along with measuring and characterizing surface roughness, the contact angle and adhesion and friction properties of these leaves are also considered. The knowledge gained by examining these properties of the leaves and by quantitatively analyzing the surface structure will help in the design of superhydrophobic and self-cleaning surfaces. Next, the techniques of producing superhydrophobic surfaces are described. Micro-, nano- and hierarchical patterned structures have been fabricated using soft lithography, photolithography, and techniques which involve the replication of micropatterns, self assembly of hydrophobic alkanes and plant waxes, and a spray coating of carbon nanotubes. They have been characterized to validate the models and to provide design guidelines for superhydrophobic and self-cleaning surfaces. To further examine the effect of meniscus force and real area of contact, scale dependence is considered with the use of AFM tips of various radii. To investigate how the effects of droplet size and impact velocity influence the transition, evaporation and bouncing studies are conducted on silicon surfaces patterned with pillars of two different diameters and heights and with varying pitch values and deposited with a hydrophobic coating. In order to generate submicron droplets, an atomic force microscopy-based technique using a modified nanoscale dispensing probe is presented. An ESEM study on the wetting behavior for a microdroplet with about 20  $\mu\text{m}$  radius on the micropatterned Si surfaces is presented. For the durability of the various fabricated surfaces, the loss of superhydrophobicity as well as wear and friction is investigated.

Artificial surfaces from shark skin, which is one of the examples found in nature for drag reduction, have been created. To investigate drag reduction efficiency on biomimetic structured surfaces, pressure drop experiments in the channel are conducted using laminar and turbulent water and air flows.

A model for predicting the oleophobic/philic nature of the surfaces is discussed. To validate the model, it is investigated how the water and oil droplets in three phase interfaces influence the wetting behavior on micropatterned surfaces with varying pitch values and the nano- and hierarchical structures as well as the shark skin replica as an example of aquatic animal.

## 20.2 Modeling of Contact Angle for a Liquid in Contact with a Rough Surface

### 20.2.1 Contact Angle Definition

The surface atoms or molecules of liquids or solids have fewer bonds with neighboring atoms, and therefore, they have higher energy than similar atoms and molecules in the interior. This additional energy is characterized quantitatively by the surface tension or free surface energy  $\gamma$ , which is equal to the work that is required to create a unit area of the surface at a constant pressure and temperature. The unit of  $\gamma$  is  $\text{J/m}^2$  or  $\text{N/m}$ , and it can be interpreted either as energy per unit surface area or as tension force per unit length of a line at the surface. When a solid is in contact with liquid, the molecular attraction will reduce the energy of the system below that for the two separated surfaces. This is expressed by the Dupré equation

$$W_{SL} = \gamma_{SA} + \gamma_{LA} - \gamma_{SL} \quad (20.1)$$

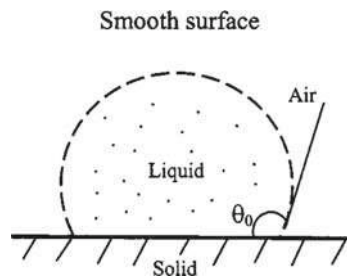
where  $W_{SL}$  is the work of adhesion per unit area,  $\gamma_{SA}$  and  $\gamma_{SL}$  are the surface energies of the solid against air and liquid, and  $\gamma_{LA}$  is the surface energy of liquid against air [22–24].

If a liquid droplet is placed on a solid surface, the liquid and solid surfaces come together under equilibrium at a characteristic angle called the static contact angle  $\theta_0$  (Fig. 20.6). This contact angle can be determined by minimizing the net surface free energy of the system [22–24]. The total energy  $E_{tot}$  is given by [27, 66]

$$E_{tot} = \gamma_{LA}(A_{LA} + A_{SL}) - W_{SL}A_{SL} \quad (20.2)$$

where  $A_{SL}$  and  $A_{LA}$  are the contact areas of the liquid with the solid and air, respectively. It is assumed that the droplet of density  $\rho$  is smaller than the capillary length,  $(\gamma_{LA}/\rho g)^{1/2}$ , so that the gravitational potential energy can be neglected. It is also assumed that the volume and pressure are constant, so that the volumetric energy does not change. At the equilibrium  $dE_{tot} = 0$ , which yields

**Fig. 20.6** Schematic of liquid droplet in contact with a smooth solid surface (contact angle,  $\theta_0$ )



$$\gamma_{LA}(dA_{LA} + dA_{SL}) - W_{SL}dA_{SL} = 0 \quad (20.3)$$

For a droplet of constant volume, it is easy to show using geometrical considerations, that

$$dA_{LA}/dA_{SL} = \cos \theta_0 \quad (20.4)$$

Combining (20.1, 20.3 and 20.4), the well-known Young equation for the contact angle is obtained

$$\cos \theta_0 = \frac{\gamma_{SA} - \gamma_{SL}}{\gamma_{LA}} \quad (20.5)$$

Equation (20.5) provides an expression for the static contact angle for given surface energies. Note that although we use the term “air”, the analysis does not change in the case of another gas, such as water vapor.

### 20.2.2 *Heterogeneous Interfaces and the Wenzel and Cassie–Baxter Equations*

In this section, we introduce and discuss the equations that govern the contact angle of liquid with a rough surface and heterogeneous interface.

We first consider a water droplet on a rough surface with a homogeneous interface. The interface area increases with respect to that for a smooth surface. Using the surface force balance and empirical considerations, the contact angle of a water droplet upon a rough solid surface,  $\theta$ , is related to that upon a smooth surface,  $\theta_0$  for a homogeneous interface (Fig. 20.7a), through the non-dimensional surface roughness factor,  $R_f > 1$ , equal to the ratio of the surface area,  $A_{SL}$ , to its flat projected area,  $A_F$  [49]

$$\cos \theta = \frac{dA_{LA}}{dA_F} = \frac{A_{SL}}{A_F} \frac{dA_{LA}}{dA_{SL}} = R_f \cos \theta_0 \quad (20.6)$$

where,

$$R_f = \frac{A_{SL}}{A_F} \quad (20.7)$$

This is called the Wenzel equation. The dependence of the contact angle on the roughness factor is presented in Fig. 20.8a for different values of  $\theta_0$ . The Wenzel model predicts that a hydrophobic surface ( $\theta_0 > 90^\circ$ ) becomes more hydrophobic with an increase in  $R_f$ , while a hydrophilic surface ( $\theta_0 < 90^\circ$ ) becomes more hydrophilic with an increase in  $R_f$  [66, 99]. As an example, Fig. 20.8b shows a

**Fig. 20.7** Schematics of configurations described by the (a) Wenzel equation for the homogeneous interface (20.6), (b) Cassie–Baxter equation for the composite interface with air pockets (20.9), and (c) the Cassie equation for the homogeneous interface (20.10) [79]

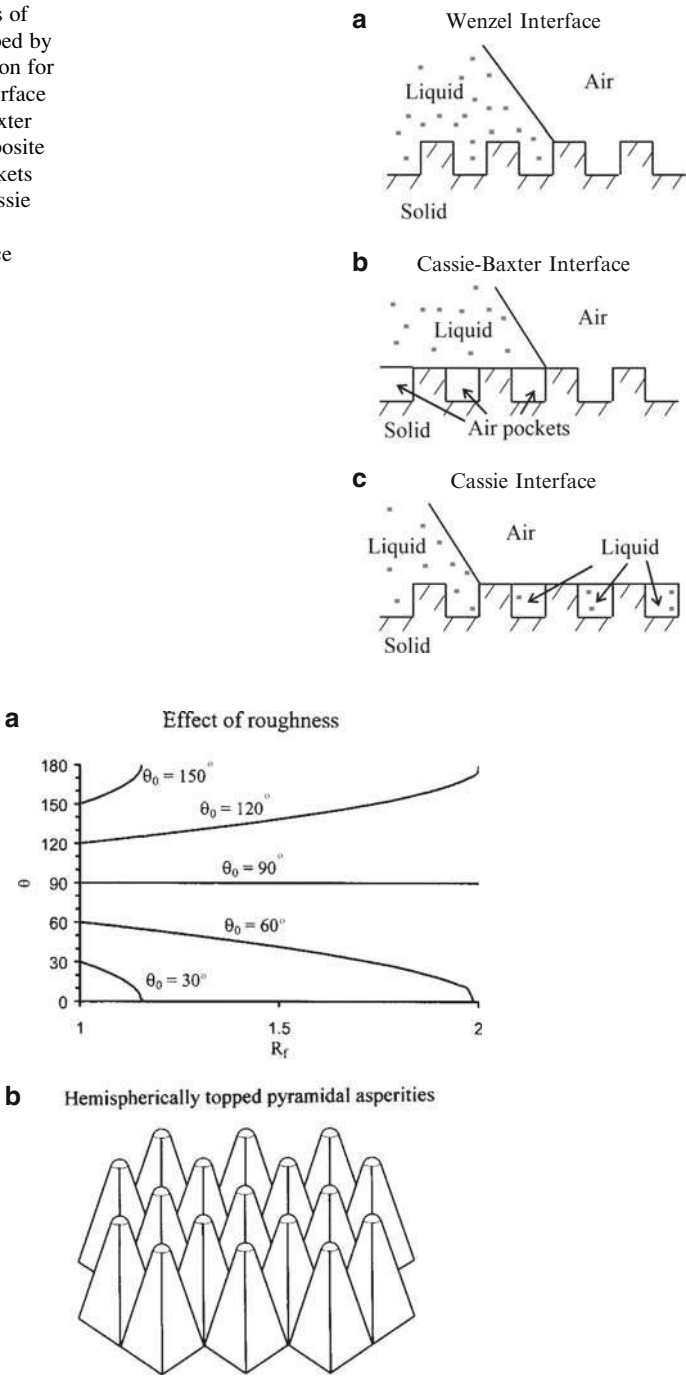


**Fig. 20.8** (a) Contact angle for rough surface ( $\theta$ ) as a function of the roughness factor ( $R_f$ ) for various contact angles of the smooth surface ( $\theta_0$ ), and (b) schematic of square-based hemispherically-topped pyramidal asperities with complete packing [66]

geometry with square-based hemispherically-topped pyramidal asperities with a rounded top, which has complete packing. The size and shape of the asperities can be optimized for a desired roughness factor.

In a similar manner, for a surface composed of two fractions, one with the fractional area  $f_1$  and the contact angle  $\theta_1$  and the other with  $f_2$  and  $\theta_2$ , respectively (so that  $f_1 + f_2 = 1$ ), the contact angle for the heterogeneous interface is given by the Cassie equation [50]

$$\cos \theta = f_1 \cos \theta_1 + f_2 \cos \theta_2 \quad (20.8)$$

For the case of a composite interface (Fig. 20.7b), consisting of a solid–liquid fraction ( $f_l = f_{SL}$ ,  $\theta_l = \theta_0$ ) and liquid–air fraction ( $f_2 = f_{LA} = 1 - f_{SL}$ ,  $\cos \theta_2 = -1$ ), combining (20.7 and 20.8) yields the Cassie–Baxter equation [50]

$$\cos \theta = R_f f_{SL} \cos \theta_0 - 1 + f_{SL}$$

Or

$$\cos \theta = R_f \cos \theta_0 - f_{LA}(R_f \cos \theta_0 + 1) \quad (20.9)$$

The opposite limiting case of  $\cos \theta_2 = 1$  ( $\theta_2 = 0^\circ$  corresponds to the water-on-water contact) yields the Cassie equation [27, 79]

$$\cos \theta = 1 + f_{SL}(\cos \theta_0 - 1) \quad (20.10)$$

Equation (20.10) is used sometimes for the homogeneous interface instead of (20.6), if the rough surface is covered by holes filled with water [131] (Fig. 20.7c).

Two situations in wetting of a rough surface should be distinguished: the homogeneous interface without any air pockets shown in Fig. 20.7a [called the Wenzel interface, since the contact angle is given by the Wenzel equation or (20.6)], and the composite interface with air pockets trapped between the rough details as shown in Fig. 20.7b (called the Cassie or Cassie–Baxter interface, since the contact angle is given by (20.9)).

Equation (20.9) for the composite interface was derived using (20.6 and 20.8), and it could also be obtained independently. For this purpose, two sets of interfaces are considered: a liquid–air interface with the ambient and a flat composite interface under the droplet, which itself involves solid–liquid, liquid–air, and solid–air interfaces. For fractional flat geometrical areas of the solid–liquid and liquid–air interfaces under the droplet,  $f_{SL}$  and  $f_{LA}$  ( $f_{SL} = 1 - f_{LA}$ ), the flat area of the composite interface is [27, 66]

$$A_F = f_{SL}A_F + f_{LA}A_F = R_f A_{SL} + f_{LA}A_F \quad (20.11)$$

In order to calculate the contact angle in a manner similar to the derivation of (20.6), the differential area of the liquid–air interface under the droplet,  $f_{LA}dA_F$ ,

should be subtracted from the differential of the total liquid–air area  $dA_{LA}$ , which yields the Cassie–Baxter equation (20.9),

$$\begin{aligned}\cos \theta &= \frac{dA_{LA} - f_{LA} dA_F}{dA_F} = \frac{A_{SL}}{A_F} \frac{dA_{LA}}{dA_{SL}} - f_{LA} = R_f f_{SL} \cos \theta_0 - f_{LA} \\ &= R_f \cos \theta_0 - f_{LA} (R_f \cos \theta_0 + 1)\end{aligned}$$

The dependence of the contact angle on the roughness factor and fractional liquid–air area for hydrophilic and hydrophobic surfaces with a composite interface (Fig. 20.9a) is presented in Fig. 20.9b.

According to (20.9), even for a hydrophilic surface, the contact angle increases with an increase of  $f_{LA}$ . At a high value of  $f_{LA}$ , a surface can become hydrophobic; however, the value required may be unachievable, or the formation of air pockets may become unstable. Using the Cassie–Baxter equation, the value of  $f_{LA}$  at which a hydrophilic surface could turn into a hydrophobic one is given as [99]

$$f_{LA} \geq \frac{R_f \cos \theta_0}{R_f \cos \theta_0 + 1} \quad \text{for } \theta_0 < 90^\circ \quad (20.12)$$

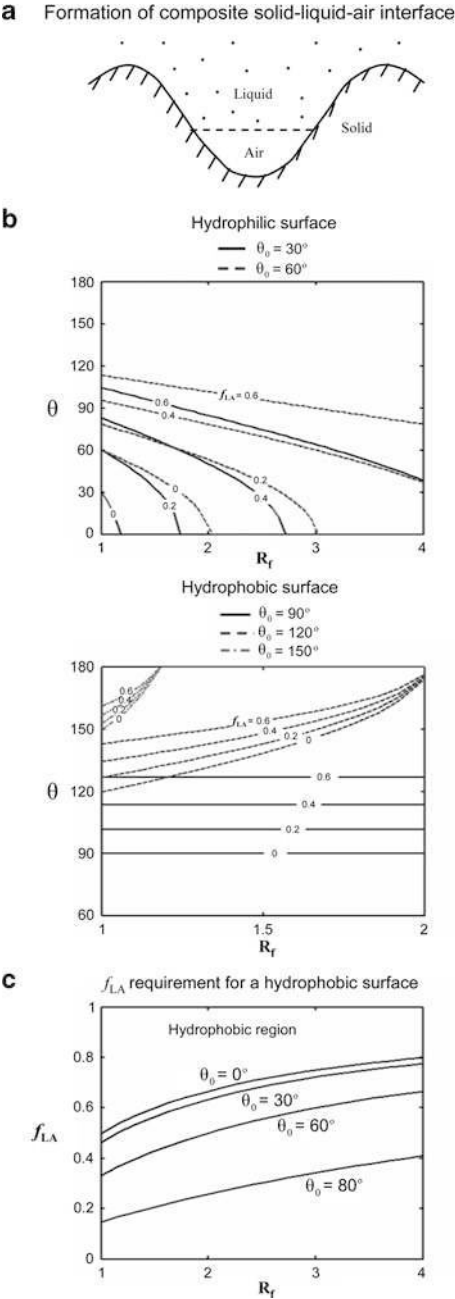
Figure 20.9c shows the value of  $f_{LA}$  requirement as a function of  $R_f$  for four surfaces with different contact angles,  $\theta_0$ . Hydrophobic surfaces can be achieved above a certain  $f_{LA}$  value as predicted by (20.12). The upper part of each contact angle line is the hydrophobic region. For the hydrophobic surface, contact angle increases with an increase in  $f_{LA}$  both for smooth and rough surfaces.

Based on Nosonovsky and Bhushan [27, 37], spreading of a liquid over a rough solid surface continues until simultaneously (20.5) (the Young equation) is satisfied locally at the triple line and the surface area is minimum over the entire liquid–air interface. The minimal surface area condition states that the sum of the inverse of the principal radii of curvature,  $R_1$  and  $R_2$  of the liquid surface, along the two mutually orthogonal planes (mean curvature), is constant at any point, which governs the shape of the liquid–air interface. The same condition is also the consequence of the Laplace equation, which relates pressure change through an interface,  $\Delta P$ , with its mean curvature,

$$\frac{1}{R_1} + \frac{1}{R_2} = \frac{\Delta P}{\gamma_{LA}} \quad (20.13)$$

Note that at the thermodynamic equilibrium (when condensation and evaporation occurs at the same speed),  $\Delta P$  is dependent on the partial vapor pressure. For contact with saturated vapor the mean curvature of the liquid–air interface is zero at equilibrium. A convex interface ( $1/R_1 + 1/R_2 > 0$ ) results in evaporation prevailing over condensation; this is why small droplets tend to evaporate. However, a concave interface ( $1/R_1 + 1/R_2 < 0$ ) results in condensation of saturated vapor prevailing over evaporation. Since the condensation prevails, a concave interface

**Fig. 20.9** (a) Schematic of formation of a composite solid–liquid–air interface for rough surface, (b) contact angle for rough surface ( $\theta$ ) as a function of the roughness factor ( $R_f$ ) for various  $f_{LA}$  values on the hydrophilic surface and the hydrophobic surface, and (c)  $f_{LA}$  requirement for a hydrophobic surface to be hydrophobic as a function of the roughness factor ( $R_f$ ) and  $\theta_0$  [99]



may be in thermodynamic equilibrium with undersaturated vapor. This is why concave menisci tend to condense even when the relative humidity is less than 100% [27, 37].



### 20.2.2.1 Limitations of the Wenzel and Cassie Equations

Based on Nosonovsky and Bhushan [27, 79], the Cassie equation (20.8) is based on the assumption that the heterogeneous surface is composed of well-separated distinct patches of different material, so that the free surface energy can be averaged. It has been argued also that when the size of the chemical heterogeneities is very small (of atomic or molecular dimensions), the quantity that should be averaged is not the energy, but the dipole moment of a macromolecule [132], and (20.8) should be replaced by [79]

$$(1 + \cos \theta)^2 = f_1(1 + \cos \theta_1)^2 + f_2(1 + \cos \theta_2)^2 \quad (20.14)$$

Experimental studies of polymers with different functional groups showed a good agreement with (20.14) [133].

Based on Nosonovsky and Bhushan [27, 79], later investigations put the Wenzel and Cassie equations into a thermodynamic framework; however, they also showed that there is no one single value of the contact angle for a rough or heterogeneous surface [51, 53, 134]. The contact angle can be in a range of values between the receding contact angle,  $\theta_{rec}$ , and the advancing contact angle,  $\theta_{adv}$ . The system tends to achieve the receding contact angle when liquid is removed (for example, at the rear end of a moving droplet), whereas the advancing contact angle is achieved when the liquid is added (for example, at the front end of a moving droplet) (Fig. 20.10a). When the liquid is neither added nor removed, the system tends to

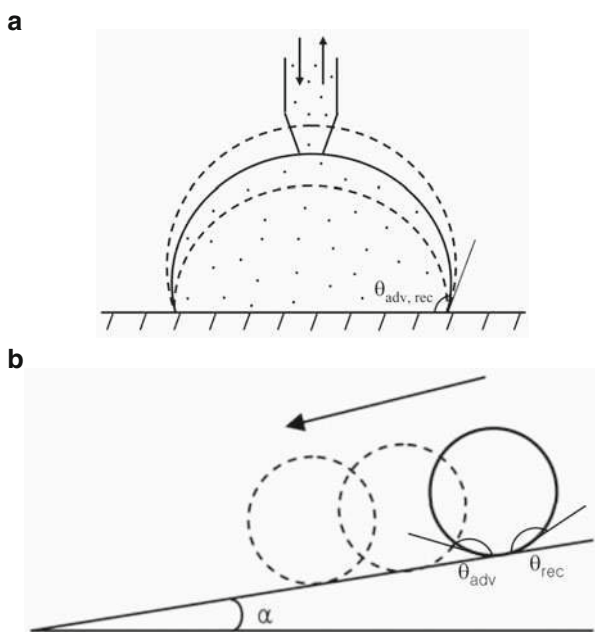


**Fig. 20.10** (a) Liquid droplet in contact with rough surface with liquid is added or removed (advancing and receding contact angles are  $\theta_{adv}$  and  $\theta_{rec}$ , respectively) and (b) tilted surface profile (tilt angle,  $\alpha$ ) with a moving liquid droplet

have a static or “most stable” contact angle, which is given approximately by (20.5, 20.6, 20.8, and 20.10).

The contact angle provided by (20.5, 20.6, 20.8, and 20.10) is a macroscale parameter, so it is called sometimes “the apparent contact angle”. Based on Nosonovsky and Bhushan [27, 33], the actual angle, under which the liquid–air interface comes in contact with the solid surface at the micro- and nanoscale, can be different. There are several reasons for that. First, water molecules tend to form a thin layer upon the surfaces of many materials. This is because of a long-distance van der Waals adhesion force that creates the so-called disjoining pressure [135]. This pressure is dependent upon the liquid layer thickness and may lead to the formation of stable thin films. In this case, the shape of the droplet near the triple line (line of contact of the solid, liquid and air, to be shown later in Fig. 20.12) transforms gradually from the spherical surface into a precursor layer, and thus the nanoscale contact angle is much smaller than the apparent contact angle. In addition, adsorbed water monolayers and multilayers are common for many materials. Second, even carefully prepared atomically smooth surfaces exhibit a certain roughness and chemical heterogeneity. Water tends first to cover the hydrophilic spots with high surface energy and low contact angle [136]. The tilt angle due to roughness can also contribute to the apparent contact angle. Third, the very concept of the static contact angle is not well defined. For practical purposes, the contact angle, which is formed after a droplet is gently placed upon a surface and stops propagating, is considered the static contact angle. However, depositing the droplet involves adding liquid while leaving it involves evaporation, so it is difficult to avoid dynamic effects. Fourth, for small droplets and curved triple lines, the effect of the contact line tension may be significant. Molecules at the surface of a liquid or solid phase have higher energy because they are bonded to fewer molecules than those in the bulk. This leads to surface tension and surface energy. In a similar manner, molecules at the concave surface and, especially, at the edge have fewer bonds than those at the surface, which leads to line tension and curvature dependence of the surface energy. This effect becomes important when the radius of curvature is comparable with the so-called Tolman’s length, normally of the molecular size [137]. However, the triple line at the nanoscale can be curved so that the line tension effects become important [138]. The contact angle, taking into account for the contact line effect, for a droplet with radius  $R$  is given by  $\cos \theta = \cos \theta_0 + 2\tau / (R\gamma_{LA})$ , where  $\tau$  is the contact line tension, and  $\theta_0$  is the value given by the Young equation [139]. Thus while the contact angle is a convenient macroscale parameter, wetting is governed by interactions at the micro- and nanoscale, which determine the contact angle hysteresis and other wetting properties. Table 20.1 shows various scale levels which affect wetting of a superhydrophobic surface.

#### 20.2.2.2 Range of Applicability of the Wenzel and Cassie Equations

Gao and McCarthy [140] showed experimentally that the contact angle of a droplet is defined by the triple line and does not depend upon the roughness under the

**Table 20.1** Wetting of a superhydrophobic surface as a multiscale process [33, 62]

Scale level	Characteristic length	Parameters	Phenomena	Interface
Macroscale	Droplet radius (mm)	Contact angle, droplet radius	Contact angle hysteresis	2-D
Microscale	Roughness detail (μm)	Shape of the droplet, position of the liquid–air interface ( <i>h</i> )	Kinetic effects	3-D solid surface, 2-D liquid surface
Nanoscale	Molecular heterogeneity (nm)	Molecular description	Thermodynamic and dynamic effects	3-D

bulk of the droplet. A similar result for chemically heterogeneous surfaces was obtained by Extrand [141]. Gao and McCarthy [140] concluded that the Wenzel and Cassie–Baxter equations “should be used with the knowledge of their fault”. The question remained, however, under what circumstances the Wenzel and Cassie–Baxter equations can be safely used and under what circumstances they become irrelevant.

Based on Nosonovsky [142], for a liquid front propagating along a rough two-dimensional profile (Fig. 20.11a,b), the derivative of the free surface energy (per liquid front length),  $W$ , by the profile length,  $t$ , yields the surface tension force  $\sigma = dW/dt = \gamma_{SL} - \gamma_{SA}$ . The quantity of practical interest is the component of the tension force that corresponds to the advancing of the liquid front in the horizontal direction for  $dx$ . This component is given by  $dW/dx = (dW/dt) (dt/dx) = (\gamma_{SL} - \gamma_{SA})dt/dx$ . It is noted that the derivative  $dt/dx$  is equal to Wenzel’s roughness factor ( $R_f$ ) in the case when the roughness factor is constant throughout the surface. Therefore, the Young equation (20.5), which relates the contact angle with solid, liquid, and air interface tensions, is modified as [142]

$$\gamma_{LA} \cos \theta = R_f(\gamma_{SA} - \gamma_{SL}) \tag{20.15}$$

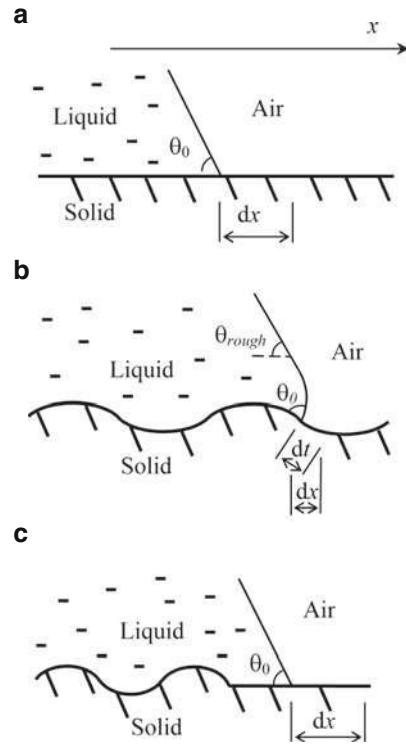
The empirical Wenzel equation (20.6) is a consequence of (20.15) combined with the Young equation.

Nosonovsky [142] showed that for a more complicated case of a non-uniform roughness, given by the profile  $z(x)$ , the local value of derivative,  $r(x) = dt/dx = (1 + (dz/dx)^2)^{1/2}$  matters. In the cases that were studied experimentally by Gao and McCarthy [140] and Extrand [141], the roughness was present ( $r > 1$ ) under the bulk of the droplet, but there was no roughness ( $r = 0$ ) at the triple line, and the contact angle was given by (20.6) (Fig. 20.11c). In the general case of a 3-D rough surface  $z(x, y)$ , the roughness factor can be defined as a function of the coordinates  $r(x, y) = (1 + (dz/dx)^2 + (dz/dy)^2)^{1/2}$ .

Equation (20.6) is valid for uniformly rough surfaces, that is, surfaces with  $r = \text{const}$ , and for non-uniformly rough surfaces the generalized Wenzel equation is formulated to determine the local contact angle (a function of  $x$  and  $y$ ) with rough surfaces at the triple line [27, 32, 142]

$$\cos \theta = r(x, y) \cos \theta_0 \tag{20.16}$$

**Fig. 20.11** Liquid front in contact with a (a) smooth solid surface and (b) rough solid surface, propagation for a distance  $dt$  along the curved surface corresponds to the distance  $dx$  along the horizontal surface. (c) Surface roughness under the bulk of the droplet does not affect the contact angle [142]



The difference between the Wenzel equation (20.6) and the Nosonovsky-Bhushan equation (20.16) is that the latter is valid for a non-uniform roughness with the roughness factor as the function of the coordinates. Equation (20.16) is consistent with the experimental results of the scholars who showed that roughness beneath the droplet does not affect the contact angle, since it predicts that only roughness at the triple line matters. It is also consistent with the results of the researchers who confirmed the Wenzel equation (for the case of the uniform roughness) and of those who reported that only the triple line matters (for non-uniform roughness). A summary of experimental results for uniform and non-uniform rough and chemically heterogeneous surfaces is shown in Table 20.2.

The Cassie equation for the composite surface can be generalized in a similar manner introducing the spatial dependence of the local densities,  $f_1$  and  $f_2$  of the solid-liquid interface with the contact angle, as a function of  $x$  and  $y$ , given by [142]

$$\cos \theta_{composite} = f_1(x, y) \cos \theta_1 + f_2(x, y) \cos \theta_2 \quad (20.17)$$

where  $f_1 + f_2 = 1$ ,  $\theta_1$  and  $\theta_2$  are contact angles of the two components.

According to Nosonovsky [142], the important question remains, what should be the typical size of roughness/heterogeneity details in order for the generalized

**Table 20.2** Summary of experimental results for uniform and non-uniform rough and chemically heterogeneous surfaces. For non-uniform surfaces, the results shown for droplets larger than the islands of non-uniformity. Detailed quantitative values of the contact angle in various sets of experiments can be found in the referred sources [142]

Experiment	Roughness/hydrophobicity at the triple line and at the rest of the surface	Roughness at the bulk (under the droplet)	Experimental contact angle (compared with that at the rest of the surface)	Theoretical contact angle, Wenzel/Cassie equations	Theoretical contact angle, generalized Wenzel–Cassie (20.16–20.17)
Gao and McCarthy [140]	Hydrophobic Rough Smooth	Hydrophilic Smooth Rough	Not changed Not changed Not changed	Decreased Decreased Increased	Not changed Not changed Not changed
Extrand [141]	Hydrophilic Hydrophobic	Hydrophobic Hydrophilic	Not changed Not changed	Increased Decreased	Not changed Not changed
Bhushan et al. [70]	Rough	Rough	Increased	Increased	Increased
Barbieri et al. [143]	Rough	Rough	Increased	Increased	Increased

Wenzel and Cassie equations (20.16–20.17) to be valid? Some scholars have suggested that roughness/heterogeneity details should be comparable with the thickness of the liquid–air interface and thus “the roughness would have to be of molecular dimensions to alter the equilibrium conditions” [144], whereas others have claimed that roughness/heterogeneity details should be small compared with the linear size of the droplet [30, 51, 69, 70, 75–77, 99, 134, 143]. The interface in the analysis proposed earlier is an idealized 2-D object, which has no thickness. In reality, the triple line zone has two characteristic dimensions: the thickness (of the order of molecular dimensions) and the length (of the order of the droplet size).

According to Nosonovsky and Bhushan [27, 32], the apparent contact angle, given by (20.16–20.17), may be viewed as the result of averaging of the local contact angle at the triple line over its length, and thus the size of the roughness/heterogeneity details should be small compared to the length (and not the thickness) of the triple line [32]. A rigorous definition of the generalized equation requires the consideration of several length scales. The length  $dx$  needed for averaging of the energy gives the length over which the averaging is performed to obtain  $r(x, y)$ . This length should be larger than roughness details. However, it is still smaller than the droplet size and the length scale at which the apparent contact angle is observed (at which local variations of the contact angle level out). Since of these lengths (the roughness size,  $dx$ , the droplet size) the first and the last are of practical importance, we conclude that the roughness details should be smaller than the droplet size. When the liquid–air interface is studied at the length scale of roughness/heterogeneity details, the local contact angle,  $\theta_0$ , is given by (20.6–20.10). The liquid–air interface at that scale has perturbations caused by the roughness/heterogeneity, and the scale of the perturbations is the same as the scale of the roughness/heterogeneity details. However, when the same interface is studied at a larger scale, the effect of the perturbation vanishes, and apparent contact angle is given by (20.16–20.17)

(Fig. 20.11c). This apparent contact angle is defined at the length scale for which the small perturbations of the liquid–air interface vanish, and the interface can be treated as a smooth surface. The values of  $r(x, y)$ ,  $f_1(x, y)$ ,  $f_2(x, y)$  in (20.16–20.17) are average values over an area  $(x, y)$  with a size larger than a typical roughness/heterogeneity detail size. Therefore, the generalized Wenzel and Cassie equations can be used at the scale at which the effect of the interface perturbations vanish, or, in other words, when the size of the solid surface roughness/heterogeneity details is small compared with the size of the liquid–air interface, which is of the same order as the size of the droplet [32].

Nosonovsky and Bhushan [27, 79] used the surface energy approach to find the domain of validity of the Wenzel and Cassie equations (uniformly rough surfaces) and generalized it for a more complicated case of non-uniform surfaces. The generalized equations explain a wide range of existing experimental data, which could not be explained by the original Wenzel and Cassie equations.

### 20.2.3 Contact Angle Hysteresis

Contact angle hysteresis is another important characteristic of a solid–liquid interface. Contact angle hysteresis occurs due to surface roughness and heterogeneity. Although for surfaces with roughness carefully controlled on the molecular scale it is possible to achieve contact angle hysteresis as low as  $<1^\circ$  [145], hysteresis cannot be eliminated completely, since even atomically smooth surfaces have a certain roughness and heterogeneity. Contact angle hysteresis is a measure of energy dissipation during the flow of a droplet along a solid surface. Low contact angle hysteresis results in a very low water roll-off angle, which denotes the angle to which a surface may be tilted for roll-off of water drops (i.e., very low water contact angle hysteresis) [28–30, 69, 75, 76] (Fig. 20.10b). Low water roll-off angle is important in liquid flow applications such as in micro/nanochannels and surfaces with self-cleaning ability.

Certain conclusions about the relationship of contact angle hysteresis to roughness can be made. It is known that the energy gained for surfaces during contact is greater than the work of adhesion for separating the surfaces, due to so called adhesion hysteresis. Factors that affect contact angle hysteresis include adhesion hysteresis, surface roughness, and inhomogeneity. Bhushan et al. [70] and Nosonovsky and Bhushan [61] assumed that contact angle hysteresis is equal to the adhesion hysteresis term and the term corresponding to the effect of roughness,  $H_r$ . They further noted that adhesion hysteresis can be assumed to be proportional to the fractional solid–liquid area  $(1 - f_{LA})$ . Using (20.9), the difference of cosines of the advancing and receding angles is related to the difference of those for a nominally smooth surface,  $\theta_{adv0}$  and  $\theta_{rec0}$ , as

$$\cos \theta_{adv} - \cos \theta_{rec} = R_f(1 - f_{LA})(\cos \theta_{adv0} - \cos \theta_{rec0}) + H_r \quad (20.18)$$

The first term in the right-hand part of the equation, which corresponds to the inherent contact angle hysteresis of a smooth surface, is proportional to the fraction

of the solid–liquid contact area,  $1 - f_{LA}$ . The second term,  $H_r$ , is the effect of surface roughness, which is equal to the total perimeter of the asperity per unit area, or in other words, to the length density of the triple line [70]. Thus (20.18) involves both the term proportional to the solid–liquid interface area and to the triple line length. It is observed from (20.9) and (20.18) that increasing  $f_{LA} \rightarrow 1$  results in increasing the contact angle ( $\cos \theta \rightarrow -1$ ,  $\theta \rightarrow \pi$ ) and decreasing the contact angle hysteresis ( $\cos \theta_{adv} - \cos \theta_{rec} \rightarrow 0$ ). In the limiting case of very small solid–liquid fractional contact area under the droplet, when the contact angle is large ( $\cos \theta \approx -1 + (\pi - \theta)^2/2$ ,  $\sin \theta \approx \theta - \pi$ ) and where the contact angle hysteresis is small ( $\theta_{adv} \approx \theta \approx \theta_{rec}$ ), based on (20.9) and (20.18) [61],

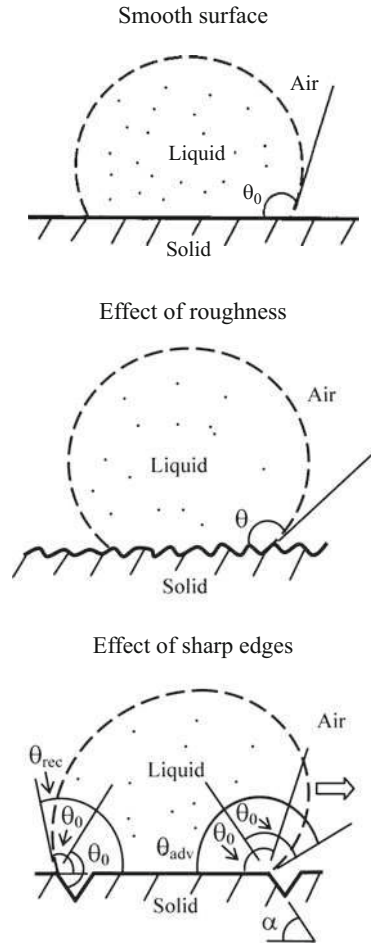
$$\pi - \theta = \sqrt{2(1 - f_{LA})(R_f \cos \theta_0 + 1)} \quad (20.19)$$

$$\begin{aligned} \theta_{adv} - \theta_{rec} &= (1 - f_{LA})R_f \frac{\cos \theta_{a0} - \cos \theta_{r0}}{-\sin \theta} \\ &= (\sqrt{1 - f_{LA}})R_f \frac{\cos \theta_{r0} - \cos \theta_{a0}}{\sqrt{2(R_f \cos \theta_0 + 1)}} \end{aligned} \quad (20.20)$$

For the homogeneous interface,  $f_{LA} = 0$ , whereas for the composite interface  $f_{LA}$  is a non-zero number. It is observed from (20.19–20.20) that for a homogeneous interface, increasing roughness (high  $R_f$ ) leads to increasing the contact angle hysteresis (high values of  $\theta_{adv} - \theta_{rec}$ ), while for the composite interface, an approach to unity of  $f_{LA}$  provides both high contact angle and small contact angle hysteresis [61, 63, 70, 99]. Therefore, the composite interface is desirable for self-cleaning.

A sharp edge can pin the line of contact of the solid, liquid, and air (also known as the “triple line”) at a position far from stable equilibrium, i.e., at contact angles different from  $\theta_0$  [146]. This effect is illustrated in the bottom sketch of Fig. 20.12, which shows a droplet propagating along a solid surface with grooves. Based on Nosonovsky and Bhushan [27, 66], at the edge point, the contact angle is not defined and can have any value between the values corresponding to contact with the horizontal and inclined surfaces. For a droplet moving from left to right, the triple line will be pinned at the edge point until it will be able to proceed to the inclined plane. As it is observed from Fig. 20.12, the change of the surface slope ( $\alpha$ ) at the edge is the cause of the pinning. Because of the pinning, the value of the contact angle at the front of the droplet (dynamic maximum advancing contact angle or  $\theta_{adv} = \theta_0 + \alpha$ ) is greater than  $\theta_0$ , whereas the value of the contact angle at the back of the droplet (dynamic minimum receding contact angle or  $\theta_{rec} = \theta_0 - \alpha$ ) is smaller than  $\theta_0$ . A hysteresis domain of the dynamic contact angle is thus defined by the difference  $\theta_{adv} - \theta_{rec}$ . The liquid can travel easily along the surface if the contact angle hysteresis is small. It is noted that the static contact angle lies within the hysteresis domain; therefore, increasing the static contact angle up to the values of a superhydrophobic surface (approaching  $180^\circ$ ) will also result in

**Fig. 20.12** A liquid droplet in contact with a solid surface – smooth surface, contact angle  $\theta_0$ ; rough surface, contact angle  $\theta$ ; and a surface with sharp edges. For a droplet moving from left to right on a sharp edge (shown by *arrow*), the contact angle at a sharp edge may take any value between the contact angle with the horizontal and inclined planes. This effect results in the difference between advancing ( $\theta_{adv} = \theta_0 + \alpha$ ) and receding ( $\theta_{rec} = \theta_0 - \alpha$ ) contact angles [66]



a reduction of the contact angle hysteresis. In a similar manner, contact angle hysteresis can also exist even if the surface slope changes smoothly, without sharp edges. There is an analogy between the two mechanisms leading to contact angle hysteresis (energy dissipation at the solid–liquid interface and pinning of the triple line) and dissipation mechanisms of dry friction (adhesion and deformation) [147].

## 20.2.4 Stability of a Composite Interface and Role of Hierarchical Structure

Stability of the composite interface is an important issue. Even though it may be geometrically possible for the system to become composite, it may be energetically



profitable for the liquid to penetrate into the valleys between asperities and form a homogeneous interface. Marmur [53] formulated geometrical conditions for a surface under which the energy of the system has a local minimum and the composite interface may exist. Patankar [56] pointed out that whether the homogeneous or composite interface exists depends on the system's history, i.e., on whether the droplet was formed at the surface or deposited. However, the above-mentioned analyses do not provide an answer to which of the two possible configurations, homogeneous or composite, will actually form.

Based on Nosonovsky and Bhushan [27, 61], formation of a composite interface is also a multiscale phenomenon which depends upon the relative sizes of the liquid droplet and roughness details. The composite interface is fragile and can be irreversibly transformed into the homogeneous interface, thus damaging superhydrophobicity. In order to form a stable composite interface with air pockets between solid and liquid, the destabilizing factors such as capillary waves, nanodroplet condensation, surface inhomogeneity, and liquid pressure should be avoided. First, the capillary waves at the liquid–air interface may destabilize the composite interface. Due to an external perturbation, a standing capillary wave can form at the liquid–air interface. If the amplitude of the capillary wave is greater than the height of the asperity, the liquid can touch the valley between the asperities, and if the angle under which the liquid comes in contact with the solid is greater than  $\theta_0$ , it is energetically profitable for the liquid to fill the valley [66, 67]. When the composite interface is destroyed and space between the asperities is filled with water, it is highly unlikely that the composite interface will be formed again because the transition from the non-composite solid–liquid interface to a composite interface would require a large activation energy. Such a transition has never been observed. The effect of capillary waves is more pronounced for small asperities with height comparable with wave amplitude. Second, nanodroplets may condense and accumulate in the valleys between asperities and eventually destroy the composite interface. Cheng et al. [148] observed condensation of submicron sized droplets on a Lotus leaf surface and found that droplets tend to condense at areas adjacent to bumps (i.e. in the valleys) and have a contact angle of less than  $90^\circ$ , whereas larger droplets have higher contact angles, thus demonstrating that the contact angle is scale dependent. The scale effect is observed for small droplets or at small distances near the triple line. Scale dependence of the contact angle has been reported by Nosonovsky and Bhushan [27, 61]. At nanoscale distances from the triple line the liquid touches the solid under a much lower contact angle. Third, even hydrophobic surfaces are usually not chemically homogeneous and can have hydrophilic spots. It is known from experiments that for droplets of submicron size, the value of the contact angle is usually smaller than for droplets at the macroscale [55]. Checco et al. [136] suggested that surface inhomogeneity is responsible for this scale effect, since nanodroplets tend to sit at the highest free surface energy (most hydrophilic) spots and thus have lower contact angles. Their phenomenological numerical simulations showed good agreement with experimental data.

For high  $f_{LA}$ , a nanopattern is desirable because whether a liquid–air interface is generated depends upon the ratio of distance between two adjacent asperities and

droplet radius. Furthermore, asperities can pin liquid droplets and thus prevent liquid from filling the valleys between asperities. High  $R_f$  can be achieved by both micropatterns and nanopatterns. Nosonovsky and Bhushan [27, 31–33, 61–64] have demonstrated that a combination of microroughness and nanoroughness (multiscale roughness) with convex surfaces can help resist the destabilization by pinning the interface. It also helps in preventing the gaps between the asperities from filling with liquid, even in the case of a hydrophilic material. The effect of roughness on wetting is scale dependent, and mechanisms that lead to destabilization of a composite interface are also scale-dependent. To effectively resist these scale-dependent mechanisms, it is expected that a multiscale roughness is optimum for superhydrophobicity.

Nosonovsky [149] considered a two-dimensional structure with rectangular pillars of height  $h$  and width  $a$  separated by distance  $b$ , covered with small semi-circular bumps (convex) and grooves (concave) of radius  $r$  (Fig. 20.13a). If the distance between the pillars is small in comparison with the capillary length, the effect of gravity is negligible, it can be assumed that the liquid–air interface is a horizontal plane, and its position is characterized by the vertical coordinate  $z$ . The free energy is given by [149]

$$W = A_{SL}\gamma_{SL} + A_{SA}\gamma_{SA} + A_{LA}\gamma_{LA} = rL\gamma_{LA}(\sin \alpha - \alpha \cos \theta_0), \quad 0 < z < h \quad (20.21)$$

where  $\alpha = \text{acos}((r-z)/r) + 2\pi N$  is the angle corresponding to vertical position of the interface  $z$ ,  $N$  is the number of ridges or grooves, and  $L$  is length of the grooves in the  $y$ -direction, which is required based on the dimensional considerations. The dependence is presented in Fig. 20.13b, for the cases of hydrophobic ( $\theta_0 = 150^\circ$ ) and hydrophilic ( $\theta_0 = 30^\circ$ ) materials for both the convex surface (with bumps) and concave surface (with grooves). It is seen that for the convex surface, there are many states of stable equilibrium (shown in Fig. 20.13a with dotted lines), separated by energy barriers which correspond to every ridge, whereas for the concave surface equilibrium states are unstable. Therefore, the ridges can pin the triple line and thus lead to a composite interface. In the case of a hydrophilic surface, each lower position of the equilibrium state corresponds to a lower value of  $W$ , therefore, when the liquid advances from one equilibrium state to the next, the total energy decreases, and thus liquid's advance is energetically profitable. When the liquid reaches the bottom of the valley and completely fills the space between the pillars forming a homogeneous interface, the total energy decreases dramatically by the value of [149]

$$\Delta W = bL(\gamma_{SA} + \gamma_{LA} - \gamma_{SL}) = bL\gamma_{LA}(1 + \cos \theta_0) \quad (20.22)$$

The opposite transition from a homogeneous interface to a composite interface requires high activation energy  $\Delta W$  and is thus unlikely, making the transition from composite interface to homogeneous interface irreversible. If the distance between the pillars  $b$  is much greater than  $r$ , the energy barriers which separate the equilibrium states,  $2\pi rL\gamma_{LA} \cos \theta_0$ , will be relatively small compared to  $\Delta W$ , and low

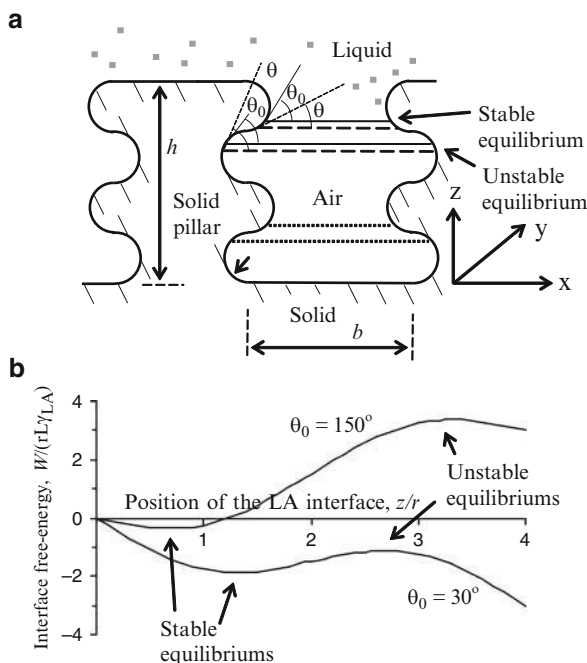


**Fig. 20.13** Two-dimensional pillars with semi-circular bumps/grooves. (a) Schematics of the structure. The bumps may pin the triple line, because an advance of the LA interface results in decrease of the contact angle ( $\theta < \theta_0$ ), making equilibrium stable. Grooves provide with equilibrium positions, which satisfy the Young equation, however, the equilibrium is unstable, because an advance of the LA interface results in increase of the contact angle ( $\theta > \theta_0$ ). (b) Energy profiles for configurations in Fig. 20.13a with bumps and grooves for hydrophilic ( $\theta_0 = 30^\circ$ ) and hydrophobic ( $\theta_0 = 150^\circ$ ) materials. Energy (normalized by  $Lr\gamma_{LA}$ ) is shown as a function of vertical position of the interface  $z$  (normalized by the radius of bumps/grooves  $r$ ). Bumps result in stable equilibriums (energy minima), whereas grooves result in unstable equilibriums (energy maxima) [149]

activation energy will be required for the liquid to spread and propagate from one equilibrium state to the other [61, 63].

For the interface to be stable, the value of the contact angle should decrease when the liquid–air interface advances, whereas for receding liquid the contact angle should increase. For a two-dimensional surface, the change of angle is equal to the change of the slope of the surface, and whether the configuration is stable or not depends on the sign of curvature of the surface. As indicated earlier, the convex surface (with bumps) leads to a stable interface, whereas a concave surface (with grooves) leads to an unstable interface. This approach was suggested for creating superoleophobic surfaces, since the surface tension of oil and organic liquids is much lower than that of water, and it is difficult to create a surface not wetted by oil [130]. Since oleophilic surfaces in air (solid–oil–air system) can become superoleophobic when immersed in water (solid–oil–water system),

underwater superoleophobicity has potential for self-cleaning anti-fouling surfaces for ships.

An experiment suggesting that the sign of curvature is indeed important for hydrophobicity was conducted by Sun et al. [60]. They produced both a positive and a negative replica of a Lotus leaf surface by nanocasting using poly(dimethylsiloxane), which has a contact angle with water of about  $105^\circ$ . This value is close to the contact angle of the wax which covers Lotus leaves (about  $103^\circ$  as reported by Kamusewitz et al. [150]). The positive and negative replicas have the same roughness factor and thus should produce the same contact angle in the case of a homogeneous interface, according to (20.6); however, the values of surface curvature are opposite. The value of contact angle for the positive replica was found to be  $160^\circ$  (same as for Lotus leaf), while for the negative replica it was only  $110^\circ$ . This result suggests that the high contact angle for Lotus leaf is due to the composite, rather than homogeneous interface, and that the sign of surface curvature indeed plays a critical role in the formation of the composite interface.

### **20.2.5 *The Cassie–Baxter and Wenzel Wetting Regime Transition***

Since superhydrophobicity requires a stable composite interface, it is important to understand the destabilization mechanisms for the Cassie–Baxter and Wenzel wetting transition. Based on Nosonovsky and Bhushan [27, 79], it is known from experimental observations that the transition from the Cassie–Baxter to Wenzel regime can be an irreversible event. Whereas such a transition can be induced, for example, by applying pressure or force to the droplet [77, 81], electric voltage [151, 152], light for a photocatalytic texture [153], and vibration [154], the opposite transition is never observed. Several approaches have been proposed for investigation of the transition between the Cassie–Baxter and Wenzel regimes, referred to as “the Cassie–Wenzel transition”. It has been suggested that the transition takes place when the net surface energy of the Wenzel regime becomes equal to that of the Cassie–Baxter regime, or, in other words, when the contact angle predicted by the Cassie–Baxter equation is equal to that predicted by the Wenzel equation. Lafuma and Quere [55] noticed that in certain cases the transition does not occur even when it is energetically profitable, and considered such a Cassie–Baxter state metastable. Extrand [141] suggested that the weight of the droplet is responsible for the transition and proposed the contact line density model, according to which the transition takes place when the weight exceeds the surface tension force at the triple line. Patankar [56] suggested that which of the two states is realized may depend upon how the droplet was formed, that is upon the history of the system. Quéré [155] also suggested that the droplet curvature (which depends upon the pressure difference between the inside and the outside of the droplet) governs the transition. Nosonovsky and Bhushan [67] suggested that the transition is a dynamic process

of destabilization and identified possible destabilizing factors. It has been also suggested that the curvature of multiscale roughness defines the stability of the Cassie–Baxter wetting regime [27, 31, 32, 61, 63, 79, 80, 147, 149] and that the transition is a stochastic gradual process [66, 154, 156, 157]. Numerous experimental results support many of these approaches, however, it is not clear which particular mechanism prevails.

Based on Nosonovsky and Bhushan [27, 79], there is an asymmetry between the wetting and dewetting processes, since less energy is released during wetting than the amount required for dewetting due to adhesion hysteresis. Adhesion hysteresis is one of the reasons that leads to contact angle hysteresis, and it also results in the hysteresis of the Wenzel and Cassie–Baxter state transition. Figure 20.14 shows the contact angle of a rough surface as a function of surface roughness parameter, given by (20.9). Here it is assumed that  $R_f \sim 1$  for a Cassie–Baxter regime with a stable composite interface, and the liquid droplet sits flat over the surface. It is noted that at a certain point, the contact angles given by the Wenzel and Cassie–Baxter equations are the same, and  $R_f = (1 - f_{LA}) - f_{LA}/\cos \theta_0$ . At this point, the lines corresponding to the Wenzel and Cassie–Baxter regimes intersect. This point corresponds to an equal net energy of the Cassie–Baxter and Wenzel regimes. For a lower roughness (e.g., larger pitch between the asperities) the Wenzel state is more energetically profitable, whereas for a higher roughness the Cassie–Baxter regime is more energetically profitable.

It is observed from Fig. 20.14 that an increase of roughness may lead to the transition between the Wenzel and Cassie–Baxter regimes at the intersection point. With decreasing roughness, the system is expected to transit to the Wenzel state. However, experiments [30, 69, 70, 75–77, 143] show that, despite the energy in

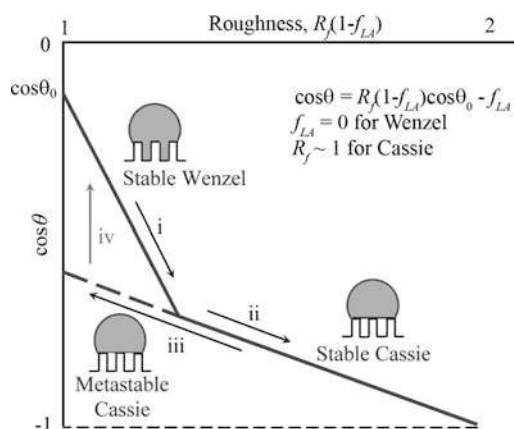


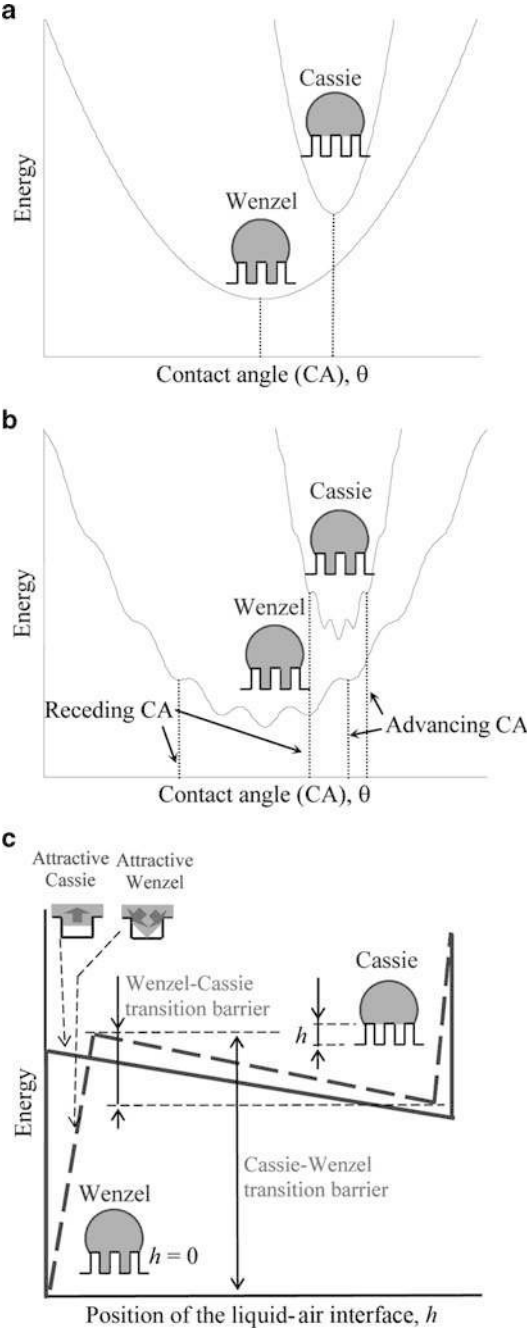
**Fig. 20.14** Wetting hysteresis for a superhydrophobic surface. Contact angle as a function of roughness. The stable Wenzel state (i) can transform into the stable Cassie state with increasing roughness (ii). The metastable Cassie state (iii) can abruptly transform (iv) into the stable Wenzel state. The transition i–ii corresponds to equal Wenzel and Cassie states free energies, whereas the transition iv corresponds to a significant energy dissipation and thus it is irreversible [79]

the Wenzel regime being lower than that in the Cassie–Baxter regime, the transition does not necessarily occur, and the droplet may remain in the metastable Cassie–Baxter regime. This is because there are energy barriers associated with the transition, which occurs due to destabilization by dynamic effects (such as waves and vibration) [27, 79].

In order to understand contact angle hysteresis and the transition between the Cassie–Baxter and Wenzel regimes, Nosonovsky and Bhushan [27, 79] analyzed the shape of the free surface energy profile. The free surface energy of a droplet upon a smooth surface as a function of the contact angle has a distinct minimum which corresponds to the most stable contact angle. As shown in Fig. 20.15a, the macroscale profile of the net surface energy allows us to find the contact angle (corresponding to energy minimums); however it fails to predict the contact angle hysteresis and Cassie–Baxter and Wenzel transition, which are governed by micro- and nanoscale effects. As soon as microscale substrate roughness is introduced, the droplet shape cannot be considered as an ideal truncated sphere anymore, and energy profiles have multiple energy minimums, corresponding to the location of the asperities (Fig. 20.15b). The microscale energy profile (solid line) has numerous energy maxima and minima due to surface asperities. While exact calculation of the energy profile for a 3-D droplet is complicated, a qualitative shape may be obtained by assuming a periodic sinusoidal dependence [51], superimposed upon the macroscale profile, as shown in Fig. 20.15b [27, 79]. Thus the advancing and receding contact angles can be identified as the maximum and minimum possible contact angles corresponding to energy minimum points. However, the transition between the Wenzel and Cassie–Baxter branches still cannot be explained. Note also that Fig. 20.15b explains qualitatively the hysteresis due to the kinetic effect of the asperities, but not the inherited adhesion hysteresis, which is characterized by the molecular length scale and cannot be captured by the microscale model.

Based on Nosonovsky and Bhushan [27, 79], the energy profile as a function of the contact angle does not provide information on how the transition between the Cassie–Baxter and Wenzel regimes occurs, because their two states correspond to completely isolated branches of the energy profile in Fig. 20.15a, b. However, the energy may depend not only upon the contact angle, but also upon micro/nanoscale parameters, such as for example the vertical position of the liquid–air interface under the droplet,  $h$  (assuming that the interface is a horizontal plane) or similar geometrical parameters (assuming a more complicated shape of the interface). In order to investigate the Wenzel and Cassie–Baxter transition, Nosonovsky and Bhushan [27, 79] studied the dependence of the energy upon these parameters. They assume that the liquid–air interface under the droplet is a flat horizontal plane. When such air layer thickness or the vertical position of the liquid–air interface,  $h$ , is introduced, the energy can be studied as a function of the droplet’s shape, the contact angle, and  $h$  (Fig. 20.15c). For an ideal situation, the energy profile has an abrupt minimum at the point corresponding to the Wenzel state, which corresponds to the sudden net energy change due to the destruction of the solid–air and liquid–air interfaces ( $\gamma_{SL} - \gamma_{SA} - \gamma_{LA} = -\gamma_{LA}(\cos \theta + 1)$ ) times the interface

**Fig. 20.15** Schematics of net free energy profiles. (a) Macroscale description; energy minimums correspond to the Wenzel and Cassie states. (b) Microscale description with multiple energy minimums due to surface texture. Largest and smallest values of the energy minimum correspond to the advancing and receding contact angles. (c) Origin of the two branches (Wenzel and Cassie) is found when a dependence of energy upon  $h$  (air layer thickness or vertical position of the liquid–air interface) is considered for the microscale description (*solid line*) and nanoscale imperfectness (*dashed line*) [79]. When the nanoscale imperfectness is introduced, it is observed that the Wenzel state corresponds to an energy minimum and the energy barrier for the Wenzel–Cassie transition is much smaller than for the opposite transition



area) (Fig. 20.15c). In a more realistic case, the liquid–air interface cannot be considered horizontal due to nanoscale imperfectness or dynamic effects such as the capillary waves [67]. A typical size of the imperfectness is much smaller than the size of details of the surface texture and thus belongs to the molecular scale level. The height of the interface,  $h$ , can now be treated as an average height. The energy dependence upon  $h$  is now not as abrupt as in the idealized case. For example, for the “triangular” shape as shown in Fig. 20.15c, the Wenzel state may become the second attractor for the system. It is seen that there are two equilibriums which correspond to the Wenzel and Cassie–Baxter regimes, with the Wenzel state corresponding to a much lower energy level. The energy dependence upon  $h$  governs the transition between the two states, and it is observed that a much larger energy barrier exists for the transition from Wenzel to Cassie–Baxter regime than for the opposite transition. This is why the first transition has never been observed experimentally [62].

To summarize, the contact angle hysteresis and Cassie–Baxter and Wenzel transition cannot be determined from the macroscale equations and are governed by micro- and nanoscale phenomena [27, 79].

## 20.3 Lotus Effect Surfaces in Nature

Many biological surfaces are known to be superhydrophobic and self-cleaning. In this section, we will discuss various plant leaves, their roughness and wax coatings in relation to their hydrophobic/hydrophilic and self-cleaning properties.

### 20.3.1 *Plant Leaves*

Hydrophobic and water-repellent abilities of many plant leaves have been known for a long time. Scanning electron microscope (SEM) studies since the 1970s have revealed that the hydrophobicity of the leaf surface is related to its microstructure. The outer cells covering a plant, especially the leaf, are called epidermis cells. The epidermis in all plant surfaces is covered by a thin extracellular membrane, called cuticle. The plant cuticle is a composite material mainly built up of a cutin network and hydrophobic waxes [4, 11, 15]. The chemical structure of the epicuticular waxes has been studied extensively by plant scientists and lipid chemists in recent decades [158, 159]. The epicuticular waxes can be either thin with a 2-D structure or thick with a 3-D structure or a combination thereof. It is believed that waxes diffuse through the cuticle via a lipidic pathway [160]. After diffusion of the wax, the tubular wax morphologies grow by crystallization or self-assembly. The plants are able to repair the wax layer by self-assembly.



The hydrophobicity of the leaves is related to another important effect, the ability to remain clean after being immersed in dirty water, known as self-cleaning. This ability is best known for the Lotus (*Nelumbo nucifera*) leaf that is considered by some Asian cultures as “sacred” due to its purity. Not surprisingly, the ability of Lotus-like surfaces for self-cleaning and water repellency was dubbed the “Lotus effect”. As far as the biological implications of the Lotus effect, self-cleaning plays an important role in the defense against pathogens binding to the leaf surface. Many spores and conidia of pathogenic organisms – most fungi – require water for germination and can infect leaves only in the presence of water.

Neinhuis and Barthlott [10] systematically studied surfaces and wetting properties of about 200 water-repellent plants (for a comprehensive review, see [4, 15]). Among the epidermal relief features are the papillose epidermal cells either with every epidermal cell forming a single papilla or cells being divided into papillae. The scale of the epidermal relief ranged from 5  $\mu\text{m}$  in multipapillate cells to 100  $\mu\text{m}$  in large epidermal cells. Some cells also are convex (rather than having real papillae) and/or had hairs (trichomes). Neinhuis and Barthlott [10] also found various types and shapes of wax crystals at the surface. Also see Koch et al. [4, 15]. Interestingly, the hairy surfaces with a thin film of wax exhibited water-repellency for short periods (minutes), after which water penetrated between the hairs, whereas hairs with a thick film led to strong water-repellency. The wax crystal creates nanoroughness, in addition to the microroughness created by the papillae. Apparently, roughness plays the dominant role in the Lotus effect.

The SEM study reveals that the Lotus leaf surface is covered by “bumps”, more exactly called papillae (papillose epidermal cells), which, in turn, are covered by an additional layer of epicuticular waxes [11]. The wax is present in crystalline tubules, composed of a mixture of long-chain aliphatic compounds, principally nonacosanol and nonacosanediols [4, 15, 161]. The wax is hydrophobic with a water contact angle of about  $95^\circ$ – $110^\circ$ , whereas the papillae provide the tool to magnify the contact angle based on the Wenzel model, discussed in the preceding section. The experimental value of the static water contact angle with the Lotus leaf was reported about the  $164^\circ$  [3, 44]. Indeed, taking the papillae density of 3,400 per square millimeter, the average radius of the hemispherical asperities  $r = 10 \mu\text{m}$  and the aspect ratio  $h/r = 1$ , provides, based on (20.6), the value of the roughness factor  $R_f \approx 4$  [66]. Taking the value of the contact angle for wax,  $\theta_0 = 104^\circ$  [150], the calculation with the Wenzel equation yields  $\theta = 165^\circ$ , which is close to the experimentally observed values [66]. However, the simple Wenzel model may be not sufficient to explain the Lotus effect, as the roughness structure forms a composite interface. Moreover, its structure has hierarchical roughness. So, a number of more sophisticated models have been developed to study the role of hierarchical roughness on contact angle [27, 31–33, 61–64, 79, 80]. A qualitative explanation for self-cleaning is that on a smooth surface contamination particles are mainly redistributed by a water droplet; on a rough surface they adhere to the droplet and are removed from the leaves when the droplet rolls off.

### 20.3.2 *Characterization of Superhydrophobic and Hydrophilic Leaf Surfaces*

In order to understand the mechanisms of hydrophobicity in plant leaves, a comprehensive comparative study of superhydrophobic and hydrophilic leaf surfaces and their properties was carried out by Bhushan and Jung [14] and Burton and Bhushan [13]. Below is a discussion of the findings of the study.

#### 20.3.2.1 *Experimental Techniques*

The static contact angles were measured using a Rame-Hart model 100 contact angle goniometer with droplets of deionized (DI) water [13, 14]. Droplets of about 5  $\mu\text{L}$  in volume (with diameter of a spherical droplet about 2.1 mm) were gently deposited on the substrate using a microsyringe for the static contact angle. All measurements were made by five different points for each sample at  $22 \pm 1^\circ\text{C}$  and  $50 \pm 5\%$  RH. The measurement results were reproducible within  $\pm 3^\circ$ .

An optical profiler (NT-3300, Wyko Corp., Tuscon, AZ) was used to measure surface roughness for different surface structures [13, 14]. A greater Z-range of the optical profiler of 2 mm is a distinct advantage over the surface roughness measurements with an AFM which has a Z-range of on the order of 7  $\mu\text{m}$ , but it has only a maximum lateral resolution of approximately 0.6  $\mu\text{m}$  [24, 25]. A commercial AFM (D3100, Nanoscope IIIa controller, Digital Instruments, Santa Barbara, CA) was used for additional surface roughness measurements with a high lateral resolution (sub nm) and for adhesion and friction measurements [14, 98]. The measurements for surface roughness were performed with a square pyramidal Si(100) tip with a native oxide layer which had a nominal radius of 20 nm on a rectangular Si(100) cantilever with a spring constant of 3  $\text{N m}^{-1}$  in the tapping mode.

Adhesion and friction force at various relative humidities (RH) were measured using a 15  $\mu\text{m}$  radius borosilicate ball [24–26]. A large tip radius was used to measure contributions from several microbumps and a large number of nanobumps. Friction force was measured under a normal load ranging from 20 to 250 nN using a  $90^\circ$  scan angle at the velocity of 100  $\mu\text{m/s}$  in 50  $\mu\text{m}$  and at a velocity of 4  $\mu\text{m/s}$  in 2  $\mu\text{m}$  scans. The quantitative measurement of friction force was calibrated by the method described by Bhushan [26]. The normal load was varied (20–250 nN), and a friction force measurement was taken at each increment. By plotting the friction force as a function of normal load, an average coefficient of friction was obtained from the slope of the fit line of the data. The adhesive force was measured using the force distance curve approach. In this technique, the AFM tip is brought into contact with the sample by extending the piezo vertically, then retracting the piezo and calculating the force required to separate the tip from the sample. The adhesive force is obtained by multiplying the cantilever spring constant with the cantilever deflection during the retraction between zero value and the maximum negative value. The method is described in detail by Bhushan [24–26].

### 20.3.2.2 SEM Micrographs

Figure 20.16 shows the SEM micrographs of two superhydrophobic leaves – Lotus (*Nelumbo nucifera*) and elephant ear or taro plant (*Colocasia esculenta*), referred to as Lotus and Colocasia, respectively – and two hydrophilic leaves – beech (*Fagus sylvatica*) and Magnolia (*Magnolia grandiflora*), referred to as Fagus and Magnolia, respectively [14]. Lotus and Colocasia are characterized by papillose epidermal cells responsible for the creation of papillae or microbumps on the surfaces, and an additional layer of 3-D epicuticular waxes which are a mixture of very long chain fatty acids molecules (compounds with chains >20 carbon atoms) and create nanostructure on the entire surface. Fagus and Magnolia are characterized by rather flat tabular cells with a thin wax film with a 2-D structure [11]. The leaves are not self-cleaning, and contaminant particles from ambient are accumulated, which make them hydrophilic.

### 20.3.2.3 Contact Angle Measurements

Figure 20.17a shows the contact angles for the superhydrophobic and hydrophilic leaves before and after applying acetone. The acetone was applied in order to remove any wax present on the surface. As a result, for the superhydrophobic leaves, the contact angle dramatically reduced, whereas for the hydrophilic leaves,

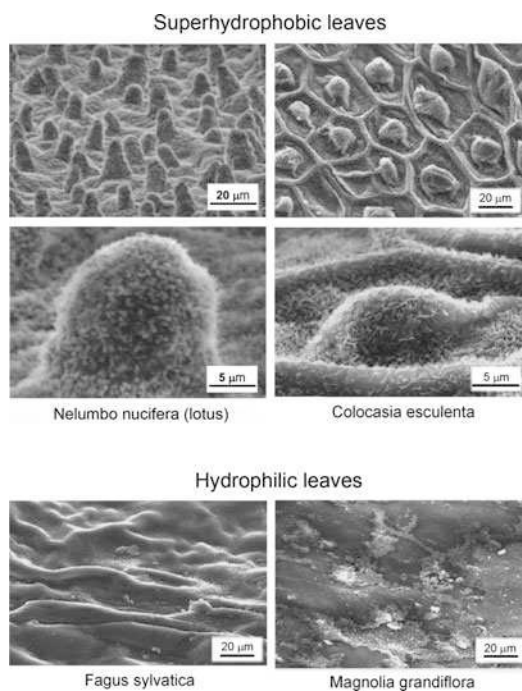


**Fig. 20.16** Scanning electron micrographs of the relatively rough, water-repellent leaf surfaces of *Nelumbo nucifera* (Lotus) and *Colocasia esculenta* and the relatively smooth, wettable leaf surfaces of *Fagus sylvatica* and *Magnolia grandiflora* [14]

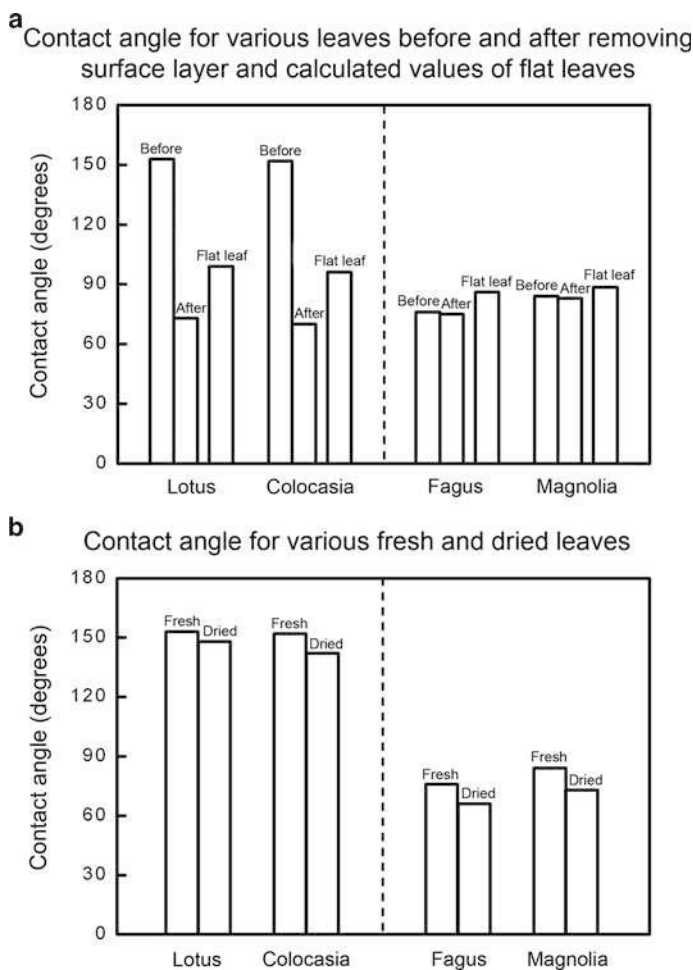


**Fig. 20.17** Contact angle measurements and calculations for the leaf surfaces, (a) before and after removing surface layer as well as calculated values, and (b) fresh and dried leaves. The contact angle on a smooth surface for the four leaves was obtained using the roughness factor calculated [14]

the contact angle was almost unchanged. It is known that there is a 2-D very thin wax layer on the hydrophilic leaves, which introduces little roughness. In contrast, superhydrophobic leaves are known to have a thin 3-D wax layer on their surface consisting of nanoscale roughness over microroughness created by the papillae, which results in a hierarchical roughness. The combination of this wax and the roughness of the leaf creates a superhydrophobic surface.

Bhushan and Jung [14] calculated the contact angles for leaves with smooth surfaces using the Wenzel equation and the calculated  $R_f$  and the contact angle of the four leaves. The results are presented in Fig. 20.17a. The approximate values of  $R_f$  for Lotus and Colocasia are 5.6 and 8.4 and for Fagus and Magnolia are 3.4 and

3.8, respectively. Based on the calculations, the contact angles on smooth surfaces were approximately  $99^\circ$  for Lotus and  $96^\circ$  for Colocasia. For both Fagus and Magnolia, the contact angles for the smooth surfaces were found to be approximately  $86^\circ$  and  $88^\circ$ . A further discussion on the effect of  $R_f$  on the contact angle will be presented later.

Figure 20.17b shows the contact angles for both fresh and dried states for the four leaves. There is a decrease in the contact angle for all four leaves when they are dried. For Lotus and Colocasia, this decrease is present because it is found that a fresh leaf has taller bumps than a dried leaf (data to be presented later), which will give a larger contact angle, according to the Wenzel equation. When the surface area is at a maximum compared to the footprint area, as with a fresh leaf, the roughness factor will be at a maximum and will only reduce when shrinking has occurred after drying. To understand the reason for the decrease of contact angle after drying of hydrophilic leaves, dried Magnolia leaves were also measured using an AFM. It is found that the dried leaf (peak-valley (P-V) height =  $7\text{ }\mu\text{m}$ , mid-width =  $15\text{ }\mu\text{m}$ , and peak radius =  $18\text{ }\mu\text{m}$ ) has taller bumps than a fresh leaf (P-V height =  $3\text{ }\mu\text{m}$ , mid-width =  $12\text{ }\mu\text{m}$ , and peak radius =  $15\text{ }\mu\text{m}$ ), which increases the roughness, and the contact angle decreases, leading to a more hydrophilic surface. The mid-width is defined as the width of the bump at a height equal to half of peak to mean line value.

#### 20.3.2.4 Surface Characterization Using an Optical Profiler

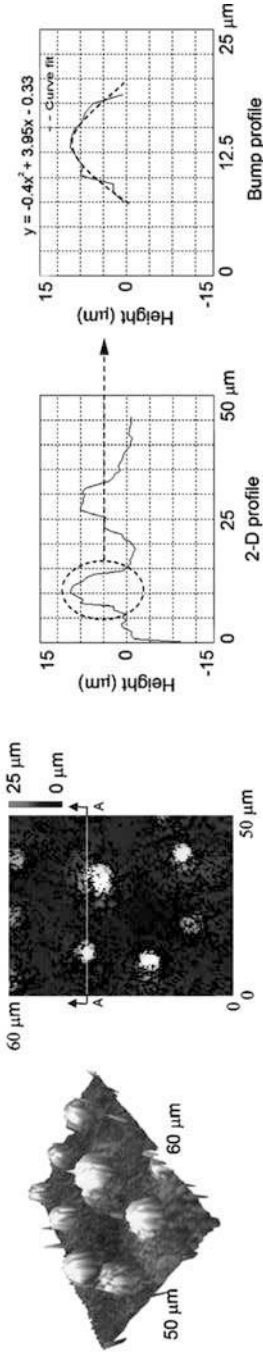
The use of an optical profiler allows measurements to be made on fresh leaves which have a large P-V distance. Three different surface height maps for superhydrophobic and hydrophilic leaves are shown in Figs. 20.18 and 20.19 [14]. In each figure, a 3-D map and a flat map along with a 2-D profile in a given location of the flat 3-D map are shown. A scan size of  $60\text{ }\mu\text{m} \times 50\text{ }\mu\text{m}$  was used to obtain a sufficient amount of bumps to characterize the surface but also to maintain enough resolution to get an accurate measurement.

The structures found with the optical profiler correlate well with the SEM images shown in Fig. 20.16. The bumps on the Lotus leaf are distributed on the entire surface, but the Colocasia leaf shows a very different structure to that of the Lotus. The surface structure for Colocasia not only has bumps similar to Lotus, but also surrounding each bump is a ridge that keeps the bumps separated. With these ridges, the bumps have a hexagonal (honeycomb) packing geometry that allows for the maximum number of bumps in a given area. The bumps of Lotus and both bumps and ridges of Colocasia contribute to the superhydrophobic nature since they both increase the  $R_f$  factor and result in air pockets between the droplet of water and the surface. In Fagus and Magnolia height maps, short bumps can be seen on the surface. This means that with decreased bump height, the probability of air pocket formation decreases, and bumps have a less beneficial effect on the contact angle.

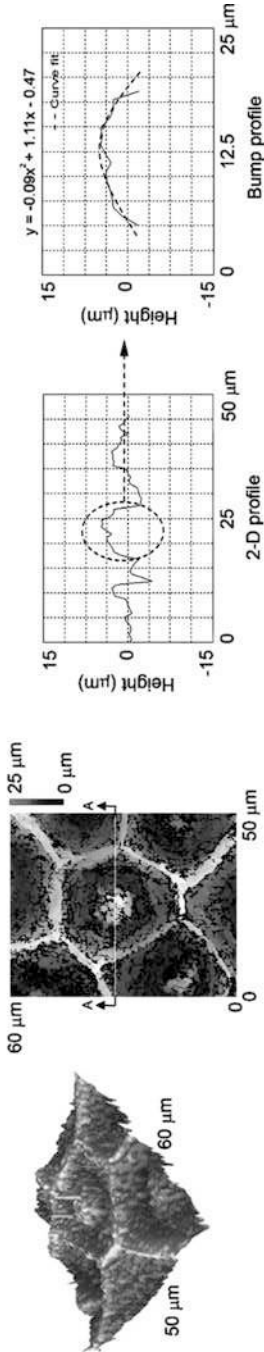
As shown in 2-D profiles of superhydrophobic and hydrophilic leaves in Figs. 20.18 and 20.19, a curve has been fitted to each profile to show exactly how

Optical surface height maps and curve fit of bumps

Superhydrophobic leaves



Fresh lotus



Fresh colocasia

**Fig. 20.18** Surface height maps and 2-D profiles of hydrophobic leaves using an optical profiler. For Lotus leaf, a microbump is defined as a single, independent microstructure protruding from the surface. For Colocasia leaf, a microbump is defined as the single, independent protrusion from the leaf surface, whereas a ridge is defined as the structure that surrounds each bump and is completely interconnected on the leaf. A curve has been fitted to each profile to show exactly how the bump shape behaves. The radius of curvature is calculated from the parabolic curve fit of the bump [14]



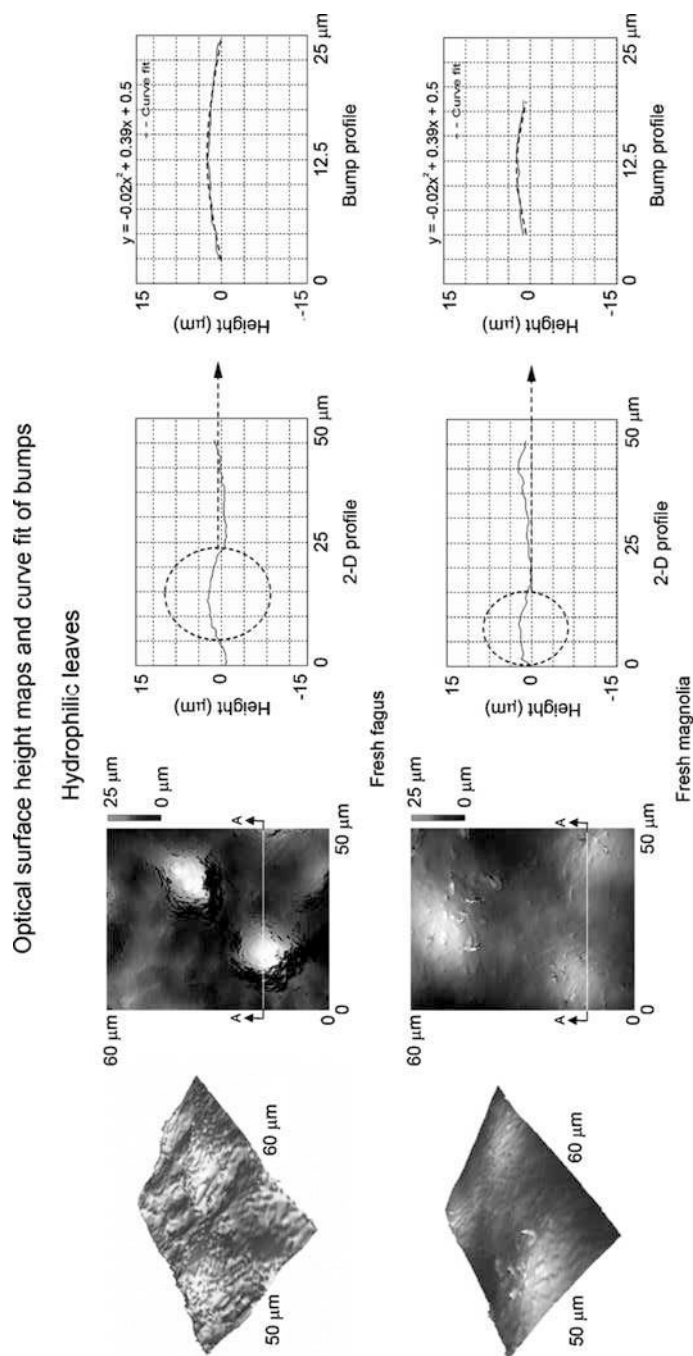


**Fig. 20.19** Surface height maps and 2-D profiles of hydrophilic leaves using an optical profiler. For *Fagus* and *Magnolia* leaves, a microbump is defined as a single, independent microstructure protruding from the surface. A curve has been fitted to each profile to show exactly how the bump shape behaves. The radius of curvature is calculated from the parabolic curve fit of the bump [14]

**Table 20.3** Microbump and nanobump map statistics for hydrophobic and hydrophilic leaves, measured both fresh and dried leaves using an optical profiler and AFM [14]

Leaf	Microbump Scan size ( $50 \times 50 \mu\text{m}$ )			Nanobump Scan size ( $2 \times 2 \mu\text{m}$ )		
	P-V height ( $\mu\text{m}$ )	Mid-width ( $\mu\text{m}$ )	Peak radius ( $\mu\text{m}$ )	P-V height ( $\mu\text{m}$ )	Mid-width ( $\mu\text{m}$ )	Peak radius ( $\mu\text{m}$ )
Lotus						
Fresh	13 <sup>a</sup>	10 <sup>a</sup>	3 <sup>a</sup>	0.78 <sup>b</sup>	0.40 <sup>b</sup>	0.15 <sup>b</sup>
Dried	9 <sup>b</sup>	10 <sup>b</sup>	4 <sup>b</sup>	0.67 <sup>b</sup>	0.25 <sup>b</sup>	0.10 <sup>b</sup>
Colocasia						
Fresh Bump	9 <sup>a</sup>	15 <sup>a</sup>	5 <sup>a</sup>	0.53 <sup>b</sup>	0.25 <sup>b</sup>	0.07 <sup>b</sup>
Ridge	8 <sup>a</sup>	7 <sup>a</sup>	4 <sup>a</sup>	0.68 <sup>b</sup>	0.30 <sup>b</sup>	0.12 <sup>b</sup>
Dried Bump	5 <sup>b</sup>	15 <sup>b</sup>	7 <sup>b</sup>	0.48 <sup>b</sup>	0.20 <sup>b</sup>	0.06 <sup>b</sup>
Ridge	4 <sup>b</sup>	8 <sup>b</sup>	4 <sup>b</sup>	0.57 <sup>b</sup>	0.25 <sup>b</sup>	0.11 <sup>b</sup>
Fagus						
Fresh	5 <sup>a</sup>	10 <sup>a</sup>	15 <sup>a</sup>	0.18 <sup>b</sup>	0.04 <sup>b</sup>	0.01 <sup>b</sup>
	4 <sup>b</sup>	5 <sup>b</sup>	10 <sup>b</sup>			
Magnolia						
Fresh	4 <sup>a</sup>	13 <sup>a</sup>	17 <sup>a</sup>	0.07 <sup>b</sup>	0.05 <sup>b</sup>	0.04 <sup>b</sup>
	3 <sup>b</sup>	12 <sup>b</sup>	15 <sup>b</sup>			

<sup>a</sup>Data measured using optical profiler<sup>b</sup>Data measured using AFM

the bump shape behaves. For each leaf a second order curve fit has been given to the profiles to show how closely the profile is followed. By using the second order curve fitting of the profiles, the radius of curvature can be found [13, 14].

Using these optical surface height maps, different statistical parameters of bumps and ridges can be found to characterize the surface: P-V height, mid-width, and peak radius [24, 25]. Table 20.3 shows these quantities found in the optical height maps for the four leaves. Comparing the superhydrophobic and hydrophilic leaves, it can be seen that the P-V height for bumps of Lotus and Colocasia is much taller than that for the bumps of Fagus and Magnolia. The peak radius for the bumps of Lotus and Colocasia is also smaller than that for the bumps of Fagus and Magnolia. However, the values of mid-width for the bumps of the four leaves are similar.

### 20.3.2.5 Surface Characterization, Adhesion and Friction Using an AFM

#### Comparison of Two AFM Measurement Techniques

To measure topographic images of the leaf surfaces, both the contact and tapping modes were first used [14]. Figure 20.20 shows surface height maps of dried Lotus obtained using the two techniques. In the contact mode, local height variation for Lotus leaf was observed in  $50 \mu\text{m}$  scan size. However, little height variation was obtained in a  $2 \mu\text{m}$  scan even at loads as low as 2 nN. This could be due to the substantial frictional force generated as the probe scanned over the sample. The frictional force can damage the sample. The tapping mode technique allows



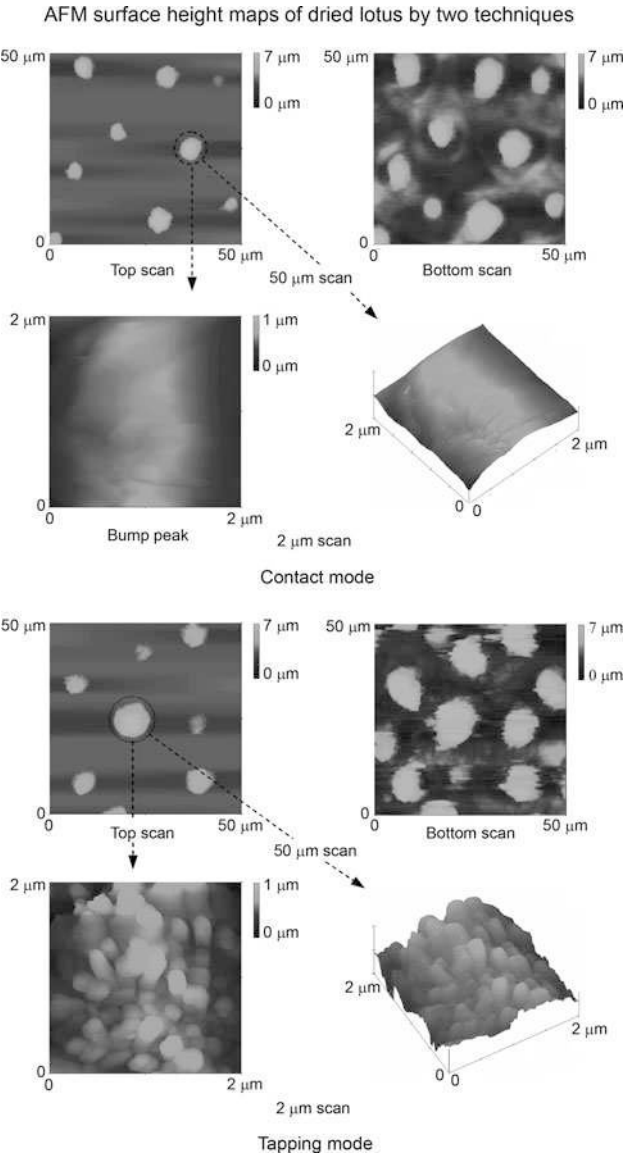


**Fig. 20.20** Surface height maps showing the top scan and bottom scan in a 50  $\mu\text{m}$  scan size and the bump peak scan selected in a 2  $\mu\text{m}$  scan size for a Lotus leaf using an AFM in contact mode and tapping mode. Two methods were used to determine a suitable method to obtain high resolution of nanotopography for a Lotus leaf [14]

high-resolution topographic imaging of sample surfaces that are easily damaged, loosely held to their substrate, or difficult to image by other AFM techniques [24, 25]. As shown in Fig. 20.20, with the tapping mode technique, the soft and fragile leaves

can be imaged successfully. Therefore tapping mode technique was used to examine the surface roughness of the superhydrophobic and hydrophilic leaves using an AFM.

### Surface Characterization

The AFM has a Z-range on the order of 7  $\mu\text{m}$ , and cannot be used for measurements in a conventional way because of the high P-V distances of a Lotus leaf. Burton and Bhushan [13] developed a new method to fully determine the bump profiles. In order to compensate for the large P-V distance, two scans were made for each height: one measurement that scans the tops of the bumps and another measurement that scans the bottom or valleys of the bumps. The total height of the bumps is embedded within the two scans. Figure 20.21 shows the 50  $\mu\text{m}$  surface height maps obtained using this method [14]. The 2-D profiles in the right side column take the profiles from the top scan and the bottom scan for each scan size and splice them together to get the total profile of the leaf. The 2  $\mu\text{m}$  surface height maps for both fresh and dried Lotus can also be seen in Fig. 20.21. This scan area was selected on the top of a microbump obtained in the 50  $\mu\text{m}$  surface height map. It can be seen that nanobumps are randomly and densely distributed on the entire surface of Lotus.

Bhushan and Jung [14] also measured the surface height maps for the hydrophilic leaves in both 50  $\mu\text{m}$  and 2  $\mu\text{m}$  scan sizes as shown in Fig. 20.22. For Fagus and Magnolia, microbumps were found on the surface, and the P-V distance of these leaves is lower than that of Lotus and Colocasia. It can be seen in the 2  $\mu\text{m}$  surface height maps that nanobumps selected on the peak of the microbump have an extremely low P-V distance.

Using the AFM surface height maps, different statistical parameters of bumps and ridges can be obtained: P-V height, mid-width, and peak radius. These quantities for the four leaves are listed in Table 20.3. It can be seen that the values correlate well with the values obtained from optical profiler scans except for the bump height, which decreases by more than half because of leaf shrinkage.

### Adhesive Force and Friction

Adhesive force and coefficient of friction of superhydrophobic and hydrophilic leaves using AFM are presented in Fig. 20.23 [14]. For each type of leaf, adhesive force measurements were made for both fresh and dried leaves using a 15  $\mu\text{m}$  radius tip. It is found that the dried leaves had a lower adhesive force than the fresh leaves. Adhesive force arises from several sources in changing the presence of a thin liquid film, such as an adsorbed water layer that causes meniscus bridges to build up around the contacting and near contacting bumps as a result of surface energy effects [24, 25]. When the leaves are fresh there is moisture within the plant material that causes the leaf to be soft, and when the tip comes into contact with the leaf sample, the sample will deform, and a larger real area of contact between the tip and sample will occur, and the adhesive force will increase. After the leaf has dried, the moisture that was in the plant material is

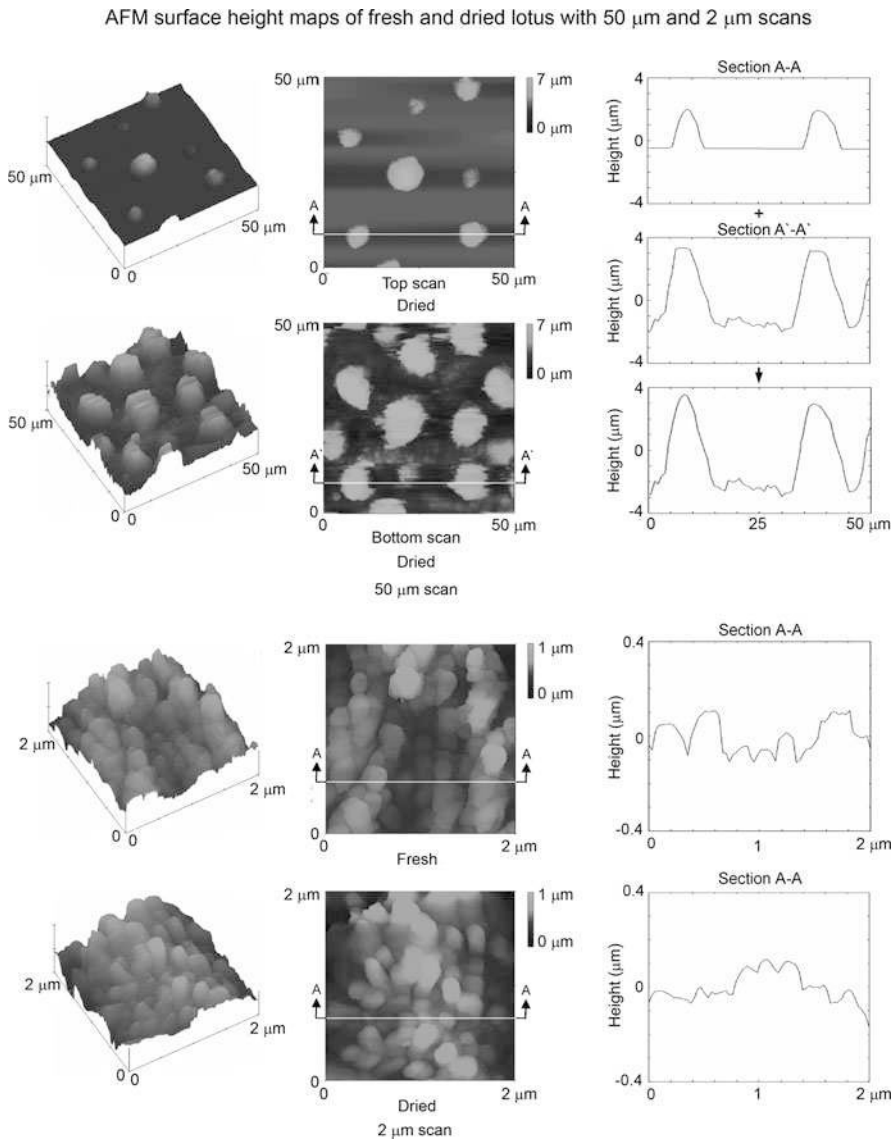


**Fig. 20.21** Surface height maps and 2-D profiles showing the top scan and bottom scan of a dried Lotus leaf in 50  $\mu\text{m}$  scan (because the P-V distance of a dried Lotus leaf is greater than the Z-range of an AFM), and the top scan of both fresh and dried Lotus in a 2  $\mu\text{m}$  scan [14]. Splicing technique was used to determine the bump profiles. In order to compensate for the large P-V distance, the total height of the bumps is embedded within the top scan and bottom scan

gone, and there is not as much deformation of the leaf when the tip comes into contact with the leaf sample. Hence, the adhesive force is decreased because the real area of contact has decreased.

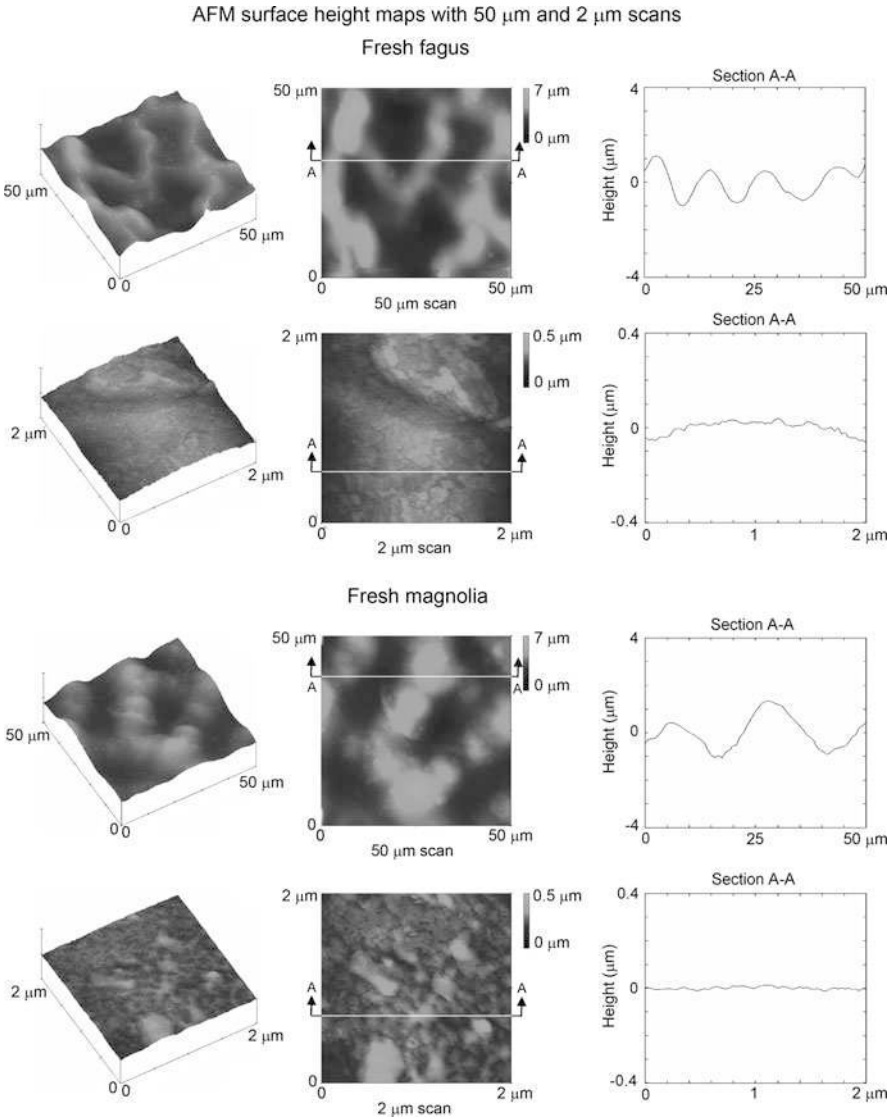
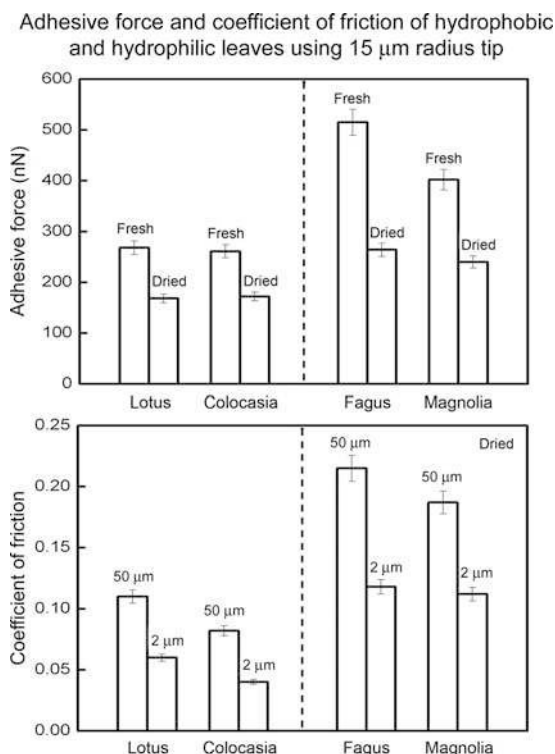


**Fig. 20.22** Surface height maps and 2-D profiles of Fagus and Magnolia using an AFM in both 50  $\mu\text{m}$  and 2  $\mu\text{m}$  scans [14]

The adhesive force of Fagus and Magnolia is higher than that of Lotus and Colocasia. The reason is that the real area of contact between the tip and leaf surface is expected to be higher in hydrophilic leaves than in superhydrophobic leaves. In addition, the Fagus and Magnolia are hydrophilic and have a high affinity to water. The combination of high real area of contact and affinity to water are responsible for higher meniscus forces [24, 25]. The coefficient of friction was only measured

**Fig. 20.23** Adhesive force for fresh and dried leaves, and the coefficient of friction for dried leaves for 50  $\mu\text{m}$  and 2  $\mu\text{m}$  scan sizes for hydrophobic and hydrophilic leaves. All measurements were made using a 15  $\mu\text{m}$  radius borosilicate tip. Reproducibility for both adhesive force and coefficient of friction is  $\pm 5\%$  for all measurements [14]



on a dried plant surface with the same sliding velocity (10  $\mu\text{m}/\text{s}$ ) in different scan sizes rather than including the fresh surface because the P-V was too large to scan back and forth with the AFM to obtain friction force. As expected, the coefficient of friction for superhydrophobic leaves is lower than that for hydrophilic leaves due to the real area of contact between the tip and leaf sample, similar to the adhesive force results. When the scan size from microscale to nanoscale decreases, the coefficient of friction also decreases in each leaf. The reason for such dependence is the scale dependent nature of the roughness of the leaf surface. Figures 20.21 and 20.22 show AFM topography images and 2-D profiles of the surfaces for different scan sizes. The scan size dependence of the coefficient of friction has been reported previously [162–164].

### 20.3.2.6 Role of the Hierarchical Roughness

The approximation of the roughness factor for the leaves on the micro- and nanoscale was made using AFM scan data [14]. Roughness factors for various leaves are presented in Table 20.4. As mentioned earlier, the open space between asperities on a surface has the potential to collect air, and its probability appears to be higher in nanobumps as the distance between bumps in the nanoscale is smaller

**Table 20.4** Roughness factor and contact angle ( $\Delta\theta = \theta - \theta_0$ ) calculated using  $R_f$  on the smooth surface for hydrophobic and hydrophilic leaves measured using an AFM, both microscale and nanoscale [14]

Leaf (Contact angle)	Scan size	State	$R_f$	$\Delta\theta$ (deg)
Lotus (153°)	50 $\mu m$	Dried	5.6	54 <sup>a</sup>
	2 $\mu m$	Fresh	20	61 <sup>b</sup>
		Dried	16	60 <sup>b</sup>
Colocasia (152°)	50 $\mu m$	Dried	8.4	56 <sup>a</sup>
	2 $\mu m$ bump	Fresh	18	60 <sup>b</sup>
		Dried	14	59 <sup>b</sup>
	2 $\mu m$ ridge	Fresh	18	60 <sup>b</sup>
		Dried	15	59 <sup>b</sup>
Fagus (76°)	50 $\mu m$	Fresh	3.4	−10 <sup>a</sup>
	2 $\mu m$	Fresh	5.3	2 <sup>b</sup>
Magnolia (84°)	50 $\mu m$	Fresh	3.8	−4 <sup>a</sup>
	2 $\mu m$	Fresh	3.6	14 <sup>b</sup>

<sup>a</sup>Calculations made using Wenzel equation  
<sup>b</sup>Calculations made using Cassie–Baxter equation. We assume that the contact area between the droplet and air is the half of the whole area of the rough surface

than those in microscale. Using roughness factor values, along with the contact angles ( $\theta$ ) from both superhydrophobic and hydrophilic surfaces, 153° and 152° in Lotus and Colocasia, and 76° and 84° in Fagus and Magnolia, respectively, the contact angles ( $\theta_0$ ) for the smooth surfaces can be calculated using the Wenzel equation (20.6) for microbumps and the Cassie–Baxter equation (20.9) for nanobumps. Contact angle ( $\Delta\theta$ ) calculated using  $R_f$  on the smooth surface can be found in Table 20.4. It can be seen that the roughness factors and the differences ( $\Delta\theta$ ) between  $\theta$  and  $\theta_0$  on the nanoscale are higher than those in the microscale. This means that nanobumps on the top of a microbump increase contact angle more effectively than microbumps. In the case of hydrophilic leaves, the values of  $R_f$  and  $\Delta\theta$  change very little on both scales.

Based on the data in Fig. 20.23, the coefficient of friction values in the nanoscale are much lower than those in the microscale. It is clearly observed that friction values are scale dependent. The height of a bump and the distance between bumps in microscale is much larger than those in nanoscale, which may be responsible for larger values of friction force on the microscale.

One difference between microbumps and nanobumps for surface enhancement of water repellency is the effect on contact angle hysteresis, in other words, the ease with which a droplet of water can roll on the surface. It has been stated earlier that contact angle hysteresis decreases and contact angle increases due to the decreased contact with the solid surface caused by the air pockets beneath the droplet. The surface with nanobumps has a high roughness factor compared with that of microbumps. With large distances between microbumps, the probability of air pocket formation decreases and is responsible for high contact angle hysteresis. Therefore, on the surface with nanobumps, the contact angle is high and contact angle hysteresis is low, and drops rebound easily and can set into a rolling motion with a small tilt angle [14].

Natural water-repellent and self-cleaning surfaces such as the Lotus leaf [4, 15] or water strider leg [5] have a hierarchical structure. However, the functionality of this hierarchical roughness remains a subject of discussion, and several explanations have been suggested. Nosonovsky and Bhushan [27, 31–33, 61–64, 79, 80] showed that the mechanisms involved in superhydrophobicity are scale dependent, and thus the roughness must be hierarchical in order to respond to these mechanisms. The surface must be able to repel both macroscopic and microscopic droplets. Fürstner et al. [165] pointed out that artificial surfaces with one level of roughness can well repel large “artificial rain” droplets; however, they cannot repel small “artificial fog” droplets trapped in the valleys between the bumps, so the hierarchy may have to do with the ability to repel droplets of various size ranges. According to Gao and McCarthy [166], the large bumps allow to maintain the composite interface while the small ones enhance the contact angle in accordance to the Wenzel model. Jung and Bhushan [76] showed that a droplet with radius of about 100–400  $\mu\text{m}$  on micropatterned surfaces goes through transition from the composite interface to the solid–liquid interface as the pitch increases, and Bhushan et al. [71, 73, 74] showed that the hierarchical structure can prevent the gaps between the pillars from filling with liquid until the droplet evaporated completely.

## 20.4 How to Make a Surface for Superhydrophobicity, Self-cleaning, Low Adhesion, and Drag Reduction

Fabrication of superhydrophobic surfaces has been an area of active research since the mid-1990s. In general, the same techniques that are used for micro- and nanostructure fabrication, such as lithography, etching, deposition and self-assembly, have been utilized for producing superhydrophobic surfaces (Fig. 20.24, Table 20.5). Pros and cons of these techniques are summarized in Table 20.6. Among especially interesting developments is the creation of switchable surfaces

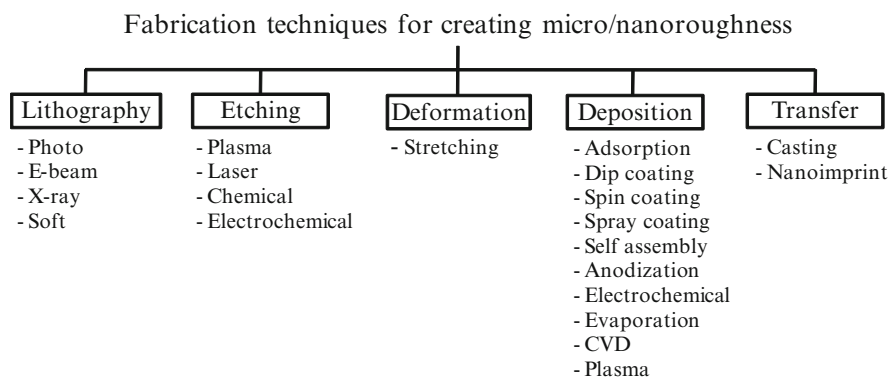


**Fig. 20.24** Typical methods to fabricate micro/nanoroughened surfaces

**Table 20.5** Typical materials and corresponding techniques to produce micro/nanoroughness

Material	Technique	Contact angle (deg)	Notes	Source
Teflon	Plasma	168		Zhang et al. [167], Shiu et al. [168]
Fluorinated block polymer solution	Casting under humid environment	160	Transparent	Yabu and Shimomura [169]
PFOS	Electro- and chemical polymerization	152	Reversible (electric potential)	Xu et al. [170]
PDMS	Laser treatment	166		Khorasani et al. [171]
PS-PDMS Block copolymer	Electrospinning	>150		Ma et al. [172]
PS, PC, PMMA	Evaporation	>150		Bornashenko et al. [173]
PS nanofiber	Nanoimprint	156		Lee et al. [174]
Polyaniline nanofiber	Chemical polymerization	175		Chiou et al. [175]
PET	Oxygen plasma etching	>150		Teshima et al. [176]
Organo-triethoxysilanes	Sol-gel	155	Reversible (temperature)	Shirtcliffe et al. [177]
Al	Chemical etching	>150		Qian and Shen [178]
Copper	Electrodeposition	160		Shirtcliffe et al. [179]
Si	Photolithography	170	Hierarchical	Bhushan and Jung [69]
Si	E-beam lithography	164		Martines et al. [180]
Si	X-ray lithography	>166		Furstner et al. [165]
PS, PMMA	AFM nanolithography			Martin et al. [181], Cappella and Bonaccorso [182]
Si	Casting	158	Plant leaf replica	Sun et al. [60], Furstner et al. [165]
Si (Black Si)	Plasma etching	>150	For liquid flow	Jansen et al. [183]
Silica	Sol-gel	150		Hikita et al. [184], Shang et al. [185]
Silica	Layer-by-layer assembly	160	Hierarchical	Zhao et al. [186]
Polyelectrolyte multilayer surface overcoated with silica nanoparticles	Self assembly	168		Zhai et al. [187]
Epoxy resin with synthetic and plant waxes	Replication and self assembly	173	Hierarchical	Bhushan et al. [71–74], Koch et al. [44]



Nano-silica spheres	Dip coating	105		Klein et al. [188]
Silica colloidal particles in PDMS	Spin coated	165	Hierarchical	Ming et al. [189]
Au clusters	Electrochemical deposition	> 150		Zhang et al. [190]
Carbon nanotubes	Chemical vapor deposition	> 165		Lau et al. [191]
Carbon nanotubes	Chemical vapor deposition	159	Hierarchical	Huang et al. [192]
Carbon nanotubes	Replication and spray coating	170	Hierarchical	Jung and Bhushan [100]
ZnO, TiO <sub>2</sub> Nanorods	Sol-gel	> 150	Reversible (UV irradiation)	Feng et al. [153]

**Table 20.6** Pros and cons of various fabrication techniques

Techniques	Pros	Cons
Lithography	Accuracy, large area	Slow process, high cost
Etching	Fast	Chemical contamination, less control
Deposition	Flexibility, cheap	Can be high temperature, less control
Self assembly	Flexibility, cheap	Require suitable precursor

that can be turned from hydrophobic to hydrophilic by surface energy modification through electrowetting, light and X-ray irradiation, dynamic effects, optical effects (e.g., the transparency, reflectivity or non-reflectivity) combined with the Lotus effect, hydrophobic interactions, and so on [153, 170, 177, 193, 194]. An important requirement for potential applications for optics and self-cleaning glasses is the creation of transparent superhydrophobic surfaces. In order for the surface to be transparent, roughness details should be smaller than the wavelength of visible light (about 400–700 nm) [195].

Two main requirements for a superhydrophobic surface are that the surface should be rough and that it should be hydrophobic (low surface energy). These two requirements lead to two methods of producing a superhydrophobic surface: first, it is possible to make a rough surface from an initially hydrophobic material and, second, to modify a rough hydrophilic surface by modifying surface chemistry or applying a hydrophobic material upon it. Note that roughness is usually a more critical property than the low surface energy, since both moderately hydrophobic and very hydrophobic materials can exhibit similar wetting behavior when roughened.

### 20.4.1 *Roughening to Create One-Level Structure*

Lithography is a well-established technique, applied for creating a large area of periodic micro/nanopatterns. It includes photo, E-beam, X-ray, and soft lithography. Bhushan and Jung [69] produced micropatterned Si using photolithography. To obtain a sample that is hydrophobic, a self-assembled monolayer (SAM) of 1, 1, -2, 2, -tetrahydroperfluorodecyltrichlorosilane ( $\text{PF}_3$ ) was deposited on the sample surfaces using a vapor phase deposition technique. They obtained a superhydrophobic surface with a contact angle up to  $170^\circ$ . Martines et al. [180] fabricated ordered arrays of nanopits and nanopillars by using electron beam lithography. They obtained a superhydrophobic surface with a static contact angle of  $164^\circ$  and contact angle hysteresis of  $1^\circ$  for a surface consisting of tall pillars with cusped tops after hydrophobization with octadecyltrichlorosilane (OTS). Fürstner et al. [165] created silicon wafers with regular patterns of spikes by X-ray lithography. The wafer was hydrophobized by sputtering a layer of gold and subsequent immersion in a hexadecanethiol solution. AFM can be used in nanolithography to produce a nanostructure with the aid of solvent [182] or electro field [181] on polystyrene (PS) and

polymethylmethacrylate (PMMA), respectively. Jung and Bhushan [99] created low aspect ratio asperities (LAR, 1:1 height-to-diameter ratio), high aspect ratio asperities (HAR, 3:1 height-to-diameter ratio), and a Lotus pattern (replica from the Lotus leaf), all on a PMMA surface using soft lithography. A self-assembled monolayer (SAM) of perfluorodecyltriethoxysilane (PFDTES) was deposited on the patterned surfaces using a vapor phase deposition technique.

One well-known and effective way to make rough surfaces is etching using either plasma, laser, chemical, or electrochemical techniques [196]. Jansen et al. [183] etched a silicon wafer using a fluorine-based plasma by utilizing the black silicon method to obtain isotropic, positively, and negatively tapered as well as vertical walls with smooth surfaces. Coulson et al. [197] described an approach in plasma chemical roughening of poly(tetrafluoroethylene) (PTFE) substrates followed by the deposition of low surface energy plasma polymer layers, which give rise to high repellency towards polar and nonpolar probe liquids. A different approach was taken by Shiu et al. [168], who treated a Teflon film with oxygen plasma and obtained a superhydrophobic surface with a contact angle of  $168^\circ$ . Fluorinated materials have a limited solubility, which makes it difficult to roughen them. However, they may be linked or blended with other materials, which are often easier to roughen, in order to make superhydrophobic surfaces. Teshima et al. [176] obtained a transparent superhydrophobic surface from a poly(ethylene terephthalate) (PET) substrate via selective oxygen plasma etching followed by plasma-enhanced chemical vapor deposition using tetramethylsilane (TMS) as the precursor. Khorasani et al. [171] produced porous polydimethylsiloxane (PDMS) surfaces with the contact angle of  $175^\circ$  using  $\text{CO}_2$ -pulsed laser etching method as an excitation source for surface. Qian and Shen [178] described a simple surface roughening method by dislocation selective chemical etching on polycrystalline metals such as aluminum. After treatment with fluoroalkylsilane, the etched metallic surfaces exhibited superhydrophobicity. Xu et al. [170] fabricated a reversible superhydrophobic surface with a double-roughened perfluorooctanesulfonate (PFOS) doped conducting polypyrrole (PPy) film by a combination of electropolymerization and chemical polymerization. Reversibility was achieved by switching between superhydrophobic doped or oxidized states and superhydrophilicity dedoped or neutral states with changing the applied electrochemical potential.

A stretching method can be used to produce a superhydrophobic surface. Zhang et al. [167] stretched a Teflon film and converted it into fibrous crystals with a large fraction of void space in the surface, leading to high roughness and the superhydrophobicity.

Deposition methods can also be used to make a substrate rough. There are several ways to make a rough surface including adsorption, dip coating, electrospinning, anodization, electrochemical, evaporation, chemical vapor deposition (CVD), and plasma. Solidification of wax can be used to produce a superhydrophobic surface. Shibuichi et al. [65] used alkylketene dimer (AKD) wax on a glass plate to spontaneously form a fractal structure in its surfaces. They obtained a surface with a contact angle larger than  $170^\circ$  without any fluorination treatments.

Klein et al. [188] obtained superhydrophobic surfaces by simply dip-coating a substrate with a slurry containing nano-silica spheres, which adhered to the substrate after a low temperature heat treatment. After reaction of the surface with a fluoroalkyltrichlorosilane, the hydrophobicity increased with a decreasing area fraction of spheres. Ma et al. [172] produced block copolymer poly(styrene-*b*-dimethylsiloxane) fibers with submicrometer diameters in the range 150–400 nm by electrospinning from a solution in tetrahydrofuran and dimethylformamide. They obtained superhydrophobic nonwoven fibrous mats with a contact angle of 163°. Shiu et al. [168] produced self-organized close-packed superhydrophobic surfaces by spin-coating the monodispersed polystyrene beads solution on a substrate surface. Abdelsalam et al. [198] studied the wetting of structured gold surfaces formed by electrodeposition through a template of submicrometer spheres and discussed the role of the pore size and shape in controlling wetting. Bormashenko et al. [173] used evaporated polymer solutions of polystyrene (PS), polycarbonate (PC) and polymethylmethacrylate (PMMA) dissolved in chlorinated solvents, dichloromethane ( $\text{CH}_2\text{Cl}_2$ ), and chloroform ( $\text{CHCl}_3$ ), to obtain self-assembled structure with hydrophobic properties. Chemical/physical vapor deposition (CVD/PVD) has been used for the modification of surface chemistry as well. Lau et al. [191] created superhydrophobic carbon nanotube forests by modifying the surface of vertically aligned nanotubes with plasma enhanced chemical vapor deposition (PECVD). Superhydrophobicity was achieved down to the microscopic level where essentially spherical, micrometer-sized water droplets can be suspended on top of the nanotube forest. Zhu et al. [199] and Huang et al. [192] prepared surfaces with two-scale roughness by the controlled growth of carbon nanotube (CNT) arrays by CVD. Zhao et al. [200] also synthesized vertically aligned multiwalled carbon nanotube (MWCNT) arrays by chemical-vapor deposition on Si substrates using a thin film of iron (Fe) as catalyst layer and aluminum (Al) film.

Attempts to create superhydrophobic surfaces by casting and nanoimprint methods have been successful. Yabu and Shimomura [169] prepared a porous superhydrophobic transparent membrane by casting a fluorinated block polymer solution under humid environment. Transparency was achieved because the honeycomb-patterned films had a sub-wavelength pore size. Sun et al. [60] reported a nanocasting method to make a superhydrophobic PDMS surface. They first made a negative PDMS template using a Lotus leaf as an original template and then used the negative template to make a positive PDMS template – a replica of the original Lotus leaf. Zhao et al. [201] prepared a superhydrophobic surface by casting a micellar solution of a copolymer poly(styrene-*b*-dimethylsiloxane) (PS-PDMS) in humid air based on the cooperation of vapor-induced phase separation and surface enrichment of PDMS block. Lee et al. [174] produced vertically aligned PS nanofibers by using nanoporous anodic aluminum oxide as a replication template in a heat- and pressure-driven nanoimprint pattern transfer process. As the aspect ratio of the polystyrene (PS) nanofibers increased, the nanofibers could not stand upright but formed twisted bundles resulting in a three-dimensionally rough surface with a contact angle of about 155°.

### 20.4.2 Coating to Create One-Level Hydrophobic Structures

Modifying the surface chemistry with a hydrophobic coating widens the potential applications of superhydrophobic surfaces. There are several ways to modify the chemistry of a surface including sol–gel, dip coating, self-assembly, electrochemical and chemical/physical vapor deposition. Shirtcliffe et al. [177] prepared porous sol–gel foams from organo-triethoxysilanes which exhibited switching between superhydrophobicity and superhydrophilicity when exposed to different temperatures. Hikita et al. [184] used colloidal silica particles and fluoroalkylsilane as the starting materials and prepared a sol–gel film with superliquid-repellency by hydrolysis and condensation of alkoxysilane compounds. Feng et al. [153] produced superhydrophobic surfaces using ZnO nanorods by sol–gel method. They showed that superhydrophobic surfaces can be switched into hydrophilic surfaces by alternation of ultraviolet (UV) irradiation. Shang et al. [185] did not blend low surface energy materials in the sols, but described a procedure to make transparent superhydrophobic surfaces by modifying silica based gel films with a fluorinated silane. In a similar way, Wu et al. [202] made a microstructured ZnO-based surface via a wet chemical process and obtained superhydrophobicity after coating the surface with long-chain alkanolic acids. Chiou et al. [175] fabricated polyaniline nanofibers using chemical oxidative polymerization to produce uniform aligned nanofibers and treated with CF<sub>4</sub> plasma treatment to create superhydrophobic surfaces with a contact angle of 175°.

Zhai et al. [187] used a layer-by-layer (LBL) self-assembly technique to create a poly(allylamine hydrochloride)/poly(acrylic acid) (PAH/PAA) multilayer which formed a honeycomb-like structure on the surface after an appropriate combination of acidic treatments. After cross-linking the structure, they deposited silica nanoparticles on the surface via alternating dipping of the substrates into an aqueous suspension of the negatively charged nanoparticles and an aqueous PAH solution, followed by a final dipping into the nanoparticle suspension. Superhydrophobicity was obtained after the surface was modified by a chemical vapor deposition of (tridecafluoro-1,1,2,2-tetrahydrooctyl)-1-trichlorosilane followed by a thermal annealing.

Zhang et al. [190] showed that the surface covered with dendritic gold clusters, which was formed by electrochemical deposition onto an indium tin oxide (ITO) electrode modified with a polyelectrolyte multilayer, showed superhydrophobic properties after further deposition of a n-dodecanethiol monolayer. Han et al. [203] described the fabrication of Lotus leaf-like superhydrophobic metal surfaces by using electrochemical reaction of Cu or Cu–Sn alloy plated on steel sheets with sulfur gas, and subsequent perfluorosilane treatment. Chemical bath deposition (CBD) has also been used to make nanostructured surfaces, thus, Hosono et al. [204] fabricated a nanopin film of brucite-type cobalt hydroxide (BCH) and achieved the contact angle of 178° after further modification of lauric acid (LA). Shi et al. [205] described the use of galvanic cell reaction as a facile method to

chemically deposit Ag nanostructures on the *p*-silicon wafer on a large scale. When the Ag covered silicon wafer was further modified with a self-assembled monolayer of *n*-dodecanethiol, a superhydrophobic surface was obtained with a contact angle of about 154° and a tilt angle lower than 5°.

### 20.4.3 *Methods to Create Two-Level (Hierarchical) Structures*

Two-level (hierarchical) roughness structures are typical for superhydrophobic surfaces in nature, as was discussed above. Recently, many efforts have been devoted to fabricating these hierarchical structures in various ways. Shirtcliffe et al. [179] prepared a hierarchical (double-roughened) copper surface by electro-deposition from acidic copper sulfate solution onto flat copper and a patterning technique of coating with a fluorocarbon hydrophobic layer. Another way to obtain a rough surface for superhydrophobicity is assembly from colloidal systems. Ming et al. [189] prepared a hierarchical (double roughened) surface consisting of silica-based raspberry-like particles. First is the attachment of epoxy and amino groups onto the silica microparticles of about 700 nm and nanoparticles of about 70 nm, respectively, using established synthetic procedures. Two suspensions in ethanol are created, one with microparticles and another one with nanoparticles. In the next step, the suspension with the silica microparticles is added dropwise to the suspension with the nanoparticles. The nanoparticles attach to the microparticles due to the reaction between the epoxy and amino groups present on the surface of the particles. Then, the suspension is centrifuged to separate any unreacted particles. A next step involves depositing these micro/nanostructured particles into an epoxy film (on silicon). Finally, since the resulting micro/nanoparticle surface is initially hydrophilic, it is made hydrophobic by a deposition of monoepoxy-end-capped poly(dimethylsiloxane) (PDMS). Northen and Turner [206] fabricated arrays of flexible silicon dioxide platforms supported by single high aspect ratio silicon pillars down to 1  $\mu\text{m}$  in diameter and with heights up to  $\sim 50 \mu\text{m}$ . When these platforms were coated with polymeric organorods of approximately 2  $\mu\text{m}$  tall and 50–200 nm in diameter, it showed that the surface is highly hydrophobic with a water contact angle of 145°. Chong et al. [207] fabricated hierarchically ordered nanowire arrays with periodic voids at the microscale and hexagonally packed nanowires at the nanoscale. This hierarchical surface was created by selective electrodeposition using nanoporous anodic alumina as a template and a porous gold film as a working electrode that is patterned by microsphere monolayers. Wang et al. [208] also developed a novel precursor hydrothermal redox method with  $\text{Ni}(\text{OH})_2$  as the precursor to fabricate a hierarchical structure consisting of nickel hollow microspheres with nickel nanoparticles in situ. The created hierarchical hollow structure exhibited enhanced coercivity and remnant magnetization as compared with hollow nickel submicrometer spheres, hollow nickel nanospheres, bulk nickel, and free Ni nanoparticles.

Kim et al. [209] fabricated a hierarchical structure which looks like the same structures as the Lotus leaf. First, the nanoscale porosity was generated by anodic aluminum oxidation, and then, the anodized porous alumina surface was replicated by polytetrafluoroethylene. The polymer sticking phenomenon during the replication created the sub-microstructures on the negative polytetrafluoroethylene nanostructure replica. The contact angle of the created hierarchical structure was about  $160^\circ$  and the tilting angle is less than  $1^\circ$ . Del Campo and Greiner [210] reported that SU-8 hierarchical patterns comprising of features with lateral dimensions ranging from 5 mm to 2 mm and heights from 10 to 500  $\mu\text{m}$  were obtained by photolithography, which comprises of a step of layer-by-layer exposure in soft contact printed shadow masks which are embedded into the SU-8 multilayer. Bhushan et al. [71–74] and Koch et al. [44] produced hierarchical structures by replication of a micropatterned silicon surface and Lotus leaf microstructure using an epoxy resin and by self assembly of synthetic and plant waxes as thin hydrophobic three-dimensional crystals to create hydrophobic nanostructures. The fabrication technique used is a low cost two step process, which provides flexibility in the fabrication of a variety of hierarchical structures. They showed that a hierarchical structure has a high propensity of air pocket formation and leads to a static contact angle of  $173^\circ$  and contact angle hysteresis and tilt angle of  $\sim 2^\circ$ . Zhao et al. [186] fabricated a hierarchical structure by using layer-by-layer assembly of silica nanoparticles on a microsphere-patterned polyimide precursor substrate combined with the fluoroalkylsilane treatment. The microstructures were created by replica molding of polyamide using two-dimensional PS microsphere arrays. They obtained a superhydrophobic surface with a static contact angle of  $160^\circ$  and sliding angle of less than  $10^\circ$ . Cortese et al. [211] applied plasma  $\text{CF}_4$  treatment on micropattern PDMS and obtained contact angle of  $170^\circ$ . Kuan et al. [212] produced a hierarchical structure by imprinting ZnO precursor films using gratings with 830 nm and 50  $\mu\text{m}$  dimensions. They achieved a contact angle of  $141^\circ$  by nanostructures deposited on sawtooth patterns without modifying the surface chemistry. Jung and Bhushan [100] produced mechanically durable CNT composite hierarchical structures with a static contact angle of  $170^\circ$  and a contact angle hysteresis of  $2^\circ$  by replication of a micropatterned silicon surface using an epoxy resin and by deposition of the CNT composite using a spray method. They showed that CNT composite structure had high mechanical strength and wear resistance led from the uniform distribution and strong bonding of CNT on substrates.

## 20.5 Fabrication and Characterization of Micro-, Nano- and Hierarchical Structured Surfaces

In this section, we will discuss experimental measurements of the wetting properties of micro-, nano- and hierarchical patterned surfaces.

## 20.5.1 *Experimental Techniques*

### 20.5.1.1 Contact Angle, Surface Roughness, and Adhesion

The static and dynamic (advancing and receding) contact angles were measured using a Rame-Hart model 100 contact angle goniometer and droplets of DI water [30, 44, 69, 71–75, 98, 99]. For measurement of the static contact angle, the droplet size should be smaller than the capillary length, but larger than the dimension of the structures present on the surfaces. Droplets of about 5  $\mu\text{L}$  in volume (with the diameter of a spherical droplet about 2.1 mm) were gently deposited on the substrate using a microsyringe for measurement of the static contact angle. The advancing and receding contact angles were measured by the addition and removal of water from a DI water sessile droplet using a microsyringe. The contact angle hysteresis was calculated as the difference between the measured advancing and receding contact angles, and the tilt angle was measured by using a simple tilting stage [30, 44, 69, 71–74]. All measurements were made at  $22 \pm 1^\circ\text{C}$  and  $50 \pm 5\%$  RH. The measurements were reproducible to within  $\pm 3^\circ$ .

For surface roughness measurement, an optical profiler (NT-3300, Wyko Corp., Tuscon, AZ) was used for different surface structures [13, 14, 30, 69]. The optical profiler has one advantage due to its greater Z-range (2 mm) over an AFM (Z-range about 7  $\mu\text{m}$ ), but it has a maximum lateral resolution of only approximately 0.6  $\mu\text{m}$  [24, 25]. Experiments were performed using three different radii tips to study the effect of scale dependence. Large radii atomic force microscope (AFM) tips were primarily used in this study. A borosilicate ball with 15  $\mu\text{m}$  radius and a silica ball with 3.8  $\mu\text{m}$  radius were mounted on a gold-coated triangular  $\text{Si}_3\text{N}_4$  cantilever with a nominal spring constant of  $0.58 \text{ N m}^{-1}$ . A square pyramidal  $\text{Si}_3\text{N}_4$  tip with a nominal radius of 30–50 nm on a triangular  $\text{Si}_3\text{N}_4$  cantilever with a nominal spring constant of  $0.58 \text{ N m}^{-1}$  was used for the smaller radius tip. Adhesive force was measured using the force distance curve approach described earlier [24–26].

### 20.5.1.2 Droplet Evaporation Studies

Droplet evaporation was observed and recorded by a digital camcorder (Sony, DCRSR100) with a 10 X optical and 120 X digital zoom for every run of the experiment. Then the decrease in the diameter of the droplets with time was determined [71, 73, 75, 76]. The frame speed of the camcorder was 0.03 s per frame. An objective lens placed in front of the camcorder during recording gave a total magnification of 10–20 times. Droplet diameter as small as a few 100  $\mu\text{m}$  could be measured with this method. Droplets were gently deposited on the substrate using a microsyringe, and the whole process of evaporation was recorded. Images obtained were analyzed using Imagetool<sup>®</sup> software (University of Texas Health Science Center) for the contact angle. To find the dust trace remaining after droplet evaporation, an optical microscope with a charge-coupled device (CCD)



camera (Nikon, Optihot-2) was used. All measurements were made in a controlled environment at  $22 \pm 1^\circ\text{C}$  and  $45 \pm 5\%$  RH [71, 73–76].

### 20.5.1.3 Bouncing Droplet Studies

The process of dynamic impact was recorded by a high speed camera (Kodak Ektapro HS Motion Analyzer, Model 4540) operated at 500 frames/s for each experimental run and then measuring the dynamic impact behavior of the droplet as a function of time. The impact velocity was calculated by varying the droplet release height. The size of the droplet was the same as that of a droplet for the static contact angle. All measurements were made in a controlled environment at  $22 \pm 1^\circ\text{C}$  and  $45 \pm 5\%$  RH [77].

### 20.5.1.4 Vibrating Droplet Studies

The process of dynamic behavior was obtained by a system producing vertical vibrations [78]. The system consists of an electrodynamic shaker (Labworks Inc. Model ET-126A/B) connected with a signal generator and power amplifier, a digital camcorder (Sony, DCRSR100, Tokyo, Japan) with an objective lens, and a lamp (Digital Instruments Inc. Model F0-50) for a light source. The specimen was placed on the top of the shaker, and a droplet was gently deposited using a microsyringe. The size of the droplet was the same as that of a droplet for the static contact angle as reported earlier. The vibration frequency was controlled between 0 and 300 Hz at 0.4 mm amplitude for measurement of the resonance frequency of a droplet. For wetting behavior of a droplet on the surface, a frequency of 30 Hz, which was less than the resonance frequency, was chosen, and the vibration amplitude was controlled between 0 and 3 mm. The vibration time applied to the droplet was 1 min for each experiment. All measurements were made in a controlled environment at  $22 \pm 1^\circ\text{C}$  and  $45 \pm 5\%$  RH [78].

### 20.5.1.5 Microdroplet Condensation and Evaporation Studies Using ESEM

A Philips XL30 ESEM equipped with a Peltier cooling stage was used to study smaller droplets [76]. ESEM uses a gaseous secondary electron detector (GSED) for imaging. The ESEM column is equipped with a multistage differential pressure-pumping unit. The pressure in the upper part is about  $10^{-6}$ – $10^{-7}$  Torr, but a pressure of about 1–15 Torr can be maintained in the observation chamber. When the electron beam (primary electrons) ejects secondary electrons from the surface of the sample, the secondary electrons collide with gas molecules in the ESEM chamber, which in turn acts as a cascade amplifier, delivering the secondary electron signal to the positively biased GSED. The positively charged ions are attracted toward the specimen to neutralize the negative charge produced by the

electron beam. Therefore, the ESEM can be used to examine electrically isolated specimens in their natural state. In ESEM, adjusting the pressure of the water vapor in the specimen chamber and the temperature of the cooling stage allows the water to condense on the sample in the chamber. For the measurement of the static and dynamic contact angles on patterned surfaces, video images were recorded. The voltage of the electron beam was 15 kV, and the distance of the specimen from the final aperture was about 8 mm. If the angle of observation is not parallel to the surface, the electron beam is not parallel to the surface but inclined at an angle, this will produce a distortion in the projection of the droplet profile. A mathematical model to calculate the real contact angle from the ESEM images was used to correct the tilting of the surfaces during imaging [76, 213].

### 20.5.1.6 Generation of Submicron Droplets

In order to generate submicron droplets, Jung and Bhushan [214] developed an AFM-based technique using a modified nanoscale dispensing (NADIS) probe as shown in Fig. 20.25. NADIS probe was fabricated from modifying a commercially available silicon nitride ( $\text{Si}_3\text{N}_4$ ) cantilever (Olympus OMCL-RC800) with lengths of 100 and 200  $\mu\text{m}$ , spring constants of 0.8 and 0.1  $\text{N m}^{-1}$ , and resonance

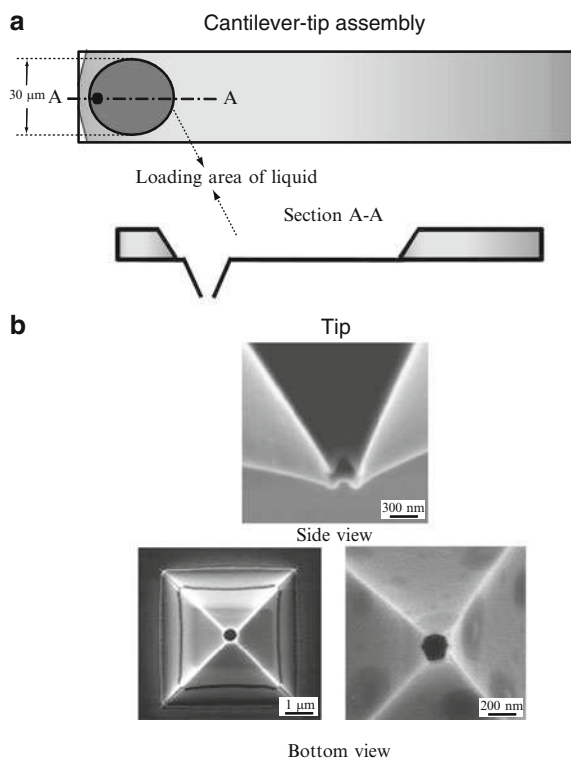


**Fig. 20.25** (a) Schematic of modified nanoscale dispensing (NADIS) probe for generation of submicron size droplets. The loaded liquid is limited to the loading area (30  $\mu\text{m}$  diameter circle), (b) scanning electron micrograph of tip in side view and bottom view with different aperture sizes (500 nm and 200 nm) at its apex [214]

frequencies of 68.94 and 122.02 kHz, respectively (Swiss Center for Electronics and Microtechnology). The probe consisted of a loading area (30  $\mu\text{m}$  diameter) for the liquid on the upper side of the cantilever. The loading area was produced by removing the material locally in and around the tip with a reflective gold layer using focused ion beam milling. The remaining gold was made hydrophobic using hexadecanethiol (in liquid phase) whereas the bare silicon nitride in the milling area remained hydrophilic. The hydrophilic–hydrophobic transition prevents spreading of the loaded liquid over the entire cantilever.

A droplet of a certain volume  $V$  is deposited on the surface. Figure 20.26 shows an idealized spherical capped droplet. Based on the thickness of the droplet  $h$  and contact diameter  $d$ , the contact angle is obtained by the following equation for a simple spherical capped geometry of droplet [214].

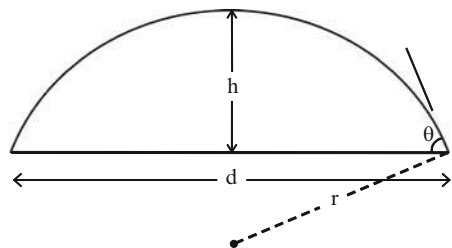
$$\theta = \sin^{-1} \left( \frac{3d}{2(\frac{3V}{\pi h^2} + h)} \right) \quad (20.23)$$

For calculation of the contact angle of the droplet, we use the following three steps:

1. For the measurement of the volume of a droplet deposited on the surface, the change in resonance frequency of the cantilever before and after depositing the droplet on the surface is measured. The resonance frequency of the cantilever is measured by performing a frequency sweep of the voltage driven oscillations by thermal tune method [215].
2. For the measurement of the thickness of a droplet deposited on the surface, the distance between the tip snap-in and the position where the tip is in contact with the surface is measured in the force calibration mode.
3. For the measurement of the contact diameter between a droplet and surface, the image of the droplet after evaporation is measured using a Si tip.

For the thickness of a droplet deposited on the surface, the force distance curve was used [24–26]. The droplet was deposited in the first approach. The force distance curve was obtained during a second approach to measure the thickness of the droplet [216–218]. The cantilever deflection is plotted on the vertical axis against the Z-position of the piezo scanner in a force distance curve as shown in Fig. 20.27. The measurement starts at a large separation (point A), where there is no

**Fig. 20.26** Droplet of liquid in contact with a surface, contact angle  $\theta$ . The thickness of droplet is  $h$ . The contact diameter between droplet and surface is  $d$ . The radius of curvature of droplet is  $r$  [214]



deflection of the cantilever. As the piezo moves to the sample, a sudden mechanical instability occurs between point B and point C, and the droplet jumps into contact with the tip and wicks up around the tip to form a meniscus. The cantilever bends downward because of the attractive meniscus force acting on the tip. As the piezo further approaches the surface, the deflection of the cantilever increases while the tip travels the thickness of the droplet and eventually contacts the underlying surface at point D, and the cantilever starts to bend upward. Once the piezo reaches the end of its designated ramp size at point E, it is retracted to its starting position. The tip goes beyond zero deflection and enters the adhesion region. At point F, the elastic force of the cantilever becomes equivalent to the adhesive force, causing the cantilever to snap back to point G. As the tip travels in the liquid, it is deflected as well. The tip deflection occurs in the same direction as the piezo travels for the AFM used in this study. The liquid film thickness ( $h$ ) is the sum of the travel distance of the piezo (described as  $h_1$  in Fig. 20.27) and the deflection of cantilever (described as  $h_2$  in Fig. 20.27). Though previous studies show that  $h$  overestimates the actual liquid film thickness, it still provides a good measurement of the thickness of droplet [216–218].

The resolution of volume (mass), thickness, and contact diameter was about  $1 \times 10^{-4} \mu\text{m}^3$  (0.12 fg), 0.1 nm, and  $<1$  nm, respectively. The resolution of volume was calculated with the measured data of the shift in the resonance frequency of the cantilever from 122.01 to 122.02 kHz during the evaporation time of 10 min. The resolutions of thickness and contact diameter measurements were from the calibration data of the z piezo and x–y piezo by AFM vendor (Veeco), respectively. The accuracy of volume, thickness, and contact diameter measurement was about  $\pm 10\%$ , 10% and  $<1$  nm, respectively.

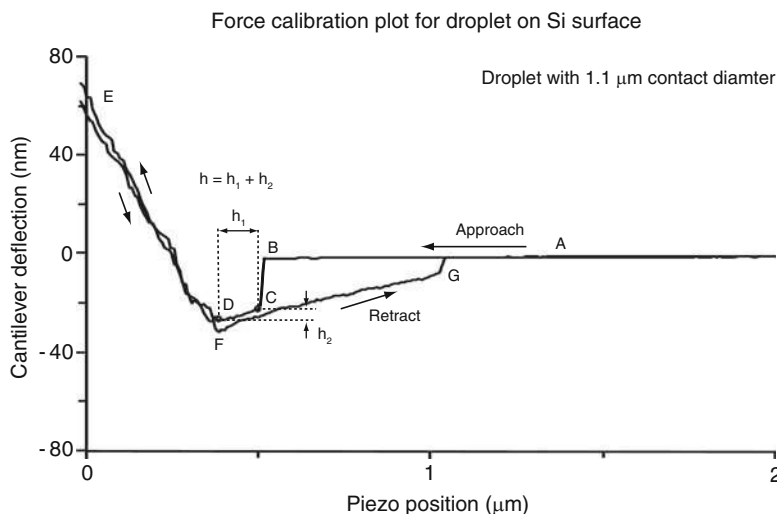
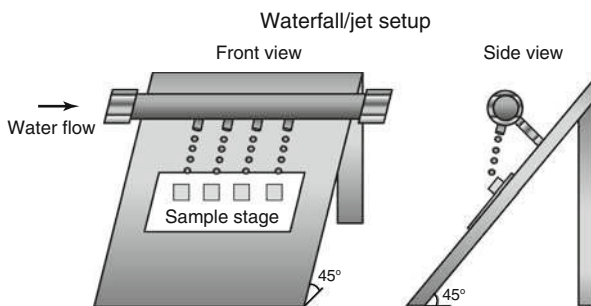


**Fig. 20.27** Force calibration plot for a droplet with 1.1  $\mu\text{m}$  contact diameter on Si surface. The  $h$  is a measure of droplet thickness on the surface

**Fig. 20.28** Schematics of waterfall/jet setup shown in front and side views [100]



### 20.5.1.7 Waterfall/Jet Tests

To investigate durability of the created surfaces in long-term exposure to water and different kinetic energies of water, a setup was constructed to provide a waterfall/jet flow as shown in Fig. 20.28 [100]. The water from the laboratory faucet flowed through a pipe. Specimens were fixed on the stage by using a double-sided adhesive tape. Specimens are placed 2 mm below the four holes in the pipe. In order to minimize flow interruption on the specimens, the runoff plate was tilted to 45°. Waterfall/jet experiments are composed of two different setups. First, water pressure was fixed at 10 kPa, and then specimens were exposed for 24 h. Next, in order to apply different kinetic energies of the water, the water pressure was controlled between 0 and 45 kPa. The exposure time applied to the specimens was 20 min for each experiment. During the tests, the change of static contact angle was measured using droplets of about 5  $\mu\text{L}$  in volume (with radius of a spherical droplet about 1 mm) gently deposited on the substrate using a microsyringe. For contact angle hysteresis, the advancing and receding contact angles were measured at the front and back of the droplet moving along the tilted surface, respectively. The image of the droplet is obtained by a digital camcorder (Sony, DCRSR100, Tokyo, Japan) with a 10x optical and 120x digital zoom. Images obtained were analyzed using Imagetool® software (University of Texas Health Science Center) for the contact angle.

### 20.5.1.8 Wear and Friction Tests

To investigate the durability of structured surfaces, wear tests on the surfaces were performed using a commercial AFM (D3100, Nanoscope IIIa controller, Digital Instruments, Santa Barbara, CA) [100]. With the AFM in contact mode, the surfaces were worn using a 15  $\mu\text{m}$  radius borosilicate ball that was mounted on a triangular  $\text{Si}_3\text{N}_4$  cantilever with a nominal spring constant of  $0.58 \text{ N m}^{-1}$ . Wear scars with dimensions of  $50 \times 50 \mu\text{m}^2$  were created and scanned for 1 cycle at two different loads of 100 nN and 10  $\mu\text{N}$ . In order to analyze the changes in the morphology of structured surfaces before and after wear tests, surface height

maps were obtained in dimensions of  $100 \times 100 \mu\text{m}^2$  using a square pyramidal Si (100) tip with a native oxide layer which has a nominal radius of 20 nm on a rectangular Si(100) cantilever with a spring constant of  $3 \text{ N m}^{-1}$  and at a natural frequency of 76 kHz in tapping mode.

In order to investigate durability at a high load, macroscale wear and friction tests on the structured surfaces were conducted based on an established procedure of using a ball-on-flat tribometer under reciprocating motion [100]. A sapphire ball with a diameter of 3 mm and surface finish of about 2 nm RMS was fixed on a stationary holder. A normal load of 10 mN was applied, and the frictional forces were measured with semiconductor strain gauges, which were then digitized and collected on a computer. Typical test conditions were: stroke length = 800  $\mu\text{m}$ , average linear speed = 1 mm/s, temperature =  $22 \pm 1^\circ\text{C}$ , and relative humidity =  $45 \pm 5\%$ . Wear was characterized by imaging the resulting scar with an optical microscope with a CCD camera (Nikon, Optihot-2) before and after wear tests. The number of cycles to failure was determined by identifying the point where a sudden change in the friction force is observed.

### 20.5.2 *Micro- and Nanopatterned Polymers*

Jung and Bhushan [99] studied two types of polymers: poly(methyl methacrylate) (PMMA) and polystyrene (PS). PMMA and PS were chosen because they are widely used in MEMS/NEMS devices. Both hydrophilic and hydrophobic surfaces can be produced by using these two polymers, as PMMA has polar (hydrophilic) groups with high surface energy while PS has electrically neutral and nonpolar (hydrophobic) groups with low surface energy. Furthermore, a PMMA structure can be made hydrophobic by treating it appropriately, for example by coating with a hydrophobic self-assembled monolayer (SAM).

Four types of surface patterns were fabricated from PMMA: a flat film, low aspect ratio asperities (LAR, 1:1 height-to-diameter ratio), high aspect ratio asperities (HAR, 3:1 height-to-diameter ratio), and a replica of the Lotus leaf (the Lotus pattern). Two types of surface patterns were fabricated from PS: a flat film and the Lotus pattern. Figure 20.29 shows SEM images of the two types of nanopatterned structures, LAR and HAR, and the one type of micropatterned structure, Lotus pattern, all on a PMMA surface [98, 99]. Both micro- and nanopatterned structures were manufactured using soft lithography. For nanopatterned structures, PMMA film was spin-coated on the silicon wafer. A UV-cured mold of polyurethane acrylate (PUA) resin with nanopatterns of interest was made which enables one to create sub-100-nm patterns with a high aspect ratio [219]. The mold was placed on the PMMA film, and a slight pressure of  $\sim 10 \text{ g/cm}^2$  ( $\sim 1 \text{ kPa}$ ) was applied and annealed at  $120^\circ\text{C}$ . Finally, the PUA mold was removed from PMMA film. For micropatterned structures, a polydimethylsiloxane (PDMS) mold was first made by casting PDMS against a Lotus leaf, followed by heating. Then, the mold was placed on the PMMA and PS film to create a positive replica of Lotus leaf. As shown in

**Fig. 20.29** Scanning electron micrographs of the two nanopatterned polymer surfaces (shown using two magnifications to see both the asperity shape and the asperity pattern on the surface) and the micropatterned polymer surface (Lotus pattern, which has only microstructures on the surface) [98, 99]

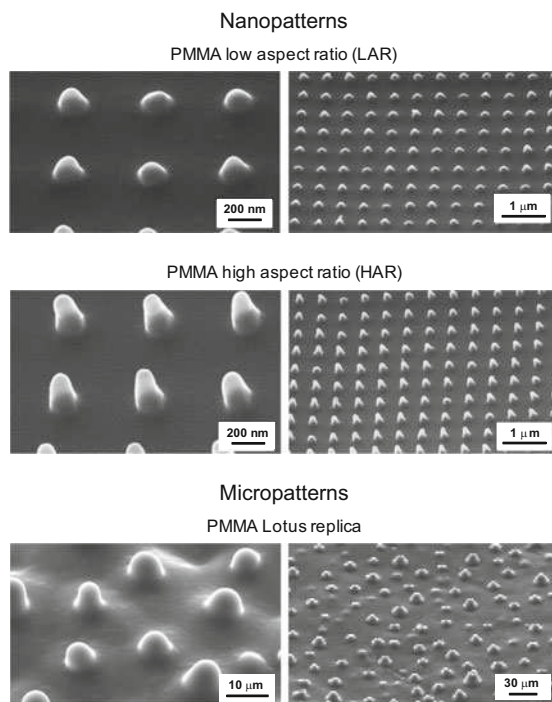
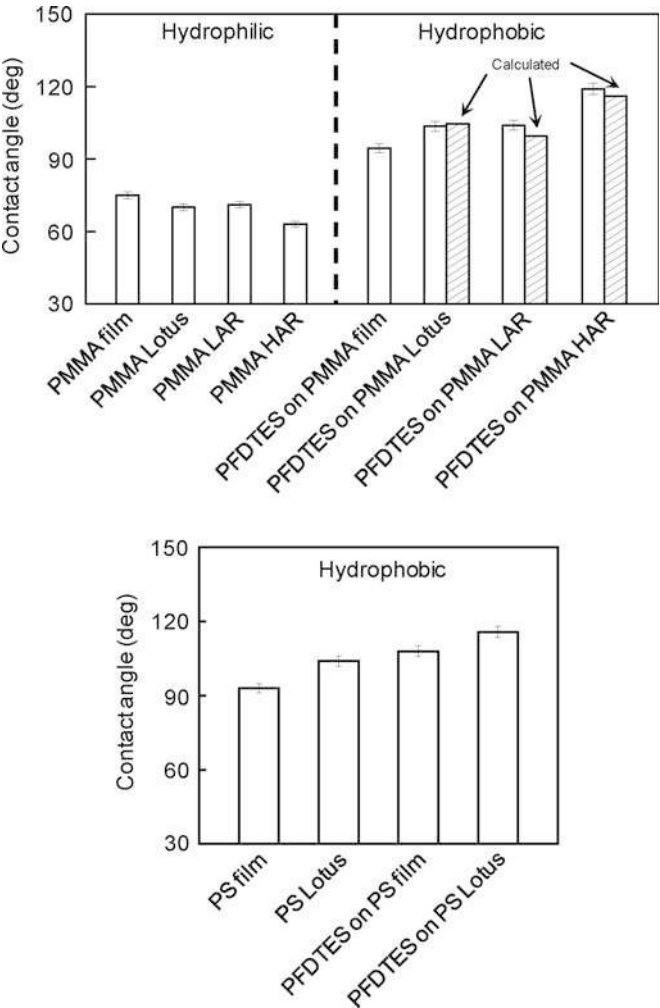


Fig. 20.29, it can be seen that only microstructures exist on the surface of Lotus pattern [99].

Since PMMA by itself is hydrophilic, in order to obtain a hydrophobic sample, a self-assembled monolayer (SAM) of perfluorodecyltriethoxysilane (PFDTES) was deposited on the sample surfaces using a vapor phase deposition technique. PFDTES was chosen because of its hydrophobic nature. The deposition conditions for PFDTES were 100°C temperature, 400 Torr pressure, 20 min deposition time, and 20 min annealing time. The polymer surface was exposed to an oxygen plasma treatment (40 W, O<sub>2</sub> 187 Torr, 10 s) prior to coating [220]. The oxygen plasma treatment is necessary to oxidize any organic contaminants on the polymer surface and to also alter the surface chemistry to allow for enhanced bonding between the SAM and the polymer surface.

### 20.5.2.1 Contact Angle Measurements

Jung and Bhushan [99] measured the static contact angle of water with the micro- and nanopatterned PMMA and PS structures; see Fig. 20.30. Since the Wenzel roughness factor is the parameter that often determines wetting behavior, the roughness factor was calculated, and it is presented in Table 20.7 for various



**Fig. 20.30** Contact angles for various micro- and nanopatterned surfaces on PMMA and PS polymers and calculated values using Wenzel equation [99]

**Table 20.7** Roughness factor for micro- and nanopatterned polymers [99]

	LAR	HAR	Lotus
R <sub>f</sub>	2.1	5.6	3.2

samples. The data show that the contact angle of the hydrophilic materials decreases with an increase in the roughness factor, as predicted by the Wenzel model. When the polymers were coated with PFDTES, the film surface became



hydrophobic. Figure 20.30 also shows the contact angle for various PMMA samples coated with PFDTES. For a hydrophobic surface, the standard Wenzel model predicts an increase of contact angle with roughness factor, which is what happens in the case of patterned samples. The calculated values of the contact angle for various micro- and nanopatterned samples based on the contact angle of the smooth film and Wenzel equation are also presented. The measured contact angle values for the Lotus pattern were comparable with the calculated values, whereas for the LAR and HAR patterns they are higher. It suggests that nanopatterns benefit from air pocket formation. For the PS material, the contact angle of the Lotus pattern also increased with increased roughness factor.

### 20.5.2.2 Effect of Submicron Droplet

Wetting phenomena have been well studied and understood at the macroscale; however, micro- and nanoscale wetting mechanisms require further investigation. The actual contact angle, under which the liquid–vapor interface comes in contact with the solid surface at the micro- and nanoscale, is known to decrease with decreasing droplet size [136, 221]. Jung and Bhushan [214] measured the contact angle of micro- and nanodroplets on various surfaces based on the contact diameter, thickness, and volume of droplets measured using the atomic force microscopy-based technique. The contact angle for different droplet sizes on various surfaces is summarized in Fig. 20.31. The data for the microdroplets with 2.4–8.1  $\mu\text{m}$  diameter and nanodroplets with 0.22–1.1  $\mu\text{m}$  diameter were compared with conventional contact angle measurements obtained with a droplet with 2.1 mm diameter (5  $\mu\text{L}$  volume). The measured values of micro- and nanodroplets using an AFM were found to be lower than those of the macrodroplet [136, 221]. There are several reasons for the scale dependence, such as the effect of contact line tension of a three-phase system (solid–liquid–vapor), which is the excess free energy of a

Contact angle for different droplet sizes on various surfaces

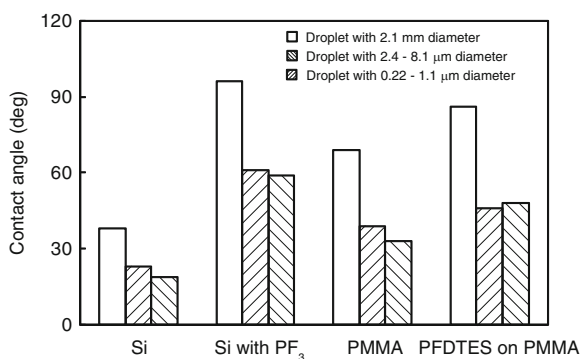


**Fig. 20.31** Contact angle measurements for different droplet sizes on various surfaces [214]

solid–liquid–vapor system per unit length of the contact line [63, 136, 221, 222]. Another reason can be surface heterogeneity [136]. For a thin fluid film present on a surface, disjoining pressure of a film is repulsive, analogous to the repulsive van der Waals force across a film, and it causes a film to spread on surfaces. It decreases with the liquid layer thickness [23]. This pressure may lead to a smaller contact angle at the nanoscale.

### 20.5.2.3 Scale Dependence on Adhesive Force

Jung and Bhushan [99] found that scale-dependence of adhesion and friction forces are important for this study because the tip/surface interface area changes with size. The meniscus force will change due to either changing tip radius, the hydrophobicity of the sample, or the number of contacting and near-contacting points. Figure 20.32 shows the dependence of the tip radius and hydrophobicity on the adhesive force for PMMA and PFDTES coated on PMMA [99]. When the radius of the tip is changed, the contact angle of the sample is changed, and asperities are added to the sample surface, the adhesive force will change due to the change in the meniscus force and the real area of contact.

The two plots in Fig. 20.32 show the adhesive force on a linear scale for the different surfaces with varying tip radius. The left bar chart in Fig. 20.32 is for hydrophilic PMMA film, Lotus pattern, LAR, and HAR, and shows the effect of tip radius and hydrophobicity on adhesive force. For increasing radius, the adhesive force increases for each material. With a larger radius, the real area of contact and the meniscus contribution increase, resulting in increased adhesion. The right bar chart in Fig. 20.32 shows the results for PFDTES coated on each material. These samples show the same trends as the film samples, but the increase in adhesion is not as dramatic. The hydrophobicity of PFDTES on material reduces meniscus forces, which in turn reduces adhesion from the surface. The dominant mechanism

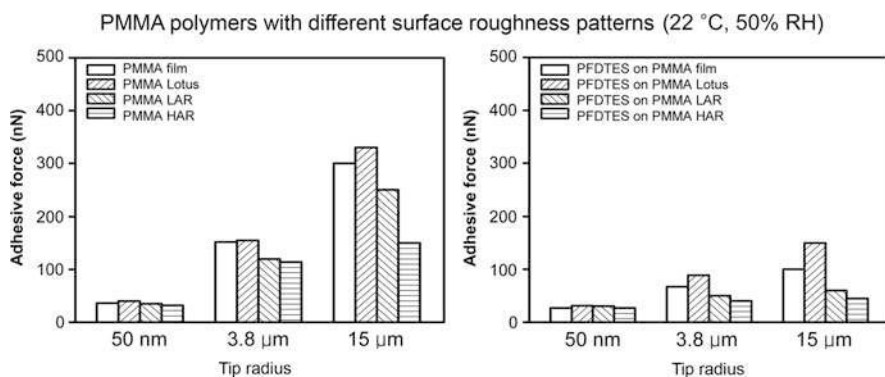


**Fig. 20.32** Scale dependent adhesive force for various micro- and nanopatterned surfaces measured using AFM tips of various radii [99]

for the hydrophobic material is real area of contact and not meniscus force, whereas with hydrophilic material there is a combination of real area of contact and meniscus forces [99].

### 20.5.3 Micropatterned Si Surfaces

Micropatterned surfaces produced from single-crystal silicon (Si) by photolithography and coated with a self-assembled monolayer (SAM) were used by Jung and Bhushan [75–77] in their study. Silicon has traditionally been the most commonly used structural material for micro/nanocomponents. A Si surface can be made hydrophobic by coating it with a SAM. One of the purposes of this investigation was to study the transition from the Cassie–Baxter to Wenzel regime by changing the distance between the pillars. To create micropatterned Si, two series of nine samples each were fabricated using photolithography [143]. Series 1 had 5- $\mu\text{m}$  diameter and 10- $\mu\text{m}$  height flat-top, cylindrical pillars with different pitch values (7, 7.5, 10, 12.5, 25, 37.5, 45, 60, and 75)  $\mu\text{m}$ , and series 2 had 14- $\mu\text{m}$  diameter and 30- $\mu\text{m}$  height flat-top, cylindrical pillars with different pitch values (21, 23, 26, 35, 70, 105, 126, 168, and 210)  $\mu\text{m}$ . The pitch is the spacing between the centers of two adjacent pillars. The SAM of 1, 1, -2, 2, -tetrahydroperfluorodecyltrichlorosilane ( $\text{PF}_3$ ) was deposited on the Si sample surfaces using a vapor phase deposition technique [143].  $\text{PF}_3$  was chosen because of the hydrophobic nature of the surface. The thickness and root mean square (RMS) roughness of the SAM of  $\text{PF}_3$  were 1.8 nm and 0.14 nm, respectively [223].

An optical profiler was used to measure the surface topography of the micropatterned surfaces [30, 69, 76, 77]. One sample each from the two series was chosen to characterize the surfaces. Two different surface height maps can be seen for the micropatterned Si in Fig. 20.33. In each case, a 3-D map and a flat map along with a 2-D profile in a given location of the flat 3-D map are shown. A scan size of 100  $\mu\text{m} \times 90 \mu\text{m}$  was used to obtain a sufficient amount of pillars to characterize the surface but also to maintain enough resolution to get an accurate measurement.

Let us consider the geometry of flat-top, cylindrical pillars of diameter  $D$ , height  $H$ , and pitch  $P$ , distributed in a regular square array as shown in Fig. 20.33. For the special case of a droplet size much larger than  $P$  (of interest in this study), a droplet contacts the flat-top of the pillars forming the composite interface, and the cavities are filled with air. For this case,  $f_{LA} = 1 - \frac{\pi D^2}{4P^2} = 1 - f_{SL}$ . Further assume that the flat tops are smooth with  $R_f = 1$ . The contact angles for the Wenzel and Cassie–Baxter regimes are given by (20.6 and 20.9) [69].

$$\text{Wenzel : } \cos \theta = \left( 1 + \frac{\pi DH}{P^2} \right) \cos \theta_0 \quad (20.24)$$

$$\text{Cassie–Baxter : } \cos \theta = \frac{\pi D^2}{4P^2} (\cos \theta_0 + 1) - 1 \quad (20.25)$$

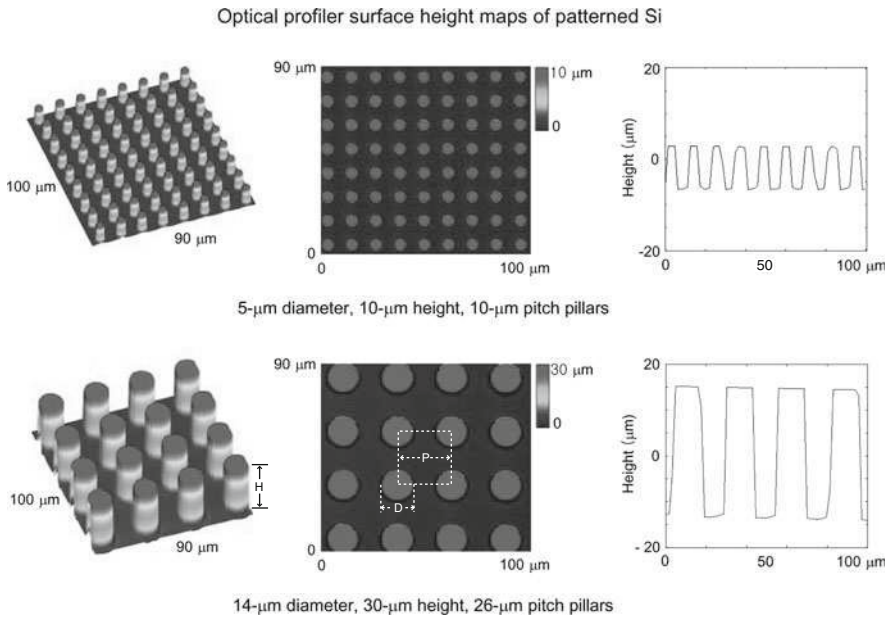


**Fig. 20.33** Surface height maps and 2-D profiles of the micropatterned surfaces using an optical profiler [69]

Geometrical parameters of the flat-top, cylindrical pillars in series 1 and 2 are used for calculating the contact angle for the above-mentioned two cases. Figure 20.34 shows the plot of the predicted values of the contact angle as a function of pitch between the pillars for the two cases. The Wenzel and Cassie–Baxter equations present two possible equilibrium states for a water droplet on the surface. This indicates that there is a critical pitch below which the composite interface dominates and above which the homogeneous interface dominates the wetting behavior. Therefore, one needs to find the critical point that can be used to design superhydrophobic surfaces. Furthermore, even in cases where the liquid droplet does not contact the bottom of the cavities, the water droplet can be in a metastable state and can become unstable, with the transition from the Cassie–Baxter to Wenzel regime occurring if the pitch is large.

### 20.5.3.1 Cassie–Baxter and Wenzel Transition Criteria

A stable composite interface is essential for the successful design of superhydrophobic surfaces. However, the composite interface is fragile, and it may transform into the homogeneous interface. What triggers the transition between the regimes remains a subject of argument, although a number of explanations have been suggested. Nosonovsky and Bhushan [61] have studied destabilizing factors for the composite interface and found that a convex surface (with bumps) leads to

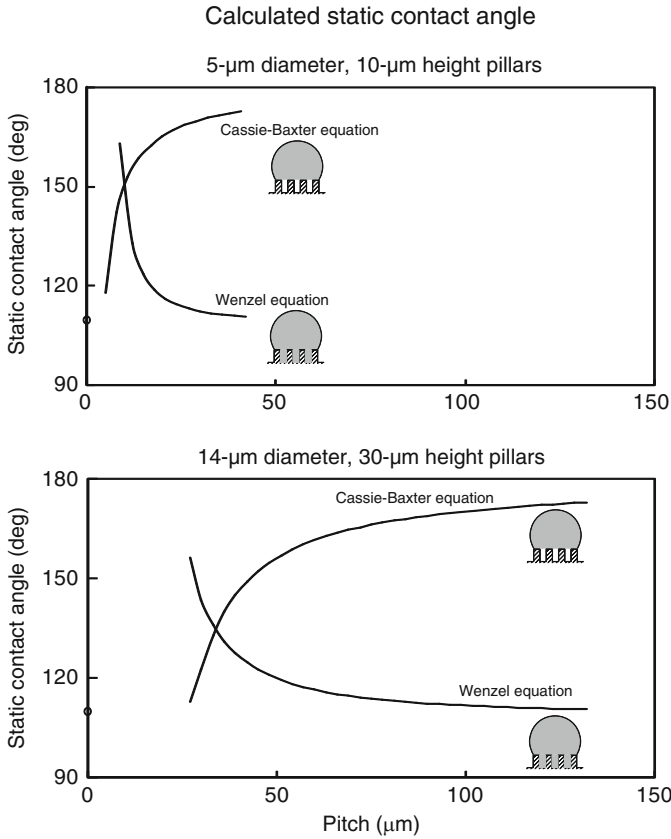


**Fig. 20.34** Calculated static contact angle as a function of geometric parameters for a given value of  $\theta_0$  using the Wenzel and Cassie–Baxter equations for two series of the micropatterned surfaces with different pitch values [69]

a stable interface and high contact angle. Also, they have suggested the effects of a droplet's weight and curvature among the factors which affect the transition.

Bhushan and Jung [30, 69] and Jung and Bhushan [75–77] investigated the effect of droplet curvature on the Cassie–Baxter and Wenzel regime transition. First, they considered a small water droplet suspended on a superhydrophobic surface consisting of a regular array of circular pillars with diameter  $D$ , height  $H$ , and pitch  $P$  as shown in Fig. 20.35. The local deformation for small droplets is governed by surface effects rather than gravity. The curvature of a droplet is governed by the Laplace equation, which relates the pressure inside the droplet to its curvature [22]. Therefore, the curvature is the same at the top and at the bottom of the droplet [63]. For the micropatterned surface considered here, the maximum droop of the droplet occurs in the center of the square formed by the four pillars as shown in Fig. 20.35a. Therefore, the maximum droop of the droplet ( $\delta$ ) in the recessed region can be found in the middle of two pillars which are diagonally across as shown in

**Fig. 20.35** A liquid droplet suspended on a superhydrophobic surface consisting of a regular array of circular pillars. (a) Plan view. The maximum droop of droplet occurs in the center of square formed by four pillars. (b) Side view in section A-A. The maximum droop of droplet ( $\delta$ ) can be found in the middle of two pillars which are diagonally across [75]

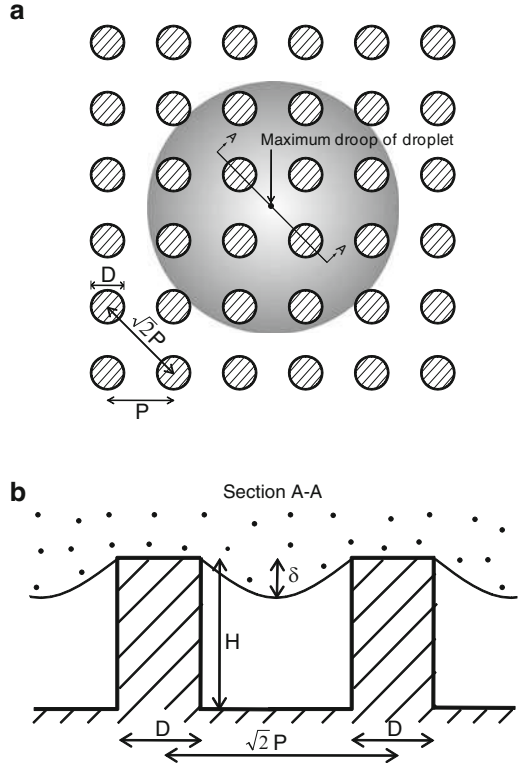


Fig. 20.35b, which is  $(\sqrt{2}P - D)^2/(8R)$ . If the droop is greater than the depth of the cavity, then the droplet will just contact the bottom of the cavities between pillars. If it is much greater, transition from the Cassie–Baxter to Wenzel regime occurs.

$$(\sqrt{2}P - D)^2/R \geq H \quad (20.26)$$

To investigate the dynamic effect of a bouncing water droplet on the Cassie–Baxter and Wenzel regime transition, Jung and Bhushan [77] considered a water droplet hitting a superhydrophobic surface as shown in Fig. 20.35. As the droplet hits the surface at velocity  $V$ , a liquid–air interface below the droplet is formed when the dynamic pressure is less than the Laplace pressure. The Laplace pressure can be written as

$$p_L = 2\gamma/R = 16\gamma\delta/(\sqrt{2}P - D)^2 \quad (20.27)$$

where  $\gamma$  is the surface tension of the liquid–air interface, and the dynamic pressure of the droplet is equal to

$$p_d = \frac{1}{2} \rho V^2 \quad (20.28)$$

where  $\rho$  is the mass density of the liquid droplet. If the maximum droop of the droplet ( $\delta$ ) is larger than the height of pillar ( $H$ ), the droplet contacts the bottom of the cavities between pillars. Determination of the critical velocity at which the droplet touches the bottom is obtained by equating the Laplace pressure to the dynamic pressure. To develop a composite interface, velocity should be smaller than the critical velocity given as

$$V < \sqrt{\frac{32\gamma H}{\rho(\sqrt{2}P - D)^2}} \quad (20.29)$$

Furthermore, in the case of large distances between the pillars, the liquid–air interface can easily be destabilized due to dynamic effects. This leads to the formation of the homogeneous solid–liquid interface [61].

Nosonovsky and Bhushan [81] used the energy barrier approach to study the Cassie–Baxter and Wenzel transition. The energy barrier is given by the product of height of the pillars,  $H$ , pillar perimeter,  $\pi D$ , pillar density,  $1/P^2$ , and the area,  $A_0$ , required to initiate the transition, and the corresponding change in the surface energy

$$\Delta E = A_0 \frac{\pi H D}{P^2} (\gamma_{SL} - \gamma_{SA}) = -A_0 \frac{\pi H D}{P^2} \gamma_{LA} \cos \theta_0 \quad (20.30)$$

where,  $A_0$  is  $\pi(R \sin \theta)^2$ .

For a short pitch, the net energy of the Cassie–Baxter state is lower than that of the Wenzel state, whereas for larger pitch values, the energy of the Wenzel state is lower (Fig. 20.15c). However, due to the energy barriers, a metastable Cassie–Baxter state with a higher energy than the Wenzel state may be found.

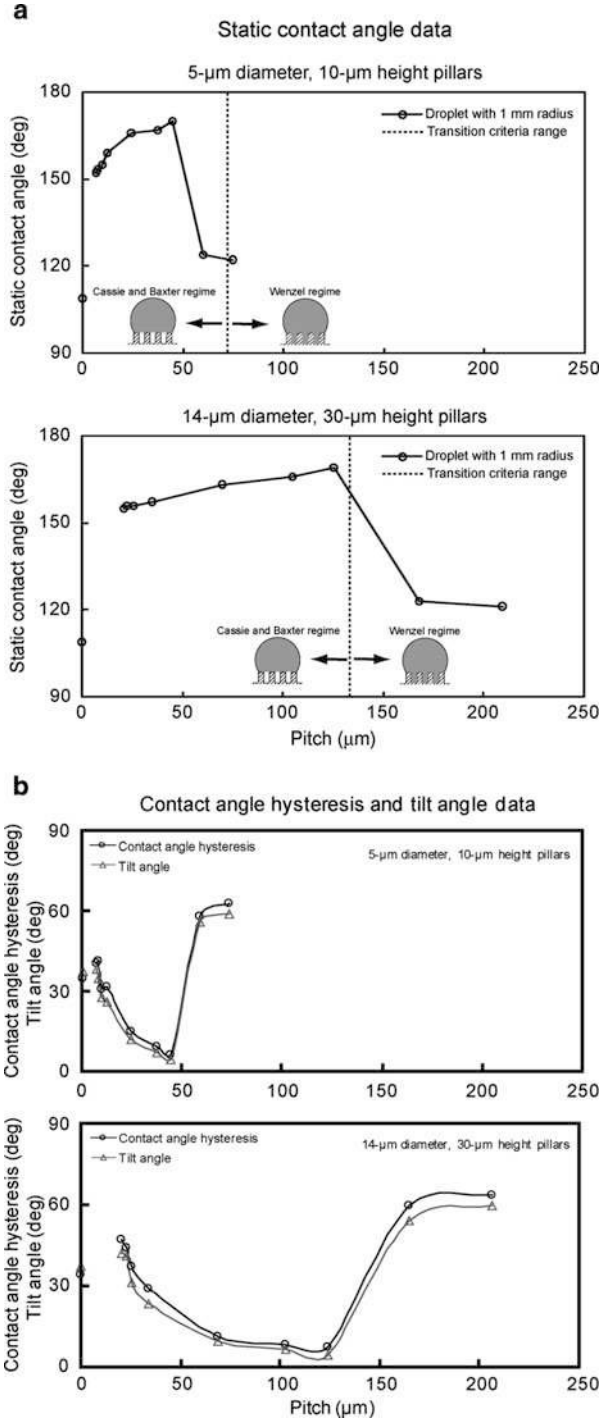
The energy barrier of the Cassie–Baxter and Wenzel transition can be estimated as the kinetic energy of the droplet. The kinetic energy of a droplet of radius  $R_0$ , mass  $m$ , and density  $\rho$  with the velocity  $V$  is given by

$$E_{kin} = \frac{(4/3)\pi\rho R^3 V^2}{2} \quad (20.31)$$

### 20.5.3.2 Contact Angle Measurements

In order to study the effect of pitch value on the transition from Cassie–Baxter to Wenzel regime, the static contact angles were measured on the micropatterned Si coated with  $\text{PF}_3$ , and the data are plotted as a function of pitch between the pillars in Fig. 20.36a [30, 69, 75–77]. A dotted line represents the transition criteria range obtained using (20.26). The flat Si coated with  $\text{PF}_3$  showed a static contact angle of

**Fig. 20.36** (a) Static contact angle (a dotted line represents the transition criteria range obtained using (20.26) and (b) contact angle hysteresis and tilt angle as a function of geometric parameters for two series of the micropatterned surfaces with different pitch values for a droplet with 1 mm in radius ( $5\text{ }\mu\text{L}$  volume). Data at zero pitch correspond to a flat sample [69, 75]





109°. The contact angle of selected micropatterned surfaces is much higher than that of the flat surfaces. It first increases with an increase in the pitch values, then drops rapidly to a value slightly higher than that of the flat surfaces. In the first portion, it jumps to a high value of 152° corresponding to a superhydrophobic surface and continues to increase to 170° at a pitch of 45  $\mu\text{m}$  in series 1 and 126  $\mu\text{m}$  in series 2 because open air space increases with an increase in pitch, responsible for propensity of air pocket formation. The sudden drop at about a pitch value of 50  $\mu\text{m}$  in series 1 and 150  $\mu\text{m}$  in series 2 corresponds to the transition from the Cassie–Baxter to the Wenzel regime. In series 1, the value predicted from the curvature transition criteria (20.26) is a little higher than the experimental observations. However, in series 2, there is a good agreement between the experimental data and the values theoretically predicted by Jung and Bhushan [75–77] for the Cassie–Baxter and Wenzel transition.

Figure 20.36b shows contact angle hysteresis and tilt angle as a function of pitch between the pillars [30, 69]. Both angles are comparable. The flat Si coated with  $\text{PF}_3$  showed a contact angle hysteresis of 34° and tilt angle of 37°. The angle first increases with an increase of pitch value, which has to do with pinning of the droplet at the sharp edges of the micropillars. Figure 20.37 shows droplets on micropatterned Si with 5- $\mu\text{m}$  diameter and 10- $\mu\text{m}$  height pillars with different pitch values. The asymmetrical shape of the droplet signifies pinning. The pinning on the micropatterned surfaces can be observed as compared to the flat surface. The micropatterned surface with low pitch (7  $\mu\text{m}$ ) has more pinning than the micropatterned surface with high pitch (37.5  $\mu\text{m}$ ), because the micropatterned surface with low pitch has more sharp edges in contact with a droplet. As the pitch increases, there is a higher propensity of air pocket formation and fewer numbers of sharp edges per unit area, which is responsible for sudden drop in the angle. The lowest contact angle hysteresis and tilt angle are 5° and 3°, respectively, which were observed on the micropatterned Si with 45  $\mu\text{m}$  of series 1 and 126  $\mu\text{m}$  of series 2. Above a pitch value of 50  $\mu\text{m}$  in series 1 and 150  $\mu\text{m}$  in series 2, the angle increases very rapidly because of transition to the Wenzel regime.

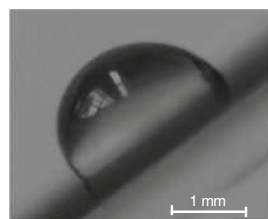
These results suggest that air pocket formation and the reduction of pinning in the micropatterned surface play an important role for a surface with both low contact angle hysteresis and tilt angle [30, 69]. Hence, to create superhydrophobic surfaces, it is important that they are able to form a stable composite interface with air pockets between solid and liquid.

### 20.5.3.3 Observation of Transition During the Droplet Evaporation

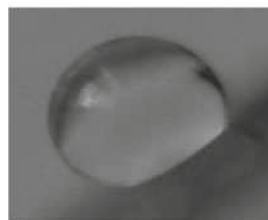
In order to study the effect of droplet size on the transition from a composite state to a wetted state, Jung and Bhushan [75, 76] performed droplet evaporation experiments to observe the Cassie–Baxter and Wenzel transition on two different micropatterned Si surfaces coated with  $\text{PF}_3$ . The series of four images in Fig. 20.38 show the successive photos of a droplet evaporating on the two micropatterned surfaces. The initial radius of the droplet was about 700  $\mu\text{m}$ , and the time interval

**Fig. 20.37** Optical micrographs of droplets on the inclined micropatterned surfaces with different pitch values. The images were taken when the droplet started to move down. Data at zero pitch correspond to a flat sample [69]

Patterned surfaces with 5- $\mu\text{m}$  diameter and 10- $\mu\text{m}$  height pillars with different pitch values



0  $\mu\text{m}$  pitch



7  $\mu\text{m}$  pitch



37.5  $\mu\text{m}$  pitch



75  $\mu\text{m}$  pitch

between first two photos was 180 s and between the latter two was 60 s. In the first three photos, the droplet is shown in a Cassie–Baxter state, and its size gradually decreases with time. However, as the radius of the droplet reached 360  $\mu\text{m}$  on the surface with 5- $\mu\text{m}$  diameter, 10- $\mu\text{m}$  height, and 37.5- $\mu\text{m}$  pitch pillars, and 423  $\mu\text{m}$  on the surface with 14- $\mu\text{m}$  diameter, 30- $\mu\text{m}$  height, and 105- $\mu\text{m}$  pitch pillars, the transition from the Cassie–Baxter to Wenzel regime occurred, as indicated by the arrow. The light passes below the first droplet, indicating that air pockets exist, so that the droplet is in the Cassie–Baxter state. However, an air pocket is not visible below the last droplet, so it is in the Wenzel state. This could result from an

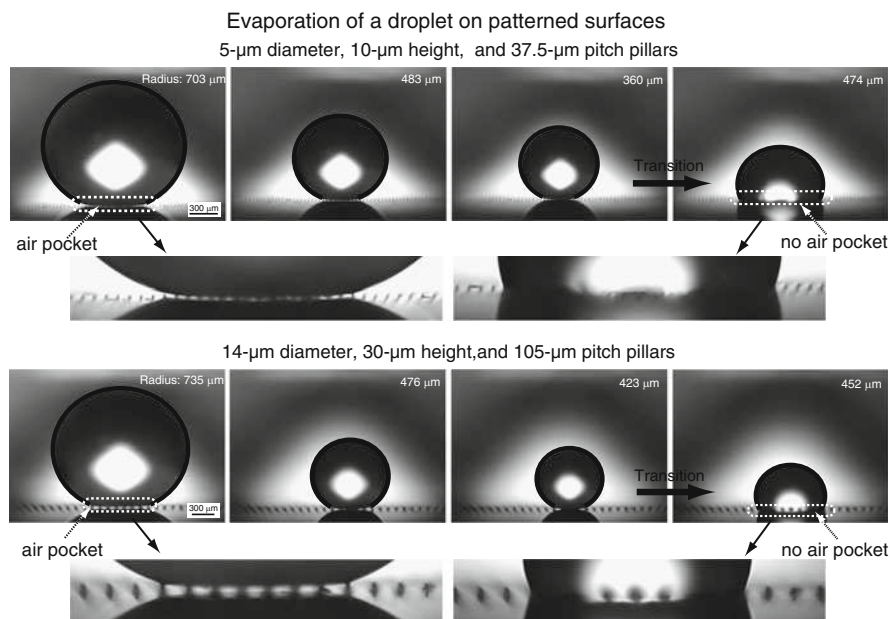


**Fig. 20.38** Evaporation of a droplet on two different micropatterned surfaces. The initial radius of the droplet is about 700  $\mu\text{m}$ , and the time interval between first two photos was 180 s and between the latter two was 60 s. As the radius of droplet reaches 360  $\mu\text{m}$  on the surface with 5- $\mu\text{m}$  diameter, 10- $\mu\text{m}$  height, and 37.5- $\mu\text{m}$  pitch pillars, and 420  $\mu\text{m}$  on the surface with 14- $\mu\text{m}$  diameter, 30- $\mu\text{m}$  height, and 105- $\mu\text{m}$  pitch pillars, the transition from the Cassie–Baxter regime to Wenzel regime occurs, as indicated by the arrow. Before the transition, air pocket is clearly visible at the bottom area of the droplet, but after the transition, air pocket is not found at the bottom area of the droplet [76]

impalement of the droplet in the micropatterned surface, characterized by a smaller contact angle.

To find the contact angle before and after the transition, the values of the contact angle are plotted against the theoretically predicted value, based on the Wenzel [calculated using (20.6)] and Cassie–Baxter (calculated using 20.9) models. Figure 20.39 shows the static contact angle as a function of geometric parameters for the experimental contact angles before (circle) and after (triangle) the transition compared to the Wenzel and Cassie–Baxter equations (solid lines) with a given value of  $\theta_0$  for two series of micropatterned Si with different pitch values coated with  $\text{PF}_3$  [76]. The fit is good between the experimental data and the theoretically predicted values for the contact angles before and after transition.

To prove the validity of the transition criteria in terms of droplet size, the critical radius of a droplet deposited on the micropatterned Si with different pitch values coated with  $\text{PF}_3$  is measured during the evaporation experiment [75, 76]. Figure 20.40 shows the radius of a droplet as a function of geometric parameters for the experimental results (circle) compared with the transition criterion (20.26) from the Cassie–Baxter regime to Wenzel regime (solid lines) for two series of

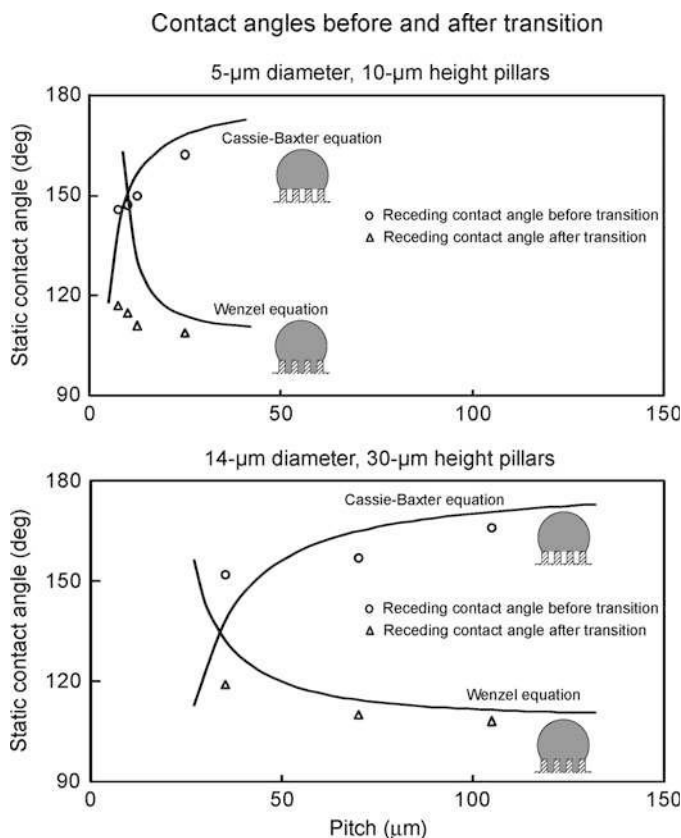


**Fig. 20.39** Receding contact angle as a function of geometric parameters before (circle) and after (triangle) transition compared with predicted static contact angle values obtained using the Wenzel and Cassie–Baxter equations (solid lines) with a given value of  $\theta_0$  for two series of the micropatterned surfaces with different pitch values [76]

micropatterned Si with different pitch values coated with  $\text{PF}_3$ . It is found that the critical radius of impalement is in good quantitative agreement with our predictions. The critical radius of the droplet increases linearly with the geometric parameter (pitch). For the surface with small pitch, the critical radius of droplet can become quite small.

To verify the transition, Jung and Bhushan [75, 76] used another approach using dust mixed in water. Figure 20.41 presents the dust trace remaining after droplet with 1 mm radius (5  $\mu\text{L}$  volume) evaporation on the two micropatterned Si surfaces. As shown in the top image, after the transition from the Cassie–Baxter regime to Wenzel regime, the dust particles remained not only at the top of the pillars but also at the bottom with a footprint size of about 450  $\mu\text{m}$ . However, as shown in the bottom image, the dust particles remained on only a few pillars with a footprint size of about 25  $\mu\text{m}$  until the end of the evaporation process. From Fig. 20.40, it is

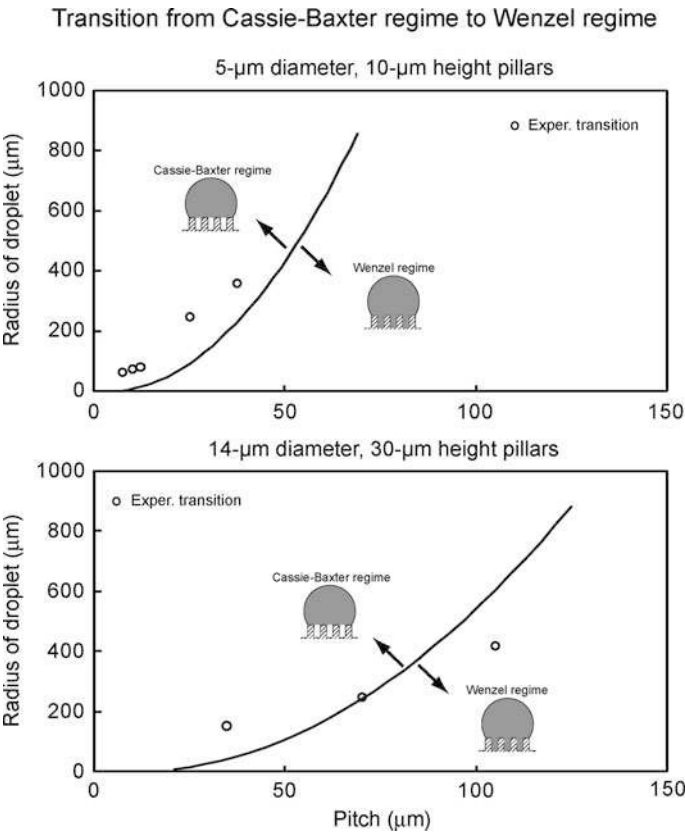


**Fig. 20.40** Radius of droplet as a function of geometric parameters for the experimental results (circle) compared with the transition criteria from the Cassie–Baxter regime to Wenzel regime (solid lines) for two series of the micropatterned surfaces with different pitch values [76]

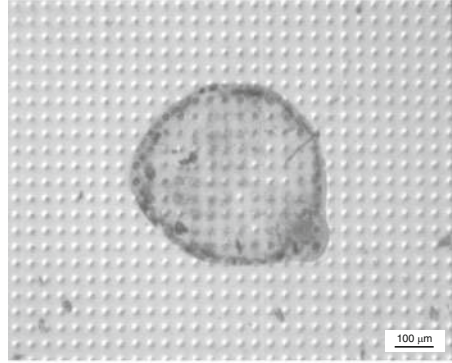
observed that the transition occurs at about 300  $\mu\text{m}$  radius of droplet on the 5- $\mu\text{m}$  diameter and 10- $\mu\text{m}$  height pillars with 37.5- $\mu\text{m}$  pitch, but the transition does not occur on the patterned Si surface with pitch of less than about 5  $\mu\text{m}$ . These experimental observations are consistent with model predictions. In the literature, it has been shown that on superhydrophobic natural Lotus, the droplet remains in the Cassie–Baxter regime during the evaporation process [224]. This indicates that the distance between the pillars should be minimized enough to improve the ability of the droplet to resist sinking.

**20.5.3.4 Scaling of the Cassie–Baxter and Wenzel Transition for Different Series**

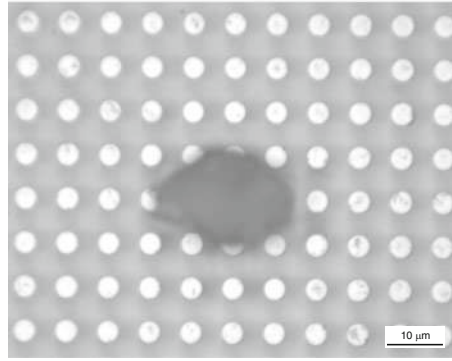
Nosonovsky and Bhushan [31, 32, 62, 63, 79] studied the data for the Cassie–Baxter and Wenzel transition with the two series of surfaces using the non-dimensional spacing factor

**Fig. 20.41** Dust trace remained after droplet evaporation for the micropatterned surface. In the top image, the transition occurred at 360  $\mu\text{m}$  radius of droplet, and in the bottom image, the transition occurred at about 20  $\mu\text{m}$  radius of droplet during the process of droplet evaporation. The footprint size is about 450 and 25  $\mu\text{m}$  for the top and bottom images, respectively [76]

Dust trace after droplet evaporation  
5- $\mu\text{m}$  diameter, 10- $\mu\text{m}$  height, and 37.5- $\mu\text{m}$  pitch pillars



5- $\mu\text{m}$  diameter, 10- $\mu\text{m}$  height, and 7- $\mu\text{m}$  pitch pillars



$$S_f = \frac{D}{P} \quad (20.32)$$

The values of the droplet radius at which the transition occurs during the evaporation plotted against the spacing factor scale well for the two series of the experimental results, yielding virtually the same straight line. Thus the two series of micropatterned surfaces scale well with each other, and the transition occurs at the same value of the spacing factor multiplied by the droplet radius (Fig. 20.42a). The physical mechanism leading to this observation remains to be determined, however, it is noted that this mechanism is different from the one suggested by (20.26). The observation suggests that the transition is a linear one-dimensional (1-D) phenomenon and that neither droplet droop (that would involve  $P^2/H$ ) nor droplet weight (that would involve  $R^3$ ) are responsible for the transition, but rather linear geometric relations are involved. Note that the experimental values approximately correspond to the values of the ratio  $RD/P = 50 \mu\text{m}$ , or the total area of the pillar tops under the droplet  $(\pi D^2/4)\pi R^2/P^2 = 6,200 \mu\text{m}^2$ .

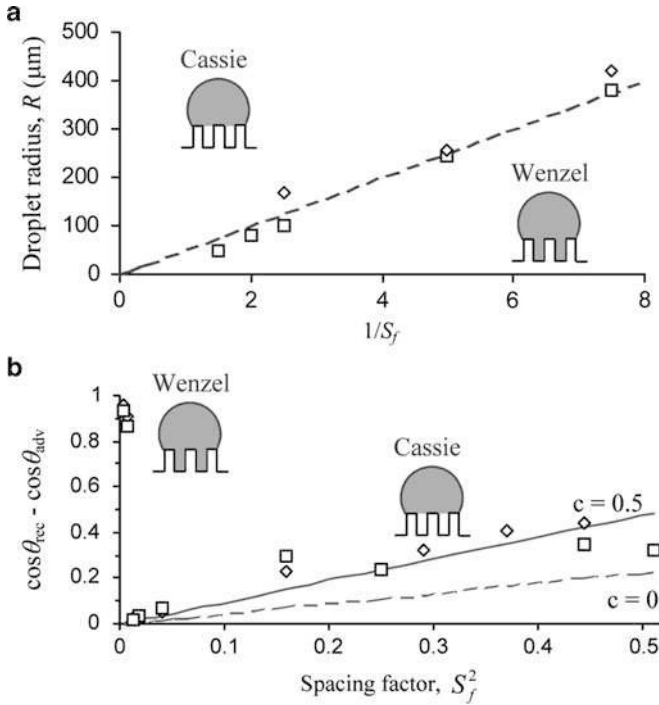


**Fig. 20.42** (a) Droplet radius,  $R$ , for the Cassie–Baxter and Wenzel transition as a function of  $P/D = 1/S_f$ . It is observed that the transition takes place at a constant value of  $RD/P \sim 50 \mu\text{m}$  (dashed line). This shows that the transition is a linear phenomenon. (b) Contact angle hysteresis as a function of  $S_f$  for the 1st (squares) and 2nd (diamonds) series of the experiments compared with the theoretically predicted values of  $\cos\theta_{\text{adv}} - \cos\theta_{\text{rec}} = (D/P)^2(\pi/4)(\cos\theta_{\text{adv}0} - \cos\theta_{\text{rec}0}) + c(D/P)^2$ , where  $c$  is a proportionality constant. It is observed that when only the adhesion hysteresis/interface energy term is considered ( $c = 0$ ), the theoretical values are underestimated by about a half, whereas  $c = 0.5$  provides a good fit. Therefore, the contribution of the adhesion hysteresis is of the same order of magnitude as the contribution kinetic effects [62]

### 20.5.3.5 Contact Angle Hysteresis and Wetting/Dewetting Asymmetry

Contact angle hysteresis can be viewed as a result of two factors that act simultaneously. First, the changing contact area affects the contact angle hysteresis, since a certain value of contact angle hysteresis is inherent for even a nominally flat surface. Decreasing the contact area by increasing the pitch between the pillars leads to a proportional decrease of the contact angle hysteresis. This effect is clearly proportional to the contact area between the solid surface and the liquid droplet. Second, the edges of the pillar tops prevent the motion of the triple line. This roughness effect is proportional to the contact line density, and its contribution was, in the experiment, comparable with the contact area effect. Interestingly, the effect of the edges is much more significant for the advancing than for the receding contact angle.

Nosonovsky and Bhushan [31, 32, 62, 63, 79] studied the wetting of two series of micropatterned Si surfaces with different pitch values coated with PF<sub>3</sub> based on the spacing factor (20.32). They found that the contact angle hysteresis involves two terms (Fig. 20.42b): the term  $S_f^2 (\pi/4)(\cos \theta_{adv0} - \cos \theta_{rec0})$  corresponding to the adhesion hysteresis (which is found even at a nominally flat surface and is a result of molecular-scale imperfectness), and the term  $H_r \propto D/P^2$  corresponding to microscale roughness and proportional to the edge line density. Thus the contact angle hysteresis is given, based on (20.18 and 20.32), by using  $R_f = 1 + \frac{\pi DH}{P^2}$  and  $f_{LA} = 1 - \frac{\pi D^2}{4P^2} = 1 - f_{SL}$  [61, 70]

$$\cos \theta_{adv} - \cos \theta_{rec} = \frac{\pi}{4} S_f^2 (\cos \theta_{adv0} - \cos \theta_{rec0}) + H_r \quad (20.33)$$

Besides the contact angle hysteresis, the asymmetry of the Wenzel and Cassie–Baxter states is the result of the wetting/dewetting asymmetry. While the fragile metastable Cassie–Baxter state is often observed, as well as its transition to the Wenzel state, the opposite transition never happens. Using (20.24 and 20.25), the contact angle with micropatterned surfaces is given by [61, 70]

$$\cos \theta = (1 + 2\pi S_f^2) \cos \theta_0 \quad (\text{Wenzel state}) \quad (20.34)$$

$$\cos \theta = \frac{\pi}{4} S_f^2 (\cos \theta_0 + 1) - 1 \quad (\text{Cassie–Baxter state}) \quad (20.35)$$

For a perfect macroscale system, the transition between the Wenzel and Cassie–Baxter states should occur only at the intersection of the two regimes (the point at which the contact angle and net energies of the two regimes are equal, corresponding to  $S_f = 0.51$ ). It is observed, however, that the transition from the metastable Cassie–Baxter to stable Wenzel occurs at much lower values of the spacing factor  $0.083 < S_f < 0.111$ . As shown in Fig. 20.43a, the stable Wenzel state (i) can transform into the stable Cassie–Baxter state with increasing  $S_f$  (ii). The metastable Cassie–Baxter state (iii) can abruptly transform (iv) into the stable Wenzel state (i). The transition point (i–ii) corresponds to equal free energies in the Wenzel and Cassie–Baxter states. Whereas the transition (iv) corresponds to the Wenzel energy much lower than the Cassie–Baxter energy and thus involves significant energy dissipation and is irreversible [62]. The solid and dashed straight lines correspond to the values of the contact angle, calculated from (20.34–20.35) using the contact angle for a nominally flat surface,  $\theta_0 = 109^\circ$ . The two series of the experimental data are shown with squares and diamonds.

Figure 20.43b shows the values of the advancing contact angle plotted against the spacing factor (20.32). The solid and dashed straight lines correspond to the values of the contact angle for the Wenzel and Cassie–Baxter states, calculated from (20.34–20.35) using the advancing contact angle for a nominally flat surface,  $\theta_{adv0} = 116^\circ$  [62]. It is observed that the calculated values underestimate the advancing contact angle, especially for big  $S_f$  (small distance between the pillars



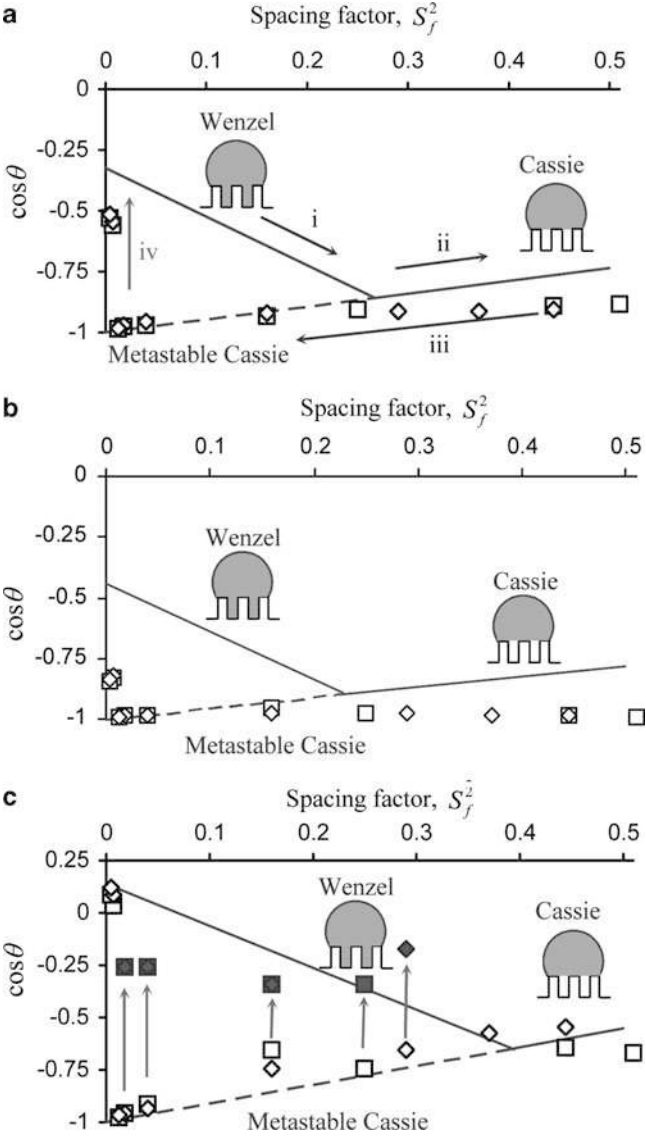


**Fig. 20.43** Theoretical (solid and dashed) and experimental (squares for the 1st series, diamonds for the 2nd series) (a) contact angle as a function of the spacing factor, (b) advancing contact angle, and (c) receding contact angle and values of the contact angle observed after the transition during evaporation (blue) [62]

or pitch  $P$ ). This is understandable, because the calculation takes into account only the effect of the contact area and ignores the effect of roughness and edge line density [it corresponds to  $H_r = 0$  in (20.33)], while this effect is more

pronounced for high pillar density (big  $S_f$ ). In a similar manner, the contact angle is underestimated for the Wenzel state, since the pillars constitute a barrier for the advancing droplet.

Figure 20.43c shows the values of the contact angle after the transition took place (squares and diamonds), as it was observed during evaporation [62]. For both series, the values almost coincide. For comparison, the values of the receding contact angle measured for millimeter-sized water droplets are also shown (squares and diamonds), since evaporation constitutes removing liquid, and thus the contact angle during evaporation should be compared with the receding contact angle. The solid and dashed straight lines correspond to the values of the contact angle, calculated from (20.34–20.35) using the receding contact angle for a nominally flat surface,  $\theta_{\text{rec0}} = 82^\circ$ . Figure 20.43c demonstrates a good agreement between the experimental data and (20.34–20.35).

In the analysis of the evaporation data of micropatterned surfaces, Nosonovsky and Bhushan [32] found several effects specific for the multiscale character of this process. First, they discussed the applicability of the Wenzel and Cassie–Baxter equations for average surface roughness and heterogeneity. These equations relate the local contact angle with the apparent contact angle of a rough/heterogeneous surface. However, it is not obvious what should be the size of roughness/heterogeneity averaging, since the triple line at which the contact angle is defined has two very different length scales: its width is of molecular size scale while its length is on the order of the size of the droplet (that is, microns or millimeters). They presented an argument that in order for the averaging to be valid, the roughness details should be small compared to the size of the droplet (and not the molecular size). They showed that while for uniform roughness/heterogeneity the Wenzel and Cassie–Baxter equations can be applied, for a more complicated case of non-uniform heterogeneity, the generalized equations should be used. The proposed generalized Cassie–Baxter and Wenzel equations are consistent with a broad range of available experimental data. The generalized equations are valid both in the cases when the classical Wenzel and Cassie–Baxter equations can be applied as well as in the cases when they later fail.

The macroscale contact angle hysteresis and Cassie–Baxter and Wenzel transition cannot be determined from the macroscale equations and are governed by micro- and nanoscale effects, so wetting is a multiscale phenomenon [31, 32, 62, 63, 79]. The kinetic effects associated with contact angle hysteresis should be studied at the microscale, whereas the effects of adhesion hysteresis and the Cassie–Baxter and Wenzel transition involve processes at the nanoscale. Their theoretical arguments are supported by the experimental data on micropatterned surfaces. The experimental study of the contact angle hysteresis demonstrates that two different processes are involved: the changing solid–liquid area of contact and pinning of the triple line. The latter effect is more significant for the advancing than for the receding contact angle. The transition between wetting states was observed for evaporating microdroplets, and droplet radius scales well with the geometric parameters of the micropattern.

### 20.5.3.6 Observation of Transition During the Bouncing Droplet

Jung and Bhushan [77] performed bouncing droplet experiments to observe how impact velocity influences the Cassie–Baxter and Wenzel transition during the droplet hitting the surface on two different micropatterned Si surfaces with  $\text{PF}_3$ . Figure 20.44 shows snapshots of a droplet with 1 mm radius hitting the surfaces. The impact velocity was obtained just prior to the droplet hitting the surface. As shown in images in the first row for the two sets of surfaces, the droplet hitting the surface under an impact velocity of 0.44 m/s first deformed and then retracted, and

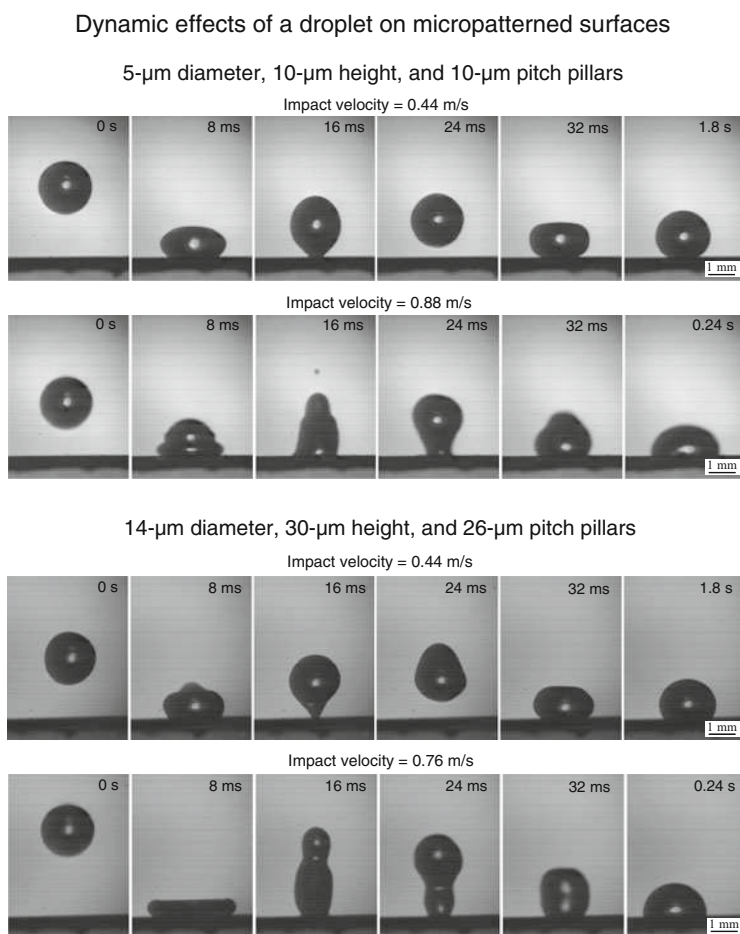


**Fig. 20.44** Snapshots of a droplet with 1 mm radius hitting on two different micropatterned surfaces. The impact velocity was obtained just prior to the droplet hitting the surface. The pinning of droplet on the surface with 5- $\mu\text{m}$  diameter, 10- $\mu\text{m}$  height and 10- $\mu\text{m}$  pitch pillars, and on the surface with 14- $\mu\text{m}$  diameter, 30- $\mu\text{m}$  height and 26- $\mu\text{m}$  pitch pillars occurred at impact velocity of 0.88 m/s and 0.76 m/s, respectively [77]

bounced off the surface. Finally, the droplet sat on the surface and had a high contact angle, which suggests the formation of a solid–air–liquid interface. Next, they repeated the impact experiment by increasing the impact velocity. The bounce off does not occur, and the wetting of the surface (and possibly pinning of droplet) occurred at an impact velocity of 0.88 m/s and 0.76 m/s, respectively, referred to as the critical velocity (described earlier). The second row of the two sets of images shows the images of the droplet at the critical velocity. After the droplet hit the surface, it wetted the surface (possibly the droplet was also pinned) after the deformation of the droplet. This is because air pockets do not exist below the droplet as a result of droplet impalement by the pillars, characterized by a smaller contact angle. These observations indicate the transition from a Cassie–Baxter to a Wenzel regime.

To identify whether one is in a Wenzel regime or a Cassie–Baxter regime, the contact angle data in the static condition and after bounce off were plotted [77]. Figure 20.45 shows the measured static contact angle as a function of geometric parameters for the droplet with 1 mm radius gently deposited on the surface (circles) and for the droplet with 1 mm radius after hitting the surface at 0.44 m/s (triangles). The data are compared with predicted static contact angle values obtained using the Wenzel and the Cassie–Baxter equations (solid lines) with a given value of  $\theta_0$  ( $109^\circ$ ) for a smooth surface for two series of the micropatterned surfaces. In the case of the droplet gently deposited on the surface, as the pitch increases up to  $45\text{ }\mu\text{m}$  of series 1 and  $126\text{ }\mu\text{m}$  of series 2, the static contact angle first increases gradually from  $152^\circ$  to  $170^\circ$ . Then, the contact angle starts decreasing sharply. The increase in the contact angle occurs because of an increase in the roughness factor and the formation of composite surface [69]. The decrease in contact angle at pitch values higher than  $60\text{ }\mu\text{m}$  for series 1 and  $168\text{ }\mu\text{m}$  for series 2 occurs due to the transition from composite interface to solid–liquid interface. In the case of the droplet hitting the surface at 0.44 m/s, it is shown that the liquid–air interface can easily be destabilized due to dynamic impact on the surface with a pitch value higher than  $12.5\text{ }\mu\text{m}$  for series 1 and  $70\text{ }\mu\text{m}$  for series 2, although the droplet is in the Cassie–Baxter regime when it is gently deposited on the surface. The static contact angle of the droplet after hitting at 0.44 m/s is lower than that of the droplet gently deposited. It can be interpreted that after hitting, the droplet contacts the bottom of the cavities between pillars and pushes out the entrapped air under the droplet, resulting in an abrupt increase of the solid–liquid surface area by dynamic impact. It will be shown in the following paragraph that the critical velocity at which wetting occurs for series 1 and series 2 samples is equal to about 0.44 m/s at pitch values larger than  $12.5\text{ }\mu\text{m}$  and  $70\text{ }\mu\text{m}$  respectively. Thus, wetting at the velocity used here is expected.

To study the validity of the transition criterion (20.29), the critical impact velocity at which wetting of the surface (possibly pinning of droplet) occurs was measured [77]. For calculations, the surface tension of the water–air interface ( $\gamma$ ) was taken at  $0.073\text{ N/m}$ , the mass density ( $\rho$ ) is  $1,000\text{ kg/m}^3$  for water, and  $1\text{ kg}\cdot\text{m/s}^2 = 1\text{ N}$  [22]. Figure 20.46 shows the measured critical impact velocity of a droplet with 1 mm radius as a function of geometric parameters (triangles).

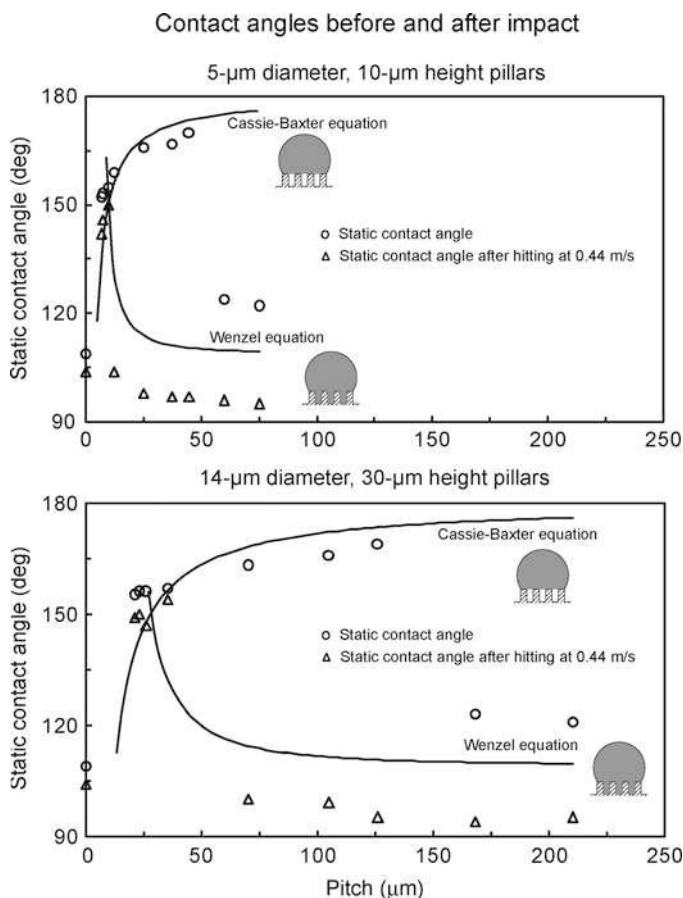


**Fig. 20.45** Measured static contact angle as a function of geometric parameters for the droplet with 1 mm radius gently deposited on the surface (*circles*) and for the droplet with 1 mm radius after hitting the surface at 0.44 m/s (*triangles*). The data are compared with predicted static contact angle values obtained using Wenzel and Cassie–Baxter equations (*solid lines*) with a given value of  $\theta_0$  ( $109^\circ$ ) for a smooth surface for two series of the micropatterned Si with different pitch values [77].

The trends are compared with the predicted curve (solid lines). It is found that the critical impact velocity at which wetting occurs is in good quantitative agreement with our predictions. The critical impact velocity of the droplet decreases with the geometric parameter (pitch). For the surface with small pitch, the critical impact velocity of droplet can be large.

The energy barrier of the Cassie–Baxter and Wenzel transition can be estimated as the kinetic energy of the droplets [81]. Figure 20.47 shows the dependence of the kinetic energy corresponding to the transition,  $E_{\text{kin}}$ , on  $\Delta E/(A_0 \cos \theta_0)$  calculated from (20.30). It is observed that the dependence is close to linear, however, the series of smaller pillars has larger energies of transition. The value of  $A_0$  is in the

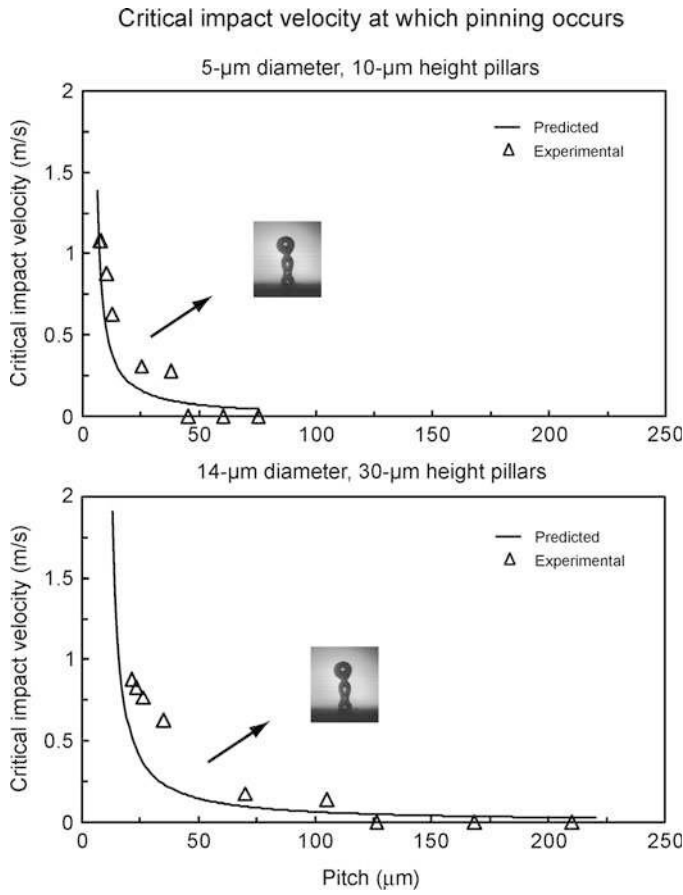
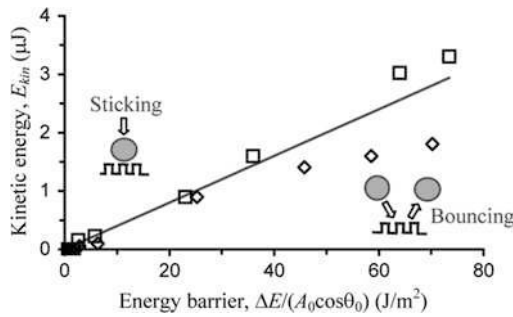


**Fig. 20.46** Measured critical impact velocity of droplet with 1 mm radius as a function of geometric parameters (*triangles*). The data are compared with the criterion of impact velocity for the pinning of droplet (*solid lines*) for two series of the micropatterned Si with different pitch values [77]

**Fig. 20.47** Bouncing droplets dependency of the kinetic energy of a droplet corresponding to the regime transition upon the energy barrier calculated from (20.30) (*squares* for series 1 and *diamonds* for series 2). The fit (*solid line*) is shown for  $A_0 = 0.12 \text{ mm}^2$  [81]



range  $0.11 \text{ mm}^2 < A_0 < 0.18 \text{ mm}^2$  for series 1 and  $0.05 \text{ mm}^2 < A_0 < 0.11 \text{ mm}^2$  for series 2, which is of the same order as the actual area under the droplet.

These results suggest that the energy barrier for the Cassie–Baxter and Wenzel transition is given by (20.30) and is proportional to the area under the droplet [81]. For droplets sitting on the surface or evaporating, the transition takes place when the size of the barrier decreases to the value of the vibrational energy,  $U$ . The vibrational energy of the droplet is the energy associated with the vibration of the droplet due to surface waves, thermal vibration etc. Assuming  $U = \text{const}$ , the proportionality of  $P/D$  and  $R$  suggests that the energy barrier is proportional to the  $RD/P$ . This is indeed true, since the area under the droplet  $A_0 = \pi(R \sin \theta)^2$ . Substitutiong  $\sin^2 \theta = 0.1$ ,  $\cos \theta_0 = \cos 109^\circ = -0.33$ ,  $\gamma_{\text{LA}} = 0.072 \text{ J/m}^2$  in (20.30) and taking the observed value  $RD/P = 50 \text{ }\mu\text{m}$  yields an estimated value of the vibrational energy  $U = 1.2 \times 10^{-10} \text{ J}$ . The transition happens because the size of the droplet is decreased or because the pitch between the pillars that cover the surface is increased. A different way to overcome the barrier is to hit the surface with a droplet with a certain kinetic energy.

Based on Nosonovsky and Bhushan [81], the vibrational energy  $U$  also plays a role in overcoming energy barriers that lead to contact angle hysteresis during liquid flow [51]. To estimate the effect of the energy barriers on contact angle hysteresis, we assume, based on (20.5), that the difference between the advancing and receding contact angle is given by

$$\cos \theta_{\text{rec}} - \cos \theta_{\text{adv}} = \Delta W / \gamma_{\text{LA}} \quad (20.36)$$

where  $\Delta W$  corresponds to the energy barrier associated with the wetting–dewetting cycle. Assuming that this energy barrier is of the same order as the vibrational energy per contact area,  $\Delta W = U/A_0$ , and taking  $A_0 = 0.1 \text{ mm}^2$ , we end up with  $\Delta W = 10^{-3} \text{ J/m}^2$ . For water ( $\gamma_{\text{LA}} = 0.072 \text{ J/m}^2$ ), (20.36) leads to a realistic value of hysteresis on a superhydrophobic surface  $\cos \theta_{\text{rec}} - \cos \theta_{\text{adv}} = 0.014$ . This number provides an estimate for contact angle hysteresis in the limit of small energy barriers comparable with  $U$ . The actual values for a micropatterned surface are dependent upon the solid–liquid contact area (that provides energy barriers due to so-called adhesion hysteresis) and the density of the solid–air–liquid contact line (that provides additional pinning) and were found to be between 0.0144 and 0.440 [70], thus showing a good agreement with the value calculated based on  $U$  as the lower limit. This indicates that the value of  $U$  is relevant both for the Cassie–Baxter and Wenzel regime transition and contact angle hysteresis.

### 20.5.3.7 Observation and Measurement of Contact Angle Using ESEM

Figure 20.48 shows how water droplets grow and merge in an ESEM [76] that was used as a contact angle analysis tool. Microdroplets (with a diameter less than 1 mm) were distributed on a micropatterned surface coated with  $\text{PF}_3$  using condensation by decreasing temperature. At the beginning, some small water droplets



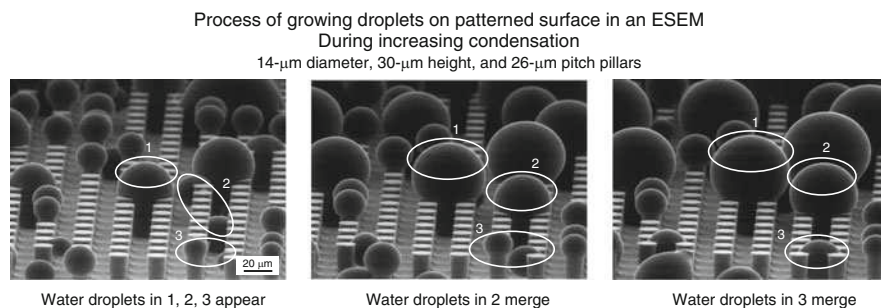


**Fig. 20.48** Microdroplet (in dimension of less than 1 mm diameter) growing and merging process under ESEM during increasing condensation by decreasing temperature. *Left image:* Some small water droplets appear at the beginning, i.e. water droplets 1, 2, 3. *Middle image:* Water droplets at locations 1 and 3 increase in size and water droplets at location 2 merge together to form one big droplet. *Right image:* Water droplets at locations 1 and 2 increase in size and water droplets at location 3 merge together to form one big droplet [76]

appeared, i.e. water droplets at locations 1, 2 and 3 in the left image. During further condensation with decreasing temperature, droplets at locations 1 and 3 gradually grew while droplets at location 2 merged together. With further condensation, droplets at locations 1 and 2 gradually grew while droplets at location 3 merged together into one big droplet in the right image. In all cases, condensation was initiated at the bottom, therefore, the droplets were in the Wenzel regime.

Compared with the conventional contact angle measurement, ESEM is able to provide detailed information about the contact angle of microdroplets on micropatterned surfaces. The diameter of the water droplets used for the contact angle measurement was 10  $\mu\text{m}$ , so that the size limit pointed out by Stelmashenko et al. [94] was avoided. For droplet size smaller than 1  $\mu\text{m}$ , substrate backscattering can distort the intensity profile such that the images are inaccurate.

As shown in Fig. 20.49, the static contact angle and contact angle hysteresis of the microdroplets on flat and micropatterned surfaces were obtained from the images using the methodology described earlier. Once the microdroplet's condensation and evaporation has reached a dynamic equilibrium, static contact angles were determined. The flat Si coated with  $\text{PF}_3$  showed a static contact angle of  $98^\circ$ . The micropatterned surfaces coated with  $\text{PF}_3$  increase the static contact angle compared to the flat surface coated with  $\text{PF}_3$  due to the effect of roughness. Advancing and receding contact angles were measured during condensation/evaporation with decreasing/increasing the temperature of the cooling stage, and the contact angle hysteresis was then calculated [76].

Figure 20.50 shows contact angle hysteresis as a function of geometric parameters for the microdroplets formed in the ESEM (triangles) for two series of micropatterned Si with different pitch values coated with  $\text{PF}_3$ . Data at zero pitch correspond to a flat Si sample. The droplets with about 20  $\mu\text{m}$  radii, which are larger than the pitch, were selected in order to look at the effect of pillars in contact with the droplet. These data were compared with conventional contact angle



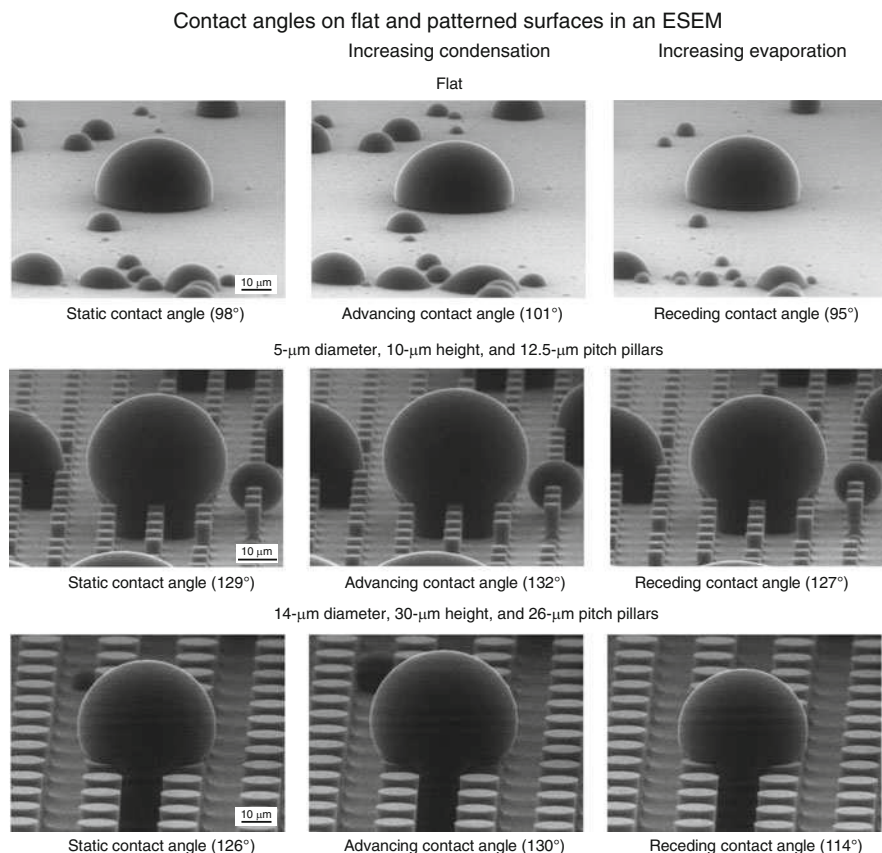


**Fig. 20.49** Microdroplets on flat and two micropatterned surfaces using ESEM. Second set of images were taken during increasing condensation, and the third set of images were taken during increasing evaporation. Static contact angle was measured when the droplet was stable. Advancing contact angle was measured after increasing condensation by decreasing the temperature of the cooling stage. Receding contact angle was measured after decreasing evaporation by increasing the temperature of the cooling stage [76]

measurements with the droplet with 1 mm radius (5  $\mu\text{L}$  volume) (circle and solid lines) [69]. When the distance between pillars increases above a certain value, the contact area between the micropatterned surface and the droplet decreases, resulting in a decrease of the contact angle hysteresis. Both droplets with 1 mm and 20  $\mu\text{m}$  radii showed the same trend. The contact angle hysteresis for the micropatterned surfaces with low pitch are higher compared to the flat surface due to the effect of sharp edges on the pillars, resulting in pinning [66]. Contact angle hysteresis for a flat surface can arise from roughness and surface heterogeneity. For a droplet advancing forward on the micropatterned surfaces, the line of contact of the solid, liquid, and air will be pinned at the edge point until it is able to move, resulting in increasing contact angle hysteresis. The contact angle hysteresis for the

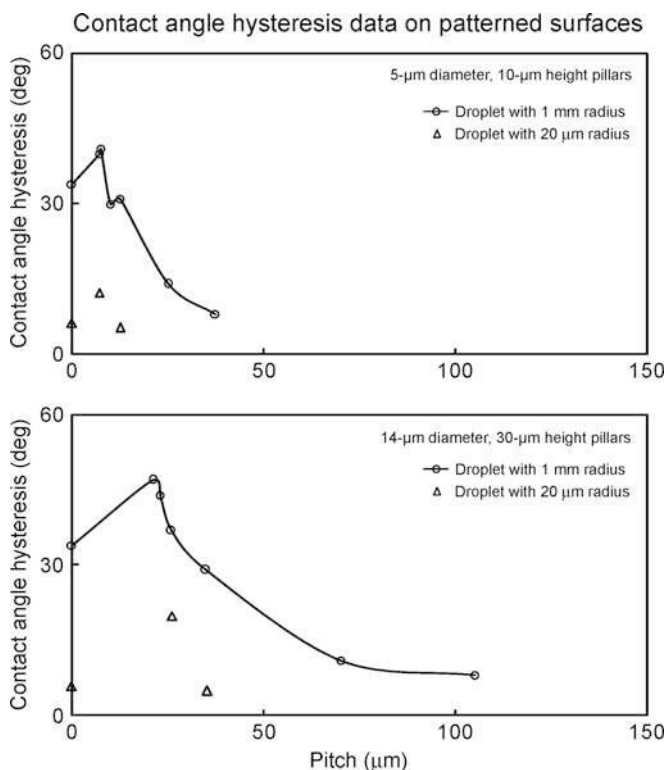


**Fig. 20.50** Contact angle hysteresis as a function of geometric parameters for the microdroplet with about 20  $\mu\text{m}$  radius from ESEM (triangle) compared with the droplet with 1 mm radius (5  $\mu\text{L}$  volume) (circle and solid lines) for two series of the micropatterned surfaces with different pitch values. Data at zero pitch correspond to a flat sample [76]

microdroplet from ESEM is lower as compared to that for the droplet with 1 mm radius. The difference of contact angle hysteresis between a microdroplet and a droplet with 1 mm radius could come from the different pinning effects, because the latter has more sharp edges in contact with a droplet compared to the former. The results show how droplet size can affect the wetting properties of micropatterned Si surfaces [76].

#### 20.5.4 Ideal Surfaces with Hierarchical Structure

It has been reported earlier that a hierarchical surface is needed to develop a composite interface with high stability. The structure of an ideal hierarchical surface is shown in Fig. 20.51. The asperities should be high enough so that the droplet does not touch the valleys. As an example, for a structure with

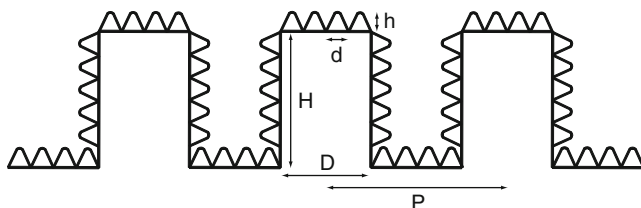


**Fig. 20.51** Schematic of structure of an ideal hierarchical surface. Microasperities consist of the circular pillars with diameter  $D$ , height  $H$ , and pitch  $P$ . Nanoasperities consist of pyramidal nanoasperities of height  $h$  and diameter  $d$  with rounded tops

circular pillars, the following relationship should hold for a composite interface;  $(\sqrt{2P} - D)^2/R < H$ , (20.26). As an example, for a droplet with a radius on the order of 1 mm or larger, a value of  $H$  on the order of 30  $\mu\text{m}$ ,  $D$  on the order of 15  $\mu\text{m}$ , a  $P$  on the order of 130  $\mu\text{m}$  (Fig. 20.36) is optimum. Nanoasperities can pin the liquid–air interface and thus prevent liquid from filling the valleys between asperities. They are also required to support nanodroplets, which may condense in the valleys between large asperities. Therefore, nanoasperities should have a small pitch to handle nanodroplets, less than 1 mm down to few nm radius. The values of  $h$  on the order of 10 nm and  $d$  on the order of 100 nm can be easily fabricated.

### 20.5.5 Hierarchical Structured Surfaces with Wax Platelets and Tubules

A hierarchical structure is composed of at least two levels of structuring in different length scales. Bhushan et al. [71–74] and Koch et al. [44] fabricated surfaces with a hierarchical structure with micropatterned epoxy replicas and Lotus leaf microstructure, and created a second level of structuring with wax platelets and wax tubules. Platelets and tubules are the most common wax morphologies found in plant surfaces and exist on superhydrophobic leaves, such as Lotus and *Colocasia esculenta* leaves. The structures developed mimic the hierarchical structures of superhydrophobic leaves. Two steps of the fabrication process include the production of microstructured surfaces by soft lithography and the subsequent development of nanostructures on top by self assembly of plant waxes and artificial wax components.

A two-step molding process was used to fabricate several structurally identical copies of micropatterned Si surface and Lotus leaves. The technique used is a fast, precise, and low cost molding process for biological and artificial surfaces [225, 226]. The technique was used to mold a microstructured Si surface with pillars of 14  $\mu\text{m}$  diameter and 30  $\mu\text{m}$  height with 23  $\mu\text{m}$  pitch [44, 71–74], fabricated by photolithography [143]. Before replication of the Lotus leaf, the epicuticular wax tubules were removed in areas of approximately 6  $\text{cm}^2$ . For this purpose,

a two-component fast hardening glue was applied on the upper side of the leaves and was carefully pressed onto the leaf. After hardening, the glue with the embedded waxes was removed from the leaf, and the procedure was repeated [44].

The replication is a two step molding process, in which first a negative replica of a template is generated and then a positive replica is generated, as shown in Fig. 20.52a [74]. A polyvinylsiloxane dental wax (President Light Body<sup>®</sup> Gel, ISO 4823, Polyvinylsiloxan (PLB), Coltene Whaledent, Hamburg, Germany) was applied via a dispenser on the surface to the surface and immediately pressed down

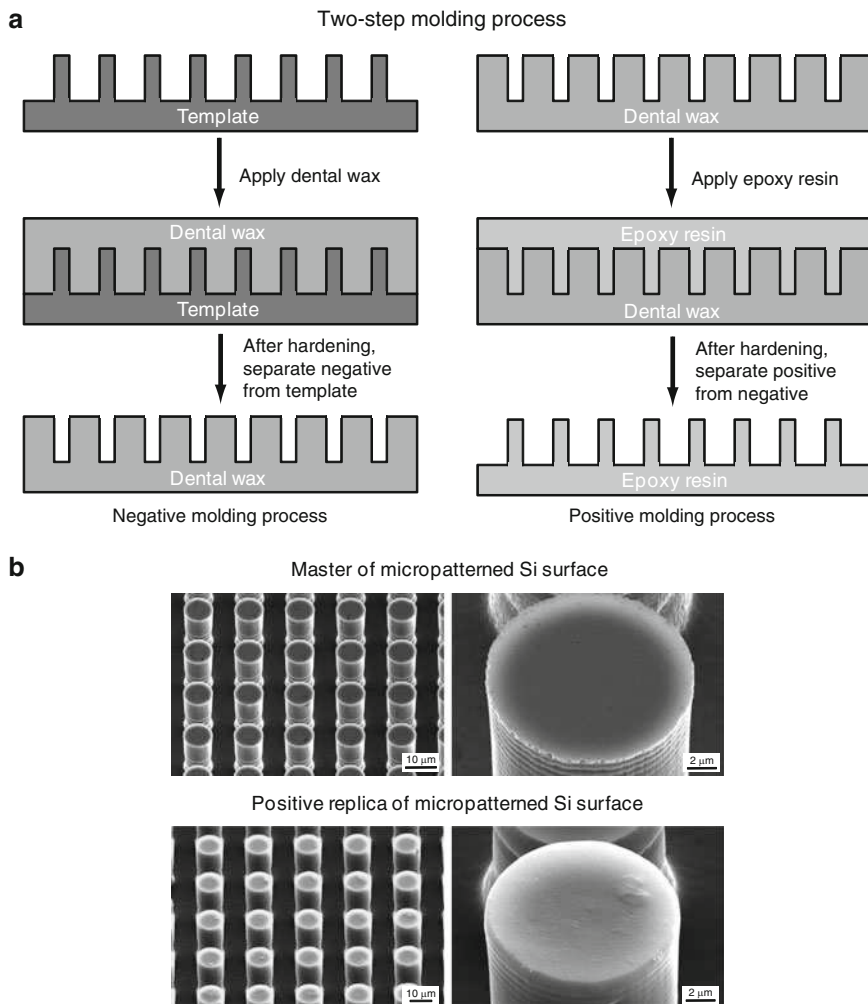


**Fig. 20.52** (a) Schematic of two-step molding process used to fabricate microstructure, in which at first a negative is generated and then a positive, and (b) SEM micrographs of the master of micropatterned Si surface and positive replica fabricated from the master surface measured at 45° tilt angle (shown using two magnifications) [74]

with a glass plate. After complete hardening of the molding mass (at room temperature for approximately 5 min at room temperature), the silicon master surface and the mold (negative) were separated. After a relaxation time of 30 min for the molding material, the negative replicas were filled with a liquid epoxy resin (Epoxydharz L<sup>®</sup>, No. 236349, Conrad Electronics, Hirschau, Germany) with hardener (Harter S, Nr 236365, Conrad Electronics, Hirschau, Germany). Specimens with microstructures were immediately transferred to a vacuum chamber at 750 mTorr (100 Pa) pressure for 10 s to remove trapped air and to increase resin infiltration through the structures. After hardening at room temperature (24 h at 22°C), the positive replica was separated from the negative replica. The second step can be repeated to generate a number of replicas. The pillars of the master surface have been replicated without any morphological changes as shown in Fig. 20.52b [74]. The nanogrooves of a couple of hundred nm in lateral dimension present on the pillars of master surface are shown to reproduce faithfully in the replica.

Bhushan et al. [71–74] and Koch et al. [44] created a nanostructure by self assembly of synthetic and plant waxes deposited by thermal evaporation. The alkane *n*-hexatriacontane (C<sub>36</sub>H<sub>74</sub>) has been used for the development of platelet nanostructures. Tubule forming waxes which were isolated from leaves of *Tropaeolum majus* (L.) and *Nelumbo nucifera*, in the following referred to as *T. majus* and Lotus, were used to create tubule structures. The chemical structure of the major components of the wax forming tubule and alkane *n*-hexatriacontane are shown in Table 20.8. The complete chemistry of the plant waxes used is presented in Koch et al. [161]. For a homogenous deposition of the waxes and alkane, a thermal evaporation system, as shown in Fig. 20.53, has been used [74]. Specimens of smooth surfaces (flat silicon replicas) and microstructured replicas were placed in a vacuum chamber at 30 mTorr (4 kPa), 20 mm above a heating plate loaded with waxes of *n*-hexatriacontane (300, 500 or 1,000 µg), *T. majus* wax (500, 1,000, 1,500 or 2,000 µg), and Lotus wax (2,000 µg) [44, 71–74]. The wax was evaporated by heating it up to 120°C. In a vacuum chamber the evaporation from the point source to the substrate occurs in a straight line; thus, the amount of sublimated material is equal in a hemispherical region over the point of source [227]. In order to estimate the amount of sublimated mass, the surface area of the half sphere was calculated by using the formula  $2\pi r^2$ , whereby the radius (*r*) represents the distance between the specimen to be covered and the heating plate with the substance to be evaporated. The amounts of wax deposited on the specimen surfaces were 0.12, 0.2 and 0.4 µg/mm<sup>2</sup> for *n*-hexatriacontane, and 0.2, 0.4, 0.6 and 0.8 µg/mm<sup>2</sup> for *T. majus* and 0.8 µg/mm<sup>2</sup> for Lotus waxes, respectively.

After coating, the specimens with *n*-hexatriacontane were placed in a desiccator at room temperature for 3 days for crystallization of the alkanes. A stable stage was indicated by no further increase of crystal sizes.

For the plant waxes which are a mixture of aliphatic components, different crystallization conditions have been chosen. It has been reported by Niemietz et al. [228] that an increase of temperature from 21°C (room temperature) to 50°C had a positive effect on the mobilization and diffusion of wax molecules, required for separation of the tubule forming molecules. It is also known that

**Table 20.8** Chemical structure of the major components of *n*-hexatriacontane, *T. majus* and Lotus waxes. The major component is shown first [44, 71, 73]

<i>n</i> -hexatriacontane		$C_{36}H_{74}$
<i>Tropaeolum majus</i>	nonacosan-10-ol	$\begin{array}{c} \text{OH} \\   \\ \text{CH}_3-(\text{CH}_2)_6-\text{CH}-(\text{CH}_2)_{18}-\text{CH}_3 \end{array}$
	nonacosane-4,10-diol	$\begin{array}{c} \text{OH} \qquad \text{OH} \\   \qquad \quad   \\ \text{CH}_3-(\text{CH}_2)_2-\text{CH}-(\text{CH}_2)_5-\text{CH}-(\text{CH}_2)_{18}-\text{CH}_3 \end{array}$
Lotus	nonacosane-10,15-diol	$\begin{array}{c} \text{OH} \qquad \text{OH} \\   \qquad \quad   \\ \text{CH}_3-(\text{CH}_2)_6-\text{CH}-(\text{CH}_2)_4-\text{CH}-(\text{CH}_2)_{13}-\text{CH}_3 \end{array}$
	nonacosan-10-ol	$\begin{array}{c} \text{OH} \\   \\ \text{CH}_3-(\text{CH}_2)_6-\text{CH}-(\text{CH}_2)_{18}-\text{CH}_3 \end{array}$

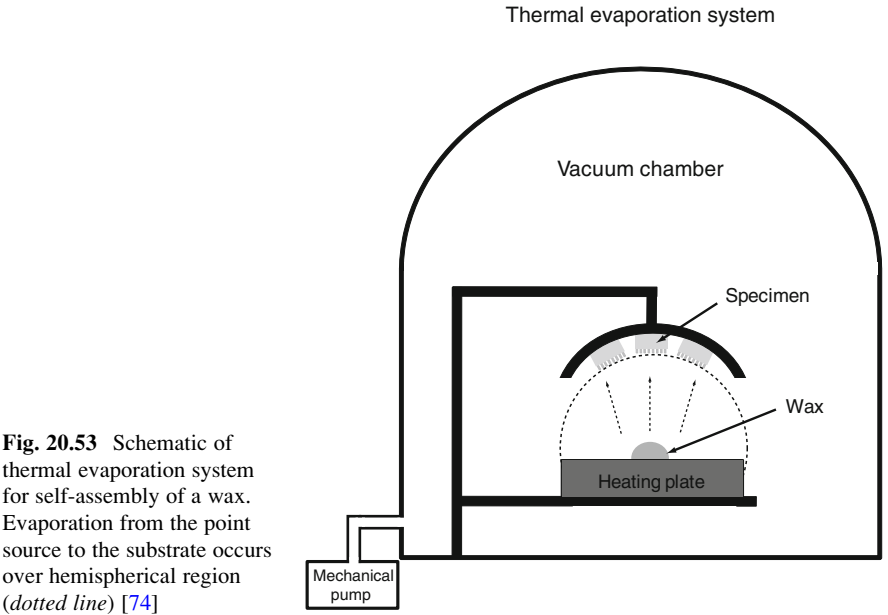


**Fig. 20.53** Schematic of thermal evaporation system for self-assembly of a wax. Evaporation from the point source to the substrate occurs over hemispherical region (dotted line) [74]

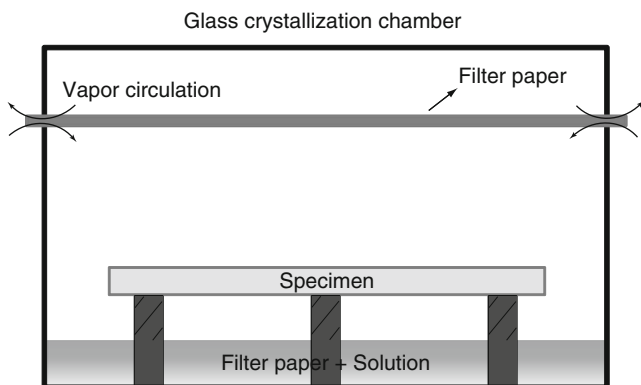


**Fig. 20.54** Schematic of a glass recrystallization chamber used for tubules formation. The filter paper placed at the bottom of the chamber was wetted with 20 mL of the solvent, and slow evaporation of the solvent was provided by placing a thin filter paper between the glass body and the cap placed above. The total volume of the chamber is about 200 cm<sup>3</sup> [3]

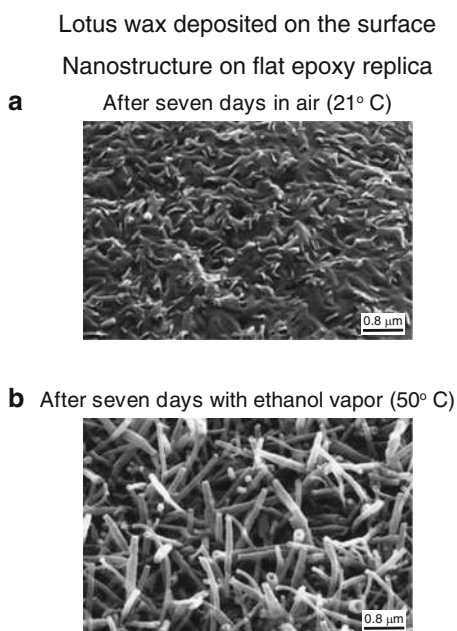
chemical ambient has an influence on the propensity of wax crystallization, thus the specimens with evaporated plant waxes (*T. majus* and Lotus) were stored for 3 days at 50°C in a crystallization chamber, where they were exposed to a solvent (ethanol) in vapor phase (Fig. 20.54). Specimens were placed on metal posts and a filter paper wetted with 20 mL of the solvent was placed below the specimens. Slow diffusive loss of the solvent in the chamber was provided by placing a thin filter paper between the glass body and the lid. After evaporation of the solvent, specimens were left in the oven at 50°C in total for 7 days. Figure 20.55 shows the nanostructures formed by Lotus wax, 7 days after wax deposition on flat surfaces. Figure 20.55a shows the nanostructure after storage at 21°C; in these no tubules were grown. Figure 20.55b shows that Lotus waxes exposed to ethanol vapor for 3 days at 50°C formed wax tubules. A detailed description of the nanostructure sizes and nanoroughness is given in the following.

Flat films of *n*-hexatriacontane and wax tubules were made by heating the substances over their melting point and rapidly cooling down. This procedure interrupts the crystallization and leads to smooth films [44, 71–74].

#### 20.5.5.1 Nanostructures with Various Platelet Crystal Densities

Figure 20.56a shows the scanning electron microscope (SEM) micrographs of a flat surface and nanostructures fabricated with various masses of *n*-hexatriacontane [71]. The nanostructure is formed by three-dimensional platelets of *n*-hexatriacontane, as shown in detail in Fig. 20.56b. Platelets are flat crystals, grown perpendicular to the substrate surface. They are randomly distributed on the surface, and their shapes and sizes show some variations. Some of the single platelets are connected to their neighboring crystals at their lateral ends. This arrangement leads to a kind of

**Fig. 20.55** SEM micrographs of morphology of the Lotus wax deposited on the flat epoxy replica surface after two treatments of specimens measured at 45° tilt angle, (a) after 7 days at 21°C (*top*), nanostructure on flat epoxy replica was found with no tubules, and (b) after 7 days at 50°C with ethanol vapor (*bottom*), tubular nanostructures with random orientation were found on the surface [44]



cross-linking of the single platelets. As shown in Fig. 20.56b, and based on additional specimens, the platelet thickness varied between 50 and 100 nm, and their length varied between 500 and 1,000 nm. The self-assembly of *n*-hexatriacontane used here, and most long chain hydrocarbons lead to layered structures with a lamellae order. In these structures, the molecular axis is orientated parallel to the substrate surface. The growth of these layers results in an ordered, crystalline 3-D structure [229]. The created nanostructures are comparable to the wax crystal morphology found on superhydrophobic leaves, e.g., *Colocasia esculenta* [10] and *Triticum aestivum* (wheat) [230]. SEM micrographs of the nanostructures fabricated with three different masses of *n*-hexatriacontane show different densities of crystals. An atomic force microscope (AFM) was used to characterize the nanostructures. Statistical parameters of nanostructures (root mean square (RMS) height, peak to valley height, and summit density ( $\eta$ )) were calculated and are presented in Table 20.9 [24, 25]. A summit is defined as a point whose height is greater than its four nearest neighboring points above a threshold value of 10% of RMS height to avoid measurement errors. The measurement results were reproducible within  $\pm 5\%$ .

To study the effect of nanostructures with different crystal density on superhydrophobicity, static contact angle, contact angle hysteresis and tilt angle, and adhesive forces were measured [71]. For contact angle hysteresis, the advancing and receding contact angles were measured at the front and back of the droplet moving along the tilted surface, respectively. The data are shown in Fig. 20.57. The static contact angle of a flat surface coated with a film of *n*-hexatriacontane was 91°.



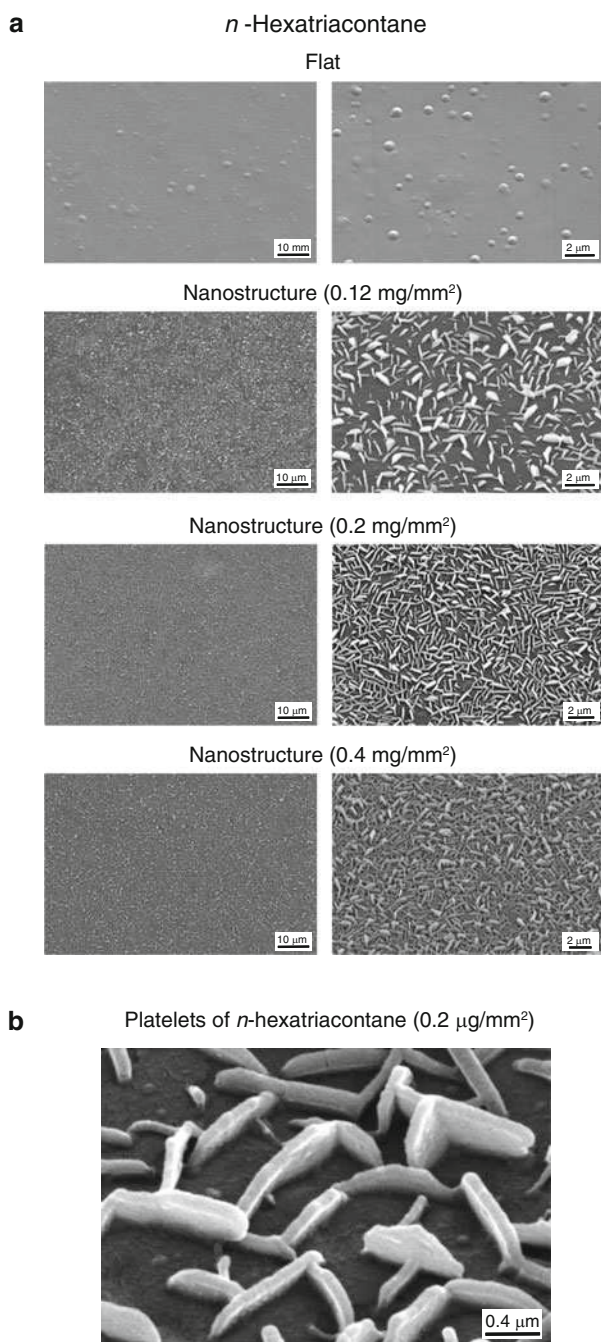


**Fig. 20.56** SEM micrographs taken at 45° tilt angle (shown using two magnifications) of (a) the flat surface and nanostructures fabricated with various mass of *n*-hexatriacontane and (b) three-dimensional platelets forming nanostructures on the surface fabricated with 0.2 μg/mm<sup>2</sup> mass of *n*-hexatriacontane. All samples are fabricated with epoxy resin coated with *n*-hexatriacontane [71]

**Table 20.9** Roughness statistics for nanostructure surface measured using an AFM (Scan size  $10\text{ }\mu\text{m} \times 10\text{ }\mu\text{m}$ ). Nanostructures were fabricated with *n*-hexatriacontane, *T. majus* and Lotus waxes [44, 71, 73]

	RMS height (nm)	Peak to valley height (nm)	$\eta$ (/sq. $\mu\text{m}$ )
<i>n</i> -hexatriacontane			
Nanostructure ( $0.12\text{ }\mu\text{g}/\text{mm}^2$ )	46	522	0.78
Nanostructure ( $0.2\text{ }\mu\text{g}/\text{mm}^2$ )	65	663	1.39
Nanostructure ( $0.4\text{ }\mu\text{g}/\text{mm}^2$ )	82	856	1.73
<i>Tropaeolum majus</i> wax			
Nanostructure ( $0.8\text{ }\mu\text{g}/\text{mm}^2$ )	180	1,570	0.57
Lotus wax			
Nanostructure ( $0.8\text{ }\mu\text{g}/\text{mm}^2$ )	187	1,550	1.47

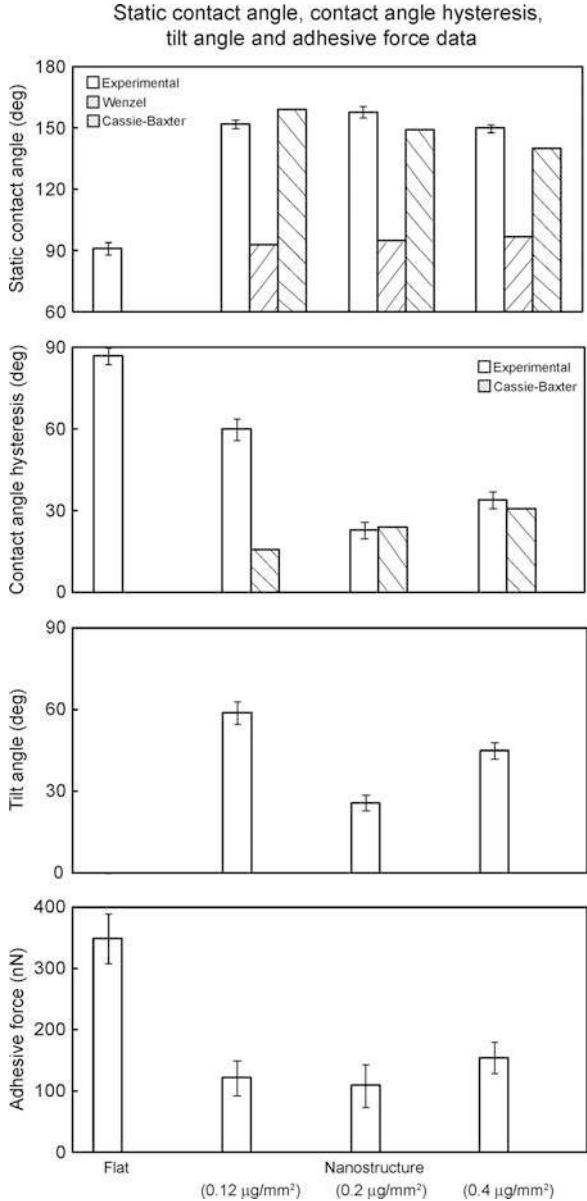
RMS root mean square

$\eta$  summit density

It showed a contact angle hysteresis of  $87^\circ$ , and the droplet still adhered at a tilt angle of  $90^\circ$ . Nanostructuring of flat surfaces with *n*-hexatriacontane platelets creates superhydrophobic surfaces with high static contact angle and a reduction of contact angle hysteresis and tilt angle. The values are a function of crystal density. Figure 20.58 shows a plot of static contact angle and contact angle hysteresis as a function of the mass of *n*-hexatriacontane deposited. As the mass of *n*-hexatriacontane increased, the static contact angle first increased, and the contact angle hysteresis decreased. Then, above a mass of  $0.2\text{ }\mu\text{g}/\text{mm}^2$ , static contact angle and contact angle hysteresis gradually decreased and increased with increasing mass, respectively. The highest static contact angle and lowest contact angle hysteresis are  $158^\circ$  and  $23^\circ$  at mass of  $0.2\text{ }\mu\text{g}/\text{mm}^2$ . As shown in Fig. 20.57, adhesive force measured using a  $15\text{ }\mu\text{m}$  radius borosilicate tip in an AFM also shows a similar trend as the wetting properties. Adhesive forces of the nanostructured surfaces were lower than for the flat surface because the contact between the tip and surface was lower than on the flat surface, because the contact between the tip and surface was reduced by surface structuring [24, 25].

In order to identify wetting regimes (Wenzel or Cassie–Baxter) as well as to understand the effect of crystal density on the propensity of air pocket formation for the nanostructured surfaces, roughness factor ( $R_f$ ) and fractional liquid–air interface ( $f_{LA}$ ) are needed. The  $R_f$  for the nanostructures was calculated using the AFM map [13, 14]. The calculated results were reproducible within  $\pm 5\%$ . The  $R_f$  for the nanostructured surfaces with masses of  $0.12$ ,  $0.2$  and  $0.4\text{ }\mu\text{g}/\text{mm}^2$  were found to be  $3.4$ ,  $4.9$  and  $6.8$ , respectively. For calculation of  $f_{LA}$  of the nanostructures, only the higher crystals are assumed to come in contact with a water droplet. The fractional geometrical area of the top surface for the nanostructures was calculated from SEM micrographs with top view ( $0^\circ$  tilt angle). The SEM images were converted to high contrast black and white images using Adobe Photoshop. The increase of contrast in SEM image eliminates the smaller platelet structures, which were visible in the original SEM image. The higher crystals led to white signals in the SEM figure. The fractional geometrical area of the top nanostructured surfaces

**Fig. 20.57** Bar chart showing the measured static contact angle, contact angle hysteresis and tilt angle; also shown are calculated static contact angles obtained using Wenzel and Cassie–Baxter equations with a given value of  $\theta_0$ , and calculated contact angle hysteresis using Cassie–Baxter equation on flat surface and nanostructures fabricated with various mass of *n*-hexatriacontane. The droplet on flat surface does not move along the surface even at tilt angle of 90°. The bar chart also shows adhesive forces for various structures, measured using a 15  $\mu\text{m}$  radius borosilicate tip [71]



with masses of 0.12, 0.2 and 0.4  $\mu\text{g}/\text{mm}^2$  was found to be 0.07, 0.15 and 0.24, leading to  $f_{\text{LA}}$  of 0.93, 0.85 and 0.76, respectively. The calculated results were reproducible within  $\pm 5\%$ . The values of static contact angle in Wenzel and Cassie–Baxter regimes for the nanostructured surfaces were calculated using the values of  $R_f$  and  $f_{\text{LA}}$  and presented in Fig. 20.57. The values of contact angle

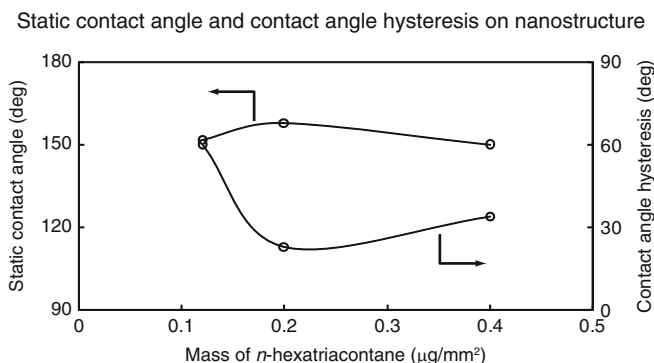


**Fig. 20.58** Static contact angle and contact angle hysteresis as a function of mass of *n*-hexatriacontane deposited on nanostructures [71]

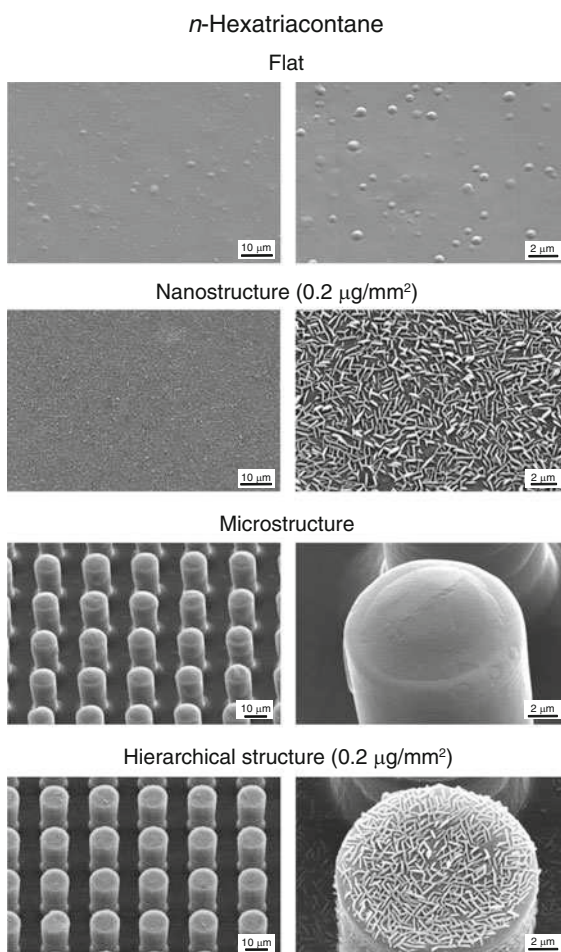
hysteresis in Cassie–Baxter regimes for various surfaces were calculated using (20.20). The data are presented in Fig. 20.57.

As shown in Fig. 20.57, the experimental static contact angle and contact angle hysteresis values for the two nanostructured surfaces with 0.2 and 0.4  $\mu\text{g}/\text{mm}^2$  were comparable to the calculated values in Cassie–Baxter regime. The results suggest that a droplet on two nanostructured surfaces should exist in the Cassie–Baxter regime. However, the experimental static contact angle and contact angle hysteresis values for the nanostructured surface with 0.12  $\mu\text{g}/\text{mm}^2$  were lower and higher than the calculated values in Cassie–Baxter regime, respectively. It is believed that neighboring crystals are separated at lower crystal density and any trapped air can be squeezed out. Whereas neighboring crystals are interconnected at higher densities and air remains trapped. At highest crystal density at a mass of 0.4  $\mu\text{g}/\text{mm}^2$ , there is less open volume compared to that at 0.2  $\mu\text{g}/\text{mm}^2$ , and that explains a droplet static contact angle going from 158° to 150° [71].

#### 20.5.5.2 The Influence of Hierarchical Structure with Wax Platelets on the Superhydrophobicity

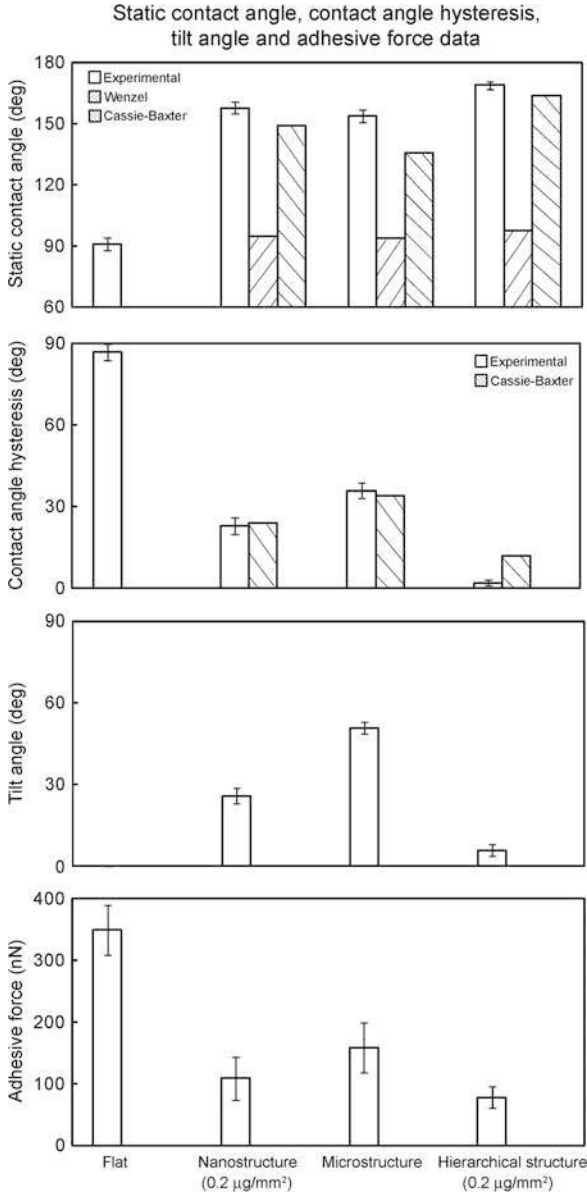
Bhushan et al. [72, 74] created surfaces with *n*-hexatriacontane of 0.2  $\mu\text{g}/\text{mm}^2$  to study the influence of hierarchical structure on superhydrophobicity. Figure 20.59 shows the scanning electron microscope (SEM) micrographs of a flat surface and nano-, micro- and hierarchical structures. To study the effect of structure on superhydrophobicity, static contact angle, contact angle hysteresis and tilt angle, and adhesive forces of four structures were measured. The data are shown in Fig. 20.60. The static contact angle of a flat surface coated with a film of *n*-hexatriacontane was 91°, and increased to 158° when *n*-hexatriacontane formed a nanostructure of platelets on it. The static contact angle on a flat specimen with a microstructure was 154°, but it increased to 169° for the hierarchical surface structure. Contact angle

**Fig. 20.59** SEM micrographs of the flat surface, nanostructure, microstructure, and hierarchical structure measured at 45° tilt angle (shown using two magnifications). All samples are fabricated with epoxy resin coated with *n*-hexatriacontane [72]



hysteresis and tilt angle for flat, micro- and nanostructured surfaces show similar trends. The flat surface showed a contact angle hysteresis of 87°, and the droplet still adhered at a tilt angle of 90°. The superhydrophobic micro- and nanostructured surfaces showed a reduction of contact angle hysteresis and tilt angle, but a water droplet still needs a tilt angle of 26° and 51°, respectively, before sliding. Only the hierarchical surface structure with static contact angle of 169° and low contact angle hysteresis of 2° exceeds the basic criteria for superhydrophobic and self-cleaning surfaces [30]. Adhesive force measured using a 15 μm radius borosilicate tip in an AFM also shows a similar trend as the wetting properties. Adhesion force of the hierarchical surface structure was lower than that of both micro- and nanostructured surfaces because the contact between the tip and surface was lower as a result of contact area being reduced [24, 25].

**Fig. 20.60** Bar chart showing the measured static contact angle, contact angle hysteresis and tilt angle; also shown are calculated static contact angles obtained using Wenzel and Cassie–Baxter equations with a given value of  $\theta_0$ , and calculated contact angle hysteresis using Cassie–Baxter equation on various structures. The droplet on flat surface does not move along the surface even at tilt angle of  $90^\circ$ . The bar chart also shows adhesive forces for various structures, measured using a  $15\text{ }\mu\text{m}$  radius borosilicate tip [72]



In order to identify wetting regimes (Wenzel or Cassie–Baxter) for the various surfaces, roughness factor ( $R_f$ ) and fractional liquid–air interface ( $f_{LA}$ ) are needed. The  $R_f$  for the nanostructure was described earlier. The  $R_f$  for microstructure was calculated for the geometry of flat-top, cylindrical pillars of diameter  $D$ , height  $H$ ,

**Table 20.10** Summary of static contact angles and contact angle hysteresis measured and calculated for droplets in Wenzel regime and Cassie–Baxter regime on the various surfaces with *n*-hexatriacontane using the calculated values of  $R_f$  and  $f_{LA}$  [72, 74]

	$R_f$	$f_{LA}$	Static contact angle (deg)			Contact angle hysteresis (deg)	
			Measured	Calculated in Wenzel regime	Calculated in Cassie–Baxter regime	Measured	Calculated in Cassie–Baxter regime
Flat			91			87 <sup>a</sup>	
Nanostructure	4.9	0.85	158	95	149	23	24
Microstructure	3.5	0.71	154	94	136	36	34
Hierarchical structure	8.4	0.96	169	98	164	2	12

<sup>a</sup>Advancing and receding contact angles are 141° and 54°, respectively

and pitch  $P$  distributed in a regular square array. For this case, roughness factor for the microstructure,  $(R_f)_{micro} = (1 + \frac{\pi DH}{P^2})$ . The roughness factor for the hierarchical structure is the sum of  $(R_f)_{micro}$  and  $(R_f)_{nano}$ . The values calculated for various surfaces are summarized in Table 20.10.

For calculation of  $f_{LA}$ , we make the following assumptions. For the microstructure, we consider that a droplet in size much larger than the pitch  $P$  contacts only the flat-top of the pillars in the composite interface, and the cavities are filled with air. For microstructure, fractional flat geometrical area of the liquid–air interface under the droplet,  $(f_{LA})_{micro} = (1 - \frac{\pi D^2}{4P^2})$  [30]. The fractional geometrical area of the top surface for the nanostructure was described earlier. For the hierarchical structure, the fractional flat geometrical area of the liquid–air interface,  $(f_{LA})_{hierarchical} = 1 - (\frac{\pi D^2}{4P^2})[1 - (f_{LA})_{nano}]$ . The values of contact angle hysteresis in Cassie–Baxter regimes for various surfaces were calculated using (20.20). The values are summarized in Table 20.10.

The values of static contact angle in the Wenzel and Cassie–Baxter regimes for various surfaces were calculated using the values of  $R_f$  and  $f_{LA}$  (Table 20.10). As shown in Fig. 20.60, the experimental static contact angle values for the three structured surfaces were larger than the calculated values in Cassie–Baxter regime. The results suggest that the droplets on three structured surfaces were in the Cassie–Baxter regime. This indicates that the microstructure and nanostructure surface induce air pocket formation. For the contact angle hysteresis, there is a good agreement between the experimental data and the theoretically predicted values for the Cassie–Baxter regime. These results show that air pocket formation in the micro- and nanostructure decreases the solid–liquid contact [44]. In hierarchical structured surfaces, the air pocket formation further decreases the solid–liquid contact and thereby reduces contact angle hysteresis and tilt angle [72, 74].



### 20.5.5.3 The Influence of Hierarchical Structure with Wax Tubules on the Superhydrophobicity

#### Morphological Characterization, Wettability and Adhesion Forces of *T. Majus* Tubules

Figure 20.61a shows the SEM micrographs of the nanostructure and hierarchical structure fabricated with two different masses ( $0.6$  and  $0.8 \mu\text{g}/\text{mm}^2$ ) of *T. majus* [73]. SEM micrographs show an increase in the tubule amount on flat and microstructure surfaces after deposition of higher masses of wax. The tubules of *T. majus* wax grown in an ethanol atmosphere are comparable to the wax morphology found on the leaves of *T. majus*. Surfaces show a homogenous distribution of the wax mass on the specimen surfaces, and tubules provide the desired nanostructure of three-dimensional tubules on flat and microstructure surfaces. The tubule morphology of *T. majus* wax is shown in detail in Fig. 20.61b. The tubular crystals are

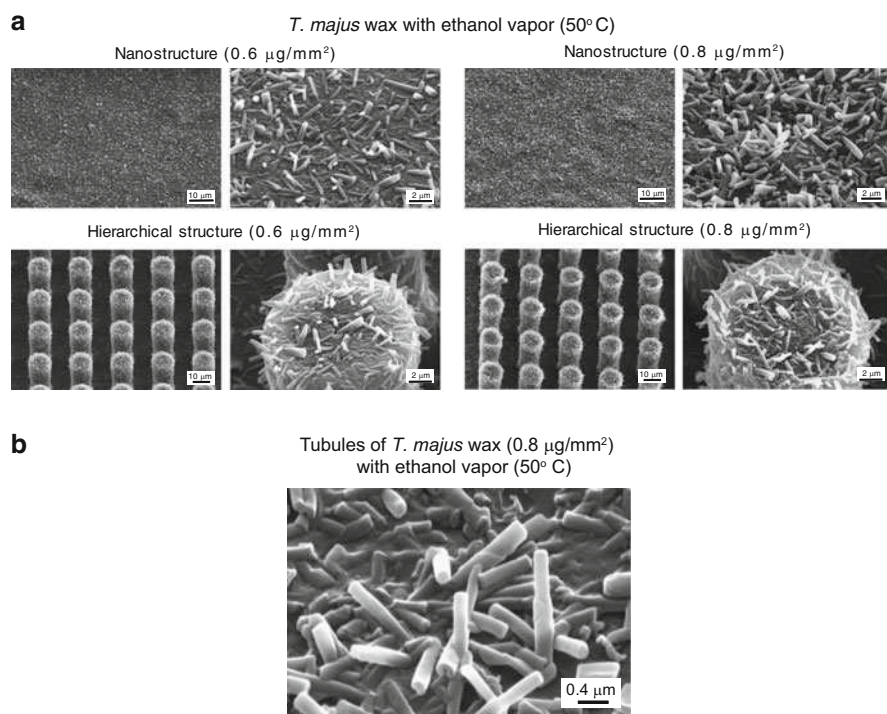


**Fig. 20.61** SEM micrographs taken at  $45^\circ$  tilt angle (shown using two magnifications) of (a) the nanostructure and hierarchical structure fabricated with two different mass ( $0.6$  and  $0.8 \mu\text{g}/\text{mm}^2$ ) of *T. majus* wax after storage at  $50^\circ\text{C}$  with ethanol vapor and (b) three-dimensional tubules forming nanostructures on the surface fabricated with  $0.8 \mu\text{g}/\text{mm}^2$  mass of *T. majus* wax after storage at  $50^\circ\text{C}$  with ethanol vapor [73]



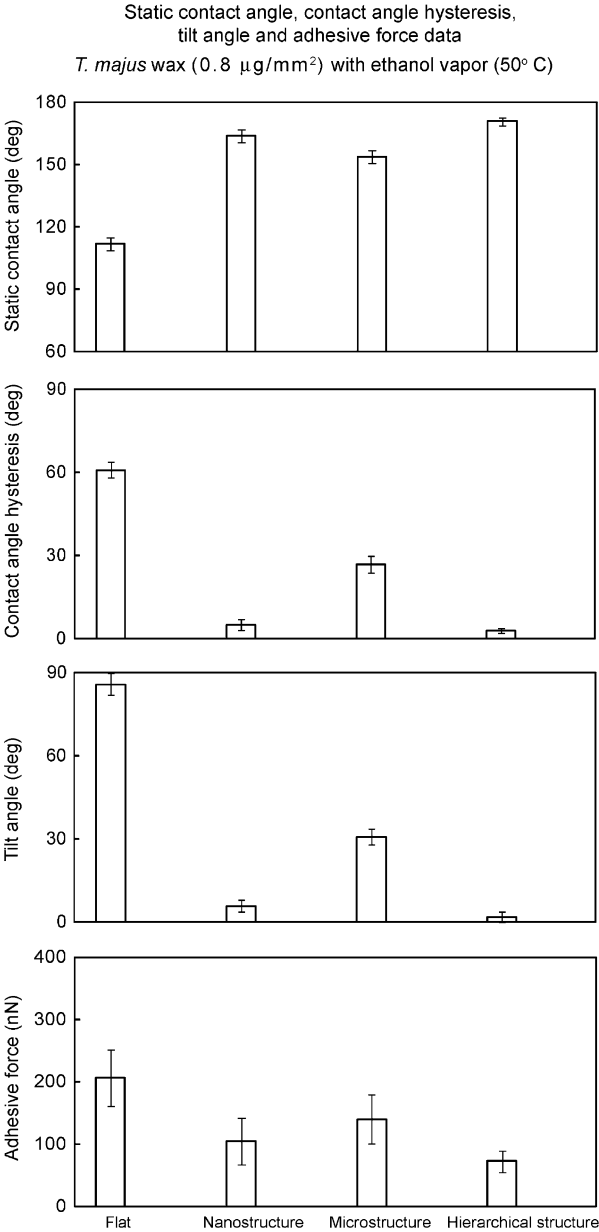
hollow structures, randomly orientated on the surface and embedded into an amorphous wax layer. They are randomly distributed on the surface, and their shapes and sizes show some variations. As shown in Fig. 20.61b, and based on additional specimens, the tubular diameter varied between 100 and 300 nm, and their length varied between 300 and 1,200 nm.

Atomic force microscopy (AFM) was used to characterize the nanostructure fabricated using *T. majus* wax of  $0.8 \mu\text{g}/\text{mm}^2$  after storage at  $50^\circ\text{C}$  with ethanol vapor [73]. Statistical parameters of the nanostructure (root mean square (RMS) height, peak to valley height, and summit density ( $\eta$ )) were calculated and are presented in Table 20.9 [24, 25]. A summit is defined as a point whose height is greater than of its four nearest neighboring points above a threshold value of 10% of RMS height to avoid measurement errors. The measurement results were reproducible within  $\pm 5\%$ .

To study the effect of structures with various length scales on superhydrophobicity, static contact angle, contact angle hysteresis and tilt angle, and adhesive forces of four structures produced using *T. majus* wax were measured [73]. Nanostructures formed on flat and microstructured surfaces were fabricated using *T. majus* wax of  $0.8 \mu\text{g}/\text{mm}^2$  after storage at  $50^\circ\text{C}$  with ethanol vapor. The data are shown in Fig. 20.62. The static contact angle of a flat surface coated with a film of *T. majus* wax was  $112^\circ$ , and increased to  $164^\circ$  when *T. majus* wax formed a nanostructure of tubules on it. On the flat specimen with a microstructure on it, the static contact angle was  $154^\circ$ , but increased to  $171^\circ$  for the hierarchical surface structure. Contact angle hysteresis and tilt angle for flat, micro- and nanostructured surfaces show similar trends. Flat surface showed a contact angle hysteresis of  $61^\circ$  and a tilt angle of  $86^\circ$ . The microstructured surface shows a reduction of contact angle hysteresis and tilt angle, but a water droplet still needs a tilt angle of  $31^\circ$  before sliding. As tubules are formed on the flat and microstructured surfaces, the nanostructured and hierarchical structure surfaces have low contact angle hysteresis of  $5^\circ$  and  $3^\circ$ , respectively. These properties are superior to plant leaves, including Lotus leaves. Adhesive force measured using a  $15 \mu\text{m}$  radius borosilicate tip in an AFM also show a similar trend as the wetting properties. Adhesion force of the hierarchical surface structure was lower than that of micro- and nanostructured surfaces because the contact between the tip and surface was lower as a result of contact area being reduced [24, 25].

To further verify the effect of hierarchical structure on the propensity of air pocket formation, Bhushan et al. [73] performed evaporation experiments with a droplet on microstructure and hierarchical structure fabricated with  $0.8 \mu\text{g}/\text{mm}^2$  mass of *T. majus* wax with ethanol vapor at  $50^\circ\text{C}$ . Figure 20.63 shows the successive photos of a droplet evaporating on two structured surfaces. On the microstructured surface, the light passes below the droplet and air pockets can be seen, so to start with the droplet is in the Cassie–Baxter regime. When the radius of the droplet decreased to  $425 \mu\text{m}$ , the air pockets are not visible anymore, and the droplet is in the Wenzel regime. This transition results from an impalement of the droplet in the patterned surface, characterized by a smaller contact angle. For the hierarchical structure, an air pocket was clearly visible at the bottom area of the droplet

**Fig. 20.62** Bar chart showing the measured static contact angle, contact angle hysteresis and tilt angle on various structures fabricated with 0.8  $\mu\text{m}/\text{mm}^2$  mass of *T. majus* wax after storage at 50°C with ethanol vapor. The bar chart also shows adhesive forces for various structures, measured using a 15  $\mu\text{m}$  radius borosilicate tip [73]



throughout, and the droplet was in a hydrophobic state until the droplet evaporated completely. It suggests that a hierarchical structure with nanostructures prevents liquid from filling the gaps between the pillars.

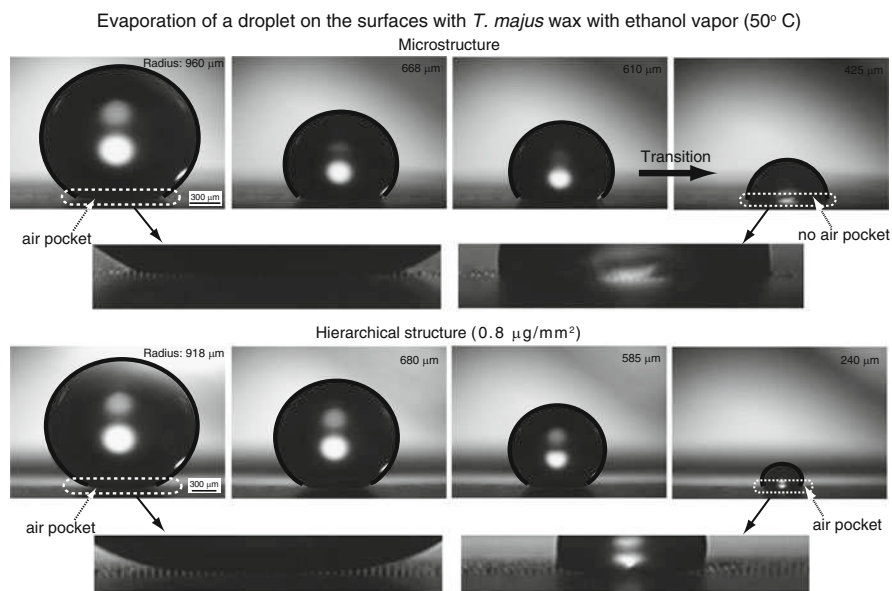


**Fig. 20.63** Evaporation of a droplet on a microstructured- and hierarchical structured surfaces fabricated with 0.8  $\mu\text{g}/\text{mm}^2$  mass of *T. majus* wax after storage at 50°C with ethanol vapor. The initial radius of the droplet was about 950  $\mu\text{m}$ , and the time interval between first two photos was 180 s and between the latter was 60 s. As the radius of droplet reached 425  $\mu\text{m}$  (foot print = 836  $\mu\text{m}$ ) on the microstructured surface, the transition from Cassie–Baxter regime to Wenzel regime occurred, as indicated by the arrow. On the hierarchical structured surface air pockets, visible at the bottom area of the droplet, exist until the droplet evaporated completely [3].

### Morphological Characterization, Wettability and Adhesion Forces of Lotus Tubules

For the development of nanostructures by tubule formation, Lotus wax was used [44]. Figure 20.64a shows the scanning electron microscope (SEM) micrographs of flat surfaces with the tubules nanostructure. Microstructures shown in Fig. 20.64b are the Lotus leaf and micropatterned Si replica covered with a Lotus wax film. Hierarchical structures were fabricated with microstructured Lotus leaf replicas and micropatterned Si replicas covered with a nanostructure of Lotus wax tubules, as shown in Fig. 20.64c. SEM micrographs show an overview (left column), a detail in higher magnification (middle column), and a large magnification of the created flat wax layers and tubules nanostructures (right column). The grown tubules provide the desired nanostructure on flat and microstructured surfaces. The recrystallized Lotus wax shows tubular hollow structures, with random orientation on the surfaces. Their shapes and sizes show only a few variations. The tubular diameter varied between 100 and 150 nm, and their length varied between 1,500 and 2,000 nm. Atomic force microscopy (AFM) was used to characterize the nanostructure of the Lotus wax tubules. The statistical parameters of the nanostructure

Lotus wax ( $0.8 \mu\text{g}/\text{mm}^2$ ) after seven days with ethanol vapor ( $50^\circ\text{C}$ )

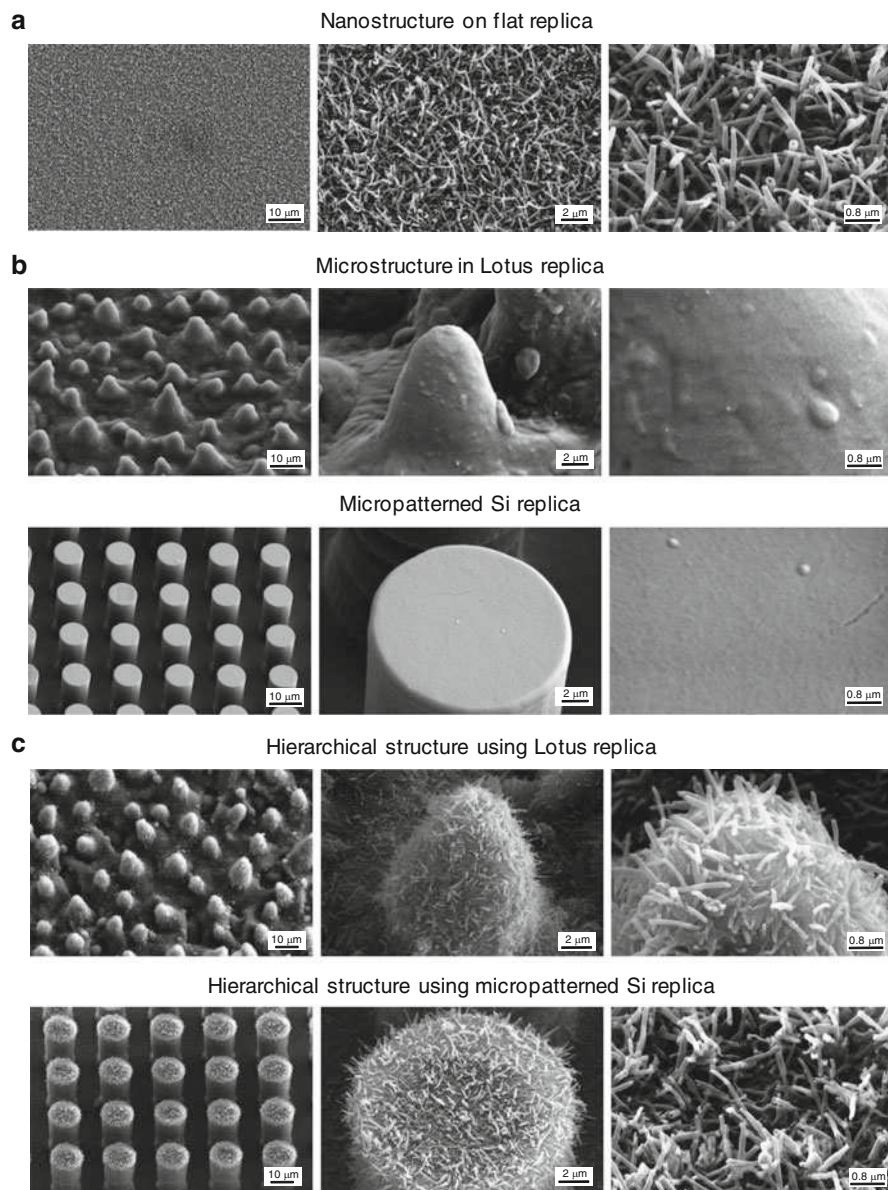


**Fig. 20.64** SEM micrographs taken at  $45^\circ$  tilt angle (shown using three magnifications) of (a) nanostructure on flat replica, (b) microstructures in Lotus replica and micropatterned Si replica, and (c) hierarchical structure using Lotus and micropatterned Si replicas. Nano- and hierarchical structures were fabricated with mass  $0.8 \mu\text{g}/\text{mm}^2$  of Lotus wax after storage for 7 days at  $50^\circ\text{C}$  with ethanol vapor. Flat epoxy resin and microstructure were covered with flat Lotus wax [44]

(root mean square (RMS) height, peak to valley height, and summit density ( $\eta$ )) were calculated and are presented in Table 20.9.

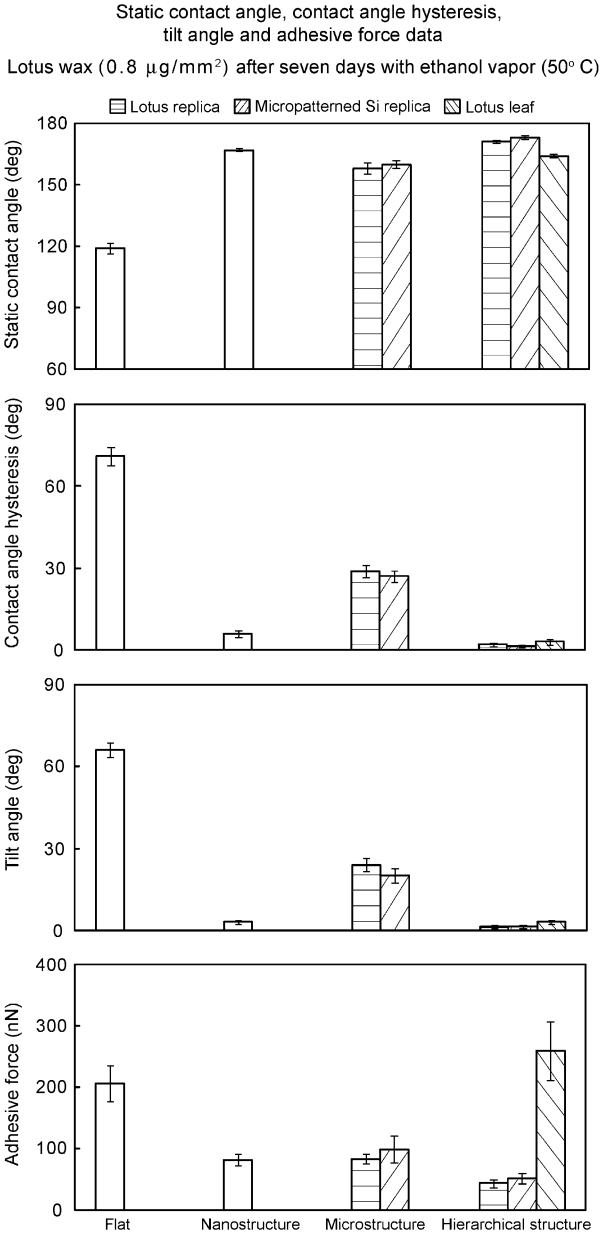
To study the effect of Lotus wax tubule nanostructures on superhydrophobicity, static contact angle, contact angle hysteresis, and tilting angle were measured on flat, microstructured Lotus replica, micropatterned Si replica, and hierarchical surfaces. Hierarchical surfaces were made of the Lotus leaf replica and micropatterned Si replica with a nanostructure of wax tubules on top. Additionally, fresh Lotus leaves were investigated to compare the properties of the fabricated structures with the original biological model.

Figure 20.65 shows that the highest static contact angles of  $173^\circ$ , lowest contact angle hysteresis of  $1^\circ$ , and tilting angle varying between  $1$  and  $2^\circ$  were found for the hierarchical structured Si replica. The hierarchical structured Lotus leaf replica showed a static contact angle of  $171^\circ$ , and the same contact angle hysteresis ( $2^\circ$ ) and tilt angles of  $1$ – $2^\circ$  as the hierarchical Si replica. Both artificial hierarchical structured surfaces show similar values as the fresh Lotus leaf surface investigated here with static contact angle of  $164^\circ$ , contact angle hysteresis of  $3^\circ$ , and a tilting angle of  $3^\circ$ . However, the artificial hierarchical surfaces showed higher static contact angle and lower contact angle hysteresis. Structural differences between the original Lotus leaf and the artificial Lotus leaf produced here are limited to a difference in wax tubules length, which are  $0.5$ – $1\text{ }\mu\text{m}$  longer in the artificial Lotus leaf [44].

The melting of the wax led to a flat surface with a flat wax film with a much lower static contact angle ( $119^\circ$ ), a higher contact angle hysteresis ( $71^\circ$ ), and a high tilting angle of  $66^\circ$ . The data of a flat Lotus wax film on a flat replica show that the Lotus wax by itself is hydrophobic. However, it has been stated that the wax on the Lotus leaf surface, by itself, is weakly hydrophilic [231]. We cannot confirm this. The data presented here demonstrate that the native, flat wax of Lotus leaves, with a static contact angle of  $119^\circ$ , is hydrophobic and can turn superhydrophobic ( $167^\circ$ ) by increasing the surface roughness after self assembly into three-dimensional wax tubules. The static contact angle of the Lotus wax film is  $119^\circ$ , which is higher than that of the wax film made of *T. majus* of  $112^\circ$ . However, films made of *n*-hexatriacontane showed static contact angles of only  $91^\circ$ . SEM investigations, made directly after contact angle measurements, revealed no morphological differences between these films. Based on the chemical composition, it should be assumed that the non-polar *n*-hexatriacontane molecules are more hydrophobic than the plant waxes, which contain high amounts of oxygen atoms. At this point these differences cannot be explained by structural or chemical differences of the films, but will be the interest for further studies.

Adhesive force measured using a  $15\text{ }\mu\text{m}$  radius borosilicate tip in an AFM also shows a similar trend as the wetting properties for the artificial surfaces (Fig. 20.65) [44]. Adhesion force of the hierarchical surface structure was lower than that of micro- and nanostructured and flat surfaces because the contact between the tip and surface was lower as a result of the contact area being reduced. However, for the fresh Lotus leaf, there is moisture within the plant material, which causes softening

**Fig. 20.65** Bar chart showing the measured static contact angle, contact angle hysteresis and tilt angle on various structures fabricated with 0.8  $\mu\text{g}/\text{mm}^2$  of Lotus wax after storage for 7 days at 50°C with ethanol vapor. The bar chart also shows adhesive forces for various structures, measured using a 15  $\mu\text{m}$  radius borosilicate tip. The error bar represents  $\pm 1$  standard deviation [44]



of the leaf, and so when the tip comes into contact with the leaf sample, the sample deforms, and a larger area of contact between the tip and sample causes an increase in the adhesive force [24, 25].

#### 20.5.5.4 Self-cleaning Efficiency of Hierarchical Structured Surfaces

For deposition of contamination on artificial surfaces, various structures were placed in a contamination glass chamber [34]. Silicon carbide (SiC) (Guilleaume, Germany) particles in two different sizes ranges of 1–10  $\mu\text{m}$  and 10–15  $\mu\text{m}$  were used as the contaminants. The SiC particles have been chosen because of their similarity in shape, sizes, and hydrophilicity to natural dirt contaminations. The number of particles per area was determined by counting them from a 280  $\mu\text{m}$   $\times$  210  $\mu\text{m}$  image taken by an optical microscope with a camera before and after water cleaning.

For the cleaning test, the specimens with the contaminants were subjected to water droplets of approximately 2 mm diameter, using two microsyringes [34]. In order to obtain a relative measure of the self-cleaning ability of hierarchical structures which exhibit the lowest contact angle hysteresis and tilt angle as compared to other structures (flat, nanostructures, and microstructures), the tilt angle chosen for the cleaning tests was slightly above the tilt angle for the hierarchical structures. Thus experiments were performed with 10° for surfaces covered with *n*-hexatriacontane and 3° for surfaces with Lotus wax. The water cleaning test was carried out for 2 min (water quantity, 10 mL) with nearly zero kinetic energy of droplets. For watering with nearly zero kinetic energy, the distance between the microsyringes and surface was set to 0.005 m (nearly zero impact velocity). The chosen impact velocity represents a low value compared to a natural rain shower, where a water droplet of 2 mm diameter can reach an impact velocity of 6 m/s (measured under controlled conditions) [232].

Figure 20.66 shows that none of the investigated surfaces was fully cleaned by water rinsing [34]. The data represent the average of five different investigated areas for each experiment. For Lotus wax, which forms tubule nanostructures, and *n*-hexatriacontane, which forms platelet nanostructures, the same tendency of particle removal was found. With the exception of hierarchical structure on all surfaces, larger particles were removed more than small ones. Most particles (70–80%) remained on smooth surfaces, and 50–70% of particles were found on microstructured surfaces. Most particles were removed from the hierarchical structured surfaces, but approximately 30% of particles remained. A clear difference in particle removal, independent of particle sizes, was only found in flat and nanostructured surfaces where larger particles were removed with higher efficiency. Observations of the droplet behavior during the movement on the surfaces showed that droplets were rolling only on the hierarchical structured surfaces. On flat, micro- and nanostructured surfaces, the droplets first applied were not moving, but the continuous application of water droplets increased the droplet volumes and led to a sliding of these large droplets. During this, some of the particles had been removed from the surfaces. However, the rolling droplets on hierarchical structures did not collect the dirt particles trapped in the cavities of the microstructures. The data clearly shows that hierarchical structures have superior cleaning efficiency.



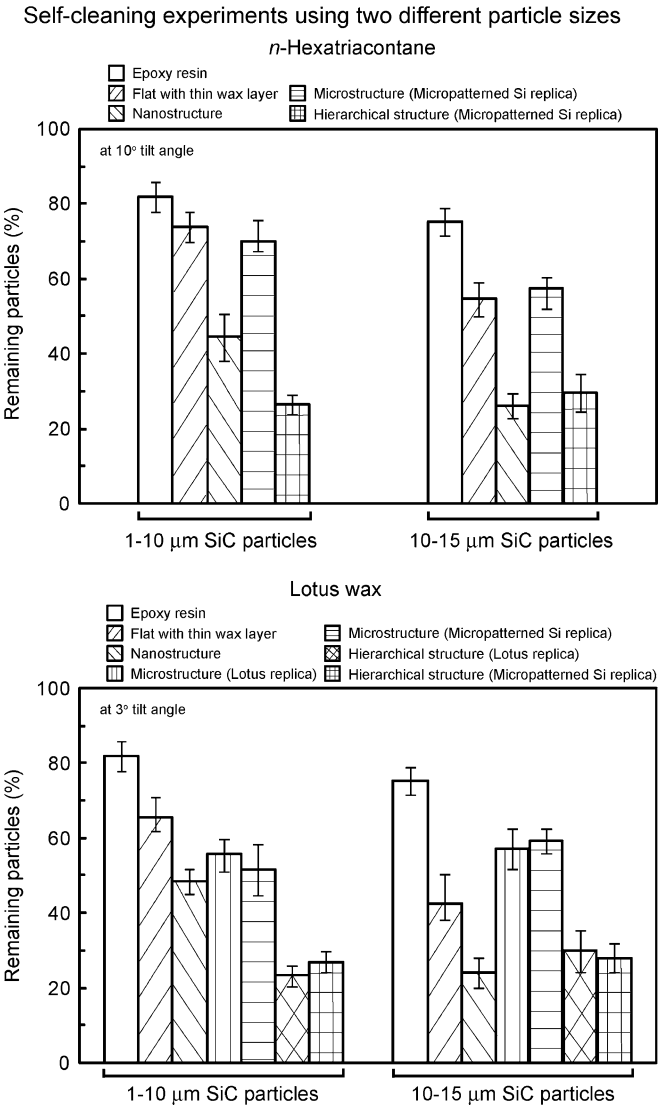


**Fig. 20.66** Bar charts showing the remaining particles after applying droplets with nearly zero kinetic energy on various structures fabricated using *n*-hexatriacontane and Lotus wax using 1–10 μm and 10–15 μm SiC particles. The experiments on the surfaces with *n*-hexatriacontane and Lotus wax were carried out on tilted stages with 10° and 3°, respectively. The error bars represent ±1 standard deviation [34]

**20.5.5.5 Observation of Transition During the Bouncing Droplet**

To observe how the impact velocity influences the transition from the composite solid–air–liquid interface to the homogeneous solid–liquid interface during droplet

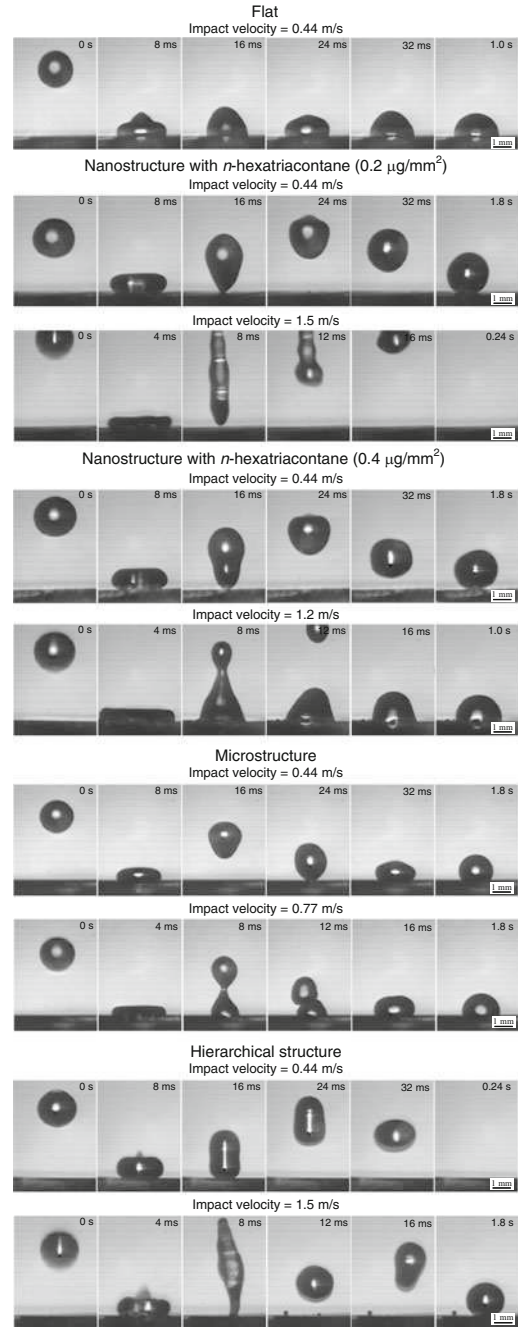


impact, Jung and Bhushan [78] performed bouncing droplet experiments on various surfaces with *n*-hexatriacontane and *T. majus* and Lotus waxes. Figure 20.67 shows snapshots of a droplet with 1 mm radius hitting various surfaces fabricated with 0.2 and 0.4  $\mu\text{g}/\text{mm}^2$  of *n*-hexatriacontane after storage at room temperature. The impact velocity was obtained just prior to the droplet hitting the surface. First, on the flat surface, it was found that the droplet did not bounce off even though the impact velocity applied was up to 1.5 m/s. As shown in the images in the first row for each nano-, micro- and hierarchical structured surface, the droplet hitting the surface under an impact velocity of 0.44 m/s first deformed and then retracted, and bounced off the surface. Finally, the droplet sat on the surface and had a high contact angle, which suggests the formation of a solid–air–liquid interface. Next, we repeated the impact experiment by increasing the impact velocity. As shown in the second row of images for nanostructure (0.4  $\mu\text{g}/\text{mm}^2$ ) and microstructure, bounce off did not occur, and the wetting of the surface (and possibly pinning of droplet) occurred at impact velocities of 1.2 m/s and 0.77 m/s, respectively, referred to as the critical impact velocity. This is because air pockets do not exist below the droplet as a result of droplet impalement by the structures, characterized by a smaller contact angle. These observations indicate the transition from the composite interface to the homogenous interface. However, as shown in the second row of images for nanostructure (0.2  $\mu\text{g}/\text{mm}^2$ ) and hierarchical structure, during applying impact velocity of up to 1.5 m/s, the bounce off always occurred and the wetting of the surface did not occur.

As shown in Fig. 20.68, the critical impact velocity of a droplet with 1 mm radius on various structures at which wetting of the surface (possibly pinning of droplet) occurs was measured [78]. The arrow indicates that the critical impact velocity can possibly be more than 1.5 m/s, or the transition has not occurred. As mentioned earlier, when the mass of *n*-hexatriacontane increased, the static contact angle of nanostructure first increased followed by a decrease at a mass of 0.2  $\mu\text{g}/\text{mm}^2$ . For the critical impact velocity, the same trends were found. It is believed that if neighboring crystals are separated on a sample with lower crystal density, any trapped air can be squeezed out whereas if the neighboring crystals are interconnected on a sample with higher density, air remains trapped. At highest crystal density at a mass of 0.4  $\mu\text{g}/\text{mm}^2$ , there is less open volume compared to that at 0.2  $\mu\text{g}/\text{mm}^2$ . For all microstructures with *n*-hexatriacontane and Lotus wax, the critical impact velocities of the droplet are lower than those on nano- and hierarchical structures due to the larger distance between the pillars, and the solid–air–liquid interface can easily be destabilized from dynamic impact on the surface. Based on (20.29), the critical impact velocity of the droplet decreases with the geometric parameter (pitch). The theoretical critical impact velocity for microstructure using (20.29) is 0.5 m/s. This value is lower than the experimental values of critical impact velocity for microstructures by about 30 ~ 50% depending on the structured surfaces. In our experiments, during applying impact velocity of up to 1.5 m/s on nano- and hierarchical structures with *n*-hexatriacontane (0.2  $\mu\text{g}/\text{mm}^2$  for nanostructure) and Lotus wax, the wetting of the surface did not occur. The data clearly shows that nano- and hierarchical

**Fig. 20.67** Snapshots of a droplet with 1 mm radius hitting various surfaces fabricated with 0.2 and 0.4  $\mu\text{g}/\text{mm}^2$  of *n*-hexatriacontane after storage at room temperature. The impact velocity was obtained just prior to the droplet hitting the surface. The pinning of droplet on the nanostructure with 0.4  $\mu\text{g}/\text{mm}^2$  mass, and on the microstructure occurred at impact velocities of 1.2 m/s and 0.77 m/s, respectively [78]

Dynamic effects of a droplet on various surfaces with *n*-hexatriacontane



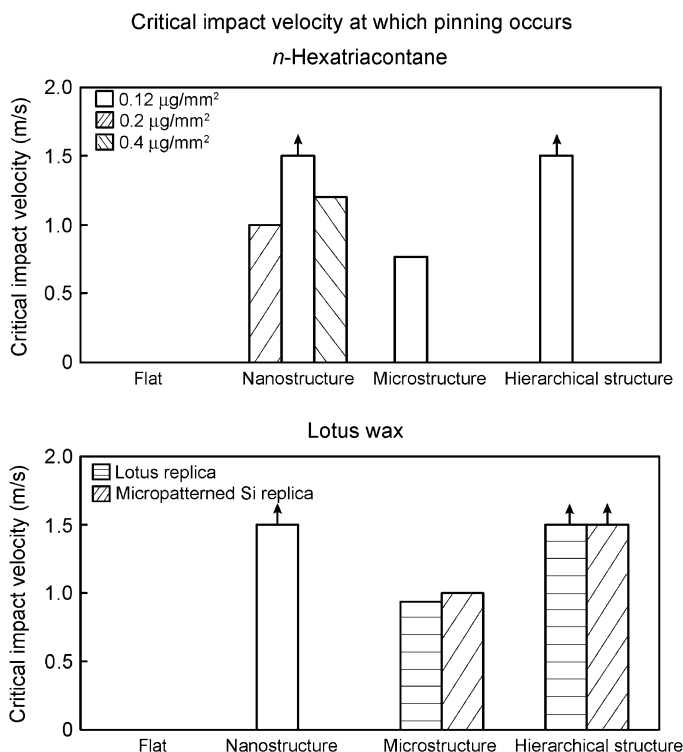


**Fig. 20.68** Bar chart showing the measured critical impact velocity of a droplet with 1 mm radius at which transition occurs on various structures. The *arrow* indicates that the critical impact velocity can possibly be more than 1.5 m/s or the transition is not occurred [78]

structures are superior to microstructure in maintaining stable composite solid–air–liquid interface.

To identify whether one is in a homogeneous solid–liquid interface or a composite solid–air–liquid interface, the contact angle data in the static condition and after bounce off were measured on various surfaces, as shown in Fig. 20.69 [78]. The contact angles of the left bar for each sample were measured using the droplet with 1 mm radius gently deposited on the surface. The contact angles of the middle and right bars for each sample were measured using the droplet after hitting the surface at 0.44 m/s and critical or highest impact velocity. Missing bars mean that the droplet, after hitting the surface, bounced off without coming to sit on the surface. The static contact angle of the droplet after impact at 0.44 m/s is lower than that of the droplet gently deposited for all of the surfaces with *n*-hexatriacontane and Lotus wax. It can be interpreted that after hitting, the droplet pushes out the entrapped air of the

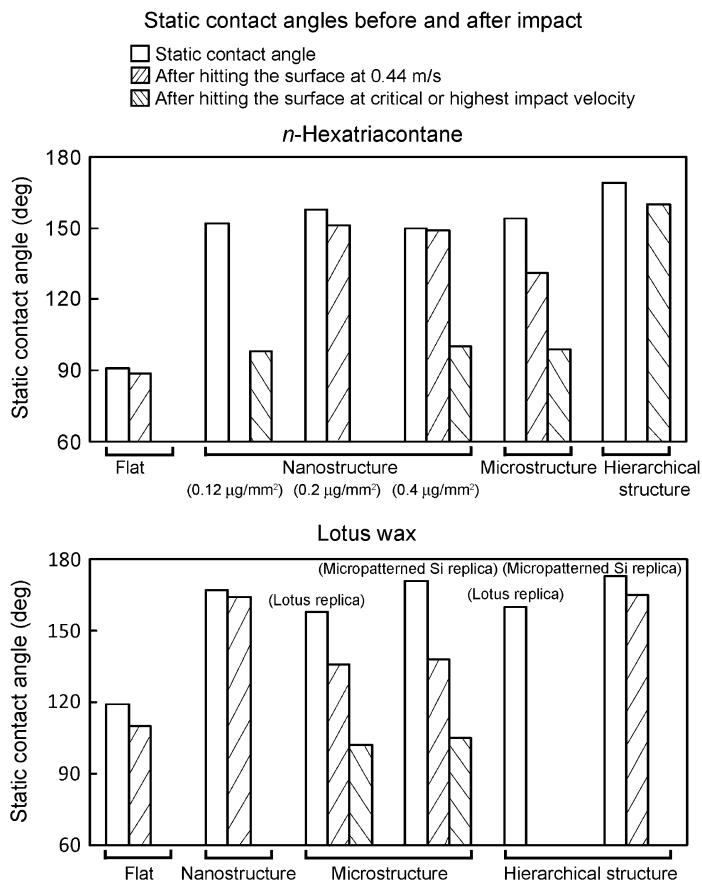


**Fig. 20.69** Bar chart showing the measured static contact angle of a droplet on various surfaces. The contact angles of the left bar for each sample were measured using a droplet with 1 mm radius gently deposited on the surface. The contact angles of the middle and right bars for each sample were measured using the droplet after hitting the surface at 0.44 m/s, and critical or highest impact velocity [78]

cavities between the pillars under the droplet, resulting in an abrupt increase of the solid–liquid surface area by dynamic impact. As mentioned earlier, after hitting the surface at a critical impact velocity, the contact angles were close to 90° and much lower than that of the droplet gently deposited for nanostructures with *n*-hexatriacontane (0.12 and 0.4 μg/mm<sup>2</sup>) and microstructures with *n*-hexatriacontane and Lotus wax. Even though the droplet is in the composite interface when it is gently deposited on the surface, these observations indicate that the composite solid–air–liquid interface was destroyed due to dynamic impact on the surface.

### 20.5.5.6 Observation of Transition During the Vibrating Droplet

#### Model for the Adhesion and Inertia Forces of the Vibrating Droplet

Jung and Bhushan [78] presented a model for vibration. In this model, they calculate expressions for adhesion force and inertia force as a function of droplet properties and operating conditions. Consider a small droplet of liquid deposited on a surface. The liquid and surface come together under equilibrium at a characteristic angle, called the static contact angle  $\theta$ , as shown in Fig. 20.70. When a droplet on a surface is vibrated, based on Lamb [233], a general expression for the resonance frequency  $f_r$  of a free oscillating liquid droplet is given as

$$f_r = \sqrt{\frac{n(n-1)(n+2)\gamma}{3\pi\rho V}} \quad (20.37)$$

where  $V$  is the volume of the droplet, and  $n$  represents the number of modes, with 2 being the 1st mode etc. For a spherical droplet with a radius  $R$  with the distance between the center of droplet and the solid  $H$ , the volume of droplet  $V$  is given by

$$\begin{aligned} V &= \frac{1}{3}\pi(R+H)^2(2R-H) \\ &= \frac{1}{3}\pi R^3(1-\cos\theta)^2(2+\cos\theta) \end{aligned} \quad (20.38)$$

Recent experimental studies were carried out by Noblin et al. [234] and Celestini and Kofman [235]. They showed that the frequency decreases with the volume of the droplet, and the trends are compared with a theoretical model.

When liquid comes in contact with a surface, the energy gained for surfaces coming into contact is greater than the energy required for their separation (or the work of adhesion) by the quantity  $\Delta W$ , which constitutes the adhesion hysteresis [38]. For a surface, the difference between the two values of the interface energy (measured during loading and unloading) is given by  $\Delta W$ . These two values

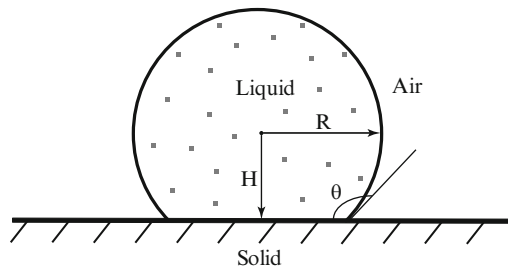


**Fig. 20.70** Droplet of liquid in contact with a solid surface – contact angle  $\theta$ ; radius of droplet  $R$ ; distance between the center of droplet and the solid  $H$  [78]

are related to the advancing contact angle,  $\theta_a$ , and receding contact angle,  $\theta_r$ , of the surface. For example, a model based on Young's equation has been used to calculate the work of adhesion from contact angle hysteresis [27, 31, 236, 237].

$$\cos \theta_a - \cos \theta_r = \frac{\Delta W}{\gamma} \quad (20.39)$$

From (20.39), the dominant force (adhesion force) responsible for the separation between the droplet and surface is given by [238, 239]

$$\begin{aligned} F_A &= L\gamma(\cos \theta_a - \cos \theta_r) \\ &= 2R \sin \theta(\gamma)(\cos \theta_a - \cos \theta_r) \end{aligned} \quad (20.40)$$

where  $L$  is the length of the triple contact line, referred to as line of contact of the solid, liquid, and air. The radius of a spherical droplet,  $R$ , depends on the contact angle and can be obtained from (20.38).

From applying vertical vibration of a droplet on a surface, the inertia force of droplet  $F_I$  is given by

$$F_I = \rho V A \omega^2 \quad (20.41)$$

where  $A$  and  $\omega$  are the amplitude and frequency of vibration, respectively. Bormeashenko et al. [154] showed that the transition occurred at a critical value of inertia force acting on the length of a triple line. However, if the inertia force of the droplet vibrated on the surface can overcome the adhesion force between the droplet and surface, which  $\Delta F$  is positive value [78],

$$\Delta F = F_I - F_A \quad (20.42)$$

the droplet can be vertically separated from the surface (bouncing off) before the composite solid–liquid–air interface is destroyed.

## Vibration Study Results

To estimate the resonance frequency of a droplet, a droplet on various surfaces was vibrated by varying the frequency with a sinusoidal excitation of relatively low amplitude (0.4 mm) [78]. Based on (20.37), the experiments were performed in the 1st and 2nd modes ( $n = 2$  and 3). Figure 20.71 shows the optical micrographs of droplets on the microstructured surface with *n*-hexatriacontane before and after vibration at an amplitude of 0.4 mm for 1st mode ( $n = 2$ ) and 2nd mode ( $n = 3$ ) of vibration. The frequencies for the 1st mode and 2nd mode were measured to be 86 Hz and 208 Hz, respectively. The resonance frequencies on various surfaces were measured, and the data are summarized in Table 20.11. For comparison, the theoretical values for the two modes were calculated using (20.37).

Vibration of a droplet on microstructured surface with *n*-hexatriacontane

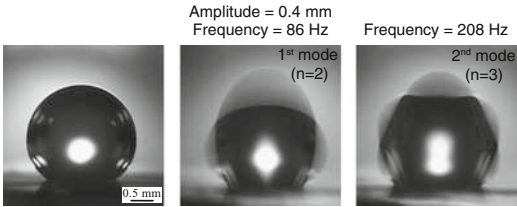


**Fig. 20.71** Optical micrographs of droplets on the microstructured surface with *n*-hexatriacontane before and after vibration at amplitude of 0.4 mm for 1st mode ( $n = 2$ ) and 2nd mode ( $n = 3$ ) of vibration. The frequencies for 1st mode and 2nd mode were measured to be 86 Hz and 208 Hz, respectively [78]

**Table 20.11** Summary of the measured resonance frequency at the fixed amplitude value of 0.4 mm, the calculated inertia force of a vibrated droplet, and adhesive force between the droplet and surface on the various surfaces fabricated with *n*-hexatriacontane and Lotus wax

	Resonance frequency (Hz)		F <sub>A</sub> (μN)	F <sub>I</sub> (μN) at transition or bouncing off	ΔF = F <sub>I</sub> − F <sub>A</sub> (μN)
	1st	2nd			
	mode (n = 2)	mode (n = 3)			
<i>n</i> -Hexatriacontane					
Flat	103	271	260 ± 3.7		
Nanostructure (0.12 μg/mm <sup>2</sup> )	63	169	45 ± 2.2	11	−34 ± 2.2 (T)
Nanostructure (0.2 μg/mm <sup>2</sup> )	50	147	10 ± 1.6	10	0 ± 1.6 (B)
Nanostructure (0.4 μg/mm <sup>2</sup> )	54	149	13 ± 2.0	11	−2 ± 2.0 (B)
Microstructure	86	208	21 ± 1.7	9	−12 ± 1.7 (T)
Hierarchical structure	49	144	0.2 ± 0.06	3.6	3.4 ± 0.06 (B)
Lotus wax					
Flat	92	243	133 ± 3.3		
Nanostructure	47	138	0.8 ± 0.08	3.2	2.4 ± 0.08 (B)
Microstructure (Lotus replica)	63	179	14 ± 1.8	11	−3 ± 1.8 (T and B)
Microstructure (Micropatterned Si replica)	66	183	10 ± 1.6	10	0 ± 1.6 (B)
Hierarchical structure (Lotus replica)	40	139	0.1 ± 0.04	3.6	3.5 ± 0.04 (B)
Hierarchical structure (Micropatterned Si replica)	38	137	0.04 ± 0.01	2.7	2.6 ± 0.01 (B)

Positive value of  $\Delta F$  means that the droplet bounced off before the transition occurs. The variation represents  $\pm 1$  standard deviation [78]

B Bouncing off

T Transition

For calculations, the surface tension of the water–air interface ( $\gamma$ ) was taken to be 0.073 N/m, the mass density ( $\rho$ ) was 1,000 kg/m<sup>3</sup> for water, and the volume of droplet ( $V$ ) was 5  $\mu\text{L}$ . The theoretical values for 1st mode ( $n = 2$ ) and 2nd mode ( $n = 3$ ) from (20.37) are 110 and 214 Hz, respectively. These values are similar to

those of flat surfaces with *n*-hexatriacontane and Lotus wax. However, with the same volume, the resonance frequencies of the structured surfaces are lower than those of flat surfaces. Celestini and Kofman [235] showed that the resonance frequency depends on the contact angle of the structured surfaces, and it decreases with increasing contact angle. The hierarchical structures with highest contact angle have the lowest resonance frequency, consistent with the results by Celestini and Kofman [235].

To observe how the vibration of the droplet influences the transition from the composite solid–air–liquid interface to the homogeneous solid–liquid interface, Jung and Bhushan [78] performed vibrating droplet experiments on various surfaces with *n*-hexatriacontane and Lotus wax. Figure 20.72 shows optical micrographs of droplets on various surfaces with *n*-hexatriacontane before and after vibrating at a frequency of 30 Hz, which is less than the resonance frequency for 1st mode ( $n = 2$ ). The vibration amplitude was increased until transition or until the droplet bounced off. First, on the flat surface, it was found that the droplet did not change much after applying vibration at amplitudes ranging from 0 to 3 mm. As shown in the images for nanostructure ( $0.12 \mu\text{g}/\text{mm}^2$ ) and microstructure, the static contact angles of the droplet before vibrating were  $152^\circ$  and  $154^\circ$ , respectively. After vibrating at amplitudes of 0.4 and 1.4 mm, the contact angles still have similar values ( $151^\circ$  for nanostructure and  $149^\circ$  for microstructure), which suggests the formation of a solid–air–liquid interface. However, after vibrating at amplitudes of 2.4 mm for nanostructure ( $0.12 \mu\text{g}/\text{mm}^2$ ) and 2.0 mm for microstructures, the static contact angles became  $125^\circ$  and  $121^\circ$ , respectively. This is because air pockets do not exist below the droplet as a result of droplet impalement by the structures, characterized by a smaller contact angle. These observations indicate the transition from the composite interface to the homogenous interface. Observations of vibration on two nanostructures ( $0.2$  and  $0.4 \mu\text{g}/\text{mm}^2$ ) and a hierarchical structure showed that the transition did not occur, but the droplet started to bounce off the surface from amplitudes of 2.2, 2.4, and 0.8 mm, respectively.

To study the validity of the proposed model (20.42), the adhesive force responsible for the separation between the droplet and surface and the inertia force of a droplet vibrated on various structures were calculated [78]. The adhesive force was obtained from (20.40) using static contact angle and contact angle hysteresis. The inertia forces were obtained from (20.41) using the amplitude and frequency of vibration as the transition or droplet bounce off occurred. The data are presented in Fig. 20.73 and summarized in Table 20.11. As shown in Fig. 20.72, it was observed that the transition occurred as a result of droplet impalement by the structures by increasing the inertia force of droplet on the surfaces. However, if the inertia force of the droplet vibrated on the surface can overcome the adhesion force between the droplet and surface ( $\Delta F$  is positive), the droplet can be vertically separated from the surface (bouncing off) before the composite solid–liquid–air interface is destroyed. The experimental results for bouncing off of the droplet appear to have the same trend as the proposed model (20.42). It is shown that hierarchical structures have the positive value of the difference between the inertia force and adhesive force for droplet bounce



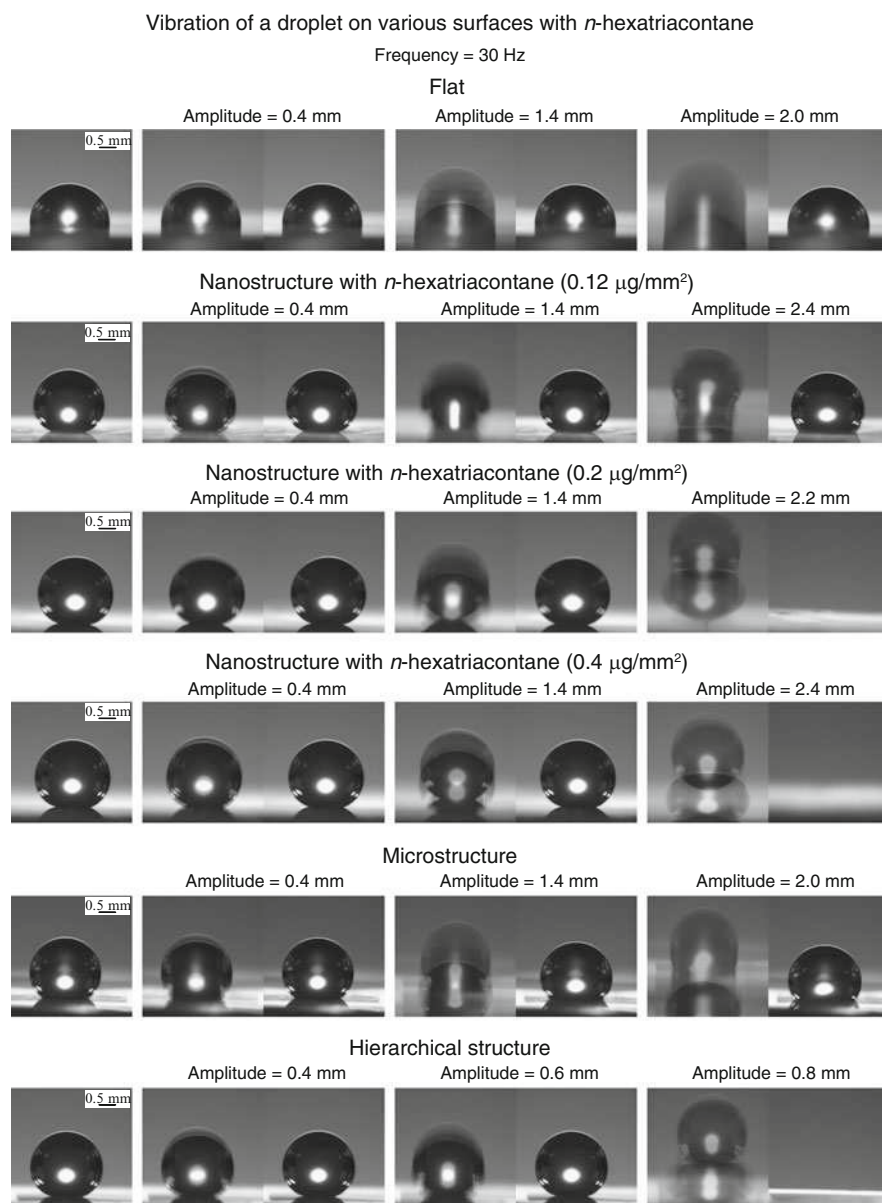


**Fig. 20.72** Optical micrographs of droplets on various surfaces with *n*-hexatriacontane before and after vibrating at frequency of 30 Hz. The transition of a droplet on the nanostructure with  $0.12 \mu\text{g}/\text{mm}^2$  mass of *n*-hexatriacontane and on the microstructure occurred at amplitudes of 2.4 mm and 2.0 mm, respectively [78]

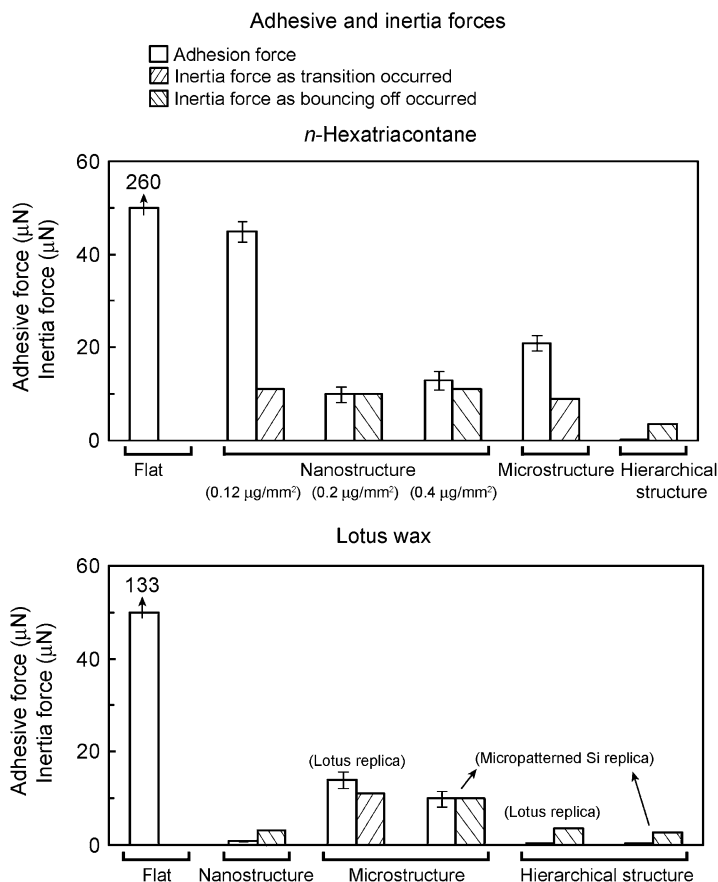


**Fig. 20.73** Bar chart showing the calculated adhesive force responsible for the separation between the droplet and surface and inertia force of a droplet vibrated on various structures. The inertia forces were obtained as the transition or droplet bounce off occurred. If the inertia force of the droplet vibrated on the surface can overcome the adhesion force between the droplet and surface ( $\Delta F$  is positive), the droplet can be vertically separated from the surface (bouncing off) before the composite solid–liquid–air interface is destroyed [78]

off responsible for superior resistance to the dynamic effects and maintain stable composite solid–air–liquid interface.

### 20.5.6 Mechanically Durable CNT-Composite Hierarchical Structured Surfaces

To create nano- and hierarchical structures with a high mechanical strength, multi-walled CNT were fabricated using catalyst-assisted chemical vapor deposition (CCVD) (Sun Nanotech Co Ltd, China). Iron catalyst was used to initiate growth

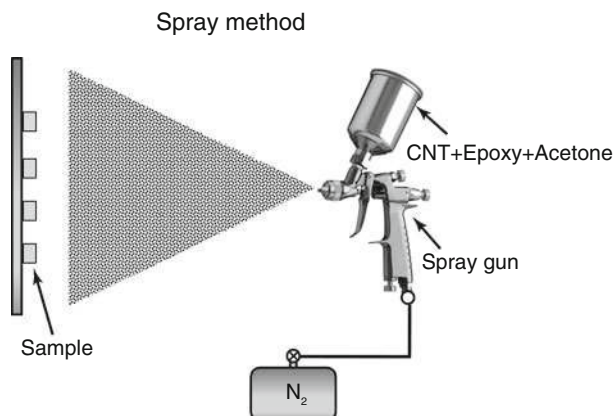


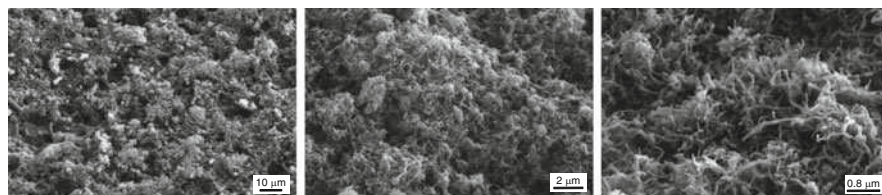
**Fig. 20.74** Schematic of spray method to deposit a mixture of CNT, epoxy, and acetone on surfaces [100]

of nanotubes using natural gas as carbon source and Ar/H<sub>2</sub> as buffer gas at 750°C. The contact angle of individual carbon nanotubes has been reported as 60° and higher. The multi-walled CNT composites were deposited on flat epoxy resin and microstructure using a spray method as shown in Fig. 20.74 [100]. Microstructures were fabricated using a microstructured Si surface with pillars of 14 μm diameter and 30 μm height with 23 μm pitch by soft lithography [3, 100]. The first step of deposition of CNT composite using the spray method was to disperse the CNT into a solvent in order to maintain a uniform distribution. Acetone was used as a solvent because it does not affect surface modification and is easily vaporized in ambient conditions. The dispersion process consisted of the sonification of 200 mg CNT in 100 mL of acetone for 4 min using a Branson Digital Sonifier with a frequency of 20 kHz at amplitude of 80%. During this process, the mixture was exposed to ultrasonic pressure waves in a sonifier in order to disperse the CNT into smaller aggregates. To provide strong bonding between CNT and the substrate, 200 mg EPON epoxy resin 1,002 F was added to the mixture of CNT and acetone, and then the mixture was sonicated for 4 more minutes. Next, the sonified mixture was poured into a spray gun and sprayed onto the specimen surfaces. The conditions for uniform deposition of the CNT on the surfaces were optimized by adjusting the concentration of CNT in the solvent. After spraying the CNT on the surfaces, the CNT composite structures were then annealed at 120°C for 3 h in order to improve the mechanical properties. This temperature, above the melting point (80 ~ 88°C) and below the burning point (180°C) of EPON epoxy resin 1,002 F, was selected to increase strong bonding between CNT and substrates. At this temperature, the epoxy which initially covered the CNT was melted and moved to the interface between the CNT and substrates, resulting in exposed CNTs which lead to high contact angle.

Figure 20.75 shows the SEM micrographs of nano- and hierarchical structures fabricated with CNT [100]. SEM micrographs show an overview (left column), a

## Carbon nanotubes (CNT) composite after three hours (120° C)

## Nanostructure with CNT



## Hierarchical structure with CNT

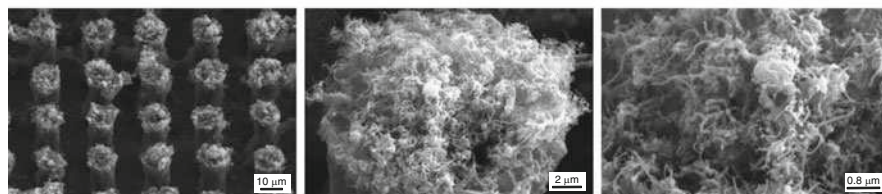


**Fig. 20.75** SEM micrographs taken at 45° tilt angle, show three magnifications of nano- and hierarchical structures fabricated with CNT after 3 h at 120°C [100]

detail in higher magnification (middle column), and a large magnification of the nanostructures with CNT (right column). All surfaces show a homogenous distribution of CNT on the specimen. The CNT were well dispersed and embedded on flat and microstructured surfaces for the desired nanostructure. The CNT diameter varied between 10 and 30 nm, and an aspect ratio varied between 160 and 200.

Lotus leaves have been the inspiration for the development of superhydrophobic and self-cleaning products. Therefore, as a benchmark for mechanical durability studies, Jung and Bhushan [100] used nano-, micro-, and hierarchical structures created by the self-assembly of Lotus wax with the amounts of 0.8  $\mu\text{g}/\text{mm}^2$  deposited on flat epoxy resin and microstructure by thermal evaporation as shown in Fig. 20.64.

### 20.5.6.1 The Influence of CNT-Composite Hierarchical Structure on the Superhydrophobicity

To study the effect of CNT composite structures for superhydrophobicity, Jung and Bhushan [100] measured the static contact angle and contact angle hysteresis on nano- and hierarchical structures with CNT. For static contact angle and contact angle hysteresis, droplets of about 5  $\mu\text{L}$  in volume (with the diameter of a spherical droplet about 2.1 mm) were gently deposited on the surface using a microsyringe. For contact angle hysteresis, the advancing and receding contact angles were measured at the front and back of the droplet moving along the tilted surface, respectively. Figure 20.76a shows that superhydrophobicity with a static contact

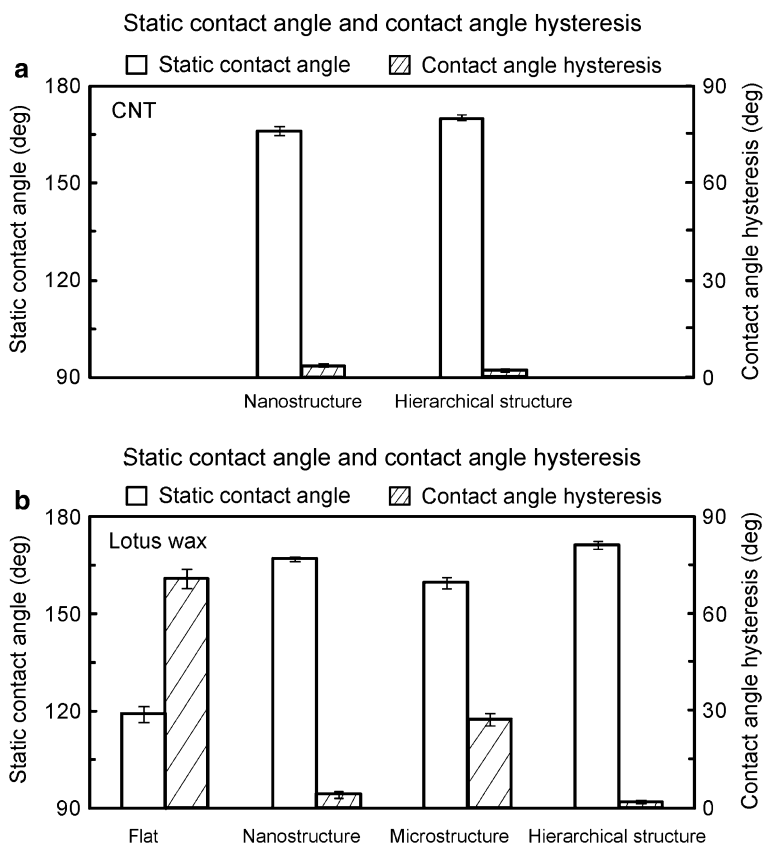


**Fig. 20.76** Bar chart showing the measured static contact angle and contact angle hysteresis on (a) nano- and hierarchical structures fabricated with CNT after 3 h at 120°C, and (b) various structures fabricated with 0.8  $\mu\text{g}/\text{mm}^2$  of Lotus wax after storage for 7 days at 50°C with ethanol vapor. The error bar represents  $\pm 1$  standard deviation [100]

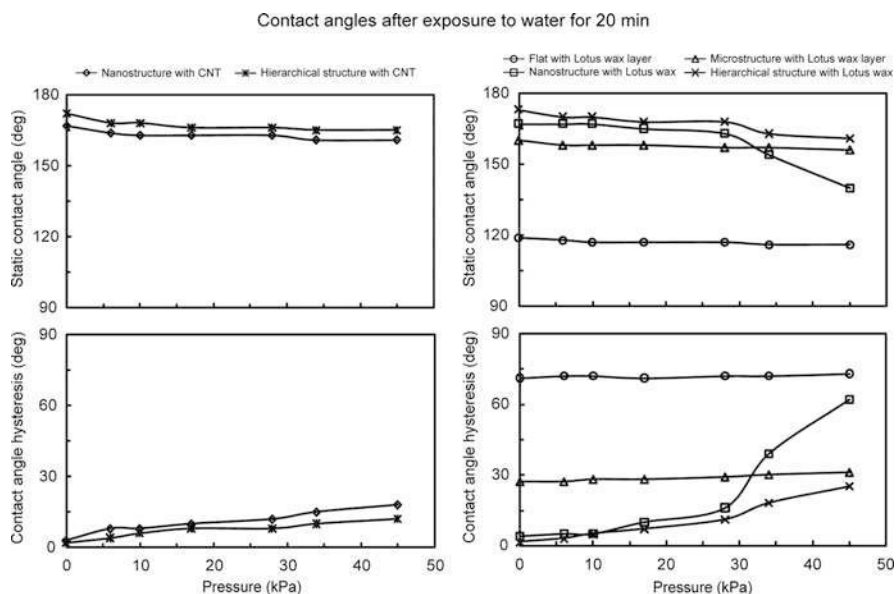
angle of 166° and a contact angle hysteresis of 4° was found in the nanostructured surface with CNT. After introducing CNT nanostructure on top of the micropatterned Si replica, the higher static contact angle of 170° and lower contact angle hysteresis of 2° were found for the hierarchical structures with CNT. Both nano- and hierarchical structures created with CNT showed superhydrophobic and self-cleaning surface, which has a static contact angle of more than 150° and contact angle hysteresis of less than 10° [100].

Figure 20.76b shows that for the hierarchical structure with Lotus wax, the highest static contact angles of 173° and lowest contact angle hysteresis of 1° were found. The recrystallized wax tubules are very similar to those of the original Lotus leaf, but are 0.5–1  $\mu\text{m}$  longer, the static contact angle is higher, and the contact angle hysteresis is lower than reported for the original Lotus leaf (static contact angle of 164° and contact angle hysteresis of 3°) [44]. Superhydrophobicity

with a static contact angle of  $167^\circ$  and a contact angle hysteresis of  $5^\circ$  was also found in the nanostructured surface with Lotus wax. The microstructured surface with Lotus wax layer has a static contact angle of  $160^\circ$ , but shows a much higher contact angle hysteresis of  $29^\circ$  than found in hierarchical structures. Melting of the Lotus wax led to a flat surface with a flat wax film and a much lower static contact angle of  $119^\circ$  and higher contact angle hysteresis of  $71^\circ$ . The data of a flat Lotus wax film on a flat replica show that the Lotus wax by itself is hydrophobic [100].

### 20.5.6.2 Durability of Various Surfaces in Waterfall/Jet Tests

To investigate the durability of the created surfaces in long-term exposure to water, and how different kinetic energies of the water hitting the surface affect wetting properties, Jung and Bhushan [100] conducted waterfall/jet tests on the surfaces created with CNT and Lotus wax. The nano- and hierarchical structures with CNT were exposed to water with pressure ranging from 0 to 45 kPa for 20 min. Figure 20.77 (left) shows static contact angle and contact angle hysteresis as a function of water pressure. As water pressure hitting the surfaces increased, the static contact angle and contact angle hysteresis decreased and increased slightly, respectively, but a significant change was not found on both nano- and hierarchical structures for superhydrophobicity. It can be interpreted that there was no deformation



**Fig. 20.77** Static contact angle and contact angle hysteresis as a function of water pressure of exposure for 20 min for the droplet with a 1 mm radius (5  $\mu$ L volume) gently deposited on the surfaces with CNT and Lotus wax. The data are reproducible within  $\pm 5\%$ . Adapted from Jung and Bhushan [100]

of CNT structures due to strong bonding with the substrate. As a result, superhydrophobic CNT composite structures showed good stability of wetting properties not only from long-term exposure to water but also high water pressure. In order to compare durability of the created surfaces with CNT and Lotus wax, Jung and Bhushan [100] also conducted waterfall/jet tests on the flat, nano-, micro-, and hierarchical structures with Lotus wax. Figure 20.77 (right side) shows static contact angle and contact angle hysteresis as a function of water pressure of exposure. As the water pressure increased up to 45 kPa, static contact angle and contact angle hysteresis of flat and microstructure with Lotus wax layer remained almost constant. However, as the water pressure increased up to 34 kPa, the static contact angle of nano- and hierarchical structures with Lotus wax first decreased slightly, and then the contact angle started decreasing sharply. It was also observed that the corresponding large change in contact angle hysteresis was found above 34 kPa. It is usually known that wax structures on the leaves can easily be induced by touching the leaf surface or by mechanical wear during transport of the leaves. As expected, it is observed that the nanostructure with Lotus wax can be damaged by water with high pressure, resulting in loss of superhydrophobicity.

### 20.5.6.3 Durability of Various Surfaces in AFM and Ball-on-Flat Tribometer Tests

To investigate the durability of the nanostructure fabricated using CNT, Jung and Bhushan [100] conducted wear tests by creating  $50 \times 50 \mu\text{m}^2$  wear scars with a  $15 \mu\text{m}$  radius borosilicate ball for 1 cycle at two normal loads of 100 nN and 10  $\mu\text{N}$  using AFM. Figure 20.78a shows surface height maps before and after wear tests for nanostructures with CNT. As the normal load of 100 nN was applied on the nanostructure with CNT, the wear scar induced on the surface after the 100 nN normal load tests was not found or very low, and it was also hard to quantify a wear depth on the nanostructure with CNT scanned with a borosilicate ball. With increasing the normal load to 10  $\mu\text{N}$ , it was found that the wear depth on the nanostructure with CNT was not significantly changed, but the morphology of the CNT differs slightly from that before wear test. It can be interpreted that the individual CNT might be expected to slide or bend by the borosilicate ball applied by high normal load of 10  $\mu\text{N}$  during the test process.

For comparison, Jung and Bhushan [100] also investigated the durability of the nanostructure fabricated using Lotus wax by applying two normal loads of 100 nN and 10  $\mu\text{N}$  using AFM. Figure 20.78b shows surface height maps before and after wear tests for nanostructures with Lotus wax. As the normal load of 100 nN was applied on the nanostructure with Lotus wax, the change in the morphology of the structured surface was observed, and a small amount of debris was generated compared to the surface before wear test, indicating that the wax nanostructure has weak mechanical strength at even small load. With increasing the normal load



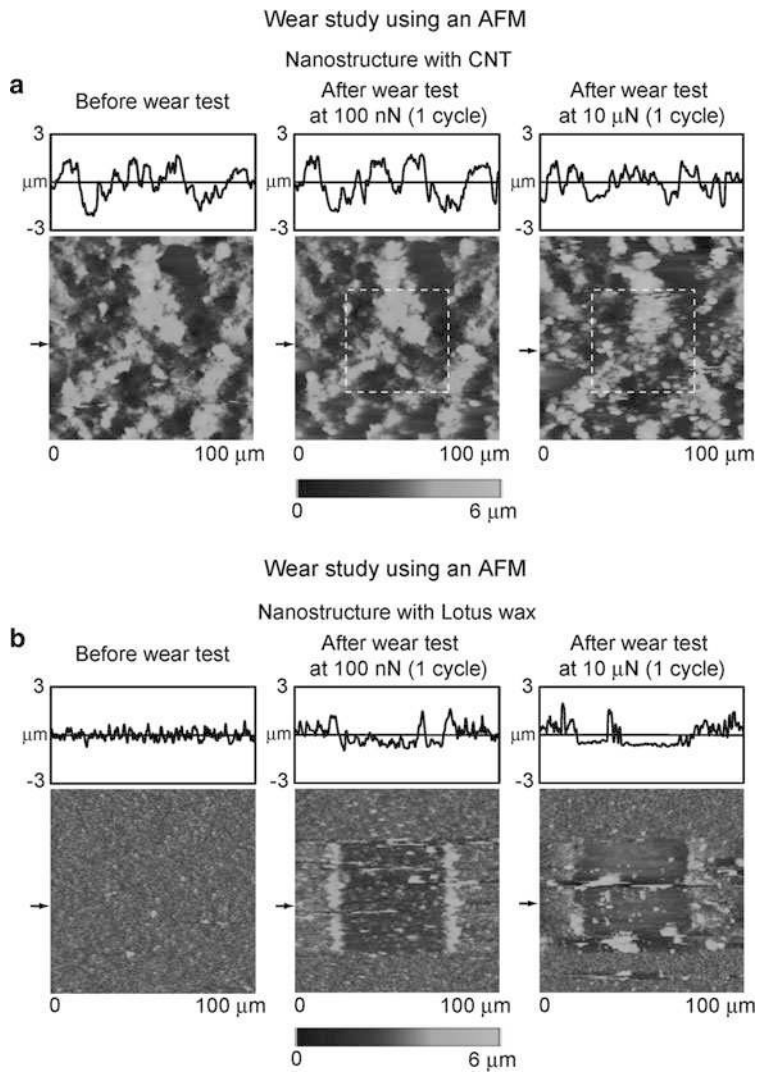


**Fig. 20.78** Surface height maps before and after wear tests with a 15  $\mu$ m radius borosilicate ball at 100 nN and 10  $\mu$ N for nanostructures with (a) CNT and (b) Lotus wax using an AFM [100]

to 10  $\mu$ N, it was found that the depth of wear mark increased, and the nanostructure with Lotus wax was fully removed from the substrate. As expected, the nanostructure with Lotus wax exhibited the greater amount of wear compared to the nanostructure with CNT as evidenced by debris build-up around the edge of the wear test region. The damage of the structured surface can cause the sticking of water droplets in the wear region, resulting in low static contact angle and high contact angle hysteresis.



In order to investigate the durability of structured surfaces at a high load, Jung and Bhushan [100] conducted conventional ball-on-flat tribometer experiments for the surfaces with CNT. Figure 20.79a shows the coefficient of friction as a function of number of cycles for the nano- and hierarchical structures with CNT. The data are reproducible within  $\pm 5\%$  based on three measurements. The coefficients of friction on both nano- and hierarchical structures with CNT first increased slightly for 20 cycles. Such a trend can be due to the elastic bending or buckling of CNT by contacting with a sapphire ball during the beginning of scan, resulting in an increase of the contact area. During the entire experiment, the coefficient of friction value of the nano- and hierarchical structures with CNT changed minimally, which indicates that the CNT was not being worn after 100 cycles. To investigate the change in the morphology of the surfaces after wear test, optical microscope images were obtained before and after wear test as shown in Fig. 20.80a. As expected, it was observed that there is no or low wear on nano- and hierarchical structures after wear tests. No or low wear on the CNT composite structure can possibly be due to the significant increase in the mechanical strength and wear resistance led from the uniform distribution and strong bonding of CNT on flat epoxy resin and micro-structure. The elastic bending or buckling exhibited by CNT make them

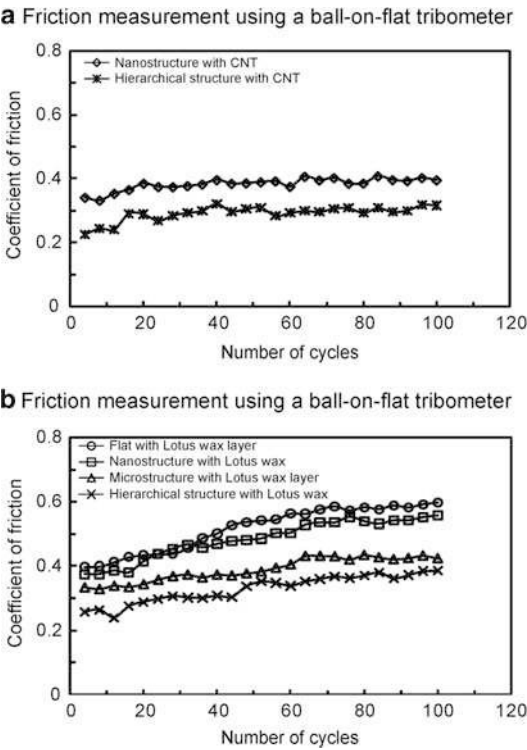


**Fig. 20.79** Coefficient of friction as a function of number of cycles using a ball-on-flat tribometer for the surfaces with (a) CNT and (b) Lotus wax at room temperature ( $22 \pm 1^\circ\text{C}$ ) and ambient air ( $45 \pm 5\% \text{ RH}$ ). The data are reproducible within  $\pm 5\%$  based on three measurements [100]



exceedingly tough materials and may be absorbing some of the force at contact acting as a compliant spring moderating the impact of the ball on the surface [240–242].

Contact diameters and contact stresses of CNT at three loads used in AFM and ball-on-flat tribometer tests were calculated [100]. Table 20.12 lists the physical properties of various specimens. It is assumed that contacts are single-asperity elastic contacts. For this case, the contact diameter [24, 25],

$$d = 2 \left( \frac{3WR}{4E^*} \right)^{1/3}$$

(20.43)

where  $W$  is the total normal load,  $R$  is the asperity radius, and  $E^*$  is the effective elastic modulus. It should be noted that contact occurs on multiple asperities, and (20.43) gives an approximate value. The calculated contact diameter and contact stress are presented in Table 20.12. The deformation of CNT appears to be elastic at the three loads applied by borosilicate ball and sapphire ball.

In order to compare the durability of the created surfaces with CNT and Lotus wax at a high load, Jung and Bhushan [100] conducted a wear study on the surfaces with Lotus wax using a conventional ball-on-flat tribometer. As shown in Fig. 20.79b, the coefficient of friction value of the surfaces with Lotus wax exhibited a gradual increase when the sliding cycle increases up to about 70 cycles, and then remains constant. This indicates that the wax nanostructure and flat wax layer could be undergoing some wear due to weak bonding between them and the substrates. The change in the morphology of the surfaces with Lotus wax was observed in optical microscope images as shown in Fig. 20.80b. As shown in the AFM study at low loads (Fig. 20.78b), it is clearly observed that the flat wax layer and wax nanostructure on flat and microstructure were fully removed from the

**Table 20.12** Typical physical properties of various specimens and calculated contact diameters and contact stresses at three loads used in AFM and ball-on-flat tribometer measurements

	Borosilicate ball with a 15 μm radius			Sapphire ball with a 1.5 mm radius		Carbon nanotube
Elastic modulus (GPa)	70 <sup>a</sup>			390 <sup>b</sup>		1,200 <sup>c</sup>
Poisson's ratio	0.2 <sup>a</sup>			0.23 <sup>b</sup>		0.2 <sup>d</sup>
Bending strength (GPa)						14.2 <sup>c</sup>
	Contact diameter (μm)			Mean contact pressure (GPa)		
	Borosilicate ball at 100 nN	Borosilicate ball at 10 μN	Sapphire ball at 10 mN	Borosilicate ball at 100 nN	Borosilicate ball at 10 μN	Sapphire ball at 10 mN
Carbon nanotube	0.05	0.24	6.62	0.076	0.33	0.44

It is assumed that contacts are singe-asperity contact [100]

<sup>a</sup>Callister [243]  
<sup>b</sup>Bhushan and Gupta [244]  
<sup>c</sup>Wong et al. [245]  
<sup>d</sup>Zhang et al. [246]

surfaces. As a result, superhydrophobic CNT composite structures showed better mechanical durability than the structured surfaces with Lotus wax to best withstand real world applications.

## 20.6 Fabrication and Characterization of Biomimetic Structures for Fluid Drag Reduction

Biomimetics allows one to mimic nature to develop materials and devices of commercial interest by engineers. Drag reduction in fluid flow is one of the examples found in nature. In this section, we discuss drag reduction efficiency on biomimetic structured surfaces in channels.

### 20.6.1 Experimental Techniques

For the measurement of pressure drop using water and air flows, an experimental flow channel with a rectangular channel was designed and fabricated as shown in Fig. 20.81 [48]. The fabricated surfaces were used for the upper and lower walls of the flow channel. Two pieces of plastic were glued between the upper and lower samples and at each end to prevent flow leak. For the measurement of pressure drop, the upper sample had two opening holes connected with a differential manometer (Model A 1000-13, Differential Pressure Plus Inc., USA). The thickness, width, and length of the resulting channel are designated as  $H$ ,  $W$ , and  $L$ , respectively.

The inlet and outlet ports were machined and connected with the plastic tubes. To introduce water into the channel in laminar flow, a syringe pump (Model NE-300, New Era Pump Systems Inc., USA) was used at a range of flow rates between 50  $\mu\text{L/s}$  and 400  $\mu\text{L/s}$  (a range of flow velocity between 0.03 m/s and 0.23 m/s). The Reynolds number of the flow applied by the syringe pump was less than 300, which is the laminar flow. To create a turbulent flow, a larger flow rate is needed than cannot be accomplished with the syringe pump. To accomplish high fluid flow, a separate plastic

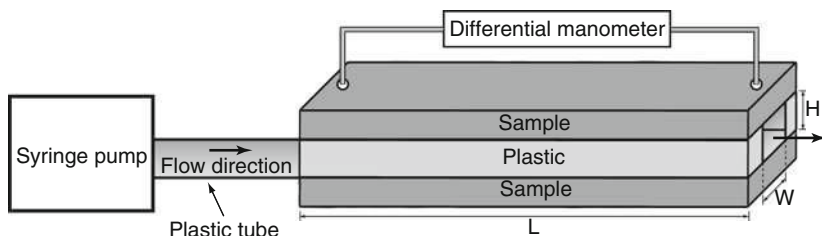


**Fig. 20.81** Schematic of the experimental flow channel connected with a differential manometer. The thickness, width, and length of the channel are  $H$ ,  $W$ , and  $L$ , respectively [48]

chamber filled with a measured amount of water was used to allow flow through the channel under the force of gravity. From measuring the amount of water and time to flow the water from a starting fluid level to an ending fluid level, the Reynolds number was calculated as 4,200 (flow velocity of 3.8 m/s), which indicates that the flow is turbulent using this setup. In order to make air flow, laboratory air outlet was connected to the channel. A flowmeter (Model FL-1478-G, Omega Engineering, Inc., USA) was used to measure air flow rate between laboratory air outlet and channel. For the experimental measurements of air flow, the calculated range of Reynolds number was between 200 and 4,600, which indicates both laminar and turbulent flows [48].

### 20.6.2 Model for Calculation of Pressure Drop and Slip Length

The pressure drop,  $\Delta p$ , of an incompressible fluid flow between two points along the channel of thickness,  $H$ , width,  $W$ , and length,  $L$ , for a hydrophilic flat surface can be calculated by [247]

$$\Delta p = \frac{\rho V^2 f L}{2 D_H} \quad (20.44)$$

where  $\rho$  is the fluid density,  $V$  is the flow velocity obtained from flow rate ( $Q$ ) divided by cross section area of the channel, and  $f$  is the friction factor which specifies the loss in pressure required to impel a flow over the surface or through the channel. The friction factor is generally a function of Reynolds number, surface roughness, and the geometry of the surface.  $D_H$  is the hydraulic diameter which is proportional to four times the flow area divided by the perimeter of the surface containing the flow. For the rectangular channel, the hydraulic diameter is

$$D_H = \frac{2WH}{W + H} \quad (20.45)$$

The friction factor for laminar flow is inversely proportional to the Reynolds number as [247]

$$f = \frac{k}{\text{Re}} \quad \text{for laminar flow} \quad (20.46)$$

$$\text{Re} = \frac{\rho V D_H}{\eta} \quad (20.47)$$

where  $\eta$  is the dynamic fluid viscosity. The Reynolds number can be used to determine whether the fluid flow will be within the laminar, turbulent, or transitional flow regimes. Since the Reynolds number is proportional to flow velocity, the pressure drop in laminar flow increases with flow velocity.  $k$  is the friction coefficient which can be found by the solution of Poisson's equation over the cross section as [247]

$$k = \frac{64}{\frac{2}{3} + \frac{11}{23} \frac{H}{W} (2 - \frac{H}{W})} \quad (20.48)$$

From (20.48), the friction coefficient is dependent only on the shapes of the cross section but it is independent of surface roughness.

To improve in the calculation of the friction factor for turbulent flow in a rectangular channel, Jones [248] developed an improved equivalent diameter,  $D_e = 64D_H/k$ , and the friction factor for turbulent flow can be modified as

$$f = \frac{64}{\text{Re}} \quad \text{for turbulent flow} \quad (20.49)$$

Next, we present an analysis to calculate slip length in the laminar flow. Using the Navier slip boundary condition, the slip length  $b$  of the two infinite parallel and smooth plates can be obtained as [121, 247]

$$b = \frac{4\eta QL}{\Delta p WH^2} - \frac{H}{3} \quad (20.50)$$

For a rectangular channel, the slip length would have the following general form [121]

$$b = \frac{c\eta QL}{\Delta p WH^2} - \frac{H}{3} \quad (20.51)$$

where  $c$  is a constant which needs to be obtained empirically. In order to obtain the constant, pressure drop measurement on a hydrophilic channel needs to be made. The (20.51) is then fitted under the assumption of zero slip length with the measured pressure drop data to obtain  $c$ . It was equal to 5 for the channel ( $H = 0.7$  mm,  $W = 2.5$  mm,  $L = 60$  mm) used in this study. Now this equation was used to calculate the slip length for hydrophobic surfaces [48].

### 20.6.3 Fabrication and Characterization of Biomimetic Structures

A shark (*Squalus acanthias*, L. Squalidae) was used for creating a shark skin replica [48]. A shark is an aquatic animal, and its skin is permanently exposed to contamination from marine organisms, e.g., bacteria and algae. The shark was conserved in FAA (formaldehyde – acetic acid – ethanol) solution. The detailed structure varies from one location to another for the shark. The scales are present over most of the shark's body. To create a replica, the right front

of shark body was selected. Before replicating the conserved shark skin, the selected area was first cleaned with acetone and then washed with deionized water. This process was repeated twice. The cleaned skin was placed in air for 1 h for drying. For the negative replica, a polyvinylsiloxane dental wax was applied via a dispenser on the upper side of the shark skin and immediately pressed down with a glass plate. After complete hardening of the molding mass (at room temperature 3–5 min), the master surface and the mold (negative) were separated. The first negative replica was made only to remove any remaining contaminations from the shark surface by embedding the dirt into the replica material. A second and third replica of the same area was made to obtain negatives without contamination. For the positive replica, a liquid epoxy resin was used in the molding process.

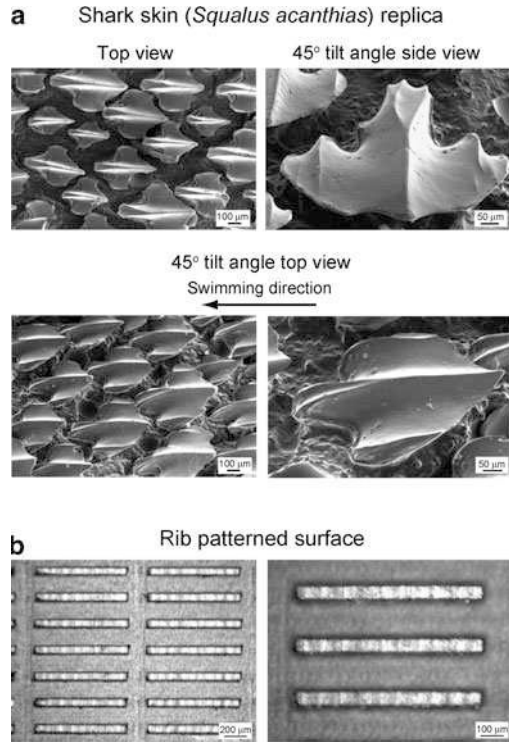
To simulate a shark skin structure, a rib patterned surface was created using a FlashCut CNC milling machine [48]. Bechert et al. [249] have reported that optimal groove depth for the rib surface should be about half of the lateral rib spacing for low drag. In the rib pattern design selected here, multiple stacks of ribs oriented along an axis were fabricated. For the fabrication, first a model of a rib patterned surface was designed in SolidWorks, and then the code for the rib's height, width, spacing and lengths, and channel dimensions was written using FeatureCAM in order to fabricate structures using the CNC milling machine. An acrylic resin was clamped onto the table of the CNC mill, and a fly cutter was used to make the top of the surface flat. The code was opened with FlashCut CNC and then the rib patterns were milled using an endmill with 130  $\mu\text{m}$  bit.

Figure 20.82a shows the SEM micrographs of the shark skin (*Squalus acanthias*) replica taken at a top view, a 45° tilt angle side view, and a 45° tilt angle top view. The shark skin replica shows that scales are lifted up at the end, and there are only three ribs on each scale. It is clearly visible that the V-shaped riblets' height varies between 200–500  $\mu\text{m}$ , and their space varies between 100–300  $\mu\text{m}$ . The ribs were oriented nearly parallel to swimming direction of the sharks. Figure 20.82b shows the optical microscope images of the rib patterned surface fabricated as a model of artificial shark skin surfaces. The height, width, and length of the created ribs were 90, 38, and 850  $\mu\text{m}$ , respectively. The spacing between the ribs was 180  $\mu\text{m}$ .

To investigate drag reduction efficiency on the surfaces with superhydrophobicity, self-cleaning, and low adhesion described earlier, Jung and Bhushan [48] used nano-, micro-, and hierarchical structures created by the self-assembly of Lotus wax with the amounts of 0.8  $\mu\text{g}/\text{mm}^2$  as shown in Fig. 20.64.

Table 20.13 summarizes the static contact angle and contact angle hysteresis measured on shark skin replica, rib patterned surface, and the structured surfaces with Lotus wax. The shark skin replica had a static contact angle of 89° and a contact angle hysteresis of 66° for a water droplet. For acrylic resin material, a static contact angle of 82° was found for flat acrylic resin. Introduction of the rib patterns on the flat surface led to a much higher static contact angle of 146° and lower contact angle hysteresis of 43°.

**Fig. 20.82** (a) SEM micrographs taken at top view, 45° tilt angle side view and 45° tilt angle top view, show shark skin (*Squalus acanthias*) replica. The shark skin replica show only three ribs on each scale. It is clearly visible that the V-shaped riblets' height varies between 200–500  $\mu\text{m}$  and their space varies between 100–300  $\mu\text{m}$ , and (b) optical microscope images (shown using two magnifications) show the rib patterned surface fabricated as a model of artificial shark skin surfaces [48]



### 20.6.3.1 Pressure Drop in the Channel Using Water Flow and Calculated Slip Length

To observe the fluid drag reduction in the channel using water flow, experiments on flat epoxy resin, flat with thin wax layer, nanostructure, microstructure, hierarchical structure, and shark skin replica were performed [48]. In Fig. 20.81, the rectangular channels with these surfaces had thickness  $H = 0.7$  mm, width  $W = 2.5$  mm, and length  $L = 60$  mm. For calculation of the pressure drop using the (20.44), the mass density ( $\rho$ ) and viscosity ( $\eta$ ) for water were taken to be 1,000  $\text{kg/m}^3$  and 0.001 Pa·s for water, respectively [250]. Figure 20.83 shows the pressure drop as a function of flow rate in the channel with various surfaces using water flow. The measured data are compared with the predicted pressure drop values for a hydrophilic surface obtained using (20.44) for laminar and turbulent flows (solid lines). The figure in the bottom is magnified in flow rate between 0 and 500  $\mu\text{L/s}$ . In both laminar and turbulent flows, the pressure drop increased linearly with flow rate for all samples. It was found that the pressure drop for the flat epoxy resin was similar to the value predicted by (20.44), while structured surfaces had values lower than the predicted. As mentioned earlier and showed in Table 20.13, the introduction of roughness increases the hydrophobicity of the surfaces responsible for reduction in drag or



**Table 20.13** Summary of the static contact angles and contact angle hysteresis measured on the various surfaces

	Static contact angle (deg)	Contact angle hysteresis (deg)
(a) Epoxy resin		
Flat epoxy resin	76 ± 0.9	67 ± 2.9 (151 <sup>a</sup> , 84 <sup>b</sup> )
Flat with thin wax layer	119 ± 2.4	56 ± 3.2 (148 <sup>a</sup> , 92 <sup>b</sup> )
Nanostructure	167 ± 0.7	6 ± 1.1 (170 <sup>a</sup> , 164 <sup>b</sup> )
Microstructure	160 ± 1.8	27 ± 2.1 (169 <sup>a</sup> , 142 <sup>b</sup> )
Hierarchical structure	173 ± 0.8	1 ± 0.6 (174 <sup>a</sup> , 173 <sup>b</sup> )
Shark skin replica	89 ± 1.7	66 ± 3.4 (155 <sup>a</sup> , 89 <sup>b</sup> )
(b) Acrylic resin		
Flat acrylic resin	82 ± 1.8	71 ± 2.6 (122 <sup>a</sup> , 51 <sup>b</sup> )
Rib patterned surface	146 ± 1.2	43 ± 1.2 (158 <sup>a</sup> , 115 <sup>b</sup> )

Nanostructures and hierarchical structures were fabricated with 0.8  $\mu\text{g}/\text{mm}^2$  of Lotus wax after storage at 50°C with ethanol vapor. Flat epoxy resin and microstructure were covered with flat Lotus wax. The variation represents  $\pm 1$  standard deviation [48]

<sup>a</sup>Advancing contact angle

<sup>b</sup>Receding contact angle

pressure drop. The hierarchical structure with highest contact angle and lowest static contact angle hysteresis provided the lowest pressure drop. It is believed that air pockets inside the grooves underneath the fluid reduce the contact area between fluid and surface, resulting in lower pressure drop. These results indicate that superhydrophobicity can lead to drag reduction in fluid flow [48].

As shown in Fig. 20.83, for shark skin replica, it was found that the pressure drop in laminar flow was higher than those of the nanostructure and hierarchical structure and the reduction of pressure drop was about 12% as compared to the theoretical pressure drop. However, in turbulent flow, the reduction of pressure drop was similar to those of nanostructure and hierarchical structure. Bechert et al. [18] showed that a turbulent boundary layer on the shark skin surface with ribs can help to reduce turbulent shear stress. The results of experimental measurements on shark skin replica showed that a reduction of pressure drop was obtained up to 30% in turbulent flow. It can be concluded that the surfaces with ribs are more beneficial in providing drag reduction in turbulent flow than that in laminar flow.

Based on the pressure drop data, the slip length on the surfaces with different wettabilities was calculated using (20.51). For calculations, it was assumed that there is a no-slip boundary condition on flat epoxy resin as verified from the experiments [116]. Figure 20.84 shows the bar chart showing the slip length in the channel with various surfaces using water flow in laminar flow ( $0 < \text{Re} < 300$ ). The average values of slip length on the surfaces were calculated over all the experimental flow rates. A slip length of 24  $\mu\text{m}$  was found for the flat surface with thin wax layer. The microstructure (covered with a flat Lotus wax film) and shark skin replica had slip lengths of 56 and 35  $\mu\text{m}$ , but the nanostructure and hierarchical structures show much higher slip lengths of 91 and 103  $\mu\text{m}$ , respectively, which implies the boundary slip increases with increasing hydrophobicity of

**Fig. 20.83** Pressure drop as a function of flow rate in the channel with various surfaces using water flow. The figure in the bottom is magnified in flow rate between 0 and 500  $\mu\text{L/s}$ . Data are compared with predicted pressure drop values for a hydrophilic surface obtained using the (20.44) for laminar and turbulent flows (solid lines) [48]

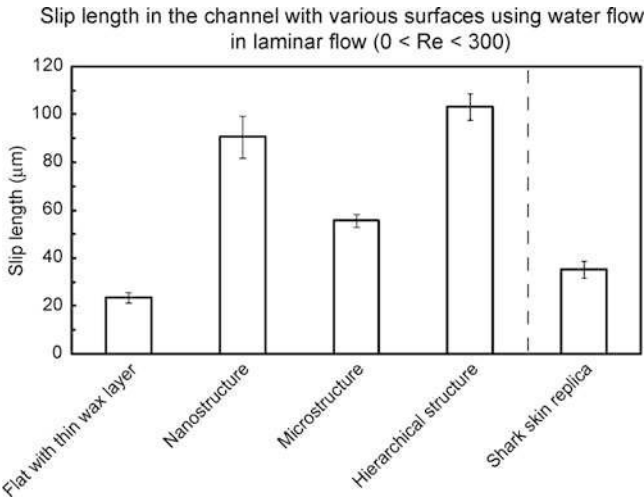
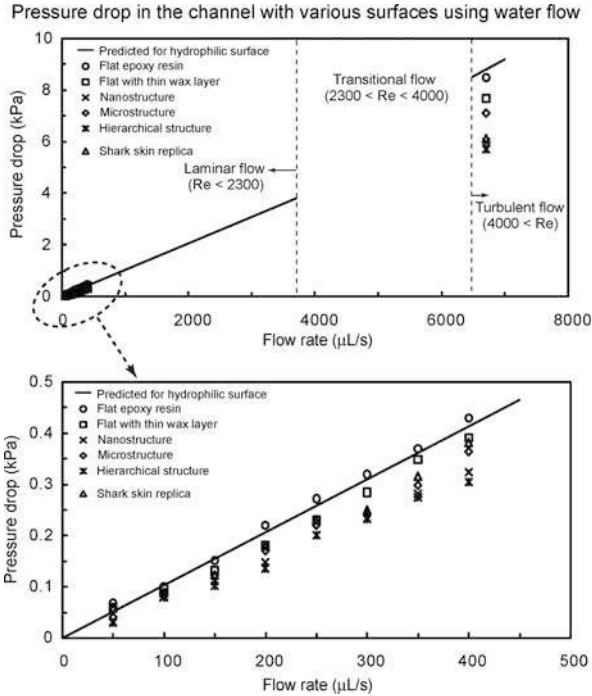


**Fig. 20.84** Bar chart showing the slip length in the channel with various surfaces using water flow in laminar flow ( $0 < Re < 300$ ). The slip length was calculated using the (20.51) and the pressure drop measured on various surfaces. The error bar represents  $\pm 1$  standard deviation [48]

solid surfaces. Zhu and Granick [251] have reported that the slip length increases from nanometer range to micrometer range as the flow rate increases.

To observe the fluid drag reduction in the channel using water flow, experiments on flat acrylic resin and rib patterned surfaces fabricated as a model of artificial shark skin were also performed [48]. In Fig. 20.81, the rectangular channels with these surfaces had thickness  $H = 1$  mm, width  $W = 2$  mm, and length  $L = 100$  mm. Figure 20.85 shows the pressure drop as a function of flow rate in the channel using water flow. The measured data are compared with predicted pressure drop values for a hydrophilic surface obtained using (20.44) for laminar and turbulent flows (solid lines). The figure in the bottom is magnified in flow rate between 0 and 500  $\mu\text{L/s}$ . In laminar flow, it was found that the pressure drop increased linearly with flow rate and was similar to the value predicted by (20.44). However, in turbulent flow, the reduction of pressure drop was obtained up to 23% as compared to the theoretical pressure drop. This result shows a similar trend to that of the shark skin replica.

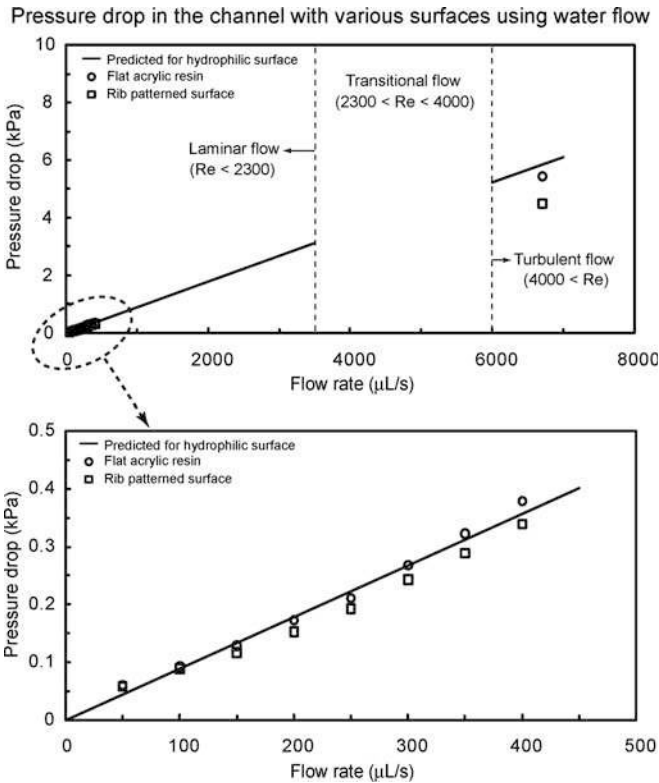


**Fig. 20.85** Pressure drop as a function of flow rate in the channel with flat acrylic resin and rib patterned surface using water flow. The figure in the bottom is magnified in flow rate between 0 and 500  $\mu\text{L/s}$ . Data are compared with predicted pressure drop values for a hydrophilic surface obtained using the (20.44) for laminar and turbulent flows (solid lines) [48]

### 20.6.3.2 Pressure Drop in the Channel Using Air Flow

To investigate the effect of air flow in the channel and compare them to water drag reduction, experiments with air flow on various surfaces were performed [48]. In Fig. 20.81, the rectangular channels had thickness  $H = 0.7$  mm, width  $W = 2.5$  mm, and length  $L = 60$  mm. For calculation of pressure drop using (20.44), the mass density ( $\rho$ ) and viscosity ( $\eta$ ) for water were taken to be  $1.204 \text{ kg/m}^3$  and  $1.837 \times 10^{-5} \text{ Pa}\cdot\text{s}$  for air, respectively [250]. Figure 20.86 shows the pressure drop as a function of flow rate in the channel with various surfaces using air flow. The measured data are compared with predicted pressure drop values for a hydrophilic surface obtained using (20.44) for laminar and turbulent flows (solid lines). The figure in the bottom is magnified in flow rate between 0 and 50 mL/s. The pressure drop of the structured surfaces is higher than that of the hydrophilic surface in the turbulent flow which is opposite to that in liquid flow. In both

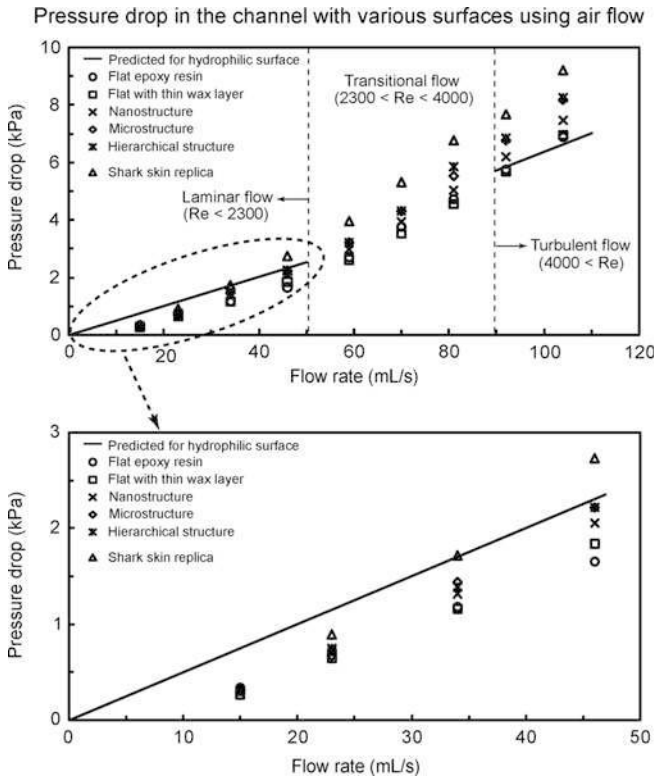


**Fig. 20.86** Pressure drop as a function of flow rate in the channel with various surfaces using air flow. The figure in the bottom is magnified in flow rate between 0 and 50 mL/s. Data are compared with predicted pressure drop values for a hydrophilic surface obtained using the (20.44) for laminar and turbulent flows (solid lines) [48]

laminar and turbulent flows, the pressure drop increased linearly with flow rate for all samples. As mentioned earlier, in the case of water flow, air pockets between the structures reduce the contact area between liquid and surface, resulting in reduction of the flow drag. The data shows that the structures are not beneficial for drag reduction in air flow. The introduction of roughness on the surfaces increases the pressure drop in the channel in the turbulent flow. It is generally known that the surfaces with a streamlined body can produce dramatic reductions of the fluid pressure drag with only a slight increase in shear stress in air flow [252]. It is also known that as the Reynolds number increases, the pressure drop becomes very large, resulting in larger pressure drag. The roughness structures on the surfaces may cause air to move around them, resulting in the formation of vortices and large fluid drag.

To observe the fluid drag reduction in the channel using air flow, experiments on flat acrylic resin and fabricated rib patterned surface were also performed [48]. The rectangular channels with these surfaces had thickness  $H = 1$  mm, width  $W = 2$  mm, and length  $L = 100$  mm. Figure 20.87 shows the pressure drop as a function of flow rate in the channel with flat acrylic resin and rib patterned surface using air flow. The measured data are compared with predicted pressure drop values for a hydrophilic surface obtained using the (20.44) for laminar and turbulent flows (solid lines). The experimental results show a similar trend to the data as shown in Fig. 20.86. It was found that the pressure drop of the rib patterned surface slightly increased due to the vortices formed at the end of the ribs in turbulent flow as compared to the theoretical pressure drop.

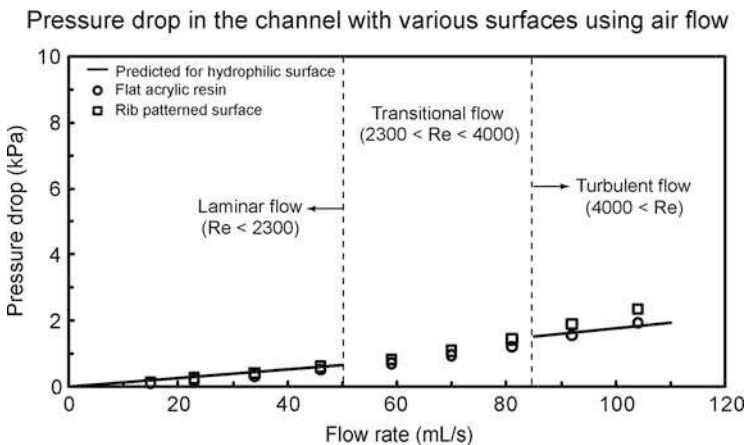


**Fig. 20.87** Pressure drop as a function of flow rate in the channel with flat acrylic resin and rib patterned surface using air flow. Data are compared with predicted pressure drop values for a hydrophilic surface obtained using the (20.44) for laminar and turbulent flows (solid lines) [48]

## 20.7 Modeling, Fabrication and Characterization of Oleophobic/philic Surfaces

Oleophobic surfaces have the potential for self-cleaning and anti-fouling from biological and organic contaminants both in air and underwater applications. In this section, we discuss a model for predicting the oleophobic/philic nature and experimental measurements of the wetting properties of the surfaces.

### 20.7.1 Modeling of Contact Angle for Various Interfaces

If a water droplet is placed on a solid surface in air, the solid–air and water–air interfaces come together with a static contact angle,  $\theta_W$ . The value of  $\theta_W$  can be determined from the condition of the total energy of the system being minimized [22, 23] and is given by the Young's equation for the contact angle,  $\theta_W$ .

$$\cos \theta_W = \frac{\gamma_{SA} - \gamma_{SW}}{\gamma_{WA}} \quad (20.52)$$

where  $\gamma_{SW}$ ,  $\gamma_{SA}$ , and  $\gamma_{WA}$  are surface tensions of the solid–water, solid–air, and water–air interfaces, respectively. If an oil droplet is placed on a solid surface in air, the Young's equation for the contact angle,  $\theta_O$ , can be expressed by

$$\cos \theta_O = \frac{\gamma_{SA} - \gamma_{SO}}{\gamma_{OA}} \quad (20.53)$$

where  $\gamma_{SO}$ ,  $\gamma_{SA}$ , and  $\gamma_{OA}$  are surface tensions of the solid–oil, solid–air, and oil–air interfaces, respectively. As predicted by (20.53), if  $\gamma_{SO}$  is higher than  $\gamma_{SA}$ , an oleophobic surface can be achieved.

To create an oleophobic surface in water, let us consider the solid–water–oil interface. If an oil droplet is placed on a solid surface in water, the contact angle of an oil droplet in water,  $\theta_{OW}$ , is given by the Young's equation

$$\cos \theta_{OW} = \frac{\gamma_{SW} - \gamma_{SO}}{\gamma_{OW}} \quad (20.54)$$

where  $\gamma_{SO}$ ,  $\gamma_{SW}$ , and  $\gamma_{OW}$  are surface tensions of the solid–oil, solid–water, and oil–water interfaces, respectively. Combining (20.52, 20.53 and 20.54), the equation for the contact angle,  $\theta_{OW}$ , of an oil droplet in water is given as

$$\cos \theta_{OW} = \frac{\gamma_{OA} \cos \theta_O - \gamma_{WA} \cos \theta_W}{\gamma_{OW}} \quad (20.55)$$

As predicted by (20.55), for a hydrophilic surface ( $\gamma_{SA} > \gamma_{SW}$ ), an oleophobic surface in the solid–water–oil interface can be created if  $\gamma_{OA} \cos \theta_O$  is lower than  $\gamma_{WA} \cos \theta_W$ . Since the surface tension of oil and organic liquids is much lower than that of water, most hydrophilic surfaces can be made oleophobic in a solid–water–oil interface. For a hydrophobic surface ( $\gamma_{SA} < \gamma_{SW}$ ) and an oleophobic surface in a solid–air–oil interface ( $\gamma_{SA} < \gamma_{SO}$ ), an oleophobic surface in a solid–water–oil interface can be created if  $\gamma_{OA} \cos \theta_O$  is higher than  $\gamma_{WA} \cos \theta_W$  and vice versa. For a hydrophobic and an oleophilic surface in solid–air–oil interface, an oleophobic surface in solid–water–oil interface cannot be created. Schematics are shown in Fig. 20.88, and the summary of philic/phobic nature in various interfaces is shown in Table 20.14. For an oleophobic surface, oil contaminants are washed away when immersed in water. This effect leads to self-cleaning that can be used against marine ship fouling [47].

### 20.7.2 Experimental Techniques

For the measurement of static contact angle, deionized water was used for water droplet and hexadecane was used for oil droplets [47]. The surface tensions of the water–air interface ( $\gamma_{WA}$ ), oil–air interface ( $\gamma_{OA}$ ), and oil–water interface ( $\gamma_{OW}$ ) are 73 [250], 27.5 [250], and 51.4 [253] mN/m, respectively. The mass densities are 1,000 and 773 kg/m<sup>3</sup> for water and hexadecane, respectively. Water and oil droplets of about 5  $\mu$ L in volume (with radius of a spherical droplet about 1 mm) in air environment were gently deposited on the specimen using a microsyringe. The process of wetting behavior of an oil droplet in water was obtained in a solid–water–oil interface system as shown in Fig. 20.89 [47]. A specimen was first immersed in water phase. Then an oil droplet was gently deposited using a microsyringe from the bottom of the system because the density of oil (hexadecane) is lower than that of water. The image of the droplet was obtained by a digital camcorder (Sony, DCRSR100, Tokyo, Japan) with a 10x optical and 120x digital zoom. Images obtained were analyzed for the contact angle using Imagetool<sup>®</sup> software (University of Texas Health Science Center). The measurements were reproducible to within  $\pm 2^\circ$ .

### 20.7.3 Fabrication and Characterization of Oleophobic Surfaces

A two-step molding process was used to replicate microstructures with varying pitch values, as described earlier. As a master template for the flat and micropatterned surfaces, a flat Si surface and micropatterned Si surfaces with pillars of 14  $\mu$ m diameter and 30  $\mu$ m height with different pitch values (21, 23, 26, 35, 70, 105, 126, 168 and 210  $\mu$ m), fabricated by photolithography, were used [47].

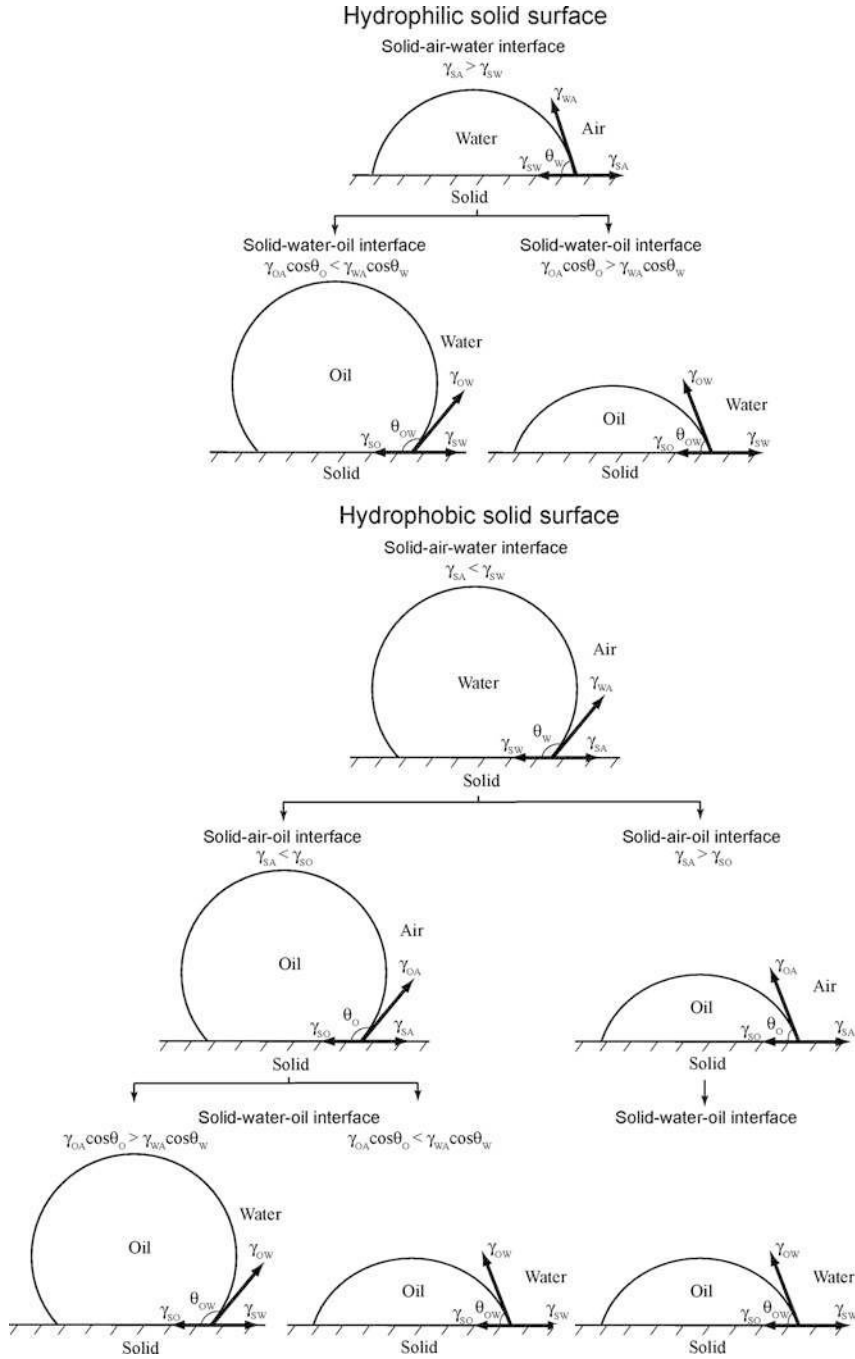


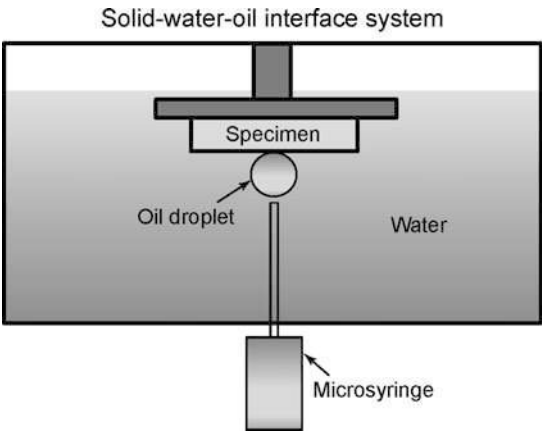
**Fig. 20.88** Schematics of a droplet of liquid showing philic/phobic nature in three different phase interface on the surface –  $\theta_w$ ,  $\theta_O$ , and  $\theta_{OW}$  are static contact angles of water droplet, oil droplet, and oil droplet in water, respectively [47]



**Table 20.14** Summary of philic/phobic nature in various interfaces [47]

Solid–air–water interface		Solid–water–oil interface	
Hydrophilic ( $\gamma_{SA} > \gamma_{SW}$ )	Solid–air–oil interface		Solid–water–oil interface
Solid–air–water interface Hydrophobic ( $\gamma_{SA} < \gamma_{SW}$ )	Oleophobic if $\gamma_{OA} \cos \theta_O < \gamma_{WA} \cos \theta_W$ Oleophilic if $\gamma_{OA} \cos \theta_O > \gamma_{WA} \cos \theta_W$		
	Oleophobic if $\gamma_{SA} < \gamma_{SO}$ Oleophilic if $\gamma_{SA} > \gamma_{SO}$		Oleophobic if $\gamma_{OA} \cos \theta_O > \gamma_{WA} \cos \theta_W$ Oleophilic if $\gamma_{OA} \cos \theta_O < \gamma_{WA} \cos \theta_W$ Oleophilic

**Fig. 20.89** Schematics of a solid–water–oil interface system. A specimen is first immersed in water phase, and then an oil droplet is gently deposited using a microsyringe, and the static contact angle in the system is measured [47]



To study surfaces with some oleophobicity, a surface coating which has a lower surface tension than that of oil is needed. For this purpose, Jung and Bhushan [47] deposited *n*-perfluoroeicosane ( $C_{20}F_{42}$ ) (268828, Sigma-Aldrich, USA) on the specimen surfaces by thermal evaporation. The surface energy of *n*-perfluoroeicosane is  $6.7 \text{ mJ/m}^2$  ( $6.7 \text{ mN/m}$ ) [254]. The specimens were mounted on a specimen holder with double-sided tape and placed in a vacuum chamber at 30 m Torr (4 kPa pressure), 2 cm above a heating plate loaded with  $6,000 \text{ }\mu\text{g}$  *n*-perfluoroeicosane [3]. The *n*-perfluoroeicosane was evaporated by heating it up to  $170^\circ\text{C}$ . In a vacuum chamber the evaporation from the point source to the substrate occurs in straight line; thus, the amount of sublimated material is equal in a hemispherical region over the point of source [227]. In order to estimate the amount of sublimated mass, the surface area of the half sphere was calculated by using the formula  $2\pi r^2$ , whereby the radius (*r*) represents the distance between the specimen to be covered and the heating plate with the substance to be evaporated. The calculated amount of *n*-perfluoroeicosane deposited on the surfaces was  $2.4 \text{ }\mu\text{g/mm}^2$  (amount of *n*-perfluoroeicosane loaded on a heating plate divided by surface area).

Hierarchical structures were fabricated using a two step fabrication process, including the production of microstructured surfaces by soft lithography and the subsequent development of nanostructures on top by self assembly of *n*-hexatriacontane with the amounts of  $0.2 \mu\text{g}/\text{mm}^2$  deposited by thermal evaporation, as described earlier [3, 71].

Jung and Bhushan [47] also used a shark skin replica described earlier (L., Squalidae).

Figure 20.90a shows the SEM micrographs taken at a  $45^\circ$  tilt angle, showing two magnifications of the micropatterned surface. Figure 20.90b shows the hierarchical structures and nanostructures covered with *n*-hexatriacontane platelets. The nanostructure is formed by three-dimensional platelets of *n*-hexatriacontane. Platelets

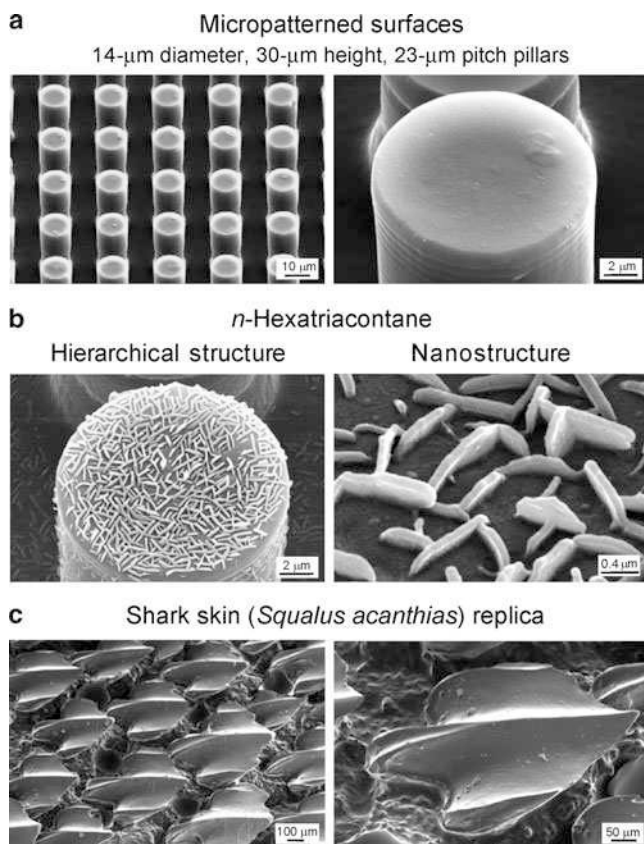


**Fig. 20.90** SEM micrographs taken at a  $45^\circ$  tilt angle showing two magnifications of (a) the micropatterned surface, (b) hierarchical structure and nanostructure with three-dimensional platelets on the surface fabricated with  $0.2 \mu\text{g}/\text{mm}^2$  mass of *n*-hexatriacontane, and (c) shark skin (*Squalus acanthias*) replica. The shark skin replica shows only three ribs on each scale. It is clearly visible that the V-shaped riblets' height varies between 200–500  $\mu\text{m}$  and their space varies between 100–300  $\mu\text{m}$  [47]

are flat crystals, grown perpendicular to the substrate surface. The platelet thickness varied between 50 and 100 nm, and their length varied between 500 and 1,000 nm. Figure 20.90c shows the shark skin replica shows only three ribs on each scale. It is clearly visible that the V-shaped riblets' height varies between 200 and 500  $\mu\text{m}$ , and their space varies between 100 and 300  $\mu\text{m}$  [47].

### 20.7.3.1 Wetting Behavior on Flat and Micropatterned Surfaces

To observe the wetting behavior of water and oil droplets for philic/phobic nature in three phase interfaces, Jung and Bhushan [47] performed experiments with droplets on both hydrophilic and hydrophobic and oleophilic surfaces in air. Figure 20.91 shows the optical micrographs of droplets in three different phase interfaces on flat epoxy resin and micropatterned surfaces. In a solid–air–water interface, the water droplet was hydrophilic for the flat epoxy resin and was superhydrophobic for the micropatterned surface with 23  $\mu\text{m}$  pitch. It is known that air pocket formation between the pillars makes a high static contact angle for micropatterned surface. However, in a solid–air–oil interface, the oil droplet was oleophilic for both surfaces. In the solid–water–oil interface system, in which the oil droplet sits on water trapped in the pillars, it is observed that the oil droplet in water was oleophobic and had contact angles of  $109^\circ$  and  $151^\circ$  for flat epoxy resin and micropatterned surface with 23  $\mu\text{m}$  pitch, respectively.

To study optimization of oleophobicity in the two solid–air–water and solid–air–oil interfaces, the static contact angles for water and oil droplets were measured on the micropatterned surfaces [47]. Figure 20.92 (top) shows the measured static contact angle as a function of pitch between the pillars for a water droplet (circle) and an oil droplet (cross) in air. The data are compared with predicted static contact angle values obtained using Wenzel and Cassie–Baxter equations (20.24 and 20.25) (solid lines) with a measured value of  $\theta_0$  for the micropatterned surfaces. In a solid–air–water interface for a water droplet, the flat epoxy resin showed a static contact angle of  $76^\circ$ . The static contact angle on micropatterned surfaces is higher than that of the flat surfaces. It first increases with an increase in the pitch values, then starts to drop rapidly to a value slightly higher than that of the flat surfaces. In the first portion, it jumps to a high value of  $150^\circ$  corresponding to a superhydrophobic surface and continues to increase to  $160^\circ$  at a pitch of 26  $\mu\text{m}$  because open air space increases with an increase in pitch responsible for propensity of air pocket formation. The sudden drop at a pitch value of about 30  $\mu\text{m}$  corresponds to the transition from the Cassie–Baxter to the Wenzel regime. The experimental observations for the transition are comparable to the value predicted from Wenzel and Cassie–Baxter equations.

At a solid–air–oil interface for an oil droplet, the flat epoxy resin showed a static contact angle of  $13^\circ$ . As shown in Fig. 20.92 (top), the oil droplets on all micropatterned surfaces were oleophilic, and the contact angle was lower than that of the flat surfaces. It increases with an increase in the pitch values as predicted from Wenzel equation. As mentioned earlier, the surface tension of the oil–air interface

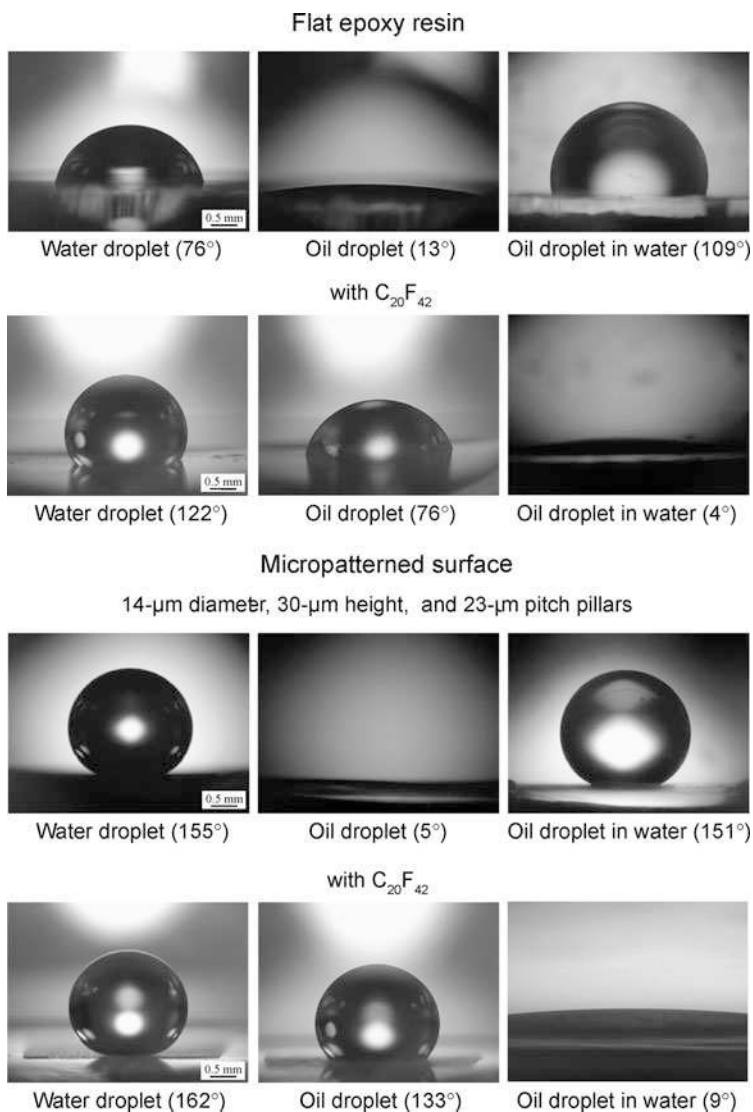


**Fig. 20.91** Optical micrographs of droplets in three different phase interfaces on flat epoxy resin and micropatterned surface without and with  $C_{20}F_{42}$ . *Left image*: a water droplet is placed on a surface in air. *Middle image*: an oil droplet is placed on a surface in air. *Right image*: an oil droplet is placed on a solid surface in water [47]

is very low for hexadecane. Therefore, it is observed that from (20.54) the surface tension of solid–oil interface ( $\gamma_{SO}$ ) is lower than that of solid–water interface ( $\gamma_{SW}$ ), resulting in oleophilic state for all micropatterned surfaces.

To study optimization of oleophobicity in a solid–water–oil interface, the static contact angles for oil droplets in water were measured on the micropatterned

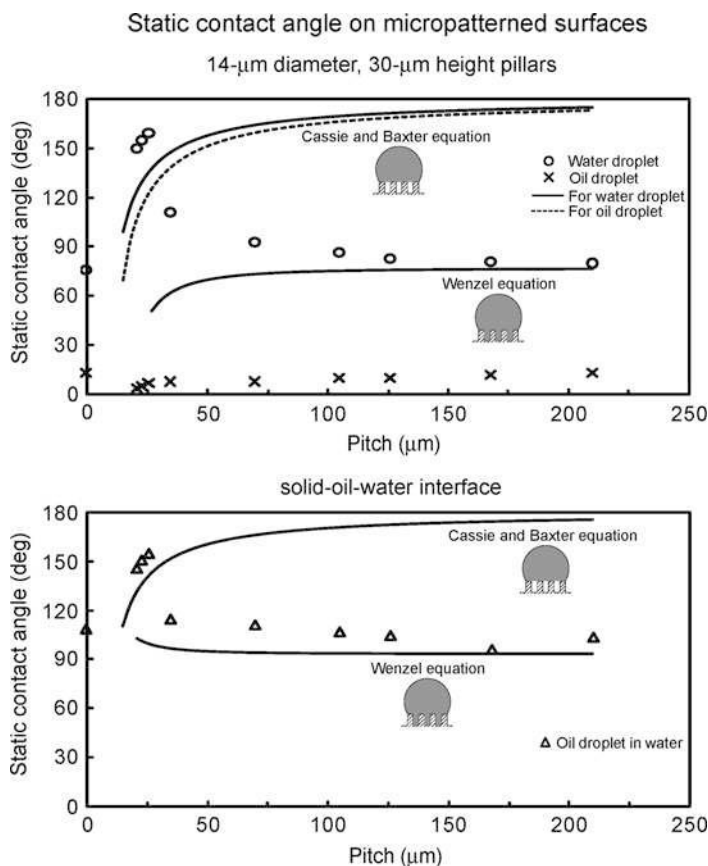


**Fig. 20.92** Static contact angle as a function of geometric parameters for water droplet (*circle*) and oil droplet (*cross*) in air (*top*), and oil droplet in water (*triangle*) (*bottom*) compared with predicted static contact angle values obtained using Wenzel and Cassie–Baxter equations (*solid lines*) with a measured value of  $\theta_0$  for the micropatterned surfaces [47]

surfaces [47]. Figure 20.92 (bottom) shows the measured static contact angle as a function of pitch between the pillars for an oil droplet in water (triangle). The data are compared with the predicted static contact angle values obtained using the Wenzel and Cassie–Baxter equations (20.24 and 20.25) (solid lines), with a measured value of  $\theta_0$  for the micropatterned surfaces. In a solid–water–oil interface, the oil droplet on the flat epoxy resin was oleophobic and had a static contact angle of  $109^\circ$ . The static contact angle of micropatterned surfaces in the solid–water–oil interface showed a similar trend to that in the solid–air–water interface. As the pitch increases up to  $26\ \mu\text{m}$ , the static contact angle first increases gradually from  $146^\circ$  to  $155^\circ$  because the oil droplet sits on water trapped in the pillars, and open space increases with an increase in pitch. Then, the contact angle starts decreasing rapidly due to the transition from the Cassie–Baxter to the Wenzel regime.

The experimental observations for the transition are comparable to the values predicted from Wenzel and Cassie–Baxter equations. The micropatterned surfaces studied here were either hydrophilic or hydrophobic and both were oleophilic. In the solid–water–oil interface, they were oleophobic. As shown in Fig. 20.88 and Table 20.14, it is observed that the data are not consistent with the model for hydrophobic surfaces. However, hydrophilic surfaces became oleophobic in the solid–water–oil interface because  $\gamma_{OA} \cos \theta_O$  is higher than  $\gamma_{WA} \cos \theta_W$ .

### 20.7.3.2 Wetting Behavior on Flat and Micropatterned Surfaces with $C_{20}F_{42}$

To study surfaces with some oleophobicity, *n*-perfluoroeicosane ( $C_{20}F_{42}$ ), which has lower surface tension than that of oil, was deposited on the surfaces, and experiments with droplets on hydrophobic and both oleophilic and oleophobic surfaces in air were performed [47]. Figure 20.91 shows the optical micrographs of droplets in three different phase interfaces on a flat epoxy resin and a micropatterned surface with  $C_{20}F_{42}$ . In a solid–air–water interface and a solid–air–oil interface, the water droplet and oil droplet showed contact angles of  $122^\circ$  and  $76^\circ$  for the flat epoxy resin with  $C_{20}F_{42}$  and contact angles of  $162^\circ$  and  $133^\circ$  for the micropatterned surface with  $23\ \mu\text{m}$  pitch with  $C_{20}F_{42}$ , respectively. However, in a solid–water–oil interface, the oil droplet in water was oleophilic and had contact angles of  $4^\circ$  and  $9^\circ$  for both surfaces, respectively. To explain why the oleophobic surfaces in air became oleophilic in water, the theoretical values for both surfaces were calculated using (20.55). For calculations, the surface tensions of the water–air interface ( $\gamma_{WA}$ ), oil–air interface ( $\gamma_{OA}$ ), and oil–water interface ( $\gamma_{OW}$ ) were taken to be 73, 27.5, and 51.4 mN/m, and the contact angles for water and oil droplets in air were taken from the measured values. The theoretical values for the flat epoxy resin and the micropatterned surface with  $23\ \mu\text{m}$  pitch with  $C_{20}F_{42}$  are  $28^\circ$  and  $10^\circ$ , respectively. These values are similar to those from the experiments. This indicates that the oleophobic surfaces become oleophilic in water.

To study optimization of oleophobicity in two solid–air–water and solid–air–oil interfaces, the static contact angles for water and oil droplets were measured on the micropatterned surfaces with different pitch values and with  $C_{20}F_{42}$  [47]. Figure 20.93 shows the measured static contact angle as a function of pitch between the pillars for a water droplet (circle) and an oil droplet (cross) in air. The data are compared with the predicted static contact angle values obtained using the Wenzel and Cassie–Baxter equations (20.24 and 20.25) (solid lines) with a measured value of  $\theta_0$  for the micropatterned surfaces with  $C_{20}F_{42}$ . In a solid–air–water interface for the water droplet, the flat epoxy resin with  $C_{20}F_{42}$  showed a static contact angle of  $122^\circ$ . The static contact angle of micropatterned surfaces with  $C_{20}F_{42}$  first increases from  $158^\circ$  to  $169^\circ$  with an increase in the pitch values, then starts to drop rapidly at a pitch value of  $110\ \mu\text{m}$ . From comparison of the experimental data to the Wenzel and Cassie–Baxter equations, this corresponds to the transition from Cassie–Baxter to Wenzel regime. All surfaces with  $C_{20}F_{42}$  had an increase in contact angle, and

the transition took place at higher pitch value than that of the micropatterned surfaces (Fig. 20.92).

At a solid–air–oil interface for an oil droplet, the flat epoxy resin with  $C_{20}F_{42}$  showed a static contact angle of  $76^\circ$ . As shown in Fig. 20.93, the highest contact angle of micropatterned surfaces with  $C_{20}F_{42}$  was  $133^\circ$  at a pitch value of  $23\ \mu\text{m}$ . Then, it decreases with an increase in the pitch values, and these values are comparable with the values predicted Wenzel equations. The contact angles of all micropatterned surfaces with  $C_{20}F_{42}$  are higher than that of the flat surfaces.

To study optimization of oleophobicity in a solid–water–oil interface, the static contact angles for oil droplets in water were measured on the micropatterned surfaces with different pitch values and with  $C_{20}F_{42}$  [47]. Figure 20.93 shows the measured static contact angle as a function of pitch between the pillars for an oil droplet in water (triangle). The data are compared with the predicted static contact

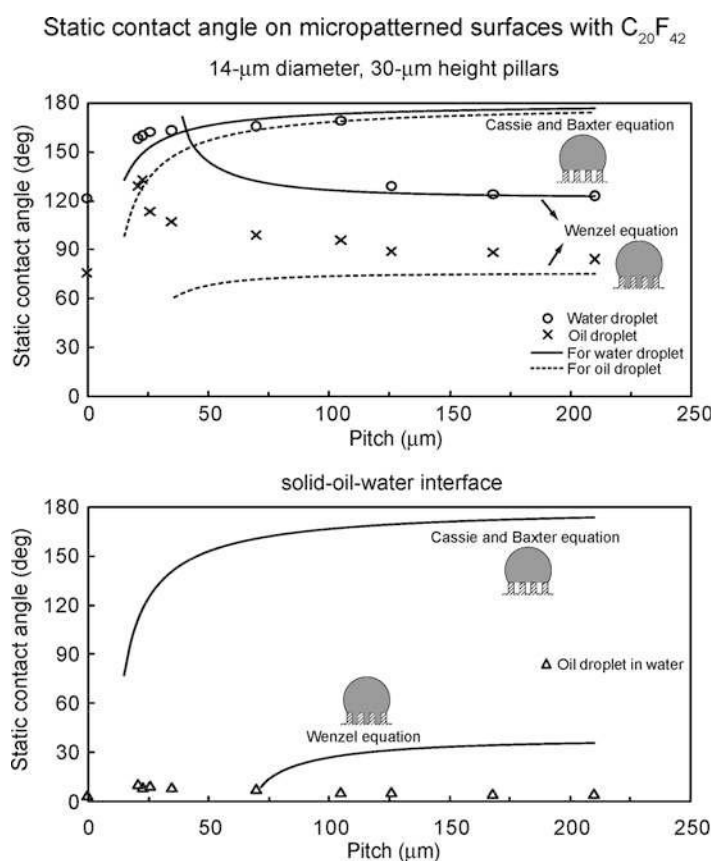


**Fig. 20.93** Static contact angle as a function of geometric parameters for water droplet (circle) and oil droplet (cross) in air, and oil droplet in water (triangle) compared with predicted static contact angle values obtained using Wenzel and Cassie–Baxter equations (solid lines) with a measured value of  $\theta_0$  for the micropatterned surfaces with  $C_{20}F_{42}$  [47]



angle values obtained using the Wenzel and Cassie–Baxter equations (20.24 and 20.25) (solid lines) with a measured value of  $\theta_0$  for the micropatterned surfaces with  $C_{20}F_{42}$ . In a solid–water–oil interface, the flat epoxy resin with  $C_{20}F_{42}$  was oleophilic and had a static contact angle of  $4^\circ$ . All micropatterned surfaces with  $C_{20}F_{42}$  were oleophilic and had contact angle lower than  $10^\circ$ . The reason why hydrophobic and oleophobic surfaces in air became oleophilic in water can be explained from Fig. 20.88 and Table 20.14. The contact angle for a water droplet is higher than that for an oil droplet on all surfaces with  $C_{20}F_{42}$ , and the surface tension of the water–air interface ( $\gamma_{WA}$ ) is higher than that of the oil–air interface ( $\gamma_{OA}$ ). Therefore, it is observed that  $\gamma_{WA} \cos \theta_W$  is higher than  $\gamma_{OA} \cos \theta_O$ , and then the surfaces become oleophilic in the solid–water–oil interface.

### 20.7.3.3 Wetting Behavior on Nano- and Hierarchical Structures and Shark Skin Replica

To observe the wetting behavior of water and oil droplets for nano- and hierarchical structures found from Lotus plant surfaces, experiments with the droplets on the surfaces were performed in the three phase interface [47]. Figure 20.94 shows the optical micrographs of droplets in three different phase interfaces on a nanostructure and a hierarchical structure fabricated with  $0.2 \mu\text{g}/\text{mm}^2$  mass of *n*-hexatriacontane.

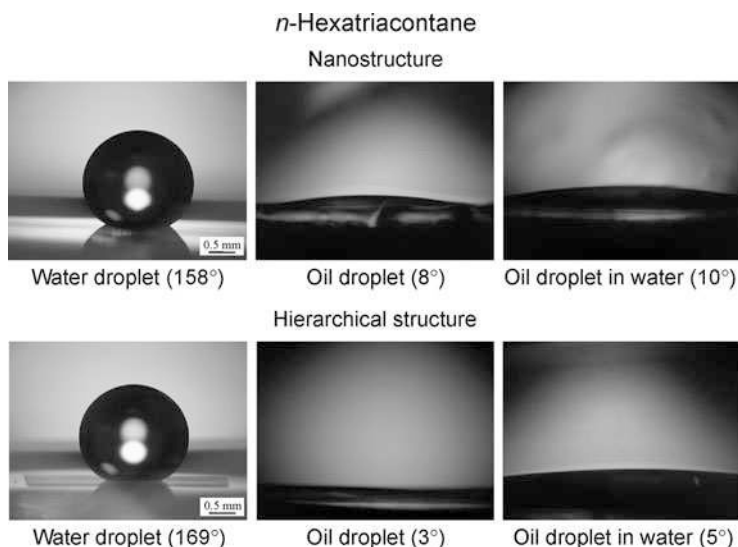


**Fig. 20.94** Optical micrographs of droplets in three different phase interfaces on nanostructure and hierarchical structure fabricated with  $0.2 \mu\text{g}/\text{mm}^2$  mass of *n*-hexatriacontane. *Left image*: a water droplet is placed on a surface in air. *Middle image*: an oil droplet is placed on a surface in air. *Right image*: an oil droplet is placed on a solid surface in water [47]



Both nano- and hierarchical structures were superhydrophobic and had a static contact angle of  $158^\circ$  and  $169^\circ$  in the solid–air–water interface, respectively. However, they are oleophilic in the solid–air–oil interface because the surface energy of *n*-hexatriacontane is  $31.4 \text{ mJ/m}^2$  ( $31.4 \text{ mN/m}$ ) [255], and this value is higher than that of an oil droplet (hexadecane). In the solid–water–oil interface, nano- and hierarchical structures had a static contact angle of  $10^\circ$  and  $5^\circ$ , respectively. As shown in Fig. 20.88 and Table 20.14, it is observed that both surfaces are oleophilic in solid–water–oil interface.

To study the surface structure on an aquatic animal, experiments with water and oil droplets on the shark skin replica were performed in a three phase interface [47]. Figure 20.95 shows the optical micrographs of droplets in three different phase interfaces on a shark skin replica without and with  $\text{C}_{20}\text{F}_{42}$ . First, the shark skin replica had contact angles of  $89^\circ$  and  $\sim 0^\circ$  for water and oil droplets, respectively. After the surface was coated with  $\text{C}_{20}\text{F}_{42}$ , the contact angles of water and oil droplets became  $142^\circ$  and  $115^\circ$ , respectively. In the solid–water–oil interface, the oil droplet in water on the shark skin replica became oleophobic and had a contact angle of  $109^\circ$ . Based on (20.55), the calculated value was  $59^\circ$  for the oil droplet in water on a shark skin replica. This difference may come from the open space under the scales of the shark skin replica responsible for the propensity of trapped water pocket formation as shown in Fig. 20.69. Shark skin replica with  $\text{C}_{20}\text{F}_{42}$  was oleophilic and had a contact angle of  $\sim 0^\circ$ . This state is the same as the micropatterned surfaces with  $\text{C}_{20}\text{F}_{42}$  as shown in Fig. 20.88 and Table 20.14.

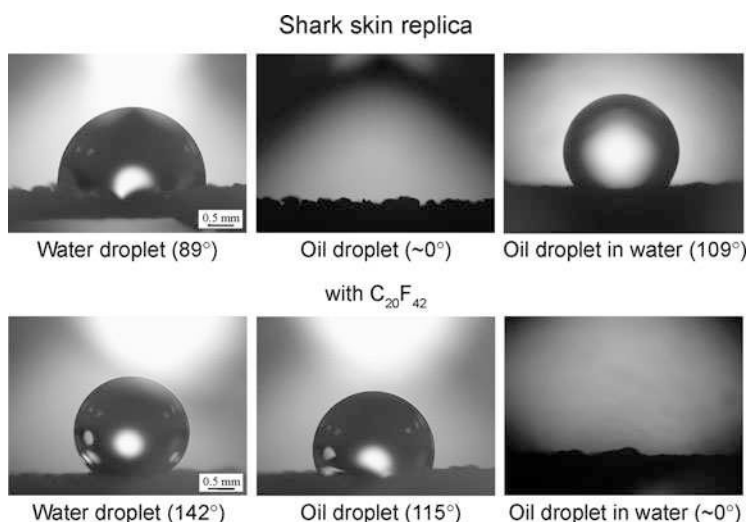


**Fig. 20.95** Optical micrographs of droplets in three different phase interfaces on shark skin replica without and with  $\text{C}_{20}\text{F}_{42}$ . *Left image*: a water droplet is placed on a surface in air. *Middle image*: an oil droplet is placed on a surface in air. *Right image*: an oil droplet is placed on a solid surface in water [47]

## 20.8 Closure

Biomimetics allows one to mimic biology or nature to develop materials and devices of commercial interest by engineers. Properties of biological materials and surfaces result from a complex interplay between surface morphology and physical and chemical properties. Hierarchical structures with dimensions of features ranging from the macroscale to the nanoscale are extremely common in nature to provide properties of interest. There are a large number of objects including bacteria, plants, land and aquatic animals and seashells, with properties of commercial interest. This article has focused on surfaces with superhydrophobicity, self-cleaning, low adhesion, and drag reduction, such as Lotus leaf and shark skin. The development of superhydrophobic and self-cleaning surfaces is important for basic research as well as various applications, including self-cleaning windows, exterior paints for buildings, navigation ships, textiles, solar panels, and applications requiring antifouling and a reduction in fluid flow, e.g., in micro/nanochannels. These surfaces can also be used in energy conversion and conservation.

In this article, the theoretical mechanisms of wetting of rough surfaces and characterization of natural and artificial surfaces with superhydrophobicity, self-cleaning, low adhesion and drag reduction has been presented. Theoretical approaches have been presented to understand these phenomena such as the transition between the Wenzel and Cassie–Baxter wetting regimes, contact angle hysteresis, the role of hierarchical roughness, and the possibility of the creation of reversible hydrophobicity. Based on learning from the theoretical background, various leaf surfaces on the micro- and nanoscale have been characterized and attempts are made to separate out the effects of the micro- and nanobumps and the wax on the hydrophobicity. The next logical step in realizing superhydrophobic surfaces is to design surfaces based on understanding of the leaves. Artificial superhydrophobic surfaces have been fabricated using various fabrication techniques. The influence of micro-, nano- and hierarchical structures on superhydrophobicity have been discussed by the investigation of static contact angle, contact angle hysteresis, evaporation, bouncing and vibration of a water droplet, and propensity of air pocket formation. In addition, their influence on adhesive force as well as efficiency of self-cleaning have been discussed. The models for the transition from Cassie–Baxter regime to Wenzel regime have been presented. Furthermore, the durability of the various fabricated surfaces has been discussed by the investigation of the loss of superhydrophobicity as well as wear and friction.

An aquatic animal, such as a shark, is another model from nature. Shark skin is covered by very small individual tooth-like scales called dermal denticles (little skin teeth), ribbed with longitudinal grooves (aligned parallel to the local flow direction of the water). These grooved scales reduce vortices formation present on a smooth surface, resulting in water moving efficiently over their surface. The artificial surfaces from the shark skin have been created and the influence of

structure has been discussed on measurement of pressure drop and fluid drag for drag reduction efficiency.

Oleophobic surfaces have the potential for self-cleaning and anti-fouling from biological and organic contaminants both in air and underwater applications. A model for predicting the contact angle of water and oil droplets has been presented. The surface tension of oil and organic liquids is lower than that of water. So to make the surface oleophobic in a solid–air–oil interface, a material with surface energy lower than that of oil should be used. The wetting behavior of water and oil droplets for hydrophobic/philic and oleophobic/philic surfaces in three phase interfaces has been investigated. For underwater applications, we have presented oleophobicity/philicity of oil droplet in water on the surfaces with different surface energies of various interfaces and contact angles of water and oil droplets in air.

This article provides a useful guide for the development of biomimetic artificial surfaces. Hierarchical structures are typical for surfaces with superhydrophobic, self-cleaning, low adhesion and drag reduction in nature. The flexible and low-cost technique demonstrates that hierarchical surfaces can be produced in the laboratory for further investigations of the properties of hierarchical structured materials. A proper control of roughness constitutes the main challenge in producing a reliable hierarchical surface and furthermore the mechanisms that trigger the Cassie–Baxter and Wenzel regime transitions still remain to be further investigated.

## References

1. B. Bhushan, Biomimetics: Lessons from nature – An overview. *Philos. Trans. R. Soc. A* **367**, 1445–1486 (2009)
2. J.E. Gordon, *The New Science of Strong Materials, or Why You Don't Fall Through the Floor*, 2nd edn. (Pelican–Penguin, London, 1976)
3. B. Bhushan, Y.C. Jung, K. Koch, Micro-, nano- and hierarchical structures for superhydrophobicity, self-cleaning and low adhesion. *Philos. Trans. R. Soc. A* **367**, 1631–1672 (2009)
4. K. Koch, B. Bhushan, W. Barthlott, Multifunctional surface structures of plants: An inspiration for biomimetics (invited). *Prog. Mater. Sci.* **54**, 137–178 (2009)
5. X.F. Gao, L. Jiang, Biophysics: Water-repellent legs of water striders. *Nature* **432**, 36 (2004)
6. H. Gao, X. Wang, H. Yao, S. Gorb, E. Arzt, Mechanics of hierarchical adhesion structures of geckos. *Mech. Mater.* **37**, 275–285 (2005)
7. W.E. Reif, Squamation and ecology of sharks. *Cour. Forschungsinst. Senckenb.* **78**, 1–255 (1985)
8. Y. Bar-Cohen, *Biomimetics: Biologically Inspired Technologies* (Taylor and Francis, Boca Raton, 2006)
9. J. Genzer, K. Efimenko, Recent developments in superhydrophobic surfaces and their relevance to marine fouling: A review. *Biofouling* **22**, 339–360 (2006)
10. C. Neinhuis, W. Barthlott, Characterization and distribution of water-repellent, self-cleaning plant surfaces. *Ann. Bot.* **79**, 667–677 (1997)
11. W. Barthlott, C. Neinhuis, Purity of the sacred lotus, or escape from contamination in biological surfaces. *Planta* **202**, 1–8 (1997)
12. P. Wagner, R. Furstner, W. Barthlott, C. Neinhuis, Quantitative assessment to the structural basis of water repellency in natural and technical surfaces. *J. Exp. Bot.* **54**, 1295–1303 (2003)

13. Z. Burton, B. Bhushan, Surface characterization and adhesion and friction properties of hydrophobic leaf surfaces. *Ultramicroscopy* **106**, 709–719 (2006)
14. B. Bhushan, Y.C. Jung, Micro and nanoscale characterization of hydrophobic and hydrophilic leaf surface. *Nanotechnology* **17**, 2758–2772 (2006)
15. K. Koch, B. Bhushan, W. Barthlott, Diversity of structure, morphology, and wetting of plant surfaces (invited). *Soft Matter* **4**, 1943–1963 (2008)
16. K. Autumn, Y.A. Liang, S.T. Hsieh, W. Zesch, W.P. Chan, T.W. Kenny, R. Fearing, R.J. Full, Adhesive force of a single gecko foot-hair. *Nature* **405**, 681–685 (2000)
17. B. Bhushan, Adhesion of multi-level hierarchical attachment systems in gecko feet. *J. Adhes. Sci. Technol.* **21**, 1213–1258 (2007)
18. D.W. Bechert, M. Bruse, W. Hage, Experiments with three-dimensional riblets as an idealized model of shark skin. *Exp. Fluids* **28**, 403–412 (2000)
19. H.-J. Jin, D.L. Kaplan, Mechanism of silk processing in insects and spiders. *Nature* **424**, 1057–1061 (2003)
20. M. Sarikaya, I.A. Aksay, *Biomimetic Design and Processing of Materials* (American Institute of Physics, Woodbury, 1995)
21. T. Mueller, Biomimetics design by nature. *Natl. Geogr.* **2008**, 68–90 (2008)
22. A.V. Adamson, *Physical Chemistry of Surfaces* (Wiley, New York, 1990)
23. J.N. Israelachvili, *Intermolecular and Surface Forces*, 2nd edn. (Academic, London, 1992)
24. B. Bhushan, *Principles and Applications of Tribology* (Wiley, New York, 1999)
25. B. Bhushan, *Introduction to Tribology* (Wiley, New York, 2002)
26. B. Bhushan, *Nanotribology and Nanomechanics – An Introduction*, 2nd edn. (Springer, Heidelberg, 2008)
27. M. Nosonovsky, B. Bhushan, *Multiscale Dissipative Mechanisms and Hierarchical Surfaces: Friction, Superhydrophobicity, and Biomimetics* (Springer, Heidelberg, 2008)
28. C.W. Extrand, Model for contact angle and hysteresis on rough and ultraphobic surfaces. *Langmuir* **18**, 7991–7999 (2002)
29. J. Kijlstra, K. Reihls, A. Klami, Roughness and topology of ultra-hydrophobic surfaces. *Colloids Surf. A Physicochem. Eng. Asp.* **206**, 521–529 (2002)
30. B. Bhushan, Y.C. Jung, Wetting, adhesion and friction of superhydrophobic and hydrophilic leaves and fabricated micro/nanopatterned surfaces. *J. Phys. Condens. Matter* **20**, 225010 (2008)
31. M. Nosonovsky, B. Bhushan, Multiscale friction mechanisms and hierarchical surfaces in nano- and bio-tribology. *Mater. Sci. Eng. R* **58**, 162–193 (2007)
32. M. Nosonovsky, B. Bhushan, Roughness-induced superhydrophobicity: A way to design non-adhesive surfaces. *J. Phys. Condens. Matter* **20**, 225009 (2008)
33. M. Nosonovsky, B. Bhushan, Biologically-inspired surfaces: Broadening the scope of roughness. *Adv. Funct. Mater.* **18**, 843–855 (2008)
34. B. Bhushan, Y.C. Jung, K. Koch, Self-cleaning efficiency of artificial superhydrophobic surfaces. *Langmuir* **25**, 3240–3248 (2009)
35. M. Nosonovsky, B. Bhushan, Superhydrophobicity for energy conversion and conservation applications. *J. Adhes. Sci. Technol.* **22**, 2105–2115 (2008)
36. M. Nosonovsky, B. Bhushan, Multiscale effects and capillary interactions in functional biomimetic surfaces for energy conversion and green engineering. *Philos. Trans. R. Soc. A* **367**, 1511–1539 (2009)
37. M. Nosonovsky, B. Bhushan, Superhydrophobic surfaces and emerging applications: Non-adhesion, energy, green engineering. *Curr. Opin. Colloid Interface Sci.* **14**, 270–280 (2009)
38. B. Bhushan, Adhesion and stiction: Mechanisms, measurement techniques and methods for reduction. *J. Vac. Sci. Technol. B* **21**, 2262–2296 (2003)
39. B. Bhushan, *Springer Handbook of Nanotechnology*, 2nd edn. (Springer, Heidelberg, 2007)
40. B. Bhushan, J.N. Israelachvili, U. Landman, Nanotribology: Friction, wear and lubrication at the atomic scale. *Nature* **374**, 607–616 (1995)

41. B. Bhushan, *Tribology and Mechanics of Magnetic Storage Systems*, 2nd edn. (Springer, New York, 1996)
42. B. Bhushan, *Tribology Issues and Opportunities in MEMS* (Kluwer, Dordrecht, 1998)
43. B. Bhushan, *Modern Tribology Handbook, Vol. 1 – Principles of Tribology; Vol. 2 – Materials, Coatings, and Industrial Applications* (CRC Press, Boca Raton, 2001)
44. K. Koch, B. Bhushan, Y.C. Jung, W. Barthlott, Fabrication of artificial Lotus leaves and significance of hierarchical structure for superhydrophobicity and low adhesion. *Soft Matter* **5**, 1386–1393 (2009)
45. X. Gao, X. Yan, X. Yao, L. Xu, K. Zhang, J. Zhang, B. Yang, L. Jiang, The dry-style antifogging properties of mosquito compound eyes and artificial analogues prepared by soft lithography. *Adv. Mater.* **19**, 2213–2217 (2007)
46. M. Liu, S. Wang, Z. Wei, Y. Song, L. Jiang, Bioinspired design of a superoleophobic and low adhesive water/solid interface. *Adv. Mater.* **21**, 665–669 (2009)
47. Y.C. Jung, B. Bhushan, Wetting behavior of water and oil droplets in three phase interfaces for hydrophobicity/phillcity and oleophobicity/phillcity. *Langmuir* **25**, 14165–14173 (2009)
48. Y.C. Jung, B. Bhushan, Biomimetic structures for fluid drag reduction in laminar and turbulent flows. *J. Phys. Condens. Matter* **22**, 035104 (2010)
49. R.N. Wenzel, Resistance of solid surfaces to wetting by water. *Ind. Eng. Chem.* **28**, 988–994 (1936)
50. A. Cassie, S. Baxter, Wettability of porous surfaces. *Trans. Faraday Soc.* **40**, 546–551 (1944)
51. R.E. Johnson, R.H. Dettre, Contact Angle Hysteresis, in *Contact Angle, Wettability, and Adhesion*, ed. by F.M. Fowkes. *Advances in Chemistry*, vol. 43 (American Chemical Society, Washington, 1964), pp. 112–135
52. J. Bico, U. Thiele, D. Quéré, Wetting of textured surfaces. *Colloids Surf. A* **206**, 41–46 (2002)
53. A. Marmur, Wetting on hydrophobic rough surfaces: To be heterogeneous or not to be? *Langmuir* **19**, 8343–8348 (2003)
54. A. Marmur, The Lotus effect: Superhydrophobicity and metastability. *Langmuir* **20**, 3517–3519 (2004)
55. A. Lafuma, D. Quéré, Superhydrophobic states. *Nat. Mater.* **2**, 457–460 (2003)
56. N.A. Patankar, Transition between superhydrophobic states on rough surfaces. *Langmuir* **20**, 7097–7102 (2004)
57. B. He, N.A. Patankar, J. Lee, Multiple equilibrium droplet shapes and design criterion for rough hydrophobic surfaces. *Langmuir* **19**, 4999–5003 (2003)
58. S. Herminghaus, Roughness-induced non-wetting. *Europhys. Lett.* **52**, 165–170 (2000)
59. N.A. Patankar, Mimicking the Lotus effect: Influence of double roughness structures and slender pillars. *Langmuir* **20**, 8209–8213 (2004)
60. M. Sun, C. Luo, L. Xu, H. Ji, Q. Ouyang, D. Yu, Y. Chen, Artificial lotus leaf by nanocasting. *Langmuir* **21**, 8978–8981 (2005)
61. M. Nosonovsky, B. Bhushan, Hierarchical roughness makes superhydrophobic surfaces stable. *Microelectronic Eng.* **84**, 382–386 (2007)
62. M. Nosonovsky, B. Bhushan, Biomimetic superhydrophobic surfaces: Multiscale approach. *Nano Lett.* **7**, 2633–2637 (2007)
63. M. Nosonovsky, B. Bhushan, Hierarchical roughness optimization for Biomimetic superhydrophobic surfaces. *Ultramicroscopy* **107**, 969–979 (2007)
64. M. Nosonovsky, B. Bhushan, Do hierarchical mechanisms of superhydrophobicity lead to self-organized criticality? *Scr. Mater.* **59**, 941–944 (2008)
65. S. Shibuchi, T. Onda, N. Satoh, K. Tsujii, Super-water-repellent surfaces resulting from fractal structure. *J. Phys. Chem.* **100**, 19512–19517 (1996)
66. M. Nosonovsky, B. Bhushan, Roughness optimization for biomimetic superhydrophobic surfaces. *Microsyst. Technol.* **11**, 535–549 (2005)
67. M. Nosonovsky, B. Bhushan, Stochastic model for metastable wetting of roughness-induced superhydrophobic surfaces. *Microsyst. Technol.* **12**, 231–237 (2006)

68. M. Nosonovsky, B. Bhushan, Wetting of rough three-dimensional superhydrophobic surfaces. *Microsyst. Technol.* **12**, 273–281 (2006)
69. B. Bhushan, Y.C. Jung, Wetting study of patterned surfaces for superhydrophobicity. *Ultramicroscopy* **107**, 1033–1041 (2007)
70. B. Bhushan, M. Nosonovsky, Y.C. Jung, Towards optimization of patterned superhydrophobic surfaces. *J. R. Soc. Interface* **4**, 643–648 (2007)
71. B. Bhushan, K. Koch, Y.C. Jung, Nanostructures for superhydrophobicity and low adhesion. *Soft Matter* **4**, 1799–1804 (2008)
72. B. Bhushan, K. Koch, Y.C. Jung, Biomimetic hierarchical structure for self-cleaning. *Appl. Phys. Lett.* **93**, 093101 (2008)
73. B. Bhushan, Y.C. Jung, A. Niemietz, K. Koch, Lotus-like biomimetic hierarchical structures developed by the self-assembly of tubular plant waxes. *Langmuir* **25**, 1659–1666 (2009)
74. B. Bhushan, K. Koch, Y.C. Jung, Fabrication and characterization of the hierarchical structure for superhydrophobicity. *Ultramicroscopy* **109**, 1029–1034 (2009)
75. Y.C. Jung, B. Bhushan, Wetting transition of water droplets on superhydrophobic patterned surfaces. *Scr. Mater.* **57**, 1057–1060 (2007)
76. Y.C. Jung, B. Bhushan, Wetting behavior during evaporation and condensation of water microdroplets on superhydrophobic patterned surfaces. *J. Microsc.* **229**, 127–140 (2008)
77. Y.C. Jung, B. Bhushan, Dynamic effects of bouncing water droplets on superhydrophobic surfaces. *Langmuir* **24**, 6262–6269 (2008)
78. Y.C. Jung, B. Bhushan, Dynamic effects induced transition of droplets on biomimetic superhydrophobic surfaces. *Langmuir* **25**, 9208–9218 (2009)
79. M. Nosonovsky, B. Bhushan, Patterned non-adhesive surfaces: Superhydrophobicity and wetting regime transitions. *Langmuir* **24**, 1525–1533 (2008)
80. M. Nosonovsky, B. Bhushan, Capillary effects and instabilities in nanocontacts. *Ultramicroscopy* **108**, 1181–1185 (2008)
81. M. Nosonovsky, B. Bhushan, Energy transitions in superhydrophobicity: Low adhesion, easy flow and bouncing. *J. Phys. Condens. Matter* **20**, 395005 (2008)
82. C.W. Extrand, Criteria for ultralyophobic surfaces. *Langmuir* **20**, 5013–5018 (2004)
83. J. Bico, C. Marzolin, D. Quere, Pearl drops. *Europhys. Lett.* **47**, 220–226 (1999)
84. D. Oner, T.J. McCarthy, Ultrahydrophobic surfaces. Effects of topography length scales on wettability. *Langmuir* **16**, 7777–778 (2000)
85. Z. Yoshimitsu, A. Nakajima, T. Watanabe, K. Hashimoto, Effects of surface structure on the hydrophobicity and sliding behavior of water droplets. *Langmuir* **18**, 5818–5822 (2002)
86. D. Richard, C. Clanet, D. Quere, Contact time of a bouncing drop. *Nature* **417**, 811 (2002)
87. D. Bartolo, F. Bouamrène, E. Verneuil, A. Buguin, P. Silberzan, S. Moulinet, Bouncing or sticky droplets: Impalement transitions on superhydrophobic micropatterned surfaces. *Europhys. Lett.* **74**, 299–305 (2006)
88. M. Reyssat, A. Pepin, F. Marty, Y. Chen, D. Quere, Bouncing transitions on microtextured materials. *Europhys. Lett.* **74**, 306–312 (2006)
89. C. Bourges-Monnier, M.E.R. Shanahan, Influence of evaporation on contact angle. *Langmuir* **11**, 2820–2829 (1995)
90. S.M. Rowan, M.I. Newton, G. McHale, Evaporation of microdroplets and the wetting of solid surfaces. *J. Phys. Chem.* **99**, 13268–13271 (1995)
91. H.Y. Erbil, G. McHale, M.I. Newton, Drop evaporation on solid surfaces: Constant contact angle mode. *Langmuir* **18**, 2636–2641 (2002)
92. G. McHale, S. Aqil, N.J. Shirtcliffe, M.I. Newton, H.Y. Erbil, Analysis of droplet evaporation on a superhydrophobic surface. *Langmuir* **21**, 11053–11060 (2005)
93. G.D. Danilatos, J.V. Brancik., Observation of liquid transport in the ESEM. In *Proceedings of the 44th Annual Meeting EMSA*, pp. 678–679
94. N.A. Stelmashenko, J.P. Craven, A.M. Donald, E.M. Terentjev, B.L. Thiel, Topographic contrast of partially wetting water droplets in environmental scanning electron microscopy. *J. Microsc.* **204**, 172–183 (2001)

95. F.G. Yost, J.R. Michael, E.T. Eisenmann, Extensive wetting due to roughness. *Acta Metall. Mater.* **45**, 299–305 (1995)
96. S. Semal, T.D. Blake, V. Geskin, M.L. de Ruijter, G. Castelein, J. De Coninck, Influence of surface roughness on wetting dynamics. *Langmuir* **15**, 8765–8770 (1999)
97. H.Y. Erbil, A.L. Demirel, Y. Avci, Transformation of a simple plastic into a superhydrophobic surface. *Science* **299**, 1377–1380 (2003)
98. Z. Burton, B. Bhushan, Hydrophobicity, adhesion, and friction properties of nanopatterned polymers and scale dependence for micro- and nanoelectromechanical systems. *Nano Lett.* **5**, 1607–1613 (2005)
99. Y.C. Jung, B. Bhushan, Contact angle, adhesion, and friction properties of micro- and nanopatterned polymers for superhydrophobicity. *Nanotechnology* **17**, 4970–4980 (2006)
100. Y.C. Jung, B. Bhushan, Mechanically durable CNT-composite hierarchical structures with superhydrophobicity, self-cleaning, and low-drag. *ACS Nano* **3**, 4155–4163 (2009)
101. S.G.G. Stokes, On the effect of the internal friction of fluids on the motion of pendulums. *Trans. Cambridge Philos. Soc.* **9**, 8–106 (1851)
102. G.K. Batchelor, *An Introduction to Fluid Dynamics* (Cambridge University Press, Cambridge, 1970)
103. S. Goldstein, *Modern Development in Fluid Dynamics* (Clarendon, Oxford, 1938)
104. S. Goldstein, Fluid Mechanics in first half of this century. *Annu. Rev. Fluid Mech.* **1**, 1–28 (1969)
105. E. Lauga, M.P. Brenner, H.A. Stone, *Handbook of Experimental Fluid Dynamics* (Springer, New-York, 2005)
106. C. Neto, D.R. Evans, E. Bonaccorso, H.-J. Butt, V.S.J. Carig, Boundary slip in Newtonian liquids: A review of experimental studies. *Rep. Prog. Phys.* **68**, 2859–2897 (2005)
107. A. Maali, B. Bhushan, Nanorheology and boundary slip in confined liquids using atomic force microscopy. *J. Phys.: Condens. Matter* **20**, 315201 (2008)
108. Y. Wang, B. Bhushan, A. Maali, Atomic force microscopy measurement of boundary slip on hydrophilic, hydrophobic, and superhydrophobic surfaces. *J. Vac. Sci. Technol. A* **27**, 754–760 (2009)
109. Y. Wang, B. Bhushan, Boundary slip and nanobubble study in micro/nanofluidics with atomic force microscope. *Soft Matter* **6**, 29–66 (2010)
110. J. Baudry, E. Charlaix, A. Tonck, D. Mazuyer, Experimental evidence for a large slip effect at a nonwetting fluid-solid interface. *Langmuir* **17**, 5232–5236 (2001)
111. Y. Zhu, S. Granick, Limits of the hydrodynamic no-slip boundary condition. *Phys. Rev. Lett.* **88**, 106102 (2002)
112. C. Cottin-Bizonne, B. Cross, A. Steinberger, E. Charlaix, Boundary slip on smooth hydrophobic surfaces: Intrinsic effects and possible artifacts. *Phys. Rev. Lett.* **94**, 056102 (2005)
113. O.I. Vinogradova, G.E. Yakubov, Dynamic effects on force measurements. 2. Lubrication and the atomic force microscope. *Langmuir* **19**, 1227–1234 (2003)
114. D.C. Tretheway, C.D. Meinhardt, Apparent fluid slip at hydrophobic microchannel walls. *Phys. Fluids* **14**, L9–L12 (2002)
115. C.D.F. Honig, W.A. Ducker, No-slip hydrodynamic boundary condition for hydrophilic particles. *Phys. Rev. Lett.* **98**, 028305 (2007)
116. A. Maali, Y. Wang, B. Bhushan, Evidence of the no-slip boundary condition of water flow between hydrophilic surfaces using atomic force microscopy. *Langmuir* **25**, 12002–12005 (2009)
117. E.T. Watts, J. Krim, A. Widom, Experimental-observation of interfacial slippage at the boundary of molecularly thin-films with gold substrates. *Phys. Rev. B* **41**, 3466–3472 (1990)
118. E. Lauga, H.A. Stone, Effective slip in pressure-driven stokes flow. *J. Fluid Mech.* **489**, 55–77 (2003)
119. C. Cottin-Bizonne, C. Barentin, E. Charlaix, L. Bocquet, J.L. Barrat, Dynamics of simple liquids at heterogeneous surfaces: Molecular-dynamics simulations and hydrodynamic description. *Eur. Phys. J. E* **15**, 427–438 (2004)

120. M. Sbragaglia, A. Prosperetti, Effective velocity boundary condition at a mixed slip surface. *J. Fluid Mech.* **578**, 435–451 (2007)
121. J. Ou, B. Perot, J.P. Rothstein, Laminar drag reduction in microchannels using ultrahydrophobic surfaces. *Phys. Fluids* **16**, 4635–4643 (2004)
122. C.-H. Choi, C.-J. Kim, Large slip of aqueous liquid flow over a nanoengineered superhydrophobic surface. *Phys. Rev. Lett.* **96**, 066001 (2006)
123. P. Joseph, C. Cottin-Bizonne, J.M. Benoit, C. Ybert, C. Journet, P. Tabeling, L. Bocquet, Slippage of water past superhydrophobic carbon nanotube forests in microchannels. *Phys. Rev. Lett.* **97**, 156104 (2006)
124. S. Shibuichi, T. Yamamoto, T. Onda, K. Tsujii, Super water- and oil-repellent surfaces resulting from fractal structure. *J. Colloid Interface Sci.* **208**, 287–294 (1998)
125. H. Li, X. Wang, Y. Song, Y. Liu, Q. Li, L. Jiang, D. Zhu, Super-“amphiphobic” aligned carbon nanotube films. *Angew. Chem. Int. Ed. Engl.* **40**, 1743–1746 (2001)
126. M. Kiuru, E. Alakoski, Low sliding angles in hydrophobic and oleophobic coatings prepared with plasma discharge method. *Mater. Lett.* **58**, 2213–2216 (2004)
127. Q. Xie, J. Xu, L. Feng, L. Jiang, W. Tang, X. Luo, C.C. Han, Facile creation of a superamphiphobic coating surface with bionic microstructure. *Adv. Mater.* **16**, 302–305 (2004)
128. M. Nicolas, F. Guittard, S. Geribaldi, Synthesis of stable super water- and oil-repellent polythiophene films. *Angew. Chem. Int. Ed. Engl.* **45**, 2251–2254 (2006)
129. H.F. Hoefnagels, D. Wu, G. de With, W. Ming, Biomimetic superhydrophobic and highly oleophobic cotton textiles. *Langmuir* **23**, 13158–13163 (2007)
130. A. Tuteja, W. Choi, M. Ma, J.M. Mabry, S.A. Mazzella, G.C. Rutledge, G.H. McKinley, R.E. Cohen, Designing superoleophobic surfaces. *Science* **318**, 1618–1622 (2007)
131. P.G. de Gennes, F. Brochard-Wyart, D. Quéré, *Capillarity and Wetting Phenomena* (Springer, Berlin, 2003)
132. J.N. Israelachvili, M.L. Gee, Contact angles on chemically heterogeneous surfaces. *Langmuir* **5**, 288–289 (1989)
133. O.N. Tretinnikov, Wettability and Microstructure of Polymer Surfaces: Stereochemical and Conformational Aspects, in *Apparent and Microscopic Contact Angles*, ed. by J. Drelich, J.S. Laskowski, K.L. Mittal (VSP, Utrecht, 2000), pp. 111–128
134. W. Li, A. Amirfazli, A thermodynamic approach for determining the contact angle hysteresis for superhydrophobic surfaces. *J. Colloid. Interface Sci.* **292**, 195–201 (2006)
135. B.V. Derjaguin, N.V. Churaev, Structural component of disjoining pressure. *J. Colloid Interface Sci.* **49**, 249–255 (1974)
136. A. Checco, P. Guenoun, J. Daillant, Nonlinear dependence of the contact angle of nanodroplets on contact line curvatures. *Phys. Rev. Lett.* **91**, 186101 (2003)
137. M.A. Anisimov, Divergence of Tolman’s length for a droplet near the critical point. *Phys. Rev. Lett.* **98**, 035702 (2007)
138. T. Pompe, A. Fery, S. Herminghaus, Measurement of Contact Line Tension by Analysis of the Three-Phase Boundary with Nanometer Resolution, in *Apparent and Microscopic Contact Angles*, ed. by J. Drelich, J.S. Laskowski, K.L. Mittal (VSP, Utrecht, 2000), pp. 3–12
139. L. Boruvka, A.W. Neumann, Generalization of the classical theory of capillarity. *J. Chem. Phys.* **66**, 5464–5476 (1977)
140. L. Gao, T.J. McCarthy, How Wenzel and Cassie were wrong. *Langmuir* **23**, 3762–3765 (2007)
141. C.W. Extrand, Contact angle hysteresis on surfaces with chemically heterogeneous islands. *Langmuir* **19**, 3793–3796 (2003)
142. M. Nosonovsky, On the range of applicability of the Wenzel and Cassie equations. *Langmuir* **23**, 9919–9920 (2007)
143. L. Barbieri, E. Wagner, P. Hoffmann, Water wetting transition parameters of perfluorinated substrates with periodically distributed flat-top microscale obstacles. *Langmuir* **23**, 1723–1734 (2007)



144. F.E. Bartell, J.W. Shepard, Surface roughness as related to hysteresis of contact angles. *J. Phys. Chem.* **57**, 455–458 (1953)
145. P. Gupta, A. Ulman, F. Fanfan, A. Korniaikov, K. Loos, Mixed self-assembled monolayer of alkanethiolates on ultrasmooth gold do not exhibit contact angle hysteresis. *J. Am. Chem. Soc.* **127**, 4–5 (2005)
146. N. Eustathopoulos, M.G. Nicholas, B. Drevet, *Wettability at High Temperatures* (Pergamon, Amsterdam, 1999)
147. M. Nosonovsky, Model for solid-liquid and solid-solid friction for rough surfaces with adhesion hysteresis. *J. Chem. Phys.* **126**, 224701 (2007)
148. Y.T. Cheng, D.E. Rodak, A. Angelopoulos, T. Gacek, Microscopic observations of condensation of water on lotus leaves. *Appl. Phys. Lett.* **87**, 194112 (2005)
149. M. Nosonovsky, Multiscale roughness and stability of superhydrophobic biomimetic interfaces. *Langmuir* **23**, 3157–3161 (2007)
150. H. Kamusewitz, W. Possart, D. Paul, The relation between Young's equilibrium contact angle and the hysteresis on rough paraffin wax surfaces. *Colloids Surf. A Physicochem. Eng. Asp.* **156**, 271–279 (1999)
151. T.N. Krupenkin, J.A. Taylor, T.M. Schneider, S. Yang, From rolling ball to complete wetting: The dynamic tuning of liquids on nanostructured surfaces. *Langmuir* **20**, 3824–3827 (2004)
152. V. Bahadur, S.V. Garimella, Electrowetting-based control of static droplet states on rough surfaces. *Langmuir* **23**, 4918–4924 (2007)
153. X.J. Feng, L. Feng, M.H. Jin, J. Zhai, L. Jiang, D.B. Zhu, Reversible super-hydrophobicity to super-hydrophilicity transition of aligned ZnO nanorod films. *J. Am. Chem. Soc.* **126**, 62–63 (2004)
154. E. Bormashenko, R. Pogreb, G. Whyman, M. Erlich, Cassie–Wenzel wetting transition in vibrated drops deposited on the rough surfaces: Is dynamic Cassie–Wenzel transition 2D or 1D affair? *Langmuir* **23**, 6501–6503 (2007)
155. D. Quéré, Non-sticking drops. *Rep. Prog. Phys.* **68**, 2495–2535 (2005)
156. C. Ishino, K. Okumura, Nucleation scenarios for wetting transition on textured surfaces: The effect of contact angle hysteresis. *Europhys. Lett.* **76**, 464–470 (2006)
157. E. Bormashenko, Y. Bormashenko, T. Stein, G. Whyman, R. Pogreb, Z. Barkay, Environmental scanning electron microscope study of the fine structure of the triple line and Cassie–Wenzel wetting transition for sessile drops deposited on rough polymer substrates. *Langmuir* **23**, 4378–4382 (2007)
158. E.A. Baker, Chemistry and Morphology of Plant Epicuticular Waxes, in *The Plant Cuticle*, ed. by D.F. Cutler, K.L. Alvin, C.E. Price (Academic, London, 1982), pp. 139–165
159. R. Jetter, L. Kunst, A.L. Samuels, Composition of Plant Cuticular Waxes, in *Biology of the Plant Cuticle*, ed. by M. Riederer, C. Müller (Blackwell, Oxford, 2006), pp. 145–181
160. K. Koch, B. Bhushan, H.-J. Enskat, W. Barthlott, Self-healing of voids in the wax coating on plant surfaces. *Philos. Trans. R. Soc. A* **367**, 1673–1688 (2009)
161. K. Koch, A. Dommisse, W. Barthlott, Chemistry and crystal growth of plant wax tubules of Lotus (*Nelumbo nucifera*) and *Nasturtium* (*Tropaeolum majus*) leaves on technical substrates. *Cryst. Growth Des.* **6**, 2571–2578 (2006)
162. C.Y. Poon, B. Bhushan, Comparison of surface Roughness measurements by stylus profiler, AFM and non-contact optical profiler. *Wear* **190**, 76–88 (1995)
163. V.N. Koinar, B. Bhushan, Effect of scan size and surface roughness on microscale friction measurements. *J. Appl. Phys.* **81**, 2472–2479 (1997)
164. N.S. Tambe, B. Bhushan, Scale dependence of micro/nano-friction and adhesion of MEMS/NEMS materials, coatings and lubricants. *Nanotechnology* **15**, 1561–1570 (2004)
165. R. Furstner, W. Barthlott, C. Neinhuis, P. Walzel, Wetting and self-cleaning properties of artificial superhydrophobic surfaces. *Langmuir* **21**, 956–961 (2005)
166. L. Gao, T.J. McCarthy, The lotus effect explained: Two reasons why two length scales of topography are important. *Langmuir* **22**, 2966–2967 (2006)

167. J.L. Zhang, J.A. Li, Y.C. Han, Superhydrophobic PTFE surfaces by extension. *Macromol. Rapid Commun.* **25**, 1105–1108 (2004)
168. J. Shiu, C. Kuo, P. Chen, C. Mou, Fabrication of tunable superhydrophobic surfaces by nanosphere lithography. *Chem. Mater.* **16**, 561–564 (2004)
169. H. Yabu, M. Shimomura, Single-step fabrication of transparent superhydrophobic porous polymer films. *Chem. Mater.* **17**, 5231–5234 (2005)
170. L. Xu, W. Chen, A. Mulchandani, Y. Yan, Reversible conversion of conducting polymer films from superhydrophobic to superhydrophilic. *Angew. Chem. Int. Ed. Engl.* **44**, 6009–6012 (2005)
171. M.T. Khorasani, H. Mirzadeh, Z. Kermani, Wettability of porous polydimethylsiloxane surface: Morphology study. *Appl. Surf. Sci.* **242**, 339–345 (2005)
172. M. Ma, R.M. Hill, J.L. Lowery, S.V. Fridrikh, G.C. Rutledge, Electrospun poly(styrene-block-dimethylsiloxane) block copolymer fibers exhibiting superhydrophobicity. *Langmuir* **21**, 5549–5554 (2005)
173. E. Bormashenko, T. Stein, G. Whyman, Y. Bormashenko, E. Pogreb, Wetting properties of the multiscaled nanostructured polymer and metallic superhydrophobic surfaces. *Langmuir* **22**, 9982–9985 (2006)
174. W. Lee, M. Jin, W. Yoo, J. Lee, Nanostructuring of a polymeric substrate with well-defined nanometer-scale topography and tailored surface wettability. *Langmuir* **20**, 7665–7669 (2004)
175. N. Chiou, C. Lu, J. Guan, L.J. Lee, A.J. Epstein, Growth and alignment of polyaniline nanofibres with superhydrophobic, superhydrophilic and other properties. *Nat. Nanotechnol.* **2**, 354–357 (2007)
176. K. Teshima, H. Sugimura, Y. Inoue, O. Takai, A. Takano, Transparent ultra water-repellent poly(ethylene terephthalate) substrates fabricated by oxygen plasma treatment and subsequent hydrophobic coating. *Appl. Surf. Sci.* **244**, 619–622 (2005)
177. N.J. Shirtcliffe, G. McHale, M.I. Newton, C.C. Perry, P. Roach, Porous materials show superhydrophobic to superhydrophilic switching. *Chem. Commun.* **25**, 3135–3137 (2005)
178. B. Qian, Z. Shen, Fabrication of superhydrophobic surfaces by dislocation-selective chemical etching on aluminum, copper, and zinc substrates. *Langmuir* **21**, 9007–9009 (2005)
179. N.J. Shirtcliffe, G. McHale, M.I. Newton, G. Chabrol, C.C. Perry, Dual-scale roughness produces unusually water-repellent surfaces. *Adv. Mater.* **16**, 1929–1932 (2004)
180. E. Martinez, K. Seunarine, H. Morgan, N. Gadegaard, C.D.W. Wilkinson, M.O. Riehle, Superhydrophobicity and superhydrophilicity of regular nanopatterns. *Nano Lett.* **5**, 2097–2103 (2005)
181. C. Martin, G. Rius, X. Borriase, F. Perez-Murano, Nanolithography on thin layers of PMMA using atomic force microscopy. *Nanotechnology* **16**, 1016–1022 (2005)
182. B. Cappella, E. Bonaccorso, Solvent-assisted nanolithography on polystyrene surfaces using the atomic force microscope. *Nanotechnology* **18**, 155307 (2007)
183. H. Jansen, M. de Boer, R. Legtenberg, M. Elwenspoek, The black silicon method: A universal method for determining the parameter setting of a fluorine-based reactive ion etcher in deep silicon trench etching with profile control. *J. Micromech. Microeng.* **5**, 115–120 (1995)
184. M. Hikita, K. Tanaka, T. Nakamura, T. Kajiyama, A. Takahara, Superliquid-repellent surfaces prepared by colloidal silica nanoparticles covered with fluoroalkyl groups. *Langmuir* **21**, 7299–7302 (2005)
185. H.M. Shang, Y. Wang, S.J. Limmer, T.P. Chou, K. Takahashi, G.Z. Cao, Optically transparent superhydrophobic silica-based films. *Thin Solid Films* **472**, 37–43 (2005)
186. Y. Zhao, M. Li, Q. Lu, Z. Shi, Superhydrophobic polyimide films with a hierarchical topography: Combined replica molding and layer-by-layer assembly. *Langmuir* **24**, 12651–12657 (2008)
187. L. Zhai, F.C. Cebeci, R.E. Cohen, M.F. Rubner, Stable superhydrophobic coatings from polyelectrolyte multilayers. *Nano Lett.* **4**, 1349–1353 (2004)

188. R.J. Klein, P.M. Biesheuvel, B.C. Yu, C.D. Meinhart, F.F. Lange, Producing superhydrophobic surfaces with nano-silica spheres. *Z. Metallkd.* **94**, 377–380 (2003)
189. W. Ming, D. Wu, R. van Benthem, G. de With, Superhydrophobic films from raspberry-like particles. *Nano Lett.* **5**, 2298–2301 (2005)
190. X. Zhang, S. Feng, X. Yu, H. Liu, Y. Fu, Z. Wang, L. Jiang, X. Li, Polyelectrolyte multilayer as matrix for electrochemical deposition of gold clusters: Toward super-hydrophobic surface. *J. Am. Chem. Soc.* **126**, 3064–3065 (2004)
191. K.K.S. Lau, J. Bico, K.B.K. Teo, M. Chhowalla, G.A.J. Amaratunga, W.I. Milne, G.H. McKinley, K.K. Gleason, Superhydrophobic carbon nanotube forests. *Nano Lett.* **3**, 1701–1705 (2003)
192. L. Huang, S.P. Lau, H.Y. Yang, E.S.P. Leong, S.F. Yu, Stable superhydrophobic surface via carbon nanotubes coated with a ZnO thin film. *J. Phys. Chem.* **109**, 7746–7748 (2005)
193. S. Wang, H. Liu, D. Liu, X. Ma, X. Fang, L. Jiang, Enthalpy driven three state switching of a superhydrophilic/superhydrophobic surfaces. *Angew. Chem. Int. Ed. Engl.* **46**, 3915–3917 (2007)
194. T.N. Krupenkin, J.A. Taylor, E.N. Wang, P. Kolodner, M. Hodes, T.R. Salamon, Reversible wetting-dewetting transitions on deelectrically tunable superhydrophobic nanostructured surfaces. *Langmuir* **23**, 9128–9133 (2007)
195. A. Nakajima, A. Fujishima, K. Hashimoto, T. Watanabe, Preparation of transparent superhydrophobic boehmite and silica films by sublimation of aluminum acetylacetonate. *Adv. Mater.* **11**, 1365–1368 (1999)
196. M. Ma, R.M. Hill, Superhydrophobic surfaces. *Curr. Opin. Colloid Interface Sci.* **11**, 193–202 (2006)
197. S.R. Coulson, I. Woodward, J.P.S. Badyal, S.A. Brewer, C. Willis, Super-repellent composite fluoropolymer surfaces. *J. Phys. Chem. B* **104**, 8836–8840 (2000)
198. M.E. Abdelsalam, P.N. Bartlett, T. Kelf, J. Baumberg, Wetting of regularly structured gold surfaces. *Langmuir* **21**, 1753–1757 (2005)
199. L. Zhu, Y. Xiu, J. Xu, P.A. Tamirisa, D.W. Hess, C. Wong, Superhydrophobicity on two-tier rough surfaces fabricated by controlled growth of aligned carbon nanotube arrays coated with fluorocarbon. *Langmuir* **21**, 11208–11212 (2005)
200. Y. Zhao, T. Tong, L. Delzeit, A. Kashani, M. Meyyappan, A. Majumdar, Interfacial energy and strength of multiwalled-carbon-nanotube-based dry adhesive. *J. Vac. Sci. Technol. B* **24**, 331–335 (2006)
201. N. Zhao, Q.D. Xie, L.H. Weng, S.Q. Wang, X.Y. Zhang, J. Xu, Superhydrophobic surface from vapor-induced phase separation of copolymer micellar solution. *Macromolecules* **38**, 8996–8999 (2005)
202. X. Wu, L. Zheng, D. Wu, Fabrication of superhydrophobic surfaces from microstructured ZnO-based surfaces via a wet-chemical route. *Langmuir* **21**, 2665–2667 (2005)
203. J.T. Han, Y. Jang, D.Y. Lee, J.H. Park, S.H. Song, D.Y. Ban, K. Cho, Fabrication of a bionic superhydrophobic metal surface by sulfur-induced morphological development. *J. Mater. Chem.* **15**, 3089–3092 (2005)
204. E. Hosono, S. Fujihara, I. Honma, H. Zhou, Superhydrophobic perpendicular nanopin film by the bottom-up process. *J. Am. Chem. Soc.* **127**, 13458–13459 (2005)
205. F. Shi, Y. Song, J. Niu, X. Xia, Z. Wang, X. Zhang, Facile method to fabricate a large-scale superhydrophobic surface by galvanic cell reaction. *Chem. Mater.* **18**, 1365–1368 (2006)
206. M.T. Northen, K.L. Turner, A batch fabricated biomimetic dry adhesive. *Nanotechnology* **16**, 1159–1166 (2005)
207. M.A.S. Chong, Y.B. Zheng, H. Gao, L.K. Tan, Combinational template-assisted fabrication of hierarchically ordered nanowire arrays on substrates for device applications. *Appl. Phys. Lett.* **89**, 233104 (2006)
208. Y. Wang, Q. Zhu, H. Zhang, Fabrication and magnetic properties of hierarchical porous hollow nickel microspheres. *J. Mater. Chem.* **16**, 1212–1214 (2006)
209. D. Kim, W. Hwang, H.C. Park, K.H. Lee, Superhydrophobic micro- and nanostructures based on polymer sticking. *Key Eng. Mat.* **334–335**, 897–900 (2007)

210. A. del Campo, C. Greiner, SU-8: A photoresist for high-aspect-ratio and 3D submicron lithography. *J. Micromech. Microeng.* **17**, R81–R95 (2007)
211. B. Cortese, S.D. Amone, M. Manca, I. Viola, R. Cingolani, G. Gigli, Superhydrophobicity due to the hierarchical scale roughness of pdms surfaces. *Langmuir* **24**, 2712–2718 (2008)
212. C.Y. Kuan, M.H. Hon, J.M. Chou, I.C. Leu, Wetting characteristics on micro/nanostructured zinc oxide coatings. *J. Electrochem. Soc.* **156**, J32–J36 (2009)
213. M. Brugnara, C. Della Volpe, S. Siboni, D. Zeni, Contact angle analysis on polymethyl-methacrylate and commercial wax by using an environmental scanning electron microscope. *Scanning* **28**, 267–273 (2006)
214. Y.C. Jung, B. Bhushan, Technique to measure contact angle of micro/nanodroplets using atomic force microscopy. *J. Vac. Sci. Technol. A* **26**, 777–782 (2008)
215. J.P. Cleveland, S. Manne, D. Bocek, P.K. Hansma, A nondestructive method for determining the spring constant of cantilevers for scanning force microscopy. *Rev. Sci. Instrum.* **64**, 403–405 (1993)
216. B. Bhushan, G.S. Blackman, Atomic force microscopy of magnetic rigid disks and sliders and its applications to tribology. *ASME J Tribol* **113**, 452–457 (1991)
217. N. Chen, B. Bhushan, Atomic force microscopy studies of conditioner thickness distribution and binding interactions on the hair surface. *J. Microsc.* **221**, 203–215 (2006)
218. R.A. Lodge, B. Bhushan, Surface characterization of human hair using tapping mode atomic force microscopy and measurement of conditioner thickness distribution. *J. Vac. Sci. Technol. A* **24**, 1258–1269 (2006)
219. S.E. Choi, P.J. Yoo, S.J. Baek, T.W. Kim, H.H. Lee, An ultraviolet-curable mold for sub-100-nm lithography. *J. Am. Chem. Soc.* **126**, 7744–7745 (2004)
220. B. Bhushan, D. Hansford, K.K. Lee, Surface modification of silicon and polydimethylsiloxane surfaces with vapor-phase-deposited ultrathin fluorosilane films for biomedical nanodevices. *J. Vac. Sci. Technol. A* **24**, 1197–1202 (2006)
221. T. Pompe, S. Herminghaus, Three-phase contact line energetics from nanoscale liquid surface topographies. *Phys. Rev. Lett.* **85**, 1930–1933 (2000)
222. D. Quere, Surface wetting model droplets. *Nat. Mater.* **3**, 79–80 (2004)
223. T. Kasai, B. Bhushan, G. Kulik, L. Barbieri, P. Hoffmann, Micro/nanotribological study of perfluorosilane SAMs for antistiction and low wear. *J. Vac. Sci. Technol. B* **23**, 995–1003 (2005)
224. X. Zhang, S. Tan, N. Zhao, X. Guo, X. Zhang, Y. Zhang, J. Xu, Evaporation of sessile water droplets on superhydrophobic natural lotus and biomimetic polymer surfaces. *Chemphyschem* **7**, 2067–2070 (2006)
225. K. Koch, A. Dommisse, W. Barthlott, S. Gorb, The use of plant waxes as templates for micro- and nanopatterning of surfaces. *Acta Biomater.* **3**, 905–909 (2007)
226. K. Koch, A.J. Schulte, A. Fischer, S.N. Gorb, W. Barthlott, A fast and low-cost replication technique for nano- and high-aspect-ratio structures of biological and artificial Materials. *Bioinspir. Biomim.* **3**, 046002 (2008)
227. R.F. Bunshah, *Handbook of Deposition Technologies for Films and Coatings: Science, Technology and Applications* (Applied Science Publishers, Westwood, 1994)
228. A. Niemietz, K. Wandelt, W. Barthlott, K. Koch, Thermal evaporation of multi-component waxes and thermally activated formation of nano-tubules for superhydrophobic surfaces. *Prog. Org. Coat.* **66**, 221–227 (2009)
229. D.L. Dorset, W.A. Pangborn, A.J. Hancock, Epitaxial crystallization of alkane chain lipids for electron diffraction analysis. *J. Biochem. Biophys. Methods* **8**, 29–40 (1983)
230. K. Koch, W. Barthlott, S. Koch, A. Hommes, K. Wandelt, W. Mamdough, S. De-Feyter, P. Broekmann, Structural analysis of wheat wax (*Triticum aestivum*, c.v. ‘Naturastar’ L.): From the molecular level to three dimensional crystals. *Planta* **223**, 258–270 (2006)
231. A. Tuteja, W. Choi, G.H. McKinley, R.E. Cohen, M.F. Rubner, Design parameters for superhydrophobicity and superoleophobicity. *Science* **318**, 1618 (2008)

232. A.I.J.M. van Dijk, L.A. Bruijnzeel, C.J. Rosewell, Rainfall intensity–kinetic energy relationships: A critical literature appraisal. *J. Hydrol.* **261**, 1–23 (2002)
233. H. Lamb, *Hydrodynamics* (Cambridge university press, Cambridge, 1932)
234. X. Noblin, A. Buguin, F. Brochard-Wyart, Vibrated sessile drops: Transition between pinned and mobile contact line oscillations. *Eur. Phys. J. E* **14**, 395–404 (2004)
235. F. Celestini, R. Kofman, Vibration of submillimeter-size supported droplets. *Phys. Rev. E* **73**, 041602 (2006)
236. R.J. Good, A thermodynamic derivation of Wenzel’s modification of Young’s equation for contact angles; together with a theory of hysteresis. *J. Am. Chem. Soc.* **74**, 5041–5042 (1952)
237. Y.L. Chen, C.A. Helm, J.N. Israelachvili, Molecular mechanisms associated with adhesion and contact angle hysteresis of monolayer surfaces. *J. Phys. Chem.* **95**, 10736–10747 (1991)
238. J.F. Joanny, P.G. de Gennes, A model for contact angle hysteresis. *J. Chem. Phys.* **81**, 552–562 (1984)
239. S.-W. Lee, P.E. Laibinis, Directed movement of liquids on patterned surfaces using non-covalent molecular adsorption. *J. Am. Chem. Soc.* **122**, 5395–5396 (2000)
240. M.S. Dresselhaus, G. Dresselhaus, Ph Avouris, *Carbon Nanotubes: Synthesis, Structure, Properties, and Applications* (Springer, Heidelberg, 2000)
241. M. Meyyappan, *Carbon Nanotubes – Science and Applications* (CRC Press, Boca Raton, 2005)
242. X.H. Chen, C.S. Chen, H.N. Xiao, H.B. Liu, L.P. Zhou, S.L. Li, G. Zhang, Dry friction and wear characteristics of nickel/carbon nanotube electroless composite deposits. *Tribol. Int.* **39**, 22–28 (2006)
243. W.D. Callister, *Materials Science and Engineering – An Introduction*, 5th edn. (Wiley, New York, 2000)
244. B. Bhushan, B.K. Gupta, *Handbook of Tribology: Materials, Coatings, and Surface Treatments* (McGraw-Hill, New York, 1991)
245. E.W. Wong, P.E. Sheehan, C.M. Lieber, Nanobeam mechanics: Elasticity, strength, and toughness of nanorods and nanotubes. *Science* **277**, 1971–1975 (1997)
246. Y.Y. Zhang, C.M. Wang, V.B.C. Tan, Examining the effects of wall numbers on buckling behavior and mechanical properties of multiwalled carbon nanotubes via molecular dynamics simulations. *J. Appl. Phys.* **103**, 053505 (2008)
247. R.D. Blevins, *Applied Fluid Dynamics Handbook* (Van Nostrand Reinhold, New York, 1984)
248. O.C. Jones, An improvement in the calculation of turbulent friction in rectangular ducts. *J. Fluids Eng.* **98**, 173–180 (1976)
249. D.W. Bechert, M. Bruse, W. Hage, J.G.T. Van Der Hoeven, G. Hoppe, Experiments on drag-reducing surfaces and their optimization with an adjustable geometry. *J. Fluid Mech.* **338**, 59–87 (1997)
250. D.R. Lide, *CRC Handbook of Chemistry and Physics*, 89th edn. (CRC Press, Boca Raton, 2009)
251. Y. Zhu, S. Granick, Rate-dependent slip of Newtonian liquid at smooth surfaces. *Phys. Rev. Lett.* **87**, 096105 (2001)
252. J.J. Bertin, *Aerodynamics for Engineers* (Prentice Hall, New Jersey, 1979)
253. K. Tajima, T. Tsutsui, H. Murata, Thermodynamic relation of interfacial tensions in three fluid phases. *Bull. Chem. Soc. Jpn.* **53**, 1165–1166 (1980)
254. T. Nishino, M. Meguro, K. Nakamae, M. Matsushita, Y. Ueda, The lowest surface free energy based on  $-\text{CF}_3$  alignment. *Langmuir* **15**, 4321–4323 (1999)
255. S. Wu, Surface-tension of solids–equation of state analysis. *J. Colloid Interface Sci.* **71**, 605–609 (1979)

# Chapter 21

## Gecko Feet: Natural Hairy Attachment Systems for Smart Adhesion

**Bharat Bhushan**

**Abstract** The leg attachment pads of several creatures, including many insects, spiders, and lizards, are capable of attaching to a variety of surfaces and are used for locomotion. Geckoes, in particular, have the largest mass and have developed the most complex hairy attachment structures capable of smart adhesion – the ability to cling to different smooth and rough surfaces and detach at will. These animals make use of about three million microscale hairs (setae) (about  $14,000 \text{ mm}^{-2}$ ) that branch off into hundreds of nanoscale spatulae (about three billion spatula on two feet). This so-called division of contacts provides high dry adhesion. This multiple-level hierarchically structured surface construction provides the gecko with the compliance and adaptability to create a large real area of contact with a variety of surfaces. Modeling of the gecko attachment system as a hierarchical spring model has provided insight into the adhesion enhancement generated by this system. van der Waals forces are the primary mechanism utilized to adhere to surfaces, and capillary forces are a secondary effect that can further increase the adhesion force. Preload applied to the setae increases adhesive force. Although a gecko is capable of producing of the order of 20 N of adhesive force, it retains the ability to remove its feet from an attachment surface at will. The adhesive strength of gecko setae is dependent on orientation; maximum adhesion occurs at  $30^\circ$ . During walking, a gecko is able to peel its foot from surfaces by changing the angle at which its setae contact the surface. Manmade fibrillar structures capable of replicating gecko adhesion have the potential for use in dry superadhesive tapes and treads for wall-climbing robots for various applications. These structures can be created using micro/nanofabrication techniques or self-assembly.

### 21.1 Overview

The leg attachment pads of several animals including many insects, spiders, and lizards, are capable of attaching to and detaching from a variety of surfaces and are used for locomotion, even on vertical walls or across the ceiling [1, 2]. Biological evolution over a long period of time has led to the optimization of their leg attachment systems. This dynamic attachment ability is referred to as reversible

or smart adhesion [3]. Many insects (e.g., beetles and flies) and spiders have been the subject of investigation. However, the attachment pads of geckoes have been the most widely studied due to the fact that they have the highest body mass and exhibit the most versatile and effective adhesion known in nature. As a result, the vast majority of this chapter will be concerned with gecko feet.

Although there are over 1,000 species of geckoes [4, 5] that have attachment pads of varying morphology [6], the Tokay gecko (*Gekko gekko*) which is native to Southeast Asia, has been the main focus of scientific research [7, 8, 9]. The Tokay gecko is the second largest gecko species, attaining lengths of  $\approx 0.3$ – $0.4$  and  $0.2$ – $0.3$  m for males and females, respectively. They have a distinctive blue or gray body with orange or red spots and can weigh up to 300 g [10]. These have been the most widely investigated species of gecko due to the availability and size of these creatures.

Almost 2,500 years ago, the ability of the gecko to “run up and down a tree in any way, even with the head downwards” was observed by *Aristotle* [11, Book IX, Part 9]. Even though the adhesive ability of geckoes has been known since the time of Aristotle, little was understood about this phenomenon until the late nineteenth century, when the microscopic hairs covering the toes of the gecko were first noted. The development of electron microscopy in the 1950s enabled scientists to view the complex hierarchical morphology that covers the skin on the gecko’s toes. Over the past century and a half, scientific studies have been conducted to determine the factors that allow the gecko to adhere to and detach from surfaces at will, including surface structure [6, 8, 12, 13, 14, 15, 16, 17], the mechanisms of adhesion [6, 7, 18, 19, 20, 21, 22, 23, 24, 25, 26, 27, 28], and adhesion strength [7, 8, 17, 25, 28, 29]. Modeling the gecko attachment system as a system of springs [3, 30, 31, 32, 33] has provided valuable insight into adhesion enhancement; van der Waals forces are widely accepted in the literature as the dominant adhesion mechanism utilized by hierarchical attachment systems. Capillary forces created by humidity naturally present in the air can further increase the adhesion force generated by the spatulae [33]. Both experimental and theoretical work support these adhesion mechanisms.

There is great interest among the scientific community to further study the characteristics of gecko feet in the hope that this information can be applied to the production of micro/nanosurfaces capable of recreating the adhesion forces generated by these lizards [2]. Common manmade adhesives such as tape or glue involve the use of wet adhesives that permanently attach two surfaces. However, replication of the characteristics of gecko feet would enable the development of a superadhesive tape capable of clean dry adhesion. These structures can bind components in microelectronics without the high heat associated with various soldering processes. These structures will never dry out in a vacuum – a common problem in aerospace applications. They have the potential for use in everyday objects such as adhesive tapes, fasteners, and toys, and in high technology such as microelectronic and space applications. Replication of the dynamic climbing and peeling ability of geckoes could find use in the treads of wall-climbing robots.

21.2 Hairy Attachment Systems

There are two kinds of attachment pads: relatively smooth and hairy. Relatively smooth pads, so-called arolia and euplantulae, are soft and deformable and are found in tree frogs, cockroaches, grasshoppers, and bugs. The hairy types consist of long deformable setae and are found in many insects (e.g., beetles, flies), spiders, and lizards. The microstructures utilized by beetles, flies, spiders, and geckoes have similar structures, as can be seen in Fig. 21.1a. As the size (mass) of the creature increases, the radius of the terminal attachment elements decreases. This allows a greater number of setae to be packed into an area, hence increasing the linear dimension of contact and the adhesion strength. Arzt et al. [17] determined that the

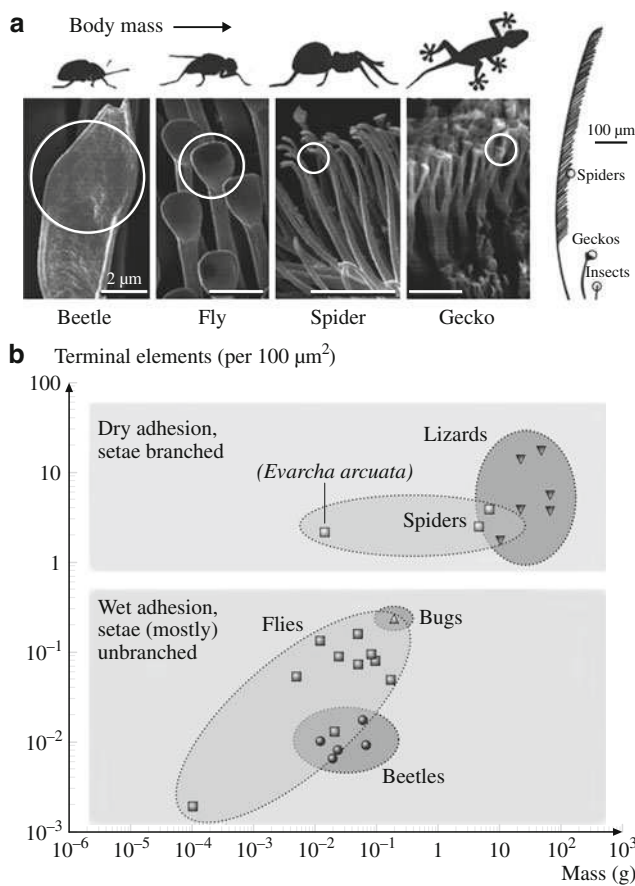


**Fig. 21.1** (a) Terminal elements of the hairy attachment pads of a beetle, fly, spider, and gecko shown at two different scales (after [17]) and (b) the dependence of terminal element density on body mass (after [34]). Data from Arzt et al. [17] and Kesel et al. [35]



density of the terminal attachment elements  $\rho_A/\text{m}^2$  strongly increases with increasing body mass  $m$  in g. In fact, a master curve can be fitted for all the different species (Fig. 21.1b)

$$\log \rho_A = 13.8 + 0.669 \log m. \quad (21.1)$$

The correlation coefficient of the master curve is 0.919. Beetles and flies have the largest attachment pads and the lowest density of terminal attachment elements. Spiders have highly refined attachment elements that cover the leg of the spider. Geckoes have both the highest body mass and greatest density of terminal elements (spatulae). Spiders and geckoes can generate high dry adhesion, whereas beetles and flies increase adhesion by secreting liquid stored generally within a spongy layer of cuticle and delivered at the contacting surface through a system of porous channels [1, 17, 35]. It should be noted that, in the smooth attachment system discussed earlier, this secretion is essential for attachment.

It should be noted that Peattie and Full [36] have revisited the scaling of terminal attachment elements with body mass using a phylogenetic approach. In their work, a larger set of species (81) over a wider range of body mass and setal morphology were considered. They found that fiber morphology is better predicted by evolutionary history and adhesion mechanism (dry or wet) than by body mass.

Figure 21.2 shows scanning electron micrographs of the end of the legs of two flies – fruit fly (*Drosophila melanogaster*) and syrphid fly. The fruit fly uses setae with flattened tips (spatulae) on two hairy rods for attachment to smooth surfaces and two front claws for attachment to rough surfaces. The front claws are also used for locomotion. The syrphid fly uses setae on the legs for attachment. In both cases, fluid is secreted at the contacting surface to increase adhesion.

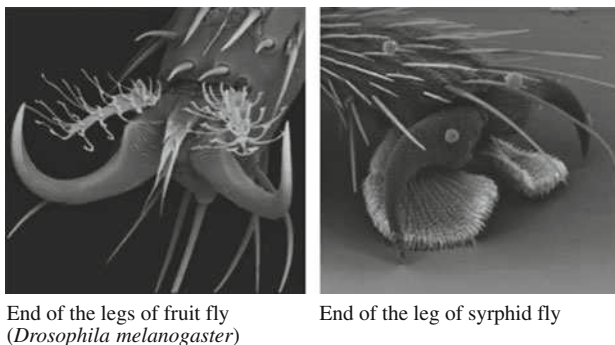


**Fig. 21.2** SEM micrographs of the end of the legs of fruit fly (*Drosophila melanogaster*) and syrphid fly (after [1])

## 21.3 Tokay Gecko

### 21.3.1 Construction of the Tokay Gecko

The explanation for the adhesion properties of gecko feet can be found in the surface morphology of the skin on the toes of the gecko. The skin is comprised of a complex hierarchical structure of lamellae, setae, branches, and spatulae [6]. Figure 21.3 shows various scanning electron microscopy (SEM) micrographs of a gecko foot, showing the hierarchical structure down to the nanoscale. Figure 21.4 shows a schematic of the structure and Table 21.1 summarizes the surface characteristics. The gecko attachment system consists of an intricate hierarchy of structures beginning with lamellae, soft ridges 1–2 mm in length [6] that are located on the attachment pads (toes) that compress easily so that contact can be made with

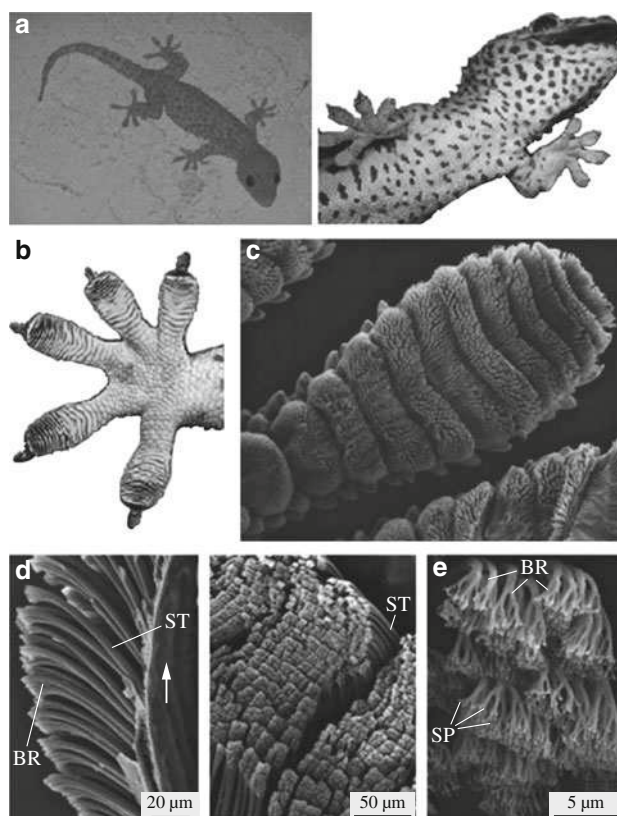


**Fig. 21.3** (a) Tokay gecko (after [25]). The hierarchical structures of a gecko foot: (b) a gecko foot (after [25]) and (c) a gecko toe (after [9]). Each toe contains hundreds of thousands of setae and each seta contains hundreds of spatulae. Scanning electron microscope (SEM) micrographs of (d) the setae (after [37]) and (e) the spatula (after [37]) (ST – seta, SP – spatula, BR – branch)

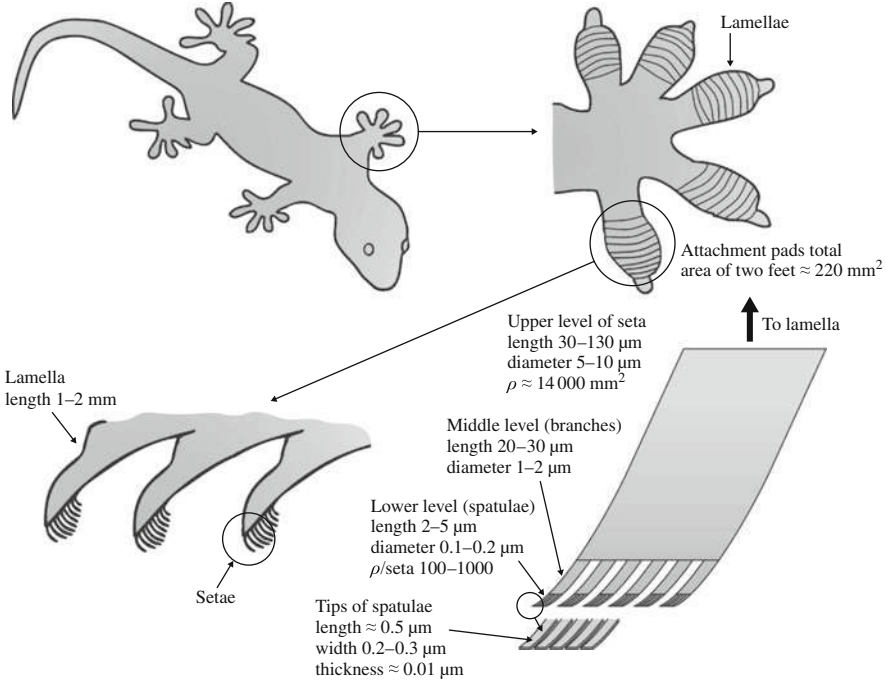


**Fig. 21.4** Schematic drawings of a Tokay gecko including the overall body, one foot, a cross-sectional view of the lamellae, and an individual seta;  $\rho$  represents the number of spatulae

**Table 21.1** Surface characteristics of Tokay gecko feet (Young’s modulus of surface material, keratin = 1–20 GPa<sup>a,b</sup>)

Component	Size	Density	Adhesive force
Seta	30–130 <sup>c,f</sup> /5–10 <sup>c,f</sup> length/diameter (μm)	≈ 14,000 <sup>g,h</sup> setae/mm <sup>2</sup>	194 μN <sup>i</sup> (in shear) ≈ 20 μN <sup>i</sup> (normal)
Branch	20–30 <sup>c</sup> /1–2 <sup>c</sup> length/diameter (μm)	–	–
Spatula	2–5 <sup>c</sup> /0.1–0.2 <sup>c,j</sup> length/diameter (μm)	100–1,000 <sup>c,d</sup> spatulae per seta	–
Tip of spatula	≈ 0.5 <sup>c,g</sup> /0.2–0.3 <sup>c,f</sup> /≈ 0.01 <sup>j</sup> length/width/thickness (μm)	–	11 nN <sup>k</sup> (normal)

<sup>a</sup>Russell [13]  
<sup>b</sup>Bertram and Gosline [45]  
<sup>c</sup>Ruibal and Ernst [6]  
<sup>d</sup>Hiller [7]  
<sup>e</sup>Russell [12]  
<sup>f</sup>Williams and Peterson [14]  
<sup>g</sup>Schleich and Kästle [15]  
<sup>h</sup>Autumn and Peattie [16]  
<sup>i</sup>Autumn et al. [25]  
<sup>j</sup>Persson and Gorb [40]  
<sup>k</sup>Huber et al. [29]

rough bumpy surfaces. Tiny curved hairs known as setae extend from the lamellae at a density of  $\approx 14,000$  per  $\text{mm}^2$  [15]. These setae are typically 30–130  $\mu\text{m}$  in length, 5–10  $\mu\text{m}$  in diameter [6, 7, 12, 14], and are composed primarily of  $\beta$ -keratin [13, 38] with some  $\alpha$ -keratin component [39]. At the end of each seta, 100–1,000 spatulae [6, 7], typically 2–5  $\mu\text{m}$  in length and with a diameter of 0.1–0.2  $\mu\text{m}$  [6], branch out and form the points of contact with the surface. The tips of the spatulae are  $\approx 0.2$ –0.3  $\mu\text{m}$  in width [6], 0.5  $\mu\text{m}$  in length, and 0.01  $\mu\text{m}$  in thickness [40] and garner their name from their resemblance to a spatula.

The attachment pads on two feet of the Tokay gecko have an area of  $\approx 220 \text{ mm}^2$ . About three million setae on their toes that branch off into about three billion spatula on two feet can produce a clinging ability of  $\approx 20 \text{ N}$  (vertical force required to pull a lizard down a nearly vertical ( $85^\circ$ ) surface) [8] and allow them to climb vertical surfaces at speeds  $\approx 1 \text{ m/s}$  with the capability to attach and detach their toes in milliseconds. In isolated setae, a 2.5  $\mu\text{N}$  preload yielded adhesion of 20–40  $\mu\text{N}$ , and thus the adhesion coefficient, which represents the strength of adhesion as a function of preload, ranges from 8 to 16 [26].

### 21.3.2 Adhesion Enhancement During Contact with Rough Surfaces

Typical rough, rigid surfaces are able to make intimate contact with a mating surface only over a very small portion of the perceived apparent area of contact. In fact, the real area of contact is typically two to six orders of magnitude less than the apparent area of contact [41, 42, 43]. Autumn et al. [26] proposed that divided contacts serve as a means for increasing adhesion. The surface energy approach can be used to calculate adhesion force in a dry environment in order to calculate the effect of division of contacts. If the tip of a spatula is considered as a hemisphere with radius  $R$ , the adhesion force of a single contact  $F_{\text{ad}}$ , based on the so-called Johnson–Kendall–Roberts (JKR) theory [44] is given by

$$F_{\text{ad}} = \frac{3}{2} \pi W_{\text{ad}} R, \quad (21.2)$$

where  $W_{\text{ad}}$  is the work of adhesion (units of energy per unit area). Equation (21.2) shows that the adhesion force of a single contact is proportional to the linear dimension of the contact. For a constant area divided into a large number of contacts or setae  $n$  the radius of a divided contact,  $R_1$ , is given by  $R_1 = R/\sqrt{n}$  (self-similar scaling) [17]. Therefore, the adhesion force of (21.2) can be modified for multiple contacts such that

$$F'_{\text{ad}} = \frac{3}{2} \pi W_{\text{ad}} \left( \frac{R}{\sqrt{n}} \right) n = \sqrt{n} F_{\text{ad}}, \quad (21.3)$$

where  $F'_{ad}$  is the total adhesion force from the divided contacts. Thus the total adhesive force is simply the adhesion force of a single contact multiplied by the square root of the number of contacts.

For contact in a humid environment, meniscus (or capillary) forces further increase the adhesion force [41, 42, 43]. The attractive meniscus force ( $F_m$ ) consists of a contribution from both Laplace pressure and surface tension (Sect. 21.4.2) [42, 46]. The contribution by Laplace pressure is directly proportional to the meniscus area. The other contribution is from the vertical component of the surface tension around the circumference. This force is proportional to the circumference, as is the case for the work of adhesion [42]. Going through the analysis presented earlier, one can show that the contribution from the component of surface tension increases on splitting into a larger number of contacts. It increases linearly with the square root of the number of contacts  $n$  (self-similar scaling) [2, 47, 48]

$$(F'_m)_{\text{surface tension}} = \sqrt{n}(F_m)_{\text{surface tension}}, \quad (21.4)$$

where  $F'_m$  is the force from the divided contacts and  $F_m$  is the force of an individual contact. This component of meniscus force is significant if the meniscus radius is very small and the contact angles are relatively large.

During separation of two surfaces, the viscous force  $F_v$  of the divided contacts is given by [47, 48]

$$F'_v = \frac{F_v}{n}, \quad (21.5)$$

where  $F'_v$  is the force from the divided contacts, and  $F_v$  is the force of an individual contact.

The models just presented only consider contact with a flat surface. Multiple-level hierarchical structure of the gecko provide compliance and conformability to rough surfaces in order to achieve high adhesion. The flexibility of the body provides conformability at the cm scale. Several toes on the feet provide conformability independently at the several mm scale. Lamellae on the bottom surfaces of the toes provide conformability at the mm scale. The setae on the lamellae provide conformability at the several  $\mu\text{m}$  scale. The tips of the setae are divided into spatulae which provide conformability at the few to several hundred nm scale. To summarize, on natural rough surfaces, the compliance and adaptability of the hierarchical structure of gecko setae allows for greater contact with a natural rough surface than a nonbranched attachment system [3, 30, 31, 32, 33, 49]. Modeling of the contact between gecko setae and rough surfaces is discussed in detail in Sect. 21.6.

Material properties also play an important role in adhesion. A soft material is able to achieve greater contact with a mating surface than a rigid material. Although gecko skin is primarily comprised of  $\beta$ -keratin, a stiff material with a Young's modulus in the range 1–20 GPa [13, 45], the effective modulus of the setal arrays on gecko feet is  $\approx 100$  kPa [50], which is approximately four orders of magnitude lower than the bulk material. The Young's modulus of gecko skin is compared with

**Table 21.2** Young's modulus of gecko skin and other materials for comparison

Material	Young's modulus
$\beta$ -keratin, mostly present in gecko skin	1–20 GPa
Steel	210 GPa
Cross-linked rubber	1 MPa
Consumer adhesive tape (uncrosslinked rubber)	1 kPa

that of various materials in Table 21.2. The surface of consumer adhesive tape has been selected to be very compliant to increase the contact area for high adhesion. Nature has selected a relatively stiff material to avoid clinging to adjacent setae. Nonorthogonal attachment angle of the seta increases the bending stiffness. Division of contacts and hierarchical structure, as discussed earlier, provide high adhesion. By combining optimal surface structure and material properties, Mother Nature has created an evolutionary superadhesive.

### 21.3.3 Peeling

Although geckoes are capable of producing large adhesion forces, they retain the ability to remove their feet from an attachment surface at will by peeling action. The orientation of the spatulae facilitates peeling. Autumn et al. [25] were the first to show experimentally that the adhesion force of gecko setae is dependent on the three-dimensional (3D) orientation as well as the preload applied during attachment. Due to this fact, geckoes have developed a complex foot motion during walking. First, the toes are carefully uncurled during detachment. The maximum adhesion occurs at an attachment angle of  $30^\circ$  – the angle between a seta and mating surface. The gecko is then able to peel its foot off surfaces one row of setae at a time by changing the angle at which its setae contact the surface. At an attachment angle  $>30^\circ$ , the gecko will detach from the surface.

Shah and Sitti [51] determined the theoretical preload required for adhesion as well as the adhesion force generated for setal orientations of  $30^\circ$ ,  $40^\circ$ ,  $50^\circ$ , and  $60^\circ$ . We consider a solid material (elastic modulus  $E$ , Poisson's ratio  $\nu$ ) to make contact with the rough surface described by

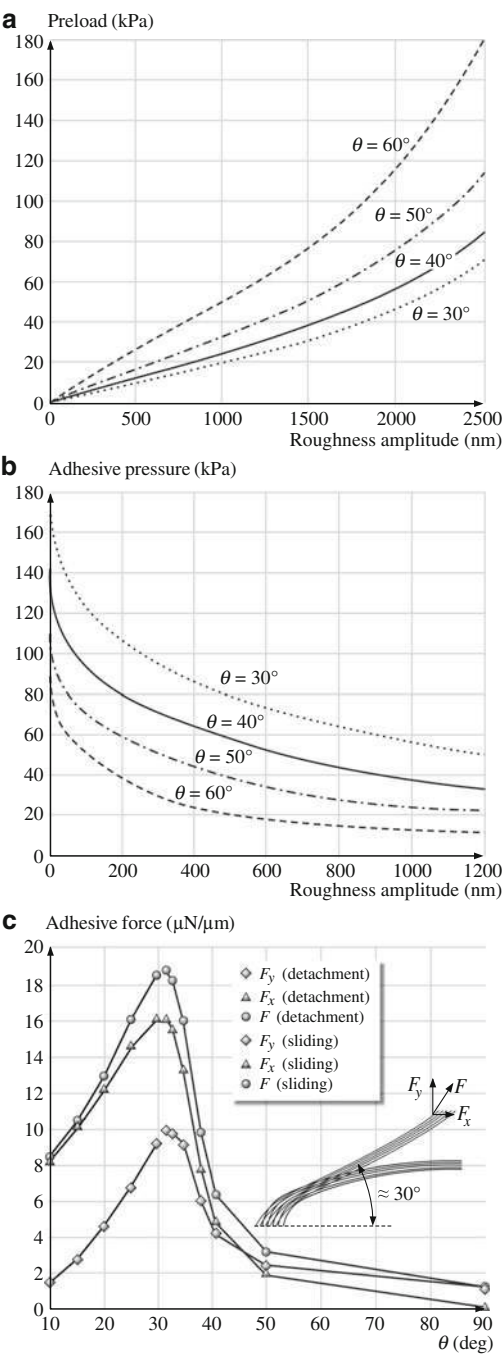
$$f(x) = H \sin^2 \left( \frac{\pi x}{\chi} \right), \quad (21.6)$$

where  $H$  is the amplitude and  $\chi$  is the wavelength of the roughness profile. For a solid adhesive block to achieve intimate contact with the rough surface, neglecting surface forces, it is necessary to apply a compressive stress  $\sigma_c$  [52]

$$\sigma_c = \frac{\pi EH}{2\chi(1 - \nu^2)}. \quad (21.7)$$

Equation (21.7) can be modified to account for fibers oriented at an angle  $\theta$ . The preload required for contact is summarized in Fig. 21.5a. As the orientation angle

**Fig. 21.5** Contact mechanics results for the effect of fiber orientation on **(a)** preload and **(b)** adhesive force for roughness amplitude of 0–2,500 nm (after [51]). **(c)** Finite-element analysis of the adhesive force of a single seta as a function of pull direction (after [37])



decreases, so does the required preload. Similarly, the adhesion strength is influenced by fiber orientation. As seen in Fig. 21.5b, the greatest adhesion force occurs at  $\theta = 30^\circ$ .

Gao et al. [37] created a finite-element model of a single gecko seta in contact with a surface. A tensile force was applied to the seta at various angles  $\theta$ , as shown in Fig. 21.5c. For forces applied at an angle  $<30^\circ$ , the dominant failure mode was sliding. On the contrary, the dominant failure mode for forces applied at angles  $>30^\circ$  was detachment. This verifies the results of Autumn et al. [25] that detachment occurs at attachment angles  $>30^\circ$ .

Tian et al. [53] have suggested that, during detachment, the angular dependence of both adhesion and friction plays a role. The pulling force of a spatula along its shaft with an angle between  $0^\circ$  and  $90^\circ$  to the substrate has a normal adhesion force produced at the spatula–substrate bifurcation zone and a lateral friction force contribution from the part of the spatula still in contact with the substrate. High net friction and adhesion forces on the whole gecko are obtained by rolling down and gripping the toes inward to realize small pulling angles of the large number of spatulae in contact with the substrate. To detach, the high adhesion/friction is rapidly reduced to a very low value by rolling the toes upward and downward, which, mediated by the lever function of the setal shaft, peels the spatula off from the substrate perpendicularly.

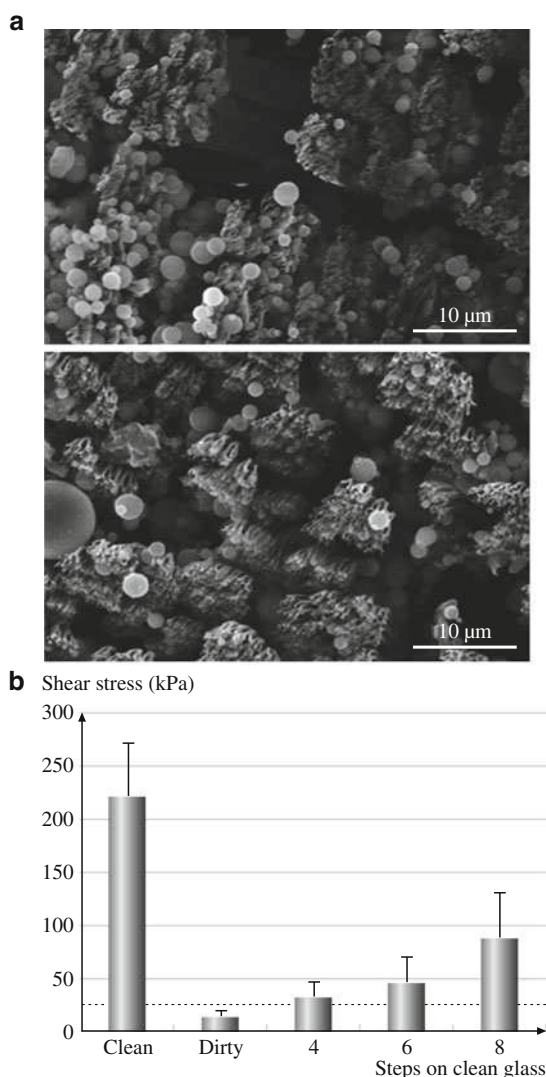
### 21.3.4 Self-cleaning

Natural contaminants (dirt and dust) as well as manmade pollutants are unavoidable and have the potential to interfere with the clinging ability of geckoes. Particles found in the air consist of particulates that are typically  $<10\ \mu\text{m}$  in diameter, while those found on the ground can often be larger [55, 56]. Intuitively, it seems that the great adhesion strength of gecko feet would cause dust and other particles to become trapped in the spatulae and that they would have no way of being removed without some sort of manual cleaning action on behalf of the gecko. However, geckoes are not known to groom their feet like beetles [57], nor do they secrete sticky fluids to remove adhering particles like ants [58] and tree frogs [59], yet they retain adhesive properties. One potential source of cleaning is during the time when the lizards undergo molting, or the shedding of the superficial layer of epidermal cells. However, this process only occurs approximately once per month [60]. If molting were the sole source of cleaning, the gecko would rapidly lose its adhesive properties as it was exposed to contaminants in nature [54].

Hansen and Autumn [54] tested the hypothesis that gecko setae become cleaner with repeated use – a phenomenon known as self-cleaning. The cleaning ability of gecko feet was first tested experimentally by applying  $2.5\ \mu\text{m}$ -radius silica–alumina ceramic microspheres to clean setal arrays. Figure 21.6a shows the setal arrays immediately after dirtying and after five simulated steps. It is noted that a significant fraction of the particles have been removed after five steps.



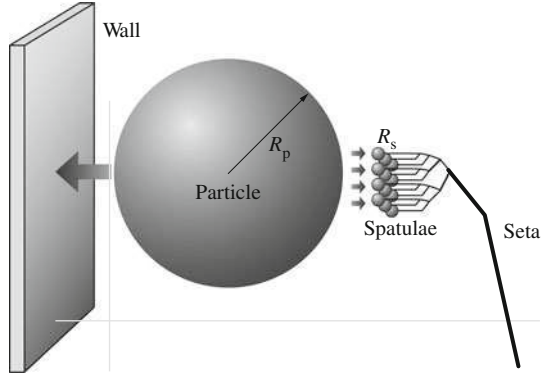
**Fig. 21.6** (a) SEM image of spatulae after dirtying with microspheres (*top*) and after five simulated steps (*bottom*). (b) Mean shear stress exerted by a gecko on a surface after dirtying. The *dotted line* represents sufficient recovery to support weight by a single toe (after [54])



The maximum shear stress that these *dirty* arrays could withstand was measured using a sensor. After each step that the gecko took, the shear stress was once again measured. As seen in Fig. 21.6b, after four steps, the gecko foot was clean enough to withstand its own body weight.

In order to understand this cleaning process, substrate–particle interactions must be examined. The interaction energy between a dust particle and a wall and spatulae can be modeled as shown in Fig. 21.7. The interaction energy between a spherical dust particle and the wall  $W_{pw}$ , can be expressed as [61]

**Fig. 21.7** Model of interactions between gecko spatulae of radius  $R_s$ , a spherical dirt particle of radius  $R_p$ , and a planar wall, enabling self-cleaning (after [54])



$$W_{pw} = \frac{-H_{pw}R_p}{6D_{pw}}, \quad (21.8)$$

where  $p$  and  $w$  refer to the particle and wall, respectively.  $H$  is the Hamaker constant,  $R_p$  is the radius of the particle, and  $D_{pw}$  is the separation distance between the particle and the wall. Similarly, the interaction energy between a spherical dust particle and a spatula  $s$ , assuming that the spatula tip is spherical, is [61]

$$W_{ps} = \frac{-H_{ps}R_pR_s}{6D_{ps}(R_p + R_s)}. \quad (21.9)$$

The ratio of the two interaction energies  $Z$  can be expressed as

$$Z = \frac{W_{pw}}{W_{ps}} = \left(1 + \frac{R_p}{R_s}\right) \frac{H_{pw}D_{ps}}{H_{ps}D_{pw}}. \quad (21.10)$$

When the energy required to separate a particle from the wall is greater than that required to separate it from a spatula ( $Z > 1$ ), self-cleaning will occur. For small contaminants ( $R_p < 0.5 \mu\text{m}$ ), there are not enough spatulae available to adhere to the particle. For larger contaminants, the curvature of the particles makes it impossible for enough spatulae to adhere to it. As a result, Hansen and Autumn [54] concluded that self-cleaning should occur for all spherical spatulae interacting with all spherical particles.

## 21.4 Attachment Mechanisms

When asperities of two solid surfaces are brought into contact with each other, chemical and/or physical attraction occurs. The force developed that holds the two surfaces together is known as adhesion. In a broad sense, adhesion is considered to

be either physical or chemical in nature [41, 42, 43, 61, 62, 63, 64, 65, 66]. Chemical interactions such as electrostatic attraction charges [20] as well as intermolecular forces [7] including van der Waals and capillary forces have all been proposed as potential adhesion mechanisms in gecko feet. Others have hypothesized that geckoes adhere to surfaces through the secretion of sticky fluids [18, 19], suction [19], increased frictional force [21], and microinterlocking [22].

Through experimental testing and observations conducted over the last century and a half many potential adhesive mechanisms have been eliminated. Observation has shown that geckoes lack any glands capable of producing sticky fluids [18, 19], thus ruling out the secretion of sticky fluids as a potential adhesive mechanism. Furthermore, geckoes are able to create large adhesive forces normal to a surface. Since friction only acts parallel to a surface, the attachment mechanism of increased frictional force has been ruled out. Dellit [22] experimentally ruled out suction and electrostatic attraction as potential adhesive mechanisms. Experiments carried out in vacuum did not show a difference between the adhesive force at low pressures compared with under ambient conditions. Since adhesive forces generated during suction are based on pressure differentials, which are insignificant under vacuum, suction was rejected as an adhesive mechanism [22]. Additional testing utilized X-ray bombardment to create ionized air in which electrostatic attraction charges would be eliminated. It was determined that geckoes were still able to adhere to surfaces under these conditions, and therefore electrostatic charges could not be the sole cause of attraction [22]. Autumn et al. [25] demonstrated the ability of a gecko to generate large adhesive forces when in contact with a molecularly smooth SiO<sub>2</sub> microelectromechanical system (MEMS) semiconductor. Since surface roughness is necessary for microinterlocking to occur, it has also been ruled out as a mechanism of adhesion. Two mechanisms, van der Waals forces and capillary forces, remain as the potential sources of gecko adhesion. These attachment mechanisms are described in detail in the following sections.

### 21.4.1 *van der Waals Forces*

van der Waals bonds are secondary bonds that are weak in comparison with other physical bonds such as covalent, hydrogen, ionic, and metallic bonds. Unlike other physical bonds, van der Waals forces are always present, regardless of separation, and are effective from very large separations ( $\approx 50$  nm) down to atomic separation ( $\approx 0.3$  nm). The van der Waals force per unit area between two parallel surfaces  $f_{vdw}$  is given by [61, 67, 68]

$$f_{vdw} = \frac{H}{6\pi D^3}, \quad \text{for } D < 30 \text{ nm}, \quad (21.11)$$

where  $H$  is the Hamaker constant and  $D$  is the separation between surfaces.

Hiller [7] showed experimentally that the surface energy of a substrate is responsible for gecko adhesion. One potential adhesion mechanism would then be

van der Waals forces [24, 25]. Assuming van der Waals forces to be the dominant adhesion mechanism utilized by geckoes, the adhesion force of a gecko can be calculated. Typical values of the Hamaker constant range from  $4 \times 10^{-20}$  to  $4 \times 10^{-19}$  J [61]. In calculation, the Hamaker constant is assumed to be  $10^{-19}$  J, the surface area of a spatula is taken to be  $2 \times 10^{-14}$  m<sup>2</sup> [6, 14, 16], and the separation between the spatula and contact surface is estimated to be 0.6 nm. This equation yields the force of a single spatula to be  $\approx 0.5$   $\mu$ N. By applying the surface characteristics from Table 21.1, the maximum adhesion force of a gecko is 150–1,500 N for varying spatula density of 100–1,000 spatulae/seta. If an average value of 550 spatulae/seta is used, the adhesion force of a single seta is  $\approx 270$   $\mu$ N, which is in agreement with the experimental value obtained by Autumn et al. [25], which will be discussed later.

Another approach to calculate the adhesion force is to assume that the spatulae are cylinders that terminate in hemispherical tips. By using (21.2) and assuming that the radius of each spatula is  $\approx 100$  nm and that the surface energy is expected to be 50 mJ/m<sup>2</sup> [17], the adhesive force of a single spatula is predicted to be 0.02  $\mu$ N. This result is an order of magnitude lower than the first approach calculated for the higher value of  $A$ . For a lower value of  $10^{-20}$  J for the Hamaker constant, the adhesive force of a single spatula is comparable to that obtained using the surface energy approach.

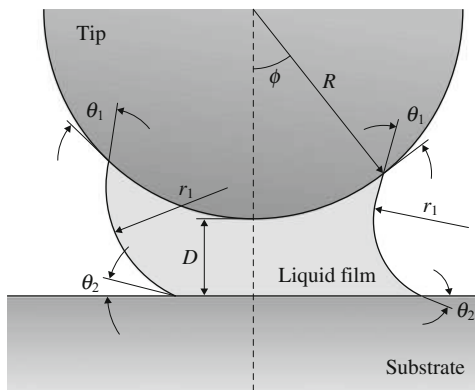
Several experimental results favor van der Waals forces as the dominant adhesive mechanism, including temperature testing [27] and adhesion force measurements of a gecko seta with both hydrophilic and hydrophobic surfaces [25]. These data will be presented in Sects. 21.5.2–21.5.4.

### 21.4.2 Capillary Forces

It has been hypothesized that capillary forces that arise from liquid-mediated contact could be a contributing or even dominant adhesive mechanism utilized by gecko spatulae [7, 24]. Experimental adhesion measurements (presented later in Sects. 21.5.3 and 21.5.4) conducted on surfaces with different hydrophobicities and at various humidity values [28] as well as numerical simulations [33] support this hypothesis as a contributing mechanism. During contact, any liquid that wets or has a small contact angle on surfaces will condense from vapor in the form of an annular-shaped capillary condensate. Due to the natural humidity present in the air, water vapor will condense to liquid on the surface of bulk materials. During contact this will cause the formation of adhesive bridges (menisci) due to the proximity of the two surfaces and the affinity of the surfaces for condensing liquid [69, 70, 71].

In the adhesion model with capillarity by Kim and Bhushan [33], the tip of the spatula in a single contact was assumed to be spherical (Fig. 21.8). The total adhesion force between a spherical tip and a plane consists of the capillary force and the solid–solid interaction. The capillary force can be divided into two components:

**Fig. 21.8** Schematic of a sphere on a plane at a distance  $D$  with a liquid film in between, forming menisci. In this figure,  $R$  is the tip radius,  $\phi$  is the filling angle,  $\theta_1$  and  $\theta_2$  are contact angles on the sphere and plane, respectively, and  $r_1$  and  $r_2$  are the two principal radii of the curved surface in two orthogonal planes (after [33])



the Laplace force  $F_L$  and the surface tension force  $F_s$ , such that the total capillary force  $F_c$  is

$$F_c = F_L + F_s. \quad (21.12)$$

The Laplace force is caused by the pressure difference across the interface of a curved liquid surface (Fig. 21.8) and depends on the pressure difference multiplied by the meniscus area, which can be expressed as [46]

$$F_L = -\pi\kappa\gamma R^2 \sin^2 \phi, \quad (21.13)$$

where  $\gamma$  is the surface tension of the liquid,  $R$  is the tip radius,  $\phi$  is the filling angle, and  $\kappa$  is the mean curvature of the meniscus. From the Kelvin equation [61], which is the thermal equilibrium relation, the mean curvature of meniscus can be determined as

$$\kappa = \frac{\Re T}{V\gamma} \ln\left(\frac{p}{p_0}\right), \quad (21.14)$$

where  $\Re$  is the universal gas constant,  $T$  is the absolute temperature,  $V$  is the molecular volume,  $p_0$  is the saturated vapor pressure of the liquid at  $T$ , and  $p$  is the ambient pressure acting outside the curved surface ( $p/p_0$  is the relative humidity). Orr et al. [46] formulated the mean curvature of a meniscus between a sphere and a plane in terms of elliptic integrals. The filling angle  $\phi$  can be calculated from the expression just mentioned and (21.14) using the iteration method. Then the Laplace force is calculated at a given environment using (21.13).

The surface tension of the liquid results in the formation of a curved liquid–air interface. The surface tension force acting on the sphere is [46]

$$F_s = 2\pi R\gamma \sin \phi \sin(\theta_1 + \phi), \quad (21.15)$$

where  $\theta_1$  is the contact angle on the sphere.

Hence, the total capillary force on the sphere is

$$F_c = \pi R \gamma \{2 \sin \phi \sin(\theta_1 + \phi) - \kappa R \sin^2 \phi\}. \quad (21.16)$$

The effect of capillarity on gecko adhesion results will be presented in Sect. 21.6.4.

## 21.5 Experimental Adhesion Test Techniques and Data

Experimental measurements of the adhesion force of a single gecko seta [25] and single gecko spatula [29] have been made. The effect of the environment, including temperature [27, 72] and humidity [28], has been studied. Some of the data has been used to understand the adhesion mechanism utilized by the gecko attachment system – van der Waals or capillary forces. The majority of experimental results point towards van der Waals forces as the dominant mechanism of adhesion [25, 27]. Recent research suggests that capillary forces can be a contributing adhesive factor [28, 33].

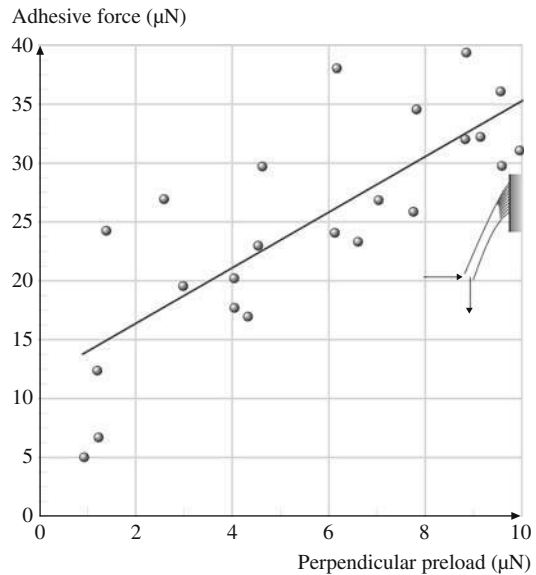
### 21.5.1 Adhesion Under Ambient Conditions

Two feet of a Tokay gecko are capable of producing  $\approx 20$  N of adhesive force with a pad area of  $\approx 220 \text{ mm}^2$  [8]. Assuming that there are  $\approx 14,000$  setae/ $\text{mm}^2$ , the adhesion force from a single hair should be  $\approx 7 \text{ } \mu\text{N}$ . It is likely that the magnitude is actually larger than this value, because it is unlikely that all setae are in contact with the mating surface [25]. Setal orientation greatly influences adhesive strength. This dependency was first noted by Autumn et al. [25]. It was determined that the greatest adhesion occurs at  $30^\circ$ . In order to determine the adhesion mechanism(s) utilized by gecko feet, it is important to know the adhesion force of a single seta. Hence, the adhesion force of gecko foot-hair has been the focus of several investigations [25, 29].

#### Adhesion Force of a Single Seta

Autumn et al. [25] used both a MEMS force sensor and a wire as a force gage to determine the adhesion force of a single seta. The MEMS force sensor is a dual-axis atomic force microscope (AFM) cantilever with independent piezoresistive sensors which allows simultaneous detection of vertical and lateral forces [73]. The wire force gage consisted of an aluminum bonding wire that displaced under a perpendicular pull. Autumn et al. [25] discovered that the setal force actually depends on the three-dimensional orientation of the seta as well as the preloading force applied

**Fig. 21.9** Adhesive force of a single gecko seta as a function of applied preload. The seta was first pushed perpendicularly against the surface and then pulled parallel to the surface, as shown in the schematic (after [25])

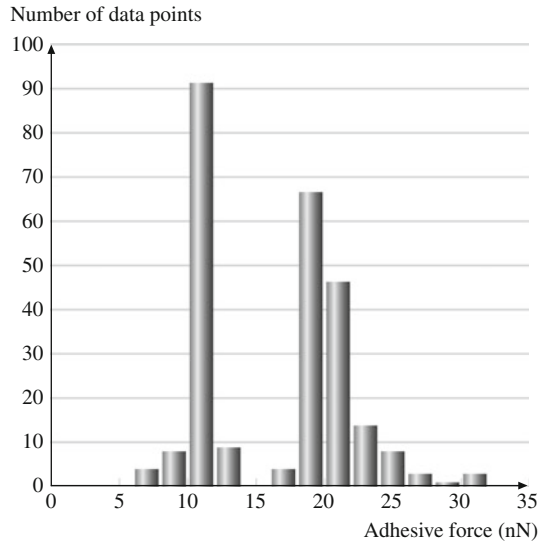


during initial contact. Setae that were preloaded vertically to the surface exhibited only one-tenth of the adhesive force ( $0.6 \pm 0.7 \mu\text{N}$ ) compared with setae that were pushed vertically and then pulled horizontally to the surface ( $13.6 \pm 2.6 \mu\text{N}$ ). The dependence of the adhesion force of a single gecko spatula on perpendicular preload is illustrated in Fig. 21.9. The adhesion force increases linearly with the preload, as expected [41, 42, 65]. The maximum adhesion force of a single gecko foot-hair occurred when the seta was first subjected to a normal preload and then slid  $5 \mu\text{m}$  along the contacting surface. Under these conditions, adhesion force measured  $194 \pm 25 \mu\text{N}$  ( $\approx 10 \text{ atm}$  adhesive pressure).

### Adhesive Force of a Single Spatula

Huber et al. [29] used atomic force microscopy to determine the adhesion force of individual gecko spatulae. A seta with four spatulae was glued to an AFM tip. The seta was then brought into contact with a surface and a compressive preload of  $90 \text{ nN}$  was applied. The force required to pull the seta off of the surface was then measured. As seen in Fig. 21.10, there are two distinct peaks on the graph – one at  $10 \text{ nN}$  and the other at  $20 \text{ nN}$ . The first peak corresponds to one of the four spatulae adhering to the contact surface, while the peak at  $20 \text{ nN}$  corresponds to two of the four spatulae adhering to the contact surface. The average adhesion force of a single spatula was found to be  $10.8 \pm 1 \text{ nN}$ . The measured value is in agreement with the measured adhesive strength of an entire gecko (of the order of  $10^9$  spatulae on a gecko).

**Fig. 21.10** Histogram of the adhesive force of a single gecko spatula. The *peak* at 10 nN corresponds to the adhesive force of one spatula and the *peak* at 20 nN corresponds to the adhesive force of two spatulae (after [29])



### 21.5.2 Effects of Temperature

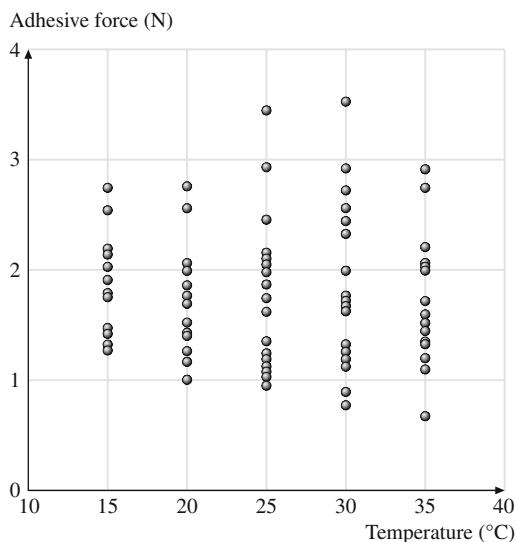
Environmental factors are known to affect several aspects of vertebrate function, including speed of locomotion, digestion rate, and muscle contraction, and as a result several studies have been completed to investigate impact of environmental on these functions. Relationships between the environment and other properties such as adhesion are far less studied [27]. Only two known studies exist that examine the affect of temperature on the clinging force of the gecko [27, 72]. Losos [72] examined the adhesion ability of large live geckoes at temperatures up to 17°C. Bergmann and Irschick [27] expanded upon this research for body temperatures ranging from 15 to 35°C. The geckoes were incubated until their body temperature reached a desired level. The clinging ability of these animals was then determined by measuring the maximum force exerted by the geckoes as they were pulled off a custom-built force plate. The clinging force of a gecko for the experimental test range is plotted in Fig. 21.11. It was determined that variation in temperature does not statistically significantly affect the adhesion force of a gecko. From these results, it was concluded that the temperature independence of adhesion supports the hypothesis of clinging as a passive mechanism (i.e., van der Waals forces). Both studies only measured the overall clinging ability on the macroscale. There have not been any investigations into the effects of temperature on the clinging ability of a single seta on the microscale, and therefore testing in this area would be extremely important.

### 21.5.3 Effects of Humidity

Huber et al. [28] employed similar methods to [29] (discussed previously) in order to determine the adhesive force of a single spatula at varying humidity.



**Fig. 21.11** Adhesive force of a gecko as a function of temperature (after [27])



Measurements were made using an AFM placed in an airtight chamber. The humidity was adjusted by varying the flow rate of dry nitrogen into the chamber. The air was continuously monitored with a commercially available hygrometer. All tests were conducted at ambient temperature.

As seen in Fig. 21.12, even at low humidity, the adhesion force is large. An increase in humidity further increases the overall adhesion force of a gecko spatula. The pull-off force roughly doubled as the humidity was increased from 1.5% to 60%. This humidity effect can be explained in two ways: (1) by standard capillarity or (2) by a change of the effective short-range interaction due to absorbed monolayers of water – in other words, the water molecules increase the number of van der Waals bonds that are made. Based on this data, van der Waals forces are the primary adhesion mechanism, and capillary forces are a secondary adhesive mechanism.

### 21.5.4 Effects of Hydrophobicity

To further test the hypothesis that capillary forces play a role in gecko adhesion, the spatular pull-off force was determined for contact with both hydrophilic and hydrophobic surfaces. As seen in Fig. 21.13a, the capillary adhesion theory predicts that a gecko spatula will generate a greater adhesion force when in contact with a hydrophilic surface as compared with a hydrophobic surface, while the van der Waals adhesion theory predicts that the adhesion force between a gecko spatula and a surface will be the same regardless of the hydrophobicity of the surface [26]. Figure 21.13b shows the shear stress of a whole gecko and the adhesive force of a single seta on hydrophilic and hydrophobic surfaces. The data shows that the

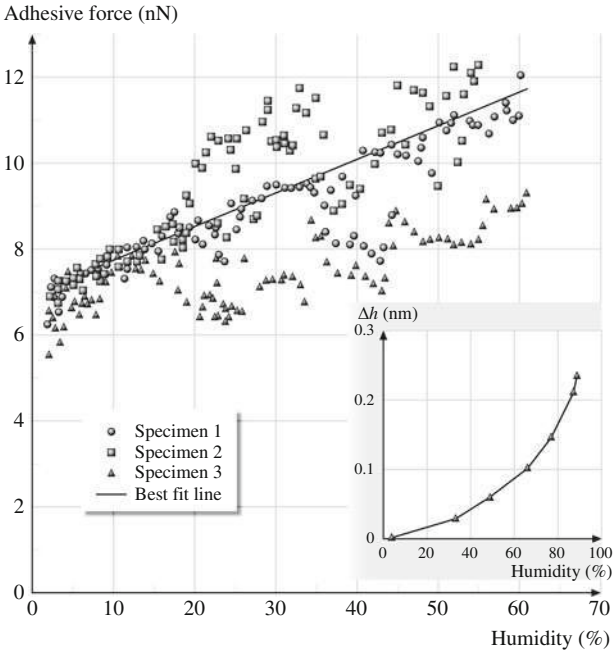


**Fig. 21.12** Humidity effects on spatular pull-off force (*inset*). The increase in water film thickness on a Si wafer with increasing humidity (after [28])

adhesion values are the same on both surfaces. This supports the van der Waals prediction of Fig. 21.13a. Huber et al. [28] found that the hydrophobicity of the attachment surface had an effect on the adhesion force of a single gecko spatula as shown in Fig. 21.13c. These results show that adhesion force has a finite value for a superhydrophobic surface and increases as the surface becomes hydrophilic. It is concluded that van der Waals forces are the primary mechanism, and capillary forces further increase the adhesion force generated.

21.6 Adhesion Modeling

With regard to the natural living conditions of the animals, the mechanics of gecko attachment can be separated into two parts: the mechanics of adhesion of a single contact to a flat surface, and the adaptation of a large number of spatulae to a natural, rough surface. Modeling of the mechanics of adhesion of spatulae to a smooth surface, in the absence of meniscus formation, was developed by Autumn et al. [26], Jagota and Bennison [52], and Arzt et al. [17]. As discussed in Sect. 21.3.2, the adhesion force of multiple contacts  $F'_{ad}$  can be increased by dividing the contact into a large number ( $n$ ) of small contacts, while the nominal area of the

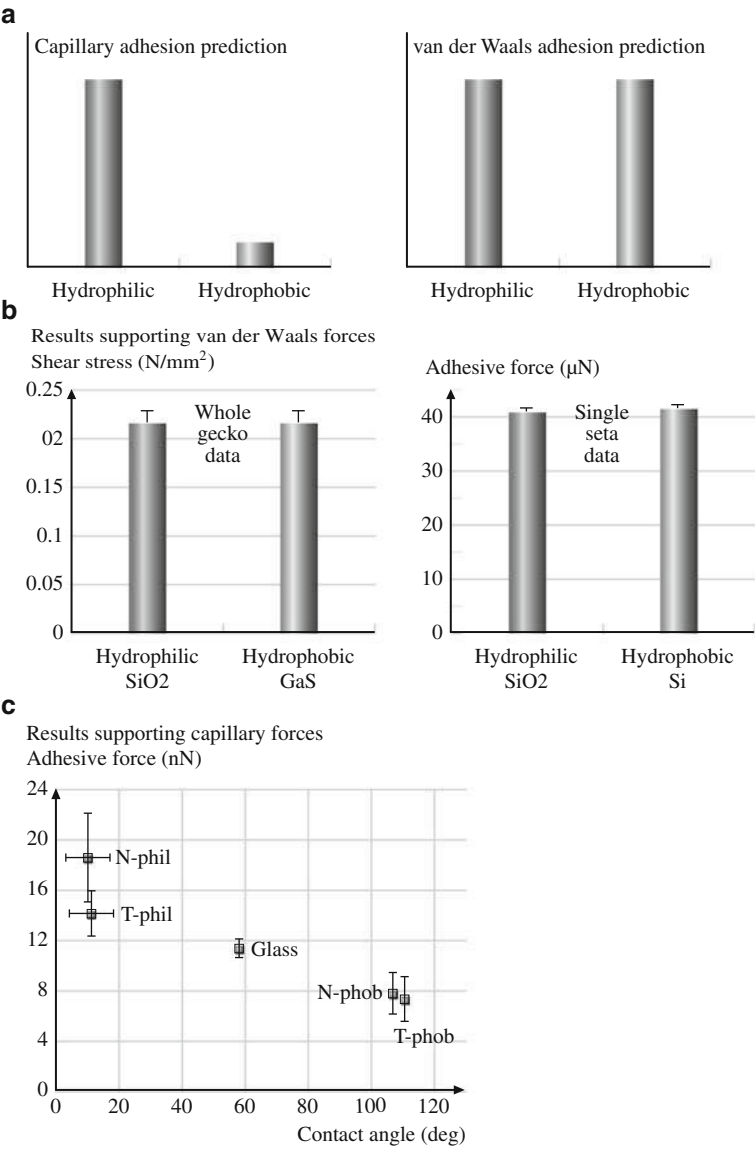


**Fig. 21.13** (a) Capillary and van der Waals adhesion predictions for the relative magnitude of the adhesive force of gecko setae to hydrophilic and hydrophobic surfaces (after [26]). (b) Results of adhesion testing for a whole gecko and single seta with hydrophilic and hydrophobic surfaces (after [26]) and (c) results of adhesive force test of a single gecko spatula with surfaces with different contact angles (after [28])

contact remains the same  $F'_{ad} \propto \sqrt{n}F_{ad}$ . However, this model only considers contact with a flat surface. On natural, rough surfaces, the compliance and adaptability of setae are the primary sources of high adhesion. As stated earlier, the hierarchical

**Table 21.3** Geometrical size, calculated stiffness, and typical densities of branches of seta for Tokay gecko [30]

Level of seta	Length ( $\mu\text{m}$ )	Diameter ( $\mu\text{m}$ )	Bending stiffness <sup>a</sup> (N/m)	Typical density ( $\#/\text{mm}^2$ )
III upper	75	5	2.908	$14 \times 10^3$
II middle	25	1	0.126	—
I lower	2.5	0.1	0.0126	$1.4\text{--}14 \times 10^6$

<sup>a</sup>for elastic modulus of 10 GPa with load applied at  $60^\circ$  to spatula long axis

structure of gecko setae allows for greater contact with a natural, rough surface than a nonbranched attachment system [49].

Bhushan et al. [3] and Kim and Bhushan [30, 31, 32, 33] have approximated a gecko seta in contact with random rough surfaces using a hierarchical spring model. Each level of springs in their model corresponds to a level of seta hierarchy. The upper level of springs corresponds to the thicker part of gecko setae, the middle spring level corresponds to the branches, and the lower level of springs corresponds to the spatulae. The upper level is the thickest branch of the seta. It is  $75 \mu\text{m}$  in length and  $5 \mu\text{m}$  in diameter. The middle level, referred to as a branch, has a length of  $25 \mu\text{m}$  and a diameter of  $1 \mu\text{m}$ . The lower level, called a spatula, is the thinnest branch, with a length of  $2.5 \mu\text{m}$  and a diameter of  $\approx 0.1 \mu\text{m}$  (Table 21.3). As reported earlier, Autumn et al. [25] showed that the optimal attachment angle between the substrate and a gecko seta is  $30^\circ$  in the single-seta pull-off experiment. This finding is supported by the adhesion models of setae as cantilever beams [37, 51] (see Sect. 21.3.3 for more details). Therefore,  $\theta$  was fixed at  $30^\circ$  in the studies by Bhushan et al. [3] and Kim and Bhushan [30, 31, 32, 33] presented below.

### 21.6.1 Single-Spring Contact Analysis

In their analysis, Bhushan et al. [3] and Kim and Bhushan [30, 31, 32, 33] assumed the tip of the spatula in a single contact to be spherical. The springs on every level of hierarchy have the same stiffness as the bending stiffness of the corresponding branches of seta. If the beam is oriented at an angle  $\theta$  to the substrate and the contact load  $F$  is aligned normal to the substrate, its components along and tangential to the direction of the beam,  $F \cos \theta$  and  $F \sin \theta$ , give rise to bending and compressive deformations,  $\delta_b$  and  $\delta_c$ , respectively, of [74]

$$\delta_b = \frac{F \cos \theta l_m^3}{3EI}, \quad \delta_c = \frac{F \sin \theta l_m}{A_c E}, \quad (21.17)$$

where  $I = \pi R_m^4/4$  and  $A_c = \pi R_m^2$  are the moments of inertia of the beam and the cross-sectional area, respectively,  $l_m$  and  $R_m$  are the length and radius of seta branches, respectively, and  $m$  is the level number. The net displacement,  $\delta_\perp$  normal to the substrate, is given by

$$\delta_\perp = \delta_c \sin \theta + \delta_b \cos \theta. \quad (21.18)$$

Using (21.17) and (21.18), the stiffness of seta branches  $k_m$  is calculated as [75]

$$k_m = \frac{\pi R_m^2 E}{l_m \sin^2 \theta \left( 1 + \frac{4l_m^2 \cot^2 \theta}{3R_m^2} \right)}. \quad (21.19)$$

For an assumed elastic modulus  $E$  of seta material of 10 GPa with a load applied at an angle of  $60^\circ$  to spatulae long axis, Kim and Bhushan [30] calculated the stiffness of every level of seta as given in Table 21.3.

In the model, both the tips of a spatula and the asperity summits of the rough surface are assumed to be spherical with constant radius [3]. As a result, a single spatula adhering to a rough surface was modeled as the interaction between two spherical tips. Because  $\beta$ -keratin has a high elastic modulus [13, 45], the adhesion force between two round tips was calculated according to the Derjaguin–Muller–Toporov (DMT) theory [76] as

$$F_{\text{ad}} = 2\pi R_c W_{\text{ad}}, \quad (21.20)$$

where  $R_c$  is the reduced radius of contact, which is calculated as  $R_c = (1/R_1 + 1/R_2)^{-1}$ ;  $R_1$  and  $R_2$  are the radii of the contacting surfaces:  $R_1 = R_2$ ,  $R_c = R/2$ . The work of adhesion  $W_{\text{ad}}$  is then calculated using (21.21) for two flat surfaces separated by a distance  $D$  [61]

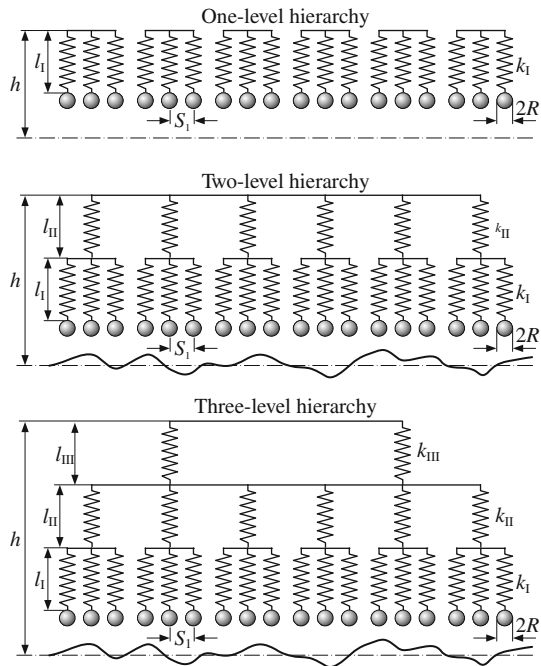
$$W_{\text{ad}} = -\frac{H}{12\pi D^2}, \quad (21.21)$$

where  $H$  is the Hamaker constant, which depends on the medium between the two surfaces. Typical values of the Hamaker constant for polymers are  $H_{\text{air}} = 10^{-19}$  J in air and  $H_{\text{water}} = 3.7 \times 10^{-20}$  J in water [61]. For a gecko seta, which is composed of  $\beta$ -keratin, the value of  $H$  is assumed to be  $10^{-19}$  J. The work of adhesion of two surfaces in contact separated by an atomic distance  $D \approx 0.2$  nm is  $\approx 66$  mJ/m<sup>2</sup> [61]. By assuming that the tip radius  $R$  is 50 nm, using (21.20), the adhesion force of a single contact is calculated as 10 nN [30]. This value is identical to the adhesion force of a single spatula measured by Huber et al. [29]. This adhesion force is used as a critical force in the model for judging whether the contact between the tip and the surface is broken or not during pull-off cycle [3]. If the elastic force of a single spring is less than the adhesion force, the spring is regarded as having been detached.

## 21.6.2 Multilevel Hierarchical Spring Analysis

In order to study the effect of the number of hierarchical levels in the attachment system on attachment ability, models with one [3, 30, 31], two [3, 30, 31], and three

**Fig. 21.14** One-, two-, and three-level hierarchical spring models for simulating the effect of hierarchical morphology on interaction of a seta with a rough surface. In this figure,  $l_{I,II,III}$  are the lengths of the structures,  $s_I$  is the space between spatulae,  $k_{I,II,III}$  are the stiffnesses of the structures, I, II, and III are level indexes,  $R$  is the tip radius, and  $h$  is the distance between the upper spring base of each model and the mean line of the rough profile (after [30])



levels [30, 31] of hierarchy were simulated (Fig. 21.14). The one-level model has springs with length  $l_I = 2.5 \mu\text{m}$  and stiffness  $k_I = 0.0126 \text{ N/m}$ . The length and stiffness of the springs in the two-level model are  $l_I = 2.5 \mu\text{m}$ ,  $k_I = 0.0126 \text{ N/m}$  and  $l_{II} = 25 \mu\text{m}$ ,  $k_{II} = 0.126 \text{ N/m}$  for levels I and II, respectively. The three-level model has additional upper-level springs with  $l_{III} = 75 \mu\text{m}$ ,  $k_{III} = 2.908 \text{ N/m}$  on the springs of the two-level model, which is identical to gecko setae. The base of the springs and the connecting plate between the levels are assumed to be rigid. The distance  $s_I$  between the neighboring structures of level I is  $0.35 \mu\text{m}$ , obtained from the average value of measured spatula density,  $8 \times 10^6 \text{ mm}^{-2}$ , calculated by multiplying  $14,000 \text{ setae/mm}^2$  by an average of  $550 \text{ spatula/seta}$  [15] (Table 21.3). A 1:10 proportion of the number of springs in the upper level to that in the level below was assumed [3]. This corresponds to each spring at level III being connected to ten springs on level II, and each spring on level II being connected to ten springs on level I. The number of springs on level I considered in the model is calculated by dividing the scan length ( $2,000 \mu\text{m}$ ) by the distance  $s_I$  ( $0.35 \mu\text{m}$ ), which corresponds to 5,700.

The spring deflection  $\Delta l$  was calculated as

$$\Delta l = h - l_0 - z, \quad (21.22)$$

where  $h$  is the position of the spring base relative to the mean line of the surface;  $l_0$  is the total length of a spring structure, which is  $l_0 = l_I$  for the one-level model,

$l_0 = l_I + l_{II}$  for the two-level model, and  $l_0 = l_I + l_{II} + l_{III}$  for the three-level model; and  $z$  is the profile height of the rough surface. The elastic force  $F_{el}$  arising in the springs at a distance  $h$  from the surface was calculated for the one-level model as [3]

$$F_{el} = -k_I \sum_{i=1}^p \Delta l_i u_i, \quad (21.23)$$

$$u_i = \begin{cases} 1 & \text{if contact} \\ 0 & \text{if no contact} \end{cases},$$

where  $p$  is the number of springs in level I of the model. For the two-level model the elastic force was calculated as [3]

$$F_{el} = -\sum_{j=1}^q \sum_{i=1}^p k_{ji} (\Delta l_{ji} - \Delta l_j) u_{ji}, \quad (21.24)$$

$$u_{ji} = \begin{cases} 1 & \text{if contact} \\ 0 & \text{if no contact} \end{cases},$$

where  $q$  is the number of springs in level II of the model. For the three-level model the elastic force was calculated as [30]

$$F_{el} = -\sum_{k=1}^r \sum_{j=1}^q \sum_{i=1}^p k_{kji} (\Delta l_{kji} - \Delta l_{kj} - \Delta l_j) u_{kji}, \quad (21.25)$$

$$u_{kji} = \begin{cases} 1 & \text{if contact} \\ 0 & \text{if no contact} \end{cases},$$

where  $r$  is the number of springs in level III of the model. The spring force when the springs approach the rough surface is calculated using either (21.23), (21.24) or (21.25) for one-, two-, and three-level models, respectively. During pull-off, the same equations are used to calculate the spring force. However, when the applied load is equal to zero, the springs do not detach due to the adhesion attraction given by (21.20). The springs are pulled apart when the pull-off force is equal to the adhesion force at the interface. The adhesion force is the lowest value of the elastic force  $F_{el}$  when the seta has detached from the contacting surface.

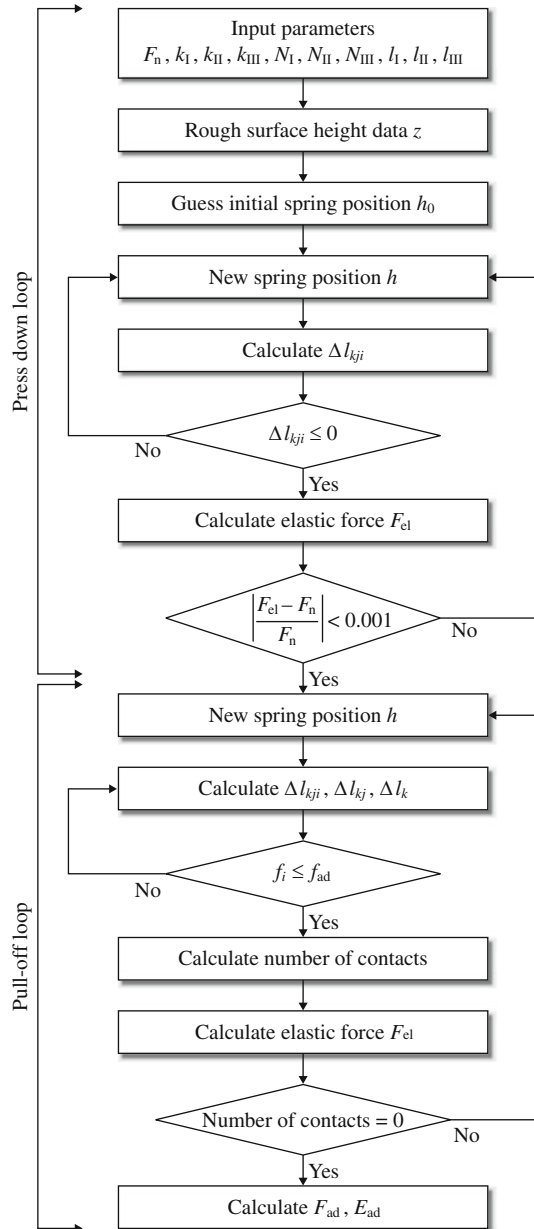
The adhesion energy is calculated as

$$W_{ad} = \int_{\bar{D}}^{\infty} F_{el}(D) dD, \quad (21.26)$$

where  $D$  is the distance that the spring base moves away from the contacting surface. The lower limit of the distance  $\bar{D}$  is the value of  $D$ , where  $F_{el}$  is first zero

when the model is pulled away from the contacting surface. Also, although the upper limit of the distance is infinity, in practice, the  $F_{el}(D)$  curve is integrated to an upper limit where  $F_{el}$  increases from a negative value to zero. Figure 21.15 shows

**Fig. 21.15** Flow chart for the calculation of the adhesion force ( $F_{ad}$ ) and the adhesion energy ( $E_{ad}$ ) for the three-level hierarchical spring model. In this figure,  $F_n$  is an applied load,  $k_{I,II,III}$  and  $l_{I,II,III}$  are stiffnesses and lengths of structures,  $\Delta l_{kji}$ ,  $\Delta l_{ki}$ , and  $\Delta l_k$  are the spring deformations on level I, II, and III, respectively,  $i, j$ , and  $k$  are spring indices on each level,  $f_i$  is the elastic force of a single spring and  $f_{ad}$  is the adhesion force of a single contact (after [30])





the flow chart for the calculation of the adhesion force and the adhesion energy employed by Kim and Bhushan [30].

The random rough surfaces used in the simulations were generated by a computer program [41, 42]. Two-dimensional profiles of surfaces that a gecko might encounter were obtained using a stylus profiler [3]. These profiles, along with the surface selection methods and surface roughness parameters [root-mean-square (RMS) amplitude  $\sigma$  and correlation length  $\beta^*$ ] for scan lengths of 80, 400, and 2,000  $\mu\text{m}$ , are presented in Sect. 21.A. The roughness parameters are scale dependent, and therefore adhesion values also are expected to be scale dependent. As the scan length was increased, the measured values of RMS amplitude and correlation length both increased. The range of values of  $\sigma$  from 0.01 to 30  $\mu\text{m}$  and a fixed value of  $\beta^* = 200 \mu\text{m}$  were used for modeling the contact of a seta with random rough surfaces. The chosen range covers values of roughnesses for relatively smooth, artificial surfaces to natural, rough surfaces. A typical scan length of 2,000  $\mu\text{m}$  was also chosen, which is comparable to a lamella length of gecko.

### 21.6.3 Adhesion Results of the Multilevel Hierarchical Spring Model

The multilevel hierarchical spring model was developed by Kim and Bhushan [30]. They obtained various useful results which will be presented next. Figure 21.16a shows the calculated spring force–distance curves for the one-, two-, and three-level hierarchical models in contact with rough surfaces of different values of RMS amplitude  $\sigma$  ranging from  $\sigma = 0.01$  to 30  $\mu\text{m}$  at applied load of 1.6  $\mu\text{N}$ , which was derived from the gecko's weight. When the spring model is pressed against the rough surface, contact between the spring and the rough surface occurs at point A; as the spring tip presses into the contacting surface, the force increases up to point B, B' or B''. During pull off, the spring relaxes, and the spring force passes an equilibrium state (0 N); tips break free of adhesion forces at point C, C' or C'' as the spring moves away from the surface. The perpendicular distance from C, C' or C'' to zero is the adhesion force. The adhesion energy stored during contact can be obtained by calculating the area of the triangle during the unloading part of the curves (21.26).

Using the spring force–distance curves, Kim and Bhushan [30] calculated the adhesion coefficient, the number of contacts per unit length, and the adhesion energy per unit length of the one-, two-, and three-level models for an applied load of 1.6  $\mu\text{N}$  and a wide range of RMS roughness ( $\sigma$ ), as seen in the left graphs of Fig. 21.16b. The adhesion coefficient, defined as the ratio of the pull-off force to the applied preload, represents the strength of adhesion with respect to the preload. For the applied load of 1.6  $\mu\text{N}$ , which corresponds to the weight of a gecko, the maximum adhesion coefficient is  $\approx 36$  when  $\sigma$  is smaller than 0.01  $\mu\text{m}$ . This means that a gecko can generate enough adhesion force to support 36 times its body weight. However, if  $\sigma$  is increased to 1  $\mu\text{m}$ , the adhesion coefficient for the three-level model is reduced to 4.7. It is noteworthy that the adhesion coefficient

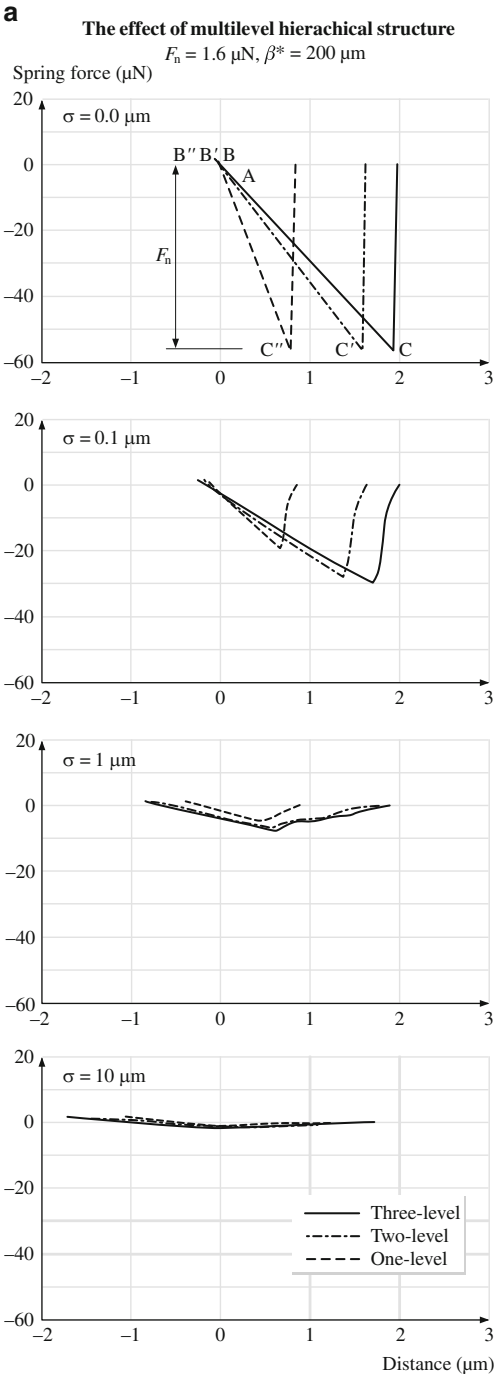
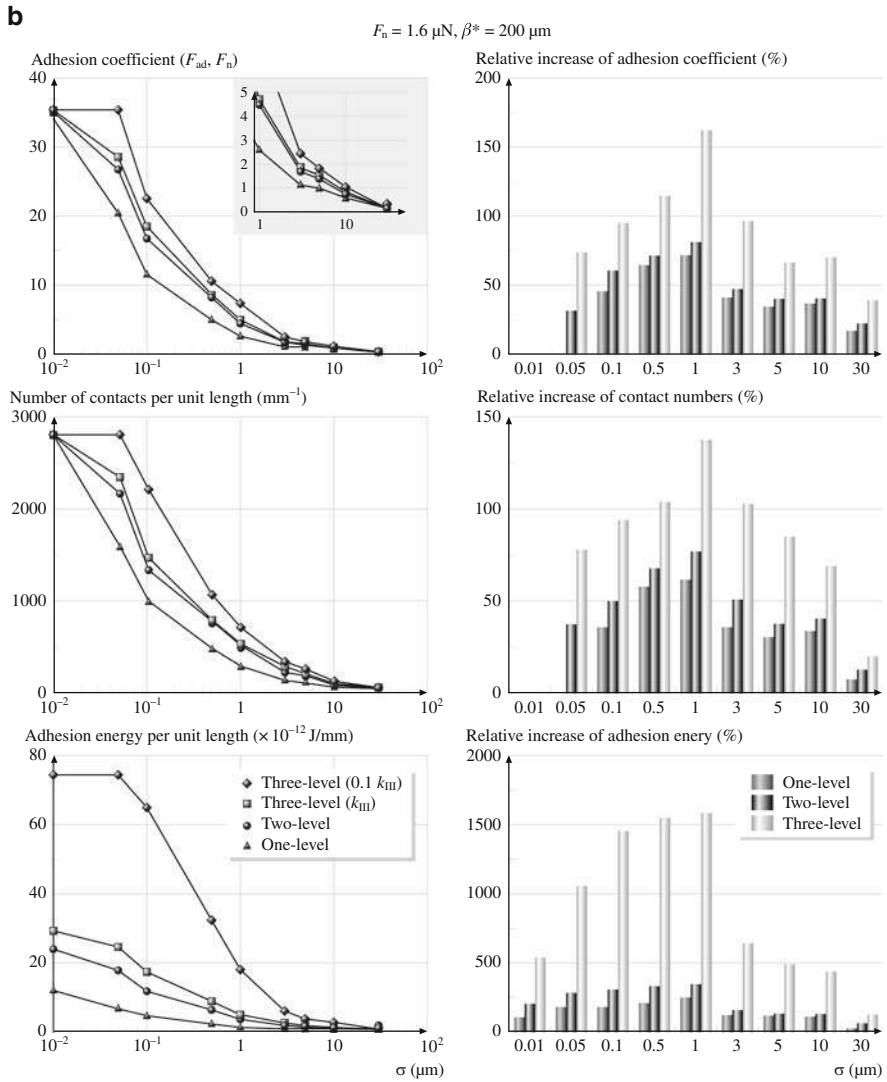


Fig. 21.16 (continued)



**Fig. 21.16** (a) Force– distance curves of the one-, two-, and three-level models in contact with rough surfaces with different  $\sigma$  values for applied load of  $1.6 \mu\text{N}$ . (b) Adhesion coefficient, number of contacts, and adhesion energy per unit length of profile for one- and multilevel models with increasing  $\sigma$  value (*left figures*), and relative increases between multi- and one-level models (*right-hand side*) for applied load of  $1.6 \mu\text{N}$ . The value of  $k_{III}$  in the analysis is  $2.908 \text{ N/m}$  (after [30])

falls  $< 1$  when the contacting surface has an RMS roughness  $\sigma > 10 \mu\text{m}$ . This implies that the attachment system is no longer capable of supporting the gecko’s weight. Autumn et al. [25, 26] showed that, in isolated gecko setae contacting with the surface of a single-crystalline silicon wafer, a  $2.5 \mu\text{N}$  preload yielded adhesion

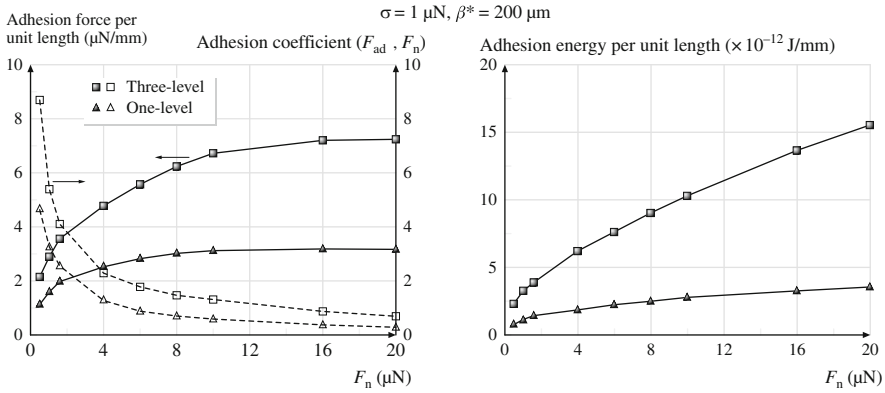
of 20–40  $\mu\text{N}$  and thus a value of adhesion coefficient of 8–16, which supports the simulation results of Kim and Bhushan [30].

Figure 21.16b (top left) shows that the adhesion coefficient for the one-level model is lower than that for the three-level model, but there is only a small difference between the values of the two- and three-level models. In order to show the effect of stiffness, the results are plotted for the three-level model with springs in level III with stiffness 10 times smaller than originally. It can be seen that the three-level model with a third-level stiffness of  $0.1 k_{\text{III}}$  has a 20–30% higher adhesion coefficient than the original three-level model. The results also show that the trends in the number of contacts are similar to that of the adhesive force. The study also investigated the effect of  $\sigma$  on adhesion energy. It was determined that adhesion energy decreased with increasing  $\sigma$ . For the smooth surface with  $\sigma = 0.01 \mu\text{m}$ , the adhesion energies for the two- and three-level hierarchical models are 2 and 2.4 times larger than that for the one-level model, respectively, but the adhesion energy decreases rapidly at surfaces with  $\sigma > 0.05 \mu\text{m}$ ; and in every model it finally decreases to zero at surfaces with  $\sigma > 10 \mu\text{m}$ . The adhesion energy for the three-level model with  $0.1 k_{\text{III}}$  is 2–3 times higher than that for the original three-level model.

In order to demonstrate the effect of the hierarchical structure on adhesion enhancement, Kim and Bhushan [30] calculated the increases in the adhesion coefficient, the number of contacts, and the adhesion energy of the two-, three- and three-level (with  $0.1 k_{\text{III}}$ ) models relative to the one-level model. These results are shown on the right side of Fig. 21.16b. It was found that, for the two- and three-level models, the adhesion coefficient increases slowly with increasing  $\sigma$  and has maximum values of  $\approx 70$  and  $80\%$  at  $\sigma = 1 \mu\text{m}$ , respectively, and then decreases for surfaces with  $\sigma > 3 \mu\text{m}$ . The condition at which a significant enhancement occurs is related to the maximum spring deformation, which is the applied load divided by the spring stiffness. If the maximum spring deformation is greater than 2–3 times larger than the  $\sigma$  value of the surface roughness, significant adhesion enhancement occurs. The three-level model with  $0.1 k_{\text{III}}$  shows significant adhesion enhancement. The relative increase of the adhesion coefficient and adhesion energy for the three-level model with  $0.1 k_{\text{III}}$  has maximum values at  $\sigma = 1 \mu\text{m}$ .

Figure 21.17 shows the variation of adhesion force and adhesion energy as a function of applied load for both one- and three-level models contacting a surface with  $\sigma = 1 \mu\text{m}$ . It is shown that, as the applied load increases, the adhesion force increases up to a certain applied load and then has a constant value, whereas adhesion energy continues to increase with increasing applied load. The one-level model has a maximum value of adhesion force per unit length of  $\approx 3 \mu\text{N}/\text{mm}$  at an applied load of  $10 \mu\text{N}$ , and the three-level model has a maximum value of  $\approx 7 \mu\text{N}/\text{mm}$  at an applied load of  $16 \mu\text{N}$ . However, the adhesion coefficient continues to decrease at higher applied loads because the adhesion force is constant even if the applied load increases.

The simulation results for the three-level model, which is close to gecko setae, presented in Fig. 21.16 show that roughness reduces the adhesion force. At surfaces with  $\sigma > 10 \mu\text{m}$ , the ratio of the adhesion force to the gecko weight indicates that it cannot support itself. However, in practice, a gecko can cling to or crawl on the



**Fig. 21.17** The adhesion force, adhesion coefficient, and adhesion energy as a function of applied loads for both one- and three-level models contacting with the rough surface (after [30])

surface of ceilings with higher roughness. Kim and Bhushan [30] did not consider the effect of lamellae in their study. The authors state that the lamellae can adapt to the waviness of a surface while the setae allow for adaptation to micro- or nano-roughness and expect that adding the lamellae of gecko skin to the model would lead to higher adhesion over a wider range of roughness. In addition, their hierarchical model only considers deformation normal to the surface and the motion of setae. It should be noted that the measurements of the adhesion force of a single gecko seta made by Autumn et al. [25] demonstrated that a load applied normal to the surface was insufficient for effective attachment of seta.

Finally the effects of spring stiffness and the number of springs on the adhesion enhancement of the multilevel hierarchical model (one- and three-level models with four different spring stiffnesses and three different numbers of springs) were analyzed by Kim and Bhushan [31]. The stiffness  $k_I$  was taken equal to 0.0126 N/m, as before. Other stiffnesses,  $k_{II}$  and  $k_{III}$  were normalized with respect to  $k_I$ . The three-level model with  $k_{III}/k_I = 100$  and  $k_{II}/k_I = 10$  had similar stiffness values to gecko seta, as presented in Table 21.3 and used in the previous example (Figs. 21.16 and 21.17). The left part in Fig. 21.18 shows the adhesion coefficient, number of contacts, and adhesion energy per unit length for the one- and three-level models with four different spring stiffnesses as a function of  $\sigma$  value for an applied load of 1.6  $\mu\text{N}$ . Trends as a function of  $\sigma$  are the same as observed previously in Fig. 21.16b. For the case of  $k_{III} = k_{II} = k_I$ , one gets the highest value (36) of the adhesion coefficient on a rough surface, and it remains high up to  $\sigma$  value of  $\approx 1 \mu\text{m}$ , and then starts to decrease. As the stiffness values  $k_{II}$  and  $k_{III}$  increase, the adhesion coefficient starts to decrease at lower values of  $\sigma$ , and it decreases rapidly with increasing  $\sigma$ . The number of contacts and adhesion energy per unit length as a function of  $\sigma$  have trends similar to that of adhesion coefficient. The right part in Fig. 21.18 shows the relative increase between the one- and three-level models. The trends are the same as discussed earlier.

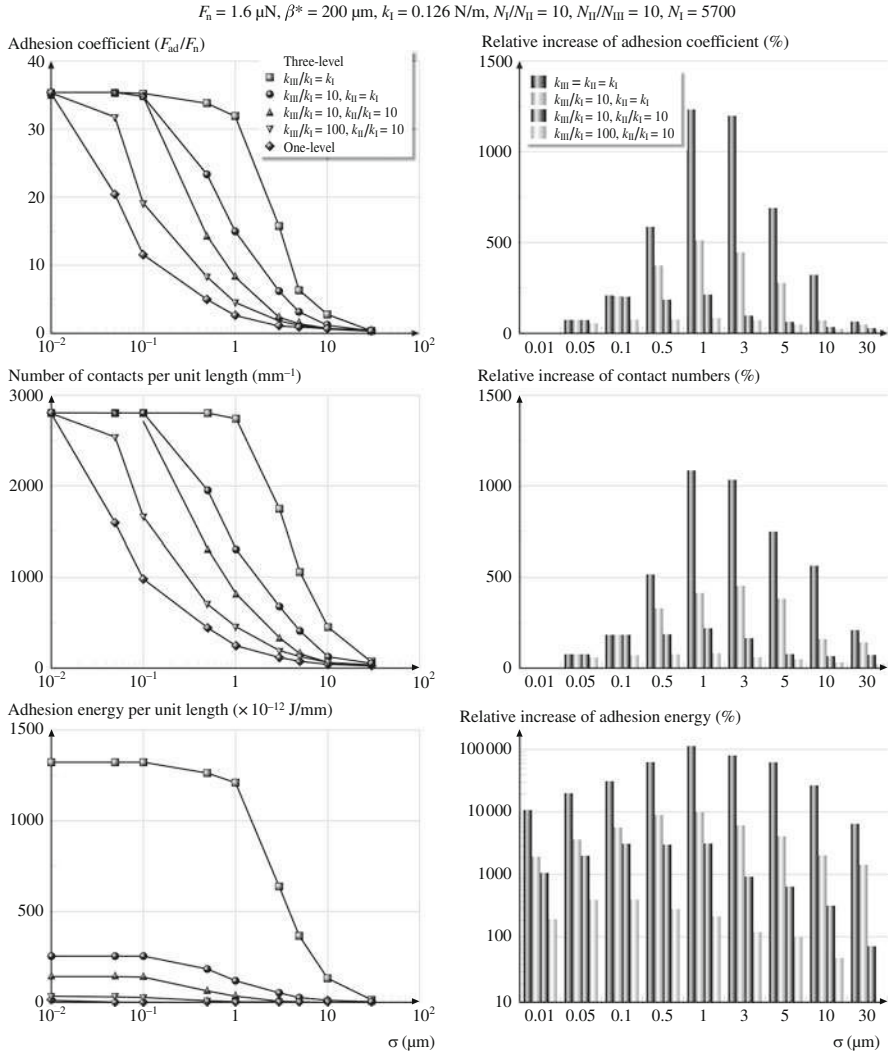
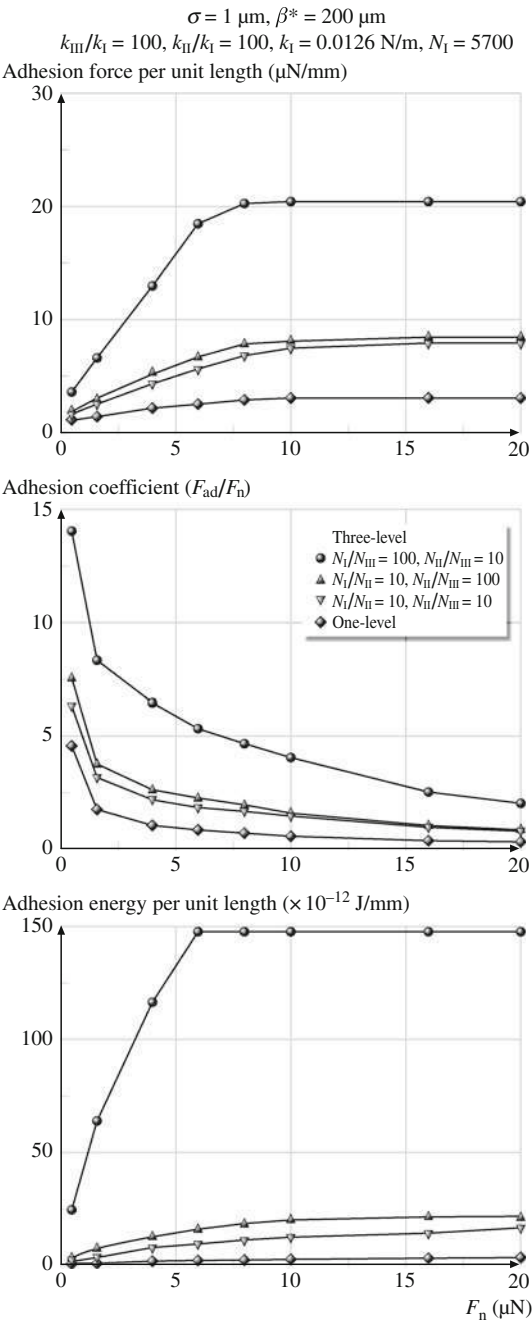


**Fig. 21.18** The adhesion coefficient, number of contacts, and adhesion energy per unit length of profile for one- and three-level models with different spring stiffnesses as a function of  $\sigma$  value (*left column*), and relative increases between one- and three-level models (*right column*) for applied load of  $1.6 \mu\text{N}$  (after [31])

To study the effect of the number of springs, three different cases of the number of springs in the upper level compared with in the lower level were considered. The three-level model with  $N_I/N_{II} = 10$  and  $N_{II}/N_{III} = 10$  is closest to the case of the gecko's setae (discussed earlier). Figure 21.19 shows the adhesion force, adhesion coefficient, and adhesion energy as a function of applied loads for one- and three-level models with different numbers of springs contacting with the rough surface.

**Fig. 21.19** The adhesive force, adhesion coefficient, and adhesion energy as a function of applied loads for one- and three-level models with different number of springs contacting with the rough surface (after [31])



The variation of the number of springs on each level affects the equivalent stiffness of the model. As the number of springs on the lower level increases, the equivalent stiffness decreases. The figure shows that the three-level model with  $N_I/N_{II} = 100$

and  $N_{II}/N_{III} = 10$  gives the largest adhesion force and adhesion energy among the models, because the equivalent stiffness is lowest.

### 21.6.4 Capillary Effects

Kim and Bhushan [33] investigated the effects of capillarity on gecko adhesion by considering the capillary force as well as the solid–solid interaction. The Laplace and surface tension components of the capillary force are treated according to Sect. 21.4.2. The solid–solid adhesive force was calculated by DMT theory according to (21.20) and will be denoted by  $F_{\text{DMT}}$ .

The work of adhesion was then calculated by (21.21). Kim and Bhushan [33] assumed typical values of the Hamaker constant to be  $H_{\text{air}} = 10^{-19}$  J in air and  $H_{\text{water}} = 6.7 \times 10^{-19}$  J in water [61]. The work of adhesion of two surfaces in contact separated by an atomic distance  $D \approx 0.2$  nm [61] is  $\approx 66$  mJ/m<sup>2</sup> in air and 44 mJ/m<sup>2</sup> in water. Assuming the tip radius  $R$  to be 50 nm, the DMT adhesion force  $F_{\text{DMT}}$  of a single contact in air and in water is  $F_{\text{DMT}}^{\text{air}} = 11$  nN and  $F_{\text{DMT}}^{\text{water}} = 7.3$  nN, respectively. As the humidity increases from 0% to 100%, the DMT adhesion force will take a value between  $F_{\text{DMT}}^{\text{air}}$  and  $F_{\text{DMT}}^{\text{water}}$ . To calculate the DMT adhesion force for intermediate humidity, an approximation method by Wan et al. [77] was used. The work of adhesion  $W_{\text{ad}}$  for the intermediate humidity can be expressed as

$$W_{\text{ad}} = \int_D^\infty \frac{H}{6\pi h^3} dh = \int_D^{h_f} \frac{H_{\text{water}}}{6\pi h^3} dh + \int_{h_f}^\infty \frac{H_{\text{air}}}{6\pi h^3} dh, \quad (21.27)$$

where  $h$  is the separation along the plane.  $h_f$  is the water film thickness at a filling angle of  $\phi$ , which can be calculated as

$$h_f = D + R(1 - \cos \phi). \quad (21.28)$$

Therefore, using (21.20), (21.27), and (21.28), the DMT adhesion force for intermediate humidity is given by

$$F_{\text{DMT}} = F_{\text{DMT}}^{\text{air}} \left\{ 1 - \frac{1}{[1 + R(1 - \cos \phi)/D]^2} \right\} + F_{\text{DMT}}^{\text{water}} \left\{ \frac{1}{[1 + R(1 - \cos \phi)/D]^2} \right\}. \quad (21.29)$$

Finally, Kim and Bhushan [33] calculated the total adhesion force  $F_{\text{ad}}$  as the sum of (21.16) and (21.29)

$$F_{\text{ad}} = F_c + F_{\text{DMT}}. \quad (21.30)$$



Kim and Bhushan [33] then used the total adhesion force as a critical force in the three-level hierarchical spring model discussed previously. In the spring model for gecko seta, if the force applied upon spring deformation is greater than the adhesion force, the spring is regarded as having been detached.

To simulate the capillary contribution to the adhesion force for a gecko spatula, Kim and Bhushan [33] set the contact angle on a gecko spatula tip to be  $\theta_1 = 128^\circ$  [28]. It was assumed that the spatula tip radius  $R = 50\text{ nm}$ , the ambient temperature  $T = 25^\circ\text{C}$ , the surface tension of water  $\gamma = 73\text{ mJ/m}^2$ , and the molecular volume of water  $V = 0.03\text{ nm}^3$  [61].

Figure 21.20a shows the total adhesion force as a function of relative humidity for a single spatula in contact with surfaces with different contact angles. Total adhesion force decreases with an increase in the contact angle on the substrate, and

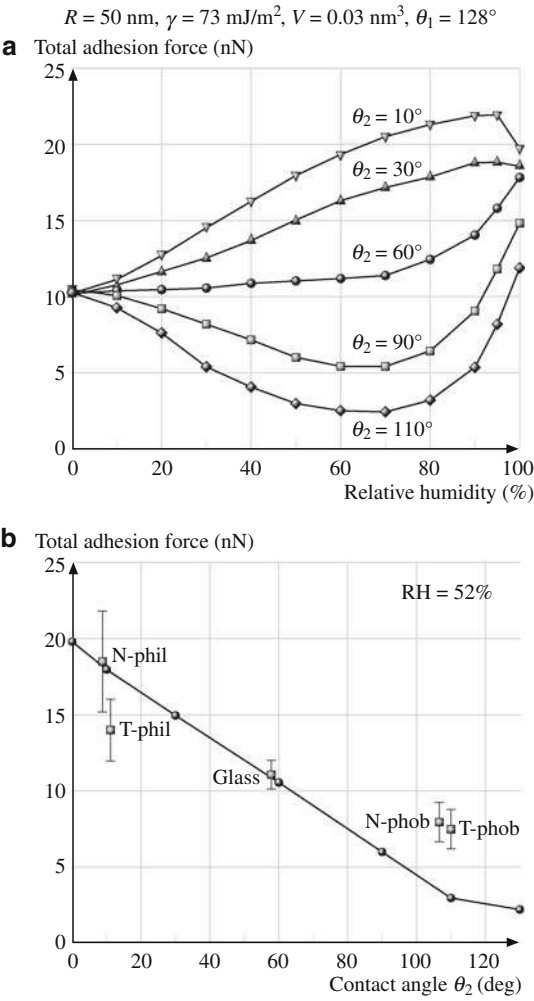


**Fig. 21.20** (a) Total adhesion force as a function of relative humidity for a single spatula in contact with surfaces with different contact angles. (b) Comparison of the simulation results of Kim and Bhushan [33] with the measured data obtained by Huber et al. [28] for a single spatula in contact with hydrophilic and hydrophobic surfaces (after [33])

the difference of total adhesion force among different contact angles is larger in the intermediate-humidity regime. As the relative humidity increases, the total adhesion force for surfaces with contact angles  $<60^\circ$  has a higher value than the DMT adhesion force not considering wet contact, whereas for contact angles  $>60^\circ$ , the total adhesion force has lower values at most relative humidity.

The simulation results of Kim and Bhushan [33] are compared with the experimental data by Huber et al. [28] in Fig. 21.20b. Huber et al. [28] measured the pull-off force of a single spatula in contact with four different types of Si wafer and glass at ambient temperature of  $25^\circ\text{C}$  and relative humidity of 52%. According to their description, wafer families “N” and “T” in Fig. 21.20b differ by the thickness of the top amorphous Si oxide layer. The “phil” type is cleaned Si oxide surface, which is hydrophilic with a water contact angle of  $\approx 10^\circ$ , whereas the “phob” type is a Si wafer covered with a hydrophobic monolayer, resulting in a water contact angle of  $>100^\circ$ . The glass has a water contact angle of  $58^\circ$ . Huber et al. [28] showed that the adhesion force of a gecko spatula rises significantly for substrates with increasing hydrophilicity (adhesive force increases by a factor of two as the mating surfaces go from hydrophobic to hydrophilic). As shown in Fig. 21.20b, the simulation results of Kim and Bhushan [33] closely match the experimental data of Huber et al. [28].

Kim and Bhushan [33] carried out adhesion analysis for a three-level hierarchical model for gecko seta. Figure 21.21 shows the adhesion coefficient and number of contacts per unit length for the three-level hierarchical model in contact with rough surfaces with different values of the RMS amplitude  $\sigma$  ranging from  $\sigma = 0.01$  to  $30\text{ }\mu\text{m}$  for different relative humidity values and contact angles of the surface. It can be seen that, for a surface with contact angle  $\theta_2 = 10^\circ$ , the adhesion coefficient is greatly influenced by relative humidity. At 0% relative humidity the maximum adhesion coefficient is  $\approx 36$  at a value of  $\sigma < 0.01\text{ }\mu\text{m}$  compared with 78 for 90% relative humidity for the same surface roughness. As expected the effect of relative humidity on increasing the adhesion coefficient decreases as the contact angle becomes larger. For hydrophobic surfaces, relative humidity decreases the adhesion coefficient. Similar trends can be noticed in terms of the number of contacts. Thus, the conclusion can be drawn that hydrophilic surfaces are beneficial to gecko adhesion enhancement.

## 21.7 Modeling of Biomimetic Fibrillar Structures

The mechanics of adhesion between a fibrillar structure and a rough surface as it relates to the design of biomimetic structures has been a topic of investigation by many researchers [31, 32, 37, 49, 52, 75, 78, 79, 80]. Kim and Bhushan [32] developed a convenient, general, and useful guideline for understanding biological systems and for improving biomimetic attachment. This adhesion database was constructed by modeling fibers as oriented cylindrical cantilever beams with spherical tips. The authors then carried out numerical simulation of the attachment system

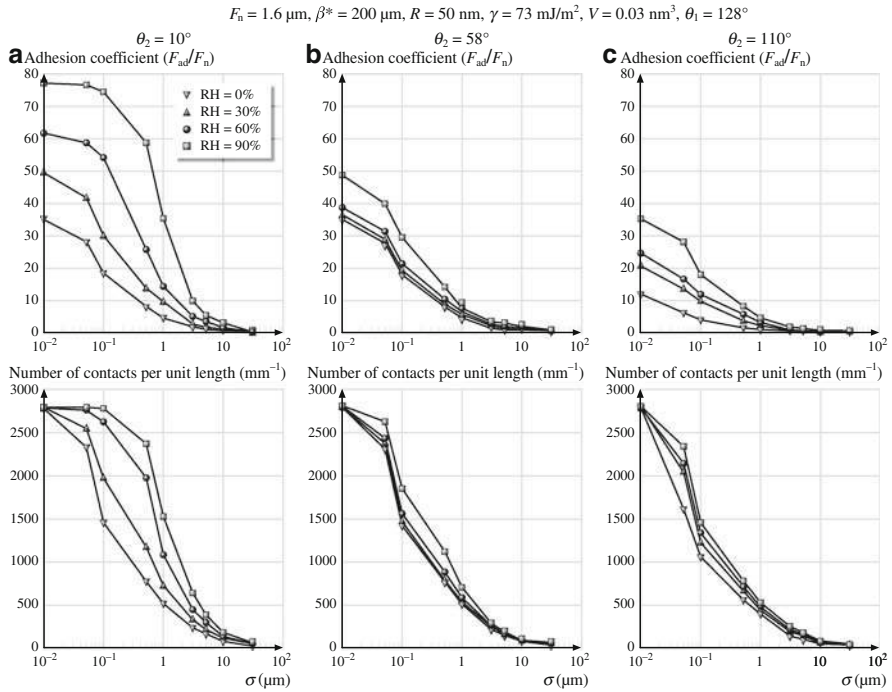


**Fig. 21.21** The adhesion coefficient and number of contacts per unit length for the three-level hierarchical model in contact with rough surfaces with different values of RMS amplitudes  $\sigma$  and contact angles for different relative humidities (after [33])

in contact with random rough surfaces considering three constraint conditions: buckling, fracture, and sticking of the fiber structure. For a given applied load and roughnesses of contacting surface and fiber material, a procedure to find an optimal fiber radius and aspect ratio for the desired adhesion coefficient was developed.

The model of Kim and Bhushan [32] is used to find the design parameters for fibers of a single-level attachment system capable of achieving desired properties, i.e., high adhesion coefficient and durability. The design variables for an attachment system are as follows: fiber geometry (radius and aspect ratio of fibers, tip radius), fiber material, fiber density, and fiber orientation. The optimal values for the design variables to achieve the desired properties should be selected for the fabrication of a biomimetic attachment system.

### 21.7.1 Fiber Model

The fiber model of Kim and Bhushan [32] consists of a simple idealized fibrillar structure consisting of a single-level array of micro/nanobeams protruding from a backing, as shown in Fig. 21.22. The fibers are modeled as oriented cylindrical

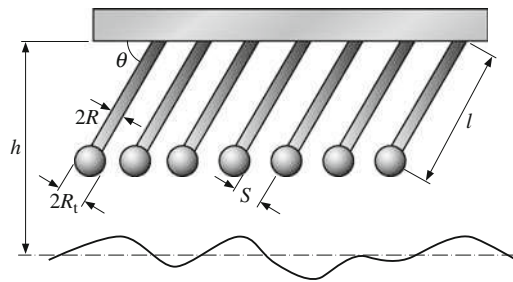


**Fig. 21.22** Single-level attachment system with oriented cylindrical cantilever beams with spherical tip. In this figure,  $l$  is the length of fibers,  $\theta$  is the fiber orientation,  $R$  is the fiber radius,  $R_t$  is the tip radius,  $S$  is the spacing between fibers, and  $h$  is the distance between the base of the model and the mean line of the rough profile (after [32])

cantilever beams with spherical tips. In Fig. 21.22,  $l$  is the length of fibers,  $\theta$  is the fiber orientation,  $R$  is the fiber radius,  $R_t$  is the tip radius,  $S$  is the spacing between fibers, and  $h$  is the distance between the upper spring base of each model and the mean line of the rough profile. The end terminal of the fibers is assumed to be a spherical tip with constant radius and constant adhesion force.

### 21.7.2 Single-Fiber Contact Analysis

Kim and Bhushan [32] modeled an individual fiber as a beam oriented at an angle  $\theta$  to the substrate, and the contact load  $F$  aligned normal to the substrate. The net displacement normal to the substrate can be calculated according to (21.17) and (21.18). The fiber stiffness ( $k = F/\delta_{\perp}$ ) is given by [75]

$$k = \frac{\pi R^2 E}{l \sin^2 \theta \left(1 + \frac{4l^2 \cot^2 \theta}{3R^2}\right)} = \frac{\pi R E}{2\lambda \sin^2 \theta \left(1 + \frac{16\lambda^2 \cot^2 \theta}{3}\right)}, \quad (21.31)$$

where  $\lambda = l/2R$  is the aspect ratio of the fiber and  $\theta$  is fixed at  $30^\circ$ .

Two alternative models dominate the world of contact mechanics: the Johnson–Kendall–Roberts (JKR) theory [44] for compliant solids, and the Derjaguin–Muller–Toporov (DMT) theory [76] for stiff solids. Although gecko setae are composed of  $\beta$ -keratin with a high elastic modulus [13, 45], which is close to the DMT model, in general the JKR theory prevails for biological or artificial attachment systems. Therefore the JKR theory was applied in the subsequent analysis of Kim and Bhushan [32] to compare materials with wide ranges of elastic modulus. The adhesion force between a spherical tip and a rigid flat surface is thus calculated using the JKR theory as [44]

$$F_{\text{ad}} = \frac{3}{2} \pi R_t W_{\text{ad}}, \quad (21.32)$$

where  $R_t$  is the radius of spherical tip and  $W_{ad}$  is the work of adhesion, calculated according to (21.25). Kim and Bhushan [32] used this adhesion force as a critical force. If the elastic force of a single spring is less than the adhesion force, they regarded the spring as having been detached.

### 21.7.3 Constraints

In the design of fibrillar structures, a trade-off exists between the aspect ratio of the fibers and their adaptability to a rough surface. If the aspect ratio of the fibers is too large, they can adhere to each other or even collapse under their own weight, as shown in Fig. 21.23a. If the aspect ratio is too small (Fig. 21.23b), the structures will lack the compliance necessary to conform to a rough surface. The spacing between the individual fibers is also important. If the spacing is too small, adjacent fibers can attract each other through intermolecular forces, which will lead to bunching. Therefore, Kim and Bhushan [32] considered three necessary conditions in their analysis: buckling, fracture, and sticking of fiber structure, which constrain the allowed geometry.

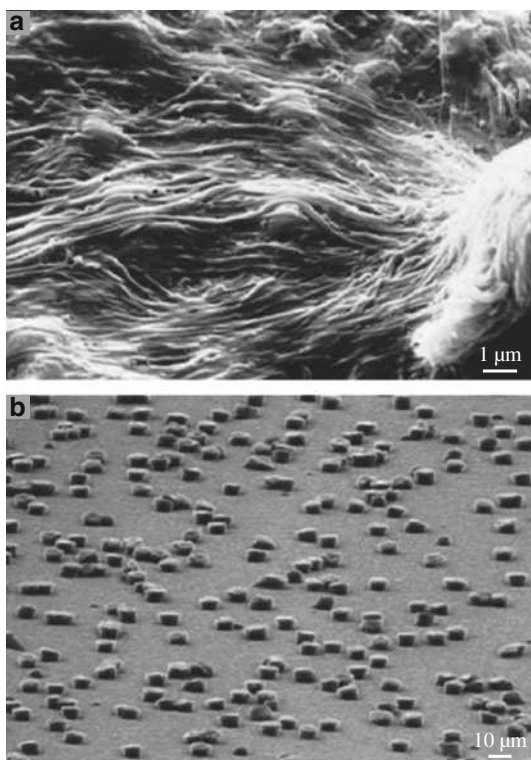


**Fig. 21.23** SEM micrographs of (a) high-aspect-ratio polymer fibrils that have collapsed under their own weight and (b) low-aspect-ratio polymer fibrils that are incapable of adapting to rough surfaces (after [49])

### Nonbuckling Condition

A fibrillar interface can deliver a compliant response while still employing stiff materials because of bending and microbuckling of fibers. Based on classical Euler buckling, Glassmaker et al. [75] established a stress–strain relationship and a critical compressive strain for buckling  $\varepsilon_{cr}$  for a fiber oriented at an angle  $\theta$  to the substrate

$$\varepsilon_{cr} = -\frac{b_c \pi^2}{3(A_c l^2 / 3I)} \left( 1 + \frac{A_c l^2}{3I} \cot^2 \theta \right). \quad (21.33)$$

where  $A_c$  is the cross-sectional area of the fibril, and  $b_c$  is a factor that depends on boundary conditions. The factor  $b_c$  has a value of 2 for pinned–clamped microbeams. For fibers having a circular cross-section,  $\varepsilon_{cr}$  is calculated as

$$\begin{aligned} \varepsilon_{cr} &= -\frac{b_c \pi^2}{3(4I^2 / 3R^2)} \left( 1 + \frac{4I^2}{3R^2} \cot^2 \theta \right) \\ &= -b_c \pi^2 \left( \frac{1}{16\lambda^2} + \frac{\cot^2 \theta}{3} \right). \end{aligned} \quad (21.34)$$

In (21.34),  $\varepsilon_{cr}$  depends on both the aspect ratio  $\lambda$  and the orientation  $\theta$  of fibers. If  $\varepsilon_{cr} = 1$ , which means the fiber deforms up to the backing, buckling does not occur. Figure 21.24 plots the critical orientation  $\theta$  as a function of aspect ratio for the case of  $\varepsilon_{cr} = 1$ . The critical fiber orientation for buckling is  $90^\circ$  at  $\lambda < 1.1$ . This means that buckling does not occur regardless of the orientation of the fiber at  $\lambda < 1.1$ . For  $\lambda > 1.1$ , the critical fiber orientation for buckling decreases with an increase in  $\lambda$ , and has a constant value of  $69^\circ$  at  $\lambda > 3$ . Kim and Bhushan [32] used a fixed value at  $30^\circ$  for  $\theta$ , because as stated earlier, the maximum adhesive force is achieved at this orientation, and buckling is not expected to occur.

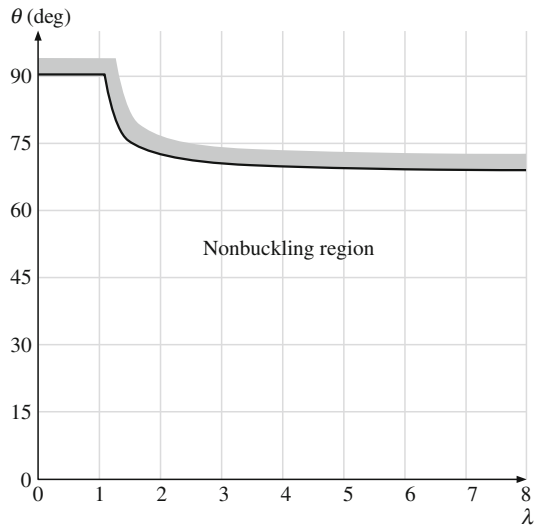


**Fig. 21.24** Critical fiber orientation as a function of aspect ratio  $\lambda$  for the nonbuckling condition for pinned–clamped microbeams ( $b_c = 2$ ) (after [32])

### No-Fiber-Fracture Condition

For small contacts, the strength of the system will eventually be determined by fracture of the fibers. Spolenak et al. [81] suggested the limit of fiber fracture as a function of the adhesion force. The axial stress  $\sigma_f$  in a fiber is limited by its theoretical fracture strength  $\sigma_{th}^f$  as

$$\sigma_f = \frac{F_{ad}}{R^2\pi} \leq \sigma_{th}^f. \quad (21.35)$$

Using (21.32), a lower limit for the useful fiber radius,  $R$ , is calculated as

$$R \geq \sqrt{\frac{3R_t W_{ad}}{2\sigma_{th}^f}} \approx \sqrt{\frac{15 R_t W_{ad}}{E}}, \quad (21.36)$$

where the theoretical fracture strength is approximated by  $E/10$  [82]. The lower limit of fiber radius for fiber fracture by the adhesion force depends on elastic modulus. By assuming  $W_{ad} = 66 \text{ mJ/m}^2$  as stated earlier, Kim and Bhushan [32] calculated the lower limits of fiber radius for  $E = 1 \text{ MPa}$ ,  $0.1 \text{ GPa}$ , and  $10 \text{ GPa}$  to be  $0.32$ ,  $0.032$ , and  $0.0032 \text{ }\mu\text{m}$ , respectively.

The contact stress cannot exceed the ideal contact strength transmitted through the actual contact area at the instant of tensile instability [81]. Kim and Bhushan [32] used this condition (21.35) to extract the limit of tip radius  $R_t$ ,

$$\sigma_c = \frac{F_{ad}}{a_c^2\pi} \geq \sigma_{th}, \quad (21.37)$$

where  $\sigma_c$  is the contact stress,  $\sigma_{th}$  is the ideal strength of van der Waals bonds, which equals  $\approx W_{ad}/b$ ,  $b$  is the characteristic length of surface interaction, and  $a_c$  is the contact radius. Based on the JKR theory, for the rigid contacting surface,  $a_c$  at the instant of pull-off is calculated as

$$a_c = \left( \frac{9\pi W_{ad} R_t^2 (1 - \nu^2)}{8E} \right)^{1/3}, \quad (21.38)$$

where  $\nu$  is Poisson's ratio. The tip radius can then be calculated by combining (21.37) and (21.38) as

$$R_t \geq \frac{8b^3 E^2}{3\pi^2 (1 - \nu^2)^2 W_{ad}^2}. \quad (21.39)$$

The lower limit of tip radius also depends on the elastic modulus. Assuming  $W_{ad} = 66 \text{ mJ/m}^2$  and  $b = 2 \times 10^{-10} \text{ m}$  [82], the lower limit of tip radius for  $E = 1 \text{ MPa}$ ,  $0.1 \text{ GPa}$ , and  $10 \text{ GPa}$  is calculated as  $6 \times 10^{-7}$ ,  $6 \times 10^{-3}$ , and  $60 \text{ nm}$ , respectively. In this study, Kim and Bhushan [32] fixed the tip radius at

100 nm, which satisfies the tip radius condition throughout a wide range of elastic modulus up to 10 GPa.

### Nonsticking Condition

A high density of fibers is also important for high adhesion. However, if the space  $S$  between neighboring fibers is too small, the adhesion forces between them become stronger than the forces required to bend the fibers. Then, fibers might stick to each other and get entangled. Therefore, to prevent fibers from sticking to each other, they must be spaced apart and be stiff enough to prevent sticking or bunching. Several authors (e.g., [49]) have formulated a nonsticking criterion. Kim and Bhushan [32] adopted the approach of Sitti and Fearing [49]. Both adhesion and elastic forces will act on bent structures. The adhesion force between two neighboring round tips is calculated as

$$F_{\text{ad}} = \frac{3}{2} \pi R'_t W_{\text{ad}}, \quad (21.40)$$

where  $R'_t$  is the reduced radius of contact, which is calculated as  $R'_t = (1/R_{t1} + 1/R_{t2})^{-1}$ ;  $R_{t1}$ ,  $R_{t2}$  – radii of contacting tips; for the case of similar tips,  $R_{t1} = R_{t2}$ ,  $R'_t = 2/R_t$ .

The elastic force of a bent structure can be calculated by multiplying the bending stiffness ( $k_b = 3\pi R^4 E / 4l^3$ ) by a given bending displacement  $\delta$  as

$$F_{\text{el}} = \frac{3}{4} \frac{\pi R^4 E \delta}{l^3}. \quad (21.41)$$

The condition for the prevention of sticking is  $F_{\text{el}} > F_{\text{ad}}$ . By combining (21.40) and (21.41), a requirement for the minimum distance  $S$  between structures which will prevent sticking of the structures is given as [32]

$$S > 2\delta = 2 \left( \frac{4}{3} \frac{W_{\text{ad}} l^3}{E R^3} \right) = 2 \left( \frac{32}{3} \frac{W_{\text{ad}} \lambda^3}{E} \right). \quad (21.42)$$

The constant 2 takes into account the two nearest structures. Using the distance  $S$ , the fiber density  $\rho$  is calculated as

$$\rho = \frac{1}{(S + 2R)^2}. \quad (21.43)$$

Equation (21.43) was then used to calculate the allowed minimum density of fibers without sticking or bunching. In (21.42), it is shown that the minimum distance  $S$  depends on both the aspect ratio  $\lambda$  and the elastic modulus  $E$ . A smaller



aspect ratio and higher elastic modulus allow for greater packing density. However, fibers with a low aspect ratio and high modulus are not desirable for adhering to rough surfaces due to lack of compliance.

### 21.7.4 Numerical Simulation

The simulation of adhesion of an attachment system in contact with random rough surfaces was carried out numerically. In order to conduct two-dimensional (2-D) simulations it is necessary to calculate the applied load  $F_n$  as a function of the applied pressure  $P_n$  as an input condition. Using  $\rho$  calculated by the nonsticking condition, Kim and Bhushan [32] calculated  $F_n$  as

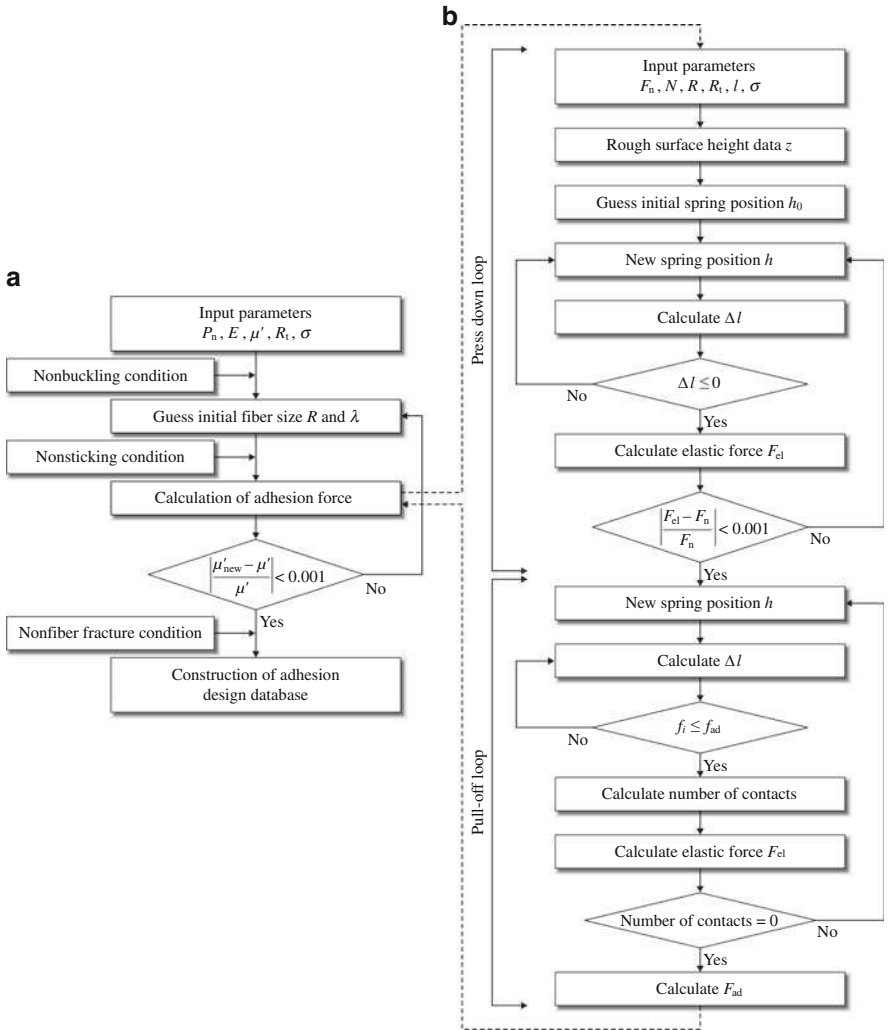
$$F_n = \frac{P_n p}{\rho}. \quad (21.44)$$

where  $p$  is the number of springs in the scan length  $L$ , which equals  $L/(S + 2R)$ .

Fibers of the attachment system are modeled as a one-level hierarchy of elastic springs (Fig. 21.14) [32]. The deflection of each spring and the elastic force arising in the springs are calculated according to (21.22) and (21.23), respectively. The adhesion force is the lowest value of the elastic force  $F_{el}$  when the fiber has detached from the contacting surface. Kim and Bhushan [32] used an iterative process to obtain the optimal fiber geometry in terms of fiber radius and aspect ratio. If the applied load, roughness of the contacting surface, and fiber material are given, the procedure for calculating the adhesion force is iterated until the desired adhesion force is satisfied. In order to simplify the design problem, the fiber material is regarded as a known variable. The next step is constructing the design database. Figure 21.25a shows the flow chart for the construction of the adhesion design database, and Fig. 21.25b shows the calculation of the adhesion force, which is part of the procedure to construct the adhesion design database.

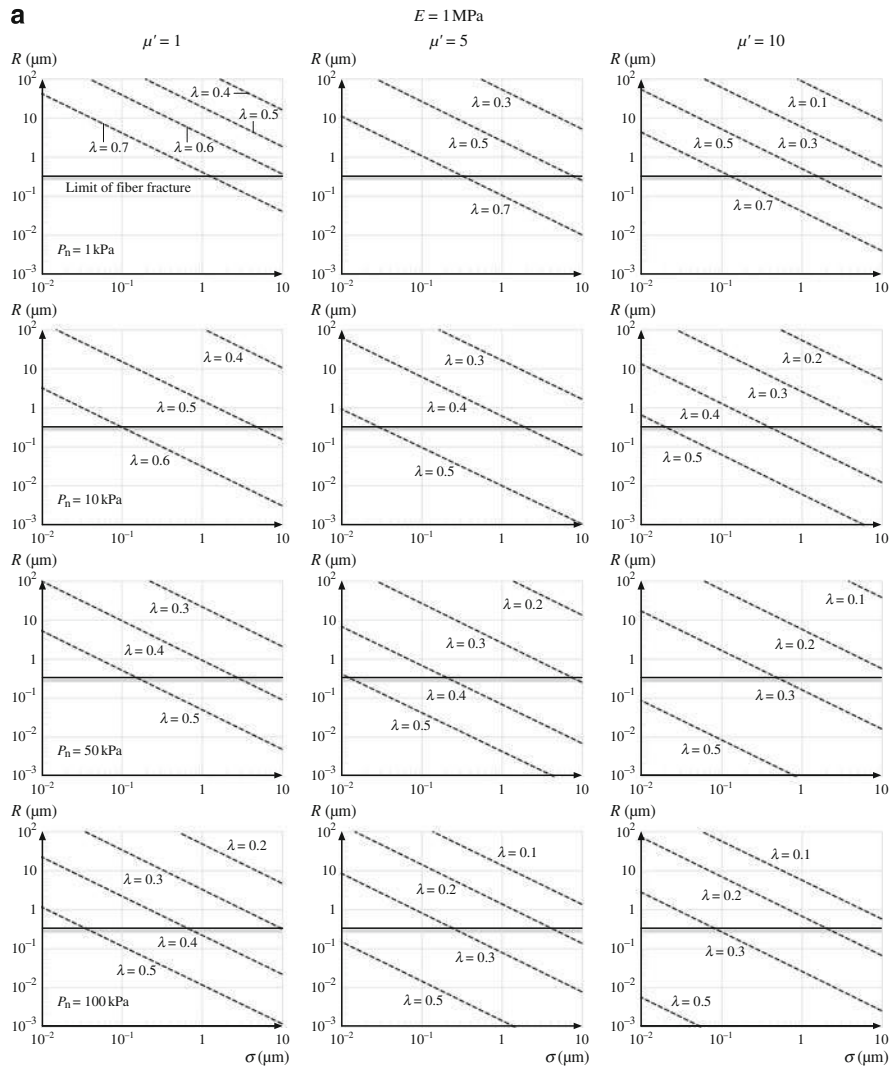
### 21.7.5 Results and Discussion

Figure 21.26 shows an example of the adhesion design database for biomimetic attachment systems consisting of single-level cylindrical fibers with an orientation angle of  $30^\circ$  and spherical tips of  $R_t = 100$  nm constructed by Kim and Bhushan [32]. The minimum fiber radius calculated by using the no-fiber-fracture condition, which plays a role of the lower limit of optimized fiber radius, is also added to the plot. The plots in Fig. 21.26 cover all applicable fiber materials from a soft elastomer material such as poly(dimethylsiloxane) (PDMS) to



**Fig. 21.25** (a) Flow chart for the construction of the adhesion design database. (b) Calculation of the adhesion force.  $P_n$  is the applied pressure,  $E$  is the elastic modulus,  $\mu'$  is the adhesion coefficient,  $R_t$  is the tip radius,  $\sigma$  is the RMS amplitude,  $R$  is the fiber radius,  $\lambda$  is the fiber aspect ratio,  $F_n$  is the applied load,  $N$  is the number of springs,  $k$  and  $l$  are the stiffness and length of structures,  $\Delta l$  is the spring deformation,  $f_i$  is the elastic force of a single spring, and  $f_{ad}$  is the adhesion force of a single contact (after [32])

stiffer polymers such as polyimide and  $\beta$ -keratin. The dashed lines in each plot represent the limits of fiber fracture due to the adhesion force. For a soft material with  $E = 1$  MPa in Fig. 21.26a, the range of the desirable fiber radius is  $>0.3 \mu\text{m}$  and that of the aspect ratio is  $\approx < 1$ . As elastic modulus increases, the feasible range of both fiber radius and aspect ratio also increase, as shown in Fig. 21.26b,c.



**Fig. 21.26** (continued)

In Fig. 21.26, the fiber radius has a linear relation with the surface roughness on a logarithm scale.

If the applied load, roughness of the contacting surface, and elastic modulus of the fiber material are specified, the optimal fiber radius and aspect ratio for the desired adhesion coefficient can be selected from this design database. The adhesion databases are useful for understanding biological systems and for guiding the fabrication of biomimetic attachment systems. Two case studies [32] are discussed below.

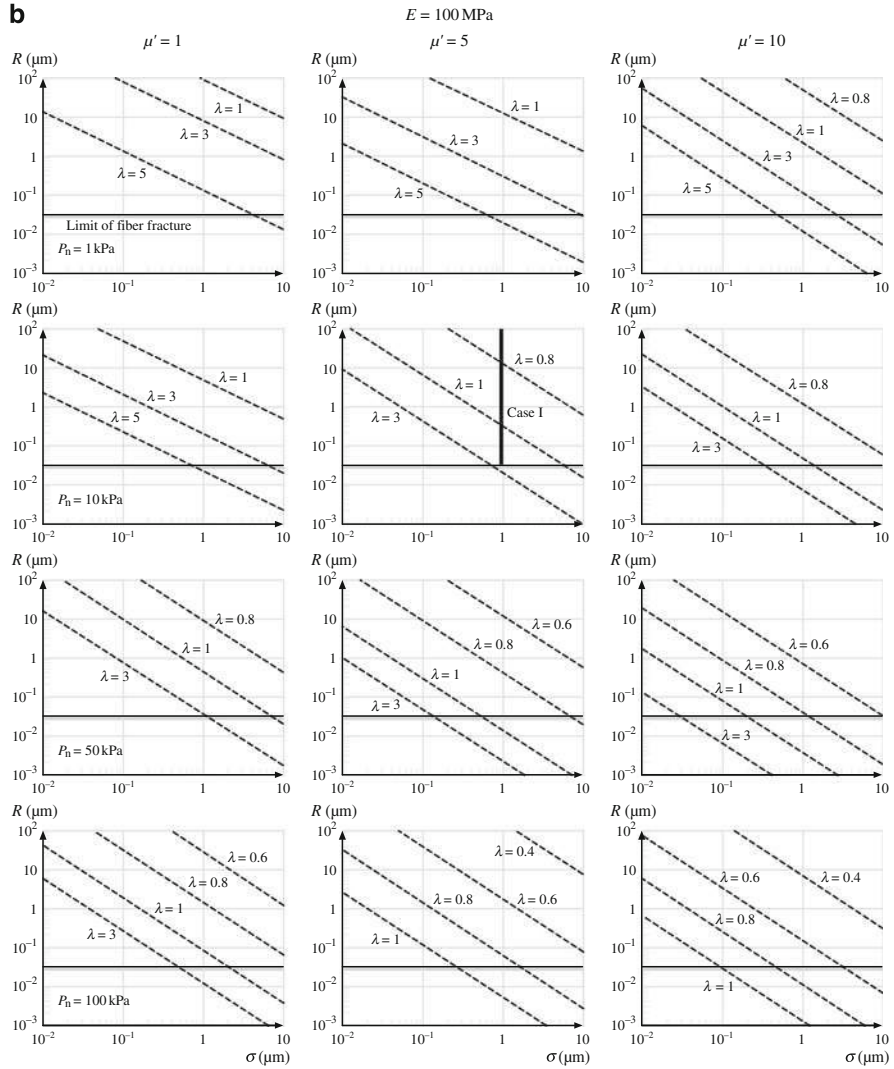
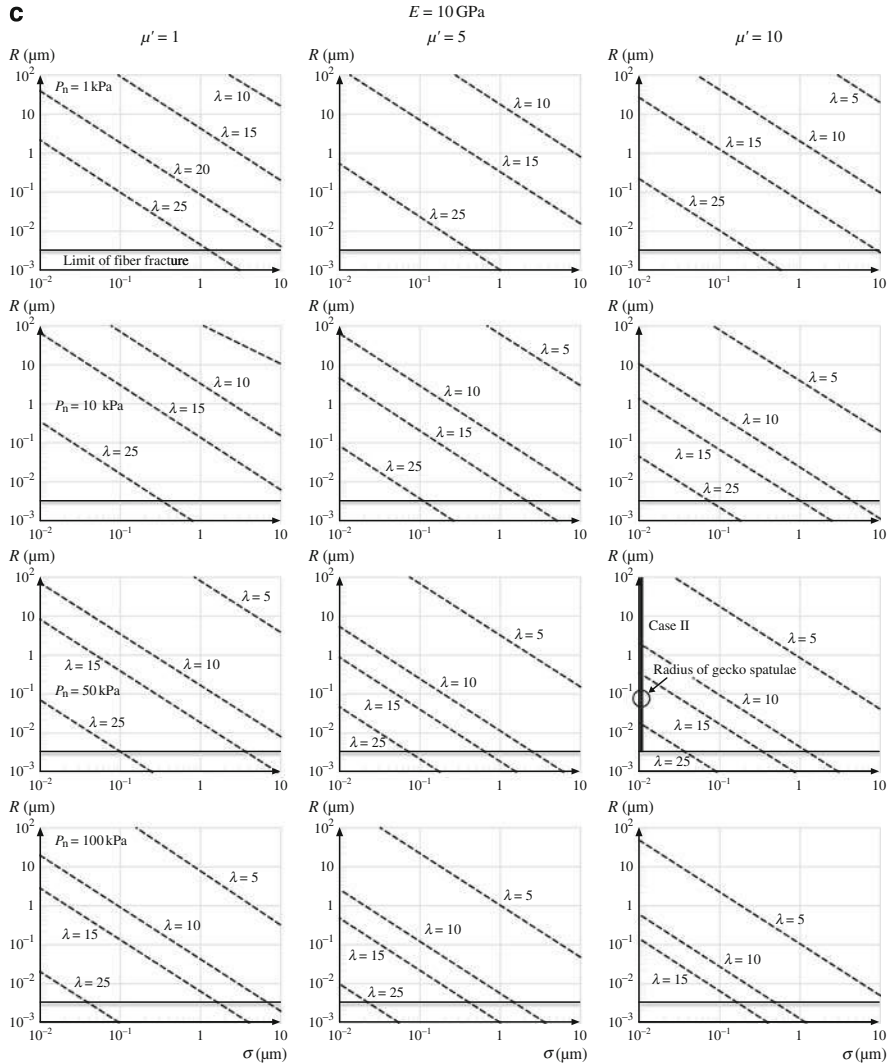


Fig. 21.26 (continued)

Case study I: Select the optimal size of fibrillar adhesive for a wall-climbing robot with the requirements:

- Material: polymer with  $E \approx 100 \text{ MPa}$
- Applied pressure by weight  $< 10 \text{ kPa}$
- Adhesion coefficient  $\approx 5$
- Surface roughness  $\sigma < 1 \mu\text{m}$



**Fig. 21.26** Adhesion design database for biomimetic attachment systems consisting of single-level cylindrical fibers with orientation angle of  $30^\circ$  and spherical tips of  $100 \text{ nm}$  for elastic modulus of (a)  $1 \text{ MPa}$ , (b)  $100 \text{ MPa}$ , and (c)  $10 \text{ GPa}$  (after [32]). The solid lines shown in (b) and (c) correspond to the case studies I and II in the text, respectively, which satisfy the specified requirements (after [32])

The subplot of the adhesion database that satisfies these requirements is found in the second column and second row in Fig. 21.26b. From this subplot, any values on the marked line can be selected to meet the requirements. For example, fiber radius of  $0.4 \mu\text{m}$  with an aspect ratio of 1 or fiber radius of  $10 \mu\text{m}$  with an aspect ratio of 0.8 would satisfy the specified requirements.

Case study II: Comparison with the adhesion test for a single gecko seta [25, 26]:

- Material:  $\beta$ -keratin with  $E \approx 10$  GPa
- Applied pressure = 57 kPa ( $2.5 \mu\text{N}$  on an area of  $43.6 \mu\text{m}^2$ )
- Adhesion coefficient = 8–16
- Surface roughness  $\sigma < 0.01 \mu\text{m}$

Autumn et al. [25, 26] showed that, in isolated gecko setae contacting the surface of a single-crystalline silicon wafer, a  $2.5 \mu\text{N}$  preload yielded adhesion of 20–40  $\mu\text{N}$  and thus a value of adhesion coefficient of 8–16. The region that satisfies the above requirements is marked in Fig. 21.26c. The spatulae of gecko setae have an approximate radius of  $0.05 \mu\text{m}$  with an aspect ratio of 25. However, the radius corresponding to  $\lambda = 25$  for the marked line is  $\approx 0.015 \mu\text{m}$ . This discrepancy is due to the difference between the simulated fiber model and the real gecko setae model. Gecko setae are composed of a three-level hierarchical structure in practice, so higher adhesion can be generated than in a single-level model [3, 30, 31]. Given the simplification in the fiber model, this simulation result is very close to the experimental result.

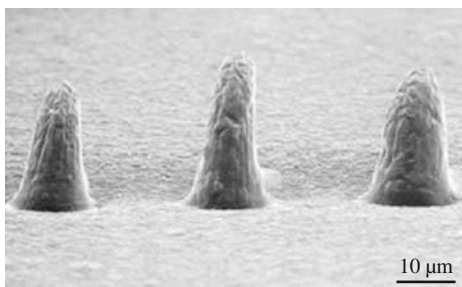
## 21.8 Fabrication of Biomimetic Gecko Skin

Based on the studies reported in the literature, the dominant adhesion mechanism utilized by gecko and spider attachment systems appears to be van der Waals forces. The hierarchical structure involving complex divisions of the gecko skin (lamellae–setae–branches–spatulae) enable a large number of contacts between the gecko skin and mating surface. As shown in previous calculations, the van der Waals adhesive force for two parallel surfaces is inversely proportional to the cube of the distance between two surfaces. These hierarchical fibrillar microstructured surfaces would be capable of reusable dry adhesion and would have uses in a wide range of applications from everyday objects such as adhesive tapes, fasteners, toys, microelectronic, and space applications, and treads of wall-climbing robots. The development of nanofabricated surfaces capable of replicating this adhesion force developed in nature is limited by current fabrication methods. Many different techniques have been used in an attempt to create and characterize bioinspired adhesive tapes. Attempts are being made to develop climbing robots using gecko-inspired structures [84, 85, 86, 87].

### 21.8.1 Single-Level Roughness Structures

One of the simplest approaches is to create a pattern by various micro/nanofabrication techniques and use it as a master template and mold with a liquid polymer to create micro/nanostructured replicas. Sitti and Fearing [49] employed an AFM tip to create a set of dimples on a wax surface. These dimples served as a mold for

**Fig. 21.27** SEM micrographs of three pillars fabricated by molding from dimples created by AFM-tip indentation (after [83])



creating polymer micropillars, shown in Fig. 21.27. The adhesive force to an individual pyramidal pillar was measured using another AFM cantilever. Although each pillar of the material was found to be capable of producing large adhesion forces, the surface failed to replicate gecko adhesion on a macroscale. This was due to the lack of flexibility in the pillars. In order to ensure that the largest possible area of contact occurs between the tape and the mating surface, a soft, compliant fibrillar structure would be desired. Compliant fibrillar structures enable more fibrils to be in close proximity to a mating surface to increase the van der Waals forces. Sitti and Fearing [49] and Cho and Choi [88] used nanoporous anodic alumina and polycarbonate membranes as a template to create polymeric nanofibers.

Geim et al. [89] created arrays of polyimide nanofibers using electron-beam lithography and dry etching in oxygen plasma (Fig. 21.28a, left). By using electron-beam lithography, thermal evaporation of an aluminum film, and lift-off, an array of nanoscale aluminum disks was prepared. These patterns were then transferred to the polyimide film by dry etching in oxygen plasma. A 1 cm<sup>2</sup> sample was able to create 3 N of adhesive force under the new arrangement. This is approximately one-third the adhesive strength of a gecko. They fabricated a Spiderman toy ( $\approx 0.4$  N) with a hand covered with molded polymer nanohairs (Fig. 21.28b). They demonstrated that it could cling to a glass plate. Bunching of the nanohairs (as described earlier) if they are closely spaced was determined to greatly reduce the both the adhesive strength and durability of the polymer tape. The bunching can be clearly seen in Fig. 21.28a (right). Therefore, an optimal geometry is required.

Davies et al. [90] fabricated mushroom-headed microfibers made of PDMS. In one of the fabrication strategies, a silicon wafer with a thickness which defined the stalk length was obtained, and the masks with mushroom-head features were first used to pattern one side of the silicon wafer with resist. Features were etched to a depth equal to that of the thickness of the mushroom head. Next, the smaller-diameter mask was used to pattern the other side of the wafer, which was then etched to produce holes through the entire thickness of the wafer, meeting the mushroom-headed cavities. This mold was first coated in a fluorocarbon release agent. A PDMS solution was then spun onto this mold and cured to produce mushroom-headed microfibers. The resulting casting comprising stalks and mushroom heads was then pulled through the mold in a single peeling process. To create



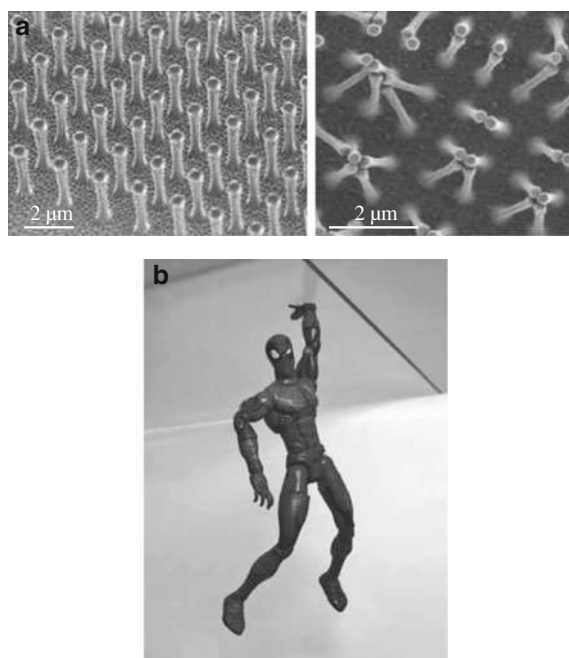


**Fig. 21.28** (a) (*left*) An array of polyimide nanohairs and (*right*) bunching of the nanohairs, which leads to a reduction in adhesive force. (b) A spiderman toy (about 0.4 N) with a hand covered with the molded polymer nanohairs, clinging to a glass plate (after [89])

angled microfiber arrays found in biological attachments using photolithography, Aksak et al. [91] simply varied the ultraviolet (UV) exposure angle by tilting the wafer during exposure. The fibers were formed at an angle not perpendicular to the substrate surface (Fig. 21.29a). This master template of angled SU-8 fibers was then used to form many copies of the fiber arrays from curable polyurethanes by molding. They reported that angled fibers exhibited reduced adhesion compared with similar vertical fibers due to a peeling moment. However, angled fibers are favored in biological attachment systems. Murphy et al. [92] modified angled fiber arrays by adding soft spherical and spatula-shaped tips via dipping in a liquid polymer of interest (Fig. 21.29b). To add tips to the fibers, the fiber array sample attached to a micropositioning stage was dipped into a liquid polyurethane layer and retracted, retaining some of the liquid polymer on the tips of the fibers. To form spherical tips, the sample was placed with the fibers facing up and allowed to cure. To form spatula tips, the fiber sample was placed onto a smooth low-energy surface and then peeled away after curing. They reported very high adhesion of these fibers with soft tips because of increased contact area.

Del Campo et al. [93, 94] fabricated pillar arrays with controlled 3D tip geometries resembling those found in biological attachments. The fabrication strategy was based on complete or partial soft molding on 2D masters made by lithography



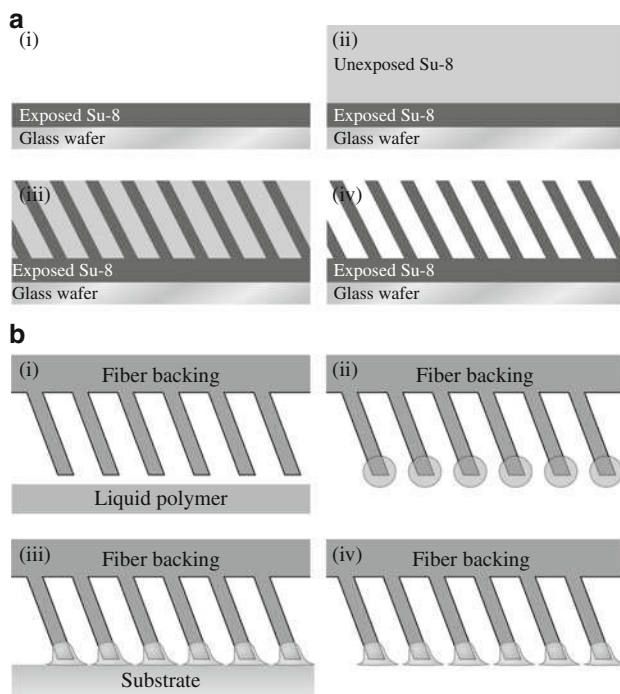


**Fig. 21.29** (a) The process steps of the polymer fiber orientation: (i) a thin layer of SU-8 is spun on a glass substrate, then exposed and cured; (ii) a thicker layer of SU-8 is spun, which will become the fibers; (iii) the thick layer is patterned with UV exposure by tilting the wafer; (iv) the SU-8 photoresist is developed, leaving the desired angled fiber array (after [91]). (b) Fiber tip fabrication process: (i) bare fibers are aligned with a layer of liquid polymer; (ii) the fibers are tipped into the liquid and retracted; (iii) the fibers are brought into contact with a substrate; (iv) the fibers are peeled away from the substrate after curing (after [92])

with elastomeric precursors followed in some cases by inking and microprinting steps. The patterned master with high-aspect-ratio cylindrical holes was produced by photolithography using SU-8 photoresist films. The SU-8 masters were filled with elastomeric precursors (PDMS supplied as Sylgard 184 by Dow Corning) to produce arrays of cylindrical pillars (Fig. 21.30a). Arrays of pillars with spherical and spatular tips were obtained by inking the Sylgard 184-structured substrates in a thin film of Sylgard 184 precursor. Curing of arrays in upside-down orientation yielded hemispherical tips as a consequence of gravity and surface tension acting on the fluid drop (Fig. 21.30b). Alternatively, the inked stamp can be pressed against a flat substrate and then cured. This leads to pillars with a flat top (Fig. 21.30c). The top can be symmetric or asymmetric depending on the tilt of the substrate during curing (Fig. 21.30c,d). They also used silicones used for dental impressions. These materials possess higher initial viscosities and faster cross-linking kinetics than Sylgard 184, which results in incomplete cavity filling. By soft-molding these materials after selected delay times after mixing, arrays of tubes and pillars with

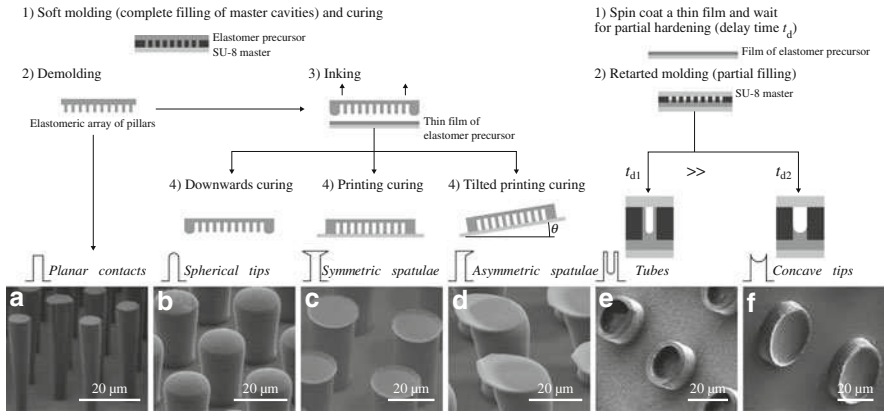
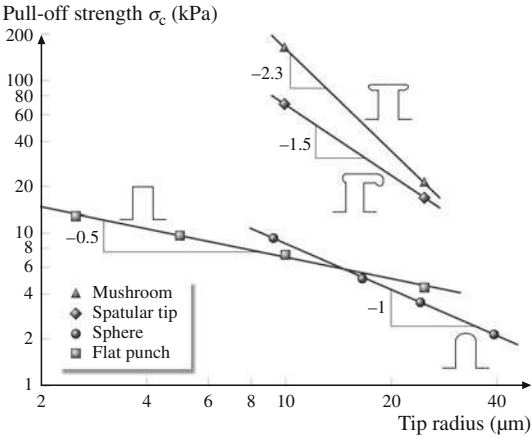


**Fig. 21.30** (a-f) Overview of the fabrication strategies and SEM images showing examples of the pillar arrays obtained with controlled 3D tip geometries (after [93])

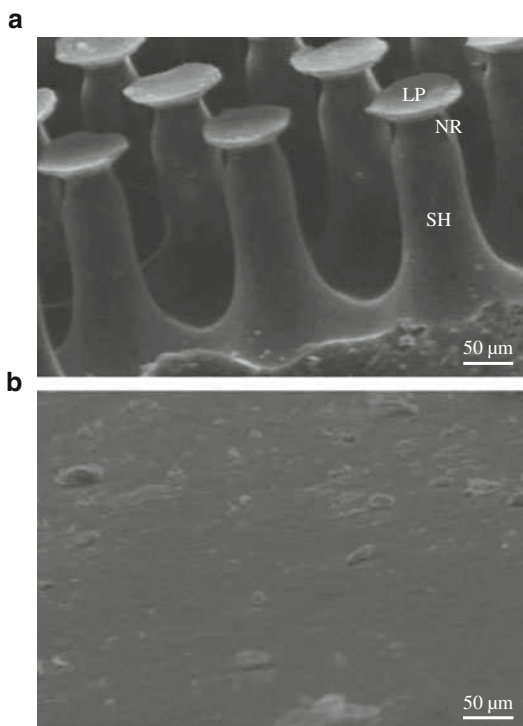
**Fig. 21.31** Tip radius dependence of the pull-off force for flat, spherical, spatular, and mushroom-like contacts at preload of 1 mN. In the case of spherical tips, the radius corresponds to the tip radius. For all other geometries, the pillar radius is used (after [94])



concave tips (Fig. 21.30e,f) were obtained. They performed adhesion tests on various geometries against a sapphire sphere. They reported that the shape of the pillar tip affects the contact area and adhesion behavior. Figure 21.31 shows pull-off strength data as a function of tip radius for various tip geometries. For a given tip radius, pillars with the flat punch geometry have significantly higher adhesion than spherical contacts. Pillars with mushroom tips have the highest adhesion.

Gorb et al. [95] and Bhushan and Sayer [96] characterized two polyvinylsiloxane (PVS) samples from Gottlieb Binder Inc., Holzgerlingen, Germany, one consisting of mushroom-shaped pillars (Fig. 21.32a) and the other an unstructured control surface (Fig. 21.32b). The structured sample is inspired by the micropatterns found in the attachment systems of male beetles from the family Chrysomelidae and is easier to fabricate. Both sexes possess adhesive hairs on their tarsi; however, males bear hair extremely specialized for adhesion to the smooth surface of

**Fig. 21.32** SEM micrographs of (a) structured and (b) unstructured PVS samples (SH – shaft, NR – neck region, LP – lip) (after [96])



female's covering wings during mating. The hairs have broad flattened tips with grooves under the tip to provide flexibility. The mushroom shape provides a larger contact area. The structured samples were produced at room temperature by pouring two-compound polymerizing PVS into the holed template lying on a smooth glass support. The fabricated sample is comprised of pillars that are arranged in a hexagonal order to allow maximum packing density. They are  $\approx 100\ \mu\text{m}$  in height,  $60\ \mu\text{m}$  in base diameter,  $35\ \mu\text{m}$  in middle diameter, and  $25\ \mu\text{m}$  in diameter at the narrowed region just below the terminal contact plates. These plates were  $\approx 40\ \mu\text{m}$  in diameter and  $2\ \mu\text{m}$  in thickness at the lip edges. The adhesion force of the two samples in contact with a smooth flat glass substrate was measured by Gorb et al. [95] using a microtribometer. Results revealed that the structured specimens featured an adhesion force more than twice that of the unstructured specimens. The adhesion force was also found to be independent of the preload. Moreover, it was found that the adhesive force of the structured sample was more tolerant to contamination compared with the control, and it could be easily cleaned with a soap solution.

Bhushan and Sayer [96] characterized the surface roughness, friction force, and contact angle of the structured sample and compared the results with an unstructured control. As shown in Fig. 21.33a, the macroscale coefficient of kinetic friction of the structured sample was found to be almost four times greater than that of the unstructured sample. This increase was determined to be a result of the structured

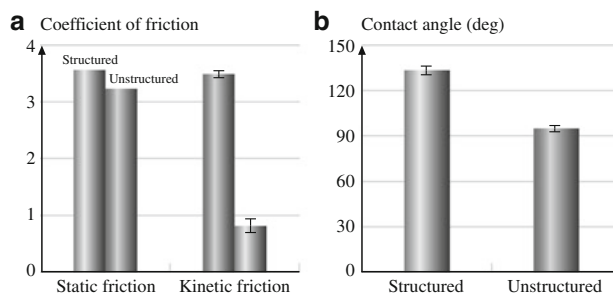
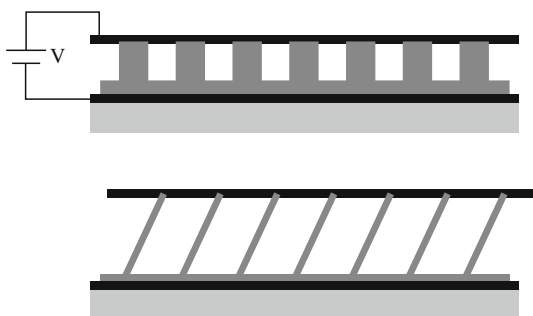


**Fig. 21.33** (a) Coefficients of static and kinetic friction for structured and unstructured samples sliding against magnetic tape with normal load of 130 mN. (b) Water contact angle for the structured and unstructured samples (after [96])

**Fig. 21.34** Directed self-assembly-based method of producing high-aspect-ratio micro/nanofibers (after [83])



roughness of the sample and not the random nanoroughness. It is also noteworthy that the static and kinetic coefficients of friction are approximately equal for the structured sample. It is believed that the divided contacts allow the broken contacts of the structured sample to constantly recreate contact. As seen in Fig. 21.33b, the pillars also increased the hydrophobicity of the structured sample in comparison with the unstructured sample, as expected due to the increased surface roughness [97–99]. A large contact angle is important for self-cleaning [100], which agrees with the findings of Gorb et al. [95] that the structured sample is more tolerant of contamination than the unstructured sample.

Directed self-assembly has been proposed as a method to produce regularly spaced fibers [83, 101]. In this technique, a thin liquid polymer film is coated on a flat conductive substrate. As demonstrated in Fig. 21.34, a closely spaced metal plate is used to apply a direct-current (DC) electric field to the polymer film. Due to instabilities in the film, pillars will begin to grow until they touch the upper metal plate. Self-assembly is desirable because the components spontaneously assemble, typically by bouncing around in a solution or gas phase until a stable structure of minimum energy is reached.

Vertically aligned multiwalled carbon nanotubes (MWCNT) have been used to create nanostructures on polymer surfaces. Yurdumakan et al. [102] used chemical

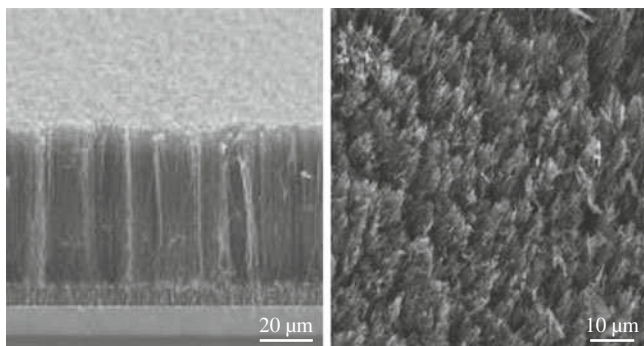


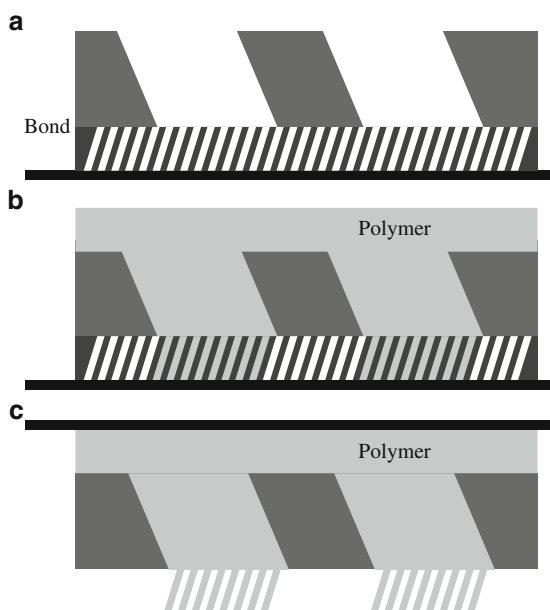
**Fig. 21.35** Multiwalled carbon nanotube structures: (a) grown on silicon by chemical vapor deposition, (b) transferred into a PMMA matrix and then exposed on the surface after solvent etching (after [102])

vapor deposition (CVD) to grow vertically aligned MWCNT that are 50–100  $\mu\text{m}$  in length on quartz or silicon substrates. A catalyst was deposited on the silicon oxide surface as patches using photolithography. The MWCNT grew selectively on the patches with controlled thickness and length and were vertically aligned. The sample with MWCNT sites facing up was then dipped in methyl methacrylate solution. After polymerization, poly(methyl methacrylate) (PMMA)-MWCNT sheets are peeled off from the silicon substrate. The MWCNTs are exposed from the silicon-facing side of the PMMA matrix by etching the top 25  $\mu\text{m}$  with a solvent. SEM images of the MWCNT grown on a silicon substrate as well as transferred into a PMMA matrix and then exposed on the surface can be seen in Fig. 21.35. On the nanoscale, the MWCNT surface was able to achieve adhesive forces two orders of magnitude greater than those of gecko foot-hairs. These structures provided high adhesion on the nanometer level and were not capable of producing high adhesion forces on the macroscale. Ge et al. [103] and others have fabricated nanostructures by transferring micropatterned, vertically aligned MWCNT arrays onto flexible polymer tape. They reported high adhesion on the macroscale. They also performed peeling experiments. Durability of the adhesive tape is an issue, as some of the nanotubes can detach from the substrate with repeated use. Qu et al. [104] measured adhesion on vertically aligned MWCNT arrays on Si substrate and reported high adhesion on the nanoscale.

### 21.8.2 Multilevel Hierarchical Structures

The aforementioned fabricated surfaces only have one level of roughness. Although these surfaces are capable of producing high adhesion on the micro/nanoscale, they are not expected to produce large-scale adhesion due to a lack of compliance and bunching.

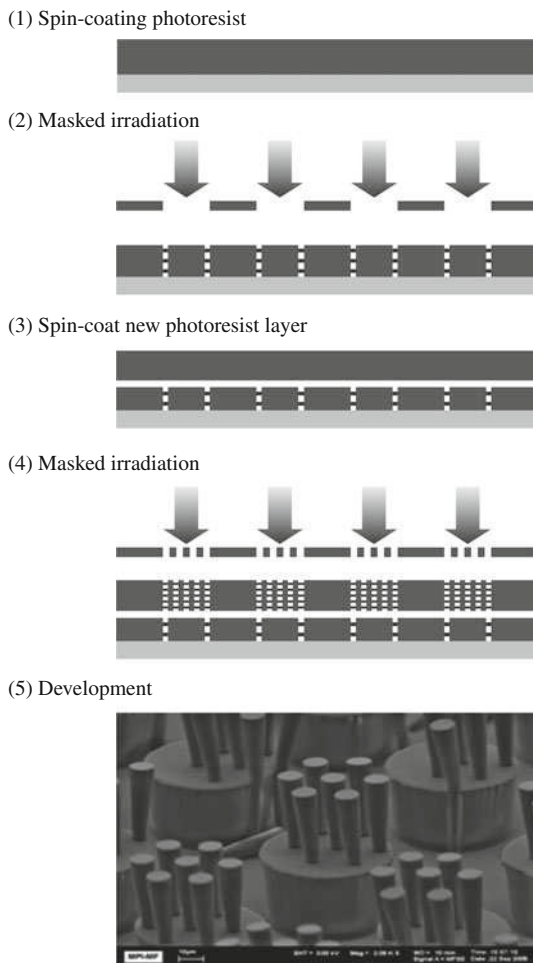
**Fig. 21.36** Proposed process for creating multilevel structures using molding. Micro- and nanometer-sized pore membranes are bonded together (a) and filled with liquid polymer through the micropore membrane site (b), followed by curing of the polymer and etching the array of both membranes in order to leave (c) the polymer surface (after [83])



Sitti [83] proposed a molding technique for creating structures with two levels. In this method two different molds are created – one with pores of the order of magnitude of micrometers in diameter and a second with pores of nanometer-scale diameter. One potential mold material is porous anodic alumina (PAA), which has been demonstrated to produce ordered pores on the nanometer scale of equal size. Pore-widening techniques could be used to create micrometer-scale pores. As seen in Fig. 21.36, the two molds would be bonded to each other and then filled with a liquid polymer. Del Campo and Greiner [105] fabricated a hierarchical structure by multilevel photolithography. Figure 21.37 shows a schematic of the process and an example of the two-level SU-8 patterns obtained.

Northen and Turner [106, 107] created a multilevel compliant structure by employing a microelectromechanical-based approach. The multiscale structures consist of arrays of organic-looking photoresist nanorods (organorods),  $\approx 2 \mu\text{m}$  tall and 50–200 nm in diameter (comparable in size to gecko spatulae) (Fig. 21.38a), atop photolithographically defined  $2 \mu\text{m}$ -thick  $\text{SiO}_2$  platforms 100–150  $\mu\text{m}$  on a side (Fig. 21.38b). The platforms of various geometries are supported by single high-aspect-ratio pillars down to 1  $\mu\text{m}$  in diameter and with heights up to  $\approx 50 \mu\text{m}$  (Fig. 21.38c). The structures are fabricated out of 100 mm single-crystal wafers using standard bulk micromachining techniques. An array of four-fingered platform structures is shown in Fig. 21.38d. Adhesion testing was performed using a nanorod surface on a solid substrate and on the multilevel structures by Northen and Turner [107]. They reported that the adhesive pressure of the multilevel structures was

**Fig. 21.37** Layer-by-layer structuring method and example of fabricated hierarchical structure in SU-8. Base pillars have 50  $\mu\text{m}$  diameter and 40  $\mu\text{m}$  height and the top pillars have 9  $\mu\text{m}$  diameter and 35  $\mu\text{m}$  height (after [105])



about four times higher than that of surfaces with only one level of hierarchy. The durability of the multilevel structure was also much greater than the single-level structure. The adhesion of the multilevel structure did not change between iterations one and five. During the same number of iterations, the adhesive pressure of the single-level structure decreased to zero.

In summary, literature clearly indicates that, in order to create a dry super-adhesive, a fibrillar surface construction is necessary to maximize the van der Waals forces by using so-called division of contacts. Hierarchical structure provides compliance for adaptability to a variety of rough surfaces. A material must be soft enough to conform to rough surfaces yet hard enough to avoid bunching, which will decrease the adhesive force. It is also desirable to have a superhydrophobic surface in order to utilize self-cleaning. Inspired by previous work on adding tips to

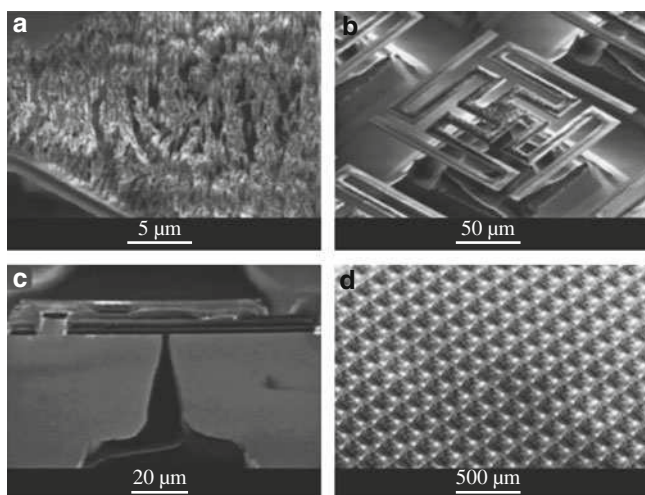


**Fig. 21.38** Multilevel fabricated adhesive structure composed of (a) organorods atop (b) silicon dioxide platforms. The platforms are supported by (c) support pillars. (d). This structure was repeated multiple times over a silicon wafer (after [106])

the fibrillar structures, the end of the fibers could be modified to enhance adhesion. For example, a soft adhesive could be used to coat fiber ends to provide added adhesion using conventional adhesives.

## 21.9 Conclusion

The adhesive properties of geckoes and other creatures such as flies, beetles, and spiders are due to the hierarchical structures present on each creature's hairy attachment pads. Geckoes have developed the most intricate adhesive structures of any of the aforementioned creatures. The attachment system consists of ridges called lamellae that are covered in microscale setae that branch off into nanoscale spatulae, of which there are about three billion on two feet. The so-called division of contacts provide high dry adhesion. Multiple-level hierarchically structured surface construction plays an important role in adapting to surface roughness, bringing the spatulae in close proximity to the mating surface. These structures, as well as material properties, allow the gecko to obtain a much larger real area of contact between its feet and a mating surface than is possible with a nonfibrillar material. Two feet of a Tokay gecko have  $\approx 220 \text{ mm}^2$  of attachment pad area, on which the gecko is able to generate  $\approx 20 \text{ N}$  of adhesion force. Although capable of generating high adhesion forces, a gecko is able to detach from a surface at will – an ability known as smart adhesion. Detachment is achieved by a peeling motion of the gecko's feet from a surface.



Experimental results have supported the adhesion theories of intermolecular forces (van der Waals) as a primary adhesion mechanism and capillary forces as a secondary mechanism, and have been used to rule out several other mechanisms of adhesion including the secretion of sticky fluids, suction, and increased frictional forces. Atomic force microscopy has been employed by several investigators to determine the adhesion strength of gecko foot hairs. The measured values of the lateral force required to pull parallel to the surface for a single seta (194  $\mu\text{N}$ ) and the adhesive force (normal to the surface) of a single spatula (11 nN) are comparable to the van der Waals prediction of 270  $\mu\text{N}$  and 11 nN for a seta and spatula, respectively. The adhesion force generated by seta increases with preload and reaches a maximum when both perpendicular and parallel preloads are applied. Although gecko feet are strong adhesives, they remain free of contaminant particles through self-cleaning. Spatular size along with material properties enables geckoes to easily expel any dust particles that come into contact with their feet.

The recent creation of a three-level hierarchical model for a gecko lamella consisting of setae, branches, and spatulae has brought more insight into the adhesion of biological attachment systems. One-, two-, and three-level hierarchically structured spring models for the simulation of a seta contacting with random rough surfaces were considered. The simulation results show that the multilevel hierarchical structure has a higher adhesion force as well as higher adhesion energy than the one-level structure for a given applied load, due to better adaptation and attachment ability. It is concluded that the multilevel hierarchical structure produces adhesion enhancement, and this enhancement increases with increasing applied load and decreasing stiffness of the springs. The condition at which significant adhesion enhancement occurs appears to be related to the maximum spring deformation. The result shows that significant adhesion enhancement occurs when the maximum spring deformation is greater than two to three times larger than the  $\sigma$  value of the surface roughness. As the applied load increases, the adhesion force increases up to a certain applied load and then has a constant value, whereas adhesion energy continues to increase with increasing applied load. For the effect of spring stiffness, the adhesion coefficient increases with a decrease in the stiffness of springs. A hierarchical model with softer springs can generate greater adhesion enhancement for lower applied load. As the number of springs in the lower level increases, the equivalent stiffness decreases. Therefore, the three-level model with a larger number of springs in the lowest level gives a larger adhesion force and energy. Inclusion of capillary forces in the spring model shows that the total adhesion force decreases with increasing contact angle of water on the substrate, and the difference of total adhesion force among different contact angles is larger in the intermediate-humidity regime. In addition, the simulation results match the measured data for a single spatula in contact with both hydrophilic and hydrophobic surfaces, which further supports van der Waals forces as the dominant mechanism of adhesion and capillary forces as a secondary mechanism.

There is great interest among the scientific community in creating surfaces that replicate the adhesion strength of gecko feet. These hierarchical fibrillar

microstructured surfaces would be capable of reusable dry adhesion and would have uses in a wide range of applications from everyday objects such as adhesive tapes, fasteners, toys, microelectronic, space applications, and treads of wall-climbing robots. In the design of fibrillar structures, it is necessary to ensure that the fibrils are compliant enough to deform easily to the mating surface's roughness profile, yet rigid enough not to collapse under their own weight. Spacing between the individual fibrils is also important. If the spacing is too small, adjacent fibrils can attract each other through intermolecular forces, which will lead to bunching. The adhesion design database developed by Kim and Bhushan [32] serves as a reference for choosing design parameters.

Nanoindentation, lithography, self-assembly, and carbon nanotube arrays are some of the methods that have been used to create fibrillar structures. The limitations of current machining methods on the micro/nanoscale have resulted in the majority of fabricated surfaces consisting of only one level of hierarchy. Bunching, lack of compliance, and lack of durability are some of the problems that may arise with the aforementioned structures. A multilayered compliant system has been created using a microelectromechanical-based approach in combination with nanorods. Multilevel photolithography has also been used to fabricate hierarchical fibrillar structures. Fibrillar structures show great promise for the creation of adhesive structures. Some of the structures have been incorporated into the design of treads of climbing robots.

## 21.10 Typical Rough Surfaces

Several natural (sycamore tree bark and siltstone) and artificial surfaces (dry wall, wood laminate, steel, aluminum, and glass) were chosen to determine the surface parameters of typical rough surfaces that a gecko might encounter. An Alpha-step 200 (Tencor Instruments, Mountain View) was used to obtain surface profiles for three different scan lengths: 80  $\mu\text{m}$ , which is approximately the size of a single gecko seta; 2,000  $\mu\text{m}$ , which is close to the size of a gecko lamella; and an intermediate scan length of 400  $\mu\text{m}$ . The radius of the stylus tip was 1.5–2.5  $\mu\text{m}$ , and the applied normal load was 3 mg. The surface profiles were then analyzed using a specialized computer program to determine the root-mean-square amplitude  $\sigma$ , correlation length  $\beta^*$ , peak to valley distance P–V, skewness Sk, and kurtosis K.

Sample surface profiles and their corresponding parameters at a scan length of 2,000  $\mu\text{m}$  can be seen in Fig. 21.39a. The roughness amplitude  $\sigma$  varies from as low as 0.01  $\mu\text{m}$  in glass to as high as 30  $\mu\text{m}$  in tree bark. Similarly, the correlation length varies from 2 to 300  $\mu\text{m}$ . The scan length dependence of the surface parameters is illustrated in Fig. 21.39b. As the scan length of the profile increases, so do the roughness amplitude and correlation length. Table 21.4 summarizes the scan-length-dependent parameters  $\sigma$  and  $\beta^*$  for all seven sampled surfaces. At a scale length of 80  $\mu\text{m}$  (size of seta), the roughness amplitude does not exceed 5  $\mu\text{m}$ , while at a scale length of 2000  $\mu\text{m}$  (size of lamella), the roughness

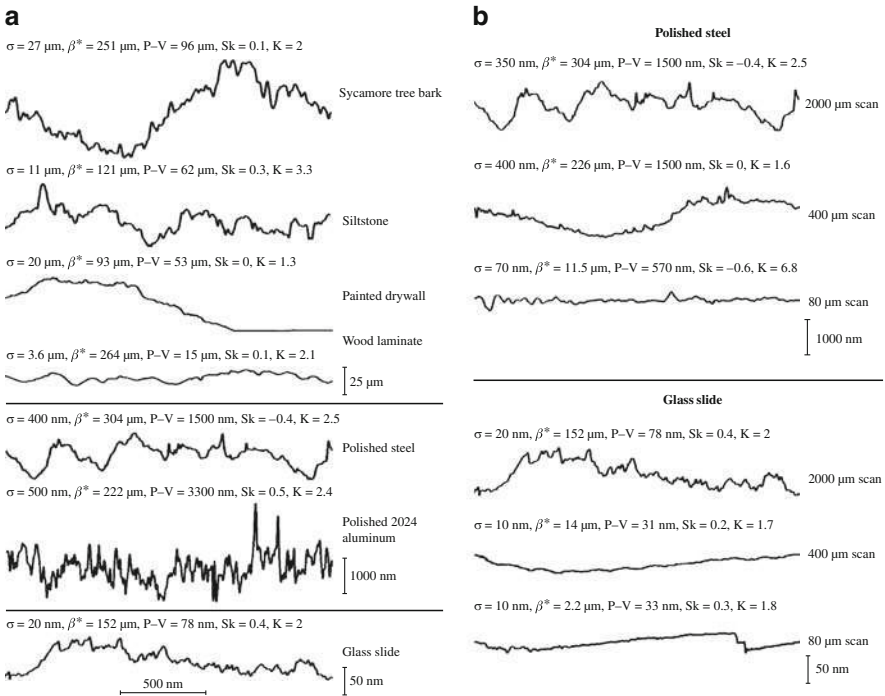


**Fig. 21.39** (a) Surface height profiles of various random rough surfaces of interest at a 2,000  $\mu\text{m}$  scan length and (b) a comparison of the profiles of two surfaces at 80, 400, and 2,000  $\mu\text{m}$  scan lengths (after [3])

**Table 21.4** Scale dependence of surface parameters  $\sigma$  and  $\beta^*$  for rough surfaces at scan lengths of 80 and 2,000  $\mu\text{m}$  [3]

Scan length	80 $\mu\text{m}$		2,000 $\mu\text{m}$	
Surface	$\sigma$ ( $\mu\text{m}$ )	$\beta^*$ ( $\mu\text{m}$ )	$\sigma$ ( $\mu\text{m}$ )	$\beta^*$ ( $\mu\text{m}$ )
Sycamore tree bark	4.4	17	27	251
Siltstone	1.1	4.8	11	268
Painted drywall	1	11	20	93
Wood laminate	0.11	18	3.6	264
Polished steel	0.07	12	0.40	304
Polished 2024 aluminum	0.40	6.5	0.50	222
Glass	0.01	2.2	0.02	152

amplitude is as high as 30  $\mu\text{m}$ . This suggests that setae should adapt to surfaces with roughness on the order of several micrometers, while lamellae should adapt to roughness on the order of tens of micrometers. Larger roughness values would be adapted to by the skin of the gecko. The spring model of Bhushan et al. [3] verifies that setae are only capable of adapting to roughnesses of a few micrometers and suggests that lamellae are responsible for adaptation to rougher surfaces.

## References

1. S. Gorb, *Attachment Devices of Insect Cuticles* (Kluwer, Dordrecht 2001)
2. B. Bhushan, Adhesion of multilevel hierarchical attachment systems in gecko feet, *J. Adhes. Sci. Technol.* **21**, 1213–1258 (2007)
3. B. Bhushan, A.G. Peressadko, T.W. Kim, Adhesion analysis of two-level hierarchical morphology in natural attachment systems for ‘smart adhesion’, *J. Adhes. Sci. Technol.* **20**, 1475–1491 (2006)
4. A.G. Kluge, Gekkotan lizard taxonomy, *Hamadryad* **26**, 1–209 (2001)
5. D. Han, K. Zhou, A.M. Bauer, Phylogenetic relationships among gekkotan lizards inferred from C-mos nuclear DNA sequences and a new classification of the Gekkota, *Biol. J. Linn. Soc.* **83**, 353–368 (2004)
6. R. Ruibal, V. Ernst, The structure of the digital setae of lizards, *J. Morphol.* **117**, 271–294 (1965)
7. U. Hiller, Untersuchungen zum Feinbau und zur Funktion der Haftborsten von Reptilien, *Z. Morphol. Tiere* **62**, 307–362 (1968), in German
8. D.J. Irschick, C.C. Austin, K. Petren, R.N. Fisher, J.B. Losos, O. Ellers, A comparative analysis of clinging ability among pad-bearing lizards, *Biol. J. Linn. Soc.* **59**, 21–35 (1996)
9. K. Autumn, How gecko toes stick, *Am. Sci.* **94**, 124–132 (2006)
10. D.W. Tinkle, Gecko, In: *Encyclopedia Americana*, Vol. 12 (Grolier, Norwich, 1992), p. 359
11. Aristotle, *Historia Animalium (The History of Animals)* (1918), transl. by D.A.W. Thompson, [http://classics.mit.edu/Aristotle/history\\_anim.html](http://classics.mit.edu/Aristotle/history_anim.html)
12. A.P. Russell, A contribution to the functional morphology of the foot of the Tokay, *Gekko gekko*, *J. Zool. London* **176**, 437–476 (1975)
13. A.P. Russell, The morphological basis of weight-bearing in the scansors of the Tokay gecko, *Can. J. Zool.* **64**, 948–955 (1986)
14. E.E. Williams, J.A. Peterson, Convergent and alternative designs in the digital adhesive pads of scincid lizards, *Science* **215**, 1509–1511 (1982)
15. H.H. Schleich, W. Kästle, Ultrastrukturen an Gecko-Zehen, *Amphib. Reptil.* **7**, 141–166 (1986), in German
16. K. Autumn, A.M. Peattie, Mechanisms of adhesion in geckos, *Integr. Comp. Biol.* **42**, 1081–1090 (2002)
17. E. Arzt, S. Gorb, R. Spolenak, From micro to nano contacts in biological attachment devices, *Proc. Natl. Acad. Sci. USA* **100**, 10603–10606 (2003)
18. J. Wagler, *Natürliches System der Amphibien* (Cotta’sche Buchhandlung, Munich 1830), in German
19. G. Simmermacher, Untersuchungen über Haftapparate an Tarsalgliedern von Insekten, *Z. Wiss. Zool.* **40**, 481–556 (1884), in German
20. H.R. Schmidt, Zur Anatomie und Physiologie der Geckopfote, *Jena. Z. Naturwiss.* **39**, 551 (1904), in German
21. S.L. Hora, The adhesive apparatus on the toes of certain geckos and tree frogs, *J. Asiat. Soc. Beng.* **9**, 137–145 (1923)
22. W.D. Dellit, Zur Anatomie und Physiologie der Geckozehe, *Jena. Z. Naturwiss.* **68**, 613–658 (1934), in German
23. J.G.J. Gennaro, The gecko grip, *Nat. Hist.* **78**, 36–43 (1969)
24. N.E. Stork, Experimental analysis of adhesion of *Chrysolina polita* on a variety of surfaces, *J. Exp. Biol.* **88**, 91–107 (1980)
25. K. Autumn, Y.A. Liang, S.T. Hsieh, W. Zesch, W.P. Chan, T.W. Kenny, R. Fearing, R.J. Full, Adhesive force of a single gecko foot-hair, *Nature* **405**, 681–685 (2000)
26. K. Autumn, M. Sitti, Y.A. Liang, A.M. Peattie, W.R. Hansen, S. Sponberg, T.W. Kenny, R. Fearing, J.N. Israelachvili, R.J. Full, Evidence for van der Waals adhesion in gecko setae, *Proc. Natl. Acad. Sci. USA* **99**, 12252–12256 (2002)

27. P.J. Bergmann, D.J. Irschick, Effects of temperature on maximum clinging ability in a diurnal gecko: evidence for a passive clinging mechanism?, *J. Exp. Zool. A* **303**, 785–791 (2005)
28. G. Huber, H. Mantz, R. Spolenak, K. Mecke, K. Jacobs, S.N. Gorb, E. Arzt, Evidence for capillarity contributions to gecko adhesion from single spatula and nanomechanical measurements, *Proc. Natl. Acad. Sci. USA* **102**, 16293–16296 (2005)
29. G. Huber, S.N. Gorb, R. Spolenak, E. Arzt, Resolving the nanoscale adhesion of individual gecko spatulae by atomic force microscopy, *Biol. Lett.* **1**, 2–4 (2005)
30. T.W. Kim, B. Bhushan, The adhesion analysis of multilevel hierarchical attachment system contacting with a rough surface, *J. Adhes. Sci. Technol.* **21**, 1–20 (2007)
31. T.W. Kim, B. Bhushan, Effect of stiffness of multilevel hierarchical attachment system on adhesion enhancement, *Ultramicroscopy* **107**, 902–912 (2007)
32. T.W. Kim, B. Bhushan, Optimization of biomimetic attachment system contacting with a rough surface, *J. Vac. Sci. Technol. A* **25**, 1003–1012 (2007)
33. T.W. Kim, B. Bhushan, The adhesion model considering capillarity for gecko attachment system, *J. R. Soc. Interface* **5**, 319–327 (2008)
34. W. Federle, Why are so many adhesive pads hairy?, *J. Exp. Biol.* **209**, 2611–2621 (2006)
35. A.B. Kesel, A. Martin, T. Seidl, Adhesion measurements on the attachment devices of the jumping spider *Evarcha arcuata*, *J. Exp. Biol.* **206**, 2733–2738 (2003)
36. A.M. Peattie, R.J. Full, Phylogenetic analysis of the scaling of wet and dry biological fibrillar adhesives, *Proc. Natl. Acad. Sci. USA* **104**, 18595–18600 (2007)
37. H. Gao, X. Wang, H. Yao, S. Gorb, E. Arzt, Mechanics of hierarchical adhesion structures of geckos, *Mech. Mater.* **37**, 275–285 (2005)
38. P.F.A. Maderson, Keratinized epidermal derivatives as an aid to climbing in gekkonid lizards, *Nature* **203**, 780–781 (1964)
39. N. Rizzo, K. Gardner, D. Walls, N. Keiper-Hrynko, D. Hallahan, Characterization of the structure and composition of gecko adhesive setae, *J. R. Soc. Interface* **3**, 441–451 (2006)
40. B.N.J. Persson, S. Gorb, The effect of surface roughness on the adhesion of elastic plates with application to biological systems, *J. Chem. Phys.* **119**, 11437–11444 (2003)
41. B. Bhushan, *Principles and Applications of Tribology* (Wiley, New York, 1999)
42. B. Bhushan, *Introduction to Tribology* (Wiley, New York, 2002)
43. B. Bhushan (Ed.), *Nanotribology and Nanomechanics – An Introduction*, 2nd edn. (Springer, Berlin, Heidelberg 2008)
44. K.L. Johnson, K. Kendall, A.D. Roberts, Surface energy and the contact of elastic solids, *Proc. R. Soc. A* **324**, 301–313 (1971)
45. J.E.A. Bertram, J.M. Gosline, Functional design of horse hoof keratin: the modulation of mechanical properties through hydration effects, *J. Exp. Biol.* **130**, 121–136 (1987)
46. F.M. Orr, L.E. Scriven, A.P. Rivas, Pendular rings between solids: meniscus properties and capillary forces, *J. Fluid. Mech.* **67**, 723–742 (1975)
47. S. Cai, B. Bhushan, Effects of symmetric and asymmetric contact angles and division of menisci on meniscus and viscous forces during separation, *Philos. Mag.* **87**, 5505–5522 (2007)
48. S. Cai, B. Bhushan, Meniscus and viscous forces during separation of hydrophilic and hydrophobic surfaces with liquid mediated contacts, *Mater. Sci. Eng. R* **61**, 78–106 (2008), (invited)
49. M. Sitti, R.S. Fearing, Synthetic gecko foot-hair for micro/nano structures as dry adhesives, *J. Adhes. Sci. Technol.* **17**, 1055–1073 (2003)
50. K. Autumn, C. Majidi, R.E. Groff, A. Dittmore, R. Fearing, Effective elastic modulus of isolated gecko setal arrays, *J. Exp. Biol.* **209**, 3558–3568 (2006)
51. G.J. Shah, M. Sitti, Modeling and design of biomimetic adhesives inspired by gecko foot-hairs, *IEEE Int. Conf. Robot. Biomim.* (2004) pp. 873–878
52. A. Jagota, S.J. Bennison, Mechanics of adhesion through a fibrillar microstructure, *Integr. Comp. Biol.* **42**, 1140–1145 (2002)

53. Y. Tian, N. Pesika, H. Zeng, K. Rosenberg, B. Zhao, P. McGuiggan, K. Autumn, J. Israelachvili, Adhesion and friction in gecko toe attachment and detachment, *Proc. Natl. Acad. Sci. USA* **103**, 19320–19325 (2006)
54. W.R. Hansen, K. Autumn, Evidence for self-cleaning in gecko setae, *Proc. Natl. Acad. Sci. USA* **102**, 385–389 (2005)
55. W.C. Hinds, *Aerosol Technology* (Wiley, New York, 1982)
56. R. Jaenicke, Atmospheric aerosol size distribution. In: *Atmospheric Particles*, ed. by R.M. Harrison, R. van Grieken (Wiley, New York, 1998) pp. 1–29
57. N.E. Stork, A comparison of the adhesive setae on the feet of lizards and arthropods, *J. Nat. Hist.* **17**, 829–835 (1983)
58. W. Federle, M. Riehle, A.S.G. Curtis, R.J. Full, An integrative study of insect adhesion: Mechanics of wet adhesion of pretarsal pads in ants, *Integr. Comp. Biol.* **42**, 1100–1106 (2002)
59. G. Hanna, W.J.P. Barnes, Adhesion and detachment of the toe pads of tree frogs, *J. Exp. Biol.* **155**, 103–125 (1991)
60. W.G. Van der Kloot, Molting. In: *Encyclopedia Americana*, Vol. 19 (Grolier, Norwich, 1992) pp. 336–337
61. J.N. Israelachvili, *Intermolecular and Surface Forces*, 2nd edn. (Academic, San Diego, 1992)
62. J.J. Bikerman, *The Science of Adhesive Joints* (Academic, New York, 1961)
63. W.A. Zisman, Influence of constitution on adhesion, *Ind. Eng. Chem.* **55**(10), 18–38 (1963)
64. R. Houwink, G. Salomon, Effect of contamination on the adhesion of metallic couples in ultra high vacuum, *J. Appl. Phys.* **38**, 1896–1904 (1967)
65. B. Bhushan, *Tribology and Mechanics of Magnetic Storage Devices*, 2nd edn. (Springer, New York, 1996)
66. B. Bhushan (Ed.), *Springer Handbook of Nanotechnology*, 2nd edn. (Springer, Berlin, 2007)
67. H.C. Hamaker, London van der Waals attraction between spherical bodies, *Physica* **4**, 1058–1072 (1937)
68. J.N. Israelachvili, D. Tabor, The measurement of Van der Waals dispersion forces in the range of 1.5 to 130 nm, *Proc. R. Soc. A* **331**, 19–38 (1972)
69. A.D. Zimon, *Adhesion of Dust and Powder* (Plenum, New York, 1969), transl. from Russian by M. Corn
70. P.L. Fan, M.J. O'Brien, Adhesion in deformable isolated capillaries, *Adhes. Sci. Technol.* **9A**, 635 (1975)
71. P.B.P. Phipps, D.W. Rice, Role of water in atmospheric corrosion, In: *Corrosion Chemistry*, ACS Symp. Ser., Vol. 89, ed. by G.R. Brubaker, P.B.P. Phipps (Am. Chem. Soc., Washington DC, 1979) pp. 235–261
72. J.B. Losos, Thermal sensitivity of sprinting and clinging performance in the Tokay gecko (*Gekko gecko*), *Asiat. Herpetol. Res.* **3**, 54–59 (1990)
73. B.W. Chui, T.W. Kenny, H.J. Mamin, B.D. Terris, D. Rugar, Independent detection of vertical and lateral forces with a sidewall-implanted dual-axis piezoresistive cantilever, *Appl. Phys. Lett.* **72**, 1388–1390 (1998)
74. W.C. Young, R. Budynas, *Roark's Formulas for Stress and Strain*, 7th edn. (McGraw-Hill, New York, 2001)
75. N.J. Glassmaker, A. Jagota, C.Y. Hui, J. Kim, Design of biomimetic fibrillar interfaces, 1. Making contact, *J. R. Soc. Interf.* **1**, 23–33 (2004)
76. B.V. Derjaguin, V.M. Muller, Y.P. Toporov, Effect of contact deformation on the adhesion of particles, *J. Colloid Interf. Sci.* **53**, 314–326 (1975)
77. K.T. Wan, D.T. Smith, B.R. Lawn, Fracture and contact adhesion energies of mica-mica, silica-silica, and mica-silica interfaces in dry and moist atmospheres, *J. Am. Ceram. Soc.* **75**, 667–676 (1992)
78. B.N.J. Persson, On the mechanism of adhesion in biological systems, *J. Chem. Phys.* **118**, 7614–7621 (2003)

79. N.J. Glassmaker, A. Jagota, C.Y. Hui, Adhesion enhancement in a biomimetic fibrillar interface, *Acta Biomater.* **1**, 367–375 (2005)
80. H. Yao, H. Gao, Mechanics of robust and releasable adhesion in biology: bottom-up designed hierarchical structures of gecko, *J. Mech. Phys. Solids* **54**, 1120–1146 (2006)
81. R. Spolenak, S. Gorb, E. Arzt, Adhesion design maps for bio-inspired attachment systems, *Acta Biomater.* **1**, 5–13 (2005)
82. G.E. Dieter, *Mechanical Metallurgy* (McGraw-Hill, London 1988)
83. M. Sitti, High aspect ratio polymer micro/nano-structure manufacturing using nanoem-bossing, nanomolding and directed self-assembly, *Proc. IEEE/ASME Adv. Mechatron. Conf.*, Vol. 2 (2003) pp. 886–890
84. K. Autumn, A. Dittmore, D. Santos, M. Spenko, M. Cutkosky, Frictional adhesion, a new angle on gecko attachment, *J. Exp. Biol.* **209**, 3569–3579 (2006)
85. K.A. Daltorio, S. Gorb, A. Peressadko, A.D. Horschler, R.E. Ritzmann, R.D. Quinn, A robot that climbs walls using micro-structured polymer adhesive, *Proc. 30th Annu. Meet. Adhes. Soc.* (2007) pp. 329–331
86. B. Aksak, M.P. Murphy, M. Sitti, Gecko inspired micro-fibrillar adhesives for wall climbing robots on micro/nanoscale rough surfaces, *Proc. ICRA 2008, Pasadena* (2008) pp. 3058–3063
87. M.R. Cutkosky, S. Kim, Design and fabrication of multi-materials structures for bio-inspired robots, *Philos. Trans. R. Soc. A* **367**, 1799–1813 (2009)
88. W.K. Choi, I.S. Choi, Fabrication of hairy polymeric films inspired by geckos: Wetting and high adhesion properties, *Adv. Func. Mater.* **18**, 1089–1096 (2007)
89. A.K. Geim, S.V. Dubonos, I.V. Grigorieva, K.S. Novoselov, A.A. Zhukov, S.Y. Shapoval, Microfabricated adhesive mimicking gecko foot-hair, *Nat. Mater.* **2**, 461–463 (2003)
90. J. Davies, S. Haq, T. Hawke, J.P. Sargent, A practical approach to the development of a synthetic gecko tape, *Int. J. Adhes. Adhes.* **29**, 380–390 (2008)
91. B. Aksak, M.P. Murphy, M. Sitti, Adhesion of biologically inspired vertical and angled polymer microfiber arrays, *Langmuir* **23**, 3322–3332 (2007)
92. M.P. Murphy, B. Aksak, M. Sitti, Adhesion and anisotropic friction enhancement of angled heterogeneous micro-fiber arrays with spherical and spatula tips, *J. Adhes. Sci. Technol.* **21**, 1281–1296 (2007)
93. A. del Campo, C. Greiner, I. Alvares, E. Arzt, Patterned surfaces with pillars with controlled 3-D tip geometry mimicking bioattachment devices, *Adv. Mater.* **19**, 1973–1977 (2007)
94. A. del Campo, C. Greiner, E. Arzt, Contact shape controls adhesion of bioinspired fibrillar surfaces, *Langmuir* **23**, 10235–10243 (2007)
95. S. Gorb, M. Varenberg, A. Peressadko, J. Tuma, Biomimetic mushroom-shaped fibrillar adhesive microstructures, *J. R. Soc. Interface* **4**, 271–275 (2007)
96. B. Bhushan, R.A. Sayer, Surface characterization and friction of a bio-inspired reversible adhesive tape, *Microsyst. Technol.* **13**, 71–78 (2007)
97. R.N. Wenzel, Resistance of solid surfaces to wetting by water, *Ind. Eng. Chem.* **28**, 988–994 (1936)
98. Z. Burton, B. Bhushan, Hydrophobicity, adhesion, and friction properties of nanopatterned polymers and scale dependence for micro- and nanoelectromechanical systems, *Nano Lett.* **5**, 1607–1613 (2005)
99. B. Bhushan, Y.C. Jung, Wetting, adhesion, and friction of superhydrophobic and hydrophilic leaves and fabricated micro/nanopatterned surfaces, *J. Phys. Condens. Matter* **20**, 22510 (2008)
100. M. Nosonovsky, B. Bhushan, *Multiscale Dissipative Mechanisms and Hierarchical Surfaces, NanoScience and Technology* (Springer, Berlin, Heidelberg 2008)
101. E. Schaffer, T. Thurn-Albrecht, T.P. Russell, U. Steiner, Electrically induced structure formation and pattern transfer, *Nature* **403**, 874–877 (2000)
102. B. Yurdumakan, N.R. Ravavikar, P.M. Ajayan, A. Dhinojwala, Synthetic gecko foot-hairs from multiwalled carbon nanotubes, *Chem. Commun.* **30**, 3799–3801 (2005)
103. L. Ge, S. Sethi, L. Ci, M. Ajayan, A. Dhinojwale, Carbon nanotube-based synthetic gecko tape, *Proc. Natl. Acad. Sci. USA* **104**, 10792–10795 (2007)

104. L. Qu, L. Dai, M. Stone, Z. Xia, Z.L. Wang, Carbon nanotube arrays with strong shear binding-on and easy normal lifting-off, *Science* **322**, 238–242 (2008)
105. A. del Campo, C. Greiner, SU-8: A photoresist for high-aspect-ratio and 3-D submicron lithography, *J. Micromech. Microeng.* **17**, R81–R95 (2007)
106. M.T. Northen, K.L. Turner, A batch fabricated biomimetic dry adhesive, *Nanotechnology* **16**, 1159–1166 (2005)
107. M.T. Northen, K.L. Turner, Meso-scale adhesion testing of integrated micro- and nanoscale structures, *Sens. Actuators A* **130/131**, 583–587 (2006)



# **Part VI**

## **Industrial Applications**

## Chapter 22

# Micro/Nanotribology and Micro/Nanomechanics of Magnetic Storage Devices

**Bharat Bhushan**

**Abstract** A magnetic recording process involves relative motion between a magnetic medium (tape or disk) against a stationary or rotating read/write magnetic head. For ever-increasing, high areal recording density, the linear flux density (number of flux reversals per unit distance) and the track density (number of tracks per unit distance) should be as high as possible. The size of a single bit dimension for current devices is typically less than  $1,000 \text{ nm}^2$ . This dimension places stringent restrictions on the defect size present on the head and medium surfaces.

Reproduced (read-back) magnetic signal amplitude decreases with a decrease in the recording wavelength and/or the track width. The signal loss results from the magnetic coating thickness, read gap length, and head-to-medium spacing (clearance or flying height). It is known that the signal loss as a result of spacing can be reduced exponentially by reducing the separation between the head and the medium. The need for increasingly higher recording densities requires that surfaces be as smooth as possible and the flying height (physical separation or clearance between a head and a medium) be as low as possible. The ultimate objective is to run two surfaces in contact (with practically zero physical separation) if the tribological issues can be resolved. Smooth surfaces in near contact lead to an increase in adhesion, friction, and interface temperatures, and closer flying heights lead to occasional rubbing of high asperities and increased wear. Friction and wear issues are resolved by appropriate selection of interface materials and lubricants, by controlling the dynamics of the head and medium, and the environment. A fundamental understanding of the tribology (friction, wear, and lubrication) of the magnetic head/medium interface, both on macro- and micro/nanoscales, becomes crucial for the continued growth of this more than \$ 60 billion a year magnetic storage industry.

In this chapter, initially, the general operation of drives and the construction and materials used in magnetic head and medium components are described. Then the micro/nanotribological and micro/nanomechanics studies including surface

roughness, friction, adhesion, scratching, wear, indentation, and lubrication relevant to magnetic storage devices are presented.

## 22.1 Introduction

### 22.1.1 *Magnetic Storage Devices*

Magnetic storage devices used for storage and retrieval are tape, flexible (floppy) disk and rigid disk drives. These devices are used for audio, video and data-storage applications. Magnetic storage industry is some \$ 60 billion a year industry with \$ 20 billion for audio and video recording (almost all tape drives/media) and \$ 40 billion for data storage. In the data-storage industry, magnetic rigid disk drives/media, tape drives/media, flexible disk drives/media, and optical disk drive/media account for about \$ 25 B, \$ 6 B, \$ 3 B, and \$ 6 B, respectively. Magnetic recording and playback involves the relative motion between a magnetic medium (tape or disk) against a read-write magnetic head. Heads are designed so that they develop a (load-carrying) hydrodynamic air film under steady operating conditions to minimize head-medium contact. However, physical contact between the medium and head occurs during starts and stops, referred to as contact-start-stops (CSS) technology [1–4]. In the modern magnetic storage devices, the flying heights (head-to-medium separation) are on the order of 5–20 nm and roughnesses of head and medium surfaces are on the order of 1–2 nm RMS. The need for ever-increasing recording densities requires that surfaces be as smooth as possible and the flying heights be as low as possible. Smooth surfaces lead to an increase in adhesion, friction, and interface temperatures, and closer flying heights lead to occasional rubbing of high asperities and increased wear. High stiction (static friction) and wear are the limiting technology to future of this industry. Head load/unload (L/UL) technology has recently been used as an alternative to CSS technology in rigid disk drives that eliminates stiction and wear failure mode associated with CSS. In an L/UL drive, a lift tab extending from the suspension load beam engages a ramp or cam structure as the actuator moves beyond the outer radius of the disk. The ramp lifts (or unloads) the head stack from the disk surfaces as the actuator moves to the parking position. Starting and stopping the disk only occur with the head in the unloaded state. Several contact or near contact recording devices are at various stages of development. High stiction and wear are the major impediments to the commercialization of the contact recording [1–7].

Magnetic media fall into two categories: particulate media, where magnetic particles ( $\gamma$ -Fe<sub>2</sub>O<sub>3</sub>, Co- $\gamma$ Fe<sub>2</sub>O<sub>3</sub>, CrO<sub>2</sub>, Fe or metal (MP), or barium ferrite) are dispersed in a polymeric matrix and coated onto a polymeric substrate for flexible media (tape and flexible disks); thin-film media, where continuous films of magnetic materials are deposited by vacuum deposition techniques onto a polymer substrate for flexible media or onto a rigid substrate (typically aluminium and more recently glass or glass ceramic) for rigid disks. The most commonly used thin

magnetic films for tapes are evaporated Co–Ni (82–18 at.%) or Co–O dual layer. Typical magnetic films for rigid disks are metal films of cobalt-based alloys (such as sputtered Co–Pt–Ni, Co–Ni, Co–Pt–Cr, Co–Cr and Co–NiCr). For high recording densities, trends have been to use thin-film media. Magnetic heads used to date are either conventional thin-film inductive, magnetoresistive (MR) and giant MR (GMR) heads. The air-bearing surfaces (ABS) of tape heads are generally cylindrical in shape. For dual-sided flexible-disk heads, two heads are either spherically contoured and slightly offset (to reduce normal pressure) or are flat and loaded against each other. The rigid-disk heads are supported by a leaf spring (flexure) suspension. The ABS of heads are almost made of Mn–Zn ferrite, Ni–Zn ferrite,  $\text{Al}_2\text{O}_3$ –TiC and calcium titanate. The ABS of some conventional heads are made of plasma sprayed coatings of hard materials such as  $\text{Al}_2\text{O}_3$ – $\text{TiO}_2$  and  $\text{ZrO}_2$  [2–4].

Figure 22.1 shows the schematic illustrating the tape path with details of tape guides in a data-processing linear tape drive (IBM LTO Gen1) which uses a rectangular tape cartridge. Figure 22.2a shows the sectional views of particulate and thin-film magnetic tapes. Almost exclusively, the base film is made of semi-crystalline biaxially-oriented poly (ethylene terephthalate) (or PET) or poly (ethylene 2,6 naphthalate) (or PEN) or Aramid. The particulate coating formulation consists of binder (typically polyester polyurethane), submicron accicular shaped magnetic particles (about 50 nm long with an aspect ratio of about 5), submicron head cleaning agents (typically alumina) and lubricant (typically fatty acid ester). For protection against wear and corrosion and low friction/stiction, the thin-film tape is first coated with a diamondlike carbon (DLC) overcoat deposited by plasma enhanced chemical vapor deposition, typically lubricated with primarily a perfluoropolyether lubricant. Figure 22.2b shows the schematic of an 8-track (along with 2 servo tracks) thin-film read-write head with MR read and inductive write. The head steps up and down to provide 384 total data tracks across the width of the tape. The ABS is made of  $\text{Al}_2\text{O}_3$ –TiC. A tape tension of about 1 N over a 12.7 mm wide tape (normal pressure  $\approx 14$  kPa) is used during use. The RMS roughnesses of ABS of the heads and tape surfaces typically are 1–1.5 nm and 5–8 nm, respectively.

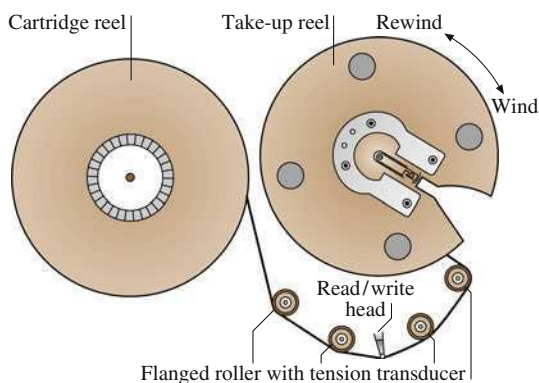


**Fig. 22.1** Schematic of tape path in an IBM Linear Tape Open (LTO) tape drive

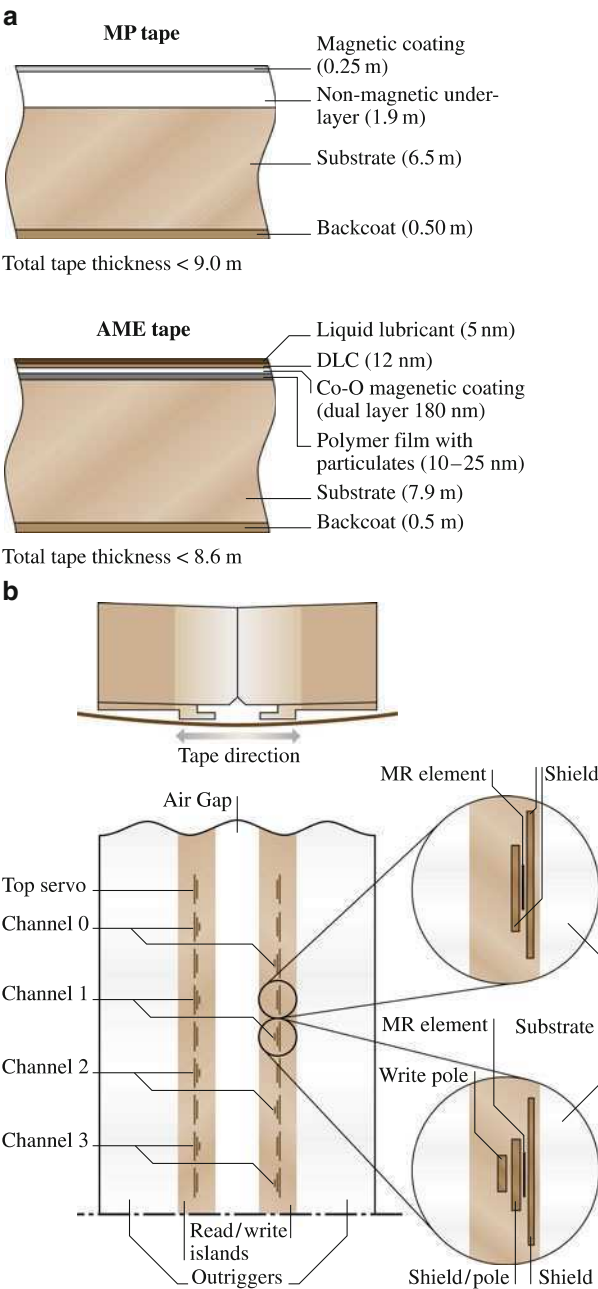


**Fig. 22.2** (a) Sectional views of particulate and thin-film magnetic tapes, and (b) schematic of a magnetic thin-film read/write head for an IBM LTO Gen 1 tape drive

Figure 22.3 shows the schematic of a data processing rigid disk drive with 22.6-, 27.4-, 48-, 63.5-, 75-, and 95-mm form factor. Nonremovable stack of multiple disks mounted on a ball bearing or hydrodynamic spindle, are rotated by an electric motor at constant angular speed ranging from about 5,000 to in excess of 15,000 RPM, dependent upon the disk size. Head slider-suspension assembly (allowing one slider for each disk surface) is actuated by a stepper motor or a voice coil motor using a rotary actuator. Figure 22.4a shows the sectional views of a thin-film rigid disk. The substrate for rigid disks is generally a non heat-treatable aluminium–magnesium alloy 5086, glass or glass ceramic. The protective overcoat commonly used for thin-film disks is sputtered DLC, topically lubricated with perfluoropolyether

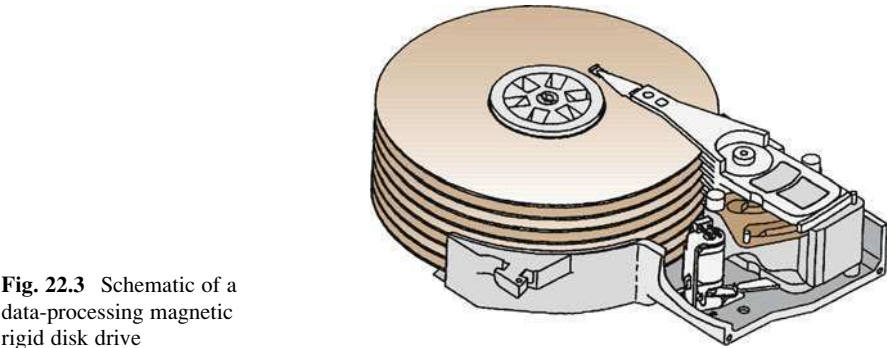


**Fig. 22.3** Schematic of a data-processing magnetic rigid disk drive

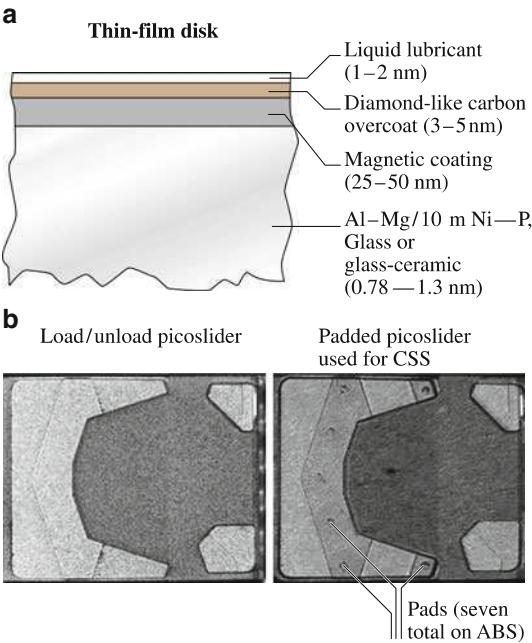


**Fig. 22.4** (a) Sectional views of a thin-film magnetic rigid disk, and (b) schematic of two picosliders – load/unload picoslider and padded picoslider used for CSS

type of lubricants. Lubricants with polar-end groups are generally used for thin-film disks in order to provide partial chemical bonding to the overcoat surface. The disks used for CSS technology are laser textured in the landing zone. Figure 22.4b shows the schematic of two thin-film head picosliders with a step at the leading edge, and GMR read and inductive write. “Pico” refers to the small sizes of  $1.25 \text{ mm} \times 1 \text{ mm}$ . These sliders use  $\text{Al}_2\text{O}_3\text{--TiC}$  (70 – 30 wt%) as the substrate material with multilayered thin-film head structure coated and with about 3.5 nm thick DLC coating to prevent the thin film structure from electrostatic discharge. The seven pads on the padded slider are made of DLC and are about  $40 \text{ }\mu\text{m}$  in diameter and 50 nm in height. A normal load of about 3 g is applied during use.

### **22.1.2 *Micro/Nanotribology and Micro/Nanomechanics and Their Applications***

The micro/nanotribological studies are needed to develop fundamental understanding of interfacial phenomena on a small scale and to study interfacial phenomena in [8–12]. Magnetic storage devices operate under low load and encounter isolated asperity interactions. These use multilayered thin film structure and are generally lubricated with molecularly-thin films. Micro/nanotribological and micro/nanomechanical techniques are ideal to study the friction and wear processes of micro/nanoscale and molecularly thick films. These studies are also valuable in fundamental understanding of interfacial phenomena in macrostructures to provide a bridge between science and engineering. At interfaces of technological applications, contact occurs at multiple asperity contacts. A sharp tip of tip-based microscopes (atomic force/friction force microscopes or AFM/FFM) sliding on a surface simulates a single asperity contact, thus allowing high-resolution measurements of surface interactions at a single asperity contacts. AFMs/FFMs are now commonly used for tribological studies.

In this chapter, we present state-of-the-art of micro/nanotribology and micro/nanomechanics of magnetic storage devices including surface roughness, friction, adhesion, scratching, wear, indentation, and lubrication.

## **22.2 Experimental**

### **22.2.1 *Description of AFM/FFM***

AFM/FFMs used in the tribological studies have been described in several papers [10, 12, 13]. Briefly, in one of the commercial designs, the sample is mounted on a PZT tube scanner to scan the sample in the  $x$ – $y$ -plane and to move the sample in the vertical ( $z$ ) direction (Fig. 22.5). A sharp tip at the end of a flexible cantilever is

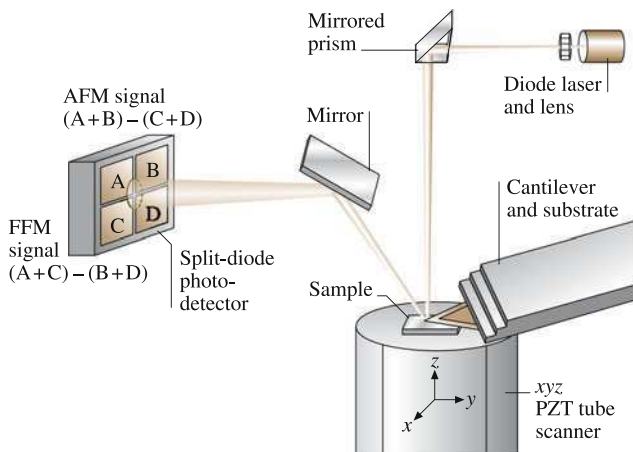
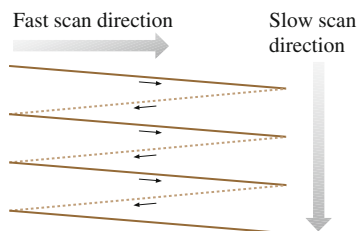


**Fig. 22.5** Principles of operation of a commercial small sample AFM/FFM

**Fig. 22.6** Schematic of triangular pattern trajectory of the AFM tip as the sample is scanned in two dimensions. During imaging, data are recorded only during scans along the solid scan lines

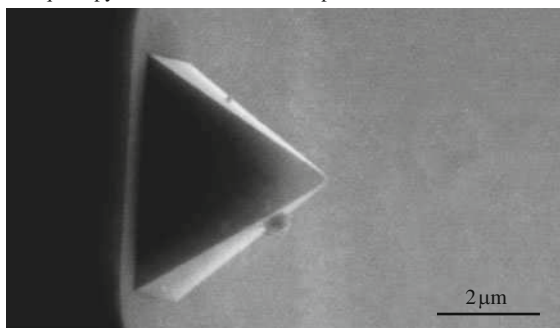


brought in contact with the sample and the sample is scanned in a raster pattern (Fig. 22.6). Normal and frictional forces being applied at the tip-sample interface are simultaneously measured using a laser beam deflection technique. Surface roughness is measured either in the contact mode or the so-called tapping mode (intermittent contact mode). For surface roughness and friction measurements, a microfabricated square pyramidal  $\text{Si}_3\text{N}_4$  tip with a tip radius of about 30 nm attached to a cantilever beam (with a normal beam stiffness of about 0.5 N/m) for contact mode or a square-pyramidal etched single-crystal silicon tip with a rectangular silicon cantilever beam (Fig. 22.7) is generally used at normal loads ranging from 10 to 150 nN. A preferred method of measuring friction and calibration procedures for conversion of voltages corresponding to normal and friction forces to force units, are described by Bhushan [10, 12, 13]. The samples are typically scanned over scan areas ranging from  $50 \text{ nm} \times 50 \text{ nm}$  to  $10 \text{ }\mu\text{m} \times 10 \text{ }\mu\text{m}$ , in a direction orthogonal to the long axis of the cantilever beam [14]. The scan rate is on the order of 1 Hz. For example, for this rate, the sample scanning speed would be  $1 \text{ }\mu\text{m/s}$  for a  $500 \text{ nm} \times 500 \text{ nm}$  scan area. Adhesive force measurements are performed in the so-called friction calibration mode. In this technique, the tip is brought in contact with the sample and then pulled away. The force required to pull the tip off the sample is a measure of adhesive force.

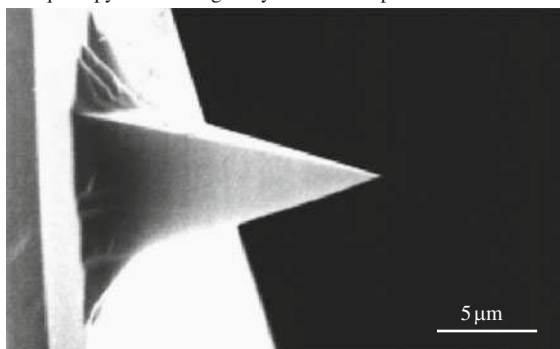


**Fig. 22.7** SEM micrographs of a square-pyramidal PECVD  $\text{Si}_3\text{N}_4$  tip with a triangular cantilever beam (*top*), a square-pyramidal etched single-crystal silicon tip with a rectangular silicon cantilever beam (*middle*), and a three-sided pyramidal natural diamond tip with a square stainless steel cantilever beam (*bottom*)

Square pyramidal silicon nitride tip



Square pyramidal single-crystal silicon tip



Three-sided pyramidal natural diamond tip



In nanoscale wear studies, the sample is initially scanned twice, typically at 10 nN to obtain the surface profile, then scanned twice at a higher load of typically 100 nN to wear and to image the surface simultaneously, and then rescanned twice at 10 nN to obtain the profile of the worn surface. For magnetic media studied by Bhushan and Ruan [15], no noticeable change in the roughness profiles was observed between the initial two scans at 10 nN and between profiles scanned at

100 nN and the final scans at 10 nN. Therefore any changes in the topography between the initial scans at 10 nN and the scans at 100 nN (or the final scans at 10 nN) are believed to occur as a result of local deformation of the sample surface. In picoindentation studies, the sample is loaded in contact with the tip. During loading, tip deflection (normal force) is measured as a function of vertical position of the sample. For a rigid sample, the tip deflection and the sample traveling distance (when the tip and sample come into contact) are equal. Any decrease in the tip deflection as compared to vertical position of the sample represents indentation. To ensure that the curvature in the tip deflection-sample traveling distance curve does not arise from PZT hysteresis, measurements on several rigid samples, including single-crystal natural diamond (IIa), were made by Bhushan and Ruan [15]. No curvature was noticed for the case of rigid samples. This suggests that any curvature for other samples should arise from the indentation of the sample.

For microscale scratching, microscale wear and nanoscale indentation hardness measurements, a three-sided pyramidal single-crystal natural diamond tip with an apex angle of  $80^\circ$  and a tip radius of about 100 nm (determined by scanning electron microscopy imaging) (Fig. 22.7) is used at relatively high loads (1  $\mu\text{N}$ –150  $\mu\text{N}$ ). The diamond tip is mounted on a stainless steel cantilever beam with normal stiffness of about 25 N/m [16–19]. For scratching and wear studies, the sample is generally scanned in a direction orthogonal to the long axis of the cantilever beam (typically at a rate of 0.5 Hz). For wear studies, typically an area of  $2\text{ }\mu\text{m} \times 2\text{ }\mu\text{m}$  is scanned at various normal loads (ranging from 1 to 100  $\mu\text{N}$ ) for selected number of cycles. Scratching can also be performed at ramped loads [20]. For nanoindentation hardness measurements, the scan size is set to zero and then normal load is applied to make the indents. During this procedure, the diamond tip is continuously pressed against the sample surface for about two seconds at various indentation loads. Sample surface is scanned before and after the scratching, wear, or nanoindentation, to obtain the initial and the final surface topography, at a low normal load of about 0.3  $\mu\text{N}$  using the same diamond tip. An area larger than the scratched, worn or indentation region is scanned to observe the scratch, wear scars, or indentation marks. Nanohardness is calculated by dividing the indentation load by the projected residual area of the indents [17]. Nanohardness and Young's modulus of elasticity (stiffness) at shallow depths as low as 5 nm are measured using a depth-sensing capacitance transducer system in an AFM [19].

Indentation experiments provide a single-point measurement of the Young's modulus of elasticity (stiffness), localized surface elasticity as well as phase contrast maps (to obtain viscoelastic properties map) can be obtained using dynamic force microscopy in which an oscillating tip is scanned over the sample surface in contact under steady and oscillating load [21–24]. Recently, a torsional resonance (TR) mode has been introduced [25, 26] which provides higher resolution. Stiffness and phase contrast maps can provide magnetic particle/polymer distributions in magnetic tapes as well as lubricant film thickness distribution.

Boundary lubrication studies are conducted using either  $\text{Si}_3\text{N}_4$  or diamond tips [27–30]. The coefficient of friction is monitored as a function of sliding cycles.

All measurements are carried out in the ambient atmosphere ( $22 \pm 1^\circ\text{C}$ ,  $45 \pm 5\%$  RH, and Class 10,000).

## 22.2.2 Test Specimens

Data on various head slider materials and magnetic media are presented in the chapter.  $\text{Al}_2\text{O}_3$ -TiC (70 – 30 w/o) and polycrystalline and single-crystal (110) Mn-Zn ferrite are commonly used for construction of disk and tape heads.  $\text{Al}_2\text{O}_3$ , a single-phase material, is also selected for comparisons with the performance of  $\text{Al}_2\text{O}_3$ -TiC, a two-phase material. An  $\alpha$ -type SiC is also selected which is a candidate slider material because of its high thermal conductivity and attractive machining and friction and wear properties [31]. Single crystal silicon has also been used in some head sliders but its use is discontinued [32].

Two thin-film rigid disks with polished and textured substrates, with and without a bonded perfluoropolyether are selected. These disks are 95 mm in diameter made of Al-Mg alloy substrate (1.3 mm thick) with a 10  $\mu\text{m}$  thick electroless plated Ni-P coating, 75 nm thick ( $\text{Co}_{79}\text{Pt}_{14}\text{Ni}_7$ ) magnetic coating, 20 nm thick amorphous carbon or diamondlike carbon (DLC) coating (microhardness  $\approx 1,500 \text{ kg/mm}^2$  as measured using a Berkovich indenter), and with or without a top layer of perfluoropolyether lubricant with polar end groups (Z-DOL) coating. The thickness of the lubricant film is about 2 nm. The metal particle (MP) tape is a 12.7 mm wide and 13.2  $\mu\text{m}$  thick (PET base thickness of 9.8  $\mu\text{m}$ , magnetic coating of 2.9  $\mu\text{m}$  with metal magnetic particles and nonmagnetic particles of  $\text{Al}_2\text{O}_3$  and  $\text{Cr}_2\text{O}_3$ , and back coating of 0.5  $\mu\text{m}$ ). The barium ferrite (BaFe) tape is a 12.7 mm wide and 11  $\mu\text{m}$  thick (PET base thickness of 7.3  $\mu\text{m}$ , magnetic coating of 2.5  $\mu\text{m}$  with barium ferrite magnetic particles and nonmagnetic particles of  $\text{Al}_2\text{O}_3$ , and back coating of 1.2  $\mu\text{m}$ ). Metal evaporated (ME) tape is a 12.7 mm wide tape with 10  $\mu\text{m}$  thick base, 0.2  $\mu\text{m}$  thick evaporated Co-Ni magnetic film and about 10 nm thick perfluoropolyether lubricant and a backcoat. PET film is a biaxially-oriented, semicrystalline polymer with particulates. Two sizes of nearly spherical particulates are generally used in the construction of PET: submicron ( $\approx 0.5 \mu\text{m}$ ) particles of typically carbon and larger particles (2–3  $\mu\text{m}$ ) of silica.

## 22.3 Surface Roughness

Solid surfaces, irrespective of the method of formation, contain surface irregularities or deviations from the prescribed geometrical form. When two nominally flat surfaces are placed in contact, surface roughness causes contact to occur at discrete contact points. Deformation occurs at these points, and may be either elastic or plastic, depending on the nominal stress, surface roughness and material properties. The sum of the areas of all the contact points constitutes the real area that would be in contact, and for most materials at normal loads, this will be only a small fraction of the area of contact if the surfaces were perfectly smooth. In general, real area of contact must be minimized to minimize adhesion, friction and wear [12].

Characterizing surface roughness is therefore important for predicting and understanding the tribological properties of solids in contact. Various measurement techniques are used to measure surface roughness. The AFM is used to measure surface roughness on length scales from nanometers to micrometers. A second technique is noncontact optical profiler (NOP) which is a noncontact technique and does not damage the surface. The third technique is stylus profiler (SP) in which a sharp tip is dragged over the sample surface. These techniques differ in lateral resolution. Roughness plots of a glass–ceramic disk measured using an AFM (lateral resolution  $\approx 15$  nm), NOP (lateral resolution  $\approx 1$   $\mu$ m) and SP (lateral resolution of  $\approx 0.2$   $\mu$ m) are shown in Fig. 22.8a. Figure 22.8b compares the profiles of the disk obtained with different instruments at a common scale. The figures show that roughness is found at scales ranging from millimeter to nanometer scales. Measured roughness profile is dependent on the lateral and normal resolutions of the measuring instrument [33–37]. Instruments with different lateral resolutions measure features with different scale lengths. It can be concluded that a surface is composed of a large number of length of scales of roughness that are superimposed on each other.

Surface roughness is most commonly characterized by the standard deviation of surface heights which is the square roots of the arithmetic average of squares of the vertical deviation of a surface profile from its mean plane. Due to the multiscale nature of surfaces, it is found that the variances of surface height and its derivatives and other roughness parameters depend strongly on the resolution of the roughness measuring instrument or any other form of filter, hence not unique for a surface [35–38] (Fig. 22.9). Therefore, a rough surface should be characterized in a way such that the structural information of roughness at all scales is retained. It is necessary to quantify the multiscale nature of surface roughness.

An unique property of rough surfaces is that if a surface is repeatedly magnified, increasing details of roughness are observed right down to nanoscale. In addition, the roughness at all magnifications appear quite similar in structure, as qualitatively shown in Fig. 22.10. The statistical self-affinity is due to similarity in appearance of a profile under different magnifications. Such a behavior can be characterized by fractal analysis [35, 39]. The main conclusion from these studies are that a fractal characterization of surface roughness is *scale independent* and provides information of the roughness structure at all length scales that exhibit the fractal behavior.

Structure function and power spectrum of a self-affine fractal surface follow a power law and can be written as (Ganti and Bhushan model)

$$S(\tau) = C\eta^{(2D-3)}\tau^{(4-2D)}, \quad (22.1)$$

$$P(\omega) = \frac{c_1\eta^{(2D-3)}}{\omega^{(5-2D)}}, \quad (22.2a)$$

and

$$c_1 = \frac{\Gamma(5-2D) \sin[\pi(2-D)]}{2\pi} C. \quad (22.2b)$$

**Fig. 22.8** Surface roughness plots of a glass–ceramic disk (a) measured using an atomic force microscope (lateral resolution  $\approx 15\text{ nm}$ ), noncontact optical profiler (lateral resolution  $\approx 1\text{ }\mu\text{m}$ ) and stylus profiler (SP) with a stylus tip of  $0.2\text{ }\mu\text{m}$  radius (lateral resolution  $\approx 0.2\text{ }\mu\text{m}$ ), and (b) measured using an AFM ( $\approx 150\text{ nm}$ ), SP ( $\approx 0.2\text{ }\mu\text{m}$ ), and NOP ( $\approx 1\text{ }\mu\text{m}$ ) and plotted on a common scale [36]

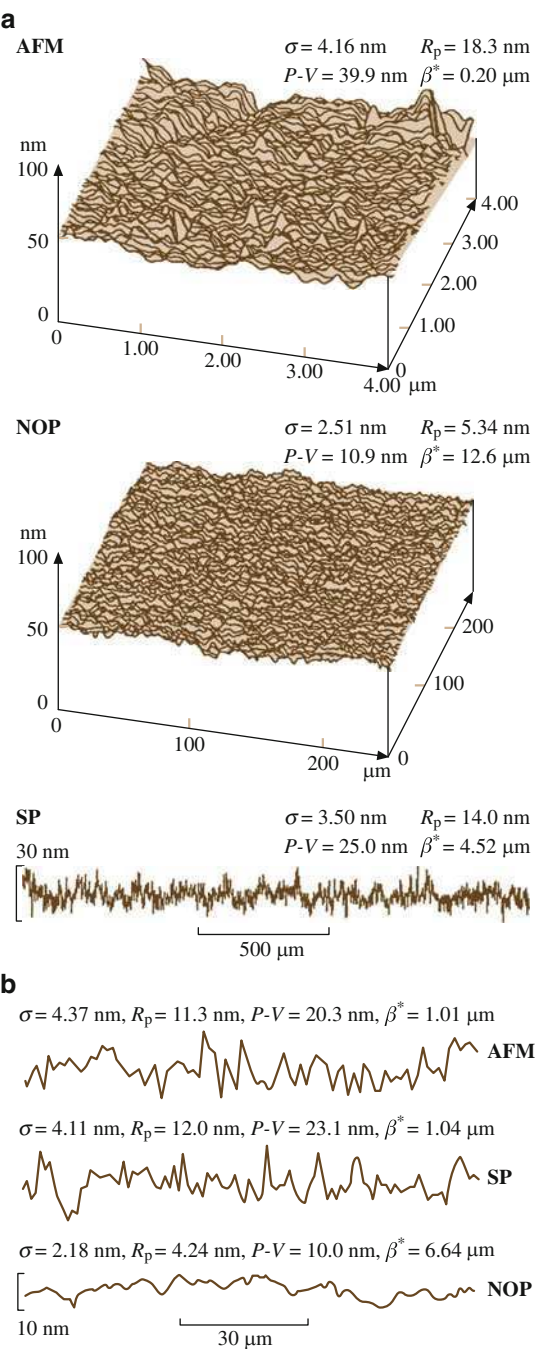


**Fig. 22.9** Scale dependence of standard deviation of surface heights for a glass–ceramic disk, measured using atomic force microscope (AFM), stylus profiler (SP), and noncontact optical profiler (NOP)

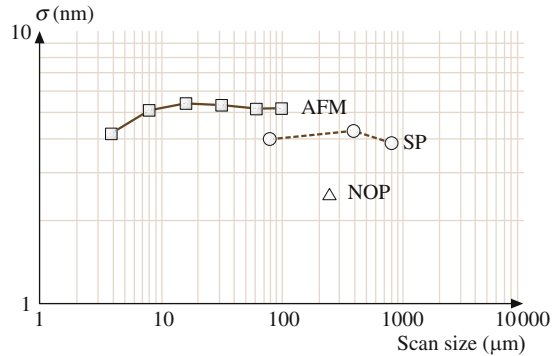
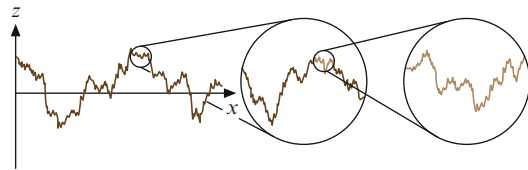


**Fig. 22.10** Qualitative description of statistical self-affinity for a surface profile



The fractal analysis allows the characterization of surface roughness by two parameters  $D$  and  $C$  which are instrument-independent and unique for each surface.  $D$  (ranging from 1 to 2 for surface profile) primarily relates to relative power of the frequency contents and  $C$  to the amplitude of all frequencies.  $\eta$  is the lateral resolution of the measuring instrument,  $\tau$  is the size of the increment (distance), and  $\omega$  is the frequency of the roughness. Note that if  $S(\tau)$  or  $P(\omega)$  are plotted as a function of  $\tau$  or  $\omega$ , respectively, on a log–log plot, then the power law behavior would result into a straight line. The slope of line is related to  $D$  and the location of the spectrum along the power axis is related to  $C$ .

Figure 22.11 present the structure function of a thin-film rigid disk measured using AFM, non-contact optical profiler (NOP), and stylus profiler (SP). Horizontal shift in the structure functions from one scan to another, arises from the change in the lateral resolution.  $D$  and  $C$  values for various scan lengths are listed in Table 22.1. We note that fractal dimension of the various scans is fairly constant (1.26–1.33); however,  $C$  increases/decreases monotonically with  $\sigma$  for the AFM data. The error in estimation of  $\eta$  is believed to be responsible for variation in  $C$ . These data show that the disk surface follows a fractal structure for three decades of length scales.

Majumdar and Bhushan [40] and Bhushan and Majumdar [41] developed a fractal theory of contact between two rough surfaces. This model has been used to predict whether contacts experience elastic or plastic deformation and to predict the statistical distribution of contact points. For a review of contact models, see Bhushan [42, 43] and Bhushan and Peng [44].

**Fig. 22.11** Structure functions for the roughness data measured at various scan sizes using AFM (scan sizes: 1  $\mu\text{m} \times 1 \mu\text{m}$ , 10  $\mu\text{m} \times 10 \mu\text{m}$ , 50  $\mu\text{m} \times 50 \mu\text{m}$ , and 100  $\mu\text{m}$ ), NOP (scan size: 250  $\mu\text{m} \times 250 \mu\text{m}$ ), and SP (scan length: 4,000  $\mu\text{m}$ ), for a magnetic thin-film rigid disk [35]

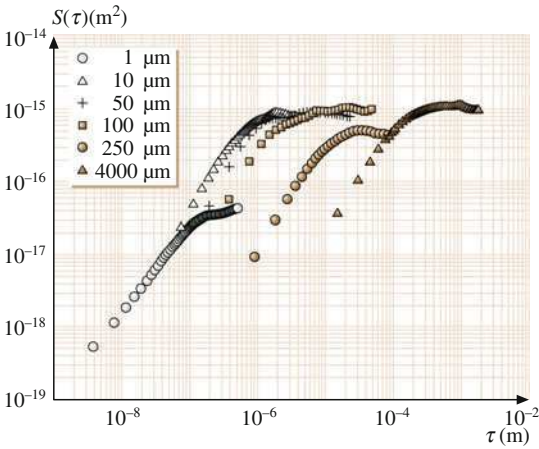


**Table 22.1** Surface roughness parameters for a polished thin-film rigid disk

Scan size ( $\mu\text{m} \times \mu\text{m}$ )	$\sigma$ (nm)	$D$	$C$ (nm)
1 (AFM)	0.7	1.33	$9.8 \times 10^{-4}$
10 (AFM)	2.1	1.31	$7.6 \times 10^{-3}$
50 (AFM)	4.8	1.26	$1.7 \times 10^{-2}$
100 (AFM)	5.6	1.30	$1.4 \times 10^{-2}$
250 (NOP)	2.4	1.32	$2.7 \times 10^{-4}$
4,000 (NOP)	3.7	1.29	$7.9 \times 10^{-5}$

*AFM* Atomic force microscope, *NOP* Noncontact optical profiler

Based on the fractal model of elastic–plastic contact, whether contacts go through elastic or plastic deformation is determined by a critical area which is a function of  $D$ ,  $C$ , hardness and modulus of elasticity of the mating surfaces. If contact spot is smaller than the critical area, it goes through the plastic deformations and large spots go through elastic deformations. The critical contact area for inception of plastic deformation for a thin-film disk was reported by Majumdar and Bhushan [40] to be about  $10^{-27} \text{ m}^2$ , so small that all contact spots can be assumed to be elastic at moderate loads.

The question remains as to how large spots become elastic when they must have initially been plastic spots. The possible explanation is shown in Fig. 22.12. As two surfaces touch, the nanoasperities (detected by AFM type of instruments) first coming into contact have smaller radii of curvature and are therefore plastically deformed instantly, and the contact area increases. When load is increased, nanoasperities in the contact merge, and the load is supported by elastic deformation of the large scale asperities or microasperities (detected by optical profiler type of instruments) [33].

Majumdar and Bhushan [40] and Bhushan and Majumdar [41] have reported relationships for cumulative size distribution of the contact spots, portions of the real area of contact in elastic and plastic deformation modes, and the load–area relationships.

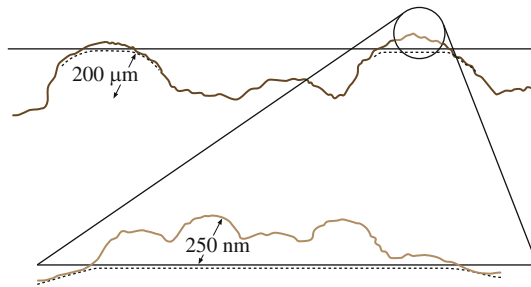


**Fig. 22.12** Schematic of local asperity deformation during contact of a rough surface, upper profile measured by an optical profiler and lower profile measured by AFM, typical dimensions are shown for a polished thin-film rigid disk against a flat head slider surface [33]

## 22.4 Friction and Adhesion

Friction and adhesion of magnetic head sliders and magnetic media have been measured by Bhushan and Koinkar [16, 45–48], Bhushan and Ruan [15], Ruan and Bhushan [14], Bhushan et al. [27], Bhushan [2, 4, 10], Koinkar and Bhushan [28, 29, 38, 49], Kulkarni and Bhushan [50], and Li and Bhushan [51, 52], and Sundararajan and Bhushan [53].

Koinkar and Bhushan [28, 29] and Poon and Bhushan [36, 37] reported that RMS roughness and friction force increase with an increase in scan size at a given scanning velocity and normal force. Therefore, it is important that while reporting friction force values, scan sizes and scanning velocity should be mentioned. Bhushan and Sundararajan [54] reported that friction and adhesion forces are a function of tip radius and relative humidity (also see [29]). Therefore, relative humidity should be controlled during the experiments. Care also should be taken to ensure that tip radius does not change during the experiments.

### 22.4.1 Magnetic Head Materials

$\text{Al}_2\text{O}_3$ –TiC is a commonly used slider material. In order to study the friction characteristics of this two phase material, friction of  $\text{Al}_2\text{O}_3$ –TiC (70 – 30 wt%) surface was measured. Figure 22.13 shows the surface roughness and friction force profiles [28]. TiC grains have a Knoop hardness of about  $2,800 \text{ kg/mm}^2$  which is higher than that of  $\text{Al}_2\text{O}_3$  grains of about  $2,100 \text{ kg/mm}^2$ . Therefore, TiC grains do not polish as much and result in a slightly higher elevation (about 2–3 nm higher than that of  $\text{Al}_2\text{O}_3$  grains). Based on friction force measurements, TiC grains exhibit higher friction force than  $\text{Al}_2\text{O}_3$  grains. The coefficients of friction of TiC and  $\text{Al}_2\text{O}_3$  grains are 0.034 and 0.026, respectively and the coefficient of friction of  $\text{Al}_2\text{O}_3$ –TiC composite is 0.03. Local variation in friction force also arises from the scratches present on the  $\text{Al}_2\text{O}_3$ –TiC surface. Thus, local friction values of a two phase materials can be measured. Ruan and Bhushan [55] reported that local



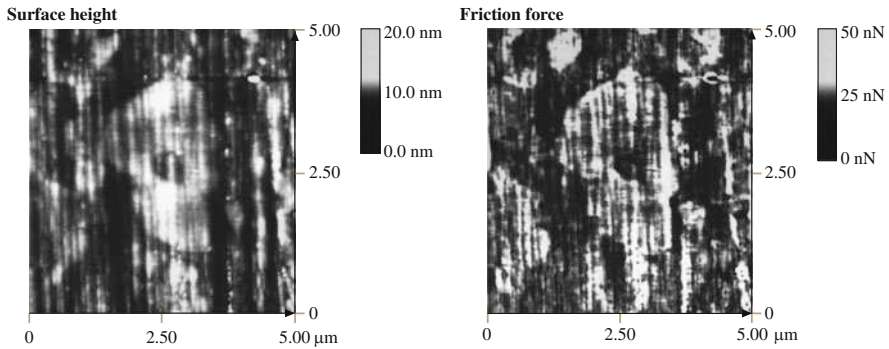


**Fig. 22.13** Gray scale surface roughness ( $\sigma = 0.97$  nm) and friction force map (mean = 7.0 nN,  $\sigma = 0.60$  nN) for  $\text{Al}_2\text{O}_3$ -TiC (70 to 30 wt%) at a normal load of 166 nN

variation in the coefficient of friction of cleaved HOP graphite was significant which arises from structural changes occurring during the cleaving process. The cleaved HOPG surface is largely atomically smooth but exhibits line shaped regions in which the coefficient of friction is more than an order of magnitude larger. These measurements suggest that friction measurements can be used for structural mapping of the surfaces.

Surface roughness and coefficient of friction of various head slider materials were measured by Koinkar and Bhushan [29]. For typical values, see Table 22.2. Macroscale friction values for all samples are higher than microscale friction values as there is less plowing contribution in microscale measurements [10, 12, 13].

### 22.4.2 *Magnetic Media*

Bhushan and coworkers measured friction properties of magnetic media including polished and textured thin-film rigid disks, metal particle (MP), barium ferrite (BaFe) and metal evaporated (ME) tapes, and poly(ethylene terephthalate)(PET) tape substrate [2, 4, 10]. For typical values of coefficients of friction of thin-film rigid disks and MP, BaFe and ME tapes, PET tape substrate (Table 22.3). In the case of magnetic disks, similar coefficients of friction are observed for both lubricated and unlubricated disks, indicating that most of the lubricant (though partially thermally bonded) is squeezed out from between the rubbing surfaces at high interface pressures, consistent with liquids being poor boundary lubricant [13]. Coefficient of friction values on a microscale are much lower than those on the macroscale. When measured for the small contact areas and very low loads used in microscale studies, indentation hardness and modulus of elasticity are higher than at the macroscale (data to be presented later). This reduces the real area of contact and the degree of wear. In addition, the small apparent areas of contact reduces the

**Table 22.2** Surface roughness ( $\sigma$  and  $P$ – $V$  distance), micro- and macro-scale friction, micro-scratching/wear, and nano- and microhardness data for various samples

Sample	Surface roughness (1 μm × 1 μm)		Coefficient of friction			Scratch depth at 60 μN (nm)	Wear depth at 60 μN (nm)	Hardness	
			Microscale	Macroscale <sup>b</sup>				Nano	Micro at 2 mN (GPa)
	σ (nm)	P–V <sup>a</sup> (nm)		Initial	Final				
Al <sub>2</sub> O <sub>3</sub>	0.97	9.9	0.03	0.18	0.2–0.6	3.2	3.7	24.8	15.0
Al <sub>2</sub> O <sub>3</sub> –TiC	0.80	9.1	0.05	0.24	0.2–0.6	2.8	22.0	23.6	20.2
Polycrystalline	2.4	20.0	0.04	0.27	0.24–0.4	9.6	83.6	9.6	5.6
Mn–Zn ferrite	1.9	13.7	0.02	0.16	0.18–0.24	9.0	56.0	9.8	5.6
Single-crystal (110)									
Mn–Zn ferrite SiC (α-type)	0.91	7.2	0.02	0.29	0.18–0.24	0.4	7.7	26.7	21.8

<sup>a</sup>Peak-to-valley distance  
<sup>b</sup>Obtained using silicon nitride ball with 3 mm diameter in a reciprocating mode at a normal load of 10 mN, reciprocating amplitude of 7 mm and average sliding speed of 1 mm/s. Initial coefficient of friction values were obtained at first cycle (0.007 m sliding distance) and final values at a sliding distance of 5 m

number of particles trapped at the interface, and thus minimize the “plowing” contribution to the friction force [8, 14, 18].

Local variations in the microscale friction of rough surfaces can be significant. Figure 22.14 shows the surface height map, the slopes of surface map taken along the sliding direction, and friction force map for a thin-film disk [8, 15, 18, 28, 38, 45–47, 56]. We note that there is no resemblance between the coefficient of friction profiles and the corresponding roughness maps, e.g., high or low points on the friction profile do not correspond to high or low points on the roughness profiles. By comparing the slope and friction profiles, we observe a strong correlation between the two. (For a clearer correlation, see gray-scale plots of slope and friction profiles for FFM tip sliding in either directions, in Fig. 22.15 to be presented in the next paragraph). We have shown that this correlation holds for various magnetic tapes, silicon, diamond, and other materials. This correlation can be explained by a “ratchet” mechanism; based on this mechanism, the local friction is a function of the local slope of the sample surface [10, 12, 13]. The friction is high at the leading edge of asperities and low at the trailing edge. In addition to the slope effect, the collision of tip encountering an asperity with a positive slope produces additional torsion of the cantilever beam leading to higher measured friction force. When encountering an asperity with a negative slope, however, there is no collision effect and hence no effect on friction. The ratchet mechanism and the collision effects thus explain the correlation between the slopes of the roughness maps and friction maps observed in Fig. 22.14.

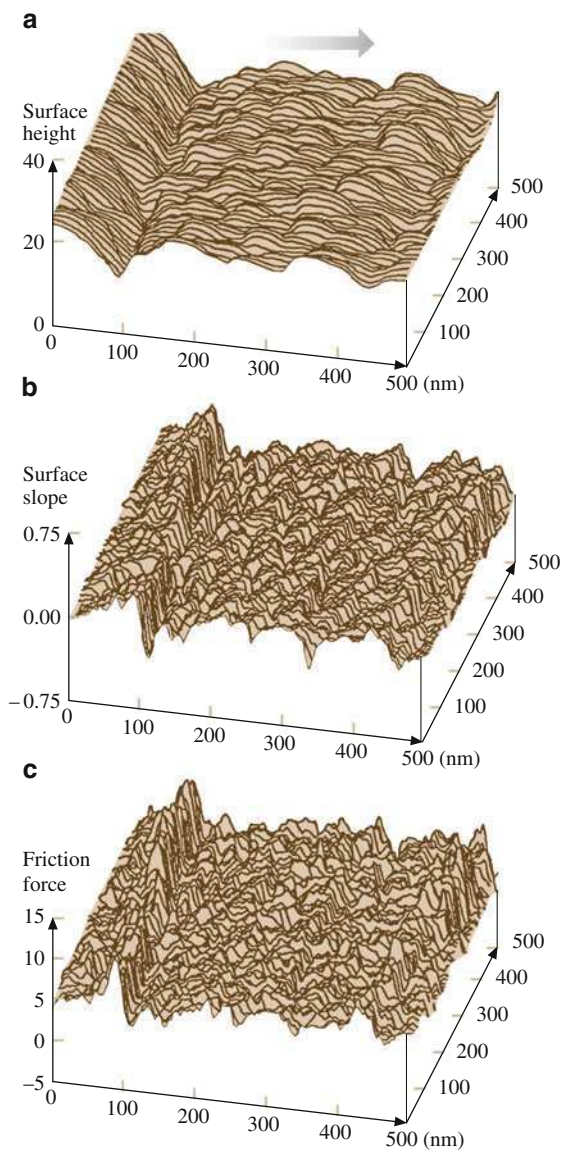
**Table 22.3** Surface roughness ( $\sigma$ ), microscale and macro-scale friction, and nanohardness data of thin-film magnetic rigid disk, magnetic tape and magnetic tape substrate (PET) samples

Sample	$\sigma$ (nm)	Coefficient of microscale friction				Coefficient of macro-scale friction	Nano-hardness (GPa)/Normal load ( $\mu$ N)			
		$10\text{ }\mu\text{m} \times 10\text{ }\mu\text{m}^a$			$1\text{ }\mu\text{m} \times 1\text{ }\mu\text{m}^a$					
		NOP $250\text{ }\mu\text{m} \times 250\text{ }\mu\text{m}^a$	AFM $1\text{ }\mu\text{m} \times 1\text{ }\mu\text{m}^a$	$10\text{ }\mu\text{m} \times 10\text{ }\mu\text{m}^a$						
Polished, unlubricated disk	2.2		3.3		4.5	0.05	0.06	–	0.26	21/100
Polished, lubricated disk	2.3		2.3		4.1	0.04	0.05	–	0.19	–
Textured, lubricated disk	4.6		5.4		8.7	0.04	0.05	–	0.16	–
Metal-particle tape	6.0		5.1		12.5	0.08	0.06	0.19	–	0.30/50
Barium-ferrite tape	12.3		7.0		7.9	0.07	0.03	0.18	–	0.25/25
Metal-evaporated tape	9.3		4.7		5.1	0.05	0.03	0.18	–	0.7 to 4.3/75
PET tape substrate	33		5.8		7.0	0.05	0.04	0.55	–	0.3/20 and 1.4/20 <sup>b</sup>

<sup>a</sup>Scan area; *NOP* Noncontact optical profiler; *AFM* Atomic force microscope

<sup>b</sup>Numbers are for polymer and particulate regions, respectively

**Fig. 22.14** (a) Surface height map ( $\sigma = 4.4$  nm), (b) slope of the roughness profiles taken in the sample sliding direction (the *horizontal axis*) (mean = 0.023,  $\sigma = 0.18$ ), and (c) friction force map (mean = 6.2 nN,  $\sigma = 2.1$  nN) for a textured thin-film rigid disk at a normal load of 160 nN [18]



To study the directionality effect on the friction, gray scale plots of coefficients of local friction of the thin-film disk as the FFM tip is scanned in either direction are shown in Fig. 22.15. Corresponding gray scale plots of slope of roughness maps are also shown in Fig. 22.15. The left hand set of the figures corresponds to

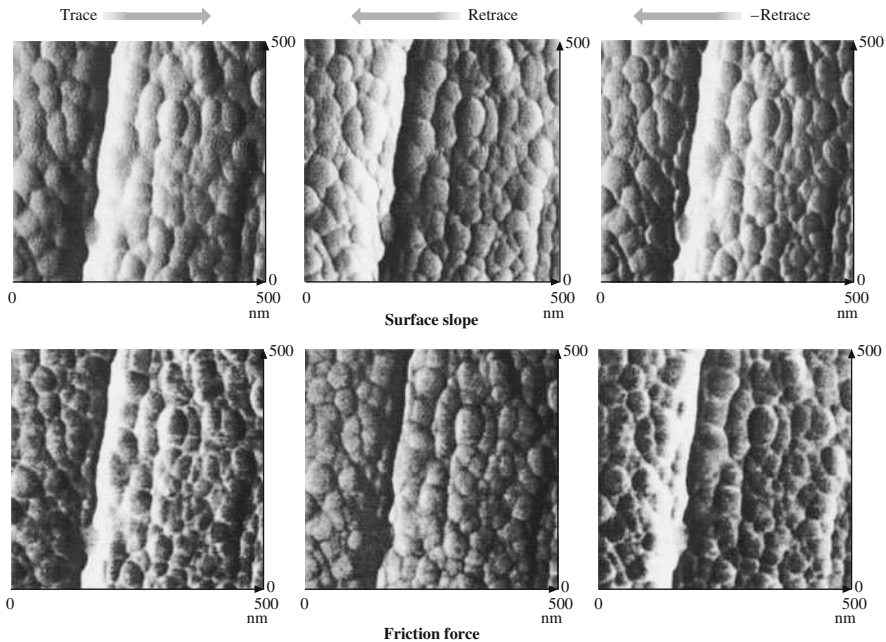
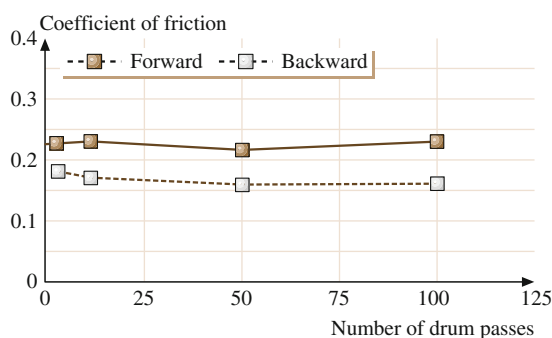


**Fig. 22.15** Gray-scale plots of the slope of the surface roughness and the friction force maps for a textured thin-film rigid disk with FFM tip sliding in different directions. *Higher points are shown by lighter color*

the tip sliding from the left towards right (trace direction), and the middle set corresponds to the tip sliding from the right towards left (retrace direction). It is important to take into account the sign change of surface slope and friction force which occur in the trace and retrace directions. In order to facilitate comparison of directionality effect on friction, the last set of the figures in the right hand column show the data with sign of surface slope and friction data in the retrace direction reversed. Now we compare trace and -retrace data. It is clear that the friction experienced by the tip is dependent upon the scanning direction because of surface topography.

The directionality effect in friction on a macroscale is generally averaged out over a large number of contacts. It has been observed in some magnetic tapes. In a macro-scale test, a 12.7 mm wide MP tape was wrapped over an aluminium drum and slid in a reciprocating motion with a normal load of 0.5 N and a sliding speed of about 60 mm/s. Coefficient of friction as a function of sliding distance in either direction is shown in Fig. 22.16. We note that coefficient of friction on a macro-scale for this tape is different in different directions.

**Fig. 22.16** Coefficient of macro-scale of friction as a function of sliding cycles for a metal-particle (MP) tape sliding over an aluminium drum in a reciprocating mode in both directions. Normal load = 0.5 N over 12.7 mm wide tape, sliding speed = 60 mm/s [7]



## 22.5 Scratching and Wear

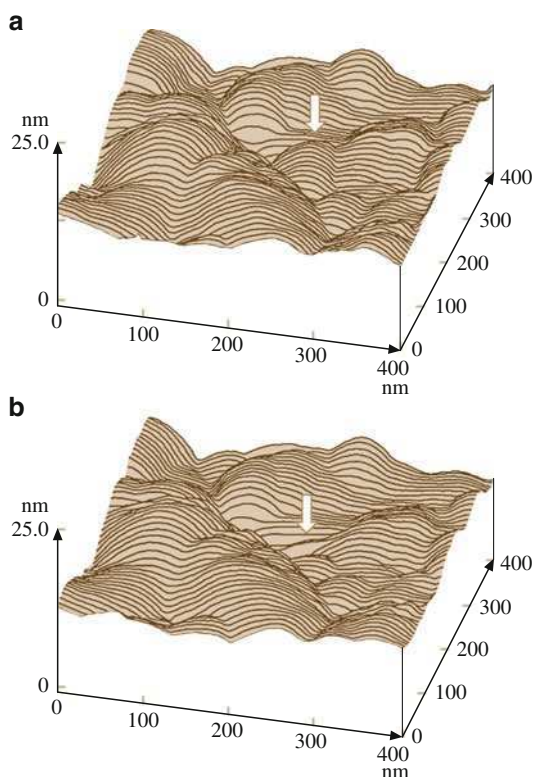
### 22.5.1 Nanoscale Wear

Bhushan and Ruan [15] conducted nanoscale wear tests on MP tapes at a normal load of 100 nN. Figure 22.17 shows the topography of the MP tape obtained at two different loads. For a given normal load, measurements were made twice. There was no discernible difference between consecutive measurements for a given normal load. However, as the load increased from 10 to 100 nN, topographical changes were observed; material (indicated by an arrow) was pushed toward the right side in the sliding direction of the AFM tip relative to the sample. The material movement is believed to occur as a result of plastic deformation of the tape surface. Similar behavior was observed on all tapes studied. Magnetic tape coating is made of magnetic particles and polymeric binder. Any movement of the coating material can eventually lead to loose debris. Debris formation is an undesirable situation as it may contaminate the head which may increase friction and/or wear between the head and tape, in addition to the deterioration of the tape itself. With disks, they did not notice any deformation under a 100 nN normal load.

### 22.5.2 Microscale Scratching

Microscratches have been made on various potential head slider materials ( $\text{Al}_2\text{O}_3$ ,  $\text{Al}_2\text{O}_3\text{-TiC}$ , Mn-Zn ferrite and SiC), and various magnetic media (unlubricated polished thin-film disk, MP, BaFe, ME tapes, and PET substrates) and virgin, treated and coated Si(111) wafers at various loads [16, 18, 28, 45–49, 53, 57, 58]. As mentioned earlier, the scratches are made using a diamond tip.

**Fig. 22.17** Surface roughness maps of a metal-particle (MP) tape at applied normal load of (a) 10 nN and (b) 100 nN. Location of the change in surface topography as a result of nanowear is indicated by arrows [15]

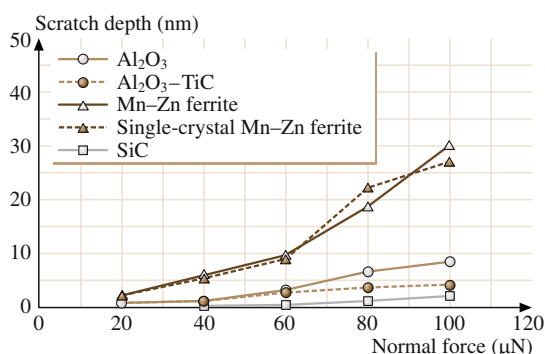


## Magnetic Head Materials

Scratch depths as a function of load and representative scratch profiles with corresponding 2D gray scale plots at various loads after a single pass (unidirectional scratching) for  $\text{Al}_2\text{O}_3$ ,  $\text{Al}_2\text{O}_3$ -TiC, polycrystalline and single-crystal Mn-Zn ferrite and SiC are shown in Figs. 22.18 and 22.19, respectively. Variation in the scratch depth along the scratch is about  $\pm 15\%$ . The  $\text{Al}_2\text{O}_3$  surface could be scratched at a normal load of  $40\text{ }\mu\text{N}$ . The surface topography of polycrystalline  $\text{Al}_2\text{O}_3$  shows the presence of porous holes on the surface. The 2D gray scale plot of scratched  $\text{Al}_2\text{O}_3$  surface shows one porous hole between scratches made at normal loads of  $40\text{ }\mu\text{N}$  and  $60\text{ }\mu\text{N}$ . Regions with defects or porous holes present, exhibit lower scratch resistance (see region marked by the arrow on 2D gray scale plot of  $\text{Al}_2\text{O}_3$ ). The  $\text{Al}_2\text{O}_3$ -TiC surface could be scratched at a normal load of  $20\text{ }\mu\text{N}$ . The scratch resistance for TiC grains is higher than that of  $\text{Al}_2\text{O}_3$  grains. The scratches generated at normal loads of  $80\text{ }\mu\text{N}$  and  $100\text{ }\mu\text{N}$  show that scratch depth of  $\text{Al}_2\text{O}_3$  grains is higher than that of TiC grains (see corresponding gray scale plot for  $\text{Al}_2\text{O}_3$ -TiC). Polycrystalline and single-crystal Mn-Zn ferrite could be scratched at a normal load of  $20\text{ }\mu\text{N}$ . The scratch width is much larger for the ferrite specimens as



**Fig. 22.18** Scratch depth as a function of normal load after one unidirectional cycle for  $\text{Al}_2\text{O}_3$ ,  $\text{Al}_2\text{O}_3\text{-TiC}$ , polycrystalline Mn-Zn ferrite, single-crystal Mn-Zn ferrite and SiC [28]



compared with other specimens. For SiC, there is no measurable scratch observed at a normal load of 20  $\mu\text{N}$ . At higher normal loads, very shallow scratches are produced. Table 22.2 presents average scratch depth at 60  $\mu\text{N}$  normal load for all specimens. SiC has the highest scratch resistance followed by  $\text{Al}_2\text{O}_3\text{-TiC}$ ,  $\text{Al}_2\text{O}_3$  and polycrystalline and single-crystal Mn-Zn ferrite. Polycrystalline and single-crystal Mn-Zn ferrite specimens exhibit comparable scratch resistance.

## Magnetic Media

Scratch depths as a function of load and scratch profiles at various loads after ten scratch cycles for unlubricated, polished disk and MP tape are shown in Figs. 22.20 and 22.21. We note that scratch depth increases with an increase in the normal load. Tape could be scratched at about 100 nN. With disk, gentle scratch marks under 10  $\mu\text{N}$  load were barely visible. It is possible that material removal did occur at lower load on an atomic scale which was not observable with a scan size of 5  $\mu\text{m}$  square. For disk, scratch depth at 40  $\mu\text{N}$  is less than 10 nm deep. The scratch depth increased slightly at the load of 50  $\mu\text{N}$ . Once the load is increased in excess of 60  $\mu\text{N}$ , the scratch depth increased rapidly. These data suggest that the carbon coating on the disk surface is much harder to scratch than the underlying thin-film magnetic film. This is expected since the carbon coating is harder than the magnetic material used in the construction of the disks.

Microscratch characterization of ultrathin amorphous carbon coatings, deposited by filtered cathodic arc (FCA) direct ion beam (IB), electron cyclotron resonance plasma chemical vapor deposition (ECR-CVP), and sputter (SP) deposition processes have been conducted using a nanoindenter and an AFM [20, 48, 49, 51–53, 59]. Data on various coatings of different thicknesses using a Berkovich tip are compared in Fig. 22.22. Critical loads for various coatings and silicon substrate are summarized in Fig. 22.23. It is clear that, for all deposition methods, the critical load increases with increasing coating thickness due to better load-carrying capacity of thicker coatings as compared to the thinner ones. In comparison of the



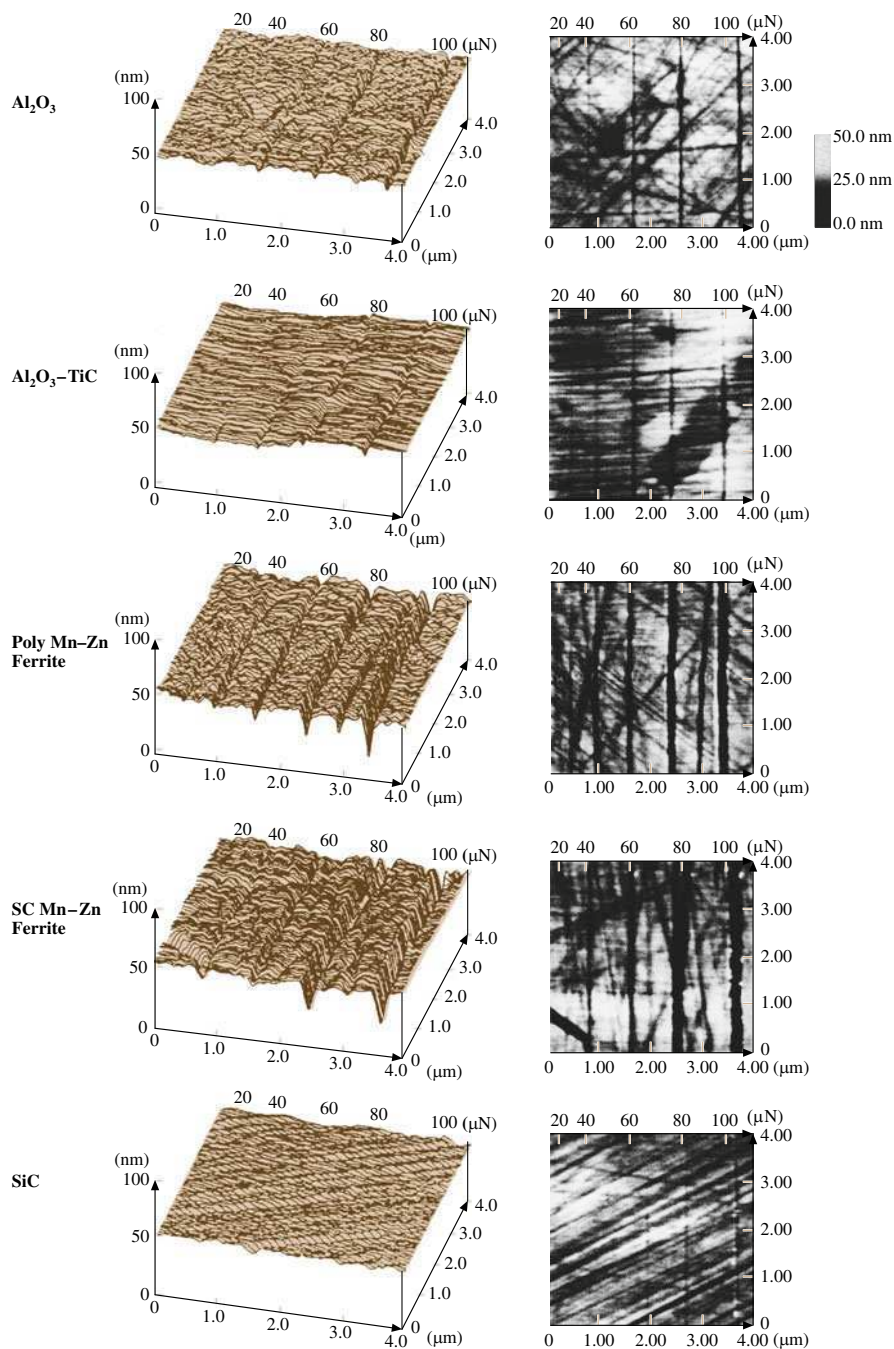


**Fig. 22.19** Surface profiles (*left column*) and 2D gray scale plots (*right column*) of scratched  $\text{Al}_2\text{O}_3$ ,  $\text{Al}_2\text{O}_3\text{-TiC}$ , polycrystalline Mn-Zn ferrite, single-crystal Mn-Zn ferrite, and SiC surfaces. Normal loads used for scratching for one unidirectional cycle are listed in the figure [28]

**Fig. 22.20** Scratch depth as a function of normal load after ten scratch cycles for unlubricated polished thin-film rigid disk, MP tape and PET film [18, 45, 47]

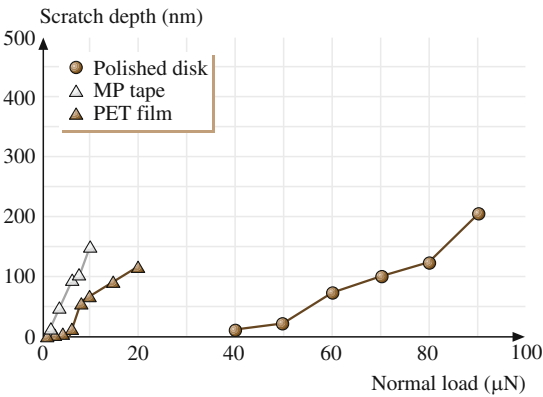
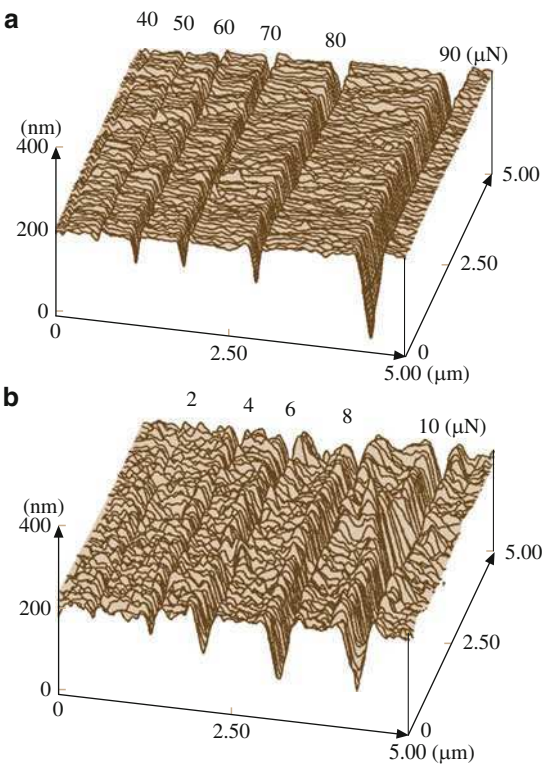


**Fig. 22.21** Surface profiles for scratched (a) unlubricated polished thin-film rigid disk and (b) MP tape. Normal loads used for scratching for ten cycles are listed in the figure [18]



different deposition methods, ECR-CVD and FCA coatings show superior scratch resistance at 20- and 10 nm thicknesses compared to SP coatings. As the coating thickness reduces, ECR-CVD exhibits the best scratch resistance followed by FCA and SP coatings.

Since tapes scratch readily, for comparisons in scratch resistance of various tapes, Bhushan and Koinkar [47] made scratches on selected three tapes only with one cycle. Figure 22.24 presents the scratch depths as a function of normal load after one cycle for three tapes – MP, BaFe and ME tapes. For the MP and BaFe particulate tapes, Bhushan and Koinkar [47] noted that the scratch depth along

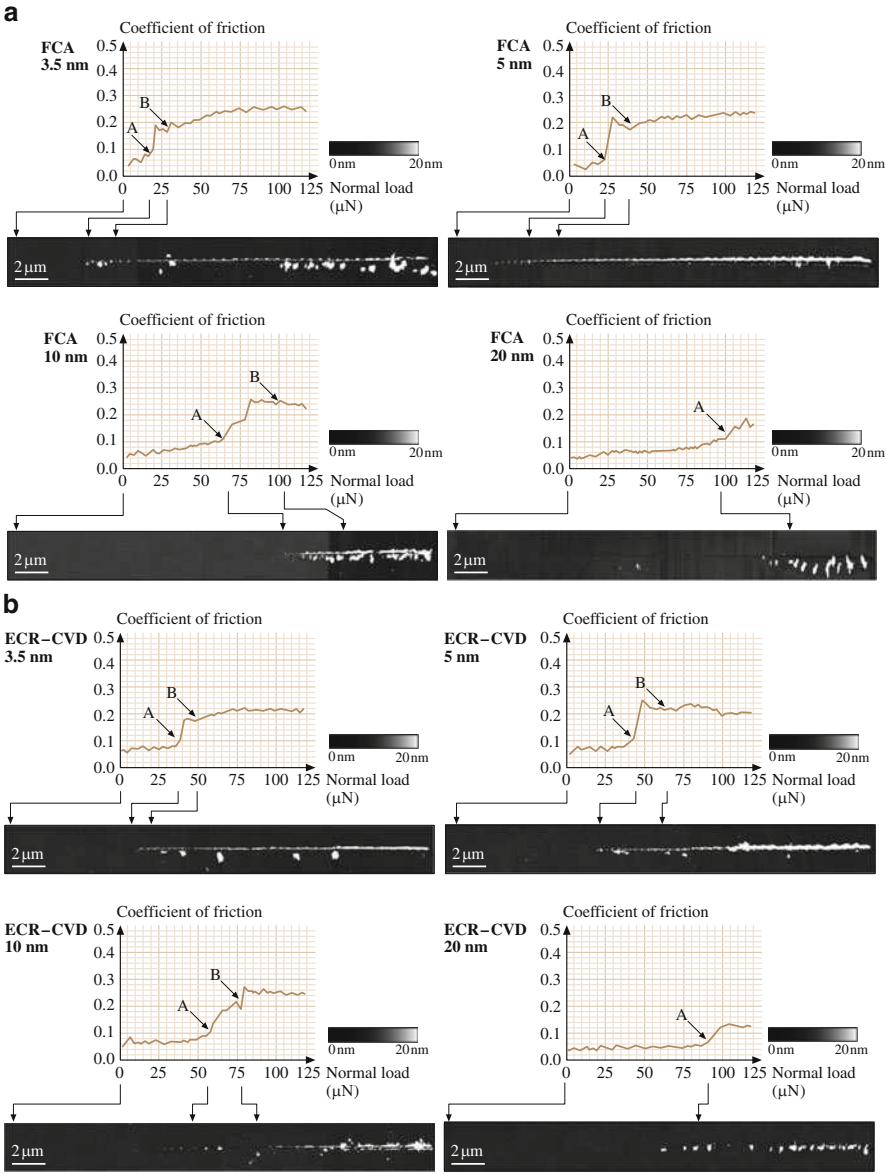
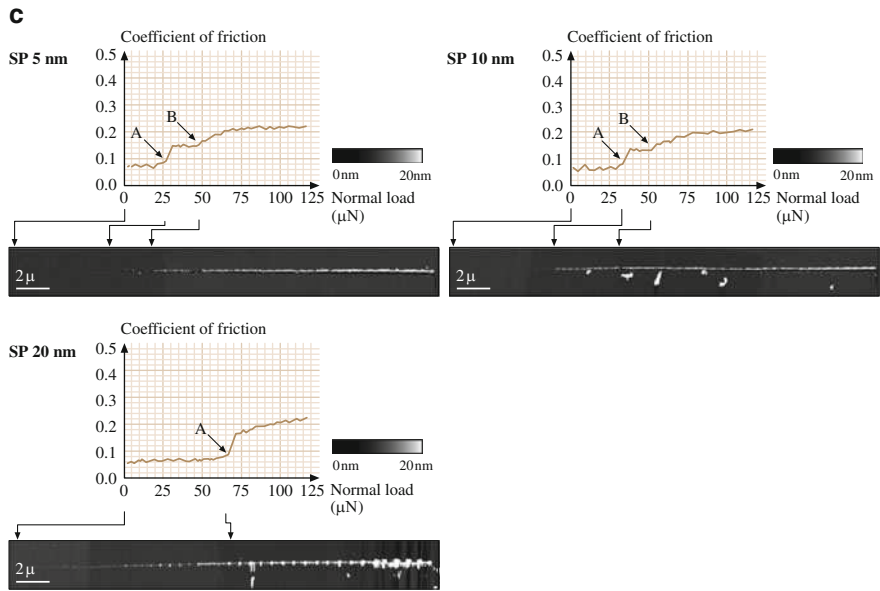
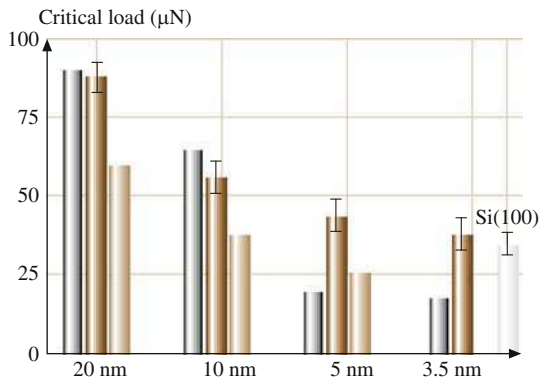


Fig. 22.22 (continued)



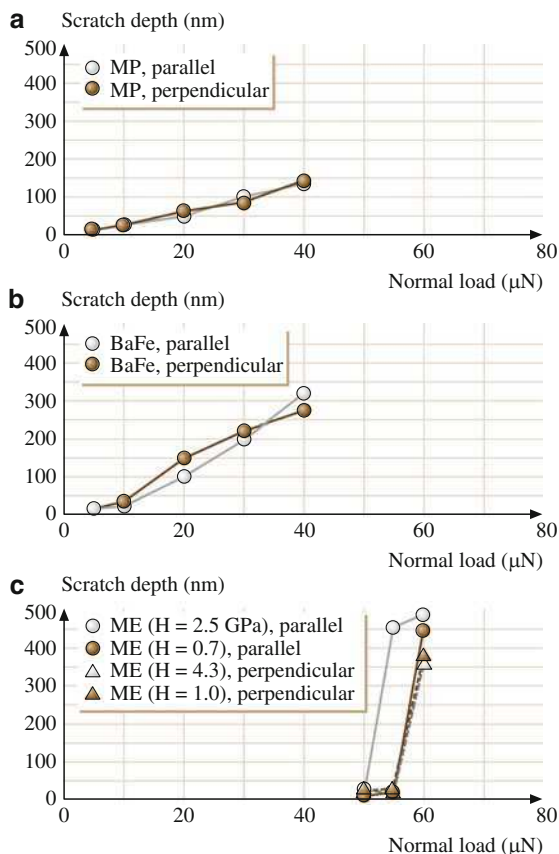
**Fig. 22.22** Coefficient of Friction profiles during scratch as a function of normal load and corresponding AFM surface height images for (a) FCA, (b) ECR-CVD, and (c) SP-coatings [20]

**Fig. 22.23** Summary of critical loads estimated from the coefficient of friction profiles and AFM images [20]



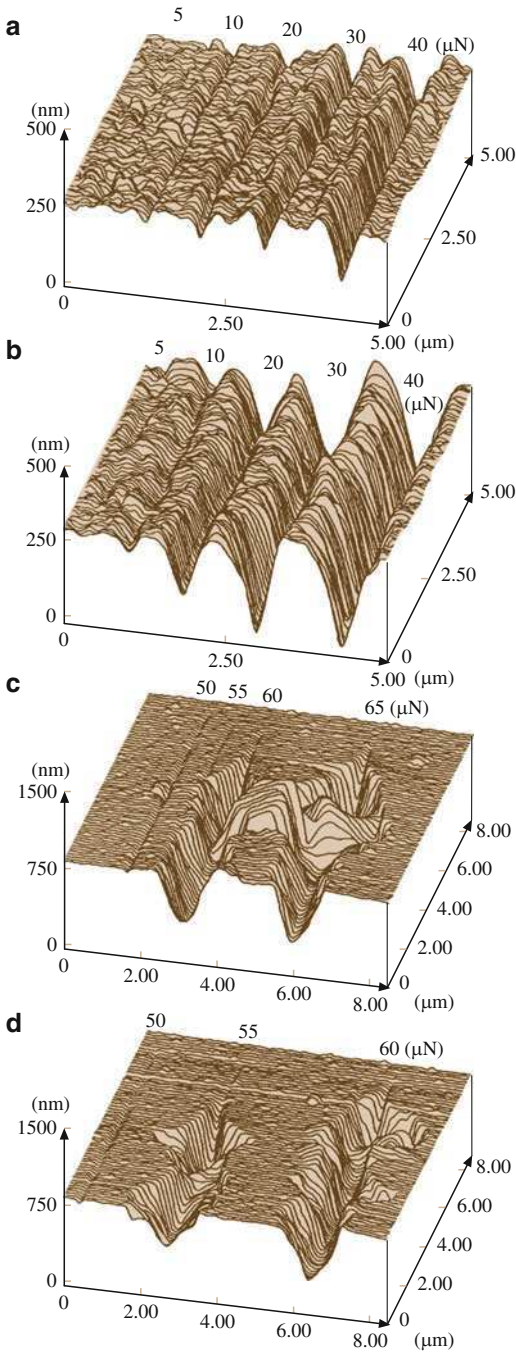
(parallel) and across (perpendicular) the longitudinal direction of the tapes is similar. Between the two tapes, MP tape appears to be more scratch resistant than BaFe tape, which depends on the binder, pigment volume concentration (PVC) and the head cleaning agent (HCA) contents. ME tapes appear to be much more scratch resistant than the particulate tapes. However, the ME tape breaks up catastrophically in a brittle mode at a normal load higher than the 50  $\mu\text{N}$  (Fig. 22.25), as

**Fig. 22.24** Scratch depth as a function of normal load after one scratch cycle for (a) MP, (b) BaFe, and (c) ME tapes along parallel and perpendicular directions with respect to the longitudinal axis of the tape [47]



compared to particulate tapes in which the scratch rate is constant. They reported that the hardness of ME tapes is higher than that of particulate tapes, however, a significant difference in the nanoindentation hardness values of the ME film from region to region (Table 22.3) was observed. They systematically measured scratch resistance in the high and low hardness regions along and across the longitudinal directions. Along the parallel direction, load required to crack the coating was lower (implying lower scratch resistance) for a harder region, than that for a softer region. The scratch resistance of high hardness region along the parallel direction is slightly poorer than that for along perpendicular direction. Scratch widths in both low and high hardness regions is about half ( $\approx 2 \mu\text{m}$ ) than that in perpendicular direction ( $\approx 1 \mu\text{m}$ ). In the parallel direction, the material is removed in the form of chips and lateral cracking also emanates from the wear zone. ME films have columnar structure with the columns lined up with an oblique angle of on the order of about  $35^\circ$  with respect to the normal to the coating surface [3, 60]. The

**Fig. 22.25** Surface maps for scratched (a) MP, (b) BaFe, (c) ME ( $H = 0.7$  GPa), and (d) ME ( $H = 2.5$  GPa) tapes along parallel direction. Normal loads used for scratching for one cycle are listed in the figure [47]



column orientation may be responsible for directionality effect on the scratch resistance. Hibst [60] have reported the directionality effect in the ME tape-head wear studies. They have found that the wear rate is lower when the head moves in the direction corresponding to the column orientation than in the opposite direction.

PET films could be scratched at loads of as low as about 2  $\mu\text{N}$  (Fig. 22.26). Figure 22.26a shows scratch marks made at various loads. Scratch depth along the scratch does not appear to be uniform. This may occur because of variations in the mechanical properties of the film. Bhushan and Koinkar [45] also conducted scratch studies in the selected particulate regions. Scratch profiles at increasing loads in the particulate region are shown in Fig. 22.26b. We note that the bump (particle) is barely scratched at 5  $\mu\text{N}$  and it can be scratched readily at higher loads. At 20  $\mu\text{N}$ , it essentially disappears.

### 22.5.3 Microscale Wear

By scanning the sample (in 2D) while scratching, wear scars are generated on the sample surface [16, 18, 28, 45–49, 53, 54, 57, 58]. The major benefit of a single cycle wear test over a scratch test is that wear data can be obtained over a large area.

#### Magnetic Head Materials

Figure 22.27 shows the wear depth as a function of load for one cycle for different slider materials. Variation in the wear depth in the wear mark is dependent upon the material. It is generally within  $\pm 5\%$ . The mean wear depth increases with the increase in normal load. The representative surface profiles showing the wear marks

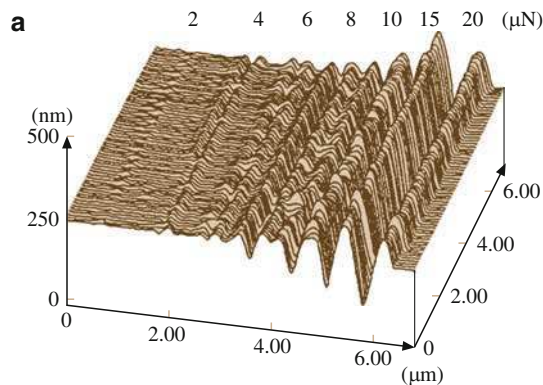
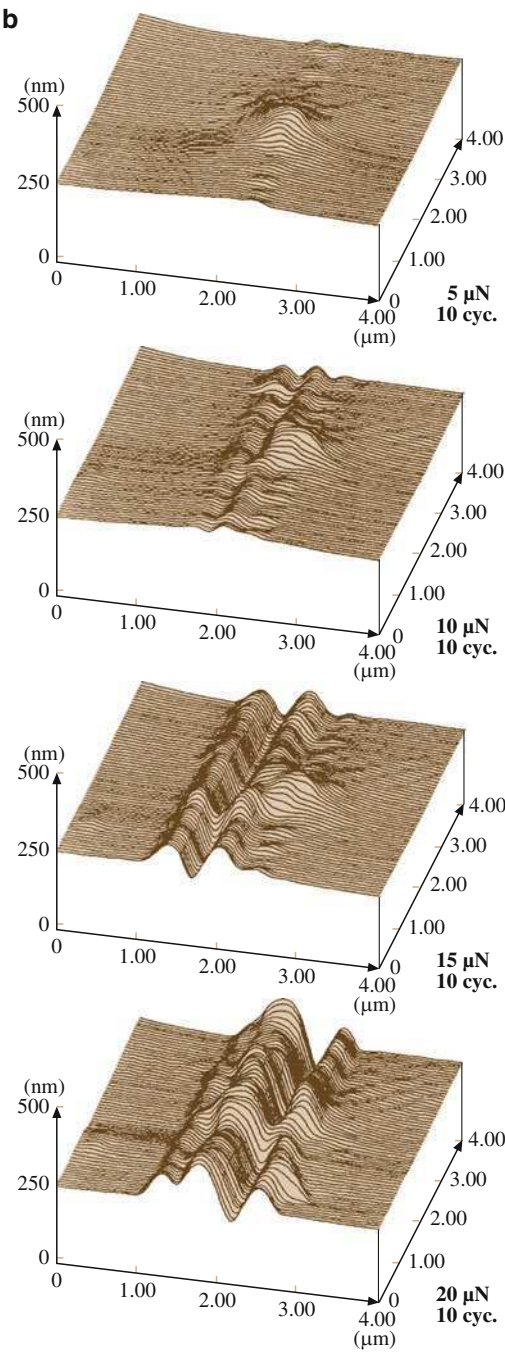


Fig. 22.26 (continued)

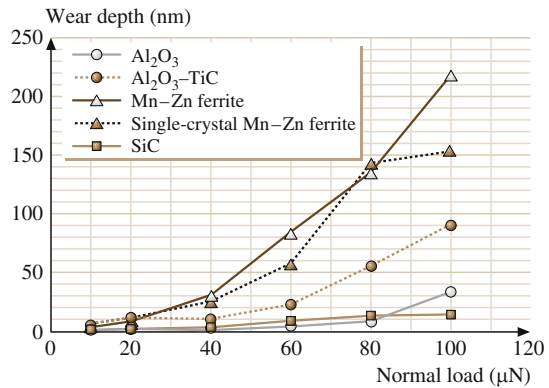


**Fig. 22.26** Surface profiles for scratched PET film (a) polymer region, (b) ceramic particulate region. The loads used for various scratches at ten cycles are indicated in the plots [45]





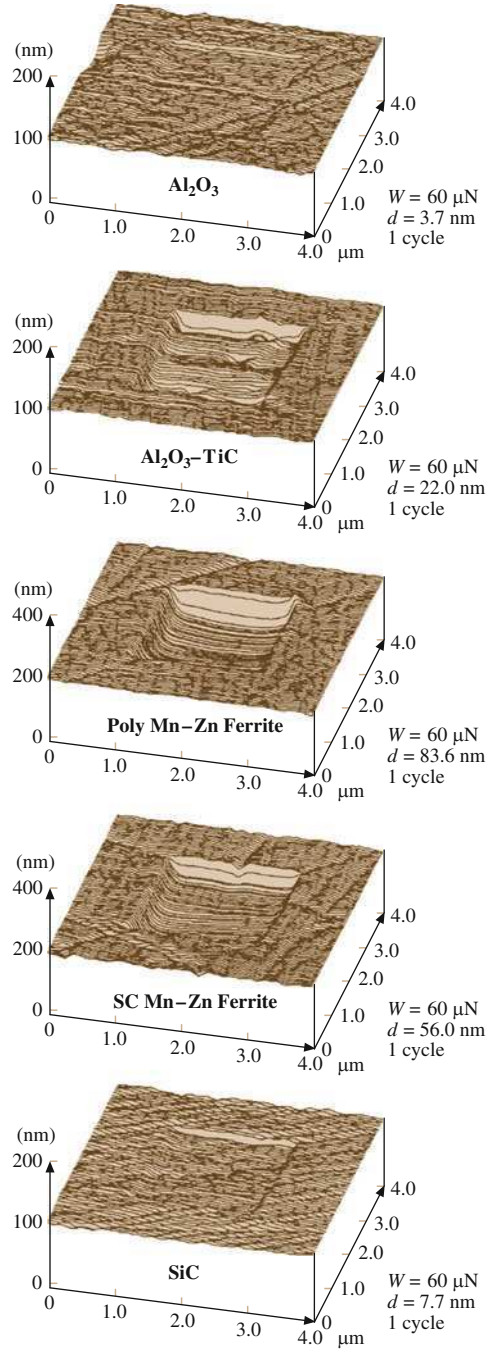
**Fig. 22.27** Wear depth as a function of normal load after one scan cycle for  $\text{Al}_2\text{O}_3$ ,  $\text{Al}_2\text{O}_3$ -TiC, polycrystalline Mn-Zn ferrite, single-crystal Mn-Zn ferrite and SiC [28]



(central  $2\ \mu\text{m} \times 2\ \mu\text{m}$  region) at a normal load of  $60\ \mu\text{N}$  for all specimens are shown in Fig. 22.28. The material is removed uniformly in the wear region for all specimens. Table 22.2 presents average wear depth at  $60\ \mu\text{N}$  normal load for all specimens. Microwear resistance of SiC and  $\text{Al}_2\text{O}_3$  is the highest followed by  $\text{Al}_2\text{O}_3$ -TiC, single-crystal and polycrystalline Mn-Zn ferrite.

Next, wear experiments were conducted for multiple cycles. Figure 22.29 shows the 2D gray scale plots and corresponding section plot (on top of each gray scale plot), taken at a location shown by an arrow for  $\text{Al}_2\text{O}_3$  (left column) and  $\text{Al}_2\text{O}_3$ -TiC (right column) specimen obtained at a normal load of  $20\ \mu\text{N}$  and at a different number of scan cycles. The central regions ( $2\ \mu\text{m} \times 2\ \mu\text{m}$ ) show the wear mark generated after a different number of cycles. Note the difference in the vertical scale of gray scale and section plots. The  $\text{Al}_2\text{O}_3$  specimen shows that wear initiates at the porous holes or defects present on the surface. Wear progresses at these locations as a function of number of cycles. In the porous hole free region, microwear resistance is higher. In the case of the  $\text{Al}_2\text{O}_3$ -TiC specimen for about five scan cycles, the microwear resistance is higher at the TiC grains and is lower at the  $\text{Al}_2\text{O}_3$  grains. The TiC grains are removed from the wear mark after five scan cycles. This indicates that microwear resistance of multi-phase materials depends upon the individual grain properties. Evolution of wear is uniform within the wear mark for ferrite specimens. Figure 22.30 shows plot of wear depth as a function of number of cycles at a normal load of  $20\ \mu\text{N}$  for all specimens. The  $\text{Al}_2\text{O}_3$  specimen reveals highest microwear resistance followed by SiC,  $\text{Al}_2\text{O}_3$ -TiC, polycrystalline and single-crystal Mn-Zn ferrite. Wear resistance of  $\text{Al}_2\text{O}_3$ -TiC is inferior to that of  $\text{Al}_2\text{O}_3$ . Chu et al. [61] studied friction and wear behavior of the single-phase and multi-phase ceramic materials and found that wear resistance of multi-phase materials was poorer than single-phase materials. Multi-phase materials have more material flaws than the single-phase material. The differences in thermal and mechanical properties between the two phases may lead to cracking during processing, machining or use.

**Fig. 22.28** Surface profiles showing the worn region (center  $2\text{ }\mu\text{m} \times 2\text{ }\mu\text{m}$ ) after one scan cycles at a normal load of  $60\text{ }\mu\text{N}$  for  $\text{Al}_2\text{O}_3$ ,  $\text{Al}_2\text{O}_3\text{--TiC}$ , polycrystalline Mn–Zn ferrite, single-crystal Mn–Zn ferrite and SiC [28]



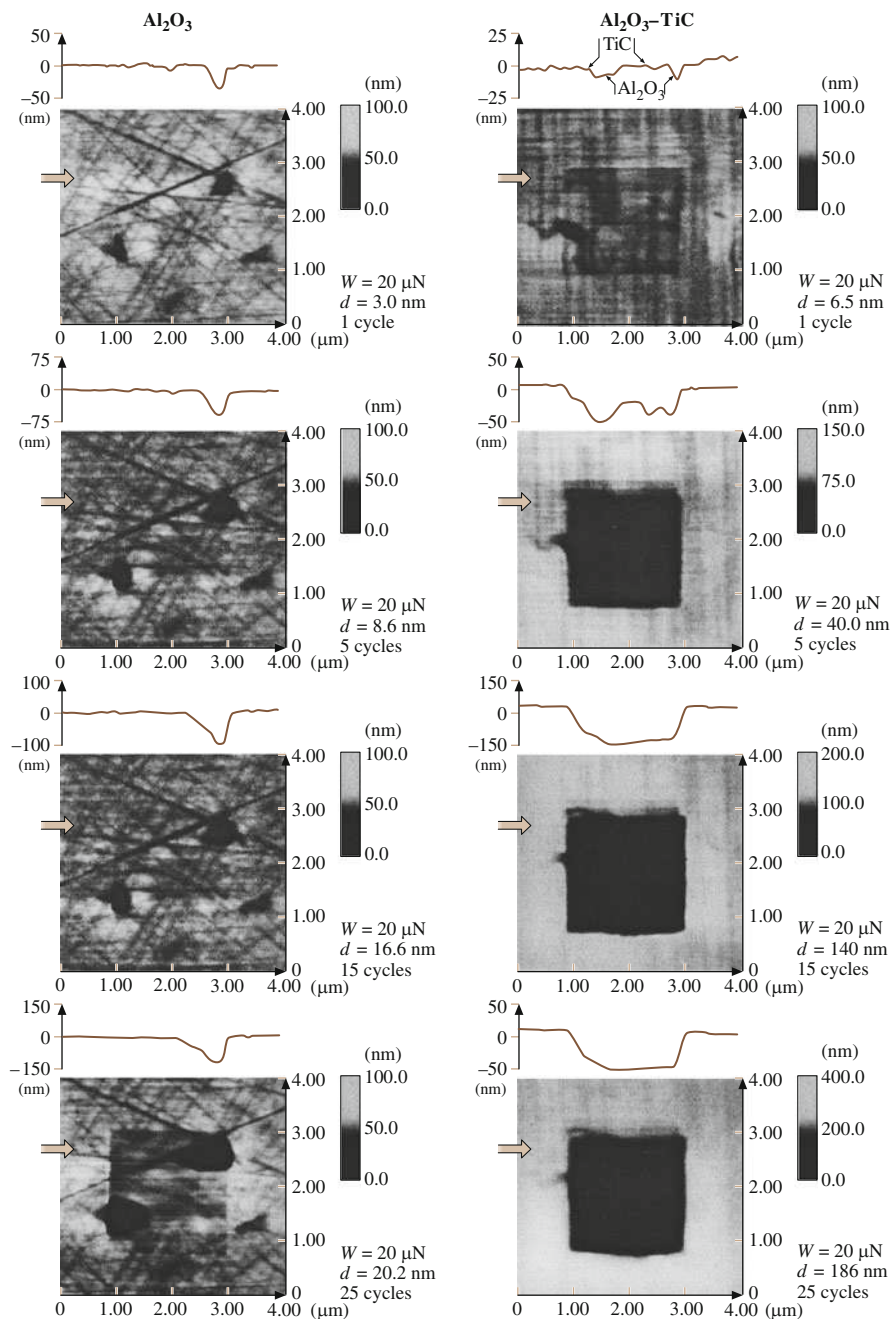


**Fig. 22.29** Gray scale 2D plots showing the worn region (center  $2\text{ }\mu\text{m} \times 2\text{ }\mu\text{m}$ ) at a normal load of  $20\text{ }\mu\text{N}$  and different number of scan cycles for  $\text{Al}_2\text{O}_3$  and  $\text{Al}_2\text{O}_3\text{-TiC}$ . The 2D section plots taken at a location shown by an arrow are shown on the top of corresponding gray scale plot. Note the change in vertical scale for gray scale and 2D section plots [28]

**Fig. 22.30** Wear depth as a function of number of cycles at a normal load of 20  $\mu\text{N}$  for  $\text{Al}_2\text{O}_3$ ,  $\text{Al}_2\text{O}_3\text{-TiC}$ , polycrystalline Mn-Zn ferrite, single-crystal (SC) Mn-Zn ferrite and SiC [28]

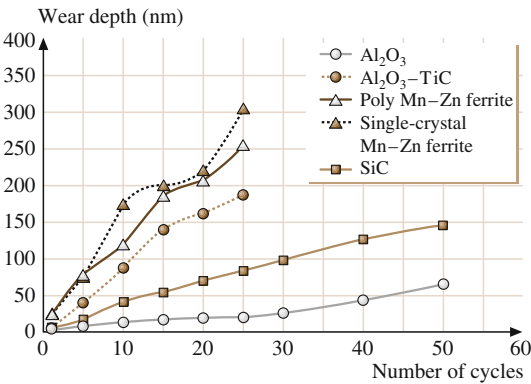
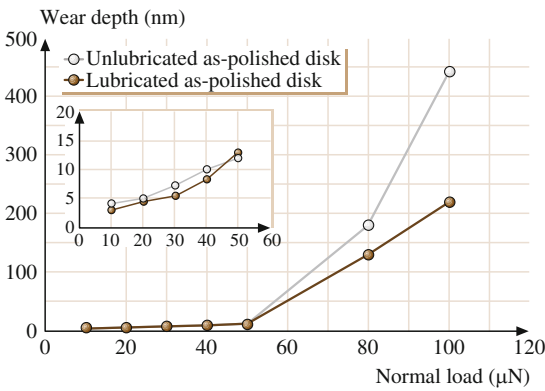


**Fig. 22.31** Wear depth as a function of normal load for polished, lubricated and unlubricated thin-film rigid disks after one cycle [18]

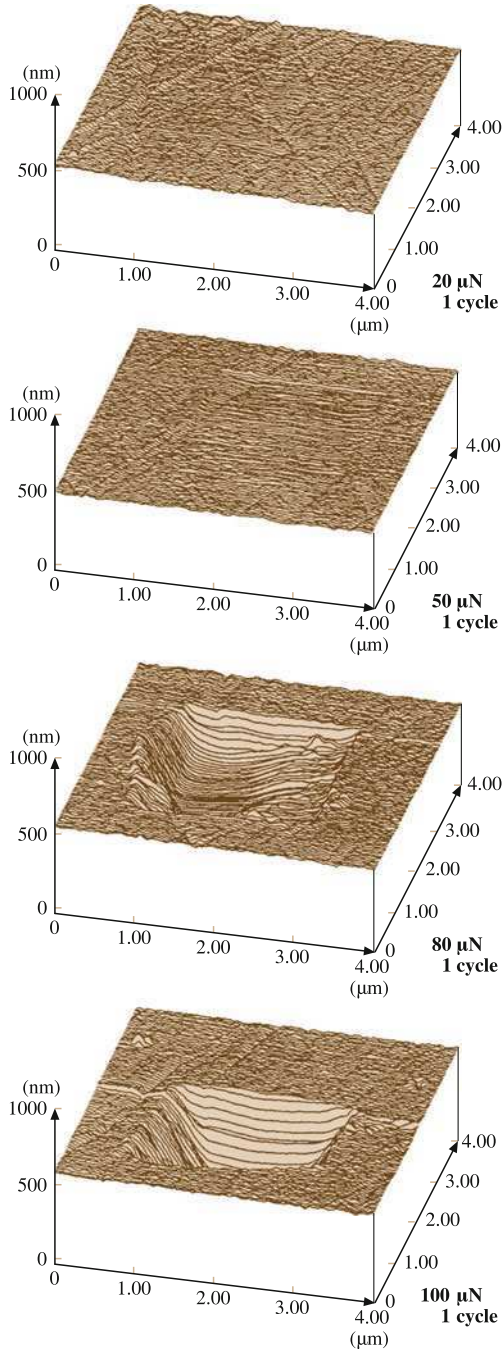


### Magnetic Media

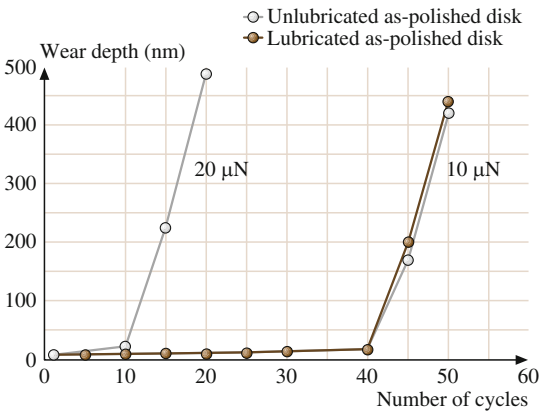
Figure 22.31 shows the wear depth as a function of load for one cycle for the polished, unlubricated and lubricated disks [18]. Figure 22.32 shows profiles of the wear scars generated on unlubricated disk. The normal force for the imaging was about 0.5  $\mu\text{N}$  and the loads used for the wear were 20, 50, 80 and 100  $\mu\text{N}$  as indicated in the figure. We note that wear takes place relatively uniformly across the disk surface and essentially independent of the lubrication for the disks studied. For both lubricated and unlubricated disks, the wear depth increases slowly with load at low loads with almost the same wear rate. As the load is increased to about 60  $\mu\text{N}$ , wear increases rapidly with load. The wear depth at 50  $\mu\text{N}$  is about 14 nm, slightly less than the thickness of the carbon film. The rapid increase of wear with load at loads larger than 60  $\mu\text{N}$  is an indication of the breakdown of the carbon coating on the disk surface.

Figure 22.33 shows the wear depth as a function of number of cycles for the polished disks (lubricated and unlubricated). Again, for both unlubricated and

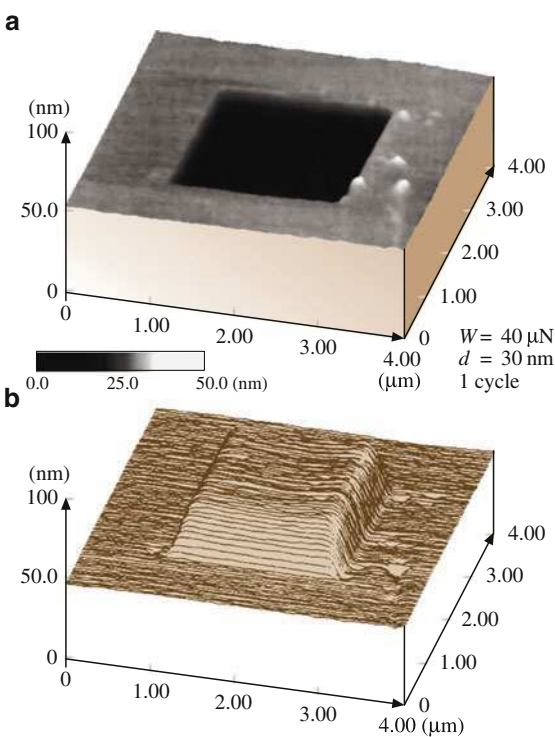
**Fig. 22.32** Surface maps of a polished, unlubricated thin-film rigid disk showing the worn region (center  $2\text{ }\mu\text{m} \times 2\text{ }\mu\text{m}$ ) after one cycle. The normal loads are indicted in the figure [18]



**Fig. 22.33** Wear depth as a function of number of cycles for polished, lubricated and unlubricated thin-film rigid disks at 10  $\mu\text{N}$  and for polished, unlubricated disk at 20  $\mu\text{N}$  [18]



**Fig. 22.34** Surface maps of a polished, unlubricated thin-film rigid disk showing the worn region (center  $2\text{ }\mu\text{m} \times 2\text{ }\mu\text{m}$ ) at 20  $\mu\text{N}$ . The number of cycles are indicated in the figure [18]



lubricated disks, wear initially takes place slowly with a sudden increase between 40 and 50 cycles at 10  $\mu\text{N}$ . The sudden increase occurred after 10 cycles at 20  $\mu\text{N}$ . This rapid increase is associated with the breakdown of the carbon coating. The wear profiles at various cycles are shown in Fig. 22.34 for a polished, unlubricated



disk at a normal load of 20  $\mu\text{N}$ . Wear is not uniform and the wear is largely initiated at the texture grooves present on the disk surface. This indicates that surface defects strongly affect the wear rate.

Hard amorphous carbon coatings are used to provide wear and corrosion resistance to magnetic disks and MR/GMR magnetic heads. A thick coating is desirable for long durability; however, to achieve ever increasing high recording densities, it is necessary to use as thin a coating as possible. Microwear data on various amorphous carbon coatings of different thicknesses have been conducted by Bhushan and Koinkar [48], Koinkar and Bhushan [49], and Sundararajan and Bhushan [53]. Figure 22.35 shows a wear mark on an uncoated Si(100) and various 10 nm thick carbon coatings. It is seen that Si(100) wears uniformly, whereas carbon coatings wear nonuniformly. Carbon coating failure is sudden and accompanied by a sudden rise in friction force. Figure 22.36 shows the wear depth of Si(100) substrate and various coatings at two different loads. FCA and ECR-CVD, 20 nm thick coatings show excellent wear resistance up to 80  $\mu\text{N}$ , the load that is required for the IB 20 nm coating to fail. In these tests, failure of a coating results when the wear depth exceeds the quoted coating thickness. The SP 20 nm coating fails at the much lower load of 35  $\mu\text{N}$ . At 60  $\mu\text{N}$ , the coating hardly provides any protection. Moving on to the 10 nm coatings, ECR-CVD coating requires about

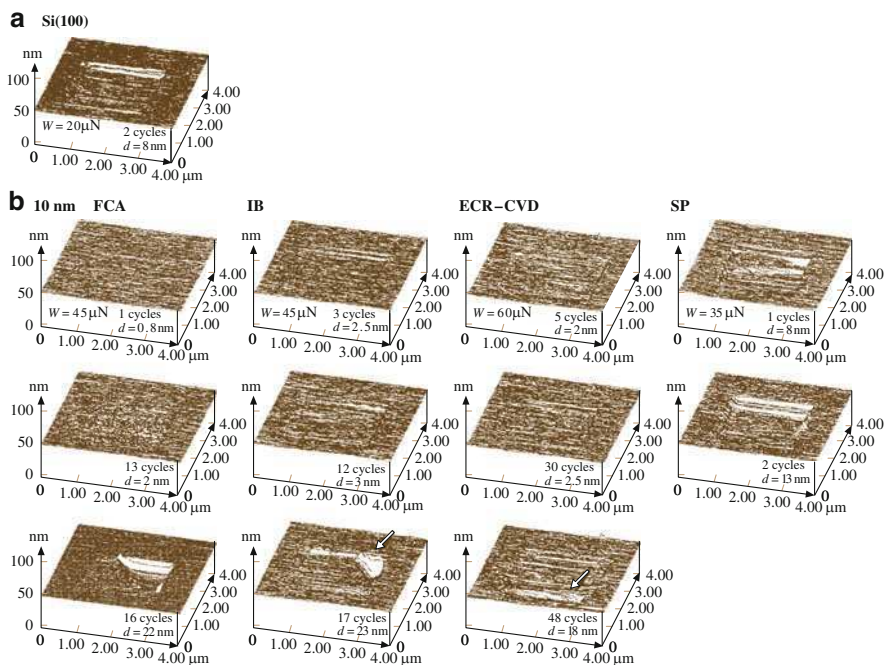


**Fig. 22.35** AFM images of wear marks on (a) bare Si(100), and (b) all 10 nm thick amorphous carbon coatings [53]

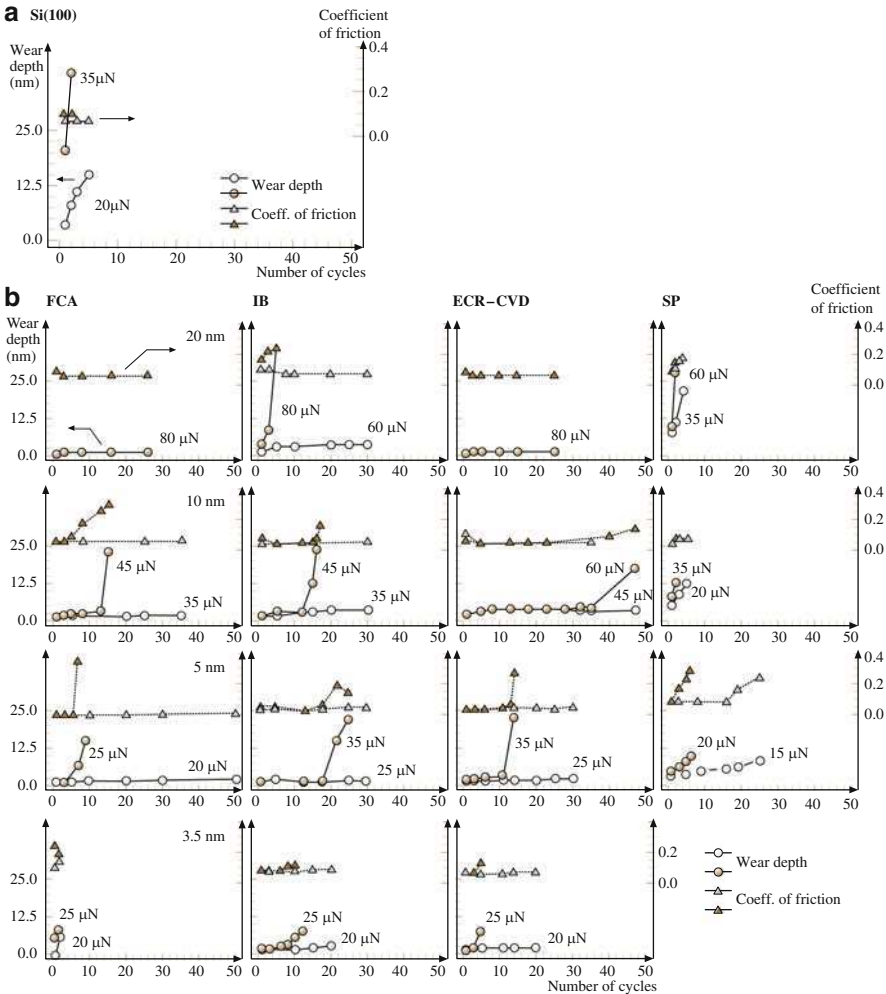


**Fig. 22.36** Wear data of (a) bare Si(100) and (b) all amorphous carbon coatings. Coating thickness is constant along each row in (b). Both wear depth and coefficient of friction during wear for a given cycle are plotted [53]

40 cycles at 60 μN to fail as compared to IB and FCA, which fail at 45 μN. the FCA coating exhibits slight roughening in the wear track after the first few cycles, which leads to an increase in the friction force. The SP coating continues to exhibit poor resistance, failing at 20 μN. For the 5 nm coatings, the load required to fail the coatings continues to decrease. But IB and ECR-CVD still provide adequate protection as compared to bare Si(100) in that order, failing at 35 μN compared to FCA at 25 μN and SP at 20 μN. Almost all the 20, 10, and 5 nm coatings provide better wear resistance than bare silicon. At 3.5 nm, FCA coating provides no wear



resistance, failing almost instantly at 20  $\mu\text{N}$ . The IB and ECR-CVD coating show good wear resistance at 20  $\mu\text{N}$  compared to bare Si(100). But IB lasts only about 10 cycles and ECR-CVD about 3 cycles at 25  $\mu\text{N}$ .

The wear tests highlight the differences in the coatings more vividly than the scratch tests data presented earlier. At higher thicknesses (10 and 20 nm), the ECR-CVD and FCA coatings appear to show the best wear resistance. This is probably due to higher hardness of the coatings (see data presented later). At 5 nm, IB coating appears to be the best. FCA coatings show poorer wear resisting with decreasing coating thickness. SP coatings showed consistently poor wear resistance at all thicknesses. The IB 2.5 nm coating does provide reasonable wear protection at low loads.

Wear depths as a function of normal load for MP, BaFe and ME tapes along the parallel direction are plotted in Fig. 22.37 [47]. For the ME tape, there is negligible wear until the normal load of about 50  $\mu\text{N}$ , above this load the magnetic coating fails rapidly. This observation is consistent with the scratch data. Wear depths as a function of number of cycles for MP, BaFe, and ME tapes are shown in Fig. 22.38. For the MP and BaFe particulate tapes, wear rates appear to be independent of the particulate density. Again as observed in the scratch testing, wear rate of BaFe tapes is higher than that for MP tapes. ME tapes are much more wear resistant than the particulate tapes. However, the failure of ME tapes are catastrophic as observed in scratch testing. Wear studies were performed along and across the longitudinal tape direction in high and low hardness regions. At the high hardness regions of the ME tapes, failure occurs at lower loads. Directionality effect again may arise from the columnar structure of the ME films [3, 60]. Wear profiles at various cycles at a normal load of 2  $\mu\text{N}$  for MP and at 20  $\mu\text{N}$  for ME tapes are shown in Fig. 22.39. For the particulate tapes, we note that polymer gets removed before the particulates do (Fig. 22.39a). Based on the wear profiles of the ME tape shown in Fig. 22.39a, we note that most wear occurs between 50 and 60 cycles which shows the catastrophic removal of the coating. It was also observed that wear debris generated during wear

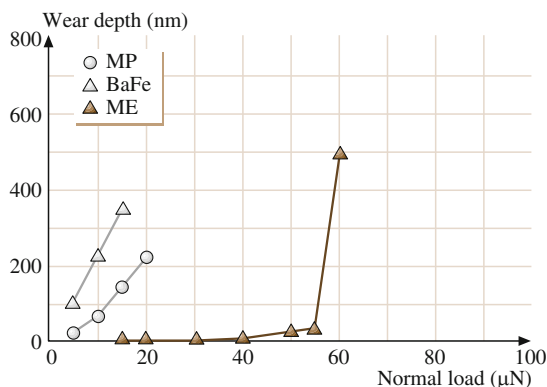
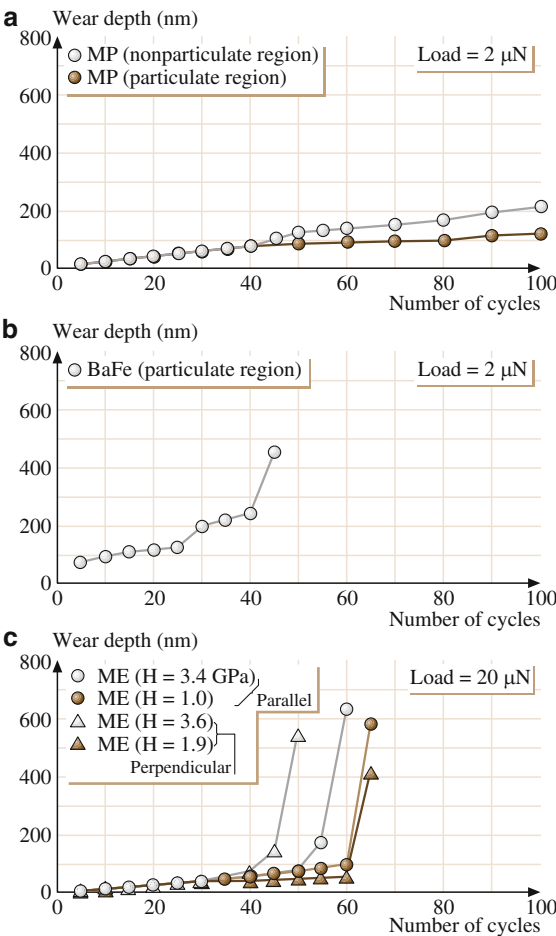


**Fig. 22.37** Wear depth as a function of normal load for three tapes in the parallel direction after one cycle [47]

**Fig. 22.38** Wear depth as a function of number of cycles for (a) MP, (b) BaFe, and (c) ME tapes in different regions at normal loads indicated in the figure. Note a higher load used for the ME tape in (c) [47]



test in all cases is loose and can easily be removed away from the scan area at light loads ( $\approx 0.3 \mu\text{N}$ ).

The average wear depth as a function of load for a PET film is shown in Fig. 22.40. Again, the wear depth increases linearly with load. Figure 22.41 shows the average wear depth as a function of number of cycles. The observed wear rate is approximately constant. PET tape substrate consists of particles sticking out on its surface to facilitate winding. Figure 22.42 shows the wear profiles as a function of number of cycles at 1  $\mu\text{N}$  load on the PET film in the nonparticulate and particulate regions [45]. We note that polymeric materials tear in microwear tests. The particles do not wear readily at 1  $\mu\text{N}$ . Polymer around the particles is removed but the particles remain intact. Wear in the particulate region is much smaller than that in the polymer region. We will see later that nanohardness of the particulate region is about 1.4 GPa compared to 0.3 GPa in the nonparticulate region (Table 22.3).

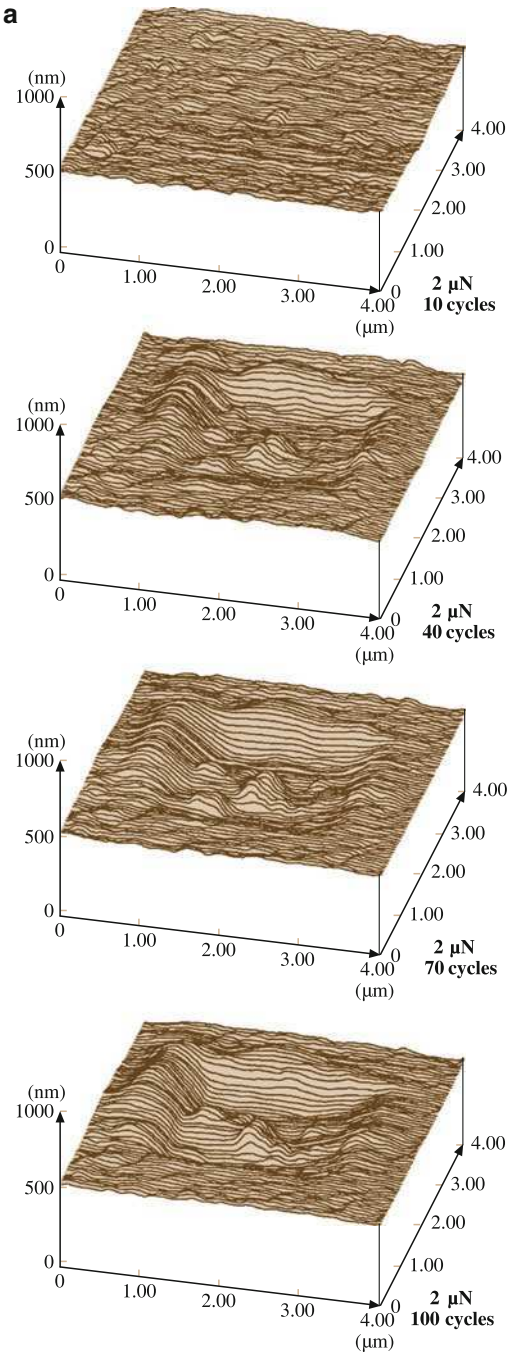
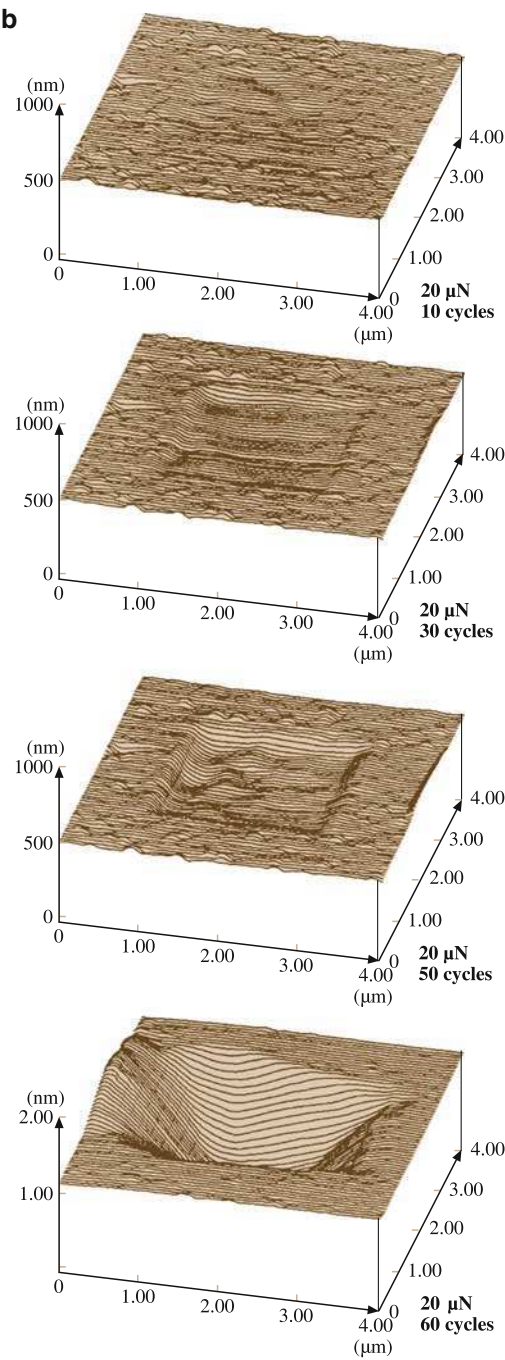
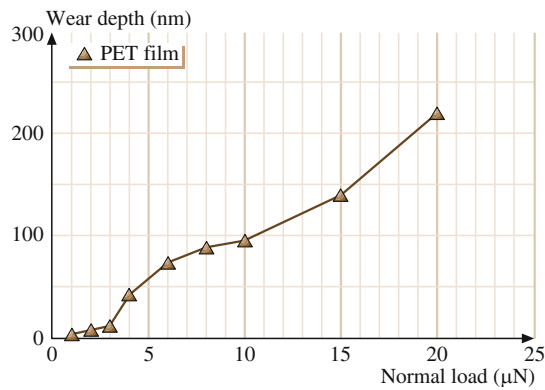


Fig. 22.39 (continued)

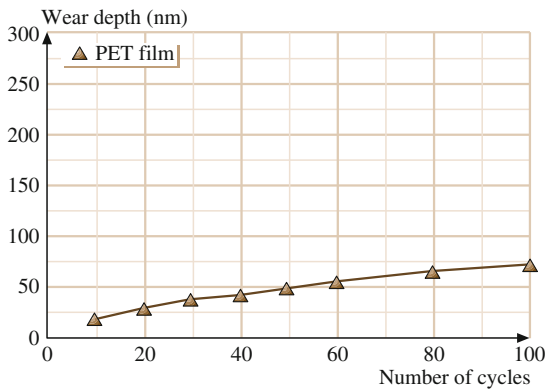
**Fig. 22.39** Surface maps showing the worn region (center  $2\text{ }\mu\text{m} \times 2\text{ }\mu\text{m}$ ) after various cycles of wear at (a)  $2\text{ }\mu\text{N}$  for MP (particulate region) and at (b)  $20\text{ }\mu\text{N}$  for ME ( $H = 3.4\text{ GPa}$ , parallel direction) tapes. Note a different vertical scale for the bottom profile of (b) [47]



**Fig. 22.40** Wear depth as a function of normal load (after one cycle) for a PET film [45]



**Fig. 22.41** Wear depth as a function of number of cycles at 1 μN for a PET film [45]



22.6 Indentation

22.6.1 Picoscale Indentation

Bhushan and Ruan [15] measured indentability of magnetic tapes at increasing loads on a picoscale, Fig. 22.43. In this figure, the vertical axis represents the cantilever tip deflection and the horizontal axis represents the vertical position ( $Z$ ) of the sample. The “extending” and “retracting” curves correspond to the sample being moved toward or away from the cantilever tip, respectively. In this experiment, as the sample surface approaches the AFM tip fraction of a nm away from the sample (point A), the cantilever bends toward the sample (part B) because of attractive forces between the tip and sample. As we continue the forward position of the sample, it pushes the cantilever back through its original rest position (point of zero applied load) entering the repulsive region (or loading portion) of the force curve. As the sample is retracted, the cantilever deflection decreases. At point D in

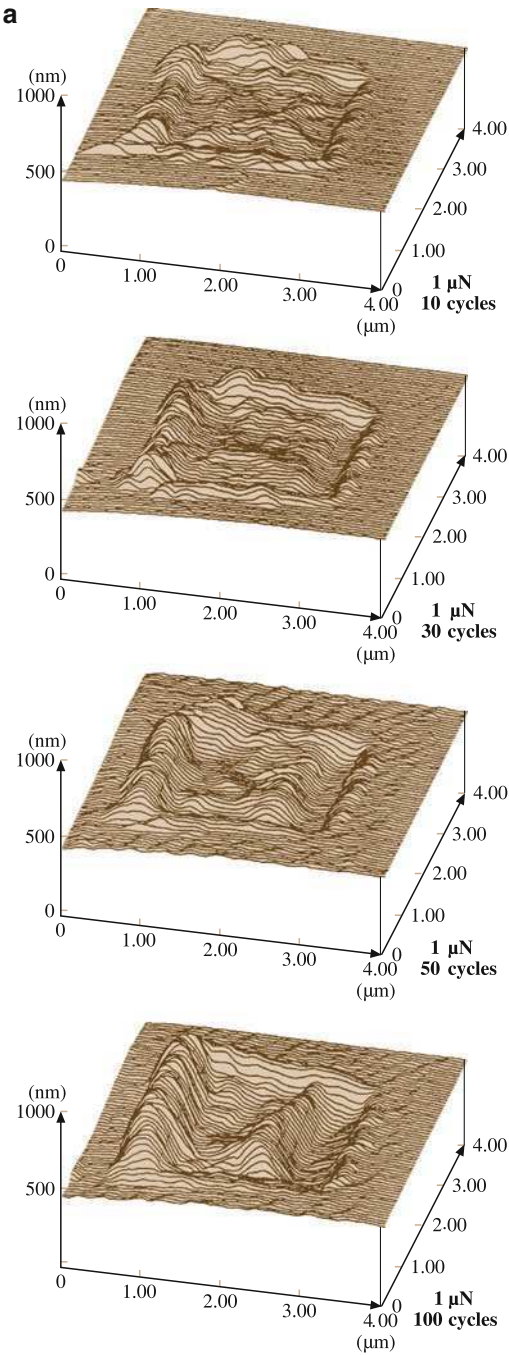
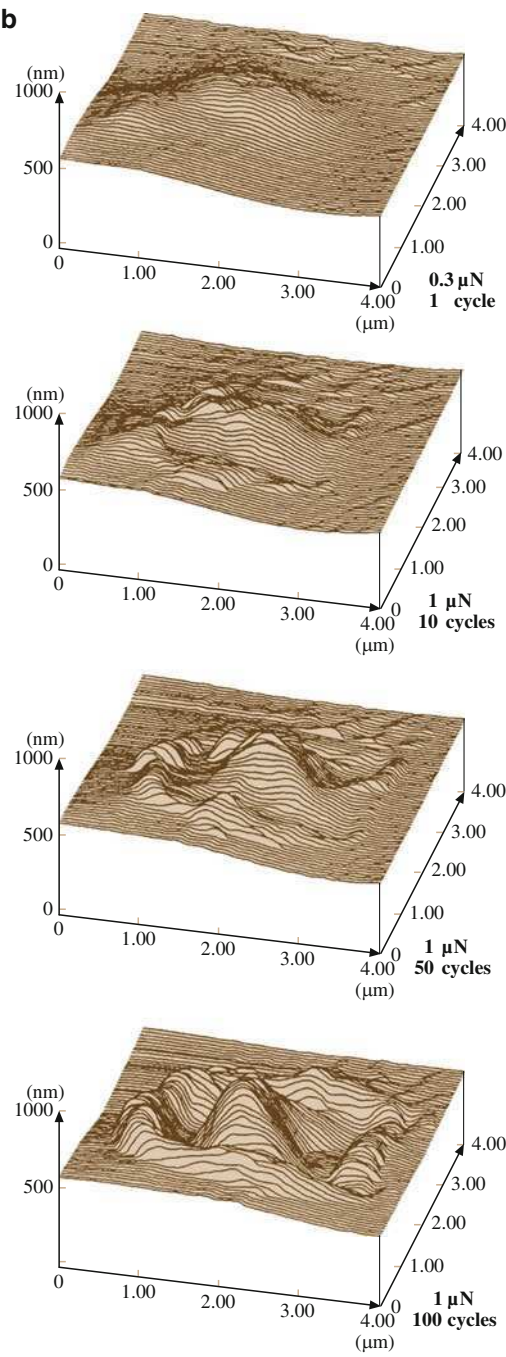
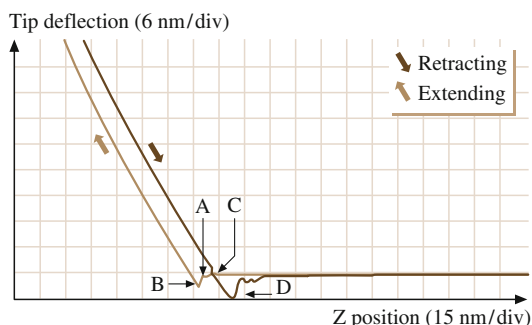


Fig. 22.42 (continued)

**Fig. 22.42** Surface maps showing the worn region (center  $2\text{ }\mu\text{m} \times 2\text{ }\mu\text{m}$ ) at  $1\text{ }\mu\text{N}$  for a PET film (a) in the polymer region, (b) in the particulate region. The number of cycles are indicated in the figure [45]



**Fig. 22.43** Tip deflection (normal force) as a function of  $Z$  (separation distance) curve for a metal-particle (MP) tape. The spring constant of the cantilever used was 0.4 N/m [15]



the retracting curve, the sample is disengaged from the tip. Before the disengagement, the tip is pulled toward the sample after the zero deflection point of the force curve (point C) because of attractive forces (van der Waals forces and longer range meniscus forces). A thin layer of liquid, such as liquid lubricant and condensations of water vapor from ambient, will give rise to capillary forces that act to draw the tip towards sample at small separations. The horizontal shift between the loading and unloading curves results from the hysteresis in the PZT tube.

The left portion of the curve shows the tip deflection as a function of the sample traveling distance during sample–tip contact, which would be equal to each other for a rigid sample. However, if the tip indents into the sample, the tip deflection would be less than the sample traveling distance, or in other words, the slope of the line would be less than 1. In Fig. 22.43, we note that line in the left portion of the figure is curved with a slope of less than 1 shortly after the sample touches the tip, which suggests that the tip has indented the sample. Later, the slope is equal to 1 suggesting that the tip no longer indents the sample. This observation indicates that the tape surface is soft locally (polymer rich) but it is hard (as a result of magnetic particles) underneath. Since the curves in extending and retracting modes are identical, the indentation is elastic up to at a maximum load of about 22 nN used in the measurements.

According to Bhushan and Ruan [15], during indentation of rigid disks, the slope of the deflection curves remained constant as the disks touch and continue to push the AFM tip. The disks were not indented.

## 22.6.2 Nanoscale Indentation

Indentation hardness with a penetration depth as low as 5 nm can be measured using AFM. Bhushan and Koinkar [17] measured hardness of thin-film disks at load of 80, 100, and 140  $\mu\text{N}$ . Hardness values were 20 GPa (10 nm), 21 GPa (15 nm) and 9 GPa (40 nm); the depths of indentation are shown in the parenthesis. The hardness value at 100  $\mu\text{N}$  is much higher than at 140  $\mu\text{N}$ . This is expected since the indentation depth is only about 15 nm at 100  $\mu\text{N}$  which is smaller than the thickness



of carbon coating ( $\approx 30$  nm). The hardness value at lower loads is primarily the value of the carbon coating. The hardness value at higher loads is primarily the value of the magnetic film, which is softer than the carbon coating [2]. This result is consistent with the scratch and wear data discussed previously.

For the case of hardness measurements made on magnetic thin film rigid disk at low loads, the indentation depth is on the same order at the variation in the surface roughness. For accurate measurements of indentation size and depth, it is desirable to subtract the original (unindented) profile from the indented profile. Bhushan et al. [18] developed an algorithm for this purpose. Because of hysteresis, a translational shift in the sample plane occurs during the scanning period, resulting in a shift between images captured before and after indentation. Therefore, the image for perfect overlap needs to be shifted before subtraction can be performed. To accomplish this objective, a small region on the original image was selected and the corresponding region on the indented image was found by maximizing the correlation between the two regions. (Profiles were plane-fitted before subtraction.) Once two regions were identified, overlapped areas between the two images were determined and the original image was shifted with the required translational shift and this subtracted from the indented image. An example of profiles before and after subtraction is shown in Fig. 22.44. It is easier to measure the indent on the subtracted image. At a normal load of 140 mN the hardness value of an unlubricated, as-polish

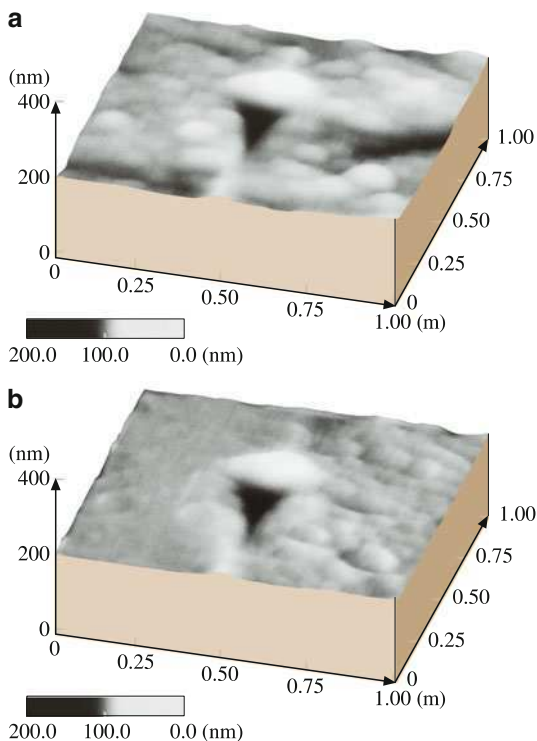


**Fig. 22.44** Images with nanoindentation marks generated on a polished, unlubricated thin-film rigid disk at 140  $\mu$ N (a) before subtraction, and (b) after subtraction [18]

magnetic thin film rigid disk (rms roughness = 3.3 nm) is 9.0 GPa and indentation depth is 40 nm.

For accurate measurement of nanohardness at very shallow indentation depths, depth-sensing capacitance transducer system in an AFM is used [19]. Figure 22.45a shows the hardness as a function of residual depth for three types of 100 nm thick amorphous carbon coatings deposited on silicon by sputtering, ion beam and cathodic arc processes [50]. Data on uncoated silicon are also included for comparisons. The cathodic arc carbon coating exhibits highest hardness of about 24.9 GPa, whereas the sputtered and ion beam carbon coatings exhibit hardness values of 17.2 and 15.2 GPa respectively. The hardness of Si(100) is 13.2 GPa. High hardness of cathodic arc carbon coating explains its high wear resistance, reported earlier. Figure 22.45b shows the elastic modulus as a function of residual depth for various samples. The cathodic arc coating exhibits the highest elastic modulus. Its elastic modulus decreases with an increasing residual depth, while the elastic moduli for the other carbon coatings remain almost constant. In general, hardness and elastic modulus of coatings are strongly influenced by their crystalline structure, stoichiometry and growth characteristics which depend on the deposition parameters. Mechanical properties of carbon coatings have been known to change over a wide range with  $sp^3$ – $sp^2$  bonding ratio and amount of hydrogen. Hydrogen is believed to play an important role in the bonding

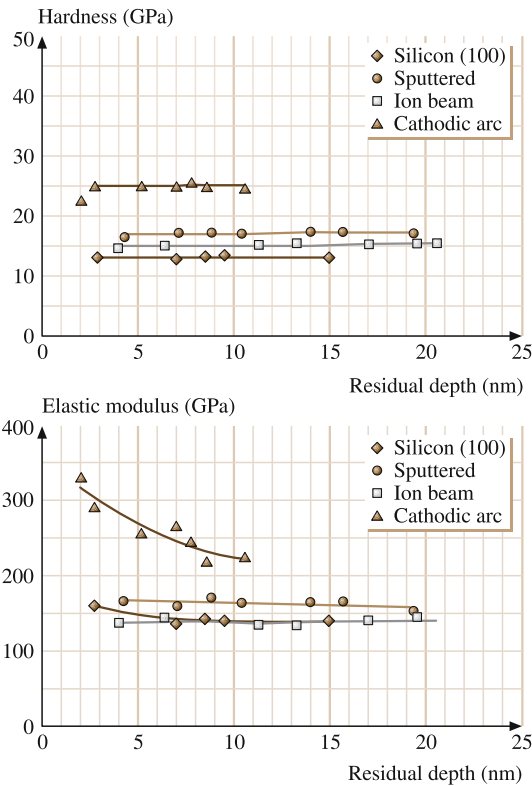


**Fig. 22.45** Nanohardness and elastic modulus as a function of residual indentation depth for Si(100) and 100 nm thick coatings deposited by sputtering, ion beam and cathodic arc processes [50]

configuration of carbon atoms by helping to stabilize tetrahedral coordination of carbon atoms. Detailed mechanical characterization of amorphous carbon coatings is presented by Li and Bhushan [51, 52] and Bhushan [59].

### 22.6.3 Localized Surface Elasticity

By using an AFM in a so-called force modulation mode, it is possible to quantitatively measure the elasticity of soft and compliant materials with penetration depths of less than 100 nm [21, 22]. This technique has been successfully used to get localized elasticity maps of particulate magnetic tapes. Elasticity map of a tape can be used to identify relative distribution of hard magnetic/nonmagnetic ceramic particles and the polymeric binder on the tape surface which has an effect on friction and stiction at the head–tape interface. Figure 22.46 shows surface height and elasticity maps on an MP tape. The elasticity image reveals sharp variations in surface elasticity due to the composite nature of the film. As can be clearly seen, regions of high elasticity do not always correspond to high or low topography. Based on a Hertzian elastic-contact analysis, the static indentation depth of these sample during the force modulation scan is estimated to be about 1 nm. The contrast seen is influenced most strongly by material properties in the top few nanometers, independent of the composite structure beneath the surface layer. The trend in number of stiff regions has been correlated to reduced stiction problems in tapes [62].

Figure 22.47 shows the surface topography and phase image of an alumina particle embedded in the MP tape using a so-called TR mode [25, 26]. The cross-section view of the particle obtained from the topographic image is shown at the bottom as a visual aid. The edges of the particle show up darker in the TR phase angle image, which suggests that it is less viscoelastic compared to the background. The magnetic particles on top of the alumina particle are clearly visible in the TR phase image. These have

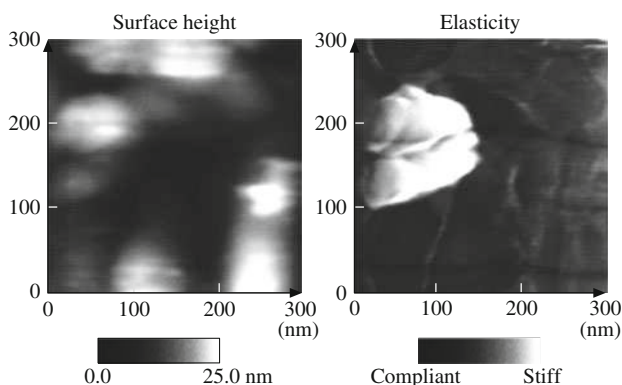


**Fig. 22.46** Surface height and elasticity maps for a metal-particle tape A ( $\sigma = 6.72$  nm and  $P-V = 31.7$  nm).  $\sigma$  and  $P-V$  refer to standard deviation of surface heights and peak-to-valley distance, respectively. The grayscale on the elasticity map is arbitrary [21]

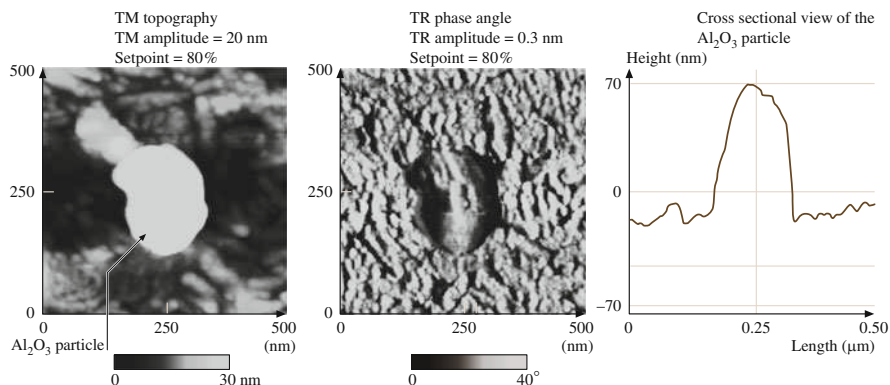


**Fig. 22.47** Tapping mode (TM) topography and TR phase angle image of an alumina particle that is used as a head cleaning agent for MP tape. A cross-sectional view of the particle is also shown [25]

a brighter contrast, which is the same as that of the background. Phase contrast mapping appears to provide better resolution than stiffness mapping for magnetic tapes.

## 22.7 Lubrication

The boundary films are formed by physical adsorption, chemical adsorption, and chemical reaction. The physisorbed film can be either monomolecular or polymolecular thick. The chemisorbed films are monomolecular, but stoichiometric films formed by chemical reaction can have a large film thickness. In general, the stability and durability of surface films decrease in the following order: chemical reaction films, chemisorbed films and physisorbed films. A good boundary lubricant should have a high degree of interaction between its molecules and the sliding surface. As a general rule, liquids are good lubricants when they are polar and thus able to grip solid surfaces (or be adsorbed). Polar lubricants contain reactive functional groups with low ionization potential or groups having high polarizability [5]. Boundary lubrication properties of lubricants are also dependent upon the molecular conformation and lubricant spreading [63–66].

Mechanical interactions between the magnetic head and the medium in magnetic storage devices are minimized by the lubrication of the magnetic medium [2, 3]. The primary function of the lubricant is to reduce the wear of the medium and to ensure that friction remains low throughout the operation of the drive. The main challenge, though, in selecting the best candidate for a specific surface is to find a material that provides an acceptable wear protection for the entire life of the product, which can be several years in duration. There are many requirements that a lubricant must satisfy in order to guarantee an acceptable life performance. An optimum lubricant thickness is one of these requirements. If the lubricant film is too thick, excessive stiction and mechanical failure of the head-disk is observed. On the other hand, if the film is too thin, protection of the interface is compromised, and

high friction and excessive wear will result in catastrophic failure. An acceptable lubricant must exhibit properties such as chemical inertness, low volatility, high thermal, oxidative and hydrolytic stability, shear stability, and good affinity to the magnetic medium surface.

Fatty acid esters are excellent boundary lubricants, and esters such as tridecyl stearate, butyl stearate, butyl palmitate, butyl myristate, stearic acid, and myristic acid are commonly used as internal lubricants, roughly 1–7% by weight of the magnetic coating in particulate flexible media (tapes and particulate flexible disks) [2, 3]. The fatty acids involved include those with acid groups with an even number of carbon atoms between  $C_{12}$  and  $C_{22}$ , with alcohols ranging from  $C_3$  to  $C_{13}$ . These acids are all solids with melting points above the normal surface operating temperature of the magnetic media. This suggests that the decomposition products of the ester via lubrication chemistry during a head-flexible medium contact may be the key to lubrication.

Topical lubrication is used to reduce the wear of rigid disks and thin-film tapes [67]. Perfluoropolyethers (PFPEs) are chemically the most stable lubricants with some boundary lubrication capability, and are most commonly used for topical lubrication of rigid disks. PFPEs commonly used include Fomblin Z lubricants, made by Solvay Solexis, Inc., Milan, Italy; and Demnum S, made by Diakin, Japan; and their difunctional derivatives containing various reactive end groups, e.g., hydroxyl or alcohol (Fomblin Z-DOL and Z-TETROL), piperonyl (Fomblin AM 2001), isocyanate (Fomblin Z-DISOC), and ester (Demnum SP). Fomblin Y and Krytox 143 AD (made by Dupont USA) have been used in the past for particulate rigid disks. The difunctional derivatives are referred to as reactive (polar) PFPE lubricants. The chemical structures, molecular weights, and viscosities of various types of PFPE lubricants are given in Table 22.4. We note that rheological properties of thin-films of lubricants are expected to be different from their bulk properties. Fomblin Z and Demnum S are linear PFPE, and Fomblin Y and Krytox 143AD are branched PFPE, where the regularity of the chain is perturbed by  $-CF_3$  side groups. The bulk viscosity of Fomblin Y and Krytox 143 AD is almost an order of magnitude higher than the Z type. Fomblin Z is thermally decomposed more rapidly than Y [5]. The molecular diameter is about 0.8 nm for these lubricant molecules. The monolayer thickness of these molecules depends on the molecular conformations of the polymer chain on the surface [64, 65].

The adsorption of the lubricant molecules on a magnetic disk surface is due to van der Waals forces, which are too weak to offset the spin-off losses, or to arrest displacement of the lubricant by water or other ambient contaminants. Considering that these lubricating films are on the order of a monolayer thick and are required to function satisfactorily for the duration of several years, the task of developing a workable interface is quite formidable. An approach aiming at alleviating these shortcomings is to enhance the attachment of the molecules to the overcoat, which, for most cases, is sputtered carbon. There are basically two approaches which have been shown to be successful in bonding the monolayer to the carbon. The first relies on exposure of the disk lubricated with neutral PFPE to various forms of radiation, such as low-energy X-ray [68], nitrogen plasma [69], or far ultraviolet

**Table 22.4** Chemical structure, molecular weight, and viscosity of perfluoropolyether lubricants

Lubricant	Formula	Molecular weight (Dalton)	Kinematic viscosity cSt(mm <sup>2</sup> /s)
Fomblin Z-25	$\text{CF}_3\text{--O--}(\text{CF}_2\text{--CF}_2\text{--O})_m\text{--}(\text{CF}_2\text{--O})_n\text{--CF}_3$	12,800	250
Fomblin Z-15	$\text{CF}_3\text{--O--}(\text{CF}_2\text{--CF}_2\text{--O})_m\text{--}(\text{CF}_2\text{--O})_n\text{--CF}_3$ ( $m/n \approx 2/3$ )	9,100	150
Fomblin Z-03	$\text{CF}_3\text{--O--}(\text{CF}_2\text{--CF}_2\text{--O})_m\text{--}(\text{CF}_2\text{--O})_n\text{--CF}_3$	3,600	30
Fomblin Z-DOL	$\text{HO--CH}_2\text{--CF}_2\text{--O--}(\text{CF}_2\text{--CF}_2\text{--O})_m\text{--}(\text{CF}_2\text{--O})_n\text{--CF}_2\text{--CH}_2\text{--OH}$	2,000	80
Fomblin AM2001	Piperonyl-O-CH <sub>2</sub> -CF <sub>2</sub> -O-(CF <sub>2</sub> -CF <sub>2</sub> -O) <sub>m</sub> -(CF <sub>2</sub> -O) <sub>n</sub> -CF <sub>2</sub> -O-piperonyl <sup>a</sup>	2,300	80
Fomblin Z-DISOC	O-CN-C <sub>6</sub> H <sub>3</sub> -(CH <sub>3</sub> )-NH-CO-CF <sub>2</sub> -O-(CF <sub>2</sub> -CF <sub>2</sub> -O) <sub>n</sub> -(CF <sub>2</sub> -O) <sub>m</sub> -CF <sub>2</sub> -CO-NH-C <sub>6</sub> H <sub>3</sub> -(CH <sub>3</sub> )-N-CO	1,500	160
Fomblin YR	$\text{CF}_3$   $\text{CF}_3\text{--O--}(\text{C--CF}_2\text{--O})_m(\text{CF}_2\text{--O})_n\text{--CF}_3$   F ( $m/n \approx 40/1$ )	6,800	1,600
Demnum S-100	$\text{CF}_3\text{--CF}_2\text{--CF}_2\text{--O--}(\text{CF}_2\text{--CF}_2\text{--CF}_2\text{--O})_m\text{--CF}_2\text{--CF}_3$	5,600	250
Krytox 143 AD	$\text{CF}_3$   $\text{CF}_3\text{--CF}_2\text{--CF}_2\text{--O--}(\text{C--CF}_2\text{--O})_m\text{--CF}_2\text{--CF}_3$   F	2,600	—

<sup>a</sup>3,4-methylenedioxybenzyl

(e.g., 185 nm) [70]. Another approach is to use chemically active PFPE molecules, where the various functional (reactive) end groups offer the opportunity of strong attachments to specific interface. These functional groups can react with surfaces and bond the lubricant to the disk surface, which reduces its loss due to spin off and evaporation. Bonding of lubricant to the disk surface depends upon the surface cleanliness. After lubrication, the disk is generally heated at 150°C for 30 min to 1 h to improve the bonding. If only a bonded lubrication is desired, the unbonded fraction can be removed by washing it off for 60 s with a non-Freon solvent (FC-72). Their main advantage is their ability to enhance durability without the problem of stiction usually associated with weakly bonded lubricants [2].

### Boundary Lubrication Studies

Koinkar and Bhushan [29] and Liu and Bhushan [30] studied friction, adhesion, and durability of Z-15 and Z-DOL (bonded and washed, BW) lubricants on Si(100) surface. To investigate the friction properties of Si(100), Z-15, and Z-DOL(BW),

the friction force versus normal load curves were obtained by making friction measurements at increasing normal loads, Fig. 22.48. An approximately linear response of all three samples is observed in the load range of 5–130 nN. From the horizontal intercept at zero value of friction force, adhesive force can be obtained. The adhesive forces for three samples were also measured using the force calibration plot technique. The adhesive force data obtained by the two techniques are summarized in Fig. 22.49, and the trends in the data obtained by two techniques are similar. The friction force and adhesive force of solid-like Z-DOL(BW) are consistently smaller than that for Si(100), but these values of liquid-like Z-15 lubricant is higher than that of Si(100). The presence of mobile Z-15 lubricant film increases adhesive force as compared to that of the Si(100) by meniscus formation. Whereas, the presence of Z-DOL(BW) film reduces the adhesive force because of absence of mobile liquid. See schematics at the bottom of Fig. 22.49. It is well known that in computer rigid disk drives, the stiction force increases rapidly with an increase in rest time between head and the disk [2]. The effect of rest time of 180 s on the friction force, adhesive force, and coefficient of friction for three samples are summarized in Fig. 22.50. It is seen that time effect is present in Si(100) and Z-15 with mobile liquid present. Whereas, time effect is not present for Z-DOL (BW) because of the absence of mobile liquid.

To study lubricant depletion during microscale measurements, nanowear studies were conducted using  $\text{Si}_3\text{N}_4$  tips. Measured friction as a function of number of cycles for Si(100) and silicon surface lubricated with Z-15 and Z-DOL (BW) lubricants are presented in Fig. 22.51. An area of  $2\text{ }\mu\text{m} \times 2\text{ }\mu\text{m}$  was scanned at a normal force of 70 nN. As observed before, friction force and coefficient of friction of Z-15 is higher than that of Si(100) with the lowest values for Z-DOL(BW). During cycling, friction force and coefficient of friction of Si(100) show a slight decrease during initial few cycles, then remain constant. This is related to the

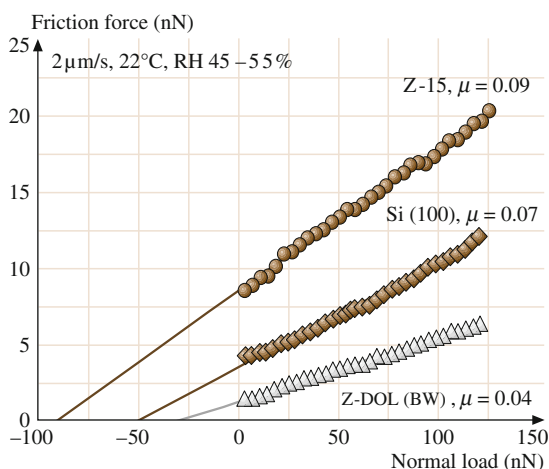


**Fig. 22.48** Friction force versus normal load curves for Si(100), 2.8 nm thick Z-15 film, and 2.3 nm thick Z-DOL (BW) film at  $2\text{ }\mu\text{m/s}$ , and in ambient air sliding against a  $\text{Si}_3\text{N}_4$  tip. Based on these curves, coefficient of friction ( $\mu$ ) and adhesive force can be calculated [30]

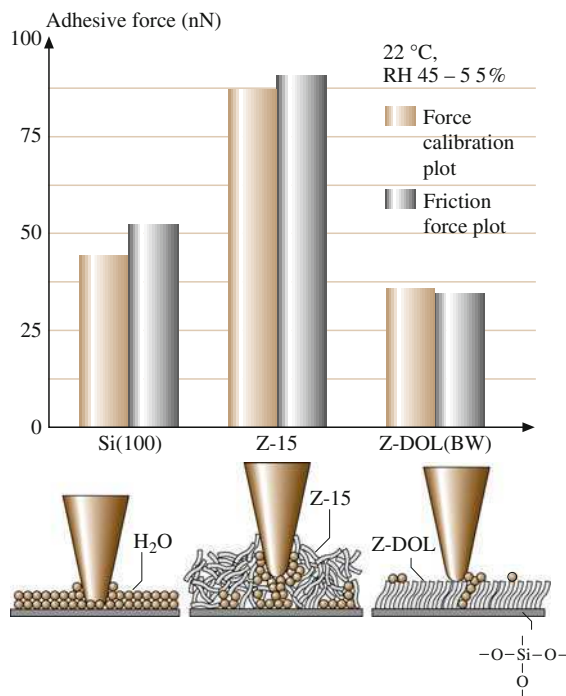


**Fig. 22.49** Summary of the adhesive forces of Si(100), 2.8 nm thick Z-15 film, and 2.3 nm thick Z-DOL(BW) film. The schematic (*bottom*) shows the effect of meniscus formation between the AFM tip and the sample surface on the adhesive and friction forces [30]

removal of the top adsorbed layer. In the case of Z-15 film, the friction force and coefficient of friction show an increase during the initial few cycles and then approach to higher and stable values. This is believed to be caused by the attachment of the Z-15 molecules onto the tip. The molecular interaction between these attached molecules to the tip and molecules on the film surface is responsible for an increase in the friction. But after several scans, this molecular interaction reaches to the equilibrium and after that friction force and coefficient of friction remain constant. In the case of Z-DOL (BW) film, the friction force and coefficient of friction start out to be low and remain low during the entire test for 100 cycles. It suggests that Z-DOL (BW) molecules do not get attached or displaced as readily as Z-15.

## 22.8 Closure

Atomic force microscope/friction force microscope (AFM/FFM) have been successfully used for measurements of surface roughness, friction, adhesion, scratching, wear, indentation, and lubrication on a micro to nanoscales. Commonly measured



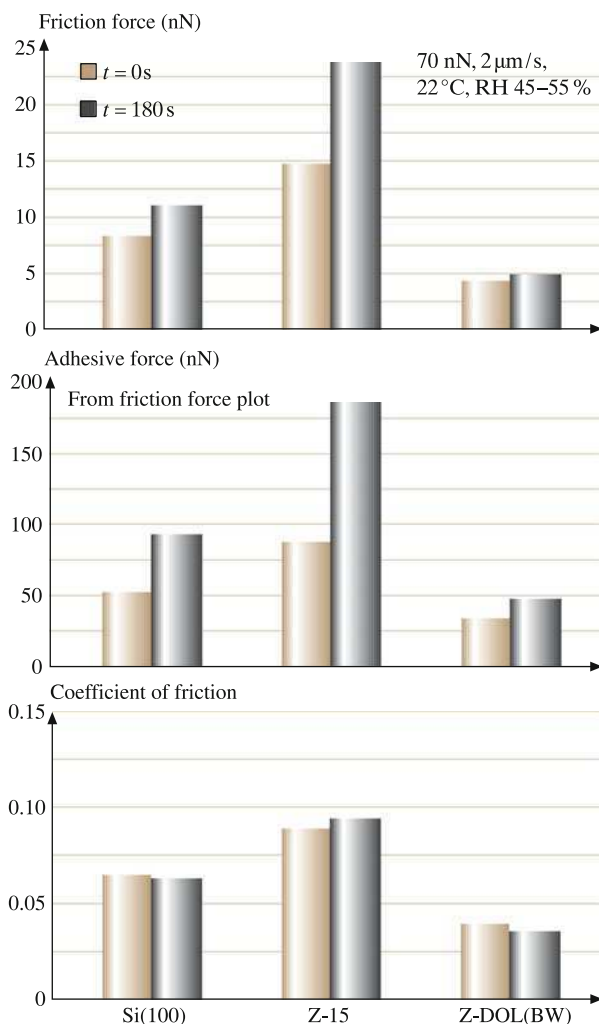


**Fig. 22.50** Summary of rest time effect on friction force, adhesive force, and coefficient of friction of Si(100), 2.8 nm thick Z-15 film, and 2.3 nm thick Z-DOL(BW) film [30]

roughness parameters are scale dependent, requiring the need of scale-independent fractal parameters to characterize surface roughness. A generalized fractal analysis is presented which allows the characterization of surface roughness by two scale-independent parameters. Local variation in microscale friction force is found to correspond to the local surface slope suggesting that a ratchet mechanism is responsible for this variation. Directionality in the friction is observed on both micro- and macro-scales because of surface topography. Microscale friction is found to be significantly smaller than the macro-scale friction as there is less plowing contribution in microscale measurements.

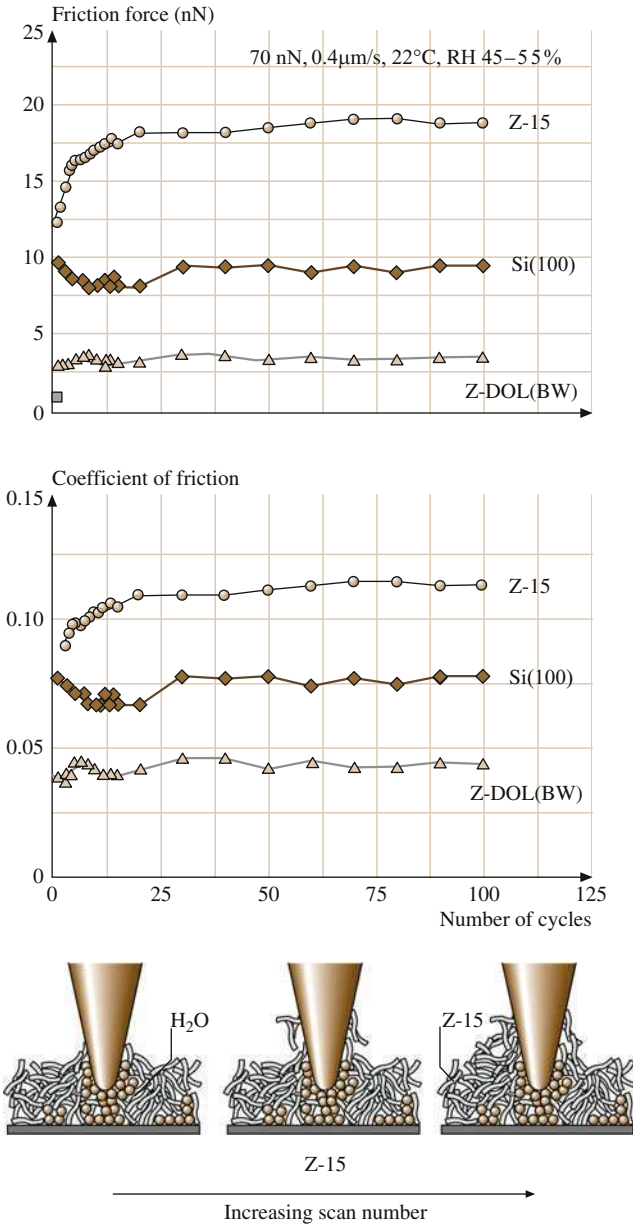


**Fig. 22.51** Friction force and coefficient of friction versus number of sliding cycles for Si(100), 2.8 nm thick Z-15, and 2.3 nm thick Z-DOL (BW) film at 70 nN, 0.8  $\mu\text{m/s}$ , and in ambient air. Schematic bottom shows that some liquid Z-15 molecules can be attached onto the tip. The molecular interaction between the attached molecules onto the tip with the Z-15 molecules in the film results in an increase of the friction force with multiscanning [30]

Wear rates for particulate magnetic tapes and polyester tape substrates are approximately constant for various loads and test durations. However, for magnetic disks and magnetic tapes with a multilayered thin-film structure, the wear of the diamondlike amorphous carbon overcoat in the case of disks and magnetic layer in the case of tapes, is catastrophic. Breakdown of thin-films can be detected with AFM. Evolution of the wear has also been studied using AFM. We find that the wear is initiated at nanoscratches. Amorphous carbon films as thin as 3.5 nm are deposited as continuous films and exhibit some wear life. Wear life increases with an increase in film thickness. Carbon coatings deposited by cathodic arc and ECR-CVD processes are superior in wear and mechanical properties followed by ion beam and sputtering processes. AFM has been modified for nanoindentation hardness measurements with depth of indentation as low as 5 nm. Scratching and indentation on nanoscales are the powerful ways of evaluation of the mechanical integrity of ultrathin films.

AFM/FFM friction experiments show that lubricants with polar (reactive) end groups dramatically increase the load or contact pressure that a liquid film can support before solid–solid contact and thus exhibit long durability. The lubricants with the absence of mobile liquid exhibit low friction and adhesion and don't exhibit rest time effect.

## References

1. B. Bhushan, *Tribology of Magnetic Storage Systems*, vol. 3 (CRC Press, Boca Raton, 1994), pp. 325–374
2. B. Bhushan, *Tribology and Mechanics of Magnetic Storage Devices*, 2nd edn. (Springer, Berlin, 1996)
3. B. Bhushan, *Mechanics and Reliability of Flexible Magnetic Media*, 2nd edn. (Springer, Berlin, 2000)
4. B. Bhushan, *Macro- and Microtribology of Magnetic Storage Devices*. Materials, Coatings, and Industrial Applications, vol. 2 (CRC Press, Boca Raton, 2001), pp. 1413–1513
5. B. Bhushan, *Magnetic Recording Surfaces* (Butterworth-Heinemann, Boston, 1993), pp. 116–133
6. B. Bhushan, *Nanotribology and its Applications to Magnetic Storage Devices and MEMS* (Kluwer, Dordrecht, 1995), pp. 367–395
7. B. Bhushan, Micro/nanotribology and its application to magnetic storage devices and mems. *Tribol. Int.* **28**, 85–95 (1995)
8. B. Bhushan, J.N. Israelachvili, U. Landman, Nanotribology: Friction, wear and lubrication at the atomic scale. *Nature* **374**, 607–616 (1995)
9. B. Bhushan, *Micro/Nanotribology and its Applications*. NATO ASI Ser. 330 (Kluwer, Dordrecht, 1997)
10. B. Bhushan, *Handbook of Micro/Nanotribology*, 2nd edn. (CRC Press, Boca Raton, 1999)
11. B. Bhushan, *Fundamentals of Tribology and Bridging the Gap Between the Macro- and Micro/Nanoscales*. NATO Sci. Ser. II (Kluwer, Dordrecht, 1997)
12. B. Bhushan, *Introduction to Tribology* (Wiley, New York, 2002)
13. B. Bhushan (ed.), *Springer Handbook of Nanotechnology* (Springer, Berlin, 2004)

14. J. Ruan, B. Bhushan, Atomic-scale friction measurements using friction force microscopy: Part i – General principles and new measurement techniques. *ASME J. Tribol.* **116**, 378–388 (1994)
15. B. Bhushan, J. Ruan, Atomic-scale friction measurements using friction force microscopy: Part ii – Application to magnetic media. *ASME J. Tribol.* **116**, 389–396 (1994)
16. B. Bhushan, V.N. Koinkar, Tribological studies of silicon for magnetic recording applications. *J. Appl. Phys.* **75**, 5741–5746 (1994)
17. B. Bhushan, V.N. Koinkar, Nanoindentation hardness measurements using atomic force microscopy. *Appl. Phys. Lett.* **64**, 1653–1655 (1994)
18. B. Bhushan, V.N. Koinkar, J. Ruan, Microtribology of magnetic media. *Proc. Inst. Mech. Eng. Part J, Eng. Tribol.* **208**, 17–29 (1994)
19. B. Bhushan, A.V. Kulkarni, W. Bonin, J.T. Wyrobek, Nanoindentation and picondentation measurements using a capacitance transducer system in atomic force microscopy. *Philos. Mag.* **74**, 1117–1128 (1996)
20. S. Sundararajan, B. Bhushan, Development of a continuous microscratch technique in an atomic force microscopy and its applications to study scratch resistance of ultra-thin hard amorphous carbon coatings. *J. Mater. Res.* **16**, 437–445 (2001)
21. D. DeVecchio, B. Bhushan, Localized surface elasticity measurements using an atomic force microscope. *Rev. Sci. Instrum.* **68**, 4498–4505 (1997)
22. V. Scherer, B. Bhushan, U. Rabe, W. Arnold, Local elasticity and lubrication measurements using atomic force and friction force microscopy at ultrasonic frequencies. *IEEE Trans. Mag.* **33**, 4077–4079 (1997)
23. W.W. Scott, B. Bhushan, Use of phase imaging in atomic force microscopy for measurement of viscoelastic contrast in polymer nanocomposites and molecularly-thick lubricant films. *Ultramicroscopy* **97**, 151–169 (2003)
24. B. Bhushan, J. Qi, Phase contrast imaging of nanocomposites and molecularly-thick lubricant films in magnetic media. *Nanotechnology* **14**, 886–895 (2003)
25. T. Kasai, B. Bhushan, L. Huang, C. Su, Topography and phase imaging using the torsional resonance mode. *Nanotechnology* **15**, 731–742 (2004)
26. B. Bhushan, T. Kasai, A surface topography-independent friction measurement technique using torsional resonance mode in an afm. *Nanotechnology* **15**, 923–935 (2004)
27. B. Bhushan, T. Miyamoto, V.N. Koinkar, Microscopic friction between a sharp diamond tip and thin-film magnetic rigid disks by friction force microscopy. *Adv. Info. Storage Syst.* **6**, 151–161 (1995)
28. V.N. Koinkar, B. Bhushan, Microtribological studies of  $\text{Al}_2\text{O}_3$ ,  $\text{Al}_2\text{O}_3$ -TiC, polycrystalline and single-crystal Mn–Zn ferrite and SiC head slider materials. *Wear* **202**, 110–122 (1996)
29. V.N. Koinkar, B. Bhushan, Microtribological studies of unlubricated and lubricated surfaces using atomic force/friction force microscopy. *J. Vac. Sci. Technol. A* **14**, 2378–2391 (1996)
30. H. Liu, B. Bhushan, Nanotribological characterization of molecularly-thick lubricant films for applications to mems/nems by afm. *Ultramicroscopy* **97**, 321–340 (2003)
31. B. Bhushan, Magnetic slider/rigid disk substrate materials and disk texturing techniques – status and future outlook. *Adv. Info. Storage Syst.* **5**, 175–209 (1993)
32. B. Bhushan, M. Dominiak, J.P. Lazzari, Contact- start-stop studies with silicon planar head sliders against thin-film disks. *IEEE Trans. Mag.* **28**, 2874–2876 (1992)
33. B. Bhushan, G.S. Blackman, Atomic force microscopy of magnetic rigid disks and sliders and its applications to tribology. *ASME J. Tribol.* **113**, 452–458 (1991)
34. P.I. Oden, A. Majumdar, B. Bhushan, A. Padmanabhan, J.J. Graham, Afm imaging, roughness analysis and contact mechanics of magnetic tape and head surfaces. *ASME J. Tribol.* **114**, 666–674 (1992)
35. S. Ganti, B. Bhushan, Generalized fractal analysis and its applications to engineering surfaces. *Wear* **180**, 17–34 (1995)
36. C.Y. Poon, B. Bhushan, Comparison of surface roughness measurements by stylus profiler, afm and non-contact optical profiler. *Wear* **190**, 76–88 (1995)

37. C.Y. Poon, B. Bhushan, Surface roughness analysis of glass–ceramic substrates and finished magnetic disks, and Ni–P coated Al–Mg and glass substrates. *Wear* **190**, 89–109 (1995)
38. V.N. Koinkar, B. Bhushan, Effect of scan size and surface roughness on microscale friction measurements. *J. Appl. Phys.* **81**, 2472–2479 (1997)
39. A. Majumdar, B. Bhushan, Role of fractal geometry in roughness characterization and contact mechanics of surfaces. *ASME J. Tribol.* **112**, 205–216 (1990)
40. A. Majumdar, B. Bhushan, Fractal model of elastic-plastic contact between rough surfaces. *ASME J. Tribol.* **113**, 1–11 (1991)
41. B. Bhushan, A. Majumdar, Elastic-plastic contact model for bifractal surfaces. *Wear* **153**, 53–64 (1992)
42. B. Bhushan, Contact mechanics of rough surfaces in tribology: Single asperity contact. *Appl. Mech. Rev.* **49**, 275–298 (1996)
43. B. Bhushan, Contact mechanics of rough surfaces in tribology: Multiple asperity contact. *Tribol. Lett.* **4**, 1–35 (1998)
44. B. Bhushan, W. Peng, Contact mechanics of multilayered rough surfaces. *Appl. Mech. Rev.* **55**, 435–480 (2002)
45. B. Bhushan, V.N. Koinkar, Microtribology of pet polymeric films. *Tribol. Trans.* **38**, 119–127 (1995)
46. B. Bhushan, V.N. Koinkar, Macro and microtribological studies of CrO<sub>2</sub> video tapes. *Wear* **180**, 9–16 (1995)
47. B. Bhushan, V.N. Koinkar, Microtribology of metal particle, barium ferrite and metal evaporated magnetic tapes. *Wear* **181–183**, 360–370 (1995)
48. B. Bhushan, V.N. Koinkar, Microscale mechanical and tribological characterization of hard amorphous carbon coatings as thin as 5 nm for magnetic disks. *Surf. Coat. Technol.* **76–77**, 655–669 (1995)
49. V.N. Koinkar, B. Bhushan, Microtribological properties of hard amorphous carbon protective coatings for thin-film magnetic disks and heads. *Proc. Inst. Mech. Eng. Part J. Eng. Tribol.* **211**, 365–372 (1997)
50. A.V. Kulkarni, B. Bhushan, Nanoindentation measurements of amorphous carbon coatings. *J. Mater. Res.* **12**, 2707–2714 (1997)
51. X. Li, B. Bhushan, Micro/nanomechanical and tribological characterization of ultra-thin amorphous carbon coatings. *J. Mater. Res.* **14**, 2328–2337 (1999)
52. X. Li, B. Bhushan, Mechanical and tribological studies of ultra-thin hard carbon overcoats for magnetic recording heads. *Z. Metallkd.* **90**, 820–830 (1999)
53. S. Sundararajan, B. Bhushan, Micro/nanotribology of ultra-thin hard amorphous carbon coatings using atomic force/friction force microscopy. *Wear* **225–229**, 678–689 (1999)
54. B. Bhushan, S. Sundararajan, Micro/nanoscale friction and wear mechanisms of thin films using atomic force and friction force microscopy. *Acta Mater.* **46**, 3793–3804 (1998)
55. J. Ruan, B. Bhushan, Frictional behavior of highly oriented pyrolytic graphite. *J. Appl. Phys.* **76**, 8117–8120 (1994)
56. S. Sundararajan, B. Bhushan, Topography-induced contributions to friction forces measured using an atomic force/friction force microscope. *J. Appl. Phys.* **88**, 4825–4831 (2000)
57. B. Bhushan, V.N. Koinkar, Microtribological studies of doped single-crystal silicon and polysilicon films for mems devices. *Sensor Actuator A* **57**, 91–102 (1997)
58. S. Sundararajan, B. Bhushan, Micro/nanotribological studies of polysilicon and SiC films for mems applications. *Wear* **217**, 251–261 (1998)
59. B. Bhushan, Chemical, mechanical and tribological characterization of ultra-thin and hard amorphous carbon coatings as thin as 3.5 nm: Recent developments. *Diam. Relat. Mater.* **8**, 1985–2015 (1999)
60. H. Hibst, *Metal Evaporated Tapes and Co–Cr Media for High Definition Video Recording* (Kluwer, Dordrecht, 1993), pp. 137–159
61. M.Y. Chu, B. Bhushan, L. DeJonghe, Wear behavior of ceramic sliders in sliding contact with rigid magnetic thin-film disks. *Tribol. Trans.* **35**, 603–610 (1992)

62. B. Bhushan, S. Sundararajan, W.W. Scott, S. Chilamakuri, Stiction analysis of magnetic tapes. *IEEE Trans. Mag.* **33**, 3211–3213 (1997)
63. V.J. Novotny, I. Hussla, J.M. Turlet, M.R. Philpott, Liquid polymer conformation on solid surfaces. *J. Chem. Phys.* **90**, 5861–5868 (1989)
64. V.J. Novotny, Migration of liquid polymers on solid surfaces. *J. Chem. Phys.* **92**, 3189–3196 (1990)
65. C.M. Mate, V.J. Novotny, Molecular conformation and disjoining pressures of polymeric liquid films. *J. Chem. Phys.* **94**, 8420–8427 (1991)
66. C.M. Mate, Application of disjoining and capillary pressure to liquid lubricant films in magnetic recording. *J. Appl. Phys.* **72**, 3084–3090 (1992)
67. B. Bhushan, Z. Zhao, Macro- and microscale studies of molecularly-thick boundary layers of perfluoropolyether lubricants for magnetic thin-film rigid disks. *J. Info. Storage Proc. Syst.* **1**, 1–21 (1999)
68. R. Heideman, M. Wirth, Transforming the lubricant on a magnetic disk into a solid fluorine compound. *IBM Technol. Disclosure Bull.* **27**, 3199–3205 (1984)
69. A.M. Homola, L.J. Lin, D.D. Saperstein. Process for bonding lubricant to a thin film magnetic recording disk (1990)
70. D.D. Saperstein, L.J. Lin, Improved surface adhesion and coverage of perfluoropolyether lubricant following far-uv irradiation. *Langmuir* **6**, 1522–1524 (1990)

# Chapter 23

## **MEMS/NEMS and BioMEMS/BioNEMS: Materials, Devices, and Biomimetics**

**Bharat Bhushan**

**Abstract** Micro-/nanoelectromechanical systems (MEMS/NEMS) need to be designed to perform expected functions in short durations, typically in the millisecond to picosecond range. The expected life of devices for high-speed contacts can vary from a few hundred thousand to many billions of cycles, e.g., over a hundred billion cycles for digital micromirror devices (DMDs), which puts serious requirements on materials. The surface-area-to-volume ratio in MEMS/NEMS is large, and in systems involving relative motion, surface forces such as adhesion, friction, and meniscus and viscous forces become very large compared with inertial and electromagnetic forces. There is a need for fundamental understanding of adhesion, friction/stiction, wear, lubrication, and the role of surface contamination and environment, all on the nanoscale. Most mechanical properties are known to be scale dependent, therefore the properties of nanoscale structures need to be measured. For bioMEMS/bioNEMS, adhesion between biological molecular layers and the substrate, and friction and wear of biological layers, can be important. Component-level studies are required to provide a better understanding of the tribological phenomena occurring in MEMS/NEMS. The emergence of the fields of nanotribology and nanomechanics, and atomic force microscopy (AFM)-based techniques, has provided researchers with a viable approach to address these problems. The emerging field of biomimetics holds promise for the development of biologically inspired nanomaterials and nanotechnology products. One example is the design of surfaces with roughness-induced superhydrophobicity, self-cleaning, and low adhesion based on the so-called lotus effect. This chapter presents an overview of nanoscale adhesion, friction, and wear studies of materials and lubrication for MEMS/NEMS and bioMEMS/bioNEMS, and component-level studies of stiction phenomena in MEMS/NEMS devices, as well as hierarchical nano-structured surfaces for superhydrophobicity, self-cleaning, and low adhesion.

### **23.1 MEMS/NEMS Basics**

Microelectromechanical systems (MEMS) refer to microscopic devices that have a characteristic length of  $<1$  mm but  $>100$  nm and that combine electrical and mechanical components. Nanoelectromechanical systems (NEMS) refer to

nanoscopic devices that have a characteristic length of  $< 100$  nm and that combine electrical and mechanical components. In mesoscale devices, if the functional components are on the micro- or nanoscale, they may be referred to as MEMS or NEMS, respectively. These are referred to as intelligent miniaturized systems comprising sensing, processing, and/or actuating functions and combining electrical and mechanical components. The acronym MEMS originated in the USA. The term commonly used in Europe is microsystem technology (MST), and in Japan it is micromachines. Another term generally used is micro-nanodevices. The terms MEMS/NEMS are also now used in a broad sense to include electrical, mechanical, fluidic, optical, and/or biological functions. MEMS/NEMS for optical applications are referred to as micro-/nanooptoelectromechanical systems (MOEMS/NOEMS). MEMS/NEMS for electronic applications are referred to as radiofrequency MEMS/NEMS (RF-MEMS/RF-NEMS). MEMS/NEMS for biological applications are referred to as bioMEMS/bioNEMS.

To put the characteristic dimensions and weights of MEMS/NEMS and bioNEMS into perspective, see Fig. 23.1 and Table 23.1. NEMS and bioNEMS shown in the figure range in size from 2 to 300 nm, and the size of MEMS is 12,000 nm. For comparison, individual atoms are typically a fraction of a nanometer in diameter, deoxyribonucleic acid (DNA) molecules are  $\approx 2.5$  nm wide, biological cells are in the range of thousands of nm in diameter, and human hair is  $\approx 75$   $\mu\text{m}$  in diameter. NEMS can be built with weight as low as  $10^{-20}$  N with cross sections of about 10 nm, and a micromachined silicon structure can have a weight as low as 1 nN. For comparison, the weight of a drop of water is  $\approx 10$   $\mu\text{N}$  and the weight of an eyelash is  $\approx 100$  nN.

Micro-nanofabrication techniques include top-down methods, in which one builds down from the large to the small, and bottom-up methods, in which one builds up from the small to the large. Top-down methods include micro-nanomachining methods and methods based on lithography as well as nonlithographic miniaturization, mostly for MEMS and fabrication of a few NEMS devices. In bottom-up methods, also referred to as nanochemistry, devices and systems are assembled from their elemental constituents for NEMS fabrication, much as nature uses proteins and other macromolecules to construct complex biological systems. The bottom-up approach has the potential to go far beyond the limits of top-down technology by producing nanoscale features through synthesis and subsequent assembly. Furthermore, the bottom-up approach offers the potential to produce structures with enhanced and/or completely new functions. It allows a combination of materials with distinct chemical composition, structure, and morphology. For a brief overview of fabrication techniques, see Appendix A.

MEMS/NEMS and bioMEMS/bioNEMS are expected to have a major impact on our lives, comparable to that of semiconductor technology, information technology, or cellular and molecular biology [4–7]. They are used in electromechanical, electronics, information/communication, chemical, and biological applications. The MEMS industry in 2004 was worth  $\approx$  US\$ 4.5 billion, with a projected annual growth rate of 17% [8]. Growth of Si-based MEMS is slowing down, while nonsilicon MEMS are picking up. The NEMS industry was worth



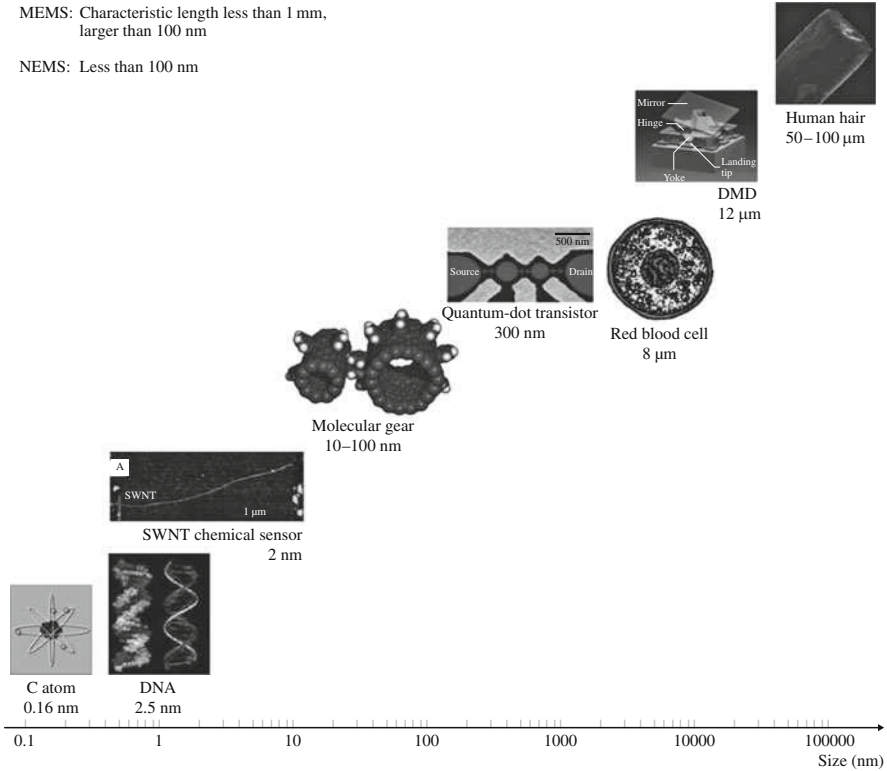


**Fig. 23.1** Characteristic dimensions of MEMS/NEMS and bioNEMS in perspective. Examples shown are a single-walled carbon nanotube (SWNT) chemical sensor [1], molecular dynamic simulations of carbon-nanotube-based gears [2], quantum-dot transistor obtained from van der Wiel et al. [3], and DMD (DLP Texas Instruments). For comparison, dimensions and weights of various biological objects found in nature are also presented

**Table 23.1** Characteristic dimensions and weights in perspective

Characteristic dimensions in perspective	
NEMS characteristic length	< 100 nm
MEMS characteristic length	<1 mm and > 100 nm
Single-walled carbon nanotube (SWNT) chemical sensor	$\approx$ 2 nm
Molecular gear	$\approx$ 10 nm
Quantum-dot transistor	300 nm
Digital micromirror	12,000 nm
Individual atoms	typically a fraction of a nm in diameter
DNA molecules	$\approx$ 2.5 nm wide
Biological cells	in the range of thousands of nm in diameter
Human hair	$\approx$ 75,000 nm in diameter
Weights in perspective	
NEMS built with cross-sections of $\approx$ 10 nm	as low as $10^{-20}$ N
Micromachines, silicon structure	as low as 1 nN
Eyelash	$\approx$ 100 nN
Water droplet	$\approx$ 10 $\mu\text{N}$

$\approx$  US\$ 10 billion dollars in 2004, mostly in nanomaterials [9]. It is expected to expand in nanomaterials and biomedical applications as well as in nanoelectronics or molecular electronics. Due to the enabling nature of these systems and because of the significant impact they can have on both commercial and defense applications, industry as well as federal governments have taken special interest in seeing growth nurtured in this field. MEMS/NEMS and bioMEMS/bioNEMS are the next logical step in the *silicon revolution*.

### 23.1.1 Introduction to MEMS

The advances in silicon photolithographic process technology since the 1960s led to the development of MEMS in the early 1980s. More recently, lithographic processes have also been developed to process nonsilicon materials. Lithographic processes are being complemented with nonlithographic processes for fabrication of components or devices made from plastics or ceramics. Using these fabrication processes, researchers have fabricated a wide variety of devices with dimensions in the submicron range to a few thousand microns (see e.g., [10, 11, 12, 13, 14, 15, 16, 17, 18, 19, 20]). MEMS for mechanical applications include acceleration, pressure, flow, and gas sensors, linear and rotary actuators, and other microstructures or microcomponents such as electric motors, gear chains, gas turbine engines, fluid pumps, fluid valves, switches, grippers, and tweezers. MEMS for chemical applications include chemical sensors and various analytical instruments. MOEMS devices include optical components, such as micromirror arrays for displays, infrared image sensors, spectrometers, barcode readers, and optical switches. RF-MEMS include inductors, capacitors, antennas, and RF switches. High-aspect-ratio MEMS (HARMEMS) have also been introduced.

A variety of MEMS devices have been produced and some are in commercial use [11, 13, 14, 15, 16, 18, 19, 20]. A variety of sensors are used in industrial, consumer, defense, and biomedical applications. The largest “killer” industrial applications include accelerometers, pressure sensors, thermal and piezoelectric inkjet printheads, and digital micromirror devices. Integrated capacitive-type silicon accelerometers have been used in airbag deployment in automobiles since 1991 [21, 22]; some 90 million units were installed in vehicles in 2004. Accelerometer technology was over a billion-dollar-a-year industry in 2004, dominated by Analog Devices followed by Freescale Semiconductor (formerly Motorola) and Bosch. It is expected to grow with an annual growth exceeding 30%. Tri-axis accelerometers are needed to describe three-dimensional motion. Multi-axis accelerometers are being used for many other applications such as vehicle stability, rollover control, and gyro sensors for automotive applications, and various consumer applications including handheld devices, e.g., laptops for free-fall detection (2003), cellular phones (2004), and personal digital assistants (PDAs) for menu navigation, gaming, image rotation, and free-fall detection. Silicon-based piezoresistive pressure sensors were launched in 1990 by GE NovaSensor for manifold absolute pressure

(MAP) sensing for engines and for disposable blood-pressure sensors; their annual sales were more than 30 million units and more than 25 million units, respectively, in 2004. MAP sensors measure the pressure in the intake manifold, which is fed to a computer that determines the optimum air–fuel mixture to maximize fuel economy. Most vehicles have these as part of the electronic engine control system. Capacitive pressure sensors for tire pressure measurements were launched by Freescale Semiconductor (formerly Motorola) in early 2000 and are also manufactured by Infineon/SensoNor and GE Novasensor (2003). Piezoresistive-type sensors are also used, manufactured by various companies such as EnTire Solutions (2003). The sensing module is located inside the rim of the wheel and relays the information via radiofrequency to a central processing unit (CPU) in order to display it to the driver. In 2005,  $\approx 9.2$  million vehicles were equipped with sensors, which translated to  $\approx 37$  million units. Their sales have grown rapidly, as they are now required in automobiles in the USA (starting in 2008), which affects 17 million vehicles (with one device in each tire) sold every year. Pressure sensors can be used to detect altitude by measuring air pressure. For example, global positioning systems (GPS) used for navigation have good lateral resolution but poor vertical resolution, which creates problems in identifying the level in the case of multiple roads stacked up. A pressure sensor is needed to determine the level (altitude) by measuring air pressure.

Thermal inkjet printers were developed independently by HP and Canon and commercialized in 1984 [23, 24, 25, 26] and today are made by Canon, Epson, HP, Lexmark, Xerox, and others. They typically cost less initially than dry-toner laser printers and are the solution of choice for low-volume print runs. Annual sales of thermal inkjet printheads with microscale functional components were  $> 500$  million units in 2004.

Micromirror arrays are used for displays. Commercial digital light processing (DLP) equipment, using digital micromirror devices (DMD), were launched in 1996 by Texas Instruments (TI) for digital projection displays in computer projectors, high-definition television (HDTV) sets, and movie projectors (DLP cinema) [27, 28, 29]. Several million projectors had been sold by 2004 ( $\approx$  US\$ 700 million revenue by TI in 2004). Electrostatically actuated, membrane-type or cantilever-type microswitches have been developed for direct-current (DC), RF, and optical applications [30]. There exists two basic forms of RF microswitches: the metal-to-metal contact microswitch (ohmic) and the capacitive microswitch. RF microswitches can be used in a variety of RF applications, including cellular phones, phase shifters, smart antennas, multiplexers for data acquisition, etc. [31]. Optical microswitches are finding applications in optical networking, telecommunications, and wireless technologies [30, 32].

Other applications of MEMS devices include chemical/biological and gas sensors [20, 33], microresonators, infrared detectors and focal-plane arrays for Earth observation, space science, and missile defense applications, picosatellites for space applications, fuel cells, and many hydraulic, pneumatic, and other consumer products. MEMS devices are also being pursued in magnetic storage systems [34], where they are being developed for supercompact and

ultrahigh-recording-density magnetic disk drives. Several integrated head–suspension microdevices have been fabricated for contact recording applications [35]. High-bandwidth servo-controlled microactuators have been fabricated for ultrahigh-track-density applications, where they serve as the fine-position control element of a two-stage coarse–fine servo system, coupled with a conventional actuator [36, 37].

Micro-nanoinstruments and micro-nanomanipulators are used to move, position, probe, pattern, and characterize nanoscale objects and nanoscale features [38]. Miniaturized analytical equipments include gas chromatography and mass spectrometry. Other instruments include micro-scanning tunneling microscope (micro-STM).

In some cases, MEMS devices are used primarily for their miniature size, while in others, as in the case of airbags, because of their low-cost manufacturing techniques. This latter fact has been possible since semiconductor processing costs have reduced drastically over the last decade, allowing the use of MEMS in many fields.

### **23.1.2 Introduction to NEMS**

NEMS are produced by nanomachining in a typical top-down approach (from large to small) and bottom-up approach (from small to large), largely relying on nanochemistry (see, e.g., [39, 40, 41, 42, 43, 44, 45]). The NEMS field, in addition to the fabrication of nanosystems, has provided impetus for the development of experimental and computation tools. Examples of NEMS include microcantilevers with integrated sharp nanotips for STM and atomic force microscopy (AFM) [46, 47], quantum corrals formed using STM by placing atoms one by one [48], AFM cantilever arrays (millipede) for data storage [49], STM and AFM tips for nanolithography, dip-pen nanolithography for printing molecules, nanowires, carbon nanotubes, quantum wires (QWRs), quantum boxes (QBs), quantum transistors [3], nanotube-based sensors [50, 51], biological (DNA) motors, molecular gears formed by attaching benzene molecules to the outer walls of carbon nanotubes [2], devices incorporating nm-thick films [e.g., in giant-magnetoresistive (GMR) read/write magnetic heads and magnetic media for magnetic rigid disk and magnetic tape drives], nanopatterned magnetic rigid disks, and nanoparticles (e.g., nanoparticles in magnetic tape substrates and nanomagnetic particles in magnetic tape coatings) [34, 52]. More than two billion read/write magnetic heads were shipped for magnetic disk and tape drives in 2004.

Nanoelectronics can be used to build computer memory using individual molecules or nanotubes to store bits of information [53], molecular switches, molecular or nanotube transistors, nanotube flat-panel displays, nanotube integrated circuits, fast logic gates, switches, nanoscopic lasers, and nanotubes as electrodes in fuel cells.

### 23.1.3 Introduction to BioMEMS/BioNEMS

BioMEMS/bioNEMS are increasingly used in commercial and defense applications (see, e.g., [54, 55, 56, 57, 58, 59, 60, 61]). They are used for chemical and biochemical analyses (biosensors) in medical diagnostics (e.g., DNA, RNA, proteins, cells, blood pressure and assays, and toxin identification) [61, 62], tissue engineering [63, 64, 65], and implantable pharmaceutical drug delivery [66, 67, 68]. Biosensors, also referred to as biochips, deal with liquids and gases. There are two types of biosensors. A large variety of biosensors are based on micro-nanofluidics [61, 69, 70, 71]. Micro-nanofluidic devices offer the ability to work with smaller reagent volumes and shorter reaction times, and perform analyses of multiple types at once. The second type of biosensors includes micro-nanoarrays which perform one type of analysis thousands of times [72, 73, 74, 75].

A chip, called lab-on-a-CD, with micro-nanofluidic technology embedded on the disk can test thousands of biological samples rapidly and automatically [69]. An entire laboratory can be integrated onto a single chip, called a lab-on-a-chip [61, 70, 71]. Silicon-based disposable blood-pressure sensor chips were introduced in early 1990s by GE NovaSensor for blood-pressure monitoring ( $\approx 25$  million units in 2004). A blood-sugar monitor, referred to as GlucoWatch, was introduced in 2002. It automatically checks blood sugar every 10 min by detecting glucose through the skin, without having to draw blood. If glucose is out of the acceptable range, it sounds an alarm so the diabetic patient can address the problem quickly. A variety of biosensors, many using plastic substrates, are manufactured by various companies including ACLARA, Agilent Technologies, Calipertech, and I-STAT.

The second type of biochips – micro-nanoarrays – is a tool used in biotechnology research to analyze DNA or proteins to diagnose diseases or discover new drugs. Also called DNA arrays, they can identify thousand of genes simultaneously [57, 72]. They include a microarray of silicon nanowires, roughly a few nm in size, to selectively bind and detect even a single biological molecule such as DNA or protein by using nanoelectronics to detect the slight electrical charge caused by such binding, or a microarray of carbon nanotubes to detect glucose electrically.

After the tragedy of September 11, 2001, concern about biological and chemical warfare has led to the development of handheld units with biological and chemical sensors for detection of biological germs, chemical or nerve agents, and mustard agents, and their chemical precursors, to protect subways, airports, water supplies, and the population at large [76].

BioMEMS/bioNEMS are also being developed for minimally invasive surgery, including endoscopic surgery, laser angioplasty, and microscopic surgery. Implantable artificial organs can also be produced. Other applications include: implantable drug-delivery devices, e.g., micro-nanoparticles with drug molecules encapsulated in functionalized shells for site-specific targeting applications, and a silicon capsule with a nanoporous membrane filled with drugs for long-term delivery [66, 77, 78, 79]; nanodevices for sequencing single molecules of DNA in the Human Genome Project [61]; cellular growth using carbon nanotubes for

spinal-cord repair; nanotubes for nanostructured materials for various applications such as spinal fusion devices; organ growth; and growth of artificial tissues using nanofibers.

### ***23.1.4 Nanotribology and Nanomechanics Issues in MEMS/NEMS and BioMEMS/BioNEMS***

Tribological issues are important in MEMS/NEMS and bioMEMS/bioNEMS requiring intended and/or unintended relative motion. In these devices, various forces associated with the device scale down with the size. When the length of the machine decreases from 1 mm to 1  $\mu\text{m}$ , the surface area decreases by a factor of a million, and the volume decreases by a factor of a billion. As a result, surface forces such as adhesion, friction, meniscus forces, viscous forces, and surface tension that are proportional to surface area become a thousand times larger than the forces proportional to the volume, such as inertial and electromagnetic forces. In addition to the consequence of large surface-to-volume ratios, the small tolerances for which these devices are designed make physical contacts more likely, thereby making them particularly vulnerable to adhesion between adjacent components. Slight particulate or chemical contamination present at the interface can be detrimental. Furthermore, the small start-up forces and the torques available to overcome retarding forces are small, and the increase in resistive forces such as adhesion and friction become a serious tribological concern that limits the durability and reliability of MEMS/NEMS [13]. A large lateral force required to initiate relative motion between two surfaces, i.e., large static friction, is referred to as *stiction* and has been studied extensively in the tribology of magnetic storage systems [34, 46, 80, 81, 82, 83, 84]. The source of stiction is generally liquid-mediated adhesion, with the source of liquid being process fluid or capillary condensation of water vapor from the environment. Adhesion, friction/stiction (static friction), wear, and surface contamination affect MEMS/NEMS and bioMEMS/bioNEMS performance and, in some cases, can even prevent devices from working. Some examples of devices that experience nanotribological problems follow.

Nanomechanical properties are scale dependent, therefore these should be measured at relevant scales.

## **MEMS**

Figure 23.2 shows examples of several microcomponents that can encounter the above-mentioned tribological problems. The polysilicon electrostatic micromotor has 12 stators and a four-pole rotor and is produced by surface micromachining. The rotor diameter is 120  $\mu\text{m}$ , and the air gap between the rotor and stator is 2  $\mu\text{m}$  [85]. It is capable of continuous rotation at up to 100,000 rpm. The intermittent

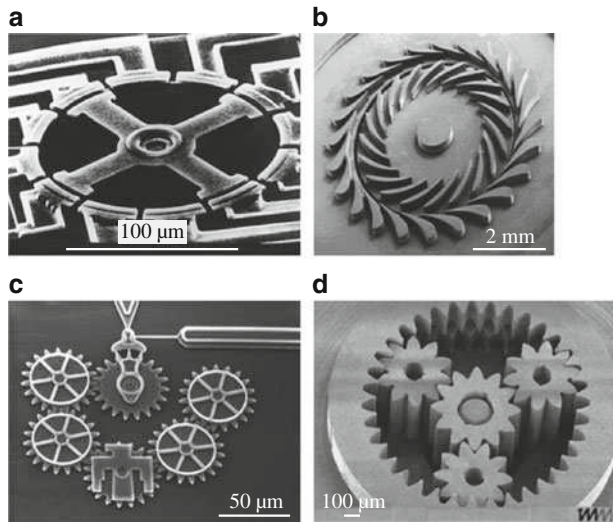


**Fig. 23.2** Examples of MEMS devices and components that experience tribological problems. (a) Electrostatic micromotor (after [85]). (b) Microturbine bladed rotor and nozzle vanes on the stator (after [86]). (c) Six-gear chain (Sandia). (d) Ni/Fe Wolfrom-type gear system produced by LIGA (after [87])

contact at the rotor–stator interface and physical contact at the rotor–hub flange interface result in wear issues, and high stiction between the contacting surfaces limits repeatability of operation or may even prevent operation altogether. Next, a bulk micromachined silicon stator–rotor pair is shown with a bladed rotor and nozzle guide vanes on the stator with dimensions  $< 1$  mm [86, 88]. These are being developed for a high-temperature micro gas-turbine engine with rotor dimension of 4–6 mm in diameter and operating speed of up to 1 million rpm (with a sliding velocity in excess of 500 m/s, comparable to velocities of large turbines operating at high velocities) to achieve high specific power, up to a total of  $\approx 10$  W. Erosion of blades and vanes and design of the microbearings required to operate at the extremely high speeds used in the turbines are some of the concerns. Ultrashort, high-speed micro hydrostatic gas journal bearings with length-to-diameter ratio ( $L/D$ ) of  $< 0.1$  are being developed for operation at surface speeds of the order of 500 m/s, which results in unique design challenges [89]. Microfabrica Inc. in the USA is developing microturbines with outer diameter as low as 0.9 mm to be used as power sources for medical devices. They plan to use precision ball bearings.

Next in Fig. 23.2 is a scanning electron microscopy (SEM) micrograph of a surface-micromachined polysilicon six-gear chain from Sandia National Lab. (For more examples of an early version, see [90].) As an example of nonsilicon components, a milligear system produced using the LIGA process for a DC brushless permanent magnet millimotor (diameter = 1.9 mm, length = 5.5 mm) with an integrated milligear box [87, 91, 92] is also shown. The gears are made of metal (electroplated Ni-Fe) but can also be made from injected polymer materials



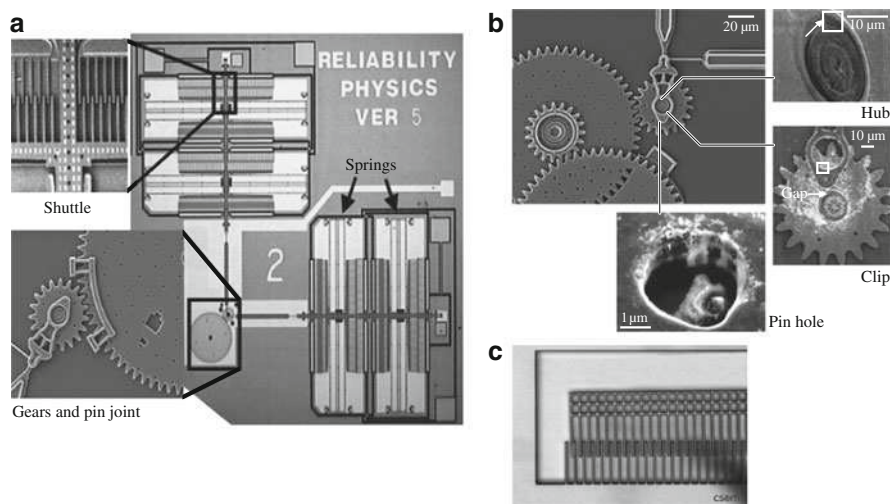


**Fig. 23.3** (a) Optical micrograph of a microengine driven by an electrostatically actuated comb drive (microengine), fabricated by Sandia Summit Technologies (after [93]). (b) The polysilicon microgear unit can be driven at speeds of up to 250,000 rpm. Various sliding components are shown after laboratory wear test for 6,000 cycles at 1.8% relative humidity (after [94]). (c) Stuck comb drive (CSEM)

(e.g., polyoxy-methylene or POM) using the LIGA process. Even though the torque transmitted at the gear teeth is small, of the order of a fraction of nN m, because of the small dimensions of gear teeth, the bending stresses are large where the teeth mesh. Tooth breakage and wear at the contact of gear teeth is a concern.

Figure 23.3 shows an optical micrograph of a microengine driven by an electrostatically activated comb drive connected to the output gear by linkages, for operation in the kHz frequency range, which can be used as a general drive and power source to drive micromechanisms [93]. Parts are fabricated from polysilicon. A microgear unit is used to convert reciprocating motion from a linear actuator into circular motion. Another drive linkage oriented at 90° to the original linkage, driven by another linear actuator, allows continuous motion to be maintained. The linkages are connected to the output gear through pin joints that allow relative motion.

One inset shows a polysilicon, multiple microgear speed reduction unit and its components after laboratory wear tests conducted for 6,000 cycles at 1.8% relative humidity (RH) [94]. Wear of various components is clearly observed in the figure. Humidity was shown to be a strong factor in the wear of rubbing surfaces. In order to improve the wear characteristics of rubbing surfaces, 20 nm-thick tungsten (W) coating deposited at 450°C using chemical vapor deposition (CVD) technique was used [95]. Tungsten-coated microengines tested for reliability showed improved wear characteristics with longer lifetimes than polysilicon microengines. However, these coatings have poor yield. Instead, vapor-deposited self-assembled monolayers of fluorinated (dimethylamino)silane are used [96]. They can be deposited with high yield; however, durability is not as good. The second inset shows a comb



drive with a deformed frame, which results in some fingers coming into contact. The contacting fingers can result in stiction.

Figure 23.4a shows a schematic of a micromachined flow modulator. Several micromachined flow channels are integrated in series with electrostatically actuated microvalves [97]. The flow channels lead to a central gas outlet hole drilled into the glass substrate. Gas enters the device through a bulk micromachined gas inlet hole in the silicon cap. The gas, after passing through an open microvalve, flows parallel to the glass substrate through flow channels and exits the device through an outlet. The normally open valve structure consists of a freestanding double-end-clamped beam, which is positioned beneath the gas inlet orifice. When electrostatically deflected upwards, the beam seals against the inlet orifice and the valve is closed. In these microvalves used for flow control, the mating valve surfaces should be smooth enough to seal while maintaining a minimum roughness to ensure low adhesion [80, 81, 82, 98].

The second MEMS device shown (Fig. 23.4b) is an electrostatically driven rotary microactuator for a magnetic disk drive, surface-micromachined by a multilayer electroplating method [37]. This high-bandwidth servo-controlled microactuator,

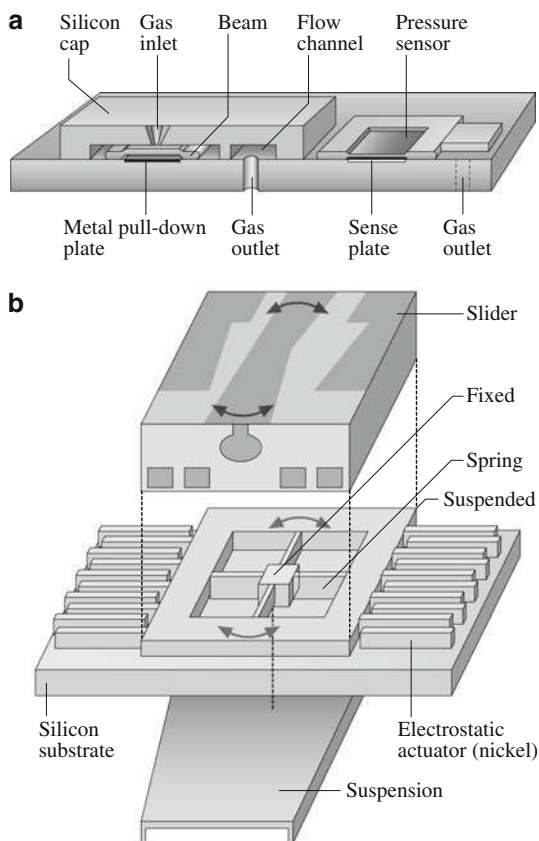


**Fig. 23.4** Examples of MEMS devices that experience tribological problems. (a) Low-pressure flow modulator with electrostatically actuated microvalves (after [97]). (b) Electroplated-nickel rotary microactuator for magnetic disc drives (after [37])

located between a slider and a suspension, is being developed for ultrahigh-track-density applications, which serves as the fine-position and high-bandwidth control element of a two-stage coarse–fine servo system when coupled with a conventional actuator [36, 37]. A slider is placed on top of the central block of a microactuator, which provides rotational motion to the slider. The bottom of the silicon substrate is attached to the suspension. The radial flexure beams in the central block give rotational freedom of motion to the suspended mass (slider), and the electrostatic actuator drives the suspended mass. Actuation is accomplished via interdigitated, cantilevered electrode fingers, which are alternately attached to the central body of the moving part and to the stationary substrate to form pairs. A voltage applied across these electrodes results in an electrostatic force which rotates the central block. The interelectrode gap width is  $\approx 2\text{ }\mu\text{m}$ . Any unintended contacts between the moving and stationary electroplated-nickel electrodes may result in wear and stiction.

Commercially available MEMS devices also exhibit tribological problems. Figure 23.5a shows an integrated capacitive-type silicon accelerometer fabricated using surface micromachining by Analog Devices, a couple of mm in dimension, which is used for airbag deployment in automobiles, and more recently for various other consumer electronic markets [21, 99]. The central suspended beam mass ( $\approx 0.7\text{ }\mu\text{g}$ ) is supported on the four corners by spring structures. The central beam has interdigitated cantilevered electrode fingers ( $\approx 125\text{ }\mu\text{m}$  long and  $3\text{ }\mu\text{m}$

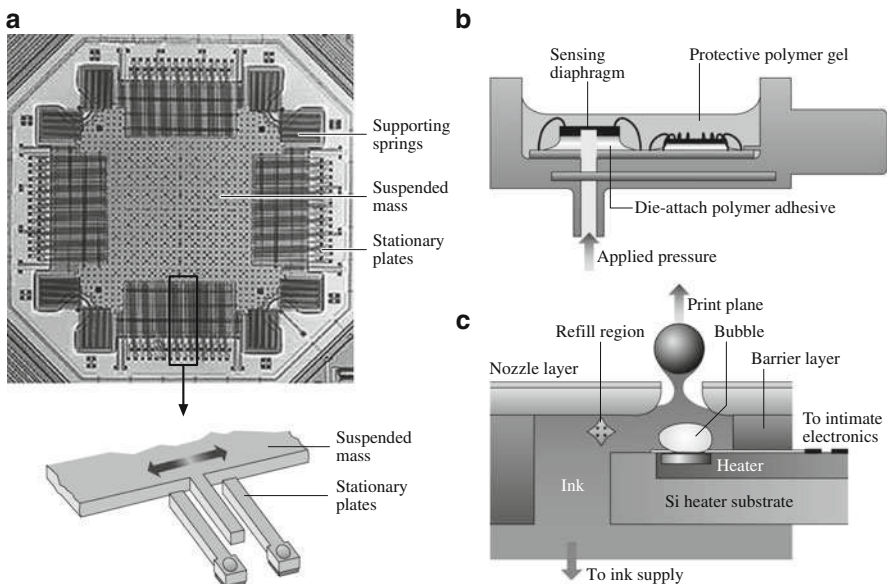


**Fig. 23.5** Examples of MEMS devices in commercial use that experience tribological problems. (a) Capacitive-type silicon accelerometer for automotive sensory applications (after [99]). (b) Piezoresistive-type pressure sensor (after [100]). (c) Thermal inkjet printhead (after [25])

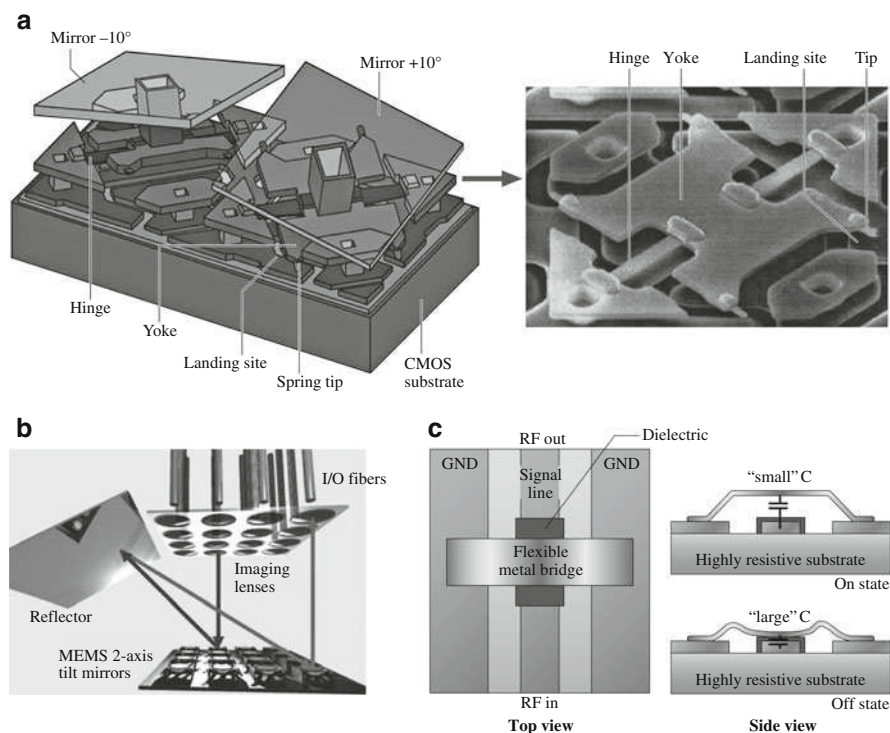
thick) on all four sides that alternate with those of the stationary electrode fingers as shown, with about a  $1.3\ \mu\text{m}$  gap. Lateral motion of the central beam causes a change in the capacitance between these electrodes, which is used to measure the acceleration. Stiction between the adjacent electrodes as well as stiction of the beam structure with the underlying substrate, under isolated conditions, is detrimental to the operation of the sensor [21, 99]. Wear during unintended contact of these polysilicon fingers is also a problem. A molecularly thick diphenyl siloxane lubricant film, resistant to high temperatures and oxidation, is applied by a vapor-deposition process on the electrodes to reduce stiction and wear [101]. For deposition, a small amount of liquid is dispensed into each package before it is sealed. As the package is heated in the furnace, the liquid evaporates and coats the sensor surface. As sensors are required to sense low- $g$  accelerations, they need to be more compliant and stiction becomes an even bigger concern.

Figure 23.5b shows a cross-sectional view of a typical piezoresistive-type pressure sensor, which is used for various applications including manifold absolute pressure (MAP) and tire pressure measurements in automotive applications, and disposable blood-pressure measurements. The sensing material is a diaphragm formed on a silicon substrate, which bends with applied pressure [100, 102]. The deformation causes a change in the band structure of the piezoresistors that are placed on the diaphragm, leading to a change in the resistivity of the material. MAP sensors are subjected to drastic conditions – extreme temperatures, vibrations, sensing fluid, and thermal shock. Fluid under extreme conditions could cause corrosive wear. Fluid cavitation could cause erosive wear. The protective gel encapsulant generally used can react with the sensing fluid and result in swelling or dissolution of the gel. Silicon cannot deform plastically, therefore any pressure spikes leading to deformation past its elastic limit will result in fracture and crack propagation. Pressure spikes could also cause the diaphragm to delaminate from the support substrate. Finally, cyclic loading of the diaphragm during use can lead to fatigue and wear of the silicon diaphragm or delamination.

The schematic in Fig. 23.5c shows a cross-sectional view of a thermal printhead chip (of the order of  $10\text{--}50\ \text{cm}^3$  in volume) used in inkjet printers [25]. They comprise an ink supply and an array of elements with microscopic heating resistors on a substrate mated to a matching array of injection orifices or nozzles ( $\approx 70\ \mu\text{m}$  in diameter) [23, 24, 26]. In each element, a small chamber is heated by the resistor, where a brief electrical impulse vaporizes part of the ink and creates a tiny bubble. The heaters operate at several kHz and are therefore capable of high-speed printing. As the bubble expands, some of the ink is pushed out of the nozzle onto the paper. When the bubble pops, a vacuum is created and this causes more ink from the cartridge to move into the printhead. Clogged ink ports are the major failure mode. There are various tribological concerns [23]. The surface of the printhead from where the ink is ejected towards the paper can become scratched or damaged as a result of countless trips back and forth across the pages, which are somewhat rough. As a result of repeated heating and cooling, the heated resistors expand and contract. Over time, these elements will experience fatigue and may eventually fail. Bubble formation in the ink reservoir can lead to cavitation erosion of the

chamber, which occurs when bubbles formed in the fluid become unstable and implode against the surface of the solid and impose impact energy on that surface. Fluid flow through nozzles may cause erosion and ink particles may also cause abrasive wear. Corrosion of the ink reservoir surfaces can also occur as a result of exposure of ink to high temperatures as well as due to ink pH. The substrate of the chip consists of silicon with a thermal barrier layer followed by a thin film of resistive material and then conducting material. The conductor and resister layers are generally protected by an overcoat layer of a plasma-enhanced chemical vapor deposition (PECVD)  $\alpha$ -SiC:H layer, 200–500 nm thick [103].

Figure 23.6a shows two digital micromirror device (DMD) pixels used in digital light processing (DLP) technology for digital projection displays in computer projectors, high-definition television (HDTV) sets, and movie projectors [27, 28, 29]. The entire array (chip set) consists of a large number of oscillating aluminum alloy micromirrors as digital light switches which are fabricated on top of a complementary metal–oxide–semiconductor (CMOS) static random-access



**Fig. 23.6** Examples of two commercial MOEMS (a,b) and one RF-MEMS (c) device that experience tribological problems. (a) Digital micromirror device for displays (after [28]). (b) Tilt mirror arrays for switching optical signal input and output fiber arrays in optical cross-connect for telecommunications (after [104]). (c) RF microswitch (© IMEC, Belgium)

memory integrated circuit. The surface-micromachined array consists of half a million to more than two million of these independently controlled reflective micromirrors, each  $\approx 12\text{ }\mu\text{m}$  square and with  $13\text{ }\mu\text{m}$  pitch, which flip backward and forward at a frequency of the order of 5,000–7,000 times a second as a result of electrostatic attraction between the micromirror structure and the underlying electrodes. For binary operation, the micromirror–yoke structure mounted on torsional hinges is oscillated  $\pm 10^\circ$  (with respect to the plane of the chip set), limited by a mechanical stop. Contact between cantilevered spring tips at the end of the yoke (four present on each yoke) and the underlying stationary landing sites is required for true digital (binary) operation. Stiction and wear during contact between aluminum-alloy spring tips and landing sites, hinge memory (metal creep at high operating temperatures), hinge fatigue, shock and vibration failure, and sensitivity to particles in the chip package and operating environment are some of the important issues affecting the reliable operation of a micromirror device [105, 106, 107, 108, 109]. A vapor-phase-deposited self-assembled monolayer of the fatty acid perfluorodecanoic acid (PFDA) on surfaces of the tip and landing sites is used to reduce stiction and wear [110, 111]. However, these films are susceptible to moisture, and to keep moisture out and create a background pressure of PFDA, a hermetic chip package is used. The spring tip is used in order to use the stored spring energy to pop up the tip during pull-off. A lifetime estimate of over 100,000 h operation with no degradation in image quality is the norm. At a mirror modulation frequency of 7 kHz, each micromirror element needs to switch  $\approx 2.5$  trillion cycles.

Figure 23.6b shows a schematic of a  $256 \times 256$ -port large optical cross-connect, introduced in 2000 by Glimmerglass (Hayward, CA) for optical telecommunication networks in order to be able to manipulate a larger number of optical signals rapidly [104]. This optical microswitch uses 256 or more movable mirrors on a chip for switching a light beam from an input fiber to a few output fibers. The mirrors are made of gold-coated polysilicon and are  $\approx 500\text{ }\mu\text{m}$  in diameter. Reliability concerns are the same as those described above for DMDs. To minimize stiction, the chipset is hermetically sealed in dry nitrogen (90%  $\text{N}_2$ , 10% He).

Figure 23.6c shows a schematic of an electrostatically-actuated capacitive-type RF microswitch for switching of RF signals at microwave and low frequencies [112]. It is of membrane type and consists of a flexible metal (Al) bridge that spans the RF transmission line in the center of a coplanar waveguide. When the bridge is up, the capacitance between the bridge and RF transmission line is small, and the RF signal passes without much loss. When a DC voltage is applied between the RF transmission line and the bridge, the latter is pulled down until it touches a dielectric isolation layer. The large capacitance thus created shorts the RF signal to ground. The failure modes include creep in the metal bridge, fatigue of the bridge, charging and degradation of the dielectric insulator, and stiction of the bridge to the insulator [30, 112]. Stiction occurs due to capillary condensation of water vapor from the environment, van der Waals forces, and/or charging effects. If the restoring force in the bridge of the switch is not large enough to pull the bridge up again after the actuation voltage has been removed, the device fails due to stiction.

Humidity-induced stiction can be avoided by hermetically sealing the microswitch. Some roughness of the surfaces reduces the probability of stiction. Selected actuation waveforms can be used to minimize charging effects.

## NEMS

Probe-based data recording technologies are being developed for ultrahigh-areal-density recording, where the probe tip is expected to be scanned at velocities up to 100 mm/s. There are three major techniques being developed: thermomechanical [49], phase change [113], and ferroelectric recording [114, 115]. We discuss the tribological issues with two of the widely pursued techniques [116].

Figure 23.7a shows the thermomechanical recording system which uses arrays of 1,024 silicon microcantilevers and playback on an  $\approx 40$  nm-thick polymer medium with a harder Si substrate [49]. The cantilevers consist of integrated tip heaters with tips of nanoscale dimensions. (The sharp tips themselves are also example of NEMS.) Thermomechanical recording is a combination of applying a local force to the polymer layer and softening it by local heating. The tip, heated to  $\approx 400^\circ\text{C}$ , is brought into contact with the polymer for recording. Readings are done using the cantilever heater, originally used for recording, as a thermal read-back sensor by exploiting its temperature-dependent resistance. The principle of thermal sensing is based on the fact that the thermal conductivity between the heater and the storage substrate changes according to the spacing between them. When the spacing between the heater and sample is reduced as the tip moves into a bit, the heater's temperature and hence its resistance will decrease. Thus, changes in temperature of

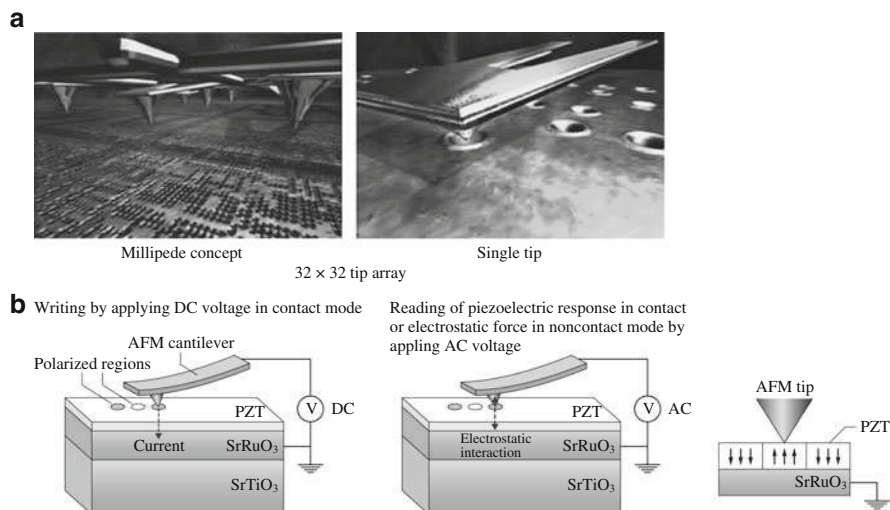


**Fig. 23.7** Two example of NEMS devices: (a) thermomechanical recording, and (b) ferroelectric recording, which experience tribological problems

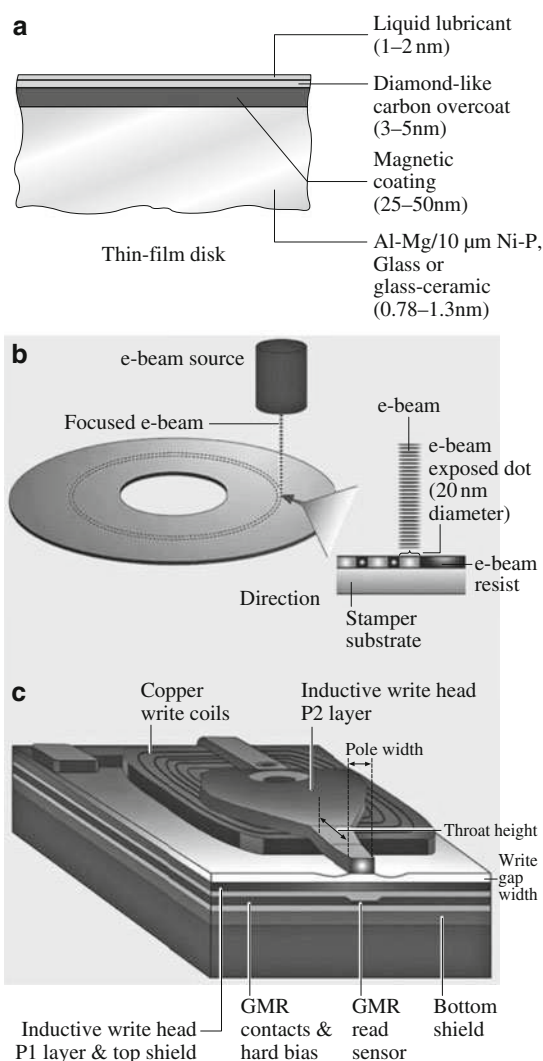


the continuously heated resistor are monitored while the cantilever is scanned over data bits, providing a means of detecting the bits. Erasing for subsequent rewriting is carried out by thermal reflow of the storage field by heating the medium to 150°C for a few seconds. The smoothness of the reflowed medium allows multiple rewriting of the same storage field. Bit sizes ranging between 10 and 50 nm have been achieved by using a  $32 \times 32$  (1,024) array write/read chip ( $3 \text{ mm} \times 3 \text{ mm}$ ). It has been reported that tip wear occurs due to contact between tip and Si substrate during writing. Tip wear is considered a major concern for the device reliability.

Figure 23.7b shows a schematic of domain writing and reading in a ferroelectric film. The electrically conductive AFM tips are placed in contact with a piezoelectric (lead zirconate titanate, PZT) film-coated medium [114, 115]. Ferroelectric domains on the PZT film are polarized by applying short voltage pulses ( $\approx 10 \text{ V}$ ,  $\approx 100 \mu\text{s}$ ) that exceed the coercive field of the PZT layer, resulting in local, nonvolatile changes in the electronic properties of the underlying film. The temperature rise during recording is expected to be of the order of 80°C. Reading out of the polarization states in the ferroelectric film can be carried out using two different methods. In one method, the static surface charge, proportional to the normal component of polarization, can be detected by electrostatic force microscopy in the noncontact mode. In the second method, an AFM is operated in contact mode and the piezoresponse force is measured by applying an alternating-current (AC) voltage. Wear of the conducting tip and the PZT layer at high scanning velocities is a major concern for device reliability. Various lubricant films are being developed to minimize wear [113, 114, 115, 116, 117, 118, 119].

In magnetic data storage, magnetic recording is accomplished by relative motion between the magnetic head slider and a magnetic rigid disk [34]. Magnetic rigid disks and heads used today for magnetic data storage consist of nanostructured films a few nm thick. Figure 23.8a shows a sectional view of a conventional multigrain magnetic rigid disk. The superparamagnetic effect poses a serious challenge for the ever-increasing areal density of disk drives. One of the promising methods to circumvent the density limitations imposed by this effect is the use of a nanopatterned disk (Fig. 23.8b). In a conventional disk, the thin magnetic layer forms a random mosaic of nanometer-scale grains, and each recorded bit consists of many tens of these random grains. In a patterned disk, the magnetic layer is created as an ordered array of highly uniform islands, each island capable of storing an individual bit. These islands may be one or a few grains, rather than a collection of random decoupled grains. This increases the density by a couple of orders of magnitude. Figure 23.8c shows a schematic of an inductive write/giant-magnetoresistive (GMR) read head structure. These are constructed from a variety of materials: magnetic alloys, metal conductors, ceramic, and polymer insulators in a complex three-dimensional structure. The multilayered thin-film structure used to construct the sensor and individual films are only a few nm thick. The head slider surface, which flies over the disk surface, is coated with  $\approx 3 \text{ nm}$ -thick diamond-like carbon coatings to protect the thin-film structure from electrostatic discharge. Any isolated contacts between the disk and sensor and lubricant pickup pose tribological concerns [34].

**Fig. 23.8** Schematic of (a) sectional view of a conventional multigrain magnetic rigid disk, (b) nanopatterned magnetic rigid disk, and (c) an inductive write/GMR read magnetic head structure for magnetic data storage (Hitachi)



## BioMEMS

An example of a wristwatch-type biosensor based on microfluidics, referred to as a lab-on-a-chip system, is shown in Fig. 23.9a [61, 70]. These systems are designed either to detect a single or a class of (bio)chemicals or for system-level analytical capabilities for a broad range of (bio)chemical species (known as a micro total analysis system, mTAS), and have the advantage of incorporating sample handling, separation, detection, and data analysis onto one platform. The chip relies on microfluidics and involves manipulation of tiny amounts of fluids in microchannels using microvalves. The test fluid is injected into the chip, generally using an



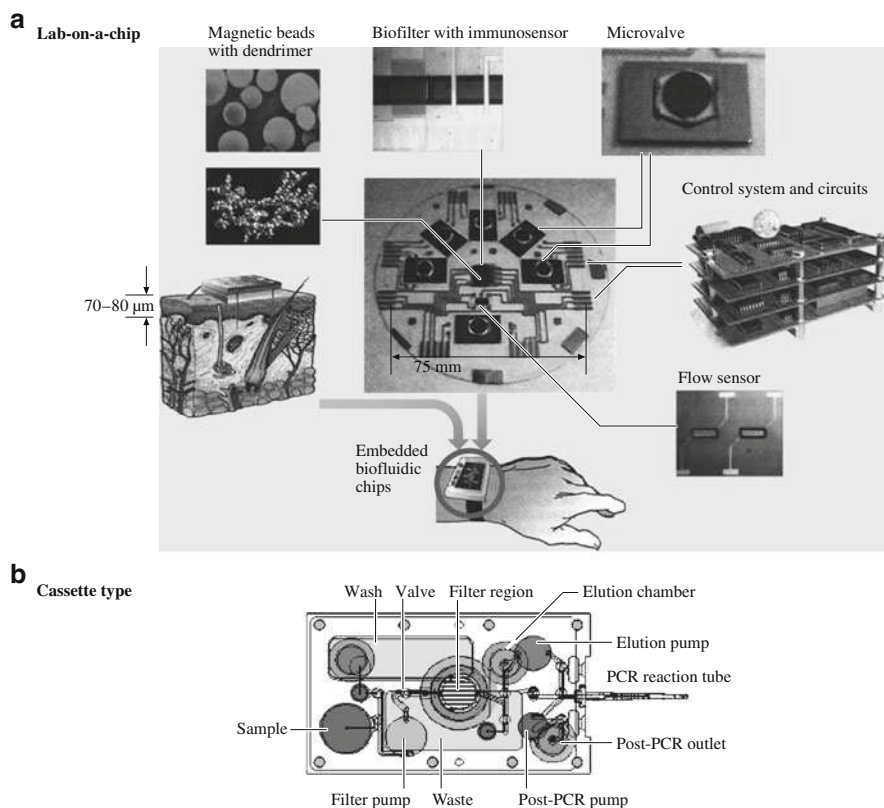
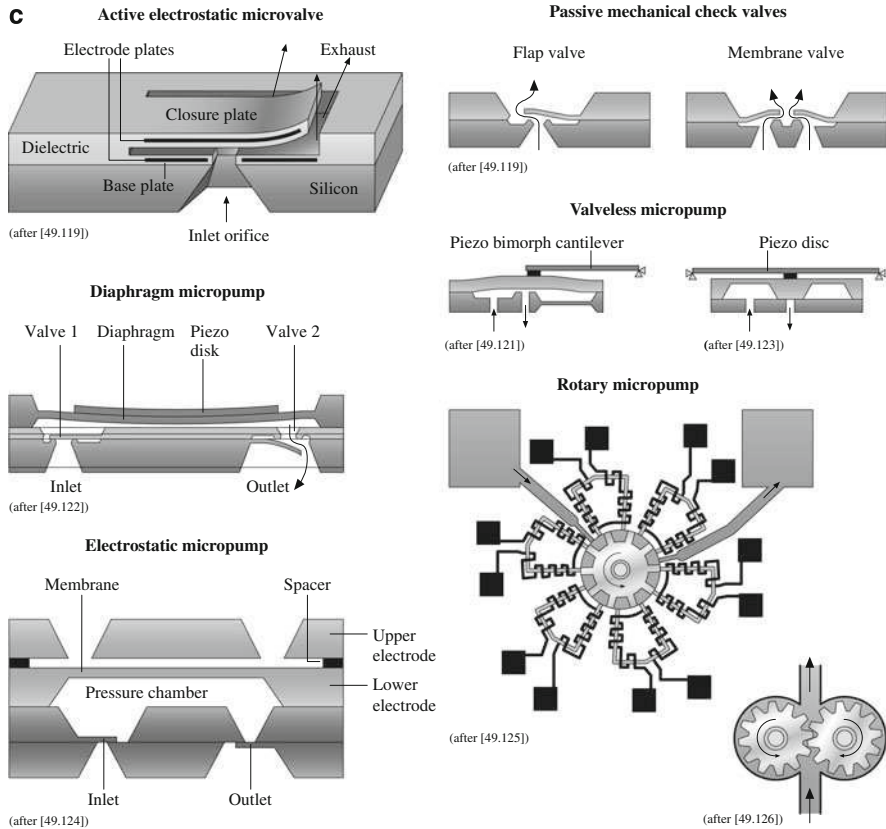


Fig. 23.9 (continued)

external pump or syringe, for analysis. Some chips have been designed with an integrated electrostatically actuated diaphragm-type micropump. The sample, which can have volume measured in nanoliters, flows through microfluidic channels via an electric potential and capillary action using microvalves (having various designs, including membrane type) for various analyses. The fluid is preprocessed and then analyzed using a biosensor. Another example of a biosensor is the cassette-type biosensor used for human genomic DNA analysis; integrated biological sample preparation is shown in Fig. 23.9b [71]. The implementation of micropumps and microvalves allows for fluid manipulation and multiple sample processing steps in a single cassette. Blood or other aqueous solutions can be pumped into the system, where various processes are performed.

Microvalves, which are found in most microfluidic components of bioMEMS, can be classified in two categories: active microvalves (with an actuator) for flow regulation in microchannels and passive microvalves integrated with micropumps. Active microvalves consist of a valve seat and a diaphragm actuated by an external actuator [62, 120, 121]. Different types of actuators are based on piezoelectric, electrostatic, thermopneumatic, electromagnetic, and bimetallic materials,



**Fig. 23.9** (a) MEMS-based biofluidic chip, commonly known as a lab-on-a-chip, that can be worn like a wristwatch (after [70]). (b) Cassette-type biosensor used for human genomic DNA analysis (after [71]). PCR, polymerase chain reaction (c) Multiple examples of valves and pumps found in bioMEMS devices. Mechanical check valves, diaphragm micropump, valveless micropump, and rotary micropump

shaped-memory alloys, and solenoid plungers. An example of an electrostatic cantilever-type active microvalve is shown in Fig. 23.9c [120]. Passive microvalves used in micropumps include mechanical check valves and a diffuser/nozzle [62, 121, 122, 123, 124]. Check valves consist of a flap or membrane that is capable of opening and closing with changes in pressure; see Fig. 23.9c for schematics. A diffuser/nozzle uses an entirely different principle and only works with the presence of a reciprocating diaphragm. When one convergent channel works simultaneously with another convergent channel oriented in a specific direction, a change in pressure is possible.

There are four main types of mechanical micropumps, which include a diaphragm micropump that involves mechanical check valves, valveless rectification pumps that use diffuser/nozzle type valves, valveless pumps without a diffuser/nozzle, electrostatic micropumps, and rotary micropumps [62, 121, 122, 123, 124].

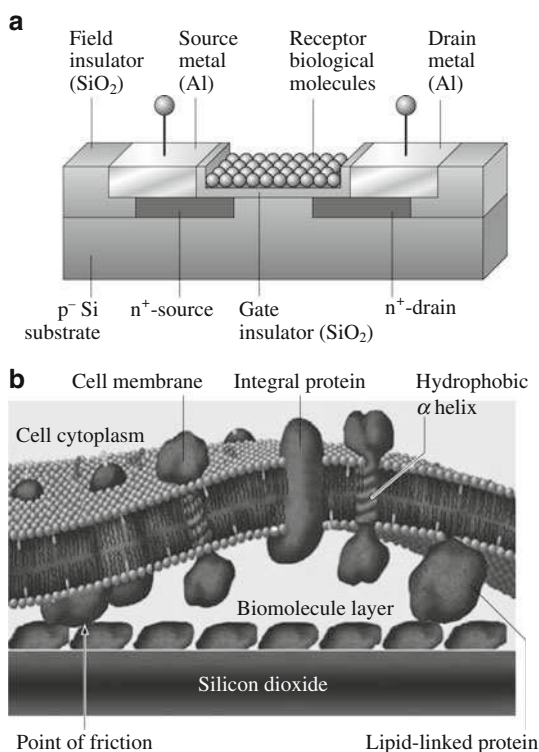
Diaphragm micropumps consist of a reciprocating diaphragm which can be piezoelectrically driven, working in synchronization with two check valves (Fig. 23.9c) [123]. Electrostatic micropumps have a diaphragm as well, but it is driven using two electrodes (Fig. 23.9c) [125]. Valveless micropumps also consist of a diaphragm, which is piezoelectrically driven, but do not incorporate passive mechanical valves. Instead, these pumps use an elastic buffer or variable-gap mechanism. Finally, a rotary micropump has a rotating rotor that simply adds momentum to the fluid by the fast moving action of the blades (Fig. 23.9c) [126, 127]. Rotary micropumps can be driven using an integrated electromagnetic motor or by the presence of an external electric field. All of these micropumps can be made of silicon or a polymer material.

During the operation of the microvalves and micropumps discussed above, adhesion and friction properties become important when contacts occur due to relative motion. During operation, active mechanical microvalves have an externally actuated diaphragm which comes into contact with a valve seat to restrict fluid flow. Adhesion between the diaphragm and valve seat will affect the operation of the microvalve. In the diaphragm micropumps, two passive mechanical check valves are incorporated into the design. Passive mechanical check valves also exhibit adhesion when the flap or membrane comes into contact with the valve seat when fluid flow is prevented. Adhesion also occurs during the operation of valveless micropumps when the diaphragm, which is piezoelectrically driven, comes into contact with the rigid outlet. Finally, adhesion and friction can also be seen during the operation of rotary micropumps when the gears rotate and come into contact and rub against one another.

If the adhesion between the microchannel surface and the biofluid is high, biomolecules will stick to the microchannel surface and restrict flow. In order to facilitate flow, microchannel surfaces with low bioadhesion are required. Fluid flow in polymer channels can produce triboelectric surface potential, which may affect the flow. Polymers are known to generate surface potential, and the magnitude of the potential varies from one polymer to another [128, 129, 130]. Conductive surface layers on the polymer channels can be deposited to reduce triboelectric effects.

As just mentioned, the microfluidic biosensor shown in Fig. 23.9a required the use of micropumps and microvalves. For example, a microdevice with 1,000 channels requires 1,000 micropumps and 2,000 microvalves, which makes it bulky and poses reliability concerns. Two methods can be used for driving the flow of fluids in microchannels: pressure and electrokinetic drive. Electrokinetic flow is based on the movement of molecules in an electric field due to their charges. There are two components to electrokinetic flow: electrophoresis, which results from the accelerating force due to the charge of a molecule in an electric field, and electroosmosis, which uses electrically controlled surface tension to drive the uniform liquid flow. Biosensors based on electrokinetic flow have also been developed. In so-called *digital-based microfluidics*, based on the electroosmosis process, electrically controlled surface tension is used to drive liquid droplets, thus eliminating the need for valves and pumps [131, 132]. These microdevices consist of a rectangular grid of gold nanoelectrodes instead of micro-nanochannels.

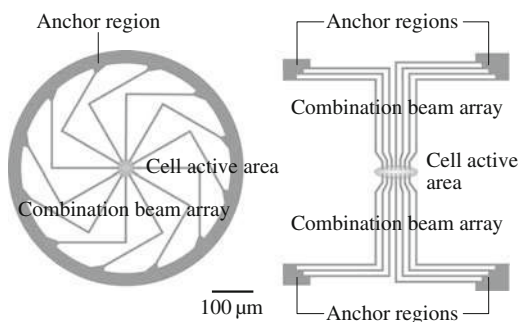
**Fig. 23.10** (a) Schematic of a bioFET sensor (after [73]), and (b) schematic showing the generation of friction and wear points due to interaction of implanted biomolecule layer on a biosensor with living tissue (after [133])



An externally applied electric field enables manipulation of a few nanoliter samples through the capillary circuitry.

An example of a microarray-type biosensor (under development in our laboratory) is based on a field-effect transistor (FET) and is shown in Fig. 23.10a [73, 134]. FETs are sensitive to the electrical field produced due to the charge at the surface of the gate insulator. In this sensor, the gate metal electrode of a metal–oxide–semiconductor field-effect transistor (MOSFET) is removed and replaced with a protein (receptor layer) whose cognate is the analyte (e.g., virus or bacteria) that is meant to be sensed. Various proteins may have 1–25 (positive or negative) charges per molecule. The binding of the receptor layer with the analyte produces a change in the effective charge, which creates a change in the electrical field. This electrical field change may produce a measurable change in the current flow through the device. Adhesion between the protein layer and silica substrate affect the reliability of the biosensor. In the case of implanted biosensors, they come into contact with exterior environment, such as tissues and fluids, and any relative motion of the sensor surface with respect to the exterior environment, such as tissues or fluids, may result in surface damage. A schematic of friction and wear points of generation, when an implanted biosensor surface comes into contact with a living tissue, is shown in Fig. 23.10b [133]. The friction, wear, and adhesion of the biosensor surface may be critical in these applications [73, 133, 135, 136].

**Fig. 23.11** Schematic of two designs for polymer bioMEMS structures to measure cellular forces (after [137])

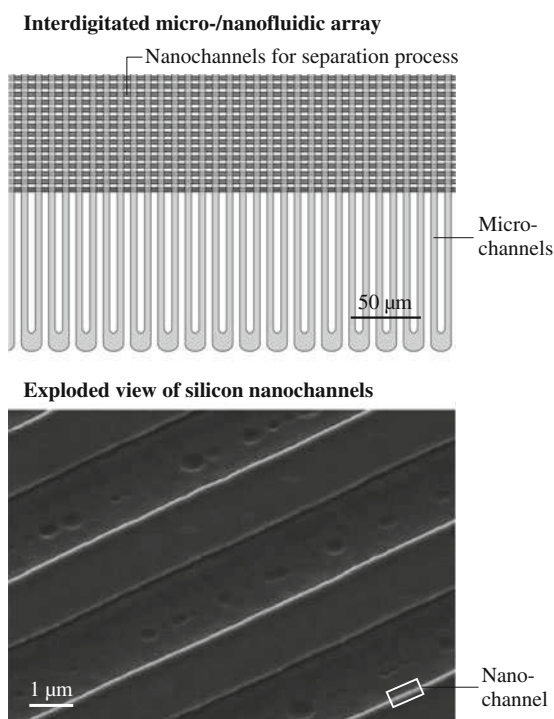


Polymer bioMEMS are designed to measure cellular surfaces. Two examples are shown in Fig. 23.11 [137]. The device on the left shows cantilevers anchored at the periphery of the circular structure, while the device on the right has cantilevers anchored at the two corners on the top and the bottom. The cell adheres to the center of the structure, and the contractile forces generated in the cell's cytoskeleton cause the cantilever to deflect. The deflection of the compliant polymer cantilevers is measured optically and related to the magnitude of the forces generated by the cell. Adhesion between cells and the polymer beam is desirable. In order to design the sensors, micro- and nanoscale mechanical properties of polymer structures are needed.

## BioNEMS

Micro-nanofluidic devices provide a powerful platform for electrophoretic separations for a variety of biochemical and chemical analysis. Electrophoresis is a versatile analytical method which is used for separation of small ions, neutral molecules, and large biomolecules. Figure 23.12 shows an interdigitated micro-nanofluidic silicon array with nanochannels for a separation process. Figure 23.13a shows a schematic of an implantable, immunoisolation submicroscopic biocapsule, aimed at drug delivery in order to treat significant medical conditions such as type I diabetes [77, 78]. The purpose of the immunoisolation biocapsule is to create an implantable device capable of supporting foreign living cells that can be transplanted into humans. It is a silicon capsule consisting of two nanofabricated membranes bonded together with the drug (e.g., encapsulated insulin-producing islet cells) contained within the cavities for long-term delivery. The pores or nanochannels in a semipermeable membrane as small as 6 nm are used as flux regulators for long-term release of drugs. The nanomembrane also protects therapeutic substances from attack by the body's immune system. The pores are large enough to provide the flow of nutrients (e.g., glucose molecules) and drug (e.g., insulin), but small enough to block natural antibodies. Antibodies have the capability to penetrate any orifice  $>18$  nm. The 50 nm pores in silicon were etched by using sacrificial-layer lithography, described in Appendix [78].

**Fig. 23.12** Interdigitated micro-nanofluidic silicon array for a separation process (after [134,138])



The main reliability concerns in the micro-nanofluidic silicon array and implantable biocapsules are biocompatibility and potential biofouling (undesirable accumulation of microorganisms) of the channels/membrane due to protein and cell adsorption from biological fluids. Biofouling can also result in clogging of the nanochannels/nanopores, which could potentially render the device ineffective. The adhesion of proteins and cells to an implanted device can also cause detrimental results such as inflammation and excessive fibrosis. Deposition of self-assembled monolayers of selected organic molecules onto the channels of the implants, which makes them hydrophobic, presents an innovative solution to combat the adverse effects of biological fluids [138, 139, 140, 141].

Figure 23.13b shows a conceptual model of an intravascular drug-delivery device: nanoparticles used to search and destroy disease (tumor) cells [79]. (The tumor cells have one or two orders of magnitude higher density of receptors than normal cells and lower pH. Some receptors are only expressed on tumor cells.) With lateral dimensions of 1  $\mu\text{m}$  or less, the particles are smaller than any blood cells. These particles can be injected into the blood stream and travel freely through the circulatory system. In order to direct these drug-delivery nanoparticles to cancer sites, their external surfaces are chemically modified to carry molecules that have lock-and-key binding specificity with molecules that support a growing cancer mass. As the particles come into close proximity with diseased cells, the ligands

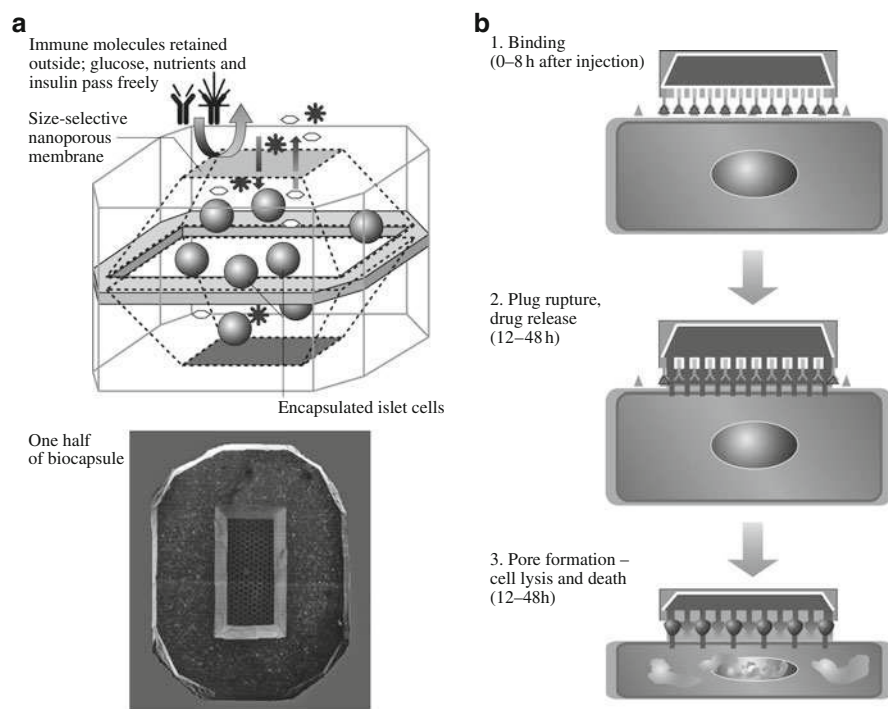
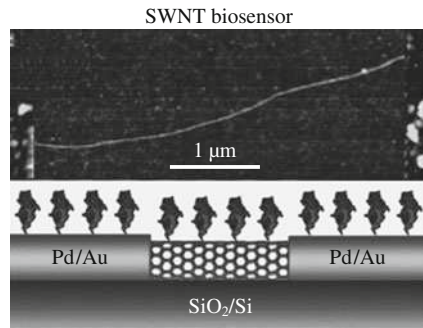


**Fig. 23.13** Schematics of (a) implantable, immunoisolation submicroscopic biocapsules (drug-delivery device) (after [78]), and (b) intravascular nanoparticles for search and destroy of diseased blood cells (after [79])

on the particle surfaces attach to the receptors on the cells. As soon as the particles dock onto the cells, a compound is released that forms a pore on the membrane of the cells, which leads to cell death and ultimately to that of the cancer mass that was being nourished by the blood vessel. The adhesive interactions are regulated by specific (ligand–receptor binding) and nonspecific (short-range van der Waals, electrostatic, and steric) interactions [142]. Adhesion between nanoparticles and disease cells is required. Furthermore, the particles should travel close to the endothelium lining of vascular arteries to facilitate the interaction between the particles and diseased cells. Decuzzi et al. [142] analyzed the margination of a particle circulating in the blood stream and calculated the speed and time for margination (drifting of particles towards the blood vessel walls) as a function of the density and diameter of the particle, based on various forces present between the circulating particle and the endothelium lining. Human capillaries can have radii as small as 4–5  $\mu\text{m}$ . They reported that particles used for drug delivery should have a radius smaller than a critical value in the range of 100 nm. Recent studies show that a lateral force on the particles assists them in faster margination towards the endothelium walls. Thus, nonspherical particles are more desirable.



**Fig. 23.14** SEM micrograph of SWNT biosensor; bottom schematic shows adsorption of protein molecules to the SWNT (after [1])



Because of their unique mechanical and electrical properties, single- and multi-walled carbon nanotubes (SWNT and MWNT) are being used for thermal management of high-power devices, reinforced composites and superstrong fiber and sheets, chemical and biological sensors, electromechanical devices, field-emission devices, and molecular electronics and computing [51, 143]. Figure 23.14 shows a SWNT biosensor [1]. The conductance of carbon nanotube (CNT) devices changes when proteins adsorb on the surface. The change in electrical resistance is a measure of protein adsorption. For high performance, adhesion should be strong between the adsorbent and SWNT.

In summary, adhesion, stiction/friction, and wear clearly limit the lifetimes and compromise the performance and reliability of MEMS/NEMS and bio-MEMS/bioNEMS. Figure 23.15a summarizes the tribological problems encountered in some of the MEMS, MOEMS, RF-MEMS, and bioMEMS devices just discussed.

## Microfabrication Processes

In addition to in-use stiction, stiction issues are also present in some processes used for the fabrication of MEMS/NEMS. For example, the last step in surface micromachining involves the removal of sacrificial layer(s), called release since the microstructures are released from the surrounding sacrificial layer(s). Release is accomplished by an aqueous chemical etch, rinsing, and drying processes. Due to meniscus effects as a result of wet processes, suspended structures can sometimes collapse and permanently adhere to the underlying substrate, as shown in Fig. 23.15b [144]. Adhesion is caused by water molecules adsorbed on the adhering surfaces and/or because of formation of adhesive bonds by silica residues that remain on the surfaces after the water has evaporated. This so-called release stiction is overcome by using dry release methods, such as CO<sub>2</sub> critical-point drying or sublimation drying [145]. CO<sub>2</sub> at high pressure is in a supercritical state and becomes liquid. Liquid CO<sub>2</sub> is used to remove wet etchant, and then it is converted back to gas phase.



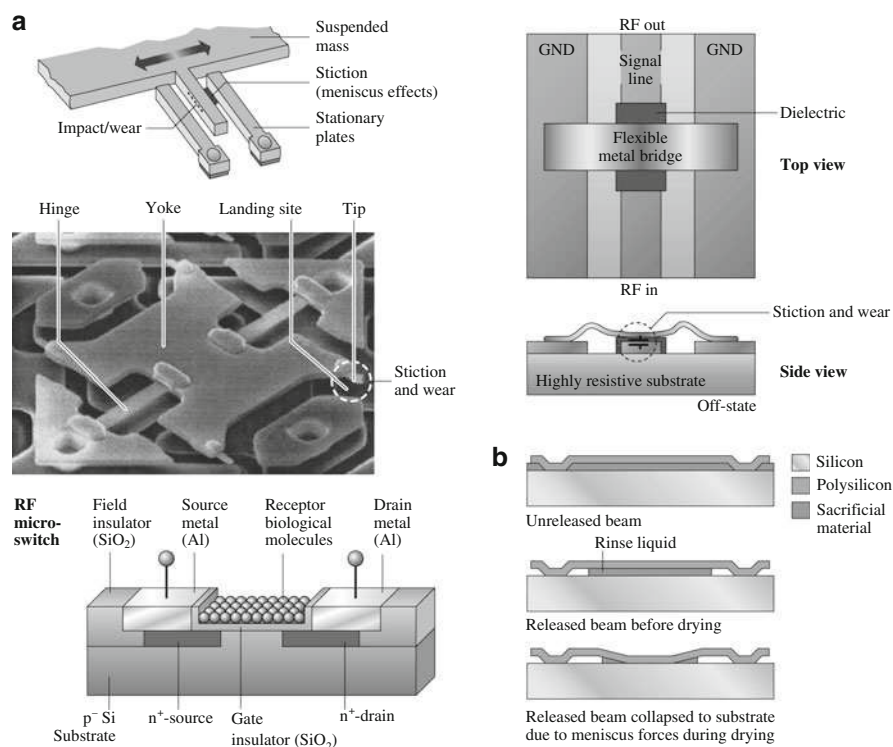


**Fig. 23.15** (a) Summary of tribological issues in MEMS, MOEMS, RF-MEMS, and bioMEMS device operation (after [73,139]), and (b) in microfabrication by surface micromachining

## Tribological Needs

Various MEMS/NEMS are designed to perform expected functions in millisecond to picosecond range. The expected life of the devices for high-speed contacts can vary from a few hundred thousand to many billions of cycles, e.g., over a hundred billion cycles for DMDs, which places stringent requirements on materials [13, 94, 146, 147, 148, 149]. Adhesion between a biological molecular layer and the substrate (referred to as *bioadhesion*), reduction of friction and wear of biological layers, biocompatibility, and biofouling for bioMEMS/bioNEMS are important. Most mechanical properties are known to be scale dependent [150]. The properties of nanoscale structures need to be measured [151]. There is a need for the development of fundamental understanding of adhesion, friction/stiction, wear, and the role of surface contamination and environment [13]. MEMS/NEMS materials need to possess good mechanical and tribological properties on the micro-nanoscale. There is a need to develop lubricants and identify lubrication methods that are suitable for MEMS/NEMS. Methods need to be developed to enhance adhesion between biomolecules and the device substrate, referred to as

bioadhesion. Component-level studies are required to provide better understanding of the tribological phenomena occurring in MEMS/NEMS.

The emergence of the field of nanotribology and nanomechanics, and atomic-force microscopy-based techniques, has provided researchers with a viable approach to address these problems [46, 47, 84, 152, 153, 154, 155]. This chapter presents an overview of nanoscale adhesion, friction, and wear studies of materials and lubrication for MEMS/NEMS and bioMEMS/bioNEMS, and component-level studies of stiction phenomena in MEMS/NEMS devices. The emerging field of biomimetics holds promise for the development of biologically inspired nanomaterials and nanotechnology products [156]. One example includes the design of roughness induced surfaces with superhydrophobicity, self-cleaning, and low adhesion based on the so-called lotus effect. An overview of hierarchical nanostructured surfaces with superhydrophobicity, self-cleaning, and low adhesion is also presented.

### 23.2 Nanotribology and Nanomechanics Studies of Silicon and Related Materials

Materials of most interest for planar fabrication processes using silicon as the structural material are undoped and boron-doped ( $p^+$ -type) single-crystal silicon for bulk micromachining, and phosphorus ( $n^+$ -type) doped and undoped low-pressure chemical vapor deposition (LPCVD) polysilicon films for surface micromachining. Since silicon-based devices lack high-temperature capabilities with respect to both mechanical and electrical properties, SiC is being developed as a structural material for high-temperature microsensor and microactuator applications [157, 158]. SiC can also be desirable for high-frequency micromechanical resonators, in the GHz range, because of its high modulus of elasticity to density ratio and consequently high resonance frequency. Table 23.2 compares selected bulk properties of SiC and Si(100). Researchers have found low-cost techniques of producing single-crystalline 3C-SiC (cubic or  $\beta$ -SiC) films via epitaxial growth on large-area silicon substrates for bulk micromachining [161] and polycrystalline 3C-SiC films on polysilicon and silicon dioxide layers for surface micromachining of SiC [162]. Single-crystalline 3C-SiC piezoresistive pressure sensors have been fabricated using bulk micromachining for high-temperature gas-turbine applications [163]. Surface-micromachined polycrystalline SiC micromotors have been

**Table 23.2** Selected bulk properties<sup>a</sup> of 3C ( $\beta$ - or cubic) SiC and Si(100)

Sample	Density (kg/m <sup>3</sup> )	Hardness (GPa)	Elastic modulus (GPa)	Fracture toughness (MPa m <sup>1/2</sup> )	Thermal conductivity <sup>b</sup> (W/(m K))	Coeff. of thermal expansion <sup>b</sup> ( $\times 10^{-6}$ K <sup>-1</sup> )	Melting point (°C)	Bandgap (eV)
$\beta$ -SiC	3,210	23.5–26.5	440	4.6	85–260	4.5–6	2,830	2.3
Si(100)	2,330	9–10	130	0.95	155	2–4.5	1,410	1.1

<sup>a</sup>Unless otherwise stated, data shown were obtained from [159]

<sup>b</sup>Obtained from [160]

fabricated and have been reported to provide satisfactory operation at high temperatures [164].

As will be shown, bare silicon exhibits inadequate tribological performance and needs to be coated with a solid and/or liquid overcoat or be surface treated (e.g., oxidation and ion implantation, commonly used in semiconductor manufacturing), which reduces friction and wear. SiC films exhibit good tribological performance. Both macroscale and microscale tribological properties of virgin and treated/coated silicon, polysilicon films, and SiC are presented next.

### ***23.2.1 Virgin and Treated/Coated Silicon Samples***

#### **Nanotribological and Nanomechanical Properties of Silicon and Effect of Ion Implantation**

Friction and wear of single-crystalline and polycrystalline silicon samples have been studied, and the effect of ion implantation with various doses of  $C^+$ ,  $B^+$ ,  $N_2^+$ , and  $Ar^+$  ion species at 200 keV energy to improve their friction and wear properties has been studied [165, 166, 167]. The coefficient of macroscale friction and the wear factor of virgin single-crystal silicon and  $C^+$ -implanted silicon samples as a function of ion dose are presented in Fig. 23.16 [165]. The macroscale friction and wear tests were conducted using a ball-on-flat tribometer. Each data bar represents the average value of four to six measurements. The coefficient of friction and wear factor for bare silicon are very high and decrease drastically with ion dose. Silicon samples bombarded with an ion dose above  $10^{17} C^+ cm^{-2}$  exhibit extremely low values of coefficient of friction (typically 0.03–0.06 in air) and wear factor (reduced by as much as four orders of magnitude). Gupta et al. [165] reported that a decrease in the coefficient of friction and wear factor of silicon as a result of  $C^+$  ion bombardment occurred because of the formation of silicon carbide rather than amorphization of silicon. Gupta et al. [166] also reported an improvement in friction and wear with  $B^+$  ion implantation.

Microscale friction measurements were performed using an atomic force/friction force microscope (AFM/FFM) [46, 47, 84, 153]. Table 23.3 presents values of surface roughness and coefficients of macroscale and microscale friction for virgin and doped silicon. There is a decrease in the coefficients of microscale and macroscale friction values as a result of ion implantation. When measured for the small contact areas and very low loads used in microscale studies, indentation hardness and elastic modulus are higher than at the macroscale. This, added to the effect of the small apparent area of contact reducing the number of trapped particles on the interface, results in less plowing contribution and lower friction in the case of microscale friction measurements. Results of microscale wear resistance studies of ion-implanted silicon samples studied using a diamond tip in an AFM [168] are shown in Fig. 23.17a, b. For tests conducted at various loads on Si(111) and  $C^+$ -implanted Si(111), it is noted that the wear resistance of the implanted sample is

**Fig. 23.16** Influence of ion doses on the coefficient of friction and wear factor on C<sup>+</sup>-ion bombarded single-crystal and polycrystalline silicon slid against an alumina ball. V corresponds to virgin single-crystal silicon, while S and P denote tests for doped single- and polycrystalline silicon, respectively (after [165])

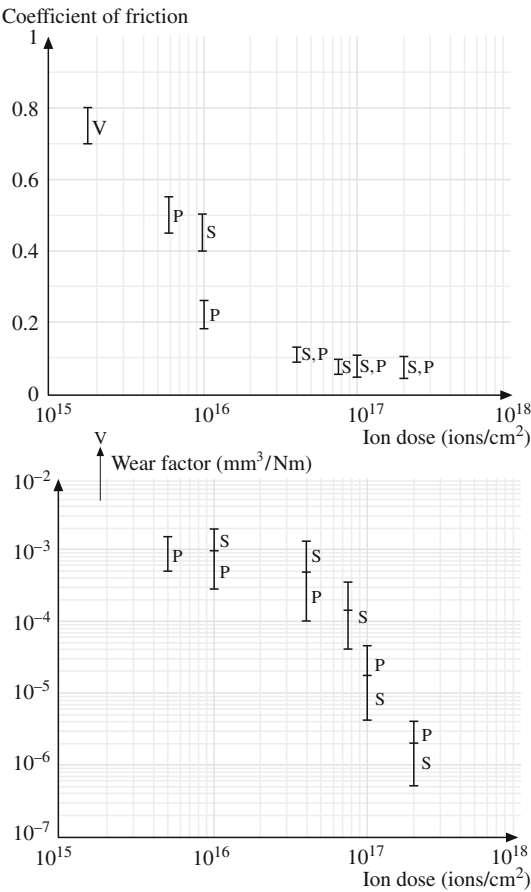


**Table 23.3** Surface roughness and micro- and macroscale coefficients of friction of selected samples

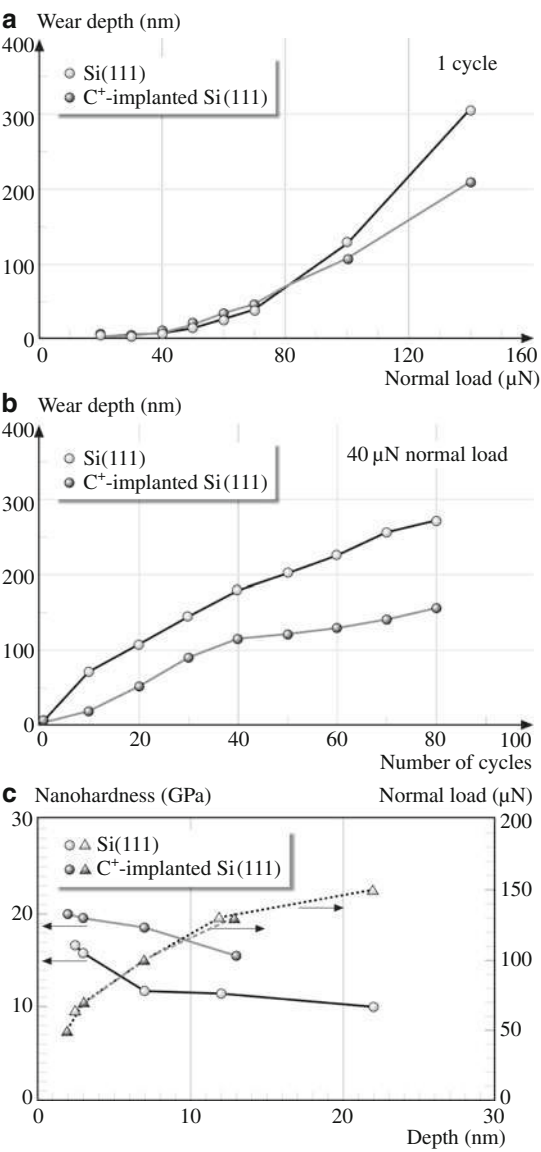
Material	RMS roughness (nm)	Coefficient of microscale friction <sup>a</sup>	Coefficient of macroscale friction <sup>b</sup>
Si(111)	0.11	0.03	0.33
C <sup>+</sup> -implanted Si(111)	0.33	0.02	0.18

<sup>a</sup>Versus Si<sub>3</sub>N<sub>4</sub> tip, tip radius of 50 nm in the load range of 10–150 nN (2.5–6.1 GPa) at a scanning speed of 5 μm/s over a scan area of 1 μm × 1 μm in an AFM

<sup>b</sup>Versus Si<sub>3</sub>N<sub>4</sub> ball, ball radius of 3 mm at a normal load of 0.1 N (0.3 GPa) at an average sliding speed of 0.8 mm/s using a tribometer

slightly poorer than that of virgin silicon up to ≈ 80 μN. Above 80 μN, the wear resistance of implanted Si improves. As one continues to run tests at 40 μN for a larger number of cycles, the implanted sample, which forms hard and tough silicon

**Fig. 23.17** Wear depth as a function of (a) load (after one cycle), and (b) cycles (normal load = 40 mN) for Si(111) and C<sup>+</sup>-implanted Si(111). (c) Nanohardness and normal load as functions of indentation depth for virgin and C<sup>+</sup>-implanted Si(111) (after [168])



carbide, exhibits higher wear resistance than the unimplanted sample. Damage from the implantation in the top layer results in poorer wear resistance; however, the implanted zone at the subsurface is more wear resistant than the virgin silicon.

Hardness values of virgin and C<sup>+</sup>-implanted Si(111) at various indentation depths (normal loads) are presented in Fig. 23.17c [168]. The hardness at a small indentation depth of 2.5 nm is 16.6 GPa, and it drops to a value of 11.7 GPa at a depth of 7 nm and a normal load of 100 μN. Higher hardness values obtained in

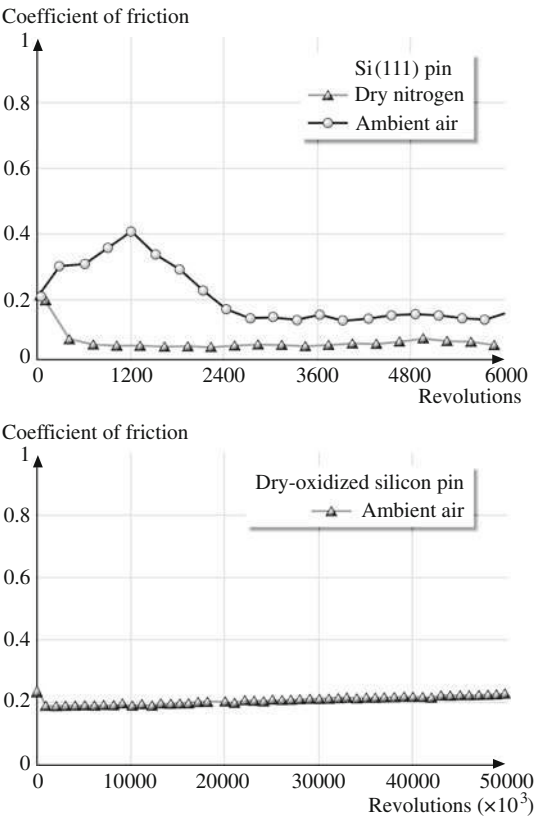
low-load indentation may arise from the observed pressure-induced phase transformation during nanoindentation [169, 170]. Additional increase in the hardness at an even lower indentation depth of 2.5 nm reported here may arise from the contribution of complex chemical films (not from native oxide films) present on the silicon surface. At small volumes there is a lower probability of encountering material defects (dislocations, etc.). Furthermore, according to the strain gradient plasticity theory advanced by Fleck et al. [171], large strain gradients inherent to small indentations lead to the accumulation of geometrically necessary dislocations that cause enhanced hardening. These are some of the plausible explanations for an increase in hardness at smaller volumes. If the silicon material were to be used at very light loads, such as in microsystems, the high hardness of surface films would protect the surface until it is worn.

From Fig. 23.17c, the hardness value of  $C^+$ -implanted Si(111) at normal load of 50  $\mu N$  is 20.0 GPa for an indentation depth of  $\approx 2$  nm, which is comparable to the hardness value of 19.5 GPa at 70  $\mu N$ , whereas the measured hardness value for virgin silicon at an indentation depth of  $\approx 7$  nm (normal load of 100  $\mu N$ ) is only  $\approx 11.7$  GPa. Thus, ion implantation with  $C^+$  results in an increase in hardness in silicon. Note that the surface layer of the implanted zone is much harder compared with the subsurface and may be brittle, leading to higher wear on the surface. The subsurface of the implanted zone (SiC) is harder than the virgin silicon, resulting in higher wear resistance, which is also observed in the results of macroscale tests conducted at high loads.

### Effect of Oxide Films on Nanotribological Properties of Silicon

Macroscale friction and wear experiments have been performed using a magnetic disk drive with bare, oxidized, and implanted pins sliding against amorphous-carbon-coated magnetic disks lubricated with a thin layer of perfluoropolyether lubricant [172, 173, 174, 175]. Representative profiles for the variation of the coefficient of friction with number of sliding cycles for an  $Al_2O_3$ -TiC slider and bare and dry-oxidized silicon pins are shown in Fig. 23.18. For bare Si(111), after an initial increase in the coefficient of friction, it drops to a steady state value of 0.1, as seen in Fig. 23.18. The rise in the coefficient of friction for the Si(111) pin is associated with the transfer of amorphous carbon from the disk to the pin and oxidation-enhanced fracture of pin material, followed by tribochemical oxidation of the transfer film, while the drop is associated with the formation of a transfer coating on the pin. Dry-oxidized Si(111) exhibits excellent characteristics, and no significant increase was observed over 500 cycles (Fig. 23.18). This behavior has been attributed to the chemical passivity of the oxide and the lack of transfer of diamond-like carbon (DLC) from the disk to the pin. The behavior of PECVD oxide (data are not presented here) was comparable to that of dry oxide, but for the wet oxide there was some variation in the coefficient of friction (0.26–0.4). The difference between the dry and wet oxide was attributed to increased porosity of the wet oxide [172]. Since tribochemical oxidation was determined to be a

**Fig. 23.18** Coefficient of friction as a function of number of sliding revolutions in ambient air for a Si(111) pin in ambient air and dry nitrogen, and a dry-oxidized silicon pin in ambient air (after [172])



significant factor, experiments were conducted in dry nitrogen [173, 174]. The variation of the coefficient of friction for a silicon pin sliding against a thin-film disk in dry nitrogen is shown in Fig. 23.18. It is seen that, in a dry nitrogen environment, the coefficient of friction of Si(111) sliding against a disk decreased from an initial value of about 0.2–0.05 with continued sliding. Based on SEM and chemical analysis, this behavior has been attributed to the formation of a smooth amorphous-carbon/lubricant transfer patch and suppression of oxidation in a dry nitrogen environment. Based on macroscale tests using disk drives, it is found that the friction and wear performance of bare silicon is not adequate. With dry-oxidized or PECVD SiO<sub>2</sub>-coated silicon, no significant friction increase or interfacial degradation was observed in ambient air.

Table 23.4 and Fig. 23.19 show surface roughness, microscale friction, and scratch data, and nanoindentation hardness for the various silicon samples [168]. Scratch experiments were performed using a diamond tip in an AFM. Results on polysilicon samples are also shown for comparison. Coefficients of microscale friction values for all the samples are about the same. These samples could be scratched at a 10  $\mu$ N load. Scratch depth increased with normal load. Crystalline

**Table 23.4** RMS, microfriction, microscratching/microwear, and nanoindentation hardness data for various virgin, coated, and treated silicon samples

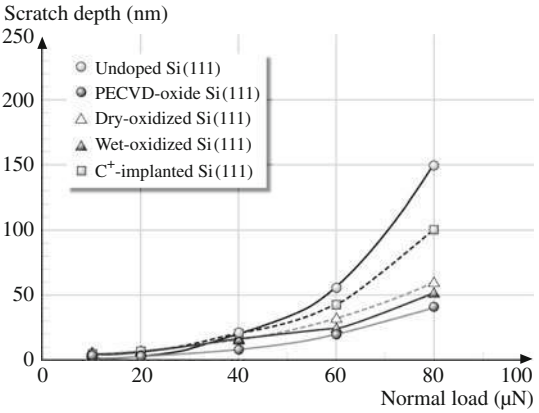
Material	RMS roughness <sup>a</sup> (nm)	Coefficient of microscale friction <sup>b</sup>	Scratch depth <sup>c</sup> at 40 μN (nm)	Wear depth <sup>c</sup> at 40 μN (nm)	Nanohardness <sup>c</sup> at 100 μN (GPa)
Si(111)	0.11	0.03	20	27	11.7
Si(110)	0.09	0.04	20	—	—
Si(100)	0.12	0.03	25	—	—
Polysilicon	1.07	0.04	18	—	—
Polysilicon (lapped)	0.16	0.05	18	25	12.5
PECVD-oxide coated Si(111)	1.50	0.01	8	5	18.0
Dry-oxidized Si(111)	0.11	0.04	16	14	17.0
Wet-oxidized Si(111)	0.25	0.04	17	18	14.4
C <sup>+</sup> -implanted Si(111)	0.33	0.02	20	23	18.6

<sup>a</sup>Scan size of 500 nm × 500 nm using AFM

<sup>b</sup>Versus Si<sub>3</sub>N<sub>4</sub> tip in AFM/FFM, radius 50 nm; at 1 μm × 1 μm scan size

<sup>c</sup>Measured using an AFM with a diamond tip of radius of 100 nm

**Fig. 23.19** Scratch depth as a function of normal load after ten cycles for various silicon samples: virgin, treated, and coated (after [168])



orientation of silicon has little influence on scratch resistance because natural oxidation of silicon in ambient masks the expected effect of crystallographic orientation. PECVD-oxide samples showed the best scratch resistance, followed by dry-oxidized, wet-oxidized, and ion-implanted samples. Ion implantation with C<sup>+</sup> does not appear to improve scratch resistance.

Wear data on the silicon samples are also presented in Table 23.4 [168]. PECVD-oxide samples showed superior wear resistance followed by dry-oxidized, wet-oxidized, and ion-implanted samples. This agrees with the trends seen in scratch resistance. In PECVD, ion bombardment during the deposition improves the coating properties such as suppression of columnar growth, freedom from pinhole, decrease in crystalline size, and increase in density, hardness, and sub-strate-coating adhesion. These effects may help in improving the mechanical integrity of the sample surface. Coatings and treatments improved the nanohardness



of silicon. Note that dry-oxidized and PECVD films are harder than wet-oxidized films as these films may be porous. High hardness of oxidized films may be responsible for the measured high scratch/wear resistance.

### ***23.2.2 Nanotribological and Nanomechanical Properties of Polysilicon Films and SiC Film***

Studies have also been conducted on undoped polysilicon film, heavily doped ( $n^+$ -type) polysilicon film, heavily doped ( $p^+$ -type) single-crystal Si(100), and 3C-SiC (cubic or  $\beta$ -SiC) film [176, 177, 178]. The polysilicon films studied here are different from the ones discussed previously.

Table 23.5 presents a summary of the tribological studies conducted on polysilicon and SiC films. Values for single-crystal silicon are also shown for comparison. Polishing of the as-deposited polysilicon and SiC films drastically affect the roughness as the values reduce by two orders of magnitude. Si(100) appears to be the smoothest, followed by polished undoped polysilicon and SiC films, which have comparable roughness. The doped polysilicon film shows higher roughness than the undoped sample, which is attributed to the doping process. Polished SiC film shows the lowest friction, followed by polished and undoped polysilicon film, which strongly supports the candidacy of SiC films for use in MEMS/NEMS devices. Macroscale friction measurements indicate that SiC film exhibits one of the lowest friction values as compared with the other samples. Doped polysilicon sample shows low friction on the macroscale as compared with the undoped polysilicon sample, possibly due to the doping effect.

Figure 23.20a shows a plot of scratch depth versus normal load for various samples [176, 177]. Scratch depth increases with increasing normal load. Figure 23.21 shows three-dimensional (3-D) AFM maps and averaged two-dimensional (2-D) profiles of the scratch marks on the various samples. It is observed that scratch depth increases almost linearly with normal load. Si(100) and the doped and undoped polysilicon film show similar scratch resistance. From the data, it is clear that the SiC film is much more scratch resistant than the other samples. Figure 23.20b shows results from microscale wear tests on the various films. For all the materials, the wear depth increases almost linearly with increasing number of cycles. This suggests that the material is removed layer by layer in all the materials. Here also, SiC film exhibits lower wear depths than the other samples. Doped polysilicon film wears less than the undoped film. Higher fracture toughness and higher hardness of SiC as compared with Si(100) is responsible for its lower wear. Also the higher thermal conductivity of SiC (Table 23.2) as compared with the other materials leads to lower interface temperatures, which generally results in less degradation of the surface [34, 80, 82]. Doping of the polysilicon does not affect the scratch/wear resistance and hardness much. The measurements made on the doped sample are affected by the presence of grain boundaries. These studies indicate that SiC film exhibits desirable tribological properties for use in MEMS devices.

**Table 23.5** Summary of micro-/nanotribological properties of the sample materials

Sample	RMS roughness <sup>a</sup> (nm)	P-V distance <sup>a</sup> (nm)	Coefficient of friction		Scratch depth <sup>d</sup> (nm)	Wear depth <sup>e</sup> (nm)	Nano-hardness <sup>f</sup> (GPa)	Young's modulus <sup>f</sup> (GPa)	Fracture toughness <sup>g</sup> , $K_{IC}$ MPa m <sup>1/2</sup>
			Micro <sup>b</sup>	Macro <sup>c</sup>					
Undoped Si(100)	0.09	0.9	0.06	0.33	89	84	12	168	0.75
Undoped polysilicon film (as deposited)	46	340	0.05	—	—	—	—	—	—
Undoped polysilicon film (polished)	0.86	6	0.04	0.46	99	140	12	175	1.11
n <sup>+</sup> -Type polysilicon film (as deposited)	12	91	0.07	—	—	—	—	—	—
n <sup>+</sup> -Type polysilicon film (polished)	1.0	7	0.02	0.23	61	51	9	95	0.89
SiC film (as deposited)	25	150	0.03	—	—	—	—	—	—
SiC film (polished)	0.89	6	0.02	0.20	6	16	25	395	0.78

<sup>a</sup>Measured using AFM over a scan size of 10  $\mu\text{m} \times 10 \mu\text{m}$

<sup>b</sup>Measured using AFM/FFM over a scan size of 10  $\mu\text{m} \times 10 \mu\text{m}$

<sup>c</sup>Obtained using a 3 mm-diameter sapphire ball in a reciprocating mode at a normal load of 10 mN and average sliding speed of 1 mm/s after 4 m sliding distance

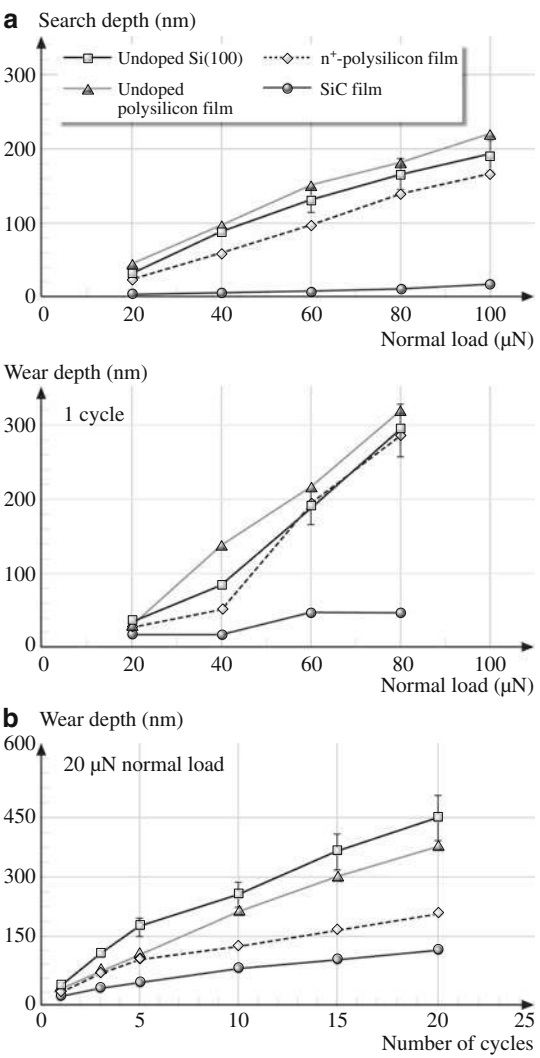
<sup>d</sup>Measured using AFM at a normal load of 40  $\mu\text{N}$  for ten cycles, scan length of 5  $\mu\text{m}$

<sup>e</sup>Measured using AFM at normal load of 40  $\mu\text{N}$  for one cycle, wear area of 2  $\mu\text{m} \times 2 \mu\text{m}$

<sup>f</sup>Measured using nanoindenter at a peak indentation depth of 20 nm

<sup>g</sup>Measured using microindenter with Vickers indenter at a normal load of 0.5 N

**Fig. 23.20** (a) Scratch depths for ten cycles as a function of normal load, and (b) wear depths as a function of normal load and as a function of number of cycles for various samples (after [176])



### 23.3 Lubrication Studies for MEMS/NEMS

Several studies of liquid perfluoropolyether (PFPE) lubricant films, self-assembled monolayers (SAMs), and hard diamond-like carbon (DLC) coatings have been carried out for the purpose of minimizing adhesion, friction, and wear [46, 47, 80, 81, 82, 83, 84, 152, 153, 154, 155, 175]. Many variations of these films are hydrophobic (low surface tension and high contact angle) and have low shear strength, which provides low adhesion, friction, and wear. Relevant details are presented below.

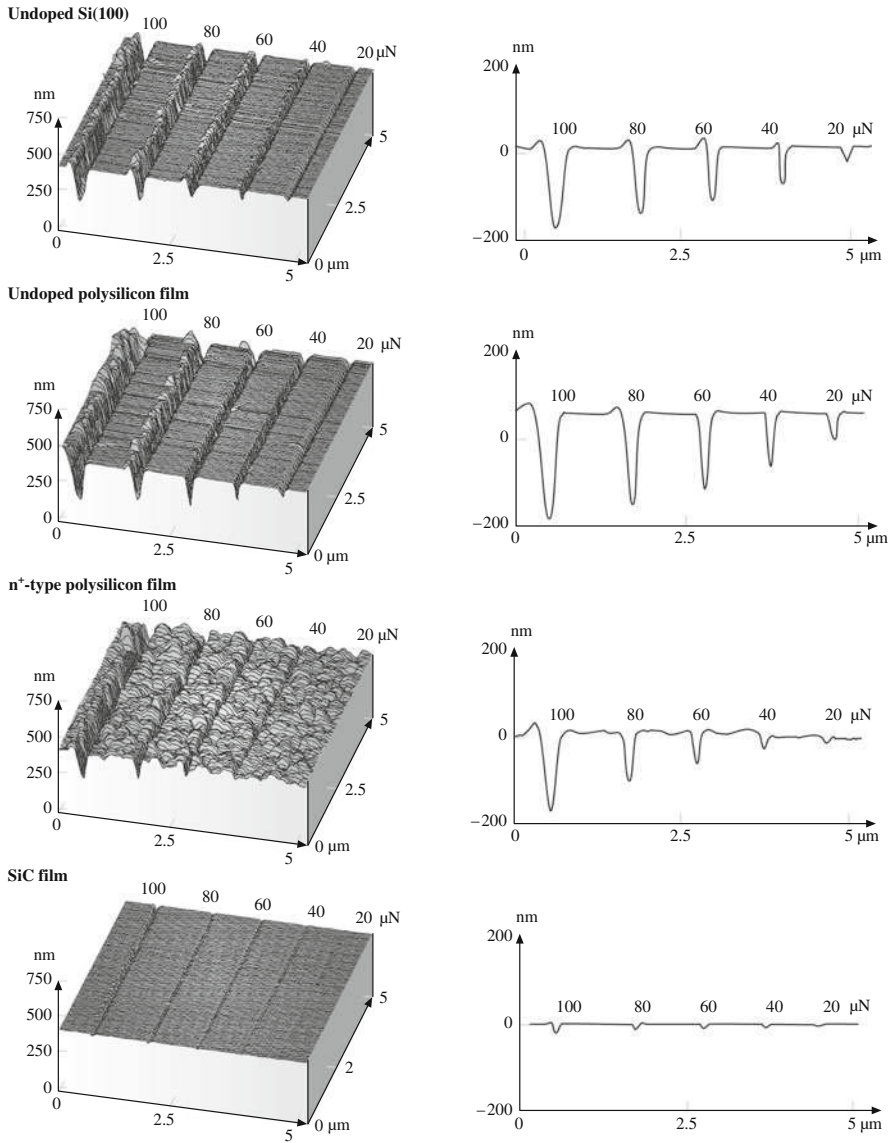


**Fig. 23.21** AFM 3-D maps and averaged 2-D profiles of scratch marks on various samples (after [176])

### 23.3.1 Perfluoropolyether Lubricants

The classical approach to lubrication uses freely supported multimolecular layers of liquid lubricants [46, 80, 82, 84]. The liquid lubricants are sometimes chemically

bonded to improve their wear resistance. Partially chemically bonded, molecularly thick perfluoropolyether (PFPE) lubricants are widely used for lubrication of magnetic storage media, because of their thermal stability and extremely low vapor pressure [34], and are found to be suitable for MEMS/NEMS devices.

Adhesion, friction, and durability experiments have been performed on virgin Si(100) surfaces and silicon surfaces lubricated with various PFPE lubricants [46, 47, 179, 180, 181, 182, 183, 184, 185]. Results of the following two PFPE lubricants will be presented here: Z-15 (with  $-\text{CF}_3$  nonpolar end groups),  $\text{CF}_3-\text{O}-(\text{CF}_2-\text{CF}_2-\text{O})_m-(\text{CF}_2-\text{O})_n-\text{CF}_3$  ( $m/n \approx 2/3$ ); and Z-DOL (with  $-\text{OH}$  polar end groups),  $\text{HO}-\text{CH}_2-\text{CF}_2-\text{O}-(\text{CF}_2-\text{CF}_2-\text{O})_m-(\text{CF}_2-\text{O})_n-\text{CF}_2-\text{CH}_2-\text{OH}$  ( $m/n \approx 2/3$ ). Z-DOL film was thermally bonded at  $150^\circ\text{C}$  for 30 min, and the unbonded fraction was removed by a solvent (fully bonded) [34]. The thicknesses of Z-15 and Z-DOL (fully bonded) films were 2.8 and 2.3 nm, respectively. Nanoscale measurements were made using an AFM. The adhesive forces of Si(100), Z-15, and Z-DOL (fully bonded) measured by force calibration plot, and friction force versus normal load plot, are summarized in Fig. 23.22. The results measured by these two methods are in good agreement. Figure 23.22 shows that the presence of mobile Z-15 lubricant film increases the adhesive force as compared

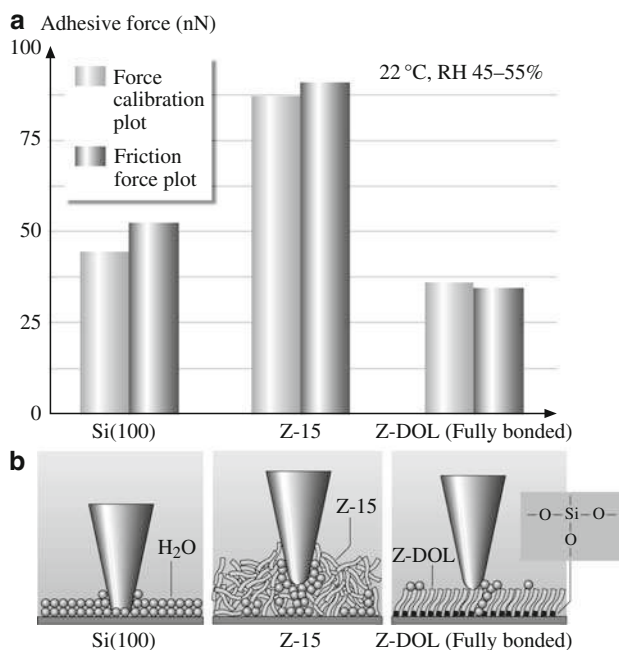


**Fig. 23.22** (a) Summary of the adhesive forces of Si(100), Z-15, and Z-DOL (fully bonded) films measured by force calibration plots and friction force versus normal load plots in ambient air. (b) Schematic showing the effect of meniscus, formed between the AFM tip and the surface sample, on the adhesive and friction forces (after [179])

with that of Si(100) by meniscus formation [80, 82, 186], whereas the presence of solid-phase Z-DOL (fully bonded) film reduces the adhesive force as compared with that of Si(100) because of the absence of mobile liquid. The schematic (bottom) in Fig. 23.22 shows the relative size and sources of meniscus. It is well known that the native oxide layer ( $\text{SiO}_2$ ) on the top of Si(100) wafer exhibits hydrophilic properties, and some water molecules can be adsorbed on this surface. The condensed water will form a meniscus as the tip approaches the sample surface. The larger adhesive force in Z-15 is not just caused by the Z-15 meniscus; the nonpolarized Z-15 liquid does not have good wettability and strong bonding with Si(100). Consequently, in the ambient environment, condensed water molecules from the environment permeate through the liquid Z-15 lubricant film and compete with the lubricant molecules present on the substrate. The interaction of the liquid lubricant with the substrate is weakened, and a boundary layer of the liquid lubricant forms puddles [180, 181]. This dewetting allows water molecules to be adsorbed onto the Si(100) surface as aggregates along with Z-15 molecules, and both of them can form a meniscus while the tip approaches the surface. Thus, the dewetting of liquid Z-15 film results in higher adhesive force and poorer lubrication performance. In addition, as the Z-15 film is fairly soft compared with the solid Si(100) surface, penetration of the tip into the film occurs while pushing the tip down. This leads to a large area of the tip being involved in forming the meniscus at the tip–liquid (mixture of Z-15 and water) interface. It should also be noted that Z-15 has a higher viscosity compared with water, therefore Z-15 film provides higher resistance to lateral motion and coefficient of friction. In the case of Z-DOL (fully bonded) film, the active groups of Z-DOL molecules are mostly bonded onto Si(100) substrate, thus the Z-DOL (fully bonded) film has low free surface energy and cannot be displaced readily by water molecules or readily adsorb water molecules. Thus, the use of Z-DOL (fully bonded) can reduce the adhesive force.

To study the effect of relative humidity on friction and adhesion, the variation of friction force, adhesive force, and coefficient of friction of Si(100), Z-15, and Z-DOL (fully bonded) as a function of relative humidity are shown in Fig. 23.23. It shows that, for Si(100) and Z-15 film, the friction force increases with a relative humidity increase up to 45% and then shows a slight decrease with further increase in relative humidity. Z-DOL (fully bonded) has smaller friction force than Si(100) and Z-15 in the whole testing range, and its friction force shows an apparent relative increase for relative humidity > 45%. For Si(100), Z-15, and Z-DOL (fully bonded), their adhesive forces increase with relative humidity, and their coefficients of friction increase with a relative humidity up to 45%, after which they decrease with further increasing of the relative humidity. It is also observed that the effect of humidity on Si(100) really depends on the history of the Si(100) sample. As the surface of the Si(100) wafer readily adsorbs water in air, without any pretreatment the Si(100) used in our study almost reaches its saturated stage of adsorbed water, and is responsible for less effect during increasing relative humidity. However, once the Si(100) wafer was thermally treated by baking at 150°C for 1 h, a greater effect was observed.

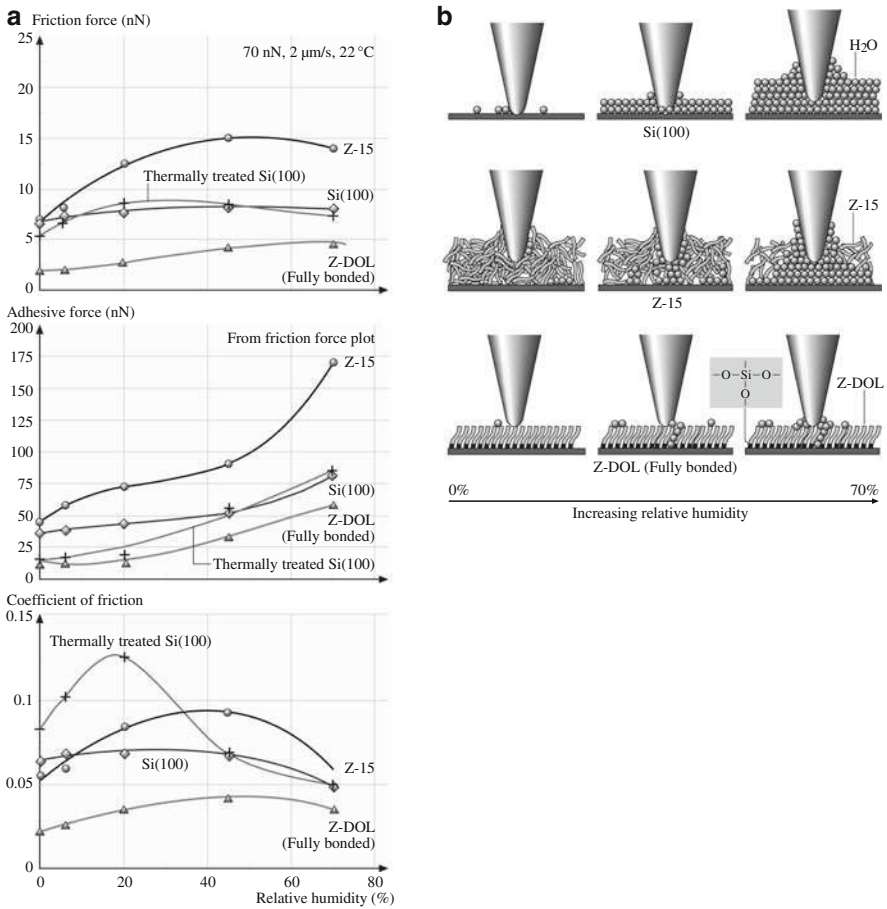


**Fig. 23.23** (a) Influence of relative humidity on the friction force, adhesive force, and coefficient of friction of Si(100), Z-15, and Z-DOL (fully bonded) films at 70 nN, 2 μm/s, and in 22 °C air. (b) Schematic showing the change of meniscus on increasing the relative humidity. In this figure, thermally treated Si(100) is Si(100) wafer that was baked at 150 °C for 1 h in an oven (in order to remove the adsorbed water) just before it was placed in the 0% RH chamber (after [179])

The schematic (right) in Fig. 23.23 shows that Si(100), because of its high free surface energy, can adsorb more water molecules with increasing relative humidity. As discussed earlier, for the Z-15 film in the humid environment, the condensed water competes with the lubricant film present on the sample surface, and interaction of the liquid lubricant film with the silicon substrate is weakened and a boundary layer of the liquid lubricant forms puddles. This dewetting allows water molecules to be adsorbed onto the Si(100) substrate mixed with Z-15 molecules [180, 181]. Obviously, more water molecules can be adsorbed on the Z-15 surface with increasing relative humidity. The more adsorbed water molecules in the case of Si(100), along with lubricant molecules in the Z-15 film case, form a bigger





during the initial few cycles and then approaches higher and stable values. This is believed to be caused by attachment of the Z-15 molecules to the tip. The molecular interaction between these molecules attached to the tip and molecules on the film surface is responsible for the increase in friction. However, after several scans, this molecular interaction reaches equilibrium, after which the friction force and coefficient of friction remain constant. In the case of the Z-DOL (fully bonded) film, the friction force and coefficient of friction start out low and remain low during the entire test for 100 cycles. This suggests that Z-DOL (fully bonded) molecules do not become attached or displaced as readily as those of Z-15.

### 23.3.2 Self-assembled Monolayers (SAMs)

For lubrication of MEMS/NEMS, another effective approach involves the deposition of organized and dense molecular layers of long-chain molecules. Two common methods to produce monolayers and thin films are the Langmuir–Blodgett (L–B) deposition and self-assembled monolayers (SAMs) by chemical grafting of molecules. L–B films are physically bonded to the substrate by a weak van der Waals attraction, while SAMs are chemically bonded via covalent bonds to the substrate. Because of the choice of chain length and terminal linking group that SAMs offer, they hold great promise for boundary lubrication of MEMS/NEMS. A number of studies have been conducted on the tribological properties of various SAMs [138, 139, 140, 141, 187, 188, 189, 190, 191, 192, 193].

Bhushan and Liu [188] studied the effect of film compliance on adhesion and friction. Based on friction and stiffness measurements, SAMs with high-compliance long carbon chains exhibit low friction; chain compliance is desirable for low friction. The friction mechanism of SAMs is explained by a so-called *molecular-spring* model. According to this model, chemically adsorbed self-assembled molecules on a substrate are just like assembled molecular springs anchored to the substrate. An asperity sliding on the surface of SAMs is like a tip sliding on the top of *molecular springs* or a *molecular brush*. The molecular-spring assembly has compliant features and can experience orientation and compression under load. The orientation of the molecular springs or brush under normal load reduces the shearing force at the interface, which in turn reduces the friction force. The orientation is determined by the spring constant of a single molecule as well as the interaction between the neighboring molecules, which can be reflected by packing density or packing energy. It should be noted that orientation can lead to conformational defects along the molecular chains, which leads to energy dissipation. SAMs with high-compliance long carbon chains also exhibit the best wear resistance [188, 190]. In wear experiments, curves of wear depth as a function of normal load show a critical normal load. Below the critical normal load, SAMs undergo orientation. At the critical load, SAMs wear away from the substrate due to weak interface bond strengths, while above the critical normal load severe wear takes place on the substrate.

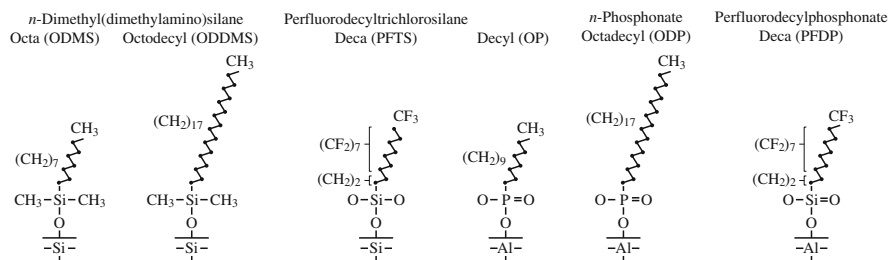


**Fig. 23.25** Schematics of the structures of perfluoroalkylsilane and alkylsilane SAMs on Si with native oxide substrates, and perfluoroalkylphosphonate and alkylphosphonate SAMs on Al with native oxide substrates

Bhushan et al. [139, 191], Kasai et al. [141], Tambe and Bhushan [192], and Tao and Bhushan [193] studied various SAMs which were vapor-phase-deposited on Si and Al substrates with native oxide films (Fig. 23.25). Perfluorodecyltrichlorosilane (PFTS), *n*-octyldimethyl(dimethylamino)silane (ODMS) ( $n = 7$ ), and *n*-octadecylmethyl(dimethylamino)silane (ODDMS) ( $n = 17$ ) were deposited on Si substrate. Perfluorodecylphosphonate (PFDP), *n*-decylphosphonate (DP) ( $n = 7$ ), and *n*-octadecylphosphonate (ODP) ( $n = 17$ ) were deposited on Al substrate. Figure 23.26 shows the static contact angle, adhesive force, friction force, and coefficient of friction of the two substrates with various SAMs under ambient conditions [139, 191]. Based on the data, all films exhibit higher contact angle and lower adhesive force and coefficient of friction as compared with corresponding substrates. Among the various films, PFTS/Si exhibits higher contact angle and lower adhesive force as compared with ODMS/Si and ODDMS/Si. Longer-chain film ODDMS/Si has superior performance than shorter-chain film ODMS. Trends for films on Al substrate are similar to that on Si substrate. Thus, substrate had little effect. The coefficients of friction of various SAMs are comparable.

The effect of relative humidity for various SAMs on Si substrate on adhesion and friction was studied. Adhesive force, friction force at 5 nN of normal load, coefficient of friction, and microwear data are presented in Fig. 23.27 [141, 191]. The result of adhesive force for silicon showed an increase with relative humidity. This is expected since the surface of silicon is hydrophilic, as shown in Fig. 23.26. More condensation of water at the tip-sample interface at higher humidity increases the adhesive force due to the capillary effect. On the other hand, the adhesive force for the SAMs showed a very weak dependency on humidity. This occurs since the surface of the SAMs is hydrophobic. The adhesive force of ODMS/Si and ODDMS/Si showed a slight increase from 75 to 90% RH. Such increase was absent for PFTS/Si, possibly because of the hydrophobicity of PFTS/Si. The friction force of silicon showed an increase with relative humidity up to  $\approx 75\%$  RH and a slight decrease beyond this point. The initial increase possibly results from the increase in adhesive force. The decrease in friction force at higher humidity could be attributed to the lubricating effect of the water layer. This effect is more pronounced in the coefficient of friction. Since the adhesive force increased and the coefficient

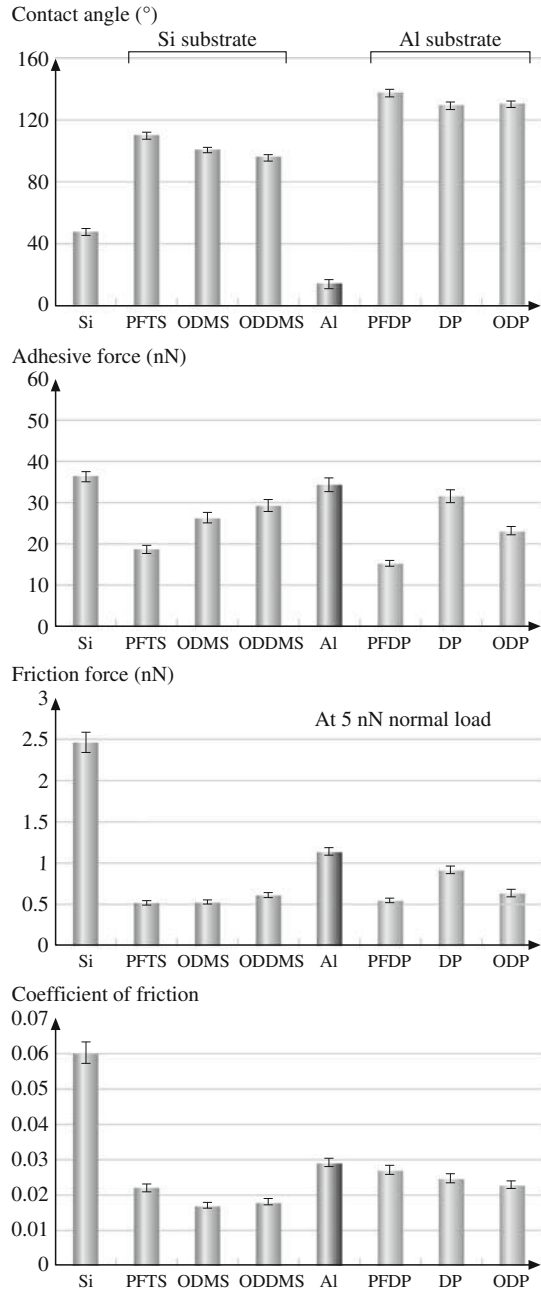


**Fig. 23.26** The static contact angle, adhesive force, friction force, and coefficient of friction measured using an AFM for various SAMs on Si and Al substrates (after [131,139,191])

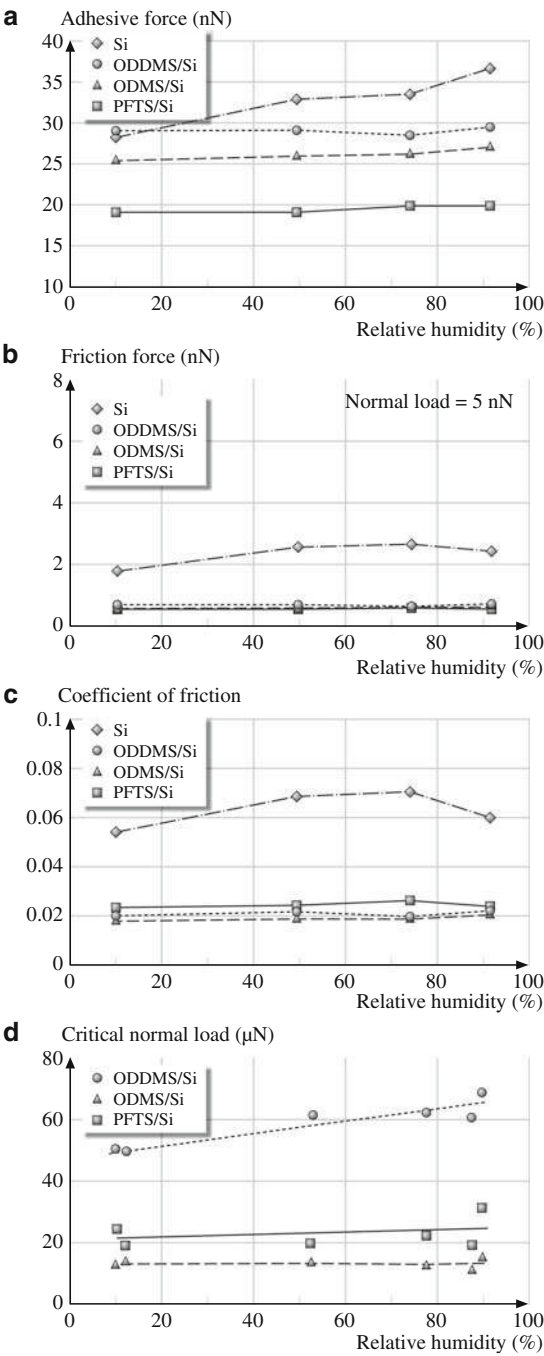


**Fig. 23.27** Effect of relative humidity on (a) adhesive force, (b) friction force, (c) coefficient of friction, and (d) microwear for various SAMs on Si substrate (after [141, 191])

of friction decreased in this range, those effects cancel out each other, and the resulting friction force showed slight changes. On the other hand, the friction force and coefficient of friction of SAMs showed very small changes with relative humidity, like that found for adhesive force. This suggests that the adsorbed water layer on the surface maintained a similar thickness throughout the tested relative humidity range. The differences among the SAM types were small, within the measurement error; however, a closer look at the coefficient of friction for ODMs/Si showed a slight increase from 75% to 90% RH as compared with PFTS/Si, possibly due to the same reason as for the adhesive force increment. The inherent hydrophobicity of SAMs means that they did not show much relative humidity dependence.

Figure 23.28a shows the relationship between the decrease in surface height as a function of the normal load during wear tests for various SAMs on Si and Al substrates [141, 191]. As shown in the figure, the SAMs exhibit a critical normal load, beyond which the surface height drastically decreases. Figure 23.28a also shows the wear behavior of the Al and Si substrates. Unlike the SAMs, the substrates show a monotonic decrease in surface height with increasing normal load, with wear initiating from the very beginning, i.e., even for low normal loads. Si (Young's modulus of elasticity,  $E = 130$  GPa [194, 195], hardness,  $H = 11$  GPa [175]) is relatively hard in comparison with Al ( $E = 77$  GPa,  $H = 0.41$  GPa), and hence the decrease in surface height for Al is much larger than that for Si for similar normal loads.

The critical loads corresponding to the sudden failure of SAMs are shown in Fig. 23.28b. Amongst all the SAMs, ODDMS shows the best performance in the wear tests, which is believed to be because of the effect of the longer chain length. Fluorinated SAMs – PFTS and PFDP – show higher critical load as compared with ODMs and DP with similar chain lengths. ODP shows higher critical load as compared with DP because of its longer chain length. The mechanism of failure of compliant SAMs during wear tests was presented earlier. It is believed that the SAMs fail mostly due to shearing of the molecule at the head group, that is, by means of shearing of the molecules off the substrate.

To study the effect of relative humidity, wear tests were performed at various humidities. Figure 23.27d shows critical normal load as a function of relative humidity. The critical normal load showed weak dependency on relative humidity for ODMs/Si and PFTS/Si, and was larger for ODMs/Si than PFTS/Si throughout the humidity range. This suggests that water molecules could penetrate into the ODDMS, which might work as a lubricant [190]. This effect was absent for PFTS/Si and ODMs/Si.

Bhushan et al. [140] and Lee et al. [138] studied various fluoropolymer multilayers and fluorosilane monolayers on Si and a selected fluorosilane on PDMS surfaces. For nanoscale devices, such as in nanochannels, monolayers are preferred. They reported that all fluorosilane films increased the contact angle. The fluorosilane monolayer – 1H,1H, 2H, 2H-perfluorodecyltriethoxysilane (PFDTES) – resulted in a contact angle of  $\approx 100^\circ$ .

Based on these studies, a perfluoro SAM with a compliant layer should have optimized tribological performance for MEMS/NEMS and bioMEMS/bioNEMS applications.

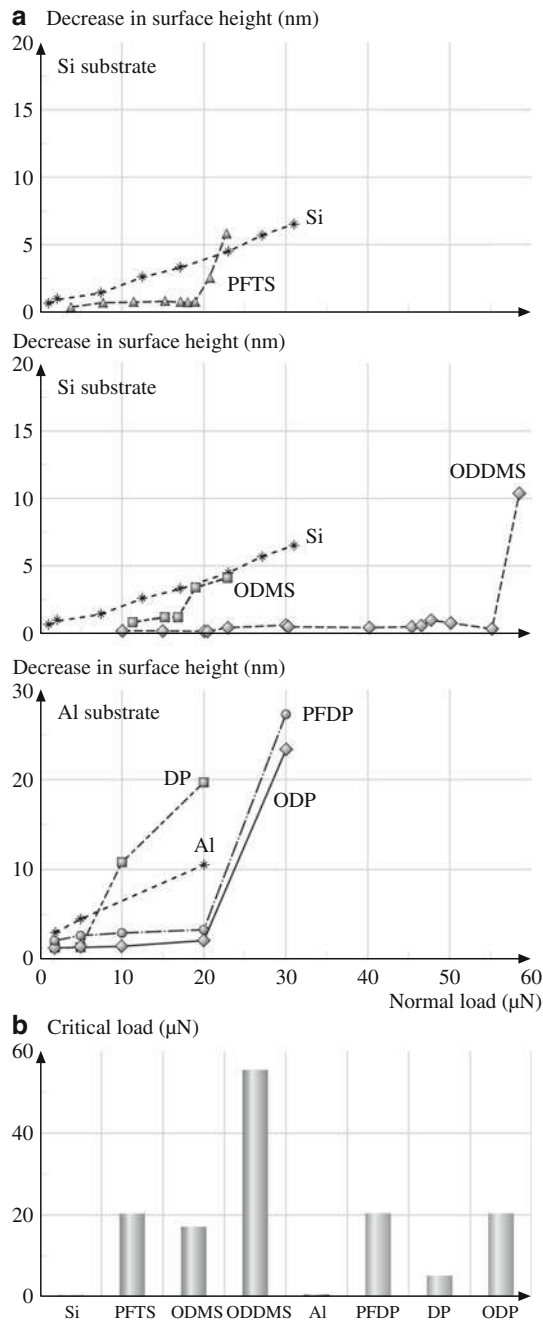


**Fig. 23.28** (a) Decrease in surface height as a function of normal load after one scan cycle for various SAMs on Si and Al substrates. (b) Comparison of critical loads for failure during wear tests for various SAMs (after [133,191])

### **23.3.3 Hard Diamond-Like Carbon (DLC) Coatings**

Hard amorphous carbon (a-C), commonly known as DLC (implying high hardness), coatings are deposited by a variety of deposition techniques, including filtered cathodic arc (FCA), ion beam, electron cyclotron resonance chemical vapor deposition (ECR-CVD), plasma-enhanced chemical vapor deposition (PECVD), and sputtering [159, 175]. These coatings are used in a wide range of applications, including tribological, optical, electronic, and biomedical applications. Ultrathin coatings (3–10 nm thick) are employed to protect against wear and corrosion in magnetic storage applications – thin-film rigid disks, metal evaporated tapes, and thin-film read/write head –, Gillette Mach 3 razor blades, glass windows, and sunglasses. The coatings exhibit low friction, high hardness and wear resistance, chemical inertness to both acids and alkalis, lack of magnetic response, and optical bandgap ranging from zero to a few electron-volts, depending upon the deposition technique and its conditions. Selected data on DLC coatings relevant for MEMS/NEMS applications are presented in a following section on adhesion measurements.

## **23.4 Nanotribological Studies of Biological Molecules on Silicon-Based and Polymer Surfaces and Submicron Particles for Therapeutics and Diagnostics**

### **23.4.1 Adhesion, Friction, and Wear of Biomolecules on Si-Based Surfaces**

Proteins on silicon-based surfaces are of extreme importance in various applications, including silicon microimplants, various bioMEMS such as biosensors, and therapeutics. Silicon is a commonly used substrate in microimplants, but it can have undesired interactions with the human immune system. Therefore, to mimic a biological surface, protein coatings are used on silicon-based surfaces as passivation layers, so that these implants are compatible with the body, avoiding rejection. Whether this surface treatment is applied to a large implant or a bioMEMS, the function of the protein passivation is obtained from the nanoscale 3-D structural conformation of the protein. Proteins are also used in bioMEMS because of their function specificity. For biosensor applications, the extensive array of protein activities provides a rich supply of operations that may be performed at the nanoscale. Many antibodies (proteins) have an affinity to specific protein antigens. For example, pathogens (disease-causing agents, e.g., viruses or bacteria) trigger the production of antigens which can be detected when bound to a specific antibody on the biosensor. The specific binding behavior of proteins that has been applied to laboratory assays may also be redesigned for in vivo use as sensing elements of a bioMEMS. The epitope-specific binding properties of proteins to various antigens are useful in therapeutics. Adhesion between the protein and substrate affects the

reliability of an application. Among other things, the morphology of the substrate affects the adhesion. Furthermore, for in vivo environments, the proteins on the biosensor surface should exhibit high wear resistance during direct contact with tissue and circulatory blood flow without washing off.

Bhushan et al. [73] studied the step-by-step morphological changes and the adhesion of a model protein – streptavidin (STA) – on silicon-based surfaces. (Also see [134, 136, 196].) Figure 23.29a presents a flowchart showing the

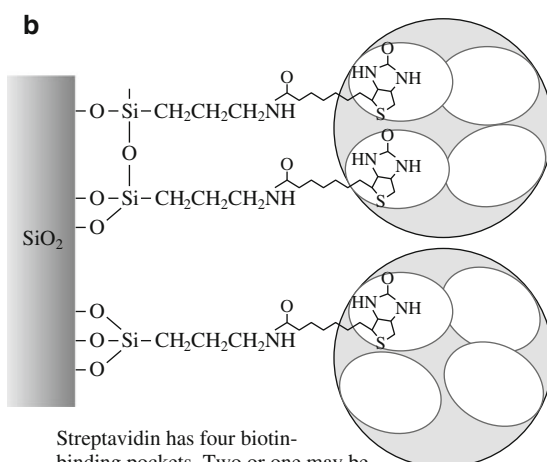
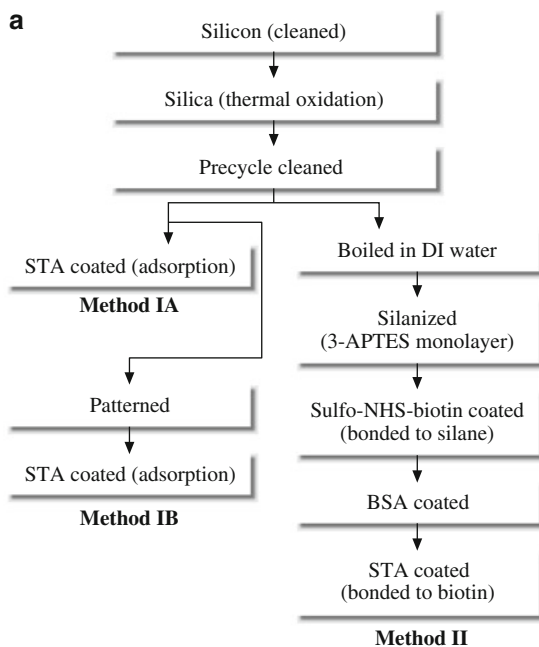


**Fig. 23.29** (a) Flowchart showing the samples used and their preparation technique. (b) Chemical structure showing streptavidin protein binding to the silica substrate by the chemical linker method

Streptavidin has four biotin-binding pockets. Two or one may be attached to the biotin on the surface, with the remaining two or three available to bind the biotin analyte



sequential modification of a silicon surface. In addition to physical adsorption, they also used nanopatterning and chemical linker methods to improve adhesion. A nanopatterned surface contains large edge surface area, leading to high surface energy which results in high adhesion. In the chemical linker method, sulfo-N-hydroxysuccinimido-biotin (sulfo-NHS-biotin) was used as a cross-linker because the bonds between the STA and the biotin molecule are one of the strongest noncovalent bonds known (Fig. 23.29b). It was connected to the silica surface through a silane linker, 3-aminopropyltriethoxysilane (3-APTES). In order to make a bond between the silane linker and the silica surface, the silica surface was hydroxylated. Bovine serum albumin (BSA) was used before STA in order to block nonspecific binding sites of the STA protein with silica surface. Figure 23.30 shows the step-by-step morphological changes in the silica surface during the deposition process using the chemical linker method. There is an increase in roughness [ $\sigma$  and peak-to-valley (P-V) distance] of the silica surface boiled in deionized (DI) water compared with the bare silica surface. After the silanization process, there are many free silane links on the surface, which caused higher roughness. Once biotin was coated on the silanized surface, the surface became smoother. Finally, after the deposition of STA, the surface shows large and small clumps. Presumably, the large clumps represent BSA, and the smaller ones represent STA. To measure adhesion between STA and the corresponding substrates, an STA-coated tip (or functionalized tip) was used and all measurements were made in phosphate-buffered saline (PBS) solution, a medium commonly used in protein analysis to simulate body fluid. Figure 23.31 shows the adhesion values of various surfaces. The adhesion value between biotin and STA was higher than that for other samples, as expected. Edges of patterned silica also exhibited high adhesion values. It appears that both nanopatterned surfaces and the chemical linker method increase adhesion with STA.

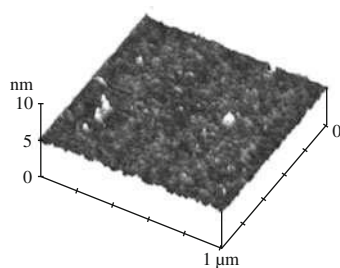
Bhushan et al. [131] studied friction and wear of STA deposited by physical adsorption and the chemical linker method. (Also see [137].) Figure 23.32 shows the coefficient of friction between the  $\text{Si}_3\text{N}_4$  tip and various samples. The coefficient of friction is less for STA-coated silica samples compared with an uncoated sample. The streptavidin coating acts as a lubricant film. The coefficient of friction is found to be dependent upon the concentration of STA, and it decreases with increasing concentration. Bhushan et al. [73] have reported that the density and distribution of the biomolecules vary with concentration. At higher concentration of the solution, the coated layer is more uniform, and the silica substrate surface is more highly covered with biomolecules than at lower concentration. This means that the surface forms a continuous lubricant film at higher concentration.

In the case of samples prepared by the chemical linker method, the coefficient of friction increases with increasing biomolecular chain length due to increased compliance. When a normal load is applied to the surface, the surface gets compressed, resulting in a larger contact area between the AFM tip and the biomolecules. Besides that, the size of STA is much larger than that of APTES and biotin. This results in a tightly packed surface with the biomolecules, which results in very little lateral deflection of the linker in the case of STA-coated biotin. Due to

**Fig. 23.30** Morphological changes in a silica surface during functionalization by the chemical linker, imaged in PBS. Streptavidin is covalently bonded at 10  $\mu\text{g/ml}$  concentration (after [73])

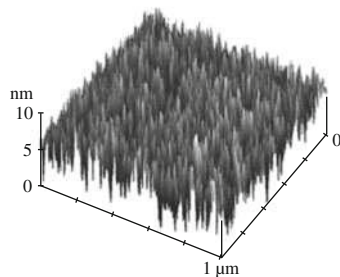
**Silica boiled in DI water**

$\sigma = 0.12 \text{ nm}$   
P-V = 3 nm



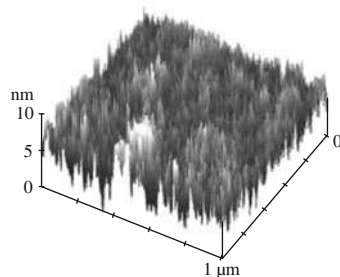
**Silanized (3-APTES monolayers) silica**

$\sigma = 1.1 \text{ nm}$   
P-V = 17 nm



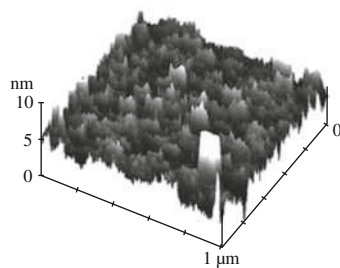
**After coating with sulphonHSH-biotin (bonded to silane)**

$\sigma = 0.96 \text{ nm}$   
P-V = 15 nm



**After coating with BSA**

$\sigma = 0.62 \text{ nm}$   
P-V = 14 nm



**After coating with streptavidin (bonded to biotin) at 10  $\mu\text{g/ml}$**

$\sigma = 0.78 \text{ nm}$   
P-V = 15 nm

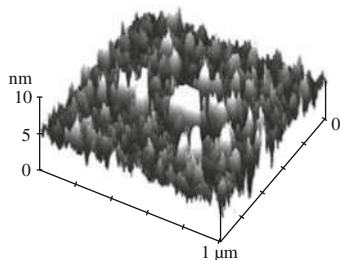


**Fig. 23.31** Adhesion measurements of silica, patterned silicon, silica boiled in DI water, and sulfo-NHS-biotin using functionalized (with streptavidin) tips obtained from force–distance curves, captured in PBS

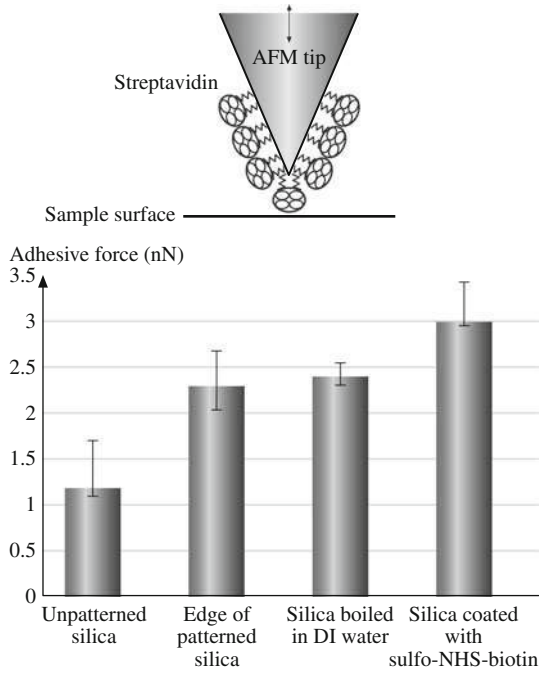
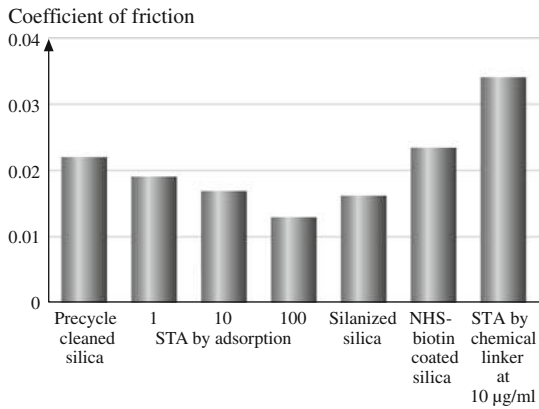


**Fig. 23.32** Coefficient of friction in PBS for various surfaces with and without biomolecules (after [133])



this high contact area and low lateral deflection, the friction force increases for the same applied normal load compared with the directly adsorbed surface. These tests reveal that surfaces coated with biomolecules reduce the friction, but if the biomolecular coating of the surface is too thick or the surface has some cushioning effect as seen in the chemical linker method, this will increase the coefficient of friction.

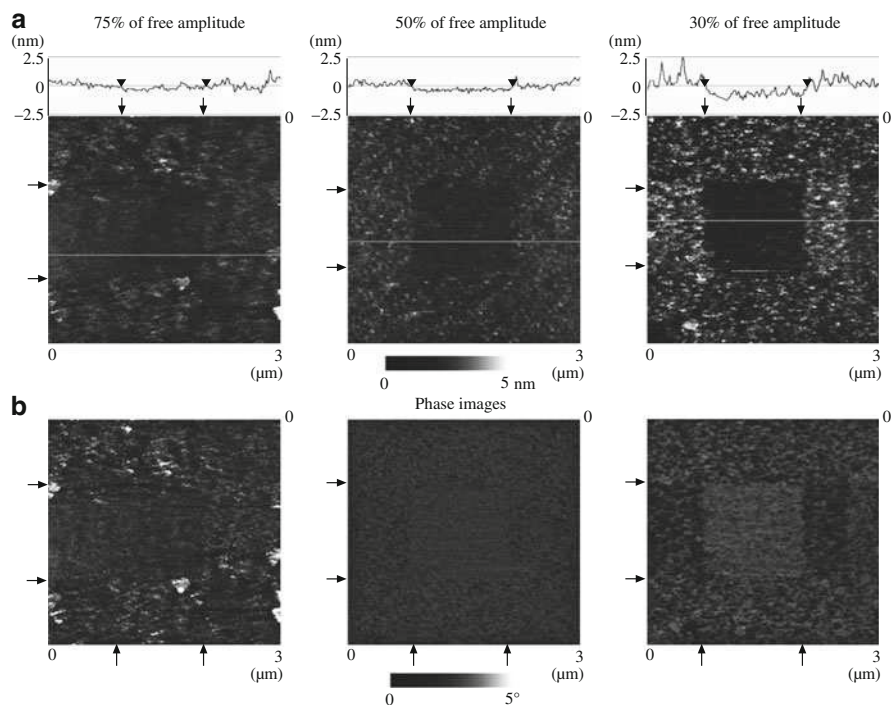


**Fig. 23.33** Surface height maps and cross-sectional profiles **(a)** and phase images **(b)** of wear marks on precycle cleaned silica coated with streptavidin by physical adsorption after wear tests at three normal loads (increasing from *left to right*). The 75, 50 and 30% of free amplitudes correspond to equivalent normal loads of 3, 6 and 8 nN, respectively (after [133])

Figure 23.33 shows the surface height maps and phase images of wear marks on STA deposited by physical adsorption after wear tests at three normal loads. The wear depth increases with increasing normal load. An increase in normal load causes partial damage to the folding structure of the streptavidin molecules. It is unlikely that the chemical (covalent) bonds within the streptavidin molecule are broken; instead, the folding structure is damaged, leading to wear marks. When the load is high,  $\approx 30\%$  of free amplitude ( $\approx 8$  nN), the molecules may have been removed by the AFM tip due to indentation effect. Because of this, there is significant increase in the wear depth from 50% of free amplitude ( $\approx 6$  nN) to 30% of free amplitude ( $\approx 8$  nN). The data show that biomolecules will be damaged during sliding.

In summary, for samples prepared using nanopatterning and the chemical linker methods, adhesion is higher compared with those prepared by the direct adsorption method. The coefficient of friction is lower for STA-coated silica prepared using the direct adsorption method as compared with an uncoated silica sample. Coefficient of friction decreases with increasing concentration of STA in the solution because protein acts as a lubricating film. Friction increases for the STA sample

prepared using the chemical linker method due to the cushioning effect and low lateral deformation. Wear of STA increases with the increasing load.

### APDMES to Improve Adhesion, Friction, and Wear of Biomolecular Films

APTES films used in the just-reported study were not very smooth, and P–V distances were substantially greater than the summed bond strengths of APTES. The biotin/STA deposited on APTES films was not very robust. APTES films are commonly described as SAMs, though this is often inaccurate [197, 198, 199]. APTES monomers can form infinite, cross-linked siloxane polymer lattices because APTES is a multivalent (trivalent) silane and can form a multilayered structure due to intermolecular polymerization with significant cross-linking between monomers. It should consist of sparse cross-links between the polymer and the substrate (Fig. 23.34) [136]. The propensity to form multilayers and its low mechanical strength makes APTES an undesirable interface material. On the other hand, 3-aminopropyldimethethoxysilane (APDMES) cannot polymerize into extensive networks because it is monovalent, forming only siloxane dimers or linkages to substrate oxides (Fig. 23.34). APDMES should therefore produce thinner films of greater mechanical robustness than APTES, and provide robustness to biomolecular layers deposited on top of it. Thinner interfaces would also theoretically increase sensor sensitivity to analyte.

Bhushan et al. [136] examined the thickness and durability of APDMES deposited on  $\text{SiO}_2$  and  $\text{Al}_2\text{O}_3$  substrates, with biotin and biotin/STA bound to them. Figure 23.35a shows the thickness and surface roughness (RMS and P–V) of APTES and APDMES and  $\text{SiO}_2$  substrate for reference. Figure 23.35b shows the surface roughness, adhesive force, and coefficient of friction for biotin and STA–biotin deposited on APTES and APDMES films. The data show that APTES film is not very smooth. It was shown in Fig. 23.30 that biotin and STA deposited on APTES were also not very smooth, with high P–V values. The thickness of the

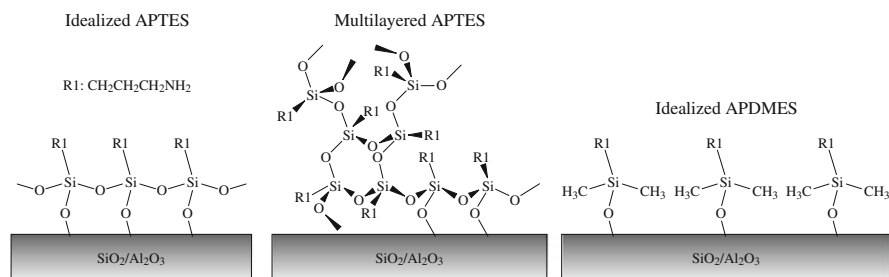


**Fig. 23.34** Chemical structure of silane polymer linker. Schematics of idealized and multilayered APTES and idealized APDMES silane polymer films on silicon/ $\text{SiO}_2$  and aluminum/ $\text{Al}_2\text{O}_3$  substrates. Idealized film corresponds to a self-assembled monolayer (after [136])

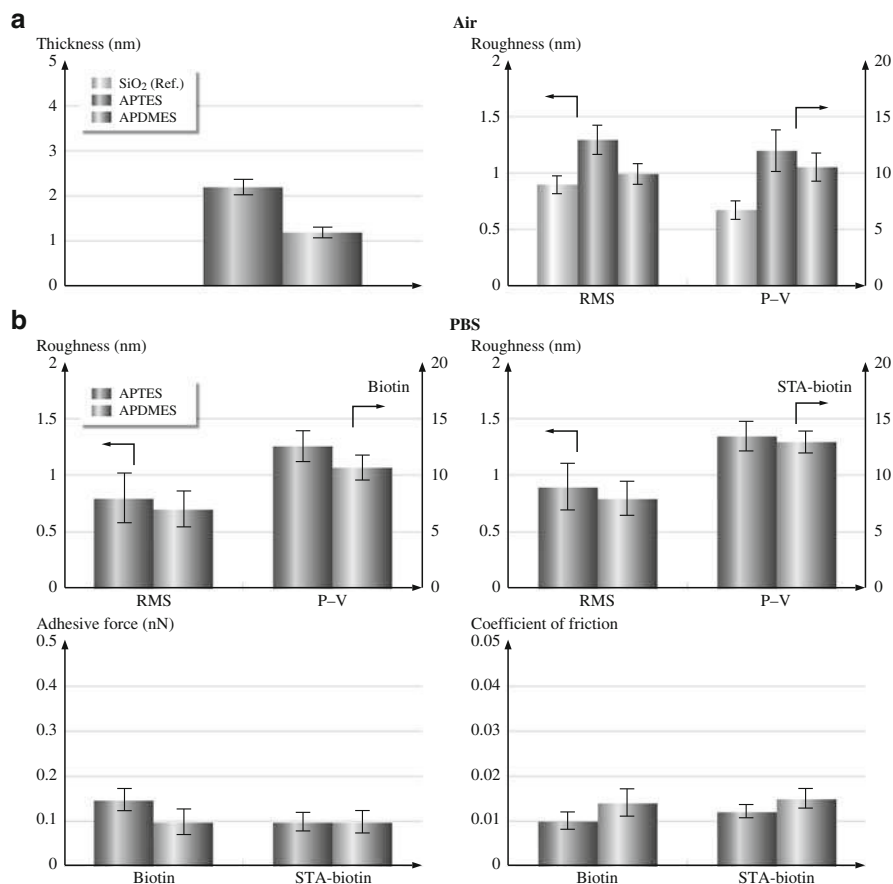


**Fig. 23.35** (a) Summary of film thickness and surface roughness (RMS and P–V distance) for APTES and APDMES in air. (b) Summary of surface roughness (RMS and P–V distance), adhesive force, and coefficient of biotin and STA–biotin on APTES and APDMES films, all in PBS buffer solution. *Error bars* represent  $\pm 1\sigma$  (after [136])

APTES layer is larger than the expected monolayer thickness. The unexpected thickness of the film represents multilayering by APTES. APDMES films produced the thinner film, with a thickness comparable to the summed bond lengths of the APDMES polymer (Fig. 23.35a). Bhushan et al. [137] reported that the APDMES film was more uniform, smoother, and nearly continuous, and that it exhibited higher contact angle and lower adhesive force as compared with the APTES film. The surface roughness and adhesive force of biotin and STA–biotin on APDMES are also slightly lower than that on APTES film. The coefficient of friction on APDMES appears to be slightly higher than that on APTES (Fig. 23.35b).

Bhushan et al. [136] also studied wear properties of various films. Contact mode always immediately stripped the surface at low loads; consequently wear

experiments were performed in tapping mode at various loads. AFM surface height and phase-angle images and cross-sectional profiles obtained after wear tests for biotin and STA-biotin on APTES and APDMES in PBS are shown in Fig. 23.36a. As controls, wear experiments of biotin and STA-biotin on  $\text{SiO}_2$  without SAM were also carried out. The biomolecular films on APDMES were more robust than on APTES. Given that each molecule of APDMES must be bonded to a surface oxide group and that intrapolymer cross-links are not possible in APDMES, it has a higher density of siloxane linkages to the substrate oxide, making it more robust. Bhushan et al. [137] also studied the effect of load on the wear of APDMES and biotin and STA-biotin deposited on APDMES (Fig. 23.36b). As expected, the wear increased with increasing load. The relationship between the average wear depth (and the coefficient of friction) and the average normal load is generally linear. The slope of the wear depth (and coefficient of friction) against load is steepest for the interface to which STA-biotin was bound because of the cushioning effect of the thick film, as suggested earlier.

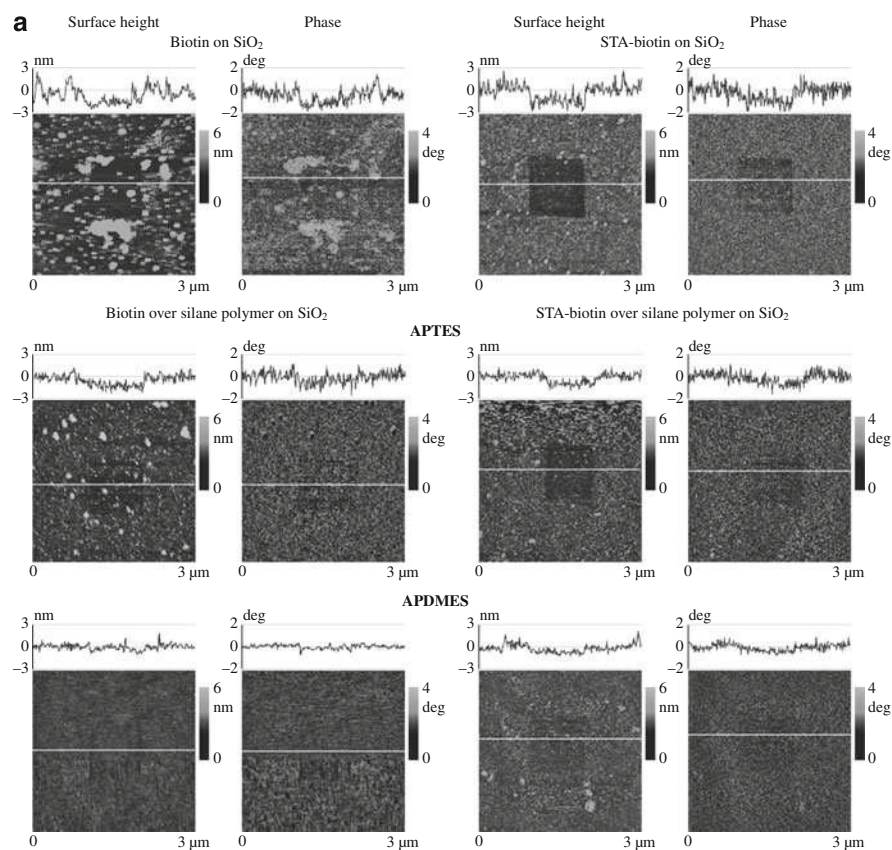
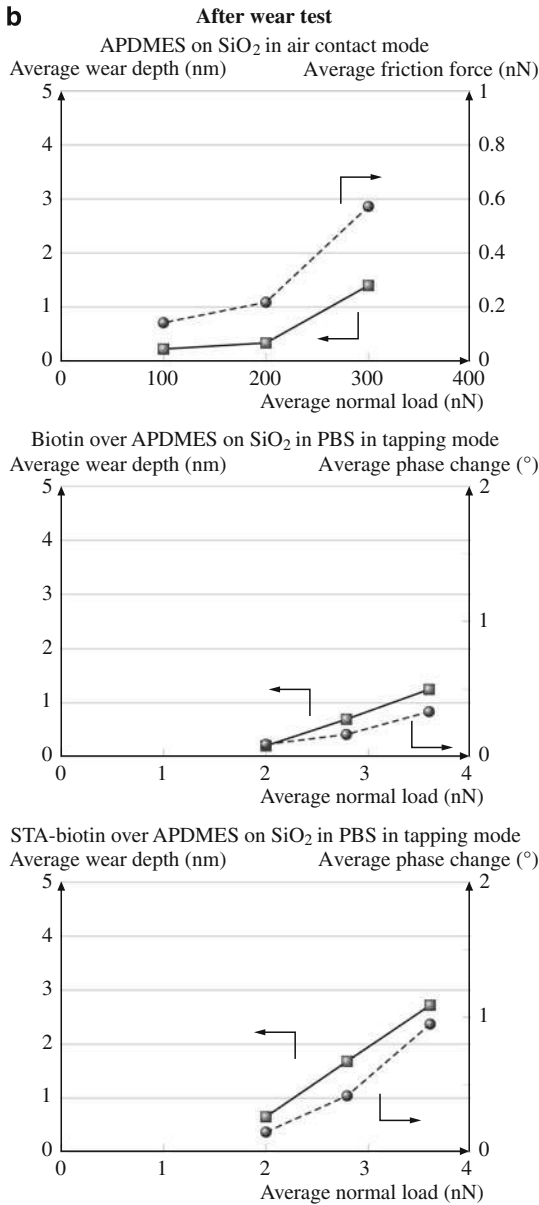


Fig. 23.36 (continued)



**Fig. 23.36** (a) AFM surface height and phase-angle images and cross-sectional profiles obtained after wear test in PBS in tapping mode at 50% of free amplitude ( $\approx 2$  nN) on biotin and STA-biotin on SiO<sub>2</sub> and APTES and APDMES films on SiO<sub>2</sub>. The *white lines* indicate the locations of the cross sections. (b) Plot of average wear depth and average friction force/phase angle as a function of average normal load for APDMES on SiO<sub>2</sub> in air in contact mode, biotin over APDMES on SiO<sub>2</sub> in PBS in tapping mode, and on STA-biotin over APDMES on SiO<sub>2</sub> in PBS in tapping mode (after [136])



In summary, APDMES film is more uniform, smoother, and nearly continuous as compared with APTES film. These properties of APDMES provide a good interfacial material for biomolecular films, providing a smooth and robust structure.

### 23.4.2 Adhesion of Coated Polymer Surfaces

As mentioned in Appendix, PMMA, PDMS, and other polymers are used in the construction of micro-nanofluidic-based biodevices. Adhesion between the moving parts needs to be minimized. Furthermore, if the adhesion between the microchannel surface and the biofluid is high, the biomolecules will stick to the microchannel surface and restrict flow. In order to facilitate flow, a surface with low bioadhesion is required.

Tambe and Bhushan [200, 201] and Bhushan and Burton [202] have reported adhesive force data for PMMA and PDMS against an AFM  $\text{Si}_3\text{N}_4$  tip and a silicon ball. Tokachichu and Bhushan [203] measured contact angle and adhesion of bare PMMA and PDMS and coated with a perfluoro SAM of perfluorodecyltriethoxysilane (PFDTES). Oxygen plasma treatment was used for hydroxylation of the surface to enhance chemical bonding of the SAM to the polymer surface. They made measurements in ambient, in PBS, and fetal bovine serum (FBS); the latter is a blood component. Figures 23.37 and 23.38 show the contact angle and adhesion data. SAM-coated surfaces have high contact angles (Fig. 23.37), as expected. The adhesion value of PDMS in ambient is high because of the electrostatic charge present on the surface. The adhesion values of PDMS are higher than PMMA because PDMS is softer than PMMA (elastic modulus = 5 GPa and hardness = 410 MPa [137]), resulting in higher contact area between the PDMS surface and the AFM tip, and PMMA does not develop electrostatic charge. When SAM is coated on PMMA and PDMS surfaces, the adhesion values are similar, which shows that electrostatic charge on virgin PDMS plays no role when the surface is coated. In the PBS solution, there is a decrease in adhesion values because of the lack of a meniscus contribution. The adhesion values for the FBS-coated tip in PBS are generally lower than for an uncoated tip in PBS.

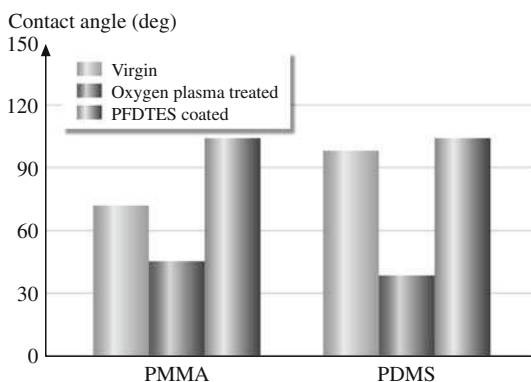
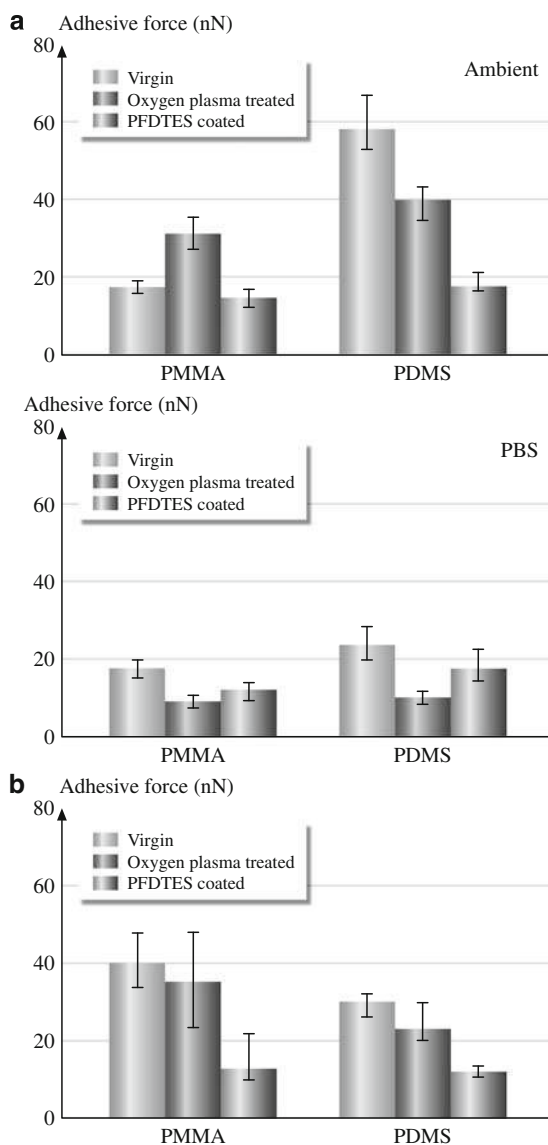


**Fig. 23.37** Sessile drop contact angle measurements of virgin, oxygen-plasma-treated, and PFDTES-coated PMMA and PDMS surfaces. The maximum error in the data is  $\pm 2^\circ$  (after [203])

**Fig. 23.38** Adhesion measurement of virgin, oxygen-plasma-treated, and PFDTES-coated PMMA and PDMS surfaces (**a**) with bare silicon nitride AFM tip in ambient, and in PBS environment, and (**b**) dip-coated tip with FBS in PBS environment (after [203])



In summary, the adhesion values of SAM-coated surfaces are lower than bare surfaces in various environments.

### 23.4.3 Submicron Particles for Therapeutics and Diagnostics

Submicron particles can be injected into the blood stream in human capillaries (as small as 4–5  $\mu\text{m}$ ) and employed to deliver drugs to diseased cells, to locate diseased

cells or tumoral masses and estimate the state of disease, and to carry diagnostic agents (fluorescent molecules) to diseased cells in order to enhance imaging [142]. Particles exhibiting one of these characteristics can be considered as smart systems, which can function as purely therapeutic agents, purely diagnostic agents, or a combination of both. Small delivery particles include nanocrystals, synthetic vesicles, liposomes, and fabricated silicon.

Particles are reservoirs containing drug or diagnostic agents. These are covered with a layer of adhesive molecules (ligands) for attaching to selected target sites. When a particle is sufficiently close to select cell surfaces (a few nm), its ligands can interact with the cellular counterpart (receptors), which leads to firm attachment. Once the particle is arrested to its target, drug or diagnostic agent is delivered. A schematic of the lifecycle of a particle injected intravenously for drug delivery is shown in Fig. 23.39. The speed and the time needed for a particle circulating in the blood stream to reach the endothelium lining of the human capillary is dependent upon the distance and interactive forces. The particle can interact with the endothelium lining through buoyancy, van der Waals (vdW), electrostatic, and steric forces. These interactions are a function of the material properties of the particles and any coating on it, in particular its relative density (particle density relative to blood), the electrostatic potential, and the dielectric constant as well as the particle radius. These properties can be optimized.

These interacting forces are weak, so the particle trajectory should be close to the endothelium lining, otherwise the particle may not get attracted to the lining to perform its intended function. Decuzzi et al. [142] developed an analytical model to predict the trajectory of a particle freely circulating in the blood stream and associated interaction forces. The model can be used to optimize the particle radii and material properties. Figure 23.40 shows a schematic of a spherical particle freely circulating in the blood stream with its center at a distance  $z$  from the

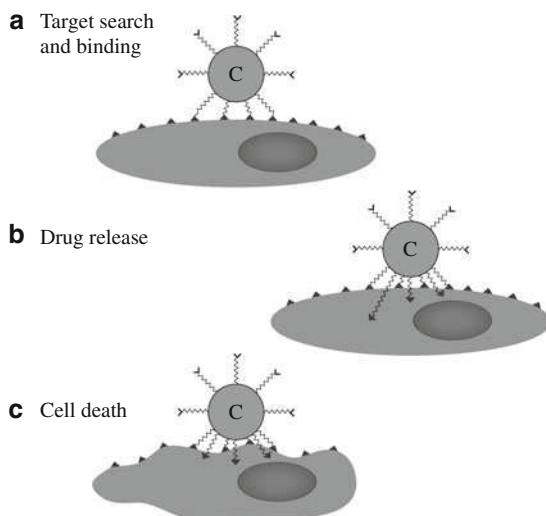


**Fig. 23.39** The life cycle of a particle injected intravenously for drug delivery: **(a)** target search and binding, **(b)** drug release, and **(c)** cell death (after [142])

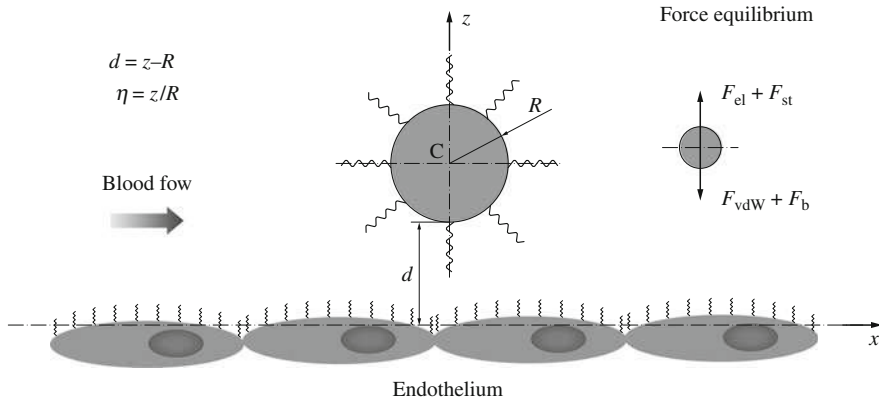


**Fig. 23.40** A spherical particle moving close to the endothelium wall in a laminar flow. In the *inset*, the balance of the forces acting on the particle are sketched:  $F_{el}$ ,  $F_{st}$ ,  $F_{vdW}$ , and  $F_b$  correspond to the electrostatic force, steric force, van der Waals force, and buoyancy force, respectively (after [142])

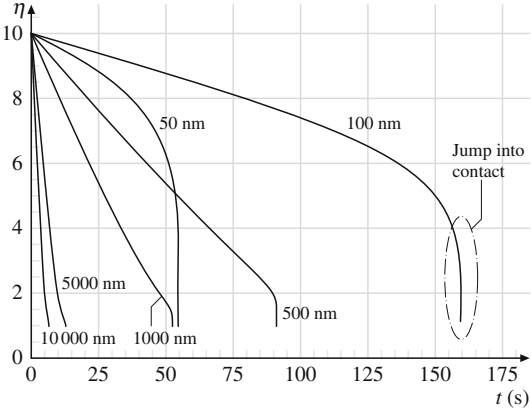
endothelium wall. The particle has a radius  $R$ , and its trajectory is governed by the forces exerted by the blood stream and gravitational and electromagnetic interactions. We assume that the particle is sufficiently far from the endothelium wall that specific interactions (such as ligand–receptor interactions) can be ignored. At short range (below 1–3 nm), solvation and other steric forces dominate. However, the most important long-range forces (5–10 nm) between particles and wall surfaces in the presence of a liquid are buoyancy, van der Waals, electrostatic, and steric forces. The buoyancy force is related to the radius of the particle  $R$  and the relative density of the particle relative to blood. The van der Waals interaction (generally attractive) is related to  $R$ , its relative position with respect to the endothelium wall  $z$ , and the Hamaker constant  $A$ , which depends upon the dielectric constants of the media involved. The electrostatic double-layer (EDL) interaction (repulsive and attractive) is related to  $R$ ,  $z$ , the ionic concentration, and the characteristic Debye length of the solution. Finally, the steric repulsive interaction is related to the unperturbed radius of gyration of polymer chains grafted onto the particle surface,  $R$ , and  $z$ . The value of various forces as a function of the particle radius  $R$  for a fixed distance from the wall  $z$  is presented in Table 23.6. The dominating force is buoyancy when the particle radius is sufficiently large, and van der Waals when the particle is sufficiently small. Electrostatic and steric forces are negligible as long as the distance is larger than the 50 nm considered in this example.

The travel time needed to reach the wall depends upon the particle size, as shown in Fig. 23.41. In this figure, the dimensionless position of the particle center with respect to the endothelium wall  $\eta$  ( $= z/R$ ) is plotted as a function of time  $t$  for different particle radii, ranging from  $R = 10 \mu\text{m}$  to 50 nm. It was assumed that particles were initially at a distance  $d_0(z_0 - R)$  equal to  $9R$  from the endothelium wall (i.e., the center of the particle is at  $z_0 = 10R$ ,  $\eta_0 = z_0/R = 10$ ). Thus the distance traveled scales with the size of the particle. The data show that, as the

**Table 23.6** Values of the buoyancy force  $F_b$ , van der Waals force  $F_{vdW}$ , electrostatic force  $F_{el}$ , and steric force  $F_{sr}$  as functions of the particle radius for a fixed distance from the wall ( $\eta = z/R = 2$  or  $d = R$ ) [142]

$R$ (nm)	$F_b$ (pN)	$F_{vdW}$ (pN)	$F_{el}$ (pN)	$F_{sr}$ (pN)
10000	41.092	0.0005	$\approx 0$	$\approx 0$
1000	$41.092 \times 10^{-3}$	0.005	$\approx 0$	$10^{-33}$
100	$41.092 \times 10^{-6}$	0.05	$10^{-52}$	$1.2 \times 10^{-3}$
50	$51.3 \times 10^{-7}$	0.1	$10^{-25}$	$3 \times 10^{-2}$

**Fig. 23.41** The dimensionless particle position  $\eta(= z/R)$  as a function of time  $t$  for different values of particle radius ( $R = 10,000, 5,000, 1,000, 500, 100$ , and  $50$  nm). There exists a critical radius  $R_c$  at which the travel time is maximum (after [142])

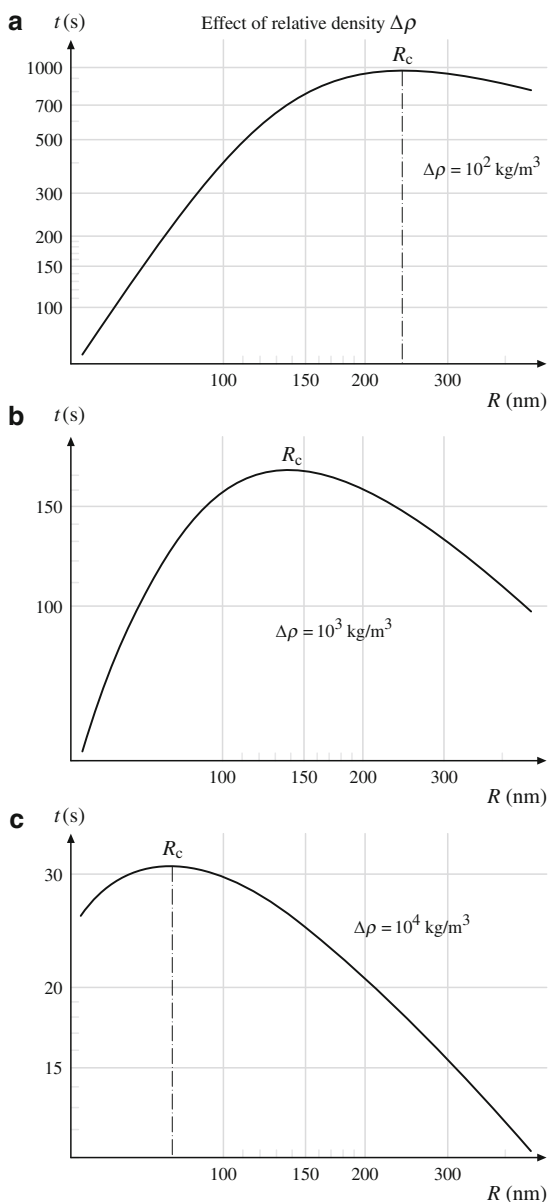


radius of the particle decreases, the time needed to reach the wall increases up to a maximum beyond which it decreases as the radius is further reduced. Larger particles are initially far from the endothelium wall; a 10  $\mu\text{m}$  particle is initially 100  $\mu\text{m}$  away from the endothelium ( $z = 10R$ ), where electrostatic and van der Waals interactions are negligible and particle motion is governed by buoyancy and hemodynamic resistance. As the particle approaches the endothelium wall, van der Waals attraction dominates, and a rapid increase in speed is observed with a *jump to contact* like behavior. Such a behavior is more clearly shown by particles with submicron radius, which are closer to the endothelium wall, so the van der Waals force dominates from the beginning. We note that there is a critical radius for which the time taken for the particle to travel to the wall is maximum. Selected radius should be smaller or larger than the critical radius (possibly smaller so that they can circulate freely even in smaller capillaries).

The effect of the relative density of the particle  $\Delta\rho$  on the critical radius  $R_c$  at which travel time is maximum is plotted in Fig. 23.42. We note that, as  $\Delta\rho$  reduces,  $R_c$  increases. As  $\Delta\rho$  decreases, the effect of buoyancy becomes less important, and van der Waals attractive forces exert a greater influence as the particle radius decreases.

In summary, the interacting forces are weak, so the particle trajectory should be close to the endothelium lining. The trajectory and interaction forces depend upon the particle radii and material properties. These results suggest that particles for

**Fig. 23.42** Travel time as a function of particle radius  $R$  for different values of relative density: (a)  $\Delta\rho = 10^2$ , (b)  $\Delta\rho = 10^3$ , and (c)  $\Delta\rho = 10^4 \text{ kg/mm}^3$ . The critical radius  $R_c$  depends upon  $\Delta\rho$  (after [142]) ◀



therapeutic and diagnostics should have a radius larger or smaller than a critical value (possibly smaller so that they can circulate freely even in smaller capillaries). The material properties of the particle and the polymer chains grafted onto it, such as the relative density of the particle, can be tuned specifically to the type of malignant tissue and the state of disease, improving the particle affinity with the diseased cells.

### 23.5 Surfaces with Roughness-Induced Superhydrophobicity, Self-Cleaning, and Low Adhesion

Various MEMS/NEMS and bioMEMS/bioNEMS require hydrophobic and self-cleaning surfaces and interfaces with low adhesion and friction. Hydrophobicity of a surface (wettability) is characterized by the static contact angle between a water droplet and the surface. If the liquid does not wet the surface, the value of the contact angle is  $90 < \theta \leq 180^\circ$ . Surfaces with a contact angle between  $150^\circ$  and  $180^\circ$  are called superhydrophobic. In addition to the high contact angle, for self-cleaning, superhydrophobic surfaces should also have very low water contact angle hysteresis  $\theta_H$ . Water droplets roll off (with some slip) on these surfaces and take contaminants with them, providing a self-cleaning ability known as the *lotus effect*. Contact angle hysteresis is the difference between advancing and receding contact angles, which are two stable values. It occurs due to surface roughness and surface heterogeneity. Contact angle hysteresis (CAH) reflects the irreversibility of the wetting/dewetting cycle. It is a measure of the energy dissipation during the flow of a droplet along a solid surface. At a low value of CAH, the droplet may roll in addition to slide, which facilitates the removal of contaminant particles. A surface with CAH of  $< 10^\circ$  is generally referred to as a self-cleaning surfaces. Surfaces with low CAH have a low water roll-off (tilt) angle, which denotes the angle to which a surface must be tilted for roll-off of water droplets. Self-cleaning surfaces are of interest in various applications, including self-cleaning windows, windshields, exterior paints for buildings and navigation ships, utensils, roof tiles, textiles, solar panels, and applications requiring antifouling and a reduction of drag in fluid flow, e.g., in micro-nanochannels in micro-nanofluidics. Superhydrophobic surfaces can also be used for energy conservation and conversion. Selection of a proper superhydrophobic surface allows the reduction of energy dissipation. Secondly, superhydrophobic and superoleophobic surfaces can be used for fuel economy. Third, the recently discovered effect of reversible superhydrophobicity provides the potential for new ways of energy conversion such as the microscale capillary engine.

Wetting may lead to the formation of menisci at the interface between solid bodies during sliding contact, which increases adhesion and friction. In some cases, the wet friction force can be greater than the dry friction force, which is usually undesirable [82, 83, 84, 126]. On the other hand, high adhesion is desirable in some applications, such as adhesive tapes and adhesion of cells to biomaterial surfaces; therefore, enhanced wetting would be desirable in these applications. Numerous applications, such as magnetic storage devices and micro-nanoelectromechanical systems (MEMS/NEMS), require surfaces with low adhesion and stiction [13, 34, 83, 152, 205].

Some natural surfaces, including leaves of water-repellent plants such as lotus, are known to be superhydrophobic and self-cleaning due to hierarchical roughness and the presence of a wax coating [205, 207]. Figure 23.43 shows SEM micrographs (shown at three magnifications) of a superhydrophobic leaf of lotus (*Nelumbo nucifera*). Lotus is characterized by papillose epidermal cells responsible for the

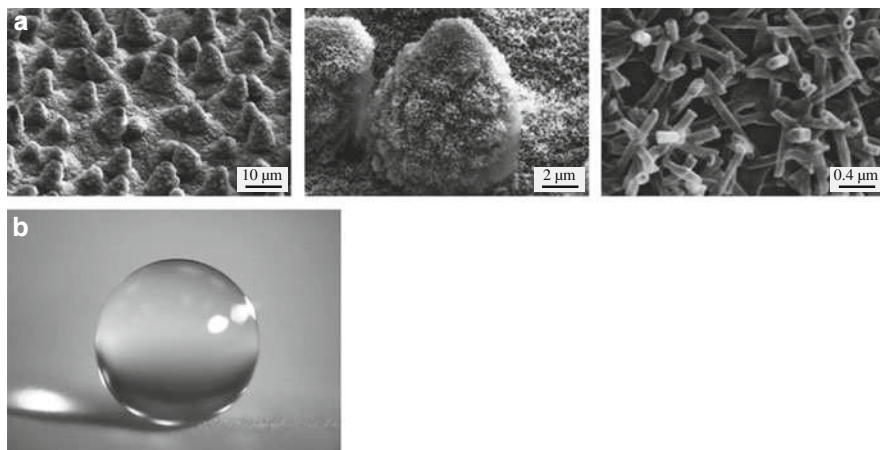


**Fig. 23.43** (a) SEM micrographs (shown at three magnifications) of *Nelumbo nucifera* (lotus) leaf surface, which consists of microstructure formed by papillose epidermal cells covered with 3-D epicuticular wax tubules on the surface, which create nanostructure [208]. (b) Image of a water droplet sitting on the lotus leaf

creation of papillae or microbumps on the surfaces, covered with three-dimensional epicuticular wax tubules which are a mixture of very long-chain fatty acids molecules (compounds with chains  $> 20$  carbon atoms) and create a nanostructure on the entire surface. The contact angle and contact angle hysteresis of the lotus leaf are  $\approx 164$  and  $3^\circ$ , respectively [207–209].

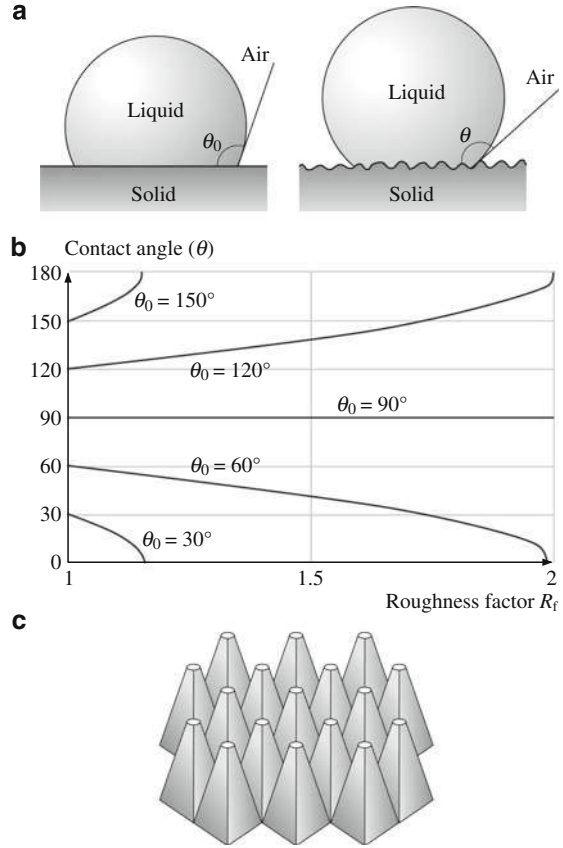
Superhydrophobic surfaces can be achieved by either selecting low-surface-energy materials/coating, or by introducing roughness. In this section, we discuss design, fabrication, and characterization of roughness-induced superhydrophobic and self-cleaning surfaces by mimicking the lotus effect [204, 205, 208–214].

### 23.5.1 Modeling of Contact Angle for a Liquid Droplet in Contact with a Rough Surface

If a droplet of liquid is placed on a smooth surface, the liquid and solid surfaces come together under equilibrium at a characteristic angle called the static contact angle  $\theta_0$  (Fig. 23.44a). The contact angle can be determined from the condition of the total energy of the system being minimized. Next, consider a rough solid surface with a typical size of roughness details smaller than the size of the droplet (of the order of a few hundred microns or larger) (Fig. 23.44a). For a droplet in contact with a rough surface without air pockets, referred to as a homogeneous interface, based on the minimization of the total surface energy of the system, the contact angle is given as by the Wenzel equation [215]



**Fig. 23.44** (a) Schematic of a liquid droplet in contact with a smooth solid surface (contact angle  $\theta_0$ ) and a rough solid surface (contact angle  $\theta$ ), (b) contact angle for rough surface ( $\theta$ ) as a function of roughness factor ( $R_f$ ) for various contact angles of the smooth surface ( $\theta_0$ ), and (c) schematic of round-topped pyramidal asperities with complete packing (after [210])



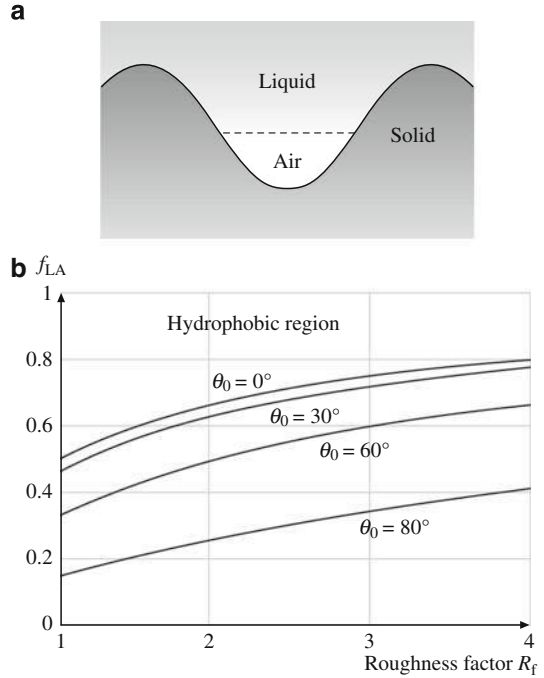
$$\cos \theta = R_f \cos \theta_0 \quad (23.1)$$

where  $\theta$  is the contact angle for rough surfaces and  $R_f$  is a roughness factor defined as the ratio of the solid–liquid area  $A_{SL}$  divided by its projection onto a flat plane  $A_F$

$$R_f = \frac{A_{SL}}{A_F}. \quad (23.2)$$

The dependence of the contact angle on the roughness factor is presented in Fig. 23.44b for different values of  $\theta_0$ , based on (23.1). It should be noted that (23.1) is valid only for moderate roughness, when  $R_f \cos \theta_0 < 1$ . The graph shows that, with an increase in the roughness factor, a hydrophobic surface becomes more hydrophobic, whereas a hydrophilic surface becomes even more hydrophilic. As an example, Fig. 23.44c shows a geometry with pyramidal asperities with rounded tops, which has complete packing. The size and shape of the asperities can be optimized for a desired roughness factor.

**Fig. 23.45** (a) Schematic of formation of a composite solid–liquid–air interface for a rough surface; (b)  $f_{LA}$  requirement for a hydrophilic surface to be hydrophobic as a function of the roughness factor ( $R_f$ ) and  $\theta_0$  [205]



For higher roughness, air pockets may be formed between the asperities on the surface, which results in a composite interface consisting of a solid–liquid and a liquid–air fraction (Fig. 23.45a). In the case of such a composite interface, the contact angle is given as by the Cassie–Baxter equation [216]

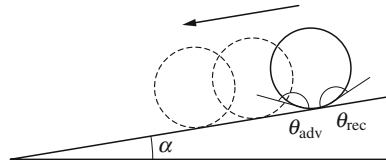
$$\cos \theta = R_f \cos \theta_0 - f_{LA}(R_f \cos \theta_0 + 1), \quad (23.3)$$

where  $f_{LA}$  is the fractional liquid–air contact area of the liquid–air interfaces under the droplet. In reality, some valleys will be filled with liquid and others with air, and the value of the contact angle is between the values predicted by (23.1) and (23.3). Examination of (23.3) shows that the contact angle increases with increasing  $R_f$  and  $f_{LA}$ . Even for a hydrophilic surface, the contact angle increases with increasing  $f_{LA}$ . At a high enough value of  $f_{LA}$ , a hydrophilic surface can become hydrophobic. The value of  $f_{LA}$  at which a hydrophilic surface could turn into a hydrophobic one is given as [206]

$$f_{LA} > \frac{R_f \cos \theta_0}{R_f \cos \theta_0 + 1} \quad \text{for } \theta < 90^\circ. \quad (23.4)$$

Figure 23.45b shows the value of  $f_{LA}$  as a function of  $R_f$  required for different contact angles  $\theta_0$  for a hydrophilic surface to become hydrophobic. The graph shows that, unlike the so-called Wenzel regime, in the so-called Cassie–Baxter

**Fig. 23.46** Tilted surface profile (tilt angle  $\alpha$ ) with a liquid droplet; advancing and receding contact angles are  $\theta_{adv}$  and  $\theta_{rec}$ , respectively



regime, even a hydrophilic surface can be made hydrophobic at a certain value of  $f_{LA}$  for a given  $\theta_0$ .

As stated earlier, low contact angle hysteresis is desirable for self-cleaning. If a droplet sits over a tilted surface (Fig. 23.46) the contact angle at the front and back of the droplet corresponds to the advancing and receding contact angle, respectively. The advancing angle is greater than the receding angle, which results in the contact angle hysteresis. Nosonovsky and Bhushan [210] derived a relationship for contact angle hysteresis as a function of roughness, given as

$$\theta_{adv} - \theta_{rec} = \left( \sqrt{1 - f_{LA}} \right) R_f \frac{\cos \theta_{r0} - \cos \theta_{a0}}{\sqrt{2(R_f \cos \theta_0 + 1)}}. \quad (23.5)$$

Equation (23.5) shows that increasing roughness (high  $R_f$ ) and decreasing fractional liquid–air contact area  $f_{LA}$  lead to an increase in contact angle hysteresis  $\theta_H$ . Increasing  $f_{LA}$  is more efficient for decreasing  $\theta_H$ ; therefore, a composite interface is desirable for self-cleaning.

Formation of a composite interface is a multiscale phenomenon which depends upon the relative sizes of the liquid droplet and roughness details. Stability of the composite interface is an important issue. Even though it may be geometrically possible for the system to become composite, it may not be energetically profitable for the liquid to penetrate into valleys between asperities to form a homogenous interface. The destabilizing factors include capillary waves, nanodroplet condensation, surface inhomogeneity, and liquid pressure. Nosonovsky and Bhushan [210] have reported that convex surfaces lead to a stable interface. Microstructure resists capillary waves present on the liquid–air surface, and nanostructures prevent nanodroplets from filling the valleys between the asperities and pin the droplet. Therefore, hierarchical structure is required to resist these scale-dependent mechanisms resulting in high contact angle and low contact angle hysteresis.

### 23.5.2 Fabrication and Characterization of Microstructures, Nanostructures, and Hierarchical Structures

Various structures have been fabricated, and characterization of contact angles and adhesion and friction has been carried out, to validate modeling predictions and provide design guidelines [205, 208, 209, 211, 214].

## Micro- and Nanopatterned Polymer Surfaces

Nanopatterned poly(methyl methacrylate) (PMMA) surfaces were fabricated using soft lithography. To realize a micropatterned sample, a low-resolution replica of a lotus leaf was made and samples were fabricated using PMMA and polystyrene (PS) [205]. Figure 23.47a shows SEM images of the samples with nanopatterns with two aspect ratios using PMMA and with micropatterns of lotus replicas using PMMA. The PMMA surfaces were hydrophilic, and were made hydrophobic by coating them with a self-assembled monolayer of perfluorodecyltriethoxysilane (PFDTES). The static contact angles of various samples are presented in Fig. 23.47b. For hydrophilic surfaces, the contact angle decreases with roughness, while for hydrophobic surfaces it increases. Using the Wenzel equation, the contact angles of the hydrophobic nanopatterned and micropatterned surfaces were calculated using the contact angle of the flat surfaces and  $R_f$ . The measured contact angles of both nanopatterned samples are higher than the calculated values, whereas for the lotus pattern these are comparable. This suggests that nanopatterns benefit from air pocket formation. Furthermore, pinning at the top of the nanopatterns stabilizes the droplet. For the PS material, the contact angle of the lotus pattern also increased with increasing roughness factor.

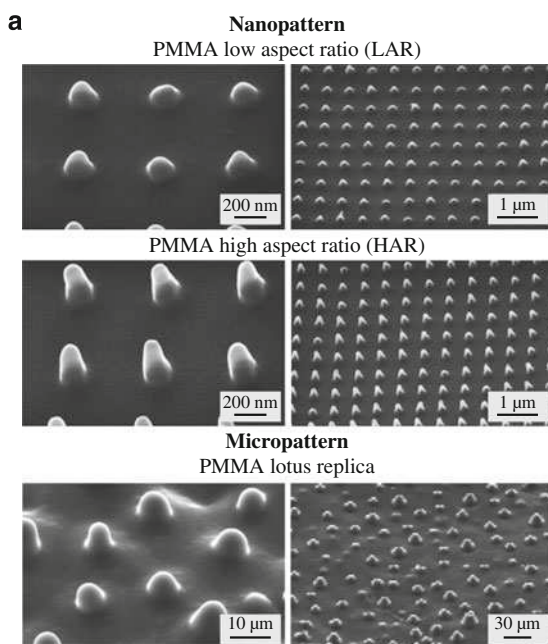
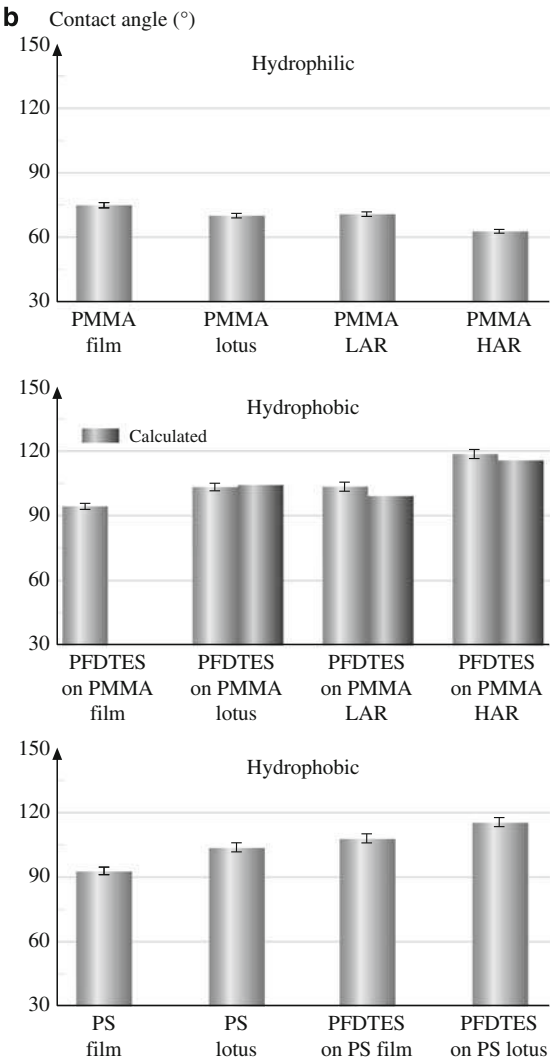


Fig. 23.47 (continued)



**Fig. 23.47** (a) SEM micrographs of the two nanopatterned polymer surfaces (shown using two magnifications to show both the asperity shape and the asperity pattern on the surface) and the micropatterned polymer surface (lotus pattern, which has only microstructures on the surface). (b) Contact angles for various patterned surfaces on PMMA and PS polymers, and calculated values using the Wenzel equation (after [205])

**Micropatterned Si Surfaces**

Micropatterned surfaces with a square grid of cylindrical pillars were produced from single-crystal silicon (Si) using photolithography and coated with a self-assembled monolayer, making them hydrophobic [205]. Micropatterns were



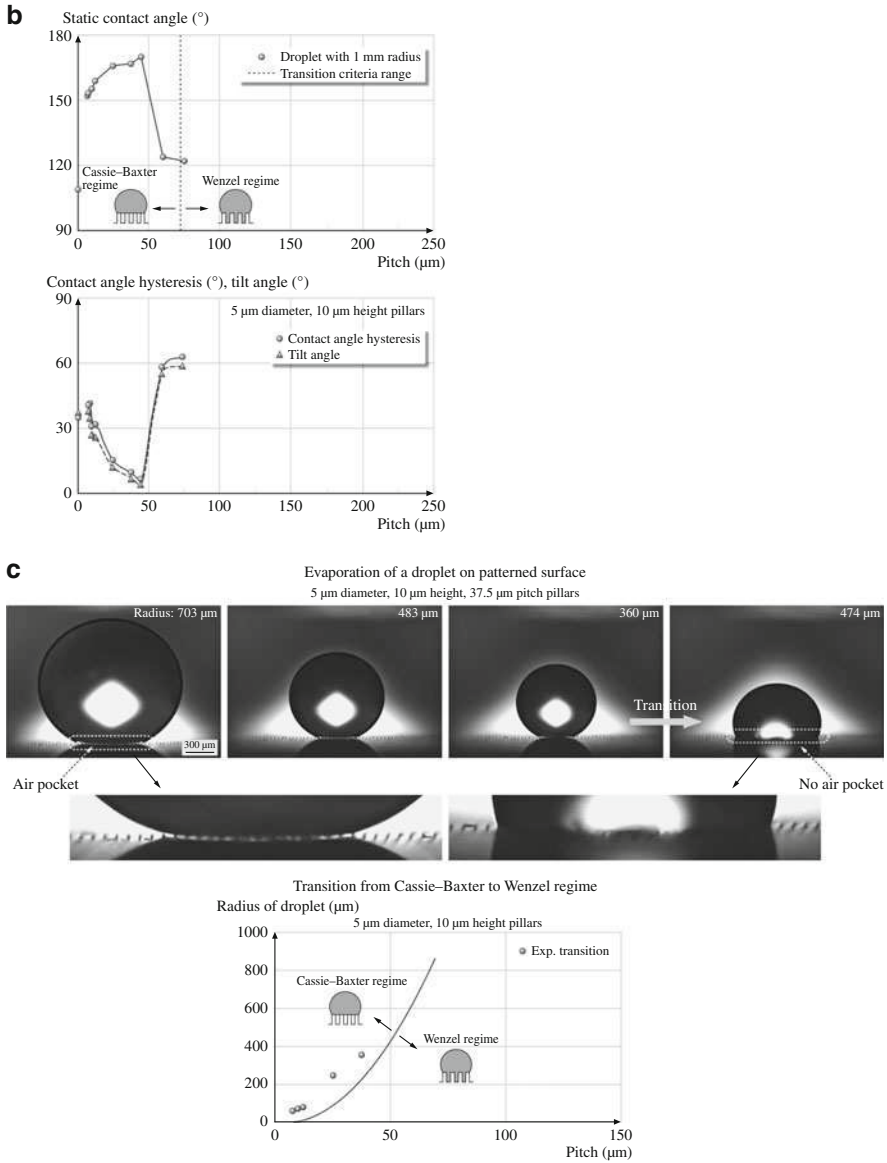


**Fig. 23.48** (a) Surface height maps of a micropatterned surface using an optical profiler and a liquid droplet on the micropatterned surface, shown to obtain the transition criteria. (b) Static contact angle [dotted line represents the transition criteria range obtained using (23.6)] and contact angle hysteresis and tilt angles as a function of pitch value for a droplet with 1 mm radius (5  $\mu\text{l}$  volume). Data at zero pitch correspond to a flat sample. (c) Radius of droplet for the regime transition as a function of pitch values. The experimental results (circles) are compared with the transition criterion (solid line, (23.6)) for the patterned surfaces with different pitch values. This figure also shows optical micrographs of a water droplet before and just after the transition (after [205])

center of the square formed by the four pillars, as shown in Fig. 23.48a. The maximum droop of the droplet can be found in the middle of two diagonally separated pillars, as shown in the figure, i.e.,  $(\sqrt{2}P - D)^2/8R$ . If the droop is greater than the depth of the cavity, then the droplet will just contact the bottom of the cavities between pillars. If it is much greater, transition occurs from the Cassie–Baxter to the Wenzel regime for

$$\frac{(\sqrt{2}P - D)^2}{R} \geq H. \quad (23.6)$$

Figure 23.48b shows the static contact angle, contact angle hysteresis, and tilt angle as a function of pitch for a droplet with 1 mm radius (5  $\mu$ l volume). The contact angle of selected patterned surfaces is much higher than that of the flat surface. It first increases with increasing pitch values, then drops rapidly to a value slightly higher than that for the flat surface. In the first portion of the curve, it jumps to a high value corresponding to a superhydrophobic surface and continues to increase because open air space increases with increasing pitch, responsible for the greater propensity for air pocket formation. The sudden drop at a pitch value of  $\approx 50$   $\mu$ m corresponds to the transition from the Cassie–Baxter to the Wenzel regime. The dotted line corresponds to the value predicted from the transition criteria presented in (23.6); the measured and predicted values are close.

Figure 23.48b shows contact angle hysteresis and tilt angle as a function of pitch. Both angles are comparable. The angle first increases with increasing pitch, which has to do with pinning of the droplet at the sharp edges of the micropillars. As the pitch increases, there is greater propensity for air pocket formation and fewer sharp edges per unit area, which is responsible for the sudden drop in angle. Above a pitch value of 50  $\mu$ m, the angle increases very rapidly because of transition to the Wenzel regime.

Droplet evaporation experiments have been conducted to investigate how droplet size influences this transition [206]. Figure 23.48c shows the radius of a droplet at which transition occurs as a function of pitch values. The experimental results (circles) are compared with the transition criterion (solid line, 23.6). It is found that the critical radius of impalement is in good agreement with our predictions. The critical radius of the droplet increases linearly with the pitch value. For surfaces with small pitch, the critical radius of the droplet can become quite small. This figure also shows optical micrographs of a water droplet before and just after transition. Before the transition, air pockets are clearly visible at the bottom area of the droplet, but after the transition, air pockets are not found at the bottom of the droplet.

Based on the data above, one can achieve a very high contact angle ( $\approx 170^\circ$ ) and very low contact angle hysteresis ( $\approx 2^\circ$ ) at the critical pitch value.

### Surfaces with Microstructure, Nanostructure, and Hierarchical Structure

It has been reported earlier that a hierarchical surface is needed to develop a composite interface with high stability. The structure of an ideal hierarchical



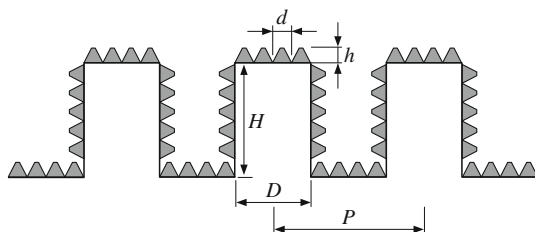


**Fig. 23.49** Schematic of an ideal hierarchical surface. Microasperities consist of circular pillars with diameter  $D$ , height  $H$ , and pitch  $P$ . Nanoasperities consist of pyramidal nanoasperities of height  $h$  and diameter  $d$  with rounded tops (after [206])

surface is shown in Fig. 23.49. The asperities should be high enough that the droplet does not touch the valleys. As an example, for a structure with circular pillars, the following relationship should hold for a composite interface:  $(\sqrt{2}P - D)^2/R < H$  (23.6). As an example, for a droplet with a radius on the order of 1 mm or larger, a value of  $H$  of the order of 30  $\mu\text{m}$ , and  $D$  of the order of 15  $\mu\text{m}$ , a  $P$  of the order of 130  $\mu\text{m}$  is optimum. Nanoasperities can pin the liquid–air interface and thus prevent liquid from filling the valleys between asperities. They are also required to support nanodroplets, which may condense in the valleys between large asperities. Therefore, nanoasperities should have a small pitch to handle nanodroplets, with radius  $< 1$  mm down to a few nm. Structures with values of  $h$  of the order of 10 nm and  $d$  of the order of 100 nm can be easily fabricated.

Bhushan et al. [208, 209, 211] and Koch et al. [214] fabricated surfaces with microstructure, nanostructure, and hierarchical structure. A two-step molding process was used to fabricate microstructures by creating identical copies of a micro-patterned Si surface and lotus leaves. Nanostructures were created by self-assembly of evaporating synthetic and plant waxes. Alkanes of varying chain length are common hydrophobic compounds of plant waxes. The alkane *n*-hexatriacontane ( $\text{C}_{36}\text{H}_{74}$ ) was used for the development of platelet nanostructures. Tubule-forming waxes, isolated from leaves of *Tropaeolum majus* (L.) and *Nelumbo nucifera* (lotus), were used to create tubule structures. Figure 23.50a shows SEM micrographs of a hierarchical structure surface using lotus wax on lotus replica and micropatterned Si replica. The amount of wax used for evaporation was 0.8  $\mu\text{g}/\text{mm}^2$ . In order to grow tubules, the specimens were placed in a chamber saturated with ethanol vapor at 50°C. The static contact angle, contact angle hysteresis, tilt angle, and adhesive forces for various samples are shown in Fig. 23.50b. Figure 23.50b shows that the highest static contact angles of 173°, lowest contact angle hysteresis of 1°, and tilting angle varying between 1 and 2° were found for the hierarchical structured Si replica. The hierarchical structured lotus leaf replica shows a static contact angle of 171°, the same contact angle hysteresis (2°), and tilt angles of 1–2°, similar to that of the hierarchical Si replica. Fresh lotus leaf surface was reported to have a static contact angle of 164°, contact angle hysteresis of 3°, and a tilt angle of 3°. Therefore, the artificial hierarchical surfaces showed higher static contact angle and lower contact angle hysteresis. Structural differences between the original lotus

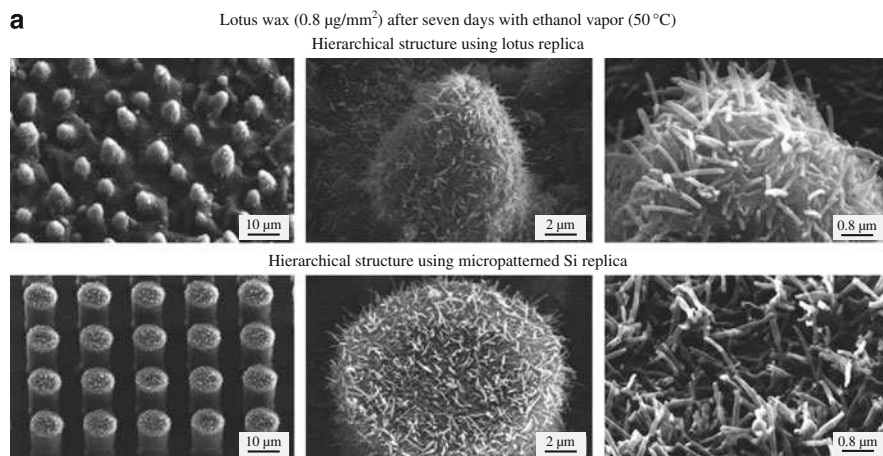


**Fig. 23.50** (continued)

leaf and the artificial lotus leaf described here are limited to a difference in wax tubule length, which is  $0.5\text{--}1 \mu\text{m}$  longer in the artificial lotus leaf.

Self-cleaning efficiency tests have also been carried out by Bhushan et al. [208]. The samples were exposed to contaminants in a contamination glass chamber and then cleaned with water droplets. Figure 23.50c shows that none of the investigated surfaces was fully cleaned by water rinsing. Most particles (70–80%) remained on smooth surfaces, and 50–70% of particles were found on microstructured surfaces. Most particles were removed from the hierarchical structured surfaces, but  $\approx 30\%$  of the particles remained. A clear difference in particle removal, independent of particle size, was only found for flat and nanostructured surfaces, where larger particles were removed with higher efficiency. Observations of droplet behavior during movement on the surfaces showed that droplets rolled only on the hierarchical structured surfaces. On flat, microstructured, and nanostructured surfaces, the first droplets applied did not move, but continuous application of water droplets increased their volumes and led to sliding of these larger droplets. During this, some of the particles were removed from the surfaces. However, the droplets rolling on hierarchical structures did not collect dirt particles trapped in the cavities of the microstructures. The data clearly show that hierarchical structures have superior cleaning efficiency.

### 23.5.3 Summary

In the Wenzel regime, an increase in roughness on a hydrophilic surface decreases the contact angle, whereas on a hydrophobic surface it increases contact angle. However, in the Cassie–Baxter regime, air pocket formation can change a hydrophilic surface to a hydrophobic surface. Based on studies to explore the effect of droplet size and roughness geometry, the transition from the Cassie–Baxter regime

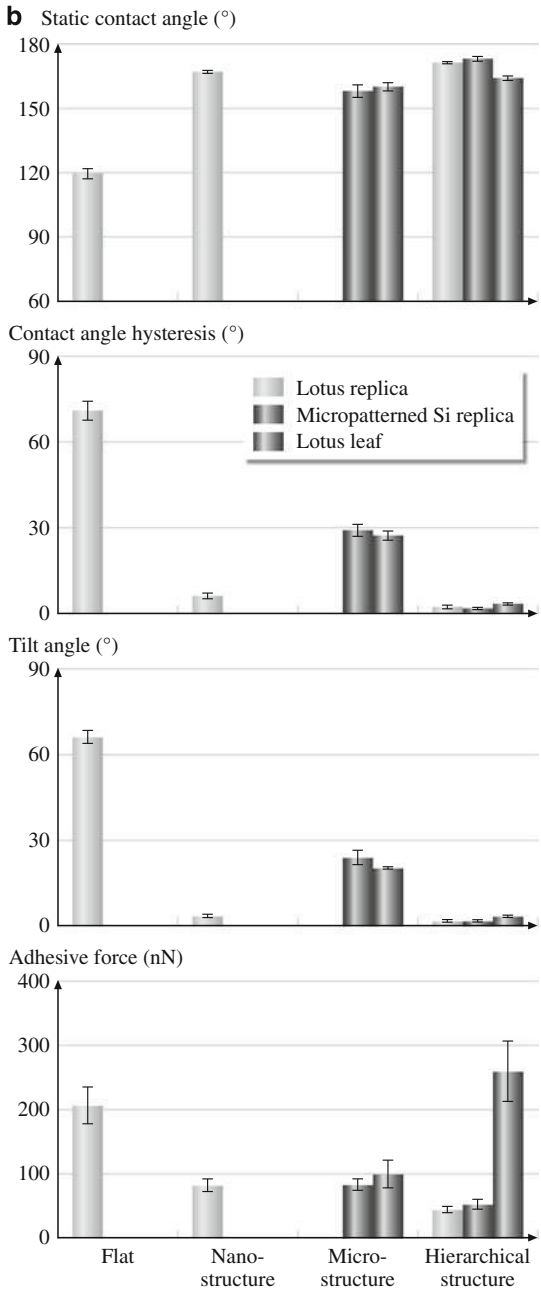
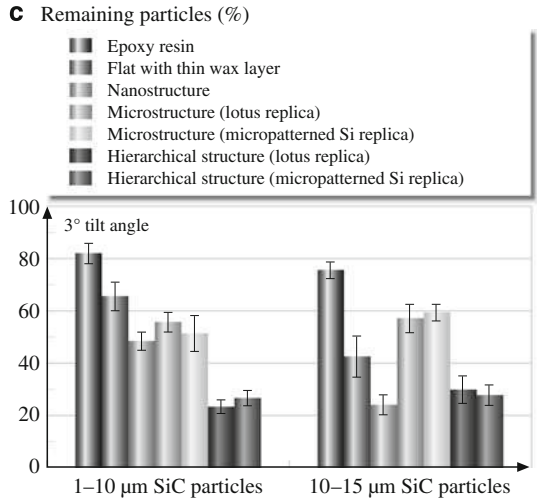


Fig. 23.50 (continued)



**Fig. 23.50** (a) SEM micrographs of hierarchical structure using lotus and micropatterned Si replicas. (b) Bar chart showing the measured static contact angle, contact angle hysteresis, and tilt angle on various structures. The bar chart also shows adhesive forces for various structures. The error bars represents  $\pm 1$  standard deviation [214]. (c) Bar charts showing remaining particles after applying droplets with nearly zero kinetic energy on various structures fabricated using lotus wax using 1–10  $\mu\text{m}$  and 10–15  $\mu\text{m}$  SiC particles. The experiments on the surfaces with lotus wax were carried out on stages tilted at  $3^\circ$ . The error bars represent  $\pm 1$  standard deviation (after [208])

to the Wenzel regime occurs below a certain radius of droplet and/or above a certain pitch value.

For fluid flow applications, for drag reduction, a surface should have high contact angle and low contact angle hysteresis. This condition should be achieved by a high value of fractional liquid–air contact area,  $f_{LA}$ , and relatively low value of roughness factor,  $R_f$ .

The fabricated hierarchical surface shows a high static contact angle of  $\approx 170^\circ$  and low contact angle hysteresis of  $\approx 2^\circ$ , which provide superior superhydrophobic and self-cleaning surfaces.

## 23.6 Component-Level Studies

### 23.6.1 Surface Roughness Studies of Micromotor Components

Most of the friction forces resisting motion in a micromotor are concentrated near the rotor–hub interface, where continuous physical contact occurs. Surface roughness usually has a strong influence on the friction characteristics on the micro–nanoscale. A catalog of roughness measurements on various components of a MEMS device does not exist in the literature. Using an AFM, measurements on

**Table 23.7** Surface roughness parameters and microscale coefficient of friction for various micromotor component surfaces measured using an AFM. Mean and  $\pm 1\sigma$  values are given

	RMS roughness <sup>a</sup> (nm)	P–V distance <sup>a</sup> (nm)	Skewness <sup>a</sup> Sk	Kurtosis <sup>a</sup> K	Coefficient of microscale friction <sup>b</sup> ( $\mu$ )
Rotor topside	21 $\pm$ 0.6	225 $\pm$ 23	1.4 $\pm$ 0.30	6.1 $\pm$ 1.7	0.07 $\pm$ 0.02
Rotor underside	14 $\pm$ 2.4	80 $\pm$ 11	– 1.0 $\pm$ 0.22	3.5 $\pm$ 0.50	0.11 $\pm$ 0.03
Stator topside	19 $\pm$ 1	246 $\pm$ 21	1.4 $\pm$ 0.50	6.6 $\pm$ 1.5	0.08 $\pm$ 0.01

<sup>a</sup>Measured from a tapping-mode AFM scan of size 5  $\mu\text{m}$   $\times$  5  $\mu\text{m}$  using a standard Si tip scanning at 5  $\mu\text{m/s}$  in a direction orthogonal to the long axis of the cantilever

<sup>b</sup>Measured using an AFM in contact mode at 5  $\mu\text{m}$   $\times$  5  $\mu\text{m}$  scan size using a standard Si<sub>3</sub>N<sub>4</sub> tip scanning at 10  $\mu\text{m/s}$  in a direction parallel to the long axis of the cantilever

various component surfaces were made for the first time by Sundararajan and Bhushan [217]. Table 23.7 shows various surface roughness parameters obtained from 5  $\mu\text{m}$   $\times$  5  $\mu\text{m}$  scans of the various component surfaces of several unlubricated micromotors using the AFM in tapping mode. A surface with a Gaussian height distribution should have a skewness of 0 and kurtosis of 3. Although the rotor and stator top surfaces exhibit comparable roughness parameters, the underside of the rotors exhibits lower root-mean-square (RMS) roughness and peak-to-valley distance values. More importantly, the rotor underside shows negative skewness and lower kurtosis than the topsides, both of which are conducive to high real area of contact and hence high friction [80, 82]. The rotor underside also exhibits a higher coefficient of microscale friction than the rotor topside and stator, as shown in Table 23.7. Figure 23.51 shows representative surface height maps of the various surfaces of a micromotor measured using the AFM in tapping mode. The rotor underside exhibits varying topography from the outer edge to the middle and inner edge. At the outer edges, the topography shows smaller circular asperities, similar to the topside. The middle and inner regions show deep pits with fine edges that may have been created by the etchants used for etching of the sacrificial layer. It is known that etching can affect the roughness of surfaces in surface micromachining. The residence time of the etchant near the inner region is high, which is responsible for the larger pits. Figure 23.52 shows the roughness of the surface directly beneath the rotors (the base polysilicon layer). There appears to be a difference in the roughness between the portion of this surface that was initially underneath the rotor (region B) during fabrication and the portion that was away from the rotor and hence always exposed (region A). The former region shows lower roughness than the latter region. This suggests that the surfaces at the rotor–hub interface that come into contact at the end of the fabrication process exhibit large real areas of contact that result in high friction.

23.6.2 Adhesion Measurements of Microstructures

Surface force apparatus (SFA) and AFMs are used to measure adhesion on micro- to nanoscales between two surfaces. In the SFA, adhesion of liquid films

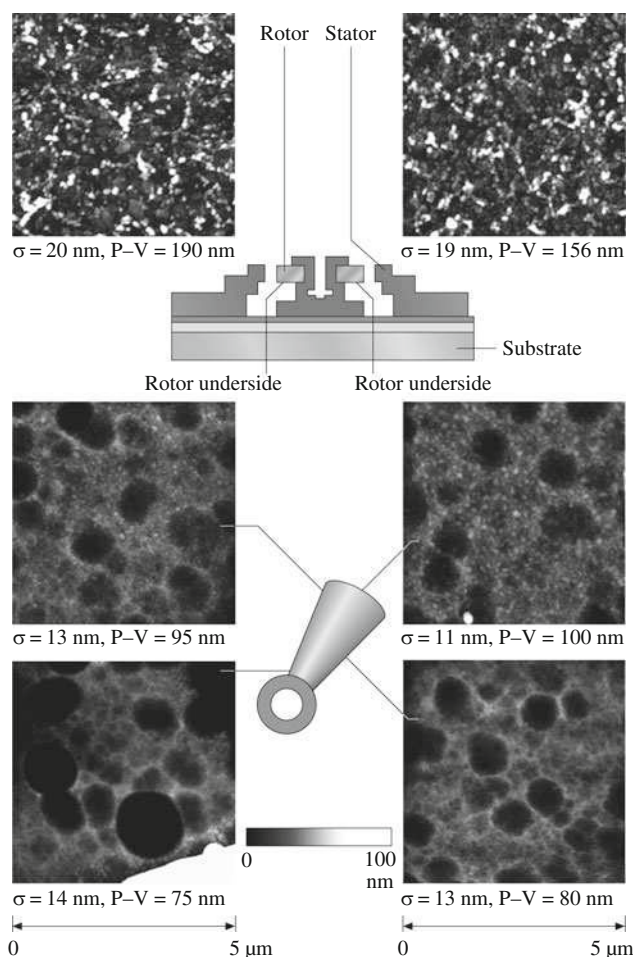
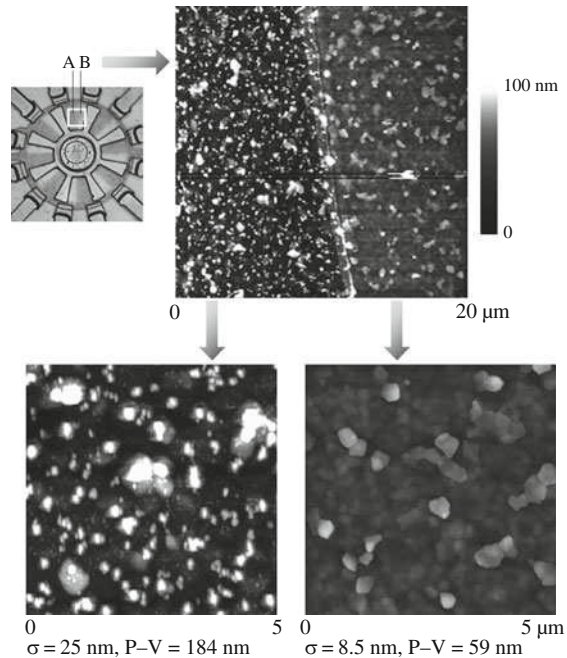


**Fig. 23.51** Representative AFM surface height images obtained in tapping mode ( $5 \mu\text{m} \times 5 \mu\text{m}$  scan size) of various component surfaces of a micromotor; root-mean-square (RMS) roughness and peak-to-valley values of the surfaces are given. The underside of the rotor exhibits drastically different topography from the topside (after [217])

sandwiched between two curved and smooth surfaces is measured. In an AFM, as discussed earlier, adhesion between a sharp tip and the surface of interest is measured. The propensity for adhesion between two surfaces can be evaluated by studying the tendency of microstructures with well-defined contact areas, covering a wide spectrum of suspension compliances, to stick to the underlying substrate. The test structures which have been used include the cantilever beam array (CBA) technique with different lengths [218, 219, 220, 221] and stand-off multiple dimples mounted on microstructures with a range of compliances, standing above a substrate [222]. The CBA technique, which is more commonly used, utilizes an array of micromachined polysilicon beams (for Si MEMS applications) on the

**Fig. 23.52** Surface height images of polysilicon regions directly below the rotor. Region A is away from the rotor while region B was initially covered by the rotor prior to the release etch of the rotor. During this step, slight movement of the rotor caused region B to be exposed (after [217])



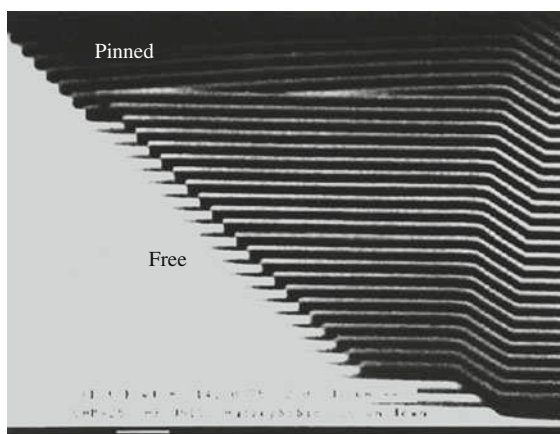
mesoscopic length scale, anchored to the substrate at one end and with different lengths parallel to the surface. It relies on peeling and detachment of cantilever beams. The change in free energy or the reversible work done to separate unit areas of two surfaces from contact is called the work of adhesion. To measure the work of adhesion, electrostatic actuation is used to bring all beams into contact with the substrate (Fig. 23.53) [218, 220]. Once the actuation force is removed, the beams begin to peel themselves off the substrate, which can be observed with an optical interference microscope (e.g., a Wyko surface profiler). For beams shorter than a characteristic length, the so-called detachment length, their stiffness is sufficient to free them completely from the substrate underneath. Beams larger than the detachment length remain adhered. The beams at the transition region start to detach and remain attached to the substrate just at the tips. For this case, by equating the elastic energy stored within the beam and the beam–substrate interfacial energy, the work of adhesion  $W_{\text{ad}}$  can be calculated by [218]

$$W_{\text{ad}} = \frac{3Ed^2t^3}{8\ell_d^4}, \quad (23.7)$$

where  $E$  is the Young's modulus of the beam,  $d$  is the spacing between the undeflected beam and the substrate,  $t$  is the beam thickness, and  $\ell_d$  is the detachment length. The technique has been used to screen methods for adhesion reduction in polysilicon microstructures.



**Fig. 23.53** SEM micrograph of a micromachined array of polysilicon cantilever beams of increasing length. The micrograph shows the onset of pinning for beams longer than  $34\ \mu\text{m}$  (after [218])



### 23.6.3 *Microtriboapparatus for Adhesion, Friction, and Wear of Microcomponents*

To measure adhesion, friction, and wear between two microcomponents, a microtriboapparatus has been used. Figure 23.54 shows a schematic of a microtriboapparatus capable of using MEMS components for tests [223]. In this apparatus, an upper specimen, mounted on a soft cantilever beam, comes into contact with a lower specimen mounted on a lower specimen holder. The apparatus consists of two piezos ( $x$ - and  $z$ -piezos) and four fiber-optic sensors ( $x$ - and  $z$ -displacement sensors, and  $x$ - and  $z$ -force sensors). For adhesion and friction studies,  $z$ - and  $x$ -piezos are used to bring the upper specimen and lower specimen into contact and to apply a relative motion in the lateral direction, respectively. The  $x$ - and  $z$ -displacement sensors are used to measure the lateral position of the lower specimen and vertical position of the upper specimen, respectively. The  $x$ - and  $z$ -force sensors are used to measure friction force and the normal load/adhesive force between these two specimens, respectively, by monitoring the deflection of the cantilever.

As most MEMS/NEMS devices are fabricated from silicon, study of silicon-on-silicon contacts is important. This contact was simulated by a flat single-crystal Si (100) wafer (phosphorus-doped) specimen sliding against a single-crystal Si(100) ball (1 mm in diameter,  $5 \times 10^{17}$  atoms/cm<sup>3</sup> boron doped) mounted on a stainless-steel cantilever [223, 224]. Both of them have a native oxide layer on their surfaces. The other materials studied were 10 nm-thick DLC deposited by filtered cathodic arc deposition on Si(100), 2.3 nm-thick chemically bonded PFPE (Z-DOL, BW) on Si(100), and hexadecane thiol (HDT) monolayer on evaporated Au(111) film to investigate their anti-adhesion performance.

It is well known that, in computer rigid disk drives, the adhesive force between a magnetic head and a magnetic disk increases rapidly with increasing rest time [34]. Considering that adhesion and friction are the major issues that lead to the failure of MEMS/NEMS devices, the effect of rest time on the microscale on Si(100), DLC,



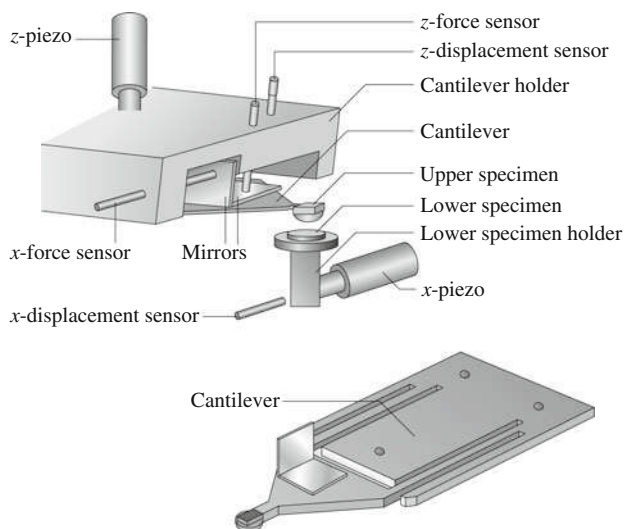
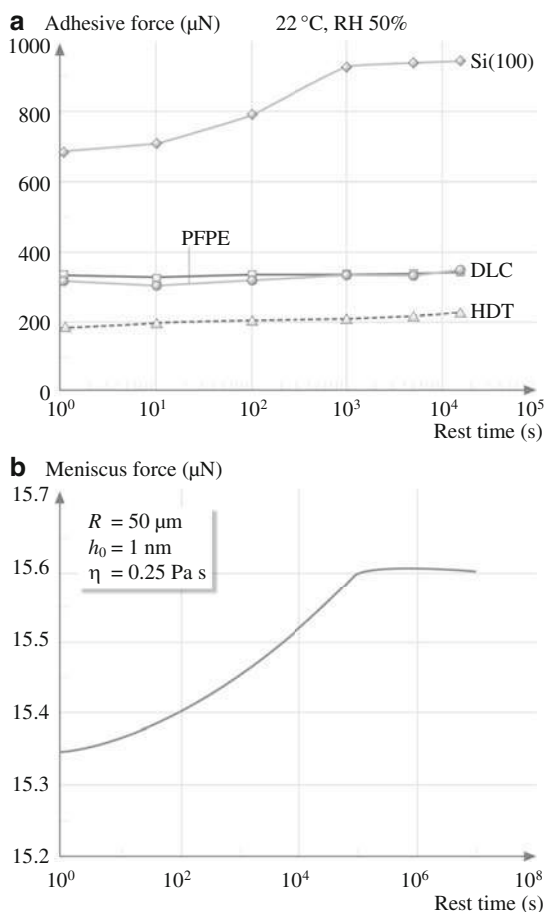


**Fig. 23.54** Schematic of the microtriboapparatus including specially designed cantilever (with two perpendicular mirrors attached to the end), lower specimen holder, two piezos ( $x$ - and  $z$ -piezos), and four fiber-optic sensors ( $x$ - and  $z$ -displacement sensors and  $x$ - and  $z$ -force sensors) (after [223])

PFPE, and HDT was studied; the results are summarized in Fig. 23.55a. It is found that the adhesive force of Si(100) increases logarithmically with rest time up to a certain equilibrium time ( $t = 1,000$  s), after which it remains constant. Figure 23.55a also shows that the adhesive force of DLC, PFPE, and HDT does not change with rest time. Single-asperity contact modeling of the dependence of meniscus force on rest time has been carried out by Chilamakuri and Bhushan [225], and the modeling results (Fig. 23.55b) verify experimental observations. Due to the presence of a thin film of adsorbed water on Si(100), a meniscus forms around the contacting asperities and grows with time until equilibrium occurs, which causes the effect of rest time on its adhesive force. The adhesive forces of DLC, PFPE, and HDT do not change with rest time, which suggests that the water meniscus is not present on their surfaces.

The measured adhesive forces of Si(100), DLC, PFPE, and HDT at rest time of 1 s are summarized in Fig. 23.56, which shows that the presence of solid films of DLC, PFPE, and HDT greatly reduces the adhesive force of Si(100), whereas HDT film has the lowest adhesive force. It is well known that the native oxide layer ( $\text{SiO}_2$ ) on top of the Si(100) wafer exhibits hydrophilic properties, and water molecules, produced by capillary condensation of water vapor from the environment, can easily be adsorbed on this surface. The condensed water will form a meniscus as the upper specimen approaches the lower specimen surface. The meniscus force is a major contributor to the adhesive force. In the case of DLC, PFPE, and HDT, the films are found to be hydrophobic based on contact angle measurements, and the amount of condensed water vapor is low as compared with

**Fig. 23.55** (a) Influence of rest time on the adhesive force of Si(100), DLC, chemically bonded PFPE, and HDT. (b) Single-asperity contact modeling results of the effect of rest time on the meniscus force for an asperity of radius  $R$  in contact with a flat surface with a water film of thickness of  $h_0$  and absolute viscosity of  $\eta_0$  (after [225])



that on Si(100). It should be noted that the measured adhesive force is generally higher than that measured in AFM, because the larger radius of Si(100) ball as compared with that of an AFM tip induces larger meniscus and van der Waals forces.

To investigate the effect of velocity on friction, the friction force was measured as a function of velocity, as summarized in Fig. 23.57a. This indicates that, for Si(100), the friction force initially decreases with increasing velocity until equilibrium occurs. Figure 23.57a also indicates that the velocity has almost no effect on the friction properties of DLC, PFPE, and HDT. This implies that the friction mechanisms of DLC, PFPE, and HDT do not change with velocity. For Si(100), at high velocity, the meniscus is broken and does not have enough time to rebuild. In addition, it is also believed that tribochemical reaction plays an important role. High velocity leads to tribochemical reactions of Si(100) (which has  $\text{SiO}_2$  native oxide) with water molecules to form  $\text{Si}(\text{OH})_4$  film. This film is removed and continuously replenished during sliding. The  $\text{Si}(\text{OH})_4$  layer at the sliding surface

**Fig. 23.56** Adhesive forces of Si(100), DLC, chemically bonded PFPE, and HDT at ambient condition, and a schematic showing the relative size of the water meniscus on different specimens

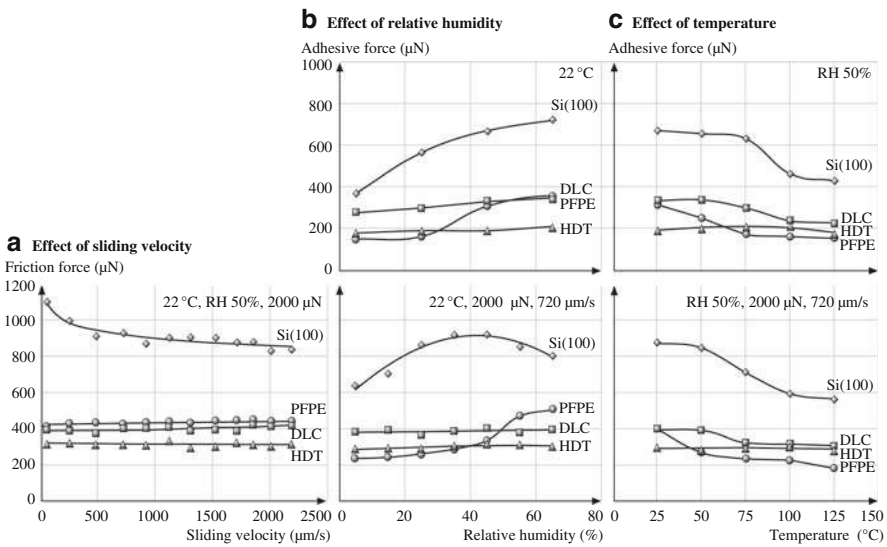
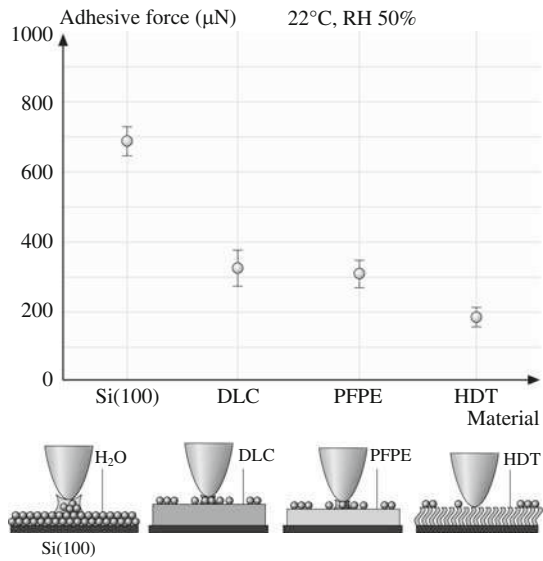


**Fig. 23.57** The influence of (a) sliding velocity on the friction forces, (b) relative humidity on the adhesive and friction forces, and (c) temperature on the adhesive and friction forces of Si(100), DLC, chemically bonded PFPE, and HDT

is known to be of low shear strength. The breaking of the water meniscus and the formation of the  $\text{Si}(\text{OH})_4$  layer results in a decrease in the friction force of Si(100). The DLC, PFPE, and HDT surfaces exhibit hydrophobic properties, and can adsorb

few water molecules under ambient conditions. The aforementioned meniscus breaking and tribochemical reaction mechanisms do not exist for these films. Therefore, their friction force does not change with velocity.

The influence of relative humidity was studied in an environmentally controlled chamber. The adhesive force and friction force were measured by making measurements at increasing relative humidity; the results are summarized in Fig. 23.57b, which shows that, for Si(100), the adhesive force increases with relative humidity, but the adhesive force of DLC and PFPE only shows a slight increase when humidity is  $> 45\%$ , while the adhesive force of HDT does not change with humidity. Figure 23.57b also shows that, for Si(100), the friction force increases with an increase in relative humidity up to  $45\%$ , and then it shows a slight decrease with further increase in the relative humidity. For PFPE, there is an increase in the friction force when humidity is  $> 45\%$ . In the whole testing range, relative humidity does not have any apparent influence on the friction properties of DLC and HDT. In the case of Si(100), the initial increase of relative humidity up to  $45\%$  causes more adsorbed water molecules, which form a larger water meniscus that leads to an increase of friction force. However, at very high humidity of  $65\%$ , large quantities of adsorbed water can form a continuous water layer that separates the tip and sample surfaces, and acts as a kind of lubricant, which causes a decrease in the friction force. For PFPE, dewetting of lubricant film at humidity  $> 45\%$  results in an increase in adhesive and friction forces. The DLC and HDT surfaces show hydrophobic properties, and increasing relative humidity does not play much of a role in their friction force.

The influence of temperature was studied using a heated stage. The adhesive force and friction force were measured by making measurements at increasing temperatures from  $22^{\circ}\text{C}$  to  $125^{\circ}\text{C}$ . The results are presented in Fig. 23.57c, which shows that, once the temperature is  $> 50^{\circ}\text{C}$ , increasing temperature causes a significant decrease of adhesive and friction forces of Si(100) and a slight decrease in the case of DLC and PFPE. However, the adhesion and friction forces of HDT do not show any apparent change with test temperature. At high temperature, desorption of water and reduction of the surface tension of water lead to the decrease of adhesive and friction forces of Si(100), DLC, and PFPE. However, in the case of HDT film, as only a few water molecules are adsorbed on the surface, the aforementioned mechanisms do not play a large role. Therefore, the adhesive and friction forces of HDT do not show any apparent change with temperature. Figure 23.57 shows that, in the whole velocity, relative humidity, and temperature test range, the adhesive force and friction force of DLC, PFPE, and HDT are always smaller than that of Si(100), whereas HDT has the smallest value.

To summarize, several methods can be used to reduce adhesion in microstructures. MEMS/NEMS surfaces can be coated with hydrophobic coatings such as PFPEs, SAMs, and passivated DLC coatings. It should be noted that other methods to reduce adhesion include the formation of dimples on the contact surfaces to reduce contact area [13, 80, 82, 84, 154, 155, 220]. Furthermore, an increase in the hydrophobicity of solid surfaces (high contact angle, approaching  $180^{\circ}$ ) can be achieved by using surfaces with suitable roughness, in addition to lowering their

surface energy [204, 205, 210]. The hydrophobicity of surfaces is dependent upon a subtle interplay between surface chemistry and mesoscopic topography. The self-cleaning mechanism or so-called *lotus effect* is closely related to the superhydrophobic properties of the biological surfaces, which usually show microsculptures on specific scales.

### 23.6.4 Static Friction Force (Stiction) Measurements in MEMS

In MEMS devices involving parts in relative motion to each other, such as micromotors, large friction forces become the factor limiting the successful operation and reliability of the device. It is generally known that most micromotors cannot be rotated as manufactured and require some form of lubrication. It is therefore critical to determine the friction forces present in such MEMS devices. To measure the static friction of a rotor-bearing interface in a micromotor in situ, Tai and Muller [226] measured the starting torque (voltage) and pausing position for different starting positions under a constant bias voltage. A friction–torque model was used to obtain the coefficient of static friction. To measure the in situ kinetic friction of the turbine and gear structures, Gabriel et al. [227] used a laser-based measurement system to monitor the steady-state spins and decelerations. Lim et al. [228] designed and fabricated a polysilicon microstructure to measure the static friction of various films in situ. The microstructure consisted of a shuttle suspended above an underlying electrode by a folded beam suspension. A known normal force was applied, and the lateral force was measured to obtain the coefficient of static friction. Beerschwinger et al. [229] developed a cantilever-deflection rig to measure the friction in LIGA-processed micromotors [230]. These techniques employ indirect methods to determine the friction forces, or involve fabrication of complex structures.

A novel technique to measure the static friction force (stiction) encountered in surface-micromachined polysilicon micromotors using an AFM has been developed by Sundararajan and Bhushan [217]. Continuous physical contact occurs during rotor movement (rotation) in micromotors between the rotor and lower hub flange. In addition, contact occurs at other locations between the rotor and the hub surfaces and between the rotor and the stator. Friction forces will be present at these contact regions during motor operation. Although the actual distribution of these forces is not known, they can be expected to be concentrated near the hub, where there is continuous contact. If we therefore represent the static friction force of the micromotor as a single force  $F_S$  acting at point  $P_1$  (as shown in Fig. 23.58a), then the magnitude of the frictional torque about the center of the motor (O) that must be overcome before rotor movement can be initiated is

$$T_S = F_S \ell_1, \quad (23.8)$$

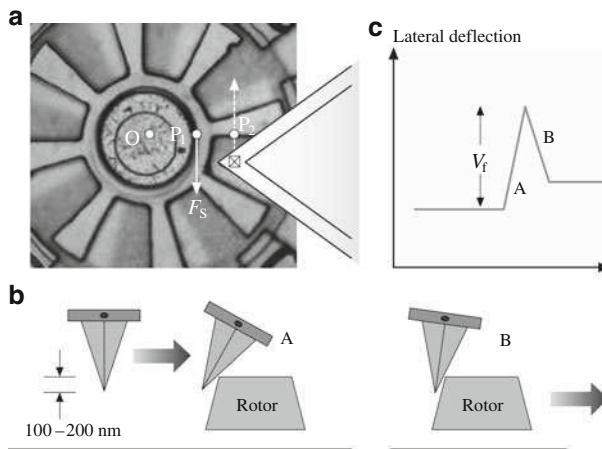
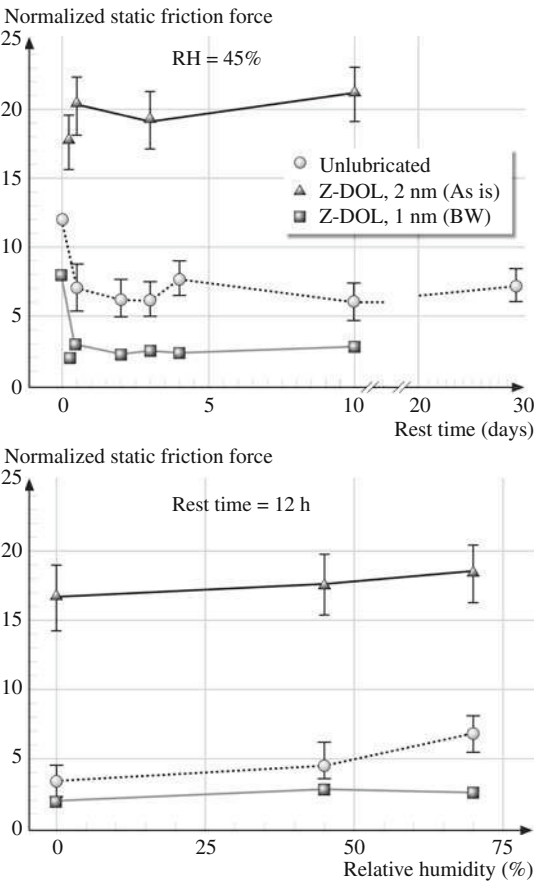


**Fig. 23.58** (a) Schematic of the technique used to measure the force  $F_s$  required to initiate rotor movement using an AFM/FFM. (b) As the tip is pushed against the rotor, the lateral deflection experienced by the rotor due to the twisting of the tip prior to rotor movement is a measure of the static friction force  $F_s$  of the rotors. (c) Schematic of the lateral deflection expected during the aforementioned experiment. The peak  $V_f$  is related to the state of the rotor (after [217])

where  $\ell_1$  is the distance  $OP_1$ , which is assumed to be the average distance from the center at which the friction force  $F_s$  occurs. Now consider an AFM tip moving against a rotor arm in a direction perpendicular to the long axis of the cantilever beam (the rotor arm edge closest to the tip is parallel to the long axis of the cantilever beam), as shown in Fig. 23.58a. When the tip encounters the rotor at point  $P_2$ , the tip will twist, generating a lateral force between the tip and the rotor (event A in Fig. 23.58b). This reaction force will generate a torque about the center of the motor. Since the tip is trying to move further in the direction shown, the tip will continue to twist to a maximum value, at which the lateral force between the tip and the rotor becomes high enough such that the resultant torque  $T_f$  about the center of the motor equals the static friction torque  $T_s$ . At this point, the rotor will begin to rotate, and the twist of the cantilever decreases sharply (event B in Fig. 23.58b). The twist of the cantilever is measured in the AFM as a change in the lateral deflection signal (in volts), which is the underlying concept of friction force microscopy (FFM). The change in the lateral deflection signal corresponding to the above-mentioned events as the tip approaches the rotor is shown schematically in Fig. 23.58c. The value of the peak  $V_f$  is a measure of the force exerted on the rotor by the tip just before the static friction torque is matched and the rotor begins to rotate.

Using this technique, the viability of PFPE lubricants for micromotors has been investigated, and the effect of humidity on the friction forces of unlubricated and lubricated devices was studied as well. Figure 23.59 shows static friction forces, normalized by the weight of the rotor, of unlubricated and lubricated micromotors as a function of rest time and relative humidity. Rest time here is defined as the time

**Fig. 23.59** Static friction force values of unlubricated motors and motors lubricated using PFPE lubricants, normalized by the rotor weight, as a function of rest time and relative humidity. The rest time is defined as the time elapsed between a given experiment and the first experiment in which motor movement was recorded (time 0). The motors were allowed to sit at a particular humidity for 12 h prior to measurements (after [217])



elapsed between the first experiment conducted on a given motor (solid symbol at time zero) and subsequent experiments (open symbols). Each open symbol data point is an average of six measurements. It can be seen that, for the unlubricated motor and the motor lubricated with a bonded layer of Z-DOL(BW), the static friction force is highest for the first experiment and then drops to an almost constant level. In the case of the motor with an as-is mobile layer of Z-DOL, the values remain very high up to 10 days after lubrication. In all cases, there is negligible difference in the static friction force at 0% and 45% RH. At 70% RH, the unlubricated motor exhibits a substantial increase in the static friction force, while the motor with bonded Z-DOL shows no increase in static friction force due to the hydrophobicity of the lubricant layer. The motor with an as-is mobile layer of the lubricant shows consistently high values of static friction force that vary little with humidity.

Figure 23.60 summarizes static friction force data for two motors, M1 and M2, along with schematics of the meniscus effects for the unlubricated and lubricated

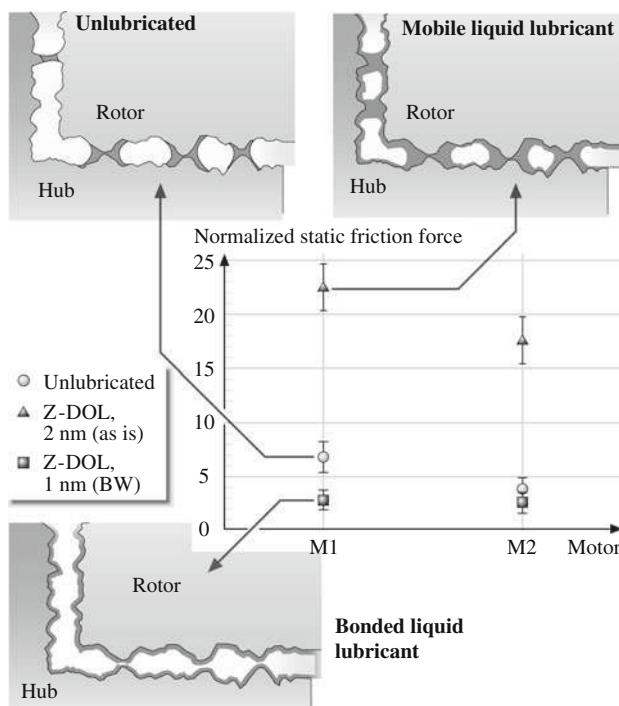


**Fig. 23.60** Summary of the effects of liquid and solid lubricants on the static friction force of micromotors. Despite the hydrophobicity of the lubricant used (Z-DOL), a mobile liquid lubricant (Z-DOL, as-is) leads to very high static friction force due to increased meniscus forces, whereas a solid-like lubricant (bonded Z-DOL, BW) appears to provide some amount of reduction in static friction force

surfaces. Capillary condensation of water vapor from the environment results in the formation of meniscus bridges between the contacting and near-contacting asperities of two surfaces in close proximity to each other, as shown in Fig. 23.60. For unlubricated surfaces, more menisci are formed at higher humidity, resulting in higher friction force between the surfaces. The formation of meniscus bridges is supported by the fact that the static friction force for unlubricated motors increases at high humidity (Fig. 23.60). Solid bridging may occur near the rotor–hub interface due to silica residues after the first etching process. In addition, the drying process after the final etch can result in liquid bridging formed by the drying liquid due to meniscus force at these areas [80, 82, 218, 219]. The initial static friction force will therefore be quite high, as evidenced by the solid data points in Fig. 23.60. Once the first movement of the rotor permanently breaks these solid and liquid bridges, the static friction force of the motors will drop (as seen in Fig. 23.60) to a value dictated predominantly by the adhesive energies of the rotor and hub surfaces, the real area of contact between these surfaces, and meniscus forces due to water vapor in the air, at which point, the effect of lubricant films can be observed. Lubrication with a



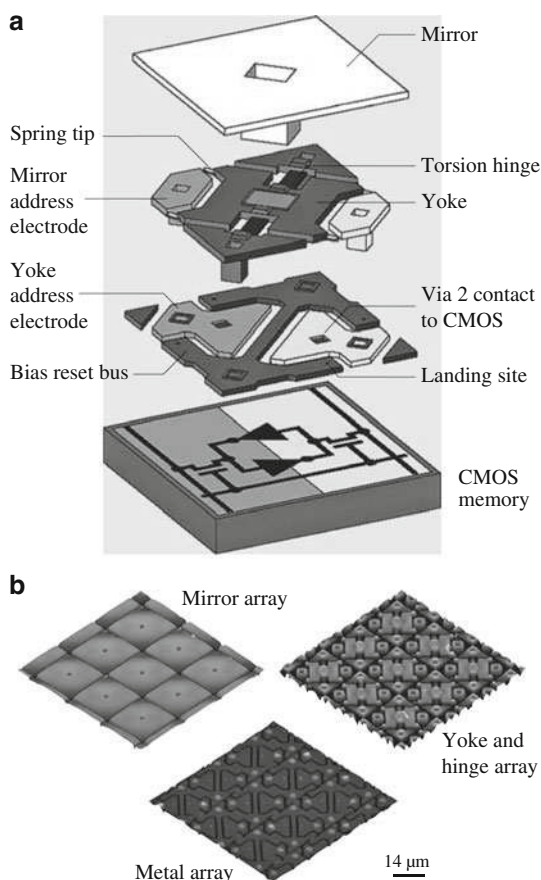
mobile layer, even a thin one, results in very high static friction forces due to meniscus effects of the lubricant liquid itself at and near the contact regions. It should be noted that a motor submerged in a liquid lubricant would result in a fully flooded lubrication regime. In this case there is no meniscus contribution, and only the viscous contribution to the friction forces would be relevant. However, submerging the device in a lubricant may not be a practical method. A solid-like hydrophobic lubricant layer (such as bonded Z-DOL) results in favorable friction characteristics of the motor. The hydrophobic nature of the lubricant inhibits meniscus formation between the contact surfaces and maintains low friction even at high humidity (Fig. 23.60). This suggests that solid-like hydrophobic lubricants are ideal for lubrication of MEMS, while mobile lubricants result in increased values of static friction force.

### **23.6.5 Mechanisms Associated with Observed Stiction Phenomena in Digital Micromirror Devices (DMD) and Nanomechanical Characterization**

DMDs are used in digital projection displays, as described earlier. The DMD has a layered structure, consisting of an aluminum alloy micromirror layer, a yoke and hinge layer, and a metal layer on a CMOS memory array [27, 28, 29]. A blown-up view of the DMD and the corresponding AFM surface height images are presented in Fig. 23.61 [108]. Single-layered aluminum alloy films are used for the construction of micromirrors; these are also sometimes used for the construction of hinges, spring tips, and landing sites. The aluminum-alloy films are overwhelmingly comprised of aluminum; trace elements (including Ti and Si) are present to suppress contact spiking and electromigration, which may occur if current densities become high during electrostatic operation. Multilayered sputtered  $\text{SiO}_2/\text{TiN}/\text{Al}$  alloy films are now generally used for the landing-site structure to minimize refraction throughout the visible region of the electromagnetic spectrum in order to increase the contrast ratio in projection display systems [231, 232]. These multilayered films are also generally used for hinges and spring tips. A low-surface-energy SAM is maintained on the surfaces of the DMD, which is packaged in a hermetic environment to minimize stiction during contact between the spring tip and the landing site. A SAM of perfluorinated  $n$ -alkanoic acid ( $\text{C}_n\text{F}_{2n-1}\text{O}_2\text{H}$ ) (e.g., perfluorodecanoic acid or PFDA,  $\text{CF}_3(\text{CF}_2)_8\text{COOH}$ ) applied by the vapor-phase deposition process is used. A getter strip of PFDA is included inside the hermetically sealed enclosure containing the chip, which acts as a reservoir in order to maintain a PFDA vapor within the package.

In order to identify a stuck mirror and characterize its nanotribological properties, the chip was scanned using an AFM [108]. It was found that it is hard to tilt the stuck micromirror back to its normal position by adding a normal load at the

**Fig. 23.61** (a) Exploded view of a DMD pixel. (b) AFM surface height images of various arrays. The DMD layers were removed by ultrasonic method (after [108])



rotatable corner of the micromirror; this is thus called a *hard* stuck micromirror. An example of a stuck micromirror is shown in Fig. 23.62a. Once the stuck micromirror was found, the region was repeatedly scanned at a large normal load, up to 300 nN. After several scans, the stuck micromirror was removed. Once the stuck micromirror was removed, the surrounding micromirrors could also be removed by continuous scanning under a large normal load (Fig. 23.62a, bottom row). The adhesive force of the landing site underneath the stuck micromirror and the normal micromirror are presented in Fig. 23.62b, which clearly indicates that the landing site underneath the stuck micromirror has much larger adhesion. A  $1\ \mu\text{m} \times 1\ \mu\text{m}$  view of landing sites under stuck and normal micromirrors are also shown in Fig. 23.62b. The landing site under the stuck micromirror has an apparent U-shaped wear mark, which is surrounded by a smeared area.

Liu and Bhushan [108] calculated contact stresses to examine if the stresses were high enough to cause wear at the spring tip–landing site interface. The calculated contact stress value was  $\approx 33\ \text{MPa}$ , which is substantially lower than the hardness,

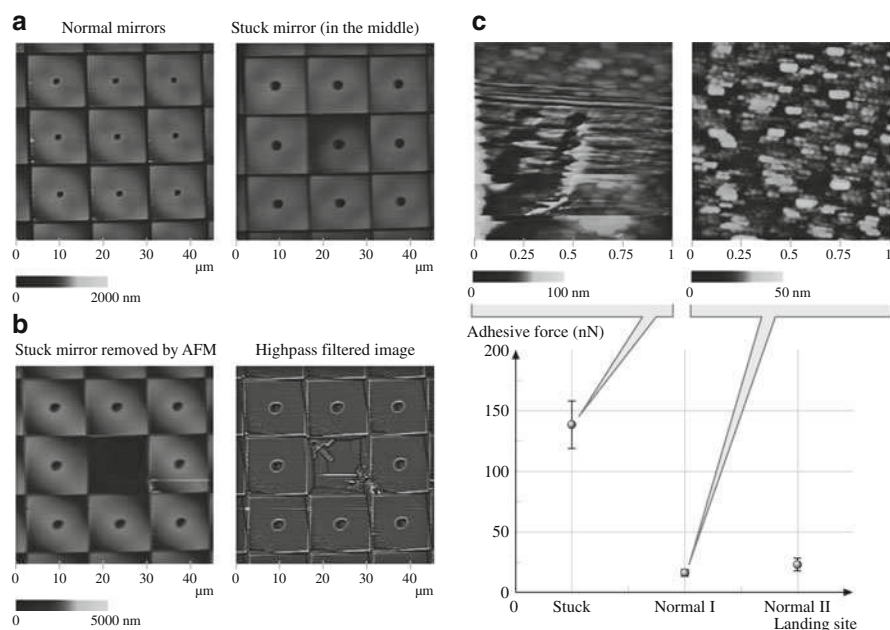


**Fig. 23.62** (a) The *top row* shows AFM surface height images of a stuck micromirror surrounded by eight normal micromirrors. (b) *Left image* shows the stuck micromirror which was removed by an AFM tip after repeated scanning at high normal load. The *right image* in the bottom row presents a high-pass-filtered image, in which the residual hinge that sits underneath the removed micromirror is clearly observed. (c) AFM surface height images and adhesive forces of the landing sites underneath the two normal micromirrors and the stuck micromirror (after [108])

therefore much plastic deformation and consequently wear was not expected. Wear mark was only found on a very few landing sites on the DMD, which means that the SAM coating can generally endure such high contact stresses. Based on data reported in the literature, coverage of vapor-deposited SAMs is expected to be  $\approx 97\%$ . The bond strength of the molecules close to the boundary of the uncovered sites is expected to be weak. Thus, the uncovered sites and the adjacent molecules are referred to as defects in the SAM coating. Occasionally, if contact occurs at the defect sites, the large cyclic stress may be close to the critical load, and lead to initial delamination of the SAM coating at the interface. The continuous contact leads to the formation of a high-surface-energy surface by exposure of the fresh substrate and formation of SAM fragments. This eventually leads to an increase in stiction by the formation of large menisci. Once this happens, the stress at the contact area is increased, which would accelerate the wear. Based on this hypothesis, suggested mechanisms for the wear and stiction of the landing site are summarized in Fig. 23.63. Wear initiates at the defect sites, and consequent high stiction can result in high wear. Improving the coverage and wear resistance of SAM coatings could enhance the yield of DMD.

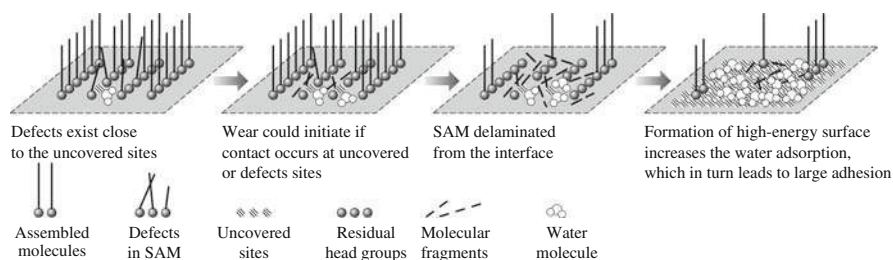


**Fig. 23.63** Suggested mechanisms for wear and stiction (after [108])

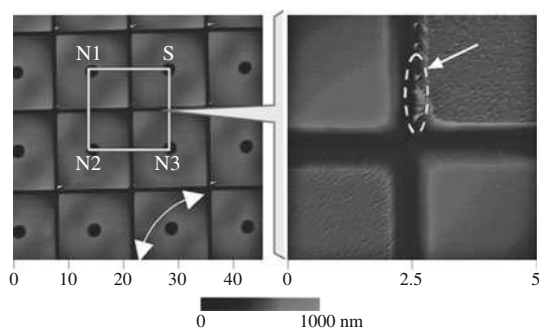


**Fig. 23.64** AFM surface height images of normal micromirrors and a soft-stuck micromirror. The soft-stuck micromirror is labeled S, and the normal micromirrors studied are labeled N1, N2, and N3 (after [109])

In some cases, the micromirrors are not fully stuck and can be moved by applying a load at the rotatable corner of the micromirror with a discontinuous motion, which is called *soft* stiction. Soft-stuck micromirrors studied by Liu and Bhushan [109] were identified in quality inspection. These micromirrors encountered slow transition from one end to the other (+1/−1). Figure 23.64 shows AFM surface height images of a location showing a stuck mirror (S) and surrounding normal micromirror array are almost the same. On the micromirrors of interest, tilting test was performed at the corner of the micromirrors; the rotatable direction of the microarray is indicated by an arrow in Fig. 23.64. A load–displacement curve for the stuck micromirror is presented in Fig. 23.65; it is not smooth and appears serrated. This clearly indicates that, although the micromirror S can be rotated, it rotates with hesitation. In regimes 1 and 2, as marked in Fig. 23.65, the slopes are much higher. In order to understand the stiction mechanisms, stiction of the landing sites of normal and stuck mirrors were measured. Unlike a hard-stuck mirror, adhesive forces of soft-stuck and normal mirrors were comparable, which suggests that the SAM coating is intact for the soft-stuck mirror. It was found that a high normal load ( $\approx 900$  nN) and of the order of a couple of hundred scans were required to remove the soft-stuck micromirrors by the AFM, whereas, only about 300 nN

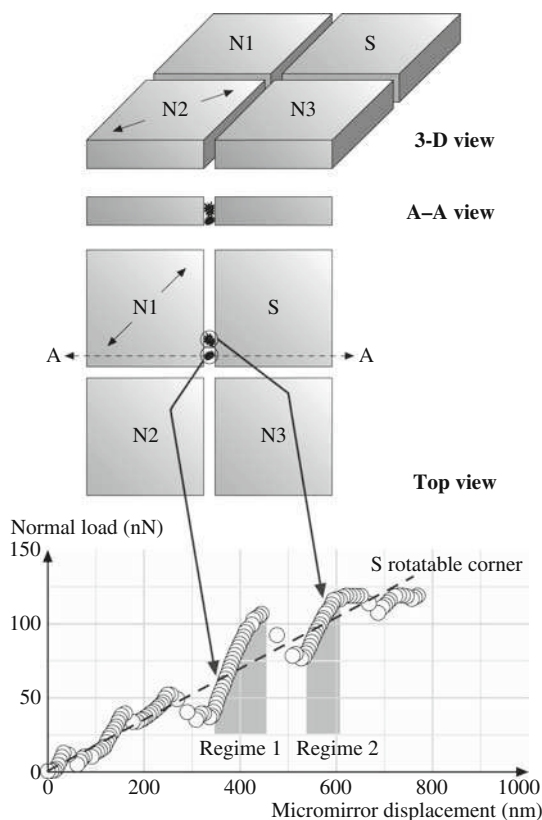
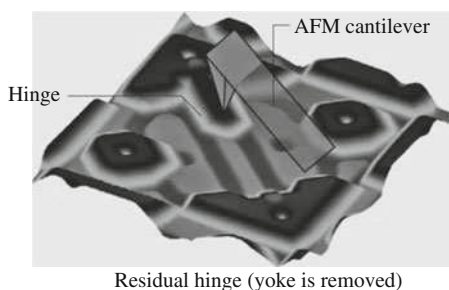


**Fig. 23.65** Load–displacement curve obtained on the rotatable corner of micromirror S, and schematic to illustrate the suggested mechanism for occurrence of soft stiction

and about ten scans were required to remove a hard-stuck mirror. After careful examination of the AFM images of the micromirror sidewalls in Fig. 23.64 (bottom left), it was noted that there were contaminant particles attached to the sidewalls of the micromirror S. It is therefore believed that, during the tilting test, for the micromirror S (see schematic in Fig. 23.65) a regime with a sharper slope will occur in the displacement curve. Extra force is required to overcome the resistance induced by these sidewall contamination particles. This is believed to be the reason for the slow transition of the micromirror during quality inspection.

Finally, nanomechanical characterization of various layers used in the construction of landing sites, hinge, and micromirror materials have been measured by Wei et al. [231, 232]. Bending and fatigue studies of hinges have been carried out by Liu and Bhushan [233] and Bhushan and Liu [234] to measure their stiffness and fatigue properties. For these studies, the micromirror was removed. During removal, the micromirror–yoke structure was removed simultaneously, leaving the hinge mounted on one end of the array (Fig. 23.66). The stiffness of the Al hinge was reported to be

**Fig. 23.66** AFM surface height image of the residual hinge and schematic diagram of the relative position of the hinge and AFM tip during the nanoscale bending and fatigue tests. The tip is located at the free end of the hinge (after [233])



comparable to that of bulk Al. The Al hinge exhibited higher modulus than the SiO<sub>2</sub> hinge. The fatigue properties depended upon the preparation of the hinge for testing.

## 23.7 Conclusions

The field of MEMS/NEMS and bioMEMS/bioNEMS has expanded considerably over the last decade. The large surface-to-volume ratio of these devices results in very high surface forces, such as adhesion and friction/stiction, that seriously undermine the performance and reliability of devices. There is a need for fundamental understanding of adhesion, friction, stiction, wear, and lubrication, and the role of contamination and environment, all on nanoscale. Most mechanical properties are known to be scale dependent, therefore the properties of nanostructures need to be measured. Using AFM-based techniques, researchers have conducted nanotribology and nanomechanics studies of materials and devices. In addition, component-level testing has been carried out to improve understanding of the nanotribological phenomena observed in MEMS/NEMS.

Macroscale and microscale tribological studies of silicon and polysilicon films have been performed. The effect of doping, oxide films, and environment on the tribological properties of these popular MEMS/NEMS materials has also been studied. SiC film is found to be a good candidate material for use in high-temperature MEMS/NEMS devices. Perfluoroalkyl self-assembled monolayers and bonded perfluoropolyether lubricants appear to be well suited for lubrication of micro-nanodevices under a range of environmental conditions. DLC coatings can also be used for low friction and wear.

For bioMEMS/bioNEMS, adhesion between biological molecular layers and the substrate, and friction and wear of biological layers can be important. Adhesion of biomolecules on Si substrate surfaces for various bioMEMS applications can be improved by nanopatterning and the chemical linker method. Friction and wear mechanisms of protein layers have been studied. The trajectory in the blood stream of submicron particles used for therapeutic and diagnostics purposes needs to be optimized in order for them to bond to target sites on the endothelium wall, for

which an analytical model has been developed. Roughness-induced hierarchical surfaces have been designed and fabricated for superhydrophobicity, self-cleaning, and low adhesion and friction.

Surface roughness measurements of micromachined polysilicon surfaces have been carried out using an AFM. The roughness distribution on surfaces is strongly dependent upon the fabrication process. Adhesion and friction of microstructures can be measured using a novel microtriboapparatus. Adhesion and friction measurements on silicon-on-silicon confirm AFM measurements that hexadecane thiol and bonded perfluoropolyether films exhibit superior adhesion and friction properties. Static friction force measurements of micromotors have been performed using an AFM. The forces are found to vary considerably with humidity. A bonded layer of perfluoropolyether lubricant is found to satisfactorily reduce the friction forces in the micromotor. Tribological failure modes of digital micromirror devices are either *hard* or *soft* stiction. In hard stiction, the tip on the yoke remains stuck to the landing site underneath. The mechanism responsible for this hard stiction is localized damage of the SAM on the landing site, whereas in soft stiction the mirror–yoke assembly rotates with hesitation. The mechanism responsible for soft stiction is contaminant particles present at the mirror sidewalls.

AFM/FFM-based techniques show the capability to study and evaluate nanotribology and nanomechanics related to MEMS/NEMS and bioMEMS/bioNEMS devices.

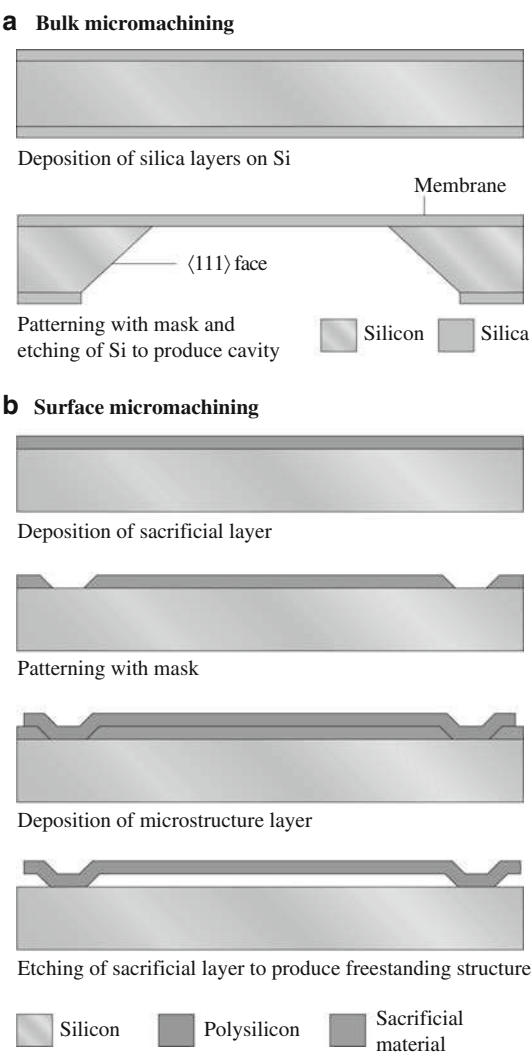
## 23.8 Appendix Micro-Nanofabrication Techniques

Micro-nanofabrication techniques include top-down methods, in which one builds down from the large to the small, and bottom-up methods, in which one builds up from the small to the large.

### 23.8.1 Top-Down Techniques

The top-down fabrication methods used in the construction of MEMS/NEMS include lithographic and nonlithographic techniques to produce micro- and nanostructures. The lithographic techniques fall into three basic categories: bulk micromachining, surface micromachining, and LIGA (a German acronym for *Lithographie Galvanoformung Abformung*, i.e., lithography, electroplating, and molding). The first two approaches, bulk and surface micromachining, mostly use planar photolithographic fabrication processes developed for semiconductor devices in producing two-dimensional (2-D) structures [13, 19, 235, 236, 237, 238]. The various steps involved in these two fabrication processes are shown schematically in Fig. 23.67. Bulk micromachining employs anisotropic etching to remove sections through the thickness of a single-crystal silicon wafer, typically

**Fig. 23.67** Schematic of process steps involved in (a) bulk micromachining and (b) surface micromachining for fabrication of MEMS



250–500  $\mu\text{m}$  thick. Bulk micromachining is a proven high-volume production process and is routinely used to fabricate microstructures such as accelerometers, pressure sensors, and flow sensors. In surface micromachining, structural and sacrificial films are alternatively deposited, patterned, and etched to produce a freestanding structure. These films are typically made of low-pressure chemical vapor deposition (LPCVD) polysilicon film with 2–20  $\mu\text{m}$  thickness. Surface micromachining is used to produce sensors, actuators, micromirror arrays, motors, gears, and grippers. The resolution in photolithography is dependent upon the wavelength of light. A commonly used light source is an argon fluoride excimer laser with 193 nm wavelength (ultraviolet, UV), used in patterning 90 nm lines and

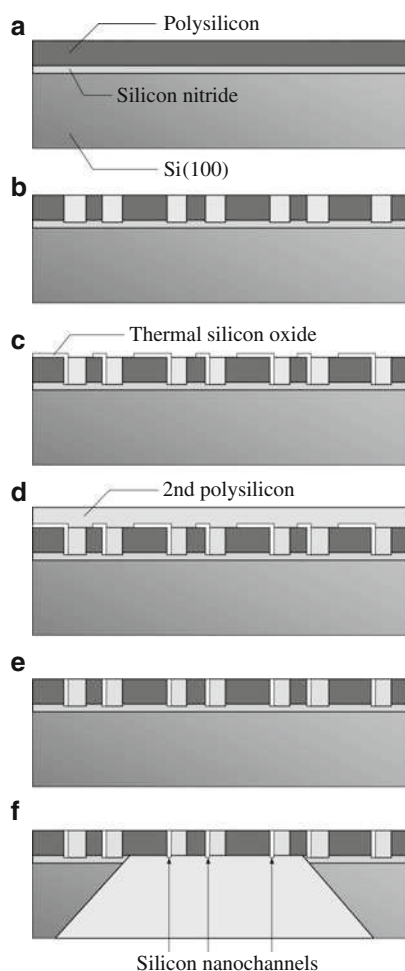


spaces. Deep-UV wavelengths, x-ray lithography, e-beam lithography, focused ion beam lithography, maskless lithography, liquid-immersion lithography, and STM writing by removing material atom by atom are some of the recent developments for sub-100 nm patterning.

The fabrication of nanostructures such as nanochannels with sub-10 nm resolution can be accomplished through several routes: electron beam (e-beam) lithography and sacrificial layer lithography (SLL). The process for e-beam lithographic technique is a finely focused electron beam that is exposed onto a resist surface; the exposure duration and location is controlled with the use of a computer [239, 240]. When the resist is exposed to the electron beam, the electrons either break or join the molecules in the resist, so the local characteristics are changed in such a way that further processes can either remove the exposed part (positive resist) or the unexposed part (negative resist). The resist material determines whether the molecules will break or join together and thus whether a positive or negative image is produced. E-beam lithography can be used either to create photolithographic masks for replication or to create devices directly. The masks that are created can be used for either optical or x-ray lithography. One limitation of e-beam lithography is that throughput is drastically reduced since a single electron beam is used to create the entire exposure pattern on the resist. While this technique is slower than conventional lithographic techniques, it is ideal for prototype fabrication because no masks are required.

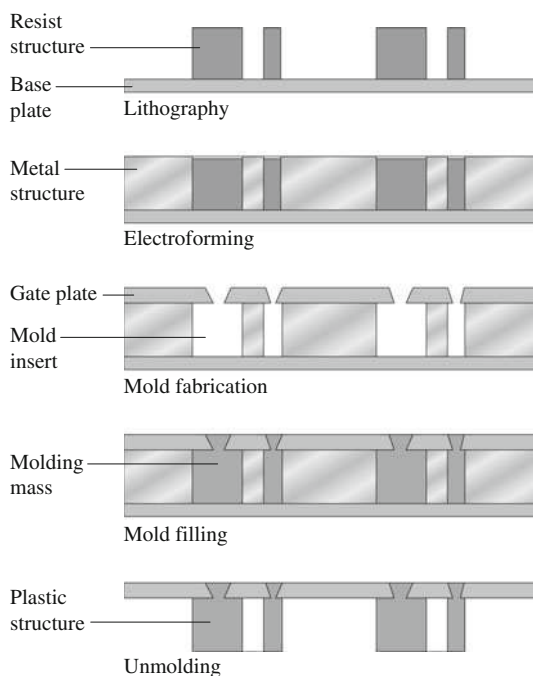
In the SLL process, the use of a sacrificial layer allows direct control of nanochannel dimensions as long as there exists a method for removing the sacrificial layer from the structural layers with absolute selectivity. A materials system with such selectivity is the silicon/silicon oxide system, which is used widely in the microfabrication of MEMS devices. The use of sidewall deposition of the sacrificial layer and subsequent etching allows for fabrication of high-density nanochannels for biomedical applications, based on surface micromachining [78]. Figure 23.68 shows a schematic of the process steps in the sacrificial layer lithography based on Hansford et al.'s [78] work on fabrication of polysilicon membranes with nanochannels. As with all membrane protocols, the first step in the fabrication is etching of the support ridge structure into the bulk silicon substrate. A low-stress silicon nitride (LSN, or simply nitride), which functions as an etch-stop layer, is then deposited using LPCVD. The base structural polysilicon layer (base layer) is deposited on top of the etch-stop layer. The plasma etching of holes in the base layer is what defines the shape of the pores. The buried nitride etch stop acts as an etch stop for the plasma etching of a polysilicon base layer. After the pore holes are etched through the base layer, the pore sacrificial thermal oxide layer is grown on the base layer. The basic requirement for the sacrificial layer is the ability to control its thickness with high precision across the entire wafer. Anchor points are defined in the sacrificial oxide layer to connect the base layer mechanically to the plug layer (necessary to maintain the pore spacing between layers). This is accomplished by using the same mask shifted from the pore holes. This produces anchors in one or two corners of each pore hole, which provides the desired connection between the structural layers while opening as much pore area as possible. After the anchor

**Fig. 23.68** Schematic of process steps involved in sacrificial layer lithography. (a) Growth of silicon nitride layer (etch stop) and base polysilicon deposition, (b) hole definition in base, (c) growth of thin sacrificial oxide and patterning of anchor points, (d) deposition of plug polysilicon, (e) planarization of plug layer, and (f) deposition and patterning of protective nitride layer through etch, followed by etching of protective, sacrificial, and etch layers for final release of the structure in HF (after [78])



points are etched through the sacrificial oxide, the plug polysilicon layer is deposited (using LPCVD) to fill in the holes. To open the pores at the surface, the plug layer is planarized using chemical mechanical polishing (CMP) down to the base layer, leaving the final structure with the plug layer only in the pore hole openings. When the silicon wafer is ready for release, a protective nitride layer is deposited on the wafer (completely covering both sides of the wafer). The backside etch windows are etched in the protective layer, exposing the silicon wafer in the desired areas, and the wafer is placed in a KOH bath to etch. After the silicon wafer is completely removed up to the membrane (as evidenced by the smooth buried etch-stop layer), the protective, sacrificial, and etch-stop layers are removed by etching in concentrated HF. Etching of the sacrificial layer in polysilicon film defines nanochannels.

**Fig. 23.69** Schematic of process steps involved in LIGA fabrication of MEMS



The LIGA process is based on combined use of x-ray lithography, electroplating, and molding processes. X-rays produced by synchrotron radiation are used to prepare the mold. The steps involved in the LIGA process are shown schematically in Fig. 23.69. LIGA is used to produce high-aspect-ratio MEMS (HARMEMS) devices that are up to 1 mm in height and only a few microns in width or length [241]. The LIGA process yields very sturdy 3-D structures due to their increased thickness. One of the limitations of silicon microfabrication processes originally used for fabrication of MEMS devices is the lack of suitable materials that can be processed. However, with LIGA, a variety of nonsilicon materials such as metals, ceramics, and polymers can be processed.

Nonlithographic micromachining processes, primarily in Europe and Japan, are also being used for fabrication of millimeter-scale devices using direct material microcutting or micromechanical machining (such as microturning, micromilling, and microdrilling) or removal by energy beams (such as microspark erosion, focused ion beam, laser ablation, and laser polymerization) [19, 242]. Hybrid technologies including LIGA and high-precision micromachining techniques have been used to produce miniaturized motors, gears, actuators, and connectors [87, 91, 92, 243]. These millimeter-scale devices may find more immediate applications.

The micro-nanofabrication technique known as *soft lithography* is a nonlithographic technique [54, 60, 244, 245] in which a master or mold is used to generate patterns, defined by the relief on its surface, on polymers by replica molding [246], hot embossing (nanoimprint lithography) [247], or by contact printing (known as

microcontact printing,  $\mu$ CP) [248]. Soft lithography is faster, less expensive, and more suitable for most biological applications than glass or silicon micromachining. Polymers have established an important role in bioMEMS/bioNEMS because of their reduced cost. The use of polymers also offers a wide range of material properties to allow tailoring of biological interactions for improved biocompatibility. Polymer fabrication is believed to be about an order of magnitude cheaper than silicon fabrication.

Replica molding is the transfer of a topographic pattern by curing or solidifying a liquid precursor against the original patterned mold. The mold or stamp is generally made of a two-part polymer (elastomer and curing agent), such as poly(dimethylsiloxane) (PDMS) from photolithographically generated photoresist master. Solvent-based embossing, or imprinting, uses a solvent to restructure a polymer film. Hot embossing, also called nanoimprint lithography, usually refers to the transfer of a pattern from a micromachined quartz or metal master to a pliable plastic sheet. Heat and high pressure allow the plastic sheet to become imprinted. These sheets can then be bonded to various plastics such as poly(methyl methacrylate) (PMMA). Nanoimprint lithography can produce patterns on a surface with 10 nm resolution. Contact printing uses a patterned stamp to transfer ink (mostly self-assembled monolayer) onto a surface in a pattern defined by the raised regions of a stamp. These techniques can be used to pattern line widths as small as 60 nm.

Replica molding is commonly used for mass-produced, disposable plastic micro-nanocomponents, for example micro-nanofluidic chips, generally made of PDMS and PMMA [245, 249]; it is more flexible in terms of materials choice for construction than conventional photolithography.

To assemble microsystems, microrobots are used. Microrobotics include building blocks such as steering links, microgrippers, conveyor system, and locomotive robots [17].

### 23.8.2 Bottom-Up Fabrication (Nanochemistry)

The bottom-up approach (from small to large) largely relies on nanochemistry [39, 40, 42, 43, 44, 45, 46, 47]. The bottom-up approach includes chemical synthesis, spontaneous *self-assembly* of molecular clusters (molecular self-assembly) from simple reagents in solution or biological molecules as building blocks to produce three-dimensional nanostructures as done by nature, quantum dots (nanocrystals) of arbitrary diameter (about  $10\text{--}10^5$  atoms), molecular-beam epitaxy (MBE) and organometallic vapor-phase epitaxy (OMVPE) to create specialized crystals one atomic or molecular layer at a time, and manipulation of individual atoms by scanning tunneling microscope, atomic force microscope, or atom optics. The self-assembly must be encoded; that is, one must be able to precisely assemble one object next to another to form a designed pattern. A variety of nonequilibrium plasma chemistry techniques are also used to produce layered nanocomposites,

nanotubes, and nanoparticles. Nanostructures can also be fabricated using mechanosynthesis with proximal probes.

## References

1. R.J. Chen, H.C. Choi, S. Bangsaruntip, E. Yenilmez, X. Tang, Q. Wang, Y.L. Chang, H. Dai, An investigation of the mechanisms of electrode sensing of protein adsorption on carbon nanotube devices. *J. Am. Chem. Soc.* **126**, 1563–1568 (2004)
2. D. Srivastava, Computational nanotechnology of carbon nanotubes. In: *Carbon Nanotubes: Science and Applications*, ed. by M. Meyyappan (CRC Press, Boca Raton, FL, 2004) pp. 25–63
3. W.G. van der Wiel, S. De Franceschi, J.M. Elzerman, T. Fujisawa, S. Tarucha, L.P. Kouwenhoven, Electron transport through double quantum dots. *Rev. Mod. Phys.* **75**, 1–22 (2003)
4. Anonymous, *Microelectromechanical Systems: Advanced Materials and Fabrication Methods, NMAB-483* (National Academy Press, Washington, DC, 1997)
5. M. Roukes, Nanoelectromechanical systems face the future. *Phys. World* **2**, 25–31 (2001)
6. Anonymous, Small Tech 101 – An Introduction to Micro- and Nanotechnology, Small Times (2003)
7. M. Schulenburg, *Nanotechnology – Innovation for Tomorrow's World* (European Commission, Research DG, Brussels, 2004)
8. J.C. Eloy, Status of the MEMS Industry 2005, Report of Yole Developpement, France, presented at SPIE Photonic West, San Jose (2005)
9. S. Lawrence, Nanotech grows up. *Technol. Rev.* **108**(6), 31 (2005)
10. R.S. Muller, R.T. Howe, S.D. Senturia, R.L. Smith, R.M. White, *Microsensors* (IEEE Press, New York, 1990)
11. I. Fujimasa, *Micromachines: A New Era in Mechanical Engineering* (Oxford University Press, Oxford, 1996)
12. W.S. Trimmer (ed.), *Micromachines and MEMS, Classic and Seminal Papers to 1990* (IEEE Press, New York, 1997)
13. B. Bhushan, *Tribology Issues and Opportunities in MEMS* (Kluwer, Dordrecht, 1998)
14. G.T.A. Kovacs, *Micromachined Transducers Sourcebook* (McGraw-Hill, Boston, MA, 1998)
15. S.D. Senturia, *Microsystem Design* (Kluwer, Boston, MA, 2000)
16. M. Elwenspoek, R. Wiegerink, *Mechanical Microsensors* (Springer, Heidelberg, 2001)
17. M. Gad-el-Hak, *The MEMS Handbook* (CRC Press, Boca Raton, FL, 2002)
18. T.R. Hsu, *MEMS and Microsystems: Design and Manufacture* (McGraw-Hill, Boston, MA, 2002)
19. M. Madou, *Fundamentals of Microfabrication: The Science of Miniaturization*, 2nd edn. (CRC Press, Boca Raton, FL, 2002)
20. A. Hierlemann, *Integrated Chemical Microsensor Systems in CMOS Technology* (Springer, Heidelberg, 2005)
21. T.A. Core, W.K. Tsang, S.J. Sherman, Fabrication technology for an integrated surface-micromachined sensor. *Solid State Technol.* **36**(10), 39–47 (1993)
22. J. Bryzek, K. Peterson, W. McCulley, Micromachines on the March. *IEEE Spectrum* **5**, 20–31 (1994)
23. J.S. Aden, J.H. Bohorquez, D.M. Collins, M.D. Crook, A. Gacia, U.E. Hess, The third-generation HP thermal inkjet printhead. *HP J.* **45**(1), 41–45 (1994)
24. H. Le, Progress and trends in ink-jet printing technology. *J. Imaging Sci. Technol.* **42**, 49–62 (1998)

25. R. Baydo, A. Groscup, Getting to the heart of ink jet: Printheads, Beyond Recharg. **10**(May), 10–12 (2001)
26. E.R. Lee, *Microdrop Generation* (CRC Press, Boca Raton, FL, 2003)
27. L.J. Hornbeck, W.E. Nelson, Bistable deformable mirror device. OSA Tech. Dig. Ser. **8**, 107–110 (1988)
28. L.J. Hornbeck, Digital Light Processing update – status and future applications. SPIE **3634**, 158–170 (1999)
29. L.J. Hornbeck, The DMD<sup>TM</sup> projection display chip: A MEMS-based technology. MRS Bulletin **26**, 325–327 (2001)
30. K. Suzuki, Micro electro mechanical systems (MEMS) micro-switches for use in DC, RF, and optical applications. Jpn. J. Appl. Phys. **41**, 4335–4339 (2002)
31. V.M. Lubecke, J.C. Chiao, MEMS technologies for enabling high frequency communication circuits. *Proceedings of the IEEE 4th International Conference Telecommunications in Modern Satellite, Cable and Broadcasting Services, Nis* (IEEE, New York, 1999) pp. 1–8
32. C.R. Giles, D. Bishop, V. Aksyuk, MEMS for light-wave networks. MRS Bulletin **4**, 328–329 (2001)
33. A. Hierlemann, O. Brand, C. Hagleitner, H. Baltes, Microfabrication techniques for chemical/biosensors. Proc. IEEE **91**, 839–863 (2003)
34. B. Bhushan, *Tribology and Mechanics of Magnetic Storage Devices*, 2nd edn. (Springer, New York, 1996)
35. H. Hamilton, Contact recording on perpendicular rigid media. J. Mag. Soc. Jpn. **15**(S2), 481–483 (1991)
36. D.A. Horsley, M.B. Cohn, A. Singh, R. Horowitz, A.P. Pisano, Design and fabrication of an angular microactuator for magnetic disk drives. J. Microelectromech. Syst. **7**, 141–148 (1998)
37. T. Hirano, L.S. Fan, D. Kercher, S. Pattanaik, T.S. Pan, HDD tracking microactuator and its integration issues. *Proceedings of the ASME International Mechanical Engineering Congress and Exposition*, vol. 2, ed. by A.P. Lee, J. Simon, F.K. Foster, R.S. Keynton (ASME, New York, 2000) pp. 449–452
38. T. Fukuda, F. Arai, L. Dong, Assembly of nanodevices with carbon nanotubes through nanorobotic manipulations. Proc. IEEE **91**, 1803–1818 (2003)
39. K.E. Drexler, *Nanosystems: Molecular Machinery, Manufacturing and Computation* (Wiley, New York, 1992)
40. G. Timp (ed.), *Nanotechnology* (Springer, New York, 1999)
41. M.S. Dresselhaus, G. Dresselhaus, P. Avouris (eds.), *Carbon Nanotubes*, Top. Appl. Phys., vol. 80 (Springer, Heidelberg, 2001)
42. E.A. Rietman, *Molecular Engineering of Nanosystems* (Springer, New York, 2001)
43. W.A. Goddard, D.W. Brenner, S.E. Lyshevski, G.J. Iafrate (eds.), *Handbook of Nanoscience, Engineering, and Technology* (CRC Press, Boca Raton, FL, 2002)
44. H.S. Nalwa (ed.), *Nanostructured Materials and Nanotechnology* (Academic, San Diego, 2002)
45. C.P. Poole, F.J. Owens, *Introduction to Nanotechnology* (Wiley, Hoboken, NJ, 2003)
46. B. Bhushan, *Handbook of Micro/Nanotribology*, 2nd edn. (CRC, Boca Raton, FL, 1999)
47. B. Bhushan, Nanotribology and nanomechanics. Wear **259**, 1507–1531 (2005)
48. J.A. Stroschio, D.M. Eigler, Atomic and molecular manipulation with a scanning tunneling microscope. Science **254**, 1319 (1991)
49. P. Vettiger, J. Brugger, M. Despont, U. Drechsler, U. Dürig, W. Häberle, M. Lutwyche, H. Rothuizen, R. Stutz, R. Widmer, G. Binning, Ultrahigh density, high data-rate NEMS based AFM data storage system. Microelectron. Eng. **46**, 11–27 (1999)
50. C. Stampfer, A. Jungen, C. Hierold, Fabrication of discrete carbon nanotube based nanoscaled force sensor. *Proceedings of the IEEE Sensors. 2004, Vienna* (IEEE, New York, 2004) pp. 1056–1059
51. C. Hierold, *Carbon Nanotube Devices* (Wiley-VCH, Weinheim, 2008)

52. B. Bhushan, *Mechanics and Reliability of Flexible Magnetic Media*, 2nd edn. (Springer, New York, 2000)
53. Anonymous, *International Technology Roadmap for Semiconductors* (2004) <http://public.itrs.net/>
54. A. Manz, H. Becker (eds.), *Microsystem Technology in Chemistry and Life Sciences*, Top. Curr. Chem., vol. 194 (Springer, Heidelberg, 1998)
55. J. Cheng, L.J. Kricka (eds.), *Biochip Technology* (Harwood Academic Publishers, Philadelphia, PA, 2001)
56. M.J. Heller, A. Guttman (eds.), *Integrated Microfabricated Biodevices* (Marcel Dekker, New York, 2001)
57. C.L.P. San, E.P.H. Yap (eds.), *Frontiers in Human Genetics* (World Scientific, Singapore 2001)
58. C.H. Mastrangelo, H. Becker (eds.), *Microfluidics and BioMEMS*. Proc. SPIE, vol. 4560 (SPIE, Bellingham 2001)
59. H. Becker, L.E. Locascio, Polymer microfluidic devices. *Talanta* **56**, 267–287 (2002)
60. D.J. Beebe, G.A. Mensing, G.M. Walker, Physics and applications of microfluidics in biology. *Annu. Rev. Biomed. Eng.* **4**, 261–286 (2002)
61. A. van der Berg (ed.), *Lab-on-a-Chip: Chemistry in Miniaturized Synthesis and Analysis Systems* (Elsevier, Amsterdam, 2003)
62. P. Gravesen, J. Branebjerg, O. Jensen, Microfluidics – A review. *J. Micromech. Microeng.* **3**, 168–182 (1993)
63. S.N. Bhatia, C.S. Chen, Tissue engineering at the micro-scale, *Biomed. Microdevices* **2**, 131–144 (1999)
64. R.P. Lanza, R. Langer, J. Vacanti (eds.), *Principles of Tissue Engineering*, 2nd edn. (Academic, San Diego, CA, 2000)
65. E. Leclerc, K.S. Furukawa, F. Miyata, T. Sakai, T. Ushida, T. Fujii, Fabrication of microstructures in photosensitive biodegradable polymers for tissue engineering applications. *Biomaterials* **25**, 4683–4690 (2004)
66. K. Park (ed.), *Controlled Drug Delivery: Challenges and Strategies* (American Chemical Society, Washington, DC, 1997)
67. R.S. Shawgo, A.C.R. Grayson, Y. Li, M.J. Cima, BioMEMS for drug delivery. *Curr. Opin. Solid State Mater. Sci.* **6**, 329–334 (2002)
68. P.A. Oeberg, T. Togawa, F.A. Spelman, *Sensors in Medicine and Health Care* (Wiley, New York, 2004)
69. J.V. Zoval, M.J. Madou, Centrifuge-based fluidic platforms. *Proc. IEEE* **92**, 140–153 (2000)
70. W.C. Tang, A.P. Lee, Defense applications of MEMS. *MRS Bulletin* **26**, 318–319 (2001), Also see <http://www.darpa.mil/mto/mems>
71. M.R. Taylor, P. Nguyen, J. Ching, K.E. Peterson, Simulation of microfluidic pumping in a genomic DNA blood-processing cassette. *J. Micromech. Microeng.* **13**, 201–208 (2003)
72. R. Raiteri, M. Grattarola, M. Butt, P. Skladal, Micromechanical Cantilever-Based Biosensor. *Sens. Actuators B: Chemical* **79**, 115–126 (2001)
73. B. Bhushan, D.R. Tokachichu, M.T. Keener, S.C. Lee, Morphology and adhesion of biomolecules on silicon based surfaces. *Acta Biomater.* **1**, 327–341 (2005)
74. H.P. Lang, M. Hegner, C. Gerber, Cantilever array sensors. *Mater. Today* **4**, 30–36 (2005)
75. F. Patolsky, C. Lieber, Nanowire nanosensors. *Mater. Today* **8**(4), 20–28 (2005)
76. M. Scott, MEMS and MOEMS for National Security Applications. In: *Reliability, Testing, and Characterization of MEMS/MOEMS II*, Proc. SPIE vol. 4980 (SPIE, Bellingham, Washington, DC, 2003) pp. xxxvii–xliv
77. T.A. Desai, D.J. Hansford, L. Kulinsky, A.H. Nashat, G. Rasi, J. Tu, Y. Wang, M. Zhang, M. Ferrari, Nanopore technology for biomedical applications. *Biomed. Devices* **2**, 11–40 (1999)

78. D. Hansford, T. Desai, M. Ferrari, Nano-scale size-based biomolecular separation technology. In: *Biochip Technology*, ed. by J. Cheng, L.J. Kricka (Harwood Academic Publishers, New York, 2001) pp. 341–361
79. F.J. Martin, C. Grove, Microfabricated drug delivery systems: Concepts to improve clinical benefits. *Biomed. Microdevices* **3**, 97–108 (2001)
80. B. Bhushan, *Principles and Applications of Tribology* (Wiley, New York, 1999)
81. B. Bhushan, *Modern Tribology Handbook*, vol. 1/2, ed. by B. Bhushan (CRC Press, Boca Raton, FL, 2001)
82. B. Bhushan, *Introduction to Tribology* (Wiley, New York, 2002)
83. B. Bhushan, Adhesion and stiction: Mechanisms, measurement techniques, and methods for reduction. *J. Vac. Sci. Technol. B* **21**, 2262–2296 (2003)
84. B. Bhushan, *Nanotribology and Nanomechanics – An Introduction*, 2nd edn. (Springer, Heidelberg, 2008)
85. Y.C. Tai, L.S. Fan, R.S. Muller, IC-processed micro-motors: Design, technology and testing. *Proc. IEEE Micro Electro Mech. Syst.* (1989) pp. 1–6
86. S.M. Spearing, K.S. Chen, Micro-gas turbine engine materials and structures. *Ceram. Eng. Sci. Proc.* **18**, 11–18 (2001)
87. H. Lehr, S. Abel, J. Doppler, W. Ehrfeld, B. Hagemann, K.P. Kamper, F. Michel, C. Schulz, C. Thurigen, Microactuators as driving units for microrobotic systems. *Proc. Microrobotics: Compon Appl.* **2906**, 202–210 (1996)
88. L.G. Fréchette, S.A. Jacobson, K.S. Breuer, F.F. Ehrich, R. Ghodssi, R. Khanna, C.W. Wong, X. Zhang, M.A. Schmidt, A.H. Epstein, High-speed microfabricated silicon turbomachinery and fluid film bearings. *J. MEMS* **14**, 141–152 (2005)
89. L.X. Liu, Z.S. Spakovszky, Effect of Bearing Stiffness Anisotropy on Hydrostatic Micro Gas Journal Bearing Dynamic Behavior, *Proc. ASME Turbo Expo 2005* (Reno 2005), Paper No. GT-2005–68199
90. M. Mehregany, K.J. Gabriel, W.S.N. Trimmer, Integrated fabrication of polysilicon mechanisms. *IEEE Trans. Electron Devices* **35**, 719–723 (1988)
91. H. Lehr, W. Ehrfeld, B. Hagemann, K.P. Kamper, F. Michel, C. Schulz, C. Thurigen, Development of micro-millimotors. *Minim. Invasive Ther. Allied Technol.* **6**, 191–194 (1997)
92. F. Michel, W. Ehrfeld, Microfabrication technologies for high performance microactuators. In: *Tribology Issues and Opportunities in MEMS*, ed. by B. Bhushan (Kluwer, Dordrecht, 1998) pp. 53–72
93. E.J. Garcia, J.J. Sniegowski, Surface micromachined microengine. *Sens. Actuators A* **48**, 203–214 (1995)
94. D.M. Tanner, N.F. Smith, L.W. Irwin, W.P. Eaton, K.S. Helgesen, J.J. Clement, W.M. Miller, J.A. Walraven, K.A. Peterson, P. Tangyonyong, M.T. Dugger, S.L. Miller, *MEMS Reliability: Infrastructure, Test Structures, Experiments, and Failure Modes, SAND2000–0091* (Sandia National Laboratories, Albuquerque, New Mexico, 2000), Download from <http://www.prod.sandia.gov>
95. S.S. Mani, J.G. Fleming, J.A. Walraven, J.J. Sniegowski, M.P. de Beer, L.W. Irwin, D.M. Tanner, D.A. LaVan, M.T. Dugger, H. Jakubczak, W.M. Miller, Effect of W coating on microengine performance. *Proceedings of 38th Annual International Reliability Physics Symposium* (IEEE, New York, 2000) pp. 146–151
96. M.G. Hankins, P.J. Resnick, P.J. Clews, T.M. Mayer, D.R. Wheeler, D.M. Tanner, R.A. Plass, Vapor deposition of amino-functionalized self-assembled monolayers on MEMS. *Proc. SPIE* **4980**, 238–247 (2003)
97. J.K. Robertson, K.D. Wise, An electrostatically actuated integrated microflow controller. *Sens. Actuators A* **71**, 98–106 (1998)
98. B. Bhushan, Nanotribology and nanomechanics of MEMS devices. In *Proceedings of the 9th Annual Workshop MEMS* (IEEE, New York, 1996) pp. 91–98



99. R.E. Sulouff, MEMS opportunities in accelerometers and gyros and the microtribology problems limiting commercialization, in *Tribology Issues and Opportunities in MEMS*, ed. by B. Bhushan (Kluwer, Dordrecht, 1998) pp. 109–120
100. M. Parsons, Design and manufacture of automotive pressure sensors. *Sensors* **18**, 32–46 (2001)
101. J.R. Martin, Y. Zhao, Micromachined Device Packaged to Reduce Stiction. U.S. Patent 5,694,740, 1997
102. G. Smith, The application of microtechnology to sensors for the automotive industry. *Microelectron. J.* **28**, 371–379 (1997)
103. L.S. Chang, P.L. Gendler, J.H. Jou, Thermal mechanical and chemical effects in the degradation of the plasma-deposited  $\alpha$ -SiC:H passivation layer in a multilayer thin-film device. *J. Mater. Sci.* **26**, 1882–1890 (1991)
104. V.A. Aksyuk, F. Pardo, D. Carr, D. Greywall, H.B. Chan, M.E. Simon, A. Gasparyan, H. Shea, V. Lifton, C. Bolle, S. Arney, R. Frahm, M. Paczkowski, M. Haueis, R. Ryf, D.T. Neilson, J. Kim, R. Giles, D. Bishop, Beam-steering micromirrors for large optical cross-connects. *J. Lightwave Technol.* **21**, 634–642 (2003)
105. S.A. Henck, Lubrication of digital micromirror devices. *Tribol. Lett.* **3**, 239–247 (1997)
106. M.R. Douglass, Lifetime estimates and unique failure mechanisms of the digital micromirror devices (DMD). in *Proceedings of the 36th Annual International Reliability Physics Symposium* (IEEE, New York, 1998) pp. 9–16
107. M.R. Douglass, DMD reliability, A MEMS success story. *Proc. SPIE* **4980**, 1–11 (2003)
108. H. Liu, B. Bhushan, Nanotribological characterization of digital micromirror devices using an atomic force microscope. *Ultramicroscopy* **100**, 391–412 (2004)
109. H. Liu, B. Bhushan, Investigation of nanotribological and nanomechanical properties of the digital micromirror device by atomic force microscope. *J. Vac. Sci. Technol. A* **22**, 1388–1396 (2004)
110. L.J. Hornbeck, Low Surface Energy Passivation Layer for Micromechanical Devices. U.S. Patent 5,602,671, (1997)
111. R.A. Robbins, S.J. Jacobs, Lubricant Delivery for Micromechanical Devices. U.S. Patent 6,300,294, B1 2001
112. I. DeWolf, W.M. van Spengen, Techniques to study the reliability of metal RF MEMS capacitive switches, *Microelectron. Reliab.* **42**, 1789–1794 (2002)
113. B. Bhushan, K.J. Kwak, Platinum-coated probes sliding at up to 100 mm s<sup>-1</sup> against coated silicon wafers for AFM probe-based recording technology. *Nanotechnology* **18**, 345504 (2007)
114. B. Bhushan, K.J. Kwak, Noble metal-coated probes sliding at up to 100 mm s<sup>-1</sup> against PZT films for AFM probe-based ferroelectric recording technology. *J. Phys. D* **20**, 225013 (2008), invited
115. K.J. Kwak, B. Bhushan, Platinum-coated probes sliding at up to 100 mm/s against lead zirconate titanate films for atomic force microscopy probe-based ferroelectric recording technology. *J. Vac. Sci. Technol. A* **26**, 783–793 (2008)
116. B. Bhushan, K. Kwak, M. Palacio, Nanotribology and nanomechanics of AFM probe-based data recording technology. *J. Phys. D* **20**, 365207 (2008)
117. B. Bhushan, M. Palacio, B. Kinzig, AFM-based nanotribological and electrical characterization of ultrathin wear-resistant ionic liquid films. *J. Colloid Interface Sci.* **317**, 275–287 (2008)
118. M. Palacio, B. Bhushan, Ultrathin wear-resistant ionic liquid films for novel MEMS/NEMS applications. *Adv. Mater.* **20**, 1194–1198 (2008)
119. M. Palacio, B. Bhushan, Molecularly thick dicationic liquid films for nanolubrication. *J. Vac. Sci. Technol. A* **27**(4), 986–995 (2009)
120. T. Ohnstein, T. Fukiura, J. Ridley, U. Bonne, Micromachined silicon microvalve. in *Proceedings of the IEEE-MEMS Workshop* (IEEE, New York, 1990) pp. 95–98
121. S. Shoji, M. Esashi, Microflow devices and systems. *J. Micromech. Microeng.* **4**, 157–171 (1994)

122. M. Stehr, S. Messner, H. Sandmaier, R. Zenergle, The VAMP – A new device for handling liquids or gases. *Sens. Actuators A* **57**, 153–157 (1996)
123. P. Woias, Micropumps – Summarizing the first two decades. in, *Proceedings of SPIE – Microfluidics and BioMEMS*, vol. 4560, ed. by C.H. Mastrangelo, H. Becker (SPIE, Bellingham, Washington, DC, 2001) pp. 39–52
124. N.T. Nguyen, X. Huang, T.K. Chuan, MEMS-micropumps: A review. *ASME J. Fluids Eng.* **124**, 384–392 (2002)
125. B. Bustgens, W. Bacher, W. Menz, W.K. Schomburg, Micropump manufactured by thermo-plastic molding. in *Proceedings of IEEE-MEMS Workshop* (IEEE, Piscataway, NJ, 1994) pp. 18–21
126. C.H. Ahn, M.G. Allen, Fluid micropumps based on rotary magnetic actuators. in *MEMS '95: IEEE 8th International Workshop on MEMS* (IEEE, Piscataway, NJ, 1995) pp. 408–412
127. J. Doepper, M. Clemens, W. Ehrfeld, S. Jung, K.P. Kaemper, H. Lehr, Micro gear pumps for dosing of viscous fluids. *J. Micromech. Microeng.* **7**, 230–232 (1997)
128. J. Henniker, Triboelectricity in polymers. *Nature* **196**, 474 (1962)
129. M. Sakaguchi, H. Kashiwabara, A generation mechanism of triboelectricity due to the reaction of mechaniradicals with mechanoions which are produced by mechanical fracture of solid polymer. *Colloid Poly. Sci.* **270**, 621–626 (1992)
130. G.R. Freeman, N.H. March, Triboelectricity and some associated phenomena. *Mater Sci. Technol.* **15**, 1454–1458 (1999)
131. S.K. Cho, H. Moon, C.-J. Kim, Creating, transporting, cutting, and merging liquid droplets by electrowetting-based actuation for digital microfluidic circuits. *J. Microelectromech. Syst.* **12**, 70–80 (2003)
132. A.R. Wheeler, H. Moon, C.A. Bird, R.R.O. Loo, C.-J. Kim, J.A. Loo, R.L. Garrell, Digital microfluidics with in-line sample purification for proteomics analysis with MALDI-MS. *Anal. Chem.* **77**, 534–540 (2005)
133. B. Bhushan, D. Tokachichu, M.T. Keener, S.C. Lee, Nanoscale adhesion, friction, and wear studies of biomolecules on silicon based surfaces. *Acta Biomater.* **2**, 39–49 (2006)
134. S.C. Lee, M.T. Keener, D.R. Tokachichu, B. Bhushan, P.D. Barnes, B.R. Cipriany, M. Gao, L.J. Brillson, Protein binding on thermally grown silicon dioxide. *J. Vac. Sci. Technol. B* **23**, 1856–1865 (2005)
135. J. Black, *Biological Performance of Materials: Fundamentals of Biocompatibility* (Marcel Dekker, New York, 1999)
136. B. Bhushan, K. Kwak, S. Gupta, S.C. Lee, Nanoscale adhesion, friction and wear studies of biomolecules on SAM-coated silica and alumina based surfaces. *J. R. Soc. Interface* **6**(37), 719–733 (2009)
137. G. Wei, B. Bhushan, N. Ferrell, D. Hansford, Microfabrication and nanomechanical characterization of polymer microelectromechanical systems for biological applications. *J. Vac. Sci. Technol. A* **23**, 811–819 (2005)
138. K.K. Lee, B. Bhushan, D. Hansford, Nanotribological characterization of perfluoropolymer thin films for BioMEMS applications. *J. Vac. Sci. Technol. A* **23**, 804–810 (2005)
139. B. Bhushan, T. Kasai, G. Kulik, L. Barbieri, P. Hoffmann, AFM study of perfluorosilane and alkylsilane self-assembled monolayers for anti-stiction in MEMS/NEMS. *Ultramicroscopy* **105**, 176–188 (2005)
140. B. Bhushan, D. Hansford, K.K. Lee, Surface modification of silicon and PDMS surfaces with vapor phase deposited ultrathin fluorosilane films for biomedical nanodevices. *J. Vac. Sci. Technol. A* **24**, 1197–1202 (2006)
141. T. Kasai, B. Bhushan, G. Kulik, L. Barbieri, P. Hoffmann, Nanotribological study of perfluorosilane SAMs for anti-stiction and low wear. *J. Vac. Sci. Technol. B* **23**, 995–1003 (2005)
142. P. Decuzzi, S. Lee, B. Bhushan, M. Ferrari, A theoretical model for the margination of particles with blood vessels. *Ann. Biomed. Eng.* **33**, 179–190 (2005)

143. B. Bhushan, Nanotribology of carbon nanotubes. *J. Phys. D* **20**, 365214 (2008)
144. H. Guckel, D.W. Burns, Fabrication of micromechanical devices from polysilicon films with smooth surfaces. *Sens. Actuators* **20**, 117–122 (1989)
145. G.T. Mulhern, D.S. Soane, R.T. Howe, Supercritical Carbon Dioxide Drying of Microstructures. in *Proceedings of International Conference on Solid-State Sensors Actuators* (IEEE, New York, 1993) pp. 296–299
146. K.F. Man, B.H. Stark, R. Ramesham, *A Resource Handbook for MEMS Reliability, Rev. A* (JPL Press, Jet Propulsion Laboratory, California Institute of Technology, Pasadena, CA, 1998)
147. S. Kayali, R. Lawton, B.H. Stark, MEMS reliability assurance activities at JPL. *EEE Links* **5**, 10–13 (1999)
148. S. Arney, Designing for MEMS Reliability. *MRS Bull.* **26**, 296–299 (2001)
149. K.F. Man, MEMS reliability for space applications by elimination of potential failure modes through testing and analysis (NASA 2001)
150. B. Bhushan, A.V. Kulkarni, W. Bonin, J.T. Wyrobek, Nano/picoindentation measurement using a capacitance transducer system in atomic force microscopy. *Philos. Mag.* **74**, 1117–1128 (1996)
151. S. Sundararajan, B. Bhushan, Development of AFM-based techniques to measure mechanical properties of nanoscale structures. *Sens. Actuators A* **101**, 338–351 (2002)
152. B. Bhushan, J.N. Israelachvili, U. Landman, Nanotribology: Friction, wear and lubrication at the atomic scale. *Nature* **374**, 607–616 (1995)
153. B. Bhushan, Nanotribology and nanomechanics of MEMS/NEMS and BioMEMS/BioNEMS materials and devices. *Microelectron. Eng.* **84**, 387–412 (2007)
154. B. Bhushan, Nanotribology, nanomechanics and nanomaterials characterization. *Philos. Trans. R. Soc. A* **366**, 1351–1381 (2008)
155. B. Bhushan, Nanotribology and nanomechanics in nano/biotechnology. *Philos. Trans. R. Soc. A* **366**, 1499–1537 (2008)
156. B. Bhushan, Biomimetics, Lessons from nature – An overview. *Philos. Trans. R. Soc. A* **367**, 1445–1486 (2009)
157. M. Mehregany, C.A. Zorman, N. Rajan, C.H. Wu, Silicon carbide MEMS for harsh environments. *Proc. IEEE* **86**, 1594–1610 (1998)
158. J.S. Shor, D. Goldstein, A.D. Kurtz, Characterization of n-type -SiC as a Piezoresistor. *IEEE Trans. Electron Devices* **40**, 1093–1099 (1993)
159. B. Bhushan, B.K. Gupta, *Handbook of Tribology: Materials, Coatings and Surface Treatments* (Krieger, Malabar, 1997), Reprint edition
160. J.F. Shackelford, W. Alexander, J.S. Park (eds.), *CRC Material Science and Engineering Handbook*, 2nd edn. (CRC Press, Boca Raton, FL, 1994)
161. C.A. Zorman, A.J. Fleischmann, A.S. Dewa, M. Mehregany, C. Jacob, S. Nishino, P. Pirouz, Epitaxial growth of 3C-SiC films on 4 in. diam Si(100) silicon wafers by atmospheric pressure chemical vapor deposition. *J. Appl. Phys.* **78**, 5136–5138 (1995)
162. C.A. Zorman, S. Roy, C.H. Wu, A.J. Fleischman, M. Mehregany, Characterization of polycrystalline silicon carbide films grown by atmospheric pressure chemical vapor deposition on polycrystalline silicon. *J. Mater. Res.* **13**, 406–412 (1998)
163. C.H. Wu, S. Stefanescu, H.I. Kuo, C.A. Zorman, M. Mehregany, Fabrication and Testing of Single Crystalline 3C-SiC Piezoresistive Pressure Sensors, Technical Digest – 11th Int. Conf. Solid State Sensors and Actuators – Eurosensors XV (Munich 2001) pp. 514–517
164. A.A. Yasseen, C.H. Wu, C.A. Zorman, M. Mehregany, Fabrication and testing of surface micromachined polycrystalline SiC micromotors. *IEEE Electron Device Lett.* **21**, 164–166 (2000)
165. B.K. Gupta, J. Chevallier, B. Bhushan, Tribology of ion bombarded silicon for micromechanical applications. *ASME J. Tribol.* **115**, 392–399 (1993)
166. B.K. Gupta, B. Bhushan, J. Chevallier, Modification of tribological properties of silicon by boron ion implantation. *Tribol. Trans.* **37**, 601–607 (1994)

167. B.K. Gupta, B. Bhushan, Nanoindentation studies of ion implanted silicon, *Surf. Coat. Technol.* **68/69**, 564–570 (1994)
168. B. Bhushan, V.N. Koinkar, Tribological studies of silicon for magnetic recording applications. *J. Appl. Phys.* **75**, 5741–5746 (1994)
169. G.M. Pharr, The anomalous behavior of silicon during nanoindentation. *Thin Films* **239**, 301–312 (1991)
170. D.L. Callahan, J.C. Morris, The extent of phase transformation in silicon hardness indentation. *J. Mater. Res.* **7**, 1612–1617 (1992)
171. N.A. Fleck, G.M. Muller, M.F. Ashby, J.W. Hutchinson, Strain gradient plasticity: Theory and experiment. *Acta Metall. Mater.* **42**, 475–487 (1994)
172. B. Bhushan, S. Venkatesan, Friction and wear studies of silicon in sliding contact with thin-film magnetic rigid disks. *J. Mater. Res.* **8**, 1611–1628 (1993)
173. S. Venkatesan, B. Bhushan, The role of environment in the friction and wear of single-crystal silicon in sliding contact with thin-film magnetic rigid disks. *Adv. Info Storage Syst.* **5**, 241–257 (1993)
174. S. Venkatesan, B. Bhushan, The sliding friction and wear behavior of single-crystal, polycrystalline and oxidized silicon. *Wear* **171**, 25–32 (1994)
175. B. Bhushan, Chemical, mechanical and tribological characterization of ultra-thin and hard amorphous carbon coatings as thin as 3.5 nm: Recent developments. *Diam. Rel. Mater.* **8**, 1985–2015 (1999)
176. B. Bhushan, S. Sundararajan, X. Li, C.A. Zorman, M. Mehregany, Micro/nanotribological studies of single-crystal silicon and polysilicon and SiC films for use in MEMS devices. In: *Tribology Issues and Opportunities in MEMS*, ed. by B. Bhushan (Kluwer, Dordrecht, 1998) pp. 407–430
177. S. Sundararajan, B. Bhushan, Micro/nanotribological studies of polysilicon and SiC films for MEMS applications. *Wear* **217**, 251–261 (1998)
178. X. Li, B. Bhushan, Micro/nanomechanical characterization of ceramic films for microdevices. *Thin Solid Films* **340**, 210–217 (1999)
179. H. Liu, B. Bhushan, Nanotribological characterization of molecularly-thick lubricant films for applications to MEMS/NEMS by AFM. *Ultramicroscopy* **97**, 321–340 (2003)
180. V.N. Koinkar, B. Bhushan, Micro/nanoscale studies of boundary layers of liquid lubricants for magnetic disks. *J. Appl. Phys.* **79**, 8071–8075 (1996)
181. V.N. Koinkar, B. Bhushan, Microtribological studies of unlubricated and lubricated surfaces using atomic force/friction force microscopy. *J. Vac. Sci. Technol. A* **14**, 2378–2391 (1996)
182. Z. Tao, B. Bhushan, Bonding, degradation, and environmental effects on novel perfluoropolyether lubrications. *Wear* **259**, 1352–1361 (2005)
183. B. Bhushan, M. Cichomski, Z. Tao, N.T. Tran, T. Ethen, C. Merton, R.E. Jewett, Nanotribological characterization and lubricant degradation studies of metal-film magnetic tapes using novel lubricants. *ASME J. Tribol.* **129**, 621–627 (2007)
184. M. Palacio, B. Bhushan, Surface potential and resistance measurements for detecting wear of chemically-bonded and unbonded molecularly-thick perfluoropolyether lubricant films using atomic force microscopy. *J. Colloid Interface Sci.* **315**, 261–269 (2007)
185. M. Palacio, B. Bhushan, Wear detection of candidate MEMS/NEMS lubricant films using atomic force microscopy-based surface potential measurements. *Scr. Mater.* **57**, 821–824 (2007)
186. T. Stifter, O. Marti, B. Bhushan, Theoretical investigation of the distance dependence of capillary and van der Waals forces in scanning force microscopy. *Phys. Rev. B* **62**, 13667–13673 (2000)
187. B. Bhushan, A.V. Kulkarni, V.N. Koinkar, M. Boehm, L. Odoni, C. Martelet, M. Belin, Microtribological characterization of self-assembled and langmuir–blodgett monolayers by atomic force and friction force microscopy. *Langmuir* **11**, 3189–3198 (1995)

188. B. Bhushan, H. Liu, Nanotribological properties and mechanisms of alkythiol and biphenyl thiol self-assembled monolayers studied by AFM. *Phys. Rev. B* **63**, 245412:1–11 (2001)
189. H. Liu, B. Bhushan, W. Eck, V. Stadler, Investigation of the adhesion, friction, and wear properties of biphenyl thiol self-assembled monolayers by atomic force microscopy. *J. Vac. Sci. Technol. A* **19**, 1234–1240 (2001)
190. H. Liu, B. Bhushan, Investigation of nanotribological properties of self-assembled monolayers with alkyl and biphenyl spacer chains. *Ultramicroscopy* **91**, 185–202 (2002)
191. B. Bhushan, M. Cichomski, E. Hoque, J.A. DeRose, P. Hoffmann, H.J. Mathieu, Nanotribological characterization of perfluoroalkylphosphonate self-assembled monolayers deposited on aluminum-coated silicon substrates. *Microsyst. Technol.* **12**, 588–596 (2006)
192. N.S. Tambe, B. Bhushan, Nanotribological characterization of self assembled monolayers deposited on silicon and aluminum substrates. *Nanotechnology* **16**, 1549–1558 (2005)
193. Z. Tao, B. Bhushan, Degradation mechanisms and environmental effects on perfluoropolyether, self assembled monolayers, and diamondlike carbon films. *Langmuir* **21**, 2391–2399 (2005)
194. Anonymous, *Properties of Silicon*, EMIS Data Rev., vol. 4 (INSPEC, London 1988)
195. Anonymous, *MEMS Materials Database* (2002) <http://www.memsnet.org/material/>
196. E. Eteshola, M.T. Keener, M. Elias, J. Shapiro, L.J. Brillson, B. Bhushan, S.C. Lee, Engineering functional protein interfaces for immunologically modified field effect transistor (immunoFET) by molecular genetics means. *J. R. Soc. Interface* **5**, 123–127 (2008)
197. K. Kallury, P.M. MacDonald, M. Thompson, Effect of surface water and base catalysis on the silanization of silica by (aminopropyl)alkoxysilanes studied by x-ray photoelectron spectroscopy and  $^{13}\text{C}$  cross-polarization/magic angle spinning nuclear magnetic resonance. *Langmuir* **10**, 492–499 (1994)
198. J.H. Moon, J.W. Shin, S.Y. Kim, J.W. Park, Formation of uniform aminosilane thin layers: an imine formation to measure relative surface density of the amine group. *Langmuir* **12**, 4621–4624 (1996)
199. Y. Han, D. Mayer, A. Offenhausser, S. Ingebrandt, Surface activation of thin silicon-oxides by wet cleaning and silanization. *Thin Solid Films* **510**, 175–180 (2006)
200. N.S. Tambe, B. Bhushan, Identifying materials with low friction and adhesion for nanotechnology applications. *Appl. Phys. Lett.* **86**, 061906–1–061906–3 (2005)
201. N.S. Tambe, B. Bhushan, Micro/nanotribological characterization of PDMS and PMMA used for BioMEMS/NEMS applications. *Ultramicroscopy* **105**, 238–247 (2005)
202. B. Bhushan, Z. Burton, Adhesion and friction properties of polymers in microfluidic devices. *Nanotechnology* **16**, 467–478 (2005)
203. D.R. Tokachichu, B. Bhushan, Bioadhesion of polymers for BioMEMS. *IEEE Trans. Nanotechnol.* **5**, 228–231 (2005)
204. M. Nosonovsky, B. Bhushan, *Multiscale Dissipative Mechanisms and Hierarchical Surfaces* (Springer, Heidelberg, 2008)
205. B. Bhushan, Y.C. Jung, Wetting, adhesion and friction of superhydrophobic and hydrophilic leaves and fabricated micro/nanopatterned surfaces. *J. Phys. D* **20**, 225010 (2008)
206. K. Koch, B. Bhushan, W. Barthlott, Diversity of structure, morphology, and wetting of plant surfaces. *Soft Matter* **4**, 1943–1963 (2008), invited
207. K. Koch, B. Bhushan, W. Barthlott, Multifunctional surfaces structures of plants: An inspiration for biomimetics. *Prog. Mater. Sci.* **18**, 843–855 (2009), invited
208. B. Bhushan, Y.C. Jung, K. Koch, Micro-, nano-, and hierarchical structures for superhydrophobicity, self-cleaning and low adhesion. *Philos. Trans. R. Soc. A* **367**, 1631–1672 (2009)
209. B. Bhushan, K. Koch, Y.C. Jung, Fabrication and characterization of the hierarchical structure for superhydrophobicity. *Ultramicroscopy* **109**(8), 1029–1034 (2009)
210. M. Nosonovsky, B. Bhushan, Roughness-induced superhydrophobicity: A way to design non-adhesive surfaces. *J. Phys. D* **20**, 225009 (2008)

211. B. Bhushan, K. Koch, Y.C. Jung, Nanostructures for superhydrophobicity and low adhesion. *Soft Matter* **4**, 1799–1804 (2008)
212. M. Nosonovsky, B. Bhushan, Multiscale friction mechanisms and hierarchical surfaces in nano- and bio-tribology. *Mater. Sci. Eng. R* **58**, 162–193 (2007)
213. M. Nosonovsky, B. Bhushan, Biologically-inspired surfaces: broadening the scope of roughness. *Adv. Funct. Mater.* **18**, 843–855 (2008)
214. K. Koch, B. Bhushan, Y.C. Jung, W. Barthlott, Fabrication of artificial lotus leaves and significance of hierarchical structure for superhydrophobicity and low adhesion. *Soft Matter* **5**, 1386–1393 (2009)
215. R.N. Wenzel, Resistance of solid surfaces to wetting by water. *Ind. Eng. Chem.* **28**, 988–994 (1936)
216. A. Cassie, S. Baxter, Wetting of porous surfaces. *Trans. Faraday Soc.* **40**, 546–551 (1944)
217. S. Sundararajan, B. Bhushan, Static friction and surface roughness studies of surface micro-machined electrostatic micromotors using an atomic force/friction force microscope. *J. Vac. Sci. Technol. A* **19**, 1777–1785 (2001)
218. C.H. Mastrangelo, C.H. Hsu, Mechanical stability and adhesion of microstructures under capillary forces – Part II: Experiments. *J. Microelectromech. Syst.* **2**, 44–55 (1993)
219. R. Maboudian, R.T. Howe, Critical review: Adhesion in surface micromechanical structures. *J. Vac. Sci. Technol. B* **15**, 1–20 (1997)
220. C.H. Mastrangelo, Surface force induced failures in microelectromechanical systems. in *Tribology Issues and Opportunities in MEMS*, ed. by B. Bhushan (Kluwer, Dordrecht, 1998) pp. 367–395
221. M.P. De Boer, T.A. Michalske, Accurate method for determining adhesion of cantilever beams. *J. Appl. Phys.* **86**, 817 (1999)
222. R.L. Alley, G.J. Cuan, R.T. Howe, K. Komvopoulos, The effect of release-etch processing on surface microstructure stiction. in *Proceedings of the Solid State Sensor and Actuator Workshop*, ed. by C.H. Mastrangelo, C.H. Hsu (IEEE, New York, 1992) pp. 202–207
223. H. Liu, B. Bhushan, Adhesion and friction studies of microelectromechanical systems/nanoelectromechanical systems materials using a novel microtriboapparatus. *J. Vac. Sci. Technol. A* **21**, 1528–1538 (2003)
224. B. Bhushan, H. Liu, S.M. Hsu, Adhesion and friction studies of silicon and hydrophobic and low friction films and investigation of scale effects. *ASME J. Tribol.* **126**, 583–590 (2004)
225. S.K. Chilamakuri, B. Bhushan, A comprehensive kinetic meniscus model for prediction of long-term static friction. *J. Appl. Phys.* **15**, 4649–4656 (1999)
226. Y.C. Tai, R.S. Muller, Frictional study of IC processed micromotors, *Sens. Actuators A* **21–23**, 180–183 (1990)
227. K.J. Gabriel, F. Behi, R. Mahadevan, M. Mehregany, In situ friction and wear measurement in integrated polysilicon mechanisms, *Sens. Actuators A* **21–23**, 184–188 (1990)
228. M.G. Lim, J.C. Chang, D.P. Schultz, R.T. Howe, R.M. White, Polysilicon Microstructures to characterize static friction, *Proceedings of the IEEE micro electro Mechanical Systems* (IEEE, New York, 1990) pp. 82–88
229. U. Beerschwinger, S.J. Yang, R.L. Reuben, M.R. Taghizadeh, U. Wallrabe, Friction measurements on LIGA-processed microstructures. *J. Micromech. Microeng.* **4**, 14–24 (1994)
230. D. Mathason, U. Beerschwinger, S.J. Yuong, R.L. Reuben, M. Taghizadeh, S. Eckert, U. Wallrabe, Effect of progressive wear on the friction characteristics of nickel LIGA processed rotors. *Wear* **192**, 199–207 (1996)
231. G. Wei, B. Bhushan, S.J. Jacobs, Nanomechanical characterization of digital multilayered thin film structures for digital micromirror devices. *Ultramicroscopy* **100**, 375–389 (2004)
232. G. Wei, B. Bhushan, S.J. Jacobs, Nanoscale indentation fatigue and fracture toughness measurements of multilayered thin film structures for digital micromirror devices. *J. Vac. Sci. Technol. A* **22**, 1397–1405 (2004)

- 233. H. Liu, B. Bhushan, Bending and fatigue study on a nanoscale hinge by an atomic force microscope. *Nanotechnology* **15**, 1246–1251 (2004)
- 234. B. Bhushan, H. Liu, Characterization of nanomechanical and nanotribological properties of digital micromirror devices. *Nanotechnology* **15**, 1785–1791 (2004)
- 235. R.C. Jaeger, *Introduction to Microelectronic Fabrication*, vol. 5 (Addison-Wesley, Reading 1988)
- 236. J. Voldman, M.L. Gray, M.A. Schmidt, Microfabrication in biology and medicine. *Annu. Rev. Biomed. Eng.* **1**, 401–425 (1999)
- 237. J.W. Judy, Microelectromechanical systems (MEMS): Fabrication, design, and applications. *Smart Mater. Struct.* **10**, 1115–1134 (2001)
- 238. C. Liu, *Foundations of MEMS* (Pearson Prentice Hall, Upper Saddle River, NJ, 2006)
- 239. G. Brewer, *Electron-Beam Technology in Microelectronic Fabrication* (Academic, New York, 1980)
- 240. K. Valiev, *The Physics of Submicron Lithography* (Plenum, New York, 1992)
- 241. E.W. Becker, W. Ehrfeld, P. Hagmann, A. Maner, D. Munchmeyer, Fabrication of microstructures with high aspect ratios and great structural heights by synchrotron radiation lithography, galvanofarming, and plastic moulding (LIGA process). *Microelectron. Eng.* **4**, 35–56 (1986)
- 242. C.R. Friedrich, R.O. Warrington, Surface characterization of non-lithographic micromachining. in, *Tribology Issues and Opportunities in MEMS*, ed. by B. Bhushan (Kluwer, Dordrecht, 1998) pp. 73–84
- 243. M. Tanaka, Development of desktop machining microfactory. *Riken Rev.* **34**, 46–49 (2001)
- 244. Y. Xia, G.M. Whitesides, Soft lithography. *Angew. Chem. Int. Ed.* **37**, 550–575 (1998)
- 245. H. Becker, C. Gaertner, Polymer microfabrication methods for microfluidic analytical applications. *Electrophoresis* **21**, 12–26 (2000)
- 246. Y. Xia, E. Kim, X.M. Zhao, J.A. Rogers, M. Prentiss, G.M. Whitesides, Complex optical surfaces formed by replica molding against elastomeric masters. *Science* **273**, 347–349 (1996)
- 247. S.Y. Chou, P.R. Krauss, P.J. Renstrom, Imprint lithography with 25-nanometer resolution. *Science* **272**, 85–87 (1996)
- 248. A. Kumar, G.M. Whitesides, Features of gold having micrometer to centimeter dimensions can be formed through a combination of stamping with an elastomeric stamp and an alkanethiol ink followed by chemical etching. *Appl. Phys. Lett.* **63**, 2002–2004 (1993)
- 249. J.C. McDonald, D.C. Duffy, J.R. Anderson, D.T. Chiu, H. Wu, O.J.A. Schueller, G.M. Whitesides, Fabrication of microfluidic systems in poly(dimethylsiloxane). *Electrophoresis* **21**, 27–40 (2000)

# Chapter 24

## Mechanical Properties of Micromachined Structures

Harold Kahn

**Abstract** To be able to accurately design structures and make reliability predictions in any field, it is first necessary to know the mechanical properties of the materials that make up the structural components. The devices encountered in the fields of microelectromechanical systems (MEMS) and nanoelectromechanical systems (NEMS), are necessarily very small, and so the processing techniques and the microstructures of the materials used in these devices may differ significantly from bulk structures. Also, the surface-area-to-volume ratios in such structures are much higher than in bulk samples, and so surface properties become much more important. In short, it cannot be assumed that the mechanical properties measured for a bulk specimen of a material will apply when the same material is used in MEMS and NEMS. This chapter will review the techniques that have been used to determine the mechanical properties of micromachined structures, especially residual stress, strength and Young's modulus. The experimental measurements that have been performed will then be summarized, in particular the values obtained for polycrystalline silicon (polysilicon).

### 24.1 Measuring Mechanical Properties of Films on Substrates

In order to accurately determine the mechanical properties of very small structures, it is necessary to test specimens made from the same materials, processed in the same way, and of the same approximate size. Not surprisingly it is often difficult to handle specimens this small. One solution is to test the properties of films that remain on substrates. Micro- and nanomachined structures are typically fabricated from films that are initially deposited onto a substrate, are subsequently patterned and etched into the appropriate shapes, and are then finally released from the substrate. If the testing is performed on the continuous film, before patterning and release, the substrate can be used as an effective *handle* for the specimen (in this case, the film). Of course, since the films are attached to the substrate, the types of tests possible are severely limited.



### 24.1.1 Residual Stress Measurements

One common measurement easily performed on films attached to substrates is residual film stress. The curvature of the substrate is measured before and after film deposition. Curvature can be measured in a number of ways. The most common technique is to scan a laser across the surface (or scan the substrate beneath the laser) and detect the angle of the reflected signal. Alternatively, profilometry, optical interferometry or even atomic force microscopy can be used. As expected, tools that map a surface or perform multiple linear scans can give more accurate readings than tools that measure only a single scan.

Assuming that the film is thin compared to the substrate, the average residual stress in the film  $\sigma_f$  is given by the Stoney equation

$$\sigma_f = \frac{1}{6} \frac{E_s}{(1 - \nu_s)} \frac{t_s^2}{t_f} \left( \frac{1}{R_1} - \frac{1}{R_2} \right), \quad (24.1)$$

where the subscripts f and s refer to the film and substrate, respectively;  $t$  is thickness,  $E$  is Young's modulus,  $\nu$  is Poisson's ratio, and  $R$  is the radius of curvature before ( $R_1$ ) and after ( $R_2$ ) film deposition [1]. For a typical (100)-oriented silicon substrate,  $E/(1 - \nu)$  (also known as the biaxial modulus) is equal to 180.5 GPa, independent of in-plane rotation [2]. This investigation can be performed on the as-deposited film or after any subsequent annealing step, provided no changes occur to the substrate.

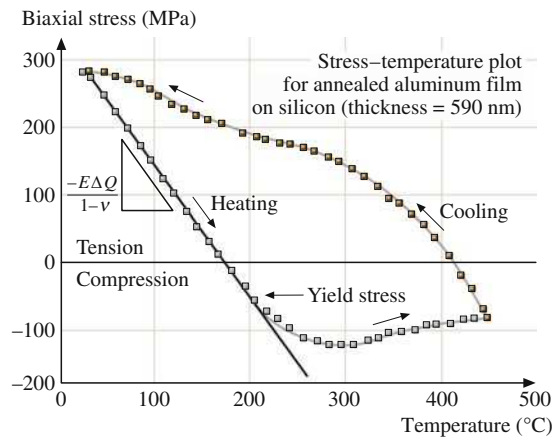
This measurement will reveal the average residual stress of the film. Typically, however, the residual stresses of deposited films will vary throughout the thickness of the film. One way to detect this, using substrate curvature techniques, is to etch away a fraction of the film and repeat the curvature measurement. This can be iterated any number of times to obtain a residual stress profile for the film [3]. Alternatively, tools have been designed that can measure the substrate curvature during the deposition process itself, in order to obtain information on how the stresses evolve [4].

An additional feature of some of these tools is the ability to heat the substrates while performing the stress measurement. An example of the results obtained in such an experiment is shown in Fig. 24.1 [5], for an aluminium film on a silicon substrate. The slope of the heating curve gives the difference in thermal expansion between the film and the substrate. When the heating curve changes slope and becomes nearly horizontal, the yield strength of the film has been reached.

### 24.1.2 Mechanical Measurements Using Nanoindentation

Aside from residual stress, it is difficult to measure the mechanical properties of films attached to substrates without the measurement being affected by the presence

**Fig. 24.1** Typical results for residual stress as a function of temperature for an aluminum film on a silicon substrate (after [5]). The stresses were determined by measuring the curvature of the substrate before and after film deposition, using the reflected signal of a laser scanned across the substrate surface



of the substrate. Recent developments in nanoindentation equipment have allowed this technique to be used in some cases. With specially designed tools, indentation can be performed using very low loads. If the films being investigated are thick and rigid enough, measurements can be made that are not influenced by the presence of the substrate. Of course, this can be verified by depositing the same film onto different substrates. By continuously monitoring the displacement as well as the load during indentation, a variety of properties can be measured, including hardness and Young's modulus [6]. This area is covered in more detail in a separate chapter.

For brittle materials, cracks can be generated by indentation, and strength information can be gathered. But the exact stress fields created during the indentation process are not known exactly, and therefore quantitative values for strength are difficult to determine. Anisotropic etching of single-crystal silicon has been performed to create 30  $\mu\text{m}$  tall structures that were then indented to examine fracture toughness [7], but this is not possible with most materials.

## 24.2 Micromachined Structures for Measuring Mechanical Properties

Certainly the most direct way to measure the mechanical properties of small structures is to fabricate structures that would be conducive to such tests. Fabrication techniques are sufficiently advanced that virtually any design can be realized, at least in two dimensions. Two basic types of devices are used for mechanical property testing: *passive* structures and *active* structures.

### 24.2.1 *Passive Structures*

As mentioned previously, the main difficulty encountered when testing very small specimens is handling. One way to circumvent this problem is to use passive structures. These structures are designed to act as soon as they are released from the substrate and to provide whatever information they are designed to supply without further manipulation. For all of these passive structures, the forces acting on them come from the internal residual stresses of the structural material. For devices on the micron scale or smaller, gravitational forces can be neglected, and therefore internal stresses are the only source of actuation force.

#### Stress Measurements

Since internal residual stresses act upon the passive devices when they are released, it is natural to design a device that can be used to measure residual stresses. One such device, a rotating microstrain gage, is shown in Fig. 24.2. There are many different microstrain gauge designs, but all operate via the same principle. In Fig. 24.2a, the large pads, labeled A, will remain anchored to the substrate when the rest of the device is released. Upon release, the device will expand or contract in order to relieve its internal residual stresses. A structure under tension will contract,

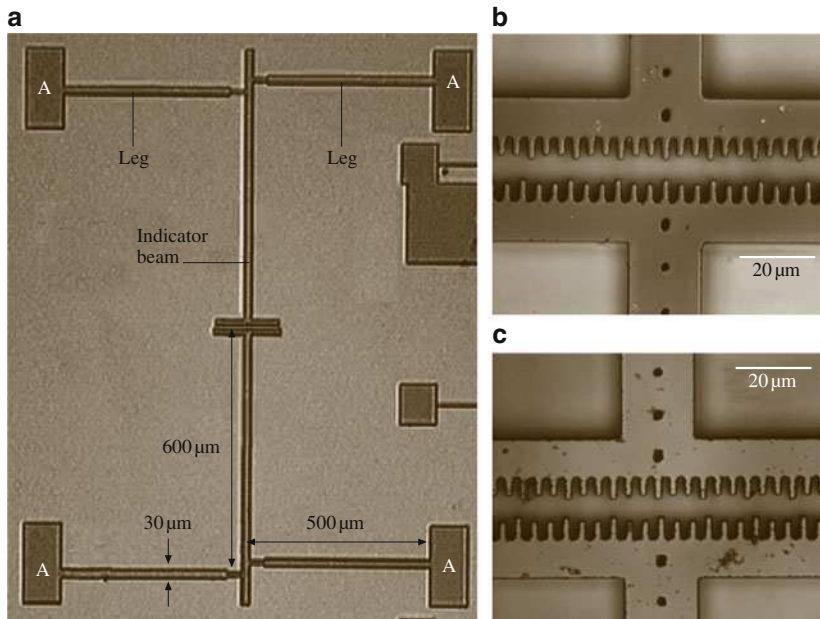


**Fig. 24.2** (a) Microstrain gauge fabricated from polysilicon; panel (b) shows a close-up of the Vernier scale before release, and panel (c) shows the same area after release

and a structure under compression will expand. For the structure in Fig. 24.2, compressive stress will cause the legs to lengthen. Since the two opposing legs are not attached to the central beam at the same point – they are offset, they will cause the central beam to rotate when they expand. The device in Fig. 24.2 contains two independent gauges that point to one another. At the ends of the two central beams are two parts of a Vernier scale. By observing this scale, one can measure the rotation of the beams.

If the connections between the legs and the central beams were simple pin connections, the strain  $\varepsilon$  of the legs (the fraction of expansion or contraction) could be determined simply by the measured rotation and the geometry of the device, namely

$$\varepsilon = \frac{d_{\text{beam}} d_{\text{offset}}}{2L_{\text{central}} L_{\text{leg}}}, \quad (24.2)$$

where  $d_{\text{beam}}$  is the lateral deflection of the end of one central beam,  $d_{\text{offset}}$  is the distance between the connections of the opposing legs,  $L_{\text{central}}$  is the length of the central beam (measured to the center point between the leg connections), and  $L_{\text{leg}}$  is the length of the leg. However, since the entire device was fabricated from a single polysilicon film, this cannot be the case; some bending must occur at the connections. As a result, to get an accurate determination of the strain relieved upon release, finite element analysis (FEA) of the structure must be performed. This is a common situation for microdevices. FEA is a powerful tool for determining the displacements and stresses of nonideal geometries. One drawback is that the Young's modulus of the material must be known in order to do the FEA as well as to convert the measured strain into a stress value. But Young's moduli are known for many micromachined materials or they can be measured using other techniques.

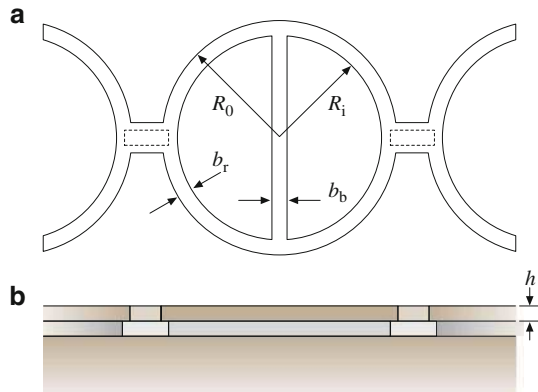
Other devices besides rotating strain gauges have been designed that can measure residual stresses. One of the simplest is a doubly clamped beam, a long, narrow beam of constant width and thickness that is anchored to the substrate at both ends. If the beam contains a tensile stress it will remain straight, but if the beam contains a compressive stress it will buckle if its length exceeds a critical value  $l_{\text{cr}}$  according to the Euler buckling criterion [8]

$$\varepsilon_r = -\frac{\pi^2}{3} \left( \frac{h}{l_{\text{cr}}} \right)^2, \quad (24.3)$$

where  $\varepsilon_r$  is the residual strain in the beam and  $h$  is the width or thickness of the beam, whichever is less. To determine the residual strain, a series of doubly clamped beams of varying lengths are fabricated. In this way, the critical length for buckling  $l_{\text{cr}}$  can be deduced after release. One problem with this technique is that during the release process, any turbulence in the solution will lead to enhanced buckling of the beams, and a low value for  $l_{\text{cr}}$  will be obtained.

For films with tensile stresses, a similar analysis can be performed using ring-and-beam structures, also called Guckel rings after their inventor, Henry Guckel.

**Fig. 24.3** Schematic showing (a) *top view* and (b) *side view* of Guckel ring structures (after [8]). The dashed lines in (a) indicate the anchors



A schematic of this design is shown in Fig. 24.3 [8]. Tensile stress in the outer ring will cause it to contract. This will lead to compressive stress in the central beam, even though the material was originally tensile before release. The amount of compression in the central beam can be determined analytically from the geometry of the device and the residual strain of the material. Again, by changing the length of the central beam it is possible to determine  $l_{cr}$ , and then the residual strain can be deduced.

### Stress Gradient Measurements

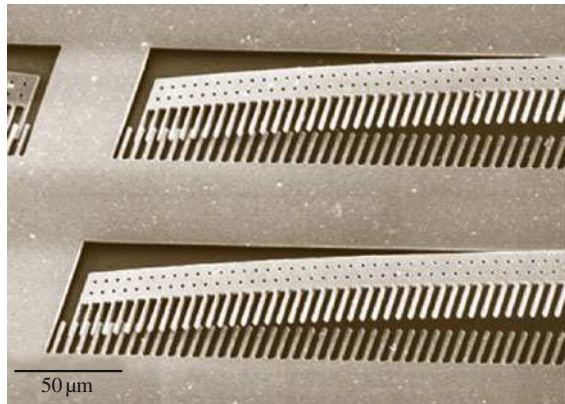
For structures fabricated from thin deposited films, the stress gradient can be just as important as the stress itself. Figure 24.4 shows a portion of a silicon microactuator. The device is designed to be completely planar; however, stress gradients in the film cause the structures to bend. This figure illustrates the importance of characterizing and controlling stress gradients, and it also demonstrates that stress gradients are most easily measured for a simple cantilever beam. By measuring the end deflection  $\delta$  of a cantilever beam of length  $l$  and thickness  $t$ , the stress gradient  $d\sigma/dt$  is determined by [9]

$$\frac{d\sigma}{dt} = \frac{2\delta}{l^2} \frac{E}{1-\nu}. \quad (24.4)$$

The magnitude of the end deflection can be measured by microscopy, optical interferometry, or any other technique.

Another useful structure for measuring stress gradients is a spiral. For this structure, the end of the spiral not anchored to the substrate will move out-of-plane. The diameter of the spiral will also contract, and the free end of the spiral will rotate when released [10].

**Fig. 24.4** Scanning electron micrograph (SEM) of a portion of a silicon microactuator. Residual stress gradients in the silicon cause the structure to bend



### Strength and Fracture Toughness Measurements

As mentioned above, if a doubly clamped beam contains a tensile stress, it will remain taut when released because it cannot relieve any of its stress by contracting. This tensile stress can be thought of as a tensile load being applied at the ends of the beam. If this tensile load exceeds the tensile strength of the material, the beam will break. Since the tensile stress can be measured, as discussed in the Sect. 24.2.1, this technique can be used to gather information on the strength of materials. Figure 24.5 shows two different beam designs that have been used to measure strength. The device shown in Fig. 24.5a was fabricated from a tensile polysilicon film [11]. Different beams were designed with varying lengths of the wider regions (marked  $l_1$  in the figure). In this manner, the load applied to the narrow center beam was varied, even though the entire film contained a uniform residual tensile stress. For  $l_1$  greater than a critical value, the narrow center beam fractured, giving a measurement for the tensile strength of polysilicon.

The design shown in Fig. 24.5b was fabricated from a tensile  $\text{Si}_3\text{N}_4$  film [12]. As seen in the figure, a stress concentration was included in the beam, to ensure the fracture strength would be exceeded. In this case, a notch was etched into one side of the beam. Since the stress concentration is not symmetric with regard to the beam axis, this results in a large bending moment at that position, and the test measures the bend strength of the material. Again, like the beams shown in Fig. 24.5a, the geometry of various beams fabricated from the same film were varied, to vary the maximum stress seen at the notch. By seeing which beams fracture at the stress concentration after release, the strength can be determined.

The fracture toughness of a material can be determined with a similar technique, but an atomically sharp pre-crack is used instead of a stress concentration. Sharp pre-cracks can be introduced into micromachined structures before release by adding a Vickers indent onto the substrate, near the device; the radial crack formed by the indent will propagate into the overlying structure [13]. Accordingly, the

**Fig. 24.5** Schematic designs of doubly clamped beams with stress concentrations used for measuring strength. (a) was fabricated from polysilicon (after [11]) and (b) was fabricated from  $\text{Si}_x\text{N}_y$  (after [12])

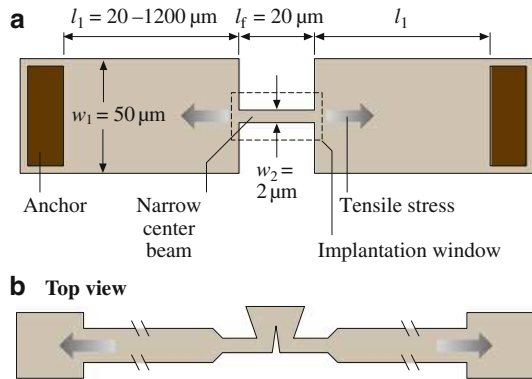
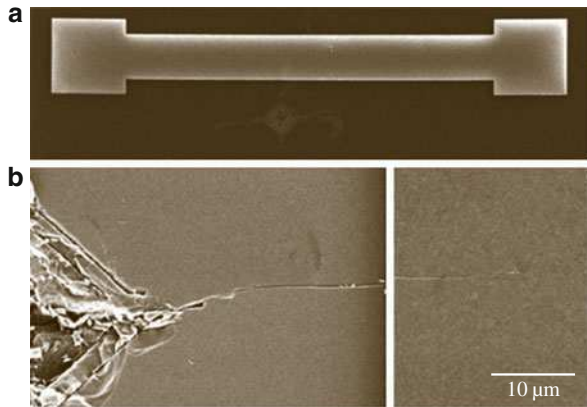


**Fig. 24.6** (a) SEM of a 500  $\mu\text{m}$ -long polysilicon beam with a Vickers indent placed near its center; (b) higher magnification SEM of the area near the indent showing the pre-crack traveling from the substrate into the beam (after [14])



beam with a sharp pre-crack, shown in Fig. 24.6, was fabricated using polysilicon [14]. Due to the stochastic nature of indentation, the initial pre-crack length varies from beam to beam. Because of this, even though the geometry of the beam remains identical, the stress intensity  $K$  at the pre-crack tip will vary. Upon release, only those pre-cracks whose  $K$  exceeds the fracture toughness of the material  $K_{Ic}$  will propagate, and in this way upper and lower bounds for  $K_{Ic}$  can be determined for the material.

For materials that do not normally contain residual tensile stresses, composite beams can be fabricated. In this technique, a portion of the beam length is fabricated from a highly tensile material, and the rest of the beam from the material to be tested. The two materials must exhibit perfect adhesion. When released, the tensile material will tend to contract, putting the rest of the beam in tension. This has been demonstrated for evaporated Al films with highly tensile CVD SiN [15].

For all of the beams discussed in this section, finite element analysis is required to determine the stress concentrations and stress intensities. Even though approximate

analytical solutions may exist for these designs, the actual fabricated structure will not have idealized geometries. For example, corners will never be perfectly sharp, and cracks will never be perfectly straight. This reinforces the idea that FEA is a powerful tool when determining mechanical properties of very small structures.

### 24.2.2 Active Structures

As discussed above, it is very convenient to design structures that act upon release to provide information on the mechanical properties of the structural materials. This is not always possible, however. For example, those passive devices just discussed rely on residual stresses to create the changes (rotation or fracture) that occur upon release, but many materials do not contain high residual stresses as-deposited, or the processing scheme of the device precludes the generation of residual stresses. Also, some mechanical properties, such as fatigue resistance, require motion before they can be studied. Active devices are therefore used. These are acted upon by a force (the source of this force can be integrated into the device itself or can be external to the device) in order to create a change, and the mechanical properties are studied via the response to the force.

### Young's Modulus Measurements

Young's modulus  $E$  is a material property critical to any structural device design. It describes the elastic response of a material and relates stress  $\sigma$  and strain  $\varepsilon$  by

$$\sigma = E\varepsilon. \quad (24.5)$$

In bulk samples,  $E$  is often measured by loading a specimen under tension and measuring displacement as a function of stress for a given length. While this is far more difficult for small structures, such as those fabricated from thin deposited films, it can be achieved with careful experimental techniques. Figure 24.7

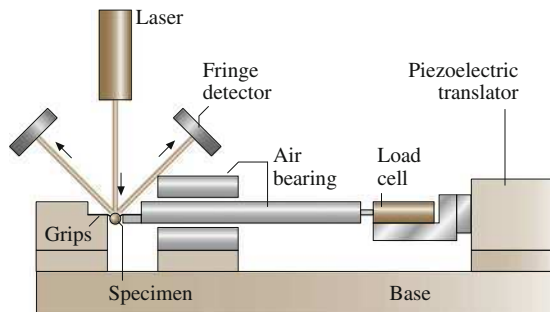


**Fig. 24.7** Schematic of a measurement system for tensile loading of micromachined specimens (after [16])



shows a schematic of one such measurement system [16]. The fringe detectors in the figure detect the reflected laser signal from two gold lines deposited onto the polysilicon specimen, which act as gauge markers. This enables the strain in the specimen during loading to be monitored. Besides gold lines, Vickers indents placed in a nickel specimen can also serve as gauge markers [17], or a speckle interferometry technique [18] can be used to determine strain in the specimen. Once the stress-versus-strain behavior is measured, the slope of the curve is equal to  $E$ . By using a constant load, such as a dead weight, and resistive heating, high-temperature creep can also be investigated with this method [19].

In addition to the tensile test, Young's modulus can be determined by other measures of stress-strain behavior. As seen in Fig. 24.8, a cantilever beam can be bent by pushing on the free end with a nanoindenter [20]. The nanoindenter can monitor the force applied and the displacement, and simple beam theory can convert the displacement into strain in order to obtain  $E$ . A similar technique, shown schematically in Fig. 24.9 [21], involves pulling downward on a cantilever beam by means of an electrostatic force. An electrode is fabricated into the substrate beneath the cantilever beam, and a voltage is applied between the beam and the bottom electrode. The force acting on the beam is equal to the electrostatic force corrected to include the effects of fringing fields acting on the sides of the beam, namely

$$F(x) = \frac{\epsilon_0}{2} \left( \frac{V}{g + z(x)} \right)^2 \left( 1 + \frac{0.65[g + z(x)]}{w} \right), \quad (24.6)$$

where  $F(x)$  is the electrostatic force at  $x$ ,  $\epsilon_0$  is the dielectric constant of air,  $g$  is the gap between the beam and the bottom electrode,  $z(x)$  is the out-of-plane deflection

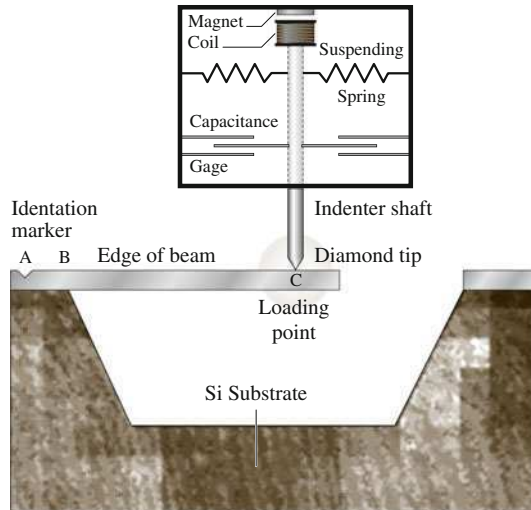


**Fig. 24.8** Schematic of a nanoindenter loading mechanism pushing on the end of a cantilever beam (after [20])

**Fig. 24.9** Schematic of a cantilever beam bending test using an electrostatic voltage to pull the beam toward the substrate (after [21])

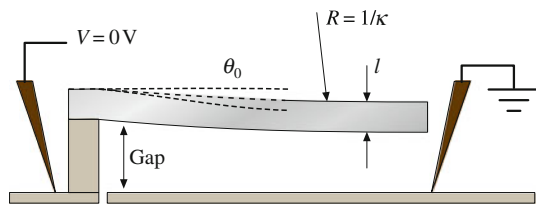
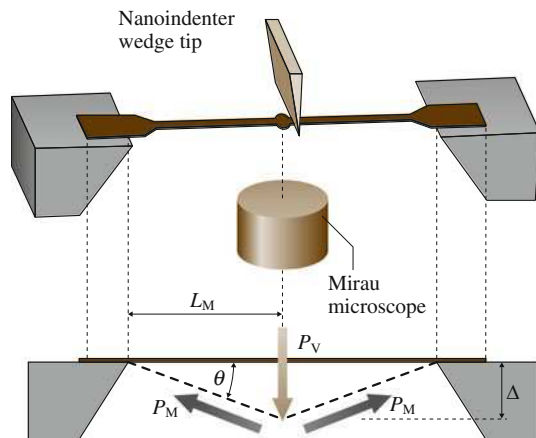


**Fig. 24.10** Schematic of an externally loaded doubly-clamped beam (after [22])



of the beam,  $w$  is the beam width, and  $V$  is the applied voltage [21]. In this work, the deflection of the beam as a function of position is measured using optical interferometry. These measurements combine to give stress-strain behavior for the cantilever beam. An extension of this technique uses doubly clamped beams instead of cantilever beams. In this case, the deflection of the beam at a given electrostatic force depends on the residual stress in the material as well as Young's modulus. This method can therefore also be used to measure residual stresses in doubly clamped beams.

Similarly, an external load can be applied to the center of the doubly-clamped beam, instead of using an electrostatic force, as shown in Fig. 24.10 [22]. The beam deflection is monitored using optical interferometry. Yet another variation is illustrated in Fig. 24.11 [23]. In this technique, the externally applied downward force is transferred to a film of any material deposited onto the device.

Another device that can be fabricated from a thin film and used to investigate stress-strain behavior is a suspended membrane, as shown in Fig. 24.12 [24]. As depicted in the schematic figure, the membrane is exposed to an elevated pressure on one side, causing it to bulge in the opposite direction. The deflection of the membrane is measured by optical or other techniques and related to the strain in the membrane. These membranes can be fabricated in any shape, typically square or circular. Both analytical solutions and finite element analyses have been performed to relate the deflection to the strain. Like the doubly clamped beams, both Young's

**Fig. 24.11** Schematic of a device that transfers external vertical loads to in-plane tensile loads in deposited films (after [23])

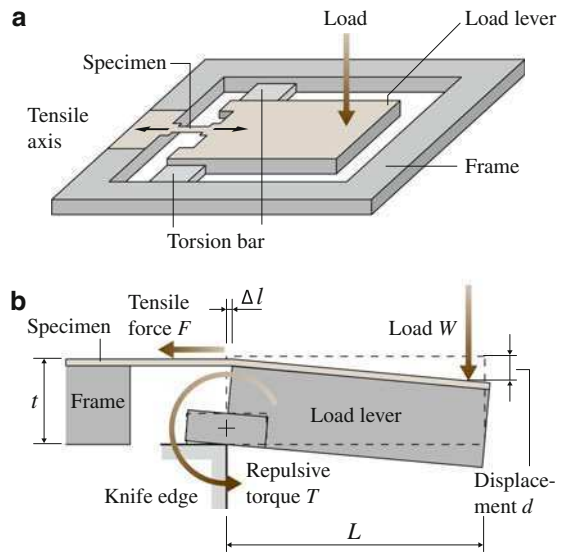
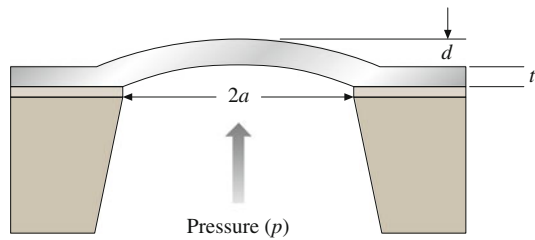


**Fig. 24.12** Schematic cross section of a microfabricated membrane (after [24])



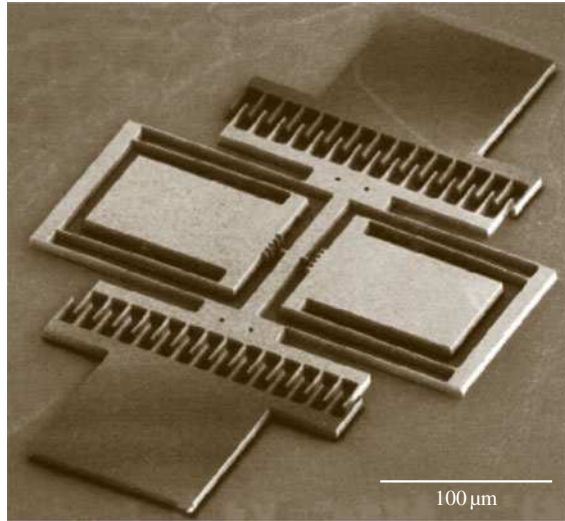
modulus and residual stress play a role in the deflected shape. Both of these mechanical properties can therefore be determined by the pressure-versus-deflection performance of the membrane.

Another measurement besides stress–strain behavior that can reveal the Young’s modulus of a material is the determination of the natural resonance frequency. For a cantilever, the resonance frequency  $f_r$  for free undamped vibration is given by

$$f_r = \frac{\lambda_i^2 t}{4\pi l^2} \left( \frac{E}{3\rho} \right)^{1/2}, \quad (24.7)$$

where  $\rho$ ,  $l$  and  $t$  are the density, length and thickness of the cantilever;  $\lambda_i$  is the eigenvalue, where  $i$  is an integer that describes the resonance mode number; for the first mode  $\lambda_1 = 1.875$  [25]. Given the geometry and density, measuring  $f_r$  allows  $E$  to be determined. The cantilever can be vibrated by a number of techniques, including a laser, loudspeaker or piezoelectric shaker. The frequency that produces the highest amplitude of vibration is the resonance frequency.

**Fig. 24.13** SEM of a polysilicon lateral resonator (after [27])



A micromachined device that uses an electrostatic comb drive and an AC signal to generate the vibration of the structure is known as a lateral resonator [26]. One example is shown in Fig. 24.13 [27]. When a voltage is applied across either set of the interdigitated comb fingers shown in Fig. 24.13, an electrostatic attraction is generated due to the increase in capacitance as the overlap between the comb fingers increases. The force  $F$  generated by the comb-drive is given by

$$F = \frac{1}{2} \frac{\partial C}{\partial x} V^2 = n\epsilon \frac{h}{g} V^2, \quad (24.8)$$

where  $C$  is capacitance,  $x$  is the distance traveled by one comb-drive toward the other,  $n$  is the number of pairs of comb fingers in one drive,  $\epsilon$  is the permittivity of the fluid between the fingers,  $h$  is the height of the fingers,  $g$  is the gap spacing between the fingers, and  $V$  is the applied voltage [26]. When an AC voltage at the resonance frequency is applied across either of the two comb drives, the central portion of the device will vibrate. In fact, since force depends on the square of the voltage for electrostatic actuation, for a time  $t$ , a dependent drive voltage  $v_D(t)$  (given by

$$v_D(t) = V_P + v_d \sin(\omega t), \quad (24.9)$$

where  $V_P$  is the DC bias and  $v_d$  is the AC drive amplitude), the time-dependent portion of the force will scale with

$$2\omega V_P v_d \cos(\omega t) + \omega v_d^2 \sin(2\omega t) \quad (24.10)$$

[26]. Therefore, if an AC drive signal is used with no DC bias, at resonance, the frequency of the AC drive signal will be one half of the resonance frequency. For this device, the resonance frequency  $f_r$  will be

$$f_r = \frac{1}{2\pi} \left( \frac{k_{\text{sys}}}{M} \right)^{1/2}, \quad (24.11)$$

where  $k_{\text{sys}}$  is the spring constant of the support beams and  $M$  is the mass of the portion of the device that vibrates. The spring constant is given by

$$k_{\text{sys}} = 24EI/L^3, \quad (24.12)$$

$$I = \frac{hw^3}{12}, \quad (24.13)$$

where  $I$  is the moment of inertia of the beams, and  $L$ ,  $h$  and  $w$  are the length, thickness, and width of each beam. Therefore, by combining these equations and measuring  $f_r$ , it is possible to determine  $E$ .

One distinct advantage of the lateral resonator technique and the electrostatically pulled cantilever technique for measuring Young's modulus is that they require no external loading sources. Portions of the devices are electrically contacted, and a voltage is applied. For the pure tension tests, as shown in Fig. 24.7, the specimen must be attached to a loading system, which can be extremely difficult for the very small specimens discussed here, and any misalignment or eccentricity in the test could lead to unreliable results. However, the advantage of the externally loaded technique is that there are no limitations on the type of materials that can be tested. Conductivity is not a requirement, nor is any compatibility with electrical actuation.

## Strength and Fracture Toughness Measurements

As one might expect, any of the techniques discussed in the previous section that strain specimens in order to measure Young's modulus can also be used to measure fracture strength. The load is simply increased until the specimen breaks. As long as either the load or the strain is measured at fracture, and the geometry of the specimen is known, the maximum stress required for fracture  $\sigma_{\text{crit}}$  can be determined, either through analytical analysis or FEA. Depending on the geometry of the test,  $\sigma_{\text{crit}}$  will represent the tensile or bend strength of the material.

If the available force is limited, or if a localized fracture site is desired, stress concentrations can be added to the specimens. These are typically notches micro-machined into the edges of specimens. Focused ion beams have also been used to carve stress concentrations into fracture specimens.

All of the external loading schemes, such as those shown in Figs. 24.7 and 24.8, have been used to measure fracture strength. Also, the electrostatically loaded doubly clamped beams can be pulled until they fracture. In this case, there is one complication. The electrostatic force is inversely proportional to the distance between the electrodes, and at a certain voltage, called the *pull-in voltage*, the attraction between the beam and the substrate will become so great that the beam

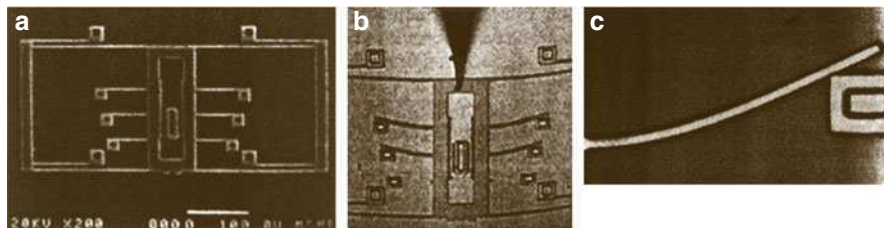


**Fig. 24.14** (a) SEM of a device for measuring bend strength of polysilicon beams; (b) image of a test in process; (c) higher magnification view of one beam shortly before breaking (after [28])

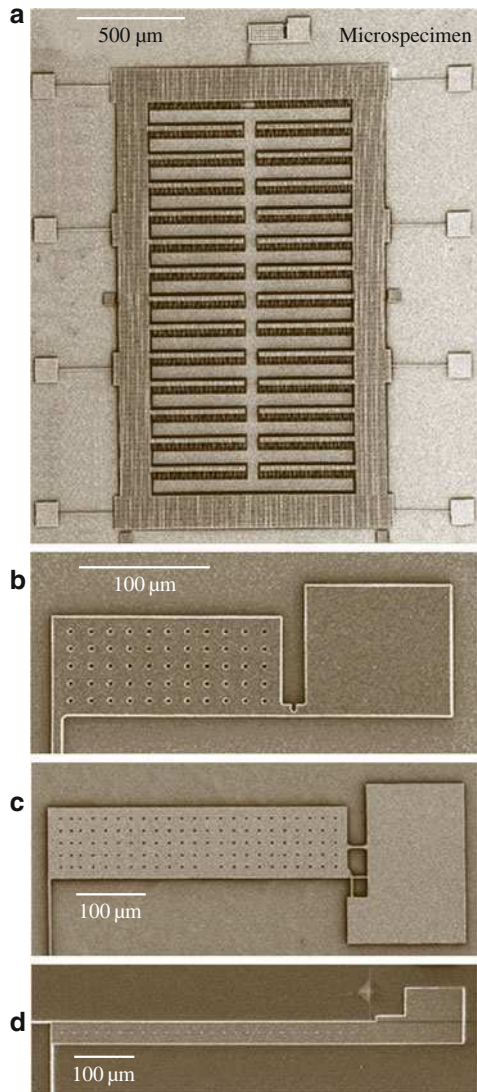
will immediately be pulled into contact with the bottom electrode. As long as the fracture takes place before the pull-in voltage is reached, the experiment will give valid results.

Other loading techniques have been used to generate fracture of microspecimens. Figure 24.14 [28] shows one device designed to be pushed by the end of a micromanipulated needle. The long beams that extend from the sides of the central shuttle come into contact with anchored posts, and, at a critical degree of bending, the beams will break off. Since the applied force cannot be measured in this technique, the experiment is continuously optically monitored during the test, and the image of the beams just before fracture is analyzed to determine  $\sigma_{\text{crit}}$ .

Another loading scheme that has been demonstrated for micromachined specimens utilizes scratch drive actuators to load the specimens [29]. These types of actuators work like inchworms, traveling across a substrate in discrete advances as an electrostatic force is repeatedly applied between the actuator and the substrate. The stepping motion can be made on the nanometer scale, depending on the frequency of the applied voltage, and so it can be an acceptable approximation to continuous loading. One advantage of this scheme is that very large forces can be generated by relatively small devices. The exact forces generated cannot be measured, so (like the technique that used micromanipulated pushing) the test is continuously observed to determine the strain at fracture. Another advantage of this technique is that, like the lateral resonator and the electrically pulled cantilever, the loading takes place on-chip, and therefore the difficulties associated with attaching and aligning an external loading source are eliminated.

Another on-chip actuator used to load microspecimens is shown in Fig. 24.15, along with three different microspecimens [14]. Devices have been fabricated with each of the three microspecimens integrated with the same electrostatic comb-drive actuator. In all three cases, when a DC voltage is applied to the actuator, it moves downward, as oriented in Fig. 24.15. This pulls down on the left end of each of the three microspecimens, which are anchored on the right. The actuator contains 1,486 pairs of comb fingers. The maximum voltage that can be applied is limited by the breakdown voltage of the medium in which the test takes place. In air, this limits the voltage to less than 200 V. As a result, given a finger height of 4  $\mu\text{m}$  and a gap of 2  $\mu\text{m}$ , and using (24.8), the maximum force generated by this actuator is limited to about 1 mN. Standard optical photolithography has a minimum feature size of

**Fig. 24.15** (a) SEM of a micromachined device for conducting strength tests; the device consists of a large comb-drive electrostatic actuator integrated with a microspecimen; (b–d) SEMs of various microspecimens for testing bend strength, tensile strength and fracture toughness, respectively (after [14])



about 2  $\mu\text{m}$ . As a result, the electrostatic actuator cannot generate sufficient force to perform a standard tensile test on MEMS structural materials such as polysilicon. The microspecimens shown in Fig. 24.15 are therefore designed such that the stress is amplified.

The specimen shown in Fig. 24.15b is designed to measure bend strength. It contains a micromachined notch with a root radius of 1  $\mu\text{m}$ . When the actuator pulls downward on the left end of this specimen, the notch serves as a stress concentration, and when the stress at the notch root exceeds  $\sigma_{\text{crit}}$ , the specimen fractures.



The specimen in Fig. 24.15c is designed to test tensile strength. When the left end of this specimen is pulled downward, a tensile stress is generated in the upper thin horizontal beam near the right end of the specimen. As the actuator continues to move downward, the tensile stress in this beam will exceed the tensile strength, causing fracture. Finally, the specimen in Fig. 24.15d is similar to that in Fig. 24.15b, except that the notch is replaced by a sharp pre-crack that was produced by the Vickers indent placed on the substrate near the specimen. When this specimen is loaded, a stress intensity  $K$  is generated at the crack tip. When the stress intensity exceeds a critical value  $K_{Ic}$ , the crack propagates.  $K_{Ic}$  is also referred to as the fracture toughness.

The force generated by the electrostatic actuator can be calculated using (24.8). However, (24.8) assumes a perfectly planar, two-dimensional device. In fact, when actuated, the electric fields extend out of the plane of the device, and so (24.8) is just an approximation. Instead, like many of the techniques discussed in this section, the test is continuously monitored, and the actuator displacement at the time of fracture is recorded. Then FEA is used to determine the magnitude of the stress or stress intensity seen by the specimen at the point of fracture.

In order to generate sufficient force to conduct tensile tests, a similar device to that shown in Fig. 24.15 has been designed which uses an array of parallel plate capacitors to provide the force, instead of comb-drives [30]. In this way the available force is increased but the maximum stroke is severely limited.

## Fatigue Measurements

A benefit of the electrostatic actuator shown in Fig. 24.15 is that, besides monotonic loading, it can generate cyclic loading. This allows the fatigue resistance of materials to be studied. Simply by using an AC signal instead of a DC voltage, the device can be driven at its resonant frequency. The amplitude of the resonance depends on the magnitude of the AC signal. This amplitude can be increased until the specimen breaks; this will investigate the low-cycle fatigue resistance. Otherwise, the amplitude of resonance can be left constant at a level below that required for fast fracture, and the device will resonate indefinitely until the specimen breaks; this will investigate high-cycle fatigue. It should be noted that the resonance frequency of such a device is about 10 kHz. Therefore, it is possible to stress a specimen for over  $10^9$  cycles in less than a day. In addition to simple cyclic loading, a mean stress can be superimposed on the cyclic load if a DC bias is added to the AC signal. In this way, nonsymmetric cyclic loading (with a large tensile stress alternating with a small compressive stress, or vice versa) can be studied.

Another device that can be used to investigate fatigue resistance in MEMS materials is shown in Fig. 24.16 [31]. In this case, a large mass is attached to the end of a notched cantilever beam. The mass contains two comb drives on opposite ends. When an AC signal is applied to one comb drive, the device will resonate, cyclically loading the notch. The comb drive on the opposite side is used as a capacitive displacement sensor. This device contains many fewer comb fingers than



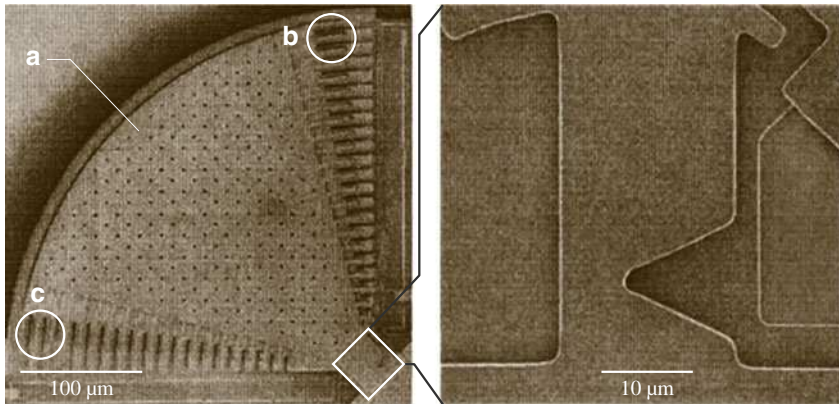


**Fig. 24.16** SEM of a device used to investigate fatigue; the image *on the right* is a higher magnification view of the notch near the base of the moving part of the structure (after [31]): (a) mass, (b) comb-drive actuator, (c) capacitive displacement sensor

the device shown in Fig. 24.15. As a result, it can apply cyclic loads by exploiting the resonance frequency of the device, but it cannot supply sufficient force to achieve monotonic loading.

Fatigue loading has also been studied using the same external loading techniques shown in Fig. 24.7. In this case, the frequency of the cyclic load is considerably lower, since the resonance frequency of the device is not being utilized. This leads to longer high-cycle testing times. Since the force is essentially unlimited, however, this technique allows a variety of frequencies to be studied to determine their effect on the fatigue behavior.

## Friction and Wear Measurements

Friction is another property that has been studied in micromachined structures. To study friction, of course, two surfaces must be brought into contact with each other. This is usually avoided at all costs for these devices because of the risk of stiction. (Stiction is the term used when two surfaces that come into contact adhere so strongly that they cannot be separated.) Even so, a few devices have been designed that can investigate friction. One of these is shown schematically in Fig. 24.17 [32]. It consists of a movable structure with a comb-drive on one end and a cantilever beam on the other. Beneath the cantilever, on the substrate, is a planar electrode. The device is moved to one side using the comb-drive. Then a voltage is applied between the cantilever beam and the substrate electrode. The voltage on the comb-drive is then released. The device would normally return to its original position, to relax the deflection in the truss suspensions, but the friction between the cantilever and the substrate electrode holds it in place. The voltage to the substrate electrode is slowly decreased until the device starts to slide. Given the electrostatic force generated by the substrate electrode and the stiffness of the truss suspensions, it

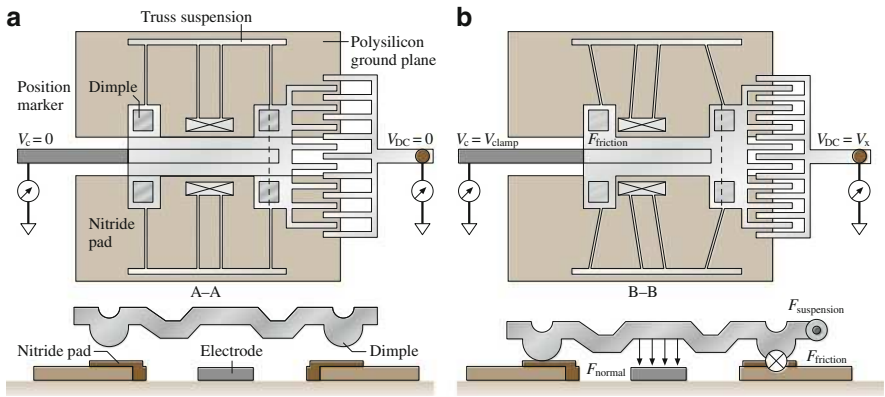


**Fig. 24.17** Schematics depicting a device used to study friction. Panel (a) shows top and side views of the device in its original position, and panel (b) shows views of the device after it has been displaced using the comb-drive and clamped using the substrate electrode (after [32])

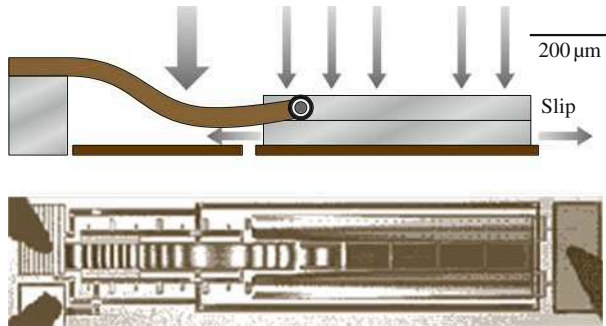


**Fig. 24.18** Schematic cross-section and top-view optical micrograph of a hinged-cantilever test structure for measuring friction in micromachined devices (after [33])

is possible to determine the static friction. For this device, bumps were fabricated on the bottom of each cantilever beam. This limited the surface area that came into contact with the substrate and so lowered the risk of stiction.

Another device designed to study friction is shown in Fig. 24.18 [33]. This technique uses a hinged cantilever. The portion near the free end acts as the friction test structure, and the portion near the anchored end acts as the driver. The friction test structure is attracted to the substrate by means of electrostatic actuation, and when a second electrostatic actuator pulls down the driver, the friction test structure slips forward by a length proportional to the forces involved, including the frictional force. This distance, however, has a maximum of 30 nm, so all measurements must be exceedingly accurate in order to investigate a range of forces. This test structure can be used to determine the friction coefficients for surfaces with and without lubricating coatings.

Wear can occur whenever friction between two contacting components is non-zero. Wear mechanisms can entail plastic deformation or brittle fracture. Adhesive wear involves fusion between asperities of two different components, followed by fracture. Wear in polysilicon devices has been investigated using transmission electron microscopy [34].

### **Metal-to-Metal Contact**

Recently, radiofrequency (RF) MEMS switches have been developed that are vast improvements over conventional technology. During operation, these devices endure unique mechanical metal-to-metal contacts that can be serious reliability concerns. An example of an RF MEMS switch is shown in Fig. 24.19 [35]. As illustrated in Fig. 24.19b, to close the switch the metal bumps are brought into contact with a metal plate, creating a short circuit. When this occurs, significant pressures are developed, depending on the roughness and asperity heights on the metal surfaces. Also, if currents are flowing, Joule heating and arcing can also take place. If the contact area becomes large, through surface roughness modification during operation, the adhesive forces between the two metal components can exceed the restoring force of the springs, and the switch can become stuck in the closed position. Alternatively, high currents can result in melting and short circuits [36]. To investigate this mechanical deformation during repeated impact, the RF switches themselves are usually examined before and after operation. A separate testing device has not been designed that could provide any accelerated testing conditions.

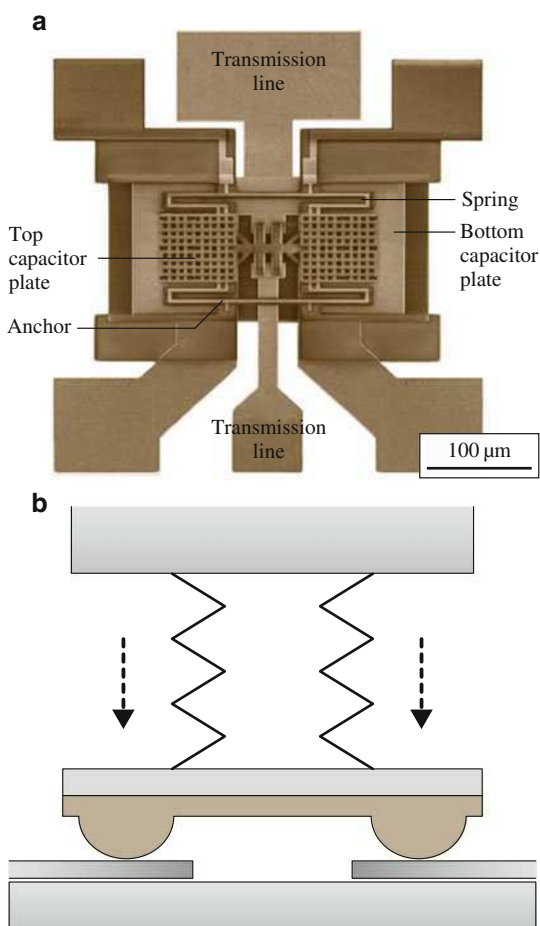
## **24.3 Measurements of Mechanical Properties**

All of the techniques discussed in Sects. 24.1 and 24.2 have been used to measure the mechanical properties of MEMS and NEMS materials. As a general rule, the results from the various techniques have agreed well with each other, and the argument becomes which of the measurement techniques is easiest and most reliable to perform. It is crucial to bear in mind, however, that certain properties (such as strength) are process-dependent, and so the results taken at one laboratory will not necessarily match those taken from another. This will be discussed in more detail in Sect. 24.3.1.

### **24.3.1 Mechanical Properties of Polysilicon**

In current MEMS technology, the most widely used structural material is polysilicon deposited by low-pressure chemical vapor deposition (LPCVD). One reason for the prevalence of polysilicon is the large body of processing knowledge for this material that has been developed by the integrated circuit community. Another

**Fig. 24.19** (a) Micrograph of an RF MEMS switch designed by Rockwell Scientific, and (b) schematic drawing showing the movement of the metal bridge as it comes into contact with the underlying metal plate during switch operation (after [35])

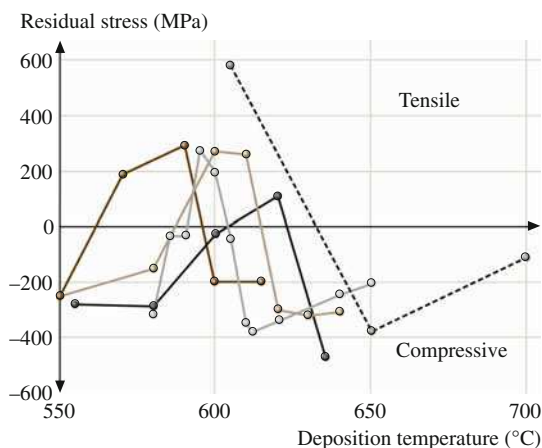


reason, of course, is that polysilicon possesses a number of qualities that are beneficial to MEMS devices, in particular high strength and Young's modulus. Therefore, most of the mechanical properties investigations performed on MEMS materials have focused on polysilicon.

### Residual Stresses in Polysilicon

The residual stresses of LPCVD polysilicon have been thoroughly characterized using both the wafer curvature technique, discussed in Sect. 24.1.1, and the micro-strain gauges, discussed in Sect. 24.2.1. The results from both techniques give consistent values. Figure 24.20 summarizes the residual stress measurements as a function of deposition temperature taken from five different investigations at five

**Fig. 24.20** Results for residual stress of LPCVD polysilicon films taken from five different investigations (after [37]). Data from the same investigation are connected by a line



different laboratories [37]. All five sets of data show the same trend. The stresses change from compressive at the lowest deposition temperatures to tensile at intermediate temperatures and back to compressive at the highest temperatures. The exact transition temperatures vary somewhat between the different investigations, probably due to differences in the deposition conditions: the silane or dichlorosilane pressure, the gas flow rate, the geometry of the deposition system, and the temperature uniformity. However, in each data set the transitions are easily discernible. The origin of these residual stress changes lies with the microstructure of the LPCVD polysilicon films.

As with all deposited films, the microstructure of the LPCVD polysilicon film is dependent on the deposition conditions. In general, the films are amorphous at the lowest growth temperatures (lower than  $\sim 570^\circ\text{C}$ ), display fine ( $\sim 0.1\ \mu\text{m}$  diameter) grains at intermediate temperatures ( $\sim 570$  to  $\sim 610^\circ\text{C}$ ), and contain columnar (110)-textured grains with a thin fine-grained nucleation layer at the substrate interface at higher temperatures ( $\sim 610$  to  $\sim 700^\circ\text{C}$ ) [37]. The fine-grained microstructure results from the homogeneous nucleation and growth of silicon grains within an as-deposited amorphous silicon film. In this regime, the deposition rate is just slightly faster than the crystallization rate. The as-deposited films will be crystalline near the substrate interface and amorphous at the free surface. (The amorphous fraction can be quickly crystallized by annealing above  $610^\circ\text{C}$ .) The columnar microstructure seen at higher growth temperatures results from the formation of crystalline silicon films as-deposited, with growth being fastest in the  $\langle 110 \rangle$  directions.

The origin of the tensile stress in the fine-grained polysilicon arises from the volume decrease that accompanies the crystallization of the as-deposited amorphous material. The origins of the compressive stresses in the amorphous and columnar films are less well understood. One proposed explanation for compressive stress generation during thin film growth postulates that an increase in the surface chemical potential is caused by the deposition of atoms from the vapor; the increase

in surface chemical potential induces atoms to flow into newly formed grain boundaries, creating a compressive stress in the film [38].

Stress gradients are also typical of LPCVD polysilicon films. The partially amorphous films contain large stress gradients since they are essentially bilayers of compressive amorphous silicon on top of tensile fine-grained polysilicon. The fully crystalline films also exhibit stress gradients. The columnar compressive films are most highly stressed at the film–substrate interface, with the compressive stresses decreasing as the film thickness increases; the fine-grained films are less tensile at the film–substrate interface, with the tensile stresses increasing as the film thickness increases [37]. Both stress gradients are associated with microstructural variations. For the columnar films, the initial nucleation layer corresponds to a very high compressive stress, which decreases as the columnar morphology develops. For the fine-grained films, the region near the film–substrate interface has a slightly smaller average grain size, due to heterogeneous nucleation at the interface. This region displays a slightly lower tensile stress than the rest of the film, since the increased grain boundary area reduces the local density.

### Young's Modulus of Polysilicon

The Young's modulus of polysilicon films has been measured using all of the techniques discussed in Sect. 24.2.2. A good review of the experimental results taken from bulge testing, tensile testing, beam bending and lateral resonators are contained in [39]. All of the reported results are in reasonable agreement, varying from 130 to 175 GPa, though many values are reported with a relatively high experimental scatter. The main origin of the error in these results is the uncertainties involving the geometries of the small specimens used to make the measurements. For example, from (24.13), the Young's modulus determined by the lateral resonators depends on the cube of the tether beam width, typically about 2  $\mu\text{m}$ . In general, the beam width and other dimensions can be measured via scanning electron microscopy to within about 0.1  $\mu\text{m}$ ; however, the width of the beam is not perfectly constant along the entire length or even throughout the thickness of the beam. These uncertainties in geometry lead to uncertainties in modulus.

In addition, the various experimental measurements lie close to the Voigt and Reuss bounds for Young's modulus calculated using the elastic stiffnesses and compliances for single-crystal silicon [39]. This strongly implies that Young's moduli of micro- and nanomachined polysilicon structures will be the same as for bulk samples made from polysilicon. This is not unexpected, since Young's modulus is a material property. It is related to interatomic interactions and should have no dependence on the geometry of the sample. It should be noted that polysilicon can display a preferred crystallographic orientation depending on the deposition conditions, and that this could affect the Young's modulus of the material, since the Young's modulus of silicon is not isotropic. However, the anisotropy is fairly small for cubic silicon.

A more recent investigation that utilized electrostatically actuated cantilevers and interferometric deflection detection yielded a Young's modulus of 164 GPa [21]. They found the grains in their polysilicon films to be randomly oriented, and calculated the Voigt and Reuss bounds to be 163.4–164.4 GPa. This appears to be a very reliable value for randomly oriented polysilicon.

## Fracture Toughness and Strength of Polysilicon

Using the device shown in Fig. 24.15a and the specimen shown in Fig. 24.15d, the fracture toughness  $K_{Ic}$  of polysilicon has been shown to be  $1.0 \pm 0.1 \text{ MPa m}^{1/2}$  [40]. Several different polysilicon microstructures were tested, including fine-grained, columnar and multilayered. Amorphous silicon was also investigated. All of the microstructures displayed the same  $K_{Ic}$ . This indicates that, like Young's modulus, fracture toughness is a material property, independent of the material microstructure or the geometry of the sample.

A tensile test, such as that shown in Fig. 24.7 but using a sample with sharp indentation-induced pre-cracks, yields a  $K_{Ic}$  of  $0.86 \text{ MPa m}^{1/2}$  [41]. The passive, residual stress loaded beams with sharp pre-cracks shown in Fig. 24.6 gave a  $K_{Ic}$  of  $0.81 \text{ MPa m}^{1/2}$  [14].

Given that  $K_{Ic}$  is a material property for polysilicon, the measured fracture strength  $\sigma_{crit}$  is related to  $K_{Ic}$  by

$$K_{Ic} = c\sigma_{crit}(\pi a)^{1/2}, \quad (24.14)$$

where  $a$  is the crack-initiating flaw size, and  $c$  is a constant of order unity. The value for  $c$  will depend on the exact size, shape and orientation of the flaw; for a semicircular flaw,  $c$  is equal to 0.71 [42]. Therefore, any differences in the reported fracture strength of polysilicon will be the result of changes in  $a$ .

A good review of the experimental results available in the literature for polysilicon strength is contained in [43]. The tensile strength data vary from about 0.5 to 5 GPa. Like many brittle materials, the measured strength of polysilicon is found to obey Weibull statistics [44, 45]. This implies that the polysilicon samples contain a random distribution of flaws of various sizes, and that the failure of any particular specimen will occur at the largest flaw that experiences the highest stress. One consequence of this behavior is that, since larger specimens have a greater probability of containing larger flaws, they will exhibit decreased strengths. More specifically, it was found that the most important geometrical parameter is the surface area of the sidewalls of a polysilicon specimen [43] and single crystal silicon [46] specimens. The sidewalls, as opposed to the top and bottom surfaces, are those surfaces created by etching the polysilicon film. This is not surprising since LPCVD polysilicon films contain essentially no flaws within the bulk, and the top and bottom surfaces are typically very smooth.

As a result, the etching techniques used to create the structures will have a strong impact on the fracture strength of the material. For single-crystal silicon specimens it was found that the choice of etchant could change the observed tensile strength by a factor of two [47] and by about 20% for polysilicon [48]. In addition, the bend strength of amorphous silicon was measured to be twice that of polysilicon for specimens processed identically [40]. It was found that the reactive ion etching used to fabricate the specimens produced much rougher sidewalls on the polysilicon than on the amorphous silicon.

The tensile strength of single crystal silicon has also been measured using a technique similar to that shown in Fig. 24.8. Sharp notches were introduced into the beams using a focused ion beam, and the apparent fracture toughness was measured for a variety of planes parallel to the notch front, along which the crack propagated. For the {110} notch plane, the fracture toughness was about  $1 \text{ MPa m}^{1/2}$ , and for the {100} notch plane it was about  $2 \text{ MPa m}^{1/2}$  [49, 50] and for the {100} notch plane it was about  $1 \text{ MPa m}^{1/2}$  [50] or about  $2 \text{ MPa m}^{1/2}$  [49].

### Fatigue of Polysilicon

Fatigue failure involves fracture after a number of load cycles, when each individual load is not sufficient by itself to generate catastrophic cracking in the material. For ductile materials, such as metals, fatigue occurs due to accumulated damage at the site of maximum stress and involves local plasticity. As a brittle material, polysilicon would not be expected to be susceptible to cyclic fatigue. However, fatigue has been observed for polysilicon tensile samples [41], polysilicon bend specimens with notches [30, 51], and polysilicon bend specimens with sharp cracks [52]. The exact origins of the fatigue behavior are still subject to debate, but some aspects of the experimental data are that the fatigue lifetime does not depend on the loading frequency [41], the fatigue behavior is affected by the ambient [14, 52], fatigue occurs faster in higher humidities [53], and the fatigue depends on the ratio of compressive to tensile stresses seen in the load cycle [14].

Fatigue in polysilicon has been found to either cause thickening of the native oxide in the highly stressed regions [54], or to cause no thickening of the native oxide in the highly stressed regions [55]. Even more strangely, fatigue cycling under certain conditions can lead to apparent strengthening of the polysilicon [56, 57]. While the exact mechanism of fatigue in polysilicon is not known, dislocations have been observed in tensile fracture of polysilicon at room temperature [58], which implies a role for dislocations in fatigue behavior.

### Friction of Polysilicon

The friction of polysilicon structures has been measured using the techniques described in Sect. 24.2.2. The measured coefficient of friction was found to vary from 4.9 [32] to 7.8 [33].



The static and dynamic friction of polysilicon coated with monolayer lubricants has been measured with a device similar to that shown in Fig. 24.17, but using a scratch-drive actuator instead of a comb-drive [59]. The dynamic friction at 0.2 m/s was approximately 80% of the static friction value; the static friction at zero applied load was due to an adhesive force of  $0.95 \text{ nN}/\mu\text{m}^2$ .

### 24.3.2 *Mechanical Properties of Other Materials*

As discussed above, of all the materials used for MEMS and NEMS, polysilicon has generated the most interest as well as the most research in mechanical properties characterization. However, measurements have been taken on other materials, and these are summarized in this section.

As discussed in Sect. 24.2.2, one advantage of the externally loaded tension test, as shown in Fig. 24.7, is that essentially any material can be tested using this technique. As such, tensile strengths have been measured to be 0.6–1.9 GPa for  $\text{SiO}_2$  [60] and 0.7–1.1 GPa for titanium [61]. The yield strength for electrodeposited nickel was found to vary from 370 to 900 MPa, depending on the annealing temperature [17]. In addition, the yield strength was strongly affected by the current density during the electrodeposition process. Both the annealing and current density effects were correlated to changes in the microstructure of the material. The fatigue behavior of electrodeposited Ni was also investigated [62]. Microstructural changes due to thermal treatments also caused the yield strength of AlCuMgMn films to vary from 400 to 1,000 MPa [63]. Young's moduli were determined to be 100 GPa for titanium [61] and 215 GPa for electrodeposited nickel [17] and 96 GPa for permalloy [23].

The tensile strength, Young's modulus, and Poisson's ratio of silicon nitride were measured to be 5.9 GPa, 0.23 and 257 GPa, respectively [64], and the same properties of amorphous diamondlike carbon were found to be 7.3 GPa, 0.17 and 759 GPa, respectively [65].

The technique of bending cantilever beams, shown in Fig. 24.8, can also be performed on a variety of materials. The yield strength and Young's modulus of gold were found to vary from 260 MPa and 57 GPa, respectively [20], to 300 MPa and 120 GPa, respectively [66], using this method. The same properties in Al were measured to be 150 MPa and 80 GPa, respectively [66], and in silicon nitride to be 6.9 and 260 GPa, respectively [67]. Using a technique similar to that shown in Fig. 24.8, except that a doubly-clamped beam was used instead of a cantilever beam, the fracture toughness of ultrananocrystalline diamond was measured to be  $4.5 \text{ MPa m}^{1/2}$  [68]. Resonating cantilever beams revealed a Young's modulus for gold of 47 GPa [69], and Young's moduli of 1.8 and 14.4 GPa for silica and alumina aerogel thin films, respectively [70].

Another technique that can be used with a number of materials is the membrane deflection method, shown in Fig. 24.12. Silicon nitride measured with this technique revealed a Young's modulus of 258 GPa [64] to 325 GPa and a burst strength of 7.1 GPa [71]. A polyimide membrane gave a residual stress of 32 MPa,

a Young's modulus of 3.0 GPa, and an ultimate strain of about four percent [24]. Membranes were also fabricated from polycrystalline SiC films with two different grain structures [72]. The film with (110)-texture columnar grains had a residual stress of 434 MPa and a Young's modulus of 349 GPa. The film with equiaxed (110)- and (111)-textured grains had a residual stress of 446 MPa and a Young's modulus of 456 GPa. Al and Ni membranes revealed Young's moduli of 70 and 200 GPa, respectively [73]. Polymeric SU-8 displayed a fracture strength of 73 MPa and a very low creep rate [74].

Other devices that are used to measure mechanical properties require more complicated micromachining, namely patterning, etching and release, in order to operate. These devices are more difficult to fabricate with materials that are not commonly used as MEMS structural materials. However, the following examples demonstrate work in this area. The structure shown in Fig. 24.5b was fabricated from  $\text{Si}_x\text{N}_y$  and revealed a apparent fracture toughness of  $1.8 \text{ MPa m}^{1/2}$  [12]. The devices shown in Fig. 24.6 revealed a fracture toughness of SiC of  $3.1 \text{ MPa m}^{1/2}$  [75]. Similar composite beams gave a yield strength of 625 MPa and a strain at crack initiation of 0.3 for Al [15]. Devices as shown in Fig. 24.10 showed a fracture toughness of diamond of  $4.6 \text{ MPa m}^{1/2}$  [22], a Young's modulus of Cu of 115 GPa [76], and a Young's modulus and yield strength of Mo of 231 and 1.76 GPa, respectively [77].

Lateral resonators of the type shown in Fig. 24.13 were processed using single crystal and polycrystalline SiC, and the Young's modulus was determined to be between 360 GPa [78] and 426 GPa [79]. Resonating beams revealed the temperature coefficient of Young's modulus to be  $-53 \text{ ppm/K}$  [80]. The device shown in Fig. 24.14 was fabricated from polycrystalline germanium, and used to measure a bend strength of 1.5 GPa for unannealed Ge and 2.2 GPa for annealed Ge [81]. The same device was also fabricated from SiC and revealed a bend strength of 23 GPa [82]. Devices similar to that shown in Fig. 24.15 revealed the tensile strength of silicon nitride to be 6.4 GPa [71], and the Young's modulus and yield strength of aluminium to be 74.6 GPa and 330 MPa, respectively [83].

The metal-to-metal contact RF switches, such as shown in Fig. 24.19 typically use Au as the contact metal, due to its low electrical resistance and high oxidation resistance. In these devices, adhesive forces were found to increase logarithmically with *cold* contact cycles (cycling with no current passing through the switch), consistent with creep as the underlying physical mechanism [34]. At high currents, no adhesion was found between the metal components, but melting led to extrusions and short circuits [36]. Both of these results are consistent with separate modeling investigations [84, 85].

## References

1. G.G. Stoney, The tension of metallic films deposited by electrolysis, Proc. R. Soc. A **82**, 172–175 (1909)
2. W. Brantley, Calculated elastic constants for stress problems associated with semiconductor devices, J. Appl. Phys. **44**, 534–535 (1973)

3. A. Ni, D. Sherman, R. Ballarini, H. Kahn, B. Mi, S.M. Phillips, A.H. Heuer, Optimal design of multilayered polysilicon films for prescribed curvature, *J. Mater. Sci.*, **38**, 4169–4173 (2003)
4. J.A. Floro, E. Chason, S.R. Lee, R.D. Twisten, R.Q. Hwang, L.B. Freund, Real-time stress evolution during  $\text{Si}_{1-x}\text{Ge}_x$  heteroepitaxy, Dislocations, islanding, and segregation, *J. Electron. Mater.* **26**, 969–979 (1997)
5. W. Nix, Mechanical properties of thin films, *Metall. Trans. A* **20**, 2217–2245 (1989)
6. X. Li, B. Bhusan, Micro/nanomechanical characterization of ceramic films for microdevices, *Thin Solid Films* **340**, 210–217 (1999)
7. M.P. de Boer, H. Huang, J.C. Nelson, Z.P. Jiang, W.W. Gerberich, Fracture toughness of silicon and thin film micro-structures by wedge indentation, *Mater. Res. Soc. Symp. Proc.* **308**, 647–652 (1993)
8. H. Guckel, D. Burns, C. Rutigliano, E. Lovell, B. Choi, Diagnostic microstructures for the measurement of intrinsic strain in thin films, *J. Micromech. Microeng.* **2**, 86–95 (1992)
9. F. Ericson, S. Greek, J. Soderkvist, J.-A. Schweitz, High sensitivity surface micromachined structures for internal stress and stress gradient evaluation, *J. Micromech. Microeng.* **7**, 30–36 (1997)
10. L.S. Fan, R.S. Muller, W. Yun, R.T. Howe, J. Huang, Spiral microstructures for the measurement of average strain gradients in thin films, *Proc. IEEE Micro Electro Mech. Syst. Workshop*, Napa Valley 1990 (IEEE, New York, 1990), pp. 177–182
11. M. Biebl, H. von Philipsborn, Fracture strength of doped and undoped polysilicon, *Proc. Int. Conf. Solid-State Sens. Actuators*, Stockholm, 1995, ed. by S. Middelhoek, K. Cammann (Royal Swedish Academy of Engineering Sciences, Stockholm, 1995) pp. 72–75
12. L.S. Fan, R.T. Howe, R.S. Muller, Fracture toughness characterization of brittle films, *Sens. Actuators A* **21-23**, 872–874 (1990)
13. H. Kahn, N. Tayebi, R. Ballarini, R.L. Mullen, A.H. Heuer, Wafer-level strength and fracture toughness testing of surface-micromachined MEMS devices, *Mater. Res. Soc. Symp. Proc.* **605**, 25–30 (2000)
14. H. Kahn, R. Ballarini, J.J. Bellante, A.H. Heuer, Fatigue failure in polysilicon is not due to simple stress corrosion cracking, *Science* **298**, 1215–1218 (2002)
15. N. André, M. Coulombier, V. De Longueville, D. Fabrègue, T. Gets, S. Gravier, T. Pardoën, J.-P. Raskin, Microfabrication-based nanomechanical laboratory for testing the ductility of submicron aluminum films, *Microelectron. Eng.* **84**, 2714–2718 (2007)
16. W.N. Sharpe Jr., B. Yuan, R.L. Edwards, A new technique for measuring the mechanical properties of thin films, *J. Microelectromech. Syst.* **6**, 193–199 (1997)
17. H.S. Cho, W.G. Babcock, H. Last, K.J. Hemker, Annealing effects on the microstructure and mechanical properties of LIGA nickel for MEMS, *Mater. Res. Soc. Symp. Proc.* **657** (2001) EE5.23.1–EE5.23.6
18. W. Suwito, M.L. Dunn, S.J. Cunningham, D.T. Read, Elastic moduli, strength, and fracture initiation at sharp notches in etched single crystal silicon microstructures, *J. Appl. Phys.* **85**, 3519–3534 (1999)
19. C.-S. Oh, W.N. Sharpe, Techniques for measuring thermal expansion and creep of polysilicon, *Sens. Actuators A* **112**, 66–73 (2004)
20. T.P. Weihs, S. Hong, J.C. Bravman, W.D. Nix, Mechanical deflection of cantilever microbeams, A new technique for testing the mechanical properties of thin films, *J. Mater. Res.* **3**, 931–942 (1988)
21. B.D. Jensen, M.P. de Boer, N.D. Masters, F. Bitsie, D.A. La Van, Interferometry of actuated microcantilevers to determine material properties and test structure nonidealities in MEMS, *J. Microelectromech. Syst.* **10**, 336–346 (2001)
22. H.D. Espinosa, B. Peng, A new methodology to investigate fracture toughness of freestanding MEMS and advanced materials in thin film form, *J. Microelectromech. Syst.* **14**, 153–159 (2005)

23. X. Li, G. Ding, T. Ando, M. Shikida, K. Sato, Micromechanical characterization of electro-plated permalloy films for MEMS, *Microsyst. Technol.* **14**, 131–134 (2007)
24. M.G. Allen, M. Mehregany, R.T. Howe, S.D. Senturia, Microfabricated structures for the in situ measurement of residual stress, Young's modulus, and ultimate strain of thin films, *Appl. Phys. Lett.* **51**, 241–243 (1987)
25. L. Kiesewetter, J.-M. Zhang, D. Houdeau, A. Steckenborn, Determination of Young's moduli of micromechanical thin films using the resonance method, *Sens. Actuators A* **35**, 153–159 (1992)
26. W.C. Tang, T.-C.H. Nguyen, R.T. Howe, Laterally driven polysilicon resonant microstructures, *Sens. Actuators A* **20**, 25–32 (1989)
27. H. Kahn, S. Stemmer, K. Nandakumar, A.H. Heuer, R.L. Mullen, R. Ballarini, M.A. Huff, Mechanical properties of thick, surface micromachined polysilicon films, *Proc. IEEE Micro Electro Mech. Syst. Workshop*, San Diego, 1996, ed. by M.G. Allen, M.L. Redd (IEEE, New York, 1996) pp. 343–348
28. P.T. Jones, G.C. Johnson, R.T. Howe, Fracture strength of polycrystalline silicon, *Mater. Res. Soc. Symp. Proc.* **518**, 197–202 (1998)
29. P. Minotti, R. Le Moal, E. Joseph, G. Bourbon, Toward standard method for microelectromechanical systems material measurement through on-chip electrostatic probing of micrometer size polysilicon tensile specimens, *Jpn. J. Appl. Phys.* **40**, L120–L122 (2001)
30. A. Corigliano, B. De Masi, A. Frangi, C. Comi, A. Villa, M. Marchi, Mechanical characterization of polysilicon through on-chip tensile tests, *J. Microelectromech. Syst.* **13**, 200–219 (2004)
31. C.L. Muhlstein, E.A. Stach, R.O. Ritchie, A reaction-layer mechanism for the delayed failure of micron-scale polycrystalline silicon structural films subjected to high-cycle fatigue loading, *Acta Mater.* **50**, 3579–3595 (2002)
32. M.G. Lim, J.C. Chang, D.P. Schultz, R.T. Howe, R.M. White, Polysilicon microstructures to characterize static friction, *Proc. IEEE Micro Electro Mech. Syst. Workshop*, Napa Valley 1990 (IEEE, New York, 1990) pp. 82–88
33. B.T. Crozier, M.P. de Boer, J.M. Redmond, D.F. Bahr, T.A. Michalske, Friction measurement in MEMS using a new test structure, *Mater. Res. Soc. Symp. Proc.* **605**, 129–134 (2000)
34. D.H. Alsem, E.A. Stach, M.T. Dugger, M. Enachescu, R.O. Ritchie, An electron microscopy study of wear in polysilicon microelectromechanical systems in ambient air, *Thin Solid Films* **515**, 3259–3266 (2007)
35. G. Gregori, D.R. Clarke, The interrelation between adhesion, contact creep, and roughness on the life of gold contacts in radio-frequency microswitches, *J. Appl. Phys.* **100**, 094904 (2006)
36. S.T. Patton, J.S. Zabinski, Fundamental studies of Au contacts in MEMS RF switches, *Tribol. Lett.* **18**, 215–230 (2005)
37. J. Yang, H. Kahn, A.Q. He, S.M. Phillips, A.H. Heuer, A new technique for producing large-area as-deposited zero-stress LPCVD polysilicon films: The MultiPoly process, *J. Microelectromech. Syst.* **9**, 485–494 (2000)
38. E. Chason, B.W. Sheldon, L.B. Freund, J.A. Floro, S.J. Heame, Origin of compressive residual stress in polycrystalline thin films, *Phys. Rev. Lett.* **88** (2002) 156103-1–156103-4
39. S. Jayaraman, R.L. Edwards, K.J. Hemker, Relating mechanical testing and microstructural features of polysilicon thin films, *J. Mater. Res.* **14**, 688–697 (1999)
40. R. Ballarini, H. Kahn, N. Tayebi, A.H. Heuer, Effects of microstructure on the strength and fracture toughness of polysilicon: A wafer level testing approach, *ASTM STP* **1413**, 37–51 (2001)
41. J. Bagdahn, J. Schischka, M. Petzold, W.N. Sharpe Jr., Fracture toughness and fatigue investigations of polycrystalline silicon, *Proc. SPIE* **4558**, 159–168 (2001)
42. I.S. Raju, J.C. Newman Jr., Stress intensity factors for a wide range of semi-elliptical surface cracks in finite-thickness plates, *Eng. Fract. Mech.* **11**, 817–829 (1979)

43. J. Bagdahn, W.N. Sharpe Jr., O. Jadaan, Fracture strength of polysilicon at stress concentrations, *J. Microelectromech. Syst.*, 302–312 (2003)
44. R. Boroch, J. Wiaranowski, R. Mueller-Fiedler, M. Ebert, J. Bagdahn, Characterization of strength properties of thin polycrystalline silicon films for MEMS applications, *Fatigue Fract. Eng. Mater. Struct.* **30**, 2–12 (2007)
45. B.L. Boyce, J.M. Grazier, T.E. Buchheit, M.J. Shaw, Strength distributions in polycrystalline silicon MEMS, *J. Microelectromech. Syst.* **16**, 179–190 (2007)
46. D.C. Miller, B.L. Boyce, M.T. Dugger, T.E. Buchheit, K. Gall, Characteristics of a commercially available silicon-on-insulator MEMS material, *Sens. Actuators A* **138**, 130–144 (2007)
47. T. Yi, L. Li, C.-J. Kim, Microscale material testing of single crystalline silicon: Process effects on surface morphology and tensile strength, *Sens. Actuators A* **83**, 172–178 (2000)
48. T. Alan, M.A. Hines, A.T. Zehnder, Effect of surface morphology on the fracture strength of silicon nanobeams, *Appl. Phys. Lett.* **89**, 091901 (2006)
49. X. Li, T. Kasai, S. Nakao, T. Ando, M. Shikida, K. Sato, H. Tanaka, Anisotropy in fracture of single crystal silicon film characterized under uniaxial tensile condition, *Sens. Actuators A* **117**, 143–150 (2005)
50. S. Koyama, K. Takashima, Y. Higo, Fracture toughness measurement of a micro-sized single crystal silicon, *Key Eng. Mater.* **297–300**, 292–298 (2005)
51. H. Kahn, R. Ballarini, R.L. Mullen, A.H. Heuer, Electrostatically actuated failure of micro-fabricated polysilicon fracture mechanics specimens, *Proc. R. Soc. A* **455**, 3807–3923 (1999)
52. W.W. Van Arsdell, S.B. Brown, Subcritical crack growth in silicon MEMS, *J. Microelectromech. Syst.* **8**, 319–327 (1999)
53. Y. Yamaji, K. Sugano, O. Tabata, T. Tsuchiya, Tensile-mode fatigue tests and fatigue life predictions of single crystal silicon in humidity controlled environments, *Proc. MEMS 2007*, Kobe (2007) pp. 267–270
54. D.H. Alsem, R. Timmerman, B.L. Boyce, E.A. Stach, J.T.M. De Hosson, R.O. Ritchie, Very high-cycle fatigue failure in micron-scale polycrystalline silicon films: effects of environment and surface oxide thickness, *J. Appl. Phys.* **101**, 013515 (2007)
55. H. Kahn, A. Avishai, R. Ballarini, A.H. Heuer, Surface oxide effects on failure of polysilicon MEMS after cyclic and monotonic loading, *Scr. Mater.* (2008), in press
56. H. Kahn, L. Chen, R. Ballarini, A.H. Heuer, Mechanical fatigue of polysilicon: Effects of mean stress and stress amplitude, *Acta Mater.* **54**, 667–678 (2006)
57. R.E. Boroch, R. Müller-Fiedler, J. Bagdahn, P. Gumbsch, High cycle fatigue and strengthening in polycrystalline silicon, *Scr. Mater.* (2008) in press
58. S. Nakao, T. Ando, M. Shikida, K. Sato, Effects of environmental condition on the strength of submicron-thick single crystal silicon film, *Proc. 14th Int. Conf. Solid-State Sens., Actuators Microsyst., Transducers Eurosens. '07*, Lyon (2007) pp. 375–378
59. A. Corwin, M.P. de Boer, Effect of adhesion on dynamic and static friction in surface micromachining, *Appl. Phys. Lett.* **84**, 2451–2453 (2004)
60. T. Tsuchiya, A. Inoue, J. Sakata, Tensile testing of insulating thin films; humidity effect on tensile strength of SiO<sub>2</sub> films, *Sens. Actuators A* **82**, 286–290 (2000)
61. H. Ogawa, K. Suzuki, S. Kaneko, Y. Nakano, Y. Ishikawa, T. Kitahara, Measurements of mechanical properties of microfabricated thin films, *Proc. IEEE Micro Electro Mech. Syst. Workshop (IEEE, New York, 1997)* pp. 430–435
62. Y. Yang, B.I. Imasogie, S.M. Allameh, B. Boyce, K. Lian, J. Lou, W.O. Soboyejo, Mechanisms of fatigue in LIGA Ni MEMS thin films, *Mater. Sci. Eng. A* **444**, 39–50 (2007)
63. R. Modlinski, R. Puers, I. De Wolf, AlCuMgMn micro-tensile samples mechanical characterization of MEMS materials at micro-scale, *Sens. Actuators A* **143**, 120–128 (2008)
64. R.L. Edwards, G. Coles, W.N. Sharpe, Comparison of tensile and bulge tests for thin-film silicon nitride, *Exp. Mech.* **44**, 49–54 (2004)
65. S. Cho, I. Chasiotis, T.A. Friedmann, J.P. Sullivan, Young's modulus, Poisson's ratio and failure properties of tetrahedral amorphous diamond-like carbon for MEMS devices, *J. Micromech. Microeng.* **15**, 728–735 (2005)

66. D. Son, J.-H. Jeong, D. Kwon, Film-thickness considerations in microcantilever-beam test in measuring mechanical properties of metal thin film, *Thin Solid Films* **437**, 182–187 (2003)
67. W.-H. Chuang, T. Luger, R.K. Fettig, R. Ghodssi, Mechanical property characterization of LPCVD silicon nitride thin films at cryogenic temperatures, *J. Microelectromech. Syst.* **13**, 870–879 (2004)
68. H.D. Espinosa, B. Peng, A new methodology to investigate fracture toughness of freestanding MEMS and advanced materials in thin film form, *J. Microelectromech. Syst.* **14**, 153–159 (2005)
69. C.-W. Baek, Y.-K. Kim, Y. Ahn, Y.-H. Kim, Measurement of the mechanical properties of electroplated gold thin films using micromachined beam structures, *Sens. Actuators A* **117**, 17–27 (2005)
70. R. Yokokawa, J.-A. Paik, B. Dunn, N. Kitazawa, H. Kotera, C.-J. Kim, Mechanical properties of aerogel-like thin films used for MEMS, *J. Micromech. Microeng.* **14**, 681–686 (2004)
71. A. Kaushik, H. Kahn, A.H. Heuer, Wafer-level mechanical characterization of silicon nitride MEMS, *J. Microelectromech. Syst.* **14**, 359–367 (2005)
72. S. Roy, C.A. Zorman, M. Mehregany, The mechanical properties of polycrystalline silicon carbide films determined using bulk micromachined diaphragms, *Mater. Res. Soc. Symp. Proc.* **657**, EE9.5.1–EE9.5.6 (2001)
73. A. Reddy, H. Kahn, A.H. Heuer, A MEMS-based evaluation of the mechanical properties of metallic thin films, *J. Microelectromech. Syst.* **16**, 650–658 (2007)
74. B. Schoeberle, M. Wendlandt, C. Hierold, Long-term creep behavior of SU-8 membranes: Application of the time-stress superposition principle to determine the master creep compliance curve, *Sens. Actuators A* **142**, 242–249 (2008)
75. J.J. Bellante, H. Kahn, R. Ballarini, C.A. Zorman, M. Mehregany, A.H. Heuer, Fracture toughness of polycrystalline silicon carbide thin films, *Appl. Phys. Lett.* **86**, 071920-1–071920-3 (2005)
76. Z.M. Zhou, Y. Zhou, C.S. Yang, J.A. Chen, W. Ding, G.F. Ding, The evaluation of Young's modulus and residual stress of copper films by microbridge testing, *Sens. Actuators A* **127**, 392–397 (2006)
77. J.-H. Kim, H.-J. Lee, S.-W. Han, J.-Y. Kim, J.-S. Kim, J.-Y. Kang, S.-H. Choa, C.-S. Lee, Mechanical behavior of freestanding Mo thin films for RF-MEMS devices, *Int. J. Modern Phys. B* **20**, 3757–3762 (2006)
78. W. Chang, C. Zorman, Determination of Young's moduli of 3C (110) single-crystal and (111) polycrystalline silicon carbide from operating frequencies, *J. Mater. Sci.* **43**, 4512–4517 (2008)
79. A.J. Fleischman, X. Wei, C.A. Zorman, M. Mehregany, Surface micromachining of polycrystalline SiC deposited on SiO<sub>2</sub> by APCVD, *Mater. Sci. Forum* **264–268**, 885–888 (1998)
80. M. Pozzi, M. Hassan, A.J. Harris, J.S. Burdess, L. Jiang, K.K. Lee, R. Cheung, G.J. Phelps, N.G. Wright, C.A. Zorman, M. Mehregany, Mechanical properties of a 3C-SiC film between room temperature and 600 °C, *J. Phys. D: Appl. Phys.* **40**, 3335–3342 (2007)
81. A.E. Franke, E. Bilic, D.T. Chang, P.T. Jones, T.-J. King, R.T. Howe, G.C. Johnson, Post-CMOS integration of germanium microstructures, *Proc. Int. Conf. Solid-State Sens. Actuators (IEE Japan, Tokyo, 1999)* pp. 630–637
82. D. Gao, C. Carraro, V. Radmilovic, R.T. Howe, R. Maboudian, Fracture of polycrystalline 3C-SiC films in microelectromechanical systems, *J. Microelectromech. Syst.* **13**, 972–976 (2004)
83. M.A. Haque, M.T.A. Saif, A review of MEMS-based microscale and nanoscale tensile and bending testing, *Exp. Mech.* **43**, 248–255 (2003)
84. J. Song, D.J. Srolovitz, Adhesion effects in material transfer in mechanical contacts, *Acta Mater.* **54**, 5305–5312 (2006)
85. O. Rezvanian, M.A. Zikry, C. Brown, J. Krim, Surface roughness, asperity contact and gold RF MEMS switch behavior, *J. Micromech. Microeng.* **17**, 2006–2015 (2007)

## Editor's Vita

Dr. Bharat Bhushan received an M.S. in mechanical engineering from the Massachusetts Institute of Technology in 1971, an M.S. in mechanics and a Ph.D. in mechanical engineering from the University of Colorado at Boulder in 1973 and 1976, respectively, an MBA from Rensselaer Polytechnic Institute at Troy, NY in 1980, Doctor Technicae from the University of Trondheim at Trondheim, Norway in 1990, a Doctor of Technical Sciences from the Warsaw University of Technology at Warsaw, Poland in 1996, and Doctor Honouris Causa from the National Academy of Sciences at Gomel, Belarus in 2000. He is a registered professional engineer. He is presently an Ohio Eminent Scholar and The Howard D. Winbigger Professor in the College of Engineering, and the Director of the Nanoprobe Laboratory for Bio- & Nanotechnology and Biomimetics (NLB<sup>2</sup>) at the Ohio State University, Columbus, OH. His research interests include fundamental studies with a focus on scanning probe techniques in the interdisciplinary areas of bio/nanotribology, bio/nanomechanics and bio/nanomaterials characterization, and applications to bio/nanotechnology and biomimetics. He is an internationally recognized expert of bio/nanotribology and bio/nanomechanics using scanning probe microscopy, and is one of the most prolific authors. He is considered by some a pioneer of the tribology and mechanics of magnetic storage devices. He has authored seven scientific books, more than 90 handbook chapters, more than 700 scientific papers (h-index – 45+; ISI Highly Cited in Materials Science, since 2007), and more than 60 technical reports, edited more than 45 books, and holds 17 US and foreign patents. He is co-editor of Springer NanoScience and Technology Series and co-editor of Microsystem Technologies. He has given more than 400 invited presentations on six continents and more than 140 keynote/plenary addresses at major international conferences.



Dr. Bhushan is an accomplished organizer. He organized the first symposium on Tribology and Mechanics of Magnetic Storage Systems in 1984 and the first international symposium on Advances in Information Storage Systems in 1990, both of which are now held annually. He is the founder of an ASME Information Storage and Processing Systems Division founded in 1993 and served as the founding chair during 1993–1998. His biography has been listed in over two dozen Who's Who books including Who's Who in the World and has received more than two dozen awards for his contributions to science and technology from professional societies, industry, and US government agencies. He is also the recipient of various international fellowships including the Alexander von Humboldt Research Prize for Senior Scientists, Max Planck Foundation Research Award for Outstanding Foreign Scientists, and the Fulbright Senior Scholar Award. He is a foreign member of the International Academy of Engineering (Russia), Byelorussian Academy of Engineering and Technology and the Academy of Triboengineering of

Ukraine, an honorary member of the Society of Tribologists of Belarus, a fellow of ASME, IEEE, STLE, and the New York Academy of Sciences, and a member of ASEE, Sigma Xi and Tau Beta Pi.

Dr. Bhushan has previously worked for the R&D Division of Mechanical Technology Inc., Latham, NY; the Technology Services Division of SKF Industries Inc., King of Prussia, PA; the General Products Division Laboratory of IBM Corporation, Tucson, AZ; and the Almaden Research Center of IBM Corporation, San Jose, CA. He has held visiting professor appointments at University of California at Berkeley, University of Cambridge, UK, Technical University Vienna, Austria, University of Paris, Orsay, ETH Zurich and EPFL Lausanne.



# Index

**Note:** Page references in Roman denote Vol. I and *Italic* page references denote Vol. II.

- $\sqrt{3}$ -Ag, 212–216
- 1,1'-biphenyl-4-thiol (BPT), 90, 91, 93, 423, 424, 426–435, 448
- 1-butyl-3-methylimidazolium hexafluorophosphate (BMIM-PF6) property, 504–527
- 3,3'-dithio-bis(sulfosuccinimidylpropionate) (DTSSP), 358, 378
- 2-pyridyldithiopropionyl (PDP) group, 359
- $\alpha$ -Al<sub>2</sub>O<sub>3</sub>(0001), 221–223
- $\gamma$ -modified geometry, 413–414
- A**
- abrasive wear, 275–277, 282–283
- abrikosov lattice, 290
- accelerated friction, 369, 389–392
- acceleration energy, 356
- accelerometer, 836, 844, 929–930
- acetylene (C<sub>2</sub>H<sub>2</sub>), 354, 357
- acoustic emission, 396, 423
- activation barrier, 368, 372–374
- actuation force, 913
- adatoms, 207–211, 222
- adhesion, 3, 4, 6, 10, 20, 23–63, 72, 84, 85, 86, 87, 89, 90, 98–100, 101, 109–113, 118–120, 131–133, 137–145, 148–164, 170, 177, 185, 349, 350, 353, 355–358, 366, 378–381, 383, 385, 392, 403, 405, 407, 408, 416, 420, 422, 424–429, 440–446, 453–455, 533–689, 833, 840, 843, 854, 855, 857–860, 866, 869, 871, 891–892, 897–910, 913–919, 924, 926, 929
  - of biomolecular film, 887–891
  - of biomolecule, 853, 859–860, 881–891, 928
  - coefficient, 707, 728–734, 737, 738, 745–747, 749, 760
  - complex, 378
  - controlled friction, 149, 151
  - design database, 744–746, 748, 761
  - energy, 726–728, 730–735, 760
  - enhancement, 702, 707–709, 731, 732, 737, 760
  - Hamaker constant, 713–715, 724, 735
  - hysteresis, 143–145, 152–153, 157, 158, 160, 161, 163, 174, 175, 186
  - hysteresis, relation to friction, 152–153, 157–161, 173
  - measurement, 4, 11–12, 881, 883, 885, 891, 892, 911–914
  - mechanics, 139–140
  - mechanics of layered system, 140
  - in microstructure, 911–914, 929
  - modeling, 721–737
  - on the nanometer level, 756
  - of polymer, 145, 155
  - primary minimum, 127, 129, 130
  - probability, 373–374
  - rate-dependent, 143–145
  - secondary minimum, 126, 127
  - test, 717–722, 749
  - tip-surface, 449
- adhesion force, 109–113, 119–120, 138–140, 142, 143, 150–156, 186, 469, 525, 526, 726, 734, 739, 740, 742, 743, 749, 754, 760
  - calculation, 727–728, 744, 745
  - gecko, 702, 709, 711, 715, 717, 719, 728, 731–733, 736, 750, 759
  - gecko foot-hair, 717, 718, 756
  - gecko spatula, 718, 720, 721, 736, 737
  - multiple contact, 707–708, 721–722
  - quantized, 129, 170
  - single contact, 707, 708, 715, 724, 727, 735, 745

- adhesion-force image, 380
- adhesive
- coating, 362
  - contact, 120, 130, 141, 144, 148, 150, 157, 161, 175
  - interaction surface, 461
- adhesive force, 12, 44, 50–57, 67–69, 72, 84–91, 93, 95, 96, 271, 404, 405, 422, 425–429, 438–445, 453, 454, 472, 487, 495, 840, 855, 871–874, 876–879, 885, 887, 888, 891, 892, 907, 909, 910, 914–918, 924–926, 928
- distribution, 473
  - finite element analysis, 710
  - influence of temperature, 482, 520
  - measurement, 10, 11, 23, 50, 52, 57, 84, 85
  - single spatula, 715, 718, 719, 760
- adsorbate, 405–406, 424
- adsorbed water, 872–874, 879, 915, 917–918, 925, 926
- AES measurement. *See* Auger electron spectroscopy measurement
- AFAM. *See* Atomic force acoustic microscopy
- AFM. *See* Atomic force microscopy
- Ag, 212–216
- trimer, 212–215
- air
- damping, 345, 346
  - induced oscillation, 73
  - pocket, 898, 900, 902, 905, 906, 908
- air-layer thickness
- Al<sub>2</sub>O<sub>3</sub>-TiC, 28, 29
- alkali halides, 216–223
- alkanethiols, 227
- alkylphosphonate SAM, 423, 424, 436–448, 454
- alkylsiloxane film, 419, 420
- all-fiber interferometer, 246
- Al<sub>2</sub>O<sub>3</sub>, 246
- Al<sub>2</sub>O<sub>3</sub>-TiC
- head, 394–395
- AM. *See* amplitude modulation
- aminopropylmethylethoxysilane (APDMES), 887–891
- aminopropyltriethoxysilane (APTES), 882–884, 887–891
- ammonium, 503, 504
- Amontons' law, 148–149, 154, 155, 157, 159, 163, 164, 270, 314
- amorphous carbon (a-C), 347–398, 864, 865, 881
- chemical structure, 358, 359
  - coating, 361, 364, 369, 392–394
  - coatings, 347, 350–352, 358–360, 363, 368, 370, 397
- amorphous surface, 109
- amplitude-mode AFM, 339
- amplitude modulation (AM), 199, 203, 319–328, 340
- mode, 47
  - scanning force microscope (SFM), 274, 275
- anatase TiO<sub>2</sub>(001), 221
- angled microfiber array, 750–751
- angle of twist formula, 86
- anisotropy, 400, 420
- of friction, 260–263
- annealing effect, 972
- anti-adhesion performance, 914
- antibody, 855, 881
- antibody-antigen complex, 373
- APCVD. *See* atmospheric pressure chemical vapordeposition
- APDMES. *See* aminopropylmethylethoxysilane
- approach-retract cycle, 379, 380
- APTES. *See* aminopropyltriethoxysilane
- aquatic animals, 534, 536, 544, 668, 687, 688
- arc discharge, 353–354
- artifacts, 242
- as-deposited film, 948, 968
- atmospheric pressure chemical
- vapordeposition (APCVD), 529, 540
- atomic force acoustic microscopy (AFAM), 17, 18, 38
- atomic force microscopy (AFM), 4–23, 26, 32, 37–39, 39, 41, 42–44, 50, 52, 57, 62, 71, 81, 96, 98–100, 110, 113–116, 120, 140, 155, 171, 172, 176, 177, 195–232, 204, 207–209, 216–218, 225, 236, 240, 242, 275, 285, 290, 292, 296, 307, 326–328, 330, 331, 357–370, 373–376, 378–382, 392–394, 401, 405, 412, 418, 420, 421, 422, 423–427, 429–435, 438–448, 451, 455, 461, 463–465, 466, 468, 469, 471, 476, 477, 479, 481, 481, 482, 489, 490, 494, 494–496, 498, 502–503, 505, 506, 509, 525, 529, 532–538, 545–552, 576, 577, 833, 838, 861, 862, 865–868, 870, 871, 877, 883, 885, 886, 889–892, 910–912, 916, 919, 920, 934
- adhesion, 422, 424–429, 440–446, 455

- bath cryostat, 245–247
  - Binnig design, 41, 50
  - calculated sensitivity, 86–87
  - cantilever, 48, 59, 61, 74, 78, 717, 750
  - cantilevers, 135–190
  - carbon nanotube tip, 463, 506
  - commercial, 50–59, 62
  - contact mode, 46–48, 51, 53, 58, 59, 848, 849, 888–890, 911
  - control electronics, 49–50, 101, 102
  - design optimization, 73
  - dual-axis, 717
  - dynamic mode, 275, 285
  - feedback loop, 100
  - friction, 420, 424–425, 430–432, 439–446
  - instrumentation, 73–104
  - interferometer, 246
  - manufacturer, 50–51
  - mode, 113–114
  - operational mode, 317–337
  - piezo creep, 242
  - probe construction, 59–65
  - static mode, 74
  - surface height image, 912, 913, 923–926, 928
  - surface height map, 380, 382, 384, 385
  - surface imaging, 3, 6, 8, 21–23, 49, 50, 65–67, 72, 76, 94
  - test, 347, 381, 385, 386
  - thermal drift, 240
  - thermal noise, 242
  - tip, 195–226, 228–232, 357–360, 365, 369, 378–380, 382, 420, 425–427, 429, 430, 435, 440, 445, 446, 464–466, 468–474, 718, 749, 750, 861, 865, 866, 871, 883, 885, 886, 891, 892, 911, 912, 916, 919–920, 924, 925, 928, 929
  - tip sliding, 3, 5, 6, 15, 26, 27, 31, 38, 43, 44, 47–49, 54–56, 63, 69, 78, 85, 98
  - for UHV application, 250
  - variable temperature, 243–245
  - vibration isolation, 243
  - wear, 422, 425–426, 432, 434, 446–448
  - atomic resolution, 37, 39, 42, 44, 45, 48, 51, 56, 59, 242, 263, 270, 276, 278, 279, 281, 283, 284, 291, 292
  - image, 207, 210, 216, 225
  - imaging, 207, 215, 218
  - atomic-scale
    - dissipation, 285
    - force measurement, 72
    - friction, 4–6, 23–27, 98, 439–440, 471, 476, 479, 483, 486, 512
    - image, 39, 40, 43, 48, 64, 248, 276–281
    - stick-slip, 480, 481, 483
  - attachment
    - element, 703–704
    - mechanism, 713–717
  - attachment system
    - micro pattern, 753
    - single-level, 738, 739, 744, 748
  - attraction
    - long-range, 118, 134, 135
  - Au(111), 255
  - auger electron spectroscopy (AES)
    - measurement, 396
  - average contact resistance, 495, 513, 517
  - avidin, 358, 361, 368, 372–374, 380, 381
- B**
- background noise, 225
  - BaF<sub>2</sub>, 218
  - ball-on-flat
    - technique, 509, 518
    - test, 509, 510, 514, 518
    - tribometer, 505, 509, 512, 517
    - tribometer testing, 512
  - bare surface, 471, 473–483
  - Barnstead Nanopure, 215
  - barrier length scale, 367
  - BDCS. *See* biphenyldimethylchlorosilane
  - beam
    - bending, 538, 559–565, 576
    - deflection AFM, 312, 317
    - deflection FFM, 246
    - deflection system, 114
  - beam-substrate interfacial energy, 913
  - Bell model, 370–371, 375
    - single energy barrier, 375
  - Bell parameter, 377
  - bending
    - quasistatic test, 532, 536, 538, 547, 549, 552
    - stiffness, 76–77
    - strength, 529, 533–535, 538, 546–550, 552, 576
  - Berkovich
    - pyramid, 406, 408, 409, 411, 413, 414, 421
    - tip, 379–380, 385
  - BFP. *See* biomembrane force probe
  - BHPET chemical structure, 506, 515–517, 519–525, 527

- BHPT chemical structure, 506, 515–517, 519–525, 527  
 bias voltage, 40–43  
 bimorph, 215, 235  
 binary compound, 216  
 bioadhesion, 853, 859–860, 891  
 biocapsule, 855–857  
 biochemical sensor, 408  
 biodevice, 891  
 biofluidic chip, 851, 852  
 biofouling, 404, 408, 856, 859  
 biological membrane, 368–379  
 biological micro-/nanoelectro-mechanical systems (bioMEMS/bioNEMS), 528, 576, 833–935  
 biological or biomedical  
   microelectromechanical system (bioMEMS), 403, 528, 530, 553, 554  
   biosensor application, 839, 881  
 biological system guideline, 737  
 biomaterials, 432  
 biomedical device, 530  
 biomembrane force probe (BFP), 363, 365, 367, 372  
 bioMEMS. *See* biological or biomedical microelectromechanical system  
 biomimetics, 533–689, 833–935  
   fibrillar structure modeling, 737–749  
   gecko skin fabrication, 749–759  
   gecko skin fabrication method, 749, 755, 757, 758  
 biomolecule, 113, 118, 358, 360–361, 366, 382  
 bioNEMS, 403, 528, 576  
   characteristic dimension, 834, 835  
 biosensor, 839, 850–854, 858, 881, 882  
 biotin surface roughness, 883, 887, 888  
 biotinylated AFM tip, 380  
 biotinylated BSA, 358  
 biphenyl, 248, 249  
 biphenyldimethylchlorosilane (BDSCS), 92, 94, 431, 432  
 birefringent crystal, 83  
 $\text{Bi}_2\text{Sr}_2\text{CaCu}_2\text{O}_{8+\delta}$  (BSCCO), 270, 271  
 bistable mode, 325  
 blister test, 392, 398  
 Bloch  
   state, 263  
   wave, 263–266  
 block-like debris, 391  
 blood-pressure sensor chip, 836–837, 839  
 BMIM-PF6, chemical structure, 504–527  
 body mass, phylogenetic approach, 704  
 Boltzmann distribution factor, 232  
 bond  
   lifetime, 357, 366, 368, 370, 372, 374–375  
   strength, 115, 117  
 bonding energy, 19  
 bond-order potential, 442, 443, 461, 463, 471, 481, 482  
 boron-ion implantation, 46  
 bottom-up  
   fabrication, 838, 934–935  
   method, 834, 929  
 boundary  
   film, 461–462  
   low-viscosity layer, 212  
   lubrication, 5, 23, 83–99, 146, 147, 168–183  
   slip, 134, 166  
 bovine serum albumin (BSA), 357–358, 882, 883  
 BPT. *See* biphenyl–4-thiol  
 BPTC. *See* cross-linked BPT  
 bridging of polymer chain, 135  
 broken coating chip, 380  
 BSA. *See* bovine serum albumin  
 bubble, 132, 133  
 buckling, 371, 372, 376–380, 383, 387, 391, 392, 737–738, 740, 741, 951  
   critical compressive strain, 741  
   stress, 378, 379  
 bulge test, 398–399  
 bulk  
   conduction band, 255, 257  
   diamond, 350, 359–360, 362, 364  
   fluid, 211, 230, 232, 236  
   graphitic carbon, 393  
   micromachining, 860–861, 929–930  
   phonon mode, 445  
   single crystal, 541, 542, 576  
   state, 254, 257, 265  
   xenon, 280  
 bulk atom, 197, 229  
 buoyancy, 893–895  
   force, 894, 895  
**C**  
 $\text{C}_{60}$ , 226, 227, 271, 348, 349  
   film, 44, 504  
   island, 261–262  
   ultralow friction, 506  
 $\text{C}_{70}$ , 348  
 CA. *See* contact angle  
 $\text{CaF}_2$ , 218, 220  
   (111), 218, 220  
   (111) surface, 280  
   tip, 280

- CaF bilayer on Si(111), 218
- CAH. *See* contact angle hysteresis
- calibration, 409–413, 416, 420
- CA mode. *See* constant amplitude mode
- cantilever, 113–116, 120, 122–127, 197–207, 216, 218, 837, 844–845, 847–849, 852, 855, 911, 913–915, 919, 920, 928
  - array, 838
  - axis, 247
  - bending, 313–315
  - deflection, 6, 8, 20, 47–49, 51, 54, 56, 58, 65, 67, 71–73, 77, 78, 79–93, 98, 197–199, 201–203, 244–246, 274, 275
  - deflection calculation, 65–67
  - effective mass, 245, 310
  - eigenfrequency, 241, 274, 275
  - elasticity, 251
  - flexible, 46, 48, 51, 66
  - force-sensing, 111, 114
  - free oscillating, 347
  - low-stiffness, 129–130
  - material, 60, 71, 198
  - microbeam, 552
  - microfabricated, 113, 114, 116, 308, 313–314
  - motion, 46
  - mount, 54–56
  - Q*-factor, 275, 307, 316, 328, 330, 338–339
  - resonance behavior, 78
  - resonance frequency, 958
  - spring constant, 364, 365–368, 370
  - stainless steel, 379–380, 386
  - stiffness, 57–59, 71, 73–78, 84
  - thermal noise, 275
  - thermomechanical noise, 275
  - thickness, 245, 246
  - trajectory, 322
  - triangular, 60–63, 77, 85
  - untwisted, 53, 69
  - V-shaped, 60, 62, 63, 247
- cantilever-based probe, 274
- cantilever beam
  - array (CBA), 912
  - fabrication procedure, 577–580
  - lateral bending, 564–565
  - torsional vibration, 18–21, 38, 39
- cantilever stiffness, 135, 140–146, 159, 163, 189
- cantilever-tip assembly, 8, 17, 18–21, 37
- capacitance detection, 49, 89–93
- capacitive
  - detection, 98
  - detector, 47
  - displacement sensor, 963–964
- capacitive-type silicon, 836, 844
- capillary
  - engine, 897
  - force, 130, 138–145, 702, 708, 714–717, 720–722, 735, 760
  - pressure gradient, 476
  - wave, 901
  - waves of water, 223
  - wave spectrum, 222
- capped nanotube, 466
  - tip, 466
- carbon, 347–398
  - crystalline, 348
  - magnetron sputtered, 359
  - unhydrogenated coating, 364–365
- carbon-carbon distance, 279
- carbon nanofiber (CNF), 112, 121
- carbon nanotube (CNT), 112, 118, 121–130, 258, 261, 263, 463, 464, 467, 468, 503, 506–508, 835, 838, 839–840, 858
  - bending, 126–130
  - structure, 121–122
  - tip, 64, 65
- carboxylates (RCOO-), 227–231
- carrier gas, 364
- Casimir force, 108
- Cassie–Baxter regime, 900–901, 904–906, 908
- catalysis, 216
- cathodic arc carbon, 368, 369, 371, 372, 374, 385, 394–395
- cation attachment scheme, 522
- CCD. *See* charge-coupled device
- CDW. *See* charge density wave
- cell death, 857, 893
- CE mode. *See* constant excitation mode
- CeO<sub>2</sub>(111), 221
- ceramic
  - nanobeam, 545–552
  - slider, 394
- chain length effect, 420, 421, 437, 441, 446, 450, 454
- charge
  - exchange interaction, 108, 120–121
  - regulation, 126
  - transfer, 120–121
  - transfer interaction, 120–121
- charge-coupled device (CCD), 112, 123
- charge density wave (CDW), 266–267, 270, 271

- charge transfer, 223
- chemical
  - binding force, 333
  - bond, 197, 230, 231
  - bonding, 199, 211, 212, 213, 215
  - bonding force, 47–48
  - characterization, 351, 358–366, 397
  - degradation, 425–426, 448–455, 462, 489–503
  - force, 196, 197, 201, 206, 226, 232
  - heterogeneity, 144
  - interaction, 714
  - interaction force, 310, 311
  - linker method, 882–887, 928
- chemically
  - active ligand, 358
  - bonded PFPE, 870–871, 914–917
- chemical mechanical polishing (CMP), 932
- chemical vapor deposition (CVD), 112, 121–125, 128, 350, 357–358, 370, 755–756
- chemisorption, 461
- Chord theorem, 136
- clay nanoparticle, 554
- cleaning process, 712
- clinging force, 719
  - of a gecko, 719
- cluster, C<sub>60</sub> molecule, 23, 24, 78
- C<sub>60</sub> multilayered film, 227
- CNF. *See* carbon nanofiber
- CNT. *See* carbon nanotube
- C=N vibration, 520
- coagulation, 132, 133
- coated
  - polymer surface adhesion, 891–892
  - Si ball-on-flat test, 509, 514
  - silicon, 861–867, 886, 903–904
  - tip, 468
- coating, 467, 468, 473, 490, 492, 493, 495, 507, 508, 509, 510, 511, 512, 513, 514, 515, 516, 517, 525, 526
  - continuity, 395–396
  - damage, 379, 382
  - durability, 509, 526
  - failure, 375, 387
  - friction and wear behavior, 448
  - friction coefficient, 470–471
  - hardness, 347, 369, 381, 386
  - mass density, 360, 364
  - microstructure, 359, 375
  - substrate interface, 367, 371, 381, 383
  - thickness, 367, 373–375, 378, 380, 383, 387–389, 392, 395
- Co clusters, 261, 262
- coefficient effective, 272
- coefficient of friction (COF), 13, 23, 27, 28, 30, 32, 35–37, 42, 51–54, 56–65, 85–91, 93, 148, 149, 155, 157, 159, 161, 165, 169, 180, 183, 249, 270–272, 282–283, 369, 379–386, 389, 390, 392–394, 420–422, 424, 426, 427, 430–434, 438–446, 448–453, 862, 865, 873, 877, 878, 885, 888
  - average, 10, 24, 32, 46, 47, 91
  - influence of temperature, 482, 520
  - lubricant, 510
  - relationship, 67
- COF. *See* coefficient of friction
- coherence length, 255, 256, 268, 289
- cold welding, 121–122, 163
- collapsed polymers, 208
- colloidal
  - force, 108
  - probe, 115, 116
- colossal-magneto resistive effect, 290
- comb drive, 959–965, 972
- complex bond, 372
- compression, 308
- compressive
  - forces nanotube, 506–507
  - stress, 364–366, 367, 371, 377–379, 951, 952, 963, 968, 969, 971
- computational study, tribological process, 439
- computer simulation, 127, 129, 133, 137, 141, 152, 163, 169, 171–173, 178, 180, 181, 183, 185
  - force, 127, 129, 133, 137, 163
  - friction, 172, 180, 185
- Concanavalin A (Con A), 378
- concentration
  - correlation, 227
  - critical, 278
- confined confinement, 108, 109, 147, 156, 184–186
- confinement of fluids, 203–204, 224
- constant
  - current mode, 40–42
  - force mode, 51, 85, 100–101
  - height mode, 40, 42, 44, 51
  - NVE, 448
- constant amplitude (CA) mode, 202, 218, 308, 336, 343
- constant excitation (CE) mode, 308, 336
- contact
  - adhesive, 120, 130, 141, 144, 148, 150, 157, 161, 175

- analysis, 723–724, 739–740
- apparent macroscopic, 156
- area, 4, 16, 23, 47, 51, 52, 54, 57, 59, 61, 114, 115, 117, 136, 139–142, 148–152, 154–157, 159–164, 180, 184, 187, 251, 257, 270–275, 278, 280, 281, 284, 396, 408–415, 419, 428
- conductance, 275
- elastic, 396, 399, 400, 402–403, 405, 406, 408, 409, 417–420
- electrification, 120
- mechanics, 710, 739
- resistance, 396, 397, 423, 424, 494, 495, 504–514, 517, 526, 527
- resistance image, 512, 513
- stiffness, 367, 375–379
- stiffness, 395, 396, 408–416, 429
- stress, 742
- contact angle (CA), 404–406, 408, 417, 420–455, 462, 471, 505, 515, 516, 520, 521, 708, 715, 716, 722, 736–738, 754, 755, 760, 869, 876, 877, 879, 888, 891, 897–903, 905–910, 915–916, 918–919
- contact angle hysteresis (CAH), 132, 143–144, 897, 898, 901, 905–910
- contacting surface, 704, 718, 724, 726–730, 738, 742, 744, 746
- contact-start-stops (CSS), 772, 775, 776
- contamination, 49, 67
- continuous stiffness measurement (CSM), 374–375, 531, 558
- continuum
  - model, 256
  - theory, 125, 130
- contrast, 253, 266–267, 270, 273, 274, 276–282, 284, 289–292
- formation, 216, 217
- controlled
  - bond formation, 249
  - desorption, 249
  - geometry (CG), 45–46
- control system, 49–50, 54, 73, 94–104
- CO on Cu(110), 248, 249
- Cooper pairs, 268, 270, 271, 289
- copper
  - surface adhesion, 449
  - surface wear, 487
  - tip, 259, 281, 473
- correlation force
  - colloidal, 126
  - computer simulation, 127
  - depletion, 134
  - double-layer, 124, 126, 127
  - double-layer (geometry dependence), 126
  - dry surface, 161
  - electromagnetic, 117, 118
  - electrostatic, 124–127
  - entropic, 108, 137
  - hydration, 108, 117, 128, 130–134, 137, 155, 161, 166
  - hydrodynamic, 108, 165
  - hydrophobic, 130–134
  - ion correlation, 124–127
  - law, 107, 109–111, 113, 119, 126, 128, 129, 131, 132, 143
  - measuring technique, 116–117
  - modulation mode, 17, 18, 22, 81
  - nonequilibrium, 108, 109
  - oscillatory, 108, 128–133, 137, 142, 143, 170, 183
  - osmotic, 108, 135
  - peristaltic, 137
  - protrusion, 108, 137
  - repulsive, 107–109, 116–117, 123, 127, 130, 131, 133, 137, 140–141, 155
  - sensor, 914, 915
  - short-range, 108, 109, 126–128, 130, 133, 155, 161, 169
  - solvation, 127–130
  - steric, 116–117, 123, 137
  - structural, 127–130
  - surface, 127
  - thermal fluctuation, 108, 137
  - undulation, 106, 108
  - van der Waals, 108–110, 112, 117–119, 122–123, 126–134, 137, 150, 151, 153, 156
  - van der Waals (geometry dependence), 112
- correlation, in-plane, 236
- Couette flow, 146, 166, 184
- Coulomb
  - force, 215
  - interaction potential, 443
  - law of friction, 265
- covalent
  - attachment, 358, 361, 362
  - bonding, modeling of material, 442
- C–O vibration, 520
- crack, 367, 371–375, 377–380, 382–383, 387, 391–392
- lateral, 78–79
- median, 78–79
- width, 73–75
- cracking of the coating, 15, 72–75

- crater formation, surface, 452
- Cr coating, 272
- creep, 240, 242, 397, 529, 531, 556, 558–559, 566, 576, 579
  - on a nanoscale, 81, 82, 99
- critical
  - concentration, 278
  - degree of bending, 961
  - load, 58, 62, 64, 66, 95, 99, 369, 370, 375, 379–383, 385–387
  - normal load, 875, 878, 879
  - pitch, 906
  - position, 252
  - radius of impalement, 906
  - shear stress, 147–149, 152, 157
  - temperature, 254–255, 270, 276, 289
  - velocity, 173, 180, 181, 183
- cross-linked BPT (BPTC), 90, 91, 93, 423, 424, 426–431, 433, 435
- cross-linker, 359–362, 364–365, 381
- cross-linking, 92, 94–95
- crosstalk, 50, 102
- cryostat, 242–246
- crystalline
  - carbon, 348
  - growth, 336
  - surface, 108, 109, 133, 149, 163, 172, 178, 179, 185
- crystal structure, 49, 95
- CSM. *See* continuous stiffness measurement
- CSS. *See* contact-start-stops
- Cu(100), 258–259, 277, 281–283
- Cu(111), 248, 251, 256, 258–259, 264, 265, 285
  - surface state, 255, 256, 262
  - tip, 281
- cube corner, 406, 413, 421
- cuprates, 272
- current density effect, 972
- cut-off distance, 119
- CVD. *See* chemical vapor deposition
- cyclic
  - fatigue, 374–375, 963, 964, 971
- D**
- damage, 121, 122, 145, 146, 155, 157, 159, 162, 163, 164, 176
  - mechanism, 381, 387, 391, 392
- damped harmonic oscillator, 314, 316
- damping, 198, 202, 218
  - constant, 338, 345, 347
  - mechanism, 346
  - pneumatic, 246
- DC-PECVD. *See* direct-current plasma-enhanced CVD
- Deborah number, 169
- debris, 380–383, 387, 390, 391, 394
- Debye
  - frequency, 446
  - interaction, 118
  - length, 124, 126, 127, 131
- decylphosphonate (DP), 423, 437, 439–442, 444–448, 876, 879, 880
- defect
  - motion, 242
  - nucleation, 417–419
  - production, 278
- deflection
  - measurement, 198
  - noise, 275
- deformation, 113, 114, 116, 122, 139, 140, 146, 164–166
  - elastic, 140, 165, 246, 251, 270, 271
  - plastic, 109, 122, 140, 146, 164
- degradation, 462, 489–503, 526
- degradation of PFPE film
  - mechanical scission, 499
- Deionized (DI), 882–885
- delamination, 69, 74, 366, 367, 371, 373, 376–380, 383, 387, 391–392, 396–397, 421–422
- delivery particle, 856, 893
- demnum-type PFPE lubricant, 472
- density of fiber, 738, 743
- dental enamel, 431, 432
- dependence
  - indentation, 457
  - MD simulation, 457, 474, 475, 479
- depletion
  - attraction, 135
  - force, 108, 129
  - interaction, 135
  - stabilization, 135
- deposition
  - rate, 354–356, 366
  - technique, 353–354, 365, 366
  - techniques, 350–359, 366–367, 370, 382, 390
- deposition (PECVD), 846, 866, 881
  - etching, 931
- depth-sensing indentation, 76, 81
- Derjaguin approximation, 111, 127, 130
- Derjaguin–Muller–Toporov (DMT)
  - adhesion force, 735, 737
  - model, 271, 275, 393, 405
  - theory, 139, 724, 735, 739



- design rule, 75
- destabilizing factor, 901
- detachment, 709, 711, 759
- detection system, 49, 73, 75, 79–93, 99
- dewetting, 472, 507, 509, 872, 873, 897, 918
- DFM. *See* dynamic force microscopy
- DFS. *See* dynamic force spectroscopy
- DI. *See* Deionized
- diagnostics, 839, 881–896, 928–929
- diamond, 349–351, 358–367, 369, 374, 379, 380, 386, 390, 393, 395, 397, 397, 409–410, 413, 422–424
  - coating, 350, 359, 361, 363–366, 396
  - film, 350, 362–364
  - friction, 478, 479, 482, 486, 498
  - nanindentation, 459, 461, 468, 470
  - tip, 6, 11, 13, 15, 62, 67, 69, 76, 77, 259, 280, 374, 379, 380, 386, 390, 468, 487, 488, 492, 512, 515, 861, 865, 866
- diamond-like carbon (DLC), 44, 45, 47–50, 56–58, 66, 69, 70, 72–74, 81, 327–331, 406, 849, 850, 864, 869, 881, 914–918, 928
  - coating, 347, 350, 351, 353, 356, 358, 360, 362, 363, 365–367, 369, 371, 374–376, 379, 381, 384–394, 396–397, 470, 471
  - coating microstructure, 359
  - matrix, 406
- diblock copolymer, 319
- dicationic ionic liquid film
  - nanotribological study, 504, 515–517
- dielectric breakdown, 397
- dielectric constant, 119, 123
- diffusion, 240, 242, 248–251
  - parameter, 250, 251
  - retardation, 234
  - rotational, 203–204, 229
  - thermally activated, 242
- diffusion coefficient, translational, 226–227
- digital
  - feedback, 42, 49–50, 100
  - micromirror device (DMD), 407, 423, 835–837, 846, 847, 859, 923–929
  - signal processor (DSP), 42, 51
- digital mirror device (DMD) pixel, 846, 923, 924
- dilation, 152, 173
- dimension, 197, 203, 230
- dimensionless particle position, 894, 895
- dimer–adatom–stacking (DAS) fault, 207
- dimer structure, 210–212
- dip coated tip, 891, 892
- dip coating, 463
- direct-current plasma-enhanced CVD (DC-PECVD), 112, 121, 126
- directed self-assembly, 755
- DI silicon nitride, 10, 63
- disjoining pressure, 466, 467, 474, 476
- dislocation
  - line tension, 420
  - motion, 147, 174
  - nanindentation, 453–455
  - nucleation, 396, 407, 418, 424
  - stick-slip, 481
- dispersion
  - force, 231
  - interaction, 118, 119, 122
- displacement sensor, 914, 915
- dissipation, 315, 324, 327, 337, 343–348
  - image, 348
  - measurement, 243, 284, 285
- dissipative interaction, 336, 337, 343
- dissociation constant, 366
- distance, cut-off, 119
- distortion, 50, 96–98, 102–103
- division of contact, 707, 709, 758, 759
- DLC. *See* diamond-like carbon
- DMT. *See* Derjaguin–Muller–Toporov
- DNA, 227, 228
  - AFM image, 342
- D<sub>2</sub>O, 258
- domain pattern, 288–289
- DOS structure, 254
- double-layer
  - force, 108, 127, 130
  - interaction, 124–126
- doubly clamped beam, 951, 953, 954, 957–958, 960, 972
- DP. *See* decylphosphonate
- drag, 533–689
- drift state, 266
- driving frequency, 79
- droplet evaporation, 905, 906
- drug
  - delivery, 528
  - delivery device, 839–840, 856–857, 893
- dry
  - sliding friction, 473, 482, 483
  - superadhesive, 701, 758
- dry surface, 120, 156–163
  - force, 120
  - friction, 120, 156–163
- DTSSP. *See* 3,3'-dithio-bis (sulfosuccinimidylpropionate)

- Dupré equation, 144
- durability, 461, 486, 487, 489, 496, 499, 500, 502–504, 508, 509, 512, 515–517, 526, 527
- dynamic
- AFM, 199–201
  - AFM mode, 313, 315, 317–337, 344, 347
  - interaction, 108
  - light scattering (DLS), 233–234
  - mode, 46–47
  - operation mode, 199–200
- dynamic AFM. *See* dynamic atomic force microscope
- dynamical response, 232–233, 236–237
- dynamic atomic force microscope (dynamic AFM), 308, 311–337, 342–349
- dynamic force microscopy (DFM), 275, 310, 331, 348, 380
- dynamic force spectroscopy (DFS), 367–368, 370, 372, 373, 375
- E**
- EAM. *See* embedded atom method
- EBD. *See* electron beam deposition
- e-beam lithography, 930–931
- EBID. *See* electron-beam-induced deposition
- EBL. *See* electron-beam lithography
- ECR-CVD. *See* electron cyclotron resonance chemical vapor deposition
- edge channel, 286–287
- EELS. *See* electron resonance loss spectroscopy
- effective
- coefficient of friction, 271–272
  - damping constant, 338, 347
  - mass, 241, 255, 257, 275
  - resonant frequency, 323
  - shear stress, 274
  - spring constant, 251, 253, 267, 275
  - viscosity, 165, 166, 168, 170, 184
- effect of
- cycling, 494
  - meniscus, 471, 475
  - viscosity, 475
- EFM. *See* electrostatic force microscopy
- EHD or EHL. *See* Elastohydrodynamic lubrication
- elastic
- contact, 396, 399, 400, 402–403, 405, 406, 408, 409, 417–420
  - deformation, 246, 251, 270, 271
  - force, 724, 726, 727, 740, 743–745
  - limit, 58, 59, 73, 75
  - modulus, 139, 140, 347, 364, 367–371, 374, 378, 379, 383, 396, 397, 398–400, 407–412, 420, 425, 427–429, 529, 530, 533–535, 538–542, 544, 546, 547, 552, 556–562, 564, 576, 579, 709, 723, 724, 739, 742–746, 748
  - tip-surface interaction, 461
- elasticity, 275
- elastohydrodynamic lubrication (EHD or EHL), 146, 147, 165, 168–170
- electrical resistance, 487, 494, 509–515
- electric force gradient, 58
- electrochemical
- AFM, 58–59
  - device, 408
  - STM, 44
- electrokinetic flow, 853
- electromagnetic force, 117
- electromagnetic trap, 363
- electron
- cyclotron resonance chemical vapor deposition (ECR-CVD), 347, 352–357, 368–370, 375, 376, 382, 384, 385, 387–391, 395–396, 398
  - energy loss spectroscopy (EELS), 347, 356, 359–363, 366, 397
  - interaction, 265
  - tunneling, 39, 49
- electron beam deposition (EBD), 112, 120–122
- electron-beam-induced deposition (EBID), 112, 126, 127
- electron-beam lithography (EBL), 129
- electron cyclotron resonance chemical vapor deposition (ECR-CVD), 347, 352–357, 368–370, 376, 382, 384, 385, 398, 881
- coating, 375, 387–388, 390, 391, 395–396
- electronegativity, 409–410
- electron-electron interaction, 255, 267
- electronic noise, 50, 103
- electron-phonon interaction, 266, 268
- electron resonance loss spectroscopy (EELS), 347, 356, 359–363, 366, 397
- electrostatic
- actuation, 844, 913
  - force, 109, 117, 124–128, 130, 166, 197, 276, 282, 286
  - force interaction, 210
  - force microscopy (EFM), 240, 286
  - interaction, 120, 123, 124, 126, 134, 217
  - potential, 265, 286, 287
- electrostatic double layer (EDL), 894

- electrostatic force microscopy (EFM), 240, 286
- embedded atom method (EAM), 443, 448, 450, 453, 455, 457, 474, 481, 489
- embedding energy, 443
- end deflection, 952
- endurance limit, 75, 76
- energy
  - dissipation, 143–144, 152, 154, 171, 174, 261, 284–287
  - landscape, 357, 366, 369, 372–378
  - MD simulation, 441, 452
  - resolution, 253–255
- energy dissipation, 202, 218
- energy (tension) stress, 383
- entangled state, 147, 184
- entropic force, 137
- environmental study, 423, 425–426, 448–453
- epicuticular wax tubule, 896–897
- equilibrium
  - binding enthalpy, 368
  - true (full) or restricted, 135, 136
- etched STM tip, 131–132
- Euler
  - buckling, 741
  - buckling criterion, 951
  - equation, 75
- evolutionary superadhesive, 709
- exchange
  - carrier plate, 251
  - force interaction, 224
  - force microscopy, 226
  - interaction, 223, 224, 226
- external
  - noise, 242, 247
  - vibrations, 39, 43
- Eyring model, 266–267
- F**
- fabricated
  - pillar array, 751
  - silicon, 844, 893, 914, 931
- face-centered cubic (fcc), 348, 349
- failure mechanism, 389–390, 394
- Fano resonance, 261
- fast-on/fast-off kinetics, 374
- fatigue, 347, 367, 369, 370, 374–379, 391, 397
  - crack, 379, 391
  - damage, 375–378
  - failure, 971
  - life, 347, 367, 369, 370, 375, 378, 379, 397, 971
  - measurement, 963–964
  - resistance, 955, 963
  - strength, 529, 536–538, 549, 576
  - test, 374, 375, 378, 927–928
- FBS. *See* fetal bovine serum
- FCA. *See* filtered cathodic arc
- fcc. *See* face-centered cubic
- Fe-coated tip, 224–226
- feedback
  - circuit, 47, 50, 51, 67, 82, 98, 100
  - loop, 42–43, 50, 53, 84, 85, 100, 101, 103, 244, 248, 249
  - network, 40
  - signal, 200, 202
- FEM. *See* finite element modeling
- Fermi
  - level, 253, 261, 267, 286
  - point, 266
- ferromagnetic probe, 288
- FET. *See* Field effect transistor
- fetal bovine serum (FBS), 891, 892
- FFM. *See* friction force microscopy
- FIB. *See* focused ion beam
- fiber
  - axial stress, 742
  - buckling condition, 737–738
  - elastic modulus, 742, 745, 746
  - fracture, 742, 745
  - material, 738, 744–746
  - model, 738–739, 749
  - morphology, 704
  - optical interferometer, 82–83
  - stiffness, 739
- fiber-optic sensor, 914, 915
- FIB-milled probe, 64
- fibrillar
  - adhesive, 737, 749, 758–759, 761
  - surface construction, 758
- fibrillar structure, 701, 737–749, 758–759, 761
  - compliant, 750
- field effect transistor (FET), 854
- field ion microscope (FIM), 312, 334
- filling angle, 716, 735
- film
  - C<sub>60</sub>, 504
  - nanindentation thickness, 463, 470
  - on substrate, 947
  - substrate interface, 968, 969
  - surface interface viscosity, 491
- film ionic liquid, 503–506
- filtered cathodic arc (FCA), 347, 353–356, 358, 370, 377, 379–385, 397, 398, 881, 914
  - coating, 368, 371, 375, 376, 379–381, 383, 387–388, 391, 392, 395–396
- deposition, 353, 368

- finite element method (FEM), 529, 535–536, 548, 552–554, 577
- finite element modeling (FEM), 411, 426
- first principle
  - calculation, 215, 222–226
  - MD simulation, 441, 475
  - simulation, 276
- flat punch, 404, 408, 409
- flexible cantilever, 46, 48, 51, 66
- flexible crosslinker
  - property, 364–365
  - spring constant, 364–365
- flocculation, 126, 131
- Flory
  - radius, 134
  - temperature, 134
- flow
  - nanoliters, 851
  - rate, 207–209, 211, 213
- fluctuation interaction, 118
- fluid
  - low viscosity, 206–208, 212, 230
  - mechanics, 207, 214
  - multicomponent, 207, 214
  - Newtonian, 206, 211–214
- fluorescence
  - correlation spectroscopy (FCS), 226–231
  - fluctuation, 226, 232, 235
  - recovery after photobleaching (FRAP), 226
  - spectroscopy, 225
- fluoride, 216–223
- fluorophore, 225–230
- FM-AFM, 202–207
- focused ion beam (FIB), 45–46, 64, 112, 119–120, 124, 126–128, 401, 428
- force
  - adhesion, 109–113, 119–110, 129, 138–140, 142, 143, 150–156, 170, 186
  - adhesion, quantized, 109–113, 119–110, 129, 138–140, 142, 143, 150–156, 170, 186
  - attractive, 108–110, 124, 127, 132–134, 153
  - calibration, 245–249
  - calibration mode, 10–12, 23, 77
  - cantilever-based, 275
  - capillary, 109
  - Casimir, 108
  - charge fluctuation, 118, 127
  - chemical force, 277, 282, 284
  - detection, 73, 75, 98
  - electrostatic force, 276, 282, 286
  - gradient, 309–313, 318, 320, 329, 330, 332, 337
  - long-range, 282
  - between macroscopic bodies, 112, 117, 125
  - measurement, 198
  - microscopy, 355–382
  - modulation, 429, 431
  - resolution, 274–276, 282, 363, 365
  - sensing tip, 49, 93
  - sensor, 51–52, 93, 202, 243, 249, 250, 280
  - spectroscopy (FS), 101
  - between surfaces in liquid, 122–137
  - between surfaces in vacuum, 108
  - van der Waals force, 277, 279, 284
- force calibration plot (FCP), 469, 470, 471, 482
- force-clamp AFM, 374
- force-distance
  - curve, 11–12, 26, 56, 57, 101, 728, 730
  - profile, 364, 366–367
- force-driven dissociation, 370
- force field spectroscopy, 3-D, 283–285
- force-free dissociation, 371
- force-probe experiment, 363, 368
- force spectroscopy (FS), 276, 279, 282, 283, 328, 335, 357, 365–380, 382
- 3D-FFS, 283–284
- site specific, 283
- force-time behavior, 357
- formate (HCOO<sup>-</sup>), 227
- formate-covered surface, 228
- four-fingered platform structure, 757
- Fourier-transform infrared spectroscopy (FTIR), 505, 520–521, 523, 527
- Fourier-transform infrared time-resolved spectroscopy (FTIR-TRS), 224
- four-quadrant photodetector, 245
- fracture, 396–397, 407, 421–422, 427, 745
- condition, 737–738, 740, 742–745
- failure, 553
- strength, 953–955, 960–963, 970–971, 973
- stress, 529, 533–536, 576
- surface, 549–551, 553, 563, 576
- toughness, 347, 367, 369–374, 379, 381–383, 386, 392, 397, 529–531, 535–536, 540–542, 547–549, 552, 576
- toughness measurement, 953–955, 960–693
- Frank–Read source, 418
- free surface energy, 472, 481
- freezing-melting transition, 176, 181
- Frenkel–Kontorova–Tomlinson (FKT) model, 254–255

- frequency
  - measurement precision, 93
  - modulation SPM (FM-SFM), 241
- frequency modulation (FM), 47, 198–200, 202–203, 206–207, 308, 329–330, 334, 336, 338–339, 343, 344, 347
  - AFM image, 277–281, 283, 286
- friction, 3–5, 10, 13, 22, 37–38, 48, 49, 53–54, 58, 59, 62, 63, 65, 76, 82, 84, 85, 86, 87, 89–91, 94, 98–100, 101, 102, 204, 230–236, 243, 248, 252–263, 275, 276, 279–283, 287, 348–351, 353, 367, 369, 379–387, 389–394, 396, 397, 403, 405, 406, 408, 416, 420–422, 424–434, 438–446, 448–455, 840, 853, 861, 862, 864–867, 871, 873, 876, 878, 886, 897, 910, 914, 918–923
  - adhesional component, 59–60
  - anisotropy, 261, 262
  - of biomolecule, 854, 881–891, 928
  - coefficient, 146, 147, 155–157, 159, 162, 164, 169, 180, 184
  - coefficient, 445–446, 470–471, 475, 476, 479, 481–482, 489–490, 498, 499, 502, 503, 507–510
  - dominant, 366
  - electrification, 120–121
  - experiments on atomic scale, 243, 255–263, 287
  - image, 259, 261
  - kinetic, 150, 152, 155, 161, 163, 169, 171–173, 177, 180, 181, 183, 184, 205, 234–235
  - load dependence, 62
  - loop, 248, 252, 253, 255–256, 263, 275, 276
  - lubrication, 440, 444
  - map, 167–168, 254–258
  - measurement, 10, 13, 21, 23, 27, 32, 33, 37, 39, 42, 56, 57, 58, 62, 64, 65, 91, 95–96, 98, 226, 232, 236, 964–966
  - measurement method, 65–71
  - measuring technique, 172
  - melting, 172
  - metal surface, 475
  - mode, 8, 22, 37, 39–41
  - molecular dynamics (MD) simulation, 243, 279–283, 287
  - plane, 115
  - profile, 542–545, 560
  - rolling, 120, 144
  - scale dependence, 56–63
  - self-assembled monolayer (SAM), 464, 466, 497, 498, 500, 502
  - sliding, 114, 120–121, 146
  - surface, 491
  - test, 420, 424, 451, 452
  - thinning, 165, 168, 170, 177
  - wave transducer, 42, 98
- frictional property, fullerene, 505
- friction and adhesion
  - influence, 472, 479, 480, 482, 500, 518, 519, 520, 525–526
  - relative humidity, 468, 470, 480, 481, 482, 483, 484, 485, 490, 518, 519, 526
  - temperature effect, 468, 480–483, 528–520
  - velocity effect, 477–479
- friction and wear, 833, 840, 854, 858, 859–862, 864, 865, 869, 881–891, 914–919, 928
  - nanoscale, 526
- friction force, 21, 23–27, 31–36, 37, 40–49, 49, 52, 53, 53–54, 58, 59, 65–73, 84–92, 94–96, 101, 102, 135–138, 159–163, 165–168, 174, 243–253, 257, 259, 261, 262, 266, 267, 269–276, 282–284, 287, 368, 379, 386, 387, 405, 420, 421, 424–426, 430–433, 438–446, 440, 447, 453, 454, 466, 469, 469, 470, 472, 473, 474, 475, 476, 476–483, 480, 485–488, 489, 490, 493, 496, 497, 500, 508, 509, 510, 512, 515, 519, 520, 522, 525, 526, 871–879, 885, 897, 910, 914, 916, 918–923
  - calibration, 54, 70–73
  - curve, 101, 102
  - magnitude, 53, 69
  - map, 273
  - measurement, 6–11, 32, 33, 37, 38, 43, 44
  - microscopy (FFM), 4, 5, 37–38, 52–55, 69–73, 115–116, 151, 155, 243–253, 257, 259, 261, 262, 266, 267, 269–276, 282–284, 287, 296, 420, 861, 866, 868, 920, 929
  - profile, 10, 23, 24, 26, 35, 36, 41
  - of Si(100), 865, 872–874, 917–918
- friction force influence of temperature, 482, 520
- friction force microscopy (FFM), 243–253, 257, 259, 261–263, 266, 267, 269–276, 281–284, 287, 440, 476, 482, 494, 498, 504, 505

- on atomic scale, 244, 251, 267, 275
- dynamic mode, 281, 284
- signal, 7, 10, 13, 42
- tip, 248, 252, 253, 257, 259, 261–263, 271–275, 282, 283
- friction model
  - cobblestone model, 148–149, 151, 153, 155
  - Coulomb model, 149
  - creep model, 177
  - distance-dependent model, 177
  - interlocking asperity model, 149
  - phase transitions model, 178–181
  - rate-and state-dependent, 180–181
  - rough surfaces model, 176–177
  - surface topology model, 176–177
  - velocity-dependent model, 177–178
- friction-torque model, 919, 920
- fringe detector, 955, 956
- fruit fly, end of the leg, 704
- FS. *See* force spectroscopy
- FTIR-TRS. *See* Fourier-transform infrared time-resolved spectroscopy
- fullerene, 348, 349
  - film, 78
  - frictional property, 505
- fundamental resonant frequency, 78
- fused silica, 400, 411–413, 420
- G**
  - GaAs/AlGaAs
    - heterostructure, 286
  - gain control circuit, 202
  - GaP(110), 278
  - gap stability, 41
  - gauge marker, 956
  - Gaussian surface, 61
  - Gd on Nb(110), 268
  - gecko
    - attachment system, 702, 705, 707, 717
    - dry adhesion, 704
    - toe, 702, 705, 707, 708, 711
  - gecko adhesion, 714, 716–717, 720, 735, 737, 750
    - macroscale, 750, 756
  - gecko foot, 712, 718, 756, 760
    - adhesion mechanism, 713–714, 717
    - setal array, 708, 711
    - surface characteristics, 705, 706
  - gecko seta
    - adhesion coefficient, 732, 733, 737, 749
    - adhesive force, 710, 718–720, 722
    - maximum adhesion coefficient, 728, 737
    - spatula, 705, 707, 713, 715, 717, 723, 725, 749, 759, 760
    - three-level model, 725–726, 728, 730–733
  - gecko skin
    - fabrication, 749–759
    - Young's modulus, 706, 708–709
  - gecko spatula
    - contact with a hydrophilic surface, 720
  - geometrically necessary dislocations (GND), 295, 297, 299–301, 335
  - geometry effects in nanocontacts, 269–275
  - germanium, 422
  - g*-factor, 255, 257, 259
  - giant MR (GMR), 773, 776, 808
  - glass
    - glassiness, 184
    - transition temperature, 134, 161–162
  - GMR. *See* giant MR
  - GND. *See* geometrically necessary dislocations
  - gold, 43, 44, 56, 61, 63
  - Grahame equation, 124, 125
  - grain
    - boundary, 121–122, 186, 968–969
    - nanindentation boundary, 454
    - size, 350
  - graphite, 242, 245–246, 255–257, 258, 261, 262, 266, 269, 271, 275, 279–281, 280, 286, 347–350, 357–362, 364, 365, 369, 370, 393, 397
    - (0001), 263, 279–281
    - cathode, 353–354
    - flake, 476, 506
    - sheet, 506
  - green chemistry, 503
  - Griffith fracture theory, 553
  - group A-specific lectin, 379
- H**
  - hairy attachment system, 701–762
  - Hall–Petch behavior, 429–430
  - Hall resistance, 287
  - Hamaker constant, 55, 56, 118, 119, 122, 123, 128, 132, 153, 197, 334, 476, 713, 714, 735, 894
    - gecko seta, 715, 724
  - Hamilton–Jacobi Method, 204
  - hard amorphous carbon coating, 347–398
  - hard coating, 866–867, 881
  - hardness, 12, 15, 16, 28, 53, 57–59, 62, 63, 66, 76, 78–81, 99, 100, 347, 349–353, 356, 358, 359, 363, 365–371, 379, 381, 383, 386, 388, 391, 392, 397, 529–531, 540–542, 544, 553, 556–562, 576, 579, 860, 861, 863–868, 879, 881, 891, 924–925, 949

- scale effect, 57, 62
- HARMEMS. *See* high-aspect-ratio MEMS
- harmonic oscillator, 309, 314–317
- harpooning
  - interaction, 108
- HDT. *See* hexadecane thiol
- heavy-ion bombardment, 290
- height profile BMIM-PF6 coating, 510, 512–514
- hemodynamic resistance, 895
- Hertzian contact model, 402, 405, 417
- Hertz model, 403, 405, 417
- Hertz-plus-offset relation, 271
- Hertz theory, 138–141, 154, 162
- heterodyne interferometer, 80–82, 84
- hexadecane thiol (HDT), 57, 90, 91, 93, 423–424, 914–918, 929
- hexagonally packed intermediate (HPI), 320
- hexa-tert-butyl-decacyclene (HtBDC) on Cu (110), 250
- hierarchical spring analysis
  - multilevel, 724–728
- hierarchical spring model, 723, 725, 727–735
- hierarchical structure, 833, 860, 901–910
  - characterization, 901–908
  - fabricated, 756–759
- hierarchical surface
  - ideal, 906–907
- high-aspect-ratio MEMS (HARMEMS), 836, 933
- higher orbital tip state, 254
- highly oriented pyrolytic graphite, 57
- highly oriented pyrolytic graphite (HOPG), 23, 25–28, 56, 58, 98, 279–280, 328–331
- high-pressure phase
  - silicon, 459
- high-resolution
  - FM-AFM, 279
  - imaging, 231
  - spectroscopy, 253–255
- high-speed data collection, 43, 44
- high-temperature
  - MEMS/NEMS, 928
  - operation STM, 243, 247
  - superconductivity (HTCS), 270
- high-temperaturesuperconductivity (HTCS), 247, 270–272
- Hill coefficient, 375
- hinged cantilever, 965
- H<sub>2</sub>O (water), 258
- homodyne interferometer, 79–80, 84
- honeycomb-chained trimer (HCT), 212–214
- Hooke's law, 274
- HOPG. *See* highly oriented pyrolytic graphite
- horizontal coupling, 42
- horizontally arranged nanotube, 506–508
- HPI. *See* hexagonally packed intermediate
- HTCS. *See* high-temperaturesuperconductivity
- H-terminated diamond, 479
- Huber-Mises, 404
- human genome project, 839–840
- human umbilical venous endothelial cell (HUVEC), 378
- humidity, 268
- HUVEC. *See* human umbilical venous endothelial cell
- hybrid
  - continuum-atomistic thermostat, 447
  - nanotube tip, 125
- hybridization, 215
- hydration
  - force, 108, 117, 128, 130–134, 137, 155, 161, 166
  - regulation, 131
- hydrocarbon, 410–414, 418, 421–422, 441, 443, 450, 451, 454
  - precursor, 357
- hydrodynamic
  - damping, 342
  - force, 108, 117, 165, 204–214, 217
  - radius, 134
  - stress, 210
- hydrogen, 210–212, 230
  - bonding, 108, 130, 132–134
  - bond network, 215, 216
  - concentration, 359, 363–366
  - content, 353, 359, 365, 366, 371
  - flow rate, 365
- hydrogenated
  - carbon, 356–358, 360, 364–365
  - coating, 359–359
- hydrogen-terminated diamond, 460, 462, 463, 466, 471, 479, 480, 481, 485, 486, 498, 506, 510
- hydrogen termination, 210
- hydrophilic, 207, 209, 215, 218–223
  - SAM, 468, 498, 499
  - surface, 109, 130–132, 139, 876, 899–902, 908
- hydrophilicity, 715, 720–722, 736, 737, 760
- hydrophobic, 204, 209, 212, 215–223
  - attraction, 212, 216, 218, 221
  - force, 130
  - interaction, 132, 133self-assembled monolayer (SAM), 468, 498, 499

- surface, 109, 132–134, 138, 139, 157, 158, 160, 207, 209, 215–223, 860, 874, 876, 897–910, 917–919, 928–929
- hydrophobicity, 403–408, 414–418, 422, 428, 437, 441, 443, 453, 455, 462, 470, 485, 715, 720–722, 736, 737, 755, 760, 833, 854, 856, 860, 869, 877, 879, 897–910, 915–919, 921–923, 929
- hysteresis, 58, 70, 96, 201, 240, 242–243, 247, 272–273, 288, 289
  - adhesion, 143–145, 152, 157, 160, 161, 163, 174, 175, 186
  - contact angle, 144
  - loop, 50, 102
- I**
- IB. *See* ion beam
- IBD. *See* ion beam deposition
- IL structure, 522–525
- image
  - effects, 429–431
  - processing software, 103
  - topography, 48, 230
- imaging
  - atomic-scale, 4, 6, 23–27, 45–48, 98
  - bandwidth, 59
  - electronic wave function, 247, 263–266
- imidazolium, 503–505, 515, 520, 522
- immunoisolation, 408
- InAs, 245–246, 255, 257, 265–266
- InAs(110), 255, 257, 265, 266, 277–278
- indentation, 3–6, 15, 16, 76–83, 98, 99, 100, 141
  - creep, 531, 558–559
  - depth, 16, 76, 78–82, 99, 367, 368, 371, 373
  - fatigue damage, 376, 377
  - hardness, 12, 15, 16, 38, 78–80, 99
  - induced compression, 377
  - rate, 452, 458
  - size effect (ISE), 419–420, 427
- inelastic regime, 529
- inelastic tunneling, 247, 249, 251, 258–259, 261
- initial contact, 418, 419
- InP(110), 207
- in-plane stresses nanoindentation, 452, 455
- in situ sharpening of the tips, 41
- instability, 201, 205
- integrated tip, 62, 86
- intensity-intensity autocorrelation, 232–233, 235
- interaction
  - charge exchange, 108, 118, 120–121
  - charge transfer, 120–121
  - Debye, 118
  - depletion, 135–136
  - Derjaguin–Landau–Verwey–Overbeek (DLVO), 116–117, 127, 128
  - dispersion, 118, 119, 122
  - double-layer, 124–126
  - double-layer (geometry dependence), 124
  - dynamic, 108
  - electrostatic, 120, 123, 124, 126, 134
  - energy, 112, 118–120, 124–127, 129, 132, 712, 713
  - energy gradient, 366
  - fluctuation, 118, 127
  - harpooning, 108
  - hydrophobic, 204, 215–223
  - hydrophobic, 132, 133
  - induction, 118
  - Keesom, 117–118
  - London dispersion, 118, 119
  - nonequilibrium, 143–145
  - orientational, 117–118
  - osmotic, 135
  - polymer, 134, 136
  - rate-dependent, 143–145
  - static, 109
  - van der Waals, 107, 112, 118, 119, 123, 129
  - van der Waals (geometry dependence), 109
- interaction force, 275, 276, 308, 309–312, 318, 320–322, 324–328, 342, 360, 362–364, 366, 368, 369, 375, 376
  - cantilever deflection, 364
- interatomic
  - attractive force, 67
  - force, 48, 308, 317
  - force constant, 199
  - interaction, 969
  - spring constant, 48
- interdiffusion, 118, 144, 152
- interdigitation, 144, 152
- interfacial
  - defect, 377, 378
  - force, 203–237
  - friction, 148, 150–156, 162, 164, 169, 172
  - stress, 375, 383, 391–392
- interferometric detection sensitivity, 83
- interleave scanning, 17, 18
- intermediate or mixed lubrication, 123, 129, 139, 146, 147, 167–170
- intermittent contact mode, 8
- internal stress, 950



intragrand transition, 255  
 intramolecular hydrogen bonding, 522  
 intrinsic  
   damping, 345, 346  
   stress, 365  
 iodine, 248, 249  
 iodobenzene, 248, 249  
 ion  
   condensation, 126  
   correlation force, 124–127  
   implantation, 861–864, 866  
   plating technique, 352–353  
   source, 354–356  
 ion beam (IB)  
   coating, 347, 352, 356, 369, 375, 387, 388, 390, 391, 394–396, 398  
   sputtered carbon, 356  
 ion beam deposition (IBD), 351–353, 355, 356  
 ionic bond, 108, 132  
 ionic liquid (IL)  
   dicationic, 504, 505, 515–525, 527  
   film, 462, 503–525, 527  
   lubrication property, 504, 505  
   physical property, 504, 505  
   thermal property, 504, 505  
   tribological property, 462, 504, 525  
 isospectral structure, 263  
 itinerant nanotube level, 261

**J**  
 jellium approximation, 443  
 Johnson–Kendall–Roberts (JKR), 707, 739–740, 742  
   model, 393, 405  
   relation, 271, 272  
   theory, 138–140, 157, 707, 739–740, 742  
 Joule  
   dissipation, 284–286  
   heating, 289  
 jump into contact, 895  
 jump-to-contact (JC), 199, 201, 276, 281, 282, 311–312, 327, 450–452, 457–458

**K**  
 KBr, 216, 218  
 KBr(100), 257, 258, 275, 277  
 KCl<sub>0.6</sub>Br<sub>0.4</sub>(001) surface, 218  
 Keesom interaction, 117–118  
 Kelvin  
   equation, 138  
   probe force microscopy (KPFM), 232  
 kinetic  
   friction, 148, 150, 152, 155, 161, 163, 169, 171–173, 177, 180, 181, 183, 184, 205, 234–235

friction coefficient, 755  
 friction macroscale coefficient, 754  
 friction ultralow, 183  
 processes, 418  
 rate, 368–372  
 knife-edge blocking, 98  
 Knoop hardness, 28  
 Kondo  
   effect, 241, 247, 261–262  
   temperature, 261–262  
 Kramers diffusion model, 370  
 K-shell EELS spectra, 360  
 kurtosis, 911

## L

lab-on-a-chip, 839, 850–852  
   system, 850  
 Lamb waves, 400  
 Landau  
   level, 242, 247, 255–257, 287  
   quantization, 255, 257  
 Langevin dynamics approach, 445  
 Langmuir–Blodgett (LB), 90, 216, 219, 221, 223, 406, 420, 462, 472–473, 494  
 Laplace  
   force, 471, 715–716, 735  
   pressure, 109, 138, 708  
 large-sample AFM, 5–8, 13, 14, 23, 27, 38, 44, 63, 76, 78, 85  
 large-scale adhesion, 756  
 laser  
   ablation, 933  
   deflection technique, 47, 51  
 lateral  
   contact stiffness, 243, 274  
   cracks, 401  
   deflection, 920  
   force, 6, 8, 17, 21, 23–24, 27, 37, 46, 47, 57, 98, 135–190, 244–249, 252–253, 255, 258, 261–266, 269, 270, 275–278, 280–282, 286, 287  
   force calculation, 86  
   force microscopy (LFM), 6, 37, 38, 115–116, 151, 155, 207, 226, 244, 267  
   resolution, 39, 41, 43, 47, 48, 52, 56  
   resonator, 959, 960, 961, 969, 973  
   spring constant, 59, 60, 245, 247, 251, 253, 274–275  
   stiffness, 76, 101, 243, 274–275  
   surface property, 5, 83  
 lattice imaging, 48  
 layered structure lubricant, 510

- layer lubricant, 487
- LB. *See* Langmuir–Blodgett
- LDOS. *See* local density of states
- leg attachment pad, 701
- Lennard–Jones (LJ) potential, 55, 56, 279, 444
- level III spring, 725, 726, 731
- LiF, 216
  - (100) surface, 280
- lifetime broadening, 247, 255, 256, 263
- lifetime-force relation, 374
- Lifshitz theory, 119, 120, 122, 123, 128, 129, 132
- lift mode, 13, 14, 17, 18, 58
- lift scan height, 17, 18
- LIGA technique, 529
- light beam deflection galvanometer, 83–84
- limit of tip radius, 742
- linearization, active, 99
- linear variable differential transformer (LVDT), 98–99
- line scan, 12, 41
- lipid
  - bilayer vesicle, 363
  - film, 261, 266, 267
- liposome, 893
- liquid, 440, 443, 448–450, 452, 464, 470, 487–484, 488, 489, 491, 510
  - bridging, 922
  - helium, 241, 242, 246
  - helium operation STM, 243
  - lubricant, 4, 5, 83, 84, 87–88, 850, 870–873, 922–923
  - lubricant, 470, 489, 510
  - lubricated surface, 157, 165–183
  - nitrogen (LN), 243, 246
- liquid-air contact, 900, 901, 910
- liquid-air interface, 716, 900, 907
- liquid film molecularly thick, 461, 462, 463, 467, 468, 482, 528, 529, 530
- liquid film thickness, 52, 95–98
- liquid-like Z–15, 464, 468, 472, 481, 525
- lithographie galvanofornung abformung (LIGA)
  - fabrication, 929, 933
  - process, 841–842, 919, 933
- lithography, 834, 836, 838, 855, 902–904, 929, 930–931, 933–934
- live cell, 378–379
- load
  - contribution to friction, 150–156
  - critical, 369, 370, 375, 379–383, 385–387
  - dependence of friction, 256–257, 271–272, 287
- load-carrying capacity, 381, 392
- load-controlled friction, 151, 159, 162, 164
- load curve, 469
- load-displacement, 530, 532–534, 538, 546, 552–554, 560–564, 574, 575
  - characteristic, 553
  - curve, 75, 78, 80, 81, 99, 367, 371–373, 532–534, 538, 546, 552–554, 563, 574, 575
  - profile, 562, 563, 564
- loading curve, 407, 414–415
- loading rate, 357, 367–374, 376–379
- local deformation, 54, 63–76
  - characterization, 4, 6, 14–15, 72–76, 99
- local density of states (LDOS), 253–254, 266–272
- localized surface elasticity, 6, 16–22, 81–83, 99
- local stiffness, 101
- London
  - dispersion interaction, 118, 119, 122
  - penetration depth, 268, 289, 291
- long-chain hydrocarbon lubricant, 489
- longitudinal piezo-resistive effect, 89
- long-range
  - attraction, 109, 118, 120, 132–135
  - force, 199–201, 217, 224, 227, 230, 282
  - meniscus force, 12
- long-range hydrophobic interaction, 204
- long-term
  - measurement, 241
  - stability, 241, 242
- loose association, 360
- loss modulus, 416, 417
- lotus, 534, 535, 538, 566–581, 639, 686
- lotus (*Nelumbo nucifera*) effect, 833, 860, 897, 898, 919
- lotus leaf
  - artificial, 907–908
  - surface, 898, 907
- lotus replica micropattern, 902, 907, 908, 910
- low-cycle fatigue resistance, 963
- low-noise measurement, 250
- low-polarizable SAM, 424
- low pressure chemical vapor deposition (LPCVD), 529, 540, 860, 930–932
- low-stress silicon nitride (LSN), 931
- low-temperature
  - AFM/STM, 49
  - microscope operation, 241–243
  - scanning tunneling spectroscopy (LT-STM), 247
  - SFM (LT-SFM), 245–246
  - SPM (LT-SPM), 241, 245

- low-viscosity, 206, 207, 212
  - fluid, 204–208, 230
- LPCVD. *See* low pressure chemical vapor deposition
- lubricant
  - chain diameter, 84
  - film, 845, 849, 869, 871–874, 883, 918, 922–923
  - failure, 452
  - thickness, 96, 99
  - flow, 467, 474, 476, 494
  - fraction, 490, 492, 508, 509, 510, 512, 515, 526, 527
  - layer, hydrophobic, 874, 921, 923
  - liquid, 5, 83, 84, 87–88, 96, 849, 870–871, 873, 922, 923
  - MEMS/NEMS application, 462, 489, 494, 504, 525
  - mobile-phase, 464, 487
  - nanotribological performance, 462, 468
  - perfluoropolyether (PFPE), 864, 870–875, 918, 920–921, 928, 929
  - PFPE, 462, 465, 467, 468, 472, 489–504, 515, 526
  - solidlike, 464, 468, 472, 481, 525
  - Z–15, 463, 468, 470, 471, 525
  - Z-DOL, 464, 465, 468, 473, 489, 525
- lubricated
  - silicon, 487, 488, 489, 490, 492, 494
  - surface, 871
- lubricating
  - film, 403, 405, 452
  - thin film, 487
- lubrication, 3–6, 23, 83–99, 859, 869–881, 919, 921–923, 928
  - elastohydrodynamic (EHD), 146, 147, 165, 169
  - intermediate or mixed, 146, 147, 168
  - mobile layer, 921–923
  - nanoscale boundary, 23, 83–99
- lubrication property
  - ceramics, 476
  - polymer, 468, 471
- LVDT. *See* linear variable differential transformer
- M**
  - macrohardness, 80
  - macromolecule, 112, 125, 134
  - macroscale friction, 99, 861, 862, 864, 865, 867
  - magnetic
    - disk, 374, 393–394
    - disk drive, 352
    - force, 196, 199, 202
    - force gradient, 58
    - quantum flux, 289
    - storage device, 351, 397
    - thin-film head, 351, 394
    - tip, 291, 292
  - magnetic force microscopy (MFM), 38, 58, 240, 288–291, 340
    - AM-MFM, 288
    - domain imaging, 288
    - FM-MFM, 288, 290
    - sensitivity, 58
    - vortex imaging, 290, 291
  - magnetoresistive (MR), 773, 808
  - magnetostatic interaction, 288
  - magnetron sputtered carbon, 359, 371, 394
  - magnon excitation, 258
  - manganite, 272, 289
  - manipulation
    - individual atom, 248, 285
    - of individual atom, 38
    - individual atoms, 248, 285
    - molecules, 249, 251, 258
  - manmade pollutant, 711
  - mass
    - of cantilever, 46
    - effective, 241, 255, 257, 275
  - material
    - lubricant, 503
    - structural, 950, 955, 962, 966, 973
  - Matrix-method, 334–335
  - maximum
    - adhesive force, 741
  - maximum load nanoindentation, 455
  - mean-field theory, 125
  - mechanical
    - coupling, 176
    - dissipation in nanoscopic device, 243
    - resonance, 182
    - scission, 498, 499
    - stability fullerene, 505
  - mechanical property, 19, 21, 61, 76, 81, 98–100, 527–580, 947–973
    - characterization, 972–973
    - of DLC coating, 379, 381, 388–389, 396–397
    - experimental technique, 530–539
  - mechanics
    - of cantilever, 73–78
    - modeling, 915, 916
    - nonadhesive, 107
    - potential difference, 286

- mechanics (*cont.*)
  - pressure, 175
  - resonance spectroscopy, 17
  - stiffness, 21
  - true molecular, 156–157
- mechanism-based strain gradient (MSG), 299
- melted SAM, 443
- membrane, 362, 363, 368–379
  - deflection method, 972
- memory distance, 107, 175, 186
- MEMS. *See* microelectromechanical system
- MEMS/NEMS. *See* micro-/nanoelectromechanical system
- meniscus
  - formation, 485, 508, 509, 515, 518
  - of liquid, 138–139
- meniscus force, 12, 45, 46, 51–56, 96, 470, 473–476, 484, 485, 708, 840, 859, 873–874, 915–918, 921–923
- meniscus force time dependent, 475
- metal
  - deposited Si surface, 212–216
  - evaporated (ME) tape, 351
  - oxide, 216–223, 227
  - particle (MP), 72–75, 83
  - particle (MP) tape, 395
  - porphyrin (Cu-TBPP), 227
  - tip, deformable, 449
- metal-evaporated (ME), 72–76
- metallic bonding, modeling of material, 442
- metallic microbeam, 552–553
- metal-oxide-semiconductor field-effect transistor (MOSFET), 854
- methylene stretching mode, 420, 421
- Meyer's law, 427
- MFM. *See* magnetic force microscopy
- MgO(001), 221, 223, 225
- mica, 44, 56, 57, 208, 212, 213, 215–217, 219, 225–226, 229–231, 234–235, 259–261, 266–267, 272, 275, 277, 278, 279, 286
- muscovite, 275, 277, 279
- surface, 260, 261, 277
- microbuckling, 741
- microcantilever, 838, 848
- microchannel, 207
- microcontact printing ( $\mu$ CP), 407
- microcrystalline graphite, 362
- microdevice, 529, 951, 959
- microelectromechanical systems (MEMS), 351, 374, 375, 397, 403, 417, 439–440, 447, 454, 462, 473, 489, 494, 504, 525, 528–530, 537, 553, 554, 566, 576, 577, 714, 717, 962, 963, 967, 972
  - device, 833–935
  - technology, 966
- microelectronics, 216
- microengine, 842
- microenvironment, 230, 233
- microfabricated silicon cantilever, 197, 198
- microfabrication, 858–859, 931, 933
- microfluidic, 850–851
- microfriction, 33–37
- microgear, 407
- microimplant, 881
- microindentation, 392, 394–396, 404–405, 420
- micromachine, 528
- micromachined
  - array, 846–847, 913, 914
  - notch, 953, 960, 962–964, 971
  - polysilicon beam, 841, 860, 912–913
  - silicon, 834, 835, 841, 843, 844, 860, 934
- micromanipulator, 122
- micromirror, 407, 437
- micromirror device (DMD)
  - digital, 835–837, 846, 923–928
- micromotor, 407, 840, 841, 910–912, 919, 922
- lubricated, 860–861, 920–921, 929
- micro-/nanoelectromechanical system (MEMS/NEMS), 84, 90, 204, 205, 209, 296, 833–935
  - characteristic dimension, 834, 835
  - device, 833–935
  - lubricant, 84
  - lubrication, 90
  - mechanical property, 528, 529, 530, 576
  - tribological property, 859, 861, 867, 868, 875, 928
- micro-/nanooptoelectromechanical systems (MOEMS/NOEMS), 834
- micropattern, 92, 94, 95
- micropatterned SAM, 429–432, 453–454
- micropatterned surface, 902–907
- micropipette aspiration, 116
- micropore membrane, 757
- micropump, 850–853
- micro-Raman spectroscopy, 392, 402, 422, 424
- microscale
  - contact resistance, 495, 512, 514, 517
  - friction, 3–6, 27–33, 37–42, 56–58, 62, 98, 505, 517–518, 861, 862, 865, 866, 911
  - hair, 759
  - scratching, 4, 6, 12–13, 63–66, 76, 99
  - seta, 759

- wear, 3, 4, 12, 57, 62, 63, 66–71, 99, 505, 517–518, 861, 867
- microscope eigenfrequency, 73
- microscopic bubbles, 218
- microscratch, 63, 65, 347, 379–388, 397–398
  - AFM, 422, 432
- microsculpture, 919
- microsensor, 860
- microslip, 38, 59
- microspark erosion, 933
- microstrain gauge, 950, 967
- microstructure, 836, 858, 901, 908, 910–914, 919, 929, 930
  - characterization, 901–908
  - surface, 897–898, 902, 903, 906–908
- microstructured surface, 749, 760–761
- microsystem technology (MST), 528, 834
- microtip, 50–52
- microtriboapparatus, 914–919, 929
- microtribometer, 754
- microwear, 347, 379–389, 397–398, 865–866, 876, 878
- millimeter-scale device, 933
- millipede, 838, 848
- misfit angle, 255, 260, 261
- mismatch of crystalline surface, 108, 109, 133, 149, 163, 172, 178, 179, 185
- Mn on Nb(110), 268, 269
- Mn on W(110), 272
- mobile lubricant, 490, 509, 510, 526
- modeling of material, 440, 442
- modulus
  - elastic, 347, 364, 367–371, 374, 378, 379, 383, 396, 397, 398–400, 407–412, 420, 425, 427–429
  - of elasticity, 16, 17, 38, 53, 58, 76, 81, 99
- MOEMS/NOEMS. *See* micro-/nanooptoelectromechanical systems
- molding process, 907, 933
- molecular
  - chain, 406, 408, 414–419, 431, 450, 452
  - cohesion, 365
  - conformation, 462–488, 525
  - dynamics (MD) calculation, 257, 280
  - dynamics simulation (MDS), 243, 279–283, 287
  - imaging, 252, 259, 263, 265
  - layer, 859, 870–871, 875, 928, 934
  - resolution, 251
  - shape, 169
  - spring, 430–431
  - spring model, 91–92, 94, 95, 99, 422, 429–432, 441, 443, 446, 453, 875
  - translational, 203–204, 226–227
- molecular-beam epitaxy (MBE), 934
- molecular dynamics (MD), 209, 234, 440, 441, 444, 445, 447–453, 455, 457–466, 468, 471–473, 475, 479–492, 495–498, 500, 502, 503, 505, 506, 510, 512
  - simulation, 209, 234, 440, 441, 444, 445, 448–452, 455, 457–466, 468, 471, 473, 475, 479–485, 487–489, 491, 495, 496, 498, 501, 502, 505, 506, 510, 512
  - constant-NVE, 448
- molecular recognition force microscopy (MRFM), 355–382
- molecular recognition force spectroscopy
  - principle, 365–368
- moment of inertia, 960
- monocationic, 505–515, 519, 522
- monohydride, 210–212
- monolayer
  - indentation, 464, 466
  - surfactant, 137, 145, 146, 157, 175, 180, 182
- monomeric bond, 375
- MoO<sub>3</sub>(010), 221
- MoO<sub>3</sub> nanoparticle, 503
- Morse potential, 334
- MOSFET. *See* metal-oxide-semiconductor field-effect transistor
- MoS<sub>2</sub> friction, 259–261
- MR. *See* magnetoresistive
- MRFM. *See* molecular recognition force microscopy
- MSG. *See* mechanism-based strain gradient
- MST. *See* microsystem technology
- multilayer, 398–400, 421, 424–431
  - thin-film, 374, 394
- multilayered APTES, 887, 888
- multilevel hierarchical model, number of
  - spring, 732
- multilevel photolithography, 757, 761
- multilevel structure durability, 758
- multimode AFM, 13, 58
- multimolecular layer, 405, 406, 870–871
- multiple-beam interferometry (MBI), 113
- multiplication of dislocations, 396, 418
- multipole interaction potential, 443
- multiwalled carbon nanotube (MWCNT), 64–65, 506, 755–756
- multiwalled nanotube (MWNT), 10, 11, 112, 121, 122, 125–126, 858
- muscovite mica, 275, 277, 279, 360

- mushroom-headed microfiber, 750
- mushroom-like contact, 753
- MWCNT. *See* multiwalled carbon nanotube
- MWNT. *See* multiwalled nanotube
- N**
- NaCl, 216, 217, 249, 257, 262, 285
  - island on Cu(111), 285
- NaCl(100), 262, 263, 273, 280
- NaCl(001) on Cu(111), 216
- NaF, 216, 259–260
- nanosperity, 405–406, 906–907
- nanobeam, 738
- nanochannel, 404, 408, 853–856, 879, 897, 931, 932
- nanoochemistry, 834, 838, 934–935
- nanoclay, 553, 554, 556, 565, 576
- nanocomposite material, 503
- nanocrystal, 893, 934
- nanocrystallite, 347, 358, 359, 397
- nanodeformation, 462–488, 525
- nanodevice, 403, 405, 407, 427, 453, 455
- nanodroplet, 901, 907
  - condensation, 907
- nanoelectromechanical systems (NEMS), 403, 417, 454, 462–488, 525, 528, 529, 537, 566, 576, 577, 833–935, 966, 972
- nanoelectronics, 407
- nanofabricated surface, 749
- nanofabrication, 12, 13, 38, 63, 99
  - parameter, 76
- nanofatigue, 374–379
- nanofluidic
  - device, 527, 833–935
  - silicon array, 855–856
- nanohair, 750
  - polyimide, 751
- nanohardness, 16, 364–366, 404
- nanoinprint lithography (NIL), 933–934
- nanointentation, 12, 15–16, 99, 367, 368, 370, 371, 373, 392–426, 428, 429, 431, 432, 448, 449, 452–461, 463, 468, 470, 472, 512, 863–866, 948–949
  - MD simulation, 448, 449, 452, 455, 457–459, 463, 512
- nanointentation relax
  - surface atom, 452
- nanointender, 81, 347, 367, 374, 380, 385, 386, 388–389, 397–398, 530–531, 538–545, 549, 552–565, 576, 577, 956, 957
- Nano–Kelvin probe, 13
- nanolithography, 838
- nanolubrication, 505
- nanomachining, 12, 13, 38, 63, 76, 99
- nanomagnetism, 272–274
- nanomanipulation, 336
- nanomaterial, biologically inspired, 833, 860
- nanomechanical characterization, 923–928
- nanomechanics, 833, 840–869, 923–929
- nanometer, 439–513
- nanometer-scale
  - device, 503
  - electronic device, 503
  - friction, 440, 476, 509–510
  - indentation, 439–513
  - lubrication, 472–473
- nanometer-scale friction ceramics, 476
- nanometer-scale property material, 448, 457
- nanomotor, 214
- nanoparticle, 487, 503–510
  - tip, 504
- nanopattern, 838, 849, 850, 883, 886, 902
- nanopatterned polymer surface, 902–903
- nano/picoindentation, 16, 77–78
- nanopores, 856
- nanopositioning, 94
- nanopump, 214
- nanorheology, 107–187
- nanoroughness, 754–755
- nanoscale
  - adhesion, 860
  - bending, 927–928
  - contact resistance, 513
  - device, 879
  - friction, 5, 6, 23–25, 42–50, 56–58, 90, 98–100
  - indentation, 3, 4, 78–81
  - spatula, 759
  - supramolecular assembly, 231
  - test, 420
- Nanoscope I, 41
- Nanoscope II, 216
- nanoscopic device, 833–834
- nanoscratch, 69, 99
- nanostucture, 839–840, 849, 860, 898, 901, 907, 908, 910, 928, 931, 934–935
  - bending test, 532–539
  - characterization, 901–908
  - indentation, 576
  - mechanical property, 949
  - roughness, 529
  - scratch, 529
  - scratch test, 530–531, 540–545, 553–560
  - stress and deformation analysis, 527–530

- nanosurface, 702
  - nanotribological properties of silicon, 861–864, 867–869
  - nanotribology, 235, 403–455, 462, 833, 840–869, 928
  - nanotube
    - bundle, 463, 506–509
    - probe, 122–126
  - nanotube-based sensor, 835, 838
  - nanowear map, 49, 50, 64
  - nanowire, 838, 839
  - Navier–Stokes equations, 207, 208
  - NbSe<sub>2</sub>, 268, 275, 290
  - Nb superconductor, 254, 290
  - NC-AFM. *See* noncontact atomic forcemicroscopy
  - near-field scanning optical microscopy (NSOM), 112, 113
  - near-field technique, 276
  - negative
    - contact force, 497
    - force gradient, 311
  - NEMS. *See* nanoelectromechanical system
  - net displacement, 723–724, 739
  - Newtonian
    - flow, 146, 168–169
    - fluid, 206, 211–214
  - NH<sub>2</sub> group tip, 360
  - NHS. *See* *N*-hydroxysuccinimidyl
  - N*-hydroxysuccinimidyl (NHS), 359, 360
  - Nickel(ii) Oxide (NiO), 245–246, 283, 284, 291, 292
  - NiO(001), 216, 221
  - NiO(001) surface, 216, 223–226
  - Ni(001) tip on Cu(100), 282
  - Ni(111) tip on Cu(110), 282
  - nitrilotriacetate (NTA), 360, 362
  - nitrogenated carbon, 358
  - noble-metal surfaces, 255, 258, 261, 263
  - n*-octadecyltrichlorosilane (*n*-C<sub>18</sub>H<sub>37</sub>SiCl<sub>3</sub>, OTS), 420, 429
  - noise
    - electronic, 50, 103
    - external, 242, 247
    - performance, 206–207
    - source, 87
  - Nomarski interferometer, 83, 84
  - nonadhesive contact, 141
  - nonbranched attachment system, 708, 722–723
  - nonbuckling condition, 741, 745
  - nonconducting film, 354
  - nonconductive
    - material, 222, 226
  - sample, 43
  - noncontact
    - AFM, 195–232
    - AFM image, 208–214, 216, 220–222, 225
    - atomic force microscopy (NC-AFM), 216, 221, 222, 225, 284–287, 330, 336–337
    - dynamic force microscopy (NC-AFM), 284
    - friction, 286
    - imaging, 47, 48, 59
    - mode, 208–210
  - noncontact atomic force microscopy (NC-AFM), 275, 330, 336–337
  - noncontact mode, 208–210
  - nonliquidlike behavior, 170
  - nonmagnetic Zn, 270
  - non-Newtonian flow, 146, 147
  - nonpolar end group, 871
  - nonsilicon MEMS, 834, 836, 933
  - nonspherical tip, 272
  - nonsticking criterion, 743
  - nonwetting, 132
  - normal friction, 145–146, 157, 159, 164
  - normalized frequency shift, 332, 333, 336
  - normal load, 4, 8, 10, 13, 15, 16, 22–24, 26, 28–31, 36–37, 39–41, 45, 48–50, 53, 54, 59, 62–70, 76–78, 84, 85, 92, 94, 95, 98, 99
  - normal stiffness, 140–159, 167, 176, 177, 180–181, 187, 188
  - Nosé–Hoover thermostat, 446, 447
  - no-slip boundary condition, 204–214
  - NSOM. *See* near-field scanning optical microscopy
  - NTA. *See* nitrilotriacetate
  - numerical modeling, 476
- O**
- octadecyldimethyl(dimethylamino)silane (ODDMS), 423, 436, 437–454, 876–880
  - octadecylphosphonate (ODP), 423, 437, 439–442, 444–448, 876, 877, 879, 880
  - octadecyltrichlorosilane (OTS), 208, 209, 420, 429
  - octadecyltriethoxysilane (OTE), 208, 216–219, 221, 223
  - octyldimethyl (dimethylamino)silane (ODMS), 423, 436–454, 876–880
  - ODDMS. *See* octadecyldimethyl (dimethylamino)silane

- ODMS. *See* octyldimethyl (dimethylamino) silane
- ODP. *See* octadecylphosphonate
- OMVPE. *See* organometallic vapor-phase epitaxy
- on-chip actuator, 961
- one-level
- hierarchical model, 728, 732
  - hierarchy elastic spring, 744
- operation, 196–200, 203, 206, 211, 232
- optical
- detector, 47
  - head, 54–56
  - head mount, 55
  - lever, 83–88, 94, 101
  - microswitch, 837, 846, 847
- optical lever
- angular sensitivity, 87
  - deflection method, 101
  - optimal sensitivity, 87
- optical tweezer (OT), 117, 363, 365
- optimal beam waist, 87
- order
- in-plane, 170
  - long-range, 108, 109, 118, 120, 124, 130, 132–135, 143, 147
  - out-of-plane, 170
  - parameter, 113, 147, 173–174
- ordered molecular assembly, 416, 453
- organic
- compound, 408–414, 426
  - monolayer film, 28
- organofunctional bond, 462
- organometallic vapor-phase epitaxy (OMVPE), 934
- orientational interaction, 117–118, 147
- Orowan strengthening, 429, 430
- oscillating
- cantilever, 6
  - tip, 53, 58
- oscillation
- amplitude, 201, 218
  - cycle, 309, 311, 313–315, 317, 320, 325, 330, 343–346
- oscillatory
- flow, 207, 208
  - force, 108, 128–133, 137, 142, 143, 169, 170, 183, 223–224
  - shear, 215
- osmotic
- force, 108, 116, 135
  - interaction, 135
  - pressure, 116, 126, 136, 155–156
  - stress technique, 116
- OT. *See* optical tweezer
- OTE. *See* octadecyltriethoxysilane
- OTS. *See* octadecyltrichlorosilane oxide
- layer, 417, 419, 424
  - sharpening, 111, 119
- oxygen content, 396
- P**
- PAA. *See* porous anodic alumina
- packed system friction, 495, 496
- packing, short-range, 236–237
- paraboloid load displacement, 409
- passive
- linearization, 97–99
  - structure, 949–955
- patterned surface, 883, 902–906
- Pb on Ge(111), 267
- PBS. *See* phosphate-buffered saline
- PDMS. *See* poly(dimethylsiloxane)
- PDP group. *See* 2-pyridyldithiopropionyl group
- peak indentation load, 367, 371, 372, 374
- peak-to-peak load, 531
- peak-to-valley (P-V), 545, 556
- peak-to-valley (P-V) distance, 883, 911
- PECVD. *See* plasma enhanced chemical vapor deposition
- peeling action, 709
- PEG. *See* polyethylene glycol
- peierls instability, 266
- perfluorinated SAM, 438, 440
- perfluorodecanoic acid (PFDA), 407, 422, 423
- perfluorodecylphosphonate (PFDP), 423, 436, 438, 439, 441, 442, 444–448, 876, 877, 879, 880
- perfluorodecyltrichlorosilane (PFTS), 423, 436–454, 876–880
- perfluorodecyltriethoxysilane (PFDTES), 879, 891, 892, 902, 903
- perfluoropolyether (PFPE), 44, 83–90, 95, 96, 869, 871, 914–918, 920, 921
- lubricant film
  - chemical degradation, 462, 489–503
  - surface topography, 472
  - nanotribological property, 462, 489, 504, 505, 525, 527
- perfluoropolyether (Z-DOL), 38, 39, 57, 84–90, 92, 95, 96
- periodic
- boundary condition (PBC), 444–445, 448, 453
  - potential, 253
- peristaltic force, 137



- permanent dipole moment, 231
- perpendicular scan, 53, 65, 68
- perturbation approach, 204
- perylene, 227
- PES. *See* photoemission spectroscopy
- PFDA. *See* perfluorodecanoic acid
- PFDP. *See* perfluorodecylphosphonate
- PFDTES. *See* perfluorodecyltriethoxysilane
- PFPE. *See* perfluoropolyether
- PFTS. *See* perfluorodecyltrichlorosilane
- phase
  - imaging, 344
  - transformation, 396, 397, 407, 422–424
    - nanindentation, 459
  - transition, shear-induced, 235
- phonon excitation, 270
- phosphate-buffered saline (PBS), 883–885, 888–892
- phosphazene lubricant, 489, 500
- photoemission spectroscopy (PES), 255
- photolithographic fabrication, 929
- photolithography (PL), 903–904, 930, 934
- photoresist
  - master, 578
  - nanorod, 757
- photothermal effect, 337
- physical wear, 492
- physisorption, 461
- pick-up tip, 125
- picoindentation system, 16, 78
- piezo
  - ceramic material, 41, 96–97, 102–103
  - effect, 95
  - excitation, 315, 318, 319, 329, 337, 347
  - hysteresis, 240, 242–243
  - relaxation, 242–243
  - stack, 99
  - tube, 42, 43, 56, 67–68, 70, 94–96, 100
- piezoelectric
  - drive, 40
  - leg, 250–251
  - positioning elements, 240
  - scanner, 113, 114, 242, 282
- piezoresistive
  - cantilever, 88
  - coefficient, 88–89
  - detection, 49, 88–89, 198
  - sensor, 717
- piezoscanner, 70, 96–97, 99, 102
- piezotranslator, 49, 50, 94, 95, 98, 102
- piezotube calibration, 43, 56
- pile-up
  - nanoindent, 401, 412, 428, 432
  - nanindentation, 452
  - surface, 460
  - surface atom, 451, 452
- pillar array fabrication, 751–753
- pinning, 268, 290, 291
- pin-on-disk tribotester, 420
- PL. *See* photolithography
- plants, 534, 535, 538, 566, 567, 579, 625, 686
- plant wax, 897, 907
- plasma enhanced chemical vapor deposition (PECVD), 60–63, 71, 351–355, 357–366, 370, 406, 540
  - carbon sample, 359–360
- plastic deformation, 367, 372, 377, 387, 452, 453, 455, 458, 460, 461, 471, 487
  - surface, 452
- platinum-iridium (Pt-Ir), 44–46
  - tip, 44, 45
- plug polysilicon, 931–932
- PMMA. *See* poly(methyl methacrylate)
- pneumatic damping, 246
- point probes, 392
- Poisson's ratio, 396, 400, 401, 403, 409–410, 413
- polishing, 350
- poly(dimethylsiloxane) (PDMS), 530, 577–579, 744–745, 750, 752, 879, 891, 892, 934
- poly(methyl methacrylate) (PMMA), 112, 126, 530, 538, 553–556, 558–563, 576–579, 891, 892, 902, 903, 934
  - physical property, 553, 555
- poly(propyl methacrylate) (PPMA), 530, 553–563, 576–579
  - physical property, 553, 555
- polycrystalline graphite, 359, 360, 362
- polydimethylsiloxane (PDMS), 407, 422
- polyethylene glycol (PEG), 359, 360, 364
- polyethylene terephthalate (PET), 72–74
- polymer
  - adsorption, 123
  - biocompatible, 530
  - bioMEMS, 530, 855, 933–934
  - brush, 166–167
  - brushes, 489
  - cantilever, 579
  - chain relaxation, 135
  - end-adsorbed, 136
  - fibril, 740, 741
  - grafted, 136–137
  - interaction, 134
  - liquid (melt), 114, 121, 147, 167, 183, 184
  - microbeam, 576–578

- polymer (*cont.*)  
  mushroom, 136–137  
  nonadsorbing, 135, 167  
  physisorbed, 134  
  in solution, 134, 167  
polymer beam, mechanical property, 559  
polymer fiber orientation, process step, 752  
polymeric  
  magnetic tape, 36–37, 63, 64, 77, 78, 82  
  microbeam, 553–565  
polypropylene (PP), 227, 348  
polysilicon  
  cantilever beam, 913, 914  
  deposition, 860, 930–932  
  doped, 861, 862, 867  
  fatigue, 971  
  film, 529, 540–545, 576, 860, 861,  
    867–869, 868, 928, 930, 951, 953,  
    968, 969, 970  
  fracture strength, 970, 971  
  fracture toughness, 970–971  
  friction, 971–972  
  mechanical property, 966–972  
  microstructure, 968, 970  
  residual stress, 967–969  
  undoped, 866–870  
  Young's modulus, 969–970  
polystyrene (PS), 530, 553–565, 576–580, 902,  
  903  
  physical property, 553, 555  
polystyrene/nanoclay composite (PS/clay),  
  553, 556–565, 576–580  
polytetrafluoroethylene (PTFE), 258, 259  
  coated Si-tip, 259  
polyurethane (PUR), 348  
polyvinyl alcohol (PVA), 556, 579–580  
polyvinylsiloxane (PVS), 753, 754  
pop-ins, 396  
pop-outs, 396, 397  
porous anodic alumina (PAA), 757  
position, accuracy, 103  
potential, 440–448, 450, 452, 453, 455,  
  457–463, 471, 474, 475, 477,  
  479–483, 485, 488, 489, 495, 500,  
  503, 509–510  
power dissipation, 284, 346, 347  
power spectra  
  MD simulation, 484  
PP. *See* polypropylene  
PPMA. *See* poly(propyl methacrylate)  
pre-crack length, 954  
pressure  
  contact, 116, 126, 154–156  
  Laplace, 109, 138  
  osmotic, 116, 126, 135–137, 155–156  
probability force distribution, 370  
probe  
  colloidal, 115, 116  
  FIB-milled, 64  
  fluorophores, 230  
  surface, 360–362, 368, 369  
probe-sample distance, 311, 319, 321, 329  
probe tip  
  performance, 116–119  
  standard, 115–116  
process, gas, 357  
processing aids, 214  
properties of a coating, 353, 381, 388–389  
property, 440, 445, 447–449, 457, 463, 466,  
  468, 470–472, 476, 482–483, 486,  
  487, 491–492, 495, 502, 503,  
  505–508, 510, 512  
  parameter, 728, 738, 761  
  phonon mode, 445  
  profiler, 913  
  separation, 129  
  ultrasmooth, 55  
protective nitride layer, 932  
protein coating, 881  
protrusion force, 108, 137  
PS. *See* polystyrene  
PS/clay. *See* polystyrene/nanoclay composite  
Pt alloy tip, 46  
PTFE. *See* polytetrafluoroethylene  
Pt-Ir. *See* platinum-iridium  
pull-off, 723, 726, 727, 742, 745, 753  
  cycle, 724  
  force (*see* Adhesion force)  
pull-off adhesion force, 217  
pulsed force mode, 17  
PUR. *See* polyurethane  
PVA. *See* polyvinyl alcohol  
P-V distance. *See* peak-to-valley (P-V)  
  distance  
PVS. *See* polyvinylsiloxane  
pyramidal tip, 115, 120, 128  
PZT (lead zirconate titanate)  
  scanner, 6–8, 16, 21  
  tube scanner, 42, 51, 54, 72
- Q**  
QCM. *See* quartz crystal microbalance  
*Q*-control system, 326  
QELS. *See* quasi-elastic light scattering  
*Q*-factor, 198, 200, 275, 282  
quad photodetector, 8, 51

- quadrant detector, 70, 85, 86, 98
- quality factor  $Q$ , 59, 75, 78, 197, 202, 314, 316, 337–342, 346, 347
- quantum
  - box (QB), 838
  - corral, 262, 263, 265
  - dot, 934
  - dot transistor, 835
  - Hall regime, 286–287
  - tunneling, 251
  - wire (QWR), 838
- quartz crystal microbalance (QCM), 440, 486
- quasi-continuum model, 458
- quasi-elastic light scattering (QELS), 226
- quasi-optical experiment, 251
- quasistatic
  - bending test, 532, 536–538, 547, 549, 552
  - mode, 201
- R**
- radial cracking, 371
- radiofrequency (RF)
  - MEMS/NEMS, 834, 836, 846, 858, 859
- radius
  - of gyration, 134, 169
  - hydrodynamic, 134
- Raleigh's method, 74
- Raman
  - spectra, 359–360, 362
  - spectroscopy, 359–363, 397
- random
  - nanoroughness, 754–755
  - rough surface, 723, 728, 737–738, 744, 760, 762
- randomly oriented polysilicon, 970
- ranking of various SAMs, 427
- ratchet mechanism, 29–30, 33, 57, 98, 478
- rate-dependent slip, 209, 214
- rate of deformation simulation, 458
- Rayleigh wave, 399–400
- RbBr, 216
- reaction force, 920
- readout electronics, 85, 86, 100, 102
- rebinding, 367
- receptor immobilization, 360–362
- receptor-ligand
  - bond, 362
  - complex, 356, 357, 365, 367
  - interaction, 108
  - pair, 358
- receptor-ligand recognition bond formation, 357
- recognition
  - force spectroscopy, 365–380
  - imaging, 379–382
- rectangular cantilever, 60–63, 245–246
- reduced modulus, 396, 408, 409
- reflection interference contrast microscopy (RICM), 117
- relative humidity (RH), 468, 470, 480–485, 490, 491, 496, 500, 508, 515, 516, 518–520, 526
  - influence, 480, 482, 518, 519, 525–526
- relative stiffness, 19
- relaxation time, 147, 169, 175, 184, 186
- remote detection system, 84
- repulsive tip-substrate, 458
- residual
  - film stress, 948, 949, 953, 968
  - stress, 364–366, 369, 371, 375, 377–380, 383, 391, 398, 399, 411, 412, 421, 428
- resisting pushing force, 496–497
- resolution vertical, 39, 47
- resonance
  - curve detection, 59
  - mechanical, 182
- rest-time effect, 473–476, 525
- retardation effect, 119, 122, 123
- retract
  - curve, 364–365
  - trace approach, 364
- Reynolds equation, 207
- RF magnetron sputtering, 351
- rheology, interfacial, 223
- rheometer, 224–225
- rhombedral R–8, 422
- RICM. *See* reflection interference contrast microscopy
- RMS. *See* root mean square
- rolling friction, 120, 144
- room temperature (RT), 443
- root mean square (RMS), 275, 276, 728, 730
  - amplitude, 728, 737, 738, 745
- rotor-hub interface, 840–841, 910, 911, 922
- rotor-stator interface, 840–841
- roughness, 115, 130, 140–144, 186, 529, 545, 560, 566–575, 577
  - amplitude, 710, 761–762
  - angle, 60–61
  - energy scale, 377
  - image, 20
  - induced hierarchical surface, 928–929
  - structure, 749–756
  - of surface, 130

roughness factor, 898–900, 902, 910

RT. *See* room temperature

rule of mixtures, 426, 429, 431

rupture force, 367–369, 373, 379

rutile TiO<sub>2</sub>(100), 221

## S

sacrificial

layer, 930

layer lithography (SLL), 855, 931, 932

oxide, 931–932

SAM. *See* scanning acoustic microscopy; self-assembled monolayer

sample holder, 243–244

SATP. *See* (S-acetylthio)propionate

scan

area, 54

direction, 50, 54, 56, 97, 103–104

frequency, 50, 54, 103

head, 244–245

range, 43–45, 49, 95–96, 98–100

rate, 4, 17, 19, 23, 43, 54, 56

size, 42–44, 54, 56, 57, 94

speed, 54, 56, 59, 98, 101

scanner, piezo, 242, 282

scanning

acoustic microscopy (SAM), 399–401

capacitance microscopy (SCM), 38

chemical potential microscopy (SCPM), 38

electrochemical microscopy (SECM), 38

electron microscopy (SEM), 11, 66, 68, 99, 112, 114–115, 120, 122, 124, 126–128, 704, 705, 712, 740, 750, 753, 754, 756

electrostatic force microscopy (SEFM), 38

head, 42

ion conductance microscopy (SICM), 38

Kelvin probe microscopy (SKPM), 38

magnetic microscopy (SMM), 38

near field optical microscopy (SNOM), 38

probe microscope, 112, 113

probe microscopy (SPM), 38, 39, 49, 94, 95, 100, 112, 113, 125, 130, 195

speed, 54, 56, 59, 98, 101

spreading resistance microscopy (SSRM), 494

system, 94–104

thermal microscopy (SThM), 38

tunneling microscopy (STM), 3, 4, 6, 23, 24, 37–46, 48–51, 60, 94, 99, 112, 113, 120, 130–132, 195, 196, 198, 202, 209, 215, 216, 221–223, 308, 317, 328, 330, 452, 464

scanning force

acoustic microscopy (SFAM), 38

microscopy (SFM), 38–39, 240–242, 245–247, 274–293

spectroscopy (SFS), 274–293

scanning force microscopy (SFM), 240–242, 245–247, 274–293

bath cryostat, 245–247

dynamic mode, 274, 275

interferometer, 246

piezo creep, 246

static mode, 275

thermal drift, 276

thermal noise, 242, 275, 276

variable temperature, 243–245

vibration isolation, 243

scanning probe microscopy (SPM), 239–293

scanning tunneling microscopy (STM), 240, 243–245, 247–274, 278, 279, 285, 289

bath cryostat, 245

cantilever, 45, 60, 71

cantilever material, 60, 71

light emission, 251, 258

piezo creep, 244

principle, 40, 41, 46

probe construction, 45–46

spectroscopy, 247–274

spin-polarized, 272, 273

thermal drift, 247

thermal noise, 242

tip, 38, 50, 244, 253, 258, 285

variable temperature, 243–245

vibration isolation, 243

scanning tunneling spectroscopy (STS), 242, 247, 253–255, 261, 263, 266–268, 270–272, 289

energy resolution, 253, 254

inelastic tunneling, 247

scratch

critical load, 369, 370, 379, 380, 391, 392

damage mechanism, 381, 387

depth, 475, 476

drive actuator, 961, 972

induced damage, 379

resistance, 432–436, 531, 542–545, 559–560, 576

test, 380, 530–531, 540–545, 553–560

scratching, 4–6, 12–13, 15, 63–77, 98–100

force, 475, 476

measurement, 38

screening, 118–119, 131, 132

selectin, 373–375

- self-assembled
    - growth, 250
    - monolayer (SAM), 208, 210, 213, 215, 216, 221, 225, 419
    - structure, 494–503
  - self-assembled monolayer (SAM), 403–455,
    - 462, 464, 466, 487, 497, 498,
    - 500–502, 847, 856, 869, 875–880,
    - 887, 889, 891, 892, 902, 918, 923,
    - 925, 926, 928, 929, 934
  - on aluminum, 422–423
  - chemically adsorbed, 92
  - coated surface, 891, 892
  - on copper, 422–423
  - deposition, 406, 407, 417, 419, 426
  - friction, 44, 90–95, 99
  - nanotribological property, 407, 420–453,
    - 462, 527
  - SAM microscopy, 399–400
  - stiffness, 91, 92, 93, 95
  - sudden failure, 879
  - tribological property, 5, 19, 90, 98, 859, 875
- self-assembly, 265
- directed, 755
- self-cleaning, 533–689, 711–713, 755, 758,
  - 760, 833, 860, 897–910, 919,
  - 928–929
- efficiency, 908
  - mechanism, 919
  - surface, 833, 860, 897–910, 929
- self-excitation mode, 308, 318, 328–337, 343,
  - 348–349
- self-lubrication, 280, 282, 287
- self-similar scaling, 707, 708
- semiconductor
- quantum dot, 263
  - surface, 207, 210
- sensitivity, 38, 42, 47, 48, 58, 59, 63, 79, 80,
  - 84, 86–89, 92, 93, 96–98, 101, 198,
  - 205, 246
- sensor, biochemical, 408
- setal orientation, 709, 717
- SFA. *See* surface force apparatus
- SFG. *See* sum-frequency generation
- SFM. *See* scanning force microscope
- shark skin, 535–536, 539, 544, 668–671, 673,
  - 680, 681, 686–688
- shear
- force (*see* Kinetic, friction; Static, friction)
  - modulus, 245, 274, 279
  - motion, 215, 219, 224
  - strength, 270
  - stress, 205, 206, 209, 211, 213
  - critical, 147–149, 152, 157–158
  - effective, 274
- shear flow detachment (SFD), 362, 365
- SH-group, 358, 360
- short-cut carbon nanotube, 263, 265
- short-range
- chemical force, 277, 282, 284
  - electrostatic attraction, 219
  - electrostatic interaction, 217
  - magnetic interaction, 216, 223–226
  - packing, 236–237
- shot noise, 84, 87
- Si(001)(2 × 1), 211
- Si(100), 368–370, 382, 385–391, 395–397
- coefficient of friction, 469, 472, 473, 474,
    - 477, 479, 480, 481, 482, 484, 485,
    - 486, 491, 497, 498, 499, 500,
    - 501, 502, 504, 508, 514, 517, 518,
    - 519
  - substrate surface, 464, 514, 515, 525, 526
- Si(111) (7 × 7), 258, 259, 281, 285, 287
- Si-Ag covalent bond, 215
- Si-based surface, 881–891
- Si cantilever, 197, 198, 245
- gold-coated, 359
- SiC film
- doped, 867
  - undoped, 867, 869
- Si(001)(2 × 1):H surface, 210–212
- silane
- bubbler, 418, 419
  - polymer film, 887
- silanization process, 883
- silanol group (SiOH), 422
- Silicon (Si), 60, 62, 63, 88, 396, 401, 402,
  - 422–424, 427, 834–836, 839, 841,
  - 843, 844, 848, 852, 854–856,
  - 859–869, 873, 881–896, 903, 914,
  - 929–934
- adatom, 207, 209
  - beam, 546, 549
  - cantilever, 10, 11, 17, 19
  - friction force, 422, 440, 441, 443
  - grain, 368
  - microimplant, 881
  - micromotor, 486
  - nanobeam, 545, 549, 566, 569, 572–575
  - nitride (Si<sub>3</sub>N<sub>4</sub>), 47, 48, 57, 60–64, 71
  - nitride layer, 931–932
  - surface, 417, 420, 464, 466, 496, 507, 509,
    - 518, 521–525
  - terminated tip, 277
  - tip, 116, 119, 125, 207, 210,

- 212–216, 223–226, 231, 276–278, 282, 283
  - single-crystal, *10, 11, 13, 19*
  - tribological performance, *861, 879*
  - trimer, 212–214
  - uncoated, *490, 492, 496, 508, 509, 510, 511, 512, 513, 514, 515, 516, 517, 518, 520*
- siloxane polymer lattice, *887*
- single
  - asperity, *3, 5, 10, 52–54, 56, 58, 59, 98, 271, 287*
  - CNT probe, *127*
  - gecko seta, *711, 717, 718, 732, 749, 761*
- single atomic bond measurement, *308–314*
- single crystal
  - silicon, *949, 969, 970, 971*
  - silicon cantilever, *60, 62, 63*
- single-crystal reactive etching and metallization (SCREAM)
  - silicon cantilever, *17, 19*
- single-crystal Si(100), *463, 490, 502, 506*
- single-crystal silicon, *860–862, 867, 903–904, 929–930*
  - hardness, *79–80*
- single-level attachment system, *738, 739*
- single molecule
  - packing density, *92*
  - recognition force detection, *362–365*
  - spring constant, *6, 46, 92*
- single-molecule force spectroscopy
  - dissociation rate, *369*
- single-particle wavefunction, *253*
- single spatula contact angle, *736–737, 760*
- single-spring contact, *723–724*
- single-walled carbon nanotube (SWNT), *64, 112, 121, 124, 125, 262, 279, 280, 284, 835*
  - biosensor, *858*
- sink-in, *401, 411, 412, 428, 432*
- sintering, *118, 121–122*
- Si<sub>3</sub>N<sub>4</sub> tip, *47, 57, 62, 115, 420, 422, 424, 426, 435, 469, 473, 474, 477, 488, 862, 866, 883, 891, 911*
- SiO<sub>2</sub>
  - beam, *545, 546, 549, 551*
  - film surface, *414, 417*
  - MEMS semiconductor, *714*
  - nanobeam, *545, 546, 566, 576*
- Si(111)-(√3 x √3)-Ag, *210–212*
- Si replica
  - hierarchical, *907, 908, 910*
- Si surface
  - micropatterned, *92, 94, 95, 903–906*
- Si(111) surface, *212, 227*
- size of lamella, *761–762*
- size of seta, *761–762*
- skewness, *911*
- sliding
  - contact, *279, 280, 281, 287*
  - direction, *161, 171, 182–183*
  - distance, *114, 175, 180, 186*
  - friction, *39, 120, 121*
  - induced chemistry, *477*
  - of tip, *244–245*
  - velocity, *4, 45–50, 99, 114, 146, 153–154, 156–158, 168, 170, 171, 174, 175, 177, 180, 181, 184, 265, 268, 425, 441–446, 454, 841, 917*
  - work, *472, 477, 487, 499, 503*
- s-like tip state, *253–254*
- slip, *205–214, 216–217*
  - length, *206, 208–210*
  - partial, *205, 206, 210, 236*
  - plane, *115, 173*
  - at the wall, *206*
- slipping and sliding regime, *172, 174*
- small specimen handling, *947, 950*
- smart
  - adhesion, *701–762*
  - system, *893*
- smooth
  - nanobeam, *567–570, 574, 575*
  - sliding, *148, 161–163, 172, 179, 180*
- snap-in, *469*
- S-N (stress-life) diagram, *75*
- SnO<sub>2</sub>(110), *221*
- soft
  - coatings, *426*
  - lithography (SL), *902, 933–934*
  - stiction, *926, 927, 929*
  - stuck micromirror, *926–927*
  - substrate, *470*
  - surface, *8, 17, 54, 81–82, 94, 344*
- solid
  - boundary lubricated surface, *148–164*
  - lubricant, *922*
  - phase Z-DOL, *470*
  - surface, *846, 872, 897–899, 918–919*
  - thin film, *487, 510*
  - xenon, *279*

- solidification, 172
  - incomplete, 233–234
- solid-like
  - behavior, 184
  - lubricant, 922, 923
- solid-liquid-air interface, 900
- solid-liquid interface, 214
- solid-lubricant interaction, 487
- solvation force, 108, 127–129, 131, 133, 137, 142, 143
- sp<sup>3</sup>
  - bonded carbon, 350, 353, 356, 361, 379
  - bonded tip, 460–461
  - bonding, 350, 359, 363, 366, 368, 370
- spacer chain, 408, 414–419, 423, 426, 435, 436, 453
- spatula-substrate bifurcation, 711
- spectroscopic resolution in scanning tunneling spectroscopy (STS), 242, 247
- spectroscopy
  - principle, 365–368
- spherical
  - particle, 893–894
  - tip, 715, 724, 737–740, 744, 748, 751, 753
- spider dry adhesion, 704
- Spiderman toy, 750, 751
- spin
  - density wave, 271
  - excitation, 247, 258
  - quantization, 255, 257
- spin-polarized STM (SP-STM), 272–274
- split-diode photodetector, 7, 20, 21
- SPM. *See* scanning probe microscopy
- spring
  - force-distance curve, 728
  - instability, 217, 219
  - level, 723, 725
  - sheet cantilever, 63, 71
  - system, 41
- spring constant, 197, 198, 202, 203, 209, 241, 245, 247, 251, 253, 256, 257, 267, 274, 274–275, 281, 282, 308–312, 332, 345, 347, 960
  - calculation, 45, 60, 62, 71, 72
  - change, 241
  - effective, 251, 253, 267, 274–275
  - lateral, 59, 60, 245, 247, 251, 274–275
  - measurement, 62–63, 71
  - vertical, 48, 59, 60, 62, 63
- (S-acetylthio)propionate (SATP), 360
- SP-STM. *See* spin-polarized STM
- sputtered coatings, physical property, 364–365
- sputtering
  - deposition, 356, 357, 366, 370
  - power, 359, 365, 366
- SrF<sub>2</sub>, 218
- SrTiO<sub>3</sub>(100), 221, 222
- SSD. *See* statistically stored dislocation
- STA. *See* streptavidin
- STA-biotin wear, 889
- stacked-cone nanotube, 122
- static
  - AFM, 198–199, 201, 308–310, 313, 344
  - deflection AFM, 309
  - friction, 148, 158, 161, 169, 172, 181, 185, 234–235, 965, 972
  - friction force, 876, 919–923, 929
  - friction force (stiction), 840, 919–923
  - friction torque, 920
  - indentation, 82
  - interaction, 109
  - mode, 198, 199, 274, 275, 282, 288
  - mode AFM, 84
- static contact angle, 424, 428, 437–440, 876, 877, 897, 898, 902, 905–910
- statistically stored dislocation (SSD), 295, 297, 299–301
- steady-state sliding, 489
- stepping motor, 250–251
- steric
  - force, 108, 117, 137
  - repulsion, 108
- stick boundary condition, 211–212
- sticking condition, 738, 740, 743
- stick-slip, 121, 148, 157, 158, 161–163, 168, 169, 187, 204, 223–224, 226, 235, 481, 482
  - behavior, 26, 27
  - friction, 474, 482, 483, 499
  - mechanism, 251, 263
  - movement, 24–25
  - phenomenon, 27, 57
- stick-slip sliding, 148, 171–183
- stiction, 82, 161, 403, 405, 407, 453, 840–841, 843–845, 847–848, 858, 859, 897, 923, 925, 926, 928, 929
  - phenomena, 860, 923–928
- stiffness, 379–380, 386, 422, 425, 426, 429–432, 441, 443, 445, 453–454
  - continuous measurement (CSM), 374–375
  - torsional, 76–77
- Stillinger–Weber potential, 442, 443, 458, 459
- STM. *See* scanning tunneling microscope

- Stoney equation, 948  
 storage modulus, 416, 417  
 strain energy difference, 374  
 strain gauge rotating, 951  
 stray capacitance, 91–92  
 strength, 947–949, 953, 954, 960–963, 966, 967, 970–973  
     of adhesion, 701–704, 707, 711, 717, 718, 728, 750, 760  
 streptavidin (STA), 361, 368, 372, 373, 377–379  
     coating, 883, 884, 886  
     protein binding, 882  
 stress, 947–958, 960, 962, 963, 967–972  
     distribution, 547, 548, 567–569, 574  
     field, 949  
     gradient, 952–953, 969  
     intensity, 536  
     maximum, 953, 960, 971  
     measurement, 948, 950–952, 957, 958  
 stress-strain  
     behavior, 956–958  
     relationship, 741  
 Stribeck curve, 146, 165, 170  
 strip domain, 289  
 structural  
     force, 108, 127–130, 134, 142  
     material, 950, 955, 962, 966, 973  
 structure, active, 949, 955–966  
 STS. *See* scanning tunneling spectroscopy  
 stuck comb drive, 841–842  
 stuck micromirror, 923–927  
 subangstrom deflection, 114  
 subangstrom positioning, 113  
 submicron particle, 881–896, 928–929  
 substrate  
     curvature technique, 948  
     particle interaction, 712  
     surface energy, 714  
 sulfonium, 503, 504  
 sum-frequency generation (SFG), 224–225  
 superadhesive tape, 702  
 superconducting  
     gap, 254, 268–271, 289  
     magnetic levitation, 41  
     matrix, 289  
 superconductivity, 241, 247, 268, 271  
     vortex, 268, 269, 289, 290  
     vortices, 268, 289–291  
 superconductor, 254–255, 268–271, 276, 289–291  
     type-I, 268, 289  
     type-II, 268, 269, 289, 290  
 superhydrophobicity, 533–689  
     roughness-induced, 833, 860, 897–910  
 superlubricity, 261  
 superlubric state, 488  
 super modulus, 398–399, 429  
 superoleophobicity, 537, 539–540, 543–544, 561–562  
 surface  
     amorphous, 109  
     atom layer, 200  
     band, 255, 256  
     characterization, 6, 72, 76, 99  
     charge, 108, 124–127, 131  
     charge density, 124–127  
     crystalline, 108, 109, 133, 149, 163, 172, 178, 179, 185  
     elasticity, 6, 16–22, 81–83, 99  
     energy, 349, 353, 405, 406, 416, 417, 422, 424, 437, 440, 454, 707, 714, 715  
     energy (tension), 121  
     film, nanotribology, 405–408  
     free energy, 437–448  
     friction, 491–492  
     height, 6, 22–25, 28–31, 34–36, 39–42, 61, 65, 69, 71, 76, 82, 83, 94, 95, 472, 492, 493, 494, 495, 506, 507, 511, 526  
     image, 494, 506, 507  
     profile, 762  
     height map, 886, 903–905, 911  
     heterogeneity, 144  
     hydrophilic, 109, 130–132, 139, 158, 160, 184  
     hydrophobic, 109, 130–134, 138, 139, 157, 158, 160  
     imaging, 23–63  
     inhomogeneity, 901  
     interaction, 3–5, 88, 97  
     lubricated, 465, 483, 492  
     material, 706  
     micromachining, 840, 844, 858–860, 911, 929–931  
     potential, 13–14, 69, 71, 99, 124, 125, 354, 489, 490, 492–495, 509–517, 526, 527  
     Fermi energy level, 492  
     mapping, 14, 69, 71  
     potential map, 493, 495, 511, 515  
     surface roughness, 29  
     protection, 403–455



- roughness, 130, 405, 426–429, 714, 728, 731, 737, 746, 747, 749, 754, 755, 759–761, 833, 848, 860–862, 865, 887, 888, 897–911, 928–929
  - state lifetime, 255
  - structure, 122, 140–143, 184–187
  - temperature, simulation, 458
  - tension, 404–405, 424, 427, 437, 453, 454, 462, 463, 471, 481, 489, 526, 708, 735, 736, 752
    - force, 716
  - topography, 15, 25, 35, 64, 71, 95, 96, 244, 275, 472
    - gray-scale plot, 25, 95, 96
  - unlubricated, 483
  - surface force apparatus (SFA), 3–5, 110, 113–116, 119, 120, 140, 151, 155, 156, 167, 172, 176, 204, 207, 212, 214–216, 223–226, 228–230, 235–237, 296, 304, 326–328, 362, 363, 365, 440, 487, 911–912
    - calibration, 228
  - surface-surface spacing, 212
  - surfactant monolayer, 146, 157
  - suspended
    - beam, 538, 560–564, 578, 579
    - membrane, 957
  - SWNT. *See* single-walled carbon nanotube
  - synthetic vesicle, 893
  - syrphid fly, end of the leg, 704
- T**
- TA. *See* tilt angle
  - tape
    - lubricated, 462, 489, 519
    - unlubricated, 519
  - tapping mode (TM), 8–10, 13, 14, 17–21, 53, 58, 61–64, 64, 65, 74, 308, 317–326, 328, 337–344, 347, 348, 888–890, 911, 912
    - AFM, 319–328
    - etched silicon probe (TESP), 62
  - teflon layer, 281
  - TEM. *See* transmission electron microscope; transmission electron microscopy
  - temperature, 121, 134, 137, 147, 153–154, 161, 171, 174, 175, 182
    - critical, 254–255, 270, 276, 289
    - dependence of friction, 269
    - Flory, 134
    - theta ( $\theta$ ), 134
  - tensile
    - load, 953, 971
    - stress, 528, 534, 547, 548–550, 553, 563, 566, 567, 569–570, 573–574, 577, 951–954, 956, 963, 968, 969, 971
    - test, 956, 962, 963, 969, 970
    - testing, 14, 15
  - terminal element, 703, 704
  - test environment, 392, 393
  - tether length, 359, 370
  - therapeutics, 881–896, 928
  - thermal
    - CVD, 121–125
    - desorption, 450
    - drift, 240, 241, 244–245, 247, 276, 289
    - effect, 263–269
    - fluctuation, 247
    - fluctuation force, 108
    - frequency noise, 242
    - processing, 530
  - thermal expansion coefficient, 199
  - thermomechanical noise, 275
  - thermostat, 445, 446–448
  - theta ( $\theta$ )
    - condition, 134, 137
    - temperature, 134
  - thin film, 391–432, 463–472, 487–512
  - thin liquid films, 204, 224, 229, 236
  - third-body molecule, 483–485, 487
    - frictional force, 483–485, 487
  - three-body deformation, contact region, 61–62
  - three-dimensional (3-D), 709, 717–718
    - bulk state, 265
    - force, 335
    - force field spectroscopy, 283–285
    - force measurement, 93–94
    - force spectroscopy, 335
  - three-level hierarchical model, 725, 727, 728, 731, 736–738, 760
  - three-level model, adhesion coefficient, 728, 730–734
  - through-thickness cracking, 367, 371–374
  - Ti atom, 222, 223, 228, 230
  - TiC grain, 28
  - tilt angle (TA), 897, 901, 905–907, 909, 910
  - tilt configuration, 433
  - TiO<sub>2</sub>
    - substrate, 229
    - (110) surface, 207, 221, 227, 229
    - (110) surface simultaneously obtained with STM and NC-AFM, 223
  - TiO<sub>2</sub>(110), 221, 223, 229

- tip, 244–249, 251–254, 256–258, 264–267, 271–276, 280–287
  - apex, 265, 266, 272, 276, 277, 280, 282, 283, 285, 285, 291
  - artifact, 209, 228
  - atom, 242, 248, 249, 272, 276–279, 281, 282, 285, 291
  - bound antibody, 378
  - bound antigen, 369
  - cantilever assembly, 120
  - carbon nanotube, 118, 121–123, 126–130
  - conductive, 130
  - electron-beam deposition, 120–121
  - fabrication, 115, 116, 119, 120, 125
  - Fe-coated, 224–226
  - focused ion beam, 119–120
  - geometry, 120, 121
  - immobilized ligand, 360, 380
  - induced atomic relaxation, 277–278
  - jumping, 481
  - mount, 43, 50
  - multiwalled carbon nanotube (MWNT), 10, 11
  - oscillation, 322, 332
  - oscillation amplitude, 284, 286
  - oscillation trajectory, 332
  - oxide-sharpened, 119
  - preparation in UHV, 249
  - preparation method, 45
  - radius, 468, 476
  - radius effect, 59, 367, 379–380, 386, 390, 483–485
- tipless cantilever, 125–126
- tip-sample
  - adhesion, 508
  - distance, 8, 17, 55, 200, 206, 212, 215, 216, 219, 222, 226, 278, 282, 285, 291, 309, 310, 314, 317, 318, 321–324, 326–329, 333, 336, 347
  - electric field, 286
  - energy dissipation, 202, 218
  - interaction, 21, 200, 205, 206, 222, 223, 284
  - interface, 441, 444
  - potential, 204
  - separation, 340
  - separation distance, 465
- tip-sample force, 196, 200–202, 205–206, 274, 281, 282, 284, 308, 309, 313, 317, 320, 322, 325–329, 332, 344, 348–349
- tip-sample force gradient, 205
- tip-sample interaction, 240, 274–276, 281, 282, 288, 291, 310, 311, 317, 318, 320, 326–332, 334, 335, 341, 343, 345, 347
  - chemical, 276, 291
  - electrostatic, 282, 286
  - van der Waals, 282
- tip-surface
  - distance, 359, 381
  - interaction, 252, 280, 461, 477, 478
  - interface, 450, 452, 478
  - potential, 251
- TIR. *See* total internal reflection
- Titanium dioxide (TiO<sub>2</sub>), 258
- TM. *See* tapping mode
- Tokay gecko, 702, 705–713, 717, 723, 759
- Tomanek–Zhong–Thomas model, 27
- Tomlinson model, 46, 243, 251–255, 257, 259, 263–266, 279
  - finite temperature, 264–266
  - one-dimensional, 251–253
  - two-dimensional, 253–254, 259
- top-down method, 834, 929
- topographical
  - asymmetry, 225, 226
  - image, 47, 51, 58, 65
- topography
  - induced effect, 33, 41
  - measurement, 47, 48, 53, 58, 59, 71
  - and recognition (TREC) image, 380–382
  - scan, 13
- topography and recognition (TREC) imaging, 380, 382
- topped pyramidal asperity, 898–899
- torsional dissipation, 286
- torsional resonance (TR), 19–22, 37–42, 83, 779, 820, 821
  - amplitude, 20, 38, 40, 41, 83
  - mode, 19–22, 37, 39–42, 83
- torsional stiffness, 142, 143, 159, 173, 174, 177, 179–184, 186, 187, 188
- torus model calculation, 96
- tosylate, 503
- total adhesion force, 707–708, 715, 735–737, 760
- total internal reflection (TIR), 224–225
  - microscopy (TIRM), 117
- TR. *See* torsional resonance
- trace and retrace, 40, 41
- transition metal oxide, 223
- translational diffusion, 226–227, 230, 233
- transmembrane transport, 378
- transmission electron microscopy (TEM), 27–28, 67–69, 99, 112, 117, 121, 124, 401, 410, 422

- transversal piezo-resistive effect, 89
  - traveling direction of the sample, 65–67, 70
  - TREC imaging. *See* topography and recognition
  - Tresca criterion, 404
  - triangular cantilever, 10, 11, 60, 61, 77, 85
  - tribochemical reaction, 86, 87, 477, 479
    - mechanism, 917–918
  - tribochemistry, 485
  - triboelectrical emission, 450
  - tribo electrification, 121
  - tribological
    - C<sub>60</sub>, 503–506
      - characterization of coating, 351, 367–396
      - performance of coating, 388–389
      - problem, 840–841, 843, 844, 846, 848, 858
  - triboluminescence, 120
  - tribometer, 861, 862
  - tribotest apparatus, 462, 494
  - triethoxysilane, 266
  - triflamide, 503, 505
  - trimer tip, 312
  - true atomic resolution, 195, 203, 207, 216, 276
    - images of insulators, 216
  - tubelike carbon nanotube, 122
  - tungsten, 41, 45
    - sphere, 247
    - tip, 45
  - tuning fork force sensor, 336
  - tunneling
    - current, 39–43, 46, 49, 50, 195, 196, 200, 202, 240, 249, 258–259, 272–274
    - detector, 47
    - tip, 251, 253, 254, 271, 272
  - two-dimensional (2-D)
    - electron gas (2-DEG), 286–287
    - electron system (2-DES), 265, 266
    - FKT model, 255
    - histogram technique, 272
  - two-layer-fluid model, 211
  - two-level
    - hierarchical model, 728, 731
    - model, 725–726
  - two-photon excitation, 228
- U**
- UHV. *See* ultrahigh vacuum
  - ultrahigh vacuum (UHV), 112, 113, 118, 131, 207, 221, 243–246, 243–251, 254, 257, 258, 261, 269, 272, 275, 276, 312, 314, 328, 330, 333, 336, 344, 346, 448, 479
    - environment, 243, 249–250, 257
  - UHV-AVM, 250
  - ultrasmooth surface, 55
  - ultrathin DLC coating, 351
  - unbinding
    - force, 358, 360, 363, 365–373, 376, 378
    - force-driven, 372, 373
  - unbonded Z-DOL film, 464, 465, 468, 473
  - uncoated Si, 490, 492, 494, 508, 509, 510–517, 520
  - undoped polysilicon, 867–870
  - undulation force, 108
  - unfilled polymer, 563, 564, 576
  - unloading curve, 456–457
  - unlubricated
    - motor, 921, 922
    - Si(100), 483, 485, 487
  - unperturbed motion, 204
  - useful fiber radius, 742
- V**
- vanadium carbide, 397
  - van der Waals (vdW)
    - adhesion, 722, 760
    - adhesive force, 720
    - attraction, 51, 470, 476
    - attractive force, 895
    - force, 12, 108, 110, 117–120, 122–123, 127–130, 133, 137, 150, 197, 209, 210, 215, 216, 309, 310, 326, 334, 702, 714–715, 717, 719–722, 749, 750, 758, 760, 847, 893–895, 916
    - interaction, 857, 894, 895
    - interaction energy, 112, 119
    - surface, 279–281
  - variable force mode, 101
  - variable temperature STM setup, 243–245
  - vdW. *See* van der Waals
  - velocity
    - critical, 173, 180, 181, 183
    - dependence of friction, 266–269
    - rescaling, 445
    - of vibration, 208
  - vertical
    - coupling, 42
    - nanotube, 508, 509
    - RMS-noise, 276
  - vertical noise, 206
  - Verwey transition temperature, 288–289
  - vibration, 309, 317, 323, 332, 333, 338, 344
    - amplitude, 208
    - external, 39, 43
  - vibrational spectroscopy, 249, 258

- Vickers  
  hardness, 394, 404  
  indentation, 531, 540, 542  
  indenter, 531  
vinylidene fluoride, 227  
viscoelastic  
  mapping, 3, 6, 16–22, 81–83  
  property, 9, 19, 83, 99  
viscoelasticity, 416–417, 432  
  mapping, 16–22, 81–83  
viscosity, 111, 115, 123, 146, 147, 165,  
  166–170, 183, 184  
viscous  
  damping, 315, 346, 365  
  dissipation, 19, 27  
  drag, 214  
  force, 108, 109, 165–167, 170  
vortex in superconductor, 268, 269, 289, 290  
V-shaped cantilever, 60, 62, 63, 247
- W**  
wafer curvature technique, 967  
wall-climbing robot, 701, 702, 747, 749, 761  
water  
  contact angle, 737, 755, 760  
  films, 215, 219–220, 222  
  film thickness, 721, 735  
  vapor, 397, 405–406  
  vapor content, 364, 392  
water-repellent plant, 897  
wear, 3, 348–351, 367, 369, 379–380,  
  386–398, 403, 405–408, 416, 420,  
  422, 424–426, 432–436, 439, 440,  
  444, 446–448, 448, 453–455,  
  472–474, 482, 487, 495, 502, 503,  
  505, 509, 510, 512, 840–842, 845,  
  849, 859, 861–869, 875, 881–883,  
  887–890, 914–919, 925, 926, 928  
  of biomolecule, 854, 881–891, 928  
  contribution to friction, 277–279  
  damage, 391–392  
  damage mechanism, 391–392  
  debris, 49, 66, 68, 71, 99  
  depth, 66, 95, 487, 488  
  fullerene, 505  
  initiation, 489, 526  
  map, 886  
  mapping, 48–50  
  mark, 886, 924, 925  
  measurement, 38  
  mechanism map, 49  
  nanoscale, 49, 63  
  process, 388–390  
  profile, 487, 488, 509  
  region, 49, 66, 71, 99  
  resistance, 350, 387–388, 391, 392, 395,  
  406, 432, 436, 454  
  test, 387–392, 398, 492, 493, 494, 500, 502,  
  509, 511, 512, 513, 515, 517, 526,  
  527, 842, 861, 867, 879, 880, 886,  
  889, 890  
  tip, 473, 474, 482  
  track, 509  
wear and stiction mechanism, 925, 926, 928  
wear detection, electrical resistance  
  measurement, 494, 509–515  
wearless friction, 487  
wear mark, AFM image, 49, 50, 66, 67  
Weibull statistics, 970  
weight function, 205  
Wenzel  
  equation, 898–899, 902, 903  
  regime, 900–901, 904, 905, 906,  
  908–910  
wet environment, 50–54, 98  
wettability, 84, 503, 504, 505, 513, 872, 897  
wetted surface, 205, 212–214  
wetting, 133, 144, 161  
  surface, 452  
wire cantilever, 45, 59  
work  
  of adhesion, 140, 143, 707, 708, 724, 735,  
  739–740  
  hardening, 404, 411, 419–420, 428  
  of indentation, 404, 414–415  
W tip, 46
- X**  
xenon, 242, 245–246, 279–281  
XPS spectra, 521, 523  
x-ray  
  lithography, 930–931, 933  
  photoelectron spectroscopy (XPS),  
  422–423, 505, 521–522
- Y**  
yield point, 147, 170  
  load, 418–420  
yield strength simulation, 458  
yield stress, 404, 419, 422, 425, 430  
Young's modulus, 60, 63, 71, 74, 101, 241,  
  242, 245, 270, 274, 706, 708–709,  
  868, 879, 913, 948, 949, 967,  
  969–970, 972–973  
  of elasticity, 16, 76, 81, 99  
  measurement, 951, 955–960, 969

**Z****Z-15**, 84–92

coefficient of friction, 468, 469, 472, 473,  
474, 477, 479, 480, 481, 482, 486

fully bonded, 464, 468, 469, 470, 471–474,  
477–482, 486, 487, 488, 525, 526

Z-DOL, 462–465, 468, 469, 470–474, 477,  
479–482, 487, 488, 525, 526

**Z-DOL**

diffusion coefficient, 467

durability, 486, 489, 490, 496, 499, 500,  
502, 503, 526

film, 38, 84–90, 92, 96, 463, 464, 487, 500

molecule, 464, 467, 472, 500

schematic, 462, 464, 477, 479, 480, 481,  
482, 483, 486, 490, 491

unbonded, 464, 465, 468, 472, 473, 525

Z-DOL (fully bonded), 84, 85–90, 92, 871–875  
durability, 482, 486, 499

hydrophobicity, 462, 470, 485  
wear depth, 487, 488

Zero-deflection (flat) line, 469

Z-15 film, 84–85, 87, 88, 90, 91

molecularly thick, 463, 483

wear depth, 487, 488

zinc, 420

Zisman plot, 424, 437

Z-15 lubricant, 84

**Z-TETRAOL**

durability, 489, 490, 496, 499, 500,  
502, 503, 504, 508, 509, 512,  
515, 526, 527

property, 489, 504, 505, 509, 512, 526

schematic, 490, 491, 507, 508, 509